

Lecture Notes in Civil Engineering

Marco Casini *Editor*

Proceedings of the 3rd International Civil Engineering and Architecture Conference

CEAC 2023, 17–20 March, Kyoto, Japan

 Springer

Lecture Notes in Civil Engineering

Volume 389

Series Editors

Marco di Prisco, Politecnico di Milano, Milano, Italy

Sheng-Hong Chen, School of Water Resources and Hydropower Engineering,
Wuhan University, Wuhan, China

Ioannis Vayas, Institute of Steel Structures, National Technical University of
Athens, Athens, Greece

Sanjay Kumar Shukla, School of Engineering, Edith Cowan University, Joondalup,
WA, Australia

Anuj Sharma, Iowa State University, Ames, IA, USA

Nagesh Kumar, Department of Civil Engineering, Indian Institute of Science
Bangalore, Bengaluru, Karnataka, India

Chien Ming Wang, School of Civil Engineering, The University of Queensland,
Brisbane, QLD, Australia

Zhen-Dong Cui, China University of Mining and Technology, Xuzhou, China

Lecture Notes in Civil Engineering (LNCE) publishes the latest developments in Civil Engineering—quickly, informally and in top quality. Though original research reported in proceedings and post-proceedings represents the core of LNCE, edited volumes of exceptionally high quality and interest may also be considered for publication. Volumes published in LNCE embrace all aspects and subfields of, as well as new challenges in, Civil Engineering. Topics in the series include:

- Construction and Structural Mechanics
- Building Materials
- Concrete, Steel and Timber Structures
- Geotechnical Engineering
- Earthquake Engineering
- Coastal Engineering
- Ocean and Offshore Engineering; Ships and Floating Structures
- Hydraulics, Hydrology and Water Resources Engineering
- Environmental Engineering and Sustainability
- Structural Health and Monitoring
- Surveying and Geographical Information Systems
- Indoor Environments
- Transportation and Traffic
- Risk Analysis
- Safety and Security

To submit a proposal or request further information, please contact the appropriate Springer Editor:

- Pierpaolo Riva at pierpaolo.riva@springer.com (Europe and Americas);
- Swati Meherishi at swati.meherishi@springer.com (Asia—except China, Australia, and New Zealand);
- Wayne Hu at wayne.hu@springer.com (China).

All books in the series now indexed by Scopus and EI Compendex database!

Marco Casini
Editor

Proceedings of the 3rd International Civil Engineering and Architecture Conference

CEAC 2023, 17–20 March, Kyoto, Japan

 Springer

Editor

Marco Casini
Sapienza University of Rome
Rome, Italy

ISSN 2366-2557

ISSN 2366-2565 (electronic)

Lecture Notes in Civil Engineering

ISBN 978-981-99-6367-6

ISBN 978-981-99-6368-3 (eBook)

<https://doi.org/10.1007/978-981-99-6368-3>

© The Editor(s) (if applicable) and The Author(s), under exclusive license to Springer Nature Singapore Pte Ltd. 2024

This work is subject to copyright. All rights are solely and exclusively licensed by the Publisher, whether the whole or part of the material is concerned, specifically the rights of translation, reprinting, reuse of illustrations, recitation, broadcasting, reproduction on microfilms or in any other physical way, and transmission or information storage and retrieval, electronic adaptation, computer software, or by similar or dissimilar methodology now known or hereafter developed.

The use of general descriptive names, registered names, trademarks, service marks, etc. in this publication does not imply, even in the absence of a specific statement, that such names are exempt from the relevant protective laws and regulations and therefore free for general use.

The publisher, the authors, and the editors are safe to assume that the advice and information in this book are believed to be true and accurate at the date of publication. Neither the publisher nor the authors or the editors give a warranty, expressed or implied, with respect to the material contained herein or for any errors or omissions that may have been made. The publisher remains neutral with regard to jurisdictional claims in published maps and institutional affiliations.

This Springer imprint is published by the registered company Springer Nature Singapore Pte Ltd.

The registered company address is: 152 Beach Road, #21-01/04 Gateway East, Singapore 189721, Singapore

Paper in this product is recyclable.

Organization

Advisory Chair

Chimay Anumba, Professor, University of Florida, USA

Conference Chairs

C. W. Lim, Professor, City University of Hong Kong, China

Tan Kiang Hwee, Professor, National University of Singapore, Singapore

Program Chairs

Ippei Maruyama, Professor, The University of Tokyo, Japan and Nagoya University, Japan

Marco Casini, Professor, Sapienza University of Rome, Italy

Kyoung Sun Moon, Associate Professor, Yale University, USA

Program Co-chairs

Ye Guang, Associate Professor, Delft University of Technology, The Netherlands

S. Joseph Antony, Associate Professor, University of Leeds, UK

Steering Committee Chairs

Nuno Dinis Cortiços, Professor, University of Lisbon, Portugal

Han Lin, Professor, Nanjing Audit University, China

Malgorzata Ulewicz, Associate Professor, Czestochowa University of Technology, Poland

Publicity Committees

Hage Chehade Fadi, Professor, Université Nice Cote d'Azur, Polytech Nice Sophia, Département Bâtiments, Lebanon

Galina Gorbacheva, Associate Professor, Bauman Moscow State Technical University, Russia

Koorosh Gharehbaghi, Doctor, RMIT University, Australia

Shadi Shaikh Yasin, Assistant Professor, American University of the Middle East, Kuwait

Duy Nguyen Phan, Lecturer, Mientrung University of Civil Engineering, Vietnam

Yi Shen, Assistant Professor, Tongji University, China

Award Chairs

Daguang Han, Associate Professor, Southeast University, China

Alcestis Rodi, Associate Professor, University of Patra, Greece

Special Session Chairs

Abeer Samy Yousef Mohamed, Professor, Effat University, KSA and Tanta University, Egypt

Ahmed Farouk Deifalla, Professor, Future University in Egypt, Egypt

Shamsul Rahman Mohamed Kutty, Associate Professor, Universiti Teknologi Petronas, Malaysia

Mohammad Arif Rohman, Associate Professor, Institut Teknologi Sepuluh Nopember, Indonesia

Regional Chairs

Ayse Ozcan Buckley, Professor, Michigan State University, USA, and Giresun University, Turkey

Bashir M. Suleiman, Professor, University of Sharjah, UAE

Zujian Huang, Doctor, Tsinghua University, China

International Technical Committees

Anizahyati Alisibramulisi, Universiti Teknologi MARA, Malaysia

Cuong Nguyen Kim, Mien Trung University of Civil Engineering, Vietnam

Dalia Augustinaite, Vilnius Gediminas technical university, Lithuania

Daniel Macek, CTU in Prague, Czech Republic

Doo-Yeol Yoo, Hanyang University, South Korea

Edoghogho Ogbeifun, University of Johannesburg, South Africa

Fernando Pachego Torgal, University of Minho, Portugal

Ghada Mohammed Younis, University of Mosul, Iraq

José Rodríguez, Universidad Peruana de Ciencias Aplicadas, Perú

Karina Vilela, Universidad Peruana de Ciencias Aplicadas, Perú

Kedsarin Pimraksa, Chiang Mai University, Thailand

Kornkamon Tantiwanit, Thammasat University, Thailand

Ludovic Jason, Université Paris-Saclay, France

Marta Skaf Revenga, Universidad de Burgos. C, Spain

Abeer Samy Yousef Mohamed, Effat University, KSA and Tanta University, Egypt

Mohammad Arif Kamal, Aligarh Muslim University, India

Moussa Leblouba, University of Sharjah, UAE

Ngoc Hieu Pham, Hanoi Architectural University, Vietnam

Omid Reza Baghchesaraei, Western Sydney University, Australia

Pimonmart Wankanapon, Thammasat University, Thailand

Rini Kusumawardani, Universitas Negeri Semarang, Indonesia

Riya Catherine George, Hiroshima University, Japan

S. J. Pawar, Motilal Nehru National Institute of Technology Allahabad, India

Sarunya Promkotra, Khon Kaen University, Thailand

Satawat Doungpan, Sukhothai Thammathirat Open University, Thailand

Sopokhem Lim, Waseda University, Japan

Susana Moya Vicuña, Universidad Tecnológica Indoamérica, Ecuador

Toshiaki Sato, Kyushu University, Japan

Trong-Phuoc Huynh, Can Tho University, Vietnam

Try Ramadhan, Universitas Pendidikan Indonesia, Indonesia

Víctor Revilla Cuesta, Universidad de Burgos. C, Spain

Yaik Wah Lim, Universiti Teknologi Malaysia, Malaysia

Yanfen Zhang, Guangdong Polytechnic of Science and Technology, China

Zbyšek Pavlík, Czech Technical University, Czech Republic
Zihni Turkan, Near East University, Cyprus
Levi Acevedo Villazana, Continental University, Peru
Steve Camargo Hinostrroza, Continental University, Peru
G. B. Estores, Mapúa University, Manila, Philippines
Lee Foo Wei, Universiti Tunku Abdul Rahman, Malaysia
Yew Ming Kun, Universiti Tunku Abdul Rahman, Malaysia
Ren Jie Chin, Universiti Tunku Abdul Rahman, Malaysia
Kun-Chi Wang, Chaoyang University of Technology, Taiwan
Kazutaka Shirai, Hokkaido University, Japan
Wen-Der Yu, Chaoyang University of Technology, Taiwan
Yashinta Irma Pratami Hematang, Universitas Musamus, Indonesia
Harry Kurniawan, Universitas Gadjah Mada, Indonesia
Ahmad Basshofi Habieb, Institut Teknologi Sepuluh Nopember, Indonesia
Ting Zhang, Wuxi Taihu University, China/Politecnico di Torino, Italy
Hiroshi Tagawa, Hiroshima University, Japan
Yu-Chuan Kao, National Taiwan University of Science and Technology, Taiwan
Rendy Thamrin, Universitas Andalas, Indonesia
Glen Wash Ivanovic, Xi'an Jiaotong-Liverpool University, China
Chung-Hao Wu, National Kaohsiung University of Science and Technology, Taiwan
Shigenobu Kainuma, Kyushu University, Japan
Masrilayanti Masrilayanti, Andalas University, Indonesia
Jafril Tanjung, Andalas University, Indonesia
Johan James Hinostrroza Yucra, Universidad Continental, Peru
Lindita Bande, United Arab Emirates University, UAE
Bolanle Deborah Ikotun, University of South Africa, South Africa
Feng-Liang Zhang, Harbin Institute of Technology, China
Masashi Ouji, Toyama University, Japan
Po-Chien Hsiao, National Taiwan University of Science and Technology, Taiwan
Mogrovejo Gutiérrez, Rubén Esaú, University of Lima, Peru
Grit Ngowtanasuwan, Mahasarakham University, Thailand
Xiaohua Li, Chongqing University, China

Preface

The 3rd International Civil Engineering and Architecture Conference (CEAC 2023) has been successfully held in Kyoto and online during March 17–20, 2023. This was a special memory because it was the first time for this conference to be held onsite after its birth due to the global epidemic.

CEAC always aims to provide a platform for scholars around the world to explore the different fields of civil engineering and architecture. It will continue to focus on quality, service, etc. to make CEAC more influential and professional. We hope all scholars are able to benefit from attending this conference.

The success of CEAC 2023 has not been possible without the contribution of all speakers, conference committee members, technical and review committee, participants, etc. We wish to record our utmost appreciation to the different parties and individuals.

After a fair and rigorous peer-review, some papers in the following representative areas in civil engineering and architecture were selected for participation and presentation at the conference, including but not limited to: cement mortar and concrete engineering, advanced building materials and properties, reinforced concrete structural engineering and structural mechanics, seismic design and seismic response of building structures, building integrated photovoltaics, building thermal environment and thermal comfort, sustainable and creative architectural design, hydraulic engineering and flood control, infrastructure projects and municipal engineering, urban architectural image and urban planning, and information technology and modeling in construction. We hope the conference proceeding will be a valuable resource for related scholars, readers, and others who share similar in the areas.

We would like to express our gratitude to all participants and contributors again. We acknowledge technical and reviewer committees' high efficiency and professional review. With their dedication, the quality of papers is ensured.

Once again, thanks for all of your support and trust! And now, everything comes back to life. CEAC 2024 will be well prepared as soon as possible. May we get together again in 2024!

C. W. Lim
Conference Chair
City University of Hong Kong
Hong Kong SAR, P. R. China

Contents

Cement Mortar and Concrete Engineering Design and Performance	
Waste Clay Brick Binders for Low-Carbon Concrete Pavement Construction	3
Janitha Migunthanna, Pathmanathan Rajeev, and Jay Sanjayan	
Effect of Superplasticizer on the Properties of Kenaf Fibre-Reinforced Geopolymer Concrete	15
F. N. A. A. Aziz, N. A. Al-Ghazali, A. D. Jasmi, N. A. M. Nasir, and I. A. Karim	
Investigation on the Effect of Pulverized Black Tea Waste (PBTW) and Eggshell Powder (ESP) as Partial Replacement of Cement on the Mechanical Properties of Normal Weight Concrete	25
Kreezel Lyra Agcaoili, Myra Alvarez, Khaira Zarene Annani, Czarina Erika Lopez, Mark Clinton Salayo, Darrell Jed Vertucio, and Cresencia Vahdanipour	
Experimental and Numerical Investigation on Carbon Fiber Reinforced Cement	35
Chang-Yu Kuo, Ying-Kuan Tsai, and Yeou-Fong Li	
Influence of Synthesized Nanosilica on Properties of Wood Ash Cement Mortar	45
B. D. Ikotun and A. A. Raheem	
Assessing the Impact of Petroleum Sludge Ash on the Compressive Strength of Fly Ash-Palm Oil Clinker Geopolymer Mortar	57
Amalina Hanani Ismail, Andri Kusbiantoro, and Yuyun Tajunnisa	

Experimental Investigation of the Effect of Water Hyacinth Extract Utilized for Curing on the Compressive and Flexural Strength of Concrete 69
 Kimberly B. Sison, Allyssa Mae C. Estanio, Christian R. Quebral, Patricia Mae D. Santos, Ron Dominic L. Alberto, and Franz D. Santos

Development of Additive for Concrete 3D Printer by Using Local Materials 81
 Mohsin Usman Qureshi, Amira Al-Shizawi, Ghassan Al-Kindi, Bushra Al-Sawafi, and Yousuf Al-Balushi

Concrete Delamination Characterization by Multi-Channel Surface Rayleigh Wave Measurement 91
 Foo Wei Lee, Yoke Bee Woon, Kok Zee Kwong, and Ming Kun Yew

Advanced Building Materials and the Properties

Mix Design for Cellular Concrete Applied in Masonry Units Using Decyl Glucoside as a Foaming Agent for Construction in High Andean Cities in 2022 101
 Flores Sánchez Diego Oswaldo, Hermosa Vargas Flor Milagros, and Montoya Torres Vladimir Simón

Compressive Strength Performance of 7-Day Non-load Bearing Concrete Hollow Blocks with Pili Shell as Partial Replacement to Sand Using Box-Behnken Design 117
 Rizza Mae T. Rea, Jonille S. Soriano, James Paul Ramos, April Noemi Q. Opinaldo, Marian Capito, and Manny Anthony Taguba

Circular Economy in Buildings: Service Life Considerations of Paint 131
 Abdul Rauf, Attoye Daniel Efurosibina, Malik Khalfan, and Shafiq Muhammed Tariq

Development of Rapid-Setting Repair Materials Through One-Part Geopolymer Technology 145
 Wei-Hao Lee, Ying-Kuan Tsai, Chien-Chin Chen, and De-Wei Gao

Reducing Embodied Energy of Floor Assembly: A Case for Using CLT in Mid-Rise Residential Buildings 157
 Abdul Rauf and Muhammed Tariq Shafiq

The Relationship Between the Surface Characteristics and Corrosion Properties of Carbon Steel Affected by Abrasive Water-Jet Treatment 165
 S. Park, S. Kainuma, T. Ikeda, Y. Toyota, and T. Arakawa

Study of Mechanical Properties of Solvent Cement Connection for PVC Pipes 177
Tao Wang and Shaowei Hu

Synthesis and Application of Graphene-Phase Biochar from Theobroma Cacao Pod Husks Using Slow Pyrolysis Technique in the Treatment of Fats, Oil, and Grease from Actual Wastewater 193
Jennice Mae D. Toledo, Karen B. Hubayan, Angel Ann M. Pacheco, Neil Harold C. Salvador, Charles Joshua O. Bravo, and Allan R. Alzona

Reinforced Concrete Structural Engineering and Structural Mechanics

An Experimental Study on the Repair Evaluation of Deteriorated RC Beams Using Natural Frequency and Mechanical Behavior Related to Damage Condition 205
Yilong Cao, Akihiko Nishimura, Xiu Luo, Masao Okoshi, Wendong Tang, and Hidekazu Nishimura

Finite Element Simulation of Externally-Prestressed Concrete Girders 223
Said Elkholy, Ahmed Godat, and Saif Elabsi

Dilated Brick Masonary Infills to Avoid the Diagonal Compression Struts During Lateral Reversed Cyclic Load 235
Jafril Tanjung, Maidiawati, Yulia Hayati, and Masrilayanti

Effect of Longitudinal Tension Bars on Performance of Composite Light Gauge Steel and Concrete of a Plate Structure 247
Sabril Haris, Rendy Thamrin, Mutia Fitriani, and Syukriati

Influence of Axial Load on the Ductility of Type “C” Reinforced Concrete Walls with Longitudinal Reinforcement Variation in the Cores 257
Meyer David Hilario Martel, Jhon Josue Canchanya Taipe, Janela Azucena Condor Gonzalez, and Johan James Hinostrroza Yucra

Study on Masonry Soil Joint Adding Rock Salt 267
Masashi Ouji

The Approximate Equation for Global Buckling Load of Grid Shell Domes 281
Baoxin Liu, Pei-Shan Chen, Jialiang Jin, and Xiangdong Yan

Experimental Test of Perforated Steel Plate Shear Wall Under Cyclic Load 291
Nidiasari, Rendy Thamrin, Sabril Haris, and Ronny Purba

Identification of Column Bases’ Stiffnesses in Steel Moment-Resisting Frames Based on Fishbone Model and Bayesian Inference 301
 Jing He and Xiaohua Li

A Finite Element Analysis on Behavior of a T-stub Type Gusset Plate in Different Bolted Connection Configurations 311
 Ruoyu Zheng and Zeyu Zhang

Seismic Design and Seismic Response of Building Structures

Displacement Performance of 8 Storeys Hotel Building Using Nonlinear Time History Analysis Method 327
 Masrilayanti, Ruddy Kurniawan, Jafril Tanjung, and Muhazir Yunus

Analysis of Energy Dissipation Structure of Reinforced Concrete Frame with Additional Metal Damping 337
 Fangqian He, Ting Zhang, and Yuchen Jiang

Discussion of “Strong Column—Weak Beam” in Capacity Design Method 349
 Lv Tao, Li Yingmin, Li Feng, Li Feng, Pan Cunrui, and Feng Liqiang

Experimental Study of Cylindrical Steel Slit Damper for Passive Energy Dissipation 365
 Shuai Feng, Hiroshi Tagawa, and Xingchen Chen

Lintel Type Damping Device for Seismic Retrofit of Shear Wall Structure 375
 GeeCheol Kim, YouSeong Kim, and Joonho Lee

Simulation Analysis of Steel Frames Supported by Foundations at Different Ground Levels with the Self-Centering Column Base Joints on the Upper Ground 383
 Yang Zhenyu and Li Yingmin

Derivation of Response Spectra and Hysteretic Energy: A Case Study on 2023 Turkey-Syria Earthquake in Consideration of Structural Ductility 399
 Weiyi Shao

Dynamic Seismic Analysis and Design of the Clock Tower Structure 409
 Osorio Lobaton Gianpol Samuel, Castañeda Avila Jhiiviana Jhasmin, and Mamani Huaman Rolando

Building Integrated Photovoltaics, Building Thermal Environment and Thermal Comfort

A Case Study on the Design Model of Sunroom in the New Rural Houses in West China from the Perspective of Carbon Emission 427
Yiming Zhang, Yu Liu, Minmin Yang, Yufei Zou, Jie Song, and Wenqiang Li

Watertightness Design and Experimental Evaluation of a Solar Panel Structure for Building Integrated Photovoltaics (BIPV) Roofs 441
Dingqiu Chen and Shaohang Shi

Evaluation of PV Utilization Potential of University Building Roofs Based on PVsyst Software Simulation 453
Yufei Zou, Yu Liu, Jie Song, Yiming Zhang, Minmin Yang, and Wenqiang Li

Reallocation of Supply Air in Large Indoor Spaces Considering Thermal Coupling 465
Bo Lan and Gongsheng Huang

Investigation on the Influence of Insolation on Winter Thermal Comfort of Outdoor Activity Space on Campus in a Cold Region of China 477
Jie Song, Yu Liu, Wenqiang Li, Yufei Zou, Minmin Yang, Yiming Zhang, and Hui Liu

A Novel Low-Temperature Personalized Radiant Cooler: Thermal Environment and Local Thermal Comfort Evaluation 491
Yuying Liang and Gongsheng Huang

An Empirical Study of the Effects of Green Roof on the Outdoor and Indoor Thermal Environment of a College Buildings in Winter 501
Minmin Yang, Yu Liu, Yiming Zhang, Yufei Zou, Jie Song, and Ni Zhang

Sustainable and Creative Architectural Design

Passive Design Strategies with Thermal Capacity in Contemporary African Educational Architecture 513
Yen-Khang Nguyen-Tran, Minato Hashimoto, and Ryo Murata

Sustainable House Design Thru Passive and Active Strategies with Python Language. Case Study Ras Al Khaimah (RAK), UAE 525
Aysha Alsheraifi, Lindita Bande, Alyazia Alsheraifi, and Muhammad Iqbal

The Art of Sustainable Architecture Creation and Evaluation 539
Dalia Augustinaite

The Effect of Geometry Parameters on Daylighting of School Buildings in the Gaza Strip 553
Tawfiq Jebril, Yang Chen, Saji Hamed, and Aly Hajjaj

Analysis Model for Industrialized Housing Design and Assembly Process 563
Yidnekachew Tesmamma Daget and Hong Zhang

Visioning New Methodology for Creative Architecture in the Third Millennium of Knowledge Society 589
Abeer Samy Yousef Mohamed

Lumiducts Implementation and Their Relation to Luminous Comfort in High Andean Homes in the District of Huamancaca-Peru in 2021 601
L. Katherine Brañez, P. Paola Segura, and T. Vladimir Montoya

Mars Habitat Design Thru Parametric Structures Based on United Arab Emirates Heritage 617
Jose Berengueres, Lindita Bande, Aysha Alsheraifi, Afra Alnuaimi, Entesar Alawthali, and Alanoud Ablooshi

An Experimental Study and Sensitivity Analysis of Design Parameters of Building Integrated Photovoltaic (BIPV) Roofs for Rain Noise Reduction 629
Dingqiu Chen and Shaohang Shi

Low Carbon Design Strategy of Regional Airport Terminal Based on *Building Carbon Emission Calculation Standard* 641
Xia Ye, Tao Li-ke, and Guo Qin-en

Hydraulic Engineering and Flood Control

Coupled Hydrologic-Hydraulic Modeling-Based Flood Inundation Mapping for a Segment of the Tullahan River in Valenzuela City, Philippines 657
Hiyasmine S. Pili, Franz D. Santos, Charena P. Baluyot, Kyla M. Manzanade, and Yunika Aloha P. Cruz

Modeling of the Submersible Plate System to Counteract Erosion in the Huallaga River, Case: Yurimaguas—Loreto 671
Amanda Giron, Stefano Rottiers, and Mitchel Jara

Soft Computing Method for Settling Velocity Prediction of Fine Sediment in Retention Structure 687
Ren Jie Chin, Sai Hin Lai, Wing Son Loh, Lloyd Ling, Eugene Zhen Xiang Soo, Yuk Feng Huang, and Ya Qi Yeo

Research on Scour Monitoring Techniques for Bridge Pile Foundations 695
 Wenting Qiao, Qianen Xu, and Yang Liu

Infrastructure Projects and Municipal Engineering

A Review of Approaches to Drainage System Management: Current Status and Future Research Directions 707
 Gabriel Lloyd C. Malinay, Clariz D. Santos, Gayle Ann Marie B. Sarmiento, Franz D. Santos, and David B. Sanson

Influence of Parameter Variation of Saturated–Unsaturated Soil on Deformation and Stability of Foundation Pit 721
 Yongbiao Xu, Yinzhen Dong, Yingyuan Jiang, Jianfen Zhou, and Qian Mao

An Urban Public Transport Resilience Assessment Methodology Based on a Two-Carbon Context 733
 Keyuan Ding, Xueliang Liu, Ran Peng, and Hanbang Ning

Advanced Intervention Phase of High-Speed Rail Construction Catenary and Track Synchronization Precise Measurement Fine Adjustment Exploration 749
 Yonggui Li and Yajun Wang

Research on the Integrated Design Method of Construction and Maintenance in the Whole Life Cycle of Expressway 757
 Xue-Feng Zhang

Urban Architectural Image and Urban Planning

Architectural Identity of the City of Tirana, Albania. Overview of the Past, Present, and Future Expectations with Focus on the Residential Buildings (Inner Circle) 769
 Lindita Bande and Brunilda Babameto

Factors Affecting the Formation of Architectural Space and Construction Systems in the Jordanian Vernacular Architecture 781
 Mohammad Tarrad and Umamah Ahmad

The Construction Typology and Its Relationship in the Architectural Image of the Buildings in the City of Oxapampa, a South German Colony Located Within the High Forest of the Department of Pasco in Central Peru 793
 Diana Villegas and Vladimir Montoya

Transformation of Architectural Elements of *Rumah Gaba-Gaba* in Merauke Old Town, South of Papua: An Embodiment of Adaptation 805
 Yashinta Irma Pratami Hematang and Harry Kurniawan

Research on the Reconstruction Strategy of Historic Districts Under the Background of Carbon Neutrality—Taking Qinzhou Historic Districts in Guangxi as an Example 817
 Chuwei Ban and Fuqiang Li

Identifying the Influencing Factors for the Walkability of Business Streets Based on Urban Multi-source Data 827
 Chendi Yang, Siu Ming Lo, and Rui Ma

Drawing the Invisible: Visualizing Patterns of Occupation in Two Streets in Shanghai 839
 Glen Wash Ivanovic and Shinya Miyazaki

The ‘Integration Mode’ of Regeneration of Industrial Heritage, Magna Science Adventure Centre 851
 Chen Zhang and Zishen Bai

Interpreting the Urban Historical Area-Huishan Ancient Town as a Case Study 863
 Ting Zhang, Fangqian He, Di Wang, and Li Tao

Before Becoming an Independent Building: A Study of the Mixed Nature of Chemistry Laboratory Space from the 16th-18th Centuries 871
 Mingzhu Lei and Tong Cui

Information Technology and Modeling in Construction

Building Information Modeling-Based Virtual Reality System for Four-Dimensional Progress Simulation and Construction Safety Training 889
 Kun-Chi Wang, Yuan-Hsiu Chou, Guan-Yu Chen, and Jun-Jie Jiang

A Method for Semantic City Modeling 903
 Rui Ma, Jiayu Chen, Chendi Yang, and Xin Li

Analyzing the Awareness, Drivers, and Barriers of Building Information Modelling (BIM) Implementation for Sustainable Construction: Indonesia Construction Industry 913
 Cakraningrat Kencana Murti and Fadhilah Muslim

Integrating Cumulative Prospect Theory into a Cellular Automata Model for Building Evacuation with Obstacles 927
 Dongli Gao, Eric Wai Ming Lee, Wei Xie, Xuanwen Liang, Ruifeng Cao, Qian Chen, and Nan Jiang

Describing Construction Hazard Images Identified from Site Safety Surveillance Video 937
Wen-Der Yu, Wen-Ta Hsiao, Tao-Ming Cheng, Hung-Sheng Chiang, and Chia-Yu Chang

A Computationally Efficient Method for Simulation-Based Evacuation Guidance Optimization 949
Zhang Botao and S. M. Lo

Optimization of the Construction Subcontractor Selection Process for Residential Building Projects by Applying Blockchain Technology Through a Smart Contract 961
Josue Janampa, Jean Pierre Pinedo, Sandra Rodriguez, and Karem Ulloa

Identifying the Stages of Fire Development from Compartment Temperatures with GMM-HMMs: A Case Study of Room Fires 973
Hongqiang Fang and S. M. Lo

Determination of the Most Suitable Location of Evacuation Center for a Flood-Prone Community Using Multi-criteria Decision Analysis: The Case of Barangay Sapang Bayan, Bulacan, Philippines 985
Charena P. Baluyot, Franz D. Santos, Clariz D. Santos, Hiyasmine S. Pili, and Allan R. Alzona

Bridge Safety State Classification Based on Unsupervised Machine Learning 999
Wei Xiang, Xiao Li, and Feng-Liang Zhang

Cement Mortar and Concrete Engineering Design and Performance

Waste Clay Brick Binders for Low-Carbon Concrete Pavement Construction



Janitha Migunthanna, Pathmanathan Rajeev, and Jay Sanjayan

Abstract This study investigated the use of waste clay bricks (WCB) as a binder constituent in developing low-carbon pavement-grade geopolymer concrete. Blends of WCB with slag and/or fly ash were used as the aluminosilicate source materials. Sodium silicate in powder form was used as the activator to produce dry geopolymer binders. Considering the practical applicability, concrete was produced under ambient curing. Concrete with WCB in the binder showed higher compressive strengths than the concrete with only fly ash and slag in the binder and, a significant difference in flexural strength was not observed for different binder types. Maximum compressive strength of around 56 MPa at 28 days was recorded for concrete made with the ternary blend of WCB + slag + fly ash. The strength of concrete with WCB + slag was around 42 MPa. Sealing of samples to avoid contact with atmospheric air resulted in better strengths. Drying shrinkage of WCB-based concrete was investigated following the standard test procedure by subjecting it to initial curing in lime-saturated water and by a non-standard procedure of sealed curing. Compared to the standard method, the non-standard method resulted in higher drying shrinkage due to loss of moisture from the specimen. The initial flexural modulus for WCB-based concrete was higher than the concrete with slag + fly ash binder indicating the higher stiffness of WCB-based concrete. The environmental performance of the different binders used in concrete was assessed by estimating the carbon emissions and energy consumption. Compared to using ordinary Portland cement, the use of geopolymer binders can reduce carbon emissions by 70% and energy consumption by 81%. Among the geopolymers investigated in this study, the binder with WCB + slag + fly ash showed the best overall performance.

J. Migunthanna (✉) · P. Rajeev · J. Sanjayan
Swinburne University of Technology, Hawthorn, Melbourne, Australia
e-mail: jmigunthannakariyaka@swin.edu.au

P. Rajeev
e-mail: prajeev@swin.edu.au

J. Sanjayan
e-mail: jsanjayan@swin.edu.au

Keywords Waste materials · Geopolymer concrete · Pavements · Strength · Durability

1 Introduction

Concrete pavements have significantly lower whole-of-life costs due to their higher durability and lower construction and maintenance costs [1]. Their simple structure, fast construction, and smooth yet skid-resistant texture make them even more attractive over other pavement types [2]. However, the high carbon emissions associated with ordinary Portland cement (OPC) used in concrete is a critical drawback and challenge to the concrete pavement industry [3].

Developing low-carbon alternatives to OPC in pavement concrete will contribute towards sustainability in the construction industry and will subsequently enhance the industrial uptake of environmentally friendly concrete pavement technologies. Geopolymer binders synthesised combining aluminosilicate source materials (i.e., precursors), such as fly ash and slag, with alkali activators, such as sodium hydroxide, are well recognised as an alternative binder material for replacing OPC in concrete [4].

The general practice in geopolymer production is to use elevated curing conditions and liquid activators [3]. However, provision of elevated temperatures is not very practical in in-situ applications, specially in pavement constructions. Furthermore, the use of liquid activators makes the geopolymer production process more complex and makes it more difficult to directly adapt existing production lines and practices optimised for OPC concrete.

As a solution, this study investigates developing pavement-grade one-part geopolymer binders using solid activators under ambient curing. Since the one-part binders are dry powders similar to OPC, their mix designs and field use is considerably more similar to the use of OPC concrete.

Recent studies have focused on developing geopolymers using non-conventional materials such as construction and demolition waste, glass waste, brick waste and volcanic ash [5–7]. Among them, the previous studies by Migunthanna et al. [8, 9] have identified one-part geopolymer binders consisting of waste clay brick (WCB) blended with fly ash and slag as aluminosilicate precursors and anhydrous sodium metasilicate as the sole activator as a promising candidate to produce pavement grade concrete under ambient curing. Therefore, the current study deals with developing concrete using the optimum binder compositions proposed in the previous literature and, assessing their performance considering mechanical characteristics, durability, serviceability, and sustainability.

Table 1 Concrete mix designs

Mix name	Binder = 400 kg/m ³				Fine agg	Coarse agg		w/b	Slump (mm)
	WCB	Fly ash	Slag	Act		14 mm	7 mm		
W + S	144	0	216	40	661.5	737.1	491.4	0.49	65
W + S + F	115.2	72	172.8	40	661.5	737.1	491.4	0.46	55
S + F	0	72	288	40	661.5	737.1	491.4	0.46	60

All the proportions are in kg/m³

Note *agg.* = aggregates, *Act.* = activator, *W* = waste clay bricks, *S* = slag, *F* = fly ash

2 Materials and Methods

2.1 Experimental Program

Two binder compositions proposed in the literature were selected based on references [8, 9]. These binders consist of WCB, slag and fly ash in the precursor. The total of the precursor and the activator was considered as the binder. All binders had an optimum activator content (i.e., Na₂SiO₃) of 10% of the weight of the binder. A 28-day target compressive strength of 40 MPa and target slump of 50–65 mm were considered following the pavement design guidelines [10]. Table 1 shows the mix proportions of concrete.

First, dry binders were prepared by mixing all precursors and activator, and then aggregates were added. Water was added in a pre-determined water-to-binder ratio (w/b) to achieve the slump in the targeted range. After wet mixing for about 15 min, test cylinders with a diameter of 100 mm and height of 200 mm were cast. Samples were subjected to ambient air curing and sealed ambient curing. In air curing samples were kept in contact with air since demoulding. In sealed curing, samples were wrapped with polythene to avoid contact with air and stored at 25 ± 2 °C. The sealing period was varied from 3 to 28 days to evaluate the effect of sealing time. Mechanical performance was assessed by compressive strength, flexural strength and split tensile strength. All the tests were carried out following Australian Standards (AS). Water absorption, apparent volume of permeable voids (AVPV) and drying shrinkage tests were conducted to assess the durability. Fatigue testing was carried out as a measure to serviceability performance.

2.2 Assessment of the Environmental Performance

The environmental performance of geopolymers were evaluated by quantifying CO₂ emissions and energy consumption. Material production, design, construction, use, maintenance and end-of-life can be considered the main phases in a pavement life cycle [11]. In this study, the focus was only given the material production since

impacts from design and construction can be assumed to be similar or have no significant difference based on the type of concrete [8]. The unavailability of durability and service performance data for geopolymer concrete pavement limits the analysis boundary up to the construction phase. In the concrete production phase, impacts from mixing and aggregates can be again considered similar for all concrete types. Therefore, significant differences and critical variations in the environmental performance can be expected related to binder production.

Inventory values for CO₂ emissions and energy consumption proposed in the literature for individual components (i.e., processing of WCB [8, 12], slag [13, 14], fly ash [15, 16]; production of Na₂SiO₃ [17, 18] and OPC [19, 20]; binder mixing [8, 12]) were used to estimate the impacts during binder production. Process-based approach was used in the analysis, where total CO₂ emissions and energy consumption related to each individual stage in raw material processing was considered. Impacts were quantified with respect to a functional unit of 1 ton of dry binder.

3 Results and Discussion

3.1 Mechanical Performance

To understand the strength development of geopolymer concrete (GPC) under ambient curing, samples were subjected to two curing environments, namely sealed and unsealed. Figure 1a shows the 28-day compressive strength for three GPC samples. Under both curing regimes, GPC with WCB binders showed strength higher than GPC with only fly ash + slag indicating the better performance of WCB-based binders. Sealing of samples improved the strength gain of all GPC types and this increment was significant for WCB-based GPC. Sealing minimizes the development of micro-cracks due to shrinkage by preventing moisture loss, and hinders the reactions with atmospheric air [21]. Under the sealed conditions, WCB-based GPC was able to exceed the target strength of 40 MPa and the highest strength was recorded for W + S + F GPC mix. The flexural strength of GPC did not show a significant variation based on the binder type (Fig. 1b). Under the sealed curing, all samples achieved flexural strength of more than 4.5 MPa which is the typical strength requirement in rigid pavement design [10].

To evaluate the effect of the sealing duration, GPC with WCB-based binders were subjected to different sealing periods up to 0, 3, 7, and 28 days and compressive strength at 28 days was recorded. As shown in Fig. 2, an increase in the sealing period increases the strength gain. GPC made with W + S + F binder was able to exceed the target strength even at 3-day sealing period indicating the better performance of the ternary blend of WCB + fly ash + slag than the binary blend of WCB + slag.

The strength development of WCB-based GPC was studied with respect to W + S + F mix, since it showed the best mechanical properties from the three GPC mixes investigated. Here samples were kept sealed only for 3 days and then kept in contact

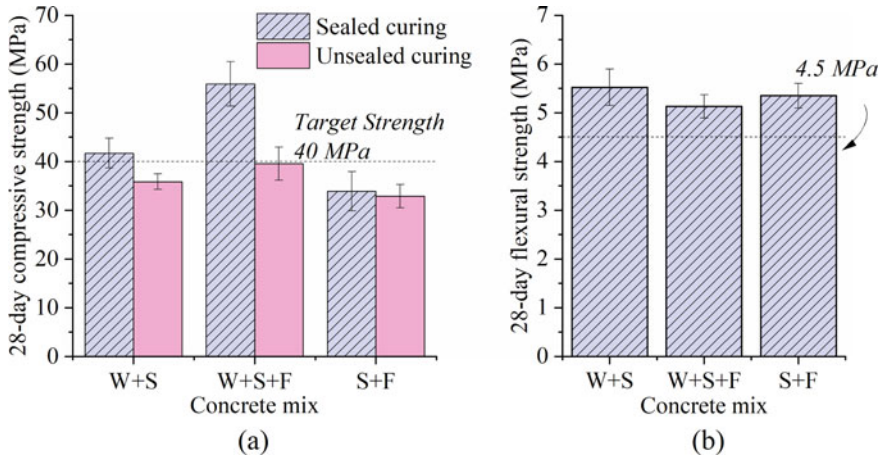


Fig. 1 **a** Compressive strength and **b** flexural strength of GPC at sealed and unsealed curing conditions. Error bars indicate mean \pm one standard deviation (SD)

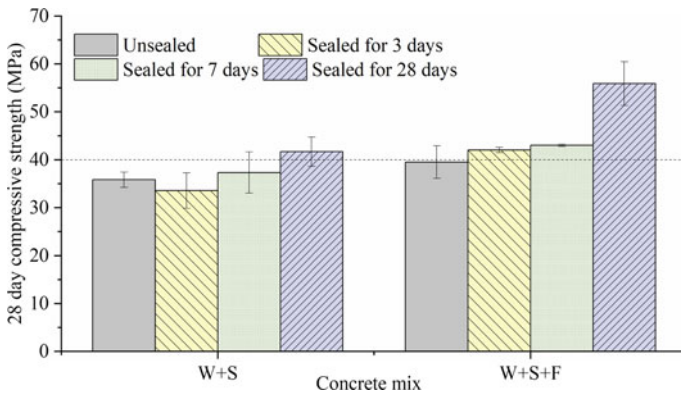


Fig. 2 Effect of sealed duration on strength development of WCB-based GPC. Error bars indicate mean \pm one SD

with air until the test date. Figure 3 shows the compressive, flexural and split tensile strengths development of W + S + F GPC. According to the Structural Concrete Design Guidelines [22], the minimum compressive strength for grade 40 concrete at 3 and 7 days should be 14 MPa and 20 MPa, respectively. The GPC mix selected in this study was well above the minimum values reporting 30.1 MPa at 3 days and 38.6 MPa at 7 days. The high early strength gain ability of GPC is an additional advantage to the concrete intended use in pavement applications [1, 3].

A significant development of compressive strength after 60 days was not observed for GPC. The selected mix reached a compressive strength of 44 MPa over a period of

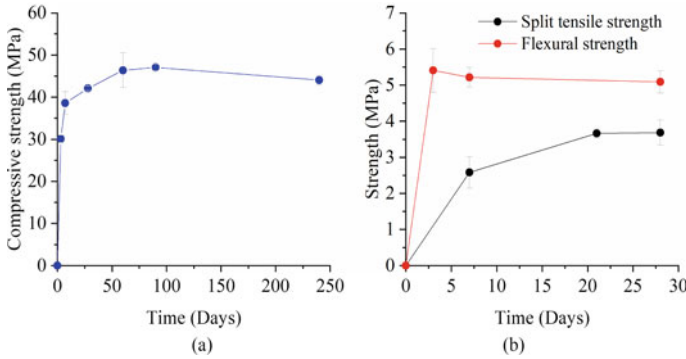


Fig. 3 **a** Compressive strength and **b** flexural and split tensile strengths development of W + S + F GPC. Error bars indicate mean \pm one SD

8 months. However, compared to the 90-day strength, this is 6% reduction. Improvement in flexural strength gain was not observed after 3 days and it was at a constant value of around 5.1 MPa throughout. Compared to the 3-day strength, a slight reduction of the flexural strength also was observed. Development of micro-cracks due to shrinkage and atmospheric carbonation can be considered as possible causes for these slight reductions in strength. The split tensile strength of selected GPC was around 3.7 MPa at 28 days.

3.2 Durability Performance

Basic durability properties of W + S + F GPC were assessed through water absorption, AVPV and shrinkage. Standard testing procedures available for OPC concrete were used following Australian guidelines (i.e., AS 1012.21). At 28 days of ageing, immersed absorption of the GPC was found to be 5.6% (SD = ± 0.75) and it was increased up to 6.1% (SD = ± 0.32) after boiling. The AVPV of WCB-based GPC was found to be 9.9% (SD = ± 0.44), which is less than 14%, the maximum allowable AVPV for concrete with target strength of 40 MPa. AVPV and absorption of concrete refer to the susceptibility of the material for ingress of impurities and foreign particles to the inner concrete environment which can subsequently result in deterioration of the material and corrosion of the embedded reinforcements [3].

3.3 Drying Shrinkage

The drying shrinkage of GPC was determined based on the standard test method following AS 1212.8.4 and a non-standard method. According to the standards,

specimens need to be cured in lime-saturated water for the first 7 days and then stored in ambient conditions under 23 °C and 50% relative humidity. However, to achieve the target strength, GPC needs sealed curing at least for 3 days. From the initial experimental work, it was found that GPC cured in water (i.e., similar to standard curing for OPC concrete) can reach only 28-day compressive strength of around 36 MPa. Therefore, to identify the shrinkage under the suggested curing method for GPC, shrinkage specimens were subjected to sealed curing for 3 days. At the end of the initial curing, samples were stored at 23 °C and 50% relative humidity.

Figure 4 shows the drying shrinkage of W + S + F GPC under standard and non-standard curing conditions. Samples subjected to the non-standard procedure showed higher shrinkage compared to the samples subjected to the standard curing procedure. Drying shrinkage in concrete occurs as a result of loss of moisture from the exposed environment causing volume reduction in binder gel products [23, 24]. For normal-strength concrete, drying shrinkage is critical during the initial period and dominant over longer periods [23]. In the standard method, samples are in a saturated state, there is no moisture loss from the concrete to the environment. Therefore, shrinkage in the entire initial curing period is zero. However, for sealed samples, drying occurred from the first day it-self. It is practically difficult to achieve a fully sealed condition and therefore, the sample starts losing moisture even under sealed conditions [25]. This moisture loss is not aggressive as the unsealed condition, however significant enough to cause drying shrinkage in the concrete.

Although GPC has several advantages over OPC concrete, the shrinkage behaviour of GPC is a critical concern. Many studies reported that GPC has a higher shrinkage compared to OPC concrete [24–26]. However, the results are often inconsistent due to variations such as mix designs, binder types, aggregate properties and curing conditions. Also, the direct use of standard test methods available for OPC concrete to determine the shrinkage of GPC is still questionable. Therefore, more studies are essential to understand the shrinkage behaviour and to develop test methods appropriate to GPC concrete.

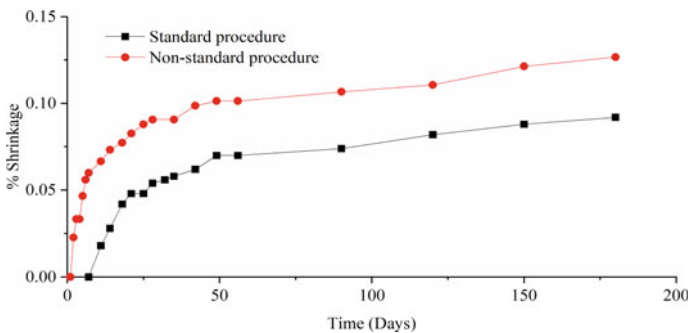


Fig. 4 Drying shrinkage of W + S + F GPC under standard procedure and non-standard procedure (i.e., sealed for 3 days)

3.4 Serviceability Performance

Pavements are always subjected to repeated loading due to the frequent movement of traffic. Although these loads are smaller than the strength of materials, pavement can fail under lower loading conditions due to fatigue damage. Therefore, investigating the fatigue behaviour of a material is important in understanding the serviceability of the pavement structure [10]. As an initiation, fatigue performance of GPC with W + S + F and S + F binders was investigated by subjecting it to cyclic loading with peak stress of 85% of the maximum. The initial flexural modulus and the fatigue life (i.e., number of loading cycles until failure) were determined.

Initial flexural modulus was calculated by averaging the flexural modulus of each load cycle with in the first 10–50 cycles. Figure 5 shows the flexural modulus for each cycle during the initial period and Table 2 summarises the average modulus and the fatigue life. At 85% stress level, GPC with WCB showed higher flexural modulus indicating the high stiffness of the material. However, to comprehensively understand the fatigue performance of these materials, detailed studies are required. It is recommended to investigate the performance of the material under several stress ratios with a higher number of specimen counts.

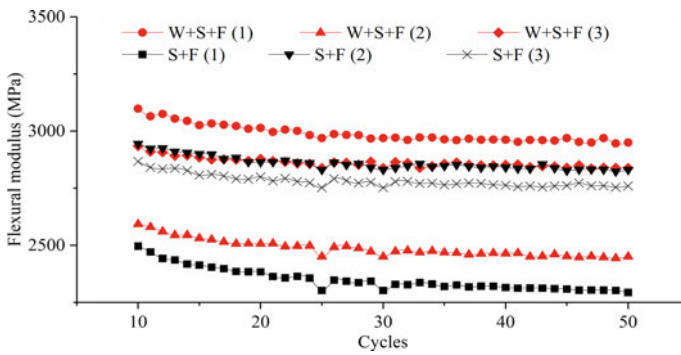


Fig. 5 Initial flexural modulus of concrete with W + S + F binder and S + F binder

Table 2 Summary of flexural fatigue test results

Concrete type	W + S + F			S + F		
	(1)	(2)	(3)	(1)	(2)	(3)
Fatigue life	5507	6805	29,995	2412	3290	286,457
Initial flexural modulus	2780 MPa			2660 MPa		

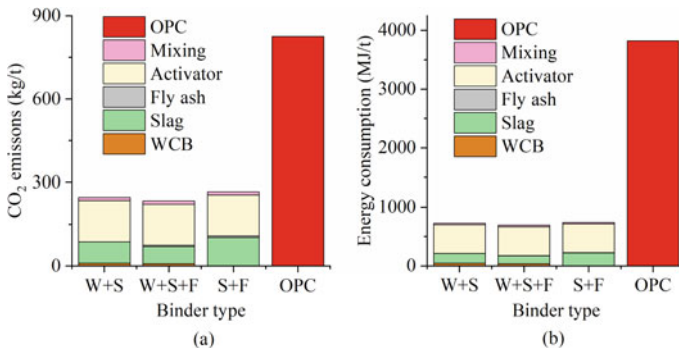


Fig. 6 **a** Comparison of CO₂ emissions and **b** energy consumptions associated with production of 1 ton of dry geopolymer binders with OPC

3.5 Environmental Performance

The environmental performance of geopolymers was assessed through CO₂ emissions and energy consumption corresponding to the binder production phase. These values were then compared with the impacts of OPC production. Figure 6 shows the CO₂ emissions and energy consumption associated with the production of three geopolymer binders initially selected in this study and their comparison with OPC.

All geopolymer binder compositions showed around 70% reduction in carbon emissions and around 81% reduction in energy consumption compared to OPC. Among the three geopolymer binders, the highest impacts were corresponding to the S + F binder due to the higher amount of slag content. Replacing part of the slag in this binder with WCB further reduced (i.e., W + S + F) the carbon emissions and energy consumption. W + S + F binder showed the best environmental performance and also the mechanical performance compared to the other binders considered in this study.

4 Conclusion

This study investigated the use of low-carbon geopolymer binders containing waste clay bricks (WCB) as an alternative to ordinary Portland cement (OPC) in producing concrete suitable for pavement construction. From the experimental studies, the following conclusions were made.

- The highest compressive strength of 56 MPa was recorded for the concrete with WCB, slag and fly ash (W + S + F) in the binder. GPC with only WCB and slag showed a 28-day compressive strength of 42 MPa.
- Concrete with only slag and fly ash showed the lowest compressive strength of 34 MPa indicating the advantage of using WCB as a binder component.

- The apparent volume of permeable voids present in the W + S + F concrete was around 9.9% which is less than the maximum allowable limit of 14% for grade 40 concrete.
- Although the sealing of samples had a positive impact on strength gain, the sealing could not provide enough resistance to prevent moisture loss. Therefore, higher drying shrinkage was observed for GPC.
- Lime-saturated water curing helped to reduce the shrinkage however, this curing method reduced the compressive strength of the WCB-based GPC down to 36 MPa.
- The initial flexural modulus of W + S + F concrete was around 2780 MPa at a stress level of 85% of the maximum.
- The use of geopolymers instead of OPC can reduce CO₂ emission by 70% and energy consumption by 81%.

Geopolymers with WCB, slag and fly ash can be considered viable low-carbon binders to replace OPC in concrete. More studies are recommended to understand the strength development, shrinkage and fatigue behaviour of these concretes.

Acknowledgements This research work is part of a research project (Project No IH18.4.2) sponsored by the SPARC Hub (<https://sparchub.org.au>) at Department of Civil Engineering, Monash University funded by the Australian Research Council (ARC) Industrial Transformation Research Hub (ITRH) Scheme (Project ID: IH180100010). The financial and in-kind support from Austroads, Swinburne University of Technology and Monash University are gratefully acknowledged.

References

1. Jayasooriya D, Rajeev P, Sanjayan J (2022) Application of graphene-based nanomaterials as a reinforcement to concrete pavements. *Sustainability* 14(10):11282
2. CCANZ (2013) Benefits of building concrete roads in New Zealand. In: *Cement Concrete Association of New Zealand (CCANZ)*, New Zealand
3. Migunthanna J, Rajeev P, Sanjayan J (2022) Waste clay bricks as a geopolymer binder for pavement construction. *Sustainability* 14(11):6456
4. Negahban E, Bagheri A, Sanjayan J (2021) Pore gradation effect on Portland cement and geopolymer concretes. *Cem Concr Compos* 104:141
5. Komnitsas K, Zaharaki D, Vlachou A, Bartzas G, Galetakis M (2015) Effect of synthesis parameters on the quality of construction and demolition wastes (CDW) geopolymers. *Adv Powder Technol* 26(2):368–376
6. Lemougna PN, MacKenzie KJD, Melo UFC (2011) Synthesis and thermal properties of inorganic polymers (geopolymers) for structural and refractory applications from volcanic ash. *Ceram Int* 37(8):3011–3018
7. Migunthanna J, Rajeev P, Sanjayan J (2023) Investigation of waste clay brick as partial replacement in geopolymer binder. *Constr Build Mater* 365:130107
8. Migunthanna J, Rajeev P, Sanjayan J (2021) Investigation of waste clay brick as partial replacement of geopolymer binders for rigid pavement application. *Constr Build Mater* 305:124787
9. Migunthanna J, Rajeev P, Sanjayan J (2022) Waste clay brick binders for rigid pavement subbase and base concretes. *Lecture Notes in Civil Engineering*, Springer International Publishing, Road and Airfield Pavement Technology

10. Austroads (2017) Guide to pavement technology. In: Part 2: Pavement structural design. Austroads, Sydney, NSW, Australia
11. Mallick RB, El-Korchi T (2013) Pavement engineering: Principles and practice. CRC Press
12. Fořt J, Vejmelková E, Kofiřáková D, Alblová N, Čáchová M, Keppert M, Rovnanříková P, Černý R (2018) Application of waste brick powder in alkali activated aluminosilicates: functional and environmental aspects. *J Clean Prod* 194:714–725
13. CTCN (2023) Blast furnace slag granulation, Climate Technology Centre & Network (CTCN), United Nations Framework Convention on Climate Change (UNFCCC). Retrieved from <https://www.ctc-n.org/technology-library/mining-production/blast-furnace-slag-granulation>. Accessed on 5 Jan 2023
14. Yuksel I (2018) Blast-furnace slag. *Waste Supplement Cemen Mater Concr* 361–415
15. ADAA (2012) Use of fly ash to achieve enhanced sustainability in construction. Fly ash technical note 11, Ash Development Association of Australia (ADAA), Wollongong, NSW, Australia
16. Ouellet-Plamondon C, Habert G (2015) Life cycle assessment (LCA) of alkali-activated cements and concretes. In: *Handbook of alkali-activated cements, mortars and concretes*, pp 663–686
17. Fawer M, Concannon M, Rieber W (1999) Life cycle inventories for the production of sodium silicates. *Int J Life Cycle Assess* 4(4):207–212
18. Sandanayake M, Gunasekara C, Law D, Zhang G, Setunge S (2018) Greenhouse gas emissions of different fly ash based geopolymer concretes in building construction. *J Clean Prod* 204:399–408
19. Golewski GL (2020) Energy savings associated with the use of fly ash and nanoadditives in the cement composition. *Energies* 13(9):2184
20. Pavlík Z, Fořt J, Záleská M, Pavlikova M, Trník A, Medved I, Keppert M, Koutsoukos PG, Černý R (2016) Energy-efficient thermal treatment of sewage sludge for its application in blended cements. *J Clean Prod* 112:409–419
21. Lee S, Van Riessen A, Chon CM (2016) Benefits of sealed-curing on compressive strength of fly ash-based geopolymers. *Materials* 9(7):598
22. VicRoads specification: Section 610. (2020) Structural concrete, VicRoads, Melbourne, Victoria
23. Brooks J (2014) *Concrete and Masonry Movements*. Elsevier Science & Technology, Oxford
24. Sadeghian G, Behfarnia K, Teymouri M (2022) Drying shrinkage of one-part alkali-activated slag concrete. *J Build Eng* 51:104263
25. Migunthanna J, Rajeev P, Sanjayan J (2023) Shrinkage model for waste clay brick-based geopolymer concrete. *Constr Build Mater* 404:133196
26. Collins F, Sanjayan JG (2000) Effect of pore size distribution on drying shrinking of alkali-activated slag concrete. *Cem Concr Res* 30(9):1401–1406

Effect of Superplasticizer on the Properties of Kenaf Fibre-Reinforced Geopolymer Concrete



F. N. A. A. Aziz, N. A. Al-Ghazali, A. D. Jasmi, N. A. M. Nasir, and I. A. Karim

Abstract The use of fibres in concrete production has attracted a lot of interest because of the low tensile properties of concrete. Lately, extensive studies have been conducted on the incorporation of different types of natural fibres in geopolymer composites as an environmentally friendly alternative to steel and synthetic fibres. However, the incorporation of natural fibres has a negative impact on workability in terms of properties in the fresh state. Several studies showed that the addition of the superplasticizer (SP) is one of the solutions to overcome this issue. But the performance of geopolymer concrete with the inclusion of kenaf fibres and different SP content is not studied yet. In this paper, the fresh and mechanical properties of kenaf fibre-reinforced geopolymer concrete (KFRGC) with the addition of different SP contents i.e., 0, 1, and 2%, are studied. The workability of KFRGC was dependent on the percentage of the SP. With the increase in the dosage of the SP, the workability was enhanced. However, the addition of the SP in a high percentage decreased the strength performance of the concrete. The best results were achieved with the addition of 1% which improved the workability of KFRGC by about 67%. These findings demonstrate the positive impact of using the appropriate percentage of SP on the performance of KFRGC in the fresh state.

Keywords Geopolymer · Fibres · Kenaf fibre · Superplasticizer · Workability · Compressive strength

1 Introduction

Geopolymer materials are inorganic polymers produced by the chemical reaction between an aluminosilicate source and an alkaline solution and are currently the material to replace ordinary Portland cement (OPC) [1]. When compared to the production

F. N. A. A. Aziz (✉) · N. A. Al-Ghazali · A. D. Jasmi · N. A. M. Nasir · I. A. Karim
Housing Research Centre, Civil Engineering Department, Faculty of Engineering, Universiti Putra Malaysia, 43400 Serdang, Malaysia
e-mail: farah@upm.edu.my

of OPC, geopolymer emits 80% less CO₂ and uses 60% less energy [2]. Additionally, numerous research that examined the characteristics of geopolymer composite (GPC) suggested excellent results, including high fire resistance [3], high early strength [4], and durability against chemical attacks [5, 6]. However, the inherent brittleness of the geopolymer exhibits drawbacks similar to OPC when subjected to flexure and tension stresses; both require fibre reinforcement to reduce crack propagation and enhance toughness and failure mode [2].

In addition to the GPC, natural fibres are gaining a lot of attention due to rising interest in maintaining long-term sustainability and environmental issues. This has prompted using more renewable resources in the building and construction sector [7]. Natural fibres are available, inexpensive, and lightweight materials. Kenaf fibre is a type of natural fibre which is an extremely useful material. Numerous research studies have suggested that using it could increase the structural performance of concrete or reinforced concrete mixtures [8]. The kenaf plant is mainly grown for its fibres. The method used to extract the fibre determines its quality.

The extraction process used to obtain plant fibres is also known as retting or degumming. Several retting techniques for plant fibres have been reported, including water retting, mechanical retting, chemical retting, enzymatic retting, and dew retting. The most widely used techniques for obtaining kenaf fibres are the water retting, enzymatic, mechanical, and chemical methods [9]. The extracted fibres could be used as building materials for construction, bio composites, textiles, and many more. However, the main obstacles to using kenaf fibre are the high moisture absorption and the weak compatibility between the fibre and the matrix, which negatively affect the performance of the composites [7].

Fibre treatment is a well-known method to reduce moisture-absorbing chemical components and enhance fibre-matrix adhesion. Lam and Yatim [10] reported that adding alkali-treated kenaf fibre to the cement-based concrete improved the tensile and flexural strength of the concrete and the samples with kenaf fibre exhibited more resistance to cracking and toughness than the plain concrete.

Recently, huge attention has been paid to geopolymer composites reinforced with steel, syntactic, and natural fibres due to their high flexural and tensile strength, ductility and crack control and excellent durability [2]. However, it has been reported that the addition of these fibres decreased the workability of the geopolymer mixtures. The type, length, shape, and content of fibres all affect the properties of fresh mixtures. Wongsu et al. [11] reported that the addition of sisal, jute, or glass fibre to geopolymer mixtures decreased the workability. Besides, the geopolymer composites prepared with sisal fibre exhibited the lowest workability performance. The authors attributed the workability loss to the rough surface, irregular stripes, and porous texture of fibres. Su et al. [12] also reported that the workability of geopolymer mixes prepared with polypropylene, glass or lignin fibres was lower than that of the plain geopolymer mixes and increasing the fibre content increased the workability reduction. Several researchers have proposed the use of a superplasticizer (SP) in fibre-reinforced concrete as a technique for maintaining concrete workability. Zhang et al. [13] reported that the addition of SP into the mixes showed three times higher

workability. Bentegri et al. [14] also reported that using 0.4% of SP results in three times lower plastic viscosity, compared to the concrete mixes without SP.

The effect of the SP on the properties of natural fibre-reinforced geopolymer is not well studied, especially, the geopolymer mixes reinforced with kenaf fibre. Therefore, this study will examine the properties of kenaf fibre-reinforced geopolymer composites with the addition of different percentages of SP. The main objectives of this research have been divided into two stages: (a) the treatment of kenaf fibre extracted by using two different methods; (i) water retting, (ii) mechanical retting, (b) the performance of geopolymer composite containing alkali treated kenaf fibre prepared with different SP percentages (1 and 2%).

2 Experimental Programme

2.1 Material

The materials used to produce kenaf fibre-reinforced geopolymer concrete (KFRGC) are low calcium fly ash class F (FA) according to ASTM C 618–12a [15], and ground granulated blast furnace slag (GGBS) as the binder materials, a combination of sodium hydroxide and sodium silicate as the alkaline activator solution, SP, fine and coarse aggregates, and kenaf fibre.

Kenaf fibres used for this study were supplied by Lembaga Kenaf dan Tembakau Negara (LKTN). The fibres were extracted by two different methods: water retting (grade A) and mechanical retting (grade D). Before adding the fibres to the geopolymer mixes, the alkaline treatment was conducted by using NaOH solution of 6% concentration and an immersion period of 3 h based on the works of [10, 16]. After the treatment, the fibres of both grades were tested for physical and mechanical properties. After testing, the fibres were cut into a length of 30 mm to be used in the geopolymer mixes.

2.2 Mix Proportions

Four different geopolymer mixes were designed, and the mix proportions are shown in Table 1. The first mix is the plain geopolymer without fibre addition, and the second mix is KFRGC with an addition of 1.25% volume fraction of kenaf fibre. The other two mixes were KFRGC with the addition of 1.0 and 2.0% of the SP (KFG-1 and KFG-2%). The alkaline activator to binder ratio, sodium hydroxide molarity and sodium silicate (SS) to sodium hydroxide (SH) ratios were fixed at 0.55, 14 M and 2.5, respectively.

Table 1 Mix proportions of KFRGC (kg/m³)

Mix	FA	GGBS	Aggregates		Solution		SP (%)
			Sand	10 mm	SS	SH	
(Ref)	261	174	704.7	1065.75	170.89	68.35	0
KFG	261	174	704.7	1065.75	170.89	68.35	0
KFG-1%	261	174	704.7	1065.75	170.89	68.35	1
KFG-2%	261	174	704.7	1065.75	170.89	68.35	2

2.3 Mixing, Casting and Curing

To achieve homogenous mixes, the coarse and fine aggregates were dry mixed for 2 min, and then the binder components were added and mixed for an additional 2 min. Then, kenaf fibres were added to the dry mix, and all the components dry mixed for another 3 min. Finally, the alkaline activator was added and mixed for 3 min. Then, the fresh mixtures were cast in the molds and the samples were cured at ambient ambient temperature (27 ± 1.5) °C under a relative humidity of 75%.

2.4 Testing

The diameter is an essential parameter for determining the tensile strength of the fibre. It was measured by using an optical microscope (Nikon LV150N). A single fibre tensile test was conducted following the guidelines of ASTM D3379-89 [17]. The workability of KFRGC mixes was evaluated by following BS EN 12350-2 [18]. The hardened properties are ultrasonic pulse velocity (UPV) based on the ASTM C597-09 [19] and compression test according to BS 12390-3 [20].

3 Results and Discussion

3.1 Properties of Kenaf Fibres

Table 2 presents the results of the diameter test of kenaf fibre grade A and D before and after treatment. The treatment decreased the diameter of kenaf fibres for both grades. The reduction in the diameter was about 20% compared to the untreated fibres. This reduction is due to the removal of the impurities, lignin, wax, and hemicellulose components from the surface of the fibres [7]. In terms of strength performance, the KF treated of type A and D achieved tensile strength of 241 and 251 MPa, respectively, which are 80 and 78% higher than the untreated fibres. This is similar to the finding from Ikhwan et al. [16]. The tensile strength of kenaf fibre type D,

Table 2 Diameter and tensile strength results for kenaf type A and D before and after treatment

Fibre type	Untreated		Treated	
	A	D	A	D
Diameter (mm)	0.0946	0.0963	0.0771	0.0780
Tensile strength MPa	134.45	141.41	241	251.58

which was extracted by mechanical retting, was higher than that of type A. Therefore, it was chosen to prepare kenaf fibre-reinforced geopolymer composites.

3.2 Workability of KFRGC

The workability of geopolymer mixtures was determined by using the slump test method. Figure 1 presents the slump heights of the KFRGC mixes and plain geopolymer without kenaf fibre. For GPC, the slump value was 172 mm, while the workability of the mixes with kenaf fibre was 43 mm. For the KFRGC prepared with SP, the slump heights were 75 and 87 mm for the mixtures with 1 and 2% of SP, respectively. The trend of workability in Fig. 1 reveals that the workability of the geopolymer mix decreased by about 75% with adding kenaf fibre. A similar trend of results was also obtained by Lam and Yatim [10] and Silva et al. [21] when kenaf fibre, jute and sisal fibres were added to the concrete mixes. However, the addition of the SP significantly improved the workability, and the slump heights of the mixes increased by about 67 and 102% with adding 1 and 2% of SP, respectively compared to KFRGC without SP. These findings are similar to another research findings where different ratios of SP were used in the steel fibre-reinforced concrete [22].

Fig. 1 Slump heights of geopolymer mixtures

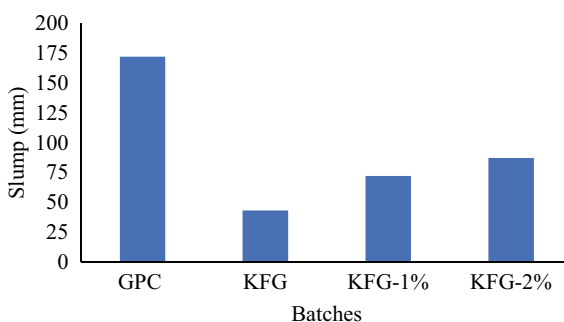
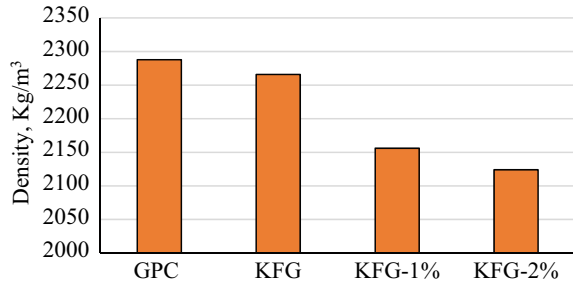


Fig. 2 Density of plain GPC and KFRGC with and without SP



3.3 Dry Density

The unit weight of the constituent materials used in the mixture has a significant impact on the density of geopolymer composites. Figure 2 displays the density of the various geopolymer mixes. KFRGC samples exhibited lower density than the plain geopolymer concrete. This reduction could be attributed to the lower density of kenaf fibre and the entrance of air voids during the mixing of the fresh mixtures. Besides, the addition of SP decreased the density and increasing the SP dosage from 1.0 to 2.0% caused a higher reduction in the density of the mixtures. Dumne et al. [23] observed a similar trend when the SP dosage increased from 0.25 to 0.35% in the concrete mixtures.

3.4 Ultrasonic Pulse Velocity (UPV)

The average UPV values of geopolymer samples at 7 and 28 days are shown in Fig. 3. All composites exhibited an increase in UPV values with a curing age of 7 to 28 days, which reflects the development of the internal structure of geopolymer with time. The results show that adding kenaf fibre to geopolymer concrete decreased the UPV values from 4584 to 4338 m/s. Besides, adding 1.0% SP decreased the UPV readings by about 8%. However, increasing the dosage of the SP to 2.0% reduced the UPV values by about 11%. Although the reduction in the UPV values with fibre and SP addition, the results demonstrated that all the KFRGC mixes with and without SP are considered to produce good-quality concrete with UPV values ranging from 3863 to 4584 m/s at 28 days [24].

3.5 Compressive Strength

Three cubes were cast for each mix and tested to determine the average compressive strength at 7 and 28 days for both plain geopolymer and KFRGC with and

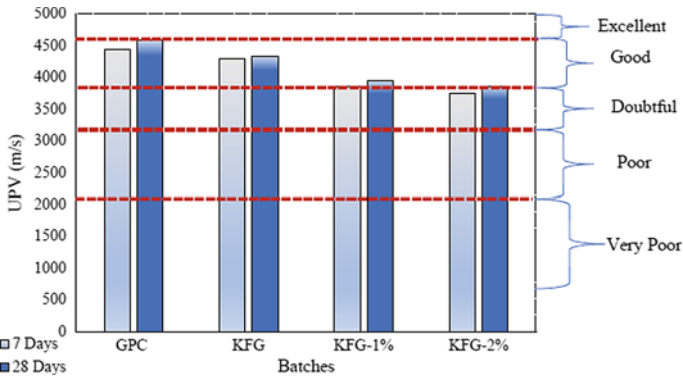


Fig. 3 UPV values of geopolymer mixtures

without SP, and the results are presented in Fig. 4. The findings demonstrate that the compressive strength increased as the curing age increased from 7 to 28 days. The highest compressive strength was achieved by the plain GPC, which is 51.5 and 64.4 MPa, after 7 and 28 days, respectively. However, adding kenaf fibre decreased the compressive strength of the plain geopolymer by about 14 and 19% after 7 and 28 days, respectively. Besides, adding the SP increased the strength reduction, and adding 1.0 and 2.0% of SP decreased the compressive strength of KFRGC by about 14 and 19%, respectively, after 28 days, compared to the fibrous composites without SP. Jithendra and Elavenil [25] and Triwulan et al. [26] also reported that increasing SP content in the geopolymer mixtures decreased the compressive strength of the samples. This could be attributed to the increased water percentage in the geopolymer mixture with increasing SP percentage ([27]. This water will take the form of evaporable water during the geopolymerization process, thus increasing the porosity of the mixes and decreasing the strength of the composites [28].

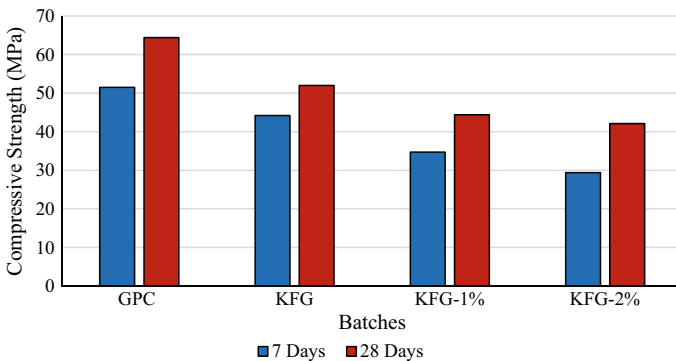


Fig. 4 Effect of kenaf fibre addition and SP percentage on the compressive strength of geopolymer mixtures

4 Conclusion

The alkaline treatment improved the tensile performance of both grades of kenaf fibre. And kenaf fibre type D (extracted by the mechanical retting method) achieved better tensile strength than that of type A. The workability results of the KFRGC mixes with SP showed that both 1.0 and 2.0% provided a workable mix with a slump height higher than 70 mm. But, increasing the SP percentage to 2.0 caused a higher reduction in the strength, and it is also not economic. Therefore, 1.0% can be considered the appropriate dosage to be used in the KFRGC to improve the workability of the mixtures.

Acknowledgements The authors gratefully acknowledge the financial support for this research by the Ministry of Education, Malaysia under the Fundamental Research Grant Scheme (FRGS/1/2020/TKO/UPM/02/32) with Vot no: 5540372 for research work entitled ‘An investigation of characterization and parametric effect of kenaf bast fibre in the properties of geopolymer kenaf reinforced concrete’.

References

1. Abbas AGN, Aziz FNAA, Abdan K, Nasir NAM (2022) Mechanical properties of natural fibre reinforced geopolymer composites: a review. *Sci Technol* 30(3):2053–2069
2. Abbas AGN, Aziz FNAA, Abdan K, Nasir NAM, Huseien GF (2022) A state-of-the-art review on fibre-reinforced geopolymer composites. *Constr Build Mater* 330:127187. <https://doi.org/10.1016/j.conbuildmat.2022.127187>
3. Jiang X, Xiao R, Zhang M, Hu W, Bai Y, Huang B (2020) A laboratory investigation of steel to fly ash-based geopolymer paste bonding behavior after exposure to elevated temperatures. *Constr Build Mater* 254:119267. <https://doi.org/10.1016/j.conbuildmat.2020.119267>
4. Xie J, Wang J, Zhang B, Fang C, Li L (2019) Physicochemical properties of alkali activated GGBS and fly ash geopolymeric recycled concrete. *Constr Build Mater* 204:384–398. <https://doi.org/10.1016/j.conbuildmat.2019.01.191>
5. Kuri JC, Sarker PK, Shaikh FUA (2021) Sulphuric acid resistance of ground ferronickel slag blended fly ash geopolymer mortar. *Constr Build Mater* 313(11):125505. <https://doi.org/10.1016/j.conbuildmat.2021.125505>
6. Kuri JC, Nuruzzaman M, Sarker PK (2022) Sodium sulphate resistance of geopolymer mortar produced using ground ferronickel slag with fly ash. *Ceram Int*. <https://doi.org/10.1016/j.ceramint.2022.09.258>.
7. Abbas AGN, Aziz FNAA, Abdan K, Nasir NAM, Norizan MN (2022) Kenaf fibre reinforced cementitious composites. *Fibers* 10:1–24
8. Solahuddin BA (2022) A critical review on experimental investigation and finite element analysis on structural performance of kenaf fibre reinforced concrete. *Structures* 35:1030–1061. <https://doi.org/10.1016/j.istruc.2021.11.056>
9. Ahmad Nadzri SNZ, Hameed Sultan MT, Shah AUM, Safri SNA, Basri AA (2020) A review on the kenaf/glass hybrid composites with limitations on mechanical and low velocity impact properties. *Polymers (Basel)* 12(6):1–13. <https://doi.org/10.3390/POLYM12061285>
10. Lam TF, Yatim JM (2015) Mechanical properties of kenaf fiber reinforced concrete with different fiber content and fiber length. *J Asian Concr Federat* 1(1):11–21

11. Wongs A, Kunthawatwong R, Naenudon S, Sata V (2020) Natural fiber reinforced high calcium fly ash geopolymer mortar. *Constr Build Mater* 241:118143. <https://doi.org/10.1016/j.conbuildmat.2020.118143>
12. Su Z, Guo L, Zhang Z, Duan P (2019) Influence of different fibers on properties of thermal insulation composites based on geopolymer blended with glazed hollow bead. *Constr Build Mater* 203:525–540. <https://doi.org/10.1016/j.conbuildmat.2019.01.121>
13. Zhang K et al (2019) How does adsorption behavior of polycarboxylate superplasticizer effect rheology and flowability of cement paste with polypropylene fiber? *Cem Concr Compos* 95:228–236. <https://doi.org/10.1016/j.cemconcomp.2018.11.003>
14. Bentegri I, Boukendakdji O, Kadri EH, Ngo TT, Soualhi H (2020) Rheological and tribological behaviors of polypropylene fiber reinforced concrete. *Constr Build Mater* 261. <https://doi.org/10.1016/j.conbuildmat.2020.119962>
15. ASTM (2010) ASTM C 618: Standard Specification for Coal Fly Ash and Raw or Calcined Natural Pozzolan for Use in Concrete. Annual Book of ASTM Standards, Volume 4.01, Cement; Lime; Gypsum. In: Annual Book of ASTM Standards, no. C, pp 3–6. <https://doi.org/10.1520/C0618>
16. Ikhwan M, Zaki M, Dolah R, Mohamed MZ (2018) Tensile behaviour for mercerization of single kenaf fiber. *Malaysian J Fundament Appl Sci* 14(4):437–439
17. “Standard Test Method for Tensile Strength and Young’s Modulus for High-Modulus Single-Filament Materials.” [Online]. Retrieved from www.astm.org
18. BS EN 12350–2 (2009) Testing fresh concrete—Part 2
19. ASTM C597–09 (2010) Standard test method for pulse velocity through concrete. In: Annual book of ASTM standards, American Society for Testing and Materials, pp 1–4
20. BS EN 12390–3 (2009) Testing hardened concrete - Part 3 : Compressive strength of test specimens
21. Silva G, Kim S, Bertolotti B, Nakamatsu J, Aguilar R (2020) Optimization of a reinforced geopolymer composite using natural fibers and construction wastes. *Constr Build Mater* 258:119697. <https://doi.org/10.1016/j.conbuildmat.2020.119697>
22. Aruntaş HY, Cemalgil S, Şimşek O, Durmuş G, Erdal M (2008) Effects of super plasticizer and curing conditions on properties of concrete with and without fiber. *Mater Lett* 62(19):3441–3443. <https://doi.org/10.1016/j.matlet.2008.02.064>
23. Dumne SM (2014) Effect of superplasticizer on fresh and hardened properties of self-compacting concrete containing fly ash. *Am J Eng Res (AJER)* 03:205–211. Retrieved from www.ajer.org
24. Awal ASMA, Mohammadhosseini H (2016) Green concrete production incorporating waste carpet fiber and palm oil fuel ash. *J Clean Prod* 137:157–166. <https://doi.org/10.1016/j.jclepro.2016.06.162>
25. Jithendra C, Elavenil S (2019) ScienceDirect Role of Superplasticizer on GGBS based Geopolymer Concrete under ambient curing. *Mater Today Proc* 18:148–154. <https://doi.org/10.1016/j.matpr.2019.06.288>
26. Wigestika P, Jaya Ekaputri J (2016) Addition of superplasticizer on geopolymer concrete. 11(24) [Online]. Retrieved from www.arpnjournals.com
27. Sharma S Influence of superplasticizer on strength of concrete.
28. Park S, Pour-Ghaz M (2018) What is the role of water in the geopolymerization of metakaolin? *Constr Build Mater* 182:360–370. <https://doi.org/10.1016/j.conbuildmat.2018.06.073>

Investigation on the Effect of Pulverized Black Tea Waste (PBTW) and Eggshell Powder (ESP) as Partial Replacement of Cement on the Mechanical Properties of Normal Weight Concrete



Kreezel Lyra Agcaoili, Myra Alvarez, Khaira Zarene Annani, Czarina Erika Lopez, Mark Clinton Salayo, Darrell Jed Vertucio, and Cresencia Vahdanipour

Abstract Pollution in the environment and the relatively high cost of solid waste disposal have been a paramount concern all throughout the world. This concern prompts the researchers to recycle black tea waste and eggshells. The purpose of this paper is to study Pulverized Black Tea Waste (PBTW) and Eggshell Powder (ESP) as a partial replacement for cement. The proponents used M20 Grade Concrete with a strength of 20 MPa on the 28th day of curing. Different concrete mixtures containing five replacement levels of cement were carried out with (2.5, 5, 7.5, 10, and 12.5% by weight of) PBTW and ESP (by 12.5, 10, 7.5, 5, and 2.5%). The compressive strength, split-tensile strength, and flexural strength tests were used to show the effect of PBTW and ESP on the mechanical properties of concrete. Results indicated that 2.5% of PBTW and 12.5% of ESP slightly increased the compressive strength of the concrete by 3.11%. In contrast, PBTW and ESP show a significant decrease in Split-Tensile Strength and Flexural Strength compared to the controlled sample ranging from 36.74–49.50% to 16.66–38.91% respectively.

Keywords Pulverized black tea waste · Eggshell powder · Compressive strength · Split tensile strength · Flexural strength

K. L. Agcaoili · M. Alvarez · K. Z. Annani · C. E. Lopez · M. C. Salayo · D. J. Vertucio · C. Vahdanipour (✉)
College of Engineering, National University-Manila, Manila, Philippines
e-mail: cmvahdanipour@national-u.edu.ph

© The Author(s), under exclusive license to Springer Nature Singapore Pte Ltd. 2024
M. Casini (ed.), *Proceedings of the 3rd International Civil Engineering and Architecture Conference*, Lecture Notes in Civil Engineering 389,
https://doi.org/10.1007/978-981-99-6368-3_3

1 Introduction

Concrete is the most common construction material used by humans [1]. It is a blended mix comprising essentially of binder cement, water, sand, and coarse aggregate [2]. The comprehensive use of concrete has increased the worldwide depletion of the earth's raw materials [3].

Cement is a grey powdery substance made by calcining lime and clay, it is mixed with water to form mortar or mixed with sand, gravel, and water to make concrete [4]. It serves as a glue that strengthens the structure. Cement produces greenhouse gas (CO₂) that affects the environment [2, 3]. About 7% of CO₂ is released into the atmosphere during cement production, which has a negative influence on ecology and the future of human beings [5], which contributes to global warming. The use of alternative materials in the production of construction materials is one of the measures to address the problems [3]. For this reason, extensive research, and development work towards exploring new ingredients for producing sustainable and environment-friendly construction materials.

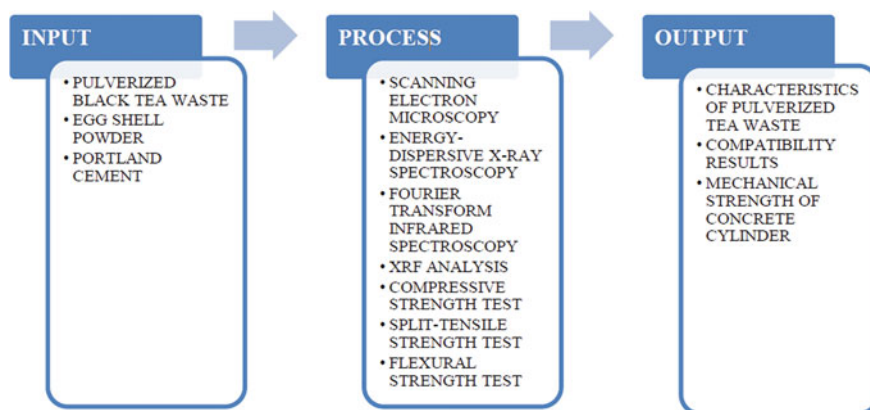
Over the next decade, the global demand for tea will continue to grow. Worldwide tea production has risen drastically to meet this growing demand which in turn produced an enormous amount of waste that causes serious environmental problems [6]. However, very limited studies have been found regarding the use of tea waste as a replacement for cement [7]. On the other hand, eggshells are bio-waste material from bakeries and fast-food chains that are disposed of in landfills, which contributes to environmental pollution [8]. From October to December 2020, the Philippine Statistics Authority (PSA) estimated that the total chicken egg production was 154.87 thousand metric tons which are 0.4% higher than the previous year's quarter output [9]. The chemical composition of Eggshell shows Carbon oxide (CaO) as its main component [8]. This experimental study assessed the use of Pulverized Black Tea Waste and Egg Shell Powder as a partial replacement for cement to determine its effect on the mechanical properties of concrete. Moreover, surface morphological characterization of composite samples was carried out to investigate the effect of integrating black tea waste and eggshell powder.

2 Materials and Methods

The method of research used for this study is experimental. The use of Black Tea Waste and Eggshell powder as a partial replacement to cement would comply with the standard on the compression strength, split tensile strength, and flexure strength of normal-weight concrete. The researchers utilized M20 grade concrete with a 1:1.5:3 ratio; the varying percentage replacement is shown in Table 1. This experiment produced three specimens for each percentage replacement. The curing days were 7, 21, and 28 days. The control sample would be the mixture without PBTW and ESP.

Table 1 Percentage of PBTW and eggshell powder

Mix name	Replacement by percentage		Total cement replacement (%)
	ESP (%)	PBTW (%)	
Control sample	0	0	0
M1	12.5	2.5	15
M2	10	5	15
M3	7.5	7.5	15
M4	5	10	15
M5	2.5	12.5	15

**Fig. 1** Conceptual framework of the study

Several tests were performed to determine the mechanical properties of the concrete samples such as the Slump Cone Test as per ASTM C143, the Compressive Strength Test to determine the compressive strength of the concrete in accordance with ASTM C39, Split Tensile Strength to determine the splitting-tensile strength of the concrete as per ASTM C496, and Flexural Strength Test as per ASTM C78. Shown in Fig. 1 is the conceptual framework that shows the flow, inputs as well as outputs of the study.

2.1 Preparation of Materials

Black Tea Waste and eggshells were collected from Macao Imperial Tea at SM Cabanatuan and from a local eatery. The collected Black Tea Waste and eggshells were rinsed thoroughly with tap water until all unnecessary substances were removed, especially the membrane within the eggshell to avoid a rotten smell. Tea wastes and

eggshells were sun-dried for several days to remove all the moisture [10]. After drying, the materials were crushed, grinded, and sieved through a No. 200 sieve.

First Phase: Characterization. X-Ray Fluorescence Analysis of pulverized black tea waste and eggshell powder samples was carried out to determine their chemical composition at NASAT Labs Muntinlupa. Scanning Electron Microscope (SEM) which provides detailed high-resolution images of the sample by raftering a focused electron beam across the surface and detecting secondary or backscattered electron signals.

Second Phase: Test of Concrete Cylinder. The compressive strength test and split tensile strength test of the concrete were performed at Mapolcom Incorporated in Norzagaray, Bulacan. The compressive strength test is the measure of the concrete's ability to resist the load that tends to compress it. Split Tensile Strength Test is conducted to determine the ability of concrete to resist cracking or breaking under tension. The samples were made using a concrete mixer. After the slump cone test, the concrete is placed in the cylindrical concrete molds leaving it for at least 24 h for hardening. The hardened concrete was removed from the mold and is placed in the water for curing. The proponents conducted 3 samples for each mixture. Depicted in Fig. 2 show different mechanical tests performed on the concrete cylinder samples (a) split tensile strength and (b) compressive strength test.

Third Phase: Test of Concrete Beams. The flexural strength test was carried out on the beams at 7, 21, and 28 curing days to determine the flexural strength. The size of the beams is $150 \times 150 \times 500$ mm. Flexural Strength Test is used to determine the bending properties of a material. The results are calculated and expressed as the modulus of rupture.

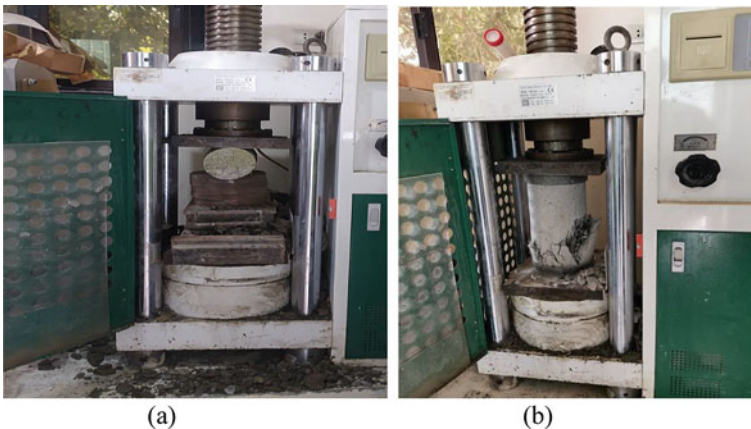


Fig. 2 Mechanical tests performed on concrete cylinder samples

Table 2 Chemical composition of pulverized black tea waste (PBTW)

Element	Cement (%)	PBTW (%)	ESP (%)
CaO	62.10	66.30	91.37
SiO ₂	22.20	0.76	0.0
Al ₂ O ₃	4.2	0.06	2.21
Fe ₂ O ₃	3.9	4.65	0.04
MnO	3.3	6.69	0.0
SO ₃	1.9	12.02	5.24

3 Results and Discussion

3.1 Properties of Materials Used

The chemical compounds reflected in Table 2 are supported by the basic chemical composition of PBTW and ESP which shows traced amounts of Calcium, Oxygen, Magnesium etc.

The high percentage composition of Calcium Oxide (CaO) means that PBTW and ESP can partially replace cement in concrete because of its similarity with lime.

3.2 Result of Tests of Concrete Specimen

The slump values for the concrete showed a continuous rise when the percentage replacement of Pulverized Black Tea Waste increased, and Egg Shell Powder decreased. The porosity and irregularity of the surface of the substituting materials is the reason for the additional water absorption properties of the concrete mixture. Moreover, the results of the slump test and its effect on the compressive strength can be seen by the increasing trend of compressive strength, split tensile strength, and flexural strength of the specimen as depicted in Tables 3, 4, and 5 respectively. Shown in Figs. 3 and 4 are the summary of compressive strength test results of PBTW and ESP.

The tests results proved that concrete mixtures containing 2.5% PBTW and 12.5% ESP shows a greater Compressive Strength and Split-Tensile Strength among the mixture with partial substitution. The M1 mixture has a compressive strength of 21.91 MPa and a split-tensile strength of 2.35 MPa. For the flexural strength test on beam samples, results are shown in Fig. 5.

From the results of testing when it comes to flexural strength, the M2 sample has the highest strength in all curing days. Generally, the M1 mixture shows greater strengths and performed best among the other mixtures. The compressive strength, split-tensile strength, and Flexural Strength tests resulted in different average strengths per specimen. This verifies that the addition of powdered eggshells and pulverized black tea waste influenced the strength of normal concrete. This may

Table 3 Summary of the compressive strength test results of PBTW and ESP

Design name	Curing days		
	7 days (MPa)	21 days (MPa)	28 days (MPa)
Control sample	16.76	19.86	21.25
M1	15.42	18.09	21.91
M2	15.24	15.68	21.14
M3	15.47	15.79	21.44
M4	15.92	16.00	21.83
M5	14.77	14.94	20.01

Table 4 Summary of the split tensile strength test results of PBTW and ESP

Design name	Curing days		
	7 days (MPa)	21 days (MPa)	28 days (MPa)
Control sample	2.38	3.65	3.72
M1	1.91	2.16	2.35
M2	1.71	1.84	2.02
M3	1.69	1.75	2.01
M4	1.70	1.89	2.02
M5	1.55	1.72	1.88

Table 5 Summary of the flexural strength of PBTW and ESP

Design name	Curing days		
	7 days (MPa)	21 days (MPa)	28 days (MPa)
Control sample	4.07	4.74	5.81
M1	3.55	4.31	4.74
M2	4.20	4.36	4.84
M3	4.20	4.20	4.41
M4	3.01	3.44	3.55
M5	3.23	3.57	3.57

mean that certain combinations tend to decrease strength development. It seemed that it is more effective at an M1 mixture of 2.5% PBTW and 12.5% ESP.

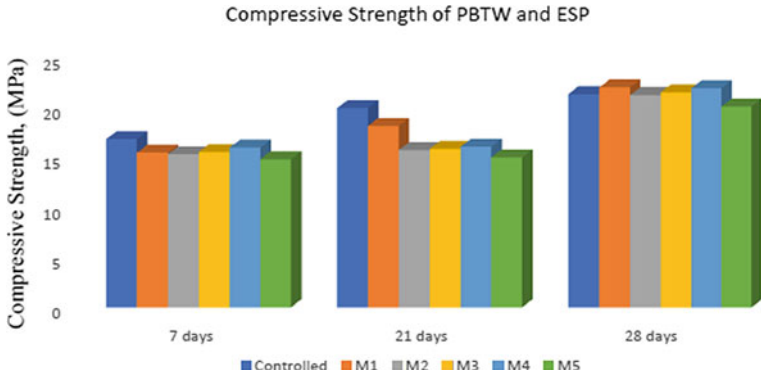


Fig. 3 Compressive strength test results of PBTW and ESP

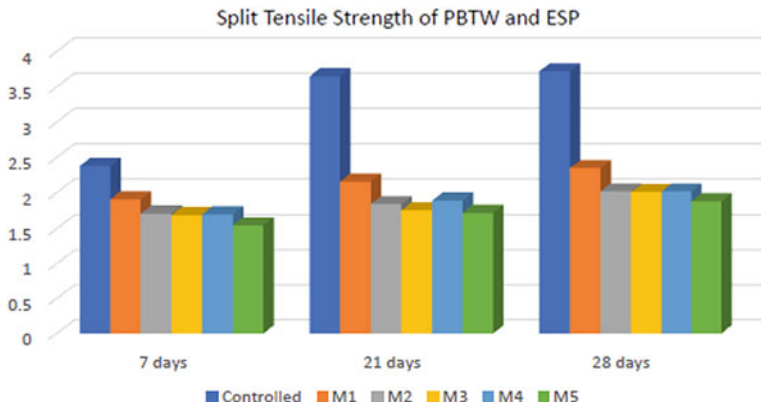


Fig. 4 Split tensile strength test results of PBTW and ESP

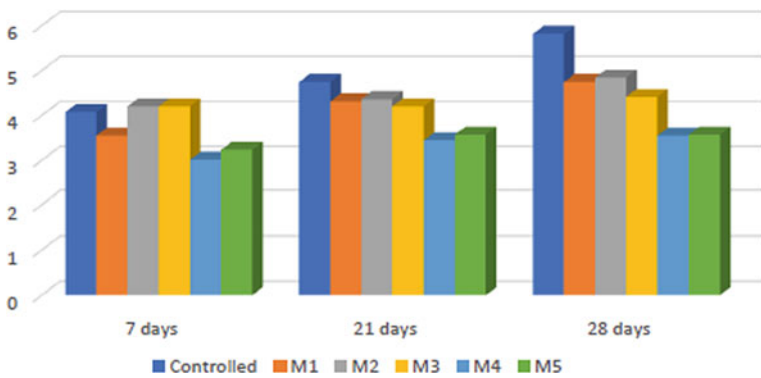


Fig. 5 Flexural strength of PBTW and ESP

3.3 SEM Analysis of Controlled and Composite Samples

The result of SEM analysis of powdered controlled and composite samples was depicted in Figs. 6 and 7, respectively. The difference in surface morphology is apparent. It is observable that the interlocking grains of the controlled sample is much smaller compared to that of the concrete containing PBTW and ESP.

It was already established that PBTW and ESP are porous materials. Because of this, the resulting concrete has bigger grains which signifies a more porous surface. The concrete without substitution has a more compact binding.

Fig. 6 Controlled sample

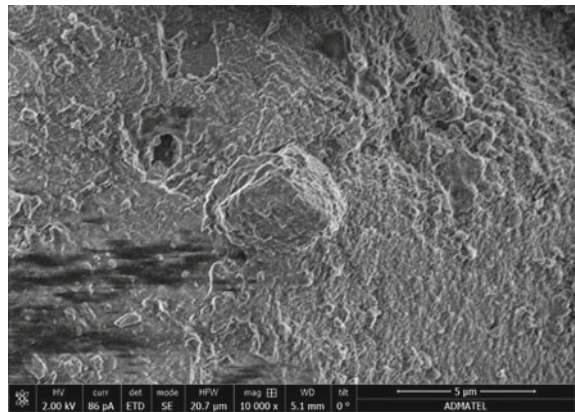
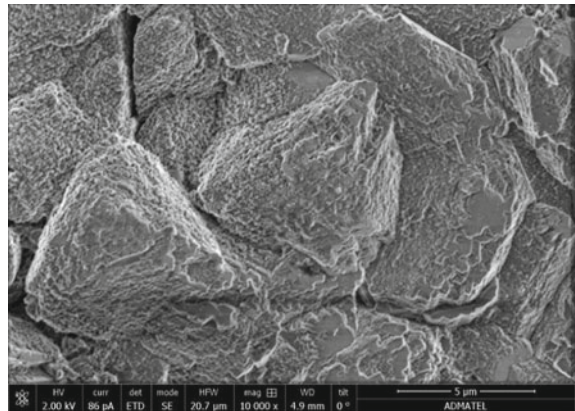


Fig. 7 Sample containing PBTW and ESP



4 Conclusion

The addition of PBTW and ESP slightly increased the compressive strength of concrete. The usage of PBTW and ESP affects the workability of concrete mixture. The suitable percentage ratio of PBTW and ESP are the peak value that passed the M20 grade concrete. M1 specimen has the overall desirable result for the partially replaced concrete mixture of PBTW and ESP with a Compressive strength at 21.91 MPa on the 28th day, Tensile Strength at 2.35 MPa on the 28th day and flexural strength is 4.84 MPa which is M2 specimen on the 28th day. The overall desirable design mixture is M1 with 2.5% PBTW and 12.5% ESP.

Acknowledgements The authors express their gratitude to the faculty and staff of the Civil Engineering Department of the National University (NU) for all their help and support. It is genuine pleasure to express our deep sense of gratitude to our thesis coordinator, Engr. Allan Alzona, for guiding us to get through this project, and our thesis adviser, Engr. Cresencia M. Vahdanipour, for her dedication and interest above all, and her overwhelming attitude, to guiding us to be responsible for completing our research. Gratitude is also given to our panelists; Engr. Allan R. Alzona, Engr. Nioro G. Furiscal, and Engr. Franz D. Santos for helping us improve our thesis. We would also like to thank the following: Macao Imperial Tea, Nanotech Analytical Services and Training (NASAT), MAPOLCOM Incorporated, N-Precision Construction Materials Testing Center, and Advanced Device and Materials Testing Laboratory (ADMATEL), for their help in the completion our data and/or for providing the materials needed for the cement replacement research. Our sincerest appreciation is also given to our family and friends without them, none of this would indeed be possible. Above all to God, deepest gratitude for the knowledge and wisdom that he bestowed on us in making this study possible.

References

1. Adesina A (2020) Recent advances in the concrete industry to reduce its carbon dioxide emissions. *Environ Challen* 1. <https://doi.org/10.1016/j.envc.2020.100004>
2. Hamid Z, Rafiq S (2020) A comparative study on strength of concrete using wood ash as partial replacement of cement. In: IOP conference series: materials science and engineering, vol 955. <https://doi.org/10.1088/1757-899X/955/1/012043>
3. Daneti SB, Tam CT (2020) Sustainability of concrete constructions: the role of materials and practices in emerging trends in civil engineering. *Lecture Notes Civil Eng* 61:381–395
4. Gwarah LS, Akatah BM, Onungwe I, Akpan PP (2019) Partial replacement of ordinary portland cement with sawdust ash in concrete. *Curr J Appl Sci Technol* 1–7. <https://doi.org/10.9734/cjast/2019/v32i630036>
5. Elahi MMA, Hossain MM, Karim MR, Zain MFM, Shearer C (2020) A review on alkali-activated binders: Materials composition and fresh properties of concrete. *Construct Build Mater* 260:10. <https://doi.org/10.1016/j.conbuildmat.2020.119788>
6. Debnath B, Haldar D, Purkait MK (2021) Potential and sustainable utilization of tea waste: a review on present status and future trends. *J Environ Chem Eng* 9(5). <https://doi.org/10.1016/j.jece.2021.106179>
7. Hilal N, Hadzima-Nyarko M (2021) Improvement of eco-efficient self-compacting concrete manufacture by recycling high quantity of waste materials. *Environ Sci Pollut Res* 28(38):53282–53297. <https://doi.org/10.1007/s11356-021-14222-9>

8. Hamada HM, Tayeh, Al-Attar A, Yahaya FM, Muthusamy K, Humada AM (2020) The present state of the use of eggshell powder in concrete: a review. *J Build Eng* 32:2020. <https://doi.org/10.1016/j.jobe.2020.101583>
9. “2_[ONSrev-cleared] SR_Q4 2020 Chicken Egg Situation Report_signed” (2020) Reterived from <https://psa.gov.ph/content/chicken-egg-situation-report-october-december-2020> Accessed on 21 Feb 2023
10. Beng Wei C, Othman R, Yee Ying C, Putra Jaya R, Shu Ing D, Ali Mangi S (2020) Properties of mortar with fine eggshell powder as partial cement replacement. *Mater Today Proceed* 46:1574–1581. <https://doi.org/10.1016/j.matpr.2020.07.240>

Experimental and Numerical Investigation on Carbon Fiber Reinforced Cement



Chang-Yu Kuo, Ying-Kuan Tsai, and Yeou-Fong Li

Abstract The objective of this study is to enhance the mechanical properties of high-early-strength cement for emergency repair of reinforced concrete infrastructure by incorporating short carbon fibers. The short carbon fibers, with weight ratios of 0.5 to 2.0% and lengths of 12 and 24 mm, were added to the high-early-strength cement and the resulting material was subjected to compressive and impact testing to determine its compressive strength and impact resistance. A micromechanical model was developed based on the results of the compressive testing to estimate the modulus of fiber-reinforced cement paste. The data from the experimental and micromechanical analyses were used as material parameters in a finite-element model, and the behavior of the fiber-reinforced cement under single impact testing was simulated using LS-DYNA.

Keywords Short carbon fiber · High-early-strength cement · Fiber reinforced cement · Impact resistant

1 Introduction

Structural elements and members are often subjected to high energy dynamic loads, which can cause significant damage or even failure. These loads may be transmitted over a short period of time through high impact velocity, or through a high projectile mass with low impact velocity. The type of material damage that occurs depends on the properties of the material and the dominant macroscopic phenomena, and can be classified as brittle, ductile, creep, or fatigue damage.

C.-Y. Kuo (✉) · Y.-K. Tsai

Department of Environmental Information and Engineering, Chung Cheng Institute of Technology, National Defense University, Taoyuan, Taiwan
e-mail: fe236912@gmail.com

Y.-F. Li

Department of Civil Engineering, National Taipei University of Technology, Taipei, Taiwan
e-mail: yfli@mail.ntut.edu.tw

Cementitious materials often experience significant deterioration during high energy impact events, resulting in reduced strength and rapid crack growth in tension. One way to improve the mechanical performance and reduce crack initiation in such materials is to add fibers [1, 2]. Carbon fibers, in particular, offer several benefits for this purpose, including high strength, high temperature resistance, corrosion resistance, better electrical conductivity, and a lower thermal expansion coefficient. The incorporation of carbon fibers into concrete can effectively increase the material's ability to absorb dynamic energy from impact and improve its mechanical performance [3–5].

Structures are often subjected to static and dynamic loads, and the response of different materials to these loads can vary significantly. Fiber-reinforced cementitious materials are widely used in construction, and simulating their behavior under dynamic loading is important. This can be done using computational tools and finite-element software such as ABAQUS, ANSYS, LS-DYNA, and AUTODYN. In this study, various lengths and proportions of short carbon fibers were added to high-early-strength cement and the resulting material was subjected to compressive and impact testing. The modulus of the fiber-reinforced cement was then calculated using micromechanical analysis, and the material's behavior under impact was simulated using LS-DYNA based on the results of the micromechanical analysis.

2 Method

The preparation of the specimens involved dispersing the carbon fibers using a pneumatic and a sieving method, adding a specific weight ratio of short carbon fibers of a certain length, and evenly mixing the well-dispersed fibers with cement in a mixer. The mixing process consisted of dry mixing for a predetermined time followed by wet mixing with the addition of water. The resulting specimens were then subjected to mechanical testing. To estimate the modulus of fiber-reinforced cement paste, a micromechanical model was developed based on the results of the compressive testing. The data from the experimental and micromechanical analyses were used as material parameters in a finite-element model.

2.1 Short Carbon Fiber

The short carbon fibers used in this study were manufactured by Tairylan Division, Formosa Plastics Corporation. Each bundle of the short carbon fibers consists of approximately 12,000 carbon fiber strands, with lengths of 12 and 24 mm, density of 1.81 g/cm³, diameter of 7.0 μm, elongation rate of 2.0%, tensile strength of 4.9 GPa, and elastic modulus of 250 GPa.

2.2 High-Early-Strength Cement

The cement used in the carbon-fiber-reinforced cement in this study was manufactured by Denka Company. When mixed with water at an appropriate water-cement ratio, the cement exhibited a strength of 28 MPa after 1 day.

3 Results

3.1 Compressive Testing

Prior to incorporating fibers into cement, compressive testing was conducted on cement paste specimens without fibers to establish a baseline. The average compressive strength of the high-early-strength cement specimens was 27.37 MPa after 3 h, 36.38 MPa after 1 day, and 50.74 MPa after 7 days. To prevent agglomeration of the fibers during the mixing process, an appropriate dispersion method was used before adding the fibers to the cementitious material.

The compressive strength of carbon-fiber-reinforced cement specimens containing 12 mm short carbon fibers with a weight percentage of 6.25‰ (12.2%), 12.50‰ (16.5%), and 18.75‰ (21.9%) was found to be higher than that of cement specimens without short carbon fibers after 7 days. The strength of the carbon-fiber-reinforced cement was also found to be increased by 28–33 and 17–30% after 3 h and 1 day, respectively, compared with the strength of cement without fibers. Among the specimens containing short carbon fibers, the one with a weight ratio of 18.75‰ performed the best in terms of strength. The compressive strength at different ages is shown in Fig. 1.

The compressive strength of carbon-fiber-reinforced cement specimens containing 24 mm short carbon fibers with a weight percentage of 6.25‰ (17.7%), 12.50‰ (23.9%), and 18.75‰ (26.8%) was found to be higher than that of cement specimens without short carbon fibers after 7 days. The strength of the carbon-fiber-reinforced cement was also found to be increased by 31–40 and 22–29% after 3 h and 1 day, respectively, compared to the strength of cement without fibers. Among the specimens containing fibers, the one with a weight ratio of 18.75‰ resulted in the highest compressive strength. The compressive strength at different ages is shown in Fig. 2.

Based on the results of the compressive testing, it was observed that most of the specimens exhibited shear failure mode. When the weight ratio of carbon fibers was the same, the distribution of fibers in the cement paste was more uniform for the 12 mm carbon fibers. The experimental results showed that the best performance in the compressive testing was achieved with a weight percentage of 18.75‰ of carbon fibers for the carbon-fiber-reinforced cement.

The incorporation of carbon fibers into the cementitious material effectively enhanced the chemical bonding between the fibers and the cement paste, leading to an

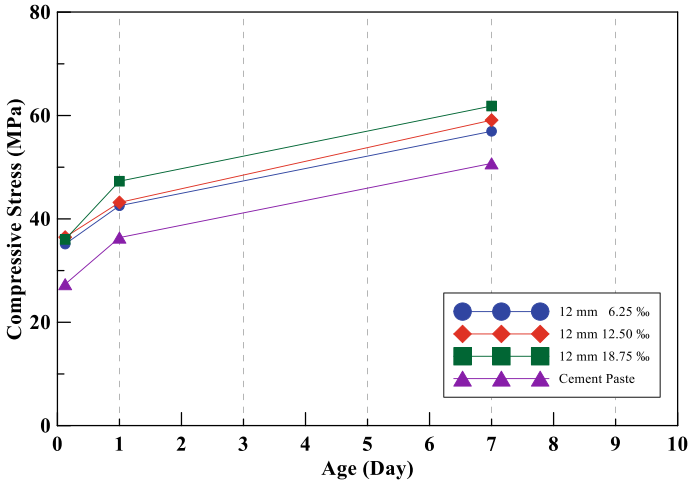


Fig. 1 The compressive strength for the specimens with 12 mm carbon fiber

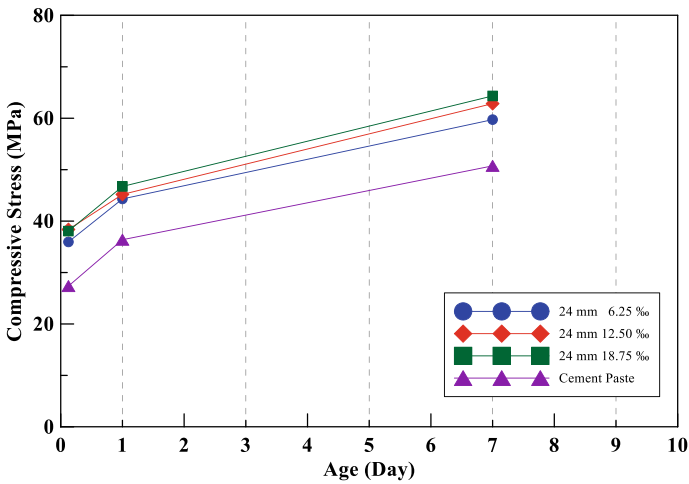


Fig. 2 The compressive strength for the specimens with 24 mm carbon fiber

increase in strength at an early age when the high-early-strength cement had not yet fully developed its resistance. This finding is particularly relevant for patching engineering applications, where early-age strength is crucial. The addition of short carbon fibers to high-early-strength cement was found to increase the strength by approximately 30% at an early age and 25% at a later age. This demonstrated the potential of using carbon fibers to improve the mechanical performance of high-early-strength cement in emergency repair of reinforced concrete infrastructures.

3.2 Micromechanical Analysis

The modulus is a significant material property that is frequently encountered in engineering applications involving cementitious composites. The overall modulus of such composites can be estimated using micromechanical theory, which takes into account the bonding between the matrix and the fibers. The interfacial transition zone (ITZ) plays a crucial role, as it represents the region where the matrix and fibers intersect. The ITZ is often considered to be the weakest zone in terms of fracture behavior, as it is where cracks typically first appear, particularly near aggregates. One approach to defining the elastic field is the Mori–Tanaka method, which is based on Eshelby’s solution for the elastic field around a fiber in an infinite, homogeneous, isotropic elastic medium. However, the Mori–Tanaka method assumes that the fibers are slender cylinder inclusions, which may not accurately represent the actual shape of the fibers in a cementitious composite. To address this limitation, the fibers were approximated as spherical fine aggregate inclusions in order to make the calculation more tractable, as depicted in Fig. 3. Continuum mechanics deals with idealized composite materials consisting of inclusions embedded in a matrix. It assumes that the inclusions are distributed throughout an infinite zone. However, in reality, the interfacial zone between the inclusions and matrix is not uniform. To account for this variability, the representative volume element (RVE) was employed to model the composite material. The referenced micromechanical modeling, a n-layered spherical inclusion embedded [6] in an infinite matrix, is illustrated in Fig. 4.

When the RVE is subjected to hydrostatic pressure, the displacements in all phases can be expressed in Eq. (1). Furthermore, the stress on the surface of each medium can be expressed as Eqs. (2–4) by Hooke’s law.

$$u_{r,j}(r) = F_i r + \frac{G_i}{r^2} \tag{1}$$

where F_i and G_i are constants and r is the radius from each phase to the center of the RVE.

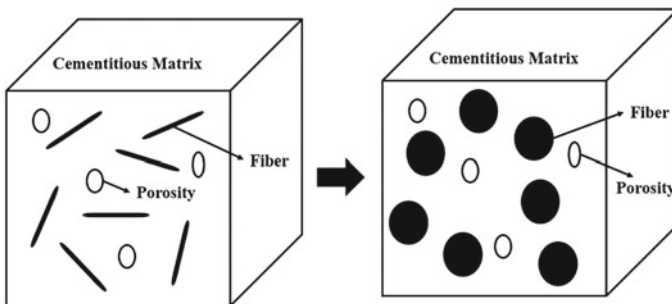


Fig. 3 The condition in RVE

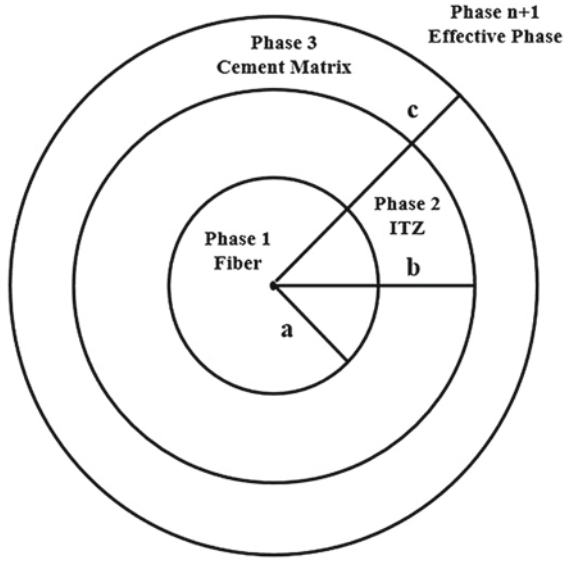


Fig. 4 The RVE of phase $n + 1$

$$\sigma_{rr,i} = 3k_i F_i - \frac{4\mu_i}{r^3} G_i \quad (2)$$

$$\sigma_{\theta\theta,i} = \sigma_{\phi\phi,i} = 3k_i F_i + \frac{2\mu_i}{r^3} G_i \quad (3)$$

$$\sigma_{r\theta} = \sigma_{r\phi} = \sigma_{\theta\phi} = 0 \quad (4)$$

The stress also can be presented in the form of a matrix and the coefficients can be obtained through the boundary conditions at the interface between the phases.

$$\vec{V}_i = \begin{bmatrix} F_i \\ G_i \end{bmatrix} \quad (5)$$

$$J_i(r) = \begin{bmatrix} r & \frac{1}{r^2} \\ 3k_i & -4\frac{\mu_i}{r^3} \end{bmatrix} \quad (6)$$

The relationship resulted from the continuity of $\sigma_{rr,k}$ and $U_{r,k}$ at the interface $r = r_i$ between phases (i) and $(i + 1)$ may be written in the form of a matrix. To avoid singularities at the origin, the constant F_{n+1} is determined by the applied state of hydrostatic pressure at infinity. In the case of the RVE with zero G_i and external displacement, F_{n+1} is equal to the macrostrain, allowing for the calculation of the spherical tensor of the original phase. The same method can be used to calculate the simple shear for the RVE.

$$J_i(r)\vec{V}_i = J_{i+1}(r)\vec{V}_{i+1} \quad (7)$$

Furthermore, the $n + 1$ phase model depicted in Fig. 4, consists of an unbounded composite body V embedded in a homogeneous elastic matrix, as well as idealized bounded inhomogeneous elastic ellipsoidal inclusions. According to the energy law, the effective bulk modulus associated with $n + 1$ phase can be expressed in the form of k_n^{eff} and k_{n-1}^{eff} .

$$k_n^{eff} = k_n + \frac{\frac{r_{n-1}^3}{r_n^3}}{\frac{1}{k_{n-1}^{eff} - k_n} + \frac{3(r_n^3 - r_{n-1}^3)}{r_n^3} \frac{1}{3k_n + 4\mu_n}} \quad (8)$$

To estimate the effective modulus E of elasticity on the surface, this study utilized a spherical container subject to uniform internal or external pressure. The theory of elasticity as proposed by Timoshenko was utilized to obtain the displacement at each phase surface. For the homogeneous medium containing an inclusion under applied traction conditions, the strain energy was determined using Eqs. (9–11). The effective modulus $E_0(a)$, was then calculated using the determined strain energy.

$$U = U_0 + \frac{1}{2} \int_{S_i} (\sigma_i^0 u_i - \sigma_i u_i^0) ds \quad (9)$$

$$U = U_0 \quad (10)$$

$$\int_{S_i} (\sigma_i^0 u_i - \sigma_i u_i^0) ds = 0 \quad (11)$$

The Eshelby's Tensor S_{ijkl} in the Cartesian coordinate system can be calculated for the case where the matrix is unbounded and the inclusion is spherical:

$$S_{ijkl} = \frac{5\nu - 1}{15(1 - \nu)} \delta_{ij} \delta_{kl} + \frac{4 - 5\nu}{15(1 - \nu)} (\delta_{ik} \delta_{jl} + \delta_{il} \delta_{jk}) \quad (12)$$

The functionals are stationary when the eigenstrain and eigenstress field, denoted as ε^* and σ^* , respectively, are in a state of corresponding consistency. The consistency condition for the eigenstrain field ε^* and eigenstress σ^* is shown below:

$$\{D'(x) - D\}^{-1} : \varepsilon^*(x) + (\Lambda : \varepsilon^*)(x) - \sigma^0 = 0 \quad (13)$$

$$\{C'(x) - C\}^{-1} : \sigma^*(x) + (\Gamma : \sigma^*)(x) - \varepsilon^0 = 0 \quad (14)$$

where Λ and Γ are the integral operators that are derived from the boundary condition in which the traction and surface displacement are zero. C and D represent the elasticity and compliance tensors, respectively. When the C' - C matrix is positive definite for any arbitrary eigenstrain field e^* and eigenstress field s^* , the average complementary strain energy W_c and W can be calculated using the follow equations:

$$W'_c - W_c \geq \frac{1}{2} \langle e^* : \{(D' - D)^{-1} + \Lambda\} : e^* \rangle - \sigma^0 : \langle e^* \rangle \quad (15)$$

$$W' - W \leq \frac{1}{2} \langle s^* : \{(C' - C)^{-1} + \Gamma\} : s^* \rangle - \langle s^* \rangle : \varepsilon^0 \quad (16)$$

where W'_c and W' represent the comparison average complementary strain energy and strain energy, respectively. σ^0 and ε^0 denote the overall stress and strain, respectively. When the D' - D matrix is positive definite for an arbitrary eigenstrain field e^* and eigenstress field s^* , the average complementary strain energy W_c and W can be calculated as below:

$$W'_c - W_c \leq \frac{1}{2} \langle e^* : \{(D' - D)^{-1} + \Lambda\} : e^* \rangle - \sigma^0 : \langle e^* \rangle \quad (17)$$

$$W' - W \geq \frac{1}{2} \langle s^* : \{(C' - C)^{-1} + \Gamma\} : s^* \rangle - \langle s^* \rangle : \varepsilon^0 \quad (18)$$

3.3 Simulation

This study investigated the impact behavior of fiber-reinforced cement under impact loading using LS-DYNA simulations. First, the uniaxial compressive testing was simulated based on experimental data and micromechanical analysis. Then, a single impact testing was analyzed using a setup comprising a steel ball, carbon-fiber-reinforced cement specimen, sand, and ground, as depicted in Fig. 5.

Because cementitious materials have complex responses to impact loads, there have been several constitutive material models available in finite-element software, such as CSCM, EPDC, KCC, Soil Concrete, and Winfrith Concrete, which are commonly used for impact simulations. This study focuses specifically on the continuous surface cap model (CSCM). The steel ball struck the specimen with varying velocity, based on the weight of the steel ball and total energy. The contact between the steel ball and specimen was modeled using AUTOMATIC SURFACE TO SURFACE. The material model for the fiber-reinforced cement specimen was CSCM, which was derived from the results of micromechanics analysis, while the sand was modeled using FHWA SOIL material model.

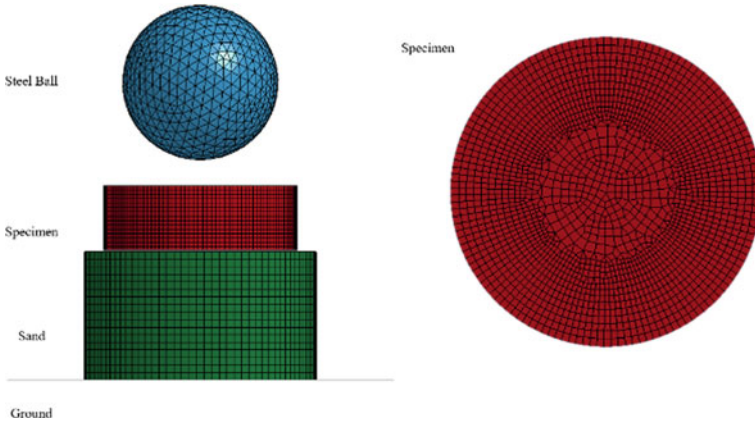


Fig. 5 Setup of the finite-element model

The results showed in Fig. 6 that impact forces are correlated with the impact energy, and the 24 mm fiber-reinforced cement specimen was effective at absorbing energy from the impact.

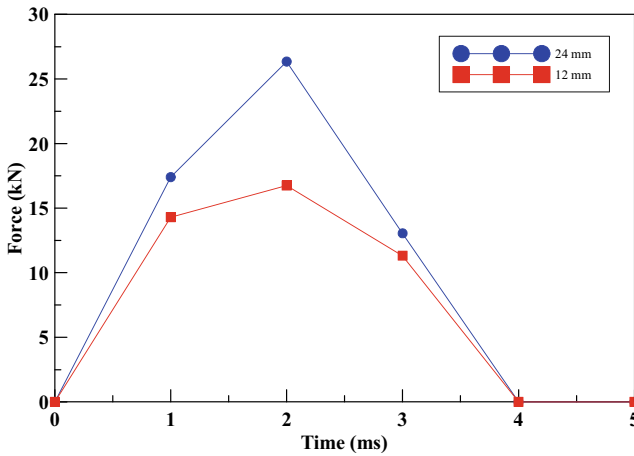


Fig. 6 The forces applied on the fiber-reinforced cement specimens in analysis of single impact testing

4 Results

1. In response to further improving the performance of high-early-strength cement, the results from this study suggests that incorporating short carbon fibers to high-early-strength cement could increase its compressive strength by approximately 30% at early age and about 25% increase at later ages.
2. The compression test suggested that adding weight ratio of 18.75% 24 mm carbon fiber resulted in the greatest strength among the weight proportions and fiber lengths investigated in this study.
3. Single impact testing showed that the impact forces are related to the impact energy and the 24 mm fiber-reinforced cement specimen exhibited strong impact resistance, making it suitable for use in applications where impact resistance is a concern.

Funding This research was funded by the Ministry of Science and Technology of Taiwan government, under contract No. MOST 107-2221-E-027-042.

References

1. Eftekhari M, Mohammadi S (2016) Multiscale dynamic fracture behavior of the carbon nanotube reinforced concrete under impact loading. *Int J Impact Eng* 87:55–64
2. Zhang D, Tu H, Li Y, Weng Y (2016) Effect of fiber content and fiber length on the dynamic compressive. *Constr Build Mater* 328:127024
3. Li Y-F, Lee K-F, Ramanathan GK, Cheng T-W, Huang C-H, Tsai Y-K (2021) Static and dynamic performances of chopped carbon-fiber-reinforced mortar and concrete incorporated with disparate lengths. *Materials* 14(4):972
4. Wu Z, Shi C, He W, Wang D (2017) Static and dynamic compressive properties of ultra-high performance concrete (UHPC) with hybrid steel fiber reinforcements. *Cem Concr Compos* 79:148–157
5. Li YF, Ramanathan GK, Syu JY, Huang CH, Tsai YK (2022) Mechanical behavior of different fiber lengths mix-proportions carbon fiber reinforced concrete subjected to static, impact, and blast loading. *Int J Protect Struct*
6. Thilakarathna PSM, Kristombu BKS, Mendis P, Lee H, Chandrathilaka ERK, Vimonsatit V (2022) Multiscale modelling framework for elasticity of ultra high strength concrete using nano/microscale characterization and finite element representative volume element analysis. *Constr Build Mater* 327:126968

Influence of Synthesized Nanosilica on Properties of Wood Ash Cement Mortar



B. D. Ikotun and A. A. Raheem

Abstract The effect of incorporating synthesised nanosilica (NS) on selected properties of wood ash (WA) cement mortar was experimentally studied. The mortar was prepared by adding 1, 2, and 3% NS by weight of binder. The binder in this case is referred to as cement alone and cement replaced with 10% WA. A constant water-binder ratio of approximately 0.4 was maintained for cement pastes samples and 0.5 for mortar samples. Control sample was maintained as sample without the addition of WA nor NS. The tests performed are, setting times, flexural strength and compressive strength. The results showed reduction in setting times of WA cement mortar with 1 and 2% NS. Increased in flexural and compressive strength compared to the control sample were observed with WA cement mortar samples with 2% NS.

Keywords Nanosilica · Wood ash · Mortar · Setting times · Flexural strength · Compressive strength

1 Introduction

Since the invention of Portland cement by Joseph Aspdin through a patent in 1842, there has been extensive research on the material to further improve its development. The use of cement-based materials such as concrete and mortar has contributed tremendously to modern building and civil engineering construction. Cement producing industries consume a lot of energy and have a high rate of carbon dioxide (CO₂) emissions. It was reported by Flower and Sanjayan [1] that production of 1.0 tonne of Portland cement emits 0.8 tonne of CO₂ into the environment. This greenhouse gases emission leads to increase in temperature and causes global warming [2]. Several attempts have been made to reduce energy consumption and

B. D. Ikotun (✉)

Department of Civil Engineering, University of South Africa, Johannesburg 1710, South Africa
e-mail: ikotubd@unisa.ac.za

A. A. Raheem

Department of Civil Engineering, Ladoko Akintola University of Technology, Ogbomoso, Nigeria

CO₂ emissions in cement industry. One way that is gaining ground now is partial replacement of Portland cement with supplementary cementitious materials (SCM), some SCM that had been studied are fly ash [3, 4]; rice husk ash [5, 6]; corn cob ash [7]; rice straw ash [8] and wood ash [9, 10]. Wood ash (WA) is obtained by incinerating wood or timber at temperature of 650–700 °C in about 8 h. Several researchers had worked on the incorporation of WA in concrete and mortar [10–12]. Findings from these studies indicated that use of WA as partial substitution for cement in concrete and mortar has adverse effects on workability and early strength development of the materials, especially at high percentage replacement level (>10%). Dawood et al. [13], alluded to the fact that wood ash can be used in the same manner as fly ash and silica fume in concrete. Hence, there will be needed to improve its effect on concrete's workability and early strength.

The advent of nanotechnology and use of nanoparticles in cement-based materials has played a major role in improving the performance of concrete and mortar incorporating pozzolanic materials like fly ash, rice husk ash and WA. This is attributed to the nano-scale size of the materials, which makes them highly reactive and act as fillers in the pores of concrete and mortar thereby refining their structural characteristics. More than a few nanomaterials had been used in cement-based products amongst which are nanosilica, nano-TiO₂, nano-Al₂O₃, nano-Fe₂O₃ and carbon nanotubes [14–16]. It was reported however that nanosilica is the most widely used nanoparticles in concrete and mortar due to its high pozzolanic activity with calcium hydroxide released during cement hydration [17].

Nanosilica had been shown to improve the properties of concrete and mortar in the fresh and hardened state as well as in short and long term [18–20]. According to Laím et al. [21], nanosilica enhances the microstructure of cement, which improves the pozzolanic reaction. However, the availability and cost of commercially produced nanosilica and other nanomaterials is a source of concern in Africa. This challenge is being addressed through green synthesis of nanoparticles. The biogenic synthesis of silver nanoparticles using pod extract of *cola nitida* and its application as an additive in paint was studied by Lateef et al. [22]. Also, Emeka et al. [23] evaluated the antibacterial activities of synthesized silver nanoparticles using pineapple. Literature is however scarce on the application of synthesized nanosilica in concrete and mortar. Therefore, this study investigated the characteristics of WA cement mortar containing synthesized nanosilica.”

2 Material and Methods

2.1 Materials

The materials used in this study were: Suretech Premium Specialist Cement (CEM 1, Grade 52.5); the silica sand used are locally produced, wood ash (WA), synthesized nanosilica and distilled water. Pretoria Portland Cement (PPC) company, South

Table 1 Chemical composition of WA used

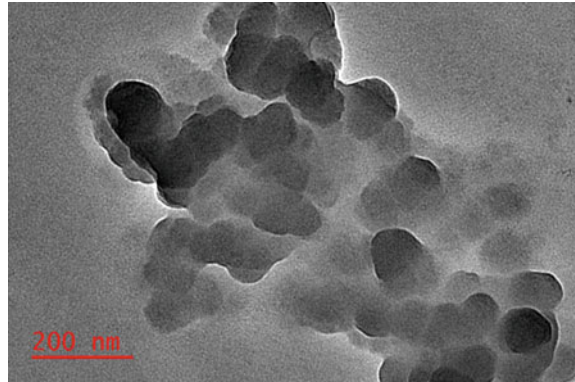
Chemical constituents	Percentage composition (%)
SiO ₂	61.18
Al ₂ O ₃	7.52
Fe ₂ O ₃	3.19
CaO	11.77
MgO	2.48
SO ₃	1.82
Na ₂ O	1.09
K ₂ O	3.81
CaCO ₃	6.22
LOI	3.05
LSF	1.28
SR	4.32
AR	7.55
Total SiO ₂ + Al ₂ O ₃ + Fe ₂ O ₃	72.58

Africa supplied the cement. The properties of the cement as stated in the product database [24] was presented by Ikotun and Raheem [25]. Silica sand of sizes 0.8–1.8, 0.4–0.85, and 600 μ m were used to produce the Local South Africa silica sand (SASS) in proportion of 14:15:8, respectively. SASS was certified as appropriate for the test based on the published grading analysis done by Ikotun and Ekelu [26]. The WA used was collected from Ladoke Akintola University of Technology (LAUTECH) bread bakery in Ogbomoso, Nigeria. The chemical composition of the WA as obtained from Raheem and Adenuga [27] is shown in Table 1. With combined SiO₂ + Al₂O₃ + Fe₂O₃ of 72.58% (>70%), the WA is a good pozzolan. The synthesized nanosilica was produced at nanotechnology research group (NANO+) laboratory in LAUTECH. The type 1 distil water used was produced at the water resources section of Civil Engineering Laboratory, University of South Africa (UNISA).

2.2 Synthesis of Nanosilica

The biogenic synthesis of the nanosilica was carried out using a pod extract of *Cola nitida* as described by Lateef et al. [22]. Approximately 1.5 g of milled pod was suspended in 150 ml of distilled water and heated in a water bath at 60 °C for 1 h to obtain the extract. The extract was then filtered using Whatman No. 1 filter paper and centrifuged at 4000 pm for 20 min. The pure liquid extract was then used to synthesize nanosilica. Solution of silicon dioxide (SiO₂) was prepared by adding 0.4 g of SiO₂ to 0.6 ml of water, after which the 120 ml of the cola pod extract (KP) was added to the solution to synthesise nanosilica. The mixture was carried

Fig. 1 Morphology of the nanosilica



out under room temperature of 30 ± 2 °C and allowed to stay for about 2 h. The formation of nanosilica (NS) was observed as a change in colour of the solution monitored visually until it stabilizes. The Nanosilica sample used was observed under the Scanning electron microscope (SEM) to visualize its sizes. The Silica used is confirmed to be of nano size and less than 200 nm as shown in Fig. 1

2.3 Preparation of Specimens

Cement Paste Samples Were Prepared for Testing Setting Times of Cement While Mortar Samples Were Prepared to Investigate the Flexural and Compressive Strength of Mortar. The samples were prepared with 10% by weight of cement WA replacement for cement and 1, 2, and 3% by weight of binder addition of NS. The sample with only CEM 1 and without WA and NS serves as the control. Based on the previous study [26], where it has been reported that 10% WA replacement is the optimum cement replacement for structural purposes, the percentage of WA used in this study was maintained at 10%. In order to maintain the water binder ratio (w/b), NS was added as a percentage substitution for mixing water. This practice was also reported by Berra et al. [28] and Horszczaruk et al. [29]. Cement paste specimen for setting times test were mixed in accordance with the provision in SANS 196-3:2006 [30]. The mix proportion for the samples is presented in Table 2.

The aqueous suspension of NS was stirred with the mixing water for about one minute to obtain uniform dispersion of the nanomaterial before adding to the binder. The cement mixer used was automated to follow the procedure described in SANS 196-3:2006 [30]. The mixing and casting were done based on the described methodology in SANS 196-3:2006 [30]. Specimens for flexural and compressive strength tests were prepared using mortar prisms of size 40 × 40 × 160 mm. The mortar prisms were made according to the SANS 196-1:2006 [31] standard. The binder

Table 2 Mix proportion of cement pastes

Sample number	Sample designation	Cement (g)	WA (g)	NS (g)	Water (g)	w/b
1	CEM 1 (control)	500	–	–	180	0.36
2	90CEM1 + 10WA	450	50	–	192	0.38
3	90CEM1 + 10WA + 1NS	450	50	5	187	0.37
4	90CEM1 + 10WA + 2NS	450	50	10	181	0.36
5	90CEM1 + 10WA + 3NS	450	50	15	177	0.35

Table 3 Mix proportion of mortar specimens

Sample code	Sample designation	Cement (g)	WA (g)	SASS (g)	NS (g)	Water (g)	w/b
A	CEM 1 + SASS (control)	450	–	1350	–	225	0.5
B	90CEM1 + 10WA + SASS	405	45	1350	–	225	0.5
C	90CEM1 + 10WA + 1NS + SASS	405	45	1350	4.5	220.5	0.5
D	90CEM1 + 10WA + 2NS + SASS	405	45	1350	9.0	216	0.5
E	90CEM1 + 10WA + 3NS + SASS	405	45	1350	13.5	211.5	0.5

to sand ratio is 1:3 and water to binder (w/b) ratio is 0.5. The setting time procedure described in SANS 196–3:2006 [30] were followed. The mix proportion of the materials is shown in Table 3.

The fresh mortar was cast in steel mould that can contain three prism samples of size 40 × 40 × 160 mm. A vibrating table designed for the mould was used to vibrate the sample for proper compaction after casting. After casting, the casted samples were covered with an impervious sheet and placed in a moist air-conditioned environment for 24 h. The specimen was demoulded after 24 h and placed in a curing tank, with maintained temperature of 20 ± 2 °C.

2.4 Testing of the Samples

Setting Times. The mould made for setting times test was placed in an automatic setting times equipment—ToniSET Compact, Model 7306.100/EN. The equipment was set to capture the initial and final setting times of the cement pastes specimen. The vicat needle EN (Ø 1.13 mm) embedded in the equipment was set to penetrate the specimen at constant interval of 5 min until the final setting time reading was

recorded. The initial and final setting time results were automatically captured on the computer and graphs were drawn from the data automatically.

Flexural and Compressive Strength. At testing age, mortar specimens were removed from the curing tank. The surface water was removed by gently mop the surface with a cloth. The samples were weighed for record purpose and placed on the appropriate load frame of the mortar flexural and compressive press -ToniPRAX, Model. The results obtained for each curing age were the average of 3 prisms for flexural strength and 6 half-prisms for compressive strength.

3 Results and Discussion

The results obtained from the various experiment conducted are discussed in the subsequent sections.

3.1 Setting Times

The effect of NS addition on the initial and final setting times of WA cement mortar in comparison to the control (CEM 1) is presented in Fig. 2(a–e). As observed from Fig. 2a, the initial and final setting times of the control (CEM1) are 203:21 and 273:06 min:sec, respectively. The introduction of 10% WA resulted to elongation of both the initial and final setting times. The initial setting time (IST) increased to 350:02 min:sec while the final setting time (FST) increased to 481:00 min:sec (Fig. 2b). This is typical of pozzolan cement mortar as they have low rate of heat of hydration especially at early ages [32].

The addition of 1% NS led to decrease in setting times of the WA cement mortar as shown in Fig. 2c. The IST and FST were 349:58 and 425:10 min:sec, respectively. Further decrease in setting times was witnessed with the addition of 2% NS as indicated in Fig. 2d. The IST and FST for 2% NS addition were 342:51 and 418:08 min:sec compared to 350:02 and 481:00 min:sec, respectively for cement mortar with 10% WA substitution. The reduction in setting times is an indication that NS contributed to faster hydration reaction [18]. According to Zhang et al. [33], the reduction in setting time may also be related to the finer particle size and higher surface area of the NS in relation to that of WA. Conversely however, addition of 3% NS resulted in increase of setting times higher than that of 2% NS incorporation with IST and FST of 343:29 and 464:22 min:sec, respectively (Fig. 2e). The increase could be caused by lack of enough calcium hydroxide to react with silica oxide in NS. This increase in setting times is an indication that the 3% dosage of NS is too much and not beneficial to the mix.

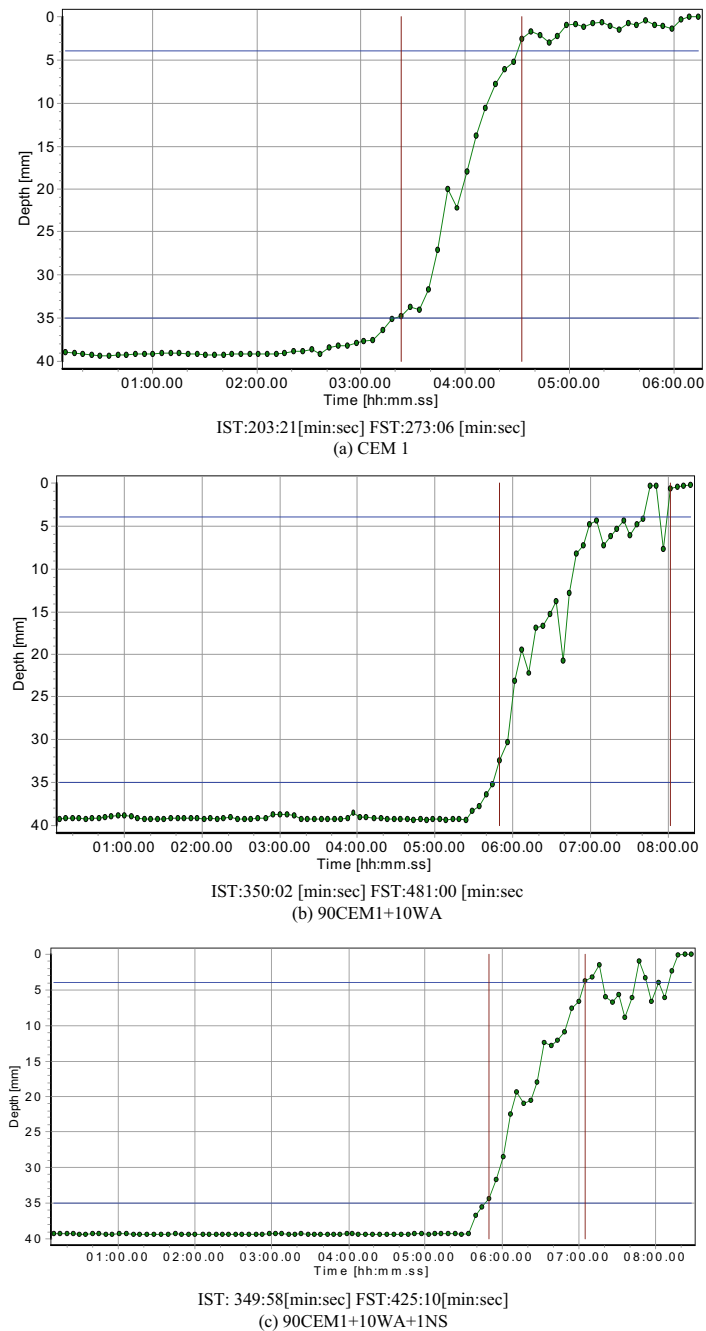


Fig. 2 Setting times of WA cement mortar

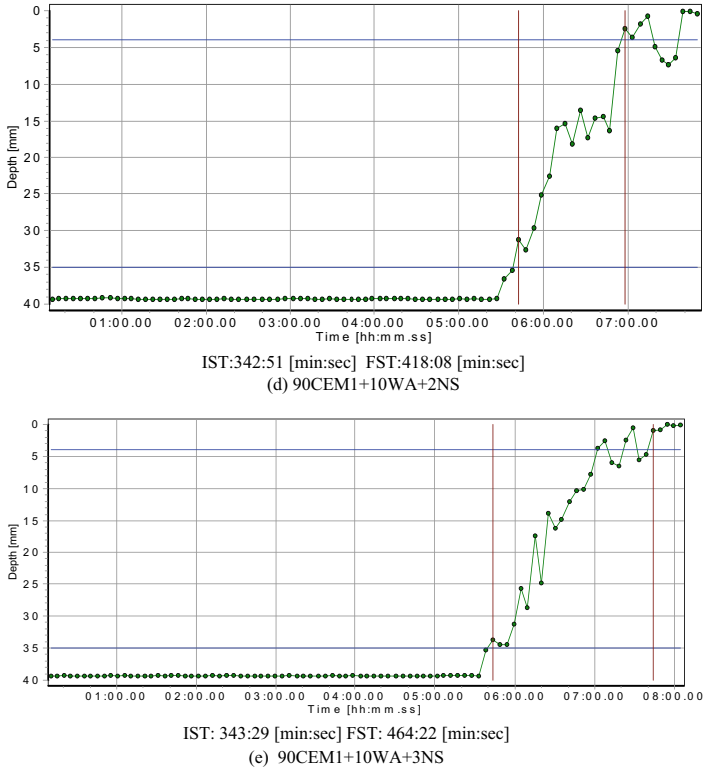


Fig. 2 (continued)

3.2 Flexural Strength

The flexural strength development of WA cement mortar incorporating NS is shown in Fig. 3. When compared with the control (CEM1), the flexural strength of mortar with 10% WA replacement for cement was lower at all curing ages. It could be observed from Fig. 3 that flexural strength of CEM1 mortar at 3, 7, 14, 28, 56 and 90 days were 6.35, 7.20, 7.38, 7.41, 8.04 and 8.11 MPa as against those of 90CEM1 + 10WA which are 3.21, 4.99, 5.56, 5.67, 5.73 and 5.90 MPa, respectively. The WA, which is a pozzolan has low rate of heat development and cement hydration hence, the lower values of flexural strength recorded. With addition of 1% NS, the flexural strength increased over those of 90CEM1 + 10WA with values ranging from 6.13 to 7.45 MPa for curing ages 3–90 days, respectively. For 2% NS addition, the flexural strength was lower than those of 1% NS at early ages but improved at later age (90 days) to surpass it. The improvement is due to continuous pozzolanic reaction of the WA at higher curing ages. The 3% NS addition resulted in lower flexural strength compared to both 1 and 2% NS with values ranging from 5.47 to 7.26 MPa for 3–90 days, respectively. The control (CEM1) has the highest flexural strength for all

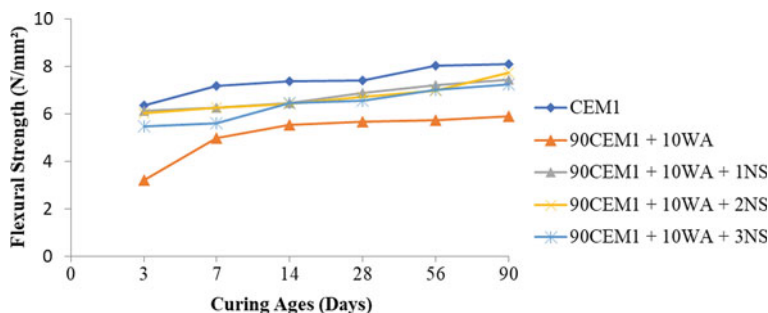


Fig. 3 Flexural strength of WA cement mortar incorporating NS

curing days irrespective of NS addition. This suggests that the effect of pozzolanic reaction of WA at later curing ages is not pronounced for flexural strength.

3.3 Compressive Strength

The influence of NS addition on compressive strength of WA cement mortar is presented in Fig. 4. Generally, the compressive strength increased with curing age and addition of NS up to 2%, beyond this percentage, the compressive strength decreases. As shown in Fig. 4, the compressive strength of mortar made with CEM1 increases from 24.66 MPa at 3 days to 49.72 MPa at 90 days. With WA incorporation, the strength reduces to 14.85 MPa at 3 days and 44.42 MPa at 90 days. This observation is typical to pozzolans and has been linked to the reduction of the rate of heat development and cement hydration caused by pozzolans, especially at lower curing ages [34]. As observed from Fig. 4, WA cement mortar with 1% NS addition recorded increase in compressive strength over that of 90CEM1 + 10WA with values ranging from 15.59 to 49.44 MPa for curing ages 3 to 90 days, respectively. However, these values are lower than those of CEM1 for all curing ages. Addition of 2% NS led to further increase in compressive strength over those of 1% NS addition and 90CEM1 + 10WA mortar. There were 35.2, 27.1, 42.2, 41.5, 39.5 and 20.9% increase in compressive strength of WA cement mortar when 2% NS was added compared to 90CEM1 + 10WA mortar at ages 3, 7, 14, 28, 56 and 90 days, respectively. This increase in compressive strength can be attributed to two factors according to Mohamed [35]. The first is due to the packing effect of small-sizes NS that acted as fillers in the pores of microstructure of mortar to increase its density and also the strength. The second is as a result of the pozzolanic effect that combines silica elements in NS and WA with calcium hydroxide from cement to produce a strong bonding strength (C-S-H), leading to higher compressive strength of the mortar. WA cement mortar with 2% NS performed better than the control (CEM1) at later curing ages. While CEM1 has compressive strength of 45.31, 47.58 and 49.72 MPa at ages 28, 56 and 90 days; 90CEM + 10WA + 2NS recorded 48.13,

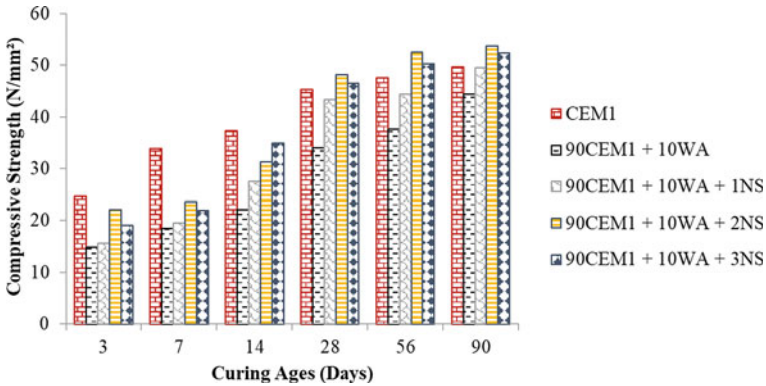


Fig. 4 Compressive strength of WA cement mortar incorporating NS

52.45, and 53.70 MPa, respectively. The increase in strength over that of CEM1 is due to continuous pozzolanic reaction of the WA at longer curing ages [10].

The incorporation of 3% NS into WA cement mortar resulted into reduction in compressive strength when compared with 2% addition, but the values are still higher than those of 1% addition and 90CEM + 10WA. This reduction in strength may be due to agglomeration of NS because they cannot be uniformly dispersed as a result of their large surface area [15]. This confirms that addition of NS beyond 2% of the weight of the binder is not beneficial to WA cement mortar.

4 Conclusion

In conclusion, based on the findings and discussion in this study, incorporation of up to 2% NS by weight of binder reduced initial and final setting times of WA cement paste. Flexural strength of WA cement mortar was increased with addition of up to 2% NS. Also, there was increase in compressive strength of WA cement mortar at various ages up to 90 days, when up to 2% NS was added. Synthesized nanosilica performed favourably in mortar at optimum percentage of 2% and may be used in lieu of commercial nanosilica upon further studies on cost analysis.

Acknowledgements The authors are grateful to Prof. A. Lateef (Head, Nanotechnology Research Group-NANO+) and Mr. P. O. Akinola, for assisting in producing the nano-SiO₂ used, at the Industrial Microbiology and Nanobiotechnology Laboratory, Department of Pure and Applied Biology, Ladoke Akintola University of Technology (LAUTECH), Ogbomoso, Nigeria. Grateful acknowledgement is made to University of South Africa (UNISA) for faculties and equipment provided for the experimental works. The authors also acknowledge PPC, South Africa for supplying the cement.

References

1. Flower DJM, Sanjayan JG (2007) Greenhouse gas emissions due to concrete manufacture. *Int J LCA* 12(5):282–288
2. Olivier GJG, Greet JM, Peters JAHW (2012) Trends in global CO₂ emissions 2012 report. Netherlands. <https://doi.org/10.2788/33777>
3. Wang W, Lu CF, Li YX, Yuan GL, Li QT (2017) Effects of stress and high temperature on the carbonation resistance of fly ash concrete. *Constr Build Mater* 138:486–495
4. Dinakar P, Babu KG, Santhanam M (2008) Durability properties of high-volume fly ash self-compacting concretes. *Cem Con Comp* 30(10):880–886
5. Ephraim ME, Akeke GA, Ukpata JO (2012) Compressive strength of concrete with rice husk ash as partial replacement of ordinary portland. *Cem Eng Res J* 2:22–26
6. Amran M, Fediuk R, Murali G, Vatin N, Karelina M, Ozbakkaloglu T, Krishna RS, Sahoo AK, Das SK, Mishra I (2021) Rice Husk Ash-based concrete composites: a critical review of their properties and applications. *Crystals* 11:168
7. Adesanya DA, Raheem AA (2009) A study of the workability and compressive strength characteristics of corn cob ash blended cement. *Con Const Build Mat* 23:311–317
8. Pandey A, Kumar B (2020) A comprehensive investigation on application of microsilica and rice straw ash in rigid pavement. *Constr Build Mater* 252:119053
9. Raheem AA, Ikotun BD (2019) Investigation of workability and compressive strength of wood ash cement concrete containing nanosilica. *Adv Mat Res* 1154:129–136
10. Orogbade BO, Raheem AA (2018) Chemical and physical characteristics of blended cements produced from softwood ash. *LAUTECH J Civil Environ Stud (LAUJOCES)* 1:1–7
11. Raheem AA, Sulaiman OK (2013) Saw dust ash as partial replacement for cement in the production of sandcrete hollow blocks. *Int J Eng Res Appl* 3(4):713–721
12. Chowdhury S, Maniar A, Suganya OM (2015) Strength development in concrete with wood ash blended cement and use of soft computing models to predict strength parameters. *J Adv Res* 6:907–913
13. Dawood ET, Al-Attar AA, Zinad OS (2020) The influence of wood ash on different cement mortar mixes. *AIP Conf Proc* 2213:020073. <https://doi.org/10.1063/5.0000392>
14. Oltulu M, Sahin R (2011) Single and combined effects of nano-SiO₂, nano-Al₂O₃ and nano-Fe₂O₃ powders on compressive strength and capillary permeability of cement mortar containing silica fume. *Mater Sci Eng A* 528:7012–7019
15. Jo BW, Kim CH, Tae GH, Park JB (2007) Characteristics of cement mortar with nano silica particles. *Constr Build Mater* 21:1351–1355
16. Saloma A, Nasution I, Imran M, Abdullah M (2015) Improvement of concrete durability by nanomaterials. *Proc Eng* 125:608–612
17. Singh LP, Karade SR, Bhattacharyya SK, Yousuf MM, Ahalawat S (2013) Beneficial role of nanosilica in cement-based materials—a review. *Constr Build Mater* 47:1069–1077
18. Zhang M, Islam J (2012) Use of nano-silica to reduce setting time and increase early strength of concretes with high volumes of fly ash or slag. *Constr Build Mater* 29:573–580
19. Rai S, Tiwari S (2018) Nano silica in cement hydration. *Mater Today Proceed* 5:9196–9202
20. Senff L, Labrincha JA, Ferreira VM, Hotza D, Repette WL (2009) Effect of nanosilica on rheology and fresh properties of cement pastes and mortars. *Constr Build Mater* 23:2489–2491
21. Laím L., Caetano H., Santia A.: Review: Effects of nanoparticles in cementitious construction materials at ambient and high temperatures *J. of Build. Engineering* 35:102008 (2021).
22. Lateef A, Azeez MA, Asafa TB, Yekeen TA, Akinboro A, Oladipo IC, Azeez L, Ajibade SE, Ojo SA, Gueguim-Kana EB, Beukes LS (2016) Biogenic synthesis of silver nanoparticles using pod extract of *Cola nitida*: Antibacterial and antioxidant activities and application as a paint additive. *J. of Taibah University for Science* 10:551–562
23. Emeka EE, Ojiefoh OC, Aleruchi C, Hassan LA, Christana OM, Rebecca M, Dare EO, Temitope AE (2014) Evaluation of antibacterial activities of silver nanoparticles green-synthesized using pineapple leaf (*Ananas comosus*). *Micron* 57:1–5

24. PPC (2018) Product data sheet PPC suretech 52.5 N cement. Retrieved from www.ppc.co.za Accessed on 19 Nov 2021
25. Ikotun BD, Raheem AA (2021) Characteristics of wood ash cement mortar incorporating green-synthesized Nano-TiO₂. *Int J Con Struc Mater* 15(19):1–9
26. Ikotun BD, Ekolu S (2010) Strength and durability effect of modified zeolite additive on concrete properties. *Constr Build Mater* 24(5):749–757
27. Raheem AA, Adenuga OA (2013) wood ash from bread bakery as partial replacement for cement in concrete. *Int J Sust Constr Eng Tech* 4(1):75–81
28. Berra M, Carassiti F, Mangialardi T, Paolini AE, Sebastiani M (2012) Effects of nanosilica addition on workability and compressive strength of Portland cement pastes. *Constr Build Mater* 35:666–675
29. Horszczaruk E, Sikora P, Cendrowski K, Mijowska E (2017) The effect of elevated temperature on the properties of cement mortar containing nanosilica and heavyweight aggregates. *Constr Build Mater* 137:420–431
30. SANS 196–3:2006. Method of testing cement—Setting times, SABS, Pretoria
31. SANS 196–1:2006. Method of testing cement—Determination of strength, SABS, Pretoria.
32. Singh NB, Singh VD (2010) Hydration of baggasse ash blended portland cement. *Cem Concr Res* 30:1485–1488
33. Zhang M, Islam J, Peethamaran S (2012) Use of nano-silica to increase early strength and reduce setting time of concretes with high volumes of slag. *Cem Con Comp* 34:650–662
34. Raheem AA, Ibiwoye EO (2018) A study of neem seed ash as partial replacement for cement in concrete. *Int J Sust Constr Eng Tech* 9(2):55–65
35. Mohamed AM (2016) Influence of nano materials on flexural behaviour and compressive strength of concrete. *Hous Build Nat Res Center HBRC J* 12:212–225

Assessing the Impact of Petroleum Sludge Ash on the Compressive Strength of Fly Ash-Palm Oil Clinker Geopolymer Mortar



Amalina Hanani Ismail , Andri Kusbiantoro , and Yuyun Tajunnisa 

Abstract Oil industries are one of the most critical industries with substantial production and closely related to the public interest. Two major oil industries, namely petroleum and palm oil, represent primary sources of consumer groups in Malaysia. However, these sectors inevitably generate waste and require disposal systems. Massive amounts of petroleum sludge generated from the refinery process, possess toxic contaminants requiring careful disposal. Similarly, palm oil production generates a hefty amount of by-products from its extraction process. Encapsulating these wastes in a cementitious medium is considered a more feasible solution than converting them for landfilling. Therefore, this study aims to utilize two wastes from palm oil and petroleum industries as binder materials in a geopolymer framework. To achieve this, palm oil clinker and petroleum sludge as the by-products from those respective industries, were subjected to mechanical grinding and incineration processes to improve their reactivity. Palm oil clinker powder (POCP) was included in the geopolymer mixture to replace 2.00–10.00% of fly ash as the source material. After obtaining the optimum POCP replacement, 0.20–1.00% of petroleum sludge ash (PSA) to be included in the geopolymer mortar to assess its impact on geopolymerization. Compressive strength was evaluated on 7, 28, and 90 days to determine the optimum proportion of fly ash, palm oil clinker, and petroleum sludge ash in geopolymer, particularly the proportion that carries the least negative effect onto the compressive strength performance. Based on the results, the ratio of 91.30% fly ash, 7.60% POCP and 1.10% PSA provided the most significant strength improvement among its peers. The encapsulation task of petroleum sludge

A. H. Ismail · A. Kusbiantoro (✉)

Department of Civil Engineering Technology, Faculty of Engineering Technology, Universiti Tun Hussein Onn Malaysia, Pagoh, Malaysia
e-mail: andri@uthm.edu.my

A. Kusbiantoro

Sustainable Engineering Technology Research Centre, Universiti Tun Hussein Onn, Pagoh, Malaysia

Y. Tajunnisa

Department of Infrastructural Civil Engineering, Faculty of Vocation, Institut Teknologi Sepuluh Nopember, Surabaya, Indonesia

ash in geopolymer has been well performed by the fly ash—palm oil clinker blend. It provides new opportunities to explore the alternative disposal method for these industrial by-products.

Keywords Palm oil clinker · Petroleum sludge · Geopolymer · Compressive strength

1 Introduction

1.1 Background

In recent years, geopolymer has emerged as a promising construction material due to its environmental and performance benefits [1]. Geopolymer production produces fewer greenhouse gas emissions in comparison to conventional concrete production methods. The elimination of the high-temperature calcination process used in traditional cement production also leads to a reduction in energy consumption and cost in the production of geopolymer.

Geopolymer is a three-dimensional polymeric Si-O-Al amorphous microstructure formed through the geopolymerization of aluminosilicate precursors in an alkaline activation solution. The four processes of geopolymerization are condensation, dissolution, reorganisation, and polymerization [2]. Aluminosilicate materials are dissolved in an alkali solution, resulting in the formation of aluminate and silicate monomers. These monomers are then rearranged and condensed into polymers, resulting in the final geopolymer structure. Aluminosilicate materials are commonly recycled from manufacturing waste, some of these wastes are, but not limited to, fly ash [3], ground granulated blast slag [4], rice husk ash [5] and the combination of these materials [6]. Out of all source materials for geopolymer, fly ash has exhibited exceptional strength and durability, owing to its amorphous nature and pozzolanic reactivity.

Fly ash is a byproduct generated from coal-fired power plants [7], with an annual production of approximately 270 million metric tons. It appears as light, fine, spherical, glassy particles with physical diameters ranging from 1 to 150 μm , and consists primarily of silica, alumina, calcium oxide, and iron oxide [8]. Fly ash has gained popularity as a binder for geopolymer due to its abundance and low cost. Combining fly ash with other pozzolanic materials can help improve some properties of geopolymer [9]. Pozzolanic materials, such as palm oil clinker, are ideal for this purpose.

Palm oil clinker is a powdery by-product generated from incinerating lignocellulosic biomass such as oil palm shells (OPS) and mesocarp fibres as a self-sufficient fuel source [10]. It is considered solid waste, with a colour ranging from blackish to grey depending on the amount of unburned carbon residues, and often has an irregular shape and porous structure. Due to the high cost of disposal, palm oil clinker is

frequently discarded in open areas or landfills, which contributes directly to pollution by impacting groundwater and altering the natural composition of the soil [11]. Utilizing palm oil clinker powder as a binder in geopolymer as an aluminosilicate material source would help to address its disposal issue.

Conversely, petroleum sludge ash is a hazardous waste generated by petroleum refineries and contains heavy metals, toxic organic compounds, and inorganic substances [12]. It is classified as hazardous waste due to its potential harm to the environment and human health. This ash is usually disposed of in landfills or incinerated to reduce environmental risks. However, petroleum sludge ash still poses a major environmental challenge due to high levels of heavy metals and other contaminants. Former research works have shown that heavy metals and toxic compounds present in petroleum sludge ash can be entrapped in geopolymer medium, whilst improving its compressive strength [13].

This study aims to investigate the impact of petroleum sludge ash on the compressive strength of fly ash-based geopolymer mortar containing palm oil clinker powder as a partial binder replacement. The results from this study would provide valuable information on the suitability of geopolymer mortar for use in construction applications and help to mitigate the environmental risks associated with the use of petroleum sludge ash.

2 Experimental Investigation

2.1 Material

This study utilized palm oil clinker (POC) and petroleum sludge (PS) as binder replacement materials in fly ash-based geopolymer after they have undergone treatment processes to reduce toxicity, and relatively increase reactivity. POC collected from a palm oil plantation at Lepar Hilir, Pahang, Malaysia, was treated in a mechanical grinding to become palm oil clinker powder (POCP) passing 75 microns sieve. Meanwhile, PS was collected from oil refinery in Malacca, Malaysia and underwent thermal and mechanical treatment to become petroleum sludge ash (PSA). Physical appearances of POCP and PSA after treatment are illustrated in Fig. 1.

Both of these materials were then tested for their chemical composition using x-ray fluorescence (XRF) analyser, compliant with ASTM C114, along with main binder fly ash. For this test, 10 g of each powdery ash was collected and kept in seal bag prior to the testing using Bruker Machine. XRF analysis was conducted to determine the proportion of major oxides that present in these raw materials, since understanding the oxides composition could help to evaluate the rate of geopolymerisation process later.

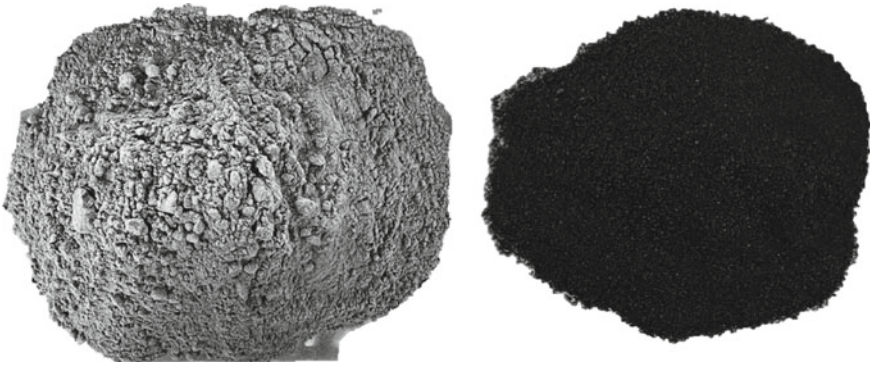


Fig. 1 Physical appearances of palm oil clinker powder (left) and petroleum sludge ash (right) after treatment process used in this study

2.2 Mix Proportion of Geopolymer Mortar with POCP

This study adopted the OPC concrete mixing procedure to ensure a homogeneous geopolymer mixture, and extend the mix proportion used in Kusbiantoro et al. (2012) work [14]. Geopolymer mortar was manually prepared by mixing dry materials, such as fly ash, POCP, PSA, and fine aggregates for 150 s. After the dry mixture has been thoroughly mixed, the alkaline activators, namely sodium silicate and sodium hydroxide, and extra water were then added into the dry mixture and continued with the wet mixing for 90 s. After the mixture has been homogeneously mixed, it was cast in $50 \times 50 \times 50$ mm cube moulds for compressive strength test purpose.

The specimens were left to harden at room temperature for 24 h, before they were demoulded and cured in electronic oven. The temperature in the oven was set at 65°C , and the specimens were covered in the plastic bag to prevent excessive moisture evaporation and cured in the oven for 24 h. After 24 h of curing, the specimens were stored at the room temperature until the testing day.

Geopolymer mortar was cast with different POCP levels at 2.0, 4.0, 6.0, 8.0 and 10.00% (by weight of fly ash) and compressive strength performance was observed on 7 and 28 days to determine optimum proportion. Pozzolanic reactivity of POCP is the evaluation highlight in the compressive strength development of geopolymer mortar. Table 1 shows the detail of geopolymer mortar mix proportion used in this study.

2.3 Mix Proportion of Geopolymer Mortar with POCP and PSA

After an optimum mix proportion is known, the addition of 0.20, 0.40, 0.60, 0.80 and 1.00% of treated PSA (by weight of POCP) into the geopolymer specimens

Table 1 Detail of fly ash-based geopolymer mortar mix proportion with POCP replacement

POCP (%)	FA (kg/m ³)	POCP (kg/m ³)	NaOH (kg/m ³)	Na ₂ SiO ₃ (kg/m ³)	Fine agg (kg/m ³)	Extra water (kg/m ³)
0.0	700.0	0.0	82.0	206.0	1290.0	25.8
2.0	686.0	14.0	82.0	206.0	1290.0	25.8
4.0	672.0	28.0	82.0	206.0	1290.0	25.8
6.0	658.0	42.0	82.0	206.0	1290.0	25.8
8.0	644.0	56.0	82.0	206.0	1290.0	25.8
10.0	630.0	70.0	82.0	206.0	1290.0	25.8

Table 2 Detail of fly ash-based geopolymer mortar mix proportion with POCP and PSA replacement

POCP (%)	PSA (%)	FA (kg/m ³)	POCP (kg/m ³)	PSA (kg/m ³)	NaOH (kg/m ³)	Na ₂ SiO ₃ (kg/m ³)	Fine agg (kg/m ³)	Extra water (kg/m ³)
0.0	0.0	700.0	0.0	0.0	82.0	206.0	1290.0	25.8
8.0	0.0	644.0	56.0	0.0	82.0	206.0	1290.0	25.8
7.8	0.2	588.0	54.6	1.4	82.0	206.0	1290.0	25.8
7.6	0.4	588.0	53.2	2.8	82.0	206.0	1290.0	25.8
7.4	0.6	588.0	51.8	4.2	82.0	206.0	1290.0	25.8
7.2	0.8	588.0	50.4	5.6	82.0	206.0	1290.0	25.8
7.0	1.0	588.0	49.0	7.0	82.0	206.0	1290.0	25.8

were introduced to understand the effectiveness of geopolymer in encapsulating the PSA from the compressive strength perspective 8.00% of POCP replacement was selected as the control specimen in this the subsequent mix proportion. The mixing method was relatively similar as mentioned previously and these geopolymer mortar specimens were tested for their compressive strength on 7, 28, and 90 days. Table 2 tabulates the detail of geopolymer mortar mix proportion in this second stage.

3 Experimental Results

3.1 Chemical Composition

The chemical composition of fly ash, petroleum sludge ash, and palm oil clinker powder was studied to understand their behaviour in geopolymer framework after undergoing mechanical treatment (palm oil clinker powder) or incineration (petroleum sludge). The chemical oxide composition is crucial in determining the properties of these binders, which are derived from combustible organic and inorganic

Table 3 Chemical composition of binder materials fly ash, palm oil clinker powder and petroleum sludge ash

Oxides	FA	POCP	PSA
Al ₂ O ₃	29.10	3.87	0.37
Na ₂ O	–	0.08	1.37
MgO	–	2.11	0.12
SiO ₂	51.70	68.30	1.17
P ₂ O ₅	1.70	1.84	0.09
SO ₃	1.50	0.16	64.30
Cl	–	0.02	0.33
K ₂ O	1.60	9.26	0.29
CaO	8.84	4.08	0.80
TiO ₂	0.70	0.31	0.28
Cr ₂ O ₃	–	0.04	0.06
MnO	–	0.11	0.24
Fe ₂ O ₃	4.76	9.63	29.10
NiO	–	0.02	0.02
CuO	–	0.02	0.04
Others			

matter. Table 3 tabulates the chemical oxides compositions of fly ash, palm oil clinker powder and petroleum sludge ash. Based on the results, major oxides compositions for all binder materials are relatively similar but with different percentage.

FA is made up of five major oxides, with percentages of 51.70, 29.10, 8.84, 4.76, and 1.70% of SiO₂, Al₂O₃, CaO, Fe₂O₃, and P₂O₅, respectively. These oxide compositions are similar, with slightly different proportion percentages, with the findings from previous research work [15]. The fly ash used in this study is classified as Class F fly ash because the sum of SiO₂ + Al₂O₃ + Fe₂O₃ = 85.86%, which is >70.00%. During geopolymerisation, Class F has a high amorphous aluminosilicate content, which reacts reactively with alkaline solution to produce 3D aluminosilicate networks. This explains the widespread use of FA as the principal binder in geopolymer.

Contrarily, the primary constituents of POCP are SiO₂, K₂O, Fe₂O₃, CaO, and Al₂O₃, with the proportion of 68.30, 9.63, 9.26, 4.08, and 3.87%, respectively. Similar to FA, the sum of SiO₂, Al₂O₃, and Fe₂O₃ in POCP used in this study was more than 70.0%, thus meets with the standard pozzolanic reactivity [16]. Different studies recorded different oxide constituents, but all have mentioned the presence of SiO₂ as a primary oxide [10, 17]. Silica is a critical component in the geopolymerization, since it is part of the backbone in the developed aluminosilicate frameworks. It shares the same function with the formation of calcium silicate framework in the pozzolanic reaction.

The composition of petroleum sludge ash (PSA) was found to be distinct from fly ash and palm oil clinker powder. PSA consists mainly of SO₃, Fe₂O₃, Na₂O and SiO₂,

with other chemical oxides making up less than 1.00%. Hazardous heavy metals like As_2O_3 , Cr_2O_3 , CuO , NiO , and MnO were present in PSA. The chemical composition of PSA can vary based on factors such as sample treatment, time, storage conditions, etc. [18]. According to Pakpahan et al. (2016), the main oxides in PSA were SiO_2 , CaO , Al_2O_3 , Na_2O , and Fe_2O_3 , at the proportion percentages of 47.28, 13.30, 12.20, 7.53, and 6.48, respectively [19]. Another study by Kankia et al. in 2021 showed the main oxides in PSA to be Fe_2O_3 , SiO_2 , SO_3 , Al_2O_3 , and CaO , with the proportion percentages of 45.90, 14.90, 11.50, 10.00, and 9.26, respectively [13]. Table 3 shows the chemical composition of binder materials used in this study.

3.2 Compressive Strength of Geopolymer Mortar with POCP

Figure 2 shows the compressive strength of geopolymer mortar with varying amounts of POCP as a replacement binder. Control specimen is referred as a specimen containing 100% fly ash without any replacement material. After 7 days of curing, the control sample had the lowest strength with 28.64 MPa, while the sample with 8.00% POCP recorded the highest strength with 44.54 MPa. The trend shows that the strength increases as the amount of POCP increases, peaking at 8.00%, but decreasing at 10.00%. The second and third highest strengths were recorded at 6.00 and 4.00% respectively. The same trend can be seen after 28 days of curing, with 8.00% still having the highest strength (45.35 MPa). No significant drop in strength was observed for any of the samples.

The strength of geopolymer mortar depends on the geopolymerization and other related chemical reaction process. Alumina and silica compounds from the source materials dissolved in an alkaline medium lead to polycondensation and formation of N-A-S-H and C-A-S-H gels [20]. The presence of POCP as a pozzolanic material, might promotes the production of secondary poly(siloxonate) and poly(sialate), contributing to the strength development of geopolymer mortar.

The compressive strength of geopolymer mortar increases with the percentage of POCP replacement, but the highest compressive strength was achieved with 8.00% of POCP replacement. Higher replacement at 10.00% of POCP resulted in a decrease in compressive strength, which may be due to the reduction in the amount of primary aluminosilicate frameworks developed from fly ash polymerisation. This finding is supported in the previous studies by Ismail et al. (2020), where they achieved a similar pattern and emphasized on a certain percentage of POCP replacement [10]. The results showed that a replacement of 8.00% POCP was the most effective, yielding the highest strength among all the samples. This proportion was therefore chosen as the standard for further testing and examination.

Figure 3 illustrates the compressive strength of geopolymer mortar with 0.20, 0.40, 0.60, 0.80 and 1.00% of PSA. The percentages were determined by subtracting the best proportion (8.00%) from previous data. The samples were tested after 7, 28 and 90 days of curing. The control sample serves as the benchmark of strength

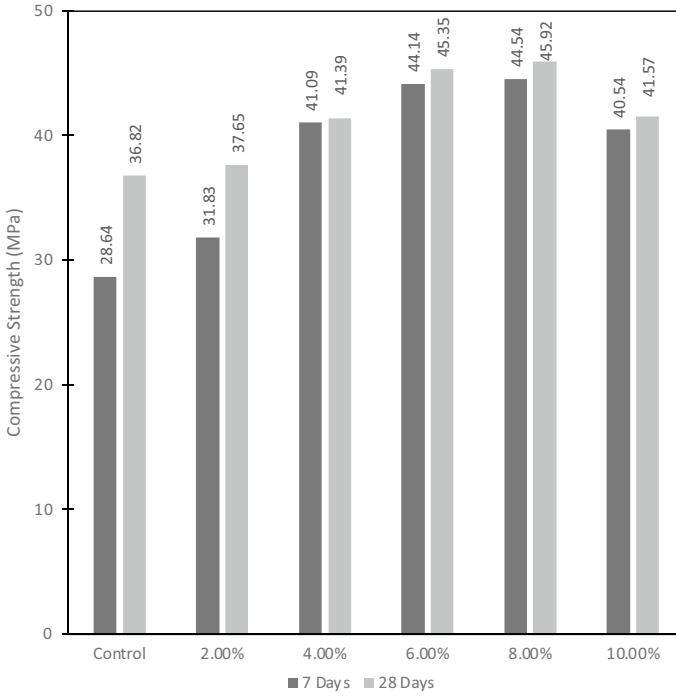


Fig. 2 Compressive strength result of fly ash-based geopolymer with various POCP replacement

designed for the mix proportion, while 8.00% indicates as the reference for strength development when using pozzolanic materials and other binders.

According to the results, control has the highest compressive strength among all samples on 7 days of curing. On 28 days, 7.20% achieved similar compressive strength with control, yet higher than the other POCP-PSA based samples. The 90 days curing showed how 7.60, 7.20, and 7.00% had surpassed the compressive strength of control with 49.60 MPa, 48.10 MPa and 56.06 MPa, respectively. However, despite the lower strength performance, control and 8.00% samples seemed had experienced a stable maturity after 24 h of oven curing, where no significant strength development was recorded from 7 to 90 days of curing. The highest compressive strength development was consistently recorded by 7.00% replacement throughout all curing days. This mixture achieved the increments of 7.58 and 37.16% on 28 and 90 days of curing, respectively.

Interestingly, the possible higher strength performance in control and 8.00% samples appeared to be caused by the higher packing density among the fine particle [21]. The lack of PSA in both control and the 8.00% specimen helped to ensure the distribution of finer fly ash and POCP particles to reach the optimum packing density. The interruption by PSA during the geopolymerization process had caused the strength disruption in every POCP-PSA based specimens. Nevertheless, after 28

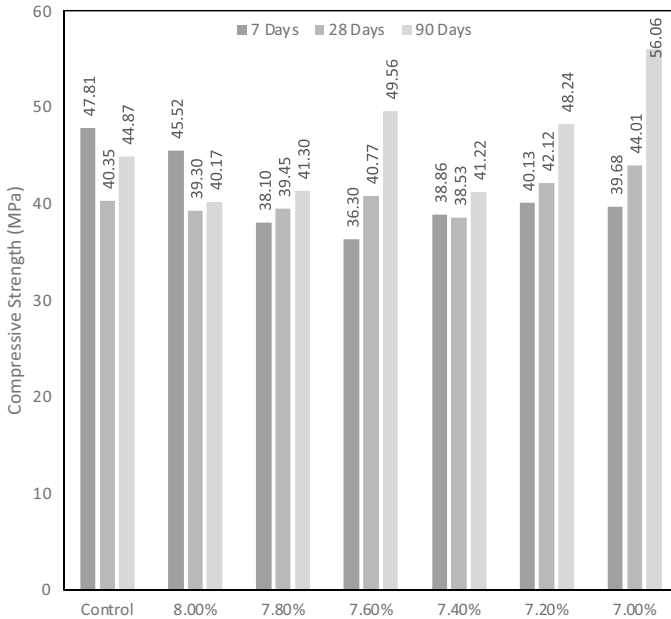


Fig. 3 Compressive strength result of fly ash-based geopolymer with optimum replacement of POCP and various PSA replacement

days of curing the compound in PSA seemed to accelerate the geopolymerization, either by liberating more alumina and silica from the unreacted fly ash to produce late poly(sialate) or poly(siloxonate), or by strengthening the weak links in the aluminosilicate frameworks. Further study is required to justify this hypothesis, by focusing on the reaction product and the chemical bonding in these specimens.

4 Conclusion

Based on the results, geopolymer mixture has presented a positive outcome in encapsulating the impurities from palm oil clinker and petroleum sludge ash in its framework without significant disruption to the compressive strength performance. The inclusion of 91.30% fly ash, 7.60% POCP and 1.10% PSA as the source material combination has displayed the highest compressive strength development after 90 days of maturity. This is obtained from the mix proportion of 7.60% which is equivalent to 588.0 kg/m³ of fly ash, 53.2 kg/m³ of POCP and 2.8 kg/m³ of PSA. This late strength development seemed to be affected by the formation of secondary aluminosilicate frameworks, e.g., poly(sialate) or poly(siloxonate) that supported the microstructure of geopolymer. Nevertheless, additional experiments that would look into the presence of certain mineral structure would be beneficial to promote this

encapsulation process further, as an alternative way to dispose hazardous waste or industrial by-products.

Acknowledgements This research was supported by the Ministry of Higher Education (MOHE) through Fundamental Research Grant Scheme (FRGS) (FRGS/1/2022/TK01/UTHM/02/4).

References

1. Thaarrini J, Ramasamy V (2016) Properties of foundry sand, ground granulated blast furnace slag and bottom ash based geopolymers under ambient conditions. *Periodica Polytechnica Civil Eng* 60(2):159–168
2. Singh NB, Middendorf B (2020) Geopolymers as an alternative to Portland cement: An overview. *Constr Build Mater* 237:117455
3. Hager I, Sitarz M, Mróz K (2021) Fly-ash based geopolymer mortar for high-temperature application—effect of slag addition. *J Clean Prod* 316:128168
4. Gupta N, Gupta A, Saxena KK, Shukla A, Goyal SK (2021) Mechanical and durability properties of geopolymer concrete composite at varying superplasticizer dosage. *Mater Today Proceed* 44:12–16
5. Pham TM, Lim YY, Pradhan SS, Kumar J (2021) Performance of rice husk ash-based sustainable geopolymer concrete with ultra-fine slag and Corn cob ash. *Constr Build Mater* 279:122526
6. Jindal BB, Jangra P, Garg A (2020) Effects of ultra fine slag as mineral admixture on the compressive strength, water absorption and permeability of rice husk ash based geopolymer concrete. *Mater Today Proceed* 32:871–877
7. Zierold KM, Odoh C (2020) A review on fly ash from coal-fired power plants: chemical composition, regulations, and health evidence. *Rev Environ Health* 35(4):401–418
8. Bhatt A, Priyadarshini S, Mohanakrishnan AA, Abri A, Sattler M, Techapaphawit S (2019) Physical, chemical, and geotechnical properties of coal fly ash: a global review. *Case Stud Constr Mater* 11:e00263
9. Shaikh FU, Supit SW (2014) Mechanical and durability properties of high volume fly ash (HVFA) concrete containing calcium carbonate (CaCO₃) nanoparticles. *Constr Build Mater* 70:309–321
10. Ismail AH, Kusbiantoro A, Chin SC, Muthusamy K, Islam M, Tee KF (2020) Pozzolanic reactivity and strength activity index of mortar containing palm oil clinker pretreated with hydrochloric acid. *J Clean Prod* 242:118565
11. Karim MR, Hashim H, Abdul Razak H (2016) Assessment of pozzolanic activity of palm oil clinker powder. *Constr Build Mater* 127:335–343
12. Johnson OA, Affam AC (2019) Petroleum sludge treatment and disposal: a review. *Environ Eng Res* 24(2):191–201
13. Kankia MU, Baloo L, Mohammed BS, Hassan SB, Haruna S, Danlami N, Samahani WN (2021) Effects of petroleum sludge ash in fly ash-based geopolymer mortar. *Constr Build Mater* 272:121939
14. Kusbiantoro A, Nuruddin MF, Shafiq N, Qazi SA (2012) The effect of microwave incinerated rice husk ash on the compressive and bond strength of fly ash based geopolymer concrete. *Constr Build Mater* 36:695–703
15. Guo X, Yang J (2020) Intrinsic properties and micro-crack characteristics of ultra-high toughness fly ash/steel slag based geopolymer. *Constr Build Mater* 230:116965
16. Yusuf MO, Johari MAM, Ahmad ZA, Maslehuddin M (2014) Influence of curing methods and concentration of NaOH on strength of the synthesized alkaline activated ground slag-ultrafine palm oil fuel ash mortar/concrete. *Constr Build Mater* 66:541–548

17. Hamada HM, Alattar AA, Yahaya FM, Muthusamy K, Tayeh BA (2021) Mechanical properties of semi-lightweight concrete containing nano-palm oil clinker powder. *Phy Chemistr Earth Parts A/B/C* 121:102977
18. Jagaba AH, Kutty SRM, Lawal IM, Birniwa AH, Affam AC, Yaro NSA, ... Yakubu AS (2022) Circular economy potential and contributions of petroleum industry sludge utilization to environmental sustainability through engineered processes-a review. *Clean Circul Bioecon* 100029
19. Pakpahan EN, Shafiq N, Isa MH, Kutty SRM, Mustafa MR (2016) Petroleum sludge thermal treatment and use in cement replacement—a solution towards sustainability. In: *Engineering challenges for sustainable future—proceedings of the 3rd international conference on civil, offshore and environmental engineering, ICCOEE*, pp 251–256
20. Cong P, Cheng Y (2021) Advances in geopolymer materials: a comprehensive review. *J Traffic Transport Eng* 8(3):283–314
21. Tadros MK, Voo Y (2016) Taking ultra-high-performance concrete to new heights. *ASPIRE* 10(3):36–38

Experimental Investigation of the Effect of Water Hyacinth Extract Utilized for Curing on the Compressive and Flexural Strength of Concrete



Kimberly B. Sison, Allyssa Mae C. Estanio, Christian R. Quebral, Patricia Mae D. Santos, Ron Dominic L. Alberto, and Franz D. Santos

Abstract This study investigates the effect of water hyacinth extract (WHE) when used as a curing agent on the compressive strength and flexural strength of the Concrete. The efficiency of Water Hyacinth Extract (WHE) was evaluated by curing concrete samples using a ponding method with varying proportions of water and WHE (100–0%, 80–20%, 60–40%, 40–60%, 20–80%, 0–100%). The mixture proportion of 1:2.5:5 and a mixture ratio of 0.5 were cured in making concrete. Universal Testing Machine was used for this investigation in determining the Compressive and Flexural Strength of Concrete. Based on the result, the compressive strength sample cured with 20% water hyacinth extract for 28 days exhibited the highest compressive strength value of 16.23 MPa, while 80% WHE yields the highest flexural strength of 2.73 MPa. Results show that Water hyacinth extract is efficient and effective when utilized as a curing agent of concrete.

Keywords Concrete curing · Compressive strength · Flexural strength · Water hyacinth extract

1 Introduction

Pasig River, the main river of the national capital region that connects Manila Bay and Laguna Lake, was a critical source of transportation, water, food, and livelihood throughout history. For this reason, due to years of environmental damage, the river developed a terrible odor and a murky green tint [1]. In addition, the transit system was troubled by issues such as the expansion of informal settlements, water lilies, and other materials clogging the rivers [2]. Water hyacinth, scientifically known as *Eichhornia crassipes*, can multiply rapidly, especially during the rainy season; it is

K. B. Sison · A. M. C. Estanio · C. R. Quebral · P. M. D. Santos · R. D. L. Alberto · F. D. Santos (✉)
Department of Civil Engineering, National University-Manila, 1008 Manila, Philippines
e-mail: fdsantos@national-u.edu.ph

© The Author(s), under exclusive license to Springer Nature Singapore Pte Ltd. 2024
M. Casini (ed.), *Proceedings of the 3rd International Civil Engineering and Architecture Conference*, Lecture Notes in Civil Engineering 389,
https://doi.org/10.1007/978-981-99-6368-3_7

known for being a good indicator of sea-level differences. On the other hand, because of its huge, deep, glossy ovate leaves, water hyacinth causes various issues in the Pasig River, including obstruction of sunlight and clogging streams, which causes flooding and impeding water transportation. Using the plant as a by-product could overcome these issues, and various studies have concluded that water hyacinth is used as a construction material [3].

Concrete comprises crushed stone, river sand, water, and cement. It is frequently utilized in construction, accounting for twice the total of all other building materials [4]. It also involves the process of determining the proper proportion and quality of concrete ingredients to control and achieve the minimum strength and durability as economically as possible [5]. Curing plays an essential role to achieve the desired strength and durability of the concrete by limiting moisture loss during cement hydration [6]. Improper curing leads to disadvantages, such as not meeting the desired strength, eventually leading to poor concrete performance [7]. Curing boosted the sequence of internal chemical reactions in hydrated cement paste. A rise in concrete's cement hydration results in a ' denser and less permeable paste microstructure that reduces ion mobility and potentially decreases the rate of micro crack formation [8].

The ponding Method, also known as immersion curing, is a process of curing test specimens per ASTM C31 [9]. It is a widely utilized concrete curing process that maintains moisture during concrete hardening. Several investigation studies were conducted to evaluate the effects of some curing methods (Ponding, Burlap, Spraying Method) on the compressive strength of Concrete, the ponding method yields the highest compressive strength value [10].

As attested by previous studies, water hyacinth is an efficient accompaniment in the innovation of concrete properties. Concluded in the research of Sathya et al. [11] wherein the influence of water hyacinth extract as a bio-mixture in cement and concrete is studied, it is claimed that the replacement of water with hydro-extract of water hyacinth increases the workability and compressive strength of concrete. In the same study, water hyacinth is also concluded to be a retarder admixture extract due to its fatty acids and lignocellulose content which causes a delay in the setting time of the concrete. To address the issue of the increasing amount of water hyacinth and to improve the properties of concrete, varying proportions of water hyacinth extract were used to cure the concrete to determine its effect on the mechanical properties of the concrete namely compressive strength and flexural strength.

2 Materials and Methods

An experimental program was carried out on this experimental investigation to assess the effect of water hyacinth extract on the compressive and flexural strength of the concrete.

2.1 Concrete

The cement and aggregates used in making the concrete samples are Ordinary Portland Cement, 3/4-inch diameter gravel, and a natural sort of sand that passed through a 4.75 mm. They are readily available in our country and purchased at Lucky 666 Hardware and Construction Supply in Bacoor, Cavite. The dimension of the concrete cylinder samples is 4 inches in diameter and 8 inches in height per ASTM C39 [12], and the dimension of the concrete beam is 6 inches wide, 6 inches in depth, and 20 inches in length following ASTM C78 [13].

Concrete Cylinder Samples. The molding procedures of the concrete cylinders follow ASTM C31 [9]. The cylindrical mold used was filled into two layers, each layer tamped with 25 strokes using a 3/8 inch rod. After tamping, tap the outside of the mold about 10–15 times using an open hand or a rubber hammer. Lastly, level the surface of the concrete mixture with the mold. Figure 1a shows the concrete cylinder molds made of PVC pipe with a diameter of four inches and a height of eight inches. Casted freshly mixed concrete in the 54 cylindrical molds is depicted in Fig. 1b, and the casted-out dry concrete cylinders from molds are in Fig. 1c.

Concrete Beam Samples. The concrete beam molds also followed the ASTM C31 [9] as shown in Fig. 2.

The rectangular molds were filled in two layers, each layer tamped once for every two square inches of the surface area using a rod. After tamping, tap the outside of the mold 10–15 times using open hands or a rubber hammer and screed any excess concrete off the mold at the end. Figure 2a shows the 6 × 6 × 20 inch rectangle molds made in Hardiflex and Marine Plywood and the 20 × 21 × 7 inch curing containers made of Liso Plane sheets. Figure 2b depicts the newly poured freshly



Fig. 1 a Cylinder molds; b Wet concrete cylinders for curing; c Cured concrete cylinders



Fig. 2 a Cylinder molds; b Wet concrete beams for curing; c Cured concrete beam samples

mixed concrete on the concrete beam molds and shown in Fig. 2c are the molded dry concrete beams.

2.2 Curing

Curing plays an essential role in achieving the appropriate strength and durability of Concrete by minimizing moisture loss during cement hydration [6]. To assess the effect of water hyacinth extract on the compressive and flexural strength of the concrete, varying proportions of water and water hyacinth extract are synthesized and used as a curing agent. The concrete samples cured in 100% water was the controlled sample of this study.

Water Hyacinth Extract. The water hyacinth extract (WHE) was used as a superplasticizer admixture in concrete production. Superplasticizers retard the setting time of the concrete. Thus, it reduced the heat of hydration produced by the hydration of cement [14]. Varying proportions of water and WHE 100–0%, 80–20%, 60–40%, 40–60%, 20–80%, and 0–100%), as shown in Table 1, were synthesized, and were later then utilized for the curing of concrete samples.

Water hyacinth plants were harvested at Pasig River, cleaned using tap water, and then transported. The plants are washed and then chopped into smaller pieces before the process starts. The extraction process, which used a centrifugal juicer. The extracted liquid is a murky green tint and foul odor, but it subsided after three days. The extraction process is done repeatedly for six months to collect 167 L of extract. Researchers kept the samples at room temperature.

Ponding. Ponding Method is one of the most well-known and widely utilized concrete curing processes for avoiding moisture loss in concrete. This method is also essential for keeping the temperature consistent throughout the concrete [10]. As per ASTM C31 [9], ponding is the curing method conducted in this study. The synthesized curing ponds are made of a Liso Plane sheet. A total of 18 ponds in 14 × 5 × 9 inch dimensions were prepared to hold the concrete cylinder samples as shown in Fig. 3a. And another 18 ponds of 20 × 21 × 7 inch as shown in Fig. 3b, were prepared to retain the concrete beam samples.

Table 1 Water-water hyacinth extract mixture

Mixture no.	Water (%)	Water hyacinth extract/WHE (%)
1 (pure water)	100	0
2	80	20
3	60	40
4	40	60
5	20	80
6 (pure WHE)	0	100

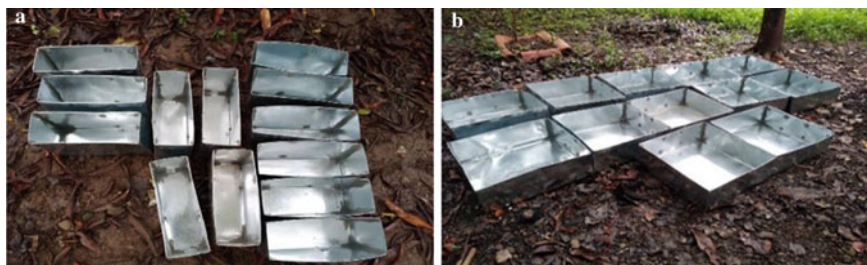


Fig. 3 a Concrete cylinders' curing containers; b Concrete beams' curing containers

2.3 Testing

Compressive Strength. Compressive strength is the most essential factor to consider when designing a structure [15]. The compressive strength of concrete cylinders with a diameter of 4" and a height of 8" is measured per ASTM C39 16, which specifies the use Universal Testing Machine for the test [16], after curing them for 7, 21, and 28 days. It depends on the mix ratio of the concrete in accordance with IS 456 as shown in Table 2. The study of [17] about the comparison of the compressive strength made with river sand (control sample) and quarry dust as fine aggregates, investigated the compressive strength in different grades of concrete. According to their study, the compressive strength of the 1:2.5:5 quality of the control concrete cured in 28 days is 13.9 MPa. For each curing agent with varying proportions of water and WHE, three specimens were tested and reported the average results.

Flexural Strength. Flexural strength, also known as the Modulus of Rupture (MR), is a material property of concrete that describes a beam's ability to resist failure in bending caused by applied loads before yielding [18]. Under the provisions of ASTM C78, the concrete beam samples with a cross-section of 6" × 6" and length of 20 were subjected to flexural tests using third point loading. The formula of flexural strength using 3rd point loading is $FS = FL/wd^2$, where FS is the flexural strength, F is the force or load at the point of failure, L is the span, w is the width and d is the depth of the beam. For the results, the metric system was used. For each curing

Table 2 Mix ratio for type of construction

Grade of concrete	Mix ratio	Type of construction
M 5	1:5:10	Generally used for PPC (plain cement concrete) works like levelling course, bedding for footing, and non-structural works
M 7.5	1:4:8	
M 10	1:3:6	
M 15	1:2:4	
M 20	1:1.5:3	Applicable for RCC (reinforced cement concrete) works for slabs, beams, and columns

agent with varying proportions of water and WHE, three specimens were tested and reported the average results.

Experimental Work. The Concrete Mixture follows the proportion of 1:2.5:5 (1 represents the ratio of Cement, 2.5 for the Sand or Fine Aggregates, and 5 for Gravel or Coarse Aggregate) and 0.5 Water-Cement Ratio by weight. The sieve analysis was performed on aggregates in this study. The slump test determines the consistency of fresh concrete to ensure the correct amount of water was added to the mixture. After 24 h of hardening the concrete, the Water-Water Hyacinth Extract mixture was prepared for the concrete curing process.

The mix of Water-Water Hyacinth Extract is as follows: (100–0%, 80–20%, 60–40%, 40–60%, 20–80%, 0–100%) and was measured by the curing container's volume. The concrete samples were submerged in the W-WHE mixtures for 7, 21, and 28 curing days. The concrete's flexural and compressive strength test was determined using UTM (Universal Testing Machine). A piston moves downward towards the concrete samples to apply loads, which tests unreinforced concrete's capacity to withstand force loads before failure ASTM C39 [12] for the Compressive Strength Test, and ASTM C78 [13] for the Flexural Strength Test.

3 Results and Discussion

3.1 Results of Mechanical Testing

Compressive Strength. Table 3 displays the average compressive strength results of this study.

The maximum compressive strength of the concrete sample after 28 days of curing in 20% water hyacinth extract is 16.23 MPa. Comparatively speaking to the WHE-cured concrete, the control sample's compressive strength of 12.24 MPa is lower. The control sample's compressive strength in the investigation was 12.241. MPa, which was higher than the desired 10 MPa compressive strength for M10 grade concrete. Therefore, the control sample passed the threshold for compressive strength.

Table 3 Summary of compressive strength results

Curing liquid ratio (Water-WHE)	Average compressive strength (MPa)		
	7 days	21 days	28 days
100–0%	11.4	11.7	12.24
80–20%	10.68	15.65	16.23
60–40%	11.84	14.78	15.95
40–60%	12.29	13.47	14.53
20–80%	12.99	13.45	14.08
0–100%	10.65	12.54	13.44

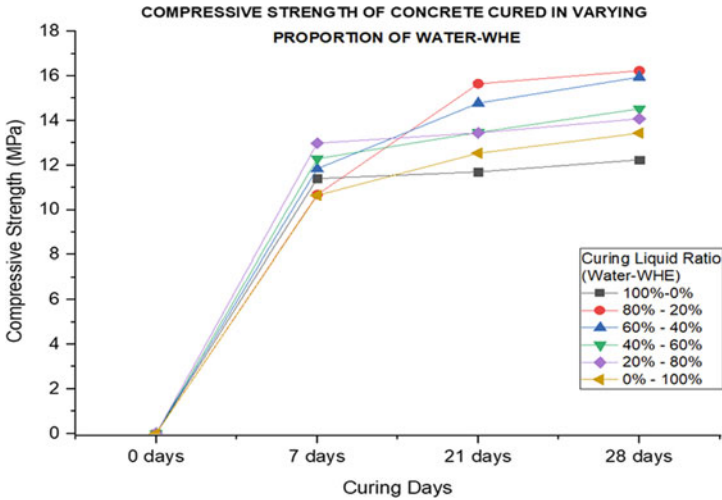


Fig. 4 Compressive strength test results

In Fig. 4, the line graph illustrates the progress in the compressive strength of the samples after curing with various amounts of water-WHE and curing times. At 28 days of curing age, the peak point of the lines showing the samples cured with 20–80% water and WHE is higher than the peak point on the line showing the progress of the cure samples in water only.

As seen on Fig. 5, the compressive strength of the samples treated with WHE grows more quickly than that of the samples cured in water alone as the number of curing days increases. Additionally, this demonstrates that compressive strength decreases as the ratio of water hyacinth extract rises. The optimal water hyacinth extract dilution is 20% with a 28-day cure age.

Flexural Strength. The concrete samples cured in 80% water hyacinth extract demonstrated the highest flexural strength values at 28 days of curing, with a value of 2.73 MPa, according to the overall results of this investigation, as shown in Table 4. However, in 20% WHE, the control sample’s flexural strength of 2.36 MPa was higher than that of the WHE-cured sample’s 2.21 MPa. Contrarily, the control sample reaches a flexural strength of 2.36 MPa, which is less than that of the WHE-cured concrete.

The line graph shown in Fig. 6 represents the progress in the flexural strength of the samples cured with varying proportions of water-WHE concerning curing days. At 28 days of curing age, the peak point of the lines representing the samples cured with 80–20% water and WHE is higher than the peak point representing the progress of the samples cured in water only.

Figure 7 shows a bar graph displaying the typical flexural strength of concrete beams. After seven days of curing in a 20–80% water-WHE ratio, the control sample had higher flexural strength than the WHE-cured sample. Despite this, the results

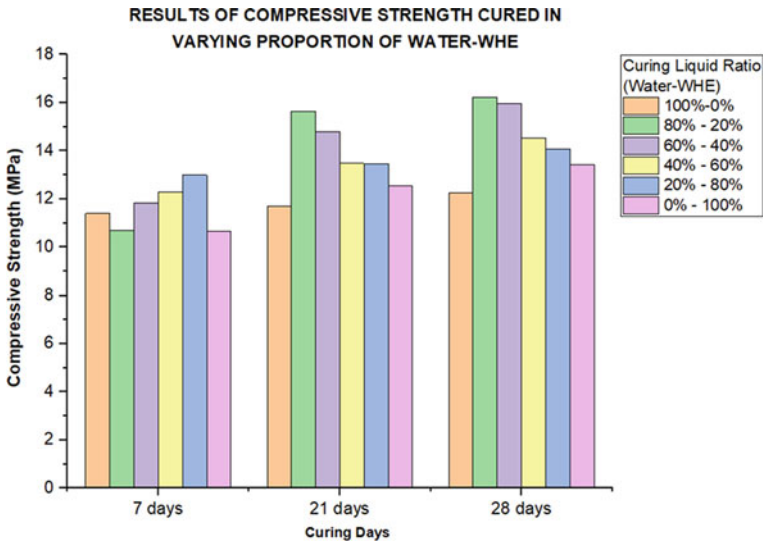


Fig. 5 Bar graph of compressive strength of concrete cured in varying proportions of W-WHE

Table 4 Summary of compressive strength results

Curing liquid ratio (water-WHE)	Average flexural strength (MPa)		
	7 days	21 days	28 days
100-0%	2.07	2.27	2.36
80-20%	2.13	2.15	2.21
60-40%	2.04	2.3	2.46
40-60%	2.17	2.4	2.53
20-80%	2.3	2.43	2.73
0-100%	2.38	2.41	2.48

showed that flexural strength increases in the 80-20% water-WHE ratio; subsequently, the following ratio demonstrates that flexural strength increases as the water hyacinth extract ratio is increased.

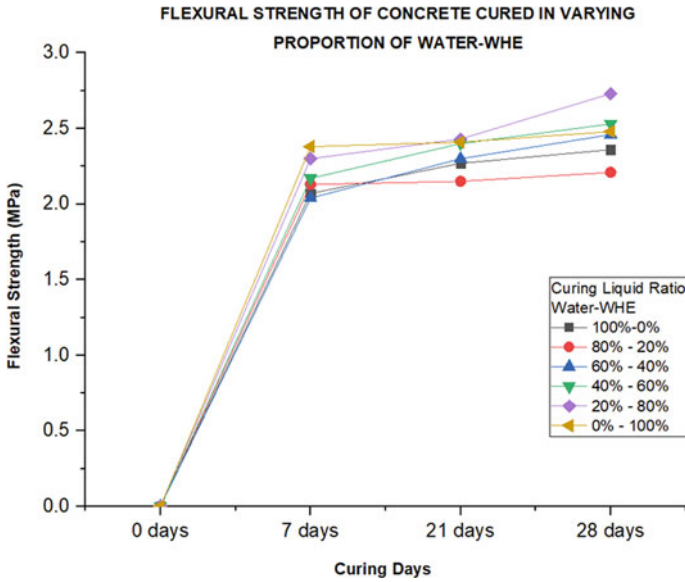


Fig. 6 Flexural strength test results

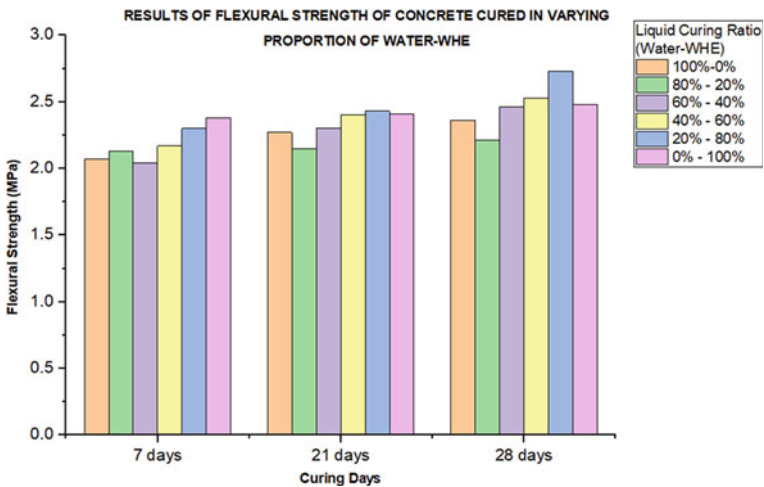


Fig. 7 Bar graph of flexural strength of concrete cured in varying proportions of W-WHE

4 Conclusion

Proliferation of water hyacinth in water streams of the country, for this study in Pasig River, has posed problems not only to the community in terms of limitation to their transport but also to the natural ecosystem. There had been constant aims to find

alternatives in improving the mechanical properties of construction materials and this study focused on using water hyacinth extract as a curing agent for concrete in an attempt to improve its compressive and flexural stress.

Based on the results of laboratory testing, it can be concluded that the concrete cured with Water Hyacinth Extract produces higher compressive and flexural strength than samples cured in pure water alone. As the curing days increased, the compressive samples cured in WHE increases more rapidly than that of samples cured in water only. The maximum compressive strength was recorded at 16.23 MPa by the sample cured in 80–20% (Water-WHE) during its 28th day as compared to the sample cured in pure water only (control sample) which was only at 12.24 MPa. This behavior could be attributed to the possible increased binding property of concrete brought about by the fiber in the extract of water hyacinth in agreement with the results of the study of [11].

For the flexural strength results, the maximum flexural strength was recorded at 2.73 MPa by the sample cured in 20–80% (Water-WHE) during its 28th day as compared to the sample cured in pure water only (control sample) which was only at 2.36 MPa. The results demonstrated that the flexural strength of the samples increases as the amount of WHE in the curing agent increases which could be attributed again to the enhanced binding property of concrete due to water hyacinth fibers [11]. In addition, to achieve a maximum result for compressive strength, the ideal dilution of water hyacinth extract on the curing agent stands at 20%, while 80% dilution gives the maximum the flexural strength as exhibited by the results of this study.

These results would be beneficial in improving the properties of concrete that is a widely used construction material in the industry while serving as a diversion for the persistent proliferation of water hyacinth in our water bodies.

Acknowledgements The proponents would like to thank Absolute Concrete Form Builders Corp., VSC Jr. Installation Services, and Mrs. Marybeth Formalejo for their contributions to the material gathering. To the Council of Barangay Natipuan, Nasugbu, Batangas for their help with materials and sample transportation. To the Council of Phase 3, Summerhills Townhomes Subdivision for allowing the use of their open area for this paper. The proponents would like to express our most incredible gratitude to all well-wishers whose enormous helps assisted to complete this report, most especially the ever-beloved parents of the researchers. Lastly, the proponents also would like to acknowledge National University – Manila particularly the Research and Development (NURD) Office for their support towards the presentation and publication of this research in the international stage.

References

1. Gorme JB, Maniquiz MC, Song P, Kim LH (2010) The water quality of the Pasig River in the City of Manila, Philippines: current status, management, and future recovery. *Environ Eng Res.* <https://doi.org/10.4491/eer.15.3.173>
2. Lazo MA, Nieto KK, Rayel MF, Sto Domingo DM, Vergara MA, Papa RD (2009) Composition, abundance, and distribution of rotifers in the Pasig River, Philippines. *The Philippine Scientist*, vol 46

3. Baccay MA (2017) Influence of varying mix design and fiber length on the properties of water hyacinth particle board. PUP J Sci Technol
4. Thandavamoorthy TS (2015) Determination of concrete compressive strength: a novel approach. Pelagia Res Library 6(10):88–96
5. Moepe R (2017) Concrete mix. Slump and concrete compression test, Botswana International University of Science and Technology
6. Verma VK, Rawat A (2018) Assessment of the effectiveness of different curing practices. J Ceram Concr Sci 3(2)
7. Liu B, Luo G, Xie Y (2018) Effect of curing conditions on the permeability of concrete with high volume mineral admixtures. Constr Build Mater 167(2018):359–371
8. Al Saffar DM, Al Saadb AJ, Tayeh BA (2019) Effect of internal curing on behavior of high-performance concrete: an overview. Case Stud Constr Mater 10(201):e00229
9. C31/C31M—19 (2018) Standard practice for making and curing concrete test specimens in the field. ASTM International, Annual Book of ASTM Standards, vol 04.02
10. Prasanth U, Kumar H, Basha S (2020) Study on utilization of zeolite and stone dust in concrete. Int J Eng Technol Manage Sci (IJETMS). <https://doi.org/10.46647/ijetms.2020.v04i05.017>
11. Sathya A, Bhuvaneshwari P, Niranjana G, Vishveswaran M (2014) Influence of bio admixture on mechanical properties of cement and concrete. Asian J Appl Sci
12. C39/C39M—01 (2001) Standard test method for compressive strength of cylindrical concrete specimens. ASTM International, Annual Book of ASTM Standards, vol. 04.02
13. C78—02 (2002) Standard test method for flexural strength of concrete (using simple beam with third-point loading). ASTM International, Annual Book of ASTM Standards, vol 04.02
14. Lazo MA, Nieto KK, Rayel MF, Sto. Domingo DM, Vergara MA, Papa RD (2009) Composition, abundance and distribution of rotifers in the Pasig River, Philippines. The Philippine Scientist, vol 46.
15. Silva RV, de Brito J, Dhir RK (2014) The influence of the use of recycled aggregates on the compressive strength of concrete: a review. Eur J Environ Civ Eng. <https://doi.org/10.1080/19648189.2014.974831>
16. Shafieifar M, Farzad M, Azizinamini A (2017) Experimental and numerical study on mechanical properties of ultra high-performance concrete (UHPC). Constr Build Mater 156:402–411
17. Chiemela C, Walter I, Ogedi I, Peter O, Mong O (2014) Comparing the compressive strengths of concrete made with river sand and quarry dust as fine aggregates. Int Lett Nat Sci 20(2014):179–189. <https://doi.org/10.18052/www.scipress.com/ILNS.20.179>
18. Supe J, Gupta MK (2014) flexural strength—a measure to control quality of rigid concrete pavements. Int J Scien Eng Res 5(11):46

Development of Additive for Concrete 3D Printer by Using Local Materials



Mohsin Usman Qureshi , Amira Al-Shizawi, Ghassan Al-Kindi, Bushra Al-Sawafi, and Yousuf Al-Balushi

Abstract This paper aims to delineate the best economical, multi-functional, and eco-friendly local materials to be used as an additive and explore its potential to revolutionize the construction industry using 3D concrete. The authors investigate different additive materials used in preparing four mixes using Ordinary Portland Cement, white cement, reservoir sediments, dune sand, commercial sand, fine marble waste and bentonite. The two mixes showed the best compressive strength and durability results, containing fine marble waste and reservoir sediments. The mix WSS (30% white cement, 50% sand, 20% sediment) has resulted in a compressive strength ranging from 18 to 21 MPa after 28 days of curing. The mix WSM (30% white cement, 50% sand & 20% fine marble waste) recorded a compressive strength range from 15 to 17 MPa after 28 days of curing. The durability of the two mixes was tested under wet & dry cycles. The mixes have achieved the best durability results with a minor reduction in durability after several cycles of wetting and drying. Both mixes successfully work as an additive for crafting in a newly developed concrete 3D printer.

Keywords 3D concrete printing · Additive manufacturing · Dune sand · Fine marble waste · Reservoir sediments

1 Introduction

The construction industry's contemporary challenges are efficiency in resources, economy, environment-friendliness, energy consumption, time, safety, etc. That necessitates developing more innovative techniques, such as digital construction. For example, layered manufacturing is a modern additive manufacturing technique that fabricates products by laying down material layer by layer. However, sustainability in using materials is still the least addressed issue in the field; therefore, the

M. U. Qureshi (✉) · A. Al-Shizawi · G. Al-Kindi · B. Al-Sawafi · Y. Al-Balushi
Faculty of Engineering, Sohar University, Sohar, Oman
e-mail: MQureshi@su.edu.om

© The Author(s), under exclusive license to Springer Nature Singapore Pte Ltd. 2024
M. Casini (ed.), *Proceedings of the 3rd International Civil Engineering and Architecture Conference*, Lecture Notes in Civil Engineering 389,
https://doi.org/10.1007/978-981-99-6368-3_8

current study will explore the feasibility of locally generated industrial waste as a material for the digital fabrication of concrete structures.

Different researchers around the globe have explored various cementitious materials and additives to investigate their feasibility in the application of digital fabrication. For example, fly Ash is one of the widely used materials as an additive in 3D concrete printing as it improves the interaction of colloidal between mixed materials due to its behavior [1]. Similarly, silica fume and fly ash increased the yield stress of the paste compared to casted samples with lower contents [2]. And it is found that Yield stress in the range of 1.5 and 2.5 kPa is found to improve both extrudability and buildability [3]. However, adding silica fume has a noticeable influence on the recovery of the viscosity, where adding 0.5 content of silica fume resulted in recovery behavior up to 13%, which is 5% higher than the control sample containing no silica fumes [4].

Abbi et al. [5] and Ferretti et al. [6] included rice rush in their mixtures and found that the mix of printing is most efficient at 0.05 kPa.s viscosity. To produce statistically grounded designs using these additives with high-quality results, the mix with a content of 0.24% is recommended to be used in 3DCP for achieving shape stability and average extrusion pressure [7]. It is also found that the reuse of paper mill sludge waste increases elastic modulus, but it drops at a certain point as stress increases [8]. Na et al. developed cement-based printing material using calcium sulfoaluminate (CSA) with sodium silicate (Na_2SiO_3), gypsum, and sand [9].

Chen et al. [10] experimented with low and high-calcined clays as an additive material, and it was found that increasing the content of high-calcined clay improves the flow consistency of the fresh mix. In contrast, other ratios of clay addition collapsed after crafting ten layers only. And it also showed a decrease in the slump and flowability [7]. In addition, printed structures with lateral support had better resistance to buckling failure and an increased number of printed layers [11].

Lee et al. [12] found that the interlayer strength decreased as the number of layers increased. However, aged samples show a steady increase in stress failure as confined [13, 14]. Matthäus et al. [15] experimented with various methods of reinforcement for the improvement of strength. Chen et al. [16] found that adding 0.2 content of Bentonite clay increases the shear stress and viscosity as well as compressive strength from 38.7 to 46.9 MPa. Yang et al. [17] found that adding nano-clay improved early and later age strength. However, it decreased the flowability by approximately 10% [18].

In contrast, the water mist did not affect the interlayer bond in any way. Finally, it was noticed that the printed samples with a four-hour gap resulted in more interface air voids compared to casted models [19]. Therefore, the present study aims to utilize local waste materials [20–26] to develop an additive for concrete 3D printer.

2 Material and Methods

Dune sand (D) used in this study was sampled from the northern part of Wahiba, located about 200 km to the southeast of Oman’s capital Muscat. The sand’s specific gravity (Gs) is 2.62, which includes fine content of 3.5%. The photomicrograph of dune sand and its elemental composition is presented in Fig. 1.

The reservoir sediments (S) used in this experiment were obtained from the Wadi Al-Jezzi Dam Reservoir, located west of Sohar city port, Oman. The sample (Fig. 2) comprises 74.1% fine content with a specific gravity (GS) of 2.38.

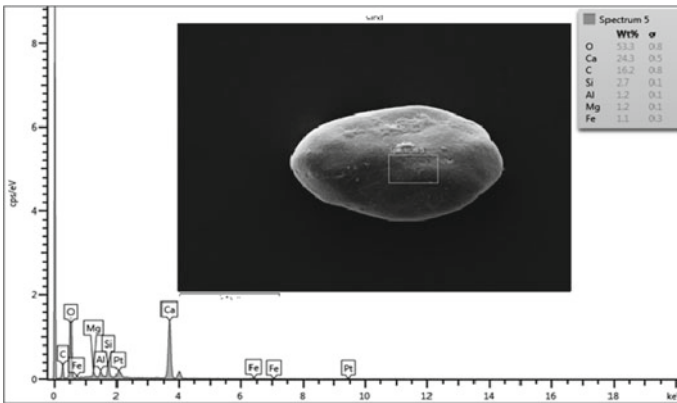


Fig. 1 Photomicrograph and elemental composition of dune sand

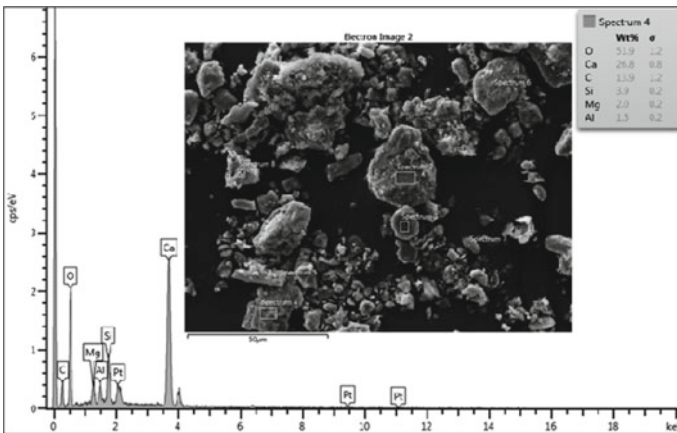


Fig. 2 Photomicrograph and elemental composition of reservoir sediments

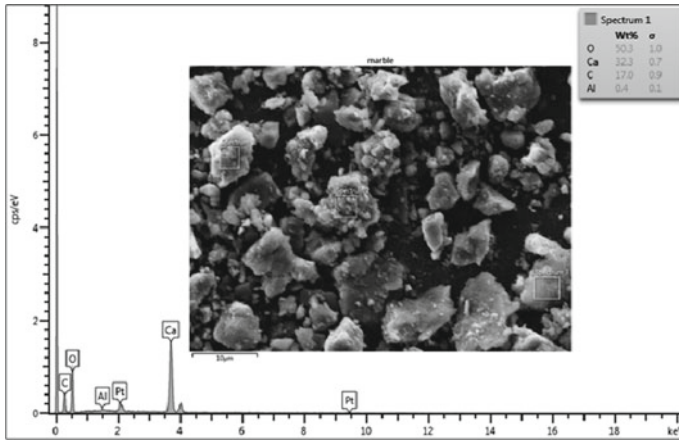


Fig. 3 Photomicrograph and elemental composition of marble waste

Waste marble dust (M) used in the study was collected from a marble quarry about 100 km to the southwest of the coastal city of AlKhaboura, Oman. The marble waste (Fig. 3) has a specific gravity (Gs) of 2.45 and fine contents of 84.1%.

For a fair comparison of additive material and its interaction with sand and binders, the mix ratio has been fixed in four different mixes as shown in Table 1. The sand content is set at 0.5% in all mixtures, 0.3 percent for binder and 0.2% for additive material. CSS and WSS contain sediment as an additive material. However, CSS has OPC, and WSS contains white cement. WSM contains fine marble waste as an additive material, and WSB contains bentonite clay.

The concrete 3D printer consists of three arms, as shown in Fig. 4. The first arm at the printer’s base is on the x-axis and is 100 cm. The second arm is on the z-axis, and it is 100 cm. Both arms are for printing the length. The third arm is on the y-axis, providing a width of the wall of up to 50 cm and 100 cm in height. The nozzle can be attached to the y-axis arm, as shown in Fig. 4. The whole function is controlled using a computer system. The concrete 3D printer is designed with total movement freedom of 100 × 100 × 50 cm.

Table 1 Trial additive and mix ratio

Mix	Material ratio		
CSS	OPC-0.3	Sand-0.5	Sediment-0.2
WSS	White cement-0.3	Sand-0.5	Sediment-0.2
WSM	White cement-0.3	Sand-0.5	Fine marble waste-0.2
WSB	White cement-0.3	Sand-0.5	Bentonite-0.2

Fig. 4 Concrete 3D printer developed at Sohar University, Oman



3 Results and Discussions

A batch of trials of the four mixes has been made, including CSS, WSS, WSM and WSB, to test its compressive strength in an automated compression machine. Casted cube test of dimension $5 \times 5 \times 5$ cm, cured at room temperature and tested after three, seven, 14 and 90 days. As shown in Fig. 5, two mixes achieved better results than others in terms of compressive strength: samples containing fine marble waste and samples containing sediment along with white cement as a binder. WSS resulted in compressive strength of 7.2 MPa after three days, which increased to about 19 MPa after 90 days. The failure modes of the tested specimens are shown in Fig. 6.

A durable building material must resist weathering of environmental conditions, including temperature and rain. This test compares the slaking index of the four mixes, including CSS (OPC, sand and sediment), WSS (white cement, sand and sediment), WSB (white cement, sand and bentonite) and WSM (white cement, sand and fine marble waste) by applying standard wet-dry cycles.

Fig. 5 Compressive strength of trial mixes of additive

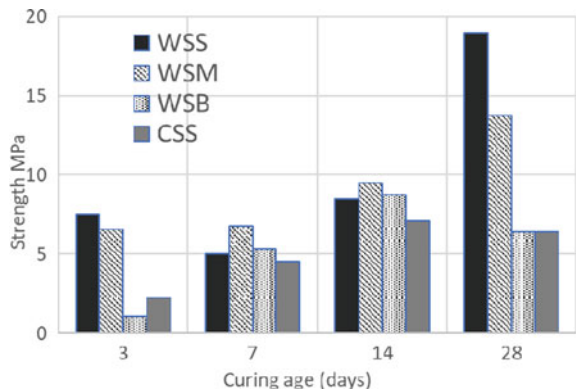
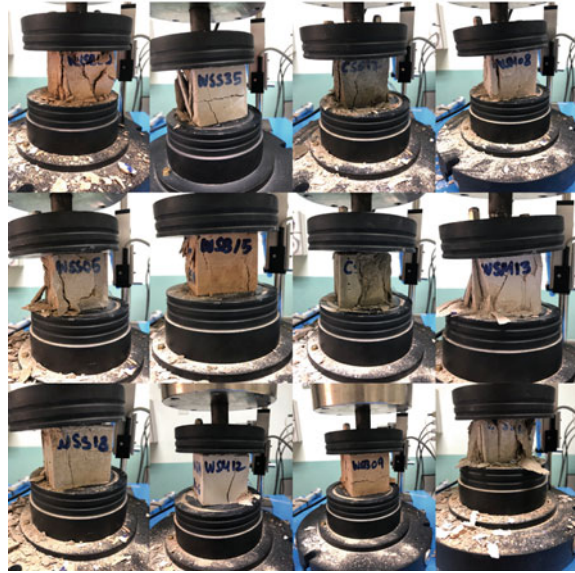


Fig. 6 Failure modes of trial mix specimens tested in a compression machine



As shown in Fig. 7, the slaking index of samples WSS, WSM and CSS behave the same and are more durable than WSB in wet-dry cycles. However, after ten cycles WSB slaking index dropped to 35.5%, which is considered very low. As well as, initially, WSB retained less weight at 84.9% compared to CSS at 96.7%, WSS at 95.8% and WSM at 98.8%. However, slaking index of WSS, CSS and WSM indicate that the material is highly durable. The additive is manufactured by the best mix of WSS (white cement, sand and sediment) and used to craft the 3D concrete structure of horizontal dimensions 60 × 20 cm. The authors successfully crafted a 30 cm high structure with 28 layers in one attempt, as shown in Fig. 8.

Fig. 7 Slake durability index of trial mixes of additive

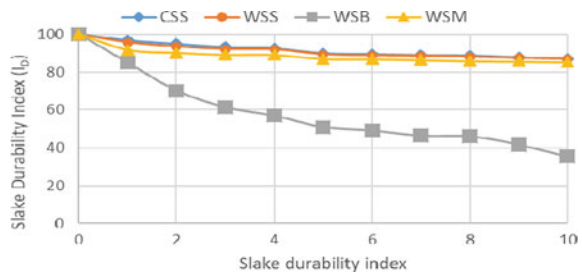


Fig. 8 Structures crafted from WSS



4 Conclusion

The following conclusion can be drawn based on the results and discussions made in this paper.

- Different local additive materials are used in preparing four mixes using Ordinary Portland Cement, white cement, reservoir sediments, dune sand, commercial sand, fine marble waste and bentonite. Two of the mixes showed promising compressive strength and durability results, containing fine marble waste and reservoir sediments, making them qualify for the trial of 3D crafting.
- The mix WSS (30%white cement, 50%sand, 20%sediment) has resulted in a compressive strength ranging from 18 to 21 MPa after 28 days of curing. The mix WSM (30%white cement, 50%sand & 20% fine marble waste) recorded a compressive strength range from 15 to 17 MPa after 28 days of curing. The durability of the two mixes was tested under wet and dry cycles. The mixes have achieved the best durability results with a minor reduction in durability index after six cycles of wet and dry.
- The layered structures are crafted by using the best mixes as an additive in a newly developed concrete 3D printer. More experiments are in progress on the assessment of buildability and structural integrity.

Acknowledgements The research leading to these results has received funding from the Ministry of Higher Education, Research and Innovation (MOHERI) of the Sultanate of Oman under the Block Funding Program, Block Funding Agreement No MOHERI/BFP/SU/01/2021/RG/02. The authors are also indebted to Sohar University, Oman, for providing in-house experimental facilities.

References

- Panda B, Unluer C, Tan MJ (2018) Investigation of the rheology and strength of geopolymers for extrusion-based 3D printing. *Cem Concr Compos* 94:307–314. <https://doi.org/10.1016/j.cemconcomp.2018.10.002>
- Ma G, Li Y, Wang L, Zhang J, Li Z (2020) Real-time quantification of fresh and hardened mechanical property for 3D printing material by intellectualization with piezoelectric transducers. *Constr Build Mater* 241. <https://doi.org/10.1016/j.conbuildmat.2019.117982>
- Bhattacharjee S, Santhanam M, Rahul A (2020) v: concrete 3D printing-Progress worldwide and in India composite cements with limestone additions: microstructure and transport properties view project national centre for safety of heritage structures view project Concrete 3D Printing-Progress Worldwide and in India
- Panda B, Tan MJ (2018) Experimental study on mix proportion and fresh properties of fly ash based geopolymer for 3D concrete printing. *Ceram Int* 44. <https://doi.org/10.1016/j.ceramint.2018.03.031>
- Abbi B, Ferretti E, Mohammed I (2022) Development of a mini 3D printer for concrete custom structures a revision of Boussinesq's solution for a homogeneous, linear-elastic and isotropic half-space subjected to point-loads perpendicular to the surface view project stability of plates and shells view project Hanane es-sebyty Université Ibn Tofail 2 Publications 0 Citations See Profile
- Ferretti E, Chiusoli A, Naldoni L (2021) Rice husk shredding as a means of increasing the long-term mechanical properties of earthen mixtures for 3D printing combined strengthening techniques to improve the out-of-plane performance of masonry walls view project stability of plates and shells view project. <https://doi.org/10.20944/preprints202112.0360.v1>
- Chen Y, Figueiredo SC, Yalçinkaya Ç, Çopuroğlu O, Veer F, Schlangen E (2019) The effect of viscosity-modifying admixture on the extrudability of limestone and calcined clay-based cementitious material for extrusion-based 3D concrete printing. *Materials* 12. <https://doi.org/10.3390/ma12091374>
- Chen Y, He S, Gan Y, Çopuroğlu O, Veer F, Schlangen E (2022) A review of printing strategies, sustainable cementitious materials and characterization methods in the context of extrusion-based 3D concrete printing. *J Build Eng* 45. <https://doi.org/10.1016/j.jobe.2021.103599>
- Na O, Kim K, Lee H, Lee H (2021) Printability and setting time of csa cement with na₂ sio₃ and gypsum for binder jetting 3d printing. *Materials* 14. <https://doi.org/10.3390/ma14112811>
- Chen Y, Romero Rodriguez C, Li Z, Chen B, Çopuroğlu O, Schlangen E (2020) Effect of different grade levels of calcined clays on fresh and hardened properties of ternary-blended cementitious materials for 3D printing. *Cem Concr Compos* 114. <https://doi.org/10.1016/j.cemconcomp.2020.103708>
- Joh C, Lee J, Bui TQ, Park J, Yang IH (2020) Buildability and mechanical properties of 3d printed concrete. *Materials* 13:1–24. <https://doi.org/10.3390/ma13214919>
- Meurer M, Classen M (2021) Mechanical properties of hardened 3D printed concretes and mortars-development of a consistent experimental characterization strategy. *Materials* 14:1–23. <https://doi.org/10.3390/ma14040752>
- Lee H, Kim J-HJ, Moon J-H, Kim W-W, Seo E-A (2019) Evaluation of the mechanical properties of a 3D-printed mortar. *Materials* 12:4104. <https://doi.org/10.3390/ma12244104>
- Wolfs RJM, Bos FP, Salet TAM (2019) Triaxial compression testing on early age concrete for numerical analysis of 3D concrete printing. *Cem Concr Compos* 104. <https://doi.org/10.1016/j.cemconcomp.2019.103344>
- Matthäus C, Kofler N, Kränkel T, Weger D, Gehlen C (2020) Interlayer reinforcement combined with fiber reinforcement for extruded lightweight mortar elements. *Materials* 13:1–17. <https://doi.org/10.3390/ma13214778>
- Chen M, Liu B, Li L, Cao L, Huang Y, Wang S, Zhao P, Lu L, Cheng X (2020) Rheological parameters, thixotropy and creep of 3D-printed calcium sulfoaluminate cement composites modified by bentonite. *Compos B Eng* 186. <https://doi.org/10.1016/j.compositesb.2020.107821>

17. Yang H, Li W, Che Y (2020) 3D Printing cementitious materials containing nano-CaCO₃: workability, strength, and microstructure. *Front Mater* 7. <https://doi.org/10.3389/fmats.2020.00260>
18. Zhang Y, Zhang Y, Liu G, Yang Y, Wu M, Pang B (2018) Fresh properties of a novel 3D printing concrete ink. *Constr Build Mater* 174:263–271. <https://doi.org/10.1016/j.conbuildmat.2018.04.115>
19. Chen Y, Chang Z, He S, Çopuroğlu O, Šavija B, Schlangen E (2022) Effect of curing methods during a long time gap between two printing sessions on the interlayer bonding of 3D printed cementitious materials. *Constr Build Mater* 332. <https://doi.org/10.1016/j.conbuildmat.2022.127394>
20. Ibrahim O, Al-Kindi G, Qureshi MU, Maghawry S (2022) AI: challenges and construction applications of solid waste management in middle East Arab Countries. *Process* 10:2289. <https://doi.org/10.3390/PR10112289>
21. Qureshi MU, Mahmood Z, Farooq QU, Qureshi QBIL, Al-Handasi H, Chang I, Qureshi MU, Mahmood Z, Farooq QU, Qureshi QBIL, Al-Handasi H, Chang I (2022) Geomechanics and engineering. *Geomech Eng* 28:547. <https://doi.org/10.12989/GAE.2022.28.6.547>
22. Al-Kindi N, Al-Moqbali A, Qureshi M, Al-Shidi A, Ala-Aldhen I (2016) Mechanical characteristics of recycled concrete aggregates as backfill material. *Int J Appl Eng Res*
23. Qureshi MU, Al-Sawafi B, Al-Washahi M, Al-Saidi M, Al-Badi S (2018) The sustainable use of fine marble waste powder for the stabilization of desert sand in Oman. Presented at the (2018). https://doi.org/10.1007/978-3-319-61612-4_25
24. Qureshi MU, Alsaaidi M, Aziz M, Chang I, Rasool AM, Kazmi ZA (2021) Use of reservoir sediments to improve engineering properties of dune sand in Oman. *Appl Sci* 11:1620. <https://doi.org/10.3390/app11041620>
25. Aziz M, Sheikh FN, Qureshi MU, Rasool AM, Irfan M (2021) Experimental study on endurance performance of lime and cement-treated cohesive soil. *KSCE J Civ Eng*. <https://doi.org/10.1007/s12205-021-2154-7>
26. Qureshi MU, Alkindi G, Alsaaidi M (2021) Experimental study to investigate dune sand improvement by adding fine waste materials. *Key Eng Mater* 902:153–159

Concrete Delamination Characterization by Multi-Channel Surface Rayleigh Wave Measurement



Foo Wei Lee, Yoke Bee Woon, Kok Zee Kwong, and Ming Kun Yew

Abstract A non-destructive testing (NDT) technique is adopted to analyse concrete delamination by utilizing multi-channel acquisition of surface Rayleigh waves (R-waves). This study embarks on examining the behaviour of R-waves propagating in concrete containing delamination. The aim is to identify the promising properties of R-wave such as wavelet transforms (WT) attenuation coefficient and phase velocity for reliable assessment. Numerical simulations of wave motions were conducted, followed by data processing to obtain correlations between the respective R-waves properties and characteristics of delamination. Results of analysis revealed that the (WT) attenuation coefficient were sensitive to the presence of delamination, inferring that simple waveform analysis can enhance the characterization of sub-surface delamination existed in concrete structures.

Keywords Concrete delamination · Phase velocity · WT attenuation coefficient · Reinforced concrete

1 Introduction

Delamination is one of the basic defects existed in the concrete structures and can be developed by over-stressing, creep, fatigue, corrosion, or thermal expansion [1, 2]. Detection of delamination at early ages is vital to avoid large-scale deterioration while an effective assessment method is essentially important in construction of the structural health monitoring system. Numerous of non-destructive testing (NDT) techniques can be applied on concrete structures, namely ultrasonic surface wave, ground penetrating radar (GPR), acoustic emission, impact echo method infra-ray and tomography method. Among, most of them are developed according to the fundamental principles of elastic wave propagation.

F. W. Lee (✉) · Y. B. Woon · K. Z. Kwong · M. K. Yew
Department of Civil Engineering, Lee Kong Chian Faculty of Engineering and Science, Universiti Tunku Aabul Rahman, Petaling Jaya, Malaysia
e-mail: leefw@utar.edu.my

Recent studies have confirmed that surface Rayleigh waves (R-waves) have satisfied NDT requirements, suggesting the possibility of utilization in assessment of defects in existing concrete infrastructures [3]. R-wave owns some specific characteristics which are superior for concrete defects assessments. Especially its low attenuation and high energy contents make it suitable to be used in concrete defects detection [4]. In addition, R-waves can be detected at large distance, preferable than other body waves. Owing to its dispersive characteristic, the displacement of R-wave's wavelength penetrates more deeply into the concrete medium. These features are potentially feasible for characterization of delamination.

The main objective of this paper is to investigate the feasibility of R-waves in evaluating concrete delamination. Key parameters of R-waves such as wavelet transform (WT) attenuation coefficient and phase velocity that are sensitive towards changes of delamination in varying depths and lengths were analysed through numerical simulation. Verification of proposed correlations through laboratory experimental examinations was then suggest the viability for assessment of delamination in concrete structure using multi- channel acquisition of R-waves.

2 Numerical Simulation

A series of numerical simulations were completed using commercial software that use finite difference method [5] to solve two dimensional (2D) elastic wave propagation problems. Figure 1 shows an example of the model of simulation, reinforced concrete section of 500 mm (width) \times 300 mm (depth) in size with a crack that lied horizontally to imitate delamination. All simulation cases have the uniform properties of concrete, assuming the material to be elastic and with no viscosity components. The elastic waves' parameters of concrete and steel reinforcement adopted in this simulation work were included, as listed in Table 1.

According to the experimental measurements, the simulated model was set up to have primary wave velocities of approximately 4300 and 6099 m/s, for concrete

Fig. 1 Schematic sketch of simulation model with inhomogeneity introduced by a delamination

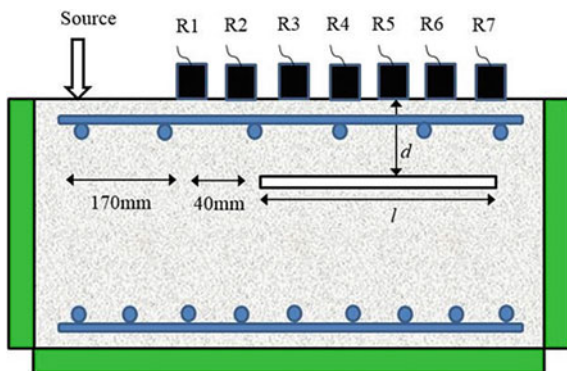


Table 1 Properties of concrete model and reinforcing steel

Parameter	Concrete Model	Reinforcing Steel
Lambda, λ (Mpa)	15,457	99,710
Mu, μ_m (Mpa)	14,600	96,160
Density, ρ_m (kg/m ³)	2313	7850
P-wave velocity, C_P (m/s)	4394	6099
R-wave velocity, C_R (m/s)	2311	3219
Wavelength of R-wave, λ_R (mm)	2.31	3.22

Table 2 Summary of delamination cases

Depth, d (mm)	Length, l (mm)	Frequency, f (kHz)
50, 90, 150 and 250	50 to 250 at 50 mm increment	7, 8, 9, 10, 15, 20, 30, 40, 50, 60, 80, 100, 150

and steel reinforcement, respectively. To receive the waves generated by the impact source, seven sensors were situated on top surface of concrete model side-by-side with an interval of 40 mm as shown in Fig. 1. The distance between the source and the first trigger sensor was configured as 170 mm. Besides, infinite boundary conditions were configured at the right, left, and bottom sides of concrete model to ensure that the transmitted waves would not reflected when it reached the edge of concrete. The parameters of R- wave propagation investigation include length and depth of delamination, and also the excitation frequencies as shown in Table 2.

The simulations were conducted with one excitation that produced a single cycle R-waves with a range of frequencies that propagated from one side to the other side of model. The effect of delamination on the waveform distortion, attenuation and phase velocity was examined. The data recording frequency was about 5×10^6 Hz samples per second. In addition, the range of excitation frequencies were chosen to study the limitation of penetration depth of R-waves to delamination detection. Taking the case of the lowest excitation frequency of 7 kHz as an example, R-waves with the deepest penetration depth was able to identify the delamination with depth of 250 mm from top face of concrete.

3 Results and Discussion

Figure 2a shows the waveform amplitude for sound concrete. The amplitude detected by four sensors is almost the same. While, Fig. 2b shows the waveform amplitude for defective concrete, and it can be noticed that the amplitude detected by S3 and S4 sensors which after the delamination are significantly lower than S1 and S2 which before the delamination. Therefore, it can be proven that the waveform amplitude is sensitive to the delamination in concrete.

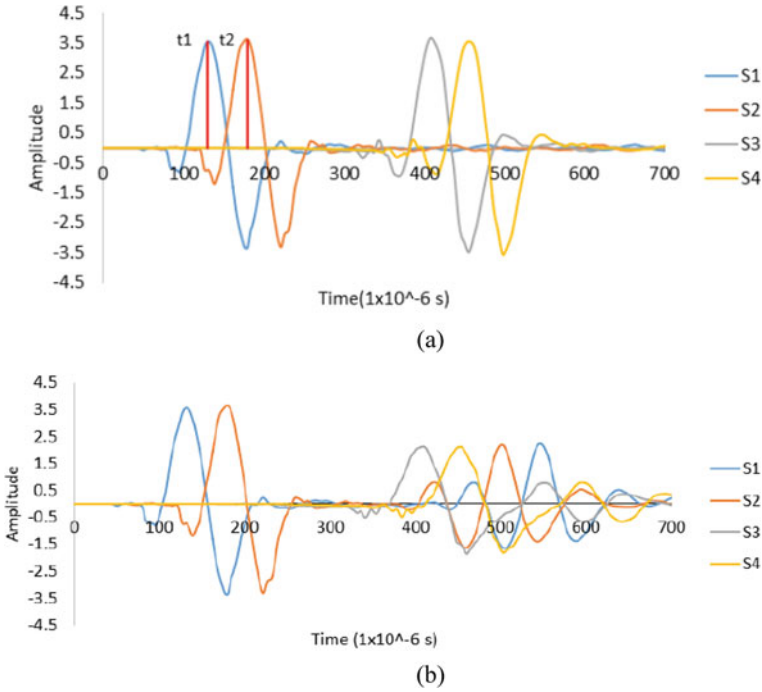


Fig. 2 Waveforms collected from **a** sound concrete and **b** delamination with 50 mm depth and length

3.1 WT Attenuation Coefficient Index

R-wave components have to be extracted and separated from the bulk waves in recorded signals before further analysis based on maximum energy concept. The processed signals were then analysed using morlet wavelet transform and the outputs were known as WT attenuation coefficient. The WT attenuation coefficient index is defined as the ratio of average R-wave WT attenuation coefficient measured in the concrete model with delamination to the average R-wave WT attenuation coefficient measured in the sound concrete model:

$$A'_{WT} = \frac{\sum_1^J A_{WTd}/7}{\sum_1^J A_{WTS}/7} \quad j = 2, 3, 4, 5, 6 \text{ and } 7 \quad (1)$$

where A_{WTI} is WT attenuation coefficient index, A_{WTd} is the R-wave WT attenuation coefficient in concrete model with delamination, A_{WTS} is the R-wave WT attenuation coefficient in sound concrete model. The time domain data are in Wavelet transformed and their responses were given as the frequency dependent attenuation known as WT attenuation coefficient.

The crack depth is practically divided by the major wavelength of R-waves to give a parameter that provides flexibility and wider coverage in comparison and evaluation [6–8]. Plotting of WT attenuation coefficient index with respect to d/l ratio yielded a reasonably good correlations polynomial regressions for all cases. It was noticeable that WT attenuation coefficient index showed either decreasing or increasing trend with respect to the d/l ratio for different excitation frequencies. WT attenuation indices decreased for the case of higher excitation frequencies due to loose energy through scattering, distortion and diffraction by the delamination.

When WT attenuation coefficient indices plotted against the depth of delamination, two different types of trends (increasing or decreasing) were observed as the depth of delamination increased as can be seen in Fig. 3. The first group of frequencies (7, 8, 9 and 10 kHz) showed increasing trend of WT attenuation coefficient index and approached towards 1.0 as the delamination depth increased. Whereas, higher excitation frequencies group (which is more than 15 kHz) showed decreasing trend for WT attenuation coefficient indices and also approaching to 1.0 as the depth of delamination increased. The phenomena of WT attenuation coefficient approaching 1.0 indicated that the WT attenuation coefficient index loose its sensitivity to delamination identification.

On the contrary, the relation between WT attenuation coefficient index and the length of delamination also showed increasing or decreasing trends but opposite to the ones mentioned above. WT attenuation coefficient index showed a decreasing trend lower than 1.0 for lower excitation frequencies (7, 8, 9 and 10 kHz). For higher excitation frequencies, WT attenuation coefficient index increased higher than 1.0 as length of delamination is increased. This mostly can be explained by the reflection of the elastic waves when they are impinged the delamination.

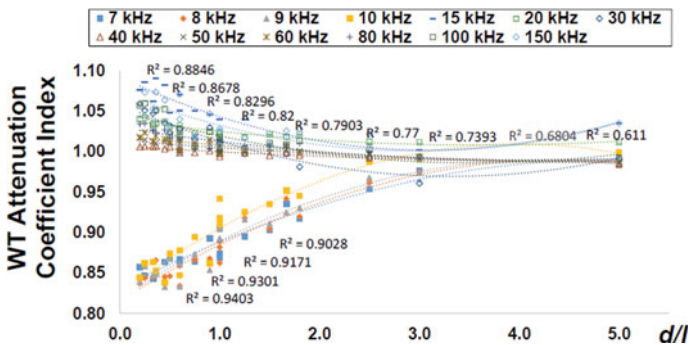


Fig. 3 WT attenuation coefficient index versus d/l ratio

3.2 Phase Velocity Index

Phase velocity is used to study and investigate dispersion of R-waves against delamination and evaluate the relationship between frequency and the depth of delamination. It is measured based on the phase different between sensors. Frequency domain function of the received signals are used to determine the effective frequency bandwidth which contain most of the signal energy and indicating by a characteristics peak frequency belonging to the propagation of R-waves by Fast Fourier Transform (FFT). The phase velocity for the crack model with delamination was found to have lower values and less uniform within the bandwidth excitation if penetration depth of excitation frequencies longer than depth of delamination. For example, lower excitation frequency of 7 kHz, the average phase velocity are lower than sound concrete model. Meanwhile in the case of highest excitation frequency which is 150 kHz, the average phase velocity obtained are quite similar to the average velocity obtained for the sound model. Phase velocity index is defined as the ratio of average phase velocity obtained from the model with delamination to the average phase velocity obtained from the sound concrete model.

$$V_P^I = \frac{\sum_1^J V_{pd(1\sim j)}/7}{\sum_1^J V_{ps(1\sim j)}/7} \quad j = 2, 3, 4, 5, 6 \text{ and } 7 \quad (2)$$

where V_{PI} is phase velocity index, V_{pd} is R-wave phase velocity in concrete model with delamination, V_{ps} is R-wave phase velocity in sound concrete model. Phase velocity index of 1.0 manifests no distortion of R-waves has occurred. Current findings showed that, delamination in concrete is confirmed to induce variation of phase velocity even though the variation would be less significant in some cases. The phase velocity index was plotted with respect to the d/l ratio as depicted in Fig. 4.

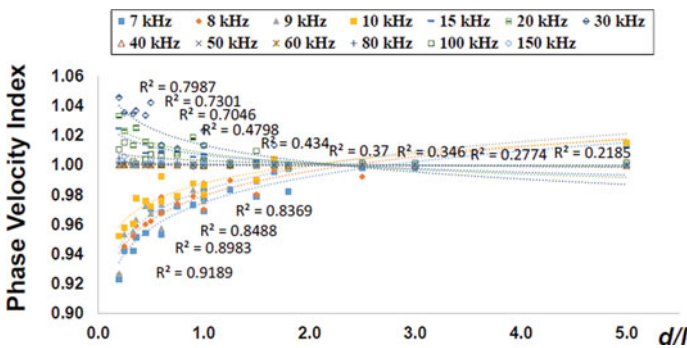


Fig. 4 Phase velocity index versus d/l ratio

4 Conclusion

In this paper, the behavior of R-waves propagating in concrete with delamination is examined through numerical simulations of wave motions. Velocity-related and energy-related parameters of R-waves were further processed by FFT and wavelet transform to extract phase velocity and wavelet coefficient data for subsequent analysis. Varying cases of depths and lengths of delamination were considered in the simulation work, in addition to excitation frequencies. Based on the results, the sensitivity of WT attenuation coefficient index of R-wave towards the delamination was better compared to the attenuation index. It can be concluded that the WT attenuation coefficient index was the most sensitive parameter towards the variation of delamination characteristics by giving a more stable trend of change and by yielding better correlations compared to other parameters. It is to be noted however that in this study two uncertainties were included, namely the length and depth of delamination. A further study will be focused on investigating the possibility of establishing feasible relationships between these two parameters, or with R-wave parameter, such as wavelength that can be computed respectively in order to formulate a useful and simple characterization methodology for delamination in concrete.

Acknowledgements This work was supported under the University Research Funding (IPSR/RMC/UTARRF/2017-C2/L02).

References

1. Carraro PA, Maragoni L, Quaresimin M (2019) Characterisation and analysis of transverse crack-induced delamination in cross-ply composite laminates under fatigue loadings. *Int J Fatigue* 129:105217
2. Kumar V, Dewangan HC, Sharma N, Panda SK (2022) Numerical prediction of static and vibration responses of damaged (crack and delamination) laminated shell structure: an experimental verification. *Mech Syst Signal Process* 170:108883
3. Yu H, Lu L, Qiao P (2021) Localization and size quantification of surface crack of concrete based on Rayleigh wave attenuation model. *Constr Build Mater* 280:122437
4. Zewer A, Polak MA, Santamaria JC (2005) Detection of surface breaking cracks in concrete members using Rayleigh waves. *J Environ Eng Geophys* 10(3):295–306
5. Wave2000, Cyber-Logic, Inc., New York. <http://www.cyberlogic.org>
6. Chai HY, Chen EJ, Chai YF, Ke WH, Zhu HX (2022) Rayleigh wave scattering at shallow cavities in layered half spaces. *Soil Dyn Earthq Eng* 156:107215
7. Xiu C, Chu X, Wan J, Wang J (2021) Numerical simulation of impulse waves in Cosserat media based on a time-discontinuous Galerkin finite element method. *Int J Numer Meth Eng* 122(17):4507–4540
8. Lee FW, Chai HK, Lim KS, Lau SH (2019) Concrete subsurface crack characterization by means of surface rayleigh wave method. *ACI Mater J* 116(1)

Advanced Building Materials and the Properties

Mix Design for Cellular Concrete Applied in Masonry Units Using Decyl Glucoside as a Foaming Agent for Construction in High Andean Cities in 2022



Flores Sánchez Diego Oswaldo , Hermosa Vargas Flor Milagros ,
and Montoya Torres Vladimir Simón 

Abstract The research aimed was to find a suitable mix design of cellular concrete applied in masonry units using decyl glucoside as a foaming agent for construction in high Andean cities, because of the advantages this offers, being the main one, thermal comfort since high Andean cities suffer from low temperatures, meeting the compressive resistance standard for masonry units and reducing the dead load, due to cellular concrete is not currently very commercial. Therefore, this study experiments with seven different proportions of water, cement, fine/coarse sand and a foaming agent to achieve better resistance. The study is of descriptive level in that the experimental method is employed in which we use an observation card; for the mixing process, an industrial cement mixer was used, which allows us to integrate the foaming water with the aggregates. The compressive resistance results were favorable obtaining results of up to 260.7 kg/cm² and lightening the weight up to about 30% of standard concrete, in the other trials lower compressive resistance were achieved, but with a weight even lighter and also a lower volume. The conclusions determine that it is possible to realize a cellular concrete using decyl glucoside meeting the strength standard for masonry units by achieving reduced volume and weight.

Keywords Cellular concrete · Decyl glucoide · Foaming agent · High Andean cities · Lightweight concrete · Masonry units · Compressive resistance · Dead load

F. S. D. Oswaldo (✉)
Arq. Universidad Continental, Huancayo 12002, Perú
e-mail: 45986421@continental.edu.pe

H. V. F. Milagros · M. T. V. Simón
Universidad Continental, Huancayo 12002, Perú
e-mail: 72912379@continental.edu.pe

M. T. V. Simón
e-mail: Vmontoya@continental.edu.pe

1 Introduction

Within the field of construction, concrete has a major commercial incidence to other type of materials, so this material was taken as a reference for the research, in this case, the low density of the concrete was taken as the focal point for partitioning since it has many advantages such as decreased dead load, having the greatest welcoming in Europe and the United States, however in Peru very little is known about low density concrete or also called cellular concrete and its development, therefore, it is almost unknown in the Peruvian market.

Cellular concrete is a special building material that is very light due to a large number of pores. According to ACI 523-3R-14 [1] Defines that cellular concrete is "A lightweight product consisting of Portland cement and/or lime with fine siliceous material, such as sand, slag or fly ash, mixed with water to form a paste that has homogeneous voids or a cellular structure". This guide addresses the materials, properties, design, production, and placement of cellular concretes with casting densities above 50 lb/ft³ (800 kg/m³). The usual density range of cellular concrete is 20–120 lb/ft³ (320–1920 kg/m³). This material has many advantages, as in addition to decreasing dead load it is also thermal insulator; which is advantageous for high Andean cities because these areas are plagued by periods of low temperature during which phenomena such as frosts, snow, and hail occur, as in ACI523.3R-14 [1] refers that cellular concrete is more thermal than a conventional concrete due to the porosity which presents acoustic properties and is non-combustible. It is because of these advantages that a suitable mix design of the cellular concrete was sought to be achieved; for this, one of the most important factors is the foaming agent that has the property of adhering to the mixture and in addition being a stable foam, given that what is required is that the specimen comes to be a cellular concrete and for this, it is needed porosity generated by the foaming agent whereby an ideal foaming agent regarding to experimentation is the Decyl Glucoside with chemical description which is fatty alcohol glycoside C8-C16 and mentions that it is a kind of soft (natural) nonionic surfactant. Which is used for foaming products such as personal hygiene and dresser (INCI), unlike other products the foam obtained is particularly stable and fine, this foaming stability and the adhesion it has to the mixture makes it compatible with experimentation.

However, a problem of cellular concrete is that containing air voids makes the material also may compromise its mechanical properties [2], but the ratio of water/cement and fine/coarse aggregate concerning the binder also influences the mechanical properties and physics of this [3], making it can get to make a block too fragile or a block that goes beyond the ranges to be a masonry unit.

Therefore, the purpose of the research is to do laboratory trials regarding water, cement, fine/coarse aggregate and Decyl Glucoside ratio to see their influence on the mechanical and physical properties by making various cellular concrete mix designs with decyl glucoside to analyze the results obtained.

2 Development

The project started with the acquisition of a foam-generating hydro washer, which expels water under pressure and when mixed with a foaming agent causes very dense foam to be generated, and also an industrial cement mixer which generates up to 750 rpm which would help mix the foam with the aggregates.

In this way with the hydro washer and the mixer, different tests were carried out with different foaming liquids to find one that meets the characteristics required for project development, experimenting with the following products: dishwasher foam of different brands, glycerin, Decyl glucoside and bath bubble oil. In this process it was concluded that the liquid that generated much more foam and has better adhesion with the mixture was the Decyl glucoside, with which he proceeded to continue experimenting, since the other products did not generate much foam or they were not finished because they did not adhere properly with the mix, generating a settlement of the sand or that the concrete block did not have sufficient porosity.

After this process, the different mix designs began to be developed which were based on having as reference the ACI 523-3R, articles and theses. 7 different mix designs were carried out (Table 1; Fig. 6). Which were carried out with the following materials: water, cement, fine sand, coarse sand and a foaming agent; they were worked with different mix designs (Fig. 1). Having the aim of achieving better consistency, and good porosity distribution; so that, the reduction of weight, but which meets the Peruvian standard of a masonry unit in compressive resistance. In the mixing process, a mechanical beater was used to obtain better adhesion of the materials (Fig. 2). During the foam manufacturing process it is recommended to produce foam for 10 s before adding it to the mixture, to let out part of the foam which does not have the proper density. After this time it is expected that the consistency of the foam will be sufficiently dense to prevent the air cells from bursting earlier than expected during the mixing of the materials [13]. In this way the mixtures were brewed with the whisk obtaining different consistencies (Fig. 3), once homogenized the mixture was poured into the probetes measuring 30 cm (Figs. 4 and 5).

3 Tests and Set-Up

The seven samples which fabricated to see their mechanical and physical properties; the drying time was seven days, then the measurements were recorded (Table 2) the weight, volume and compressive resistance were measured (Table 3). Whose results analyzed were the most important to define the most optimal mix design for the realization of masonry units.

Table 1 Mix design for 7 different probes of cellular concrete

ID	Specimen	Mix design for 1m ³							
		Portland cement		Fine sand		Gross sand		Water with foam	
		m ³	%	m ³	%	m ³	%	m ³	%
Cellular concrete for masonry units	1	0.25	25.00	0.13	12.50	0.13	12.50	0.50	50.00
	2	0.20	20.00	0.10	10.00	0.10	10.00	0.60	60.00
	3	0.40	40.00	0.10	10.00	0.10	10.00	0.40	40.00
	4	0.33	33.33	0.83	8.33	0.83	8.33	0.50	50.01
	5	0.16	16.50	0.91	9.10	0.91	9.10	0.50	65.30
	6	0.27	27.27	0.90	9.09	0.90	9.09	0.54	54.54
	7	0.23	23.07	0.76	7.69	0.76	7.69	0.46	46.15

Fig. 1 Materials cement, fine and coarse sand, water and foaming agent (Hydro-Washer)



Fig. 2 Mix the materials with the whisk



Fig. 3 Mix ready for the probes



Fig. 4 Used probe of 30 cm



Fig. 5 Mixture poured to the probes



Fig. 6 7 probes with different blends



Table 2 Factory date data, average diameter and area of the cross section

ID	Specimen	Age (days)	Rehearsal date	Average diameter (mm)	Cross sectional area (mm ²)
Cellular concrete for masonry units	1	7	24/10/2022	151.40	18,002.90
	2	7	24/10/2022	151.20	17,955.30
	3	7	24/10/2022	151.30	17,979.10
	4	7	24/10/2022	151.40	18,002.90
	5	7	24/10/2022	151.20	17,955.30
	6	7	24/10/2022	151.10	17,931.60
	7	7	24/10/2022	151.30	17,979.10

Table 3 Weight, density and compressive resistance results

ID	Specimen	Weight (Kg)	Density (Kg/m ³)	CompeSSION resistance (Mpa)	CompeSSION resistance (Kg/cm ²)
Cellular concrete for masonry units	1	7.37	1389.81	4.60	46.90
	2	5.51	1038.68	1.20	12.00
	3	10.04	1893.40	26.00	260.70
	4	8.17	1541.89	8.30	83.30
	5	7.33	1383.02	2.30	23.30
	6	7.44	1404.53	5.70	57.80
	7	5.51	1038.87	1.20	12.10

Table 4 Characteristic resistance of masonry Mpa (kg/cm²)—National building regulations E.070 2021 [12]

Denomination	Unit
Type P block concrete	4.9 (50)
	6.4 (65)
	7.4 (75)
	(85)

Bold indicates the minimum required in compressive strength according to the national building regulations

4 Aim

The main objective of this project is to find a suitable mix design that complies with standard 0.70 of the national strength building regulation for masonry joints having a lower weight, thus reducing the dead load.

The minimum compressive resistance for P-type block concrete masonry units is 50 kg/cm² (Table 4).

5 Results

The obtained results are favorable and achieve the proposed objectives, it is possible to generate stable foam produced by a hydro washer (Fig. 7), different mix designs were carried out and cellular concrete of different consistencies (Fig. 8), densities, weights (Figs. 9 and 10) and resistors (Figs. 11 and 12).

Fig. 7 Hydro-washer foam generator



Fig. 8 Cellular concrete of different consistencies



Fig. 9 Density and weight



The laboratory trials were carried out in “C3—Specialized Engineering” giving the following result:

The results show the trial of seven different mix designs, cellular concrete is very sensitive to dosages of foaming additive, regarding its properties in fresh state [4], the decrease in unit weight not only depends on the dosage of the additive foaming but also of the time that the cellular concrete is mixed, the longer the mixing time the lower the unit weight of the mix, but a prolonged mixing time results in the disappearance of the bubbles and an increase in the unit weight [4].

Fig. 10 Density and weight**Fig. 11** Resistance test

5.1 Weight

The weight results show that the specimen with the highest weight is number 3 with a weight of 10.04 kg at the same time being the one with the highest % of cement in the design. And the one with the least weight is specimen number 2 with a weight of 5.51 kg (Table 5; Fig. 13). The cell concrete with foaming additive can be defined as a type of concrete with an expanding agent that increases its volume while gaining work-ability qualities and weight loss [5], the bubbles remain stable and maintain their shape throughout the setting process and become discrete air cells in the cement

Fig. 12 Resistance test



Table 5 Weight results per specimen

ID	Specimen	Weight (Kg)
Cellular concrete for masonry units	1	7.37
	2	5.51
	3	10.04
	4	8.17
	5	7.33
	6	7.44
	7	5.51

matrix. The presence of air bubbles gives the aerated concrete its lightweight property [6].

5.2 Density

The density results show that design number 3 has the highest density with 1893.40 kg/m^3 and the one with the least density is design number 2 with 1038.68 kg/m^3 (Table 6; Fig. 14)., the density can vary from 300 to 2000 kg/m^3 on comparison with normal concrete which has a density of around $2300\text{--}2400 \text{ kg/m}^3$ [6].

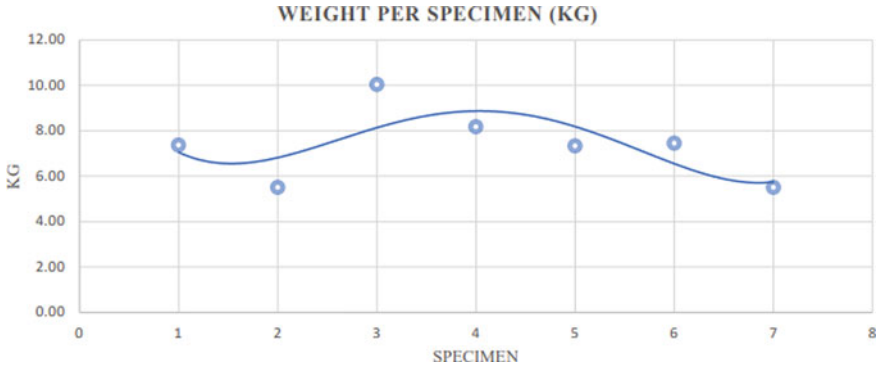


Fig. 13 Weight results by probeta

Table 6 Density results per specimen

ID	Specimen	Density (Kg/m ³)
Cellular concrete for masonry units	1	1389.81
	2	1038.68
	3	1893.40
	4	1541.89
	5	1383.02
	6	1404.53
	7	1038.87

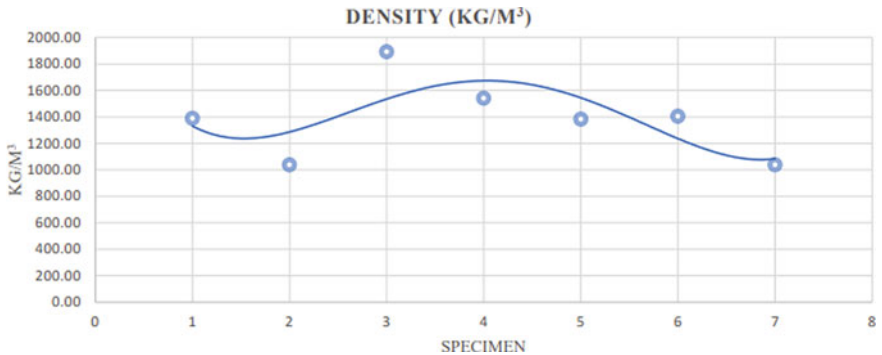


Fig. 14 Density results

Table 7 Specimen compressive resistance results.

ID	Specimen	Compression resistance (kg/cm ²)
Cellular concrete for masonry units	1	46.90
	2	12.00
	3	260.70
	4	83.30
	5	23.30
	6	57.80
	7	12.10

5.3 Compressive Resistance

The compressive resistance results show that test number 3 has a higher resistance with 260.70 kg/cm² (Table 7) for a lightweight concrete having structural applications, its compressive resistance must be greater than 176 kg/cm² at 28 days and its weight should not exceed 1920 kg/m³ [7], cellular concrete offers physical characteristics and mechanical properties, apart from compressive resistance and water absorption, such as: thermal conductivity, acoustic characteristics, resistance to fire [7].

5.4 Resistance to Compression in Relation to Weight

The results show that weight and compressive resistance go in a direct relation, so greater weight greater resistance, as shown the specimen weighing 10.04 kg has a strength of 260.70 kg/cm² (Figs. 15 and 16), and the lightest specimen weighing 5.51 kg has a strength of 12.00 kg/cm² because when applying cellular concrete in structural support areas the addition of foam would be minimal, since by adding more foam the density of concrete lowers and its resistance as well [8].

The results show that specimens 3 and 4 exceed the minimum required widely being very optimal for their manufacture, specimen 6 also exceeds the minimum required being optimal for their manufacture, specimen 1 is unoptimal by not reaching a 93.8% of the required, specimens 2, 5 and 7 are not optimal for being below the required minimum (Table 8; Fig. 17).

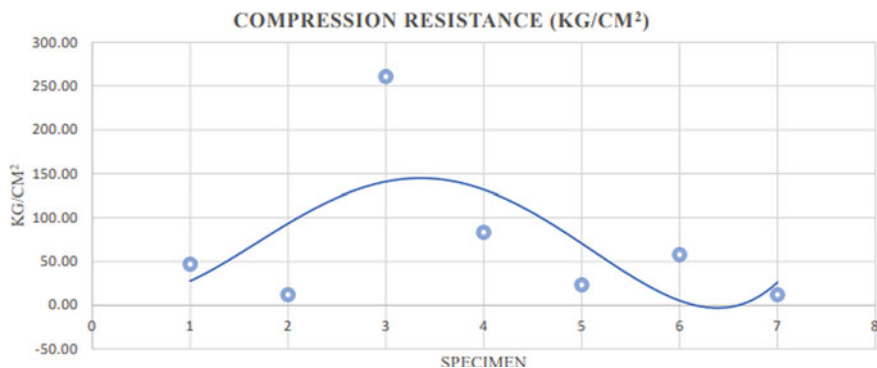


Fig. 15 Compressive resistance results

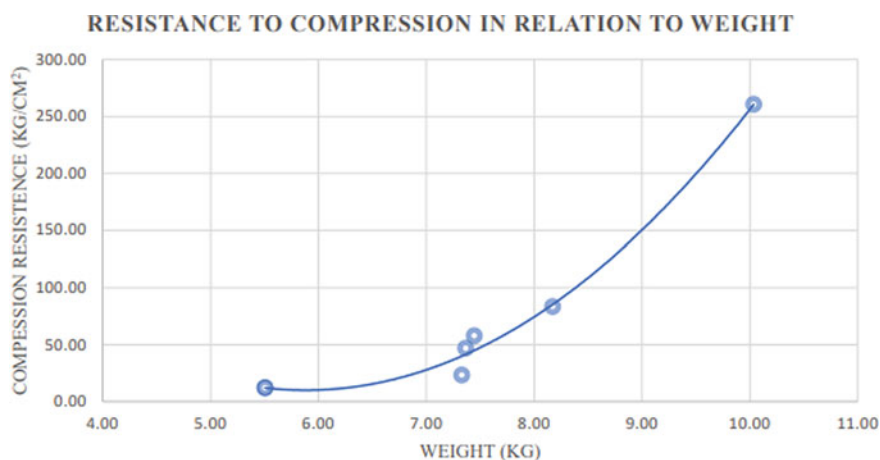


Fig. 16 Results of compressive resistance about weight

Table 8 Status results by specimen

Specimen	Required compressive strength (kg/cm ²)	Compression resistance (Kg/cm ²)	Percentage of required compressive strength (%)	Specimen status
1	50	46.90	93.8	Less than optimal
2	50	12.00	24	Not optimal
3	50	260.70	521.4	Very optimal
4	50	83.30	166.6	Very optimal
5	50	23.30	46.6	Not optimal
6	50	57.80	115.6	Optimal
7	50	12.10	24.2	Not optimal

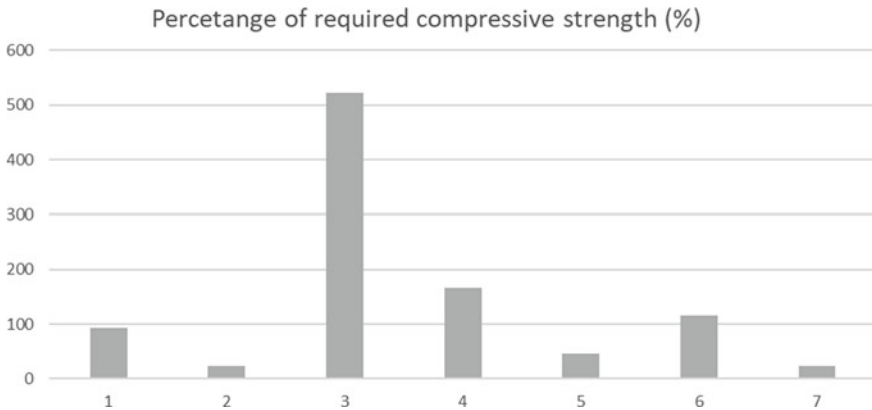


Fig. 17 Percentage results of required compressive resistance (%)

6 Conclusion

The research proved that it is possible to make cellular concrete with decyl glucoside with the help of a hydro washer and a cement mixer. For making cellular concrete it is suggested to make a proper mix design and control the quality and quantity of materials in work, as well as the use of an additive in amounts recommended by the manufacturer [9].

The research proved that the weight and compressive resistance in a cellular concrete specimen has a direct proportion, that is if the weight is higher the compressive resistance is higher, and the hardened mix presents a reduction in density, so that the fresh density of CCA mixture will increase, knowing that to higher density higher compressive resistance [10].

The research proved as a result that cellular concrete loses compressive capacity so it is not recommended for structures, when applying cellular concrete in structural support areas foam addition would be minimal, so when adding more foam the density of concrete is low and hence its resistance [8].

The research showed that changed in dosage can generate large changes in weight, density and compressive resistance. In the design of concrete mixes many factors are involved, among the most important can be mentioned: the type and consumption of cement by cubic meter, the ratio of water, cement, types of aggregates and their characteristics, gravel sand ratio, characteristics and amounts of the additives used, etc., to obtain concrete mixtures with certain desired characteristics of the economy, reventing, volumetric weight, compressive resistance, indirect stress resistance, etc. [11].

References

1. ACI "American Concrete Institute" (2015) Guide for Cellular Concretes above 50 lb/ft³ (800 kg/m³) ACI523.3R-14, 2-7
2. Zhang S, Cao K, Wang C, Wang X, Deng G, Wei P (2019) Influence of the porosity and pore size on the compressive and splitting strengths of cellular concrete with millimeter-size pores 1-2
3. Amran M, Farzadnia N, Ali AAA (2015) Properties and applications of foamed concrete; a review 1-3
4. Lazo J (2017) Diseño de concreto celular para diferentes densidades, análisis de sus propiedades y sus aplicaciones 106
5. Izquierdo M, Ortega O (2017) Desarrollo y aplicación del concreto celular a base de aditivo espumante para la elaboración de bloques macizos destinados a tabiquerías no portantes en edificaciones 24
6. Zamora L (2015) Diseño de un bloque de concreto celular y su aplicación como unidad de albañilería no estructural 12
7. Yoc J (2018) Fabricación y evaluación experimental de unidades de mampostería de concreto celular de espuma preformada 88
8. Mathios M, Cotrina N (2021) Propuesta de diseño sismorresistente y su relación con el desempeño de un edificio multifamiliar de albañilería confinada, con bloques de concreto celular, distrito de la banda de Shilcayo, provincia y departamento de san Martín, vol 21
9. Góngora H, Huamán F (2015) Análisis y diseño estructural comparativo de una vivienda multifamiliar de muros de ductilidad limitada de concreto celular y concreto estructural en Chachapoyas 138
10. Barcia K, Lindao A (2020) Estudio de factibilidad para la aplicación de bloques de concreto celular a edificaciones en la ciudad de Guayaquil (Doctoral dissertation. Universidad de Guayaquil-Facultad de Ciencias Matemáticas y Físicas Carrera de Ingeniería Civil 87
11. Organista E (1999) Optimización en el diseño de mezclas, dosificación, producción y propiedades de concreto celular hecho a base de agentes espumantes 42
12. Reglamento Nacional Edificaciones E.070.: (s.f.) (2021) Obtenido de <https://cdn.www.gob.pe/uploads/document/file/2366661/56%20E.070%20ALBA%C3%91ILERIA.pdf?v=1636060379>, 15
13. Fócil A (2006) Caracterización del Concreto Celular Elaborado con Espuma Preformada-Edición Única 73

Compressive Strength Performance of 7-Day Non-load Bearing Concrete Hollow Blocks with Pili Shell as Partial Replacement to Sand Using Box-Behnken Design



Rizza Mae T. Rea, Jonille S. Soriano, James Paul Ramos,
April Noemi Q. Opinaldo, Marian Capito, and Manny Anthony Taguba

Abstract The Philippines is one of the leading distributors of Pili (*Canarium ovatum*) nut worldwide. Along with the rise of production of pili nut is the increase in the generation of residual waste specifically the pili nutshell. The present study aims to investigate the compressive strength of 7-day of non-load bearing concrete hollow block (CHB) using waste pili nutshell as partial replacement to sand in the production of non-load bearing concrete hollow block (CHB) using Box-Behnken design. The compressive strength blocks made with varying proportion of waste pili shells for fine aggregates, pili shell size, and cement-sand ratio were also evaluated for a constant curing day of seven days. The Pili shell proportions used were 3%, 6% and 9% of total sand volume. Pili shell size retained at sieve no.10, no.20 and no.30 were used. And lastly a cement-to-sand ratios of 0.5:7, 1:7, and 1.5:7 were adopted. Compressive test results showed that most of the CHB with Pili shells possessed higher compressive capacity compared to the ordinary CHB. Among the prepared 7-day composites, the highest compressive strength was 671.28 pound per square inch (psi) that was obtained by the sample with 6% pili shells that retained at sieve #10 with a mix ratio of 1.5: 7. Moreover, the present paper examines the interaction among the three parameters using Response Surface Methodology—Box Behnken Design (RSM-BBD) using three level factorial designs was used in this study. Sigma XL software suggested fifteen (15) experimental runs. Statistical testing such as Variance Inflation Factor (VIF) and ANOVA revealed the adequacy of the generated model to describe the fit of experimental data to predictor model.

R. M. T. Rea · J. S. Soriano · J. P. Ramos · A. N. Q. Opinaldo · M. Capito · M. A. Taguba (✉)
Department of Civil Engineering, National University, 1008 Manila, Philippines
e-mail: mmtaguba@national-u.edu.ph

M. A. Taguba
Department of Environmental and Sanitary Engineering, National University, 1008 Manila,
Philippines

Keywords Pili nutshell · Non-load bearing concrete hollow blocks · Box-Behnken design · Compressive strength

1 Introduction

Construction material cost, on a global market platform, has been rising and inflating which leads to expensive housing, building, and real estate development. Because of this, for most members of the middle and lower socioeconomic sector of the society, home possession has been becoming a luxury. Scarcity of the raw materials (or sustainability of the construction materials) and continuous upsurge of material cost drive researchers and engineers to explore for alternative, innovative and relatively affordable construction materials. Researchers and scientists are committed to utilizing local materials to substitute these costly traditional materials partially or fully. Moreover, attention has been drawn to waste reusability thru incorporation of agricultural wastes and residues to some construction materials. The use of agricultural wastes to supplement other conventional materials in construction offers both practical and economical gains. These wastes commonly have no commercial value and being locally available generation and transportation cost become minimal [1].

Concrete with oil palm shells as coarse aggregate and the effect of fly ash as partial cement replacement was examined by [2]. Osei and Jackson investigated the effects of replacing crushed granite in concrete with palm kernel shells on the strength and workability of concrete [1]. Moreover, Emiero examined the compressive strength and workability of concrete using palm kernel shell and palm kernel fiber as a replacement for coarse aggregate [3]. A synthesis of study on the performance of coconut shell as coarse aggregate in concrete was summarized by Kanojia and Jain and reviewed the works done on the use of waste coconut shell for concrete production [4].

In the Philippines, Bicol region is the leading distributor of pili nuts (*Canarium ovatum*) worldwide. Some of these trees can also be found in some parts of Visayas and Mindanao since it has wide adaptations to varying agro-climatic condition which can be grown alone or intercropped with other crops. Like the coconut tree, pili nut is also regarded as tree of life with all its parts being valuable. However, along with the rise of pili nuts production rate is the increase also of the agricultural wastes produced by pili, and one of the residual wastes is the nutshell.

On the other hand, concrete hollow block (CHB), which forms significant part of buildings and engineering structure, is one of the most widely used walling materials in the Philippines. Sometimes called concrete masonry unit (CMU), CHB is a mixture of Portland cement, sand, and gravel. Lower density blocks may use agricultural or industrial wastes, such as fly ash, post-consumer glass and recycled aggregate [5].

The present study aims to investigate the suitability of using waste pili nutshell as partial replacement to sand in the production of non-load bearing concrete hollow block (CHB). The compressive strength blocks made with varying proportion of waste pili shells for fine aggregates, pili shell size, and cement-sand ratio were also

Fig. 1 A Preparation of waste Pili shell by manual crushing of waste pili shell using hammer



evaluated. Moreover, the interaction of the variables was examined using Sigma XL software (version 7.0) adopting the Response Surface Methodology (RSM).

2 Methodology

2.1 Materials Preparation

Waste Pili nutshells used in this study were sourced from various pili nut production sites at Sorsogon, Albay, Philippines. Collected pili shells were flushed with running water to remove dust and other impurities that could influence the concrete. They were sun-dried for a day, crushed manually using a hammer and then sieved, as shown in Fig. 1. Pili shells retained at Sieve number 10, 20, and 30 were collected and packed in plastic sheets to prevent contact with water (see Fig. 2).

2.2 Batching and Casting of CHB

The cement used in this study was Ordinary Portland Cement (OPC), purchased in a local hardware in Manila, was fresh, of good quality, and without lumps. The fine aggregate used for the experiment were manufactured sand obtained also from local hardware in Manila. Potable water that is clean and free from visible impurities was used for mixing. Cement, sand, sieved waste pili shell, and water were mixed on a mixing tray until it reached a good consistency (plastic state). The study utilized three control mix ratios (cement: sand) namely: 0.5:7, 1:7, and 1.5:7 batched by volume. Moreover, the percentage replacements of sand by waste pili shells were 0, 3, 6 and 9% of total sand volume. The casting was done in a semi-automatic CHB molding machine with mold dimension of 400 × 93 × 194 mm. The concrete mixture was

Fig. 2 Sieved and categorized crushed waste Pili nutshells (Sieve No. 10, 20, and 300)



cast into machine and compacted. A straight edge tool was used to level off the concrete.

The CHB specimens were then stored in a room free from vibration and outside dust, not exposed to direct sunlight, and then subjected to curing for 7 days. The curing was carried out by wetting the specimens with water twice a day to promote hydration and absorb heat of hydration until the age of test.

Determination of Compressive Strengths. Measurement of compressive strength of CHB was done by crushing the block specimens. The CHBs were crushed using the Universal Testing Machine which gauges the compression load and the compressive stresses at failure and shows the results on the gauge screen. The blocks were properly centered under the compression equipment before the load was applied (shown in Fig. 3). The dimension and the mass of the specimens were measured before crushing. For all tests, each value was taken as the average of three samples. Compressive strength tests were performed at 7 days after casting. All tests were carried out at the Bureau of Research and Standards (BRS) of Department of Public Works and Highways- National Capital Region (DPWH-NCR).

Statistical Design of Experiment. In order to evaluate the interaction of operating parameters, design of experiment using Box-Behnken Design was utilized. It uses the three-level incomplete factorial design at its basis [6]. Moreover, BBD requires only 12 runs plus a replicate at center point for a three-factor design. Three levels (three values) would be assigned for each factor which is a vital feature in experimental situations [7]. In the present study, operating parameters such as waste pili percentage, pili size, and cement: sand ratio are assigned as independent variables. The optimum values were generated by Response Surface Methodology (RSM) using Sigma XL.

Fig. 3 Placement of the CHB specimen for compressive strength test



3 Results and Discussion

3.1 Parametric Study

Effect of varying percentage of crushed pili shell by volume for different pili shell size and cement: sand ratio to compressive strength were investigated in this study. The effects of replacement of sand by pili shell on compressive strengths of the specimens are shown in Figs. 4, 5 and 6, respectively.

Compressive strength was determined for CHB after 7 curing days. It is seen from the figures (Figs. 4, 5 and 6) that compressive strength of all design mixtures for all particle sizes increases from 3 to 6% and dropped when 9% total volume of sand replacement by pili shell was made—a pattern that is observed for all mixtures. The compressive strength of all design mixtures is maximum at 6% replacement of sand by pili shell for all pili shell sizes. The 7-day compressive strength obtained from 6% replacement CHB samples were within the range of 299.38 psi to 671.28 psi. Thus,

Fig. 4 Variation of compressive strength (in lb/in²) with pili shell content at 0.5: 7 ratio for different pili shell sizes

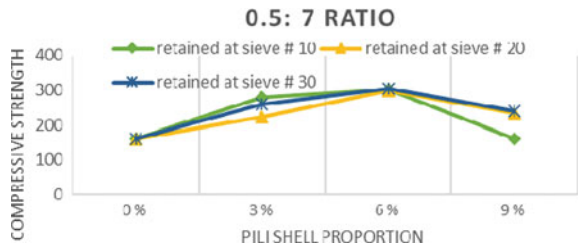


Fig. 5 Variation of compressive strength (in lb/in²) with pili shell content at 1.5: 7 ratio for different pili shell sizes

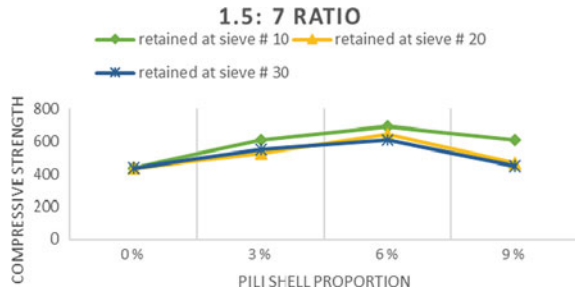
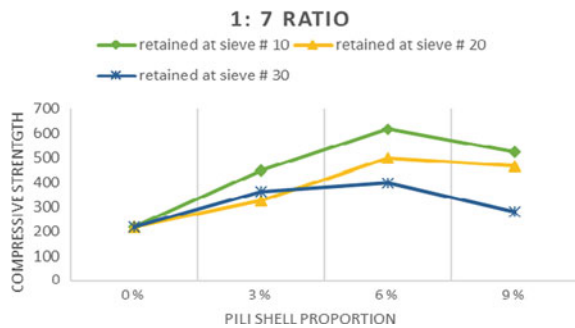


Fig. 6 Variation of compressive strength (in lb/in²) with pili shell content at 1: 7 ratio for different pili shell sizes



waste pili shell, at 6% volume replacement, is an effective substitute for fine aggregate. An increase in compressive strength is due to the effective bonding of pili shell (as fine aggregate) and cement. However, as pili shell content continuous to increase, the specific area increases, hence requiring more cement paste to bond effectively with the shells. Subsequently, with constant cement concentration, the bonding is inadequate resulting to decrease in the compressive strength at 9% replacement of sand by pili shell. The compressive strength diminishes as a consequence of the continuous increase in percentage replacement of sand.

Summary of data obtained from compressive test on volume batched CHB are presented in Fig. 7 and Table 1 It is notable that even though the curing was only set to seven (7) curing days only, five (5) samples already passed the minimum requirement for 600 psi non-load bearing capacity. Furthermore, as depicted in Fig. 8, the compressive strength attained by 1.5: 7 mixture is higher than that of 0.5: 7 and 1: 7 mixtures at seven curing days. It is therefore advisable to use 1.5: 7 cement-to-sand mixture for the production of CHB with waste pili shell as partial replacement to sand.

The effect of varying the size of pili shell was also examined by the proponents at sieve numbers 10 (2 mm), 20 (0.85 mm), and 30 (0.60 mm). As shown in Fig. 8, the CHB with pili shell size of sieve # 10 experienced the highest compressive strength at 6% replacement of fine aggregate with 1.5:7 mixture recorded at 671.28 psi which passed the minimum compressive strength for non-load bearing block. For 6% replacement, it was observed that for 1: 7 and 0.5: 7 cement-sand ratio, as the

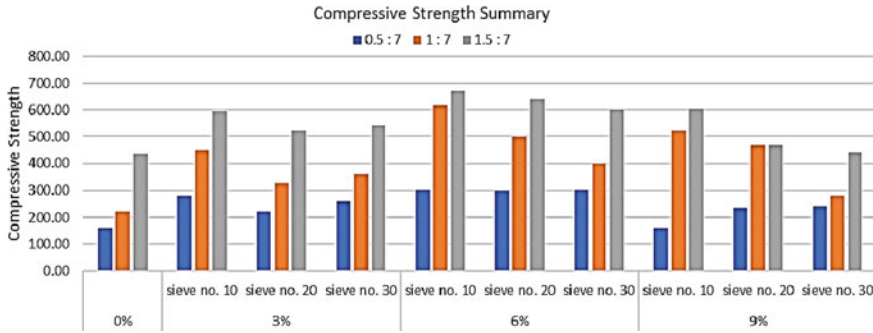
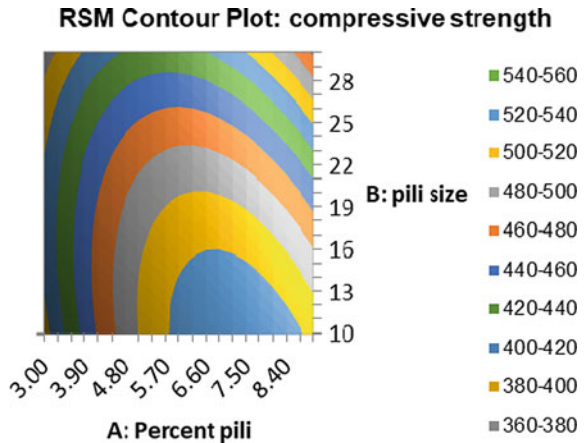


Fig. 7 Development of compressive strength (psi) for each proportion (cement: sand ratio) at different pili shell concentration (% replacement by volume) at varying pili shell sizes

Table 1 Compressive strength performance of CHB with pili shells of varying sieve sizes, % replacement of total sand volume by pili shell and cement-sand mixtures

Cement: sand ratio	Compressive strength (psi)									
	0%	3% Replacement			3% Replacement			9% replacement		
		Sieve # 10	Sieve # 20	Sieve # 30	Sieve # 10	Sieve # 20	Sieve # 30	Sieve # 10	Sieve # 20	Sieve # 30
0.5: 7	161.32	279.56	223.21	260.02	301.28	299.33	303.43	160.33	233.38	240.27
1: 7	221.18	447.80	328.48	361.89	615.06	498.96	399.66	522.19	466.40	279.99
1.5: 7	437.41	595.26	523.00	540.68	671.28	641.66	600.44	602.23	466.43	438.50

Fig. 8 RSM contour plot of interaction between % pili and pili shell size in the development of compressive strength of CHB with pili shells



size of pili shell decreases, the compressive strength of the samples also decreases. Hence, given a constant cement-to-sand ratio at 6% replacement of fine aggregate by waste pili shell, it was found out that the mean compressive strength of the pili shell increases with the increasing aggregate size which supports the result of a published study of Roy et al. [8]. Moreover, the relationship between the compressive strength and aggregate size is due to the fact that aggregate size influences the workability [9] and is directly proportional to aggregate size [8].

3.2 Statistical Analysis Using Box-Behnken Design

To evaluate the interaction among the chosen independent variables, Response Surface Methodology (RSM) is utilized in this study as a tool in the laboratory analysis or statistical design of experiment (DOE). RSM is an empirical model that covers mathematical and statistical technique and optimization is one of its features. Sigma XL software (version 7.0) was employed to determine the number of runs (series of tests). Since the study examined three independent variables, the experimental design used is Box-Behnken Design (BBD) which adopts three factors. From the BBD of Sigma XL, fifteen (15) runs were suggested to evaluate the interactions of these independent variables and to determine the optimize model, as shown in Table 2. Runs were carried out in duplicate to optimize the level of chosen variables.

Table 2 Summary of experimental runs with experimental values of compressive strength

Run Order	A: % pili	B: pili size	C: cement-sand ratio	Compressive strength (psi)
1	3	20	1.5	523
2	6	10	0.5	301.28
3	6	20	1	498.96
4	3	30	1	361.89
5	6	30	0.5	303.43
6	6	20	1	498.96
7	6	20	1	498.96
8	9	20	0.5	466.43
9	3	10	1	447.8
10	6	30	1.5	600.44
11	9	20	1.5	466.43
12	6	10	1.5	671.28
13	3	20	0.5	223.21
14	9	30	1	279.9
15	9	10	1	522.19

The minimum and maximum value for % pili as sand replacement and pili size used in the parametric study was adopted. Since the compressive strength continues to rise as the cement-to-sand ratio increases, the values used for optimization were in the range of 0.5–1. The encoded compressive strengths of all runs in the design of experiment were mean values of three samples per run. RSM can predict the model equation using multiple regression analysis. The Eq. (1) is the fundamental equation for multiple regression observation:

$$f(\%) = \beta_0 + \beta_1 A + \beta_2 B + \beta_3 C \quad (1)$$

where β_0 , β_1 , β_2 , and β_3 are the regression coefficients, while A, B, and C are pili proportion, particle size, and cement-sand ratio, respectively.

Based on the experimental data, an empirical relationship between the response was generated by Sigma XL (version 7.0) that relates the compressive strength to the independent variables and is presented in Eq. (2).

$$\begin{aligned} \text{RSM Regression Model : } Y = & (481.9014286) + (22.38125)*A : \text{Percent pili} \\ & + (-49.61125)*B : \text{pili size} + (120.85)*C : \text{cement ratio} + (-39.095)*AB \\ & + (-74.9475)*AC + (-70.54517857)*AA \end{aligned} \quad (2)$$

where Y is the predicted response (compressive strength), and A, B, and C are the coded values for the three independent variables as mentioned previously.

From the generated model equation, displayed in Eq. (2), the positive coefficients indicate the favorable effect of independent variables on the compressive stress of CHB with pili shell. Hence, the percentage of pili shell and the cement-to-sand ratio are significant in prediction of compressive stress.

Among the significant factors, the ratio of cement to sand is highly significant exhibited by low p-value (0.0007), as shown in Table 3. This implies that the compressive strength of CHB with pili nut is highly influenced by the cement-to-sand mixture. As shown in the generated model equation, a high positive coefficient of cement-to-sand ratio was produced implying that independent variable contributed greatly to the compressive stress of CHB. This is attributed to the excellent bonding of cement and sand that contributes to workability and compressive strength of the block. Moreover, it was found also that there is a synergistic interaction between the percentage of pili as partial replacement to sand and the cement-sand ratio displayed by low p-value (<0.05).

Another statistical criterion that most regression analyst relies on is the variance inflation factor or VIF which measures whether factors or independent parameters are correlated to each other (i.e., multicollinearity) which could affect the p-value [10]. It is imperative that the operating parameters or input variables are not correlated so as not to cause “tipping effect” of error or amplified standard error of estimates [11]. If the VIF is equal or closer to 1, then the model is much stronger and reliable, implying the factors re not impacted by correlation with others. From Table 3, all

Table 3 Box-Behnken design's parameter estimates of the surface quadratic model

Term	Coefficient	p	VIF
Constant	481.9014286	0.0000	
A: Percent pili	22.38125	0.3560	1
B: pili size	-49.61125	0.0617	1
C: cement-sand ratio	120.85	0.0007	1
AB	-39.095	0.2609	1
AC	-74.9475	0.0490	1
AA	-70.54517857	0.0680	1

factors acquired a value of 1.0 which means factors are not correlated. Hence, the parameters are proven to be independent with one another.

Result of summary of analysis of variance (ANOVA) revealed a p-value of 0.0061 of the model. The smaller the value of the p-value (<0.0001), the more significant is the model [7]. Hence, the generated model is significant in describing the compressive strength of CHB with pili shell. On checking the coefficient of determination or R^2 of the model, it was found out to be 0.8489 and an adjusted R^2 of 0.7355, suggesting a satisfactory predictor model performance. It shows that 15.11% of the variations cannot be explained satisfactorily by the model. Hence, the generated model and the corresponding actual measurements showed and established an acceptable satisfactory correlation.

Additional elucidation was carried out using RSM plots and contour plots. Interaction between factors % pili replacement of total sand volume and the pili shell size and compressive strength (in psi) of CHB with pili shells as the response are established in the contour plot and three-dimensional response surface plots in in Figs. 8 and 9, respectively.

The compressive strength of CHB with pili shells increases as the percentage of pili shell size increases from 3 to 6% indicating this range of value was favorable to for the enhancement of compressive strength. Moreover, the compressive strength improved when the pili shell size used larger particle size (or smaller sieve number). As shown in Fig. 12, the relationship among these three variables is curvilinear relationship showing regions of high and low values.

On the other hand, for the RSM contour plot and 3D surface plot of the interaction between cement: sand ratio and % pili replacement of sand, as depicted in Figs. 10 and 11, the progress in compressive strength of CHB with pili shells happened with increasing cement: sand ratio at growing percentage of pili from 3 to 6% of total volume. However, the result showed that the maximum point is outside the experimental region. Hence, a research extension on exploring higher cement: sand ratio with sand replacement by pili shells in the range of 3–6% is recommended.

Lastly, the interaction of pili shell size thru sieve number and cement: sand ratio was investigated and the result is displayed in Figs. 12 and 13. It was viewed that the maximum compressive stress was produced from larger pili shell (as fine aggregate) size.

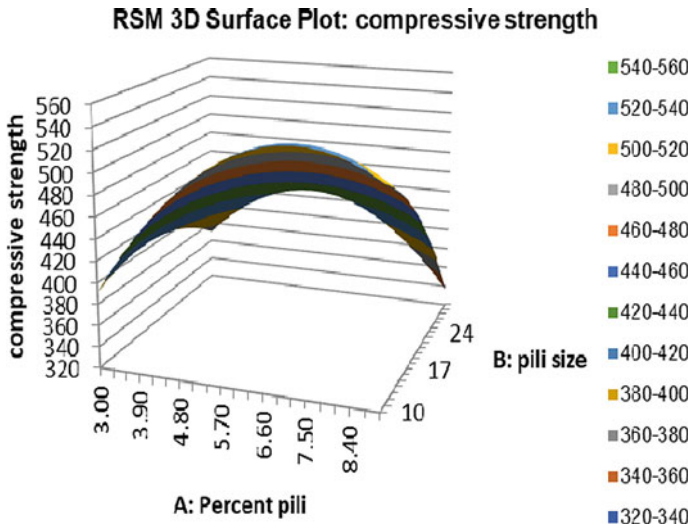
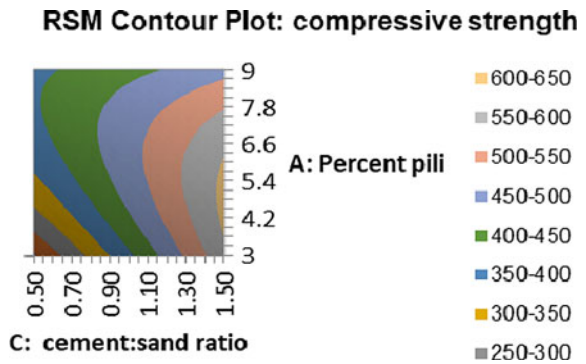


Fig. 9 RSM Three-dimensional surface plot of interaction between % pili and pili shell size in the development of compressive strength (psi) of CHB with pili shells

Fig. 10 RSM contour plot of interaction between cement: sand ratio and % pili by volume in the development of compressive strength of CHB with pili shells



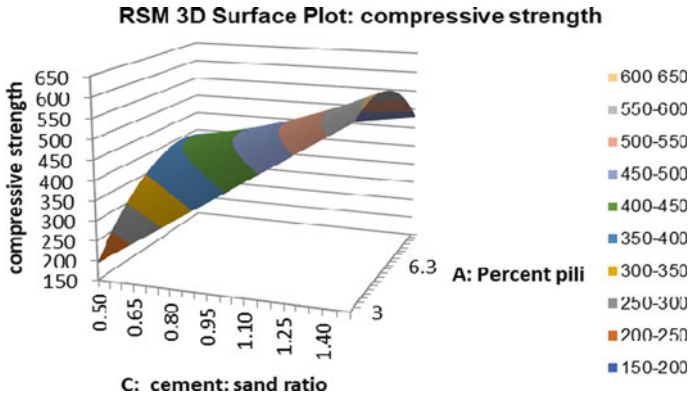


Fig. 11 RSM Three-dimensional surface plot of interaction between cement: sand ratio and % pili by volume in the development of compressive strength (psi) of CHB with pili shells

Fig. 12 RSM contour plot of interaction between pili size by sieve number and cement: sand ratio in the development of compressive strength of CHB with pili shells

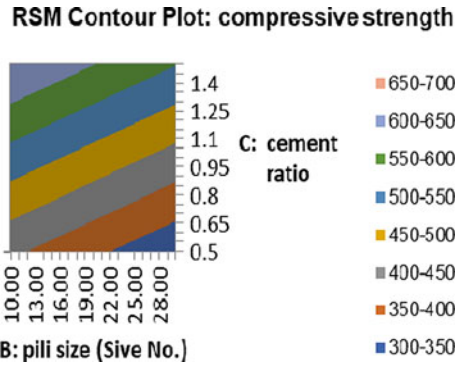
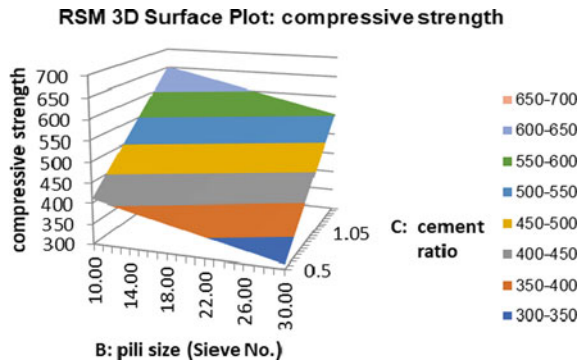


Fig. 13 RSM Three-dimensional surface plot of interaction between pili size by sieve number and cement: sand ratio in the development of compressive strength (psi) of CHB with pili shells



4 Conclusion

In this work, the possibility of using pili (*Canarium ovatum*) nutshell as partial replacement to sand in non-load bearing concrete hollow blocks batched at 7th day was investigated by evaluating the compressive strength of synthesized CHB with pili shells. The following conclusions are drawn from the output of the present study and can be summarized as follows:

The possibility exists for the partial replacement of sand with waste pili shells to produce non-load bearing CHB. Considering a constant seven (7) day curing period only, majority of the synthesized CHBs with pili shells surpassed the control sample in terms of compressive strength. It is also worth note taking that despite of short curing period, five batched samples passed the minimum requirement of 6,000 psi for non-load bearing blocks.

Waste pili shell at 6% volume replacement, is an effective substitute for fine aggregate. Compressive strength of CHB increases with the size of pili shells as partial replacement to sand. A significant rise in compressive strength of samples as the cement-to-sand ratio increases.

The use of Response Surface Methodology (RSM) has facilitated the evaluation of the compressive strength optimization of CHB with pili shell in this study. Box-Behnken Design (BBD) produced the suggested number of runs to investigate the interactions of three factors (i.e., % pili shell by volume as replacement to sand, pili shell size expressed in terms of sieve number, and cement-to-sand ratio) and their influence on the compressive strength of CHB with pili shells.

Contour-response surface plots and three-dimensional surface plots clearly demonstrate the effect of increasing the percentage of pili shell as replacement to sand, cement-to-sand ratio, and pili shell size on the compressive strength. The variable cement-to-sand ratio exhibited the highest influence in the increase of compressive strength as suggested by its high positive coefficient value in the generated model, low p-value, and high coefficient value.

Statistical testing such as Variance Inflation Factor (VIF), and ANOVA revealed the adequacy of the generated model to describe the fit of experimental data to predictor model. Moreover, the coefficient of determination (R^2) of the predictor model implies that the quadratic model utilized is satisfactory in predicting the performance of the compressive strength of CHB with pili shells.

From the result of the study and the inference made from the result, possible research extensions can be made by future researchers. Moreover, regarding various constraints and limitations incurred in the study, there will be numerous opportunities to improve the validity of the study. Thus, the following considerations are recommended:

- (1) Consider more variations in the cement-to-sand ratio. From the RSM plot of the study, it was found out that the optimized compressive strength influenced by cement: sand ratio is outside the set maximum value.
- (2) From the results of this preliminary study suggested the possible use of waste pili shells as a replacement to fine aggregates in CHB, it is recommended to

observe the development of compressive strength of CHB with pili shells in 14, 21 and 28 curing days. Furthermore, the long-term behavior of pili shells should be investigated to strengthen the feasibility of utilizing and incorporating pili shells to CHB.

- (3) Effect of using plasticizers and its influence to compressive strength should be considered since it is well known that it aids in workability.
- (4) Additional significant independent variables can be considered in the optimization study to improve the value of R^2 and other statistical parameters.

It is recommended that broader parametric study and further validation of the interaction between percent pili by volume and cement-sand ratio should be conducted in order to achieve an optimized condition. Other operating parameters such as effect of heat and chemical treatment should be investigated to evaluate their effect to compressive strength of composite.

References

1. Osei DY, Jackson EN (2012) Experimental study on palm kernel shells as coarse aggregates in concrete. *Int J Sci Eng Res* 3(8):1–6
2. Basri HB, Mannan MA, Zain MFM (1999) Concrete using waste oil palm shells as aggregate. *Cem Concr Res* 29(4):619–622. [https://doi.org/10.1016/S0008-8846\(98\)00233-6](https://doi.org/10.1016/S0008-8846(98)00233-6)
3. Oyedepo OJ, Emiero C (2012) An investigation on the strength and workability of concrete using palm kernel shell and palm kernel fibre as a coarse aggregate. *Cem Concr Res* 21(4):551–557. [https://doi.org/10.1016/0008-8846\(91\)90105-Q](https://doi.org/10.1016/0008-8846(91)90105-Q)
4. Kanojia A, Jain SK (2015) Performance of coconut shell as coarse aggregate in concrete: a review. *Int Res J Eng Technol* 2395–56
5. Elgaali E, Elchalakani M (2012) Concrete hollow blocks made with recycled coarse aggregate and recycled water ‘Green blocks’
6. Luis S et al. (2007) Statistical designs and response surface techniques for the optimization of chromatographic systems. 1158:2–14. <https://doi.org/10.1016/j.chroma.2007.03.051>
7. Bai Y, Saren G, Huo W (2014) Response surface methodology (RSM) in evaluation of the vitamin C concentrations in microwave treated milk. <https://doi.org/10.1007/s13197-014-1505-5>
8. Roy B, Vilane T, Sabelo N (2016) The effect of aggregate size on the compressive strength of concrete. *J Agric Sci Eng* 2(6):66–69. [Online]. Available: <http://www.aiscience.org/journal/jase%5Cn>, <http://creativecommons.org/licenses/by/4.0/>
9. Ajamu SO, Ige JA (2015) Effect of coarse aggregate size on the compressive strength and the flexural strength of concrete beam. *J Eng Res Appl* 5(4):2248–962267. www.ijera.com ISSN, [Online]. Available: www.ijera.com
10. Santos FD et al. (2020) Optimization of the compressive strength of hair fiber reinforced concrete using central composite design. In: *IOP conference series: materials science and engineering*, 2020, vol 771(1). <https://doi.org/10.1088/1757-899X/771/1/012059>
11. Santos F, Alzona A, Taguba MA, John M, Santos D (2019) Optimization of the bulk specific gravity of plastic waste bituminous binder using box-behnken design. pp 1–5

Circular Economy in Buildings: Service Life Considerations of Paint



Abdul Rauf, Attoye Daniel Efurosibina, Malik Khalfan,
and Shafiq Muhammed Tariq

Abstract Buildings and built environment are responsible for 40% of global CO₂ emissions and resulting in climate change and other environmental issues. Life cycle research is a vital tool in understanding and resolving the myriad of multifaceted challenges which have made addressing the status quo complicated. Previous studies show that embodied energy research provides an opportunity to investigate the environmental impact of building materials. However, the emerging field of circular economy has recently presented a platform for a critical appraisal of the association between the lifespan of a material and the potentials for its circularity, as a means of increasing its sustainability. This paper embraces this challenge but further argues that extending the lifespan of a material has quantifiable benefits. The aim of this paper is to explore how the service life considerations of paint as a finishing material in buildings, can help to achieve the goals of circular economy and help reduce the life cycle embodied energy of buildings. The assessment was carried out using an input–output based hybrid approach (IOBHA) to calculate the life cycle embodied energy of the building with a service life of 50 years, and 10 years for the paint. Next, a sensitivity analysis was carried out and it was assumed that the MSL was increased by 20% up to 100%, and then the LCEE was recalculated. The findings show that while the LCEE of the paint was 161.8 GJ, increasing the MSL by 80–100% can lead to a drop in the LCEE of the paint by up to 40%. Specific strategies were also recommended to facilitate the extension of the service life and enhance the circularity of paint.

A. Rauf (✉) · A. D. Efurosibina · S. M. Tariq
Architectural Engineering Department, United Arab Emirates University, Al Ain, UAE
e-mail: a.rauf@uaeu.ac.ae

A. D. Efurosibina
e-mail: danielattoye@uaeu.ac.ae

S. M. Tariq
e-mail: muhammad.tariq@uaeu.ac.ae

M. Khalfan
Department of Management Science and Engineering, Khalifa University, Abu Dhabi, UAE
e-mail: malik.khalfan@ku.ac.ae

Keywords Service life · Circular economy · Embodied energy · Paint · Input–Output Based Hybrid Assessment

1 Introduction

Buildings and built environment are responsible for 40% of global CO₂ emissions and resulting in climate change. This situation requires urgent actions. Circular economy (CE) encourages the use of strategies such as reducing, reusing and recycling that eliminate waste, lower resource consumption and reduce greenhouse gas emissions. One of the most prominent definitions of CE is a statement by the Ellen MacArthur Foundation [1, 2]. It reads, “[CE] an industrial system that is restorative or regenerative by intention and design. It replaces the ‘end-of-life’ concept with restoration, shifts towards the use of renewable energy, eliminates the use of toxic chemicals, which impair reuse, and aims for the elimination of waste through the superior design of materials, products, systems, and, within this, business models.” [3]. Geissdoerfer et al. examined 114 definitions of CE and found that the most common component in the definitions was recycling (79%), then reuse (74%) and reduce (54–55%) [1]. The literature also supports strategies that aim to extend the useful life of a product with strategic gains such as economic benefits [4], future reusability [5], reduction of a product’s environmental footprint [6, 7] and overall sustainability to advance the CE agenda. CE replaces ‘end-of-life’ product concept with reducing, or reusing, recycling and the recovering materials and at its core, is targeted towards sustainable development. This bridges key issues relating to good environmental quality, economic prosperity and equity in the social/community sphere.

Several authors have corroborated the 3Rs of CE: reduction, reuse, and recycling [1, 8–11] with the goal of promoting cyclical resource usage in connection with CE [10]. Generally, broad discussions of CE resonate with an identification “indicators” which mostly prioritize material preservation with “recycling” notably mentioned in the literature [1, 10]. Though several other indicators have been mentioned, this paper is primarily focused on one which fits the broad dimensions of life cycle assessments in association with CE. Our attention, therefore, is given to embodied energy (EE). Although EE is a fundamental part of life cycle assessments -which predates the current CE awareness, the association between CE and life cycle embodied energy, is a healthy reasoning. There are, however, gaps in the knowledge within the construction industry which quantitatively justify and establish this relationship and proceed to explain how this can be operationally carried out using actual case examples. This is important since at its core, circularity requires quantifiable metrics that allow us to track our progress [12].

This investigation is part of a larger project to investigate the critical importance of embodied energy assessment in the construction industry of the United Arab Emirates (UAE), investigating variations in the service life and renewable energy integration [13, 14], and deriving adaptable lessons for wider regional and global applications. The current study provides a connection between embodied energy research and

circular economy. Our focus within the purview of the 3R concept is not simply to reduce, reuse, recycle but to justify and engage in strategies that extend the useful life of the selected wall finish as a means of ensuring material and environmental sustainability. This resonates with the concepts of lifetime extension and closed-loop recycling which are vital two circular economy approaches that aim to reduce exploitation of virgin materials, environmental demand, and life cycle waste [15].

2 Background

2.1 Circular Economy: A Working Definition

The construction industry is the one of the major economic driving forces within the UAE. But the industry has been criticized for unsustainable practices and low resource efficiency. One of the ways to deal with the above criticism is to move towards a Circular Economy (CE) approach that promises streamlining practices to be more sustainable, better resource-efficient, and environmentally-friendly [16, 17]. The European Parliament defines CE as a production and consumption model that relies on ‘sharing, leasing, reusing, repairing, refurbishing and recycling existing materials and products as long as possible’, hence lengthening products’ and materials’ life cycles [18].

Within the context of construction industry, the CE is referred to as ‘an economic system that supersedes the conventional ‘end-of-life’ ethos; the focus of its strategies is on minimizing, creatively repurposing, recycling and salvaging materials from manufacturing or distribution and consumption practices to retain the materials for the longest possible time in the cycle, thus limiting the exploitation of natural resources in projects’ [17]. Figure 1 shows some of these strategies and the connection between CE, embodied energy assessment and the objective of this investigation.

2.2 Embodied Energy: An Overview

With growing interest in embodied energy research, there have been several factors identified which have a definitive impact on the associated embodied energy of a building, either at the initial stage (cradle to site) or over the life cycle (cradle to cradle). Some other factors investigated include: material service life [19–21], building service life [20, 21], assessment method [20, 21], material specification, [22], energy source, [23], and the construction method [24]. In our previous studies, the service life of both materials and buildings were reported as having a definitive impact on the embodied energy of buildings; noting however, that the service life of materials is very different [19–21]. While a material life concrete may last up to 50 years, paint may last only 10 years.

Strategy	Description
Strategy 1	Preserve the functions of products or services using business models, and scheme which promote product multifunctionality.
Strategy 2	Preserve the product itself via lifetime extension or increase aided by durability, reuse, restore, refurbish, and remanufacture.
Strategy 3	Preserve the product's components via reuse, recovery and repurposing of existing parts.
Strategy 4	Preserve the materials through recycling and downcycling.
Strategy 5	Preserve the embodied energy through energy recovery at incineration facilities and landfills.
Strategy 6	Measure and compare the reference linear economy side-by-side CE objectives to show status: positive or negative

Identifies the objective of lifetime /life cycle extension as a strategic option

Identifies embodied energy of materials as a resource to be preserved.

Fig. 1 Annotated CE strategies in line with LCEE objectives (Adapted from [10])

From a comparative point of view, some authors have reported that it is possible to reduce the embodied energy of a representative case study by up to 20% [25] and up to 50% [26] when then building materials used are changed for alternative options. Thus, it stands to reason that if the variation in service life of different materials impacts their total embodied energy, extending the service life of a single material would have a similar positive effect on the goal to reduce embodied energy. This standpoint directs the current investigation, and this is clearly expressed in the research design (See Sect. 3).

2.3 United Arab Emirates: Study Context

In the UAE, there is a growing awareness of shifting to the CE approach. The government, practitioners and university researchers agree on the benefits of adopting CE within the construction industry and recognize its potential for moving the industry towards sustainable practices [27]. However, there is no substantial research done in this area and hence some initial work is presented in this paper.

While the concept of recycling of a material is considered as a one-off activity, the CE concept takes it to the next level, that is a never-ending circle of use, reuse, repair and recycling of material where waste is considered as commodity and reinjected into the economy as useful resource. In addition to the above, CE also looks at the design phase of construction activity, where the materials and resources are being specified and procured, in order to make sure that the circularity is kept in mind whilst specifying and procuring construction materials.

2.4 Paint as a Building Material

Paint is used in large quantities in buildings as a finishing material, and can have significant environmental impacts. On average, the embodied energy for paint is about 117 MJ/kg compared to 3.5 MJ/kg for clay bricks and 263 MJ/kg for wallpaper [28]. Therefore, it is important to investigate the way to improve its circularity and extend its usefulness. Re-using, extending the life of materials and recycling are among important strategies for a material to secure the benefits of circular economy. Unused water-based and latex paints can be recycled to manufacture new paint products. Unused Oil based paints can be used as a source of energy. However, unlike most materials used in buildings, paint which has been used once, cannot be re-used or recycled. In this scenario, extending the service life of paint becomes extremely important to improve its circularity and reduce its environmental impacts.

The manufacture of paint is mostly carried out in coordinated batch processes. There are two major steps which make up the production, there are the premix and dispersion, and then, the finishing and tinting (See Fig. 2). In some cases, these steps are done in one tank, or divided up in two consecutive tanks: a disperser or mixer tank, and a let-down tank [29].

In general, there are few to no chemical reactions which occur as the operations are mostly mechanical. Once the assembling of raw materials is done, mixing, dispersing, and the thinning/adjusting are concluded; final filling into containers and batching into warehouses comes last [31]. As per the raw materials used in paint manufacture, they are a range of solids, liquids, powders, pastes and slurries. The pigments used are titanium dioxide, zinc oxide, mineral solvents such as turpentine, as well as resins and some additives [32]. By-products and waste produced include Volatile Organic Compounds (VOCs), wastewater, waste solvents, and sludge. These have negative environmental effect and need various systems and strategies implemented to reduce their impact [33].

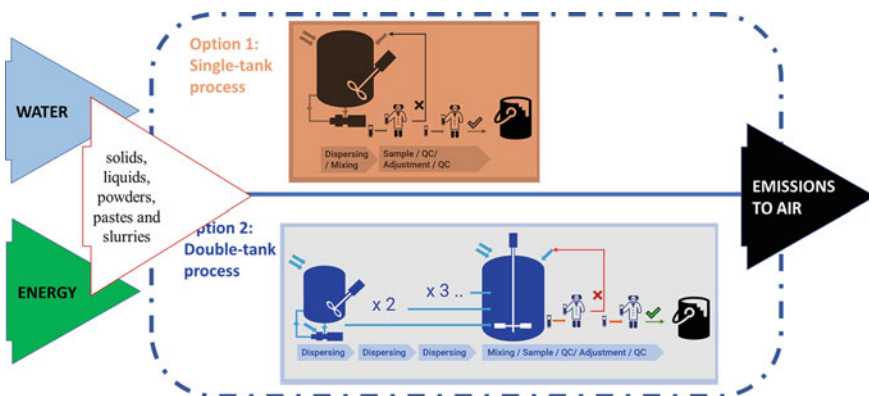


Fig. 2 Manufacture of paint [29, 30]

There is a close association between a systematic review of the sub-processes critical in any manufacturing process, and the steps leading to an assessment of the circularity of the product. Fundamentally, both allow for evaluating strengths and weaknesses across the production line. But circular economy encourages the shifting of material use from linear to circular by using materials again and again, a concept known as closing the loop [34, 35].

Circular strategies also encourage narrowing or slowing resource loops with the objective of maintaining the value of materials or extending their usefulness [36]. This strategy is applied for as long as it is practically possible and is intended to maximize the material's primary use before it is reused or recycled into another product. It has been argued that the disadvantages of material recovery associated with recycling may be addressed by extending a product's service life of products before attempts to repurposing or recycle it [37, p. 2]. Furthermore, when materials are used to their maximum extent, there are several benefits such as avoidance of resource losses, savings on raw materials and energy, reduction of emissions and by-products by significantly reducing in the volume of material waste generated [38]. These in-turn lead to, low embodied energy consumption and resource intensive construction activities, as well as less dependency on virgin materials, and material extraction from primary sources [36].

3 Research Method

As stated earlier, this study focuses on assessing the embodied energy of paint, as the selected building material, extending its service life, and then re-evaluating the life cycle embodied energy impacts to assess the applicability of benefits the aim as a circular economy strategy.

3.1 Case Study Villa

This investigation was facilitated by using an already-built residential villa in the UAE to provide real-world material usage based on the actual bill of quantities used in the construction. The representative case study building selected is located in Al Ain, UAE. It is a two-storey house with a Floor area of 532 m² (See Fig. 3).

The bill of quantities was used to quantify the life cycle embodied energy of the house by extracting the following: material unit and quantity delivered. The material quantities of the paint used in the villa extracted are listed in Table 1 below. The wastage factor was derived from literature [19, 20], and the Energy intensity (EI) unit was extracted from the Environmental Performance in Construction (EPiC) database [28].

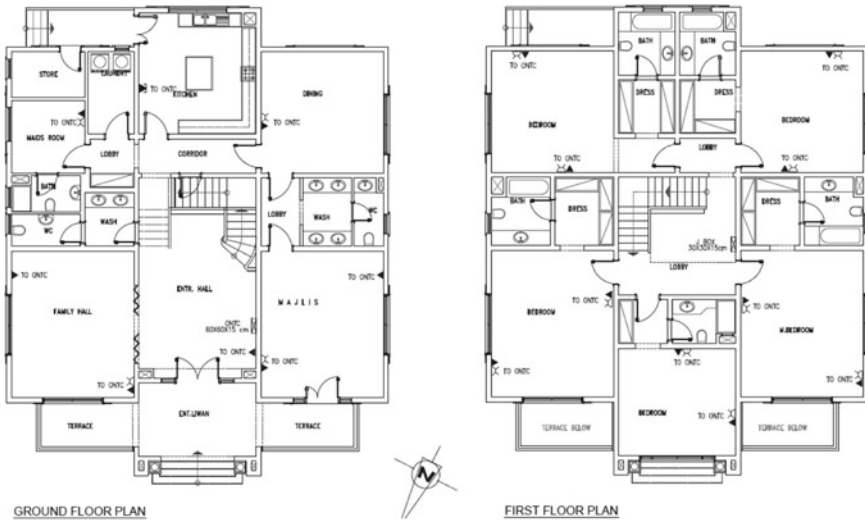


Fig. 3 Floor plans of the view of representative case study villa

Table 1 Material quantities and embodied energy assessment data for paint

Item	Unit	Qty	Wastage factor	Delivered quantity	EI GJ/unit	
<i>Interior</i>						
1	Wall finishing (W2) (Washable emulsion paint) 1530 m ²	kg	169	1.05	177.7191	0.111
2	Ceiling finishing (C2, C3) (Washable emulsion paint) 320 m ²	kg	35.4	1.05	37.17	0.111
3	Ceiling finishing (C6, C7) (Washable and oil paint) 16 m ²	kg	1.77	1.05	1.8585	0.111
4	Ceiling finishing (C6, C7) (Washable and oil paint) 16 m ²	kg	1.70	1.05	1.78416	0.124
<i>Exterior</i>						
1	Acrylic paint 70 m ²	kg	7.744	1.05	8.130938	0.111

3.2 *Embodied Energy Assessment*

The assessment protocol used for the quantification of both the embodied energy of the villa and the paint was a rigorous input–output based hybrid approach (IOBHA). In previous studies, this approach has been presented as the most comprehensive and procedurally reliable method for such assessments [19, 21, p. 206], [21]. A full breakdown of the steps for the IOBHA is provided in referenced literature. The critical formula used –for each material and component of the villa, is as shown below:

$$\begin{aligned} &\text{Process – based hybrid embodied energy(PB)} = \\ &\text{Delivered quantities of materials} + \text{Hybrid embodied energy} \end{aligned} \quad (1)$$

The process-based (PB) hybrid embodied energy value is then added to the results of a series of mathematical investigations to account for embodied energy consumed by non-material inputs. These are the provision of finance, insurance, transport etc., which are needed supporting measures to facilitate the villa construction. This addition was done to complete the system boundary for the assessment and is called the “remainder” which is then added to the PB value to arrive at the comprehensive IOBHA value of the associated embodied energy.

3.3 *Base Case and Alternative Scenarios*

The current investigation was designed to provide an extension of our on-going research trajectory to cover the much spoken and critical aspect of Circular Economy. In order to apply the listed steps above in connection with the objective of this study on “service life extension”, this study adopts a scenario approach. Using the average service life of paint at 10 years as the base case, we projected possible variations which will lead to an extension of the service life. These may include improved product quality, better manufacturing processes or maintenance. These factors are elaborated in Sect. 4.2.

To create an analytical basis for these scenarios, we assumed an incremental variation in the service life. Table 2 shows these scenarios and service life improvements which were investigated in details and the results presented in the next section.

Table 2 Base case and service life scenarios

Material under review: paint	Material service life (MSL) in years
Base case	10
Scenario 1 (+20%)	12
Scenario 2 (+40%)	14
Scenario 3 (+60%)	16
Scenario 4 (+80%)	18
Scenario 5 (+100%)	20

4 Results and Discussion

The findings of this study are presented on two levels. Firstly, the life cycle embodied energy of the case study villa is presented relative to the initial and recurrent embodied energies. Next, the selected building materials, paint, is focused on. A similar presentation of its LCEE is provided as well as an extended investigation of five (5) scenarios; this is the sensitivity analysis where the material service life of the paint is varied as explained in the previous section. As stated, Fig. 4 shows the results of the IOBHA for the villa; its LCEE over 50 years was 13,096.5 GJ which is made up of the IEE which was 7390.5 GJ (56%) and the REE which was 5690.01 GJ (43%).

4.1 Life Cycle Embodied Energy of the Paint Used in the Villa

With specific reference to the focus of this paper, Fig. 5 shows the combined IEE and REE of all the paint used in the finishing of the villa. This figure represents the base

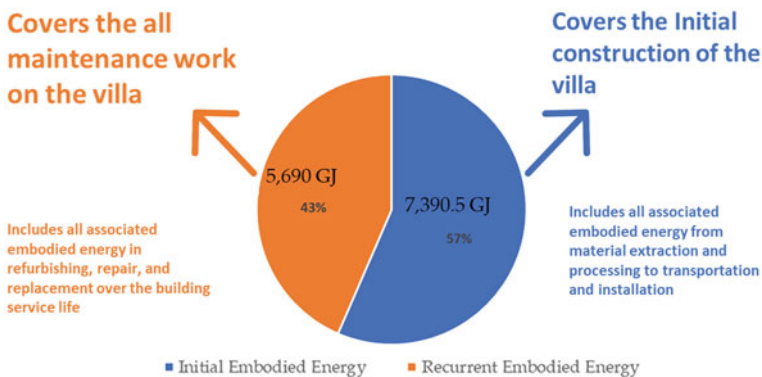
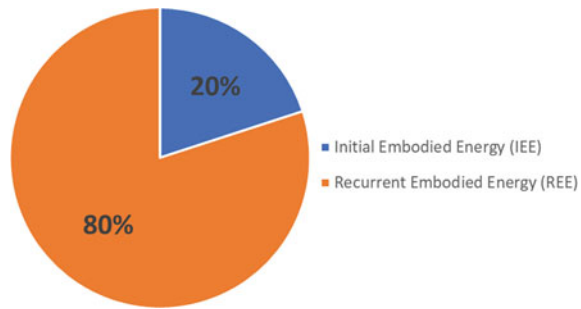


Fig. 4 Annotated LCEE of the case study villa

Fig. 5 IEE and REE of the paint used in the case study villa



case where the average material service life of the paint used is 10 years. It shows that the IEE was 32.5 GJ (20%) while the REE was 129.4 GJ (80%).

Recurrent embodied energy for the paint is assumed to be the same for all types of paint used for the purpose of simplifying this investigation. The figure shows that the REE of the paint is 4 times its IEE at a MSL of 10 years and a BSL of 50 years. This implies that there will be 4 replacements (or repainting) over the building's useful life span. There are some factors, which may however, alter these projections. For example, socially, a change in the resident; a new tenant may prefer a different colour of the walls even if the initial paint does not need any maintenance; environmentally, weathering and climate change rates may quite easily vary in the next 50 years, leading to a faster rate of degradation of both the exterior walls, and the paint used on it. Also, economically, the cost of paint and affordability may significantly drop or rise which may make the occupants decide to repaint villa before its MSL (10 years) or not repaint even after 10 years, if too expensive. Due to these unforeseen scenarios, it is important to have a well-understood assessment of how the service life of the paint, may or may not impact its circularity.

4.2 Sensitivity Analysis

Based on the foregoing, this section investigates the impact of improvement in the service life of the paint used, as a strategy to increase its useful life, reduce its environmental impact, and extend the timeline of its circularity and value. Thus, the MSL was increased by 20, 40, 60, 80 and 100%. For each scenario, the corresponding LCEE of the paint was recalculated. Figure 6 visually shows the impact of the MSL variations, as well as the incremental reduction in the LCEE relative to the base case for each scenario.

The figure shows that when the service life of paint is increased by 100%, there is a 40% reduction in its LCEE. This confirms that there is a significant advantage in extending the loop and increasing circularity by improving the service life of building materials. While this finding resonates with the objective of the paper, practical strategies which allow for this to be achieved need to be investigated. In previous

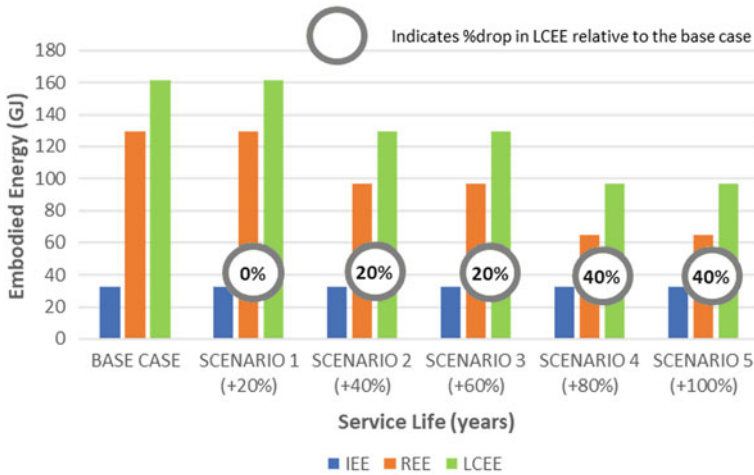


Fig. 6 Comparison of life cycle embodied energies associated with the 5 different scenarios

studies, the factors method or ‘factoring’ has been presented, debated and positioned as a possible approach or strategy to accomplish this [20]. It is associated with the ISO 15686–1 (2000) and ISO 15686–2 (2003) which set standards for service life planning in relation to both buildings and building components. Based on the factors approach, some possible strategies are recommended below for each “factor”:

1. **Quality of materials:** proper selection of water- or fire- resistant materials where needed
2. **Design level of a component’s or an assembly’s installation:** reduce design complexity
3. **Installer skill level:** ensure installation in made by certified, competent and well-trained painters
4. **Indoor environment:** Protection of painted areas from immediate negative indoor impact such as water spills, extreme friction, wear and tear, and loading
5. **Outdoor environment:** Protection of painted surfaces from direct or indirect outdoor impact from the environment (sun, rain or snow) or human activity
6. **In-use condition:** Advocate for trained or mature handling of product or component
7. **Maintenance level:** Provide planned periodic maintenance

For each factor, further research may reveal other strategies which may be applied. Although this lies outside the scope of the current paper, it is important to state that such strategies may be investigated either qualitatively based on industry trends, or quantitatively to evaluate LCEE aspects, financial expenses or environmental impacts.

5 Conclusion

This research was carried out to investigate the benefit of extending the service life of building materials as a circular economy strategy. To explore this objective, an IOBHA was carried out on a representative case study villa to calculate the associated embodied energy. Next, the service life was gradually increased, and the embodied energy recalculated. The results showed that for the selected case, the life cycle embodied energy of the paint was 161.8 GJ, IEE was 20% and REE was 80% of the LCEE. For the sensitivity analysis, the various scenarios show that when the MSL of paint is increased by 20% there is no change in LCEE. But when it increases by 40–60%, the LCEE drops by 20% and when the MSL is increased by 80–100%, LCEE drops by 40%.

This research was carried out as the first step in providing evidence to show that service life extension of paint can be used in reducing their embodied energy but also improving their circularity. This is because, the longer a material is useful, the greater the economic and environmental benefits, less resources extraction needed, and thus, promotes the transition towards the circular economy in the construction industry for sustainable development. It also serves as a vital step in promoting material sustainability by improving waste generated and closing the loop.

References

1. Geissdoerfer M, Savaget P, Bocken NMP, Hultink EJ (2017) The circular economy—a new sustainability paradigm? *J Clean Prod* 143:757–768. <https://doi.org/10.1016/j.jclepro.2016.12.048>
2. Schut E, Crielaard M, Mesman M (2016) Circular economy in the Dutch construction sector: a perspective for the market and government
3. Ellen MacArthur Foundation (2013) Towards the circular economy economic and business rationale for an accelerated transition, vol 3. [Online]. Available: https://www.werktrends.nl/app/uploads/2015/06/Rapport_McKinsey-Towards_A_Circular_Economy.pdf
4. von Freeden J, Husemann A, Caba S (2022) Component reuse strategy (CRS) for continuous reinforced thermo-sets enabling circular economy. *J Remanuf* 1–17
5. Jockwer R, Goto Y, Scharn E, Crona K (2020) Design for adaption—making timber buildings ready for circular use and extended service life. In: *IOP conference series: earth and environmental science*, 2020, vol 588(5). pp 052025
6. Brimacombe L (2018) Thinking life cycle in a circular economy. In: *Designing for the circular economy*, Routledge, pp 157–166
7. Halstenberg FA, Stark R (2019) Introducing product service system architectures for realizing circular economy. *Proc Manuf* 33:663–670. <https://doi.org/10.1016/j.promfg.2019.04.083>
8. Huang B, Wang X, Kua H, Geng Y, Bleischwitz R, Ren J (2018) Construction and demolition waste management in China through the 3R principle. *Resour Conserv Recycl* 129:36–44
9. Mohammed M et al (2021) Modeling of 3R (reduce, reuse and recycle) for sustainable construction waste reduction: a partial least squares structural equation modeling (PLS-SEM). *Sustainability* 13(19):10660
10. Moraga G et al (2019) Circular economy indicators: what do they measure? *Resour Conserv Recycl* 146:452–461. <https://doi.org/10.1016/j.resconrec.2019.03.045>

11. Yeheyis M, Hewage K, Alam MS, Eskicioglu C, Sadiq R (2013) An overview of construction and demolition waste management in Canada: a lifecycle analysis approach to sustainability. *Clean Technol Environ Policy* 15(1):81–91
12. Steinmann ZJN, Huijbregts MAJ, Reijnders L (2019) How to define the quality of materials in a circular economy? *Resour Conserv Recycl* 141:362–363. <https://doi.org/10.1016/j.resconrec.2018.10.040>
13. Rauf A (2022) Reducing life cycle embodied energy of residential buildings: importance of building and material service life. *Buildings* 12(11):1821
14. Rauf A, Attoye DE, Crawford R (2022) Embodied and operational energy of a case study villa in UAE with sensitivity analysis. *Buildings* 12(9):1469
15. Mirletz H, Ovaitt S, Sridhar S, Barnes TM (2022) Circular economy priorities for photovoltaics in the energy transition. *PLoS ONE* 17(9):e0274351. <https://doi.org/10.1371/journal.pone.0274351>
16. Elmualim A, Mostafa S, Chileshe N, Rameezdeen R (2018) Construction and the circular economy: smart and industrialised prefabrication. In: *Unmaking waste in production and consumption: towards the circular economy*, Emerald Publishing Limited
17. Shooshtarian S, Caldera S, Maqsood T, Ryley T, Khalfan M (2021) An investigation into challenges and opportunities in the Australian construction and demolition waste management system. *Engineering, construction and architectural management*
18. European Parliament (2015) Circular economy: definition, importance and benefits | News | European Parliament. 12 Feb 2015. <https://www.europarl.europa.eu/news/en/headlines/economy/20151201STO05603/circular-economy-definition-importance-and-benefits>. Accessed 16 Dec 2022
19. Rauf A, Attoye DE, Crawford RH (2021) Life cycle energy analysis of a house in UAE. In: *ZEMCH 2021 International conference*, Dubai, United Arab Emirates, 26–28 October 2021, pp 13–23. [Online]. Available: <http://zemch.org/proceedings/2021/ZEMCH2021.pdf>
20. Rauf A (2016) The effect of building and material service life on building life cycle embodied energy, PhD Thesis, The University of Melbourne, Melbourne, VIC, Australia
21. Rauf A, Crawford RH (2015) Building service life and its effect on the life cycle embodied energy of buildings. *Energy* 79:140–148
22. Tavares V, Lacerda N, Freire F (2019) Embodied energy and greenhouse gas emissions analysis of a prefabricated modular house: the “Moby” case study. *J Clean Prod* 212:1044–1053
23. Ajayi SO, Oyedele LO, Ilori OM (2019) Changing significance of embodied energy: a comparative study of material specifications and building energy sources. *J Build Eng* 23:324–333. <https://doi.org/10.1016/j.jobe.2019.02.008>
24. Wen TJ, Siong HC, Noor ZZ (2015) Assessment of embodied energy and global warming potential of building construction using life cycle analysis approach: case studies of residential buildings in Iskandar Malaysia. *Energy and Build* 93:295–302
25. Huberman N, Pearlmuter D (2008) A life-cycle energy analysis of building materials in the Negev desert. *Energy and Build* 40(5):837–848
26. Reddy BV, Jagadish KS (2003) Embodied energy of common and alternative building materials and technologies. *Energy and Build* 35(2):129–137
27. UAE Government, ‘UAE Policy (2021) UAE Circular Economy 2021–2031 policy. Google Search’. [https://www.google.com/search?q=UAE+Policy+\(2021\)%2C+UAE+Circular+Economy+2021-2031+policy.&dq=UAE+Policy+\(2021\)%2C+UAE+Circular+Economy+2021-2031+policy.&aq=chrome..69i57j0i54614j0i30i546j69i64j69i60.390j0j7&sourceid=chrome&ie=UTF-8](https://www.google.com/search?q=UAE+Policy+(2021)%2C+UAE+Circular+Economy+2021-2031+policy.&dq=UAE+Policy+(2021)%2C+UAE+Circular+Economy+2021-2031+policy.&aq=chrome..69i57j0i54614j0i30i546j69i64j69i60.390j0j7&sourceid=chrome&ie=UTF-8). Accessed 19 Dec 2022
28. Crawford R, Stephan A, Prideaux F (2019) Environmental performance in construction (EPiC) database. Melbourne, VIC, Australia: The University of Melbourne. <https://doi.org/10.26188/5dc228ef98c5a>
29. Fluidan (2022) Manufacturing of paint | RheoStream®—Fluidan. <https://fluidan.com/manufacturing-of-paint/>. Accessed 19 Dec 2022
30. Yacout DMM, El-Zahhar M (2018) Environmental impact assessment of paints production in Egypt. In: *e 4th International conference of biotechnology, environment and engineering*

- sciences (ICBE 2018), Alexandria, Egypt, 2018. [Online]. Available: <http://fms-kursk.ru/wp-content/uploads/2019/01/LCAPaint-61-66.pdf>
31. Michael M (2011) Paint and coating manufacture. <https://www.iloencyclopaedia.org/part-xii-57503/chemical-processing/item/380-paint-and-coating-manufacture>. Accessed 19 Dec 2022
 32. HPS (2021) How paint manufacturers can overcome raw material price hikes in 2021. HPS Hygienic Pigging Systems 19 Mar 2021. <https://www.hps-pigging.com/how-paint-manufacturers-can-overcome-raw-material-price-hikes-in-2021/>. Accessed 19 Dec 2022
 33. Community Repaint (2022) 'How is paint made?'. Community RePaint 2021 https://communityrepaint.org.uk/news_and_stories/how-is-paint-made/. Accessed 19 Dec 2022
 34. Brydges T (2021) Closing the loop on take, make, waste: investigating circular economy practices in the Swedish fashion industry. *J Clean Prod* 293:126245. <https://doi.org/10.1016/j.jclepro.2021.126245>
 35. Hobson K (2016) Closing the loop or squaring the circle? Locating generative spaces for the circular economy. *Prog Hum Geogr* 40(1):88–104. <https://doi.org/10.1177/0309132514566342>
 36. Densley Tingley D, Giesekam J, Cooper-Searle S (2018) Applying circular economic principles to reduce embodied carbon. In: *Embodied carbon in buildings*, Springer, pp 265–285
 37. Zhang Z, Takeyama K, Ohno H, Matsubae K, Nakajima K, Nagasaka T (2019) An estimation of the amount of dissipated alloy elements in special steel from automobile recycling. *Matériaux Techniques* 107(1):105. <https://doi.org/10.1051/mattech/2019007>
 38. Stahel WR (2016) The circular economy. *Nature* 531(7595):435–438

Development of Rapid-Setting Repair Materials Through One-Part Geopolymer Technology



Wei-Hao Lee, Ying-Kuan Tsai, Chien-Chin Chen, and De-Wei Gao

Abstract The development of geopolymer materials has been over 35 years. Compared with ordinary portland cement (OPC), geopolymer materials have many excellent properties such as high-early strength, nice durability, low carbon emission...etc. Therefore, geopolymer materials have great potential to replace OPC. In particular, geopolymer's high early strength characteristics are very suitable as repair materials. However, the traditional geopolymer manufacturing process is mixed alkaline solution and aluminosilicate materials. The transportation and storage of alkaline solution will cause a significant burden on the factory, limiting the application and market willingness of geopolymer material. This study focuses on using solid-state activator to develop one-part geopolymer, which is "only adding water" to produce geopolymer. This study will try to develop [Rapid-setting repair geopolymer paste] and [Rapid-setting repair geopolymer mortar] and discuss the effect of solid activator dosage amount, type of solid activator, and solid activator fineness on the mechanical and workability properties of geopolymer materials. According to the experiment results, after curing for 2h, the compressive strength of [Rapid-setting repair geopolymer paste] can reach over 30 MPa, and the compressive strength can reach 100 Mpa after curing for 28 days. The compressive and flexural strength of [Rapid-setting repair geopolymer mortar] can reach over 60 and 10MPa, after curing for the day. The shrinkage rate can be controlled at lower than 0.1%. This study succeeded in developing a suitable repair material using one-part geopolymer technology. It is hoped that the practical application can be carried out after more testing in the future.

Keywords Geopolymer · Pavement repair materials · High early strength

W.-H. Lee (✉) · D.-W. Gao

Institute of Mineral Resources Engineering, National Taipei University of Technology, Taipei 10608, Taiwan
e-mail: whlee@ntut.edu.tw

Y.-K. Tsai · C.-C. Chen

Department of Environmental Information and Engineering, Chung Cheng Institute of Technology, National Defense University, Taoyuan 335, Taiwan

1 Introduction

Cement manufacturing is one of the highest carbon dioxide emission industries. It releases 880 kg carbon dioxide for every ton of cement produced. The annual global cement production has reached 2.8 billion tonnes [1]. The OPC production contributes approximately 5–8% of global CO₂ emissions [2].

Geopolymer materials have been developed for over 30 years. Until recently, geopolymer have been heeded by global research institutes and many countries due to geopolymers containing excellent properties, simple production equipment, and fabrication process at room temperature. It has good development potential for replacing OPC cement to use in engineering applications [3–9].

In the traditional way of making geopolymers, it is necessary to mix reactive binder materials with alkaline solutions [10, 11]. However, there are many limitations in transporting and storing a large amount of alkaline solution, which limits the application and market willingness of geopolymer material.

Therefore, this study uses solid-state activator and aluminosilicate material to form geopolymer. It is expected to improve the current way of adding alkaline solution by mixing it with water. This study will discuss the effect of solid-state activator dosage amount, type of solid-state activator, and solid-state activator fineness on rapid-setting repair geopolymer material's mechanical and workability properties.

At the same time, this study will discuss the influence of various parameters on the workability and mechanical properties of rapid-setting repair geopolymer materials when made into mortar.

2 Material and Experiment Method

This study uses sodium metasilicate anhydrate (SMA) and sodium carbonate (SC) as solid-state activators to prepare the geopolymer. The chemical composition of sodium metasilicate anhydrate (Na₂SiO₃) is 46 wt.% of SiO₂ and 51 wt.% of Na₂O. The purity of sodium carbonate is 99%. All the solid activators were purchased from Emperor Chemical Co., Ltd.

In this study, Ground granulated blast furnace slag (GGFBS) has been selected as binder material. China Steel produced GGBFS in southern Taiwan. The chemical composition and particle size of the GGBFS are in Table 1. The crystal phase of GGBFS, shown in Fig. 1a, reveals that GGFS is almost amorphous. To form geopolymer mortar, this study purchased natural sand as fine aggregate, and the F.M. of natural sand is 3.0.

Table 1 Chemical composition of GGBS

Oxide	CaO	SiO ₂	Al ₂ O ₃	MgO	Other	D ₅₀ of GGBFS
Wt.%	40.2	34.7	14.1	7.1	3.9	12.02μm

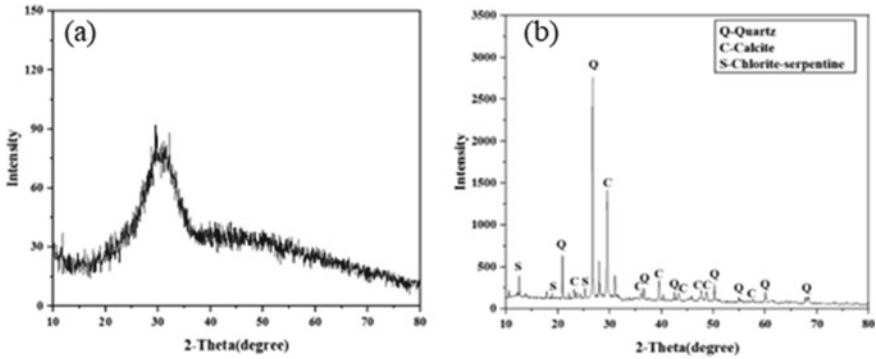


Fig. 1 a The XRD pattern of the GGBFS. b The XRD pattern of the natural sand

The experiment procedure and parameters of this study can be divided into two part to discuss. The first part is [Rapid-setting repair geopolymer paste], experimental procedure and parameters were shown in Fig. 2 and Table 2. The second part is [Rapid-setting repair geopolymer mortar], experimental procedure and parameters were shown in Fig. 2 and Table 3.

The setting times analysis method of geopolymer paste were followed by CNS 786 and determined through Vicat equipment. The setting time analysis method of geopolymer mortar were followed by CNS 14,220. The compressive and flexural strength analysis method of all specimens were followed by CNS 1232 and CNS 1234 The shrinkage analysis method of all specimens were followed by CNS 14,603.e Size, Margins and Font.

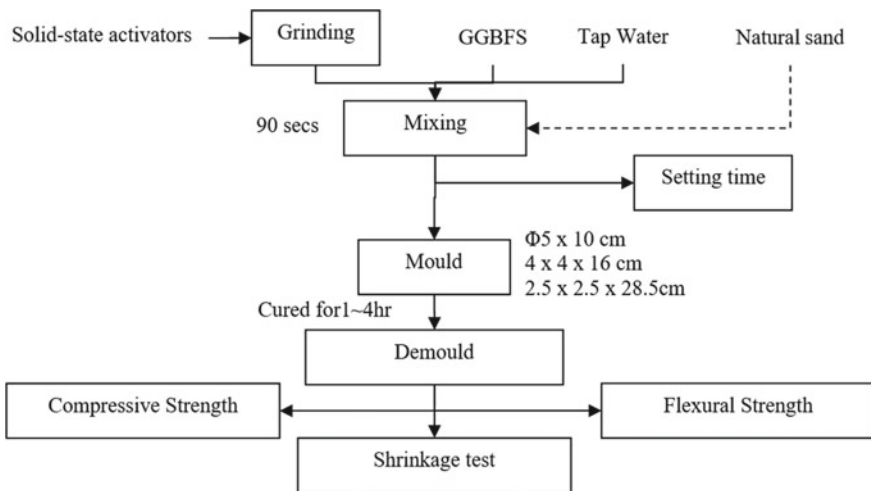


Fig. 2 Overall experiment procedures

Table 2 [Rapid-setting repair geopolymer paste] experiment parameters

Mix ID	Solid activator grinding time	Binder (wt. %)		
		SMA	SC	GGBFS
12-0-15	15	12	0	88
15-0-15	15	15	0	85
18-0-15	15	18	0	82
20-0-15	15	20	0	80
15-10-15	15	13.5	1.5	85
15-15-15	15	12.7	2.3	85
15-20-15	15	12	3.0	85
15-30-15	15	10.5	4.5	85
15-50-15	15	7.5	7.5	85
15-15-0	0	12.7	2.3	85
15-15-30	30	12.7	2.3	85

Table 3 [Rapid-setting repair geopolymer mortar] experiment parameters

Mix ID	Solid activator grinding time	Binder (wt. %)			Fine aggregate to binder ratio
		SMA	SC	GGBFS	
12-15-0-1.2	0	10.2	1.8	88	1.2
12-15-15-1.2	15	10.2	1.8	88	1.2
12-15-30-1.2	30	10.2	1.8	88	1.2
12-15-15-1.5	15	10.2	1.8	88	1.5
12-15-15-2.0	15	10.2	1.8	88	2.0
12-15-15-2.75	15	10.2	1.8	88	2.75

3 Result and Discussion

3.1 Effect of Various Factors on the Setting Time of [Rapid-Setting Repair Geopolymer Paste]

Table 4 shows the influence of each factor on [Rapid-setting repair geopolymer paste] setting time. According to the experimental results, it is found that the three factors have a significant effect on the initial setting time of [Rapid-setting repair geopolymer paste]. The main factor was the SC replacement amount.

In addition, through the experimental results, it is found that the amount of SC replacement amount and the solid-state activator dosage amount has a significant effect on the final setting time of [Rapid-setting repair geopolymer paste], while the grinding time of the solid activator has no apparent effect; based on the above-related

Table 4 The effect of various factors on the setting time of [Rapid-setting repair geopolymer paste]

Mix ID	Initial setting time (min)	Final setting time (min)
12-0-15	17	32
15-0-15	7	11
18-0-15	6	11
20-0-15	5	8
15-10-15	8	15
15-15-15	17	23
15-20-15	15	32
15-30-15	24	40
15-50-15	45	80
15-15-0	17	38
15-15-30	11	25

results, it is found that the SC replacement amount is the main factor affecting the setting time of [Rapid-setting repair geopolymer paste].

3.2 Effect of Various Factors on the Compressive Strength of [Rapid-Setting Repair Geopolymer Paste]

The influence of various factors on the compressive strength of [Rapid-setting repair geopolymer paste] is shown in Fig. 3. The experimental results show that the solid activator grinding time and the amount of sodium carbonate substitution significantly affected the 4-h compressive strength of the [Rapid-setting repair geopolymer paste]. In addition, according to the results of 1-day compressive strength, only the solid-state activator dosage amount significantly affect the 1-day compressive strength of [Rapid-setting repair geopolymer paste], and the solid-state activator dosage amount is the only one that affects [Rapid-setting repair geopolymer paste] 1-day compressive strength. The analysis results of the [Rapid-setting repair geopolymer paste] 7-day compressive strength show that the solid-state activator dosage amount and the grinding time of the solid activator significantly affect it.

The influence of various factors on the 28-day compressive strength of [Rapid-setting repair geopolymer paste] was found that only the solid-state activator dosage amount significantly affects the 28-day compressive strength of the [Rapid-setting repair geopolymer paste]. The main factor of the 28-day compressive strength of the slurry is the amount of solid activator added.

Therefore, based on the above results, it is found that the main factor affecting the development of compressive strength of [Rapid-setting repair geopolymer paste] is the solid-state activator dosage amount.

In addition, this study conducted experimental tests on the short-term compressive strength development of [Rapid-setting repair geopolymer paste], and the related

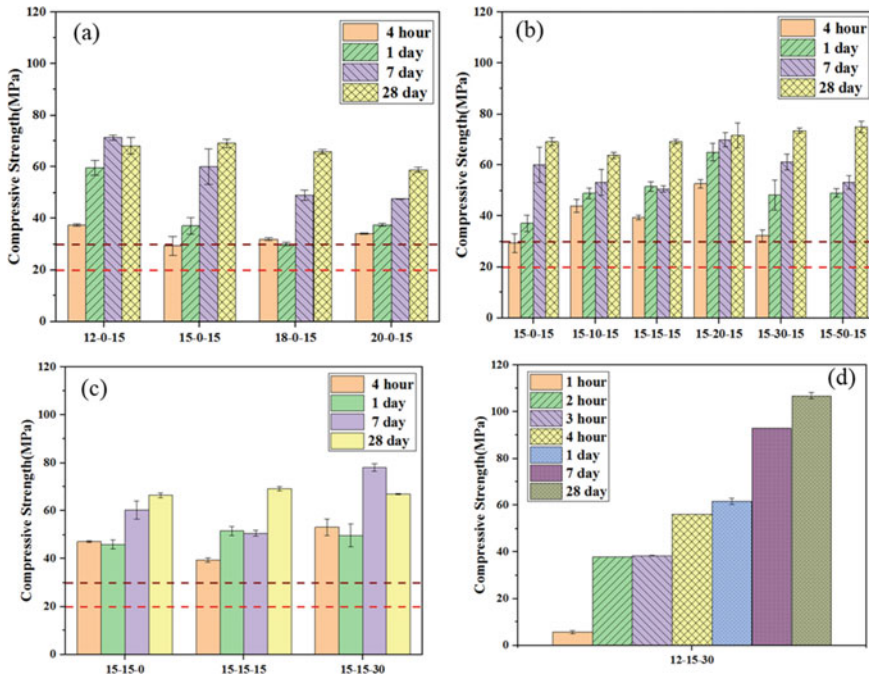


Fig. 3 Effect of various factors on the compressive strength of [Rapid-setting repair geopolymer paste]. **a** The solid-state activator dosage amount. **b** SC replacement amount. **c** Solid activator grinding time. **d** Development of compressive strength (cured from 1 h to 28 days)

results are shown in Fig. 3d. The compressive strength of [Rapid-setting repair geopolymer paste] developed in this study develops rapidly, and it only needs two hours of curing to exceed the 28 Mpa required by general engineering. It can be seen from this that the [Rapid-setting repair geopolymer paste] developed in this research has the feasibility of a practical application.

3.3 Effect of Various Factors on Flexural Strength of [Rapid-Setting Repair Geopolymer Paste]

The influence analysis of various factors on the flexural strength of [Rapid-setting repair geopolymer paste] is shown in Fig. 4. The experimental results showed that the solid-state activator dosage amount and SC replacement amount significantly affect the 4-h flexural strength of the [Rapid-setting repair geopolymer paste], and the influence of the solid-state activator dosage amount is higher than that of the SC replacement amount. The experimental results also found that the three factors have

no significant influence on the 1-day flexural strength of the [Rapid-setting repair geopolymer paste].

In addition, according to the 7-day flexural strength results of [Rapid-setting repair geopolymer paste], only the solid activator’s grinding time significantly affects the 7-day flexural strength. Regarding the 28-day flexural strength, the experimental results found that none of the three factors significantly affected [Rapid-setting repair geopolymer paste].

In addition, this study conducted experimental tests on the short-term flexural strength development of [Rapid-setting repair geopolymer paste], and the relevant results are shown in Fig. 4d. The flexural strength of [Rapid-setting repair geopolymer paste] developed in this study also developed rapidly. It can be seen from this that the [Rapid-setting repair geopolymer paste] developed in this research has the feasibility of a practical application.

Therefore, based on the above results, it is found that the main factor affecting the development of compressive strength of [Rapid-setting repair geopolymer paste] is the solid-state activator dosage amount.

In addition, this study conducted experimental tests on the short-term compressive strength development of [Rapid-setting repair geopolymer paste], and the related

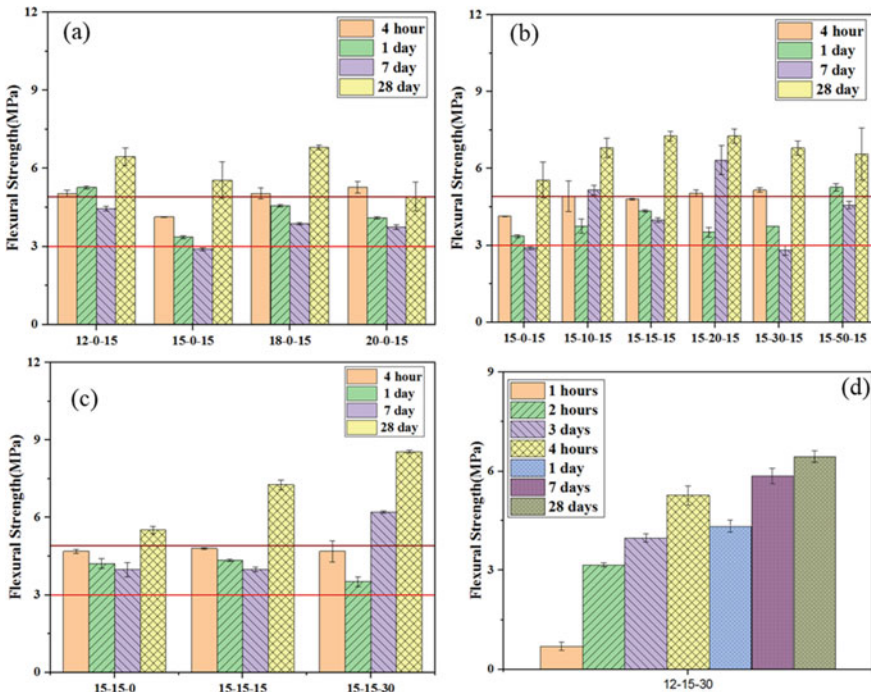


Fig. 4 Effect of various factors on the flexural strength of [Rapid-setting repair geopolymer paste]. **a** The solid-state activator dosage amount. **b** SC replacement amount. **c** Solid activator grinding time. **d** Development of flexural strength (cured from 1h to 28 days)

results are shown in Fig. 3d. The compressive strength of [Rapid-setting repair geopolymer paste] developed in this study develops rapidly, and it only needs two hours of curing to exceed the 28Mpa required by general engineering. It can be seen from this that the [Rapid-setting repair geopolymer paste] developed in this research has the feasibility of a practical application.

3.4 Effect of Various Factors on Shrinkage of [Rapid-Setting Repair Geopolymer Paste]

The influence analysis of various factors on the shrinkage of [Rapid-setting repair geopolymer paste] is shown in Fig. 5. The results show that the shrinkage will decrease when the solid-state activator dosage amount increases.

When the solid-state activator dosage amount is higher enough, the shrinkage of the specimen can be controlled at around 0%. However, these two factors will not significantly affect the shrinkage, including SC replacement amount and Solid activator grinding time.

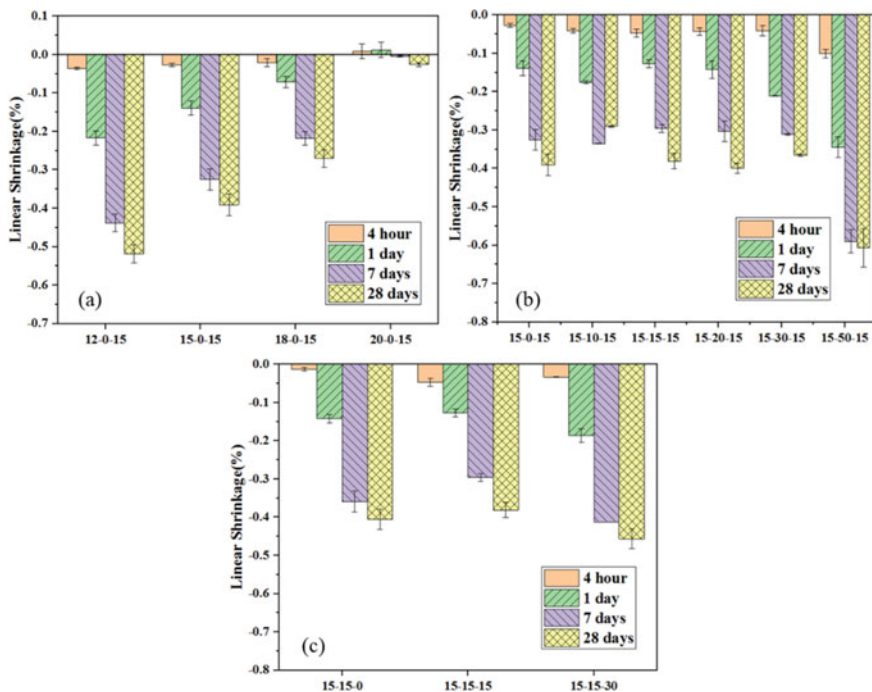


Fig. 5 Effect of various factors on the shrinkage of [Rapid-setting repair geopolymer paste]. **a** The solid-state activator dosage amount. **b** SC replacement amount. **c** Solid activator grinding time

Table 5 Effect of various factors on the setting time of [Rapid-setting repair geopolymer mortar]

Mix ID	Initial setting time (min)	Final setting time
12-15-0-1.2	17	31 min
12-15-15-1.2	11	25 min
12-15-30-1.2	11	23 min
12-15-15-1.5	11	23 min
12-15-15-2.0	23	54 min
12-15-15-2.75	65	193 n

3.5 Effect of Various Factors on the Setting Time of [Rapid-Setting Repair Geopolymer Mortar]

Table 5 shows the influence of various factor on [Rapid-setting repair geopolymer mortar] setting time. According to the experimental results, it is found that the fine aggregate amount have a significant effect on the initial and final setting time of [Rapid-setting repair geopolymer mortar]. Because when the additional amount of fine aggregate increases, the overall content of the paste will decrease, thereby delaying the overall reaction rate and achieving the effect of retarding the setting time.

In addition, through the experimental results, it is found that the grinding time of solid-state activator also slightly affects setting time. As the grinding time increases, the overall reaction speeds up. But when the grinding time exceeds 15 min, there will not have any change.

3.6 Effect of Various Factors on the Compressive Strength of [Rapid-Setting Repair Geopolymer Mortar]

The influence of various factors on the compressive strength of [Rapid-setting repair geopolymer mortar] is shown in Fig. 6. According to the experimental results, as the Solid activator grinding time prolongs, the compressive strength of the specimen cured for 4 h increases. The reason is speculated because when the Solid activator grinding time is extended, the particle size of the Solid activator becomes finer. The specific surface area increases, which makes the Solid activator react better, thereby increasing the compressive strength of the specimen. However, as the curing age was prolonged, the compressive strength was not significantly affected by it.

In addition, as the proportion of fine aggregates increases, the 4-h strength will decrease. This trend is mainly because the fine aggregates themselves cannot participate in the reaction and can only provide the strength of the aggregate itself. Therefore, when the proportion of fine aggregates increases After that, the early strength decreases, but as the curing time elongated, the proportion of fine aggregates had no significant effect on the compressive strength.

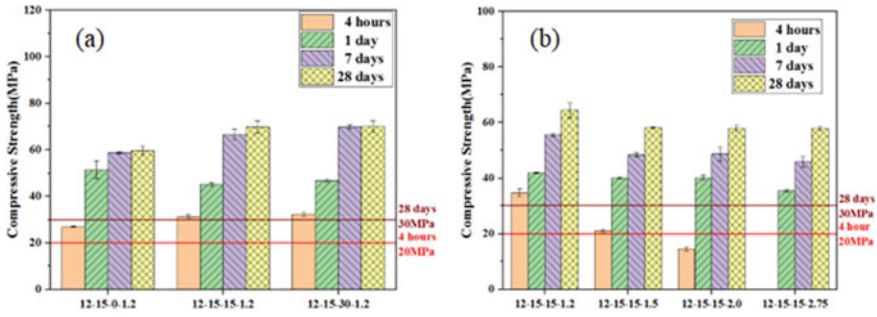


Fig. 6 Effect of various factors on the compressive strength of [Rapid-setting repair geopolymer mortar]. **a** Solid activator grinding time. **b** Fine aggregate to Binder ratio

3.7 Effect of Various Factors on the Flexural Strength of [Rapid-Setting Repair Geopolymer Mortar]

The influence of various factors on the compressive strength of [Rapid-setting repair geopolymer mortar] is shown in Fig. 7. According to the experimental results, the flexural strength trend of [Rapid-setting repair geopolymer mortar] increases with the increase of Solid activator grinding time. In addition, it is known that when fine aggregates are added to the material, the fine aggregates can effectively inhibit the shrinkage of the specimen and then promote the development of the flexural strength of [Rapid-setting repair geopolymer mortar], compared with [Rapid-setting repair geopolymer paste] is stable. The trend is similar to the compressive strength results for the proportion of fine aggregate added.

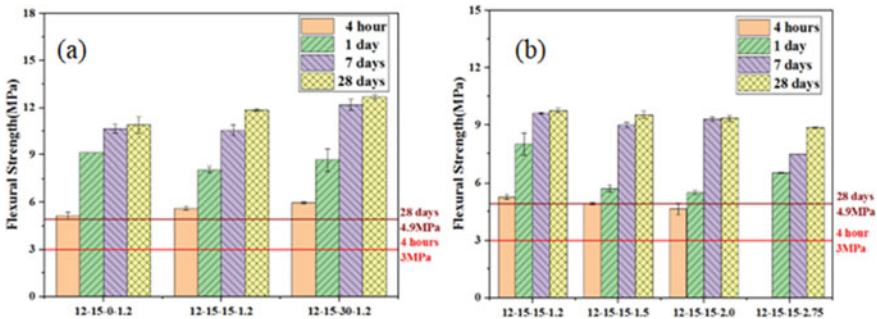


Fig. 7 Effect of various factors on the flexural strength of [Rapid-setting repair geopolymer mortar]. **a** Solid activator grinding time. **b** Fine aggregate to Binder ratio

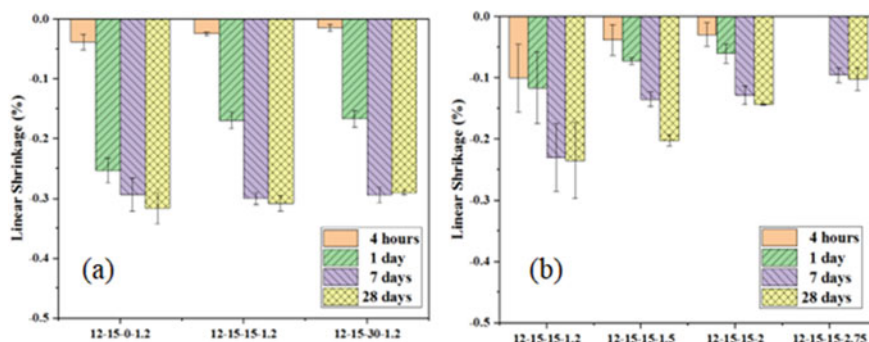


Fig. 8 Effect of various factors on the shrinkage of [Rapid-setting repair geopolymer mortar]. **a** Solid activator grinding time. **b** Fine aggregate to Binder ratio

3.8 Effect of Various Factors on the Shrinkage of [Rapid-Setting Repair Geopolymer Mortar]

The influence of various factors on the shrinkage of [Rapid-setting repair geopolymer mortar] is shown in Fig. 8. According to the experimental results, the shrinkage becomes smaller as the solid activator grinding time increases. It is speculated that the reason is that when the solid activator grinding time is prolonged, the particle size of the solid activator becomes finer, and the specific surface area increases, which makes the solid activator reaction better. The test body's structure developed completely, and the shrinkage properties declined.

In addition, as the additional amount of fine aggregate increases, the shrinkage rate will also decrease. The additional amount of fine aggregates can inhibit the shrinkage of the specimen, and there is no obvious change in shrinkage after curing 7 days. However, although the addition of fine aggregates will help inhibit the specimen's shrinkage, it still needs to be considered carefully because of its poor early strength development.

4 Conclusion

According to the experimental results, it is found that the workability properties and mechanical properties of [Rapid-setting repair geopolymer paste] can be adjusted by adjusting the different parameters. When the solid-state activator dosage amount is too much, there is no obvious effect on the specimen's early compressive and flexural strength. Still, as the age is extended to 28 days, the surface of the test body will produce white blooms of carbonates to reduce the strength of the specimen. When sodium carbonate replaces sodium metasilicate $\geq 15\%$, the setting time of [Rapid-setting repair geopolymer paste] is prolonged.

According to the test results, [Rapid-setting repair geopolymer paste] No. 15–15–15, its setting time can meet the target range of repair material requirements, and the compressive and flexural strength can also reach the target strength of the repair material. In addition, through relevant data analysis, the main factor affecting the setting time is SC replacement amount, followed by solid-state activator dosage amount; the main factor affecting the early compressive strength is Solid activator grinding time; the main factor affecting the development of the compressive strength of the specimen is solid -state activator dosage amount.

About [Rapid-setting repair geopolymer mortar], according to the experimental results, it is found that through the adjustment of the different parameters, the workability properties and mechanical properties of [Rapid-setting repair geopolymer mortar] can be adjusted so that [Rapid-setting repair geopolymer mortar] can achieve repair the target strength and working performance of the material. The different ratio of fine aggregate significantly affects the setting time and early strength development of [Rapid-setting repair geopolymer mortar]; according to the current experimental results, the setting time can be controlled within the target range of the repair material demand, and the compressive and flexural strength can also reach the target strength of the repair material.

References

1. Schneider M, Romer M, Tschudin M, Bolio H (2011) Sustainable cement production-present and future. *Cem Concr Res* 41:642–650
2. Van Deventer JSJ, Provis JL, Duxson P (2012) Technical and commercial progress in the adoption of geopolymer cement. *Miner Eng* 29:89–104
3. Aiken TA, Kwasny J, Sha W, Soutsos MS (2018) Effect of slag content and activator dosage on the resistance of fly ash geopolymer binders to sulfuric acid attack. *Cem Concr Res* 111:23–40
4. Aliques-Granero J, Tognonvi MT, Tagnit-Hamou A (2019) Durability study of AAMs: sulfate attack resistance. *Constr Build Mater* 229:117110
5. Lahoti M, Tan KH, Yang EH (2019) A critical review of geopolymer properties for structural fire-resistance applications. *Constr Build Mater* 221:514–526
6. Liu Y, Su P, Li M, You Z, Zhao M (2020) Review on evolution and evaluation of asphalt pavement structures and materials. *J Traffic and Transport Eng* 7:573–599
7. Shill SK, Al-Deen S, Ashraf M, Hutchison W (2020) Resistance of fly ash based geopolymer mortar to both chemicals and high thermal cycles simultaneously. *Construct Build Mater* 239:117886
8. Vafaei M, Allahverdi A, Dong P, Bassim N (2018) Acid attack on geopolymer cement mortar based on waste-glass powder and calcium aluminate cement at mild concentration. 193:363–372
9. Cong P, Cheng Y (2021) Advances in geopolymer materials: a comprehensive review. *J Traffic and Transport Eng* 8:283–314
10. Luukkonen T, Abdollahnejad Z, Yliniemi J, Kinnunen P, Illikainen M (2018) One-part alkali-activated materials: a review. *Cem Concr Res* 103:21–34
11. Wang YS, Alrefaei Y, Dai JG (2021) Roles of hybrid activators in improving the early-age properties of one-part geopolymer pastes. *Construct Build Mater* 306:124880

Reducing Embodied Energy of Floor Assembly: A Case for Using CLT in Mid-Rise Residential Buildings



Abdul Rauf and Muhammed Tariq Shafiq

Abstract Buildings' energy consumption is estimated between 30 and 40% of its global use, resulting in various environmental impacts. There is a need to reduce the energy consumption by buildings in the construction phase, along with the operation phase, which is well-studied. Concrete is a construction material that is being used widely in the construction industry but has high embodied energy. In the move towards using low-energy materials, new materials and construction technologies are being developed and studied. In this regard, Cross laminated timber (CLT) can be a sustainable alternative due to its excellent load-carrying capabilities, and therefore has become an emerging choice in buildings as a low embodied energy material alternative. This paper aims to explore the potential initial embodied energy reduction benefits by comparing the initial embodied energy consumption of concrete floor systems and CLT floor systems for mid-rise residential buildings. An eight-story apartment building was used for this analysis. This study shows that replacing the reinforced concrete floor with a CLT floor results in more than four times reduction in embodied energy associated with floor construction. This demonstrates the need for careful selection of materials in buildings at the design stage to reduce their embodied energy and consider the use of CLT instead of reinforced concrete in this context. Results from this initial study also indicate the need for more studies to address the challenges associated with the adoption of this low embodied energy material.

Keywords Initial embodied energy · Cross-laminated timber · Floor assembly · Input–output based hybrid assessment · Construction materials

A. Rauf (✉) · M. T. Shafiq
Department of Architectural Engineering, College of Engineering, United Arab Emirates University, 15551 Al Ain, Abu Dhabi, UAE
e-mail: a.rauf@uaeu.ac.ae

M. T. Shafiq
e-mail: muhammad.tariq@uaeu.ac.ae

© The Author(s), under exclusive license to Springer Nature Singapore Pte Ltd. 2024
M. Casini (ed.), *Proceedings of the 3rd International Civil Engineering and Architecture Conference*, Lecture Notes in Civil Engineering 389,
https://doi.org/10.1007/978-981-99-6368-3_14

157

1 Introduction and Background

There is a consensus among researchers about the contribution of energy consumption to global warming and climate change. Increasing heat waves, more frequent floods, and other weather-related catastrophes show the extent of climate change. Atmospheric CO₂ concentration has now reached well above the upper safety limit with a value of 419 parts per million [1]. Buildings consume significant amounts of energy during their life cycle. This includes the energy required for their initial construction including the energy required for the production of materials, as well as the operation of buildings during their use phase [2, 3]. Energy is also consumed through maintenance activities during a building's lifetime. Multidimensional approaches are required to minimize energy consumption across all life cycle stages of buildings.

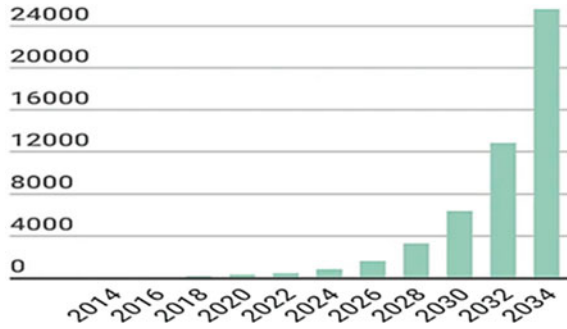
Buildings-related energy consumption is estimated between 30 and 40% of global energy consumption [4]. A significant share of building-related energy is attributed to residential buildings. Growth in the global population and rapid urbanization is resulting in a strain on the housing needs in cities. This situation is resulting in the construction of more and more mid-rise residential projects in urban and suburban areas. There is an urgent need for action from all the stakeholders in the construction industry to form strategies for the reduction in energy consumption by the building sector. Energy associated with the operations of buildings is well understood and significant work has been done in this area [3].

A considerable amount of energy is associated with the manufacture of materials and products. This includes the energy consumed in the extraction of raw materials, their processing, manufacturing, transportation to the site, and construction and is known as Initial embodied energy [5]. Due to the large amounts of energy inputs, this phase of the building life cycle may potentially cause the greatest environmental impacts. An understanding of the impacts associated with this phase is essential in the selection of suitable materials at the design stage in efforts to reduce the greenhouse gases associated with the building sector.

Within this context, timber is one of those materials which is considered low energy material. As a building material, timber requires significantly less production energy compared to other major building materials, such as concrete and steel [6]. Significant amounts of greenhouse gases are emitted due to the large amount of energy required for the manufacturing of cement and steel. Therefore, timber is considered a key component of more environmentally conscious buildings.

Mid-rise residential buildings are gaining popularity in urban areas around the world. The overall trend of mid-rise residential buildings is due to the rising population and rapid urbanization sustained by a widespread shift from low-rise buildings. Therefore, reducing the energy embodied in the materials of mid-rise residential buildings is becoming important [7]. Using timber as a construction material in these types of buildings may offer an opportunity to reduce embodied energy of materials. In addition to the environmental benefits, timber as a building construction material offers many advantages in terms of cost, ease of construction, time savings in construction time, and safety of the workforce during construction [8].

Fig. 1 Construction projection of mass timber buildings in the U.S. (Anderson et al. [6])



Until recently, timber has been used for low-rise buildings only, with concrete and steel frames the dominant types for medium-rise buildings worldwide [9]. Massive timber construction is an emerging technology, which offers the construction industry a viable alternative to steel and concrete [10]. The use of massive timber construction and cross-laminated timber has recently started to grow around the world, particularly in the developed world [11]. Many buildings have been constructed in Europe, America, Canada, and Australia. The use of massive timber construction is expected to grow significantly in the coming years and decades [6], as shown in Fig. 1.

Massive timber construction is a method that makes use of large solid timber sections and panels to replace concrete slabs and steel framing for walls and floors [10]. Cross-laminated timber is the main type of ‘massive timber construction’ which has become increasingly popular in the last decade. The use of massive timber for walls, floors, and roofs in the form of CLT in medium-rise buildings results in a considerably lower weight of the building as compared to concrete and steel. This means there may be huge cost savings associated with foundation systems [8]. Other cost advantages come principally from reduced build time with the lighter prefabricated material [6]. Compared to steel or concrete, massive timber is reasonably easy to work with on-site. Prefabricated sections arrive on a truck, are quickly craned into place, and simply joined together with a skeleton crew [11]. Improved safety during construction is also a significant advantage. The two key drivers behind the wide use of massive timber in Europe for more than a decade are undoubtedly its cost-effectiveness and sustainability.

This study takes the position that there is a need to better understand the energy associated with the construction materials and initial construction of buildings at the design stage. A better comprehension of embodied energy consumption can help professionals in the construction industry to make informed decisions leading to a reduction in energy associated with the initial construction of buildings [12]. Therefore, this study aimed to explore the potential initial embodied energy reduction benefits by comparing the initial embodied energy consumption of concrete floor systems and CLT floor systems for mid-rise residential buildings.

2 Research Method

A typical eight-story apartment building was created in Autodesk Revit. The model consists of a CLT floor (without floor finishes). Floors were supported by 135 mm thick CLT wall panels. Quantity of the CLT floor panels calculated by material takeoff in Revit. A hybrid analysis is considered the most appropriate method for the calculation of embodied energy [13]. The embodied energy of these CLT floor panels was calculated using the input–output-based hybrid analysis method. Embodied energy co-efficient for CLT was used from the EPIC database [14] and multiplied by the total quantity of CLT used in the apartment building, resulting in a process-based hybrid embodied energy figure. To complete the system boundary, the energy embodied in non-material inputs was calculated, referred to as the remainder of energy inputs, and added to the process-based hybrid embodied energy figure. More detail about using input output-based hybrid analysis method can be found in the previous publications by the author [15–17].

The same apartment building was then recreated in Revit with reinforced concrete floors and a concrete frame structure, with a slab thickness of 150 mm. The floor was supported by concrete columns. Quantities of the floor materials for this model were also extracted and embodied energy of the concrete floors was calculated as per the method described for CLT floors. Embodied energy results for both the CLT and concrete floor assembly were compared.

3 Results and Discussion

This section presents the embodied energy results of CLT floors and reinforced floor systems for the apartment building.

The embodied energy of CLT floors. The total volume for CLT for floor assembly with a panel thickness of 175 mm on a typical floor was 75.3 m^3 . Embodied energy associated with the initial construction of a typical floor with was found to be 162 GJ (0.321 GJ/m²). For the seven floors of the apartment building assumed to be built by CLT, embodied energy was 1134 GJ, as shown in Fig. 3.

The embodied energy of reinforced concrete floors. The total volume of concrete for floor assembly with a floor panel thickness of 200 mm on a typical floor was 100.7 m^3 . Embodied energy associated with the use of concrete for the initial construction of a typical floor with was found to be 388.6 GJ (0.77 GJ/m²). For the seven floors of the apartment building, embodied energy associated with concrete use was 2720.6 GJ, as shown in Fig. 2. The amount of steel used for reinforcement of the floor slab was calculated by using the thumb rule of 1% steel for the consumed volume of concrete. This amount resulted in 7905.6 kg of steel per floor. Embodied energy associated with this amount of steel was 298.5 GJ (0.59 GJ/m²). For the seven floors of the apartment building, embodied energy associated with the use of steel was found to be 2089.64 GJ. Combined embodied energy associated with the use of

concrete and steel for the reinforced concrete floor system was found to be 4810.3 GJ.

Embodied energy results for the floor assembly of both construction systems show that the reinforced concrete floor system is responsible for significantly higher embodied energy consumption as compared to the CLT floor system. The individual amount of embodied energy for Concrete (2720.6 GJ) and steel (2089.6 GJ) is more than double the amount for CLT (1134.1 GJ). The combined embodied energy of both materials in a reinforced concrete floor system (4810.3 GJ) is 4.24 times more than the embodied energy associated with the use of CLT. As embodied energy results in a significant amount of GHG emissions and related environmental impacts, the use of CLT in mid-rise buildings can help to significantly reduce the environmental impacts of buildings.

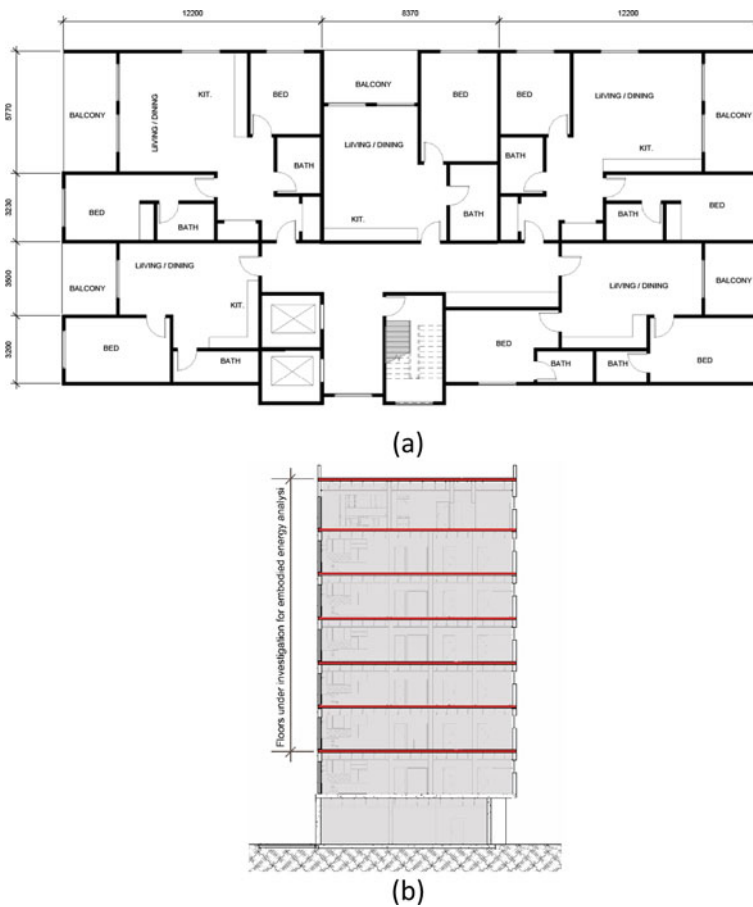


Fig. 2 a Floor plan of the apartment building b Cross section of the apartment building showing the floors (in red) under investigation for embodied energy analysis

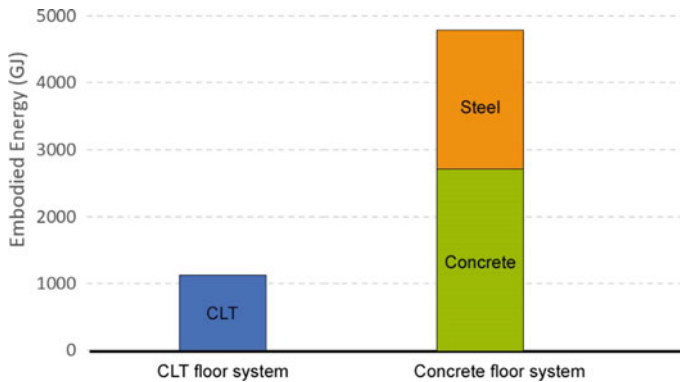


Fig. 3 Embodied energy of CLT and reinforced concrete floor systems for the apartment building

By replacing the reinforced concrete system for floor construction with a CLT floor system, this apartment building can reduce 3676.1 GJ of embodied energy. Using the Emission rate of 70 kg CO₂-e/GJ [12, 13], this reduction in embodied energy amounts to 52.52 t CO₂-e. This saving of greenhouse emissions is equal to the emissions by a bus passenger traveling 299,656 km, based on 159 g CO₂-e per passenger km in Melbourne [12, 18]. In addition to these benefits of using CLT as a construction material, its use in mid-rise buildings results in a reduction of building weight significantly. This may result in further embodied energy savings due to the reduced size of the foundation/footing system as a result of less building weight.

Keeping in mind the environmental impacts of embodied energy associated with the construction of buildings, and embodied energy reductions associated with the appropriate selection of materials and construction systems as shown by this study, all stakeholders in the building industry need to make efforts to reduce the embodied energy. Policymakers should encourage the use of low-embodied energy materials through incentives and embed embodied energy into building codes incrementally. Similarly, designers and developers should exploit any opportunity to reduce embodied energy including the careful selection and efficient use of materials.

4 Conclusion

This study compared the embodied energy associated with the CLT floor system and reinforced concrete floor system for an eight-story apartment building. Both floor systems were modeled in BIM and quantities were extracted. These quantities were used to calculate the embodied energy using input–output-based hybrid analysis. Results show that the CLT floor system consumed significantly less amount (4.24 times less) of embodied energy than the reinforced concrete system. This study also shows appropriate materials selection is important at the design stage to reduce the embodied energy consumption and related environmental impacts of the buildings.

References

1. NOAA (2023) Trends in atmospheric carbon dioxide. Retrieved Aug 15 2015, from <http://www.esrl.noaa.gov/gmd/ccgg/trends/>
2. Crawford RH, Bontinck P-A, Stephan A, Wiedmann T, Yu M (2018) Hybrid life cycle inventory methods—a review. *J Clean Prod* 172:1273–1288
3. Rauf A (2022) Reducing life cycle embodied energy of residential buildings: importance of building and material service life. *Buildings* 12(11):1821
4. IEA and UNEP (2018) 2018 Global status report—towards a zero-emission, efficient and resilient buildings and construction sector
5. Crawford R (2011) *Life cycle assessment in the built environment*. Routledge
6. Anderson R, Atkins D, Beck B, Dawson E, Gale C (2020) 2020 State of the industry—North American Mass timber. Forest Business Network, USA
7. Smyth M (2018) A study of the viability of cross laminated timber for residential construction. Master thesis Master thesis. KTH Royal Institute of Technology, Stockholm, Sweden
8. Wells M (2011) Tall timber buildings: Application of solid timber in Multistory buildings. *CTUBH* (1):24–27
9. FWPA (2012) Massive timber construction systems—cross-laminated timber (CLT). NSW, Australia, Forest and Wood Products Australia Limited
10. Harte AM (2017) Mass timber—the emergence of a modern construction material. *J Struct Integrity Maintenance* 2:121–132
11. Ahmed S, Arocho I (2020) Mass timber building material in the U.S. construction industry: determining the existing awareness level, construction-related challenges, and recommendations to increase its current acceptance level. *Cleaner Eng Technol* 1:100007
12. Rauf A (2016) The effect of building and material service life on building life cycle embodied energy. PhD, University of Melbourne
13. Crawford RH (2008) Validation of a hybrid life-cycle inventory analysis method. *J Environ Manage* 88(3):496–506
14. Crawford RH, Stephan A, Prideaux F (2019) Environmental performance in construction (EPiC) database
15. Rauf A, Crawford RH (2015) Building service life and its effect on the life cycle embodied energy of buildings. *Energy* 79:140–148
16. Rauf A (2021) Role of building and material service life in life cycle embodied energy demand of buildings. In: 8th zero energy mass custom home (ZEMCH) 2021 international conference. United Arab Emirates University, UAE
17. Rauf A, Attoye D, Crawford R (2022) Embodied and operational energy of a case study villa in UAE with sensitivity analysis. *Buildings* 12. <https://doi.org/10.3390/buildings12091469>
18. Glover L (2009) Carbon emissions trading and Australia’s urban transport. Australasian Centre for the Governance and Management of Urban Transport

The Relationship Between the Surface Characteristics and Corrosion Properties of Carbon Steel Affected by Abrasive Water-Jet Treatment



S. Park, S. Kainuma, T. Ikeda, Y. Toyota, and T. Arakawa

Abstract Abrasive water-jet treatment (AWT) is applied in this study as a promising surface cleaning method for steel structures. This study aimed to evaluate the effect of changes in the surface properties of steel on the corrosion characteristics of the base steel plate by AWT. The changes in the surface configuration and microstructure of the steel plate obtained at different standoff distances from AWT were compared to those of abrasive blasting. The surface characteristics of the specimens were evaluated for their roughness and micro-structural features. The test results showed that the smaller the standoff distance, the changes in microstructures generated from the increased plastic deformation layers during the AWT became distinct. As the energy reaching the substance during the AWT increased, found the increased surface hardening and the reduced grain size on the plastic deformation sections, which resulted in enhanced corrosion resistance. Hence, it was verified that AWT has a positive effect on the corrosion properties of the base metal as a surface cleaning technic for steel structures.

Keywords Abrasive water-jet treatment · Blast treatment · Surface roughness · Microstructure · Corrosion resistance

S. Park (✉) · S. Kainuma
Department of Civil Engineering, Kyushu University, 744 Motooka, Nishi-Ku,
Fukuoka 819-0395, Japan
e-mail: qkrpsh1@gmail.com

T. Ikeda
Ikeda Kogyo Co., Ltd., 218-3 Nakano-Dori, Hokuto 049-0156, Hokkaido, Japan

Y. Toyota
Technical Development Bureau, West Nippon Expressway Co., Ltd., 1-6-20 Dojima, Kita-Ku,
Osaka 530-0003, Japan

T. Arakawa
Production Management Department, Sugino Machine Ltd., 2880 Kuriyama, Surikawa,
Toyama 936-8577, Japan

1 Introduction

Surface cleaning is a significant procedure to maintain the quality of steel structures and their lifespan. The durability of painting and under coating corrosion mainly depends on steel surface conditions after treatment. In current, abrasive blasting is one of the most widely used methods for steel surface preparation. However, it still has poor cleaning efficiency in the bottom of the corrosion pit of severely corroded steel members. The initial corrosion under the painting and film occurred due to chloride or corrosion products that have not been removed is another disadvantage of blast treatment. On the other hand, abrasive water-jet developed originally as a new type of special steel cutting technology is a potential surface cleaning method to break through such problems. A recent study showed that abrasive water-jet was used for polishing steel surfaces by adjusting the various operating parameters [1]. The abrasive water-jet which provided the Mach 2 level of ultra-high pressure water to abrasive materials allowed to make large energy penetrate to the compact rust layer. During the high-pressure process of abrasive water-jet, the water temperature raised to more than 60 °C washed away the residue on the surface without the risk of fire and dust generation. Due to these benefits, the abrasive water-jet was more excellent than typical surface treatment methods in relation to the removal of thick rust as well as the cleaning of surface residues in narrow areas such as crevices between structures. Furthermore, the abrasive water-jet was shown to modify the surface characteristics of the substance because the huge energy from the abrasive water-jet produces alterations in surface hardening and microstructure [2]. Changes in surface properties were generally due to plastic deformation layers that have a positive effect on corrosion resistance [3]. This study aimed to investigate the changes in steel surface properties and their effects on corrosion properties according to standoff distances during abrasive water-jet treatment (AWT) with the convergent nozzle. The surface roughness and microstructures after AWT were evaluated and compared with the electrochemical test results to establish the effects of AWT on the corrosion properties of carbon steel plates. To assess treatment efficiency, results were compared to blast treatment.

2 Experimental

2.1 Specimens

The material used for AWT and blast treatment was JIS G 3106 SM490A steel (carbon steel) specified by Japanese Industrial Standard, and the dimensions of the test samples were 70 × 70 × 6 mm. AWT and blast treatment were conducted with Australian garnet of which mesh size is #30–60. AWT and blast treatment conditions are listed in Tables 1 and 2, respectively. The nozzle used in the AWT was set in one direction at a speed of 1 m/min by selecting a water-jet conversion nozzle used for

Table 1 AWT processing parameters

Specimen	Standoff distance (mm)	Abrasive supply (g/min)	Pressure (MPa)	Garnet mesh size (#)	Traverse speed AWT machining (m/min)	Nozzle diameter (mm)	Water flow (L/min)
AWT100	100	600	230	30–60	1	2	11.9
AWT200	200						
AWT300	300						

Table 2 Blast treatment parameters

Specimen	Standoff distance (mm)	Abrasive supply (g/min)	Pressure (MPa)	Garnet mesh size (#)	Blasting time (s)	Nozzle diameter (mm)	Blasting angle (°)
Blast200	200	1,740	0.7	30–60	5	8	90

metal cutting, and in the case of blasting, it was projected for 5 s at a 90° angle. AWT specimens according to standoff distances 100, 200, and 300 mm are nominated as AWT100, AWT200, and AWT300. A blasted specimen corresponding to a standoff distance of 200 mm is labeled as Blast200. Prior to the surface treatment, all surfaces of the samples were polished to remove the mill scale on the surface and provide cleaned surface conditions.

2.2 Surface Profile and Roughness

The surface morphology after both types of treatments was measured by microscope. Those properties are described by surface profiles. The surface profile is referred to as the treatment range and maximum erosion depth after surface treatment. Hereby, the treatment range illustrates the affected area and eroded area. The affected area has a surface condition analogous to the blasted surface. The eroded area is a fully treated area, placed on the track of AWT or blasting. The maximum erosion depth is the depth from the eroded area. Figure 1a shows a detailed overview of the AWT process applied to steel plate. Figure 1b exhibits the surface profile of the surface after blast treatment and AWT as a 3D image. Figure 2 presents the morphology of the treatment range as an actual processed photo and a 2D image.

After AWT and blast treatment, the cross-sectional profile and roughness of the test samples were performed by laser scanning microscope and the calculation of the affected area and eroded area can be determined using the inflection point of the mapping graph, which is the maximum curvature [4]. Surface roughness was assessed for the arithmetic mean roughness (Ra) and the mean width of the roughness (RSm) calculated based on an average of 11 lines with a base length of 10 mm. the Ra is the most commonly used parameter for general engineering purposes [5].

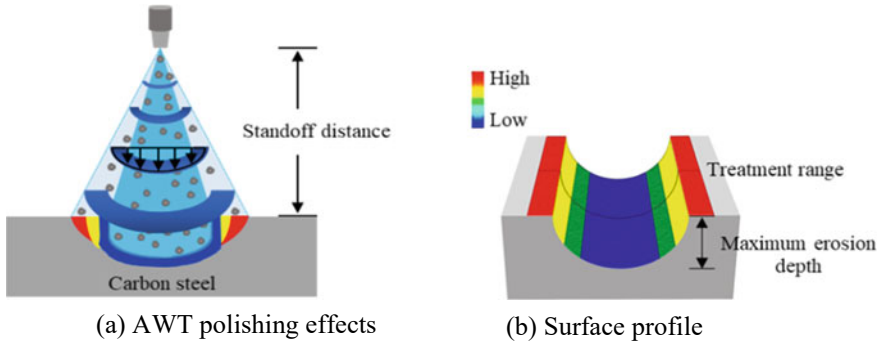


Fig. 1 Schematic diagram of AWT polishing effects

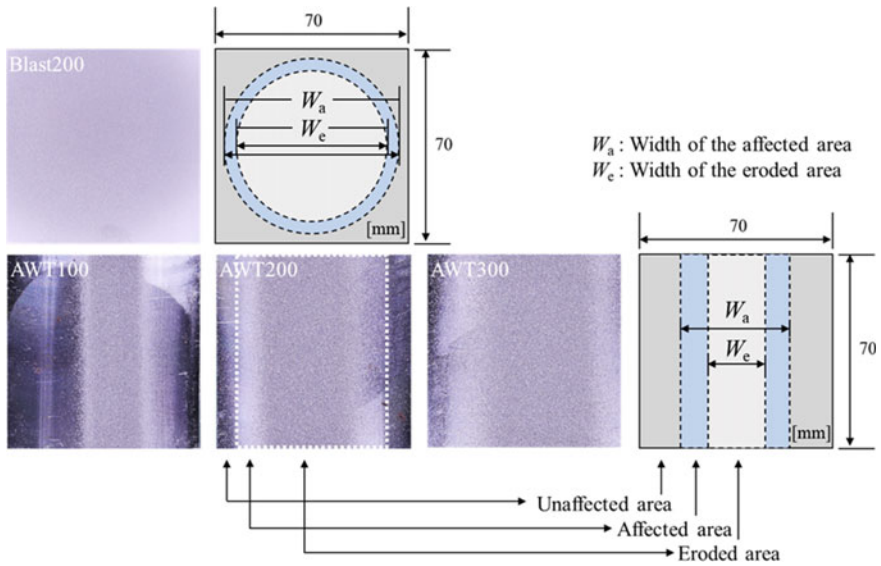


Fig. 2 Surface conditions of carbon steel plate by blast treatment and AWT

2.3 Hardness and Microstructure

The microhardness values of the treated steel specimens were measured using a Vickers hardness test. In order to analyze changes in the microstructure, the cross-section of the treated sample was investigated with a microscopic photograph. The cross-section of the samples was prepared, etched with 2% nital, and the microstructure of the samples was examined under a microscope.

2.4 Electrochemical Test

Electrochemical tests were measured using a potentiostat. All electrochemical tests were conducted on the reference electrode (Ag/AgCl) and counter electrode (platinum foil) with a measurement area of 100 mm². Open circuit potential (OCP), polarization curve (PC), and electrochemical impedance spectroscopy (EIS) measurements were tested in a 3.5 wt% NaCl aq for all treated samples. The OCP of the test sample was measured with an AC amplitude of 10 mV for 24 h, and the PC was tested in the range of ± 250 mV at a scanning speed of 10 mV/min. Corrosion current (i_{corr}) and corrosion potential (E_{corr}) were measured using Tafel extrapolation. EIS was performed in the range of 10 MHz to 100 kHz with respect to OCP.

3 Test Result

3.1 Surface Profile in the Treated Surface

Figure 3 shows the quantitative values of the surface profile after blast treatment and AWT. In Fig. 3a, for the treatment range, the blasted specimen was larger than the AWT specimens, whereas, in Fig. 3b, the maximum erosion depth tended to be larger in AWT specimens. In particular, under the same standoff distance of 200 mm condition, the Blast200 specimen was 1.5 times larger than the AWT200 specimen for the treatment range, while the maximum erosion depth was 2 times smaller. This means that although the entirely treated for blast treatment had a larger treated area than the AWT due to the influence of the divergent nozzle, the maximum erosion depth during AWT was greater because the energy that touches the substrate was significantly larger than the blast treatment. Hence, the larger erosion depth of AWT could be ideal for the removal of the thick rust and inside chlorides than blasting. During AWT, as standoff distance increased, the treatment range tended to increase, while the maximum erosion depth decreased. This is because the larger the standoff distance during AWT, the wider the injection angle due to the divergent of the jet, and the kinetic energy of the particle is gradually lost when the abrasive materials particles collide with the jet entry and move toward the jet exit [6].

Figure 4 exhibits microphotographs of the surface morphologies of the specimens after blasting and AWT. The AWT specimens had a surface peak to the valley two to three times higher than the blasted specimen. In particular, the AWT100 specimen had the largest peak value of 300 μm , and the peak tended to increase as the standoff distance decreased during AWT. As the standoff distance decreases, the kinetic energy transmitted to the target substance increases, leading to increase the density of energy, amplifying the force for erosion. Consequently, as the standoff distance decreases, the impact force on the target substrate increases, the existing peak is destroyed on the surface particle impact and the groove deepens because of creating a new groove [7]. Figure 5 presents the actual roughness values in the

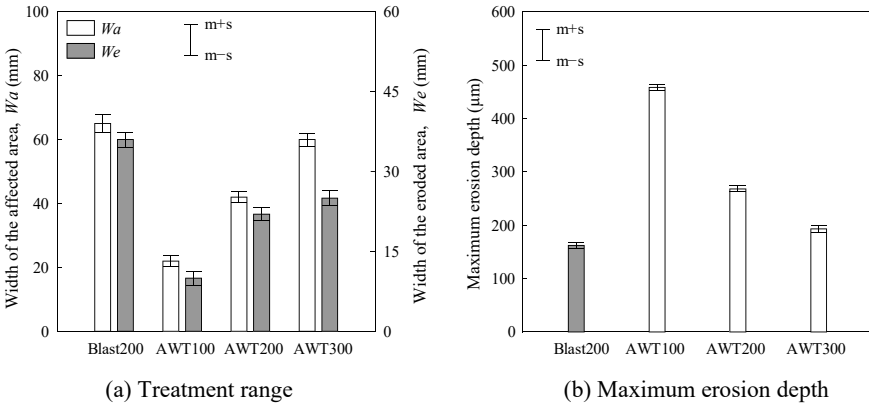


Fig. 3 Surface profile of Blasted and AWT specimens

corresponding treated specimens. It was exhibited that all AWT specimens had 1.5–2 times greater roughness (R_a , R_{Sm}) than the blasted specimen. In addition, for the AWT specimens, the roughness decreased as the standoff distance increased. Distinctly, the greater the energy reaching the substrate allowed for the increase of the roughness.

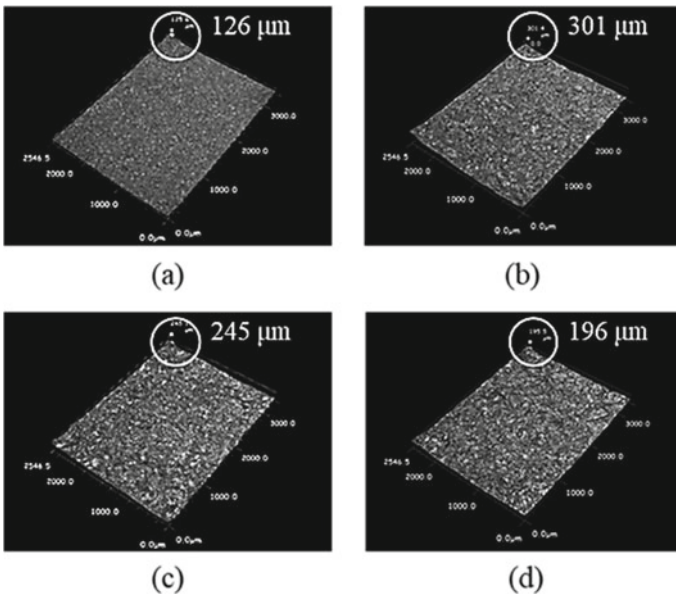
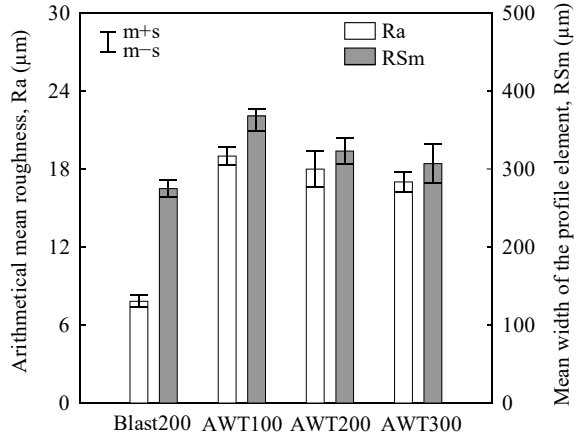


Fig. 4 Surface morphologies of **a** Blast200 specimen, **b** AWT100 specimen, **c** AWT200 specimen, and **d** AWT300 specimen

Fig. 5 Surface roughness of blasted specimen and AWT specimens



3.2 Changes in Hardness and Microstructure of AWT Specimens According to Standoff Distance

Figure 6 shows the microhardness value graph of the specimens. It can be seen in this graph that the untreated specimen (base material) had an average hardness value of 150–200 HV. All specimens after both types of treatment had increased hardness and observed the maximum value on the treated surface. Especially, the AWT100 specimen which is the smallest standoff distance obtained the largest value of 268 HV. AWT200, AWT300, and Blast200 obtained 253, 242, and 224 HV, respectively. The improvement in microhardness values can be attributed to the hardening of the surface of steel plates.

The change in surface deformation after treatment is shown in Fig. 7. After both types of treatment, a plastically deformed surface layer was formed in each specimen, and the depth of the modified layer was 90 µm, 40 µm, 25 µm, and 10 µm for AWT100, AWT200, AWT300, and Blast200 specimens, respectively. Especially, the plastically deformed layer was the densest in the AWT100 specimen, followed by the AWT200 specimen, and less dense in the case of the AWT300 specimen and the Blast200 specimen. For the blast treatment, the plastic deformation layer was the smallest. In addition, it was shown that the plastic deformation layer and the surface hardness increase section were almost the same. As a result, it was indicated that the energy strength of AWT reaching the surface is higher than that of the blast treatment, and as the standoff distance is decreased during the AWT, the energy strength of the surface is increased to form the maximum depth and section of the plastic deformation layer. It was also deduced that maximum compressive residual stress is generated in the maximum plastic deformation part [8]. Therefore, it was inferred that the energy absorbed in the steel plate during AWT influenced the increase in microhardness below the sample surface and the change in microstructure.

Fig. 6 Microhardness values of the treated specimens

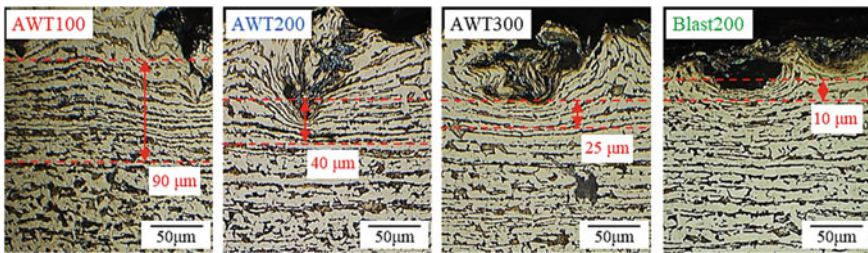
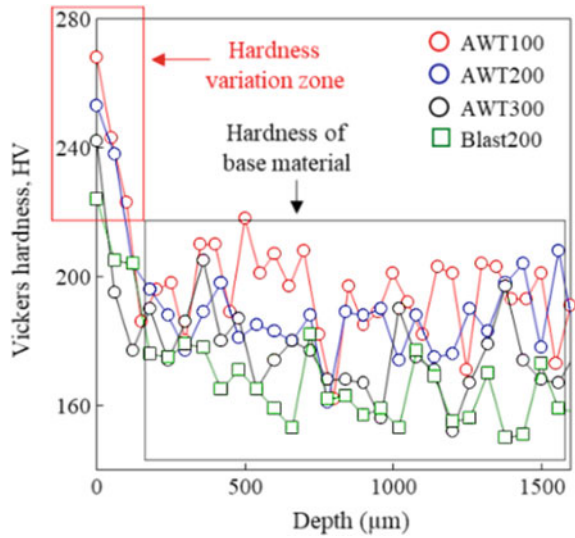


Fig. 7 Microscopic images of microstructure on the cross-section of the treated specimens

3.3 Difference in Corrosion Properties

The OCP values for all specimens are shown in Fig. 8a. AWT100 specimen possessed the highest OCP value, thus it was obvious that this specimen was the noblest potential value. The blasted specimen exhibited the most cathodic potential value. Figure 8b presents the PC values obtained using the Tafel extrapolation method of all specimens. E_{corr} values of the AWT100 specimen reached the highest stable value of $-707 \text{ mV}_{\text{Ag}/\text{AgCl}}$, followed by the AWT200 of $-736 \text{ mV}_{\text{Ag}/\text{AgCl}}$, AWT300 of $-748 \text{ mV}_{\text{Ag}/\text{AgCl}}$, and Blast200 of $-814 \text{ mV}_{\text{Ag}/\text{AgCl}}$. When the i_{corr} values were investigated, the blasted specimen had the highest i_{corr} ($1.56 \mu\text{A}/\text{cm}^2$) than those of AWT ($0.3\text{--}1 \mu\text{A}/\text{cm}^2$). In addition, in the case of AWT specimens, those of AWT specimens had tend to decrease slightly as the standoff distance decreased. Particularly, the AWT100 specimen was the lowest at $0.37 \mu\text{A}/\text{cm}^2$. Generally, i_{corr} is one of the

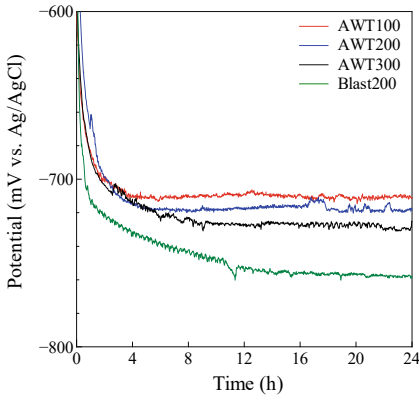
most important parameters for evaluating corrosion performance. A lower i_{corr} indicates better corrosion resistance. Therefore, the AWT specimens had better corrosion resistance than that of the blasted specimen, and the smaller the standoff distance during AWT, the higher the corrosion resistance of the treated specimen. The EIS results of all specimens are shown in Fig. 8c. The diameter of the Nyquist loop in the AWT specimens was larger than that of the blasted specimens, indicating that AWT had positive effects on corrosion resistance rather than blast treatment. Notably, the AWT100 specimen possessed the largest semicircle, followed by the AWT200 specimen, AWT300 specimen, and Blast200 specimen. Thus, the AWT100 specimen had the largest capacitive loop diameter which manifests the highest corrosion resistance. EIS data were fitted by adopting an electrical equivalent circuit as shown in Fig. 8d. Randles circuit is adequate for representing the situation of the steel surface without the film [9]. The equivalent circuits were composed of solution resistance (R_s), the constant phase element of the double electrical layer (CPE_{dl}), and the charge transfer resistance (R_{ct}). Table 3 lists the results of R_{ct} values of the AWT specimens and the blasted specimen. The AWT specimens had larger R_{ct} values than those of the blasted specimen and for AWT, the R_{ct} value reduced as the standoff distance increased at AWT100, AWT200, and AWT300 specimens, respectively. It can be said that the larger the R_{ct} value, the greater the corrosion resistance value.

Generally, as the roughness of the steel surface increases, the corrosion rate increases [10]. However, in Fig. 5 the roughness of the AWT-treated specimens was more than three times that of the blasted specimen, but as illustrated in Fig. 8, the corrosion resistance of the AWT specimens was higher than that of the blasted specimen. In terms of AWT, roughness and corrosion resistance also increased as standoff distance decreased. The result was contrary to conventional literature and indicated that factors other than roughness among surface properties have a greater influence on the corrosion resistance of specimens treated in this study. Changing corrosion resistance could be ascribed to the plastic deformation layer of the surface after the treatment. Namely, it can be seen that corrosion resistance improved after AWT, due to as the section of the plastic deformation layer increases, the compressive residual stress increases. The result was coherent with studies by Wang et al. [3]. Therefore, it can be indicated that the formation of a deformed surface layer and hardening in the AWT has a desirable influence on corrosion resistance.

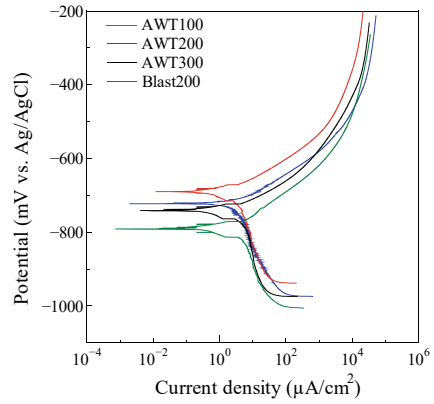
4 Conclusion

To identify the effect of AWT on the corrosion characteristics of carbon steel plates, the surface roughness, hardness, microstructure, and electrochemical properties were investigated. The main conclusions obtained from this study are as follows.

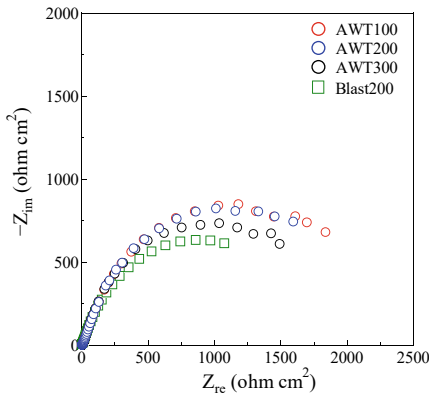
- (1) AWT-treated steel plate exhibited a lower treatment range, and larger maximum erosion depth under the same standoff distance in comparison to blasted steel plate.



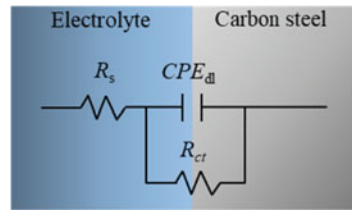
(a) Open circuit potential



(b) Potentiodynamic polarization curves



(c) EIS test by Nyquist plots



(d) Randle circuit

Fig. 8 Electrochemical test results

Table 3 Fitted impedance parameters from EIS of the treated specimens

Specimen	R_s ($\Omega \text{ cm}^2$)	CPE_{dl} ($\Omega^{-1} \text{ s}^n \text{ cm}^{-2}$) $\times 10^{-3}$	R_{ct} ($\Omega \text{ cm}^2$)	Chi-squared χ^2 ($\times 10^{-3}$)
AWT100	8.05	1.62	2640	4.31
AWT200	10.0	1.58	2600	5.52
AWT300	7.16	1.40	2090	6.38
Blast200	8.19	3.72	1650	2.58

- (2) Surface roughness of AWT-treated steel plates was larger than that of the blast treatment. The roughness of the treated surface with respect to AWT processing is reduced as increasing standoff distance.
- (3) AWT-treated steel plates had larger hardness and plastic deformation in comparison with blasted steel plate. Those properties in relation to AWT processing increased as the standoff distance decreased.
- (4) Electrochemical test results indicated that AWT improved the corrosion properties more than those of the blast treatment. The improvement in corrosion resistance is due to the modified microstructure by increasing surface hardness and plastic deformation according to an increase in energy received from the surface of the specimen.

Future studies should investigate a surface physics analysis to assess the quantitative values of changes in microstructure under the surface of the steel plate during AWT. Additionally, the assessment of coating qualities for AWT-treated steel plates is also essential for actual structure application.

References

1. Natarajan Y, Murugesan PK, Mohan M, Liyakath Ali Khan SA (2020) Abrasive water jet machining process: a state of art of review. *J Manuf Processes* 49:271–322
2. Mieszala M, Torrubia PL, Axinte DA, Schwiedrzik JJ, Guo Y, Mischler S, ..., Philippe L (2017) Erosion mechanisms during abrasive waterjet machining: model microstructures and single particle experiments. *J Mater Process Technol* 247:92–102
3. Wang T, Yu J, Dong B (2006) Surface nanocrystallization induced by shot peening and its effect on corrosion resistance of 1Cr18Ni9Ti stainless steel. *Surf Coat Technol* 200:4777–4781
4. Goldman R (2005) Curvature formulas for implicit curves and surfaces. *Comput Aided Geom Des* 22(7):632–658
5. Jamil M, He N, Huang X, Zhao W, Gupta MK, Khan AM (2022) Measurement of machining characteristics in novel dry ice blasting cooling assisted milling of AISI 52100 tool steel. *Measurement* 191(1):10821
6. Mohamad WNF, Kasim MS, Norazlina MY, Hafiz MSA, Izamshah R, Mohamed SB (2020) Effect of standoff distance on the kerf characteristic during abrasive water jet machining. *Results Eng* 6:100101
7. Li F (2007) Experimental and numerical investigation of abrasive waterjet polishing technology. *Public Health* 125
8. Kovacı H, Bozkurt YB, Yetim AF, Aslan M, Çelik A (2019) The effect of surface plastic deformation produced by shot peening on corrosion behavior of a low-alloy steel. *Surf Coat Technol* 360:78–86
9. He S, Wang Z, Hu J, Zhu J, Wei L, Chen Z (2018) Formation of superhydrophobic nanostructured iron oxide for corrosion protection of N80 steel. *Mater Des* 160:84–94
10. Toloei A, Stoilov V, Northwood D (2013) The relationship between surface roughness and corrosion. *ASME Int Mech Eng Congr Exposition* 2B(11)

Study of Mechanical Properties of Solvent Cement Connection for PVC Pipes



Tao Wang and Shaowei Hu

Abstract For the mechanical properties of pipe joints, existing studies have mainly focused on flexible joints of ductile iron pipes and concrete pipes, and there is a lack of research on the mechanical properties of adhesive bonded joint of PVC pipes. By combining axial pullout prototype tests and numerical simulations using ABAQUS, this study investigated the effects of pipe diameter, socket gap, and loading rate on the axial mechanical properties of PVC pipe adhesive joints. Moreover, by building a buried PVC pipeline with 4 pipe sections, this study investigated the dynamic response of the adhesive bonded joint under different load amplitudes and different travel directions. The results showed that the seismic performance of the adhesive bonded joint is weak, and its axial pullout force is inversely proportional to the socket gap and proportional to the pipe diameter, while the loading rate has limited effect on it; under buried conditions, the longitudinal stress distribution at the top of the pipe is highly discontinuous, and the maximum stress in the socket is proportional to the traffic load amplitude, and the longitudinal travel direction is more likely to cause the failure damage of the buried PVC pipeline with adhesive bonded joint.

Keywords PVC pipes · Solvent cement connection · Parametric analysis · Numerical simulation · Adhesive bonded joint · Experiments

1 Introduction

Underground pipeline system is the infrastructure for transporting water in cities, and is the underground lifeline to ensure residents' life and production [1]. Polyvinyl chloride (PVC) pipes, as a national effort to promote the development of eco-friendly

T. Wang (✉)

Department School of Civil Engineering, Chongqing University, Chongqing 400045, China
e-mail: wangtaobenny@163.co

S. Hu

Yellow River Laboratory, Zhengzhou University, Zhengzhou 450001, China
e-mail: hushao-wei@zzu.edu.cn

pipes, have the advantages of flexibility, low flow resistance, reliable sealing, and corrosion resistance [2]. Many studies have pointed out [1, 3–5] that the interface area of pipes is the weak part in the mechanical properties of buried pipelines and is more prone to damage during earthquakes, so it is crucial to effectively improve the mechanical properties of water pipeline interfaces.

Currently in the Chinese standard regarding PVC pipes [6, 7], the interface connections of PVC pipelines are mainly divided into two types of flexible connections and rigid connections. And rigid connection mainly includes solvent cement connection, flange connection and other connection methods, of which the most applied is the solvent cement connection (adhesive bonded joint, or adhesive interface), whose applicable range is less than 225 mm nominal diameter.

A major evaluation indicator for buried pipelines is seismic capacity, Chen et al. [8] concluded that the flexible interface has good seismic energy dissipation capability by conducting axial pull-out test on foot-rule cast iron pipeline; Han et al. [3] proposed the axial stiffness equation of socketed flexible interface by conducting axial pull-out test on ductile iron pipeline; Ren et al. [4] studied the damage form of flexible interface of ductile iron pipeline under eccentric stretching; Li et al. [9] obtained the hysteresis curves of flexible interfaces of ductile iron pipes under reciprocal loading and found that the magnitude of seismic capacity was positively correlated with the size of pipe diameter through tests; Zhong et al. [5] studied the bending performance of the flexible interface of ductile iron pipeline; Duan [10] studied the seismic performance of the socket interface of cast iron pipeline by bending test; Wang et al. [11, 12] investigated the mechanical response of flexible interfaces of buried concrete pipes under coupled traffic and operational loads through three-dimensional numerical simulations; Zhai et al. [13] studied the failure mode of the socket of PCCP pipes and found that the increase of joint gap is not conducive to socket joint protection; Chen et al. [14] compared the seepage resistance of flexible and rigid interfaces through the leakage test of concrete drainage pipes and found that flexible interfaces such as rubber rings have better impermeability; Zhang et al. [15] obtained the analysable solution of internal force and displacement of arbitrary cross-section of gas transmission pipeline under rainfall conditions; Wu et al. [16] established the calculation model and calculation method of vertical displacement of flexible interface pipeline under vertical load.

The above-mentioned studies in the field of buried pipes are more on the mechanical response of the interfaces of cast iron and concrete pipes, but rarely on the interfaces of PVC pipes, and mostly focus on the flexible interface as the connection form, lacking studies on the adhesive connection form.

In this study, based on the previous studies, the axial mechanical properties of PVC pipes with adhesive bonded joints under different pipe diameters, loading rates, and socket gaps by means of a three-dimensional solid numerical model established by ABAQUS software were investigated. Further, the three-dimensional solid model of the interaction between the road structure and the buried PVC pipeline with adhesive bonded joint of multiple pipe joints is established, and the mechanical response of the buried PVC pipeline with adhesive interface is studied by applying different traffic

load amplitudes and different travel directions. The results of this study will provide guidance for practical engineering.

2 Axial Mechanical Properties

The seismic data over the years show that the bending deformation of buried pipes caused by seismic wave propagation can be almost negligible compared to the axial deformation [3], so it is necessary to study the axial mechanical response of PVC pipes with adhesive bonded joints.

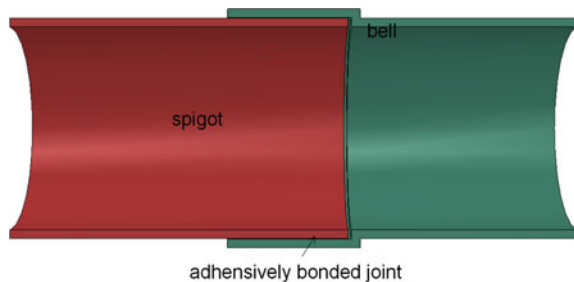
2.1 Finite Element Model

To investigate the mechanical response of the adhesive interface under different loading regimes, the 3D solid model of the adhesive bonded joint is established in ABAQUS as Fig. 1, which consists of three components: bell, spigot and adhesive layer [17, 18]. In this simulation, the end of the bell is fixed while the end of the spigot is loaded according to the displacement to simulate the pulling process of the adhesive interface.

The material of the PVC pipe composed of bell and spigot was set as an elastoplastic material, and the elastic modulus and Poisson's ratio were respectively set to 0.3 GPa and 0.35 [3], with C3D8R cell type and hourglass control.

The finite element model approach for the adhesive interface is mainly surface-based cohesive and using solid cells, among which the simulation results obtained by using the solid cell approach are more realistic and accurate compared to the former [19, 20]. For the above reasons, this study adopted the method of establishing solid cells for finite element simulation of PVC adhesive interfaces, and its intrinsic model is the BK composite mode under energy-based damage evolution [21–23]. The adhesive layer was processed using the COH3D8 cell type as shown in Fig. 2 in ABAQUS software, where the upper surface of the adhesive layer was designated as the top surface. Connect the outer wall of the spigot to the inner wall of the adhesive

Fig. 1 Structure of solvent cement connection



layer and the inner wall of the bell to the outer wall of the adhesive layer using a Tie connection in ABAQUS.

At present, research on the performance of adhesive interface materials is mainly focused on the aerospace and chemical industry, and less research has been conducted on the adhesive layer used for PVC adhesive interfaces. The bonding properties of different base materials and adhesives are not consistent, to obtain the material parameters for characterizing the adhesive layer, the material property tests were carried out according to the standards [24–26], and the normal tensile test and shear test were performed as shown in Fig. 3. According to the stress–strain curve obtained from the test results, the values of the material parameters used in this paper are shown in Table 1.

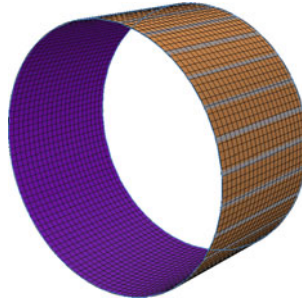
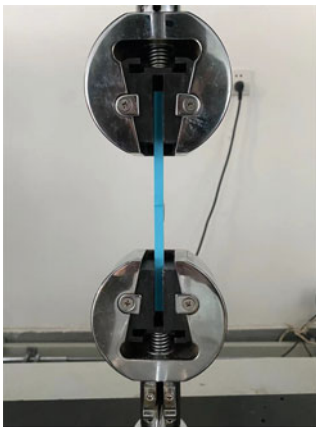
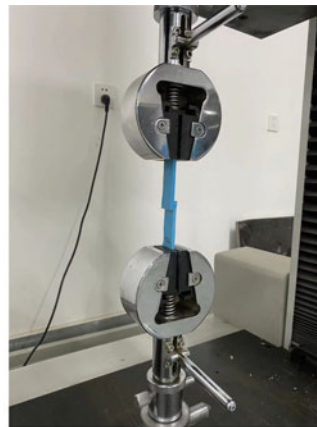


Fig. 2 Orientation of the adhesive layer mesh



(a) normal tensile test



(b) shear test

Fig. 3 Adhesive mechanical properties materiality test

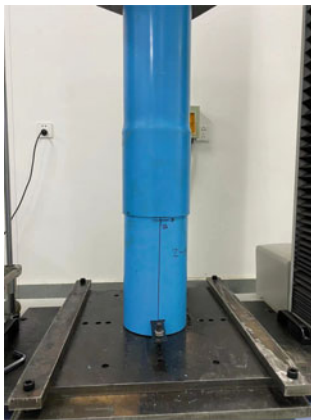
Table 1 Parameters for characterizing adhesive materials in ABAQUS

E_{nn}	E_{ss}	E_{tt}	σ_{nn}	σ_{ss}	σ_{tt}	G_{IC}	C_{IIC}	G_{IIIc}
0.671	2.143	2.143	0.612	5.892	5.892	1.365	10.178	10.178

2.2 Results and Discussion

The response of the axial mechanics of the PVC pipe line was accessed by simulating the pulling process of adhesive bonded joint. To verify the accuracy of the numerical simulation and ensure the validity of the subsequent results, a proposed static test of the axial pullout of the adhesive interface is designed in this paper, and the test setup and procedure of this test are shown in Fig. 4 where bell and spigot of the pipeline were fixed at the two ends of the loading device respectively. A universal testing machine was used for displacement loading, and the axial pulling force and displacement of the specimen during the press-pulling process were collected by force and displacement sensors. The experimental results are compared with the results of the numerical simulation in Fig. 5, from which it can be seen that the results of the simulation are quite consistent with the experimental ones, which ensures that the finite element model used in this simulation is valid.

Loading Rate. The relationship between the measured axial pullout force and socket displacement (F-D curves) is shown in Fig. 6 when different loading rates (10 mm/s, 20 mm/s, 50 mm/s) were applied to a socket with DN200 and a socket gap of 1 mm. In Fig. 6, for PVC pipelines with adhesive bonded joints, increasing the pullout rate does not change the nominal stiffness of the interface to resist pullout, but can increase the maximum failure load to some extent, although the change was relatively small and its effect can be ignored in practical engineering applications. In the early pulling



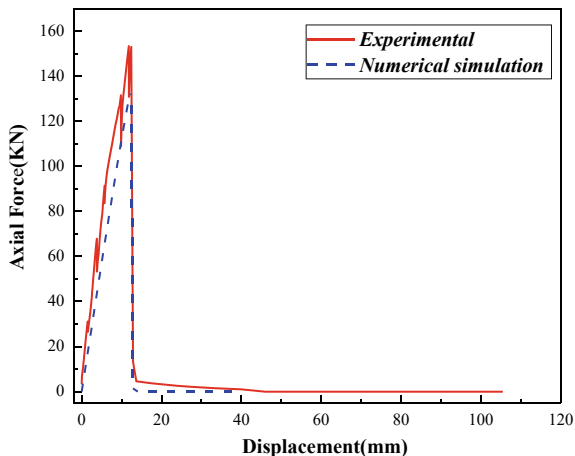
(a) Prototype test site



(b) The pipeline prepared for the test

Fig. 4 Prototype test of PVC pipeline with solvent cement connection

Fig. 5 Comparison of prototype test results and numerical simulation results for PVC pipelines with solvent cement connection



period, the adhesive interface in the axial pulling force basically maintained linear elasticity, when the ultimate load was reached, rapid tearing damage occurred and the interface collapsed. This explained that the change in velocity of seismic waves in earthquake was less influential in producing damage to the adhesive interface. Nevertheless, the PVC pipe with adhesive interface of DN200 failed by pull-out damage after 12 mm of socket displacement, which indicated that the resistance of interface to seismic damage is very weak and much lower than that of flexible interface. But compared to the flexible joint, DN200, socket gap of 1 mm adhesive bonded joint limited pullout force of about 250 KN, while the same specifications of the flexible joint limit pullout force were often only about 600 N, which makes the adhesive bonded joint has a much higher than the flexible interface stopping ability. Therefore, for the buried PVC pipeline with adhesive interface, it is not necessary to set up sup-port piers along the laying direction, which will greatly save the project cost in the short and medium distance water transmission project with small diameter requirements.

Pipe Diameter. To study the effect of pipe diameter size on the mechanical properties of the interface, three nominal diameters of PVC pipes, DN200, DN160 and DN110, were taken for simulation in ABAQUS, and the obtained F-D curves are shown in Fig. 7.

From Fig. 7, for PVC pipelines with adhesive bonded joints, not only the maximum pullout force would increase significantly with the increase of pipe diameter, but also the nominal stiffness of the interface to resist pullout could be increased. Further, the maximum pullout force does not simply increase linearly with the increase in pipe diameter. The maximum pullout load per week increased with the increase of pipe diameter, which indicated that the increase of pipe diameter changes the mechanical mechanism of the adhesive interface. Since the bonding force of the adhesive interface comes from the cohesive force of the adhesive and the bonding force between the adhesive and the pipe wall, the increase of the pipe diameter did

Fig. 6 Relationship between tensile force and interface displacement of PVC pipe socket with DN200 adhesive interfaces at different loading rates

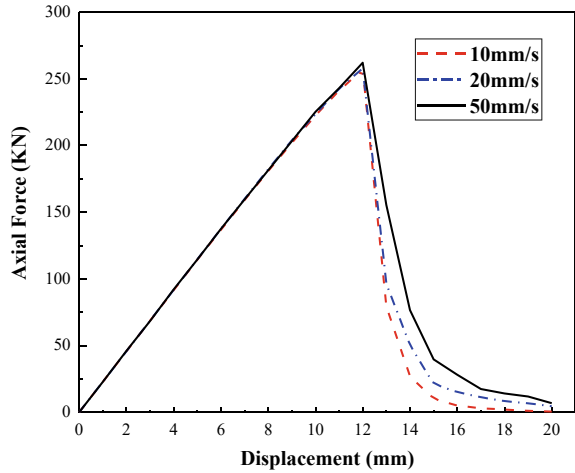
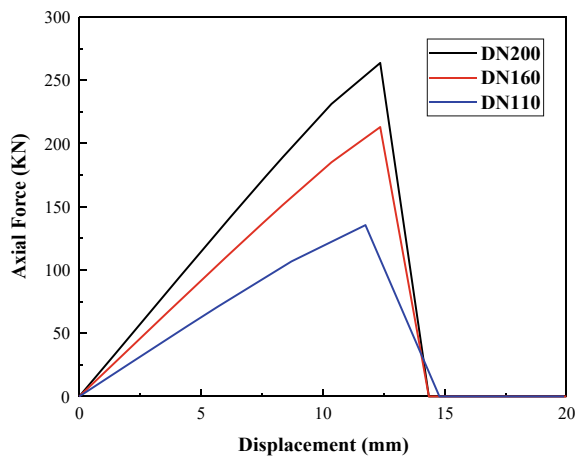


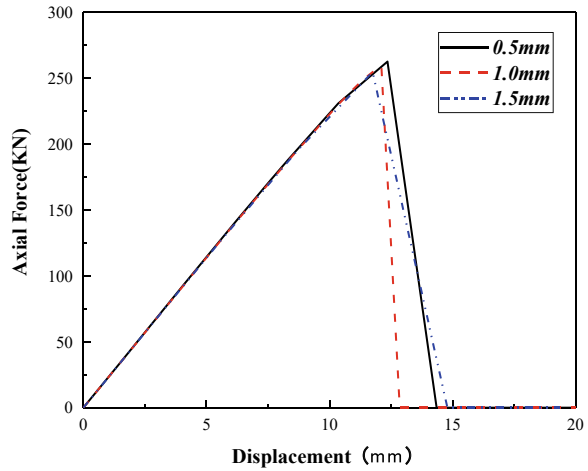
Fig. 7 Relationship between pull-out force and interface displacement of PVC pipe socket for adhesive interfaces at different pipe diameters



not change the cohesive force of the adhesive, which indicated that the increase of the pipe diameter will increase the bonding force between the adhesive and the pipe wall and there was a size effect.

Socket Gap. In the assembly process, the socket gap of the adhesive interface will affect the bonding ability between the adhesive and the bonding interface, so the size of the socket gap is an important factor affecting the mechanical properties of joint. To investigate the effect of different gap sizes on the axial pullout force of the adhesive interface, different assembly gaps were set as variables in this section, and the F-D curve about axial mechanical response of the adhesive interface is shown in Fig. 8. As it can be seen from Fig. 8, for the adhesive interface, the increase of the socket gap did not change the magnitude of the nominal stiffness of the interface to

Fig. 8 Relationship between pull-out force and interface displacement of PVC pipe socket for adhesive interfaces at different socket gap



resist pullout, while its maximum pullout force decreased with the increase of the socket gap, which led to the forward shift of the appearance of the maximum pullout force. Although increasing the socket gap means using more adhesive to bond bell and spigot, it reduced the tensile strength of the socket, so it was more economical and beneficial to avoid using adhesive interfaces with large socket gaps in the project. The increase of the socket gap did not change the adhesive mechanics of the adhesive interface, but only makes the bonding force between the adhesive and the pipe wall reduced, thus weakening the working ability of the adhesive interface.

3 Buried Pipeline Mechanical Properties

3.1 Finite Element Model

The whole model consists of two major parts: the pipeline model and the road model. The pipeline model consisted of 4 sections of the same length connected to each other, and the two adjacent sections were connected by adhesive joints, each with an effective length of 2 m and a nominal diameter of DN 200. The material parameters of the PVC pipeline and adhesive joints were set as before. The overall model of the pipeline is shown in Fig. 9 (P1, P2, P3, P4 represent the 1st, 2nd, 3rd, 4th pipe sections, S1, S2, S3 represent the 1st, 2nd, 3rd adhesive bonded joint).

The road model consisted of three parts: road surface, roadbed and sand subcrust, and the overall model size is 7 m × 8 m × 8 m. The thickness of the road surface was 0.25 m and adopted the linear elastic principal structure. The thicknesses of roadbed and sand subcrust were 6.75 m and 0.25 m respectively, and the width of sand sub-crust was 0.60 m. Both the roadbed and sand subcrust used the Moore

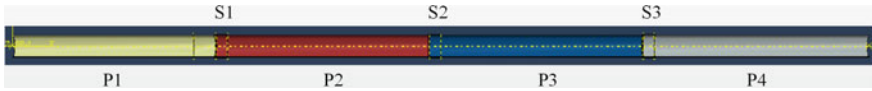


Fig. 9 Modeling of pipeline entities

Coulomb elastoplastic principal structure model. The relevant material parameters are shown in Table 2 [11, 12, 27], and the overall mesh is divided as shown in Fig. 10. To simulate the boundary conditions of the buried pipeline more realistically, the displacement degrees of freedom of the bottom 3 directions and the displacement degrees of freedom of the 4 lateral normal directions are constrained in the road model.

Table 2 Material parameters of road structures

Material	Density ρ / ($\text{kg}\cdot\text{m}^{-3}$)	Elastic modulus E / (MPa)	Poisson's ratio μ	Cohesive force c /(kPa)	Angle of internal friction φ /($^{\circ}$)
Road surface	2400	240	0.3	–	–
Roadbed	2000	15	0.26	20	25.4
Sand subcrust	2200	1400	0.25	1×10^{-3}	37

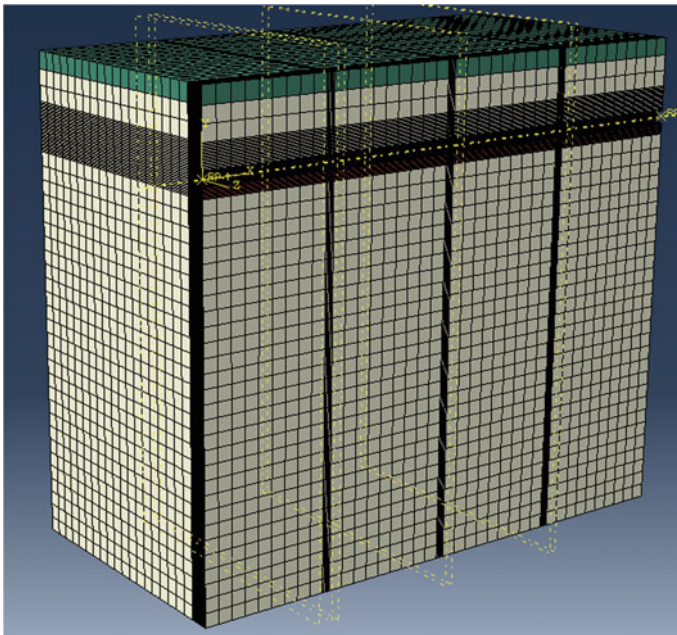


Fig. 10 Meshing of the overall structure

Frictional contact was set at the intersection of roadbed and pipeline, tangentially as a penalty contact and normally as a hard contact. The friction coefficient of the pipe and soil contact surface was taken according to the following equation [28].

$$\mu = \frac{A}{H/D - B} + C \quad (1)$$

where, H is the embedment of the pipe from the mudline to the upper of pipe, A, B and C are fitting constants, depending on the undrained shear strength of the soil, which were taken as 0.756, 0.461 and 0.204 in this study [27], respectively.

3.2 Analysis and Discussion

On the established preface of road model, the impulse load measurement curve of the falling hammer bending instrument is used with an action area of 0.4 m × 0.2 m and a wheel spacing of 1.2 m, acting directly above and on both sides of S2, respectively, with reference to the literature [11, 12]. To make the simulation results of the road structure more realistic, the soil structure has been equilibrated before loading in this paper.

Comparison of Mechanical Response of PVC Pipelines under Different Load Magnitudes. The traffic load was applied to the road surface at the point directly above the pipe section S2, and the mechanical response of the buried pipeline with adhesive interface was studied under three different magnitude sizes of traffic load (0.6, 0.8 and 1.0 MPa). The longitudinal Mises stress distribution curves are shown in Fig. 11 for a point at each end of the pipe top to determine the path. To study the circumferential stress distribution of the pipe, the circumferential paths of the bell and the spigot at S2 were taken and the Mises stresses of the socket are analyzed under the action of traffic loads of three amplitudes. The stress comparison curves are shown in Fig. 12.

Due to the geometrical asymmetry of the socket structure, the Mises stresses at the top of the pipe in Fig. 11 were not symmetrical about the longitudinal centerline of the pipe and were highly discontinuous at the pipe joints. With the increase of the traffic load, the longitudinal Mises stresses of P2 and P3 pipe joints showed a significant increase, while the longitudinal Mises stresses of P1 and P4 pipe joints did not change significantly, which indicates that the influence of traffic load on the adhesive bonded joint was about 2 pipe joints (4 m).

As can be seen from Fig. 12, the stress distribution of the buried adhesive bonded joint of PVC pipe line bell and spigot had obvious peaks and valleys. The peaks of Mises stress distribution for the socket appeared at the top (0°) and the side (90°, 270°) of the pipe, and the valleys of Mises stress distribution are located at the shoulder (45°, 315°) and the bottom (360°) of the pipe. From the top to the bottom of the pipe, the Mises stress showed the distribution characteristics of first falling,

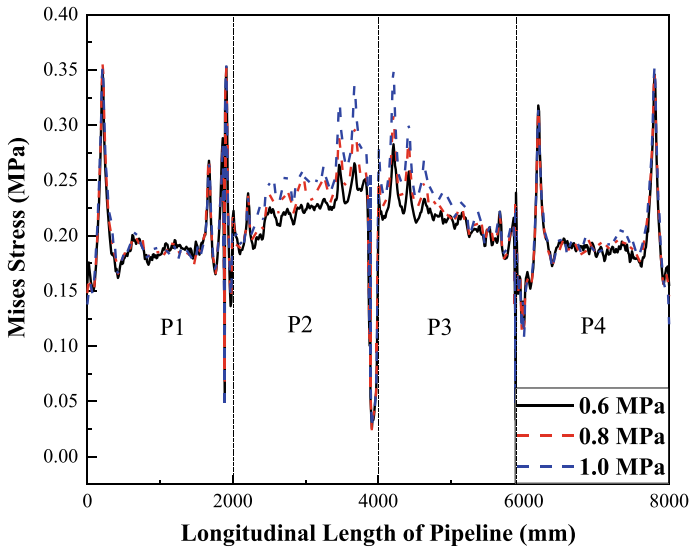


Fig. 11 Comparison curve of Mises stress at the top of the pipeline under different magnitude of traffic load

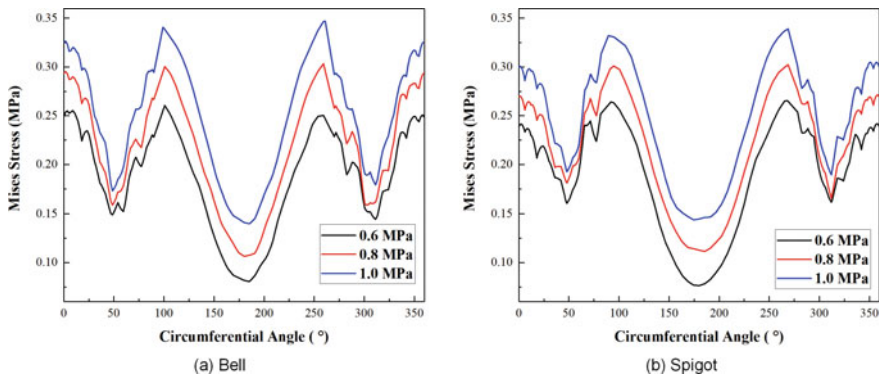


Fig. 12 Mises stress comparison curves for bearing sockets in the circumferential direction under different traffic load magnitudes

then rising and then falling. The maximum Mises stress appeared at the side of the pipe (90°, 270°) and the minimum Mises stress appeared at the bottom of the pipe (180°). Comparing the Mises stress distribution in the bell and the spigot, it can be found that the minimum and maximum Mises stresses in the spigot are smaller than those in the bell, but the minimum Mises stresses in the spigot are larger than those in the bell at the tube side (90°, 270°), where the spigot is at the valley. In addition, with the increase of the traffic load amplitude, the circumferential Mises stress of the socket increased, and the effect of the Mises stress distribution law was especially

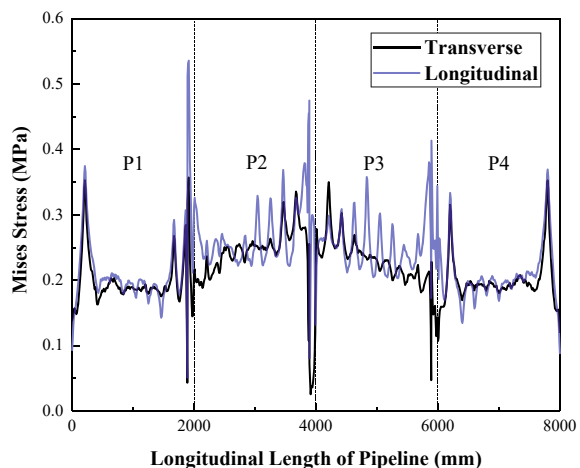
obvious for the lower part of the pipe (90° – 270°), while the effect of the Mises stress distribution law was relatively small for the upper part of the pipe, especially the pipe shoulders.

Comparison of Mechanical Response of PVC Pipelines under Different Traffic Direction. The direction of the traffic load may be either perpendicular to the buried pipeline (transverse) or parallel to the buried pipeline (longitudinal). The traffic load in two different traffic directions is now applied to the road surface at the point directly above the pipe joint S2 to study the mechanical response of the buried pipeline with adhesive interface. The longitudinal Mises stress distribution curves are shown in Fig. 13 for a point at each end of the pipe top to determine the path. To study the stress distribution around the pipe perimeter, the circumferential paths of bell and spigot at S2 are taken, and the Mises stresses generated at bell and spigot by the traffic load under two traffic directions are analyzed. The stress comparison curves are shown in Fig. 14.

From Fig. 13, the direction of travel changed from transverse to longitudinal, the distribution pattern of Mises stress at the top of the pipe did not change significantly, but the magnitude of its stress increased significantly which was most obvious at the interface and smaller at the body of the pipe. This indicates that, under the same conditions, buried pipes laid along the road are more prone to rupture failure than buried PVC pipes with adhesive bonded joints across the road. In addition, the change in the direction of traffic did not significantly affect the Mises stresses at the top of the two pipe sections P1 and P4, which again indicates that the mechanical response of the traffic load on the buried pipeline is limited to the middle two pipe sections (4 m).

As can be seen from Fig. 14, the direction of travel had a greater effect on the circumferential dynamic response. When the direction of travel changes from transverse to longitudinal, the valley of the Mises stress distribution changed, and the

Fig. 13 Comparative Mises stress curves at the top of the pipeline under the traffic load in different traffic directions



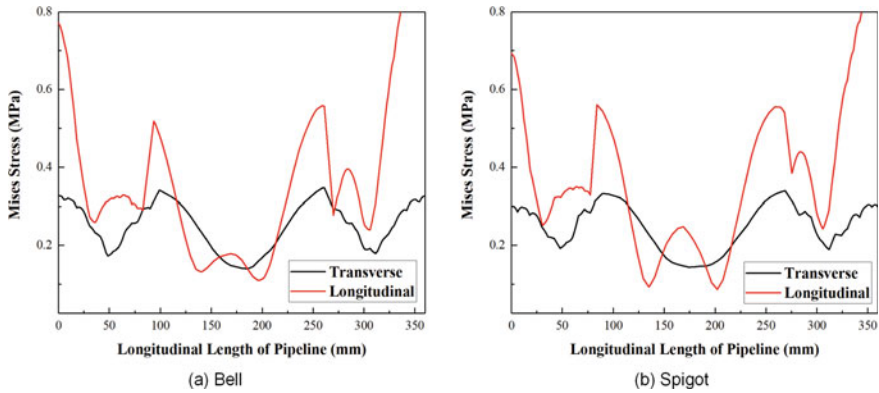


Fig. 14 Mises stress comparison curves in the circumferential direction of the bearing socket under traffic loads in different directions of travel

shoulder (45° , 315°) and the bottom (180°) are no longer the minima, but the minima fell symmetrically near the shoulder (30° , 75° , 285° , 320°) and near the bottom (145° , 215°). In addition, the change in the direction of travel caused the Mises stress in the upper part of the pipe to increase significantly, and the increase was much higher than that in the lower part of the pipe, which indicates that the Mises stress distribution pattern in the upper part of the pipe is more sensitive to the longitudinal direction of travel.

As can be seen from Fig. 13, the direction of travel has a greater effect on the circumferential dynamic response. When the direction of travel changes from transverse to longitudinal, the location of the valleys of the Mises stress distribution were relocated, and the number of both valleys and peaks both changed from three to six. The shoulders (45° , 315°) and the bottom (180°) were no longer the minima, but the new minima fall symmetrically on both sides of the shoulders (30° , 75° , 285° , 320°) and on both sides of the bottom (145° , 215°), which makes the weakest point of the interface that the lowest value of the circumferential stress distribution of the interface, became the hips (145° , 215°) of pipe. The Mises stress at the bottom of the pipe under the longitudinal direction of travel is higher than that under the transverse direction of travel. In addition, the change in the direction of travel caused a significant increase in the Mises stress in the upper part of the pipe, which is much higher than that in the lower part of the pipe, indicating that the Mises stress distribution pattern in the upper part of the pipe was more sensitive to the longitudinal direction of travel, which is opposite to the effect of the transverse direction of travel on the stress distribution pattern.

4 Conclusion

In this study, the axial mechanical performance and buried mechanical response of the adhesive bonded joint of PVC pipes were calculated numerically on basis of existing studies, the following conclusions were obtained.

1. The seismic performance of PVC pipe adhesive interface is poor, and the axial pullout displacement is very small, so it is difficult to resist the axial deformation under seismic damage like the flexible interface; the ultimate axial pullout force of adhesive interface is inversely proportional to the socket gap and proportional to the pipe diameter, while the influence of loading rate on the pullout force is limited and can be negligible.
2. Under the action of traffic load, the stress on the top and side of buried PVC adhesive bonded joint is obviously larger and prone to damage. And the maximum Mises stress by circumferential distribution of the bell is larger than that of the spigot, so bell is more susceptible to damage than the spigot in buried situations.
3. Different traffic directions have a greater influence on the mechanical response of the adhesive bonded joint. In the longitudinal traffic direction, the maximum circumferential Mises stress on the interface is significantly greater than that in the transverse traffic direction, and the location of the circumferential stress valley is relocated. The number of valleys is increased to 6 from 3, but it does not change the location of the circumferential stress Mises peak, so it does not change the location of damage accordingly.

References

1. Sun SP, Han Y (2003) State-of-the-art of the research on lifeline earthquake engineering. *China Civ Eng J* (05):97–104
2. Wang Q, Guo MJ et al (2022) High performance PVC axial hollow wall pipes in urban drainage projects. *Water Wastewater Eng* 58(S1):406–411
3. Han Y, Li GC et al (2020) Experimental study on axial mechanical properties of pipeline under pseudo-static loading. *J Earthquake Eng Vibr* 40(05):44–51
4. Ren XZ, Han Y, Yang JC (2019) Experimental study on mechanical properties of ductile iron pipe flexible joint under eccentric tension. *J Henan Univ Urban Constr* 28(05):37–40
5. Zhong ZL, Wang SR et al (2019) Experimental study on mechanical properties of ductile iron pipeline rehabilitated by corrosion protection lining. *J Harbin Inst Technol* 51(06):141–147
6. CJJ 101-2016 (2016) Technical specification for buried plastic pipeline of water supply engineering
7. CJJ 143-2010: Technical specification for buried plastic pipeline of sewer engineering
8. Chen CG, Yang et al (2012) Experimental research on seismic capability of cast-iron pipe with rubber gasket joints. *J Earthquake Eng Eng Vibr* 32(03):104–108
9. Li GC, Ren XZ, Han Y (2020) Experimental study on mechanical properties of socket type flexible joint of pipeline under reciprocating load. *J Henan Univ Urban Constr* 29(01):29–33
10. Duan JF (2011) Experimental study on mechanical behavior of rubber gasketed joint with ductile cast iron pipe. Henan University of Technology

11. Wang FM, Fang HY et al (2018) Dynamic response analysis of drainage pipes with gasketed bell and spigot joints subjected to traffic loads. *Chin J Geotech Eng* 40(12):2274–2280
12. Wang FM, He H et al (2020) Study on mechanical response of the bell-and-spigot joints of pipeline under the coupling of traffic and running load. *J Zhengzhou Univ (Eng Sci)* 41(04):1–6
13. Zhai KJ, Fang HY et al (2020) Mechanical properties and failure mode simulation analysis of joints in PCCP. *China Water Wastewater* 36(20):10–18
14. Chen LP, Wang JS et al (2021) Study on joint leakage law of municipal concrete drainage pipeline. *Water Resour Hydropower Eng* 52(6):223–232
15. Zhang ZG, Fang L et al (2021) Influence analyses on force of gas pipeline with discontinuous joints induced by landslide on rainfall condition. *Chin J Geotech Eng* 1–10
16. Wu WY, Zhang TQ et al (2002) Calculation of longitudinal mechanics of flexible interface pipes under vertical load. *China Water Wastewater* (09):58–60
17. CJT 493-2016: High performance unplasticized poly (vinyl chloride) pipes and fittings for water supply
18. GB/T 10002.1-2006: Pipes and fittings made of unplasticized poly (vinylchloride) (PVC-U) for water supply—specifications
19. Guo S (2019) Methods and mechanisms of toughening of adhesively bonded joints. Tsinghua University
20. He X (2011) A review of finite element analysis of adhesively bonded joints. *Int J Adhes Adhes* 31(4):248–264
21. Camanho PP, Davila CG (2002) Mixed-mode decohesion finite elements for the simulation of delamination in composite materials. NASA/TM-2002–211737, pp 1–37
22. Camanho PP, Davila CG, De Moura MF (2003) Numerical simulation of mixed-mode progressive delamination in composite materials. *J Compos Mater* 37(16):1415–1438
23. Benzeggagh ML, Kenane M (1996) Measurement of mixed-mode delamination fracture toughness of unidirectional glass/epoxy composites with mixed-mode bending apparatus. *Compos Sci Technol* 56:439–449
24. GB/T 6329-1996 (1996) Adhesives-determination of tensile strength of butt joints
25. GB/T 33799-2017 (2017) Adhesives-determination of the bond strength of engineering-plastic joints
26. QB/T 2568-2002 (2002) Solvent cements for poly (vinyl Chloride) (PVC) plastic piping system
27. Fang H, Tan PL et al (2020) Numerical and experimental investigation of the effect of traffic load on the mechanical characteristics of HDPE double-wall corrugated pipe. *Appl Sci* 10(2):627
28. Wang J, Yang Z (2016) Axial friction response of full-scale pipes in soft clays. *Appl Ocean Res* 59:10–23

Synthesis and Application of Graphene-Phase Biochar from *Theobroma Cacao* Pod Husks Using Slow Pyrolysis Technique in the Treatment of Fats, Oil, and Grease from Actual Wastewater



Jennice Mae D. Toledo, Karen B. Hubayan, Angel Ann M. Pacheco, Neil Harold C. Salvador, Charles Joshua O. Bravo, and Allan R. Alzona

Abstract This research reports the applicability of the produced graphene-phase biochar (GPB) adsorbent in the treatment of actual wastewater contaminated by fats, oil, and grease (FOG) through the process of packed-bed column adsorption. The GPB was synthesized using acetic acid pre-treatment and heat treatment from biochar generated from the pod husks of *Theobroma cacao*. Column adsorption studies were performed by modification of the column parameters, specifically: the flow rate, bed height, and the initial influent concentration. The highest percentage removal was 99.70% which was recorded by employing the 20 ml min⁻¹ flow rate, 150 mm bed height, and 78,880.0 mg L⁻¹ of influent concentration. With these findings, it can be inferred that *Theobroma cacao* pod husks waste can be successfully employed for the treatment of fats, oil, and grease from actual wastewater from quick-service restaurants.

Keywords Column adsorption · Fats · Oil · and Grease (FOG) · Graphene · *Theobroma cacao*

J. M. D. Toledo · K. B. Hubayan · A. A. M. Pacheco · N. H. C. Salvador · C. J. O. Bravo · A. R. Alzona (✉)
Civil Engineering Department, National University, Manila, Philippines
e-mail: aralzona@national-u.edu.ph

J. M. D. Toledo · A. R. Alzona
Environmental and Sanitary Engineering Department, National University, Manila, Philippines

© The Author(s), under exclusive license to Springer Nature Singapore Pte Ltd. 2024
M. Casini (ed.), *Proceedings of the 3rd International Civil Engineering and Architecture Conference*, Lecture Notes in Civil Engineering 389,
https://doi.org/10.1007/978-981-99-6368-3_17

1 Introduction

Fats, oil, and grease, collectively referred to as FOG, are one of the principal causes of problems in sewer systems, which continues to be a global challenge. FOG is toxic organic waste that has a low affinity to water and is used in or is a by-product of cooking or any food preparation processes. FOG exists in various forms: animal and vegetable fats, butter, margarine, and lard. These organic substances appear harmless because they liquefy at high water temperature, a reason it is usually poured directly into the drain. However, once FOG enters the sewer system, it cools down and accumulates within the pipes. Over time, this accumulation restricts flow and leads to sewer blockages [1]. Blockages result in raw sewage backups and sanitary sewer overflows (SSO) into public areas and other bodies of water posing severe environmental threats and health hazards [2].

FOG in wastewater generated by Quick Service Restaurants (QSRs) in the country often causes sewer blockages [3]. FOG is challenging to treat since they are insoluble in water [4]. Also, oil and grease are considered “one of the most complicated pollutants to remove” in wastewater [5].

FOG-containing wastewater has no currently acceptable treatment technology [3]. However, there have been growing bodies of literature on the application of biochar produced from several types of biomasses in water treatment, specifically in removing various contaminants in water through adsorption processes. Organic sorbents in the form of biochar have long been used in water treatment due to their abundant source, cheap cost, adsorptive abilities, economic advantages, and reduced environmental impact [6].

Meanwhile, graphene, isolated in 2004, has received a great deal of attention in the field of science and technology since first reported. Graphene is an allotrope of carbon, and one of the most promising nanomaterials. The potential of graphene applications includes photoelectric elements, various medical applications, semiconductor materials, and adsorbents for environmental pollutants. Due to its nanopores, or sieve-like form, it can filter and adsorb contaminants in water. Graphene is a material that provided both functional adsorptive capacity and good kinetics, implying that it could be used as a sorbent for soluble oil removal from wastewater [7].

To take advantage of the advancements in both graphene and biochar technologies, this study used graphene-phase biochar. The said biochar was produced from the waste biomass of *Theobroma cacao* pod husks. Cacao is an important crop at the industrial level since cocoa beans are the main ingredient of chocolate [8]. Subsequently, cocoa beans only represent 25–30% of the whole weight of the cacao fruit, only 10% of which are commercially valuable beans [6]. And because only a few percent of the fruit is utilized, results in cacao plantations having extensive quantities of waste, which makes the cacao pod husks a significant biomass source.

This study aims to evaluate the applicability of graphene-phase biochar derived from *Theobroma cacao* pod husks as an adsorbent to FOG from wastewater of quick-service restaurants (QSRs).

2 Materials and Methods

2.1 Synthesis of Adsorbent

The utilized biomass material, *Theobroma cacao* pod husks (TCPH), was obtained from San Jose City, Nueva Ecija. Collected TCPH were cut into pieces at approximately 30 by 20 by 3 mm³ in length, width, and height, respectively, and sundried for four days to remove all moisture content present. Afterward, these TCPH pieces were loaded into a muffle furnace and were heated at 350 °C for an hour to convert them into biochar materials. Consequently, the produced biochar was immersed under the CH₃COOH solution for pretreatment at room temperature for 14 days.

For the heat treatment process, this CH₃COOH-pretreated biochar was dried at 105 °C for an hour. It then underwent slow pyrolysis using a muffle furnace at 1100 °C under a vacuum for another hour. The pyrolyzed GPB was powdered using mortar and pestle and sieved between Sieve No. 30 and 40 meshes to obtain the desired particle size. This method is an operative procedure in preparing high rapheme-sheet content carbon materials [9].

2.2 Packed-Bed Column Adsorption Experiments

A glass column of 20 mm internal diameter and 400 mm height was used in carrying out the continuous packed-bed column adsorption experiments as shown in Fig. 1. The bed was supported by layers of glass wool and glass beads to prevent the distribution of beds throughout the column and to ensure uniform inlet flow. The experiments were performed using actual wastewater containing FOG, which was then pumped continuously, through the column, in an up-flow mode using an adjustable peristaltic pump. Effect of adjustment of parameters, namely the bed height (50, 100, and 150 mm), initial FOG concentration (2,551.6, 16,996.8, and 78,880.8 mg L⁻¹), and flow rate (20, 40, and 60 ml min⁻¹), were studied for the filtering of FOG using the synthesized GPB. Experiments were executed by varying the parameter under study and holding the other parameters constant. All the experiments were employed at room temperature. Samples of filtered wastewater were withdrawn at specific time intervals, and the concentrations of effluents were analyzed using the U.S. Environmental Protection Agency, Method 1664, Revision B: n-Hexane Extractable Material (HEM; Oil and Grease) by Extraction and Gravimetry (US EPA 1664B) [10]. The effluent volume can be calculated using Eq. (1),

$$(Q)(t_{total}) = V_{eff} \quad (1)$$

where Q is the volumetric flow rate in ml min⁻¹, and t_{total} is the total flow time in minutes. By calculating the area under the curve multiplied by the flow rate, the total FOG adsorbed FOG_{ad} (mg) in the fixed bed can be determined using Eq. (2),

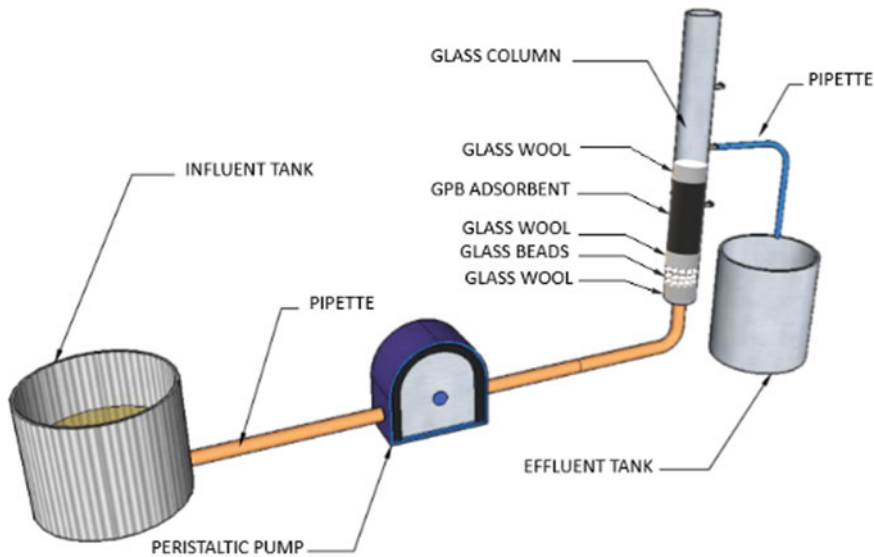


Fig. 1 Packed-bed column adsorption experimental setup

$$\frac{Q}{1000} \int_{t=0}^{t=total} C_{eff} dt = FOG_{ad} \tag{2}$$

where C_{ad} is the concentration of FOG removal ($mg L^{-1}$). The total amount of FOG entering the column (FOG_{total}) is calculated from Eq. (3),

$$\frac{(C_{in})(Q)(t_{total})}{1000} = FOG_{total} \tag{3}$$

and the total FOG removal percentage can be obtained using Eq. (4),

$$\left(1 - \frac{FOG_{ad}}{FOG_{total}}\right)(100) = \% Removal \tag{4}$$

2.3 Analysis of FOG in Wastewater

To measure the amount of FOG present in the wastewater sample to be used, the researchers adopted the standards mandated by the U.S. Environmental Protection Agency (U.S. EPA), Method 1664, Revision B: n-Hexane Extractable Material (HEM; Oil and Grease) by Extraction and Gravimetry. This analysis determines the amount of FOG present quantitatively on the sample based on its mass.

Wastewater containing FOG was obtained from a local fast-food chain. Amber bottles were used for the storage of the wastewater to avoid oil accumulation along the surface of the container. The collected wastewater underwent acidification by mixing an amount of hydrochloric acid needed to obtain a sample having a pH of not greater than 2.0.

A 250 ml of acidified sample was poured into the sample bottle of the separatory funnel. Then, 7.5 ml of n-Hexane was mixed with the sample by manually shaking it for two minutes. Thereafter, the layers of water and oil-hexane solution were allowed to settle for 10 min for them to separate. After 10 min, the water was drained from the separator. This process was repeated two more times totaling three separations to ensure that no water was left in the solution. After the third time of draining water out of the separatory funnel, only the n-Hexane and oil were left in the separator. The mixture left was then poured into a flask with a predetermined tare weight.

Using a rotary evaporator, the n-Hexane was efficiently removed from the mixture. This equipment vaporized the n-Hexane out of the mixture, having a boiling point of approximately 70 °C. Subsequently, what was left was the fats, oils, and grease in the flask. Finally, the flask containing the FOG obtained from this process was then weighed. The amount of FOG concentration in mg L⁻¹ was obtained based on Eq. (5),

$$\frac{W_{FOG}}{V_s} = FOG(mgL^{-1}) \quad (5)$$

where W_{FOG} is the weight of FOG and V_s is the sample volume.

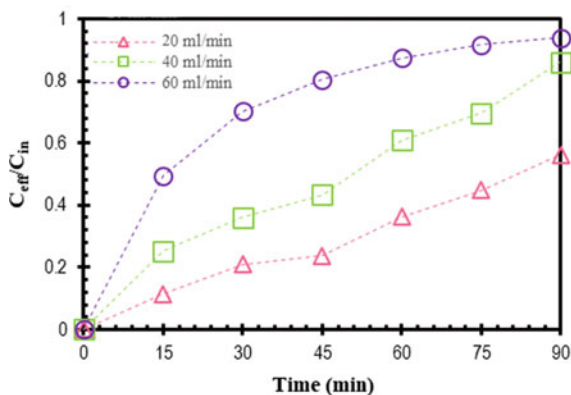
3 Results and Discussion

3.1 Parametric Studies

The influence of varying the three process parameters, namely, flow rate, bed height, and influent concentration, were determined in this study. The column sorption data at different varied factors were presented in tables and were used to plot the C_{eff}/C_{in} versus time graphs of the packed bed column adsorption experiments. C_{eff} is the concentration of FOG analyzed in the effluent sample taken at specific time intervals while C_{in} pertains to the influent concentration entering the packed-bed column adsorption system.

Effect of Flow Rate. One of the most critical parameters to be studied in packed bed column adsorption is the flow rate of the influent used in the study. Figure 2 shows the plot of the C_{eff}/C_{in} versus time obtained for different flow rates of the influent, and sorption column data are presented in Table 1. From the results, it can be observed that as the flow rate increased from 20 to 60 ml min⁻¹, the total FOG removal percentage substantially decreased. This reduction in percentage removal

Fig. 2 Effect of flow rate variation on the percentage removal of FOG



can be attributed to the decrease in the residence time of the adsorbate. At lower flow rates, the influent had greater chances of contact with the adsorbent which resulted in higher removal of adsorbate in the column [11]. This phenomenon can be explained that as the rate of mass transfer gets increased, the amount of adsorbate adsorbed onto unit bed height (mass-transfer zone) gets increased with increasing flow rate leading to a lower removal rate of the contaminant.

Effect of Bed Height. The effect of bed height on the percentage removal of FOG is shown in Fig. 3 and the sorption column data are presented in Table 2. With an increase in bed height, the removal rate of FOG also significantly increased; this is due to more contact time at a greater bed depth. The increase in percentage removal at higher bed heights is due to the availability of a greater number of surface sites [12]. Since the flow rate is optimized prior to bed height, the lower flow rate facilitates increased residence time for the adsorbates at higher bed depths. These results indicated that the bed height of 150 mm offered the highest removal percentage among the three tested bed depth values. Therefore, subsequent experiments were carried out with this bed height.

Effect of Influent Concentration. The effect of varying influent concentrations was investigated using actual wastewater samples with resulting FOG concentrations of 2,551.6 mg L⁻¹, 16,996.8 mg L⁻¹, and 78,880.0 mg L⁻¹. At the same time, the flow rate of 20 ml min⁻¹ and a bed height of 150 mm were kept constant. The impact on the removal percentage of FOG at various influent concentrations was shown in Fig. 4 and sorption column data are presented in Table 3. Generally, and as proven in previous

Table 1 Maximum percentage removal on flow rate variation

Flow rate (ml min ⁻¹)	Time (min.)	Maximum percentage removal (%)
20	15	88.59
40	15	74.71
60	15	50.43

Fig. 3 Effect of bed height variation on the percentage removal of FOG

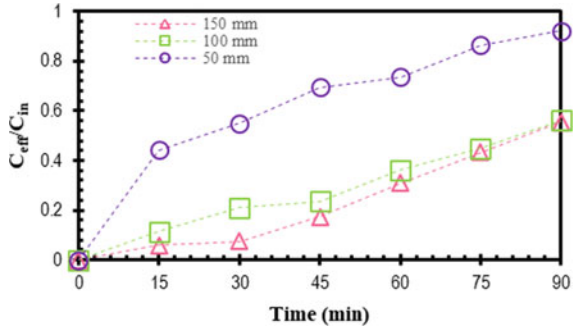


Table 2 Maximum percentage removal on bed height variation

Bed height (mm)	Time (min.)	Maximum percentage removal (%)
50	15	55.71
100	15	88.59
150	15	94.14

studies, decreasing influent concentration lowers the removal percentage of the adsorbent. This can be explained by the fact that a higher concentration gradient caused faster transport due to increased mass transfer [12]. As expected, the loading capacity also increased with an increase in initial concentration. The percentage removal of FOG was found to increase with a gradual increase in initial inlet concentration. Similar observations have been reported by other researchers [13].

Fig. 4 Effect of influent concentration variation on the percentage removal of FOG

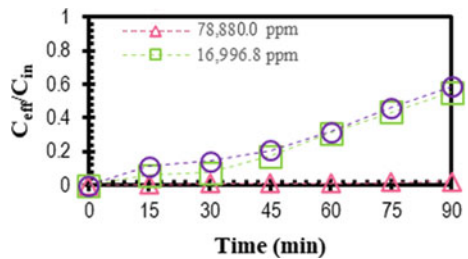


Table 3 Maximum percentage removal on influent concentration variation

Influent concentration (mg L ⁻¹)	Time (min.)	Maximum percentage removal (%)
78,880.0	15	99.70
16,996.8	15	94.14
2,551.6	15	88.72

4 Conclusion

To sum up, the study has successfully demonstrated the applicability of the produced graphene-phase biochar (GPB) adsorbent in the treatment of actual wastewater contaminated by fats, oil, and grease (FOG) through the process of packed-bed column adsorption.

- a. The GPB was synthesized via a two-step process (CH_3COOH pretreatment followed by heat treatment) from biochar generated from the pod husks of *Theobroma cacao*.
- b. The percentage removal of FOG was found to increase with a gradual increase in initial inlet concentration. The highest percentage removal was 99.70% which was recorded by employing the 20 ml min^{-1} flow rate, 150 mm bed height, and $78,880.0 \text{ mg L}^{-1}$ of influent concentration.
- c. Meanwhile, the results of the performed parametric runs showed that the column adsorption performance of GPB is influenced by the studied operating parameters, namely inlet flow rate, bed height, and influent concentration. The adsorption of FOG via a packed-bed column adsorption process is largely influenced by the inlet flow rate. As the flow rate increased from 20 to 60 ml per minute, the percentage removal also substantially decreased. The depth of the adsorbent bed has a significant impact on the adsorption ability of the synthesized GPB on FOG. With the increase in bed height, the removal percentage of FOG also increased significantly. Influent concentration also affects the FOG removal rate of the adsorbent. Increasing the concentration of the influent that passes through the column resulted in a gradual increase in the removal efficiency of GPB.

References

1. Williams JB, Clarkson C, Mant C, Drinkwater A, May E (2012) Fat, oil and grease deposits in sewers: characterization of deposits and formation mechanisms. *Water Res* 46(19):6319–6328
2. Environmental Protection Agency (EPA) (2016) Why control sanitary sewer overflows? Retrieved from https://www3.epa.gov/npdes/pubs/sso_casestudy_control.pdf
3. Department of Science and Technology—Industrial Technology Development Institute: ITDI develops FOG treatment for QSR wastes. Retrieved from <http://itdi.dost.gov.ph/index.php/18-technological-services/106-tsd-publications-press-releases> (2016)
4. Matsumiya Y, Wakita D, Kimura A, Sanpa S, Kubo M (2007) Isolation and characterization of a lipid-degrading bacterium and its application to lipid-containing wastewater treatment. *J Biosci Bioeng* 103(4):325–330
5. Rhee CH, Martyn PC, Kremer JG (1989) Removal of oil and grease in oil processing wastewaters. In: Proceedings of the 42nd Purdue industrial waste conference, pp 1–15. Retrieved from <http://infohouse.p2ric.org/ref/02/01442.pdf>
6. Vriesmann LC, de Mello Castanho Amboni RD, De Oliveira Petkowicz CL (2011) Cacao pod husks (*Theobroma cacao L.*): composition and hot-water-soluble pectins. *Ind Crops Prod* 34(1):1173–1181
7. Wang N, Zhang Y, Zhu F, Li J, Liu S, Na P (2014) Adsorption of soluble oil from water to graphene. *Environ Sci Pollut Res* 21(10):6495–6505

8. Mansur D, Tago T, Masuda T, Abimanyu H (2014) Conversion of cacao pod husks by pyrolysis and catalytic reaction to produce useful chemicals. *Biomass Bioenerg* 66:275–285
9. Liou YJ, Huang WJ (2015) A process for preparing high graphene sheet content carbon materials from biochar materials. *Electroplating Nanostruct*
10. U.S. Environmental Protection Agency: Method 1664, Revision B: n-Hexane Extractable Material (HEM; Oil and Grease) and Silica Gel Treated n-Hexane Extractable Material (SGT-HEM; Non-polar Material) by Extraction and Gravimetry. Retrieve from <http://www.epa.gov/environmental-topics/water-topics> (2010)
11. López-Cervantes J, Sánchez-Machado DI, Sánchez-Duarte RG, Correa-Murrieta MA (2018) Study of a fixed-bed column in the adsorption of an azo dye from an aqueous medium using a chitosan–glutaraldehyde biosorbent. *Adsorpt Sci Technol* 36(1–2):215–232
12. Uddin MT, Rukanuzzaman M, Khan MR, Islam MA (2009) Adsorption of methylene blue from aqueous solution by jackfruit (*Artocarpus heterophyllus*) leaf powder: a fixed-bed column study. *J Environ Manage* 90:3443–3450
13. Baral SS, Das N, Ramulu TS, Sahoo SK, Das SN, Chaudhury GR (2009) Removal of Cr(VI) by thermally activated weed *Salvinia culcullata* in a fixed-bed column. *J Hazard Mater* 161:1427–1435

Reinforced Concrete Structural Engineering and Structural Mechanics

An Experimental Study on the Repair Evaluation of Deteriorated RC Beams Using Natural Frequency and Mechanical Behavior Related to Damage Condition



Yilong Cao, Akihiko Nishimura, Xiu Luo, Masao Okoshi, Wendong Tang, and Hidekazu Nishimura

Abstract This study aims to quantitatively evaluate the repair of deteriorated RC beams for reuse through natural frequency and proposes a method that describes the mechanical behavior of structures. A static loading test was conducted to determine the load-carrying capacity and deformation performance of structures. To investigate the soundness of the RC beam based on the change of the natural frequency at each load stage, an impact vibration test (IVT) was conducted. Then, a higher vibration mode of natural frequencies, which can better reflect the degree of damage of a frame, was used as an evaluation index to represent the mechanical behavior of structures. The result confirmed that, although in case where IVT is challenging to perform due to location limitations, the damage condition can be estimated from the axial stiffness (EA) of RC beams by axial impact to measure the natural frequencies. Regarding the defined model of mechanical behavior, the results in each deteriorated pattern or load stage to be organized by level of damage. Accordingly, the reliability of the quantitative evaluation of repair effectiveness using the proposed method was verified.

Keywords RC Beam · Repair · Quantitative assessment · Mechanical behavior · Impact vibration test

Y. Cao (✉) · H. Nishimura

Graduate School of System Design and Management, Keio University, Hiyoshi 4-1-1, Kohoku-Ku, Yokohama 223-8521, Japan
e-mail: tonycaoyilong1988@keio.jp

A. Nishimura · W. Tang

Nishimura Seismic and Disaster Prevention Institute, Shimorenjaku 3-3-50 5F, Mitaka 181-0013, Tokyo, Japan

X. Luo · M. Okoshi

JR Soken Engineering Co. Ltd, Higashi 1-4-13 8F, Kunitachi 186-0002, Tokyo, Japan

1 Introduction

Recently, with aging of structures, especially in developed countries, maintenance and repair of structures has become a major problem. As structures and their components age, deterioration risks increase, such as corrosion of reinforcing steel and sectional defects of concrete depending on service conditions and environments. The potential risk is extremely high because these changes have a strong influence on the deterioration related to safety. In the current maintenance systems in Japan, for example, general inspections of railroad bridges are carried out once every 2 years through visual inspection, but subsequent detailed inspection are carried out if necessary [1, 2]. However, some cases emerge wherein the scale of inspection becomes enormous due to the aging of bridges and the rapid response sometimes required after disasters (e.g., large earthquakes). Accordingly, to ensure safety and realize efficient maintenance management plans at the relevant sites, the life cycle management concept has been considered; this concept includes an evaluation of the damage level of a structure and a quantitative evaluation of the required repair and reinforcement [3]. Meanwhile, from the sustainability viewpoint, problems related to maintenance automation (e.g., investigation, monitoring, diagnosis, and assessment) and life extension of concrete and structures have recently received lots of attention [4]. Further, the lifecycle management frameworks, which focus on preventative maintenance, have been considered for quick implementation [5]. Due to the characteristics of structures and their preventative maintenance, both the stages from the start of service to repair or reinforcement and the stages of reuse after repair or reform should be discussed [6, 7]. To restart service for repaired structures, understanding and quantitatively evaluating the mechanical behavior are necessary. To grasp the mechanical behavior of structures after repair, static loading experiments must be conducted. However, from a practical perspective, a nondestructive inspection method for accurately investigating the effects of repair or reinforcement in a relatively easy process at maintenance sites should be used. Moreover, an inspectable evaluation index that can clearly express the effects of repair with quantifiably high reliability is required [8].

To quantitatively evaluate the repair effects of RC beams, including the case wherein the condition of boundaries (e.g., conditions of support) are difficult to investigate (Fig. 1), first, the beams are repaired. Subsequently, the strength of the repaired beams is examined through concrete core tests. In this process, static loading experiments were carried out after the repair to understand the bearing capacity and deformation performance. As a nondestructive test method, impact vibration tests (IVTs), commonly used by railway companies in Japan, were conducted at each loading stage to measure the bending and axial natural frequencies by impact vibration test. Moreover, the effectiveness of repair to the deteriorated beam was quantitatively evaluated in terms of natural frequencies at each load stage and mechanical behavior [9–11].



Fig. 1 Example for the damaged RC beam wherein the condition of the support is difficult to investigate

2 Experimental Method

2.1 Details of the Experiment

Due to corrosion induced by salt, RC beams become severely deteriorated (e.g., falling concrete covers and exposure of reinforcing rebars, including a decrease in the cross-sectional area. In the case of moderate deterioration (e.g., exfoliation of the concrete cover caused by corrosive expansion of rebars), structures' safety is severely compromised. However, to plan the maintenance work with high accuracy and efficiency, the effectiveness of the repair should be evaluated. To evaluate the effects of the repair on the model beam from the aspects of mechanical behavior and material strength, the sound model beam (Case 1) and the model beam with moderate (Case 2) and severe (Case 3) deteriorations were created (Fig. 2). The concrete core test applied for Case 2. The mechanical behavior was observed for Cases 1 and 3, Case 3-D for the deteriorated condition case, and Case 3-R for after the repair. To artificially present deteriorated model beams, based on the sound model beam (Case 1), we removed part of the bottom concrete cover in Case 2, and additionally removed part of stirrup rebars in Case 3-D [12]. Then, the load-carrying capacity and deformation performance in each case could be clarified under a static loading experiment. Table 1 presents the details of the experimental case.

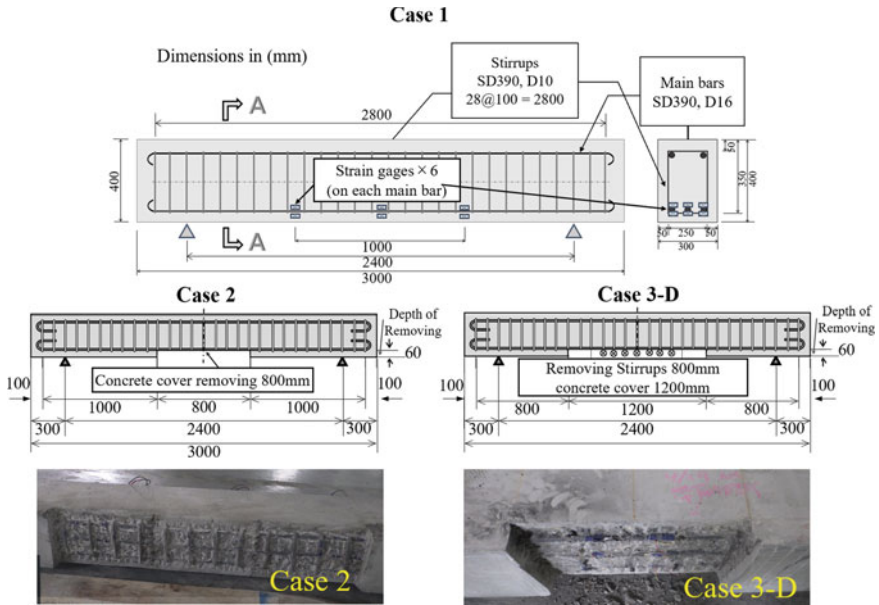


Fig. 2 Elevation view and section view of the RC model beam

Table 1 Details of the experimental cases

Case No.	Level of deterioration		Condition
	Removal of the bottom concrete cover (mm)	Removal of stirrups (mm)	
Case 1	0	0	Sound
Case 2	800	0	Moderate
Case 3-D	1200	800	Severe
Case 3-R	0	0	Repaired

2.2 Repair Method

For the repair method of the deteriorated model beams for Cases 2 and 3-D, we selected the inside pressure hardening (IPH) method, which is considered effective when the damage level is high [13]. In the repair process (Fig. 3), we first checked whether a sectional defect occurs in the member, repaired the defective part if necessary, and sealed the crack. Then, the repair area was drilled, and resin was injected using a specifically built tool. Tables 2 and 3 present the conditions in repair and the repair overview of experimental cases, respectively. Case 3-D has wider and deeper cracks than Case 2. Therefore, more epoxy resin is used.

The IPH method is adopted by using a high-fluidity epoxy resin and dedicated injection tool to control the injection pressure to an ultralow level of 0.06 ± 0.01

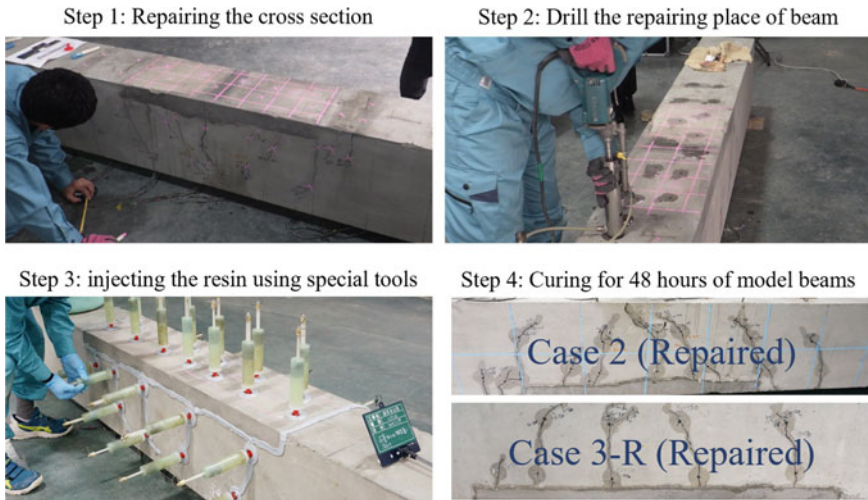


Fig. 3 IPH procedure to repair the RC beam

Table 2 Conditions of the experimental cases before repair

Case	Load stage	Load deflection relationship (P- δ)		Residual deflection (mm)
		Load (kN)	Deflection (mm)	
2	1.6 δ_y	175	8.83	4.77
3-D	δ_y	160	5.63	1.87

Table 3 Repair overview of the experimental cases

Case	Sectional repair	Consumption of epoxy resin (g)	Curing Period (hrs.)
2	Yes	180.3	48
3-D	Yes	236.9	48

to 0.02 N/m². Simultaneously, the injected resin is replaced with the air inside the concrete. Thereafter, capillary action occurs inside the sealed member, and the resin diffuses radially from the inside of the drilled hole. Accordingly, a high-density filling can be achieved. Table 4 presents the material details and testing results of IPH epoxy resin.

2.3 Method of the Material Test

To confirm the concrete strength in the model beams, concrete-compression tests were conducted using the collected test specimens, whereas the model beams were

Table 4 Material property of IPH epoxy resin

Items	Main agent	Curing agent
Component	Epoxy resin	Metamorphic polyamines
Appearance	Transparent	Pale yellow
Viscosity at mixing	550 ± 200 (mPa s 23 °C)	
Mixing ratio (main/curing)	2:1	
Usable time	60 ± 20 (min 23 °C)	
Specific gravity	1.15 0.1	

created. Their curing period was 28 days. Tables 5, 6 and 7 present the details of test specification and results. To confirm the yield and tensile strengths of the main and stirrup rebars, tensile tests of the main rebar were conducted in advance. Table 8 and 9 provide the specifications and results. To confirm the strength of the concrete after repair, concrete cores were extracted for the model beam of Case 2, and the same equipment and procedures were used.

Table 5 Results of the concrete-compression test

Specimen size (Cube in mm)	Compression strength (kN/m ²)	Young's module (kN/m ²)
150	4.01×10^4	2.74×10^7

Table 6 Results of the rebar tensile test

Type	Spec.	Strength (kN/m ²)		E_s (kN/m ²)
		Yield	Tensile	
Main	HRB400-D16	4.48×10^5	6.19×10^5	2.05×10^8
Stirrup	HRB400-D10	5.65×10^5	7.35×10^5	

Table 7 Specification of the accelerometer (for the bending impact vibration test, IVT)

Type	Specifications
Type of sensor	Piezoelectric accelerate type
Charge sensitivity	6.42 pC/(m/s ²)
Max acceleration measurement	± 5000 m/s ²
Frequency range of measurement	1–7000 Hz
Size	17.5 mm (Hex.) × 18 mm (H)

Table 8 Specification of the accelerometer (for the axial IVT)

Type	Specifications
Type of sensor	Piezoresistance accelerate type
Voltage sensitivity	0.44 mV (m/s ²)
Max acceleration measurement	± 5000 m/s ²
Frequency range of measurement	3 Hz ~ 20,000 Hz
Size	7 mm (Hex.) × 11 mm (H)

Table 9 Result of the core compression test of Case 2

No.	Dimensions of specimens (mm)		Pressure receiving area (mm ²)	Ultimate load (kN)	Strength (N/mm ²)
	Diameter	Height			
53-1	98	98	7543	395.27	43.9
53-2	99	99	7697	302.22	41.5
10-1	99	99	7697	330.78	51.4
106-2	98	98	7543	319.48	40.1
196-1	99	99	7697	296.78	45.0
196-2	98	98	7543	342.70	43.9

2.4 Procedure of the Static Loading Test

For the static loading test, the loading device comprises a loading frame and oil jack with a maximum loading capacity of 500 kN. The loading force on the model beam was applied at the center position, and the load value was recorded by an electric load cell. Displacement sensors were installed at the center position and fulcrums of the frame (Fig. 4). At each load stage, the deflection value was calculated from the relative displacements between the center and ends of the beam.

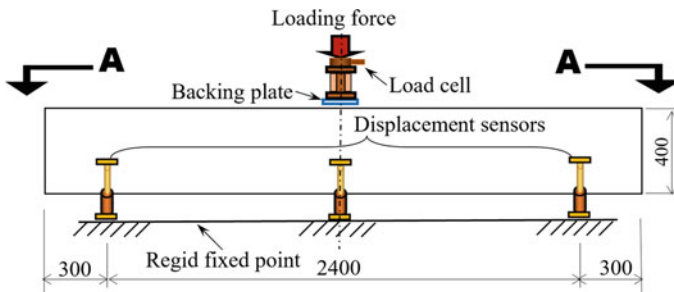


Fig. 4 Installing condition of the displacement sensors in an elevation view

Subsequently, the relationship between the damage (in each load stage) and deflection was determined using the following processes. Both sides of the beam were observed at an elevated view to determine the crack occurrence point. To determine the deflection at the time of yielding (yield point), the load–displacement relationship for each loading step and the measured values of strain gauges attached to the main bars when the model beams were created in advance were considered. The value was an integer of the yield strain in the design calculated using Eq. (1). Further, it was set at the point when the strain reached 2200μ (main bar) and was obtained from the result of the tensile strength testing. Here ε_y is the yield strain in the design, F_y denotes the yield strength of the main bar, and E_s is Young's modulus of the main bar.

$$\varepsilon_y = \frac{F_y}{E_s} \quad (1)$$

The subsequent load stages after the yield point, which are multiples of the yield deflection value (δ_y), were used for the target loading deflection. At a load stage of the yield point or after this stage, the loading force was controlled according to the deflection. Further, three-time cyclic loadings were performed in each load stage. To ensure that the damage of the model beams did not exceed the condition for reuse after repair, the end of loading was determined by decreasing the load-carrying capacity three times that of cyclic loading, amount of residual deflection, and progress of cracks in each experimental case.

2.5 Method of the IVT

To understand the bending stiffness (EI) of a member when the support conditions are difficult to investigate, a simply supported beam with a low degree of fixation of the support points and a large influence of instability of the support conditions was formed. IVTs were conducted to clarify the relationship between the degree of damage and natural frequency of the model beam before and after different deterioration degrees and at each load stage from the beginning to the end of loading. In this static loading experiment, the load is applied from the perpendicular direction of the frame of model beam. Further, the EI of the member is considered to decrease as the load stage progresses. Therefore, as this ensures an accurate estimation of the EI from the natural frequency, the pulse should be applied from the vertical direction. Specifically, since the weight of the model beam to be measured is not large, the input of impact was applied using a hammer. Pulse inputs from small hammer to a structure or member can easily be collected by the accelerometer over a wide range of frequencies. Then, a Fourier spectrum analysis is performed on the measured waveforms to determine the prevailing frequency from the amplitude and phase spectrum, which is available used as the natural frequency. The case of IVT in this study, the mass of the simply supported beam is constant, the natural frequency

is only affected by the stiffness. Unless the condition of frame or support is changed (e.g. crack occurred) by pulse input in measurement, the ratio between acceleration and displacement which depending on the stiffness does not change. Therefore, there are differences with force input to be acceptable in applying the IVT.

Previous studies have shown that the lower vibration mode (1st mode of vibration) is affected by boundaries (e.g., the spring constant of the fulcrum), whereas the higher vibration modes are less affected and tend to reflect the EI of the model beam frame [14, 15]. The support conditions or further information regarding boundaries may difficult to investigate in certain maintenance sites. Therefore, we decided to focus on the high vibration modes of natural frequencies, which are considered to be less affected by the boundary conditions (up to the fourth vibration modes, including the lower mode ϕ). To measure these modes of natural frequencies, five accelerometers were installed to record the response waveforms to follow the central axis of the top of the beam within the supports of the model beam when installed on the load frame. The impact positions were set at the center of the beam support to measure the lower or higher odd-modes, as well as at 1/4 of the beam support distance for the measurement of higher even-modes. Table 7 presents the details of the accelerometer.

In case IVTs in the vertical direction impact are difficult to conduct due to location limitations on maintenance sites, axial natural frequencies to be measured can verify the reliability by applying an impact to the axial direction of the member.

The axial IVT was used to measure the axial natural frequencies to estimating the axial stiffness (EA) [16]. For the model beam in the sound condition, the transmission speed of axial vibration is fast up to 3000–4000 m/s. In this case, accelerometers with very high accuracy should be required in measurement. In a static load test, the EA of the member is considered to decrease as the load stage progresses caused by crack expanding and main bars yielded. However, for the deteriorated model beam, the transmission speed is reduced due to detouring or reflection at the defect positions (e.g., crack or bottom concrete cover removal). Basis on this characteristic, the response acceleration of the axial impact can be accurately calculated from the natural frequencies to estimate the defect of the model beam. The natural frequency of the axial impact is expressed in Eq. (2).

$$f_i = i \frac{v_i}{2l}, \quad (2)$$

where f_i is the natural frequency in the i mode of vibration, l is the axial length, and v_i is the response velocity in the i mode of vibration. Then, the response velocity is transformed in Eq. (3).

$$v_i = 2l \frac{f_i}{i} \quad (3)$$

Young's modulus E can be expressed in Eq. (4), where v_i is the response velocity of concrete, ρ is the density, and ν is Poisson's ratio.

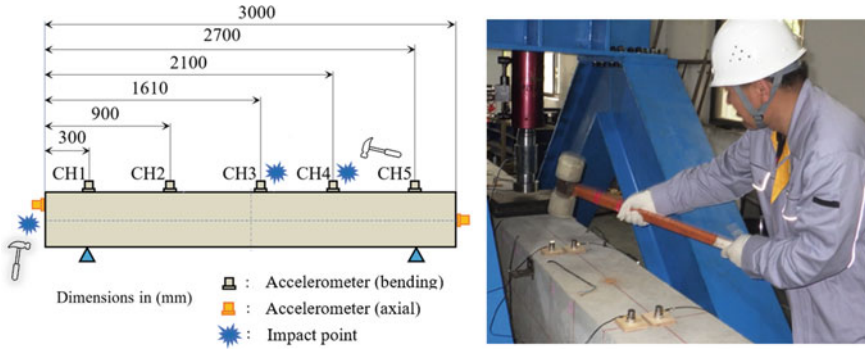


Fig. 5 Positioning of accelerometers and impact points

$$E = V_i^2 \frac{\rho(1 + \nu)(1 - 2\nu)}{1 - \nu} \tag{4}$$

For the axial IVT (Fig. 5), the accelerometers were placed at both ends of the model beam, and the center of the beam was hammered in axial manner. As a relatively higher range of natural frequencies was measured in the test, a wider range of accelerometers were installed. To control the impact, a smaller hammer be used in this test. Table 8 provides the specifications.

3 Result of the Experiment

3.1 Result of the Concrete Core Test

The results of the material test after the repair are described as follows. Figure 6 displays the conditions of resin injection in each specimen and the positional relationship between the model beam. To check the condition of the injection, we extract the core from areas where cracks were concentrated and where without cracks, respectively. Table 12 presents the results. Among these specimens, core specimen #53, without cracks, was not injected with epoxy resin, core specimen #106 was obtained from the location where the cracks were relatively concentrated, and core specimen #196 was obtained from the location where the cracks were relatively sparse. Therefore, the injection of epoxy resin contributes to the strength at the core specimen level. Through visual inspection by ultraviolet irradiation, epoxy resin was confirmed to have been injected into specimens #106 and #196 without any gap space across the rebar.

A compressive strength test of Case 2 was conducted using a square specimen. However, compressive strength tests conducted on cylindrical cores were removed from the Case 2. According to Kikuta et al., the size effect was equal between the

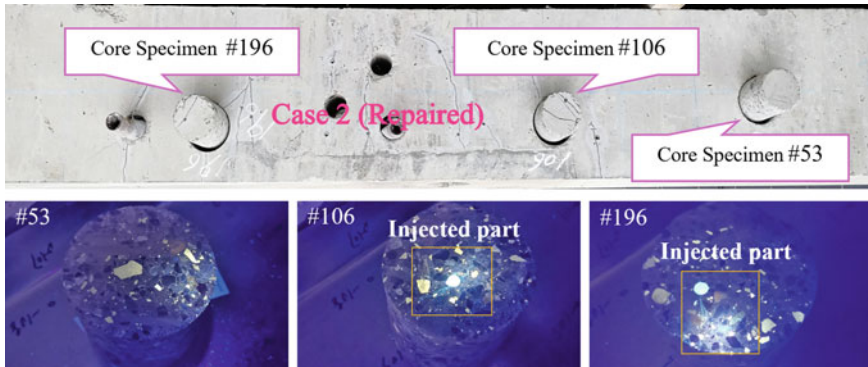


Fig. 6 Positioning of the model beam and specimens in Case 2

square and cylindrical specimens, although the effect of the cross-sectional shape requires correction [17, 18]. Accordingly, through a comparison between the results of pre- and post-repair, it can be considered that all core specimens, namely, #106–1, #106–2, #196–1, and #196–2, in Case 2 are partially in equivalent level or above compared with the sound condition.

3.2 Result of the Static Loading Test

For the overview of the static loading test, the envelope diagram in Fig. 7 shows the first load deflection relationship in each experimental case. Evidently, the 1200 mm concrete cover and 800 mm stirrup rebars of both the sound model beam (Case 1) and severely deteriorated (Case 3-D) were removed, and the yield deflection value (δ_y) was reached at a load stage of 160 kN. These results are consistent with the analysis of Case 1. Tables 10 and 11 present the physical properties used in the analysis. Meanwhile, the yield point of the repaired model beam Case 3-R was measured at 175 kN.

Then, the inelastic characteristics of the experimental cases, showing the rate of decrease when the load-carrying capacity of the first-time loading after yielding in each case and the third-time loading in a cyclic loading (including the yield strength reduction at a yield deflection point in Case 3-D), were compared. The decrease rate of the first- and third-time loading at the same load stage when deflection was controlled was compared. The sound model beam (Case 1) exhibited a reduction rate (4%) in the load capacity at a load stage of 178 kN in equivalent $2 \delta_y$. However, at this load stage, the residual deflection was 7.83 mm, the crack width was 5 mm, and the cracks progressed to a deeper position. The load test terminated at this stage considering the aim of reuse. Case 3-D designed the condition of severe deteriorations created at the bottom, where the concrete cover and stirrup rebars were removed. The deflection measurement at the yield deflection value in 5.63 mm and was the same

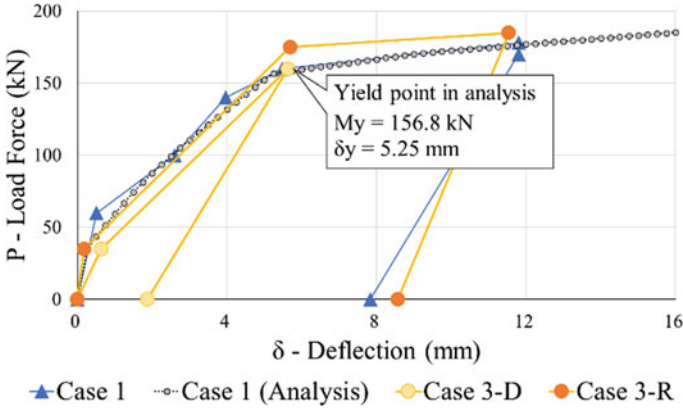


Fig. 7 Load deflection diagram in the envelope diagram

Table 10 Characteristics value of the concrete and main bar

Items	Indexes	Unit	Value
Concrete-compression strength	f'_{ck}	kN/m ²	4.01×10^4
Concrete Young's module	E_c		2.74×10^7
Main bar tensile strength	f_y		4.48×10^5
Main bar Young's module	E_s		2.05×10^8

Table 11 Bending moments and curvatures at the load stage

Items	Indexes	Unit	Value
Bending moment of crack occurrence	M_c	kN m	19.50
Bending moment of yield deflection (δ_y)	M_y		96.00
Bending moment of correspond to Max. loading	M_m		120.00
Curvature of crack occurrence	φ_c	1/m	3.88×10^{-4}
Curvature of yield deflection (δ_y)	φ_y		3.22×10^{-3}
Max curvature	φ_m		6.00×10^{-2}

as that in Case 1. Meanwhile, an intense reduction in the load-carrying capacity was measured at this timing using three times as that of the cyclic loading. The reduction rate was 18%, the cracks progressed to the same depth as that in Case 1 at equivalent 2 δ_y , the residual deflection was 1.87 mm, and the load test was terminated. Compared with that in Case 1, the deflection measurement at the yield deflection value 5.69 mm was in Case 3-R after repair. When the test developed to a load stage 2 δ_y , the load force was 188 kN with 11.54 mm deflection. The residual deflection was 8.57 mm at the end of the test. Combining the results of the material test after repair and static

Table 12 Result of the IVT in the vertical impact

Case	Load deflection relationship (P- δ)		Load stage (condition of damage)	4th mode in the vertical impact (Hz)
	Load (kN)	Deflection (mm)		
1	0	0	Sound	422
	160	5.53	Yield point (δ_y)	360
	177	11.50	Equivalent $2\delta_y$	327
	End	7.83	/	/
3-D	0	0	Sound	422
	0	0	Deteriorated	388
	160	5.63	Yield point (δ_y)	363
	End	1.87	/	/
3-R	0	0	Repaired	401
	185	11.54	Equivalent $2\delta_y$	330
	End	8.57	/	/

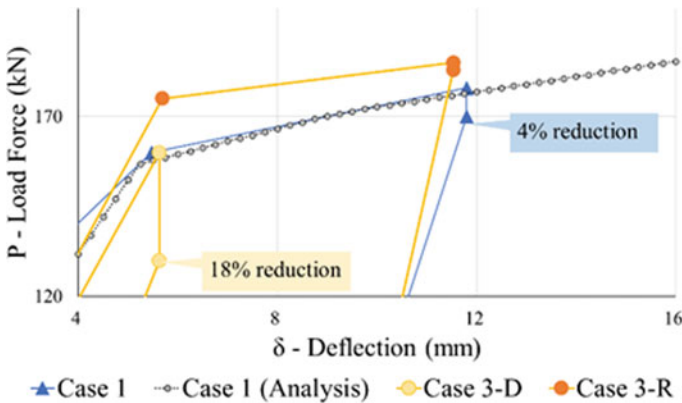


Fig. 8 Load capacity drops in the third-time test during cyclic loading

loading tests, it was found that the Case 3-R after repair could achieve a mechanical behavior comparable to Case 1 (Fig. 8).

3.3 Result of the IVT and Quantitative Evaluation for Repair

Table 12 presents the relationship between bending natural frequency and deflection. This study aims to estimate the damage of frame (Fig. 9). The discussion here focuses on the higher mode (4th mode) of natural frequencies, which is less influenced by

boundary conditions and better represents the degree of damage. At the initial loading stage, the natural frequency was 424 Hz in Case 1. Case 3-D has a natural frequency of 388 Hz due to severe sectional defects. In comparison with the obtained main bars, a natural frequency of 363 Hz was obtained for Case 3-D. This value is lower when compared to the natural frequency of 375 Hz for Case 1, as measured at the yield deflection value. Therefore, a beam with a severe deterioration level, as in that in Case 3-D, has already lost the carrying capacity in the initial stage or earlier stage of loading without reaching the yield deflection value, it is consistent with the previous study [19]. The natural frequency of Case 3-R after repair in the initial stage was 401 Hz, which was almost 5% lower compared with Case 1. The reason for this phenomenon is because Case 3-R is in a yielded condition and involves a condition of the yielded main rebars after repair. This result is consistent with other conclusions of existing studies [20]. As the relationship between the deflection and natural frequency is almost linear, when estimating the natural frequency that corresponds to the yield deflection, Case 3-R and Case after repair 1 have a close value. Therefore, the target should be set to more than the value of 95% in the residual natural frequency if epoxy resin injection (e.g., IPH) is implemented as the method of repairs. Here, the carrying capacity and deformation performance are equivalent to the sound beam.

In the results of the axial IVT provided in Table 13, the natural frequency of the severely deteriorated model beam, Case 3-D, at a yield deflection value 5.63 mm was 1874 Hz. The value of Case 3-R after repair recovered to 1939 Hz. Then, the value in the load stage $2\delta_y$ was 1585 Hz in the end of the static loading test (Fig. 10). From the result of axial natural frequency before and after repair, Table 14 presents the value comprising the bending natural frequency with Case 3 in the reduction rate from the natural frequency perspective. Based on those result, the reduction rate of axial natural frequencies are consistent with bending natural frequencies in each level of damage. As simply supported beams were used in this study, the vibration overall in frame as first vibration mode are not observed in this case. The considered reason

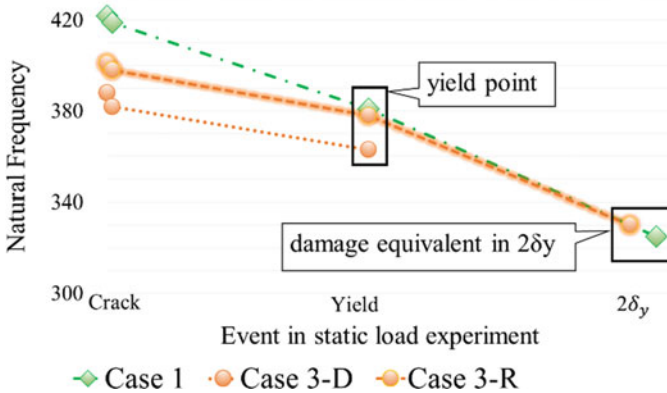


Fig. 9 Comparison rate of the decreasing natural frequency in experimental cases

for the small difference in axial natural frequencies before and after the repair is because the static loading test for Case 3-D was terminated only after the yield point for reuse. In this case, the residual deflection was relatively in a smaller level.

Table 13 Result of the IVT in the axial impact

Case	Load deflection relationship (P- δ)		Load stage (condition of damage)	4th mode in axial impact (Hz)
	Load (kN)	Deflection (mm)		
3-D	0	0	Deteriorated	/
	160	5.63	Yield point (δ_y)	1874
	End	1.88	/	/
3-R	0	0	Repaired	1939
	185	11.54	Equivalent $2\delta_y$	1585
	End	8.57	/	/

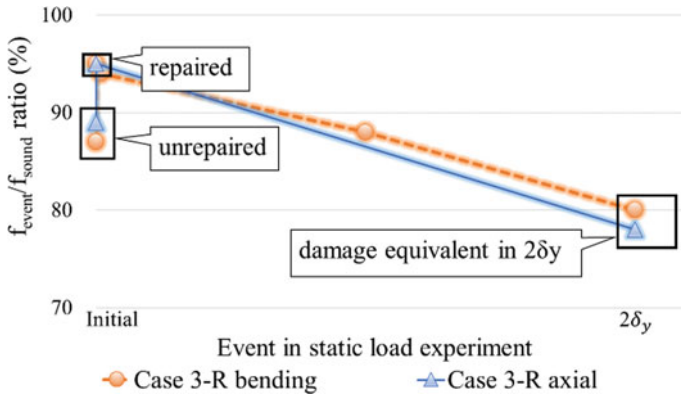


Fig. 10 Comparison rate of the decreasing natural frequency in vertical and axial impact of IVT

Table 14 Comparing of the IVT result using the event sound ratio in natural frequency

Event	Case 1	Case 3-R		Deviation (% in Case 3-R)
		Bending	Axial	
Initial	100	92	/	/
Yield point (δ_y)	85	87	90	3%
Repaired	/	95	95	0%
Equivalent $2\delta_y$	79	78	78	0%

4 Conclusion

This study quantitatively evaluated the repair effect using natural frequency as the evaluation index, and an RC beam with severe deterioration was used as an example. To evaluate the repair effect in the RC beam by natural frequency, an appropriate vibration mode of natural frequency should be determined depending on the boundary condition and purpose when selecting the type of IVT as the nondestructive inspection method. The results indicate that, when beam damage is determined from the EI of the frame, the natural frequency in a higher vibration mode (4th natural frequency) can also reflect the yield condition and repair effect. Additionally, although a bending IVT was difficult to conduct, damage condition can be estimated from the axial stiffness of RC beams, which is determined by decreasing the natural frequencies through the axial IVT. This study is expected to contribute to the quantitative evaluation of the soundness in structures and members, as well as the repair effect in the perspective of seismic design and disaster prevention (e.g., earthquakes or flood). However, the axial natural frequencies before and after repair have a small difference. It was considered that condition with small cracks and relatively small residual deflection reflected the axial natural frequency in a small difference between before and after repair in the RC beam. In a future study, an eigenvalue analysis is required to elucidate the mechanism of axial IVTs. Further, as this study was conducted with only one sample, more data should be collected to improve the accuracy.

References

1. Maintenance standards for railway structures and commentary (concrete structures) (in Japanese), Railway Technical Research Institute, Tokyo, Maruzen Publishing Co, Ltd (2007)
2. Design standards for railway structures and commentary (concrete structures) (in Japanese), Railway Technical Research Institute, Tokyo, Maruzen Publishing Co, Ltd (2007)
3. Mazda T, Miyatake S, Kajita Y (2022) A study on assessing the damage of a bearing and a pier with neural network using the acceleration responses of a bridge. *J Japan Soc Civ Eng* 78(4):344–353
4. Homepage of Japan Society of Science and Technology Agency: Cross-minstrel strategic innovation promotion program: infrastructure maintenance renewal and management. Accessed 01 Dec 2022
5. Achillopoulou DV, Mitoulis SA, Argyroudou SA, Wang Y (2020) Monitoring of transport infrastructure exposed to multiple hazards: a roadmap for building resilience. *Sci Total Environ* 746:141001
6. Iwaki I, Kamiharako A, Koda Y, Naito H, Minagawa H, Suzuki M (2010) Evaluation on properties of concrete and steel in PC bridge girders severely damaged by chloride induced deterioration (in Japanese). *J Mater Concr Struct Pavements* 66(4):413–432
7. Tanaka Y, Yamaguchi T, Shimomura T (2010) Loading test and numerical evaluation of reinforced concrete bridge beam deteriorated by salt attack (in Japanese). *J Mater Concr Struct Pavements* 66(4):466–482
8. Cao Y, Nishimura A, Luo X, Okoshi M, Tang W, Nishimura H (2021) Study on a roadmap model to describe the mechanical behavior related to damage condition of RC beam quantitatively (in Japanese). *J Jpn Soc Exp Mech* 21–23:199–207

9. Nishimura A, Haya H (1991) Assessment of the structural integrity of bridge foundation by impact vibration test. *Int Conf Geotech Eng* 719–724
10. Nishimura A, Haya H (1995) Evaluation of bridge piers soundness on Japanese railway, ERRI (European rail Research Ins.) In: Conference on maintenance of railway bridges and civil engineering structures in Holland, pp 1–13
11. Nishimura A, Haya H (1996) Evaluating the soundness of san-yo Shinkansen by impact vibration test. *Found Eng Equipment (monthly)* 24–9:73–79
12. Yokota T, Wijayawardane I, Mutsuyoshi H (2018) Study on load carrying capacity and analytical performance evaluation method of PC beams having damaged prestressing tendons (in Japanese). *J Japan Soc Civ Eng Ser E2* 74(4):218–233
13. Technical evaluation on design and construction method of IPH method for concrete structures (in Japanese). Organization for Promotion of Civil Engineering Technology, Tokyo, Society of Civil Engineers, Japan (2017)
14. Watanabe G, Tomohiro F, Goto S, Emoto H (2014) Health monitoring and identification of dynamic characteristic of a skewed bridge based on the vibration test using a moving vehicle (in Japanese). *J Struct Eng* 60A:513–521
15. Miyamura M, Naito H, Nakano S, Kado M, Iwaki I, Suzuki M (2016) Study on evaluation of structural performance in 15-years-old PC road bridge after reconstruction under severe chloride environment. *J Japan Soc Civ Eng Ser E2(72–2)*:41–55
16. Iwano S, Morihama K, Gokudan K, Sakai T (2003) Measurement of thickness of concrete by the impact vibration method. *Proce Japan Concr Inst* 25(1):1637–1642
17. Kikuta H, Goto M, Sawamoto T, Shinozaki T, Morihama K (2012) Effect of form and measure of BOSS specimens on compressive strength of concrete. *J Monozukuri Univ* 3:68–73
18. Watanabe H, Tamai T, Masuda H, Kasami H (2006) On the effects of sizes of cylindrical specimens on compressive strength of high strength concrete. *Proc Japan Concr Inst* 28(1):1175–1180
19. Seki M, Nishimura A, Sano H, Nakano S (2003) Study on the evaluation of damage levels of RC rigid frame railway bridges in the case of earthquakes (in Japanese). *J Japan Soc Civ Eng Ser* 2003(731):51–64
20. Watanabe S, Seno K, Kagawa J, Niwa J (2008) Effect of epoxy resin injection on seismic performance of existing RC beam. *Proc Japan Concr Inst* 30(3):1615–1620

Finite Element Simulation of Externally-Prestressed Concrete Girders



Said Elkholy, Ahmed Godat, and Saif Elabsi

Abstract The external prestressing (EP) technique has been noticeably used in either the strengthening of deteriorated reinforced concrete (RC) structures or the construction of long-span girders. This technique has many advantages in terms of its contribution to both flexural and shear capacity of RC girders, the ease of installation, and more convenient maintenance for tendons' inspection and replacement. Considerable number of research have been experimentally investigated the contribution of EP tendons to enhance the capacity of RC girders. However, numerous factors were found to affect the performance of EP RC girders that require further investigation. The main purpose of this study is to develop a three-dimensional finite-element model that is able to simulate the entire behavior of EP RC girders. In this model, appropriate geometrical elements are used to represent the behavior of the concrete, steel reinforcement and EP tendons. The EP tendons are modelled with truss elements connected to the concrete at specific locations, as was the case for the laboratory experiments. Sensitivity analysis is performed for finite element modelling of specimens in order to optimize the mesh size and the number of nodes per element. The numerical predictions of the finite element model are compared with various configurations and materials of EP tendons. It is shown that the numerical predictions compare very well with experimental measurements in terms of ultimate loading capacities, load–deflection relationships and failure modes. The numerical predictions are used to provide useful information of the cracking progress and strain profiles of the simulated girders.

S. Elkholy
Fayoum University, Fayoum, Egypt

A. Godat (✉)
Ajman University, Ajman, UAE
e-mail: a.godat@Ajman.ac.ae

S. Elabsi
United Arab Emirates University, Al-Ain, UAE

Keywords Finite element simulation · Externally-prestressed beams · Geometrical modelling · Finite element predictions · Ultimate loading capacity · Cracking progress

1 Introduction

External prestressing is considered as an effective option for design and strengthening of RC girders due to its great contribution to both flexural and shear capacities since the EP tendons force are applied to the concrete girders [1]. Moreover, the EP technique is characterized with the ease of installation, and convenient of tendons' inspection and replacement without affecting the use of the structure. However, limited number of studies were carried out to investigate the behavior of EP girders compared to the internally-prestressed ones. EP girders exhibit complex behavior that is controlled by many parameters. As summarized in the existing literature, these parameters are the contact bond between the reinforcing steel and concrete, contact bond between the EP tendons and concrete, tendon profile, prestressing losses, anchors deviators [2–7].

In this study, a versatile three-dimensional finite-element model is developed in this research to accurately predict the response of EP girders using the ATENA finite-element package [8]. The proposed three-dimensional numerical model is applied to several cases of EP girders having various configurations. The accuracy of the model is evaluated by comparing the numerical predictions with the experimental results. Once the accuracy of the model is established, the numerical predictions are used to provide useful information of the cracking progress and pattern of the girders. The significance of the present findings with respect to the various results is discussed.

2 Finite Element Model

The numerical analysis was carried out using the finite-element software package ATENA [8] to simulate the entire nonlinear load–deflection behavior of EP girders. The model was modified to accommodate different characteristics and schemes of tendons. The software formulations for the concrete, steel and FRP tendons are detailed in the software guide, and summarized below.

2.1 Concrete

The three-dimensional nonlinear cementitious material model of the FE package (CC3DNonLinCementitious2) was used to simulate the behavior of concrete. The concrete model combines three features to simulate the basic characteristics of

the concrete: (i) a nonlinear stress–strain relation to allow for the strain softening behavior of the material under increasing compressive stresses; (ii) a failure fracture for concrete is used to define the cracking stress in tension and the failure envelope in compression, and (iii) the failure envelopes account for multiaxial stress conditions and a fixed smeared crack model is used to describe the post-cracking behavior of the concrete. The compressive model consists of an ascending branch that represents the hardening phase, as shown in Fig. 1a, and a descending branch that represents the softening phase. In the hardening phase, the material behaves linearly up to a certain value; then, the hardening phase become nonlinear and is governed with the following equation:

$$\sigma_c = f_{co} + (f_c' - f_{co}) \sqrt{1 - \left(\frac{\varepsilon_{cp} - \varepsilon_p}{\varepsilon_{cp}} \right)^2} \tag{1}$$

where σ_c is the compressive stress in the nonlinear hardening part; f_c' is the cylinder compressive strength; ε_p is plastic strain; ε_{cp} is the plastic strain corresponding to the compressive strength. In the softening phase, the material is assumed to behave linearly, as depicted in Fig. 1a. The tension model is assumed linear elastic up to the material tensile strength (f_t), followed by an exponential softening response after the peak point at which concrete has cracked, as presented in Fig. 1b. The slope of the linear ascending branch is taken equal to the material elastic modulus. For the

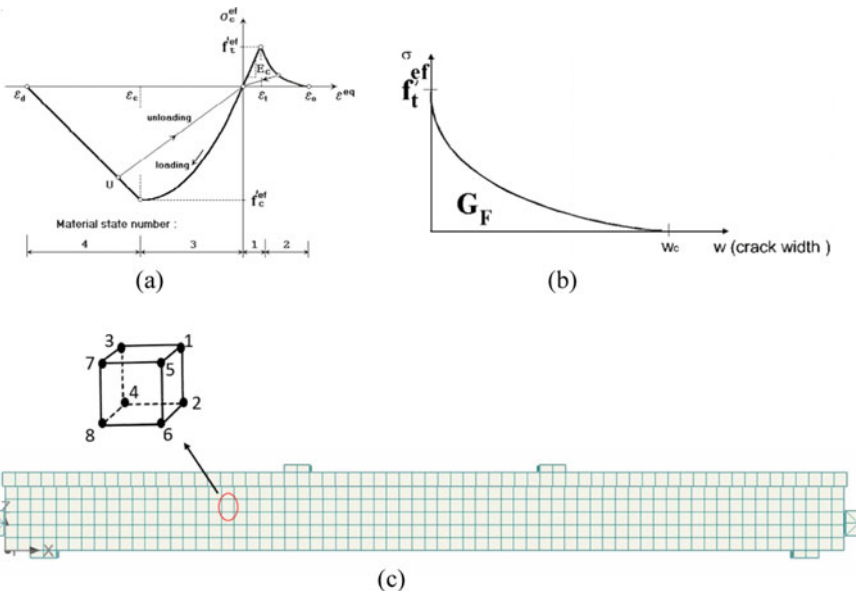


Fig. 1 Typical finite element model [8]: **a** concrete stress–strain relationship; **b** concrete softening behavior under uniaxial tension, and **c** concrete brick element

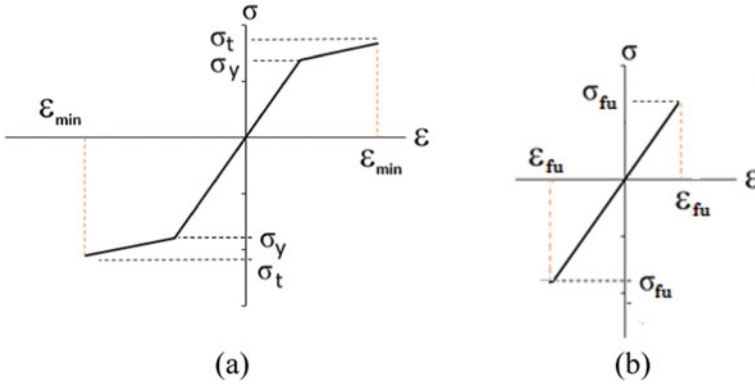


Fig. 2 ATENA constitutive laws [8]: **a** bilinear stress–strain relationship for steel reinforcement, and **b** linear stress–strain relationship for external tendons

finite element implementation, the values of the f'_c , f_t and E_c (MPa) were taken from the relevant set of experimental data.

The concrete behavior was simulated using a hexahedron brick elements that was defined by height-node element, as shown in Fig. 1c. The element has the ability to simulate the nonlinear behavior of the concrete due to its cracking capability in tension, in the three orthogonal directions, and crushing in compression. Each node in this element has three translational degrees of freedom in the x, y and z-directions.

2.2 Steel Reinforcement

The steel reinforcement was represented by a bilinear elastic–plastic constitutive relation with linear strain hardening (Fig. 2a). The ratio between the slopes in the elastic range to the plastic range was taken from the corresponding experimental results. The steel reinforcement embedded in the concrete was modelled using two-node truss elements with three degrees of freedom at each node. A perfect bond was assumed between the steel elements and the concrete elements, since no debonding was experimentally observed between the two components.

2.3 External Tendons

The steel and FRP external tendons were simulated as linear elastic up to failure, as shown in Fig. 2b. A rupture point on the stress–strain relationship was provided to define the maximum stress and strain of the tendons. The response of the two materials was identical in tension and compression. For structural modelling, the external tendons were simulated as truss elements that were directly connected to

the concrete elements at specific locations following the experimental tests. It is of interest to mention that one end of the external tendons (called anchors) was subjected to prestressing force, whereas the other end was passive force. At the location of the deviator, zero friction coefficient was assumed between the cables and the concrete.

2.4 Loading Conditions, Mesh Size and Steel Plates

The loading type employed in this study was displacement-based until failure in order to represent the actual loading scheme as performed experimentally. The displacement-based loading allows to capture the entire load deflection plateau. For the numerical simulation of EP girders, the symmetry of the girders is neglected and the entire girder was considered in order to maintain the stability of the girder and to avoid having numerical errors.

The mesh size at the state of accuracy verification was varied to accommodate the numerical predictions. For each set of experimental tests, mesh sensitivity study was performed in order to examine the effect of the mesh size on the loading capacity of the specimens. Once the accuracy of the model was established for the control specimen, the mesh size was maintained identical for the rest of the specimens. In this study, steel plates located at the loading points, supports and anchorage zones were modelled as an isotropic linear elastic material. Perfect connection between the steel plates and the concrete was assumed, whereas the thickness of the steel plates was taken from the corresponding experimental tests. Monitoring points were determined at the top surface of the loading plate under the applied load, where the prescribed displacements were applied. Another point was specified at the beam mid-span at the bottom surface of the concrete to record the mid-span deflections. In this study, the EP tendons were assumed fully bonded to the concrete at the points of contact as experimentally described. It is necessary to note that no debonding failure was experimentally observed between the EP tendons and the concrete.

2.5 Investigated Specimens

In this study, the numerical investigation involves eight specimens tested: five specimens were tested by Bennitz et al. [9] and three specimens were tested by Wang et al. [10]. Complete details of the specimens considered can be found in their corresponding references. These specimens were selected for numerical analysis to cover various ranges of EP girders. All specimens were simply supported T-section girders, with girder height ranged between 300 and 500mm, and girder span length of 3.30–6.00 m.

The girders were EP with carbon or basalt FRP tendons having prestressing level between 14 and 50% of the tendons' ultimate tensile strength. The numerical simulation considered specimens having three different tendon configurations: no deviator,

one deviator, and two deviators. Table 1 summarizes the mechanical properties of the specimens, and Fig. 3 presents a typical presentation of experimental tests' configurations. It should be emphasized that for a given set of specimens with and without EP, the same values of the various material properties were used.

Table 1 Mechanical Properties of simulated specimens

Beam	Type of support	Type of cross-section	Concrete comp Strength (MPa)	External tendon material	Ultimate strength (MPa)	Tendon profile	Number of deviations
B2[9]	Simply supported	T-section	35.2	CFRP	2800	Straight	1
B3[9]	Simply supported	T-section	33.4	CFRP	2800	Straight	1
B4[9]	Simply supported	T-section	35.9	CFRP	2800	Straight <td>1</td>	1
B5[9]	Simply supported	T-section	28.4	CFRP	2800	Straight	1
B6[9]	Simply supported	T-section	40.6	CFRP	2800	Straight	0
B7[9]	Simply supported	T-section	35.9	CFRP	2800	Straight	0
BD 0.38[10]	Simply supported	T-section	40.5	BFRP	1192	U shape	2
BD 0.5[10]	Simply supported	T-section	40.5	BFRP	1192	U shape	2
BS 0.5[10]	Simply supported	T-section	40.5	BFRP	1192	Straight	0

*CFRP indicates the carbon fiber reinforced polymers; BFRP indicates the basalt fiber reinforced polymers

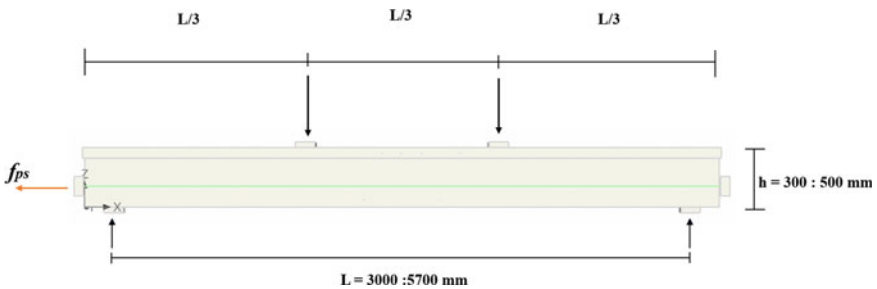


Fig. 3 Geometry and load location of tested beams. (h indicates beam height; f_{sp} indicates tensile strength of prestressing tendons)

3 Numerical Results and Discussions

The primary objective of the numerical investigations is to establish the ability of the proposed model to simulate the behavior of EP girders. The accuracy of the numerical model is evaluated by comparing the numerical predictions to experimental results. Then, having verified the accuracy, the numerical model is utilized to obtain some information of the girders that are difficult to measure experimentally.

3.1 *Ultimate Loading Capacities and Failure Modes*

Table 2 summarizes the predicted loading capacities compared to the experimental results for the various specimens. The table shows that the finite element model was able to accurately predict the loading capacities for the simulated specimens. The predictions for the ultimate load ranged between -12.2 to 12.9% with an average of -5.1% and a standard deviation of 8.2%. This indicates the high agreement between the numerical predictions and the experimental results. It can be observed that the numerical results are, in many cases, lower than the experimental ones. This can be attributed to the assumptions applied for the concrete cover, percentage of prestressing force, concrete tensile strength and percentage of prestressing losses. It should be mentioned that reasonable assumptions were made when any of these values were not provided in the relevant set of experimental data. For the mid-span deflection values correspond to the ultimate loading capacity, the predicted deflections were always lower than those obtained experimentally, as shown in Table 2. The average numerical-to-experimental mid-span deflection is -6.9% with standard deviation of 4.7%. The lower numerical deflection magnitudes can be explained based on the fact that the experimental deflection at failure may not be accurate due to the full bond assumption in the numerical model that produced stiffer results. As shown in Table 2, the numerical model is able to predict failure modes identical to those observed experimentally. The position of the failure in the numerical model corresponds to experimental observations.

3.2 *Applied Load-Midspan Deflection Relationships*

The numerical model used to simulate the experimental beams proves to be capable of correctly modelling general trends and behavior of the applied load-midspan deflection relations with very good accuracy for the specimens considered, as shown in Fig. 4a–h. As it can be observed in the figures, the numerical model shows very good agreement with experimental results. In the initial elastic stiffness and before the cracking appearance, identical curves of the experimental and the numerical results are obtained. It is clear that there is small discrepancy between the stiffness of

Table 2 Comparison between experimental and numerical results

Number of deviators	Beam label	Experimental results		Numerical results		Num. / Exp. Results		Mode of failure
		Ultimate load (kN)	Midspan deflection (mm)	Ultimate load (kN)	Midspan deflection (mm)	% of ultimate load	% of midspan deflection	
<i>No</i>	BS 0.5 [10]	189	81	166	74.6	– 12.17	– 7.90	Flexure
	B6 [9]	140	65	158	56	12.86	– 13.85	Flexure
	B7 [9]	153	42.6	143	38.5	– 6.54	– 9.62	Flexure
<i>One</i>	B2 [9]	147.09	45.4	146.5	45	– 0.40	– 0.88	Flexure
	B3 [9]	171	39.6	162.6	38.5	– 4.91	– 2.78	Flexure
	B5 [9]	178	60	161	53	– 9.55	– 11.67	Flexure
<i>Two</i>	BD0.35 [10]	204	90	185	84	– 9.31	– 6.67	Flexure
	BD0.5 [10]	220	101	196.17	99	– 10.83	– 1.98	Flexure

the experimental curves and numerical predictions. For the post-yield behavior, the numerical model does not accurately describe the applied load-midspan deflection relations. This can be attributed to the failure mode, which occurs earlier in the numerical model compared to the experimental results. Indeed, this phenomenon affected numerical predictions of the maximum deflections.

3.3 Crack Pattern at Failure

Since the numerical model proved its capability to simulate the behavior of EP tendons, the model is used to obtain the crack pattern at failure. The experimental results of the crack pattern was compared to the numerically predicted ones in Fig. 5a, b for girders BD0.5 and BD 0.35, respectively. A very good agreement between the predicted and experimental crack patterns can be observed in the figures. Both the experimental and predicted crack patterns indicate that the failure mode of these girders is flexural failure, which is yielding of longitudinal reinforcement followed by concrete crushing. As can be seen in the figure, vertical cracks are located in the region between the points of applied loads. The cracks' heights and widths are increased as the applied load increase. The cracks extend up to the flange before the failure. This finding indicates that the presence of EP does not change the ductile mode of failure of the girders. It is necessary to mention that few shear cracks appeared in the region between the applied load and the support. As experimentally reported, the failure was characterized by concrete crushing under the points of applied load, which is captured by the numerical model.

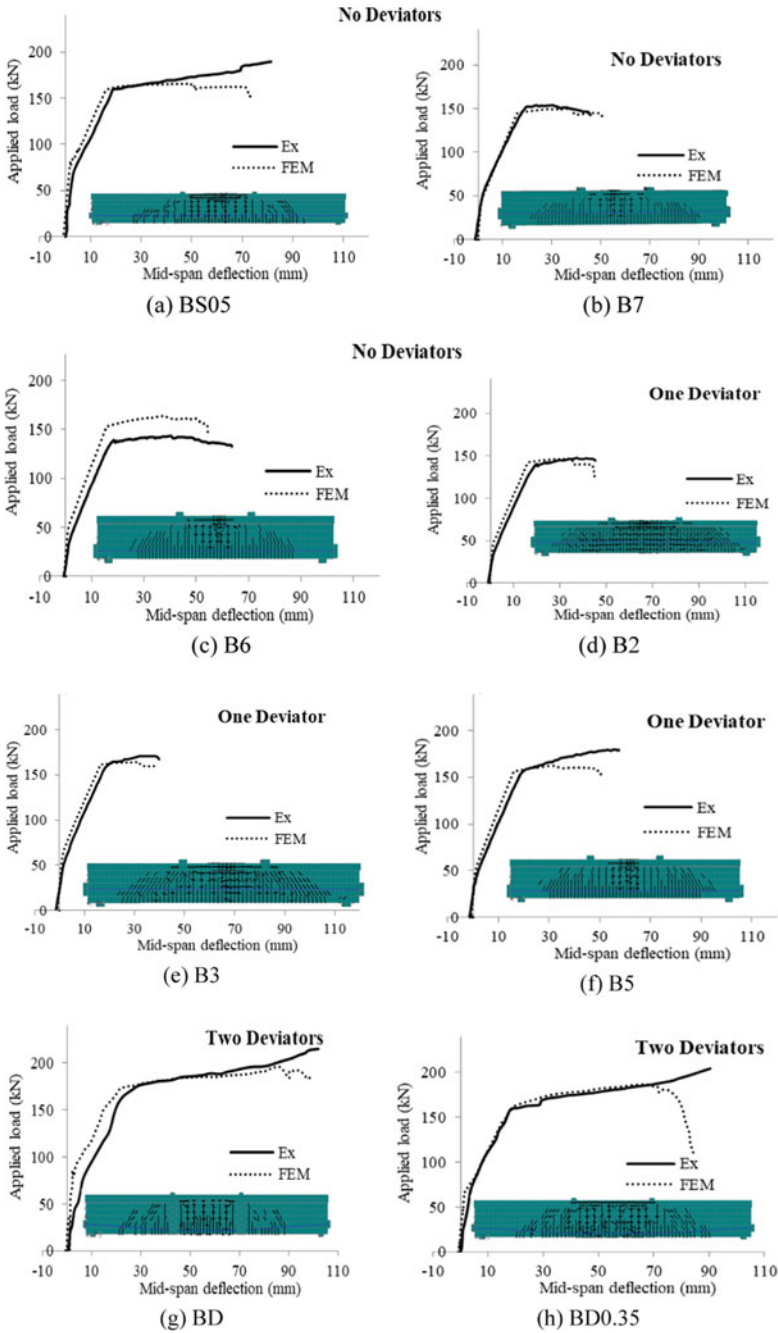


Fig. 4 Experimental versus numerical applied load-midspan deflection relations

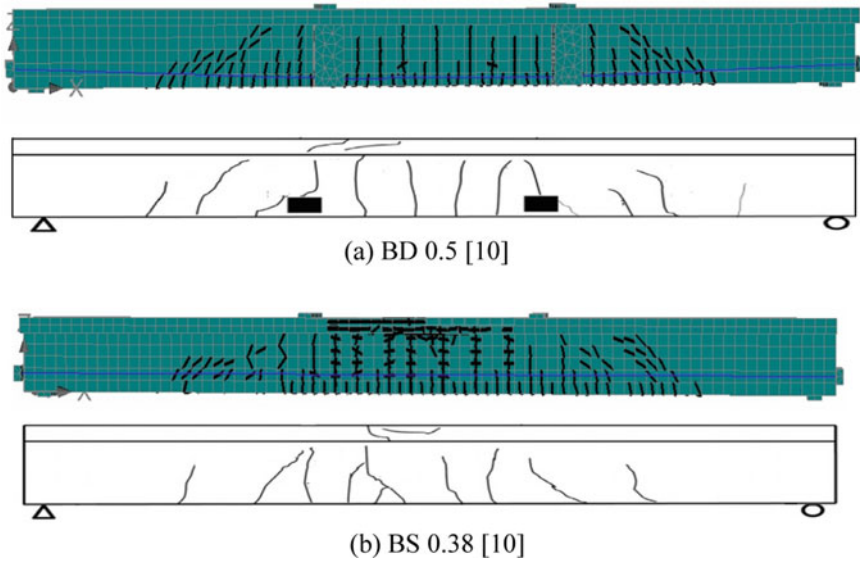


Fig. 5 Numerical and experimental crack patterns at failure

Since the numerical model proved its capability to simulate the behavior of EP tendons, the model is used to obtain the crack pattern at failure. The experimental results of the crack pattern was compared to the numerically predicted ones in Fig. 5a, b for girders BD0.5 and BD 0.35, respectively. A very good agreement between the predicted and experimental crack patterns can be observed in the figures. Both the experimental and predicted crack patterns indicate that the failure mode of these girders is flexural failure, which is yielding of longitudinal reinforcement followed by concrete crushing. As can be seen in the figure, vertical cracks are located in the region between the points of applied loads. The cracks' heights and widths are increased as the applied load increase. The cracks extend up to the flange before the failure. This finding indicates that the presence of EP does not change the ductile mode of failure of the girders. It is necessary to mention that few shear cracks appeared in the region between the applied load and the support. As experimentally reported, the failure was characterized by concrete crushing under the points of applied load, which is captured by the numerical model.

4 Conclusion

This study investigated the numerical modelling of EP girders, which has been rarely examined in the literature, using a non-linear finite-element model that was developed using the ATENA finite element package. The accuracy of the model was

validated using two sets of experimental results having various mechanical properties, prestressing levels and tendon profiles. The numerical predictions for the ultimate loading capacities, load–deflection relationships, and crack patterns at failure were compared to the experimental results. Based on the comparison between the experimental and numerical results, the following conclusions can be proposed:

- The ratios of the predicted-to-experimental ultimate loading capacities at failure of the tested girders ranged between -12.2 and 12.9% with an average and standard deviation of -5.1% and 8.2% respectively. These results indicated the high accuracy of the numerical models to predict the performance of EP girders;
- The numerical model was successful to predict the general trends of the applied load-midspan deflection relations for the experimental results. The predicted mid-span deflections corresponding to the ultimate loading capacity at failure were smaller than the experimental results with an average of 6.9% and standard deviation of 4.7% ;
- Both the experimental results and numerical model showed a flexural failure mode. In addition, the numerical model was able to track the failure progress with similar cracking scenario as the ones observed experimentally. It is necessary to indicate that the use of deviator with no friction had neither effect on the failure progress nor on the ultimate loading capacities compared to the experimental ones.

References

1. Lin TY, Burns NH (1981) Design of prestressed concrete structures, 3rd edn. Wiley, New York
2. Zona A, Ragni L, Dall'Asta A (2008) Finite element formulation for geometric and material nonlinear analysis of beams prestressed with external slipping tendons. *Finite Elem Anal Des* 44(15):910–919
3. Lou T, Lopes SM, Lopes AV (2012) Numerical analysis of behaviour of concrete beams with external FRP tendons. *Constr Build Mater* 35:970–978
4. Lou T, Xiang Y (2010) Numerical analysis of second-order effects of externally prestressed concrete beams. *Struct Eng Mech* 35(5):631–643
5. Lou TJ, Lopes AV, Lopes SMR (2012) Influence of span-depth ratio on behavior of externally prestressed concrete beams. *ACI Struct J* 109(5):687–695
6. Lou T, Lopes S, Lopes AA (2014) Finite element model to simulate long-term behavior of prestressed concrete girders. *Finite Elem Anal Des* 81(1):48–56
7. Elkholy S, El-Ariss B (2016) Improving the robustness of reinforced concrete framed structures under sudden column losses. *J Protective Struct* 7(2):282–300
8. Cervenka V, Jendele L, Cervenka J (2020) ATENA program documentation theory. Cervenka Consulting
9. Bennitz A, Schmidt JW, Nilimaa J, Täljsten B, Goltermann P, Ravn DL (2012) Reinforced concrete T-beams externally prestressed with unbonded carbon fiber-reinforced polymer tendons. *ACI Struct J* 109(4):521–530
10. Wang X (2015) Effectiveness of basalt FRP tendons for strengthening of RC beams through the external prestressing technique. *Eng Struct* 101:34–44

Dilated Brick Masonry Infills to Avoid the Diagonal Compression Struts During Lateral Reversed Cyclic Load



Jafril Tanjung, Maidiawati, Yulia Hayati, and Masrilayanti

Abstract In high seismicity areas such as Indonesia, brick masonry has been widely applied as a partition as well as infills in reinforced concrete (RC) buildings. One of the disadvantages of using brick masonry infilled in RC buildings is that the diagonal compression struts may occur during the earthquake shaking, which may influence the seismic performance of its structure. Due to its diagonal strut, the columns will undergo additional axial and shear loads. The situation may collapse columns early. This study proposes the dilated brick masonry infill to overcome the above disadvantage. The advantage of its dilated brick masonry was obtained through structural testing of three 1:4 scaled-down RC frame specimens applied to lateral reversed cyclic loading. The specimens include one bare frame, one with full masonry infill, and one with dilated masonry infill. For the specimen with the dilatation masonry, there was a dilatation of about 20 mm between the masonry and columns. During structural testing, the deformations of specimens were measured. The cracks pattern of the columns and masonry was also drawn to observe the failure mechanism of the specimens. Comparing the experimental results shows that the dilated masonry infill has suitably avoided the diagonal strut on the masonry infill. As we predicted, the ductility of the frame with dilated masonry was similar to the bare frame without significantly reducing its seismic capacity. The observation during the test showed that the interface between masonry infills and the beams was weak. The applied static reversed lateral loading made the area experience shear stress—the cracks on the masonry started from its area. Strengthening of its interface areas is required to apply this proposed dilated masonry infill.

Keywords RC building · Masonry infill · Seismic performance · Cyclic loading

J. Tanjung (✉) · Masrilayanti
Andalas University, Padang 25163, Indonesia
e-mail: jafriltanjung@eng.unand.ac.id

Maidiawati
Padang Institute of Technology, Padang 25143, Indonesia

Y. Hayati
Syiah Kuala University, Banda Aceh 23373, Indonesia
e-mail: yuliahayati@unsyiah.ac.id

1 Introduction

Indonesia is known as one of the most earthquake-prone areas in the world. The United States Geological Survey (USGS) recorded that Indonesia experiences earthquakes with a significant magnitude [1]. During 2016 and 2018, for instance, Indonesia experienced several major earthquakes, such as the 2016 Pidie Jaya earthquake (M6.5) [2], the 2018 Lombok earthquake (M6.4, M7.0, M6.9) [3], and the 2018 Palu earthquake (M7.4) [4]. These earthquake shocks have caused damage to many residents and buildings, including those supported by RC frame structures.

Several researchers have conducted post-earthquake observations to determine the cause of damage to RC buildings due to earthquake motions. For instance, the EERI [5] conducted observations after the 2009 West Sumatra earthquake, and Choi et al. [6] predicted the structural response of the damaged RC building due to the 2009 West Sumatra earthquake. Maidiawati et al. [7] analyzed the causes of the collapse of the RC buildings due to the 2018 Palu earthquake. The main reasons for damage and collapse to the buildings were dominated by using low-quality construction materials and poor detailing of reinforcement of the RC frame structures; the detailing reinforcement has inadequate earthquake-resistant building standards. Despite having experienced a major West Sumatra earthquake in 2009, the RC buildings' construction processes have not yet wholly followed the current Indonesian provisions, as observed by Wardi et al. [8]. They observed the construction process of almost one hundred RC buildings in West Sumatra several years after the 2009 earthquake. Based on the authors' experience when observing damages to the buildings after the 2009 West Sumatra, 2016 Pidie Jaya, 2018 Lombok, and 2018 Palu earthquakes have also concluded similar results.

In Indonesia, burned red brick masonry is commonly used as the infill walls in RC buildings. The walls are used for partitioning between rooms and as the exterior walls of the buildings. Because the final stress distribution of the masonry infill to the RC frame structure has not been unknown in many cases, engineers have not taken it into account in the design process of the buildings. The masonry was assumed to be non-structural components, where their interaction with the columns was not considered. Therefore, the structure response may deviate from what we expected in design. However, the post-earthquake observation and laboratory tests conducted by Maidiawati et al. showed that masonry infills increase the capacity of RC structures [9, 10]. Their test used the cropped brick masonry wall from the surviving building due to the 2007 West Sumatra earthquake to search for the advantage of the masonry infill when shaken by the earthquake.

Indeed, experimental research regarding the effect of brick masonry infills on RC frame structures has been performed and well documented by the researchers, see Tanjung et al. [11], Maidiawati et al. [12], and Cavaleri et al. [13]. They tested several scaled-down RC frame specimens subjected to lateral static monotonic and cyclic loadings, including full and partial infill, where the bricks were produced locally. Most of their experimental results arrive at the masonry infill plays an important role in the performance of the RC frame structures when subjected to lateral cyclic loads.

The existence of the infills has completely changed the responses of the RC frame structure. The lateral strength, ductility, and failure modes of the structures depend on the properties of the infills. Particularly related to the failure modes of the infill in RC frame structures were explained by Cavaleri et al. [13]. Meanwhile, the research on how to derive the mathematical expression for the infill in the RC frame structure has been well explained by Catherin et al. [14] and Durai et al. [15]. Tanjung et al. [16] also conducted an analytical study to determine the seismic capacity of a multistory RC frame structure infilled with brick masonry to verify the results obtained from the post-earthquake observation.

Although the infills contribute to the excellent performance of the RC building during the earthquake, however, the infill causes several undesirable effects such as short columns, soft story, torsion, and out-of-plane collapse. When the infill failed and collapsed, it often caused fatalities. The researchers developed and proposed strengthening methods to overcome the disadvantage of the infill in RC structures. Akhoundi et al. [17] strengthened them using textile-reinforced mortar. Tanjung et al. [18] proposed the strengthening method by embedding the plain steel bars on the masonry infill and subjecting them to lateral monotonic static loading. Tanjung et al. [19] and Maidiawati et al. [20] have extended their previous research by applying cyclic static lateral loads to the specimens. Another simple strengthening method has also been proposed by Tanjung et al. [21]. They skew the chicken wire mesh on the diagonal area of the masonry infill. This wire mesh is cheaper and easy to find in the local market in Indonesia. Their study aims to define a strengthening method that an effective, cheaper, and easy to apply.

Post-earthquake observation and experimental results showed that the infill interferes with the deformation of the RC frame structures. Tensile will take along one diagonal of the infill, causing the separation between the infill and RC frame components. Meanwhile, the compression strut forms take place along the other diagonal. Consequently, the infill will add lateral stiffness to the structure. Load transfers of the structures will change from frame action to predominant truss action. The columns experience increased axial forces, reduced bending, and shear forces. This situation may cause the premature collapse of the columns.

This paper presents the experimental study to avoid the diagonal struts in the infill during lateral loading of infilled RC frame structures. The dilated brick masonry infill is proposed. The works used structural testing facilities at the Structure and Construction Material Laboratory of Syiah Kuala University, Banda Aceh, Indonesia.

2 Materials and Methods

2.1 The Specimens

Figure 1 depicts the geometry and reinforcement arrangement of the RC frame specimens. Yield in flexure before shear failure was designed into the columns. Following the 1:4 scaled-down of the low-rise building in West Sumatera, INDONESIA, the cross-section of the columns was set to 125 mm \times 125 mm, and the height of the columns was 750 mm. The reinforcement of 4D10 longitudinal bars and 4@50 transverse hoops were installed on these columns. A beam on the top of the specimen was constructed 200 mm \times 200 mm and 1550 mm long, where the loading will apply. Its beam used 4D13 and ϕ 6@50 longitudinal bars and transverse stirrups, respectively. A beam supported the specimen with a 700 mm \times 150 mm cross-section and a span 1650 mm long. Its reinforcements were 12D16 longitudinal bars and ϕ 6@50 transverse stirrups. Standard laboratory testing procedures were applied to obtain the material properties for constructing the specimens. Table 1 tabulates the compressive strengths of the cylindrical concrete and the brick masonry. The concrete cylinder was tested 28 days after casting. For the reinforcements, standard tensile testing was operated. The testing results are shown in Table 2.

Figure 2 shows the sketch of the specimens tested for this study, i.e., bare frame (Fig. 2a), frame with full infill (Fig. 2b), and frame with dilated infill (Fig. 2c). For a frame with dilated infill specimen. There was a dilatation of about 20 mm between the infill and columns.

2.2 The Experimental Setup, Instrumentation, and Loading

At first, a specimen was positioned on the rigid floor. We fastened the lower beam to the rigid floor using six post-tensioning rods to keep the specimen in position during structural testing. A double-action lateral actuator force equipment, including a built-in load cell, was attached and fastened to the strong wall using four post-tensioning rods—the actuator was directly connected to a portable data logger for recording the applied load to the specimen. A manual jack pump was used to supply the pressure to the actuator. The double steel beams were horizontally installed on the top beam to prevent the specimen deforms out-of-plane when the lateral force was applied during testing. These horizontal double steel beams were linked to the actuator, which was mounted on the strong wall. The schematic experimental setup for the current study is shown in Fig. 3a. For measuring the deformation of the RC frame specimen during testing, the displacement transducers (LVDTs) have been installed at certain points, as shown in Fig. 3b.

The lateral static reversed cyclic loading was subjected to the top beam of the RC frame specimens. The loading procedure has followed FEMA461 [22]. The lateral displacement control with a loading speed of approximately 0.05 mm/s was applied.

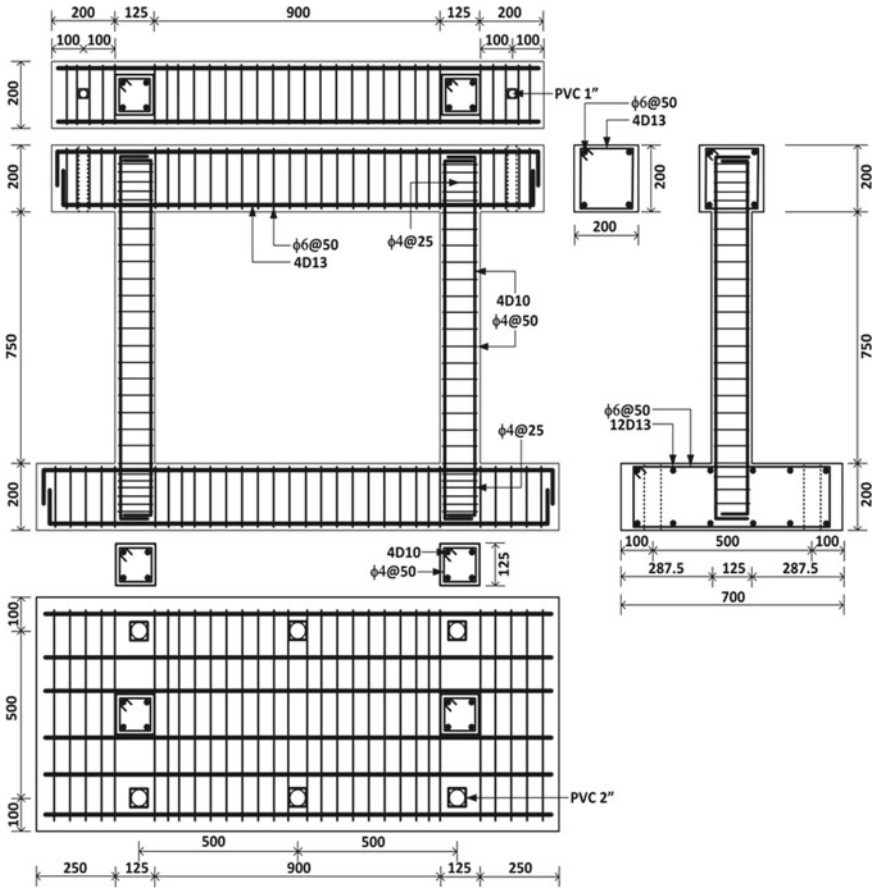


Fig. 1 The geometry and reinforcements of the RC frame specimen

Table 1 Mechanical properties of concrete and brick masonry

Material	Compressive strength (MPa)
Concrete	30.6
Brick	9.40

Table 2 Mechanical properties of reinforcements

Type	Yield strength (MPa)	Tensile strength (MPa)
phi 4	390.20	574.90
phi 6	346.80	446.30
D10	324.60	449.50
D13	374.30	535.40

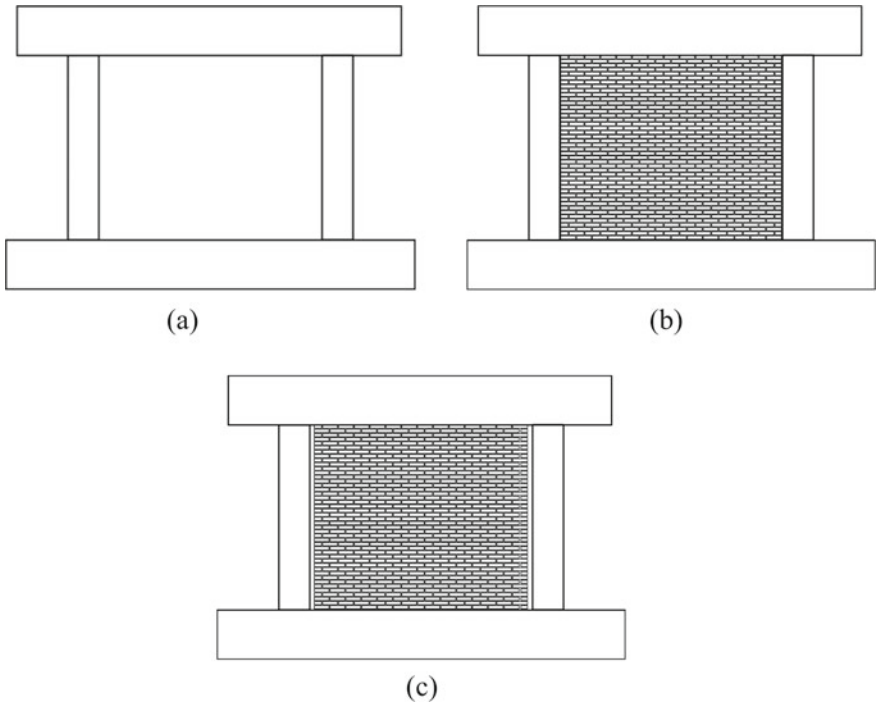


Fig. 2 The RC frame specimens, **a** Bare Frame (BF-S), **b** Frame with Masonry Infill (IF-SW), **c** Frame with Dilated Masonry Infill (IF-DL)

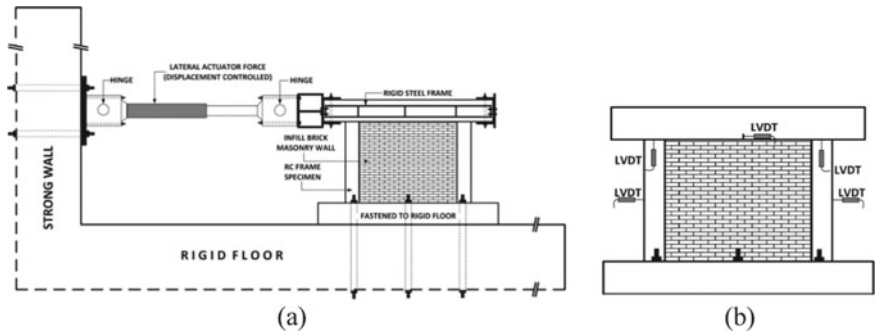


Fig. 3 The Experimental setup and its instrumentation, **a** the experimental setup, **b** the arrangement of LVDTs

An LVDT apparatus on the top beam’s bottom face was used as a displacement control point. The lateral static loading on the top beam was controlled by the drift ratio of the column $R = \delta/H$, where δ is the lateral displacement at the center of the top beam measured by the displacement transducer, and H is the distance between

the transducer and the bottom of the column. The loading program was $R = 1/800$, $R = 1/400$, $R = 1/200$, $R = 1/100$, $R = 1/50$, $R = 1/25$, and $R = 1/12.5$ rad, followed by a pushover to $R = + 1/10$. Except for the first drift ratio $R = + 1/800$, two cycles were applied for each drift ratio. Incremental lateral static load and specimen deformation were monitored and recorded throughout the tests. An initial crack and crack propagation was drawn on the RC frame and brick masonry infill in every loading cycle to recognize the failure mechanism of the specimens.

3 Results and Discussion

Figure 4 shows a comparison of the experimental results. The figure includes the crack pattern after the first cycle of drift ratio $R = 1/25$ (Fig. 4a) and the hysteresis loop displaying the relation between applied lateral load and displacement on the top beam (Fig. 4b). The drift ratio $R = 1/25$ was considered for an observation comparison because the collapsed pattern of the test object could be observed.

For the BF-S specimen, an initial flexural crack appeared at the top side of the tensile column after the drift ratio $R = 1/400$ (0.25% radian), approximation at about the lateral displacement of 1.2 mm. An initial shear crack on the compressive column occurred during the drift ratio $R/200$ (0.5% radian); the lateral displacement at that time was 3.8 mm. The ultimate lateral strength was 51.3 kN. The compressive column experienced shear failure at the lateral displacement of 57.8 mm after the last cycle of drift ratio $R = 1/12.5$ (8% radian). As we expected, the RC columns in the specimen exhibited flexural failure before experiencing the shear failure.

In the IF-SW specimen, the brick masonry infill causes a significant increase in its lateral strength. The increase of the lateral stiffness was indicated by increasing the lateral strength of the specimen, i.e., 127.7 kN, as shown in Fig. 4b. It increased about 2.5 times compared to the bare-frame specimen BF-S lateral strength. The column and brick masonry infill separation started at the applied loading ($R = 1/800$). The initial flexure crack on the column was observed at the lateral displacement of about 1.3 mm within the drift ratio $R = 1/400$ (0.25% radian). When reaching the lateral displacement of about 3.4 mm, the brick masonry began to crack on the diagonal area of the infill, which was within the drift ratio $R = 1/200$ (0.5% radian). The diagonal crack developed and failed at the drift ratio $R = 1/50$ (2% radian). After that, the lateral strength of the specimen was significantly degraded, and the path of lateral strength seemed to follow the bare frame specimen.

One of the disadvantages of brick masonry infilled in the RC frame is the existence of diagonal compression struts on the brick masonry during loading. These compression struts caused diagonal shear cracks on the diagonal area of the brick masonry infills, and the column suffered additional axial and shear loads. Comparing the experimental results of the BF-S and IF-SW specimens after the drift ratio $R = 1/25$ shows that the columns in the IF-SW specimen resisted larger forces than that of the BF-S specimen, as indicated by cracks that occurred in these columns.

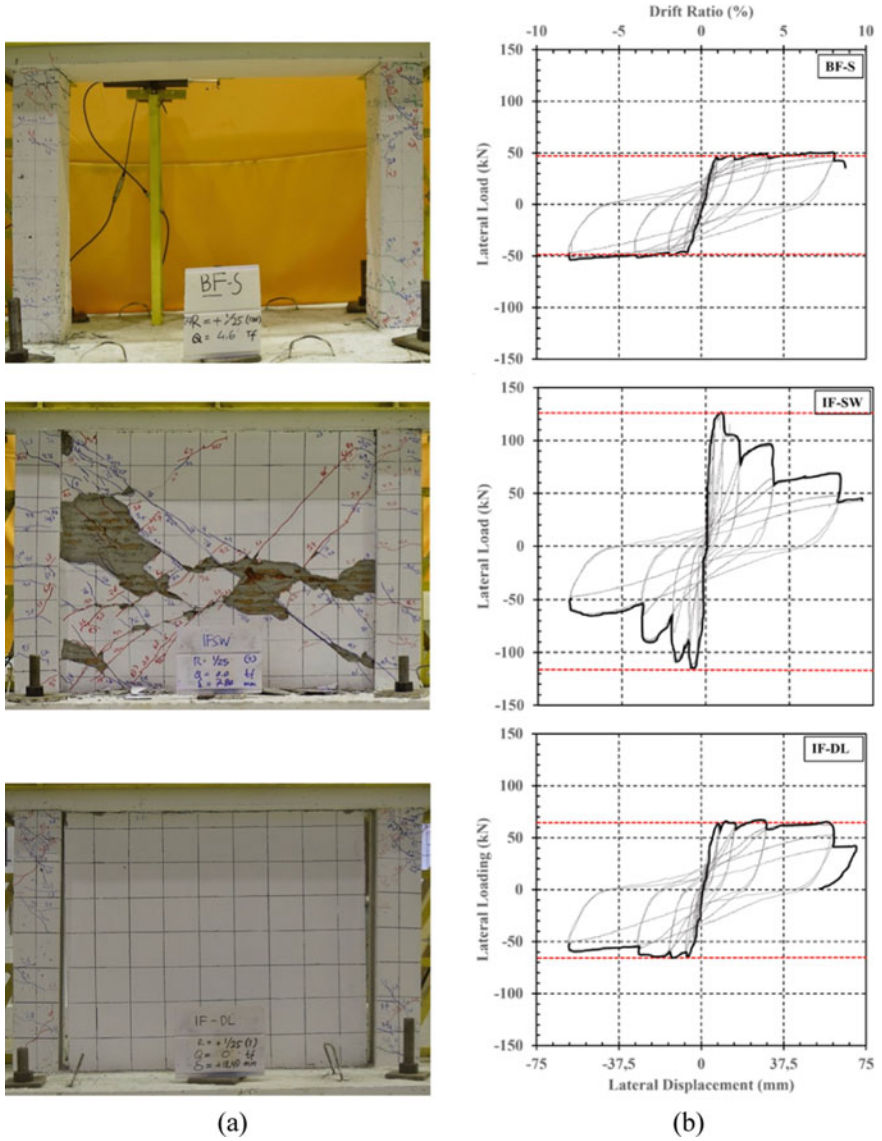


Fig. 4 The comparison of experimental results, **a** crack pattern after 1st cycle of 1/25 rad, **b** hysteresis curves

For the IF-DL specimen case, the dilatation of the masonry infill did not significantly increase the lateral strength and stiffness of the RC frame structure compared to the bare frame specimen. The maximum lateral strength was 67.8 kN. The lateral strength was much lower than the infilled frame without dilatation (IF-SW). Significant differences in crack patterns and failure mechanisms between IF-DL and IF-SW

specimens, as shown in Fig. 4. An initial flexural crack occurred at the top tensile column at a drift angle of $1/800$ of cyclic lateral load. The initial shear crack appeared at the tensile column at $1/400$ of the cyclic loading. The shear cracks were developed at the ends of both columns. Finally, the columns failed in shear during the loading cycles of $R = 1/12.5$. The brick infill began to crack during the cyclic loading of $R = 1/12.5$. It failed in shear in these cycles.

The ultimate lateral strength of the BF-S specimen was 51.0 kN, and the average lateral strength in each cycle was about 49.5 kN. Similar behavior was also seen in the test results of the IF-DL specimen, where the ultimate strength was 67.8 kN, and the average lateral strength for each cycle was about 65.5 kN. These results indicate that the masonry infills in the RC frame specimen of IF-DL did not affect the performance of the specimen. In contrast to the IF-SW test results, the masonry infill significantly increases the lateral strength of the specimen, and the lateral strength decreases after the masonry infills cracks. The lateral strength path BF-S and IF-DL will eventually be similar after the masonry infills collapse.

Based on the hysteresis loop and crack propagation of the IF-DL specimen, its performance was very different from the IF-SW specimen but similar to the bare frame specimen (BF-S), as shown in Fig. 4. The results indicate that the masonry infilled RC frame structure using dilatation spacing has no significant effect on the performance of the RC frame. Therefore, this method may ignore the existence of masonry infill in the seismic design calculation.

4 Conclusion

An experimental study to evaluate the performance of the brick masonry-infilled RC frames with and without dilatation spacing was performed under a cyclic lateral loading test. The testing specimens include RC bare frame, brick masonry infilled frame, and brick masonry infilled frame with dilatation spacing. Comparing the experimental results of these specimens concluded that the brick masonry infill does not affect the performance of the RC frame when the masonry infill dilatates to the columns. Therefore the existence of masonry infill may be ignored in seismic design calculation.

Acknowledgements The first author gratefully acknowledges financial support from the Engineering Faculty of Andalas University for the grand under contract number 030/UN.16.09.D/PL/2020 to publish this article. The authors also sincerely acknowledge the staff of the Structure and Construction Material Laboratory, Engineering Faculty, Syiah Kuala University, for supporting during the preparation of the specimens, providing the structural testing facilities, and conducting the structural tests.

References

1. Seismicity of the Earth 1900–2012 Sumatra and vicinity: U.S. Geological Survey Open-File Report 2010–1083-L, scale 1:6,000,000. <https://pubs.usgs.gov/of/2010/1083/l/>. Access 12 June 2022
2. Irsyam M, Hanifa NR, Djarwadi D (2017) A Study of Aceh Pidie Earthquake, Aceh Province, Indonesia (in Bahasa), Research Institute for Human Settlements, Bandung
3. Irsyam M, Hanifa NR, Djarwadi D (2018) A Study of the Lombok Earthquake Series, West Nusa Tenggara Province (in Bahasa), Research Institute for Human Settlements, Bandung
4. Irsyam M, Hanifa NR, Djarwadi D (2018) A Study of Palu Earthquake, Central Sulawesi Province (in Bahasa), Research Institute for Human Settlements, Bandung
5. EERI, Learning from Earthquakes: The Mw 7.6 Western Sumatra Earthquake of September 30, 2009, EERI Special Earthquake Report (2009)
6. Choi H, Sanada Y, Kashiwa H, Watanabe Y, Tanjung J, Jiang H (2016) Seismic response estimation method for earthquake-damaged RC buildings. *Earthquake Engng Struct Dyn* 45:999–1018
7. Maidiawati, Tanjung J, Sanada Y, Nugroho F, Wardi S (2020) Seismic analysis of damaged buildings based on post-earthquake investigation of the 2018 Palu Earthquake. *Int J GEOMATE* 18(70):116–122
8. Wardi S, Sanada Y, Kita M, Tanjung J, Maidiawati (2018) Common structural details and deficiencies in Indonesian RC buildings: preliminary report on field investigation in Padang City, West Sumatra. *Int J Adv Sci Eng Inf Technol* 8(2):418–425
9. Maidiawati, Sanada Y, Konishi D, Tanjung J (2011) Seismic performance of nonstructural brick walls used in Indonesian R/C buildings. *J Asian Archit Build Eng* 10(1):203–210
10. Maidiawati, Sanada Y (2016) R/C frame–infill interaction model and its application to Indonesian buildings. *Earthquake Eng Struct Dyn* 46:221–241
11. Tanjung J, Ismail FA, Maidiawati Nur OF, Mahlil (2019) Experimental study for evaluating the seismic performance of RC frame structure with partially infilled by brick masonry. *Int J GEOMATE* 16(57):189–194
12. Maidiawati, Agus, Sanada Y, Tanjung J (2017) Seismic performance evaluation of Indonesian existing R/C building considering brick infill. In: *Proceedings of Sustainable civil engineering structures and construction materials, SCESCM 2016, Procedia Engineering*, vol 171, pp 1043–1051
13. Cavaleri L, Trapani FD (2014) Cyclic response of masonry infilled RC frames: experimental results and simplified modeling. *Soil Dyn Earthq Eng* 65:224–242
14. Catherin JM, Jayalekshmi BR, Venkataramana K (2013) Modeling of masonry infills—a review. *Am J Eng Res* 2:59–63
15. Durai TNP, Arunachalam J, Karthich LA (2016) Computational model for infill walls under cyclic loads. *Int J Appl Eng Res* 11(4):2786–2790
16. Tanjung J, Maidiawati, Alfajri A (2019) Effect of brick masonry infills to seismic capacity of Indonesia multistory RC building. *Int J GEOMATE* 16(57):42–48
17. Akhoundi F, Vasconcelos G, Lourenço P, Silva LM, Cunha F, Figueiro R (2018) In-plane behavior of cavity masonry infills and strengthening with textile reinforced mortar. *Eng Struct* 156:145–160
18. Tanjung J, Maidiawati, Nugroho F (2017) experimental investigation of the seismic performance of the R/C frames with reinforced masonry infills. In: *Proceedings of the international conference of global network for innovative technology and AWAM international conference in civil engineering (IGNITE-AICCE'17)*, AIP Conference Proceedings, vol 1892, paper 020009-1-020009-8
19. Tanjung J, Maidiawati (2020) Cyclic behavior of the R/C frames with reinforced masonry infills. In: *The 4th international conference on earthquake engineering and disaster mitigation, 4th ICEEDM 2019, E3S Web of Conference*, vol 156, paper 05014

20. Maidiawati, Tanjung J, Hayati Y, Agus, Rangga S (2020) Seismic performance of brick masonry infilled frame structures with bed joint reinforcements. In: The 4th international conference on earthquake engineering and disaster mitigation, 4th ICEEDM 2019, E3S Web of Conference, vol 156, paper 03004
21. Tanjung J, FIsmail FA, Maidiawati, Putra R (2020) A simple method for strengthening the brick masonry infilled in the reinforced concrete frame structure Int J GEOMATE 18(66):118–123
22. FEMA 461, Interim Testing Protocols for Determining the Seismic Performance Characteristics of Structural and Nonstructural Components, Federal Emergency Management Agency, California (2007)

Effect of Longitudinal Tension Bars on Performance of Composite Light Gauge Steel and Concrete of a Plate Structure



Sabril Haris, Rendy Thamrin, Mutia Fitriani, and Syukriati

Abstract This paper studied the performance of composite light gauge steel and concrete applied on a plate structure. A light gauge steel section is initially proposed to replace longitudinal bars on resisting tension stress at the lower zone of the plate section. Experimental tests have been conducted for six specimens: three specimens of composite light gauge steel and concrete and three other composite specimens with longitudinal reinforcing bars, which were so-called hybrid specimens. A static monotonic load was applied to each specimen until the ultimate condition reached. It was observed that the first crack occurred at the bending moment zone for the hybrid section and around the two-point loads. Compression crushes on the top fiber and diagonal shear failure resist the specimen to obtain a higher capacity. The structural stiffness decreased for additional tension bars within the range of 10.2–20.8%. About the structural ductility, the hybrid specimens had 1.55–1.71 lower than the composite specimens.

Keywords Composite structures · Hybrid section · Ultimate condition · Crack pattern · Ductility

1 Introduction

Light gauge steel materials have been applied primarily on roof structures and wall partitions. This material has some advantages in its strength, lightweight section, and installation convenience. However, the use of light gauge steel materials for other structural applications, for example, for composite structures, has been studied by some researchers.

One of the pioneers in the studies of composite light gauge steel and concrete beams was reported in [1]. It was found that the lip part of the lip-channel section steel plays a significant role in resisting the slip between concrete and light gauge steel

S. Haris (✉) · R. Thamrin · M. Fitriani · Syukriati
Department of Civil Engineering, Universitas Andalas, Padang, Indonesia
e-mail: sabril.haris@eng.unand.ac.id

© The Author(s), under exclusive license to Springer Nature Singapore Pte Ltd. 2024
M. Casini (ed.), *Proceedings of the 3rd International Civil Engineering and Architecture Conference*, Lecture Notes in Civil Engineering 389,
https://doi.org/10.1007/978-981-99-6368-3_21

247

material. Therefore, the composite beams had significant bending moment capacity with good bond strength. In [2], the channel sections with circular embossments were observed to increase the slip resistance between concrete and light gauge steel material. Based on the test results of 32 specimens, simplified formulations to calculate the shear-bond resistance and the flexural capacities were proposed.

Tsu et al. [3] investigated another composite structural system. Light gauge steel beams supported the reinforced concrete structural plate on a corrugated cold-formed metal deck. Meanwhile, the channel section in reversed position was studied in [4]; this was opposite to the light gauge steel arrangement in [1, 2]. Stand-off screws as shear connectors played a significant role in providing sufficient resistance for composite action. In [5, 6], light gauge steel and concrete are also investigated for a column element. It was found that light gauge steel can be used to substitute the steel bar reinforcement.

In this paper, the effect of longitudinal tension bars on performance of composite light gauge steel and concrete of a plate structure was studied for a plate structure. Six specimens were tested in this experimental study: 3 specimens of composite light gauge steel and concrete and 3 other specimens with additional longitudinal bars. The plate width was 300 mm, which was wider than the specimen used in the previous study [7]. Section depths of the plate structures were 80, 100, and 120 mm, which are within the range of typical plate thickness. A standard channel section of light-gauge steel, denoted as C.75.35.075, was used in the composite specimen.

2 Methodology

Experimental tests for six specimens were conducted at the Material and Structures Laboratory, Department of Civil Engineering, Universitas Andalas, Indonesia. All of the specimens were subjected to a static monotonic load. Behavior of the specimens were observed until the ultimate load obtained.

2.1 Specimens

This study tested two types of plate specimens, as illustrated in Fig. 1. The first type of specimen was a composite of light gauge steel and concrete structures. Four-channel sections of light-gauge steel were put on the bottom of the specimen, and arranged side by side. Dimension of the channel section was 75 mm in height, 35 mm in width, and 0.75 mm in thickness resulting in the total area for four-channel sections being 468 mm².

The second type of specimen was named the hybrid section. Along with the light gauge steel section, four longitudinal tension bars were placed 25 mm from the bottom of the specimen. Therefore, there was a contribution from both the tension

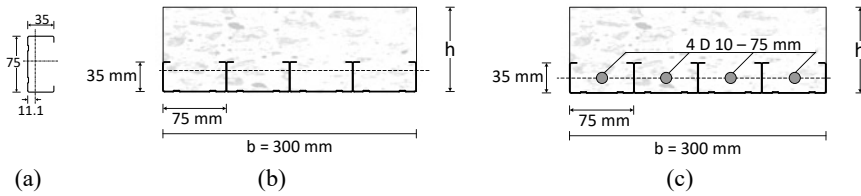


Fig. 1 Specimen: **a** light gauge steel section, **b** composite section, and **c** hybrid section

Table 1 Data of specimen

Type	Specimen's name	Specimen's Id	Reinforcement	Depth (mm)
Composite	Comp-80	CR0.h80.b300	–	80
	Comp-100	CR0.h100.b300	–	100
	Comp-120	CR0.h120.b300	–	120
Hybrid	Hybrid-80	CR10.h80.b300	4 D10	80
	Hybrid-100	CR10.h100.b300	4 D10	100
	Hybrid-120	CR10.h120.b300	4 D10	120

bars and the light gauge steel section in the tension zone. The diameter of tension bar is 10 mm.

All plate specimens had the same total length of 2300 mm and width of 300 mm. The plate depth (h) was varied for 80, 100, and 120 mm for each type of specimen. Data of specimens are given in Table 1. A commercial ready mix concrete company supplied concrete material with a target strength of 35 MPa. However, the compression test gave a slightly lower result at a strength of 33 MPa. For the longitudinal tension bars, the average yield stress from three tensile specimens was 515 MPa. Meanwhile, the average yield stress for the light gauge steel material was 481 MPa, less than expected at 550 MPa.

2.2 Experimental Setup

Figures 2 and 3 show the experimental setup scheme and a photo of the typical tested specimen. The specimen was placed on the pin and rolled supports with a clear distance of 2000 mm. With the 2300 mm length of the specimen, it will be 150 mm remaining length for end anchorage at each support. A 500 kN capacity hydraulic jack loaded the specimens monotonically until the ultimate condition occurred. The load cell, placed under the hydraulic jack, measured the monotonic load. The monotonic load was transferred to the specimen using a steel spreader beam and steel saddles to produce two points loading scenario. The pure bending moment span between two steel saddles was 400 mm, leaving 800 mm of the shear span length. Three LVDTs

measured displacements in three locations: at the mid-span and the two-point loads. A data logger recorded all deflection data from the and the load data from the load cell.

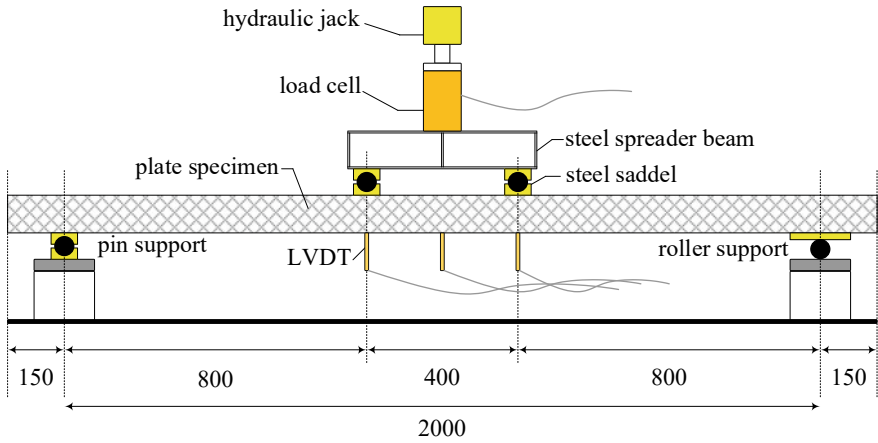


Fig. 2 Experimental setup

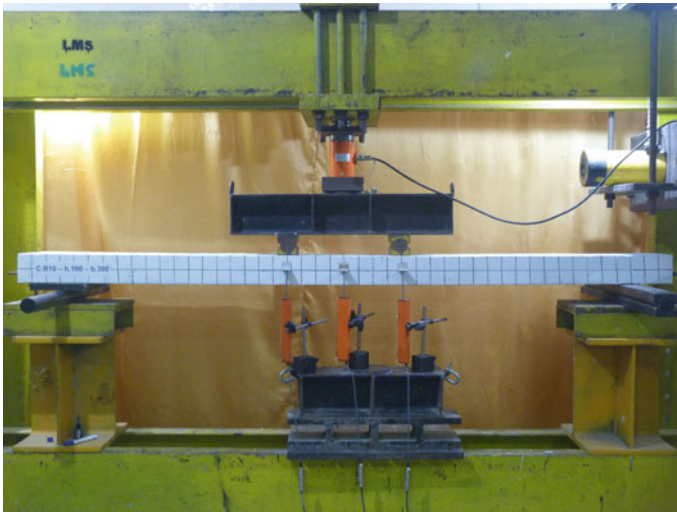


Fig. 3 Photo of hybrid specimen CR10.h100.b300

3 Result and Discussion

The load and displacement curves for composite and hybrid specimens are shown in Fig. 4. As expected, structural stiffness and the ultimate load were consistently increased for the thicker specimens. In each curve, the first crack and the ultimate load are denoted, marked by a circle and a triangle, respectively. The values of those loads are given in Table 2. The hybrid specimen exhibited later crack than the composite ones; the first crack occurred within the range of 67.2–96.3% of the ultimate load. The composite specimens cracked earlier at the 36.6–53.6% of the maximum load.

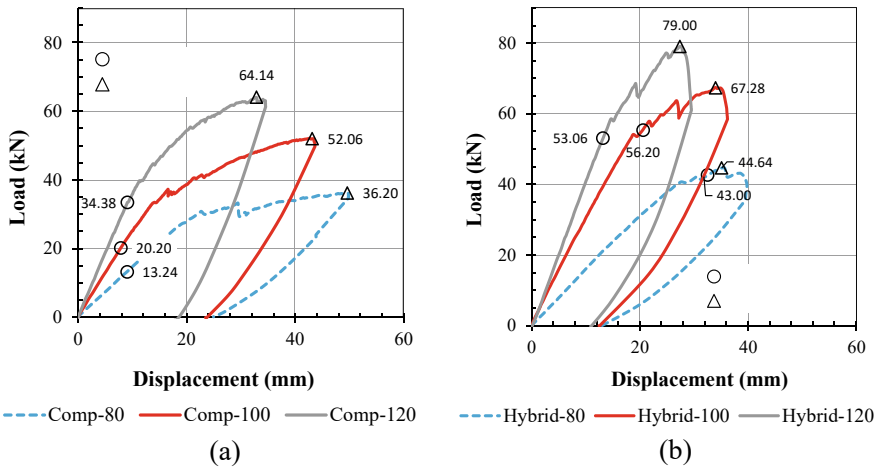


Fig. 4 Load and displacement curves: **a** composite specimen, **b** hybrid specimen

Table 2 First crack and the ultimate load (in kN)

Type	Specimen's name	First crack	Ultimate	%
Composite	Comp-80	13.24	36.20	36.6
	Comp-100	20.20	52.06	38.8
	Comp-120	34.38	64.14	53.6
Hybrid	Hybrid-80	43.00	44.64	96.3
	Hybrid-100	56.20	67.28	83.5
	Hybrid-120	53.06	79.00	67.2

3.1 Crack Pattern

The first crack occurred at the pure bending moment zone or area around two-point loads location. For composite specimen with the thickness of 120 mm, the first crack was at 34.38 kN and located about 340 mm from the center point of the specimen, outside the pure bending moment zone (Fig. 5a). Crack at this point developed significantly became a diagonal shear failure. More several cracks were founded on the area around two-point loads. However, there was no crack founded at the support zone. As shown in Fig. 5b and c, significant diagonal shear failure and compression crash at the top fiber resisted the specimen to obtain a higher resistance. It stopped at 64.14 kN.

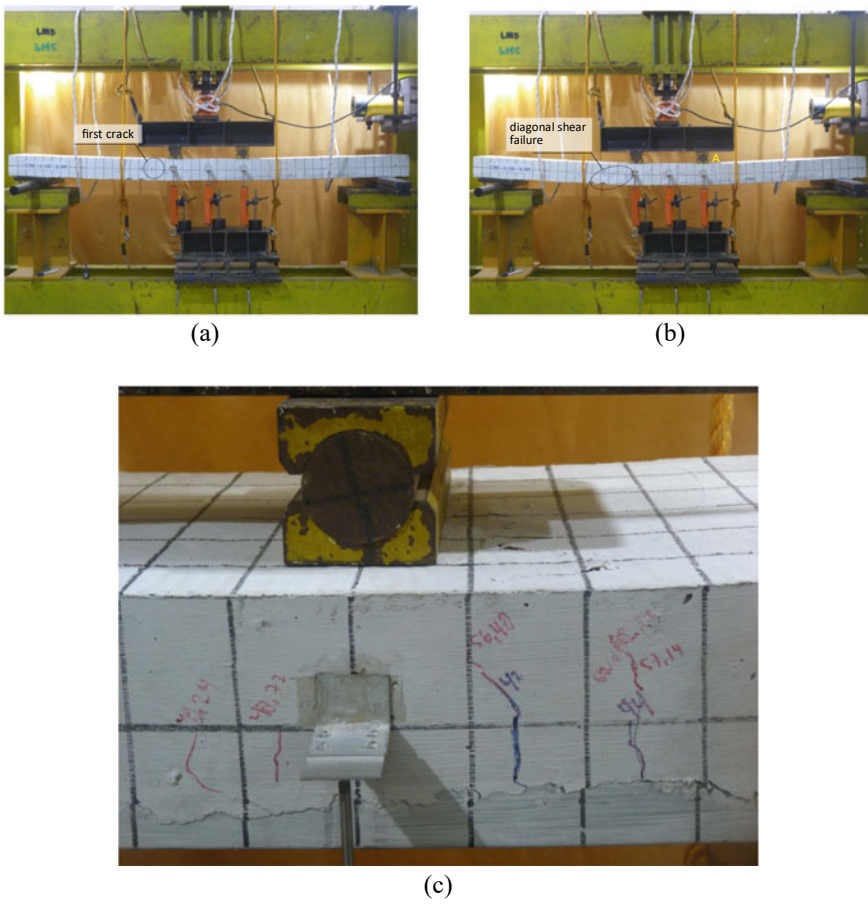


Fig. 5 Crack pattern composite specimen with thickness of 120 mm: **a** first crack, crack pattern at the ultimate condition, **c** compression crash at the top fiber

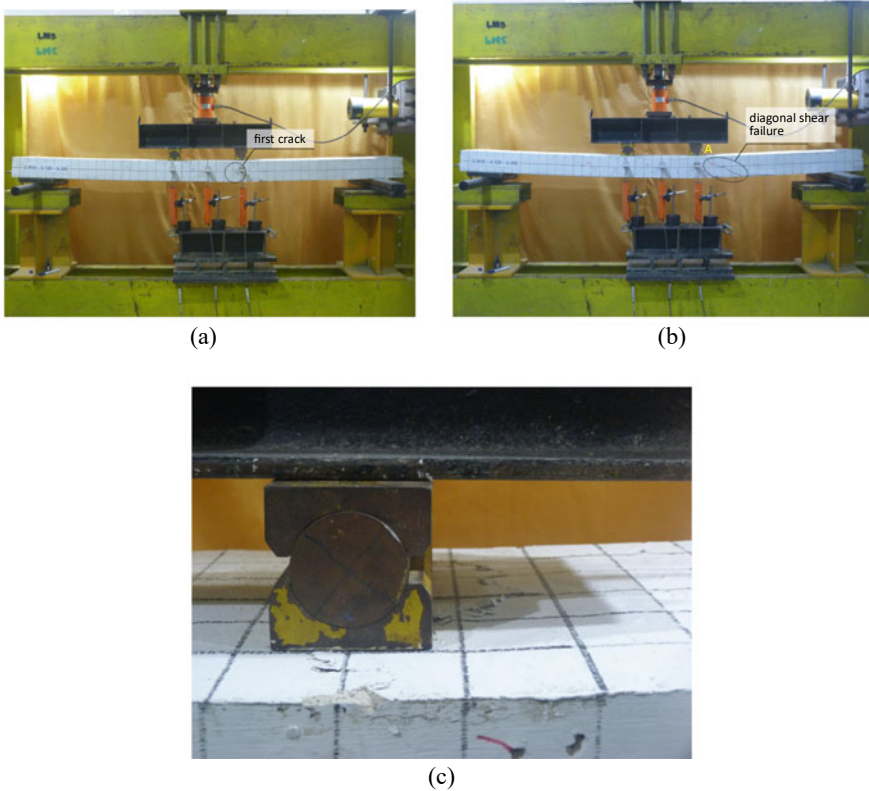


Fig. 6 Crack pattern hybrid specimen with thickness of 120 mm: **a** first crack, crack pattern at the ultimate condition, **c** compression crash at the top fiber

For the thickest hybrid specimen, the first crack was founded at 170 mm from the center point of the specimen at at 53.06 kN (Fig. 6a). At the ultimate condition, additional cracks were founded on the area around two-point loads. There was also no crack founded at the support zone. The push-over loading process was stopped 79.00 kN due to compression crash at the top fiber around steel saddle and significant diagonal shear failure.

3.2 Structural Stiffness

In Table 3, the structural stiffness for the composite and hybrid section are given. Additional tension bars to composite section may increase the stiffness of the specimen within the range of 10.2–20.8%.

Table 3 Structural stiffness (k)

Thickness (mm)	k (kN/mm)		Increment %
	Composite	Hybrid	
80	1.37	1.51	10.2
100	2.40	2.90	20.8
120	3.56	4.07	14.3

Table 4 Ductility of the specimen

Type	Specimen's name	Displacement		Ductility
		Yield	Ultimate	
Composite	Comp-80	22.72	49.40	2.17
	Comp-100	14.06	42.70	3.04
	Comp-120	11.32	32.90	2.91
Hybrid	Hybrid-80	27.56	35.08	1.27
	Hybrid-100	18.80	33.94	1.81
	Hybrid-120	14.62	27.36	1.87

3.3 Ductility

The ductility of the specimens are listed in Table 4. The displacement yield for different types of specimens with same thickness were almost similar, but the displacement at the ultimate load differed. At average, the composite specimen could displace 1.3 larger than the hybrid specimen. Thus, the ductility decreased within the range of 1.55–1.71 due to the addition of tension bars.

4 Conclusion

Experimental tests of the composite and hybrid sections of plate structures have been conducted in this study. The crack was initiated at the bending moment zone and around two-point loads for six observed specimens. No crack founded at the support zone. A similar ultimate condition is denoted by compression crash at the top fiber of the specimen. Additional tension bars can increase the load capacity of the specimen as well as the stiffness of the structures. On the contrary, the structural ductility will decrease at about 1.55–1.71 times.

References

1. Abdel-Sayed G (1982) Composite cold-formed steel concrete structural systems. In: Proceeding 6th international specialty conference on cold-formed steel structures. Rolla, Missouri, pp 485–510
2. Nguyen RP (1988) Strength of composite cold-formed steel-concrete beams. In: Proceeding 9th international specialty conference on cold-formed steel structures. Rolla, Missouri, pp 405–442
3. Hsu CTT, Punurai S, Punurai W, Majdi Y (2014) *Eng Structures* 71:187–200
4. Wehbel N, Bahmani P, Wehbe A (2013) *Int J Concr Struct Mater* 7:51–59
5. Abdel-Sayed G, Chung KC (1987) *Canadian J Civ Eng* 14:295–301
6. Alenezi K, Tahir MM, Alhajri T, Badr MRK, Mirza J (2015) *Constr Build Mater* 84:39–45
7. Haris S, Zaidir, Thamrin R, Buthi L, *Int J Civ Eng Technol* 8:1191–1198

Influence of Axial Load on the Ductility of Type “C” Reinforced Concrete Walls with Longitudinal Reinforcement Variation in the Cores



Meyer David Hilario Martel, Jhon Josue Canchanya Taipe,
Janela Azucena Condor Gonzalez, and Johan James Hinostroza Yucra

Abstract Type “C” shear walls are structural elements with a great capacity to absorb seismic forces that are commonly used in elevator boxes. The present research aims to show the effect of the axial load from 980.6 to 7844.8 KN on the ductility of the walls called (M1) and (M2), also evaluating the ductility in relation to variation of reinforcement longitudinal in the cores, for which trilinear diagrams of moment–curvature of both walls were generated. The results showed that the increase in axial load is inversely proportional to the ductility of the wall. On the other hand, the increase in axial load is directly proportional to the values of moments at each point of the moment–curvature diagram, but inversely proportional to the curvature at the points of the yield of steel and exhaustion of the maximum capacity. The increase in the amount of steel in the cores in the M1 was not optimal, since when comparing the ductility in both walls, the M1 presents less ductility because there is more steel in the traction zone.

Keywords Cutting walls · Moment curvature · Axial load · Numerical analysis

M. D. H. Martel (✉) · J. J. C. Taipe · J. A. C. Gonzalez · J. J. H. Yucra
School of Civil Engineering, Universidad Continental, Huancayo, Perú
e-mail: 73331527@continental.edu.pe

J. J. C. Taipe
e-mail: 73991701@continental.edu.pe

J. A. C. Gonzalez
e-mail: 75388855@continental.edu.pe

J. J. H. Yucra
e-mail: jhinostrozay@continental.edu.pe

1 Introduction

The shear walls have been used especially in high-rise buildings to resist seismic loads [1]. These walls are critical in seismically active areas since there is an increase in shear force in the structure [2]. Which are designed to have a no-linear behavior in severe seismic, where the input seismic energy is absorbed [3].

Likewise, the design of shear walls requires to estimate of their load capacity as well as their resistance for lateral displacement; in addition, the seismic events raised have highlighted their seismic performance [4]. However, pre-existing buildings show that shear walls lack some ductility [5]. One of the most appropriate options for concrete structures against seismic loads is to increase their ductility [6]. Due to this, it is necessary to simulate its behavior with greater precision, where the curvature moment relationship of concrete elements is considered as well as the stress-deformation relationship of confined and unconfined concrete [7].

Studies of shear walls have been observed in which the curvature moment decreased when the axial loads increased, resulting in the concrete's immediate deformation. Likewise, parameters such as material properties, amount of reinforcement and geometry of the section influence the calculation of the curvature moment diagram [8].

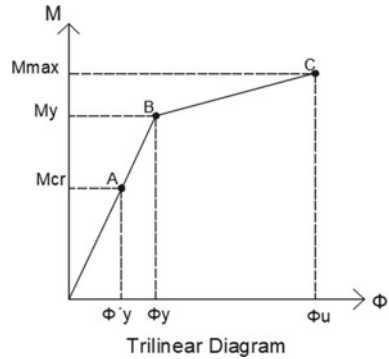
2 Methodology

In this study, the "C" shaped reinforced concrete walls M1 and M2 were analyzed with variability in the longitudinal reinforced of the cores. With the intention of comparing the ductility of both walls with a variation of axial loads from 980.6 to 7844.8 KN, also evaluating the ductility in relation to the change of longitudinal reinforced in the cores. With a positive "y" eccentricity. Considering $f'c$ 2059.4 N/cm² and the perfect elastoplastic model of steel with f_y 41,187.93 N/cm².

3 Construction of the Curvature Moment Diagram

The models of idealization of curvature moment allow validating the behavior of the wall, therefore, in the present study the proposed model from the Book of Eng. Ottazzi was used, which details the cracking point of the concrete and limits the yield point that requires variability of the stiffness of the section in study [10]. (See Fig. 1).

Fig. 1 Curvature Moment Diagram. Adapted of “Apuntes del Curso de Concreto Armado 1” [10]



3.1 Hypothesis to Consider Generating the Moment–Curvature Diagram

The following points were taken into consideration for the numerical analysis proposed by the research: The section under analysis is flat and remains flat. There is no early failure by cutting, or by lateral buckling. The bending tensile strength of concrete can be estimated as $2\sqrt{f_c}$ ($\frac{\text{kgf}}{\text{cm}^2}$). There is a perfect adhesion between concrete and steel [10].

3.2 Cracking Point (Point A—Mcr)

The point at which the section under analysis reaches the maximum tensile strength of the concrete, thus initiating the cracking of the concrete. After this point, the cracked area of the concrete was neglected in the numerical analysis, so the only one that provides tensile strength is steel [10]. When comparing the moment of cracking and the last moment of a wall this is significantly greater than the moment of cracking which demonstrates low plasticity or seen otherwise allows very little inelastic deformation [11]. Minimal reinforcement in concrete walls can increase the cracking moment up to 1.5 times its value [11].

3.3 Creep Point (Point B—My)

Steel creep starting point, the unit deformation of the steel reaches $\epsilon_y = 0.0021$ (0.21%). One of the most representative states of a moment–curvature diagram, which precedes the failure point of the section and in turn represents the end of elastic behavior, relating the yield moment (M_y) and the creep curvature (ϕ_y) [10].

To appreciate the behavior of the concrete wall depends on variables such as the form of application of loads, and the relationship between steel and concrete, which is the reason for the existence of several constitutive laws, therefore, we worked with the constitutive law of Hognestad that represents the model of stress deformation related to maximum effort and with a deformation of exhaustion of $\varepsilon_0 = 0.002$ [9]. “Eq. (1) and (2)” defines Hognestad’s proposed constitutive law.

$$f_c = f''_c * \left[\frac{2\varepsilon_c}{\varepsilon_0} - \left(\frac{\varepsilon_c}{\varepsilon_0} \right)^2 \right] \left(\frac{\text{kgf}}{\text{cm}^2} \right); 0 \leq \varepsilon_c \leq 0.002 \quad (1)$$

where:

$$\varepsilon_0 = \frac{2 * f''_c}{E_c} \quad (2)$$

When performing tests on columns placed vertically with eccentric loads, an average value of maximum bending stress, f'' , which is equal to $0.85f'_c$ (kgf/cm^2) [9] was found.

Point of Depletion (Point C—Mmax). After exceeding the admissible stresses, the section does not fail, it still has a reserve that is used in the design for resistance which we call a point of exhaustion or maximum capacity. The ACI and Peruvian regulations accept the simplification of an equivalent block of compressions or Whitney rectangle [10].

3.4 Ductility

Ductility is the property that allows deforming the plastic state without reaching the fault. Consequently, the ductility of curvature is the ratio of the curvature of the concrete at its point of exhaustion, which means the concrete has reached a deformation $\varepsilon_c = 0.003$ without any steel failing by breakage and the first creep of the steel to tension [10]. Ductility is the ability of a material or structure under inelastic conditions to withstand loads [12]. During an earthquake, the energy is absorbed by the structure which will be dissipated by the plastic deformation of the components [13]. “Eq. (3) defines the ductility of the section under analysis”.

$$\mu_\varphi = \frac{\varphi_{max}}{\varphi_y} \quad (3)$$

4 Results

The following figures show the reinforcements used in the M1 and M2 walls (see Figs. 2 and 3).

The following table shows the summary of the values calculated at each point of the Moment—curvature of the M1 Diagram (see Table 1).

The following figure shows the moment—curvature diagram as a function of the variation of the axial load on wall M1 (see Fig. 4).

The following table shows the summary of the values calculated at each point of the Moment—curvature of the M2 Diagram (see Table 2).

The following figure shows the moment—curvature diagram as a function of the variation of the axial load on wall M2 (see Fig. 5).

The following tables summarize the ductility calculations in walls M1 and M2 as a function of the variation of the axial load (see Tables 3 and 4).

The following figure shows the comparison of ductility in walls M1 and M2 as a function of axial load variation (see Fig. 6).

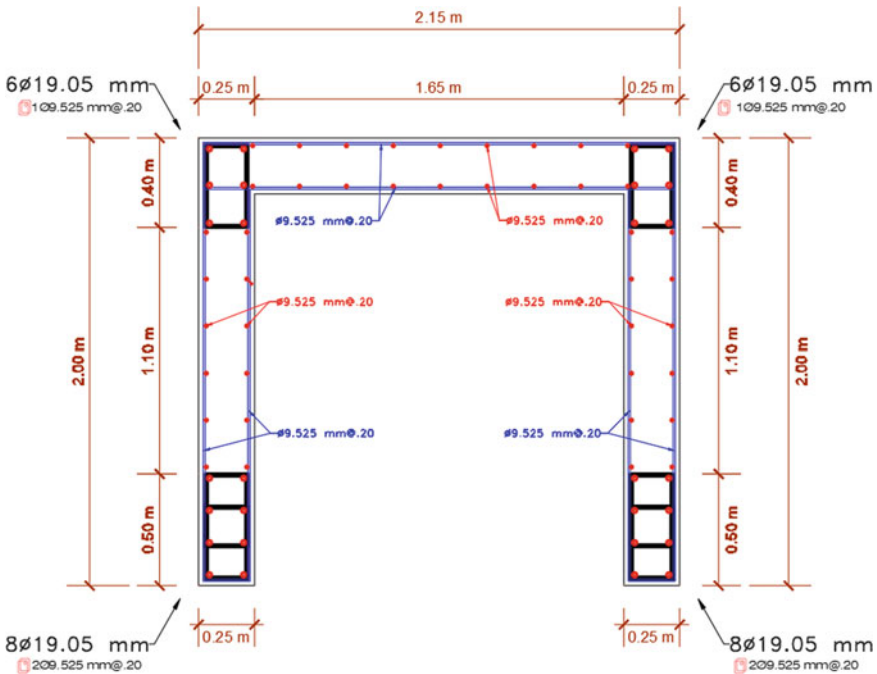


Fig. 2 M1 reinforcement proposal 1

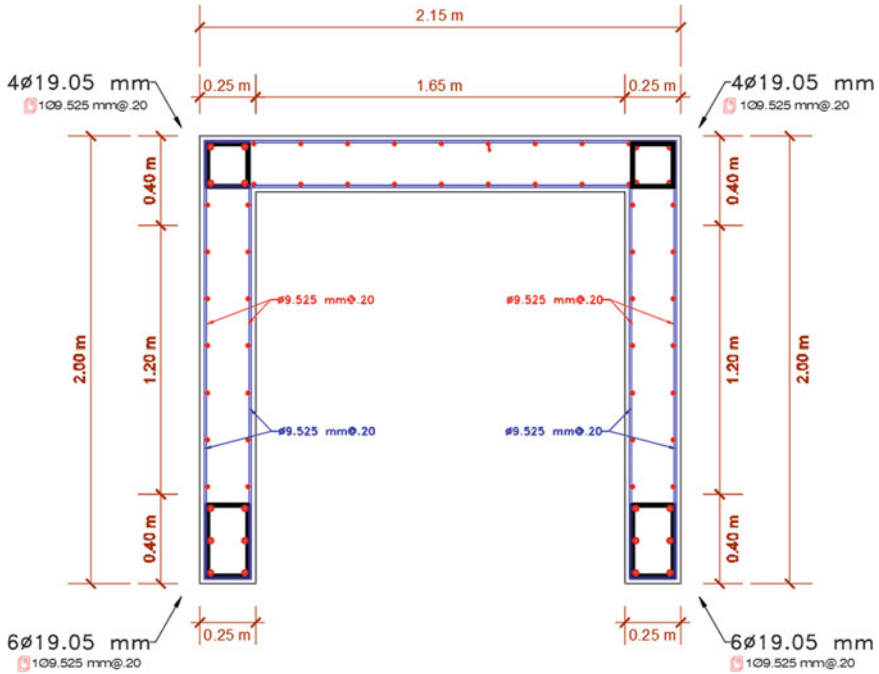


Fig. 3 M2 reinforcement proposal 2

Table 1 Result of generating the moment—curvature diagram with axial load variation of wall 1 Type C

Wall 1 Type C						
Axial load	Concrete cracking point		Steel creep point		Point of failure o maximum capacity	
	M cr	φ	My	φ_y	M max	φ_{max}
KN	KN m	$10^{-3} \frac{1}{m}$	KN m	$10^{-3} \frac{1}{m}$	KN m	$10^{-3} \frac{1}{m}$
980.6	1716.05	0.25	4095.38	1.32	5141.38	23.59
1961.2	2036.80	0.33	5114.71	1.38	6169.74	20.23
3922.4	2678.31	0.49	7114.74	1.51	8186.83	15.23
5883.6	3319.76	0.65	9063.59	1.64	10,114.30	12.11
7844.8	3961.23	0.81	10,961.74	1.77	11,950.33	9.88

5 Discussion of Results

When performing an analysis of the formulas used and the results obtained in the research it was observed that the parameter “c” represents the distance or compressed area in the direction in which the analysis was performed, when increasing its value

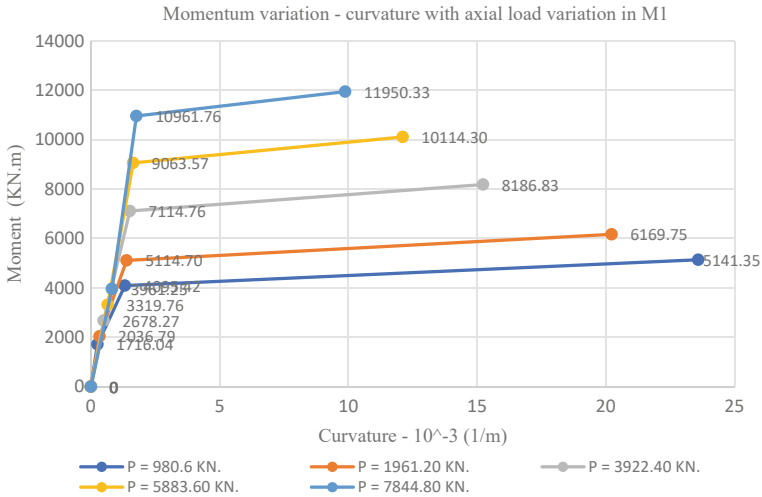


Fig. 4 Result of generating the moment—curvature with axial load variation of the M1 type C

Table 2 Result of generating the moment—curvature diagram with axial load variation of M2 Type C

Wall 2 type C						
Axial load	Concrete cracking point		Steel Creep Point		Point of failure o maximum capacity	
	M cr	φ	My	φy	M max	φmax
KN	KN m	10 ⁻³ 1/m	KN m	10 ⁻³ 1/m	KN m	10 ⁻³ 1/m
980.6	1700.93	0.26	3683.23	1.30	4441.94	28.36
1961.2	2021.64	0.34	4720.07	1.37	5500.34	22.98
3922.4	2663.07	0.50	6752.58	1.50	7542.79	17.08
5883.6	3304.49	0.66	8731.02	1.63	9514.16	13.25
7844.8	3945.92	0.82	10,656.90	1.76	11,413.58	10.69

this inversely influences the curvature, in the same way to ductility; In other words, if the compressed area is larger the ductility will be lower. To increase the ductility in any section you have to reduce the value of this parameter, for which you had to increase the amount of steel in the compressed area and increase the f’c, another option was to increase the width of the compressed area.

The proposal to place more steel in the compressed area is not possible in all cases since many of the structural elements in which they act forces in flexion or flexo-compression, these forces act in different directions, which can vary the compressed area making the steel that was placed to decrease the parameter “c” in that direction of analysis, It can be more detrimental in a reverse direction since the parameter “C” depends not only on the width of the compressed zone and the steels in it, but

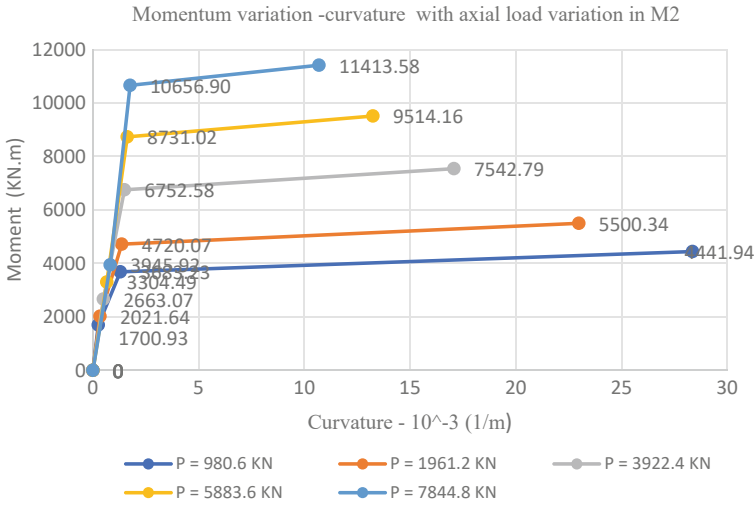


Fig. 5 Result of generating the moment—curvature diagram with axial load variation of wall 2 type C

Table 3 Axial load versus wall ductility 1 Type C

Axial load (KN)	Ductility
980.6	17.88
1961.2	14.61
3922.4	10.08
5883.6	7.39
7844.8	5.58

Table 4 Axial load versus wall ductility 2 Type C

Axial load (KN)	Ductility
980.6	21.85
1961.2	16.83
3922.4	11.42
5883.6	8.15
7844.8	6.08

also the steels that are in the tensile zone. Seen another way if there is more steel in the traction zone, the parameter “c” must have a higher value to balance the internal forces in the section.

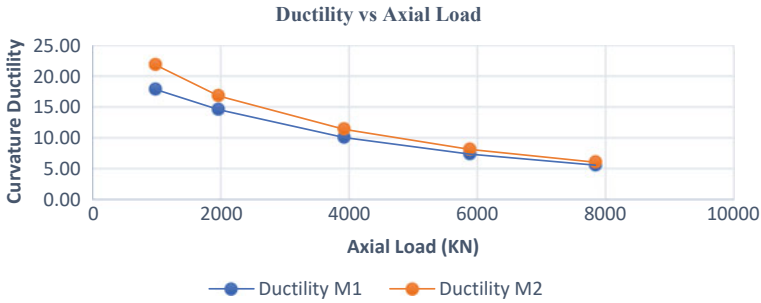


Fig. 6 Comparison of the ductility of both diagrams moment—curvature with respect to the variation of the axial load

6 Conclusion

To sum up, the axial load significantly influences each point of the Moment – Curvature diagram, since in both analyzes as the axial load increases it is necessary to apply a greater moment to reach the cracking points of the section (M_{cr}), the yield point of the steel (M_y) and point of exhaustion or maximum capacity (M_{max}).

- (1) In M1 and M2 the (M_{cr}) with axial load of 980.6 KN. is 1716.04 KN.m and 1700.93 KN.m for axial loads of 1961.2, 3922.4, 5883.6, 7844.8 KN the value of (M_{cr}) for M1 increases by 18.69%, 56.07%, 93.45% 130.84% respectively and for M2 the increase is 18.86%, 56.57%, 94.28% 131.99% respectively.
- (2) In M1 and M2 the (M_y) with axial load of 980.6 KN. is 4095.42 KN.m and 3683.23 KN.m, for the axial loads of 1961.2, 3922.4, 5883.6, 7844.8 KN. the value of (M_y) for the first wall increases by 24.89%, 73.72%, 121.31% 167.66% respectively and for the second wall the increase is 28.15%, 83.33%, 137.05% 189.34% respectively.
- (3) In M1 and M2 the (M_{max}) with axial load of 980.6 KN. is 5141.35 KN.m and 4441.94 KN.m, for the axial loads of 1961.2, 3922.4, 5883.6, 7844.8 KN. the value of (M_{max}) for the first wall is increased by 20%, 59.23%, 96.72% 132.44% respectively and for the second wall the increase is 23.83%, 69.81%, 114.19% 156.95% respectively.
- (4) It can also be observed that the greater the axial load, the cracking points (M_{cr}), and the steel yield point (M_y) have greater curvature as the axial load increases.

If the diagrams of both walls in the analysis are compared with the same axial load, the wall with less longitudinal reinforcement in the cores requires a lower moment value to bring to each point of the diagram, but the curvature at the points of cracking of the section and of exhaustion or maximum capacity is greater except for the yield point at which the wall with the greatest reinforcement in the cores has a greater curvature.

When increasing the value of the axial load the ductility of the wall decreases, since, for an axial load of 980.6 KN the ductility of the first and second wall is 17.88

and 21.85, for the axial loads of 1961.2, 3922.4, 5883.6, 7844.8 KN the ductility in the first wall decreases by 18.28, 43.63, 58.64, 68.77% and in the second wall decreases by 22.96, 47.73, 62.70 and 72.19%.

Finally, the way in which the amount of steel in the core was increased was not optimal, since it did not help greatly to increase the ductility of wall 1, and even this was more harmful. Thanks to the analysis of formulas used and results, it was concluded that it is necessary to increase the steel in the cores in such a way that, when performing the analysis in opposite directions, the wall presents a balanced ductility in both directions.

References

1. Marzok A, Lavan O, Dancygier AN (2020) Predictions of moment and deflection capacities of RC shear walls by different analytical models. In: Structures. Elsevier, pp 105–127. <https://doi.org/10.1016/j.istruc.2020.03.059>
2. Fadallah R et al (2022) Experimental investigation of small-scale shear walls under lateral loads. *J Eng Appl Sci* 2022 69(1):1–19. <https://doi.org/10.1186/s44147-022-00141-0>
3. Gu A et al (2019) Experimental study and parameter analysis on the seismic performance of self-centering hybrid reinforced concrete shear walls. *Soil Dyn Earthq Eng* 116:409–420. <https://doi.org/10.1016/j.soildyn.2018.10.003>
4. Mangalathu, S et al (2020) Data-driven machine-learning-based seismic failure mode identification of reinforced concrete shear walls. *Eng Struct* 208:110331. <https://doi.org/10.1016/j.engstruct.2020.110331>
5. Paulay T (1975) Design aspects of shear walls for seismic areas. *Can J Civ Eng* 2(3):321–344. <https://doi.org/10.1139/l75-030>
6. Mohebbi M (2022) An algorithm to obtain moment-curvature diagram for reinforced concrete sections. In: International conference on civil engineering. Springer, Singapore, pp 31–45. https://doi.org/10.1007/978-981-19-1260-3_4
7. Foroughi S, Yüksel B (2020) Investigation of nonlinear behavior of high ductility reinforced concrete shear walls. *Int Adv Res Eng J* 4(2):116–128. <https://doi.org/10.35860/iarej.693724>
8. Wang B, Cai W, Shi Q (2019) Simplified data-driven model for the moment curvature of T-shaped RC shear walls. *Adv Civ Eng* 2019. <https://doi.org/10.1155/2019/9897827>
9. Hognestad E (1951) Study of combined bending and axial load in reinforced concrete members. University of Illinois at Urbana Champaign, College of Engineering. Engineering Experiment Station
10. Ottazzi G (2016) Apuntes del curso Concreto Armado 1. 15ava edición. Lima-Perú Pontificia Universidad Católica del Perú
11. Houlst R, Goldsworthy H, Lumantarna E (2018) Plastic hinge length for lightly reinforced rectangular concrete walls. *J Earthq Eng* 22(8):1447–1478. <https://doi.org/10.1080/13632469.2017.1286619>
12. Nurjannah S et al (2023) The analysis of numerical self-compacting concrete wall panel models with variations of shear reinforcement. *Eng Solid Mech* 11(1):89–102. <https://doi.org/10.5267/j.esm.2022.8.002>
13. Zhang L et al (2022) Experimental study on the seismic behavior of squat SRC shear walls with high axial load ratio. *Buildings* 12(8):1238. <https://doi.org/10.3390/buildings12081238>

Study on Masonry Soil Joint Adding Rock Salt



Masashi O uji

Abstract This study is about strengthening joints in masonry construction, commonly used in Nepal's mountainous areas. Generally, mud mortar has been used for joints of masonry buildings in Nepal. However, after the 2015 Gorkha earthquake, the use of cement is recommended to ensure earthquake resistance, but it has not been widely used due to the high cost of the material. Therefore, we are attempting to strengthen the earthquake resistance of masonry buildings by reinforcing locally available soil with inexpensive materials. We have already reported on the joint properties using soil and lime in a separate paper. In the present paper, the addition of rock salt in addition to soil and lime has been used, and a large increase in strength was observed. Although the strength increase was more pronounced when red soil was used, the strength increase due to rock salt was also observed for other soils. This is different from the effect of lime. This paper reports the results of the strength increase when rock salt and other materials were added.

Keywords Rock-salt · Masonry joint · Reinforced soil · Magnesium · Red soil · Yellow soil

1 Introduction

This study is a follow-up to a report presented at ACE 2018. The Nepal Gorkha earthquake in 2015 caused significant damage to masonry buildings in mountainous areas. This major earthquake revealed a lack of seismic resistance in masonry buildings built using traditional methods in Nepal [1]. The Nepalese government took measures to improve earthquake resistance, such as limiting the number and size of stories in masonry buildings and requiring the use of cement mortar as a jointing material [2]. This is correct as a measure to mitigate damage to masonry buildings. However, in mountainous areas where many residents have low incomes,

M. O uji (✉)
Toyama University, Takaoka City, Toyama Pref., Japan
e-mail: ouji@tad.u-toyama.ac.jp

© The Author(s), under exclusive license to Springer Nature Singapore Pte Ltd. 2024
M. Casini (ed.), *Proceedings of the 3rd International Civil Engineering and Architecture Conference*, Lecture Notes in Civil Engineering 389,
https://doi.org/10.1007/978-981-99-6368-3_23

267

cement itself is not easy to obtain economically, and there are limits to the spread of government-recommended methods unless the income problem is solved. There is also the problem that modern materials such as cement are discouraged in masonry buildings with historical value. To address both of these issues, we planned to use locally available soil as the main material and to add lime to the joints to ensure water resistance and to improve the strength of the joints by adding easily available materials.

The idea of using improved soil as joints are based on “Tataki,” a type of improved soil traditionally used in Japan for flooring. “Tataki” is a traditional ground improvement method that is made by adding sand, slaked lime, and bittern to decomposed granite soil. Although not used frequently in modern times, it boasts high durability despite using only traditional materials. Before the start of this study, we surveyed “Tataki” in Japan. The ratio of soil to slaked lime is generally considered to be about 2:1, although there are some differences depending on the type of soil. The amount of bittern added is generally about 10% by weight, and the amount of moisture is about the same as that of a loose mass when held in the hand. Although the amount of moisture is a matter of feelings, we decided to follow the traditional Japanese method as closely as possible in the beginning.

Compression test pieces were produced using paper mold (50φ, H = 100 mm) formwork and compacted in the three parts by a 1.5kgf rammer. This is by the compaction test method of improved soil testing commonly performed in Japan. After compaction, the test was conducted after a curing period of at least 2 months in a cool and dark place.

The test results for the case without rock salt addition have already been published but will be briefly reviewed for reference. Red soil was commonly used as joints in mountain villages in Sindhupalchowk District, northeast of Kathmandu, the capital of Nepal, or other readily available soil, and the effect of varying the ratio of lime in addition to the compressive strength was checked (N1). Compression tests were also conducted to verify the effect of adding straw (N2) and sand and straw (N3) in the same manner. In addition, direct shear tests were conducted using brick blocks (N4). From this series of results, the following was found [3].

- The best mixing ratio of soil and quicklime is about 3:1. When slaked lime is used, a ratio of 2:1 is best.
- Compared to the soil-only case, the lime-added case showed a slight increase in compressive strength, but this increase was 20–50%.
- Cracking failure was more common than shear failure.
- In the case of lime-added lime, the compressive strength increased slightly, but by 20–50%, and the cracking failure was more frequent than the shear failure. However, the deformation capacity was doubled.
- No significant increase in strength was observed even when sand was mixed in.
- When only straw was added without lime, the compressive strength increased to the same level as when lime was added.

A similar use of “Tataki” for joints exists in Japan, where a man-made stonework method called “Choshichi-Tataki” existed nearly 100 years ago. Although

“Choshichi-Tataki” disappeared with the spread of cement, traces of it can still be seen in Japan today, and it retains its durability for more than 100 years. However, the details of its manufacturing process have been lost, and although component analysis has been conducted, it is unknown.

Similarly, at Pashupatinath, one of the World Heritage sites in Kathmandu, Nepal, we have confirmed that a material similar to “Tataki” was used as the surface finish of the masonry structure. Although the analysis has not yet been conducted at this stage due to the difficulty of traveling to Nepal due to corona infection, we intend to proceed with it in the future.

2 Rock Salt Addition Case (N5)

Next, the following experiment was conducted to see how the compressive strength of the improved soil changes with the addition of rock salt in addition to soil and lime, using the aforementioned traditional Japanese Tataki as a reference.

The various parameters are as follows. However, in the experiments reported here, the moisture content was not yet treated as a parameter, and the moisture content was adjusted by human senses following the traditional method. The amount of rock salt added was determined on a trial basis and has no basis.

2.1 Parameters of N5 Case (Fig. 3)

Date of production: 26–27/Mar/2018

Date of test: 16/Sep/2018

Soil type (1: common Red Soil that can be collected in the village, 2: fine Red Soil)

- Wet Soil Condition

The weight ratio of soil to Lime (1: [2:1], 2: [1.5:1], 3: [3:1], 0: [No Lime])

Weight of straw added (A: [0 g], B: [15 g]/1000 g: [Soil + Lime])

Weight of rock salt added (1: [0 g], 2: [15 g], 3: [30 g]/1000 g: [Soil + Lime])

The following findings were obtained from the experimental results by adding rock salt.

- The strength of the case without rock salt is slightly lower than that of the case with rock salt compared to the N1 result because the moisture content was not controlled.
- The strength of the case with rock salt was 1.5–5.0 times higher than that without rock salt (2.78 times higher on average) under the same conditions (Tables 1, 2 and 3).

Table 1 N5 case: average of maximum intensity per case

		N/mm ²	
Adding rock salt	Str. average Case A without Case 0-A	1.892	(a)
	Str. average Case B	1.333	(b)
	Str. average Case 0-A	1.639	(c)
No rock salt	Str. average Case A	0.653	(d)
	Str. average Case B	0.779	(e)
Average strength increasing ratio	(a)/(d)	2.897	
	(b)/(e)	1.712	
	(c)/(d)	2.509	

- The case of adding straw also increased strength by rock salt, but at a lower rate than without the addition of rock salt (Figs. 1, 2 and 4).
- The strength increased significantly with the addition of rock salt even in the case where lime was not added, and lime did not contribute significantly to the increase in strength (Table 2).
- In the range of the amount of rock salt added (15 and 30 g), there is no clear tendency to say that the strength increases with increasing the amount of rock salt added (Figs. 1, 2 and 4).

Even when all cases are compared, the strength-enhancing effect of rock salt is evident. And the most stable ratio of soil to quicklime is 3:1 (Figs. 1 and 5).

3 Magnesium Addition Case (N6)

Since the strength enhancement by rock salt was found in N5, we decided to investigate which substances in rock salt have an effect. Rock salt generally contains Na, Mg, K, Ca, and other ions. First, we focused on magnesium, examining the strength change due to the addition of magnesium hydroxide (MgCl₂), magnesium oxide (MgO), and the addition of both. In addition, following traditional Japanese methods, the test specimens were produced while considering the minimum amount of water to be given in this case, especially in a sticky situation. Therefore, the amount of water added per 1070 g of soil and lime was set at 80 g. However, the amount was changed to 90 g and 100 g during the creation of the test specimens because of a perceived lack of adhesion due to insufficient moisture. Rock salt was also added for comparison with N5. The amount of rock salt added was less than in the case of N5 to check the effect of rock salt.

Table 2 Result of reinforced soil test within rock salt (Case: N5)

Soil No.	Mixing ratio	Straw case	Rock salt case	Average max strength N/mm ²	Standard deviation N/mm ²	Adopted value N/mm ²	Remarks	Strength increasing ratio
(1)	1 [2:1]	A 0 g	1	0.508	0.024	0.496	No rock salt	1.000
			2	1.742	0.032	1.726	15 g	3.480
			3	1.907	0.526	1.644	30 g	3.315
		B 15 g	1	0.351	0.056	0.323	1 piece defective	1.000
			2	NG	NG	NG	All pieces defective	NG
			3	1.434	0.096	1.386		4.291
	2 [1.5:1]	A	1	0.688	0.015	0.681		1.000
			2	1.385	0.276	1.247		1.832
			3	2.577	0.164	2.495		3.666
		B	1	0.419	0.108	0.365		1.000
			2	1.303	0.049	1.279		3.503
			3	1.062	0.152	0.986		2.701
	3 [3:1]	A	1	0.428	0.067	0.395	1 piece defective	1.000
			2	1.343	0.206	1.240		3.143
			3	1.739	0.136	1.671		4.236
B		1	0.794	0.094	0.747		1.000	
		2	1.514	0.091	1.469		1.966	
		3	1.128	0.201	1.028		1.376	
0	A	2	2.015	0.097	1.967		4.985	
		3	1.551	0.122	1.490	1 piece defective	3.777	
(2)	1	A	1	1.266	0.044	1.244		1.000
			2	2.042	0.064	2.010		1.616
			3	1.927	0.076	1.889		1.518
		B	1	1.371	0.016	1.363		1.000
			2	1.228	0.071	1.193		0.875
			3	2.014	0.019	2.005		1.471
	2	A	1	0.604	0.084	0.562	Water too much	1.000
			2	1.392	0.158	1.313	Water too much	2.336
			3	1.405	0.184	1.313		2.336

(continued)

Table 2 (continued)

Soil No.	Mixing ratio	Straw case	Rock salt case	Average max strength N/mm ²	Standard deviation N/mm ²	Adopted value N/mm ²	Remarks	Strength increasing ratio
		B	1	0.864	0.145	0.792		1.000
			2	1.286	0.161	1.206		1.523
			3	0.870	0.136	0.802	Water too much	1.013
	3	A	1	0.596	0.107	0.543		1.000
			2	3.207	0.328	3.043		5.609
			3	3.219	0.201	3.119		5.748
		B	1	1.211	0.257	1.083		1.000
			2	1.864	1.039	1.345		1.242
			3	2.008	0.083	1.967		1.817
0	A	2	1.846	0.060	1.816		3.347	
		3	1.369	0.169	1.285		2.368	

The strength increasing ratio compares the no rock salt case with adding case italic is 3 times higher on the no rock salt case

Table 3 N5 case: strength increasing ratio average

SIR average Case A without Case 0-A	3.236
SIR average Case B	1.980
SIR average Case 0-A	3.619
SIR average All Case	2.781

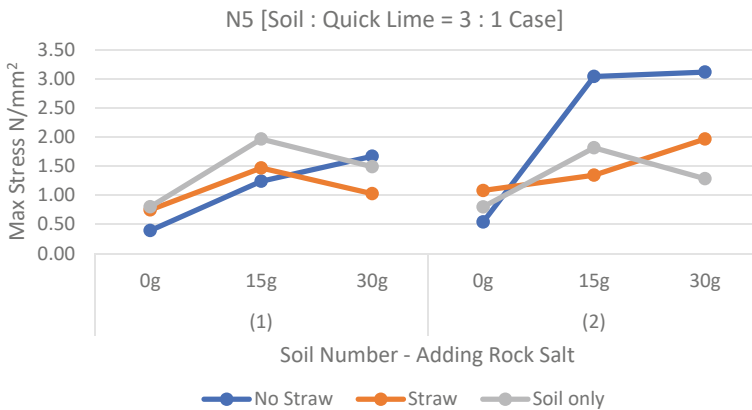


Fig. 1 Rock salt effect: N5[Soil: Lime = 3:1] case

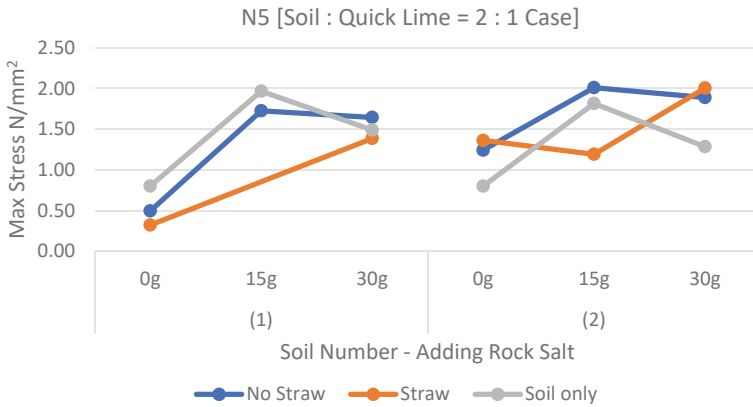


Fig. 2 Rock salt effect: N5[Soil: Lime = 2:1] case



Fig. 3 N5-(2)-3-B-3-1

3.1 Parameters of N6 Case

Date of production: 16–19/Nov/2018

Date of test: 23–25/Mar/2019

Soil type (Fixed: common Red Soil that can be collected in the village)

- Dry Soil Condition

The weight ratio of soil to Lime (Fixed: [3:1])

Weight of Water (Fixed 80 g: But increasing to 100 g on the way to testing)

Weight of straw added (A: [0 g], B: [15 g]/1000 g: [Soil + Lime])

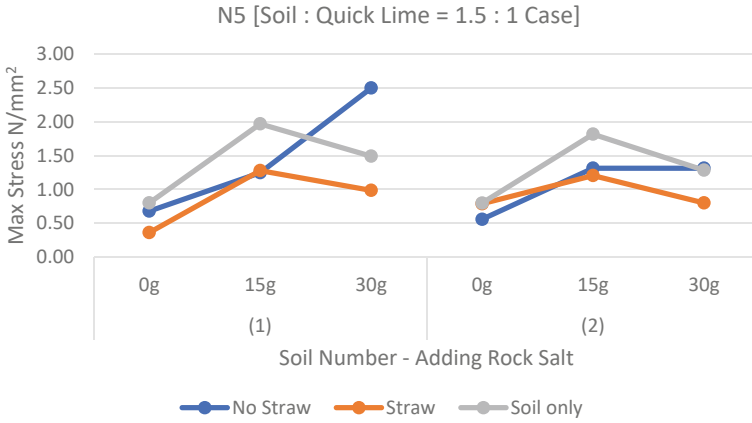


Fig. 4 Rock salt effect: N5[Soil: Lime = 1.5:1] case

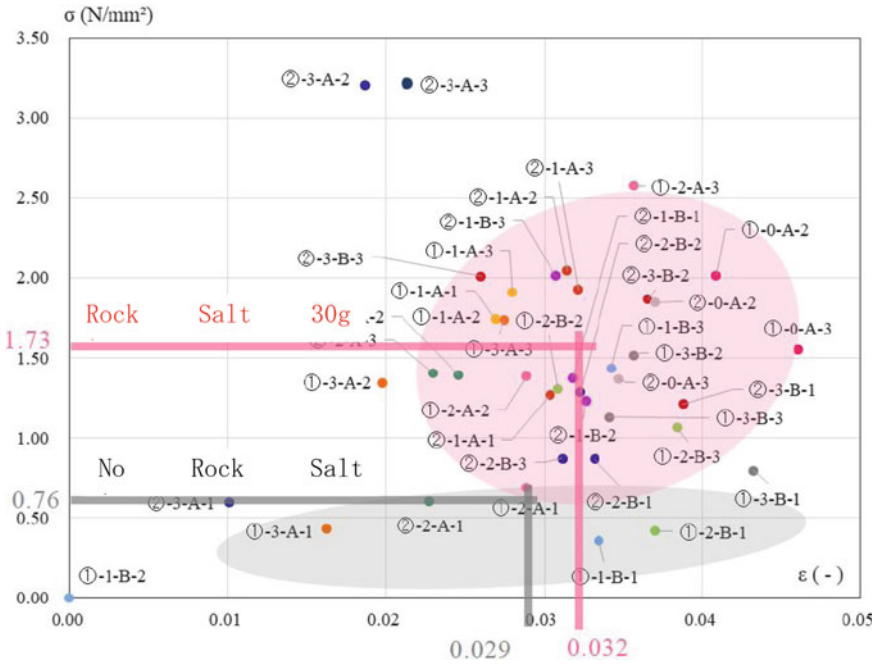


Fig. 5 Rock salt effect: total case [4]

Weight of adding Materials (1: [Nothing], 2: [Rock Salt 5 g], 3: [Rock Salt 10 g], 4: [MgCl₂ 1 g], 5: [MgCl₂ 5 g], 6: [MgCl₂ 10 g], 7: [MgCl₂ 20 g], 8: [MgO 10 g], 9: [MgO 30 g], 10: [MgO 50 g], 11: [MgO 100 g], 12: [MgO 150 g], 13: [MgO 25 g + MgCl₂ 5 g], 14:

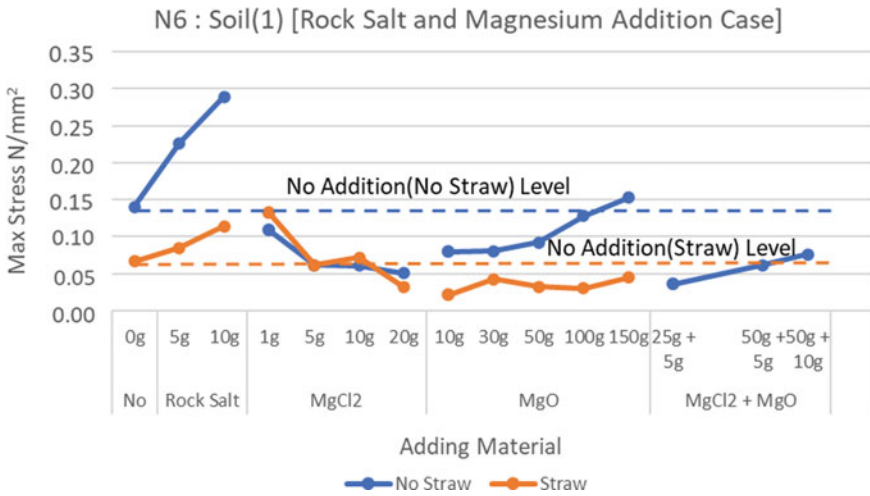


Fig. 6 Magnesium effect: total case

In the N6 case, both specimens had lower compressive strength than the soil-only case due to insufficient moisture content. For verification, a comparison with the rock salt identified in N5 is shown in the table above. It was found that the amount of water had a significant effect on the strength development of the improved soil (Fig. 6).

Although it is not clear because the amount of water used during mixing was small, it is clear again that the strength is improved by rock salt. On the other hand, the strength of $MgCl_2$ decreased in proportion to the amount of magnesium added, while the strength of MgO increased with the amount of $MgCl_2$ added, but even at the maximum amount of 150 g, the strength reached only that of case where nothing was added.

The strength is also considerably lower when both $MgCl_2$ and MgO are added. However, a separate test should be conducted to determine the situation when moisture is increased.

4 Effect of Water Ratio (N7)

The effect of moisture content is verified after the results with N6. The soil used in this study was somewhat dry as in N6.

4.1 Parameters of N7 Case

Date of production: 26/Mar/2019

Date of test: 23/May/2019

Soil type (Fixed: common Red Soil that can be collected in the village)

- Dry Soil Condition

The weight ratio of soil to Lime (Fixed: [3: 1])

Weight of Rock Salt added (Fixed: [10 g])

Weight of straw added (A: [0 g], B: [15 g]/1,000 g: [Soil + Lime])

Weight of Water (1: [80g], 2: [100g], 3: [120g], 4: [150g], 5: [200g], 6: [250g], 7: [300g], 8: [350g])

Essentially, the amount of moisture to be added varies depending on the wetness of the soil being used. To be accurate, the moisture content of the soil should be measured each time, but this is not practical. Therefore, we believe it is desirable to classify the soil into two broad categories: wet and dry soil.

On the other hand, it was found that the moisture content significantly affects the strength of the improved soil, including the results of the experiment presented here. Moreover, it is taking a clear peak. Solidification does not progress if too little, and strength is reduced due to cracking during drying (Fig. 7, Table 4).

It can be assumed that the amount of moisture is not specified in traditional Japanese methods because the appropriate amount of moisture may vary depending on the moisture content of the soil used in this way. In addition, it was understood that “Tataki” is used for ground-level floors, so a lower moisture content is easier to improve quality, but when used as joints, sufficient moisture content is required to the extent that it does not become too much and does not increase adhesion.

Fig. 7 Water effect: total case [5]

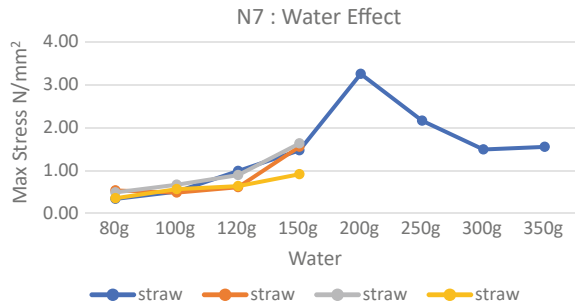


Table 4 Water effect: strength increasing ratio

Water	Straw			
	0 g	5 g	10 g	15 g
80 g	1.000	1.000	1.000	1.000
100 g	1.496	0.904	1.369	1.591
120 g	2.909	1.142	1.826	1.788
150 g	4.326	2.897	3.330	2.566
200 g	9.560			
250 g	6.356			
300 g	4.385			
350 g	4.565			
Strength increasing ratio				

5 Yellow Soil Case (N9)

In Durbar Square at Patan, one of the World Heritage Sites, yellow clay is used for joints. Therefore, this experiment was conducted as a case other than red clay. Other N8 experiments have been conducted to explore the potential of recycled soil, but they are omitted in this report.

5.1 Parameters of N7 Case

Date of production: 18–19/Sep/2019

Date of test: 5/Dec/2019

Soil type (Fixed: Patan Yellow Soil)-Wet Soil Condition

The weight ratio of soil to Lime (Fixed: [3: 1])

Weight of Rock Salt added (Fixed: [10 g])

Weight of straw added (A: [0 g], B: [10 g]/1,000 g: [Soil + Lime])

Weight of rock salt added (1: [0 g], 2: [10 g], 3: [20 g]/1,000 g: [Soil + Lime])

Weight of Water (1: [80g], 2: [100g], 3: [120g], 4: [150g], 5: [200g])

Although the basic strength of Yellow Soil is lower than that of the Red Soil case in this test, the effect of the rock salt addition is evident. Moisture content also peaked at approximately 100 g (/1000 g: [soil + lime]) (Figs. 8 and 9).

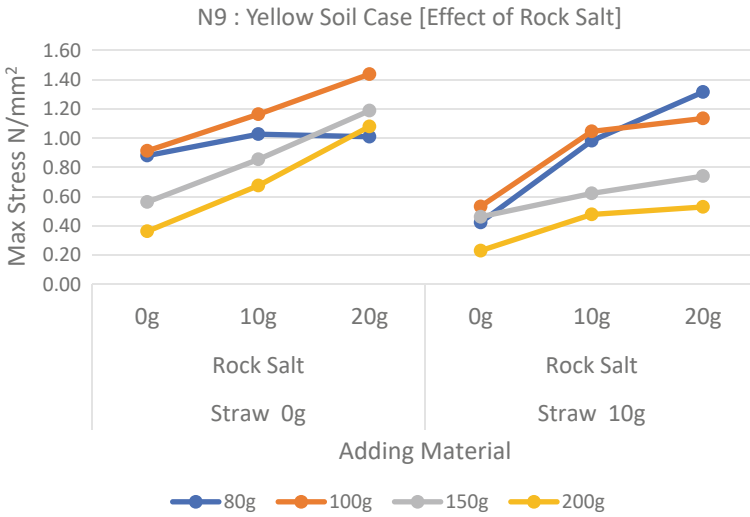


Fig. 8 Rock salt effect: yellow soil case

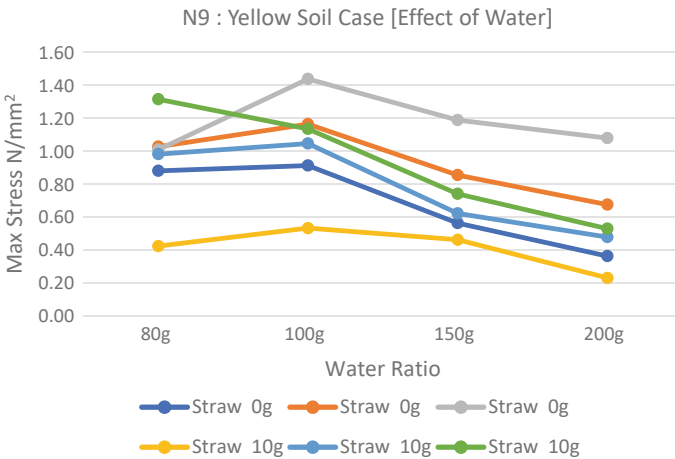


Fig. 9 Water effect: yellow soil case

6 Conclusion

The effect of water added during mixing is very significant, and strength development is considerably worse with less water. The amount of water added is influenced by the moisture content of the original soil. Based on the results of this study, 150–200 g of water was appropriate for dry soils, and 80–120 g for wet soils.

- Rock salt increased the compressive strength of the soil by a factor of 2 or more in many cases.
- We are currently verifying which components in the Rock Salt are causing the strength increase.
- We are also continuing to test the behavior of Red Soils from outside Nepal using Japanese Red Soils.

I would like to thank Mr. Kumar Yonjan for his many assists and Dr. Sanjaya Uprety for his coordination in Nepal. Special thanks to Ms. Mayuko Hashimoto and Ms. Seina Ichikawa for their help in organizing the data. This study was supported by Toyama Nepal Cultural Exchange Association.

Acknowledgements This work was supported by JSPS KAKENHI Grant Number JP19KK0112.

References

1. Architectural Institute of Japan, Technical Information for Disaster Mitigation of Masonry Structures, 2017
2. Nepal Department of Urban Development and Building Construction, Design Catalogue for Reconstruction of Earthquake Resistant Houses, 2015
3. Ouji M, Yonjan K (2018) A basic study on one of reinforcement method for masonry structure. In: Annual international conference on architecture and civil engineering, pp 152–161
4. Hashimoto M (2019) Study on reinforced joint of masonry—about housing in Nepal, Graduation Thesis, University of Toyama
5. Ichikawa S (2021) Study on masonry joints in Nepal-moisture content and reactants. Graduation Thesis, University of Toyama

The Approximate Equation for Global Buckling Load of Grid Shell Domes



Baoxin Liu , Pei-Shan Chen , Jialiang Jin , and Xiangdong Yan 

Abstract The goal of this study is to propose an approximate equation to evaluate the global buckling load of dome grid shell. For considering the influence of overall stiffness for grid shells, the effective stiffness is defined according to past research. Different from conventionally mechanical methods, this study adopts regression analysis based on a software named “1stOpt” to forecast the relationship between buckling load factors λ , geometric parameter and effective stiffness. Through the linear buckling analysis, the dome grid shell models with different geometric parameters, in a total of 1225 cases, are analyzed to build the relationship and establish the dataset. By inputting the dataset into the 1stOpt, a suitably approximate equation is fitted with high precision.

Keywords Dome grid shells · Buckling analysis · Buckling load · Effective stiffness · Regression analysis · Approximate equation

B. Liu

Department of Civil Engineering and Architecture, Kyushu Institute of Technology,
Kitakyushu 804-8550, Japan
e-mail: wuyezi894427800@gmail.com

P.-S. Chen (✉)

Graduate School of Engineering, Kyushu Institute of Technology, Kitakyushu 804-8550, Japan
e-mail: chen@civil.kyutech.ac.jp

J. Jin

Graduate School of Environmental Studies, Nagoya University, Nagoya 464-8601, Japan
e-mail: j1822238004@gmail.com

X. Yan

Department of Civil and Environmental Engineering, University of Pittsburgh, Pittsburgh,
PA 15216, USA
e-mail: yan.xiangdong760@mail.kyutech.jp

1 Introduction

Currently, there are two kinds of primary methods to evaluate global buckling load of grid shells or space frames, which are the continuum shell analogy [1] and the finite element method [2]. The continuum shell analogy is suitable for manual calculation, which provides a basis for some researchers to propose the evaluation equations of the dome grid shells [3–5]. But as a kind of approximate method, it can only be used with specific shapes and grids. The finite element method applied in buckling analysis can analyze the buckling characteristics of space frames exactly, however, it is complex and inconvenient to be used for common engineers and/or designers. Therefore, the authors devote to searching a method to evaluate the buckling load of dome grid shells easily.

In the research by Aitziber Lopez [6], Altuna Zugasti [7], etc., the authors notice that a clear statistical relationship can be found between the buckling load and geometric parameters of grid shells. Moreover, regression analysis, which associates with large scales of statistical data analysis, is applied more and more in the evaluation of global buckling load for space frames [8]. Accordingly, the author LIU assume that within the conventional structural design (conventional shape, span, height and so on), the relationship between geometric parameters and buckling loads may be expressed into formulations and/or equations. The past research by authors realized that assumption which fitted an approximate equation for the single-layer space frames [9]. Based on the same method and principle, an equation are proposed to evaluate the buckling loads for dome grid shells in this paper.

For the early stage of this study, this paper mainly introduces the methodology with dome grid shells with pipe-shaped members, and consider the analytical models as ideal linearly elastic structures. The geometric parameters are introduced as grid-density n , arc-angle θ , span L , and diameter of member section \emptyset . In addition, the influence of initial imperfection, non-linear buckling features et cetera will be investigated as effect factors to adjust the evaluation equation in the next stage.

2 Design Parameters and Analytical Cases

2.1 Geometric Parameters and Effective Stiffness

In this study, the design parameters for a dome grid shell are separated as the geometric parameters and effective stiffness. Figure 1 introduces the geometric parameters as span $L = L_x = L_y$, angle θ (related to Rise h), grid-density $n = n_x = n_y$, and the diameter of pipe members \emptyset .

As well known, the overall stiffness significantly affects the buckling capacity of a grid shell dome. For considering the influence of overall stiffness, the authors have compared the previous studies on the equivalent/effective stiffness related to the buckling characteristics of single-layer grid shells [10–12], and consequently

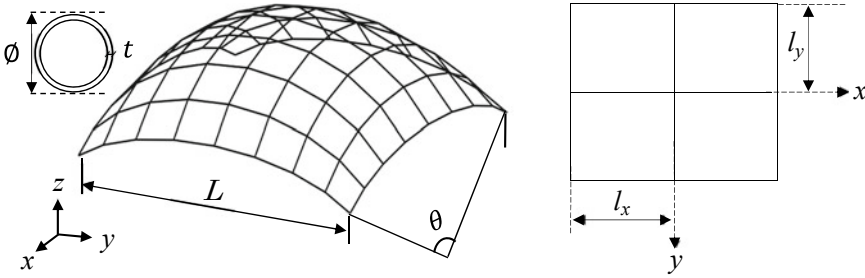


Fig. 1 Geometric parameters and grid for a dome

adopt the effective stiffness proposed by Dong [12], which is separated as membrane stiffness B and flexural stiffness D .

$$B_x = \frac{EA_x}{l_x} \quad B_y = \frac{EA_y}{l_y} \tag{1}$$

$$D_x = \frac{EI_x}{l_x} \quad D_y = \frac{EI_y}{l_y} \tag{2}$$

where the subscripts x, y indicate the directions shown in Fig. 1, I_x, I_y are the second moment of area of members, A_x, A_y are the area of members, l_x, l_y are the spacing of members, E is Young’s modulus of members. In this study, $B_x = B_y, D_x = D_y$, because the spans and grid density are set as the same in x and y directions, respectively, $L_x = L_y, n_x = n_y$.

2.2 Analytical Cases

As shown in Fig. 2, 5 kinds of span L , 7 kinds of angle θ , 7 kinds of grid-density n , and 5 kinds of diameters ϕ , in a total of 1225 cases for linear buckling analysis are carried out. In addition, the diameters of member sections are uniformed as pipe for each analysis case (for each diameter case), and the pipe thickness is kept as a constant of $t = 6$ mm. The member material is assumed as SS400 (JIS) with Young’s modulus of $E = 2.05 \times 10^5$ N/mm² and Poisson’s ratio $\nu = 0.3$. The vertical distributed load acting on the horizontal projection plane is 1 kN/m². The boundary condition is pin-supported at four edges. In addition, the analysis models are set as ideal linearly elastic structures, all initial imperfections are ignored.

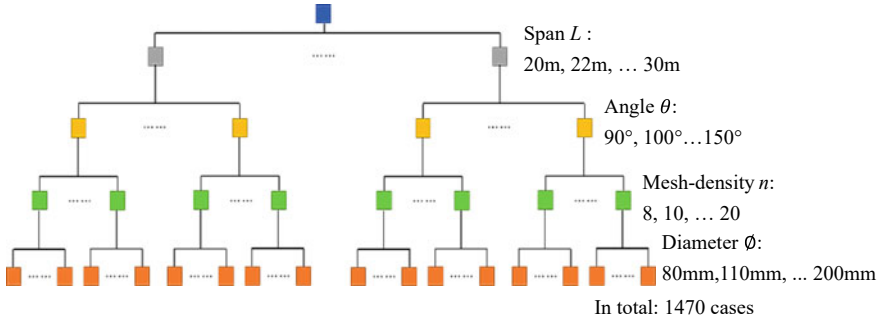


Fig. 2 A hierarchical tree for illustrating the analysis cases

3 Principle of Fitting Method

In this study, to build the relationship among the buckling load factors λ , geometric parameters and effective stiffness, a large number of linear buckling analyses are carried out. Linear and non-linear buckling analysis are contacted well by pioneer researchers. Nevertheless, nonlinear buckling analysis is associated with incremental convergence analysis and bifurcation searching, which will cost much CPU time. Moreover, many researchers like S. Kato discussed and verified the effectiveness of linear buckling analysis [5]. Accordingly, a buckling analysis program “CPS” [13] developed by author Chen is used for the linear buckling analysis in this study. In general, the linear buckling analysis can be handle as eigenvalue problems [14]:

$$(\mathbf{K}_L + \lambda^{(i)} \mathbf{K}_G) \mathbf{U}^{(i)} = 0 \tag{3}$$

where \mathbf{K}_L and \mathbf{K}_G are the matrices representing the linear and geometric stiffness, respectively, $\lambda^{(i)}$ is the linear buckling load parameter associated with the i_{th} buckling mode $\mathbf{U}^{(i)}$. In this study, the authors use the first eigenvalue value λ as the buckling load factor.

In subsequence, the buckling load factors λ , geometric parameters and effective stiffness are set as the variables to compose a dataset for being inputted into the 1stOpt, which is a powerful software that can conduct statistical analysis and regression analysis [15]. This study applies two kinds of internal functions of 1stOpt: the function of mathematical formulation generation and the regression analysis based on the optimization algorithms. The function of mathematical formulation generation can randomly combine ten thousand kinds of mathematical formulations via its database. According to the dataset, the regression analysis fits the formulations one by one to output the regression equations with coefficients, where the optimization algorithms optimize the coefficients in the fitting process. The outputted equations are ranked according to the coefficient of determination R^2 which is defined as following [16]:

$$R^2 = 1 - \frac{\sum_i (\lambda_i - \lambda_{api})^2}{\sum_i (\lambda_i - \bar{\lambda})^2} \tag{4}$$

where λ_i is the buckling factors gained by linear buckling analysis, $\bar{\lambda}$ is the average value of λ_i , λ_{api} are the results calculated by the regression equations, and i indicate the analytical case number. For the best case, the λ_{api} should exactly match the λ_i , while the R^2 should be almost equal to 1.

4 Numerical Analysis

In this section, the influence of geometric parameters on buckling load factors λ and effective stiffness is first demonstrated. Subsequently, the process of fitting the approximate equation by 1stOpt is introduced.

4.1 Analytical Results

Figure 3 shows the influence of span L , grid-density n , angle θ , and diameter ϕ on buckling load factors λ , where the 5 lines with colors in every figure correspond to 5 kinds of diameter ϕ . It can be found that only the trends of θ on λ is non-monotonic changed, span L has negative correlations on λ , while the influence of grid-density n and diameter ϕ on λ is opposite. In order to build the dataset of 1stOpt for fitting the equation, same as past research by authors [9], the present study also sets $K = \sqrt{BD} \times 10^{-13}$, n , $\sinh \theta$, L as independent variables, and buckling load factors λ as dependent variables. As illustrated in Fig. 4a shows the relation of λ between $\sinh \theta$ and K with different n for span $L = 20$ m; (b) is the perspective of (a). Through the 1stOpt, the distribution of Fig. 4 is projected into λ - N plane as shown in Fig. 5 (a), the distribution of analysis results for all spans can be found in Fig. 5 (b), where the horizontal axis N represents the analysis case number (referring to Fig. 2).

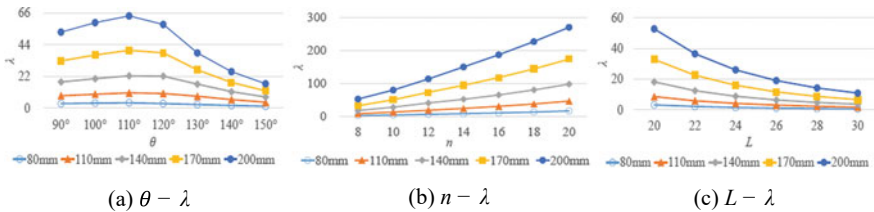


Fig. 3 Influence of geometric parameters on buckling load factors λ

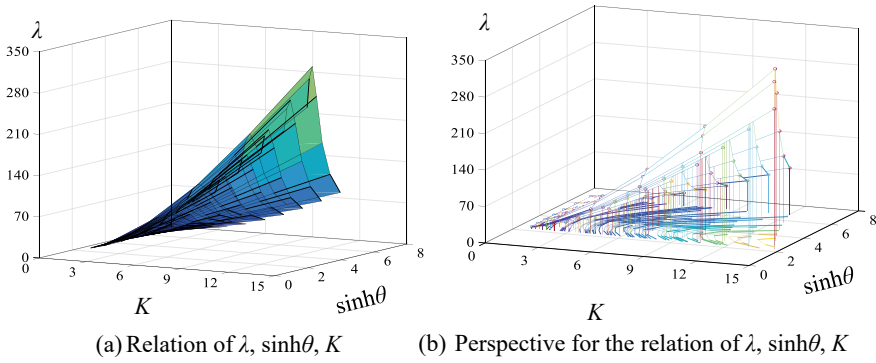


Fig. 4 The distribution of analysis result for the cases of $L = 20$ m with $n = 8-20$

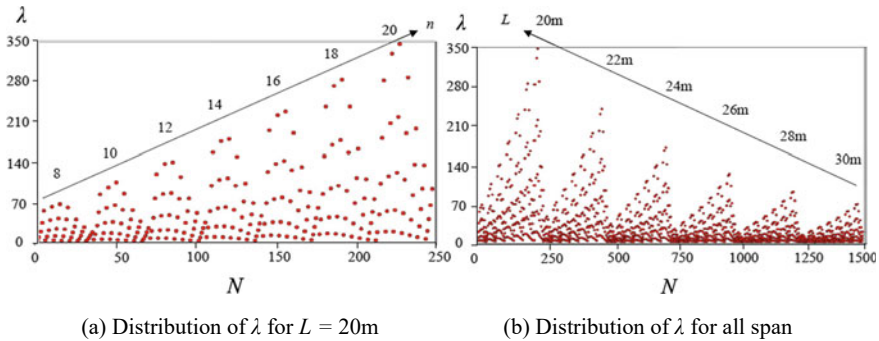


Fig. 5 The projection of distribution of analysis result in λ - N plane

4.2 The Fitting of the Approximate Equation

In Fig. 5b, it can be found that the same variation trends of analysis results appear for different spans from span 20–30 m. When carrying out the regression analysis, the internal algorithm of 1stOpt automatically ignores the precision of the smaller values for span 30 m. Therefore, the authors divide the distribution of all analysis results into six parts corresponding to six kinds of spans respectively, and use the distribution of $L = 20$ m shown in Fig. 5a as a foundational dataset to fit a foundational equation. As a result, a concisely and precisely foundational regression equation for the foundational dataset of $L = 20$ m is found as expressed in Eq. (5) with $R^2 = 0.9771$, where its high compatibility is shown in Fig. 6a.

$$\lambda_{20} = -5.578 - 0.554K \sinh \theta + 0.499K^2 \sinh \theta + 0.235Kn + 0.0215K \sinh \theta n + 6.699K - 0.0821K^2 \sinh^2 \theta \tag{5}$$

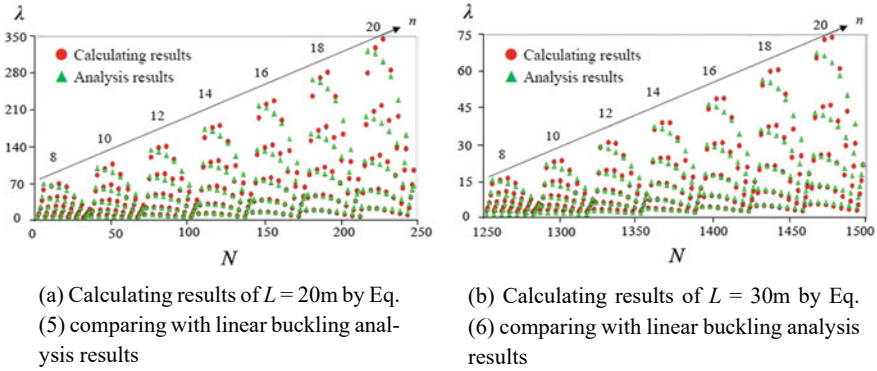


Fig. 6 Calculating results comparing with linear buckling analysis results

Table 1 Attenuation coefficient α_L and R^2

$L(\text{m})$	20	22	24	26	28	30
α_L	1	0.788	0.631	0.512	0.421	0.350
R^2	0.9771	0.9785	0.9790	0.9787	0.9779	0.9767

Then through a series of statistical analyses and regression analyses, the approximate equation is fitted as Eq. (6). The attenuation coefficients α_L and R^2 for each span L are shown in Table 1.

$$\lambda_{ap} = \alpha_L \lambda_{20} \tag{6}$$

As illustrated in Fig. 6b, the calculating results of span 30m by Eq. (6) match the linear buckling analysis result very well, while Fig. 7 shows all cases from span 20m to 30m. It should be noted that the λ calculated by Eq. (6) is the multiplier of the vertically distributed load p acting on the horizontal projection plane. This study carries out buckling analysis with setting $p = 1 \text{ kN/m}^2$ as a standard load, so that the buckling load P_{cr} of a single-layer grid shell is calculated as $P_{cr} = \lambda \text{ kN/m}^2$.

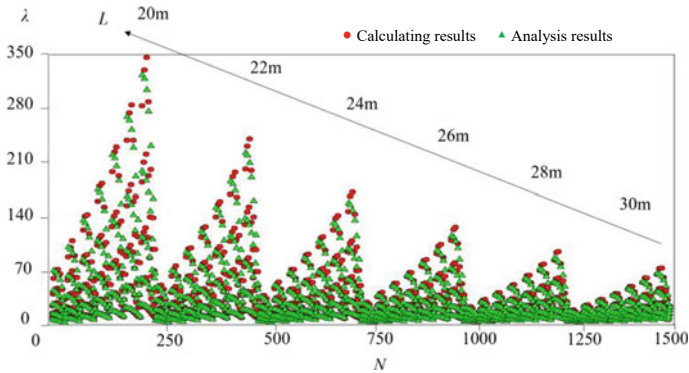


Fig. 7 Calculating results comparing with linear buckling analysis results for all cases

5 Conclusion

This study analyzes 1225 cases of dome grid shells with various geometric parameters by linear buckling analysis. According to the regression analysis based on 1stOpt, an approximate equation for estimating the global buckling load is fitted as Eq. (6), which consists of foundational equations Eq. (5) and attenuation coefficient α_L shown in Table 1. The high coefficient of determination R^2 illustrates that the proposed equation is enough to evaluate the global buckling load factors for the dome grid shell with pipe-shaped members, where its buckling load P_{cr} can be calculated as $P_{cr} = \lambda \text{ kN/m}^2$.

However, though the influence of span L and grid-density n are considered in this paper, the buckling evaluating equations for structures with different spans and meshing-density in x and y directions, $L_x \neq L_y$ and $n_x \neq n_y$ are expected to be reported in coming issue. Moreover, the influence of initial form imperfection and verification and validation for non-linear buckling analysis remains an interesting topic. In addition, the authors will extend this research to the other grid shells with various shapes and boundary conditions.

Acknowledgements The author LIU would like to show his sincere gratitude to ASSURAN International Scholarship Foundation for supporting his life of studying abroad.

References

1. Wright DT (1965) Membrane forces and buckling in reticulated shells. In: Proceedings of the American society of civil engineers. J Struct Div 21:175–201
2. Yamada S (1991) Relationship between non-linear numerical experiments and a linear lower bound using finite element method on the overall buckling of reticular partial cylindrical space

- frames. In: Proceedings of the 4th international conference on computing in civil and building engineering, pp 259–266
3. Hangai Y (1987) Structural behaviors of single-layer space frames (Part 1)—formulae for buckling loads of single-layer domes. *SEISAN KENKYU* 39(12):17–20. (In Japanese)
 4. Chen X, Wang N, Shen SZ (1994) Ultimate loading capacity of braced domes. In: IASS-ASCE, Symposium, pp 539–546
 5. Kato S, Yamashita T (2002) Evaluation of elasto-plastic buckling strength of two-way grid shells using continuum analogy. *Int J Space Struct* 17(4):249–261
 6. López A, Puente Iñigo, Serna MA (2007) Direct evaluation of the buckling loads of semi-rigidly jointed single-layer latticed domes under symmetric loading. *Eng Struct* 29(1):101–109
 7. Altuna-Zugasti AM, Lopez-Arancibia A, Puente I (2012) Influence of geometrical and structural parameters on the behaviour of squared plan-form single-layer structures. *J Constr Steel Res* 72:219–226
 8. Zhu S, Ohsaki M, Guo Z (2021) Prediction of non-linear buckling load of imperfect reticulated shell using modified consistent imperfection and machine learning. *Eng Struct* 226
 9. Liu B, Chen PS, Yan X, Jin J (2022) Approximate equation for evaluating global buckling load of single-layer cylindrical space frames with crossing pattern. In: 2022 annual symposium of international association for shell and spatial structures, 13th Asian-Pacific conference on shell and spatial structures
 10. Makowski ZS (1984) Analysis, design and construction of braced domes. New York
 11. Heki K (1977) Structural mechanics II. Japan (In Japanese)
 12. Dong S (1958) Analysis of lattice flat shells consisting of lamella arch system. *China Civ Eng J* 18(3):3–19 (in Chinese with English abstract)
 13. Jin J, Qian X, Chen PS (2021) Study on buckling characteristics of cylindrical and domed 1.5-layer space frames with lap-units. *J Struct Eng Architectural Inst Japan* 67B:251–260
 14. Chair of Working Group 8, Draft Guide to Buckling Load Evaluation of Metal Reticulated Roof Structures. The International Association for Shell and Spatial Structures (2014)
 15. Cheng X, Wang Y, Liu H (2009) Study on optimal regulation modelling of reservoir discharge. In: Advances in water resources and hydraulic engineering. Springer, Berlin
 16. Zhang D (2016) A coefficient of determination for generalized linear models. *The American Statistician* 71(4)

Experimental Test of Perforated Steel Plate Shear Wall Under Cyclic Load



Nidiasari, Rendy Thamrin, Sabril Haris, and Ronny Purba

Abstract Steel Plate Shear Wall is a steel frame system with stiffeners that are effective in resisting lateral forces. The shear wall functions as a fuse, so the failure mechanism is expected to occur in the plate first. The shear wall plate is designed to be relatively thin to achieve this mechanism, but the appropriate thickness will be challenging in low-rise buildings. The perforations given to the shear wall panels aim to reduce the shear capacity and stiffness of the plate. This research is an experimental test on three specimens of shear wall plates. Tests are only carried out on shear wall plates without beams and columns. Variations in the form of the percentage of perforation area are given to the specimen to see the cyclic behavior of the plate when receiving lateral loads. The percentage is obtained from the ratio of the perforation area to the total plate area. The type of perforation used is circular, with a diameter of 65 mm. The test results show that the shear wall plate has a stable hysteresis curve for all specimens. The different inelastic behavior can be seen from the hysteresis curve pattern formed during the test.

Keywords Steel plate shear wall · Lateral load · Perforation · Experimental study · Cyclic load · Hysteretic curve

1 Introduction

Earthquakes are an unavoidable natural phenomenon. The structural system receives the effects of an earthquake. Most of the structural damage caused by earthquakes is the result of the structure's response to ground shaking [1]. Earthquakes that can damage structures demonstrate the importance of improving design quality in earthquake-resistant construction [2]. Structural damage due to the earthquake, in

Nidiasari (✉) · R. Thamrin · S. Haris
Civil Engineering Department, Universitas Andalas, Padang, Indonesia
e-mail: nidia@eng.unand.ac.id

R. Purba
Civil Engineering Department, Universitas Bandar Lampung, Lampung, Indonesia

© The Author(s), under exclusive license to Springer Nature Singapore Pte Ltd. 2024
M. Casini (ed.), *Proceedings of the 3rd International Civil Engineering and Architecture Conference*, Lecture Notes in Civil Engineering 389,
https://doi.org/10.1007/978-981-99-6368-3_25

addition to impacting high-rise buildings, also affects low-rise buildings and residential houses. Data on the damage caused by the earthquake that hit West Sumatra due to the September 30, 2009 earthquake shows that the types of buildings that suffered the most were government offices, schools, and shop houses [3]. The building is generally classified as a low-rise building. Low-rise buildings are buildings with a number of story less than four [4] or have a height of less than 60 ft (18.3 m) [5].

Earthquake forces are called lateral forces, these forces are applied horizontally to the structural system. For the structure to withstand earthquake forces, the structure must have adequate lateral stiffness. Shear walls have stiffness in a relatively high to withstand lateral forces [6]. The type of shear wall used in steel structures is Steel Plate Shear Wall/Special Plate Shear Wall (SPSW). SPSW consists of thin steel plates framed by Vertical Boundary Elements (VBE) and Horizontal Boundary Elements (HBE). The plate is installed in one or more cavities along the structure's total height to form a cantilevered wall [7–9]. The characteristics used as infill panels in steel plate shear walls are very slender plates and are prone to diagonal buckling [10]. SPSW mechanism in resisting lateral loads through diagonal stress on the web plate [11, 12].

The difficulty in plate selection in the SPSW system is that the available plate material may be stronger or thicker than the required design. This will increase the size of the structural members (beams and columns) and the foundation, as these structural components are generally designed for plate strength. The application of the SPSW system to withstand lateral loads due to earthquakes is not only limited to high-rise buildings; this system can also be applied to residential houses and low-rise buildings [11]. In the design of low-rise buildings, the required steel plate is thinner than in high-rise structures. One way to reduce the capacity of the plate is to give perforations (holes) on the plate. Tests on web plates with perforations show that the plates have adequate ductility. So the plate with perforation can be used as an alternative to reduce the capacity of the plate [7]. This study aims to obtain the effect of the percentage of perforation area on the SPSW plate on the shear capacity through experimental testing.

2 Methodology

Experimental testing was carried out at the Department of Civil Engineering, Universitas Andalas, at the Materials and Structures Laboratory. In this study, only the infill plate was tested. The plate was tested without vertical and horizontal boundary elements. The dimensions of the plate used were 900 × 900 mm. These dimensions follow the availability of space that can be accommodated by the main frame available in the laboratory.

2.1 Experimental Setup and Loading Protocol

The test setup in this study is a modification of the shear wall test carried out by Setiawan et al. [13]. In that study, the testing set follows the research conducted by Egorova et al. (Fig. 1) [14]. Modification is done by changing the orientation of the direction of the load given by the load cell. In the previous, the load cell was placed vertically, while in this study, the load cell is placed in the horizontal direction (Fig. 2). This modification makes the plate installation and disassembly work easier.

To model the relationship of the plate to the support, VBE, and HBE, the four sides of the plate are clamped by canal steel sections. So that the plate is free to experience translation, the four corners are given a pin mechanism. In addition to avoiding displacement in the out-of-plane direction, steel turnbuckles were placed at four positions of the top beam. Each side has two slings placed at the left and right corners. So that the sling mechanism does not interfere with the movement in the system, the connecting plate between the sling and the upper beam must be ensured



Fig. 1 Experimental Set-up by a Egorova et al. and b Setiawan et al.

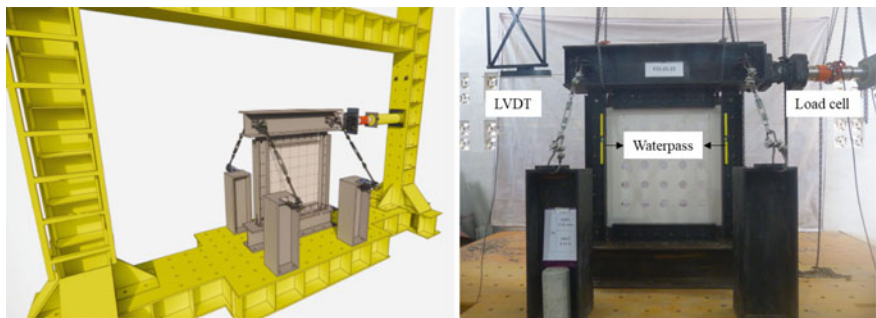


Fig. 2 Experimental setup

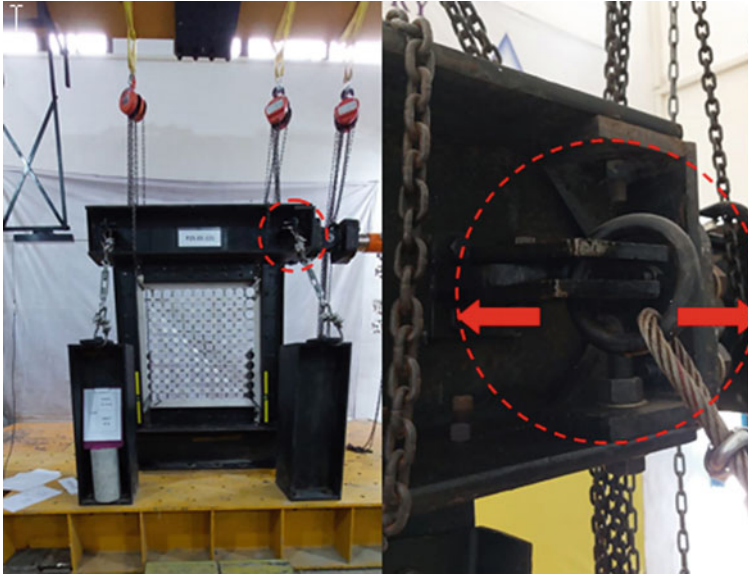


Fig. 3 Sling connection

to be able to move freely to the right or the left according to the direction of loading (Fig. 3). To monitor the out-of-plane condition during loading, two water passes are placed.

Loading considers the provisions of AISC 341-16 [15]. In the first cycle, the load is applied until a drift of 0.25% or equivalent to a displacement of 2.25 mm, and then the load is continued until the maximum drift. The maximum drift applied in this test was 11% drift of the specimen. Figure 4 shows the loading protocol used during the test.

2.2 Specimens Detail

The plates tested in this study were made of steel plates with a thickness of 2 mm. The dimensions and thickness of the plate refer to the research conducted by Setiawan et al. [13]. The test variable in this study was the perforation area. Three specimens were designed to study the shear capacity under the cyclic load and the effect of the perforation area observed. The perforation on the plate is a circle with a diameter of 65 mm. Different percentages of area are obtained by placing a different number of holes in each specimen. The details of the plate test specimens can be seen in Table 1.

Each specimen has an ID indicating the specimen type, thickness, perforation layout, diameter, and several perforations on the plate (Fig. 5.). The S notation in

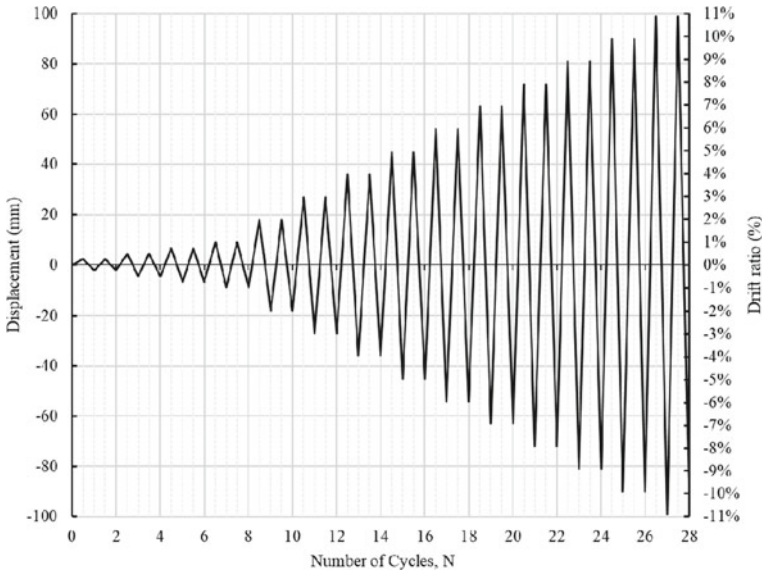


Fig. 4 Cyclic loading protocol

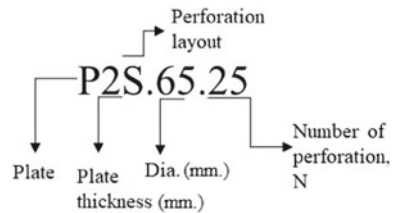
Table 1 Specimen size

Model	D (mm)	N _{pr}	% of perforation
P2S.65.25	65	25	10.25
P2S.65.81	65	81	33.20
P2S.65.121	65	121	49.59

P2S indicates the hole arrangement in the specimen, which is parallel in a straight configuration.

The perforation pattern is made on the plate using a waterjet cutting machine to ensure the holes are neatly formed and have a smooth surface. The specimens are shown in Fig. 6. The plates are painted white, so it is easy to observe.

Fig. 5 Description of specimen ID



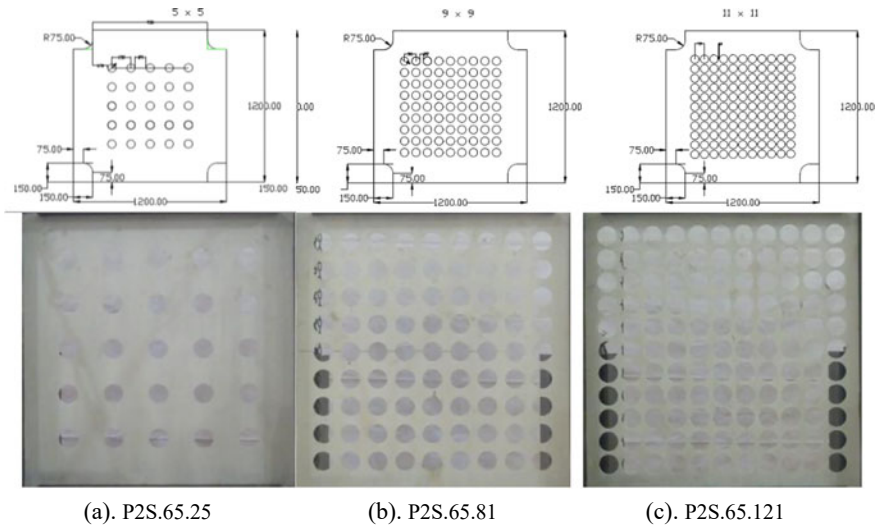
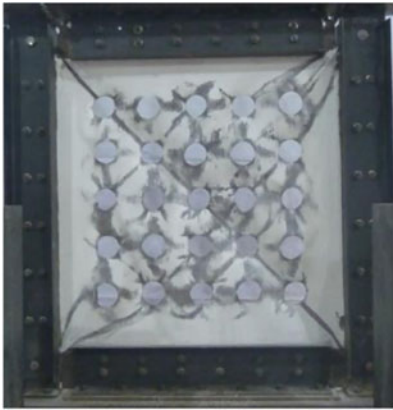


Fig. 6 Specimen object

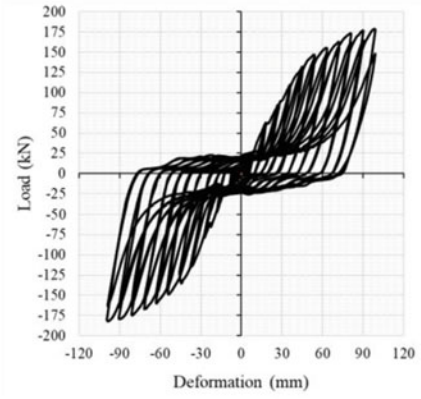
3 Result and Discussion

The test results were obtained based on the loading protocol applied to the specimen. The initial loading was at a drift of 0.25% and continued until the test object experienced a decrease in strength. Observations were made during the loading process. The paint on the specimen surface begins to peel off as the plate begins to deform. The tension field action can be seen from the formation of a diagonal line on the surface of the plate. During the loading cycle, buckling occurs parallel to the diagonal direction. The loading cycle is stopped if there is an indication of a decrease in the load or the stroke of the load cell has reached 99 mm (Figs. 7, 8 and 9a). At the end of loading, tears appeared in the center of the plate in specimen P2S.65.25 and the upper and lower right corners of the plate in specimen P2S.65.121. There are no tears in specimen P2S.65.81.

The data obtained from the experimental tests are shown in a hysteresis curve (Figs. 7, 8 and 9b). From this curve, it can be seen the maximum shear capacity in each cycle, as well as the inelastic behavior during the loading protocol. Specimen P2S.65.25 has the highest shear capacity for each loading cycle. The inelastic behavior of the plate became more ductile in the P2S.65.81 and P2S.65.121.

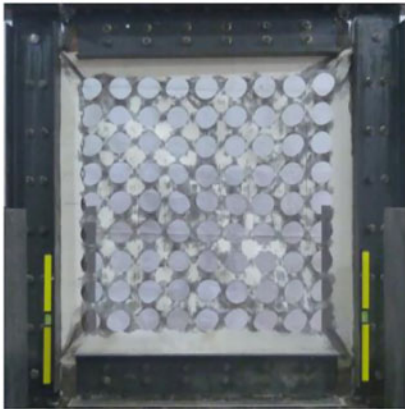


(a)

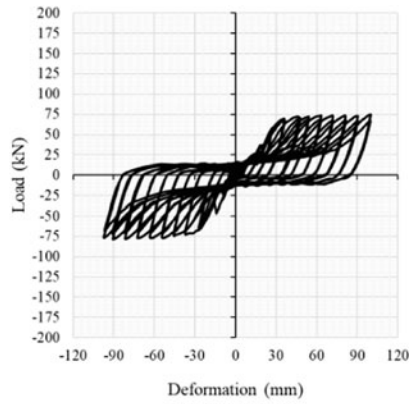


(b)

Fig. 7 a Specimen at max drift 11% and b hysteresis curve of P2S.65.25



(a)



(b)

Fig. 8 a Specimen at max drift 11% and b hysteresis curve of P2S.65.81

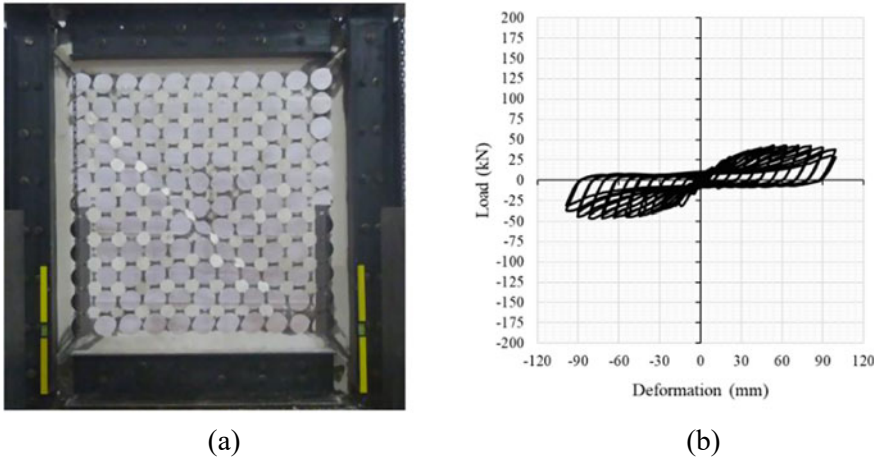


Fig. 9 **a** The specimen at max drift 11% and **b** hysteresis curve of P2S.65.121

4 Conclusion

The experimental study was carried out on three SPSW specimens. The following are some conclusions obtained from the test results:

1. Perforation percentage affects the plate's shear capacity and inelastic behavior.
2. The larger the percentage of perforations, the smaller the shear capacity of the plate.
3. The plate with a 33.2% perforation proportion exhibits inelastic behavior and has more ductile than the other two specimens.

Acknowledgements This study was supported by the Civil Engineering Department and Engineering Faculty of Universitas Andalas.

References

1. Hamburger RO (2009) Earthquakes and Seismic Design. In: Facts for steel building. American Institute of Steel Construction, United States of America pp i–64. [Online]. Available: <https://www.aisc.org/globalassets/aisc/publications/facts-for-steel-buildings-3-earthquakes-and-seismic-design.pdf>
2. Applied Technology Council, "Building Safety and Earthquakes Part A: Earthquake Shaking and Building Response." ATC/SEAOC Joint Venture Training Curriculum. [Online]. Available: <https://www.atccouncil.org/pdfs/bp1a.pdf>
3. EERI, "Learning from Earthquakes The Mw 7.6 Western Sumatra Earthquake of September 30, 2009," EERI, December 2009
4. Mujagic JRJ (ed) (2012) Structural design of low-rise buildings in cold-formed steel, reinforced masonry, and structural timber. McGraw-Hill, New York

5. American Society of Civil Engineers (2017) (ed) Minimum design loads and associated criteria for buildings and other structures. American Society of Civil Engineers, Reston, Virginia
6. Coull A, Smith BS (1967) Analysis of shear wall structures. In: Tall buildings. Elsevier, pp 139–155. <https://doi.org/10.1016/B978-0-08-011692-1.50012-2>
7. Roberts TM, Ghomi SS (1991) Hysteretic characteristics of unstiffened plate shear panels. *Thin-Walled Struct* 12(2):145–162. [https://doi.org/10.1016/0263-8231\(91\)90061-M](https://doi.org/10.1016/0263-8231(91)90061-M)
8. Astaneh-Asl A (2001) Seismic behavior and design of steel shear walls. Structural steel educational council. Moraga, California
9. Bruneau M, Uang C-M, Sabelli R (2011) Ductile design of steel structures, Second. The McGraw-Hill Companies
10. Zhao Q, Sun J, Li Y (2017) Analyses on seismic behavior of corrugated steel plate shear walls. In: Proceedings of the annual stability conference. San Antonio, Texas
11. Sabelli R, Bruneau M (2006) Steel plate shear wall. American Institute of Steel Construction Inc., United State of America
12. Vian D, Bruneau M (2005) Steel plate shear walls for seismic design and retrofit of building structure. University at Buffalo, New York, Technical Report MCEER-05-0010
13. Setiawan D, Bellisca W, Purba RH, Haris S, Thamrin R, Moestopo M (2022) Dinding Geser Pelat Baja Sebagai Sistem Pemikul Beban Gempa untuk Mitigasi Kerusakan Struktur Bangunan Bertingkat Rendah. In: Seminar Tahunan dan Pameran HAKI “Ketahanan Gempa pada Bangunan Gedung dan Infrastruktur. Jakarta, Indonesia
14. Egorova N, Eatherton MR, Maurya A (2014) Experimental study of ring-shaped steel plate shear walls. *J Constr Steel Res* 103:179–189. <https://doi.org/10.1016/j.jcsr.2014.09.002>
15. ANSI/AISC 341-16, Seismic provisions for structural steel buildings. American Institute of Steel Construction, United States of America

Identification of Column Bases' Stiffnesses in Steel Moment-Resisting Frames Based on Fishbone Model and Bayesian Inference



Jing He and Xiaohua Li

Abstract This paper presents a method of identifying the stiffness of column bases in steel frames based on the fishbone model and the hierarchical Bayesian update method. In this study, the fishbone model considering the flexibility of column bases can be used to update the rotational and shear stiffness of the column base, which is impossible in the traditional model updating method because the previous model assumes that the column bases are fully rigid. First, the steel frame is simplified into a fishbone model considering the flexibility of the column bases, and thus the eigenvalue problem of the fishbone model is established. Then, the shear stiffness and rotational stiffness of the column base of the fishbone model are identified using incomplete modal data based on the hierarchical Bayesian model updating algorithm. The effectiveness of this method is numerically studied by using a 5-story steel frame model using the first fourth frequencies and the corresponding lateral components of the mode shapes.

Keywords Stiffness identification · Column base · Fishbone model · Hierarchical Bayesian update algorithm · Steel frame

1 Introduction

The steel moment-resisting frame structures used in earthquake-prone areas can reduce damage caused by earthquakes [1]. Previous earthquakes [2, 3] and experiments [4, 5] showed that local buckling and cracks could be observed at the beam ends and column bases of steel frames due to the accumulation of plastic strain under strong earthquakes.

So far, most studies have focused on identifying damage at beam ends. Li et al. [6] proposed a method to assess post-earthquake damage of beam ends in steel frames based on the fishbone model with column bases assumed to be fully rigid. Wang

J. He · X. Li (✉)

School of Civil Engineering, Chongqing University, Chongqing, China
e-mail: lixiaohua@cqu.edu.cn

© The Author(s), under exclusive license to Springer Nature Singapore Pte Ltd. 2024
M. Casini (ed.), *Proceedings of the 3rd International Civil Engineering and Architecture Conference*, Lecture Notes in Civil Engineering 389,
https://doi.org/10.1007/978-981-99-6368-3_26

301

et al. [7] proposed a method based on convolutional neural networks (CNN) using acceleration response to detect fractures at beam ends. However, this method required acceleration sensors arranged at each beam end. Iyama et al. [8] proposed a method to detect cracks at the beam ends after earthquakes. The local stiffness calculated from the measured acceleration and strain response data was compared with the local stiffness estimated from Pushover and modal analysis, and the result was used as a detection threshold to determine if cracks were present, but the stress transfer mechanism of this method might not always be similar to that of actual structures.

Although many studies have proposed methods to identify damage at beam ends, most were limited to the assumption that the column bases were rigid or semi-rigid. However, since the dynamic properties are sensitive to changes in the support conditions and it is difficult to estimate the initial state of the support conditions [9], the accuracy of the identified results is low, so it is important to consider the flexibility of the column bases.

This paper proposes a method for identifying the stiffness of column bases. The steel frame is simplified as a fishbone model considering the flexibility of the column bases. Then, the stiffnesses of the column bases can be identified using incomplete modal data based on the hierarchical Bayesian algorithm. The effectiveness of the presented method can be verified by the numerical results of a 5-story, 2-bay steel frame model.

2 Column Base Stiffness Identification Method

2.1 Shear and Rotational Stiffness of the Column Base

The embedded column can be idealized as a Bernoulli–Euler beam, which is placed on an elastic base with a rotational spring, as shown in Fig. 1. The equations for the shear stiffness and rotational stiffness of the column base are

$$k_{tt} = \frac{V_{\text{column}}}{s} \quad (1)$$

$$k_{\text{oo}} = \frac{M_{HB}}{\alpha} \quad (2)$$

where M_{HB} and V_{column} are the moment and shear at the top of the base [10], respectively, calculated by idealizing the force transfer of the column base based on experimental observations and finite element simulations [11]. s and α are the horizontal displacement and the rotational displacement at the top of the column base, respectively, which can be solved by summing the horizontal and rotational displacements at the top of the column base caused by the three loads M_{HB} , M_{base} and V_{column} [12], respectively, depicted in Fig. 1. M_{base} is the moment at the bottom of the base, which can be obtained from the rotational spring stiffness k_s [13].

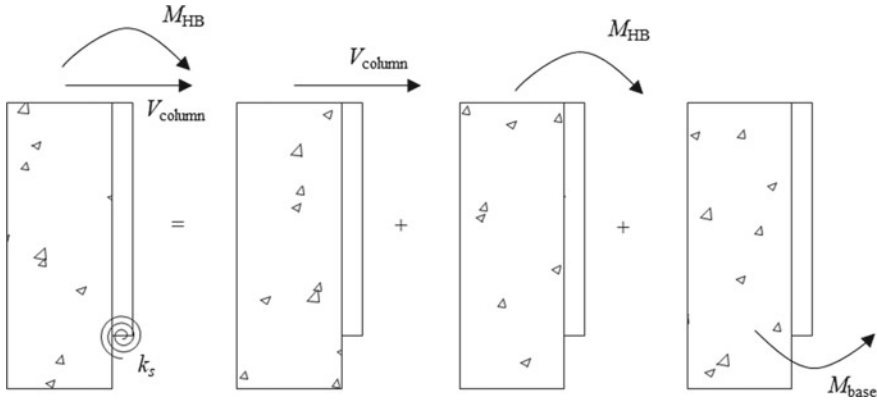


Fig. 1 Simplified model of the embedded column

2.2 Eigenvalue Problem of Fishbone Model

An n -story r -bay steel frame can be simplified to a fishbone model considering the flexibility of column bases, which is a solution to the problem of assuming fully rigid column bases in previous studies, as shown in Fig. 2.

The lumped mass of the i th floor m_i is obtained by adding half of the mass of the i th column and $i + 1$ th column to the mass of the beam on the i th floor. The lumped mass of the column base m_0 is half of the mass of the column on the first floor.

The shear stiffness of the column base k_t and the rotational stiffness of the column base can be respectively calculated as

$$k_t = \sum_{j=1}^{r+1} k_{tj} \tag{3}$$

$$k_o = \sum_{j=1}^{r+1} k_{ooj} \tag{4}$$

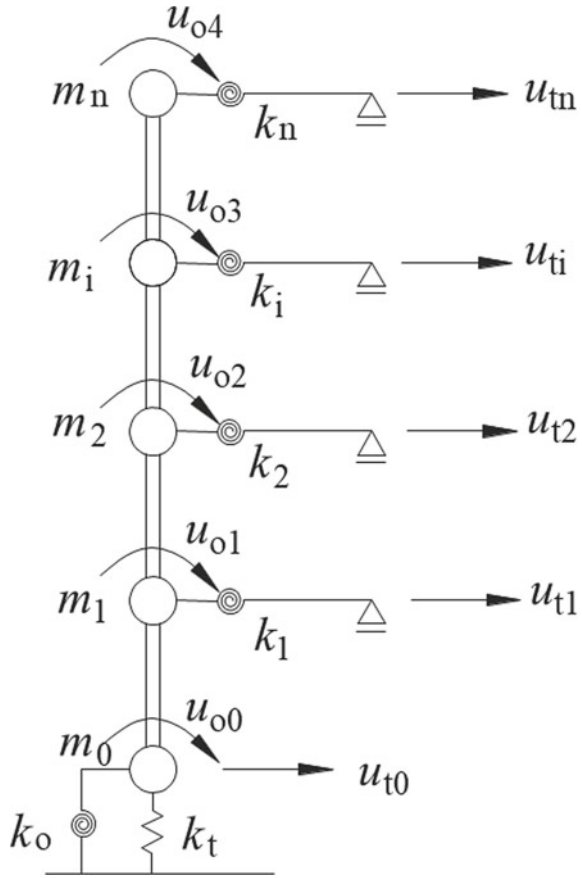
where k_{tj} and k_{ooj} are the shear stiffness and rotational stiffness of the j th column base given by Eqs. (1) and (2), respectively.

The stiffness of the rotational spring located at the i th story k_i is calculated as

$$k_i = 2 \sum_{j=1}^r k_{Bij} = 2 \sum_{j=1}^r \frac{6EI_{Bij}}{L_{ij}} \tag{5}$$

where k_{Bij} is the stiffness of the j th beam on the i th floor; E is the elastic modulus of the steel; I_{Bij} and L_{ij} are the moments of inertia and the length of the j th beam on the i th floor, respectively.

Fig. 2 Fishbone model considering the flexibility of column bases



The flexural rigidity of the representative column on the i th floor k_{ci} is expressed as

$$k_{ci} = \sum_{j=1}^{r+1} k_{C_{ij}} = \sum_{j=1}^{r+1} EI_{C_{ij}} \tag{6}$$

where $k_{C_{ij}}$ is the flexural rigidity of the j th column on the i th floor; $I_{C_{ij}}$ is the moment of inertia of the j th column on the i th floor.

Considering the lateral displacements $\mathbf{u}_t \in \mathbf{R}^{n+1}$ and the rotational displacements $\mathbf{u}_o \in \mathbf{R}^{n+1}$, the undamped free vibration equation of the fishbone model can be established as [14]

$$\mathbf{MR} + \mathbf{Ku} = \mathbf{0} \tag{7}$$

where $\mathbf{u} = [\mathbf{u}_t^T \ \mathbf{u}_o^T]^T \in \mathbf{R}^{2n+2}$ is displacement vector; $\mathbf{M} = \text{diag} (m_0, m_1, \dots, m_n, 0, \dots, 0) \in \mathbf{R}^{(2n+2) \times (2n+2)}$ is the mass matrix established by the lumped mass method; $\mathbf{K} \in \mathbf{R}^{(2n+2) \times (2n+2)}$ is the stiffness matrix.

Then frequencies and mode shapes could be obtained by solving the eigenvalue problem in Eq. (8).

$$\mathbf{K}\varphi_i = \omega_i^2 \mathbf{M}\varphi_i \tag{8}$$

where ω_i^2 and $\varphi_i \in \mathbf{R}^{2n+2}$ represent the i th frequency and the corresponding mode shapes, respectively.

2.3 Fishbone Model Updating

It is assumed that the flexural rigidities of the column are known, because they can be obtained from theoretical calculation. The stiffnesses to be updated are the shear stiffness and rotational stiffness of the column base and the stiffness of the rotational springs located at each story. Therefore, the vector for the unknown stiffness is defined as $\boldsymbol{\theta} = [\theta_1, \theta_2, \dots, \theta_{n+2}]^T = [k_t, k_o, k_1, \dots, k_n]^T \in \mathbf{R}^{n+2}$.

Then, the stiffness matrix of the fishbone model can be parameterized by $\boldsymbol{\theta}$ as

$$\mathbf{K}(\boldsymbol{\theta}) = \mathbf{K}_0 + \sum_{l=1}^{n+2} \theta_l \mathbf{K}_l \tag{9}$$

where \mathbf{K}_l is the stiffness matrix of the substructure for the l th stiffness parameter; \mathbf{K}_0 is the stiffness matrix after removing the parameters θ_i ($i = 1, 2, \dots, n + 2$).

Assume that the currently known data have the first $m (< 2n + 2)$ orders of frequencies $\hat{\omega}^2 = [\hat{\omega}_1^2, \hat{\omega}_2^2, \dots, \hat{\omega}_m^2]^T \in \mathbf{R}^m$ and the corresponding mode shapes

$\hat{\varphi} = [\hat{\varphi}_1^T, \hat{\varphi}_2^T, \dots, \hat{\varphi}_m^T]^T \in \mathbf{R}^{m \times s}$, where s is the number of observed components.

The parameters to be obtained are frequencies $\boldsymbol{\omega}^2 \in \mathbf{R}^{2n+2}$, the corresponding mode shapes $\boldsymbol{\varphi} \in \mathbf{R}^{(2n+2) \times (2n+2)}$ and the stiffness parameters $\boldsymbol{\theta} \in \mathbf{R}^{n+2}$.

According to Bayes' theorem, the posterior probability density function for the unknown parameters $\boldsymbol{\omega}^2$, $\boldsymbol{\varphi}$ and $\boldsymbol{\theta}$ is given as [15]

$$p(\boldsymbol{\omega}^2, \boldsymbol{\varphi}, \boldsymbol{\theta} | \hat{\omega}^2, \hat{\varphi}, \hat{\theta}) = \kappa p(\hat{\omega}^2, \hat{\varphi} | \boldsymbol{\omega}^2, \boldsymbol{\varphi}, \boldsymbol{\theta}, C) p(\boldsymbol{\omega}^2, \boldsymbol{\varphi}, \boldsymbol{\theta} | C) \tag{10}$$

where κ is a constant. $p(\hat{\omega}^2, \hat{\varphi} | \boldsymbol{\omega}^2, \boldsymbol{\varphi}, \boldsymbol{\theta}, C)$ is a Gaussian likelihood probability density function with mean $[(\boldsymbol{\omega}^2)^T, (\mathbf{L}_o \boldsymbol{\varphi})^T]^T$ and covariance matrix of the measurement errors $\boldsymbol{\Sigma}_\epsilon$, and $\mathbf{L}_o \in \mathbf{R}^{ms \times 2mn}$ is the "1 s" or "0 s" observation matrix that selects the components of $\boldsymbol{\varphi}$ in correspondence to the s measured degrees of freedom, $p(\boldsymbol{\omega}^2, \boldsymbol{\varphi} | \boldsymbol{\theta}, C)$ is a prior probability density function whose expression is

$$p(\omega^2, \varphi, \theta|C) = p(\omega^2, \varphi|\theta, C)p(\theta|C) \quad (11)$$

where $p(\omega^2, \varphi|\theta, C)$ is a prior probability density function conforming to the Gaussian distribution with a prescribed equation error variance σ_{eq}^2 , $p(\theta|C)$ is a Gaussian prior probability density function with the nominal value of the unknown stiffness parameter $\theta_\eta \in \mathbf{R}^{n+2}$ as the mean and the covariance matrix of the unknown parameter $\Sigma_\theta \in \mathbf{R}^{(n+2) \times (n+2)}$ as the covariance.

The objective function of independent variables ω^2 , φ and θ is the negative logarithm of the posterior probability density function $p(\omega^2, \varphi|\theta, C)$ excluding κ , obtained as

$$J(\omega^2, \varphi, \theta) = \frac{1}{2}(\theta - \theta^\eta)^T \sum_{\theta}^{-1} (\theta - \theta^\eta) + \frac{1}{2\sigma_{eq}^2} \sum_{i=1}^m \|(\mathbf{K}(\theta) - \omega_i^2 \mathbf{M})\varphi_i\|^2 + \frac{1}{2} \begin{bmatrix} \hat{\omega}^2 - \omega^2 \\ \hat{\varphi} - \mathbf{L}_0 \varphi \end{bmatrix}^T \sum_{\epsilon}^{-1} \begin{bmatrix} \hat{\omega}^2 - \omega^2 \\ \hat{\varphi} - \mathbf{L}_0 \varphi \end{bmatrix} \quad (12)$$

The optimum values of the shear stiffness and rotational stiffness of the column base can be determined by minimizing the objective function $J(\omega^2, \varphi, \theta)$ until the specified convergence criterion is met.

3 Numerical Example

A 5-story 2-bay moment-resisting frame model with column bases' embedded depth of 0.5 m, the width of 0.7 m and the flange width of 0.4 m was considered. The mass density of beams and columns was 2×10^4 kg/m. For the beams, the length was 6 m, and the stiffness values were $k_{B1j} = k_{B3j} = k_{B5j} = 80$ MN·m/rad and $k_{B2j} = k_{B4j} = 70$ MN·m/rad. For the columns, the heights were $h_1 = 3.5$ m, $h_2 = 5$ m, $h_3 = h_4 = h_5 = 4$ m, and the flexural rigidities were $k_{C1j} = k_{C2j} = 150$ MN·m², $k_{C3j} = k_{C4j} = 120$ MN·m², $k_{C5j} = 100$ MN·m² ($j = 1, 2$).

The model could be simplified to a fishbone model considering the flexibility of the column bases with lumped masses of $m_0 = 1.05 \times 10^5$ kg, $m_1 = 4.95 \times 10^5$ kg, $m_2 = 5.1 \times 10^5$ kg, $m_3 = 4.8 \times 10^5$ kg, $m_4 = 4.8 \times 10^5$ kg and $m_5 = 3.6 \times 10^5$ kg, flexural rigidities of representative columns of $k_{c1} = 450$ MN·m², $k_{c2} = 450$ MN·m², $k_{c3} = 360$ MN·m², $k_{c4} = 360$ MN·m² and $k_{c5} = 300$ MN·m² and rotational springs stiffness values of $k_1 = 320$ MN·m/rad, $k_2 = 280$ MN·m/rad, $k_3 = 320$ MN·m/rad, $k_4 = 280$ MN·m/rad and $k_5 = 320$ MN·m/rad. The shear stiffness and rotational stiffness of the column base were $k_t = 3.667 \times 10^4$ MN/m and $k_o = 644$ MN·m/rad, respectively. The first four orders of the model were $\omega_1^2 = 1.63$ Hz, $\omega_2^2 = 5.67$ Hz, $\omega_3^2 = 10.68$ Hz and $\omega_4^2 = 15.56$ Hz.

The shear stiffness of the column base of the fishbone was supposed to be constant and could be calculated from Eq. (3). Then the first four frequencies and the corresponding lateral components of the mode shapes were known. The nominal value of each stiffness parameter was chosen to be 400 MN·m/rad with a standard deviation of 400 MN·m/rad. The covariance matrix Σ_ϵ of the measurement errors was set to 1.0% for the measured frequencies and the diagonal standard deviations of the mode shapes. The variance of the equation error σ_{eq}^2 was 0.01.

Figure 3 shows that the lateral component and rotational component of the modal shapes could be accurately identified by the limited lateral component of modal shapes by the proposed method. The method can be used to obtain the rotational component of mode shapes with high accuracy by using a limited number of the lateral components. The identified stiffness values are compared with the actual stiffness values, as shown in Fig. 4. The identified rotational stiffness of the column base was 666.75 MN·m/rad with an error of 0.02%, which verified that the proposed method could accurately identify the rotational stiffness of the base column using the first fourth frequencies and the corresponding lateral components of the mode shapes.

4 Conclusion

This paper proposed a method for identifying the stiffness of the column bases based on fishbone model and Bayesian inference. The frame structure was simplified to a fishbone model considering the flexibility of column bases. The shear stiffness and rotational stiffness of the column bases could be identified using incomplete modal data based on hierarchical Bayesian update algorithm. The effectiveness of the method was verified by a numerical model of a 5-story steel frame.

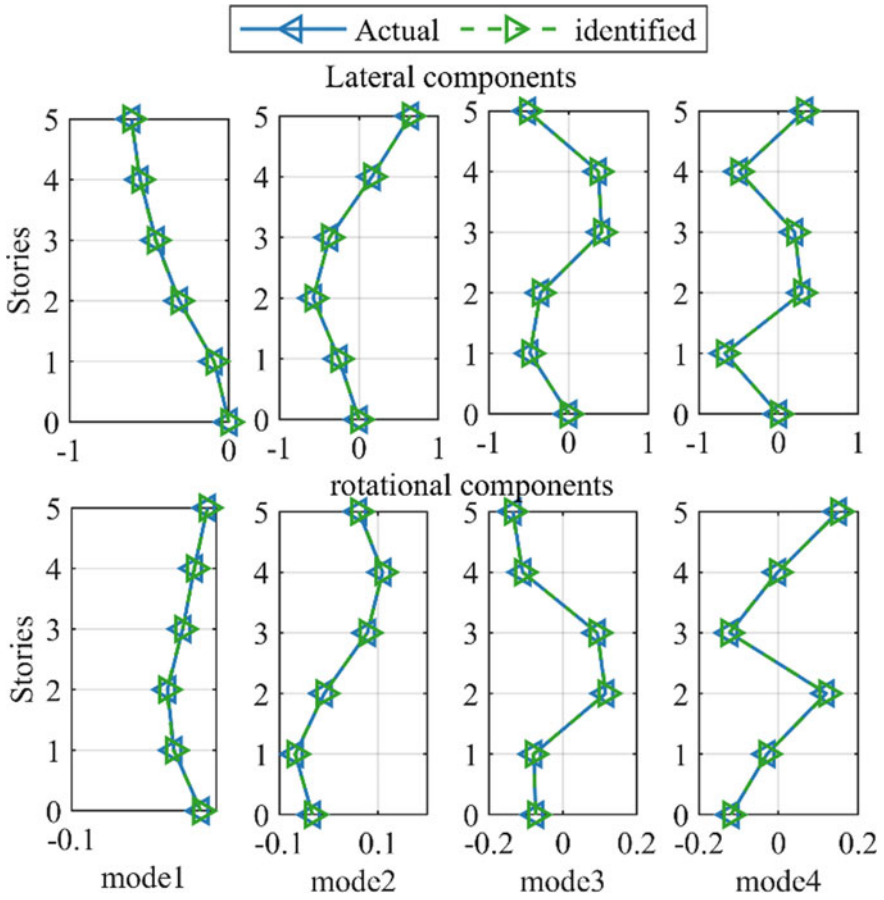


Fig. 3 Comparison between actual values and identified values for mode shapes

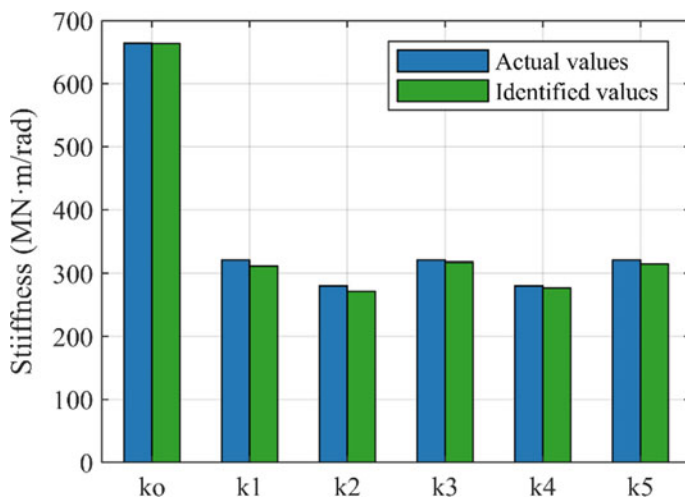


Fig. 4 Comparison between actual values and identified values for stiffnesses

Acknowledgements This work was supported by the National Natural Science Foundation of China (Grant No. 52178454).

References

1. Liang J, Gu LS, Hu MH (2016) Experimental study on seismic performances of steel frame bent structures. *Earthquakes Struct* 10(5):1111–1123
2. Tremblay R, Filiatrault A, Bruneau M, Nakashima M, Prion HG, DeVal R (1996) Seismic design of steel buildings: lessons from the 1995 Hyogo-ken Nanbu earthquake. *Can J Civ Eng* 23(3):727–756
3. Akiyama H (2000) Evaluation of fractural mode of failure in steel structures following Kobe lessons. *J Constr Steel Res* 55(1–3):211–227
4. Chen M, Huo JH, Xing YW (2020) Seismic behavior of cold-formed steel frames with bolted moment connections. *J Struct Eng* 146(3):04019212
5. Jiang L, Zhang X, Ye J, Jiang L, Zhou L (2021) Seismic behavior and damage assessment of mid-rise cold-formed steel-framed buildings with normal and reinforced beam-column joints. *Archives Civ Mech Eng* 21(3):1–16
6. Li X, Kurata M (2019) Probabilistic updating of fishbone model for assessing seismic damage to beam–column connections in steel moment-resisting frames. *Comput Aided Civ Infrastruct Eng* 34(9):790–805
7. Wang L, Dang J, Wang X, Shrestha A (2021) Waveform-based fracture identification of steel beam ends using convolutional neural networks. *Struct Control Health Monit* 28(9):e2777
8. Iyama J, Fukushima Y, Hasegawa T, Nakagawa H, Kaneshiro Y (2021) Detection of beam-end fractures in steel members based on local stiffness calculated by strain response. *Eng Struct* 241:112419
9. Lin YZ, Nie ZH, Ma HW (2017) Structural damage detection with automatic feature-extraction through deep learning. *Comput Aided Civ Infrastruct Eng* 32(12):1025–1046

10. Grilli DA, Kanvinde AM (2017) Embedded column base connections subjected to seismic loads: Strength model. *J Constr Steel Res* 129:240–249
11. Grilli D, Jones R, Kanvinde A (2017) Seismic performance of embedded column base connections subjected to axial and lateral loads. *J Struct Eng* 143(5):04017010.1–04017010.10
12. Hetényi M, Hetbenyi MI (1946) *Beams on elastic foundation: theory with applications in the fields of civil and mechanical engineering*, 1st edn. University of Michigan press, Ann Arbor
13. Richards PW, Barnwell NV, Tryon JE, Sadler AL (2018) Flexural strength and stiffness of block-out connections for steel columns. *Eng Struct* 173:404–415
14. Chopra AK (2011) *Dynamics of structures*, 4th edn. Prentice Hall, Upper Saddle River
15. Yuen KV (2010) *Bayesian methods for structural dynamics and civil engineering*. Wiley, Singapore

A Finite Element Analysis on Behavior of a T-stub Type Gusset Plate in Different Bolted Connection Configurations



Ruoyu Zheng and Zeyu Zhang

Abstract Configurations play a crucial role in the mechanical behaviors of bolted connections in steel structures. This study provides a visual characterization of the influence of different configurations on the bolted connection by introducing three configurations, namely the collinear, rectangular, and circular bolt configurations. A popular T-stub type steel gusset plate is introduced, and three types of loading conditions are implemented. A three-dimensional numerical analysis is comprehensively developed in a linear elastic framework, followed by a mathematical derivation to interpret the results. Instead of a one-rules-all condition, the results imply that different configurations excel under different loading conditions. The study provides an instructive guidance in choosing the most effective bolted connection configuration in the practical field of resisting the corresponding primary loading condition for connecting different structural components.

Keywords Bolted connection · T-Stub type gusset plate · Bolt configuration · Three-dimensional modeling · Finite element analysis (FEA)

1 Introduction

Bolt connections are widely used in connecting structural or mechanical members such as columns to columns, columns to beams, and beams to girders via gusset plates or endplates. In typical circumstances, bolt connections will withstand tensions or/and shear forces that come from different loading scenarios acting on structures. However, bolt connections may undergo severe shear force loadings caused by axial torsions under some unusual situations, such as seismic activities causing structural members to develop lateral buckling deformation. During such geological events,

R. Zheng
Unit 1203, Build 3, Xuhuaiaodu, Chaoyang District, Beijing 100022, China

Z. Zhang (✉)
Unit 2 Apt 301, 12-1 Zhengjie Rd, Haizhou District, Lianyungang 222023, Jiangsu, China
e-mail: zz5@evansville.edu

© The Author(s), under exclusive license to Springer Nature Singapore Pte Ltd. 2024
M. Casini (ed.), *Proceedings of the 3rd International Civil Engineering and Architecture Conference*, Lecture Notes in Civil Engineering 389,
https://doi.org/10.1007/978-981-99-6368-3_27

311

the structure needs to remain as integrated as possible. However, structural designs should also follow the principles of economics. It is unreasonable and unacceptable to design all buildings as strong as fortresses. Therefore, when the number of bolts is a determining parameter, the configuration pattern of the bolted connection will play a crucial role in the mechanical behavior of the gusset plate, such as stress concentrations and displacements. Smaller stress concentrations and displacements at the bolted connections imply less possibility of reaching the ultimate capacity of the connections, which reduces the likelihood of the building to fail at these critical structural nodes.

Numerous researchers have conducted various studies on bolt connections in steel structures using experimental methods, finite element simulation analysis, or a combination of both. Pawar and Waghmode [1] used the finite element method to study several T-stub connections connected with various bolt configurations: circular, rectangular, and inline. They applied tensile force to each model and recorded the separation distance data of the two paired gusset plates. Kim and Kuwamura [2] used the finite element analysis method to investigate the structural behavior of bolted shear connections with thin-walled stainless steel plates. Non-linear material and non-geometric analysis were carried out to predict the load–displacement curves of bolted connections and the ultimate behaviors. Crosti and Duthinh [3] used the finite element analysis to predict the behavior of gusset plates in tension, resulting in possible failure by block shear after the Federal Highway Administration issued guidelines for the load rating of bolted and riveted gusset plates in truss bridges. Rogers and Hancock [4] described the failure behavior of bearing and net sections of bolt connections under shear load. El-Hadary et al. [5] conducted a parametric non-linear finite element study on the apex knee connection of a portal frame constructed with cold-formed back-to-back double-lipped C sections for both the rafter and the column and identified five failure modes. Francavilla et al. [6] developed a simple simplified finite element model of a bolted T-stub with only one bolt row, which was developed using the SAP2000 computer program aiming to show how even a widespread commercial software could be used to estimate the plastic deformation capacity of bolted joints' components. Prinz et al. [7] experimentally studied the strengthening of bolted beam-column connections without column web stiffeners using multiple bolts on each side of the column web. Gödrich et al. [8] focused on the design approach of T-stub components, which played a consequential role in the analytical and numerical prediction of the behavior of bolted end plate connections by the component-based finite element method. Swanson and Leon [9] conducted tests on 48 T-stub specimens, which were carried out as part of a SAC Phase II project, to provide insight into the behavior, failure modes, and ductility of these components. Tartaglia et al. [10] studied the bolts and their arrangements that strongly influenced stiffness, strength, and ductility of T-stub connections. Saberi et al. [11] presented a paper that aimed to compare the sensitivity of the bolted connections to the thickness of the end plate and T-stub flange using a numerical method. Bezerra et al. [12] investigated the effect of the thickness of T-stub connections fixed to a rigid support base using non-linear finite element models. Hu et al. [13] developed mechanical models used to simulate the complete behavior of full-scale bolted T-stub connections under

cyclic loads. Bezerra et al. [14] again presented a comprehensive experimental and numerical study on the structural behavior of bolted T-stub connections when fixed onto a rigid base. Liu et al. [15] investigated failure modes, and their corresponding tension strengths of thread-fixed one-side bolted T-stub both experimentally and theoretically. Lemonis and Gantes [16] developed and studied an incremental model for predicting the mechanical characteristics of T-stub steel connections. Latour and Rizzano [17] aimed to enhance the energy-dissipation capacity of classical rectangular T-stubs by recommending an hourglass shape for the T-stub flange. Wang et al. [18] investigated the behavior of the blind-bolt Hollobolt when used in moment-resisting connections. Coelho et al. [19] investigated a finite element model for the characterization of the non-linear behavior of bolted T-stub connections that idealized the tension zone of bolted joints. Gil and Goñi [20] aimed at beam to column connections subjected to loads in the beam minor axis direction and their behavior that relied mainly on the characterization of the components acting on the T-stub under out-of-plane bending. Yuan et al. [21] conducted a comprehensive experimental study on the structural behavior of stainless-steel bolted T-stub connections. A total of 27 stainless steel bolted T-stubs with various geometric configurations were fabricated from hot-rolled stainless-steel plates and assembled with stainless steel bolts. Abidelah et al. [22] investigated the impact of the bolt bending on the behavior of the T-stubs. Gantes and Lemonis [23] presented the development and implementation of a finite element model for simple T-stub steel connections with parameters of material and geometric non-linearities as well as contact and friction. Spyrou and Davison [24] described the use of an image acquisition and processing technique for the measurement of deformations in steel T-stub connections, representing the tension component in a steel joint. Zhang et al. [25] experimentally studied the ultimate tensile behavior of 16 bolted T-stub connections and 2 bolted angle counterparts, regarding horizontal plate thickness, bolt diameter, bolt pitch, and bolt preload. Bravo and Herrera [26] presented a part of a research program conducted to study the response of built-up T-stubs under cyclic loadings. Hantouche et al. [27] investigated experimental and finite element studies that built-up T-stub connections could be successfully detailed for use in special and intermediate moment frames in seismic areas. Hu et al. [28] presented the development of refined three-dimensional finite element models with the ability to reliably simulate the mechanical behavior of full-scale bolted T-stub connections. Herrera et al. [29] investigated the behavior of built-up T-stubs subjected to tensile loading through the stem through both numerical and experimental models. Anwar et al. [30] studied the behavior of T-stub components of beam to column end plate bolted connections under large deformation demands associated with column loss scenario. Xu et al. [31] investigated the performance of steel frames with partially restrained connections fabricated from bolted T-stubs following damage to load-bearing columns. Girão Coelho et al. [32] presented simplified methods for determining the monotonic deformation response of T-stub connections.

The purpose of this study is to find the most relatively effective bolted connection configurations to serve for different structural purposes in the engineering application by understanding the mechanical behaviors of each type of bolted configurations

under typical and severe loading scenarios. Three-dimensional numerical analysis is conducted using the finite element analysis package ABAQUS/CAE ver. 2022. Three common bolt configurations, namely the circular, collinear, and rectangular configurations are applied to the gusset plates. To study the mechanical behaviors of the bolted connections undergoing typical and severe circumstances, three principal types of loading scenarios are considered. The typical loading conditions studied are tension and shear forces, while the severe loading condition is axial torque. To simplify the analysis and make the results straightforward, each loading condition is applied to the bolted connection individually.

2 Numerical Modeling

The bolted connection is composed of one base plate and two identical T-stub type gusset plates on each side of the base plate, connected with bolts. A total of 12 bolts are on the connection, as shown in Fig. 1. Both the X- and Z- axes of the Cartesian coordinate system are perpendicular to the thickness of the base plate. The X-axis is parallel to the short side of the base plate, and the Z-axis is parallel to the long side of it. The Y-axis is parallel to the thickness of the base plate.

The base plates are $500 \times 300 \times 15$ mm in dimensions, and the gusset plates are $200 \times 200 \times 15$ mm in dimensions. The bolts are 45 mm in length, 12.7 mm in diameter, 8 mm in both heads and nuts, 22.23 mm in across corners, and 19.25 mm in across flats. The base plate employs A50 steel which Young's modulus, yield stress, and Poisson's ratio are 210,000 MPa, 345 MPa, and 0.3, respectively. The gusset plates employ A36 steel which Young's modulus, yield stress, and Poisson's ratio are 200,000 MPa, 270 MPa, and 0.3, respectively. The bolts are A325 steel which Young's modulus, yield stress, and Poisson's ratio are 210,000 MPa, 660 MPa,

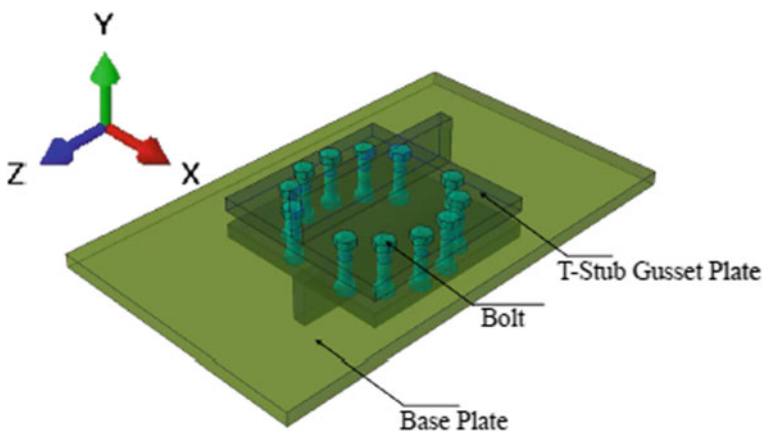


Fig. 1 Primary view of the bolted connection with transparency

and 0.36, respectively. The three-dimensional numerical models are assembled with everything identical to each other except for the bolt configurations, making it a total of three separate models. The plan view of the numerical models with different bolt configurations are illustrated in Fig. 2.

In the numerical analysis, the shear force applied on the corresponding models is 75,000 Newtons which is on one side of the T-stub gusset plate and develops along the Z-axis. The tensile force is 240,000 Newtons which is on the upper end of the T-stub gusset plate web and develops along the Y-axis. The torque is 3,000 N-meters applied at the geometric center of the web of the T-stub gusset plate around the positive Y-axis. To ensure control variables, all gusset plates are set as fixed ends on the other end ($U1 = U2 = U3 = UR1 = UR2 = UR3 = 0$). A three-dimensional hexahedral eight-node linear block with reduced integration, also known as C3D8R element, is applied to properly mesh all components in the numerical model. This type of element has proved to be suitable for simulating lap-bolted connections.

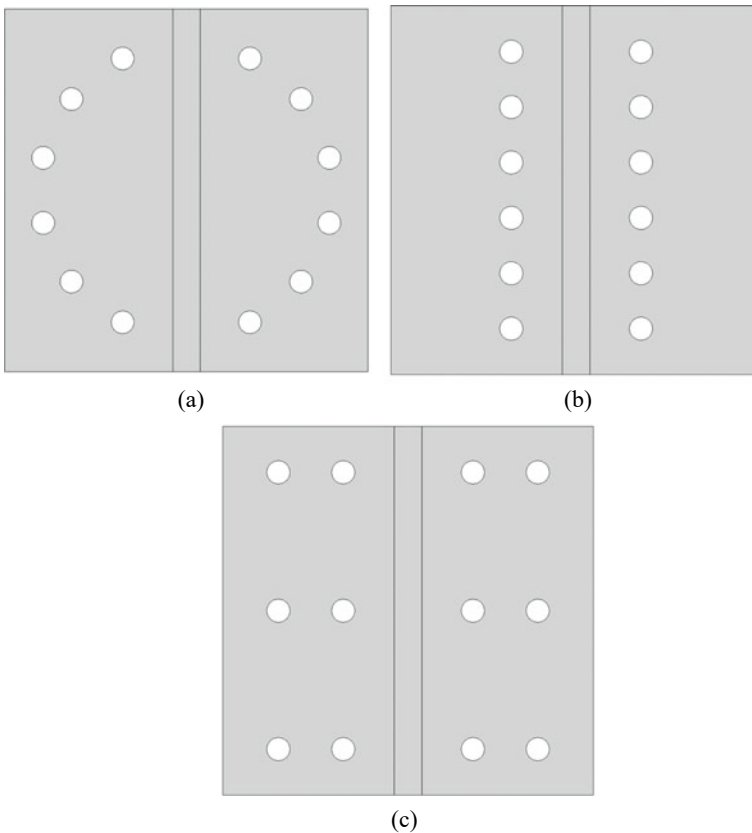


Fig. 2 Plan views of the numerical models with different bolt configurations: **a** circular; **b** collinear; **c** rectangular

3 Result and Comparison

Data acquired from the three-dimensional models in different bolt configurations under different loading conditions were collected, processed, and compared. Figure 3 is an example of the visualization of the end result of the circular bolt configuration under tensile force loading. By focusing on the nodes with maximum stress, displacement, and rotation behaviors on each gusset plate, the stress–strain, time–displacement, and time–angle curves are plotted. Figure 4a–c illustrate the stress–strain curves of the selected nodes under shear, tension, and axial torque, respectively. The same rule applies to the time–displacement curves for shear and tensile load cases in Fig. 5 and the time–angle of rotation curves for the axial torque load case in Fig. 6.

Due to the fact that the thickness of the gusset plate is comparatively much smaller than the length and width of the plate, and for simplicity of mathematical derivations, it is fair to assume the bolted connection is in a plane stress condition when individual one-dimensional loads are applied.

In the case where the three bolted connections are subjected to shear forces, the models can be viewed as a “competition” between the forces and number of bolts. In the circular bolt configuration, there are two bolts that are collinear with the applied shear force in the Z-axis direction. In the rectangular configuration, three bolts are collinear with the shear force in the Z-axis direction. In the collinear configuration, six bolts are collinear with the shear force in the Z-axis direction. As a result, the reaction force acting at each bolt interface is ideally equal to the applied force divided by the number of bolts.

Therefore, the largest stress concentration in the bolt interface occurs in the circular bolt configuration, followed by the rectangular configuration, and the

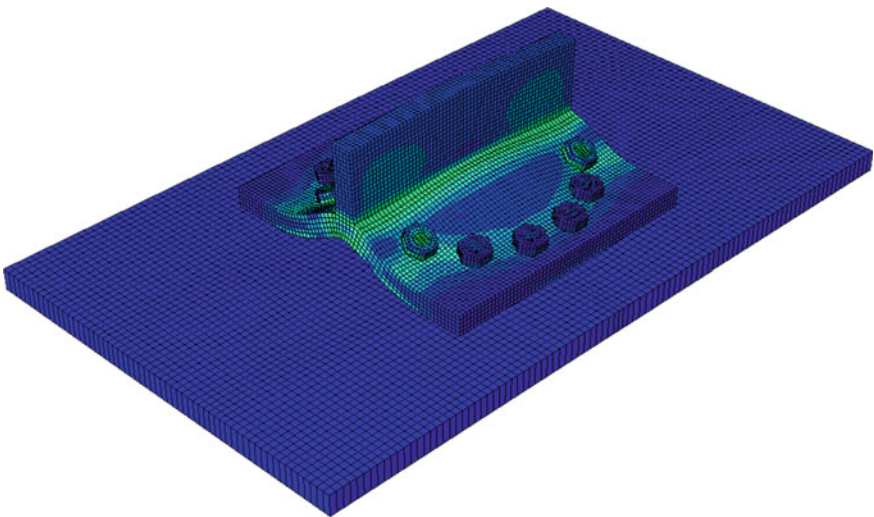
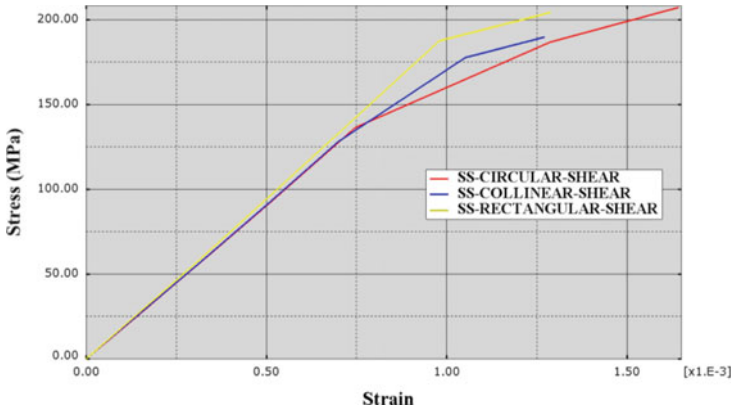
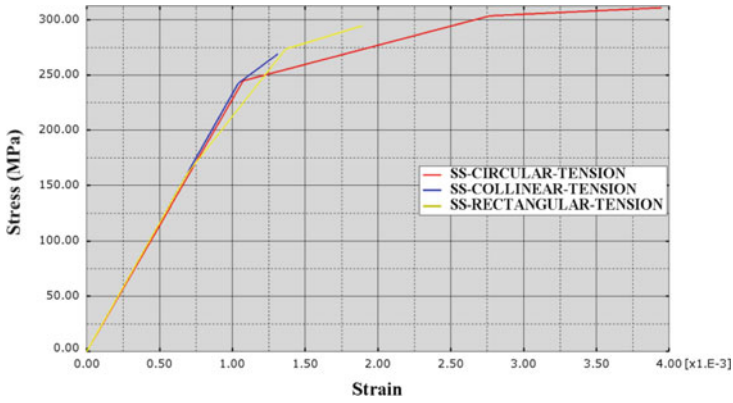


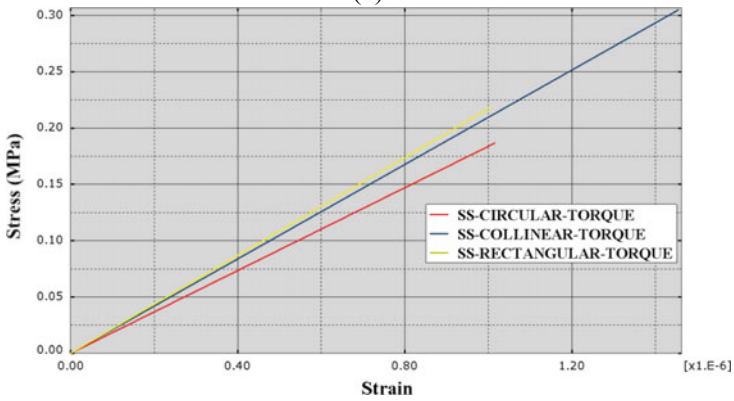
Fig. 3 Visualization of circular bolt configuration under tensile force



(a)



(b)



(c)

Fig. 4 Stress–strain curves for three bolt configurations under: a shear force; b tensile force; c axial torque

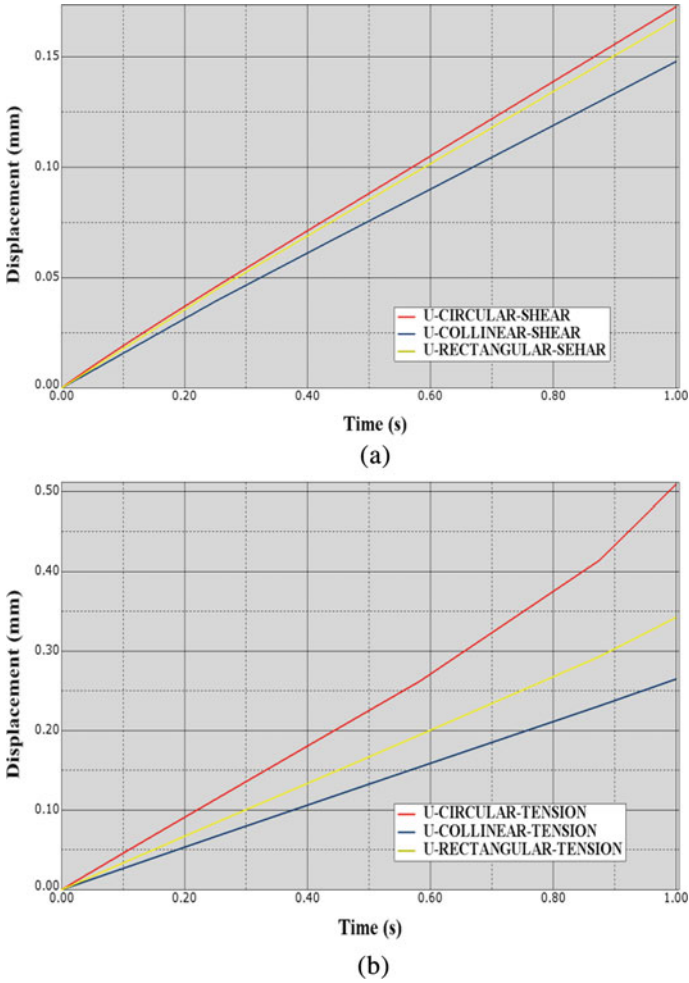


Fig. 5 Time-Displacement curves for three bolt configurations under: **a** shear force and **b** tensile force

collinear configuration. The following diagram (Fig. 7) can be more concise and clearly illustrate the above “competition” theory. As shown in the diagram, the bolt in “competition” to withstand the load is highlighted by the red dashed rectangle.

In the case where the three bolted connection configurations are subjected to tensile force, the geometric center of the bolt configuration plays a chief role in interpreting the experiment results. The geometric center of each configuration can be calculated according to the following formula:

$$x_C = \frac{\sum_i x_i A_i}{\sum_i A_i} \tag{1}$$

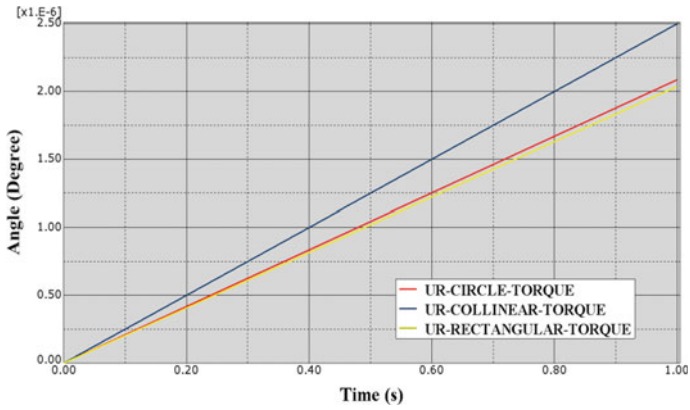


Fig. 6 Time-angle of rotation curves for bolt configurations under axial torque

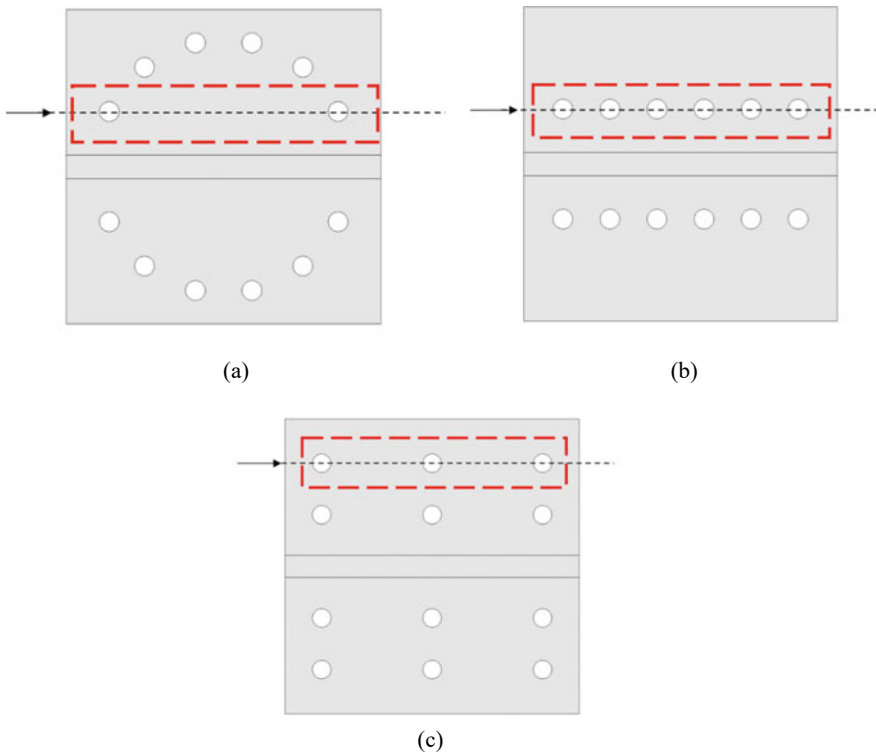


Fig. 7 Illustrations of the “competition” theory, compared among: a circular; b collinear; c rectangular configurations

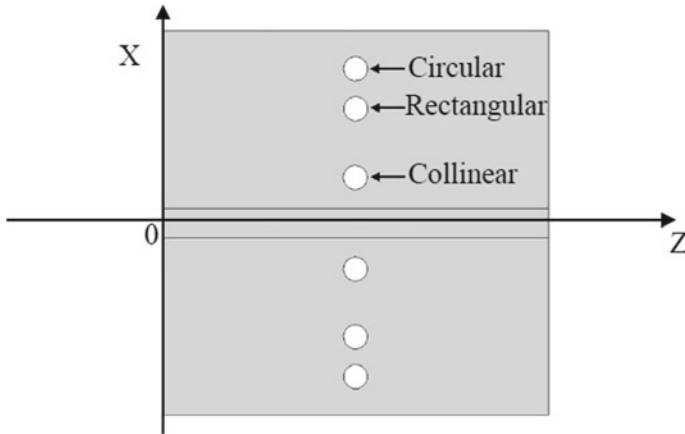


Fig. 8 Relative positions of the geometric centers to the center line (Z-axis)

$$y_c = \frac{\sum_i y_i A_i}{\sum_i A_i} \tag{2}$$

where A_i is the bolt area, and x_i and y_i are the z- and x- bolt locations, respectively.

The geometric center coordinates of the circular, rectangular, and collinear bolt configurations are (100, 58.94), (100, 52.53), and (100, 35.02), respectively. Figure 8 presents the relative positions of the geometric centers to the center line (Z-axis) on the gusset plate for the three bolt configurations.

When the gusset plate begins to deform along the Y-axis direction due to the tensile force, the magnitude of the vertical component stress acting on the bolt hole along the Y-axis is proportional to the distance from the geometric center of the bolt configuration to the center line. This explains that the further away the geometric center of the bolt configuration is from the centerline, the greater the stress concentration is, and vice versa.

The same theory can be applied when the three bolted connection configurations are subjected to axial torque. From the above formula for calculating the geometric center of the bolt configuration, it can be known that the distance between the geometric center and the center line of the collinear bolt configuration is the shortest, the circular one is the longest, and the rectangular one is in between. Based on the principle of static equilibrium of moment, the sum of the moment is equal to zero. The shorter the moment arm, the greater the force. Therefore, the geometric center of the collinear bolt configuration is closest to the center line, and its stress concentration is the largest. According to the finite element analysis results, the magnitude of stress is ranked from high to low: collinear, rectangular, and circular. The math derivation agrees with the finite element analysis results.

4 Conclusion

This study aims to investigate the mechanical behaviors of T-stub type gusset plates connected in circular, collinear, and rectangular bolt configurations under shear, tension, and axial torque, facilitated with a three-dimensional finite element analysis in a linear elastic framework. By summarizing and analyzing the results of this experiment, when the gusset plate is subjected to shear or tensile force, the collinear bolt configuration will produce less stress concentration at the bolt hole, and the maximum displacement developed on the gusset plate will be smaller. Both the smaller stress concentrations and displacements indicate that the collinear bolt configuration will make the connections more stable during severe geological activities. However, when the gusset plate is subjected to axial torque, the circular and rectangular bolt configurations perform better than the collinear ones. Therefore, it is reasonable to use circular or rectangular bolt configurations at the joints where the members are prone to axial buckling deformation due to eccentric loads. Structural engineers should reasonably select the appropriate bolt configuration to connect the members according to the specific situation.

This research is limited to one assembly of bolted connection with only three bolted configurations, and the numerical analysis is conducted within the linear elastic framework. The effects of various parameters such as number of bolts, bolt spacing, edge spacing, etc., are not taken into considerations. These effects will be systematically investigated in the next paper. The shear, tension, and torsion loads are applied to the bolted connection individually without eccentricity. Future research will be made on the mechanical responses of the bolted connection under combined loading conditions, with proper discussion on the influence of eccentricity in the plane and normal to the plane. In future works, the mechanical framework should also expand to non-linear elastic and plastic ranges with power laws and yield criteria involved.

References

1. Pawar GB, Waghmode LY (2014) Analysis of bolted joints with different bolt patterns using non-linear finite element analysis. *Int J Eng Res Technol (IJERT)*
2. Soo Kim T, Kuwamura H (2007) Finite element modeling of bolted connections in thin-walled stainless steel plates under static shear. *Thin-Walled Struct* 45(4)
3. Crosti C, Duthinh D (2010) Block shear failure of Steel Gusset plates. *Bridge maintenance, safety, management and life-cycle optimization*
4. Rogers CA, Hancock GK (2000) Failure modes of bolted-sheet-steel connections loaded in shear. *J Struct Eng* 126(3)
5. El-Hadary MR, El-Aghoury IM, Ibrahim AA-B (2022) Behavior of different bolted connection configurations in frames composed of cold-formed sections. *Ain Shams Eng J* 13(1)
6. Francavilla AB, Latour M, Piluso V, Rizzano G (2015) Simplified finite element analysis of bolted T-stub connection components. *Eng Struct* 100

7. Prinz GS, Nussbaumer A, Borges L, Khadka S (2014) Experimental testing and simulation of bolted beam-column connections having thick extended endplates and multiple bolts per row. *Eng Struct* 59
8. Gödrich L, Wald F, Kabeláč J, Kuříková M (2019) Design finite element model of a bolted T-stub connection component. *J Constr Steel Res* 157
9. Swanson JA, Leon RT (2000) Bolted steel connections: Tests on T-stub components. *J Struct Eng* 126(1)
10. Tartaglia R, D'Aniello M, Zimbru M (2020) Experimental and numerical study on the T-stub behaviour with preloaded bolts under large deformations. *Structures* 27
11. Saberi V, Gerami M, Kheyroddin A (2014) Comparison of bolted end plate and T-stub connection sensitivity to component thickness. *J Constr Steel Res* 9
12. Bezerra LM, Bonilla J, Silva WA, Matias WT (2020) Experimental and numerical studies of bolted T-stub steel connection with different flange thicknesses connected to a rigid base. *Eng Struct* 218
13. Hu JW, Leon RT, Park T (2012) Mechanical models for the analysis of bolted T-stub connections under cyclic loads. *J Constr Steel Res* 78:45–57
14. Bezerra LM, Bonilla J, Freitas CS, Massicotte B (2022) Behavior of T-stub steel connections bolted to rigid bases. *J Constr Steel Res* 192
15. Liu M, Zhu X, Wang P, Tuoya W, Hu S (2017) Tension strength and design method for thread-fixed one-side bolted T-stub. *Eng Struct* 150
16. Lemonis M, Gantes C (2006) Incremental modeling of T-stub connections. *J Mech Mater Struct* 1(7)
17. Latour M, Rizzano G (2021) Experimental behavior and mechanical modeling of dissipative T-stub connections
18. Wang ZY, Tizani W, Wang QY (2010) Strength and initial stiffness of a blind-bolt connection based on the T-stub model. *Eng Struct* 32(9)
19. Girão Coelho AM, Simões da Silva L, Bijlaard FS (2006) Finite-element modeling of the nonlinear behavior of bolted T-stub connections. *J Struct Eng* 132(6)
20. Gil A, Goñi R (2015) T-stub behaviour under out-of-plane bending. I: Experimental research and finite element modelling. *Eng Struct* 98
21. Yuan HX, Hu S, Du XX, Yang L, Cheng XY, Theofanous M (2019) Experimental behaviour of stainless steel bolted T-stub connections under monotonic loading. *J Constr Steel Res* 152
22. Abidelah A, Bouchair A, Kerdal DE (2014) Influence of the flexural rigidity of the bolt on the behavior of the T-Stub Steel Connection. *Eng Struct* 81
23. Gantes BJ, Lemonis ME (2003) Influence of equivalent bolt length in finite element modeling of T-stub steel connections. *Comput Struct* 81(8–11)
24. Spyrou S, Davison JB (2001) Displacement measurement in studies of steel T-stub connections. *J Constr Steel Res* 57(6)
25. Zhang Y, Gao S, Guo L, Qu L, Wang S (2022) Ultimate tensile behavior of bolted t-stub connections with preload. *J Build Eng* 47
26. Bravo MA, Herrera RA (2014) Performance under cyclic load of built-up T-stubs for Double t moment connections. *J Constr Steel Res* 103
27. Hantouche EG, Rassati GA, Kukreti AR, Swanson JA (2012) Built-up t-stub connections for moment resisting frames: experimental and finite element investigation for prequalification. *Eng Struct* 43
28. Hu JW, Kim DK, Leon RT, Choi E (2011) Analytical studies of full-scale steel T-stub connections using delicate 3D finite element methods. *ISIJ International* 51(4)
29. Herrera RA, Bravo M, Gómez G, Aedo G (2013) Performance of built-up T-stubs for Double t moment connections. *J Constr Steel Res* 88
30. Anwar GA, Dinu F, Ahmed M (2018) Numerical study on ultimate deformation and resistance capacity of bolted T-stub connection. *Int J Steel Struct* 19(3)

31. Xu G, Ellingwood BR (2011) Disproportionate collapse performance of partially restrained steel frames with bolted T-stub connections. *Eng Struct* 33(1)
32. Girão Coelho AM, Simões da Silva L, Bijlaard FSK (2004) Characterization of the nonlinear behaviour of single bolted t-stub connections. *Connections in steel structures V*

Seismic Design and Seismic Response of Building Structures

Displacement Performance of 8 Storeys Hotel Building Using Nonlinear Time History Analysis Method



Masrilayanti, Ruddy Kurniawan, Jafril Tanjung, and Muhazir Yunus

Abstract Acknowledging the responses of a structure under a particular type of loading is the utmost importance aspect of structure's designing and analysing. Seismic load are one of the most important type of loading, therefore dynamic analysis should be performed in order to evaluate the performance of a structure which is subjected to earthquake load. Among all the dynamic analysis methods, non-linear time history seismic analysis method is more accurate, because it generates a real earthquake load on a structure and analyzes the response of the structure. In this study, the structural behavior of reinforced concrete building is observed subjected to an earthquake motion by nonlinear time history analysis method. Different parametric studies have been performed to investigate its responses during an earthquake. An eight storeys hotel building is analyzed using finite element analysis software. Two earthquakes ground motion, namely El Centro (1940) and Kobe earthquake are applied at the base of the structure and the seismic capacities at structural and element levels are evaluated according to the guideline of ATC-40. Formation of plastic hinges is used as the basis of local performance evaluation and storey drift is used as the basis for evaluating global performance. It has been observed that for Kobe and El Centro earthquake ground motions, the structure meets the performance objective in serviceability of ATC-40 as Immediate Occupancy (IO) and Damage Control (DC).

Keywords Performance based · Earthquake · Building · Nonlinear time history

Masrilayanti (✉) · R. Kurniawan · J. Tanjung · M. Yunus
Universitas Andalas, Padang Sumatera Barat 25163, Indonesia
e-mail: masrilayanti@eng.unand.ac.id

© The Author(s), under exclusive license to Springer Nature Singapore Pte Ltd. 2024
M. Casini (ed.), *Proceedings of the 3rd International Civil Engineering and Architecture Conference*, Lecture Notes in Civil Engineering 389,
https://doi.org/10.1007/978-981-99-6368-3_28

327

1 Introduction

1.1 Background of the Study

Indonesia is a country located at the confluence of three tectonic plates, namely the Eurasian plate, the Pacific plate and the Indian plate. These plates keep moving to collide with each other or move away from each other, the result could be that one of the plates will break or even stick out above the earth's surface, resulting in an earthquake.

Earthquakes become dangerous if they occur in areas that have life and livelihoods where activities are very dependent on buildings. Building collapse due to earthquakes is the most real threat from the impact of earthquakes. As a solution, a building is needed that can withstand earthquake loads with minimal damage so as to ensure the survival and livelihood of its inhabitants. Therefore it is necessary to design buildings that have resistance to earthquake loads [1].

According to the National Earthquake Information Center, there are an average of 20,000 earthquakes each year—16 of them being major disasters. On August 14, 2021, a magnitude 7.2 earthquake struck the southwest region of Haiti and killed over 2000 people. As with other earthquakes, much of the damage was caused by buildings collapsing with people inside them, making earthquake-proof buildings a must.

West Sumatra is one of the provinces that is prone to earthquakes. According to the BMKG, in 2019 alone there have been recorded 460 earthquakes. The largest earthquake that ever occurred in West Sumatra occurred in 2009. According to Satkorlak PB data, as many as 1117 people died as a result of this earthquake spread over 3 cities and 4 districts in West Sumatra, 1214 people were seriously injured, 1688 people were slightly injured, the victims missing 1 person. Meanwhile, 135,448 houses were heavily damaged, 65,380 houses were moderately damaged, and 78,604 houses were slightly damaged [1, 2].

Based on those facts, many researches have been conducted in West Sumatera to ensure that the victims can be reduced if the dreadful disaster occurs again in that province. One of the researches is this study which tries to acknowledge the performance of a ten stories building under three different ground motions by using nonlinear time history analysis.

2 Literature Review

Buildings are physical forms resulting from construction work that are integrated with their domicile, partly or wholly located on/or in the ground/or water, which functions as a place for humans to carry out their activities, whether for residence or residence, religious activities, business activities, social, cultural and special activities. It generally accepted that most building structures shall exhibit a nonlinear response when

subjected to medium–high intensity earthquakes. It is currently known, however, that this phenomenon is not properly modelled in the majority of cases, especially at the design stage, where only simple linear methods have effectively been used [3, 4]. The response of a building to an accelerated ground motion is carried by a number of physical mechanisms developed by a complex association of structural elements. These elements are assembled together to grant civil engineering structures with three fundamental components: stiffness, resistance and ductility [5, 6].

Performance-based seismic design concept with Performance Based Earthquake Engineering (PBEE) is a combination of aspects of custody and aspects of service. PBEE concept can be used to design new as well as evaluation of existing buildings.

According to ATC-40, the criteria for earthquake resistant building structures are as follows [7]:

1. Immediate Occupancy (IO) is the condition of the building when an earthquake occurs, the structure is able to withstand the earthquake, the structure does not experience structural damage and does not experience non-structural damage so that it can be directly used.
2. Life Safety (LS) is the condition of the building when an earthquake occurs, the structure is able to withstand earthquakes, with little structural damage, the people who live or are in the building are kept safe from earthquakes.
3. Collapse Prevention (CP) is a condition where the building structure experiences very heavy structural damage but does not collapse.
4. Structural Stability (SS) is where the structure has suffered partial/total damage, the damage that occurs causes a degradation of the strength and stiffness of the lateral force resisting system.

The performance level of structures based on total lateral shear forces and lateral displacement at roof can be seen from the Fig. 1.

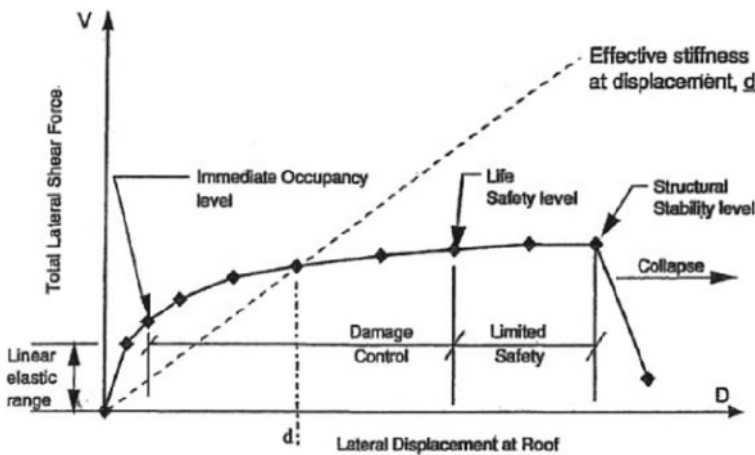


Fig. 1 Performance level of structures based on ATC-40

Earthquake loads are function of time, so that the response that occurs in the building structure also depends on the loading time.

Time history dynamic analysis is a method of analysis to determine the time history of the dynamic response of building structures that behave linearly or nonlinearly to ground motion due to an earthquake. Dynamic response in each time interval is calculated using the step-by-step integration method. As a result of the design earthquake load, the structure will still behave elastically for linear analysis and inelastic for nonlinear analysis. Usually time history analysis is more often used for nonlinear conditions, but not infrequently it is also used for linear conditions only. To get the response of the structure due to loading from Accelerograms records, (accelogram; recording the acceleration of the movement of the earth's base when an earthquake occurs) the use of modal analysis cannot be carried out, direct numerical integration with respect to the structure as a couple equation is the basis of Time History analysis where the integration method that is generally used is the Newmark method [3].

3 Methodology of Research

Indonesia standard of earthquake-resistant building designs refer to SNI 1726 2019 Concerning Procedures for Planning Earthquake Resistance for Building & Non-Building Structures. The analytical method used in this study is the nonlinear time history analysis method. In this study the object of the building to be studied is eight storeys hotel located in Padang City.

The building is modelled by using structural analysis software, and then assess with nonlinear time history analysis. Based on ATC-40, maximum displacements and interstorey drift of the structure due to different earthquake are analysed and discussed.

3.1 Structural Modelling

The object of this research has eight storeys which has been modelled based on the dimensions and quality of materials in accordance with the shop drawings that have been obtained. The calculated load is the weight of the building itself and shearwall is taken into account as a building structural element. Nonlinear response analysis is conducted using ETABS software according to ATC-40 code. The input earthquake parameters that used are accelerogram data from the El Centro, California (1940) and the Kobe, Japan (1995) earthquakes. The reason for choosing these two earthquakes is to see how these earthquake ground motions with different characteristics will affect the deviations that occur in the structure.

Figure 2 describes the modelling of the eight floors of building. This reinforced concrete building has 45 m height, 26 m length, and 28 m width. The function of

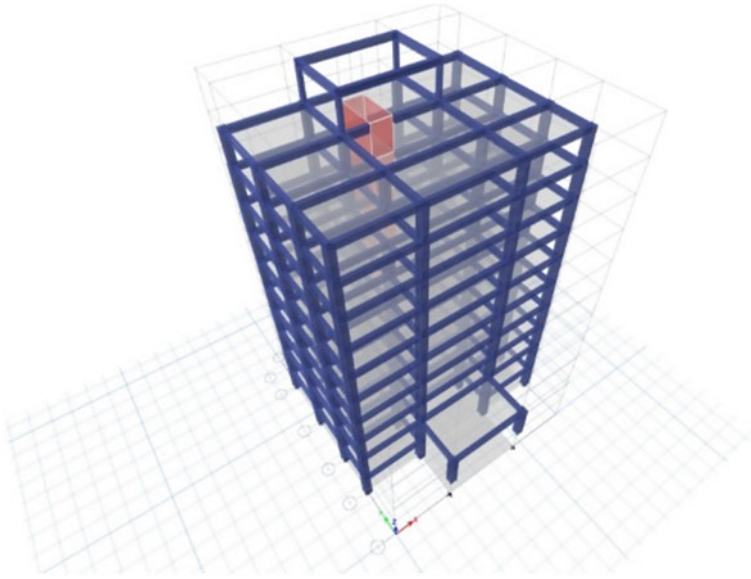


Fig. 2 Structure modelling

the building is as a hotel which is classified as a structure risk category II and the priority factor of the earthquake (I_e) is 1.0.

The plan of fourth floor of the building is can be seen in Fig. 3.

The acceleration earthquake groundmotions used is as below:

From Fig. 4, it can be observed that the pattern and the value of the earthquakes are different, so that from that it can be suggest that the pattern and the value of response structure will also be different.

4 Results and Discussion

The stages of dynamic time history analysis include two stages, these are response spectral analysis and time history analysis. Spectral response analysis refers to SNI 1726:2019 concerning the procedures for planning earthquake resistance for building and non-building structures by the Indonesian Standardization Agency. According to SNI 1726-2019 the ultimate limit performance of a building structure is determined by the maximum inter-storey deviation of the building structure due to the influence of the planned earthquake in conditions the building structure is on the verge of collapse, namely to limit the possibility of a collapse of the building structure which can cause human casualties.

In Indonesia Standard for Earthquake Design, Article 5.6, it is stated that the fundamental natural period must be limited to prevent the use of building structures

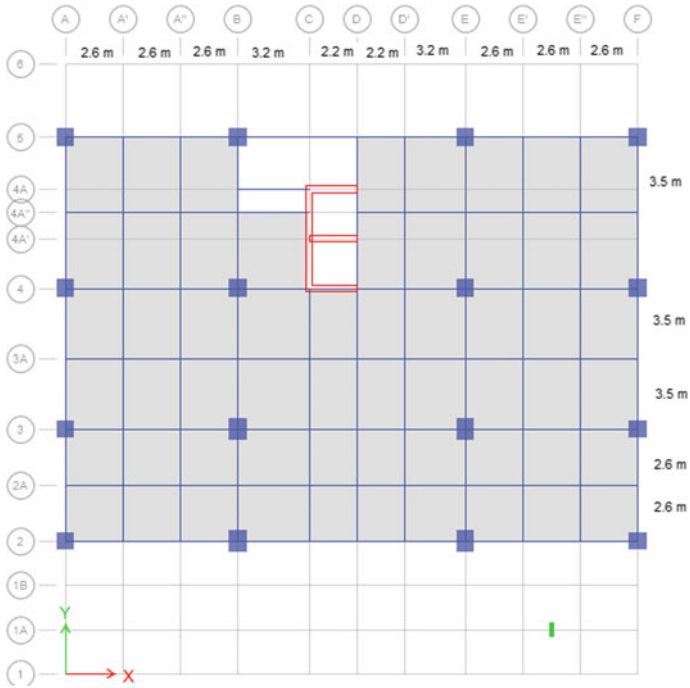


Fig. 3 Layout of fourth floor

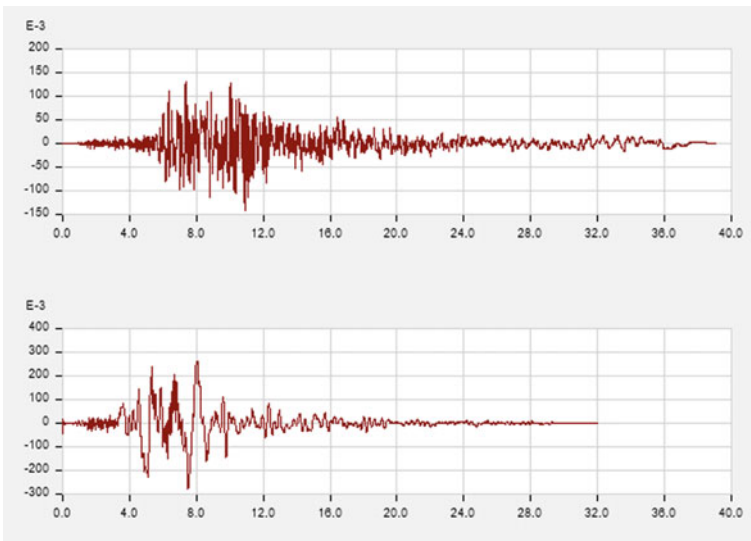


Fig. 4 Groundmotion of El-Centro (above) and Kobe (below)

that are too flexible with the requirement $T_1 < \zeta n$, where n is the number of floors, T_1 is the period at mode shape 1, and the coefficient ζ depends on the earthquake zone. T_1 is obtained from the structural analysis and it is defined that the natural period of the structure is 1.359.

For Padang City, the value of ζ is 0.18, so that:

$$T_1 < \zeta \times n.$$

$$1.359 < 0.18 \times 8 \rightarrow 1.359 < 1.44$$

From the results it can be seen that the natural period of the structure is not beyond the limit value. Results also show that the displacements obtained from dynamic analysis using time history analysis is quite different among those two ground motions. These graphs below (Figs. 5, 6 and 7) are the behaviour at the top roof of the building under the earthquake ground motions.

Fig. 5 The comparison of displacement of the building in longitudinal direction

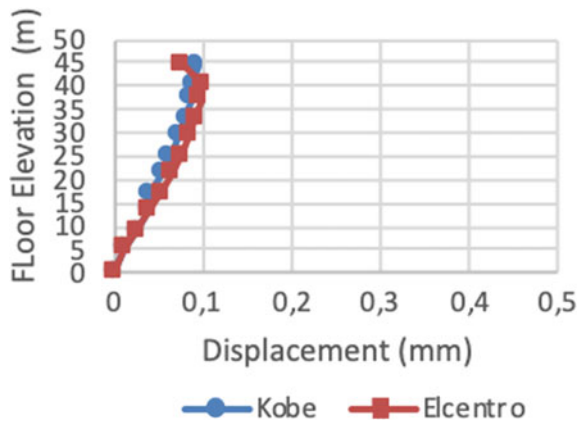
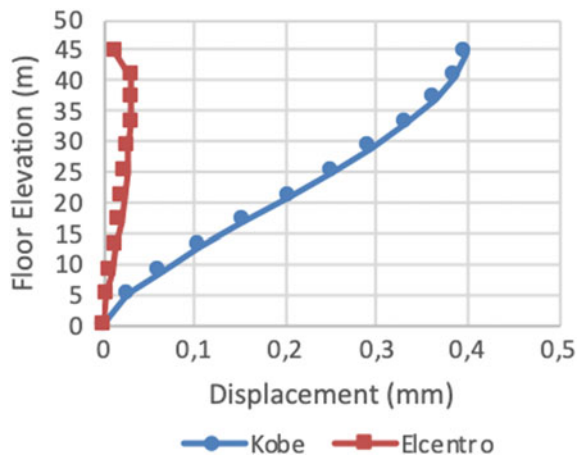


Fig. 6 The comparison of displacement of the building in longitudinal direction



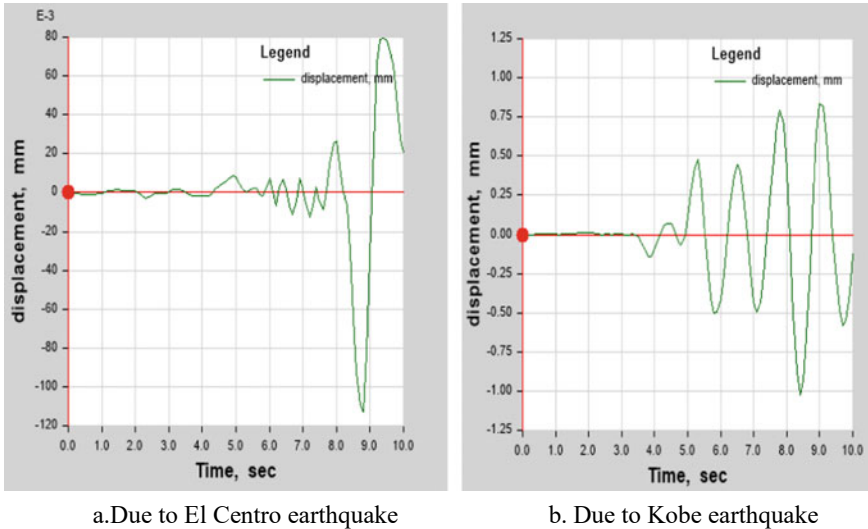


Fig. 7 Differences of roof top displacement time history due to the earthquake groundmotions

From Fig. 7, it can be seen that the patterns and the values of roof top displacement of the building are not the same. The pattern is related to the earthquake acceleration ground motions.

When a high-scale earthquake hits a building, the structure of the building will experience plastic hinges in several places, and the building no longer behaves linearly but behaves nonlinearly. Thus, nonlinear analysis is needed to determine the behavior of the structure when experiencing a large earthquake.

The amount of horizontal drift (drift) must be considered in accordance with applicable regulations, namely service limit performance and ultimate limit performance. According to [7] structural drift can be expressed in the form of index drift, as:

$$Maximum\ Drift = \frac{D_t}{H_{total}} \tag{1}$$

$$Maximum\ In\ Elastic\ Drift = \frac{D_t - D_1}{H_{total}} \tag{2}$$

As D_t is maximum displacement, and D_1 is known as minimum deformation.

As the results of this study, it can be seen that the performance of the structure based on ATC-40 due to ground motion of Kobe and El-Centro are as can be seen in Tables 1 and 2.

Table 1 Performance of building (X direction) based on ATC-40

G. motion	Maximum frift	Maximum in-elastik drift	Drift performance	In-elastic drift performance
El-centro	0,00,227,586	0,002	IO	IO
Kobe	0,00,216,092	0,001,885,057	IO	IO

Table 2 Performance of building (Y direction) based on ATC-40

G. motion	Maximum drift	Maximum in-elastik drift	Drift performance	In-elastic drift performance
El-centro	0,000,712,644	0,00,062,069	IO	IO
Kobe	0,009,126,437	0,008,505,747	IO	LS

5 Conclusion

Assessing a structure relating to its performance under earthquake loads is very important to be conducted especially for high risk earthquake area. From the analysis of the building, it can be concluded that:

- a. According to ATC-40, if a building is subjected to El Centro earthquake loads, the building’s performance comes into the IO (Immediate Occupancy) category. This means that if it is hit by an earthquake, the building structure is safe, the risk of casualties from structural failure is insignificant, the building does not suffer significant damage, and can immediately function or can operate again.
- b. According to ATC-40, if a building is subjected to the Kobe earthquake load, the building’s performance is included in the LS (Life Safety) category. This means that if an earthquake hits the structure is able to withstand an earthquake, with little structural damage, the people who live or are in the building are still safe and protected from earthquakes effects.

References

1. Aryanti R, Masrilayanti M (2021) State of the art of seismic risk and loss assessment in structures. E3S Web Conf 331:07013. <https://doi.org/10.1051/e3sconf/202133107013>
2. Chaudhary MT, Piracha A (2021) Natural disasters—origins, impacts, management, pp 1101–1131
3. Fajfar P, Krawinkler H (2005) Nonlinear seismic analysis and
4. Villaverde R (2009) Fundamental concepts of earthquake engineering

5. Masrilayanti, Kurniawan R, Budi AL, Sourkan SH (2021) Pushover analysis of 10-floors reinforced concrete building (Case Study: Mahkota Majolelo Sati Boutique Hotel). IOP Conf Ser Mater Sci Eng 1041(1):012003. <https://doi.org/10.1088/1757-899x/1041/1/012003>
6. Carvalho G, Bento R, Bhatt C (2013) Nonlinear static and dynamic analyses of reinforced concrete buildings-comparison of different modelling approaches. Earthq Struct 4(5):451–470. <https://doi.org/10.12989/eas.2013.4.5.451>
7. (Applied Technology Council) ATC-40, “ATC-40 (Applied Technology Council),” ATC 40, Appl Technol Counc, 1995

Analysis of Energy Dissipation Structure of Reinforced Concrete Frame with Additional Metal Damping



Fangqian He, Ting Zhang, and Yuchen Jiang

Abstract The seismic performance curve of single-particle-system is used to investigate the damping amount of additional dampers for reinforced concrete frame structures. The damping amount of the additional metal damper is researched and calculated. First, the original structure is simplified to a single-particle-system. The inter displacement angle of the structure is calculated according to the response spectrum. Then the target interlayer displacement angle of the original structure is set, the damping of the single-particle-system is calculated according to the target interlayer displacement angle. Finally, the damping amount of the multi-particle-system is derived from the damping amount of the single-particle-system, and the damping amount of the additional metal damping required for the multi-particle-system structure is calculated. The time history analysis of seismic response of the calculation model is carried out by Wilson- θ method, and the response value is obtained. At the same time, the hysteretic curve of the damper under earthquake action is drawn, the energy dissipation capacity of the damper is researched by the hysteretic curve. Some considerations are put forward for the design of reinforced concrete energy dissipation frame structures in the future.

Keywords Reinforced concrete frame · Energy dissipation · Metal damper · Time history analysis · Performance design

1 Introduction

Energy dissipation structures and technologies are more and more widely used due to their good seismic performance. Domestic and foreign scholars have done relevant researches on the damping amount of additional dampers for energy dissipation structures.

F. He · T. Zhang (✉) · Y. Jiang
Wuxi Taihu University, Wuxi Jiangsu 214064, China
e-mail: zhangt_wxu_edu@163.com

© The Author(s), under exclusive license to Springer Nature Singapore Pte Ltd. 2024
M. Casini (ed.), *Proceedings of the 3rd International Civil Engineering and Architecture Conference*, Lecture Notes in Civil Engineering 389,
https://doi.org/10.1007/978-981-99-6368-3_29

337

XU calculated the additional damping ratio of the optimized scheme based on the method of determining the reasonable location of the additional viscous dampers in the steel structure according to the structural static analysis [1]. Zhao studied the seismic reduction effect of different optimal arrangement methods of mild steel dampers in frame structures by using the layer-by-layer arrangement method, the location parameter method and the genetic algorithm, and found that the hysteretic curves of the three methods of dampers were relatively full [2]. Li studied the energy dissipation and damping system through the design concept of “energy dissipation as strength supplement”, and obtained the method to determine the relevant parameters of the damper [3]. Le used the energy method to study the distribution ratio of the total energy consumption of dampers between floors in energy dissipation and damping, and obtained the distribution ratio of the total energy consumption of dampers between floors with dampers [4]. Cheng used the concept of reliability to study the arrangement scheme of energy-dissipation braces, and reached the conclusion that the optimal arrangement scheme of energy-dissipation braces was determined according to the sequential approximation method [5]. Milman used simulated annealing algorithm to study the arrangement of dampers, the optimal arrangement scheme of dampers is obtained by using annealing algorithm [6]. Li studied the arrangement of metal dampers by using genetic algorithm and SAP2000 application program interface, and concluded that the arrangement of dampers can be more efficient by reading the hysteretic energy dissipation curve data of dampers [7]. Pan studied the energy dissipation and damping structure system with metal dampers, and obtained the design principle of equal damping ratio of energy dissipation and damping structure [8]. Zhang studied the position of VED in the non-uniform shear structure, the design method of optimizing the position of VED in the structure is obtained by taking the maximum value of the root mean square of the interlayer displacement of each floor as the objective function [9]. Singh study the damping distribution of the structure by using gradient method and genetic algorithm, and the optimal arrangement method of dampers was obtained [10]. Bei studied the optimization of damper, and the damper position optimization method was obtained based on improved genetic algorithm and equivalent quadratic performance index method [11].

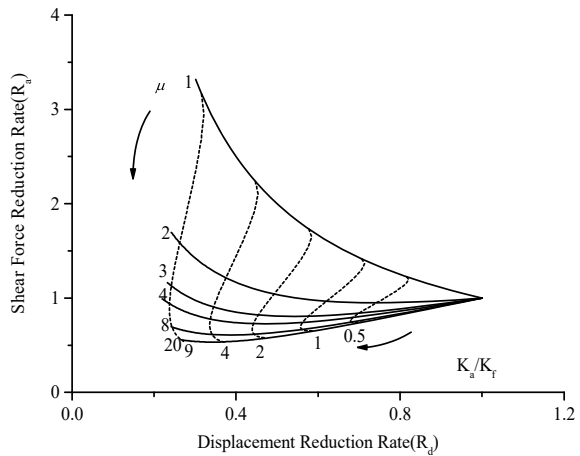
Great progress has been made in the research and application of energy dissipation technology. However, the technology needs to be further improved in the damping amount of the energy dissipation, vibration reduction effects of different structural forms with different dampers, and the optimal damping amount. In addition, the damping amount study of additional dampers for concrete frame structures is also to be carried out. Based on the above situation, the method of combining the seismic performance curve of single-particle-system with the response spectrum used in China’s design is adopted to conduct the damping amount, which should be installed on the reinforced concrete frame structure. It establishes a foundation for the standardized design of the design method of additional metal damping of reinforced concrete structures. This method reduces the repeated trial calculation and design process, and the time history analysis is only used as the verification of

the final damping effect, which not only reduces the difficulty, but also improves the efficiency. It has a broad prospect.

2 Damping Performance Curve of Single-Particle-System with Metal Damping

The damping performance curve shows the reduction degree of the maximum response value of the single-particle-system structure with and without dampers [12]. The damping effect is expressed by the displacement reduction rate (R_d) and the acceleration reduction rate (R_a). The damping performance curve of the structure with additional metal damping is a function of the displacement reduction rate (R_d) and the acceleration (shear) reduction rate (R_a) expressed by the two basic parameters of the system, which are ductility coefficient (μ) and the elastic stiffness ratio of the additional system (K_a/K_f). It is shown in Fig. 1. The maximum displacement and shear force of the energy dissipation system can be obtained by multiplying the reduction rate of displacement and shear force with the maximum displacement and the shear force of the original structure. The calculation formula of displacement reduction rate R_d , acceleration reduction rate R_a and ductility coefficient μ , the elastic stiffness ratio of the additional system (K_a/K_f) is in the literature [13].

Fig. 1 The seismic performance curve



3 Computational Mode

The 10-story reinforced concrete frame structure model is established. The structure plan is shown in Fig. 2. The bottom floor is 3.6 m high, and the rest floor is 3 m high. The concrete grade is C40. Rectangular section is adopted for beam and column sections. The section sizes of beams and columns are shown in Table 1. The mass of the bottom floor is 600 tons, and that of the rest is 558 tons.

The frame model is designed with structural design software, and the structural design meets the requirements. The calculation period is $T = 1.2$ s. According to the empirical formula of the basic natural vibration period of high-rise structures, $T = (0.1-0.15)n$, (n is the number of floors), the calculation period conforms to the empirical value.

Two artificial seismic waves are used to analyze the elastic–plastic time history of the structure, which are KOBE wave and TOHOKU wave. Their acceleration time-history curves are shown in Fig. 3. The seismic fortification intensity is set as 8° , the design earthquake group is Group I, and the site category is Class II. The acceleration conversion value is set as 70 cm s^{-2} when considering frequent earthquakes and 400 cm s^{-2} when considering rare earthquakes. The time interval of seismic wave is 0.01 s, and its action time is 30 s.

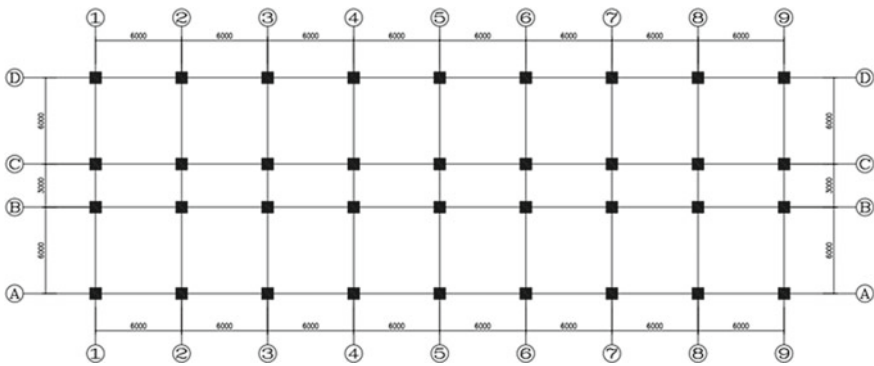


Fig. 2 Structure layout plan

Table 1 Dimensions of frame structure members

Storey	Structure member	Section size (mm)
1–10 storey	Column	800 × 800
1–10 storey	Peripheral transverse beam	300 × 850
1–10 storey	Internal transverse beam	250 × 700
1–10 storey	External longitudinal beam	300 × 700
1–10 storey	Internal longitudinal beam	300 × 750

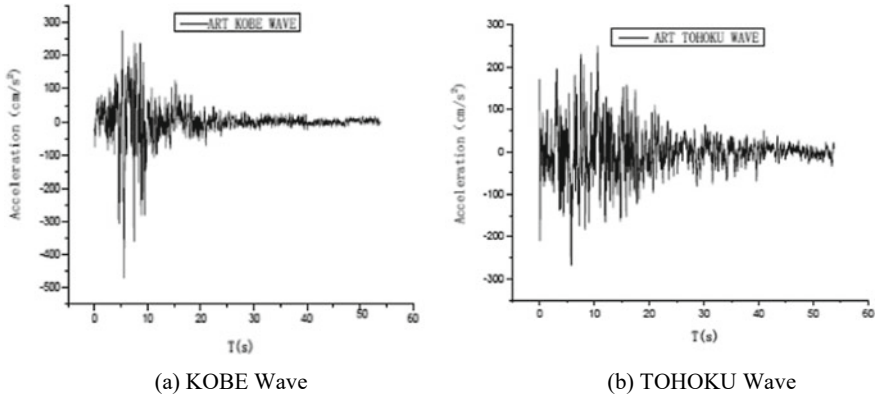


Fig. 3 Seismic waves

The static nonlinear analysis of the structure is carried out by using Pushover method, and the relationship between the interlayer shear force and the interlayer displacement of the structure is shown in Table 2.

The time history analysis of the original structure is carried out, and the response values under the action of two waves are obtained, as shown in Fig. 4. The overall change trend of the structure is relatively close in the action of two waves.

Table 2 The elastic lateral stiffness of the structure

Storey	Elastic lateral stiffness K_{fi}
10	1.17E + 08
9	3.85E + 08
8	4.80E + 08
7	4.89E + 08
6	4.96E + 08
5	5.10E + 08
4	5.30E + 08
3	6.04E + 08
2	8.45E + 08
1	1.22E + 09

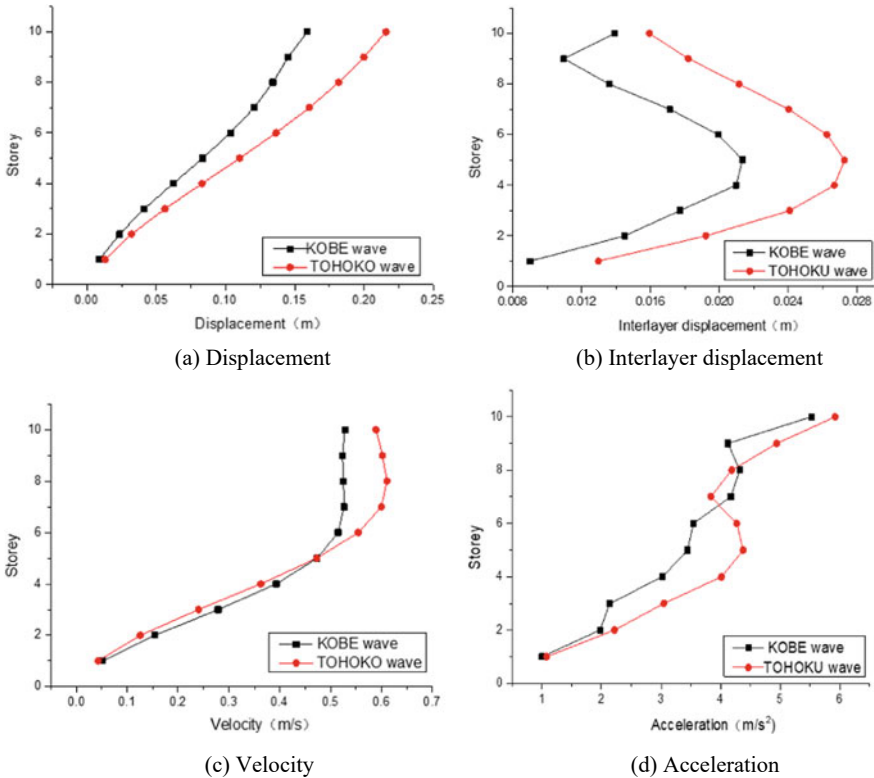


Fig. 4 Response value under the action of two seismic waves

4 The Calculation Process of Additional Metal Damping

The reinforced concrete frame structure with additional metal damping is called energy dissipation damping structure. It consists of energy dissipation and shock absorption system and the main structure. The energy dissipation and damping system is composed of supporting member, damper and the main structure. The support and damper constitute the structural additional system, the additional system and the main structure constitute the energy dissipation and the damping system; the stiffness of the additional system is K_a , the stiffness of the main structure is K_f , the stiffness of the energy dissipation and damping system is K , the stiffness is calculated as shown in Eqs. (1) and (2).

$$K_a = \frac{1}{1/K_b + 1/K_d} \tag{1}$$

$$K = K_a + K_f \tag{2}$$

The damping amount of additional metal damping required by the structure is calculated by using the method of energy dissipation and shock absorption based on the damping performance curve. The main calculation process is as follows:

Firstly, the elemental point system is converted into a multi-particle-system. The total height of the multi-particle-system is 30.6 m. Its effective height is 20.87 m after converting the multi-particle-system into the single-particle-system. The response value of displacement response spectrum of the single-particle-system is 0.15 m. The interlayer displacement angle of the single-particle-system is 1/140. Based on the performance design, the target interlayer displacement angle can be set as 1/300 of the target displacement value. The ratio of the target interlayer displacement angle to the calculated interlayer displacement angle is the target displacement reduction rate.

Secondly, the damping amount of the additional system of metal dampers, which are required for the structure to achieve the target displacement reduction rate, is calculated by using the damping performance curve method of the single-particle-system in the early stage.

Thirdly, the value of ductility coefficient (μ) is been set and continuously adjust the elastic stiffness ratio (K_a/K_f) until the difference between the calculated displacement reduction rate and the target displacement reduction rate is zero, which is the value of ductility coefficient and elastic stiffness ratio meet the requirements. When the ductility coefficient (μ) is 4 and the elastic stiffness ratio (K_a/K_f) is 3.3, the requirements are met. At this time, the displacement reduction rate (R_d) is 0.46, and the shear reduction rate (R_a) is 0.66. The calculated stiffness of the additional system of the structure is shown in Table 3.

Table 3 Damping of additional system of concrete frame structure

Storey	Additional system yield displacement $\mu_{ay,i}$ (m)	Elastic stiffness of additional system K_{ai} (N/m)	Additional system yield strength $F_{ay,i}$ (N)
10	0.0025	3.86E + 08	9.65E + 05
9	0.0025	8.43E + 08	2.11E + 06
8	0.0025	1.47E + 09	3.67E + 06
7	0.0025	2.01E + 09	5.02E + 06
6	0.0025	2.34E + 09	5.84E + 06
5	0.0025	2.53E + 09	6.32E + 06
4	0.0025	2.63E + 09	6.58E + 06
3	0.0025	2.55E + 09	6.38E + 06
2	0.0025	2.02E + 09	5.04E + 06
1	0.003	6.83E + 08	2.05E + 06

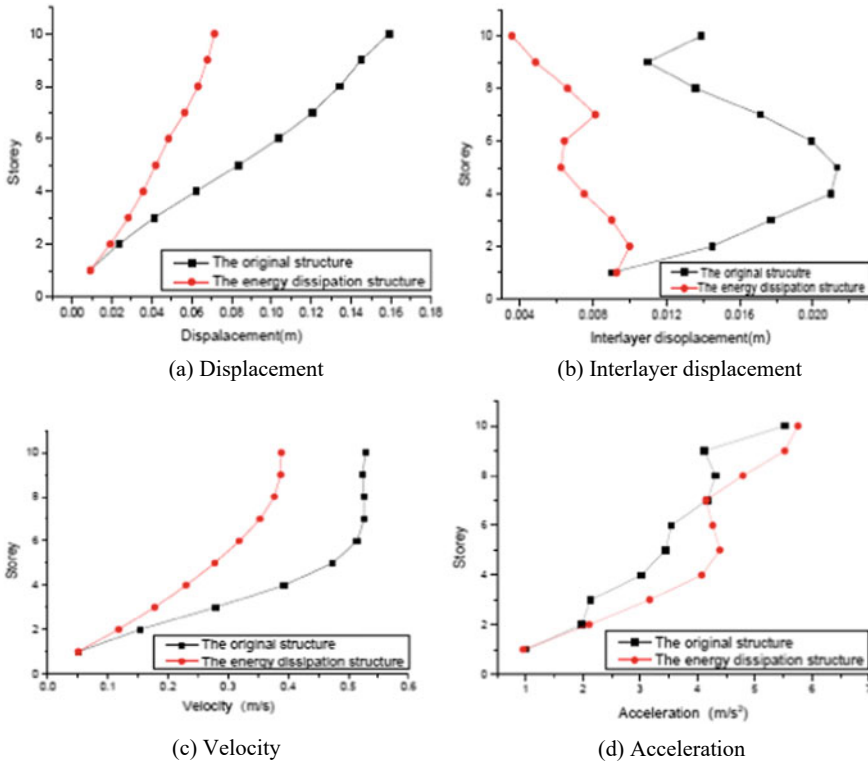


Fig. 5 The displacement, interlayer displacement, velocity and acceleration response of KOBE wave

At last, take the elastic stiffness of additional system (K_{ai}) as the optimal damping amount of the additional system with metal damping. The calculated damping amount is added to the main structure, and the total damping amount of each floor is evenly distributed to each frame. One damper is respectively set for AB span and CD span of each frame.

The time history analysis of the energy dissipation and damping structure with metal dampers is carried out, and compared with the original structure. The seismic response values are shown in Figs. 5 and 6. The displacement response values and the interlayer displacement values have greatly decreased. The speed response values decrease significantly on the upper floor, while the reduction in the bottom floor is not significant. The acceleration response values decrease slightly, even exceeding the original structure on some floors. This is because the additional system with metal damping increases the stiffness of the energy dissipation structure.

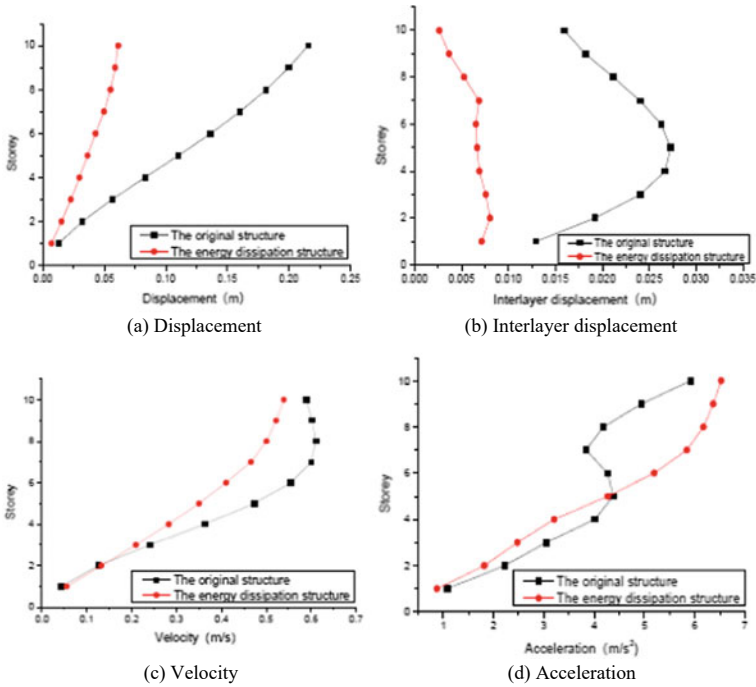


Fig. 6 The displacement, interlayer displacement, velocity and acceleration response of TOHOKO wave

The energy consumption of additional metal damping in each floor is researched. The energy dissipation hysteresis curve of each damper is shown in Figs. 7, 8 and 9. LINK-1, LINK-3, LINK-5, and LINK-19 correspond to the 1st, 2nd, 3rd and 10th floor respectively. It can be seen that the hysteresis curve of dampers from the 1st to 5th floors is fuller than that of the upper part from the hysteretic curve of the additional system. It means that the absorption capacity of the lower damper of the structure is higher than that of the upper floor. The energy dissipation curves of the 7th and 10th floors are approximate straight lines, it means that the dampers of these two floors consume less energy.

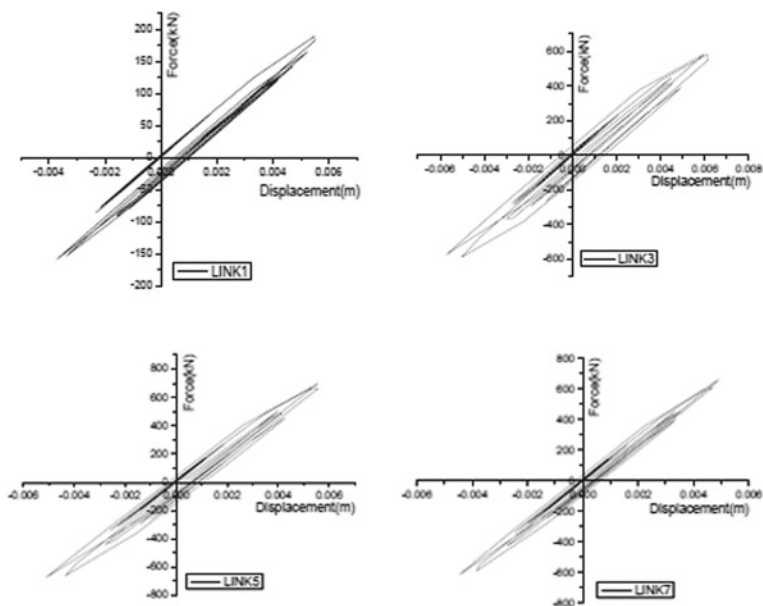


Fig. 7 Hysteresis curve of dampers form the 1st to 4th floors

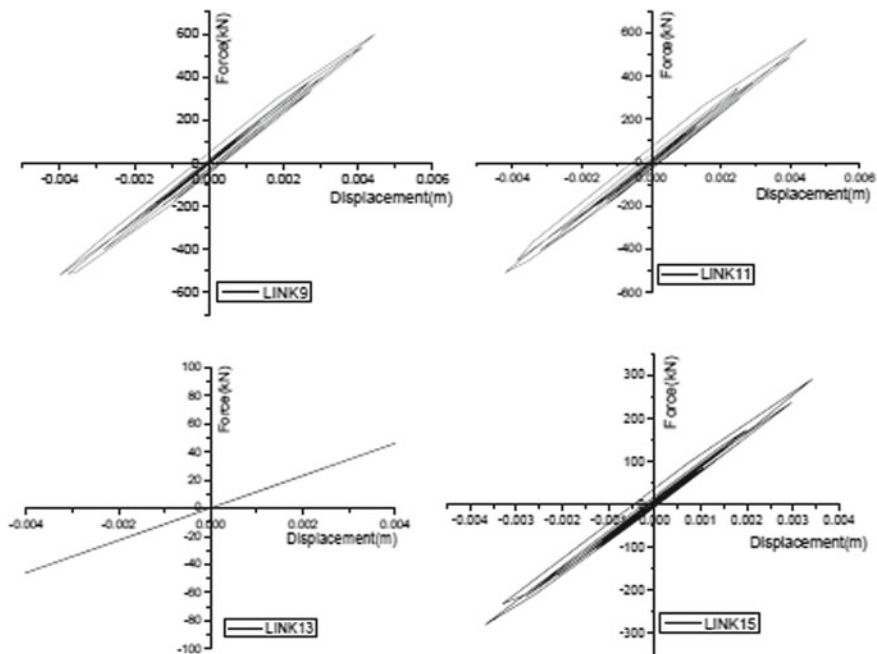


Fig. 8 Hysteresis curve of dampers form the 5th to 8th floors

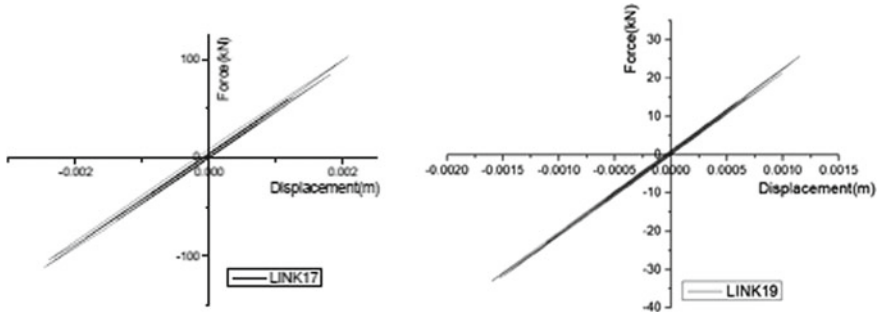


Fig. 9 Hysteresis curve of dampers form the 5th to 6th floors

5 Conclusion

The damping amount of additional metal damping of reinforced concrete frame structure is calculated. The main methods and conclusions are as follows.

First, a reinforced concrete frame structure is designed to meet the specification requirements, which meets the specification requirements through structural design. The static nonlinear analysis is carried out and the stiffness of each floor is obtained. Then the time history analysis is carried out under the action of two kinds of seismic waves, the response values of the structure are obtained. The change trend of displacement and velocity of the original structure is relatively close under the action of two kinds of seismic waves.

Second, the multi-particle-system is converted into a single-particle-system. The displacement angle of the single-particle-system is calculated through the displacement spectrum, and the target interlayer displacement angle of the structure is set. The damping amount of additional metal damping required is calculated to achieve the target displacement reduction rate according to the damping performance curve of additional metal damping. The damping amount is converted into a single damper and added to the structure, and the energy dissipation structure of reinforced concrete frame with metal damping is analyzed. It is found that the displacement response values and the interlayer displacement values have greatly decreased. The speed response values decrease significantly on the upper floor, while the reduction in the bottom floor is not significant. The acceleration response values decrease slightly, even exceeding the original structure on some floors. This is because the additional system with metal damping increases the stiffness of the energy dissipation structure.

At last, the energy consumption of additional metal damping in each floor is researched. It is found that the energy dissipation curve of the additional system is plump at the bottom floor than at the upper floor, it means that the metal dampers at the bottom consumes more energy, while the damper at the top consumes less energy. In addition, the damper energy dissipation curve area of the second floor is the largest and the energy dissipation is large, however, the energy dissipation curves of the 7th and 10th floors are approximate straight lines, and the dampers of these

two floors consume less energy. The damping amount of additional metal damping at the upper part can be appropriately reduced in the later optimization design, so that the upper damper can also give full play to its damping efficiency. The study of the hysteretic curve of the additional system establishes a foundation for the further optimization design of the additional damping in the later stage.

Acknowledgements This study is supported by Natural Science foundation of Jiangsu Higher Education, the project number is 20KJB560011, 22KJD560006, and is also supported by the Philosophy and Social Science of Jiangsu Higher Education, the project number is 2021SJA0913, the Soft Science Research Project of Wuxi Association for Science and Technology (KX-22-C143).

References

1. Weizhi XU, Dongsheng DU (2022) Optimization layout of viscous dampers and its application in retrofitting of a high-rise steel structure. *J Build Struct* 43(8):32–44
2. Jie Z, Tong-ling Z (2017) The application of the different optimal allocation methods of hysteretic dampers in the frame structure. *Earthquake Resistant Eng Retrofitting* 39(3):79–85
3. Gang LI, Hong-nan LI (2007) Direct displacement-based design for buildings with passive energy dissipation devices. *Eng Mech* 24(9):88–94
4. Deng Y, Zhou Y, Deng X (2009) Research on the total energy consumption ratio of dampers between stories in passive energy dissipation structures. *Earthquake Resistant Eng Retrofitting* 31(3):26–33
5. Cheng FY, Pantelides CP (1988) National center for earthquake engineering research (US). Optimal placement of actuators for structural control. National Center for Earthquake Engineering Research, State University of New York at Buffalo
6. Milman MH, Chu CC (2007) Optimization methods for passive damper placement and tuning
7. Dan LI, Ying ZHOU (2013) Optimally distribution of metallic dampers based on genetic algorithm and sap 2000 application programming interface. *Struct Eng* 29(06):69–75
8. Chao P, Ruifu ZH, Hao L, Jingzhou L (2018) Constant damping ratio design method for damping controlled structures with metallic yielding dampers. *J Build Struct* 03(39):39–47
9. Zhang RH, Soong TT (1992) Seismic design of viscoelastic dampers for structural applications. *J Struct Eng* 118(5):1375–1392
10. Singh MP, Moreschi LM (2001) Optimal seismic response control with dampers. *Earthq Eng Struct Dynam* 30:553–572
11. Bei W, Li H (2006) Optimal placement of semi-active control devices in controlled structures. *J Disaster Prev Mitig Eng* 26(1):28–33
12. Japan Vibration Isolation Construction Association (2008) Design and construction manual of passive damping structures. China Architecture & Building Press
13. Xingzhu P, He F (2013) Research on the design method of energy dissipation structure. *Bulid Struct* 43(4):60–65

Discussion of “Strong Column—Weak Beam” in Capacity Design Method



Lv Tao, Li Yingmin, Li Feng, Li Feng, Pan Cunrui, and Feng Liqiang

Abstract The ideal failure mode of structures under strong earthquakes is one of the key factors to achieve the seismic fortification goal. The capacity design method is an important tool to ensure the failure mode of “strong column—weak beam” in different country design codes, but there are various differences in the design application, as well as in the observed failure modes after earthquake disasters. In terms of structural damage, this failure mode advocated by the capacity design method has not been totally realized. In order to explore the reasons, this paper takes the reinforced concrete frame structure as an example, sorts out the relevant provisions on “strong column—weak beam” in the capacity design method in New Zealand, the United States, Europe, Japan and China, summarizes the similarities and differences. Additionally, this paper also reflects on the inadequacies about design method of column moment magnification in China.

Keywords Capacity design method · Seismic code · Strong column—weak beam

1 Introduction

The “capacity design method” proposed by Paulay et al. [1–4] describes how to make the RC frame structure have good ductility deformation capacity, and to form the failure mode of beam end hinge under strong earthquakes. This method is widely used in different country design codes. However, many earthquake disasters show that the failure mode of RC frame structure is still dominated by the column hinge or

L. Tao · L. Yingmin (✉) · L. Feng · L. Feng
Chongqing University, Chongqing 400045, China
e-mail: 2890310258@qq.com

P. Cunrui · F. Liqiang
Gansu Construction Investment (Holdings) Group Co., Ltd, Lanzhou 730000, China

P. Cunrui
Gansu Construction Investment Technology Research Co., Ltd, Lanzhou 730000, China

© The Author(s), under exclusive license to Springer Nature Singapore Pte Ltd. 2024
M. Casini (ed.), *Proceedings of the 3rd International Civil Engineering and Architecture Conference*, Lecture Notes in Civil Engineering 389,
https://doi.org/10.1007/978-981-99-6368-3_30

the beam-column mixed hinge, so the column end moment amplification coefficient method adopted in China still needs to be further improved. This paper will summarize the characteristics of the capacity design method, compare the similarities and differences of design codes among New Zealand, the United States, Europe, Japan and China, and re-examine the shortcomings of the column end moment amplification coefficient method in China.

2 Capacity Design Method

Based on the ductility design idea, the capacity design method is the main design tool to control the nonlinear response and ensure the realization of the preset failure mode. In detail, the concept of the capacity design method [1] is: firstly, determine the energy dissipation mechanism of the structure, specify the ductile member (beam) to dissipate the earthquake energy, take strict structural measures, and then calculate the internal force demand of the ductile member based on the reduced seismic action. At the same time, the bearing capacity of the non-ductile member (column) is amplified to a certain extent, so that the non-ductile member has sufficient strength reservation and always remains elastic without yielding, whereas the ductile member is close to the ultimate strength level in the process of sufficient energy dissipation.

The capacity design method has the following characteristics [2–4]:

- (1) Clarify the energy dissipation mechanism of the structure. Firstly, the plastic hinge position of the building structure is specified, and the section of the plastic hinge area is designed based on the reduced seismic action, and strict structural measures are taken to ensure that the ductile members can meet the expected ductility requirements and energy dissipation capacity. In addition, ductile members should be easy to be repaired and have little effect on the stability of non-ductile members or the integrity of the system. Take a typical multi-story frame structure as an example, the energy dissipation mechanism of beam hinges has better ductility or lower ductility requirements than the energy dissipation mechanism of column hinges, and the corresponding structural measures are easier to implement [5].
- (2) Avoid unexpected brittle failure modes of ductile members. In order to achieve the expected ductile failure mode of the whole structure, all members should have sufficient strength reservation to avoid the occurrence of brittle failure mode, such as ensuring that the beam is “strong shear—weak bending” and avoiding shear failure before the plastic hinge is formed at the beam end.
- (3) The capacity of non-ductile members is not obtained by the structural analysis of reduced seismic action, but by enlarging the bearing capacity of ductile members. In Chinese code, the flexural bearing capacity of the beam calculated from the reduced seismic action is amplified, and then the flexural bearing capacity of the non-ductile component column is obtained from the beam capacity. The resistance of non-ductile members comes from ductile members

with plastic hinges. The design is carried out by keeping the strength of non-ductile members in a certain proportion to the internal forces that may occur when the plastic hinge section exceeds the expected strength. Therefore, no matter how strong the ground motion intensity is under earthquakes or how large the degree of nonlinear deformation of the structure is, non-ductile members can always maintain elastic and reduce the sensitivity of the structure to ground motion characteristics.

3 The Concrete Practice of Capacity Design Method in National Codes

At the end of the twentieth century, European and American scholars fully studied the R - μ - T relationship of single-degree of freedom systems [6–8]. Based on this, the seismic codes of various countries generally accepted the R - μ seismic design criteria. The capacity design method is the main design tool to achieve structural ductility and seismic fortification objectives. At present, the codes of various countries have applied the concept of capacity design method more or less. The following summarizes the provisions on “strong column—weak beam” failure mode in New Zealand, the United States, Europe, Japan and China.

3.1 New Zealand Code

In the Appendix CD of “Concrete structures standard: Part 1- The design of concrete structures” (NZS 3101) [9], measures are taken to ensure that the bearing capacity of the structure with column hinge failure mechanism is greater than that with beam hinge failure mechanism, and two design methods (A and B) are provided. The difference between the two methods is that method A only allows plastic hinges at the bottom of column in the first floor and the top of column in the top floor, and does not allow plastic hinges at the column ends of other floors; method B does not allow premature plastic hinges at the column end, but allows the structure to eventually have a failure mechanism of beam-column mixed hinges. This method is stricter with the structural measures of the column. Both methods do not allow the structure to appear the story yield failure mode.

In method A, the failure mode of “strong column—weak beam” is mainly achieved by calculating the design bending moment of the column end section (M_{col}^*), Eq. (1) defines the design bending moment of the column end section, where R_m is the reduction coefficient of the design value of the bending moment of the column end. When the axial compression ratio of the column is small or under tension, the column is similar to the beam placed vertically, and the ductility is better. Considering the economy, the design moment can be minimized.

$$M_{\text{col}}^* = R_m(\beta\omega\phi_0 M_{\text{EC}} - 0.3h_b V_{\text{col}}^*) \quad (1)$$

The dynamic amplification coefficient ω and the correction coefficient β are considered when the structure enters the nonlinear state. The analysis results of the column end moment under the dynamic force and the static condition are different. $\phi_{o, fy}$ is the over strength ratio; M_{EC} is the sum of the bending moments at the column end at the center of the joint under the combined seismic action, h_b is the height of the beam, and V_{col}^* is the maximum design shear force of the column.

The New Zealand code comprehensively considers the contribution of the actual reinforcement in the floor to the flexural bearing capacity of the beam end, the reinforcement material overstrength, the dynamic response of the structure, the axial force in the column, the economy and other factors. The above factors are transformed into a series of bending moment amplification factors and then the design moment of the column end is multiplied by these factors. In addition, the difference between the bending moment at the column end at the center of the beam-column joint and the bending moment at the column end section is also considered.

3.2 American Code

In Sect. 21.6 of the “Building code requirements for structural concrete and commentary” (ACI318-11) [10], the minimum bending capacity of the column is specified, inequality (2) defines the minimum bending capacity of the column, so that there is a difference between the bending capacity of the column and that of the beam, which reduces the possibility of yielding at the end of the column and avoid the failure mode of yielding at the lower story of the column hinge mechanism.

$$\sum M_{nc} \geq (6/5) \sum M_{nb} \quad (2)$$

where, $\sum M_{nc}$ is the sum of nominal flexural strengths of columns framing into the joint, evaluated at the faces of the joint. The flexural capacity of the column should be calculated under the axial pressure of the coefficient multiplied by the minimum flexural capacity which is consistent with the direction of the lateral force considered. $\sum M_{nb}$ is the sum of nominal flexural strengths of the beams framing into the joint, evaluated at the faces of the joint. The nominal strength is roughly equivalent to the standard value of material strength in China. In addition, for structures using T-section beams, the contribution of slab reinforcement to M_{nb} within the effective width of the floor should be considered.

The American code mainly considers the contribution of the steel bar in the floor to the bearing capacity of the beam end, the reinforcement material overstrength, and the influence of the axial force on the reduction of the flexural bearing capacity of the column. The actual flexural bearing capacity of the column end is moderately increased based on the actual flexural bearing capacity of the beam end, so that it

forms a clear flexural bearing capacity difference to avoid the column hinge yield mechanism.

3.3 *European Code*

In Euro Code 4.4.2 Ultimate limit state of Euro Code 8 [11], it is emphasized that the structure should have good ductility, mainly through the bearing capacity difference between different types of components to avoid brittle failure mode. For the frame structure, the plastic hinge should appear at the beam end. Or it should first appear at the beam end before the plastic hinge appears at the column end to avoid the story yield mechanism dominated by column hinge.

Considering the combination of seismic action, the flexural capacity of beams and columns is checked by inequality (3).

$$\sum M_{Rc} \geq 1.3 \sum M_{Rb} \quad (3)$$

where, $\sum M_{Rc}$ is the sum of the design values of the bending capacity of the column at the center of the frame joint, and the minimum bending capacity of the column in the range of axial force variation under the combined action of earthquake is taken. $\sum M_{Rb}$ is the sum of the design values of the flexural capacity of the beam at the center of the frame joint. The $\sum M_{Rc}$ and $\sum M_{Rb}$ are calculated according to the standard value f_k and the partial coefficient γ_M of the material, and the contribution of the steel bar to the flexural capacity of the beam within the effective width of the floor needs to be considered.

The European code mainly considers the reinforcement material overstrength, the contribution of the steel bar to the flexural capacity of the beam in the effective width range of the floor flange, and the influence of the axial force change in the column on the flexural capacity of the column. It ignores the difference between the bending moment at the center of the joint and the section. Through the calculation of the bearing capacity of the beam and column and other components, in order to achieve the bearing capacity difference between different components, so as to avoid the brittle failure mode dominated by column hinge. It is worth noting that the European code uses the material design value rather than the standard value to calculate the bearing capacity.

3.4 *Japanese Code*

At present, several seismic design methods in Japan are implemented at the same time. The new seismic design method [12–15] is one of them. The core content is the second design stage which is divided into two steps: “design limit state” and

“safety limit state”. The corresponding calculation processes are “yield mechanism design” and “yield mechanism guarantee design”. “Design limit state” refers to the requirement that the structure still has sufficient bearing capacity when it reaches the design limit deformation (1/100) under the action of large earthquakes. The bearing capacity is guaranteed by the expected bearing capacity of the plastic hinge. “Safety limit state” refers to considering the randomness of ground motion, the possible strengthening of the plastic hinge and the inaccuracy of the elastic–plastic model. When the safety guarantee deformation (1/67) is achieved, it is required to ensure the bearing capacity of the non-plastic hinge area of the component, and to ensure that all components do not appear failure modes other than bending failure.

The Japanese code is to design and calculate the overall yield mechanism of the structure, rather than to calculate the difference of the bearing capacity of the joints. For the frame structure, the overall yield mechanism is the beam hinge yield mechanism, and all plastic hinges are required to be flexural plastic hinges with sufficient ductility. In addition, plastic hinges are allowed to appear at the bottom end of column in the first floor and the top of column in the top floor, and some frame columns that do not bear the horizontal action of the earthquake are also allowed to appear plastic hinges, forming the overall yield mechanism of the beam-column mixed hinge. Japanese new seismic design method is a direct quantitative calculation under the level of large earthquakes, including bearing capacity requirements and deformation capacity requirements. This method comprehensively considers the factors such as the reinforcement material exceeds expected strength, and the influence of axial force changes on the bending capacity of the column, which needs high requirements for designers.

3.5 Chinese Code

The provisions of Article 6.2.2 of Chinese “Code for seismic design of buildings” (GB 20011-2010 (2016 Edition)) [16] indicate that the seismic collapse resistance of frame structures is closely related to its failure mechanism. The beam-end yielding frame has a large internal force redistribution and energy dissipation capacity. The seismic performance is good, and the column end yielding collapse mechanism should be avoided. “Strong column—weak beam” refers to the actual flexural bearing capacity of the beam end at the joint M_{by}^a , and the actual flexural bearing capacity of the column end M_{cy}^a satisfies the inequality (4):

$$\sum M_{cy}^a > \sum M_{by}^a \quad (4)$$

It is stipulated in Article 6.2.2 of the specification as follows:

At the beam-column joints of the first, second, third and fourth-level frames, except that the axial compression ratio of the top layer of the frame and the column is less than 0.15 and the joint of the frame-supported beam and the frame pillar,

Eq. (4) defines requirements of the bending moment design value of the column end combination:

$$\sum M_c = \eta_c \sum M_b \quad (5)$$

The first-level frame structure and the first-level frame in the regions of seismic intensity 9 degrees may not meet the requirements of the above formula, Eq. (5) defines the requirements that should also be met:

$$\sum M_c = 1.2 \sum M_{bua} \quad (6)$$

where, $\sum M_c$ is the sum of the bending moment design values of the upper and lower column ends in the clockwise or counter clockwise direction, and the bending moment design values of the upper and lower column ends can be distributed according to the elastic analysis. $\sum M_b$ is the sum of the bending moment design values of the anticlockwise or clockwise combination of the left and right beam sections of the joint. When the left and right beam ends of the first-stage frame joint are negative bending moments, the bending moment with smaller absolute value should be zero. $\sum M_{bua}$ is the sum of the bending moment values corresponding to the bending capacity of the normal section of the anticlockwise or clockwise section of the left and right beam ends of the joint, which is determined based on the area of the actual reinforcement (including the compression reinforcement of the beam and the related floor reinforcement) and the standard value of material strength; η_c is column end moment amplification coefficient. For the frame structure, the first, second, third and fourth levels can be taken as 1.7, 1.5, 1.3 and 1.2 respectively.

Chinese code mainly calculates the design value of the column end moment through column end moment amplification coefficient. It is expected that the frame structure can realize the beam hinge yield mechanism of “strong column—weak beam”, and take different column end moment amplification coefficients for different seismic intensities. It should be said that Chinese code is convenient for engineering design and use. In addition to the first-level frame, different factors such as the reinforcement material overstrength, the contribution of floor slabs to the flexural capacity of beam ends, and the difference in bearing capacity between the center of beam-column joints and the interface are all considered uniformly and roughly by the column end moment amplification coefficient. In addition, the sum of the bending moment design value of the beam end is different from the sum of the bending capacity of the beam end, and the actual bending capacity of the beam-column section at the joint is not checked.

3.6 *The Similarities and Differences of National Codes*

In the process of applying the capacity design method, there are many similarities and differences between the codes among various countries, which are compared from the aspects of yield mechanism type, different influencing factors and methodology.

In terms of yield mechanism: all national codes emphasize the avoidance of column hinge-based story yield mechanism, which is a brittle failure mode. The difference is that the New Zealand code method B and the Japanese code allow the mixed hinge yield mechanism of beam hinge + partial column hinge; the codes of Europe, the United States and China are not clear, but it is required to reduce the possibility of the hinge at the column end, or the plastic hinge should first appear at the beam end before appearing at the column end. In addition, the New Zealand code and the Japanese code allow plastic hinges at the bottom of column in the first floor and the top of column in the top floor, but the European and American codes are not clear, and the Chinese code allows plastic hinges at the top of the column. It should be said that the complete beam hinge yield mechanism is ideal and perfect, but it is difficult to achieve. Plastic hinges are allowed at the bottom of column in the first story and some column ends, but it is necessary to ensure that the bearing capacity cannot be reduced after the column ends hinges appear.

In terms of influencing factors: the reinforcement material overstrength, the contribution of steel bar to the flexural bearing capacity of beam within the effective width of floor flange, and the influence of axial force in column on the reduction of flexural bearing capacity of column are considered in the codes of various countries, but the consideration methods are different. New Zealand, European and American codes consider different factors separately; the Japanese code is directly calculated under large earthquakes, and the above factors can be directly considered. Chinese code is relatively rough on various influencing factors and do not determine the degree of each influencing factor separately.

From the perspective of methodology, both the New Zealand code and the Chinese code consider the seismic load combination conditions in the design process, and amplify the bending moment internal force values of the column end and the beam end respectively, so as to obtain the design value of the column end moment, in order to achieve the bearing capacity difference between different components. Both American and European codes check the bending capacity of beams and columns to ensure that the sum of the bearing capacity of columns is greater than the sum of the bearing capacity of beam ends. The American code calculates the actual bending strength or nominal bending strength by using the standard value of the material, and the European code adopts the bending strength design value considering the reduction coefficient for the bearing capacity. The Japanese code is a nonlinear calculation under large earthquakes, which directly analyzes the overall yield mechanism of the structure, rather than designing the moment amplification of the column end under small earthquakes or simply comparing the flexural capacity of the joints.

4 The Influence of Column End Moment Amplification Coefficient on the Difference of Bending Capacity Between Beam and Column

Chinese code adopts the column end moment amplification coefficient for seismic design, but the actual bending capacity of the column end under strong earthquakes will change due to the change of axial force. Whether the column end moment amplification coefficient can achieve the capacity difference of beam-column bearing capacity remains to be investigated. The ratio of the sum of the seismic bearing capacity of the normal section of the column end and the beam end is analyzed when parameter of the column end moment amplification coefficient changes.

4.1 Typical Frame Design

In this paper, a typical RC frame structure is designed by using YJK structural design software. The design seismic acceleration is 0.20 g, class II site, earthquake group is the first group, the basic wind pressure is 0.45 kN/m², the ground roughness is class B, class C building, the floor height is 3.3 m, the number of floor is 7, the total height is 23.1 m, the seismic grade is two, the axial compression ratio of the column and the maximum interstory drift ration are close to the code limit, the axial compression ratio of the model is 0.74, less than the axial compression ratio limit of 0.75, the maximum displacement angle is 1/573, less than the limit of 1/550, which meets the code requirements. The section size of the middle column is 450 mm × 450 mm, the side column is 400 mm × 400 mm, the section size of the beam is 250 mm × 600 mm, the thickness of the slab is 120 mm, the thickness of the protective layer of the beam and column is 20 mm, the steel bar of the beam and column is HRB400, the steel bar and stirrup of the floor are HPB300, the strength grade of the beam and column concrete is C35, the strength grade of the slab concrete is C30, the dead load of the roof is 1.5 kN/m², the live load of the roof is 2.0 kN/m², and the linear load of the parapet wall is 3.5 kN/m. The dead load of the standard floor is 2.0k N/m², the live load is 2.0 kN/m², and the linear load of the outer partition wall is 7.0 kN/m. Figure 1 shows the structural plan layout, Fig. 2 shows the elevation.

Through the OpenSees structural analysis platform, a frame of the structure is modeled, and the elastic–plastic analysis of the large earthquake is carried out. The load combination condition is: 1.0 times of constant load + 0.5 times of live load + 1.0 times of horizontal seismic action (rare earthquake). The cross-section size of the beam and column of the model are unchanged, by adjusting the seismic grade and construction measures in the YJK seismic parameters, whereas the column end moment amplification coefficient η_c is changed.

Fig. 1 Layout plan

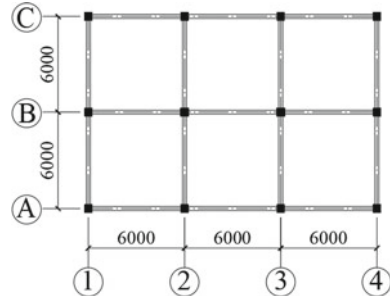
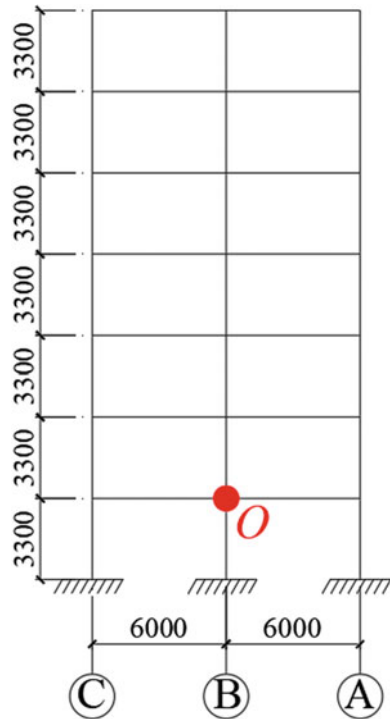


Fig. 2 Structural elevation



4.2 Calculation of Flexural Bearing Capacity of Column End and Beam End

The calculation method of the ratio of the sum of the flexural bearing capacity of the normal section of the column end and the beam end is as follows: Corresponding to the O node in Figs. 2 and 3 shows the bearing capacity of the beam and column, and the flexural bearing capacity of the beam end is $\sum M_{bu1}^a$ and $\sum M_{bu2}^a$, respectively, calculated by the area of the actual reinforcement in the beam, and considering

the reinforcement overstrength. The flexural bearing capacity of the column end is $\sum M_{cu1}^a$ and $\sum M_{cu2}^a$, respectively. The column is a compression-bending member, and its flexural bearing capacity is closely related to the vertical axial force. Figure 4 shows the M-N bearing capacity curve of the column. The axial force and internal force bending moment coordinates of the column are (N_1, M_1) , and the corresponding flexural bearing capacity is M_{cu1}^a . Equation (7) defines the ratio of the sum of the flexural bearing capacity of the column end to the beam end, without considering the improvement of the flexural bearing capacity of the beam by the floor.

$$\frac{\sum M_{cy}^a}{\sum M_{by}^a} = \frac{M_{cy1}^a + M_{cy2}^a}{M_{by1}^a + M_{by2}^a} \tag{7}$$

Fig. 3 Bending bearing capacity of beam and column at the middle joint O

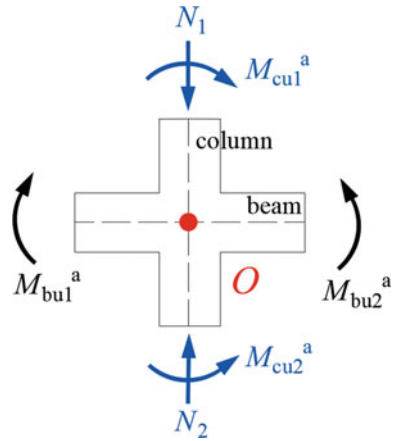
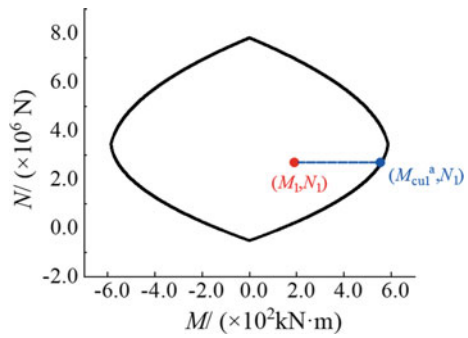


Fig. 4 Relationship curve of column M and N



4.3 *The Ratio of Flexural Capacity of Column End to Beam End Under Strong Earthquake*

Figure 5 shows the initial ratio of the sum of the bending capacity of the column end and the beam end of the frame under different column end moment amplification coefficient η_c . It can be seen from the diagram that when η_c increases from 1.2 to 1.7, the ratio of the flexural bearing capacity of the column end to the beam end increases, but it is still not fully guaranteed that the bearing capacity of the column end is greater than that of the beam end. The flexural bearing capacity of the column end of most joints is less than that of the beam end, and the expected bearing capacity difference is not formed. The side joint is only connected to one beam, so it is often easy to meet the bearing capacity ratio greater than 1, and the ratio is greater than the middle joint.

It should also be noted that the example in this paper does not consider the strengthening effect of the floor on the beam. In practical engineering, the flexural capacity of the beam will be further improved, and the ratio will be reduced to a certain extent.

5 **Thoughts on the Column End Moment Amplification Coefficient Method**

Whether the column end moment amplification coefficient can achieve the bearing capacity difference remains to be discussed. This paper analyzes the reliability and deficiency of the “strong column—weak beam” provisions of Chinese code from the perspective of methodology. As shown in Fig. 6, under the combined conditions of frequent earthquakes, the sum of the design values of the bending moment at the column end $\sum M_c$ is the product of the sum of the design values of the bending moment at the beam end $\sum M_b$ and the bending moment increase coefficient η_c , in order to realize the structure encountering strong earthquakes (rare earthquakes or earthquakes with larger acceleration peaks). During the process, the sum of the flexural bearing capacity of the column end $\sum M_{cu}^a(t)$ is always greater than the sum of the flexural bearing capacity of the beam end $\sum M_{bu}^a(t)$. The code transforms the difference of bending capacity into the relationship between the design value of beam and column internal force. With the increase of seismic grade, the column end moment amplification coefficient needs further increase.

- (1) Under strong earthquakes, the difference of flexural bearing capacity between beam end and column end needs to be further investigated. If the column end moment amplification coefficient can realize the equivalent transformation of bearing capacity, the failure mode of the structure “strong column—weak beam” can be effectively guaranteed. However, from the perspective of seismic damage

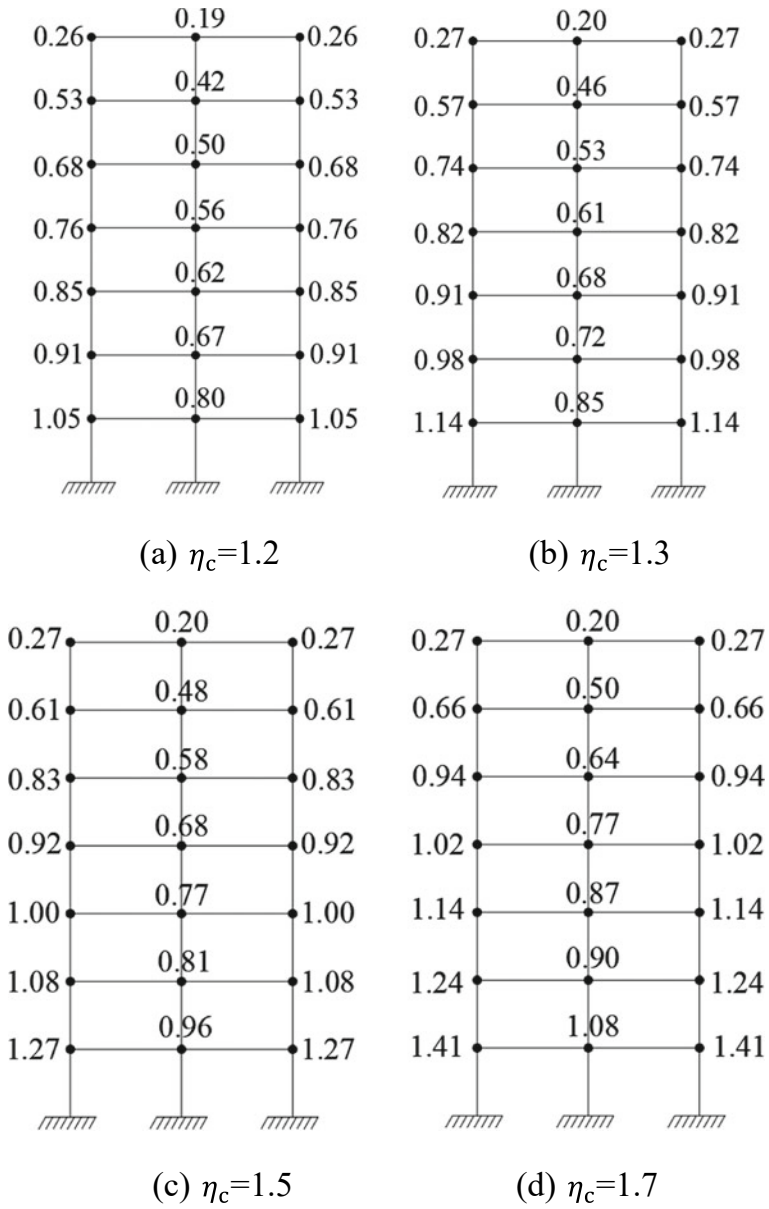


Fig. 5 Moment resisting capacity ratio of column to beam

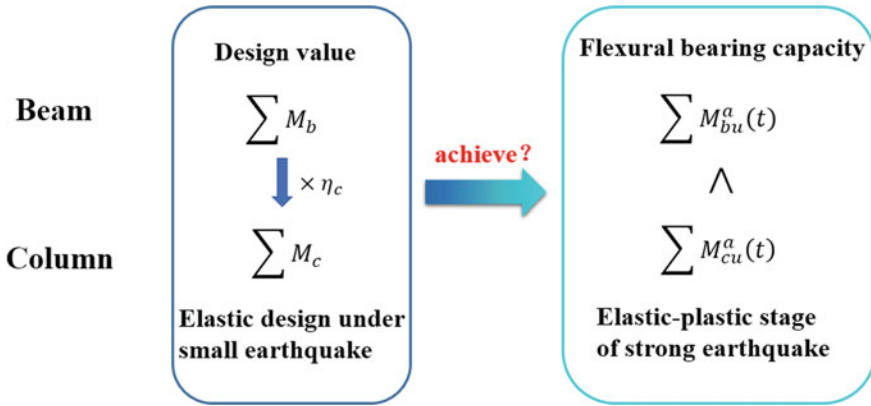


Fig. 6 Realization method of ‘strong column and weak beam’

and the numerical simulation results of Sect. 3.3, in order to meet the requirements of “strong column—weak beam”, the column end moment amplification coefficient needs to be further improved.

- (2) The reduction of flexural capacity of columns under strong earthquakes is not fully considered. The bending capacity of the column $\sum M_{cu}^a(t)$ changes under strong earthquakes, that is, the bearing capacity $\sum M_{cu}^a$ corresponding to different time is not the same. Under strong earthquakes, the axial force in the column may change dramatically, resulting in a decrease in the flexural capacity. References [17–19] studied the influence of vertical ground motion on the seismic performance of RC frame structures. It is found that the vertical seismic action has a significant effect on the axial force distribution of concrete frame columns. When the vertical seismic action intensity is large, the maximum axial pressure of the frame column can reach 2–3 times of the initial axial pressure, and tension appears in some floor frame columns. In addition, for the frame structure with a large height-width ratio, the horizontal seismic action will produce a large overturning moment, which will have a great influence on the axial force of the side column. The above reasons will lead to a significant reduction in the bending capacity of the column $\sum M_{cu}^a(t)$, so it is difficult to ensure that the structure meets the requirements of “strong column—weak beam” under strong earthquakes. Although the European, New Zealand and American codes consider the influence of the axial force in the column to varying degrees, they only consider the influence of the maximum axial force of the design condition combination, not the axial force in the column under strong earthquakes.

In summary, “Code for seismic design of buildings” attempts to achieve the difference in flexural capacity between the column end and the beam end under strong earthquakes through the method of increasing the bending moment coefficient of the column end under small earthquakes. This method may have some shortcomings.

6 Conclusion

By summarizing the concept and characteristics of the capacity design method and comparing the relevant provisions of the “strong column—weak beam” in the codes of various countries, the following conclusions are obtained:

- (1) At present, all countries have adopted the capacity design method to ensure that the ductile members fully dissipate energy while the non-ductile members are not damaged, but the specific application methods are different, and the practical effects are also different.
- (2) Whether the column end moment amplification coefficient method used in China can realize the difference of flexural bearing capacity of beams and columns needs to be verified.
- (3) At present, the reduction of the flexural capacity of columns under strong earthquakes is not fully considered, and it is difficult to ensure the realization of the failure mode of “strong column—weak beam”. There may be some deficiencies in the method of column end moment amplification coefficient.

References

1. Fardis MN (2018) Capacity design: early history. *Earthq Eng Struct Dynam* 47(12):2887–2896
2. Paulay T (1983) Deterministic seismic design procedures for reinforced concrete buildings. *Eng Struct* 5(1):79–86
3. Paulay T (1980) Deterministic design procedure for ductile frames in seismic areas. *Deterministic design procedure for ductile frames in seismic areas*, pp 357–381
4. Paulay T, Priestley MJN (2011) *Seismic design of reinforced concrete and masonry buildings*. China Architecture & Building Press, Beijing
5. Feng P (2016) *Ductility seismic analysis of RC frame structures under different failure modes*. Changsha University of Science & Technology
6. Vidic T, Fajfar P, Fischinger M (1994) Consistent inelastic design spectra: Strength and displacement. *Earthq Eng Struct Dynam* 23(5):507–521
7. Miranda E, Bertero V (1994) Evaluation of strength reduction factors for earthquake-resistant design. *Earthq Spectra—EARTHQ SPECTRA*, 10
8. Miranda E (1993) Site-dependent strength-reduction factors. *J Struct Eng-ASCE* 119
9. NZS 3101 (2006) *Concrete structures standard: Part 1-The design of concrete structures*. Standards New Zealand, Wellington, New Zealand
10. ACI 318-11 (2011) *Building code requirements for structural concrete and commentary*. American Concrete Institute MI, USA, Hills, Farmington
11. European Standard EN 1998-1-2004 (2004) *Eurocode 8: design of structures for earthquake resistance-part 1: general rules, seismic actions and rules for buildings*. Cen, Bruxelles, Belgium
12. Umemura K (1981) *New seismic design building standard method new seismic design standard*. Japan Architecture Center
13. Architectural Society of Japan (1990) *Final strength type seismic design guidelines for reinforced concrete buildings. Explanation*. Japan
14. Ye LP, Sun YP (2010) Introduction of design method for RC structures under severe earthquake in Japan. *Build Struct* 40(6):114–118, 43
15. Sun YP, Zhao SC, Ye LP (2011) Comparative study of seismic design method for reinforced concrete structures in China and Japan. *Build Struct* 41(5):13–19

16. GB50011-2010 Code for seismic design of buildings. Building Industry Press of China, Beijing
17. Lin JX (2012) Study on seismic behavior of RC frames under horizontal and vertical seismic excitation. Chongqing University
18. Yi WJ, Wang WY (2012) Effect of vertical ground motion on seismic behavior of RC frame in near-fault region. Chin Civil Eng J 45(10):81–88
19. Zhao WF, He FP, Zhou J (2014) Research on the distribution mode of axial force for RC frame columns subjected to near-fault vertical ground motions. Earthq Resistant Eng Retrofitting 36(4):29–35

Experimental Study of Cylindrical Steel Slit Damper for Passive Energy Dissipation



Shuai Feng, Hiroshi Tagawa, and Xingchen Chen

Abstract This paper presents a novel cylindrical steel slit damper, named the CSSD, designed for passive energy dissipation. The CSSD consists of a steel cylinder with multiple axial slit cuts to form strips, which dissipates energy by flexural yielding under the torsional deformation of the cylinder. In this study, we derived formulas to evaluate the initial torsional stiffness and torsional yield strength of the device. We then conducted cyclic loading tests on three specimens to verify the device's performance, and found that all specimens exhibited stable hysteretic behavior. The relationships between torque moment and torsional angle for the three specimens were discussed. The torsional stiffness and yield strength showed good consistency with the theoretical prediction. Results of this study indicate that the stiffness and strength of the CSSD can be easily modified or scaled up to meet actual structural requirements.

Keywords Slit damper · Structural control · Energy dissipation · Cyclic loading test

1 Introduction

Increasing interest in the structural control systems has been leading significant progress to energy dissipation devices in the last decades [1]. Metallic dampers are a highly effective and cost-efficient means of passive energy dissipation, which has attracted the attention of many researchers [2]. Metallic dampers have been developed in various forms including, such as ADAS [3], buckling restrained braces [4], honeycomb dampers [5], U dampers [2] and steel slit dampers (SSD). Among them, SSDs have the potential to significantly dissipate energy through flexural yielding [6].

S. Feng · H. Tagawa (✉) · X. Chen
Graduate School of Advanced Science and Engineering, Hiroshima University,
Higashihiroshima 739-8527, Japan
e-mail: htagawa@hiroshima-u.ac.jp

© The Author(s), under exclusive license to Springer Nature Singapore Pte Ltd. 2024
M. Casini (ed.), *Proceedings of the 3rd International Civil Engineering and Architecture Conference*, Lecture Notes in Civil Engineering 389,
https://doi.org/10.1007/978-981-99-6368-3_31

365

In 2008, Chan and Albermani studied the hysteretic behavior of SSD made from wide flange sections by cyclic loading tests [7]. Ghabraie et al. utilized a topology optimization technique to optimize the shape of the slit damper [8]. In 2015, Teruna et al. demonstrated that SSDs with convex-shaped edges exhibit more stable hysteresis cycles, which helps to prevent low cycle fatigue [9]. In 2017, Lee et al. proposed a novel box-shaped steel slit damper composed of four steel slit plates for the seismic retrofitting of structures [10]. Amiri et al. further extended the concept of slit dampers to those with a very low height-to-thickness ratio, introducing the block slit damper and conducting hysteretic behavior tests [11]. Mohamed et al. investigated the seismic capacity of a hybrid damper consisting of a steel slit plate damper and two shape memory alloy bars through fragility analysis and life-cycle cost evaluation [12]. Naeem et al. proposed multi-slit damper by combining weak and strong steel slit dampers in series [13]. Oh and Park examined the effect of unexpected additional tensile loads on a flexural yield-type steel slit damper [14].

Given the aforementioned information, this study develops the cylindrical steel slit damper (CSSD), a novel device designed to dissipate energy through torsion. The CSSD is fabricated from a steel cylinder with a specific number of axial slit cuts. The proposed device arranges the strips in a circular form, which is the first application among slit dampers. The mechanical characteristics and configuration of the CSSD are presented, along with derived formulas to evaluate its initial torsional stiffness and torsional yield strength. Cyclic loading tests with increasing amplitudes on three specimens were conducted to investigate the hysteretic performance of the proposed CSSD. The accuracy of the evaluation formulas was confirmed by the test results.

2 Theoretical Study of CSSD

2.1 CSSD Configuration

Figure 1 shows the geometric design of the novel CSSD. The cylindrical steel slit damper (CSSD) is fabricated by cutting a series of slits into a steel cylinder, resulting in a specific number of strips that are arranged in a circular pattern. To connect the device, two end plates are welded to the ends of the cylinder. The strip ends are rounded to prevent stress concentration. Each end plate features bolt holes for connection, eliminating the need for in-situ welding and enabling easy replacement.

2.2 Torsional Stiffness and Strength of CSSD

Consider CSSD, the energy is dissipated through torsion of the device. It is worth mentioning that slight deformation occurs in the bases.

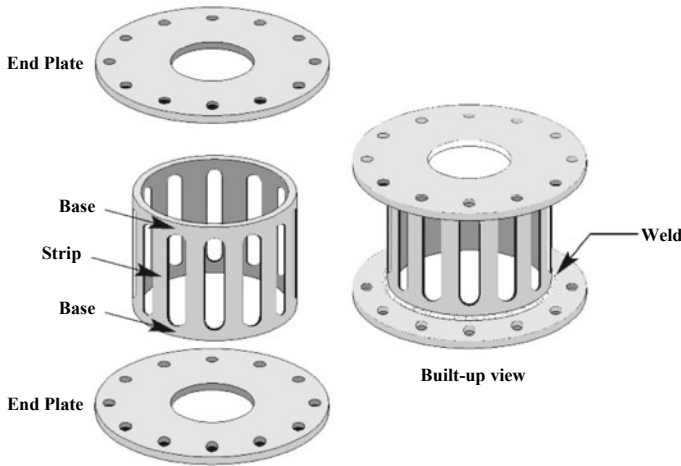


Fig. 1 Geometric design of CSSD

The total deformation of each strip can be separated into bending and shearing components as the two end plates rotate relative to each other. Due to the round ends, the strip should be calculated in equivalent strip length l' (Fig. 2a) [15, 16]. The moment increases linearly from the midpoint of the strip to its two ends (Fig. 2b).

Equations (1, 2) define the stiffness of each strip k_s and the plastic yield strength of each strip F_s respectively.

$$k_s = \frac{1}{\frac{l'^3}{Etb^3} + \frac{l'}{1.2Gtb}} \tag{1}$$

$$F_s = \frac{2M_P}{l'} = \frac{\sigma_y t b^2}{2l'} \tag{2}$$

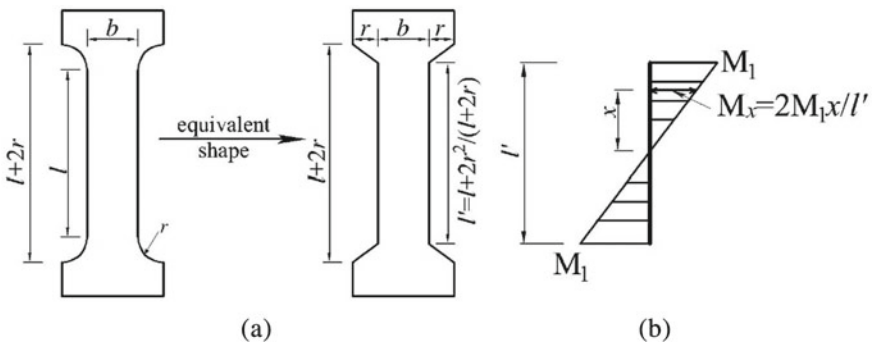


Fig. 2 The strip: a equivalent length; b bending moment distribution

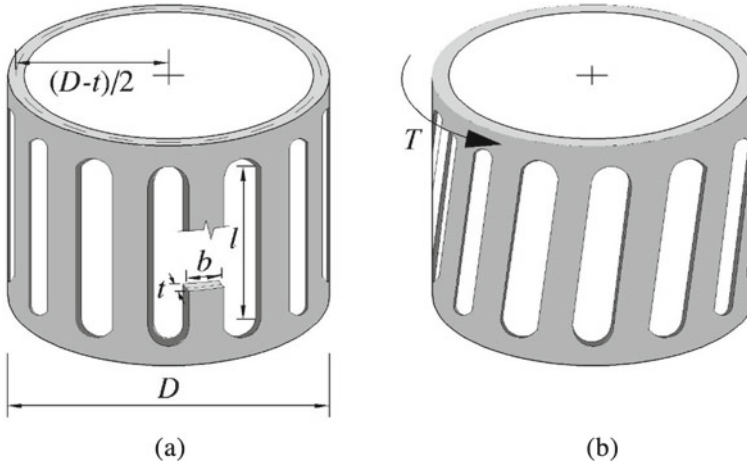


Fig. 3 Configuration of CSSD: **a** initial configuration; **b** deformed configuration

The initial configuration and deformed configuration of the damper are shown in Fig. 3.

Equations (3, 4) define the initial torsional stiffness of the damper S_{eval} and the torsional strength of the damper T_{eval} .

$$S_{eval} = cnk_s \left(\frac{D-t}{2} \right)^2 \quad (3)$$

$$T_{eval} = nF_s \frac{D-t}{2} \quad (4)$$

where E and G represents Young's modulus and shear modulus respectively, M_P means the full plastic moment of the strip section, the stiffness reduction factor c reflects the deformation of the bases, which will be determined by experiments, σ_y signifies the material yield stress, t denotes the thickness, b denotes the strip width, n is the strips number, D represents the outside diameter of CSSD.

3 Cyclic Loading Tests

3.1 Test Setup

The experimental setup for the loading test is depicted in Fig. 4. To test the CSSD, a twisting system was employed, which was derived from a seesaw system. The loading frame had a span and height of 2200 and 1568 mm, respectively, and all connections in the loading system were fully hinged to facilitate free movement. A

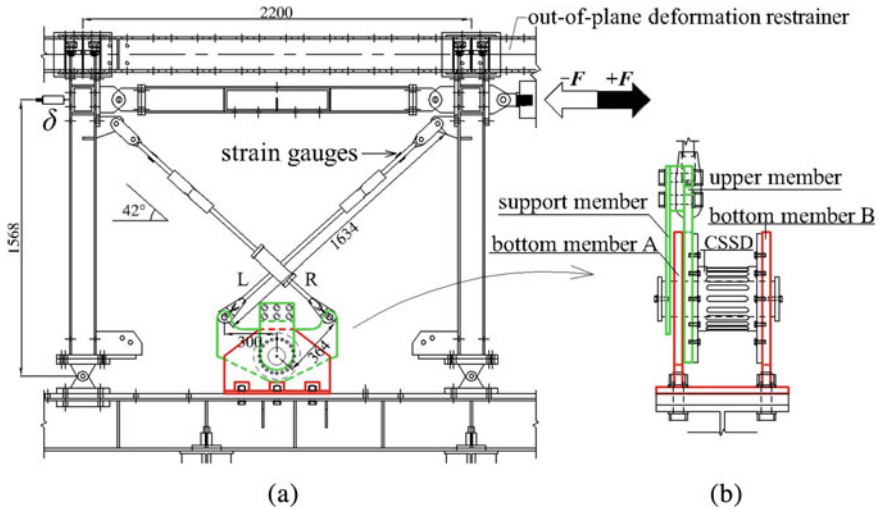


Fig. 4 Test arrangement: **a** elevation; **b** damper connection details (units: mm)

horizontal load denoted as “ F ” was applied at the right beam-to-column connection, and the brace members were made of steel rods with a diameter of 25 mm and steel grade SS400. Axial forces of the brace members were measured during the loading process using strain gauges. To restrain any out-of-plane displacement of the loading system, a larger support frame was employed.

Figure 4b provides details on the connection of the damper. The red bottom member is securely fixed to the beam, with a pin passing through it to serve as the rotation center. The green upper member is free to rotate around this center. To install the CSSD, one side of the device is connected to the bottom member, while the other side is screwed to the upper member. Brace members are used to connect the edges of the upper member to the opposite beam-column joint. In addition, a support member is added to prevent any warping of the CSSD. When a lateral load is applied to the frame, the resulting lateral displacement causes the upper member to rotate, leading to torsion of the specimen.

3.2 Test Specimens and Loading Histories

Figure 5 and Table 1 present the specifications of the CSSD used in this experimental study. Three specimens were utilized to investigate the hysteretic behavior of the damper. The aspect ratio of each strip is denoted by column l/b . All dampers had the same diameter of 146 mm and thickness of 8 mm, with a weight of approximately 11.6 kg each. Specimen T-A had longer strips compared to T-B, whereas T-C had wider strips. The material properties for all specimens were the same, with

a yield stress of 267 N/mm², ultimate stress of 472 N/mm², and elongation of 39%. During the experiment, two sides of the specimens were fastened to the stationary bottom member and the upper member, respectively. The braces' reciprocal traction facilitated free rotation of the upper member around the pin, inducing torsion in the specimen. Remarkably, the installation of the damper did not require any in-situ welding, making it easy to replace after a severe earthquake. During the loading program, the braces were pre-tensioned to maintain their tensile state throughout the loading process.

In accordance with the experimental setup illustrated in Fig. 4, the lateral load was applied to the beam-column connection on the right side, where the convention of setting rightward loading and displacement as positive. Figure 6 illustrates the

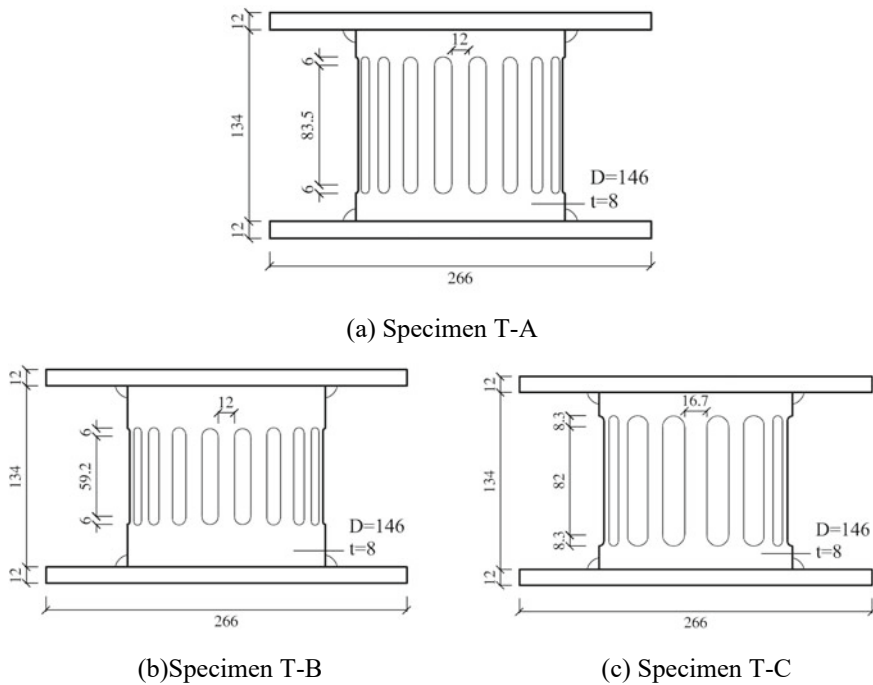


Fig. 5 Damper dimensions (units: mm)

Table 1 Specifications of CSSD (units: mm)

Specimen	<i>D</i>	<i>t</i>	<i>l</i>	<i>b</i>	<i>l'</i>	<i>l'/b</i>	<i>n</i>
T-A	146	8	83.5	12.0	84.3	7	18
T-B	146	8	59.2	12.0	60.2	5	18
T-C	146	8	82.0	16.7	83.4	5	13

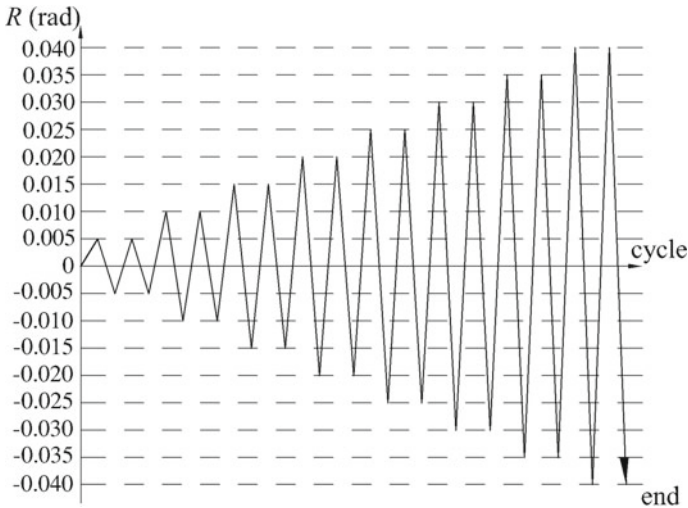


Fig. 6 Loading history

loading history, where the story drift angle $R (= \delta / 1568 \text{ mm})$ increased from 0.005 to 0.04 in increments. At each amplitude, two full cycles were repeated.

3.3 Test Results and Discussion

Figure 7 shows the relationships between the torque moment and torsional angle for the three specimens. The torque moment exerted on the specimens was calculated by analyzing the brace forces.

All specimens completely experienced the experiments and maximum torsional angle exceeds 0.12 rad without fracture. The hysteresis curves obtained in this experiment exhibited a plump spindle shape. Notably, the torsional strength of specimens T-B (which had shorter strips) and T-C (which had wider strips) was found to be greater than that of T-A.

Table 2 shows the initial torsional stiffness S_{test} and torsional strength T_{test} measured in the tests. The strength was determined as the torque moment at which the stiffness decreased to one-third of the initial value. The theoretical stiffness S_{eval} and strength T_{eval} are obtained by Eqs. (3, 4). For the stiffness calculation, the stiffness reduction factor c determined by the experiments is 0.7. As shown by the ratios between the theoretical values and test values, the theoretical evaluation is in satisfactory correspondence with the experimentally measured values.

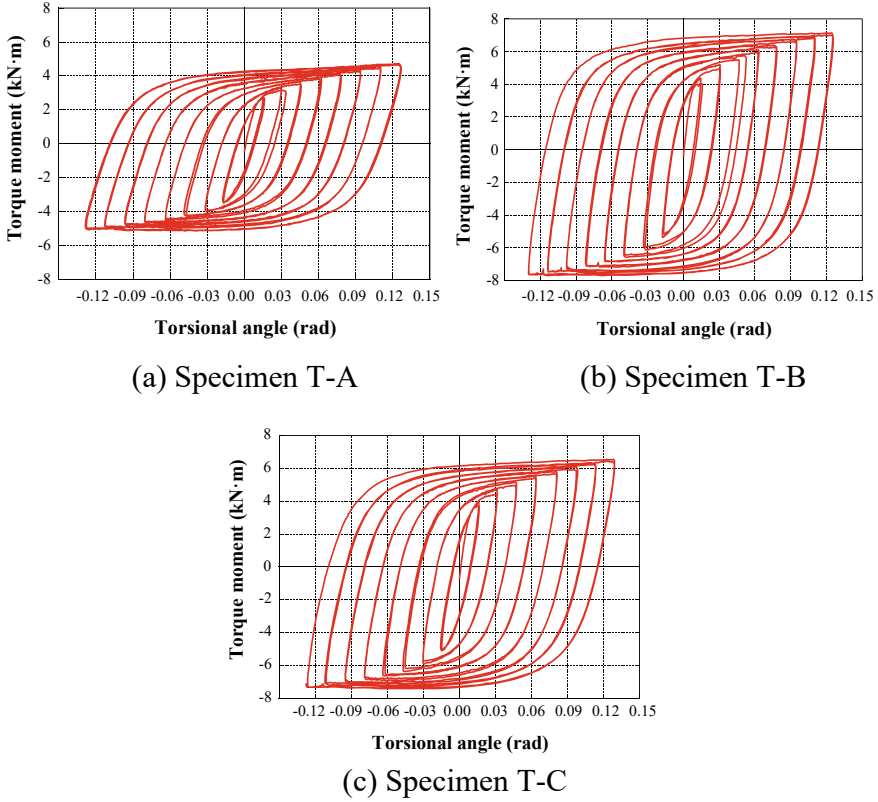


Fig. 7 Torque moment and torsional angle relationships

Table 2 Test and theoretical results (units: kN·m/rad, kN·m)

	S_{eval}	S_{test}	S_{eval}/S_{test}	T_{eval}	T_{test}	T_{eval}/T_{test}
T-A	270	250	1.28	2.3	2.6	0.89
T-B	700	562	1.24	3.2	3.6	0.89
T-C	505	381	1.33	3.2	3.4	0.94

4 Conclusion

In this paper, a novel cylindrical steel slit damper (CSSD) was proposed, and the formulas for its torsional stiffness and strength were derived. The damper’s hysteretic performance was validated through cyclic loading tests on three specimens. The primary findings of this study could be summarized as follows:

1. The device exhibited highly stable hysteretic behavior across various specifications.

2. The theoretical formulas demonstrate a good agreement with the experimental results for the initial torsional stiffness and torsional strength.
3. Adjusting the width, length, and thickness of the strips allows for easy customization of the torsional stiffness and strength of the damper, providing flexibility in the design process. Additionally, this approach enables the stiffness and strength to be independently tailored to meet specific project requirements.

Acknowledgements This work was supported by JST SPRING, Grant Number JPMJSP2132.

References

1. Kang JD, Tagawa H (2013) Seismic performance of steel structures with seesaw energy dissipation system using fluid viscous dampers. *Eng Struct* 56:431–442
2. Tagawa H, Gao J (2012) Evaluation of vibration control system with U-dampers based on quasi-linear motion mechanism. *J Constr Steel Res* 70:213–225
3. Alehashem SMS, Keyhani A, Pourmohammad H (2008) Behavior and performance of structures equipped with ADAS&TADAS dampers (a comparison with conventional structures). In: 14th world conference on earthquake engineering, Beijing, China
4. Mateus JAS, Tagawa H, Chen XC (2019) Buckling-restrained brace using round steel bar cores restrained by inner round steel tubes and outer square steel tube. *Eng Struct* 197:109379
5. Lee M, Lee J, Kim J (2017) Seismic retrofit of structures using steel honeycomb dampers. *Int J Steel Struct* 17(1):215–229
6. Tagawa H, Yamanishi T, Takaki A, Chan RWK (2016) Cyclic behavior of seesaw energy dissipation system with steel slit dampers. *J Construct Steel Res* 117:24–34
7. Chan RWK, Albermani F (2008) Experimental study of steel slit damper for passive energy dissipation. *Eng Struct* 30:1058–1066
8. Ghabraie K, Chan RWK, Huang XD, Xie YM (2010) Shape optimization of metallic yielding devices for passive mitigation of seismic energy. *Eng Struct* 32:2258–2267
9. Teruna DR, Majid TA, Budiono B (2015) Experimental study of hysteretic steel damper for energy dissipation capacity. *Adv Civil Eng* 2015:631726
10. Lee J, Kim J (2017) Development of box-shaped steel slit dampers for seismic retrofit of building structures. *Eng Struct* 150:934–946
11. Amiri HA, Najafabadi EP, Estekanchi HE (2018) Experimental and analytical study of block slit damper. *J Constr Steel Res* 141:167–178
12. NourEldin M, Naeem A, Kim J (2019) Life-cycle cost evaluation of steel structures retrofitted with steel slit damper and shape memory alloy-based hybrid damper. *Adv Struct Eng* 22(1):3–16
13. Naeem A, Kim J (2019) Seismic performance evaluation of a multi-slit damper. *Eng Struct* 189:332–346
14. Oh SH, Park HY (2022) Experimental study on seismic performance of steel slit damper under additional tensile load. *J Build Eng* 50:104110
15. Benavent-Climent A (2010) A brace-type seismic damper based on yielding the walls of hollow structural sections. *Eng Struct* 32:1113–1122
16. Oh SH, Kim YJ, Ryu HS (2009) Seismic performance of steel structure with slit dampers. *Eng Struct* 31:1997–2008

Lintel Type Damping Device for Seismic Retrofit of Shear Wall Structure



GeeCheol Kim, YouSeong Kim, and Joonho Lee

Abstract The methods for improving the seismic performance of the structure are the increasing the strength or the ductility capacity of the structure. In order to increase the strength of the shear wall structure, there are methods to increase the cross section of the structural member as like the shear wall or beam, and increase the rebar amount, but these are unreasonable in terms of design and construction. Therefore, in order to improve the seismic performance of the shear wall structure, it is reasonable to improve the ductility capacity by using the damping device. In this study, the seismic performance of shear wall structures with the lintel type damping device was analyzed. It can be seen that the energy dissipation of the damping device is greatly increased after the nonlinear behavior of the shear wall structure, thereby reducing the damage of the main structural members.

Keywords Damping device · Lintel beam · Shear wall structure · Nonlinear static analysis

1 Seismic Behavior of Shear Wall Structure

In the seismic design of shear wall structure, the plastic hinge generation of coupling beams (lintel beams) connecting shear walls is generally allowed. Therefore, in the case of shear wall type structure, it is possible to apply the lintel type damping device using the plastic hinge characteristic of lintel beam subjected to seismic load as shown in Fig. 1 [1, 2].

The behavior of the parallel shear wall system is greatly influenced by the behavior of the entire structural system according to the behavior of the coupling beams. As shown in Fig. 2a, if wall A and wall B are connected by a pin joint, each wall resists

G. Kim (✉) · J. Lee
Department of Architecture, Seoul University, Seoul, Republic of Korea
e-mail: 20040012@seoil.ac.kr

Y. Kim
Plus Structure Engineering, Seoul, Republic of Korea

© The Author(s), under exclusive license to Springer Nature Singapore Pte Ltd. 2024
M. Casini (ed.), *Proceedings of the 3rd International Civil Engineering and Architecture Conference*, Lecture Notes in Civil Engineering 389,
https://doi.org/10.1007/978-981-99-6368-3_32

375

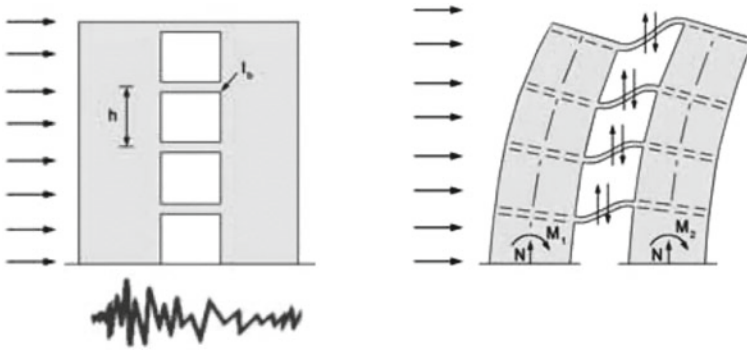


Fig. 1 Seismic behavior of shear wall structure

the external moment while acting as a cantilever. Therefore, the stress of the wall is linearly distributed in each individual wall, and the neutral axis of the bending stress is located at the center line of each individual wall. In contrast, As shown in Fig. 2b, if the ends of wall A and wall B are connected by a strong joint, the entire left and right walls resist external moment while acting as a single cantilever structure. In this case, the stress is linearly distributed throughout the entire parallel shear wall system, and each wall acts as a ‘tension wall’ and a ‘compression wall’ and forms a couple force. The behavior of the actual parallel shear wall system is shown in Fig. 2c will behave between the two cases described above in Fig. 2a, b [3, 4].

Since the lintel beam yields due to the shear force and bending moment caused by the earthquake, it is possible to dissipate a lot of energy in the lintel beam where shear

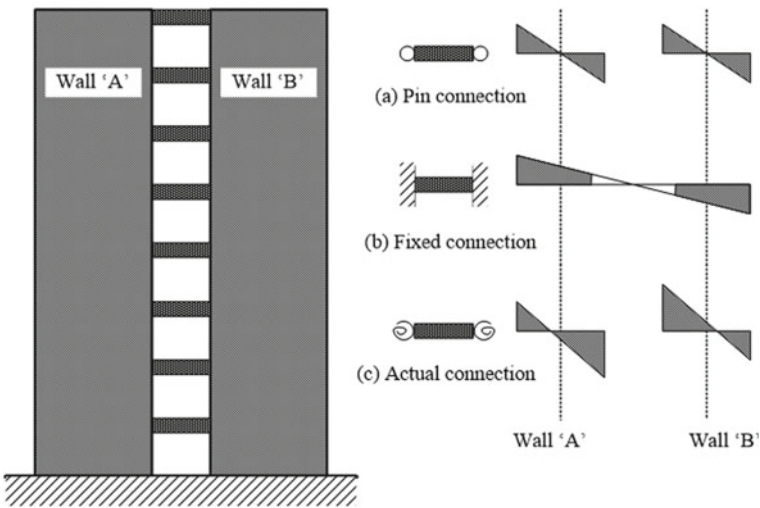


Fig. 2 Coupling effect of shear wall system

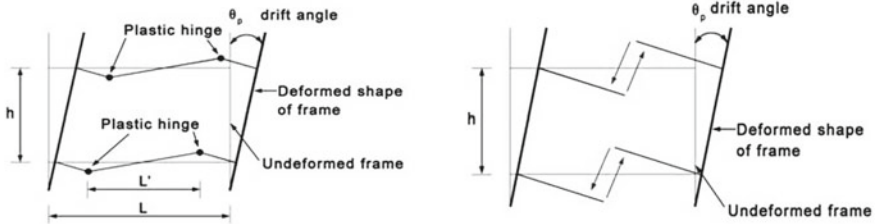


Fig. 3 Behavior of lintel beam

force and bending moment occur a lot. Therefore, the lintel type damping device is developed to have plastic behavior of the damping device in the center of the lintel beam by the shear force and the bending moment.

This lintel type damping device has elastic behavior under wind load conditions and plastic behavior under seismic load conditions to dissipate energy as shown in Fig. 3.

2 Hysteric Characteristic of Lintel Type Damping Device

Experiments were conducted to analyze the ductility of lintel type damping device. This device is composed of steel plate and steel wire as shown in the Fig. 4a. As shown in Fig. 4b, the lintel type damping device has a nonlinear hysteric characteristic. This device exhibits plastic behavior and excellent ductility after the displacement of 2 mm. This nonlinear hysteric characteristic is applied to evaluate the seismic performance of the shear wall structure having the lintel type damping device [5, 6].

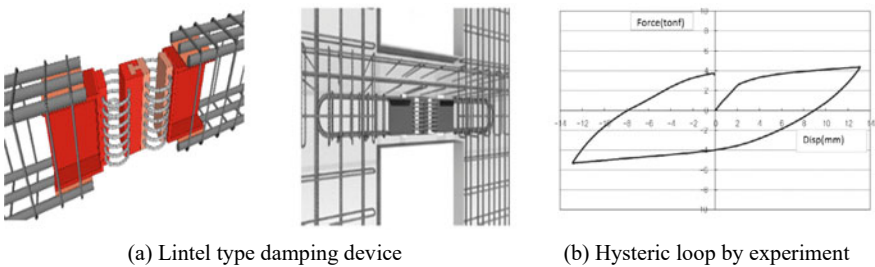


Fig. 4 Lintel type damping device

3 Numerical Analysis of the Shear Wall Structure

Nonlinear analysis of shear wall structure was performed by using Perform 3D program. In case of the damping device is applied to the lintel beam connecting the shear walls, the shear wall structures have nonlinear behavior.

This shear wall structures model is 19 stories and dimension of each floor are $36.2 \times 9.5 \times 3.0$ m.

Due to the lintel type damping device, the ductile capacity of the shear wall structure increases, thereby minimizing damage to the main structural members such as the shear wall or beam. In order to analyze the seismic performance of shear wall structure having the lintel type damping device, the nonlinear static analysis of the shear wall structure as shown in Fig. 5 was performed. Figure 5b shows the location of the lintel beam. The hysteric loop in Fig. 4b was applied to the nonlinearity of the lintel beam of example structure.

Figure 6 shows the performance curve of the example shear wall structure by nonlinear static analysis (pushover analysis). The performance point and the ductility of the shear wall structure having the lintel type damping device is excellent. In the case of shear wall structures without damping device, the seismic behavior of the shear wall structure depends on the stiffness and strength of the shear wall after the lintel beam is broken. However, the shear wall structure having a lintel type damping device exhibits a coupling effect of shear walls due to the plastic behavior of the lintel type damping device. Therefore, the shear wall structure resists seismic load due to the interaction of shear wall and shear wall.

Figure 7 shows the performance points for MCE Level and DBE Level. The base shear for the performance point was 10.6 and 9.4% lower for the shear wall structure having the lintel type device than the shear wall structure at the DBE Level and MCE

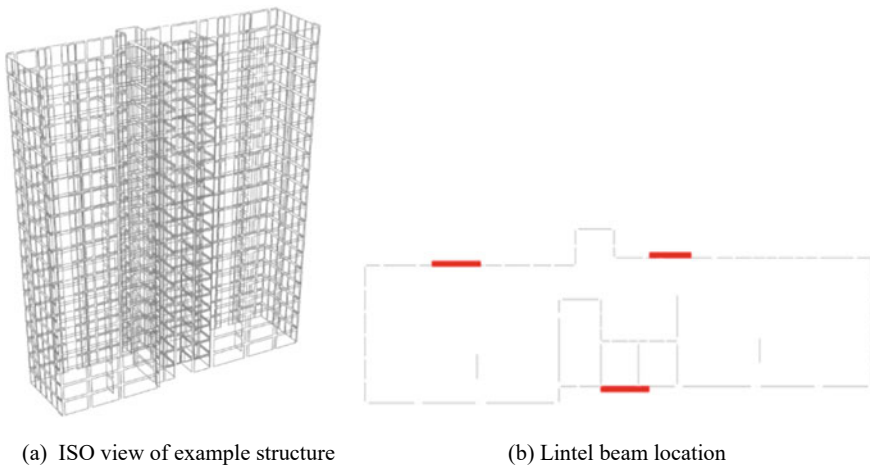


Fig. 5 Shear wall structure example

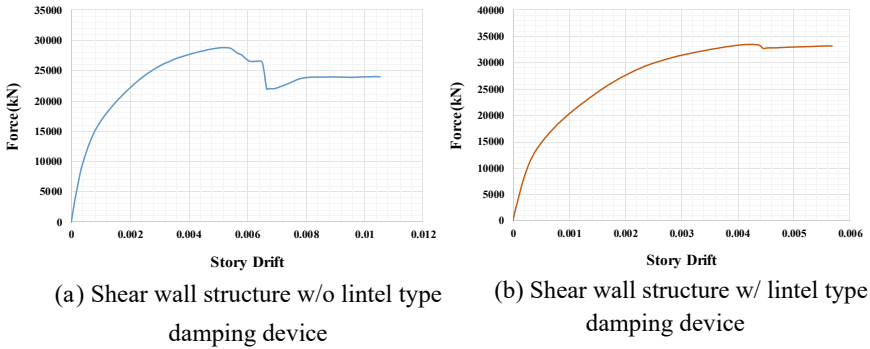


Fig. 6 Performance curves of shear wall structure

Level, respectively. This is considered to be because the demand spectrum is lowered by the effective damping ratio considering the damping ratio of the lintel type device.

Figure 8 is showing the wall axial strain and rotation angle for the performance point at the MCE level. The CP level criteria for the axial strain and rotation angle of the shear wall structure were set to 0.004 rad and 0.2%, respectively, and red color is the member exceeding the CP level. The shear wall structure did not satisfy the CP level in the axial strain and rotation angle in the 1st to 4th floor, but the axial strain and rotation angle of the shear wall structure having the lintel type device satisfied with the CP level.

Figure 9 is a graph showing the story drift ratio at the performance point. The LS level and CP level standards for the story drift ratio of shear wall structures were set at 1.5 and 2%, respectively. The story drift ratio for the performance point was 46.1, 47.7% lower for the shear wall structure having the lintel type device than the shear wall structure for the DBE Level and MCE Level, respectively, but the acceptance criteria for the DBE Level and MCE Level for both analytical models were satisfied.

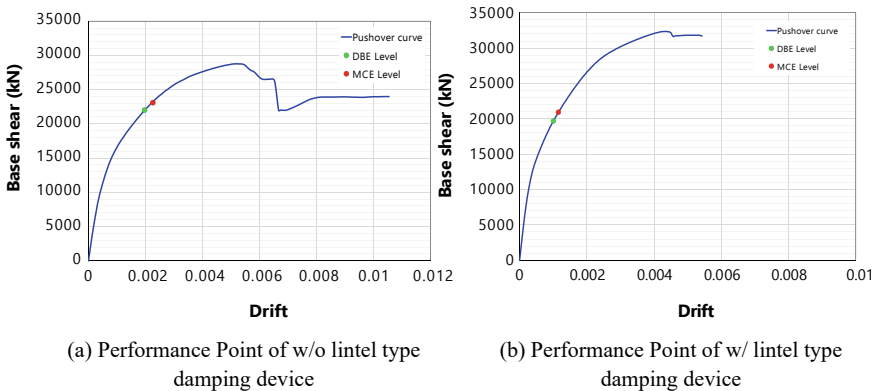


Fig. 7 Performance point of analytical model

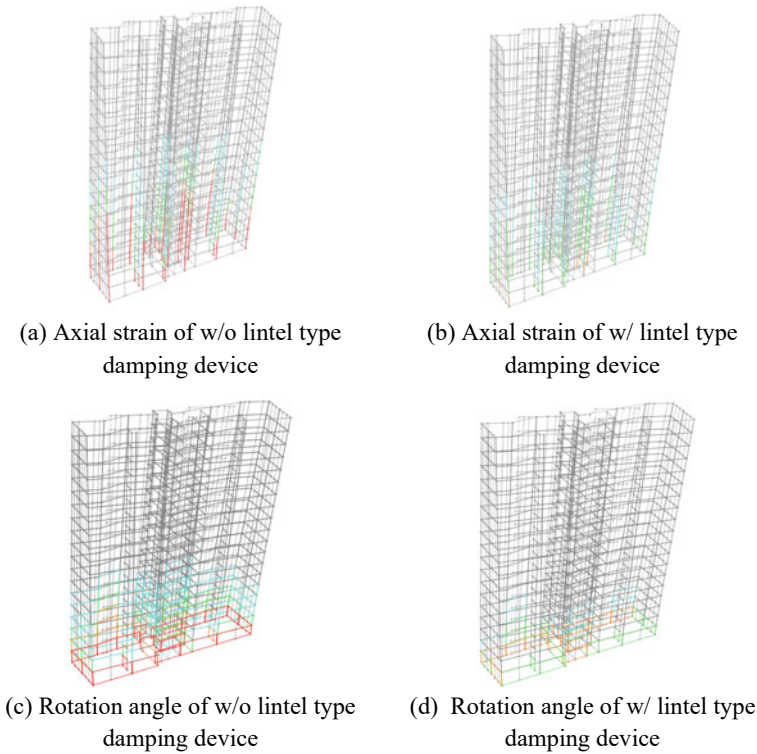
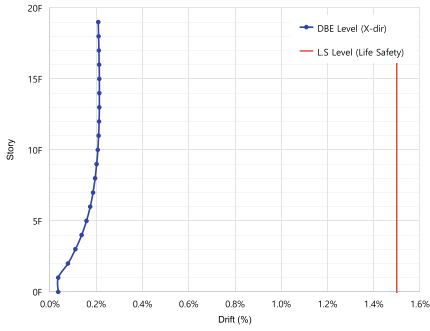


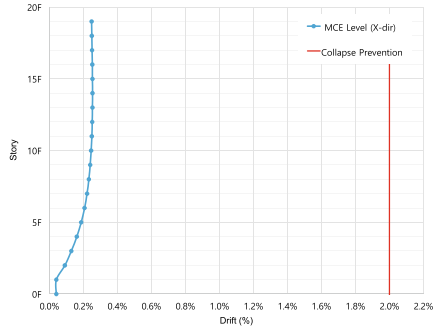
Fig. 8 Axial strain and rotation angle of shear wall

Figure 10 shows the energy dissipation capacity from the nonlinear time history analysis of shear wall structure having the lintel type damping device. The red color shows the energy dissipation of the entire shear wall structure, and the yellow color shows the energy dissipation of the lintel type damping device.

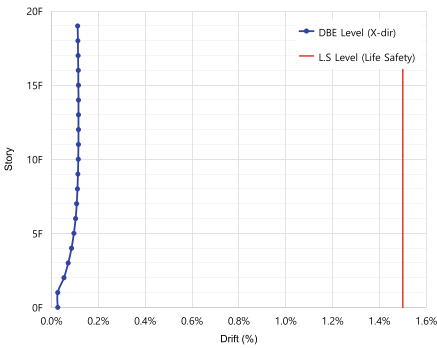
As shown in Fig. 10, the energy dissipation of the lintel type damping device increases significantly after the nonlinear behavior of the shear wall structure. This means that energy is dissipated by the additional damping caused by the nonlinear behavior of the lintel type damping device. It can be seen that about 75% of the total energy dissipation is dissipated by the lintel type damping device. In case of the shear wall structure having a lintel type damping device, the energy is almost dissipated by the lintel type damping device, thereby reducing damage to the main structural members as like shear wall or beam. damping device.



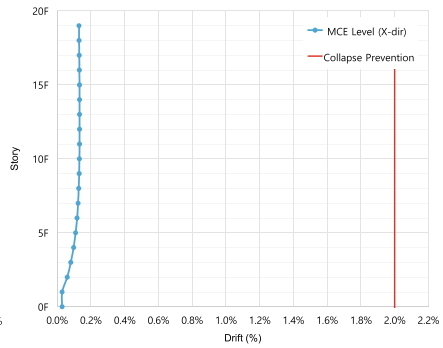
(a) Story drift ratio of w/o lintel type damping device (DBE Level)



(b) Story drift ratio of w/o lintel type damping device (MCE Level)



(c) Story drift ratio of w/ lintel type damping device (DBE Level)



(d) Story drift ratio of w/ lintel type damping device (MCE Level)

Fig. 9 Story drift ratio of analytical model at performance point

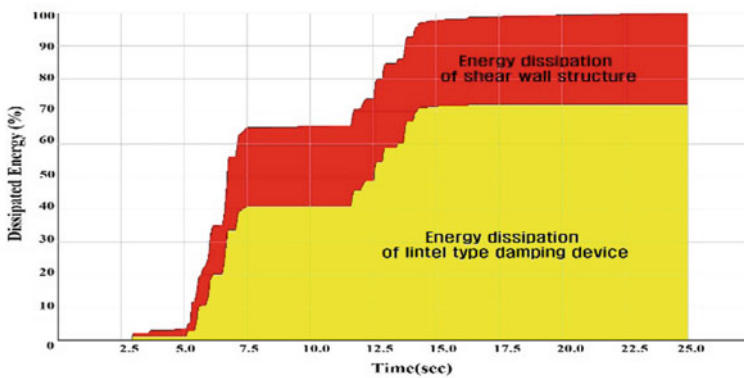


Fig. 10 Energy dissipation capacity of shear wall structure lintel type damping device

4 Conclusion

In this study, nonlinear static analysis and nonlinear time history analysis were performed to evaluate the seismic performance of shear wall structure with the lintel type damping device. The shear wall structure having the lintel type damping device has more excellent performance point and ductility compared with the general seismic design structure. In addition, it can be seen that the damage of the main structural members is reduced due to the great energy dissipation capacity of the lintel type damping device.

Acknowledgements This work has supported by the National Research Foundation of Korea(NRF) grant funded by the Korea government(MSIT) (No. 2021R1A2C1094642).

References

1. Ro KM, Kim MS, Lee YH (2017) Experimental evaluation of seismic performance for lintel beam type steel damper. *J Korean Assoc Spatial Struct* 17(4):77–84
2. Chung HS, Min KW (2009) The behavior of reinforced concrete coupling elements in wall-dominant system. *J Korea Concr Inst* 14(1)
3. Chang KK, Seo DW, Chun YS (2012) The behavior of reinforced concrete coupling elements in wall-dominant system. *J Korea Concr Inst* 24(1)
4. Cho MJ, Kim JS (2014) Research on efficient installation method of device of lintel beam type, technical article. *SH Urban Res Insight* 4(2)
5. Yi WH, Kim HG, Jang DW, Ahn TS, Kim YJ (2012) Characteristics of coupling beam dampers for application of domestic apartment buildings. *J Korean Soc Steel Constr* 24(3)
6. Kim YJ, Ahn TS, Kim HG, Park JH (2012) Experimental study on new metallic damper for seismic retrofit of building structure. *Proc CESEIK Ann Conferen* 25(1)

Simulation Analysis of Steel Frames Supported by Foundations at Different Ground Levels with the Self-Centering Column Base Joints on the Upper Ground



Yang Zhenyu and Li Yingmin

Abstract Due to the strong constraint conditions, the column on the upper ground of frames supported by foundations at different ground levels will have large residual deformation after the earthquake, the self-centering structure is useful to reduce the residual deformation. At present, there is no research on the application of self-centering structure to the structures supported by foundations at different ground levels. Therefore, in this paper, the self-centering structure is applied to the upper grounding to study the seismic performance of the steel structures supported by foundations at different ground levels. The seismic performance of the frame is simulated by finite element software and the results are analyzed. To study the seismic performance of steel frames, the structure of the self-centering column base joints and the form of steel frames are designed. Considering three design parameters, including the size of the slotted hole of the buckling restrained steel (BRS) plate and the connecting plate on foundation, the width of the dissipated section of the BRS plate and whether the connecting plate on foundation is arranged, five frame models are established by using the finite element software ABAQUS to simulate under the lateral cyclic loading. The effects of hysteretic curves, stiffness degradation, energy dissipation capacity, residual deformation and other seismic properties of each specimen were compared and analyzed. Research results show that the steel frame with the self-centering column on the upper ground has good self-center ability. However, the parameters of the steel frame with the self-centering column on the upper ground will affect the self-centering ability and seismic performance. The slotted hole can delay the plastic time of BRS plate, but has little effect on the overall residual deformation. The width of the dissipating position has a great influence on the self-centering effect and energy-dissipating capacity of the whole specimen. With the increase of the width, the dissipating capacity and stiffness of the structure increase, but the self-centering effect decreases. The connecting plate on foundation

Y. Zhenyu (✉) · L. Yingmin
Chongqing University, Chongqing 400045, China
e-mail: 475775082@qq.com

can provide certain energy dissipation capacity and stiffness under earthquake, but the overall residual deformation will increase.

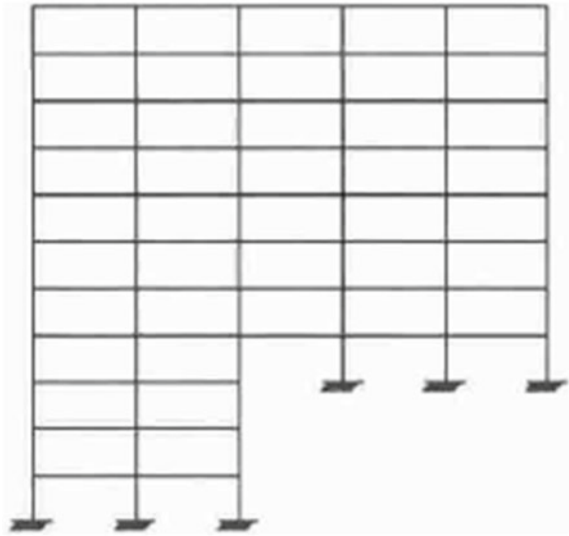
Keywords Steel frames supported by foundations at different ground levels · Self-centering · BRS plate · Seismic performance

1 Introduction

Structures supported by foundations at different ground levels is representative structure of mountain building structure, refers to the same unit with two partial fixing is not in the same plane, as shown in Fig. 1. Due to the existence of two different grounding points. The stress characteristics and seismic performance of the column on the upper ground are significantly different from that of the ordinary structure. The rigidity of the column on the upper ground is much larger than that of the step-terrace position due to the restriction of the ground. Structures supported by foundations at different ground levels may not collapse after the earthquake of fortification intensity, but the column on the upper ground cannot be repaired and reused due to large residual deformation, resulting in huge waste [1]. Therefore, in order to reduce the residual deformation of the column on the upper ground after the earthquake and not affect the normal functions, the column on the upper ground is set as self-centering structure to reduce the cost of repairing the structure and ensure the seismic performance of the structure. By adding the prestressed bar and energy-dissipating elements on the main components, the self-centering structure can realize self-centering after the earthquake, significantly reduce the residual deformation and have good energy-dissipating capacity.

So far, there have been many research results about self-centering structural systems. Chi et al. [2] proposed a kind of column base joints form of replaceable energy-consuming components, which is provided with prestressed bar inside the column to provide self-centering capability, and a slab with weakened section is set at the column base joints. After the lateral cyclic loading of the column base joints, the research results show that the column base joints can withstand the lateral displacement under 4% displacement angle, and the cover plate with weakened section shows the deformation characteristics of tension and compression without breaking, and the replacement of the cover plate after earthquake can restore the seismic performance of the column base joints. Mirzaie et al. [3] proposed a new type of self-centering steel frame column base joints, which concentrated the deformation on T-stubs energy dissipation device, effectively avoiding the occurrence of plastic hinge at the column base joints, and used Open SEES software to accurately predict the characteristic behavior of the self-centering column base joints like that of the common self-centering column under the lateral cyclic loading. Fabio et al. [4] proposed the bidirectional friction energy dissipation self-centering rocking steel column base joints, and carried out the lateral cyclic loading simulation and nonlinear elastic-plastic time-history analysis on it. The results show that the self-centering

Fig. 1 Elevation of frame on slope



column base joints remains elastic under the rare earthquake, and effectively dissipates the seismic energy through the friction plate. Kamperinis et al. [5] proposed the composite steel frame structure with self-centering column base joints, and carried out quasi-static test loading on it. The research results show that the steel frame structure has good functional recoverability, and the overall damage is small. Cui Y et al. [6] carried out shaking table test on the controlled self-centering reinforced concrete frame with self-centering column base joints, and the results show that under the rare earthquake, the structure only suffered small damage, and had good self-centering ability. Liu Yang et al. [7] proposed a column base joints form with core square steel pipe connectors and replaceable energy consumption parts. Due to the existence of core square steel pipe, it can be better applied to various forms of column members. Combined with the low cycle reciprocating load test, the research results show that the column base joints have good ductility and hysteretic energy dissipation performance, and the plastic deformation is concentrated on the replaceable energy dissipation components. After the earthquake, the seismic performance can be better restored by replacing the damaged replacement parts.

In order to study the self-centering effect and energy dissipation capacity of the steel frame supported by foundations at different ground levels with self-centering column on the upper ground, the finite element parameter analysis is carried out by considering the width of the energy dissipation section of the buckling restrained steel (BRS) plate, the size of the slotted hole of the BRS plate and the connecting plate on foundation, and whether the connecting plate on foundation is set, to design the specimen model. ABAQUS software can display the deformation and stress changes at the self-centering structure better. Therefore, ABAQUS software is used to analyze the parameters and study the seismic performance of the frame.

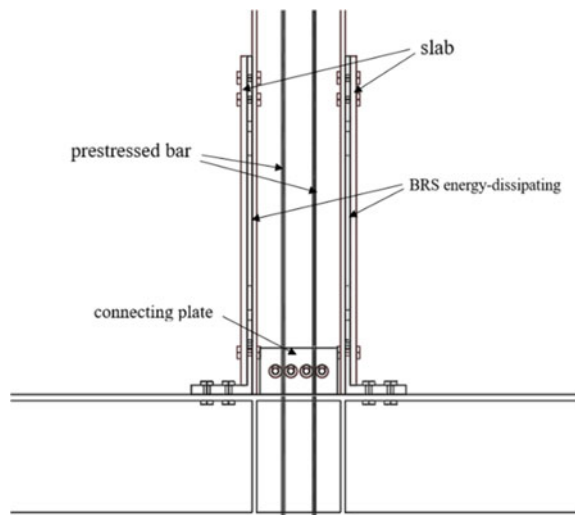
2 Structural Design of Steel Frames Supported by Foundations at Different Ground Levels with Self-Centering Column Base Joints on the Upper Ground

2.1 Structure of Self-Centering Column Base Joints

The column body of the self-center column base joint is disconnected from the foundation, an H-shaped steel foundation is set at the bottom of the column to contact the column bottom, and energy dissipation is set at the joint between the top of the foundation and the column body to prevent the column body from lateral displacement under horizontal load. In the middle of the column, an unbonded prestressed bar is set up that runs through the column body until the base. When the column moves sideways, the contact surface at the bottom of the column rotates to open, and the tensile force of the steel strand increases. The self-centering function of the column base joints is realized by using the tensile force of the steel strand.

The BRS plate is used as energy dissipating element, and the cover plate is arranged on the outside of it. The dissipating element is closely connected with the column body through bolt connection. The connecting plate is arranged on the foundation, and bolts are used to connect the column on the upper ground and the foundation, which provides certain energy consumption for the frame. When the bottom of the column rotates, one side of the BRS plate is tensioned and the other side of the BRS plate is compressed to yield, realizing energy consumption. As shown in Fig. 2.

Fig. 2 Self-centering column base joints



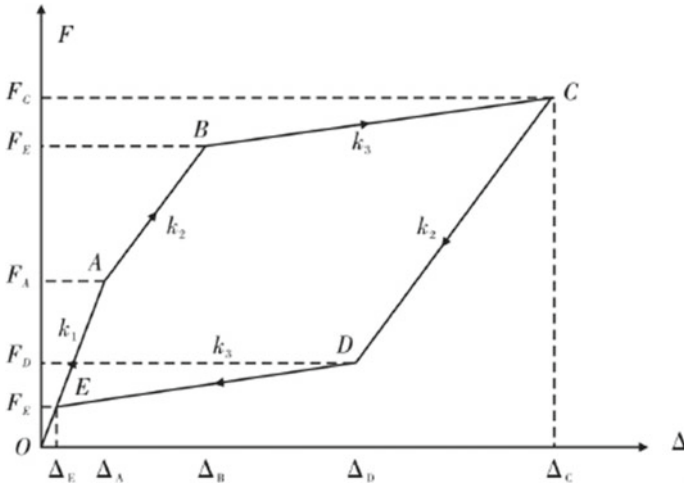


Fig. 3 Horizontal load–displacement curves of self-centering column base joints

2.2 Force Mechanism of Self-Center Column Base Joints

The mechanical properties of the self-center column base joints are mainly determined by the prestressed bar, energy dissipating elements and steel columns. During the whole loading process, the prestressed bar is always in elastic state, and the energy-dissipating element and column steel produce plastic deformation. The whole loading process of column base joints can be divided into 6 stages, and the specific load–displacement relationship is shown in Fig. 3.

The OA section is only subject to axial force, and the bending stiffness K_1 is provided by the column itself; the bottom of the column in section AB and the foundation have openings, and the bending stiffness K_2 is provided by the energy dissipating element and steel strand, and the energy dissipating element yields at point B; the energy dissipating element of BC section has been in tension strengthening state, and the bending stiffness K_3 is provided by the prestressed bar; the energy-consuming elements and prestressed bar in CD section are in elastic unloading state, and the energy-consuming elements yield under compression at point D; the energy consuming elements of DE section are strengthened under pressure, and the column and foundation openings are closed at point E [8]

2.3 The Structure of the Steel Frames Supported by Foundations at Different Ground Levels

The steel frame supported by foundations at different ground levels with two layers and three spans is taken as the research object, and a self-centering column on the

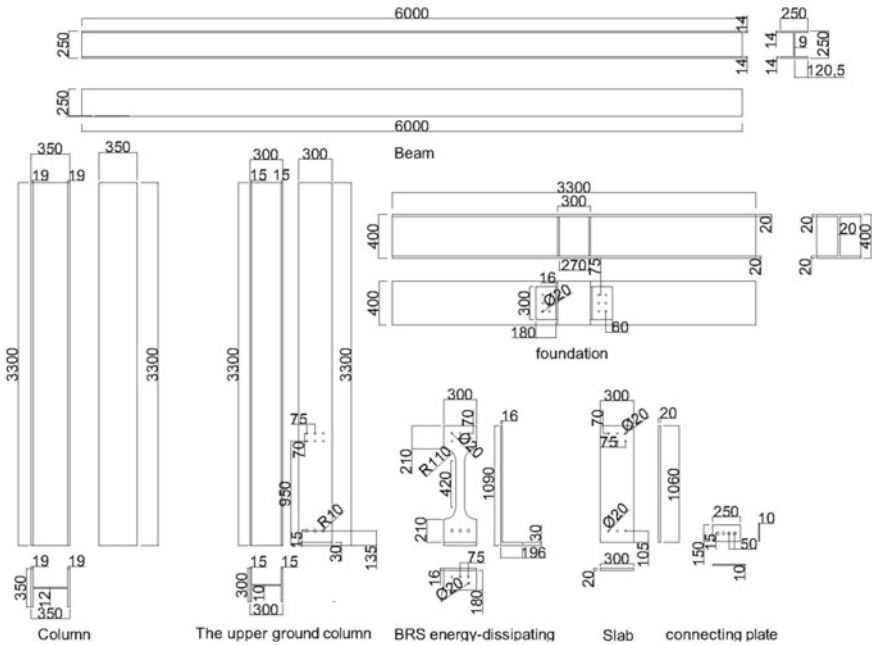


Fig. 4 Structural component

upper ground is set. Both beams and columns are made of H-shaped steel, and an H-shaped steel beam is set at the lower end of the column on the upper ground to replace the foundation. Beams, columns, BRS plates and cover plates are made of Q345 steel; using 10.9 M20 high strength bolts to connect the column on the upper ground, BRS plate, cover plate and foundation; the two prestressed bar are 7 strands of wire which the diameter is 15.2 mm. The standard value of ultimate strength is 1860 MPa and the initial stress is controlled at 150 kN. The design drawing of each component is shown in Fig. 4, and the steel frame supported by foundations at different ground levels is shown in Fig. 5.

3 Finite Element Model

3.1 Model Design

According to the material selection of each member and the detailed design drawing, the beam section size is $H250 \times 250 \times 14 \times 14$, the length is 6 m; the cross-section size of the foundation beam is $H400 \times 400 \times 20 \times 20$; the section size of the column on the upper ground is $H300 \times 300 \times 10 \times 15$, and the length is 3.3 m. The section

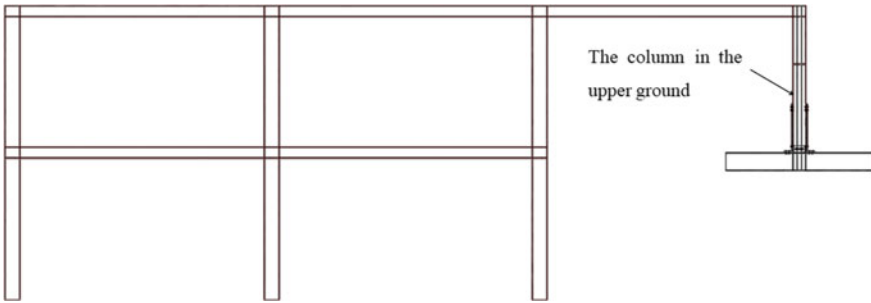


Fig. 5 Design of test specimens

Table 1 Main design parameters of specimens

Test specimens	Size of slotted hole (mm)	Width of BRS energy-dissipating (mm)	The number of connection plate
A-DCKJ1	Fixed connection		
B-DCKJ2	10	80	1
B-DCKJ3	15	80	1
B-DCKJ4	10	60	1
B-DCKJ5	10	80	0

size of the other columns is $H350 \times 350 \times 12 \times 19$, and the length is 3.3 m. The self-centering column on the upper ground considers three design parameters, including the slotted hole size of the lower end of the BRS plate and the connecting plate of the foundation, the width of the dissipated section of the BRS plate, and whether the connecting plate of the foundation is arranged. By using the finite element software ABAQUS, a fixing frame model and four self-centering frame models are established, and the seismic performance under the cyclic loading is numerically simulated. The specific parameters of specimens are designed in Table 1. Main design parameters of specimens.

3.2 Geometric Model

The finite element software ABAQUS was used to establish 6 finite element models. Firstly, each component is created through the component module. Each component is a deformed solid component, and then the material property of each component is given. Then the component is assembled into a whole through the assembly module. In the mesh Module, the cell types of components were all C3D8R. In order to improve the efficiency of finite element, only half of the models were built by symmetric operation. XY symmetric planes were defined in the boundary conditions

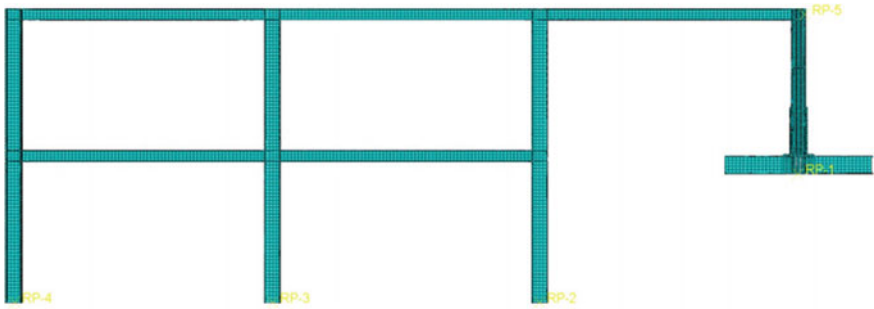


Fig. 6 The geometrical model of specimens

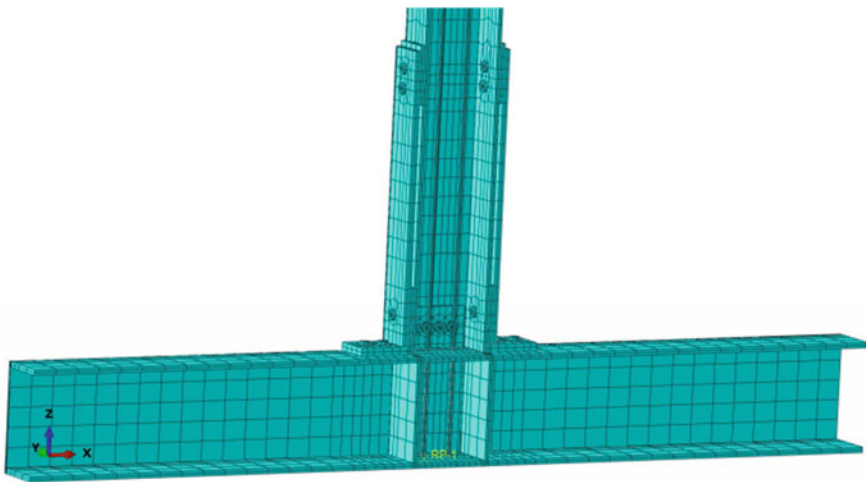


Fig. 7 The geometrical model of column base joints

manager of the load module, and YSYMM constraints were set. The finite element geometric model is shown in Fig. 6, and the geometric model column base joints on the upper ground is shown in Fig. 7.

3.3 Steel Constitutive

The steel is simplified as an ideal homogeneous and isotropic material. Because the high-strength bolts and prestressed bar are always in the elastic stage during the actual loading process, the constitutive models of other steel members, except high-strength bolts and pretensions, adopt the linear strengthening elastoplastic model [9], and the specific expression is as follows:

$$\sigma = \begin{cases} E_s \varepsilon & (\varepsilon \leq \varepsilon_y) \\ \sigma_y + E_{st}(\varepsilon - \varepsilon_y) & (\varepsilon \geq \varepsilon_y) \end{cases} \quad (1)$$

where E_s is the elastic modulus of steel; σ_y is the yield stress of steel; ε_y is the yield strain of steel; E_{st} is the strengthening modulus of steel.

3.4 Interaction

Binding and surface—to—surface contact are two types of interaction. All welding parts are bound. The friction coefficient between steel and steel is set at 0.3 [10]. Four contact surfaces are set between BRS plate and cover plate, BRS plate and column, BRS plate and foundation and column and foundation.

3.5 Loading Scheme

The horizontal load is applied by displacement loading, and the loading point is the coupling point at the top of the column on the upper ground. The first eight loading stages are respectively increased by 0.125% of the height of the column on the upper ground until 1%, and then each stage is increased by 0.25% of the height until 2%. The loading scheme is shown in Fig. 8.

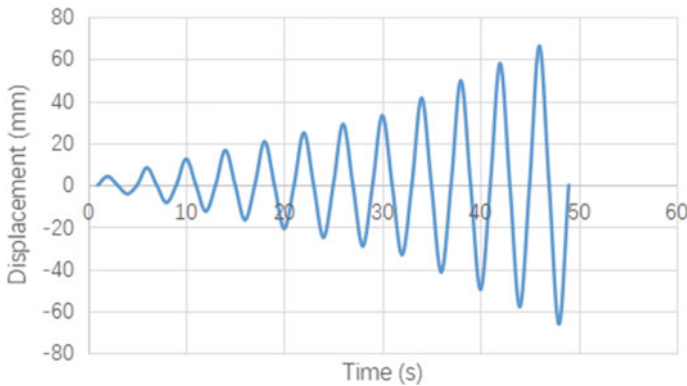


Fig. 8 Loading protocol of the specimens

4 Analysis of Simulation Results

4.1 Hysteretic Properties of Specimens

Through processing the simulation results of the finite element software ABAQUS, the hysteretic curves of the column on the upper ground of each specimen were obtained, using these data to study the seismic performance of the steel frame supported by foundations with the self-centering column on the upper ground. The hysteretic curves of specimens are shown in Fig. 9.

Analysis of the results in Fig. 9 shows that:

- (1) In the whole loading process, A-DCKJ1, whose column on the upper ground is fixing joined, relies on the column itself for energy dissipation. The overall lateral stiffness and bearing capacity are large, and the residual deformation is large. At the end of loading, the maximum forward bearing capacity reaches 450.16 kN and the maximum reverse bearing capacity reaches 447.85 kN.
- (2) The specimen B-DCKJ1, which is set with the self-center column on the upper ground, overcomes the preloading force of the prestressed steel bar at the initial loading stage, and the energy dissipation of the hysteretic curve of the specimen is not obvious until the preloading force is completely cancelled out. When the load reaches 8.25 mm, the the lower row bolts of the BRS plate reach the top of the slotted hole, and the BRS plate is stretched and begins to produce elastic deformation. When the loading reaches 33 mm, the BRS plate enters the yield state, and the energy consumption begins to increase. As the loading continues, the residual deformation of the frame also gradually increases. During the unloading process, when the displacement reaches 33 mm in reverse, the

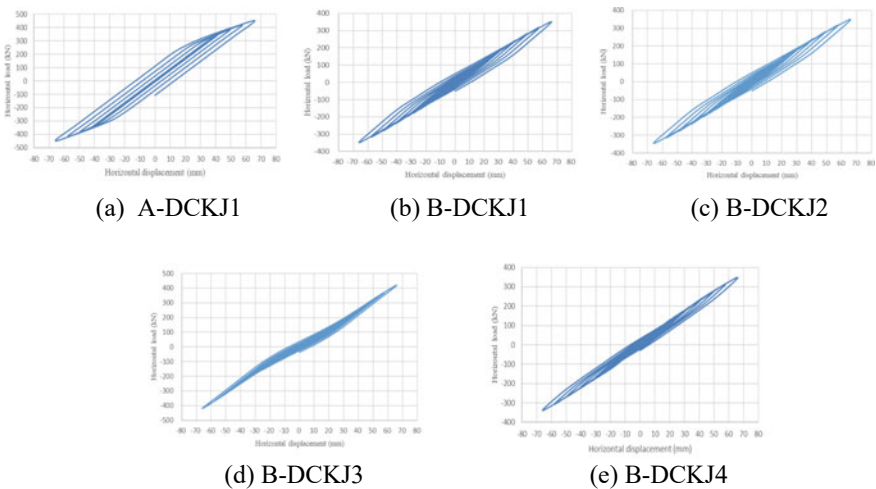


Fig. 9 Hysteresis curves of the specimens

BRS plate will yield under compression and consume energy. Compared with A-DCKJ1, the residual deformation of the frame is smaller, but the energy dissipation capacity is lower. At the end of loading, the maximum forward bearing capacity reaches 350.07 kN and the maximum reverse bearing capacity reaches 347.63 kN.

- (3) The hysteresis curve of specimen B-DCKJ2 is basically the same as that of specimen B-DCKJ1, because the BRS plate and the column body are connected by circular bolt holes, and the BRS plate and the foundation are also connected by circular bolt holes. As a result, the effect of slotted holes at the BRS plate is not obvious, and the energy dissipation is basically the same.
- (4) The specimen B-DCKJ3 reduces the width of the dissipating section of BRS plate, which reduces the dissipating capacity, but improves the self-centering ability, which can effectively reduce the residual deformation of the frame. When loading to 41.25 mm, the bearing capacity increases, the maximum positive bearing capacity reaches 420.61 kN, the maximum negative bearing capacity reaches 419.54 kN.
- (5) Compared with B-DCKJ1, the specimen B-DCKJ4, which does not have a connection plate between the column on the upper ground and the foundation, the result show that its energy dissipation capacity and maximum bearing capacity are weakened, but the residual deformation is reduced.

5 Stiffness Degradation

With the continuous increase of horizontal cyclic load, the lateral stiffness of the specimen gradually degrades, which further reflects the damage of the structure. The peak stiffness curve of the specimen is shown in Fig. 10.

As can be seen from Fig. 10, the stiffness of the laminar-steel structures supported by foundations at different ground levels fixed with the column on the upper ground

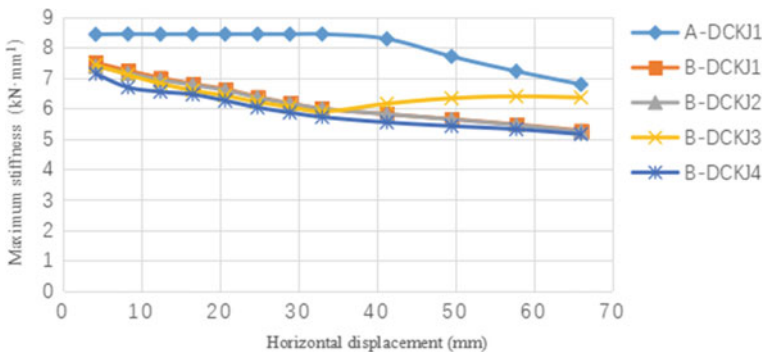


Fig. 10 Maximum stiffness curves of the specimen

remain basically unchanged under the pre-loading condition, but the stiffness degradation is faster than that of other specimens after the displacement is loaded to 41.25 mm, while the stiffness degradation of the specimen set with the self-centering column on the upper ground become slower after the displacement is loaded to 33 mm, indicating that the fixed connection can ensure the seismic performance under small deformation. However, if it exceeds a certain limit value, it will lose great seismic performance. Setting self-centering can effectively improve the stiffness degradation ability. Changing the slotted hole size has little effect on the stiffness change because the bolt has not reached the edge of the slotted hole when loading the 66 mm horizontal displacement. The larger the width of the dissipated section of the BRS plate, the larger the initial stiffness will be. When the BRS plate with the dissipated section width of 60 mm is used, the bolt will reach the edge of the slip hole when the horizontal displacement of 33 mm is loaded, resulting in the increase of the stiffness.

5.1 Energy Dissipation Capacity

The area of the hysteresis loop of the specimen under the horizontal cyclic load reflects its energy dissipation capacity. The energy dissipation curves of each specimen are obtained by processing the hysteresis curves. The energy dissipation curves of specimens with different parameters are shown in Fig. 11.

According to the analysis of the energy dissipation of each specimen, the specimen with the column on the upper ground fixed is always elastic in the early loading, and no energy dissipation occur. When the loading displacement reaches 41.25 mm, the energy dissipation begins to increase, and the increase amplitude is larger than that of the structure with self-center. Compared with DCKJ2 and DCKJ4, the larger the width of the dissipating section of BRS plate, the better the dissipating capacity. In addition, setting the connecting plate on foundation can also improve the energy

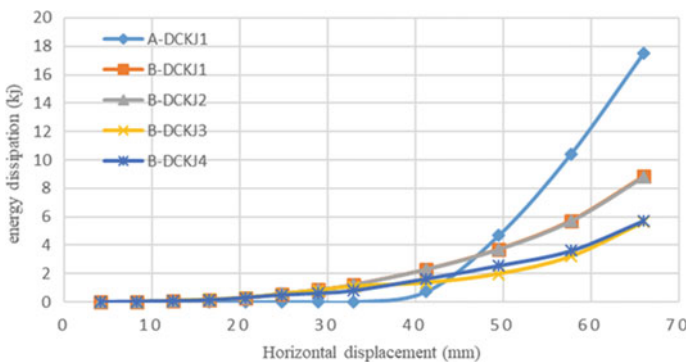


Fig. 11 Hysteretic energy-dissipation curves

dissipation capacity, but the energy dissipation capacity provided by the connecting plate on foundation is limited. The energy dissipation capacity of DCKJ4 is larger than that of DCKJ5 before the loading displacement of 66 mm, but the energy dissipation capacity of the two specimens is basically the same when the displacement reaches 66 mm.

5.2 Residual Deformation

The size of the residual deformation of the specimen reflects the size of the self-centering ability. The residual deformation curves of each specimen are obtained by processing the finite element results, as shown in Fig. 12.

The specimen with self-center column on the upper ground increases gently with the gradual increase of loading, while the specimen with fixed column on the upper ground has no residual deformation at the initial loading stage. After the loading displacement reaches 41.25 mm, the residual deformation increases rapidly and the structural deformation is large. When the loading displacement reaches 66 mm, the residual deformation of the specimens with the self-centering column on the upper ground is only 40% of that of the specimens with the column on the upper ground fixed, showing good self-centering ability. Comparing the four specimens with the self-center column on the upper ground, the larger the width of the dissipating section of BRS plate, the larger the residual deformation; The slip hole size has little effect on the residual deformation. A small amount of residual deformation will be increased if a connecting plate is set on the foundation and connected to the column on the upper ground.

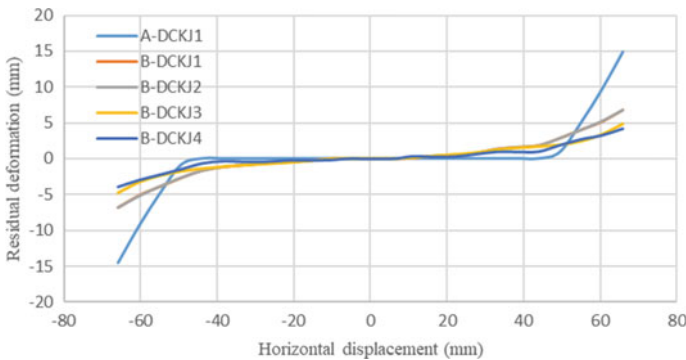


Fig. 12 Residual displacement curves

5.3 Stress Distribution

The 4 specimens with self-center column on the upper ground all consume seismic energy through BRS plate and reduce residual deformation through prestressed bar to achieve self-center capability. There is little difference in the stress conditions of the self-centering specimens. The overall stress nephogram of specimen B-DCKJ1 is intercepted to analyze the stress conditions, as shown in Fig. 13.

By analyzing the overall stress nephogram, the column on the upper ground of the steel structures supported by foundations at different ground levels is damaged first, and the BRS plate enters plastic yield to consume energy, and the stress of the frame node and the column base joint on the lower ground is relatively large.

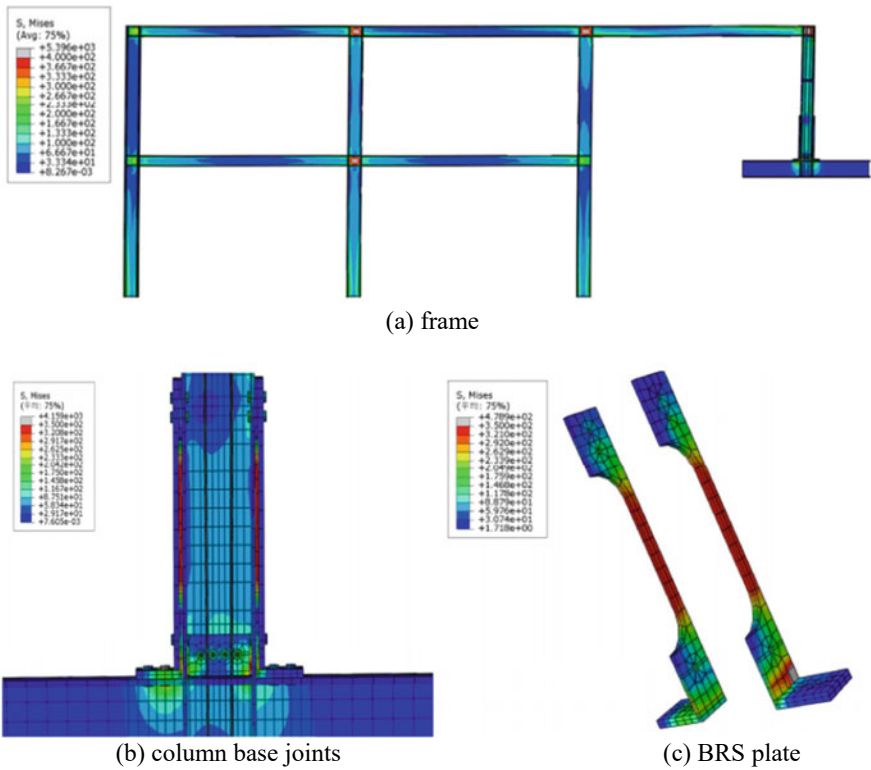


Fig. 13 Mises stress distribution of the specimens

5.4 Application Limitations

Comparing specimens, A-DCKJ1 and B-DCKJ3, the maximum bearing capacity, stiffness and energy dissipation capacity of the frame are reduced by setting the self-centering structure. With the increase of the number of layers, the seismic performance of the frame will be further reduced. If the self-centering structure is applied to the high-rise frame structure, the seismic performance of the frame may not meet the requirements. Therefore, the high-rise frame structure needs to be further analyzed.

6 Conclusion

In this paper, a steel structures supported by foundations at different ground levels with a self-centering column on the upper ground is taken as the research object. Firstly, compared with the ordinary steel structures supported by foundations at different ground levels with fixing joint, then the three design parameters of slotted hole, the width of the dissipated section of BRS plate and the connecting plate on foundation in the self-centering structure are considered. Then, the finite element software ABAQUS is used to model and simulate the seismic performance. The comparative analysis draws the following conclusions:

- (1) When the column on the upper ground of the steel structures supported by foundations at different ground levels is set as a self-centering structure, the bearing capacity and stiffness will be slightly reduced, but the overall residual deformation can be greatly improved. Finally, the residual deformation after a large earthquake does not exceed the limit of 0.5%, achieving a good self-centering effect.
- (2) Setting slotted holes can delay the plastic entry of BRS plates. Energy dissipation is mainly provided by prestressed bar in the early stage of loading. However, the change of the size of slotted holes has little influence on the overall energy dissipation and residual deformation within the specified range.
- (3) During the whole loading process, the plastic deformation is mainly concentrated at the BRS plate. The BRS plate has a great influence on the self-center effect and energy-dissipating capacity of the whole specimen. Increasing the width of the energy-dissipating section of the BRS plate increases the energy-dissipating capacity and stiffness of the specimen, but the overall residual deformation increases.
- (4) Because of the slotted holes, the connecting plate on foundation can guarantee the seismic performance of the specimen and provide certain energy dissipation capacity and stiffness in the event of an earthquake, but the overall residual deformation will increase.
- (5) With the increase of the number of layers, the seismic performance of the frame will be further reduced. If the self-centering structure is applied to the high-rise frame structure, the seismic performance of the frame may not meet

the requirements. Therefore, the high-rise frame structure needs to be further analyzed.

References

1. Han J, Li YM, Tang GL et al (2014) Influence of ground support types on the seismic performance of structures supported by foundations at different ground levels. *Chin Civil Eng J* 47(2):93–100
2. Chi H, Liu J (2012) Seismic behavior of post-tensioned column base for steel self-centering moment resisting frame. *J Constr Steel Res* 78:117–130
3. Mirzaie M, Bahaari MR, Emam SH (2014) Numerical simulation of the new post tensioned column base with bolted T-stubs. *ISIJ Int* 54(1):179–187
4. Fabio F, Chrisoforos A (2017) Rocking damage-free steel column base with friction devices: design procedure and numerical evaluation. *Earthquake Eng Struct Dynam* 46(14):2281–2300
5. Kamperidis VC, Karavasilis TL, George V (2018) Self-centering steel column base with metallic energy dissipation devices. *J Constr Steel Res* 149:14–30
6. Cui Y, Lu XL, Jiang C (2017) Experimental investigation of tri-axial self-centering reinforced concrete frame structures through shaking table tests. *Eng Struct* 132:684–694
7. Liu Y, Guo ZX, Jia LP et al (2020) Experimental study on seismic performance of innovative replaceable composite columns[J]. *J Build Struct* 41(7):45–54
8. Yang P, Hong JH, Yang YM et al (2019) Simulation analysis of self-centering EC column base joints. *Xi'an Univ Arch Tech* 51(6):775–783
9. Wang YX, Fang YZ, Shen XM et al (2017) Numerical simulation of inter-story seismic performance of composite frame connected with new-type PEC column-steel beam T-type jointer. *World Earthquake Eng* 33(1):100–109
10. GB50017–2017 Standard for design of steel structures. Beijing: Building Industry Press of China (2017)

Derivation of Response Spectra and Hysteretic Energy: A Case Study on 2023 Turkey-Syria Earthquake in Consideration of Structural Ductility



Weiye Shao

Abstract Structural response under strong ground motion has always been of concern in engineering seismology due to low predictability of seismic events and their devastating impact. The energy-based seismic design (EBSD) is proposed to capture the cumulative damage of the structure in terms of evaluating hysteretic energy, which is a more reasonable design method considering inelastic deformation of structures. On the other hand, structural ductility demand is another significant aspect of design. In this paper, the response spectra and hysteretic energy under different ductility factors are derived and quantified based on a selection of ground motion records from the recent 2023 Turkey-Syria earthquake mainshock (M7.7) and aftershock (M7.6). The results show that for the selected data, the peak value of acceleration response spectra significantly exceeds the design acceleration, and the hysteretic energy for M7.7 presents a relatively high value while the value for M7.6 is comparatively lower. Even if the evaluation for the M7.6 event is minor, it is worth considering the structural vulnerability under cumulative damage and residual influence from the mainshock.

Keywords Response spectra · Hysteretic energy · Energy-based seismic design · Structural ductility · Single-degree-of-freedom system

1 Introduction

Structural response under strong ground motion is acknowledged as one of the most significant issues in engineering seismology due to the low predictability of seismic events and their destructive impact on structures. The mainstream of structural reliability and performance assessment is probabilistic seismic hazard analysis (PSHA), which is extensively used as method for potential damage estimation under earthquakes, and its efficiency and accuracy have been proved over the past few decades

W. Shao (✉)
University of Bristol, Bristol BS8 1TR, UK
e-mail: ql21598@alumni.bristol.ac.uk

© The Author(s), under exclusive license to Springer Nature Singapore Pte Ltd. 2024
M. Casini (ed.), *Proceedings of the 3rd International Civil Engineering and Architecture Conference*, Lecture Notes in Civil Engineering 389,
https://doi.org/10.1007/978-981-99-6368-3_34

399

[1]. The dedication that has been devoted to this topic is prominent, and the works of performing simulation on models, creating design spectra and hazard maps based on specific events have improved the seismic risk assessment at design stage as well as in post-hazard investigation.

On the one hand, the code-based seismic design mainly targets on elastic response of structures. For instance, force-based seismic design and displacement-based design, which are the most commonly used method for earthquake-resistant structural design [2, 3]. However, it has been conventionally acknowledged that structures not only suffer from elastic displacement under ground motion, but also experience inelastic hysteretic deformation which is closely associated with energy-based seismic design (EBSD) [2, 4]. The application of EBSD which takes the impact of cumulative damage into account in design codes is less prevalent, but has gradually been adopted in seismic design and risk assessment, and this design method can better predict the structural response compared with ordinary code-based seismic design under some circumstances, where the energy spectra present distinctive peak response while the spectral acceleration would probably fail to capture [4].

From seismic input energy perspective, the total input seismic energy can be classified into recoverable energy and dissipated energy, while recoverable energy consists of elastic strain energy and kinetic energy, and dissipated energy can be further classified into damping energy and hysteretic energy [2, 4]. The hysteretic energy, in particular, is related to the inelastic behavior that may cause permanent damage to the structure. Consequently, in EBSD, the priority of design resides in the overall hysteretic energy demand and corresponding inelastic deformation [2].

On the other hand, structural damage is correlated with ductility demand, and it is stressed in seismic design codes that the ductility demand is vital in seismic-prone regions; therefore, the investigation of desired ductility level of structures resisting strong ground motion is critical [5]. Hatzigeorgiou evaluates the ductility demand of single-degree-of-freedom (SDOF) systems under multiple near-fault and far-fault earthquakes, and it has been concluded that the design earthquake is insufficient to estimate structural performance under real earthquake sequences [5]. Therefore, as a complementary aspect, the hysteretic energy for different structural ductility under real earthquake records can provide a better quantification of seismic demand.

In general, this paper presents the conventional response spectra and the estimation of hysteretic energy for SDOF system of the recent Turkey-Syria earthquake (2023) in order to quantify the difference between the code-based seismic design and EBSD. In Sect. 2, a brief introduction of this seismic event is stated, and the formulation of calculating hysteretic energy as well as the selection of ground motion records is clarified in Sect. 3. The result is discussed in Sect. 4 in order to compare the acceleration spectra and hysteretic energy for different categories. Finally, conclusions are drawn in Sect. 5 based on the results obtained, the scope of the analysis and proposal of future research directions.

2 Case-Study Event: 2023 Turkey-Syria Earthquake

On February 6th, 2023, a strong earthquake with magnitude 7.8 (M7.7 for AFAD inspection) struck south-eastern Turkey with thousands of aftershock sequences, influencing north-western Syria as well [6]. According to the engineering report and Turkish database AFAD, the earthquake is featured with 3 major events: first and mainshock with Mw of 7.7 (01:17 UTC), second event which happened closely after the mainshock with Mw of 6.6 (01:28 UTC) and another unexpected strong aftershock happened within 12 h with Mw of 7.6 (10:24 UTC) [6, 7]. All of them are caused by strike-slip mechanism. The epicentre of the M7.7 earthquake is 37.288°N, 37.043°E with a depth of 8.6 km, while for the M7.6 earthquake, the epicentre is around 10 km away with depth of 7 km (38.089°N, 37.239°E) [7].

Despite that it is suggested to evaluate the impact of the second M6.6 earthquake, the main analysis relies on the first M7.7 and the third M7.6 ground motion. Nevertheless, the acceleration time-histories of the M7.7 and the M6.6 earthquakes for station 2708 (37.099°N, 36.648°E) are illustrated in Fig. 1. For each ground motion, the station recorded the data in 3 directions: east-west (EW), north-south (NS) and up-down (UD). For the M7.7 earthquake, the peak ground acceleration (PGA) values reach 0.93, 1.32, and 0.69 g for the three components respectively, but for M6.6 event, the PGA value is lower (0.36, 0.32, and 0.22 g). However, the latest 2019 Turkish earthquake code TEC 19 indicates design acceleration at 0.3 g, and it is unreasonable to design structures at high acceleration level even in earthquake-prone region [8]. As a result, the impact on structure is severe, including demolition of buildings, inundation in coastal area and small tsunamis [9, 10].

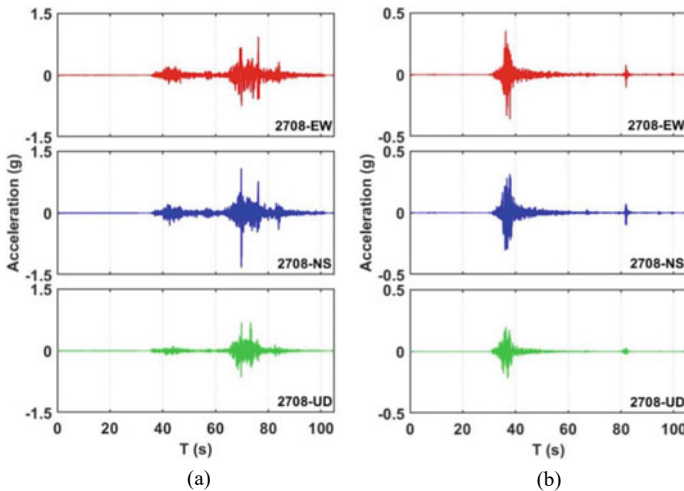


Fig. 1. Acceleration time-history at Station 2708 (37.099°E, 36.648°N): **a** Mw 7.7, 01:17 (UTC) and **b** Mw 6.6, 01:28 (UTC)

3 Methodology

3.1 Estimation of Seismic Input Energy and Hysteretic Energy

The first theoretical identification of seismic energy concept is proposed by Housner [11], followed by several studies on analysis of SDOF systems evaluating the damage from energy perspective (e.g. Akiyama (1985), Fajfar and Vidic (1994)) [12, 13]. The formulation that has been used in this paper to estimate the total input and hysteretic energy is proposed by Khashae (2004) [14]. For the total input seismic energy EI per unit mass m, the formulation is shown as Eq. 1:

$$\frac{E_I}{m} = \bar{f} \cdot f_T \cdot \frac{1}{2} \cdot \left(\frac{Sa}{\omega} \right)^2 \quad (1)$$

where $\frac{Sa}{\omega}$ is the pseudo-spectral velocity (evaluated with 5% damping ratio), \bar{f} and f_T can be calculated as follow (Eq. 2–3):

$$\begin{cases} f_T = 0.572e^{(-4.283T_n)} + 0.6 \text{ for } \mu = 1 \\ f_T = 1 \text{ for } \mu = 2, 3, 4, 5 \end{cases} \quad (2)$$

$$\bar{f} = \frac{4.256}{\sqrt{\mu - 0.5}} + 0.318I_c \quad (3)$$

where μ is the ductility of structure, and I_c is the intensity index which can be calculated as Eq. 4:

$$I_c = (a_{rms})^{1.5} (t_{di})^{0.5} \quad (4)$$

where a_{rms} is the root-mean square ground acceleration and t_{di} is the 5–95% duration of strong motion (Eq. 5–6).

$$a_{rms} = \left(\frac{1}{T_2 - T_1} \cdot \int_{T_1}^{T_2} [a(t)]^2 dt \right)^{0.5} \quad (5)$$

$$t_{di} = T_{0.95} - T_{0.05} \quad (6)$$

Eventually, the hysteretic energy E_H can be evaluated as Eq. 7:

$$\begin{cases} E_H = 0 \text{ for } \mu = 1 \\ E_H = 0.72(1 - \mu^{-1})^{0.7} E_I \text{ for } \mu = 2, 3, 4, 5 \end{cases} \quad (7)$$

The benefit of these formulae is the efficiency and accuracy of predicting input and hysteretic energy based on regression analysis of 160 accelerograms, and it does not involve the cyclic ductility variable [14].

3.2 Selection of Ground Motion Records

The selection of ground motions was made based on the nearest stations for each event listed in preliminary engineering report, and corresponding acceleration time-history was available on AFAD [6, 7]. For the mainshock (M7.7) and aftershock (M7.6), 20 records are selected from the database respectively in terms of source-to-site distance and availability of record data to proceed further analysis. The basic information of the stations is shown in Table 1.

Table 1 Selected stations and basic information (adapted from Baltzopoulos et al. [6])

M7.7, 01:17 (UTC)			M7.6, 10:24 (UTC)		
Station No	V_{S30} (m/s) / EC8 Ground type	R_{epi} (km)	Station No	V_{S30} (m/s) / EC8 Ground type	R_{epi} (km)
0201	391 (B)	120.12	0129	965 (A)	91.84
2703	758 (A)	37.34	0141	/	161.28
2704	721 (B)	74.10	0213	/	68.73
2708	523 (B)	40.77	3802	305 (C)	77.41
2709	555 (B) 90	37.45	3803	499 (C)	157.41
2712	/	29.79	3804	637 (B)	102.93
3123	470 (B)	143.00	4405	579 (B)	100.81
3125	448 (B)	142.15	4406	815 (A)	70.17
3126	350 (C)	143.54	4408	654 (B)	56.74
3129	447 (B)	146.39	4409	/	56.86
3135	460 (B)	142.15	4410	/	94.59
3137	688 (B)	82.48	4412	/	99.89 99.89 99.89
3141	338 (C)	125.42	4611	731 (B)	38.21
3142	539 (B)	106.49	4612	246 (C)	66.68
4615	484 (B)	13.83	4614	671 (B)	67.35
4616	390 (B)	20.54	4617	574 (B)	66.50
4629	382 (B)	22.50	4620	484 (B)	63.46
4630	347 (C)	21.89	4628	186 (C)	32.41
4632	428 (B)	24.09	4631	543 (B)	21.43
NAR	/	15.35	5807	445 (B)	70.94

4 Results and Analysis

4.1 Response Spectra

The response spectra are illustrated in Fig. 2 for M7.7 and M7.6 event, and each component, respectively. The preliminary acceleration time-history was downloaded from AFAD [8], and processed in MATLAB [15] and SeismoSignal [16]. It should be noted that the damping ratio ζ equals to 5% as it is generally defined in pseudo-spectral acceleration (PSA) calculation. For PSA spectra, the mean value as well as plus/minus one standard deviation is evaluated for each event and component in order to assess central tendency as well as the variability and significance range of each sample.

From Fig. 2a, c, and e, it can be observed that the mean value and plus/minus standard deviation is similar for EW and NS with maximum mean value of 1.42 and 1.54 g, but relatively lower for UD especially after $T = 0.3$ s, where the mean value of UD only presents half of the mean value for EW and NS. This minor PSA value indicates less significance of acceleration in UD direction compared with EW and NS component, however, the peak mean value for UD still reaches 1.18 g which is far more notable with respect to the design acceleration level (0.3 g).

The comparison between Fig. 2a–f is made, and the differences between two events are prominent. Even though the mean value and plus/minus standard deviation falls beneath 0.4 g, the maximum value of sample mean for EW (0.32 g) and NS (0.29 g) is close to design acceleration. In addition, the damage that structures suffered from the mainshock is not negligible, which suggests that the structures are much more vulnerable when experiencing this strong aftershock. As a result, the impact of the spectral acceleration for M7.6 is also pronounced and destructive.

4.2 Hysteretic Energy

Having the PSA values, the mean value and plus/minus standard deviation of hysteretic energy per unit mass (E_H/m) for each ductility category ($\mu = 2, 3, 4$ and 5) is derived using the equations mentioned in Sect. 3.1.

The results are shown in Fig. 3, where for both two events NS component presents higher average hysteretic energy than EW and UD, and M7.7 event apparently possesses larger hysteretic energy for all of the components. The maximum value of mean for M7.7 usually appears within the period range of $T = 1.0$ – 2.3 s, but for M7.6 this range as well as the variability range is narrower ($T = 1.3$ – 1.7 s). Specifically, for UD component of M7.7 and M7.6, the peak falls in $T = 2.0$ – 3.0 s, and its value is excessively lower than EW and NS. In terms of different ductility level of SDOF systems, lower ductility presents higher hysteretic energy under most of the scenarios, however, for M7.7 EW and NS (Fig. 3a, c), the most distinct hysteretic

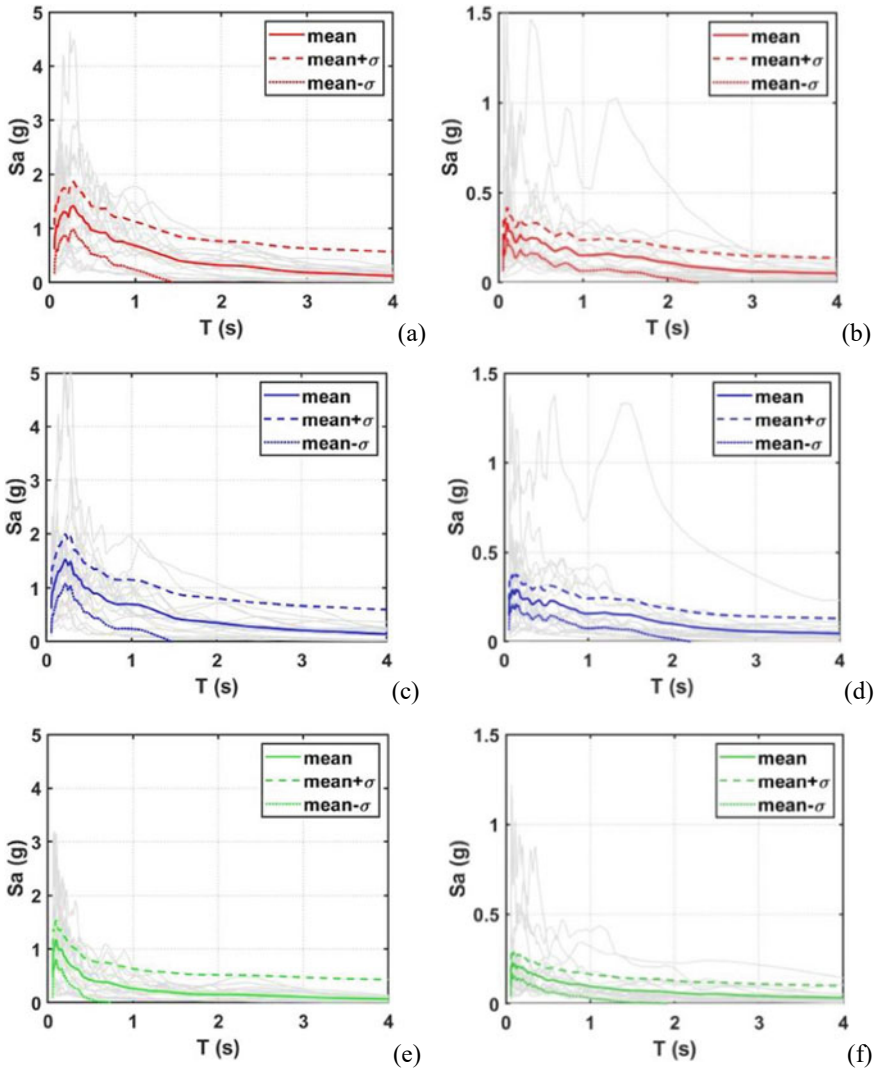


Fig. 2 Response spectra (acceleration) ($\zeta = 5\%$) for: **a** M7.7, EW; **b** M7.6, EW; **c** M7.7, NS; **d** M7.6, NS; **e** M7.7, UD and **f** M7.6, UD

energy is observed in $\mu = 3$ rather than $\mu = 2$. It is true as the ductility level indicates the ability of structures withstanding large displacement under strong ground motions, and also the ability to dissipate seismic energy during an earthquake. Consequently, a higher ductility level usually suggests better performance. However, for SDOF systems under actual scenario, the overall stiffness would be higher than MDOF systems using the same material, so the ductility level is more essential to

prevent brittle structures. With a certain capacity of deformation defined by structural ductility, the energy dissipation is in direct proportion to ductility, so it is more profitable to improve the ductility to achieve better energy dissipation.

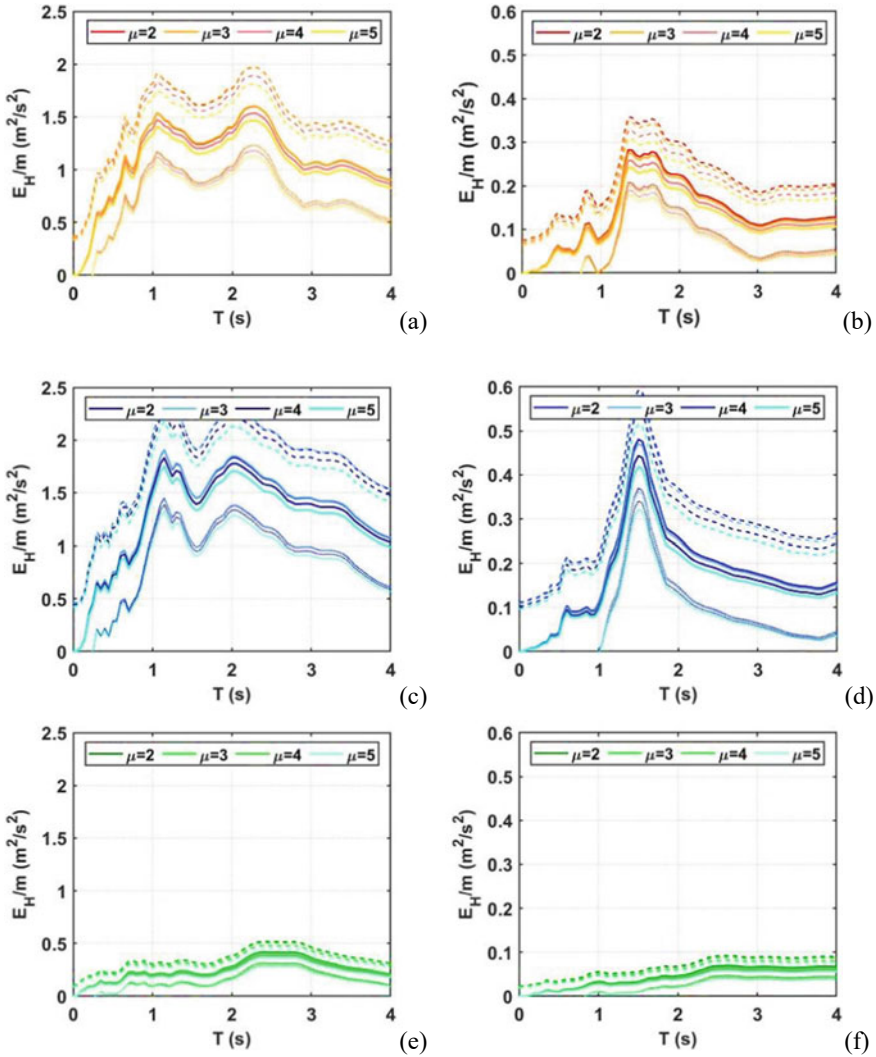


Fig. 3 Hysteretic energy spectra for SDOF systems with different ductility μ ($\zeta = 5\%$): **a** M7.7, EW; **b** M7.6, EW; **c** M7.7, NS; **d** M7.6, NS; **e** M7.7, UD and **f** M7.6, UD

5 Conclusion

In this paper, general information on EBSD and empirical formulation on hysteretic energy estimation as well as geotechnical details of 2023 Turkey-Syria earthquake is introduced. PSA and E_H/m are chosen as intensity measures to describe M7.7 and M7.6 events. The implementation of response spectra shows an excessive high maximum value of average PSA for M7.7 (1.42, 1.54, and 1.18 g for EW, NS and UD) compared with design level (0.3 g), and the maximum value of average PSA reaches design acceleration for M7.6 (0.32, 0.29, and 0.24 g for EW, NS and UD). However, the residual effect of the mainshock should be taken into account when evaluating the second major aftershock M7.6 for potential damage and vulnerability (e.g. interior cracking) of structures.

In terms of hysteretic energy, higher energy level is observed in NS component, while the M7.7 earthquake presents larger hysteretic demand than M7.6 earthquake. The peak value of average E_H/m depends on the event and component, for UD shows late peak value which falls in medium-to-long period ($T = 2.0-3.0$ s), and the period range in which peak value appears for M7.6 ($T = 1.3-1.7$ s) event is more concentrated than M7.7 ($T = 1.0-2.3$ s). The overall tendency of ductility-related analysis on SDOF systems is as expected, for the hysteretic energy decreased as ductility increased for most of the cases except for some individual cases, in which distinction is subtle to be visualized between $\mu = 2$ and $\mu = 3$.

Even though the study is carried out based on the formulation with great accuracy and efficiency of predicting input and hysteretic energy based on regression analysis of 160 accelerograms without the requirement of considering cyclic ductility variables, a comparison between total input and hysteretic energy expression proposed by different scholars and the real earthquake scenario was made, and the results indicated that the ratio of hysteretic energy over input seismic energy generally overestimates the real energy demand [2]. However, conservative prediction is necessary in determining structural response, for rationally raised seismic demand can better ensure the safety of structures under ground motions which are extremely intensive.

Despite the fact that the consistency between the data obtained from PSHA and the actual response caused by real earthquakes is controversial, it is comparatively reliable if the derivation and assessment process has taken various factors into consideration (e.g. site condition, geotechnical and rupture mechanism, etc.) [17]. For further work orientation, the selection of 20 records for each event is insufficient due to the deficiency of stations, unavailability of records and limitation of database. Therefore, a more extensive selection of ground motion records should be made and data that shows low consistency should be eliminated. Moreover, the pulse-like ground motions can cause more severe damage to structures than ordinary records, and the identification of pulse-like content in this seismic event has been carried out [18]. Further investigation into the influence of pulse-like records on different structural systems should be simulated and evaluated, and the potential inadequacy of the model or analysis should be discussed.

References

1. Mulargia F, Stark PB, Geller RJ (2017) Why is probabilistic seismic hazard analysis (PSHA) still used? *Phys Earth Planetar Inter* 264:63–75, ISSN 0031–9201. <https://doi.org/10.1016/j.pepi.2016.12.002>
2. Mezgebo MG (2015) Estimation of Earthquake Input Energy, Hysteretic Energy and its Distribution in MDOF Structures”. Dissertations—ALL, pp 228. Retrieved from <https://surface.syr.edu/etd/228>
3. Eurocode 8 (2004) Design of structures for earthquake resistance. British Standards Institution, London: BSI
4. Ying Z, Ge S, Ping T (2019) Hysteretic energy demand for self-centering SDOF systems. *Soil Dynam Earthquake Eng* 125:105703, ISSN 0267–7261. <https://doi.org/10.1016/j.soildyn.2019.105703>
5. Hatzigeorgiou GD (2010) Ductility demand spectra for multiple near- and far-fault earthquakes. *Soil Dynam Earthquake Eng* 30(4):170–183, ISSN 0267–7261, <https://doi.org/10.1016/j.soildyn.2009.10.003>
6. Baltzopoulos G, Baraschino R, Chioccarelli E, Cito P, Iervolino I (2023) Preliminary engineering report on ground motion data of the Feb. 2023 Turkey seismic sequence V2.0—10/02/2023. <https://doi.org/10.13140/RG.2.2.31375.25767>
7. Ground motion records AFAD. Retrieved from <https://tadas.afad.gov.tr/list-waveform>. Accessed 20/02/2023 9:35 UTC
8. AFAD (2019) The disaster and emergency management authority of Turkey. “Turkish Building Earthquake Code, TEC 19”
9. Ravilius K (2023) Geological impact of Turkey-Syria earthquake slowly comes into focus. *The Guardian*
10. Damaskinos I (2023) Earthquake in Turkey caused ‘small tsunamis’ off Famagusta coast. *Cyprus Mail*. Archived from the original on 6 February 2023. Accessed on February 2023
11. Housner GW (1956) Limit design of structures to resist earthquakes. In: Proceedings of the first world conference on earthquake engineering, EERI, Berkeley, CA
12. Akiyama H (1985) Earthquake-resistant limit state design for building. University of Tokyo Press, Tokyo
13. Fajfar P, Vidic T (1994) Consistent inelastic design spectra: hysteretic and input energy. *Earthquake Eng Struct Dynam* 23:523–537
14. Khashaee (2004) Energy-based seismic design and damage assessment for structures. PhD dissertation, Southern Methodist University, Dallas, Texas, pp. 266
15. MATLAB and Statistics Toolbox Release R (2019a) The MathWorks, Inc., Natick, Massachusetts, United States
16. SeismoSignal v2022 Release-1 Build-50, Seismosoft Ltd. Retrieved from www.seismosoft.com
17. Iervolino I (2013) Probabilities and fallacies: why hazard maps cannot be validated by individual earthquakes. *Earthq Spectra* 29(3):1125–1136. <https://doi.org/10.1193/1.4000152>
18. Chen G (2023) Report on pulse-like ground motions in the Feb 2023 Turkey earthquakes. <https://doi.org/10.13140/RG.2.2.31375.25767>

Dynamic Seismic Analysis and Design of the Clock Tower Structure



Osorio Lobaton Gianpol Samuel, Castañeda Avila Jhiiviana Jhasmin,
and Mamani Huaman Rolando

Abstract The project includes the analysis and structural design, according to the National Building Regulations of a building of 06 levels, the construction of a clock tower located in the district of Huaró—Province of Quispicanchi- Department of Cusco-Peru. The building has the following structural elements: The structure consists of reinforced concrete elements. It is a structure with a system of *aporticado* in the longitudinal and transversal directions. The roof system consists of columns, reinforced concrete beams, lightened slabs, stairs and masonry partitions. For the seismic analysis a three-dimensional model was elaborated considering all structural elements representing the beams and columns as linear elements (Frame), the lightened slabs as membrane elements (Membrane). Three degrees of freedom were considered at each level of the building (two translational and one rotational). The design spectrum of the seismic standard was used and a dynamic spectral analysis was performed. For the design of the elements, the values obtained in the dynamic analysis were scaled up to values equivalent to 80–90% of the static analysis using the regulatory formula $H = ZUCS/R$ multiplied by the total weight of the building. The required design combinations are established according to the RNE Standard E.060 for reinforced concrete elements, being that the structure complies with symmetry, both in the distribution of masses and in the stiffness, adequate resistance, continuity

O. L. G. Samuel · C. A. J. Jhasmin · M. H. Rolando (✉)
Professional Academic School of of Civil Engineering, Universidad Continental, Huancayo,
Junín, Perú
e-mail: 70380248@continental.edu.pe

O. L. G. Samuel
e-mail: 75453151@continental.edu.pe

C. A. J. Jhasmin
e-mail: 48427575@continental.edu.pe

in the structure, both in plan and in elevation, ductility of the connections, hyperstability and monolithism, lateral stiffness and rigid diaphragm. It is concluded that the design of the structure complies with all the regulatory bases of the RNE and also of the seismic-resistant analysis that is zoned according to its location.

Keywords Seismic analysis · Structure · Construction

1 Introduction

Dynamic seismic analysis carried out in the clock tower of the main square of the district of Huaro, province of Quispicanchi, Cusco region. The loads in a building are vertical loads that interact throughout the useful life of the building and horizontal loads, these loads are transferred from the slabs to the beams and then to the columns that go to the foundations and finally to the ground [1]. The behaviour of structures in buildings under the action of seismic loads can sometimes be modified by taking into account the Dynamic Ground-Structure Interaction [2]. Structural element that transfers seismic waves into a building, which could cause damage to the structure leading to instability and deterioration [3]. A method for seismic design of buildings that considers shear deformations, it is a new method with respect to the traditional method, used to study any structure that is subjected to the ground. A typical reinforced concrete section is composed of unconfined concrete fibres plus confined concrete fibres and steel fibres [4]. Dynamics is the behaviour of structures subjected to dynamic forces (actions that have high acceleration) [5]. Dynamic loads can be people, wind, traffic, waves, explosions and earthquakes [6]. Dead loads are the weight of the structural and non-structural elements of a building [7]. Gravity loads from objects external to the structure, working personnel, equipment, among others, are defined as live loads [8]. Earthquake loads generate higher axial force values in the elements in all cases of two-way combinations [9]. Soil conditions and topographical characteristics change with earthquakes and are decisive for the seismic-resistant design of buildings [10]. Generation of a building project in which cost and time are related, these parameters being important for decision making [11]. The design of a building project in which cost and time are related, being these parameters important for decision making [12]. The design of a building project in which cost and time are related, being these parameters important for decision making [13]. The design of a building project is based on the following parameters.

2 Methodology

2.1 Standards Used

The standards used for the preparation of the following document are: standard RNE E020: Loads, standard RNE E050: Soils and Foundations, standard RNE E030: Earthquake Resistant Design and standard RNE 060: Reinforced Concrete [12].

2.2 Design Loads

For the design of the reinforced concrete elements of this building we will mainly consider three types of loads: Dead Cargo (D).

2.3 Dead Cargo (D)

Made up of the self-weight of the structural elements: slabs, beams, plates and columns. Considering the weight of: Ceiling First Level to Sixth Level

2.4 Ceiling First Level to Sixth Level

Floor finishes = 100 kg/m^2
Movable partitioning = 100 kg/m^2

2.5 Live Cargo (L)

It is that which is generated by the weight of occupants, furniture, equipment and other movable elements that together are called overload.

2.6 Ceiling First Level to Sixth Level

Overload = 200 kg/m^2

Table 1 Seismic loads

COMB1 = 1.4 D + 1.7 L
COMB2 = 1.25 (D + L) + SX
COMB3 = 1.25 (D + L) – SX
COMB4 = 1.25 (D + L) + SY
COMB5 = 1.25 (D + L) – SY
COMB6 = 0.9 D + SX
COMB7 = 0.9 D – SX
COMB8 = 0.9 D + SY
COMB9 = 0.9 D – SY

Table 2 Reduction factor

Application	Reduction factor (Φ)
Pure flexion	0.90
Flexure with axial tensile load	0.90
Shear and torsion	0.85
<i>Compression and flexo compression</i>	
Elements with spirals	0.75
Elements with stirrups	0.70

2.7 Earthquake Load (S_x , S_y)

These are those generated by the seismic action on the structure through a dynamic spectral analysis. The Design Combinations required according to the E.060 Standard for reinforced concrete elements, for the purposes of this project, Table 1 are shown below:

Where: Dead loads (D), live loads (L) and seismic (S_x , S_y).

Reinforced concrete structures and structural elements shall be designed to obtain in all their sections resistances at least equal to the required or ultimate resistances (R_u) calculated for the amplified loads in the combinations stipulated in NTE E060, this method is called Design by Ultimate Resistance (Design Resistance > Required Resistance). On the other hand, in order to take into account the effects of variability of the nominal resistance (R_n), resistance reduction factors (ϕ) are introduced according to the stress to which the element is subjected, Table 2 shows factors that are:

2.8 General Conditions for Design

The structural modelling will be based on a three-dimensional modal analysis with the seismic spectrum that governs the Seismic Resistant Standard, which will be scaled to the minimum static force required by the standard (See 29.4.1 Minimum

Fig. 2 Floor 5th level to 6th level

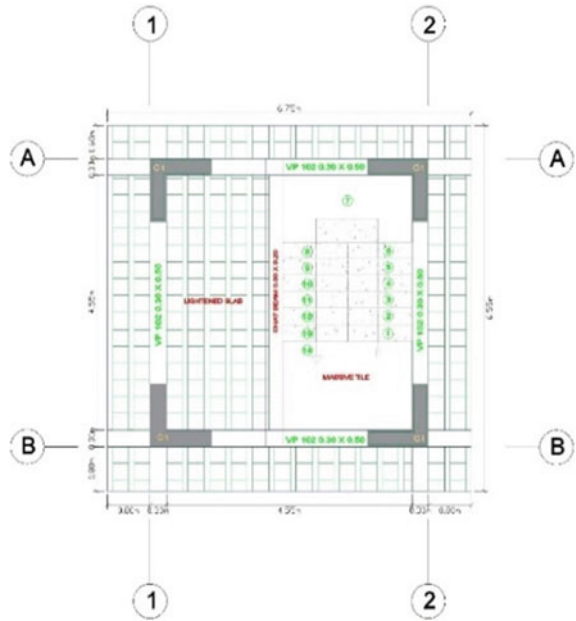


Table 3 Geotechnical condition periods

Soil factor "S"				
Soil and area	S0	S1	S2	S3
Z4	0.80	1.00	1.05	1.10
Z3	0.80	1.00	1.15	1.20
Z2	0.80	1.00	1.20	1.40
Z1	0.80	1.00	1.60	2.00

Table 4 Geotechnical condition factor soil

Periods "TP" Y "TL"				
	Soil profile			
	S0	S1	S2	S3
TP (S)	0.3	0.4	0.6	1.0
TL (S)	3.0	2.5	2.0	1.6

2.10 Seismic Amplification Factor

The indications of Standard E-030 for the fundamental period shall be considered, considering the provisions of chapter "2.5 Seismic Amplification Factor (C): This coefficient is interpreted as the amplification factor of the structural acceleration with

respect to the acceleration in the ground. According to the site characteristics, the seismic amplification factor (C) is defined by the following expressions:

$$T < T_P \quad C = 2, 5 \tag{1}$$

$$T_P < T < T_L \quad C = 2, 5 \cdot \left(\frac{T_P}{T} \right) \tag{2}$$

$$T > T_L \quad C = 2, 5 \cdot \left(\frac{T_P \cdot T_L}{T^2} \right) \tag{3}$$

where: T is the fundamental period of the structure.

As stipulated in Standard E-030 number 4.5.4 Fundamental Period of Vibration, for each direction it shall be estimated with the following expression:

$$T = \frac{h_n}{C_T} \tag{4}$$

CT = 35 For buildings whose resistant elements in the direction considered are only reinforced concrete frames without shear walls.

$$h_n = 18.20 \quad T_x = 0.52 \quad T_y = 0.52 \tag{5}$$

Therefore, we have the following fundamental periods of vibration:

$$T_P = 0.6 > T_x = 0.52; \text{ por lo tanto, } C_x = 2.50 \tag{6}$$

$$T_P = 0.6 > T_y = 0.52; \text{ por lo tanto, } C_y = 2.50 \tag{7}$$

2.11 Building Category and Use Factor

Buildings where large numbers of people gather such as cinemas, theatres, stadiums, coliseums, shopping centres, passenger terminals, correctional facilities or those housing valuable heritage such as museums and libraries. These are in category B of important buildings with a U-factor of 1.30.

2.12 Structural Configuration of the Building

According to Chap. 3.5 of the E.030 Seismic Resistant Design Standard: “structures must be classified as regular or irregular in order to determine the appropriate analysis procedure and the appropriate values of the seismic force reduction factor”. According to the above, we must analyse the structure and determine whether it qualifies as regular or irregular, for which we must evaluate the building both in height and in plan. A regular behaviour is estimated, which will be determined later with the dynamic seismic analysis.

2.13 Structural System and Seismic Reduction Coefficient

According to the reinforced concrete structural system, the frames have a basic reduction coefficient R_0 (*) of 8 ($R_{0X} = 8$ $R_{0Y} = 8$), (see Fig. 3).

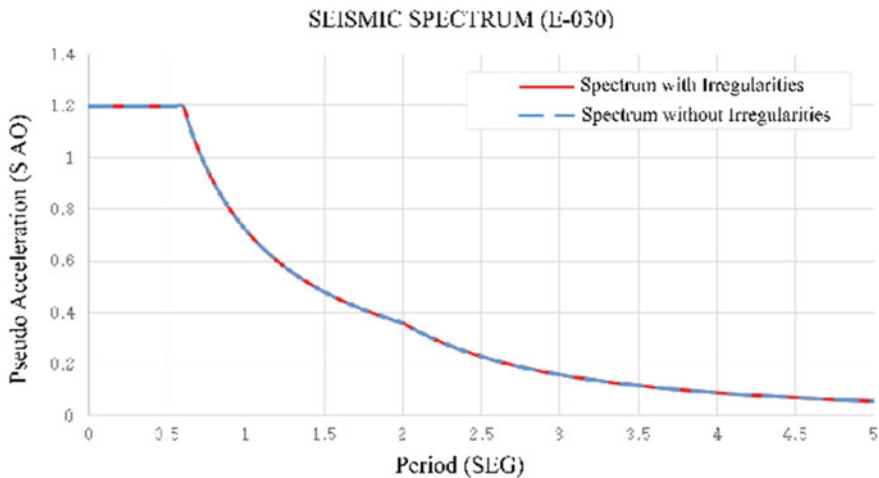


Fig. 3 Seismic spectrum for X, Y directions

3 Results

3.1 Weight of the Building

It will be considered what is indicated in the Standard E-030 for the weight of the structure we consider what is established in the chapter “4.3 Estimation of the Weight (P)” for which: “b. In category C buildings, which indicates that 50% of the live load shall be taken”, for which the following estimated weights shown in Table 5 are used:

$$\text{Weight Structure} = 100\% (\text{Own Weight} + \text{Finishes} + \text{Partitioning}) 50\% (\text{C. Viva}).$$

Weight Structure = 1.00 (245.93) + 0.50 (37.04). Statistical data is displayed in the following Table 6, also the first 3 data are displayed in (Figs. 4, 5, and 6) as an example.

Table 5 Results of gravity loads

Story	Load	P (ton)	Load	P (ton)
Base	Dead	245.93	LIVE	37.04

Table 6 Periods and modes of vibration

Case	Mode	Periodo(s)	UX	UY	RZ	SumRX	SumRY	SumRZ
Modal	1	0.540	0.777	0.000	0.000	0.777	0.000	0.000
Modal	2	0.538	0.000	0.777	0.001	0.777	0.777	0.001
Modal	3	0.471	0.000	0.001	0.189	0.777	0.777	0.789
Modal	4	0.131	0.123	0.000	0.000	0.899	0.777	0.789
Modal	5	0.131	0.000	0.122	0.000	0.899	0.899	0.790
Modal	6	0.117	0.000	0.000	0.108	0.899	0.899	0.898
Modal	7	0.055	0.033	0.000	0.000	0.932	0.899	0.898
Modal	8	0.055	0.000	0.032	0.000	0.932	0.931	0.898
Modal	9	0.052	0.000	0.000	0.030	0.932	0.932	0.928
Modal	10	0.030	0.011	0.000	0.000	0.943	0.932	0.928
Modal	11	0.030	0.000	0.011	0.000	0.943	0.943	0.928
Modal	12	0.029	0.000	0.000	0.011	0.943	0.943	0.940
Modal	13	0.019	0.000	0.005	0.000	0.943	0.948	0.940
Modal	14	0.019	0.005	0.000	0.000	0.948	0.948	0.940
Modal	15	0.018	0.000	0.000	0.006	0.948	0.948	0.945
Modal	16	0.013	0.000	0.003	0.000	0.948	0.950	0.945
Modal	17	0.013	0.003	0.000	0.000	0.960	0.950	0.945
Modal	18	0.013	0.000	0.000	0.003	0.960	0.950	0.949
Modal	19	0.010	0.000	0.000	0.000	0.960	0.950	0.949
Modal	20	0.010	0.050	0.000	0.000	1.000	0.950	0.949

Fig. 4 Deformation of the structure due to the mode 1

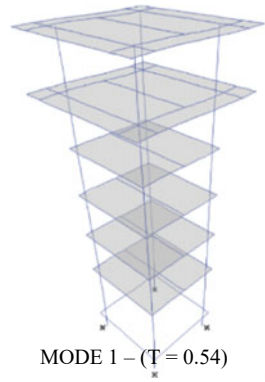


Fig. 5 Deformation of the structure due to the mode 2

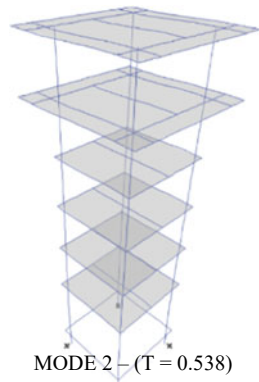


Fig. 6 Deformation of the structure due to the mode 3

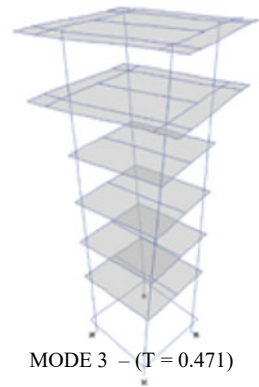
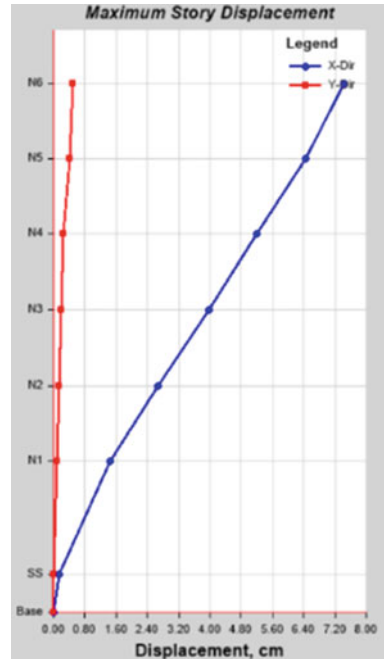


Fig. 7 Maximum displacement per level by earthquake “Sx”



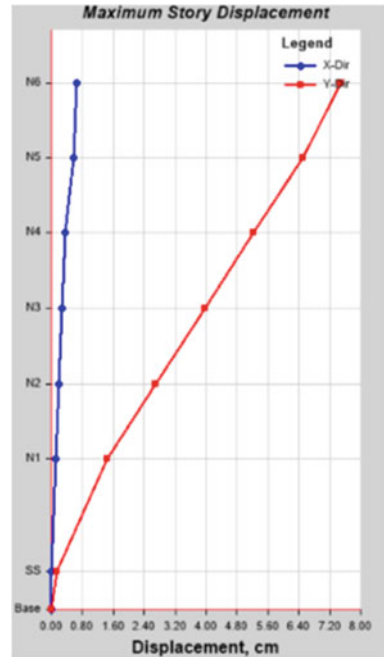
3.2 Lateral Displacement Control

The Standard establishes that the calculation of lateral displacements for regular structures shall be done by multiplying by 0.75 times the value of R the results of the displacements obtained in the analysis, and for irregular structures by multiplying by 0.85 times the value of R the results of the displacements obtained in the analysis. The Standard also establishes that the maximum relative displacement of the floor-to-ceiling ratio shall not exceed the fraction of the floor-to-ceiling height, which for reinforced concrete structures is equal to 0.007. the resulting graphs can be seen in (Figs. 7 and 8).

3.3 Foundation Design

In (Fig. 9a) shows the soil pressure diagram for the in-service case S1(D + L). The maximum pressure is $1.0 \text{ kg/cm}^2 < 1.25 \text{ kg/cm}^2$ (Soil pressures case S1 in kg/cm^2). (Fig. 9b) shows the soil pressure diagram for the service case S2 (D + L + 0.8.SX). The maximum pressure is $1.16 \text{ kg/cm}^2 < 1.25(1.3) = 1.63 \text{ kg/cm}^2$ (Soil pressures case S2 in kg/cm^2). (Fig. 9c) shows the diagram of soil pressures for the in-service case S3 (D + L + 0.8.SY). The maximum pressure is $1.16 \text{ kg/cm}^2 < 1.25(1.3) =$

Fig. 8 Maximum displacement per level per earthquake “Sx”



1.63 kg/cm² (Soil pressures case S3 in kg/cm²). (Fig. 9d) bending resistance (bending moment (tonf-m/m) of footing).

The design of the footing foundation is based on the combination of several processes, including: soil investigation, structural analysis, foundation design [13]. In (Fig. 10) it can be seen that the construction project of the clock tower ends based on this investigation.

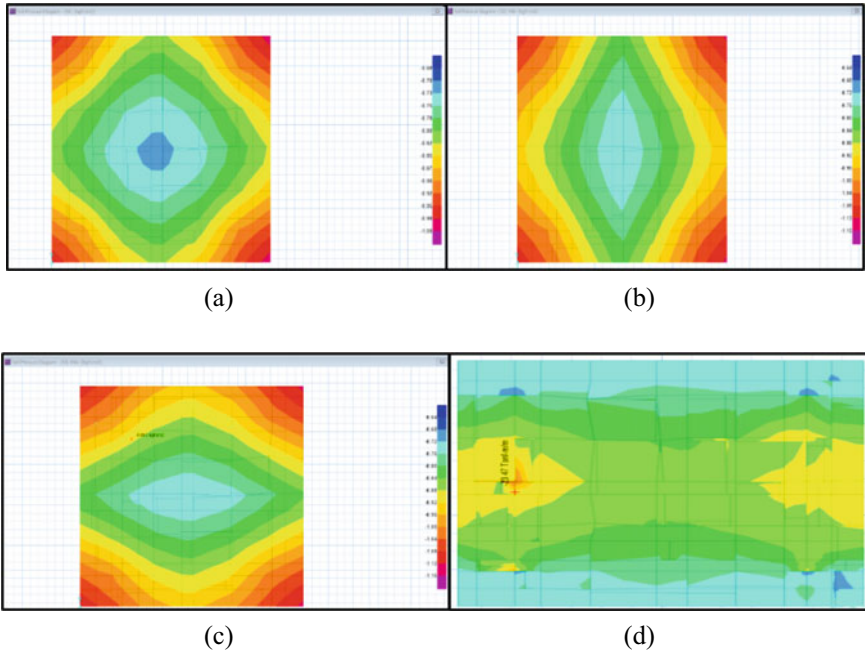


Fig. 9 Soil pressure diagram

Fig. 10 Clock tower completed



4 Conclusion

Required Design Combinations are established according to RNE Standard E.060 for reinforced concrete elements. of the RNE for reinforced concrete elements, for the purposes of this project was designed and reinforced concrete structural elements with the Ultimate Strength Design method with sections of required strengths calculated for the amplified loads in the combinations that are stipulated in the NTE E060. That it was demonstrated under the structural modeling based on a three-dimensional modal analysis with the seismic spectrum that governs the Seismic Resistant norm in mention, that will be scaled to the minimum static force that demands the norm Norm E 0.30 of the RNE, being that the structure fulfills the symmetry, as much in the distribution of masses as in the rigidities, adequate resistance, continuity in the structure, as much in plant as in elevation, ductility of the connections, hyperstaticity and monolithism, lateral rigidity and rigid diaphragm. In addition, it is established that the displacement control shall not exceed the fraction of the floor-to-ceiling height that for reinforced concrete structures, which is complied with in the regulations. It is concluded that the design of the structure complies with all the regulatory bases of the RNE and also of the seismic-resistant analysis that is zoned according to its location, therefore this dynamic seismic analysis in the structure of the clock tower according to the type of soil, the Clock Tower which was executed and designed satisfactorily for the locals of Quispicanchi, being this a convenient background of the importance of a well-designed structure according to the regulations in the location of the land above all the welfare of the population.

References

1. Shamim M (2022) Dynamic seismic analysis of multi storey buildings in seismic zone V. *Int J Res Appl Sci Eng Technol (IJRASET)* 10(2)
2. Fundora Sautié N, Braña Nuez P, Gamón Payret R, Martínez Cid JO (2022) Influence of height on the consideration of dynamic soil-structure interaction in buildings with mixed typology located in high seismic hazard zones. *Eng Develop* 40(01):6–27. <https://doi.org/10.14482/inde.40.01.621.852>
3. Del Carpio F, Soto Chacon A (2022) Analysis of the magnitude of the seismic wave energy transferred to the foundation of a building. *Constr. Eng. Magazine* 37(2):131–146. <https://doi.org/10.7764/ric.00022.21>
4. Luévanos Rojas A (2011) Analysis of two models by the dynamic method for seismic building design. *Architect Eng Magazine* 5(3). Retrieved from <https://dialnet.unirioja.es/servlet/articulo?codigo=4727196>
5. Caysevíc M, Mitrovic S (2011) Comparison between non-linear dynamic and static seismic analysis of structures according to European and US provisions. *Bull Earthquake Eng* 9
6. Khan M, Ali M, Karimuddin K, Charan S (2022) Comparative study of linear static and linear dynamic method of seismic analysis of RCC multistoried building using ETABS. *Int J Res Appl Sci Eng Technol (IJRASET)* 10(5)
7. Escobedo L, David D, Albino T, Carlos J (2020) Comparison between 3 alternative connection types in a steel building under seismic loads. *Eng Res Technol* 21(3):00008. Epub 02 December of 2020. <https://doi.org/10.22201/ri.25940732e.2020.21.3.028>

8. Li J, Li F, Cai Z (2019) Seismic analysis of a multi-storey office building based on SAP 2000. In: Dhileep M, Arumairaj PD, Hemalatha G (eds) IOP conference series: earth and environmental science “a dynamic correction for the seismic analysis of structures” innovative infrastructure solutions
9. Patricia M, Vivian E (2012) Seismic analysis of Cuban models of self-supporting telecommunication towers. *Cuban J Eng* 3(2)
10. Calderín-Mestre F, Almenarez-Labañino D, Boada-Fernández D (2020) Consideration of the soil-structure interaction phenomenon in prefabricated building. *Science* 1(4):79–94. ISSN: 1027–2887. Disponible en: <https://www.redalyc.org/articulo.oa?id=181366194007>. Accessed on 21 Nov 2022
11. Lemar M, Akcay C, Manisali E (2019) Time-cost optimization using harmony search algorithm in construction projects. *Constr. Magazine* 18(2):226–237. <https://doi.org/10.7764/rdlc.18.2.226>
12. National Training Service for the Construction Industry [Internet]. Gob.pe. Retrieved from <https://www.gob.pe/institucion/sencico/informes-publicaciones/887225-normas-del-reglamento-nacional-de-edificaciones-rne>. Accessed on 19 Dec 2022
13. What is the process of designing a support base? (2019) [Internet]. SkyCiv | cloud structural analysis software and calculators. Retrieved from <https://skyciv.com/es/docs/tutorials/foundation-design-tutorials/the-process-of-designing-a-footing-foundation/>. Accessed on 19 Dec 2022

**Building Integrated Photovoltaics,
Building Thermal Environment
and Thermal Comfort**

A Case Study on the Design Model of Sunroom in the New Rural Houses in West China from the Perspective of Carbon Emission



Yiming Zhang, Yu Liu, Minmin Yang, Yufei Zou, Jie Song, and Wenqiang Li

Abstract In the solar radiation enriched areas of west China, solar heat gain has a significant impact on the heating demand of houses, thus the application of solar energy technology in new rural houses is becoming popular. Taking a new rural house project in west China as a case, this paper studied a number of factors influencing solar energy utilization in sunroom with Design Builder software and came up with some results and recommendations for the design of sunroom from the perspective of carbon emission reduction: (1) If local new rural house has the attached sunroom and it is oriented to south direction, the carbon emissions of rural house can be reduced by about 20% per unit area. (2) Sunroom roof with southward slope can well reduce the heat load of the rural house. (3) Height of the sunroom should be not higher than that of its adjacent back wall, otherwise opaque partition structure is preferable to be used. (4) With the same land area and construction area of the case project, the recommendable width and depth of the south-facing sunroom is 4.8 and 3.9 m respectively.

Keywords Case study · Sunroom · Rural house · Carbon emission

Y. Zhang · Y. Liu (✉) · M. Yang · Y. Zou · J. Song · W. Li
School of Mechanics, Civil Engineering and Architecture, Northwestern Polytechnical University,
Xi'an, China
e-mail: liuyu@nwpu.edu.cn

Sustainable Building and Environmental Research Institute, Northwestern Polytechnical
University, Xi'an, China

J. Song
School of Architecture, University of Liverpool, Liverpool, United Kingdom

© The Author(s), under exclusive license to Springer Nature Singapore Pte Ltd. 2024
M. Casini (ed.), *Proceedings of the 3rd International Civil Engineering and Architecture
Conference*, Lecture Notes in Civil Engineering 389,
https://doi.org/10.1007/978-981-99-6368-3_36

1 Introduction

Solar energy utilization in buildings can improve their thermal comfort in winter and effectively reduce carbon emissions during operation [1]. Literature review also shows that “carbon emission” has become a new perspective on the research of passive solar energy utilization.

Qinghai locates in a cold & severe cold climate zone in west China. It is rich in solar energy resources with long and cold winters and large daily temperature differences, so has a good potential for solar energy utilization. Passive solar energy utilization in Qinghai rural houses has the advantages of low cost and high efficiency. With increasing emphasis on green energy-saving technologies, there is a trend to develop passive solar energy utilization for buildings in west China. Among different types of passive solar energy utilization in buildings, sunroom is more commonly used in west China.

In 2008, Liu et al. [2] tested and analyzed the solar house performance in the Qinghai-Tibet Plateau region and found that the collector-storage wall solar house has good heat collection and storage performance, and calculated the optimal use pattern of the collector-storage wall. In 2017, Bai Yang et al. [3] from the perspective of solar energy utilization potential, several settlement forms in severe cold regions were measured and simulated, and the solar radiation intensity distribution was analyzed with EnergyPlus software and IESVE software. In 2019, Weixian Jiang [4] used Designbuilder to analyze the solar energy consumption of three regions of Qinghai Xining, Tibet Lhasa and Xinjiang Turpan, so that the solar energy utilization of the scheme could be improved. In 2022, Yang Xiaojing [5] carried out post-use evaluation on the 24 Zhuangkuo Profiles under the Riyueshan Mountains (hereinafter referred to as Project) in Qinghai Province, she obtained the environmental performance data analysis and post-use subjective evaluation of the project, and explored the relationship between typical sunroom scale and indoor thermal environment.

While existing studies have already improved the research tools and pathways for passive solar energy utilization, with the emergence of the “double carbon” target, “carbon emission” has become a new perspective for measuring building energy consumption. Therefore, in this paper, from the perspective of “carbon emission”, we extract the typical house types of new rural houses in Qinghai Province, west China from “24 Zhuangkuo”, and study the effect of the orientation, depth, and height of additional sunrooms and atrium sunrooms on the energy consumption of buildings using the Design Builder dynamic simulation analysis technology. Based on the results of the analysis, we further propose the design pattern of sunrooms in West China.

Fig. 1 Number and location of buildings. *Source* Edited by the author based on the UAV photos of the project team



2 Project Overview

The project is located in Huangyuan County, Qinghai Province, with a continental monsoon climate and annual average temperature of 3 °C. The project site is flat with no obvious sunlight shading around.

There are 10 buildings on the site, including 24 rural houses, 1 restaurant, 1 art center, and 1 activity center (Fig. 1), in which two rural houses (building 4# and 5#) with different type of sunrooms are analyzed in this paper.

3 Typical Buildings



Two typical buildings (4# and 5#) were selected according to the form and shape coefficient of their sunroom, more information of which is shown in Table 1.

4 Software Simulation

4.1 Tool Selection

There are many software for building energy simulation, and most of these software are based on OpenStudio, EnergyPlus kernel, which can derive the annual heat/cooling load, energy consumption and carbon emission of the building through the input of building information, thermal information and human activities. This paper focuses on the impact of sunroom on carbon emissions in the process of building

Table 1 Basic information of the two typical buildings

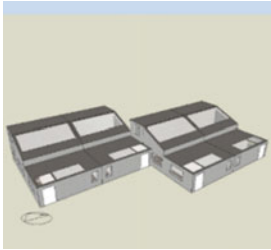
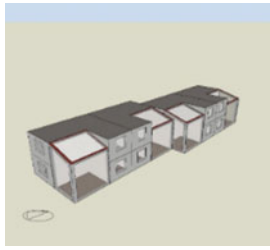
	Building 4#	Building 5#
First floor plan		
Building volume/m ³	1471.08	1306.20
Building area/m ²	433.6	466.4
Building surface area/m ²	915.72	782.3
Body shape factor	0.622	0.599
Sunroom area/m ²	32.44	16.69
Form of sunroom	Atrium-type sunroom	Attached sunroom

operation. Through comparative analysis, DesignBuilder was finally selected for simulation and calculation.

4.2 Model Setting

The above two building units were simulated using DesignBuilder software. Parameters of the buildings construction were set as follows: the heat transfer coefficient of exterior wall (80 mm concrete slab + 130 mm graphite polystyrene b1 + 240 mm modified rammed earth wall) was 0.32 W/m²·K, the south window-wall ratio was 0.25. The parameters of the indoor environment were set as follows: air changes in the building was 0.5 times/h, heating temperature of bedroom was 20°C, heating temperature of living room, dining room and bathroom was 18°C, starting temperature of heating system was 0.5 times/h. 18°C, starting temperature of heating was 12°C. Sun room was not heated. According to the Thermal Design Code for Civil Buildings (GB 50,176–2016) in China, the number of air-conditioning degree days in Qinghai Province is 0, so the air-conditioning in summer was not considered in the setting. Original model based on the above setting is shown in Table 2.

Table 2 Design builder model

Building 4#	Building 5#
	

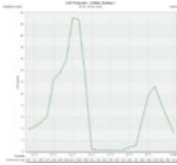
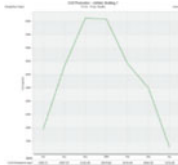
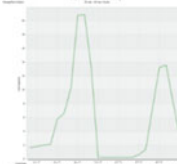
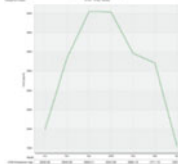
4.3 Results of Simulation

Two Representative time period were selected: (1) the heating period (October 15th–April 15th); (2) the Big Cold Day (January 20th, a solar term in the traditional Chinese calendar) to further analysis. Results of a preliminary simulation based on the original model and typical scenario is shown in Table 3.

The following conclusions are drawn:

The daily CO₂ emissions per unit area on the Big Cold Day are basically consistent with that in the heating period, with a difference within ± 5%.

Table 3 Preliminary results of simulation

	Big cold day (January 20th)		Heating period (October 15th–April 15th)	
	Carbon emission/kg	Daily carbon emission per unit area/kg·(m ² ·d) ⁻¹	Carbon emission/kg	Daily carbon emission per unit area/kg·(m ² ·d) ⁻¹
4#	167.76	0.386900369	27,642.47	0.348366579
				
5#	136.04	0.291680961	25,172.44	0.294927781
				

The per unit energy consumption of building 4# is higher than that of building 5#, the reason of which need to be further explored.

5 Correlation Analysis

5.1 Orientation

To study relationship between sunroom and CO₂ emissions of rural houses, it is necessary to first determine the optimal orientation of them. Based on the typical model, orientation of the building was set at 45°SW, 30°SW, 15°SW, S, 15°SE, 30°SE, and 45°SE for the simulation. The result shows that (Fig. 2):

- (1) When the building is facing due south, the sunlight is best utilized and the CO₂ emission per unit area of the building is the least.
- (2) Taking 15° as a step, the CO₂ emission per unit area of the building is approximately parabolic with the angle. The larger the angle of orientation offset, the larger the CO₂ emissions per unit area for each step.

Therefore, further study was conducted based on the due south orientation of the building.

5.2 Sunroom

With or Without Sunroom. Experimental models were established to determine whether the presence or absence of sunroom has an impact on building’s CO₂ emissions. The original sunroom of building 4# and 5# were deleted and set as unheated indoor space, and the rest of the conditions remained unchanged (Table 4).

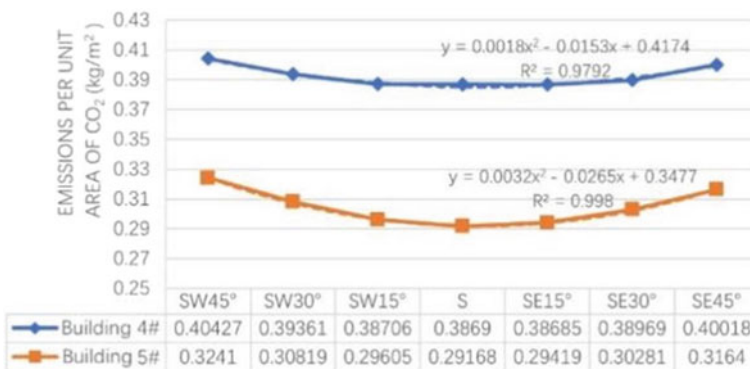
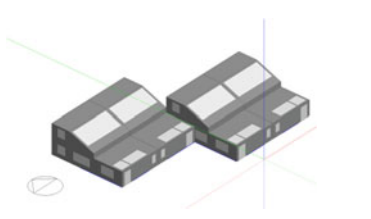
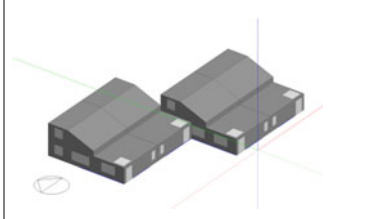
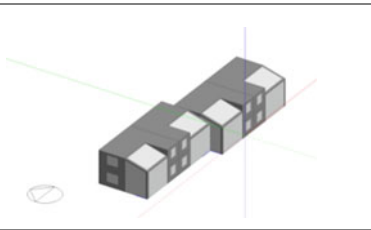
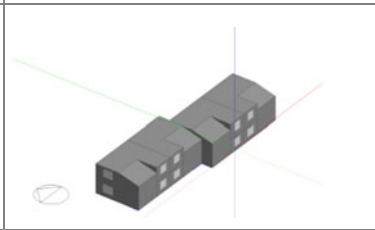


Fig. 2 Relationship between CO₂ emissions and building orientation

Table 4 Experimental modeling with and without sunroom simulation comparison

	With sunroom	Without sunroom
Building 4#		
Building 5#		







The results show that the CO₂ emissions of building 4# and 5# increased by 16.67 and 28.80% respectively after deleting their sunroom (Table 5).

Slope of Sunroom Roof. The slope of sunroom roof can affect the angle of sunlight incidence, thus affecting the heating load of the building. Different slope of roof of sunroom were set and with the rest conditions remained unchanged. Result are shown in Table 6 and Fig. 3.

Table 5 Experimental results of comparison between with and without sunroom

	With sunroom		Without sunroom		
	Carbon emission/kg	Carbon emission per unit area/kg/m ²	Carbon emission/kg	Carbon emission per unit area/kg/m ²	Percentage of change (%)
4#	167.76	0.386900369	195.74	0.451429889	+16.67
5#	136.04	0.291680961	175.21	0.375664666	+28.80

Table 6 Sunroom roof slope simulation experiment grouping and modeling

Sunroom roof slope		0°	15°	30°
4#	East elevation			
5#	East elevation			

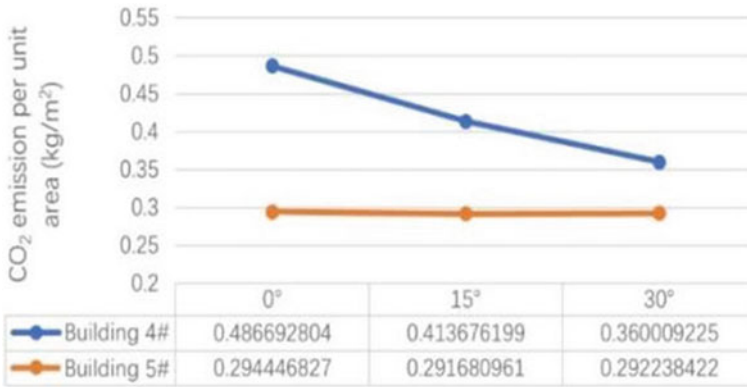


Fig. 3 Analysis of the relationship between CO₂ emissions and the slope of the sunroom roof

The slope of the sunroom roof is negatively correlated with the CO₂ emissions of building 4# (Fig. 3). There are user activities in the atrium sunroom, a larger transparent roof can provide better lighting conditions of such space and effectively reduce heating load of the building. On the contrary, roof slope of sunroom has little impact on building 5#, and only exists as a buffer cavity between the building and the outdoor environment, which would not affect indoor environment.

Height of Sunroom. Height of sunroom can affect indoor ventilation and lighting and indoor flow of hot and cold air, which affects the heating load and CO₂ emissions of buildings. In this study, height of sunroom was changed, with other conditions remain. Detailed settings are shown in Tables 7 and 8.

The height of sunroom may be higher than that of the main building envelop. In such case, the north direction can be a glass or a solid wall, the former of which will let in more light, and the latter can reflect more sunlight to the interior (Fig. 4).

Results shows that: (1) Decreasing height of sunroom could increase heating load of south-facing rooms, thus increase CO₂ emission of the building. (2) Increasing height of sunroom could increase heating load and CO₂ emissions of the building. (3) When height of sunroom is equal to that of the building envelop at the same side, heating load and CO₂ emissions of the building are the least (Fig. 4). When height of the sunroom is higher than that of the building envelop, heating load and CO₂

Table 7 Sunroom height simulation experiment grouping and modeling of building 4#

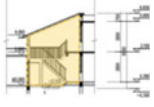
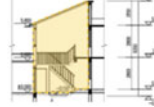
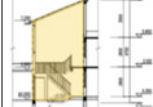
Sections			
Sunroom height/m	4.4	5.8	7.2

Table 8 Sunroom height simulation experiment grouping and modeling of building 5#

Sections					
Sunroom height/m	2.8	4.2	5.6	7	8.4

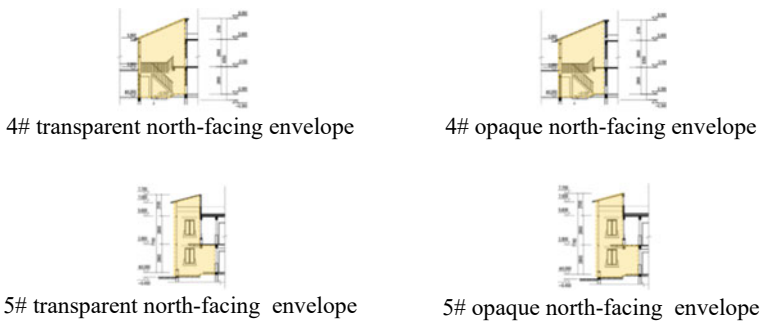
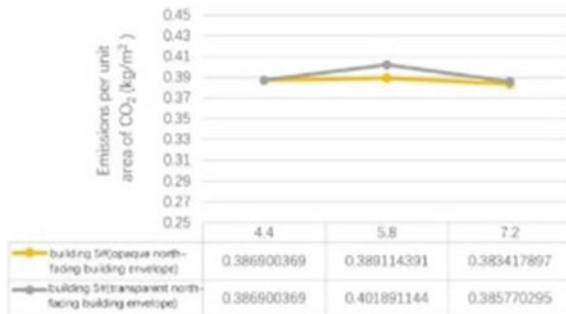


Fig. 4 Material comparison test group for the northward part of the sunroom

emission of the north-facing space enclosed with solid walls is smaller than that of the enclosed with glass (Figs. 5 and 6).

Width of Sunroom. Width of the sunroom has the potential to directly affect the floor area of the sunroom, and thus the sun’s heating of the adjacent room in the sunroom and the flow of hot air in the sunroom. The atrium sunroom of building 4# would also change the user activities inside it if it was changed, so experiment was conducted only for the south-facing sunroom of building 5#. While keeping the total

Fig. 5 Building 4# CO₂ emissions versus height of sunroom



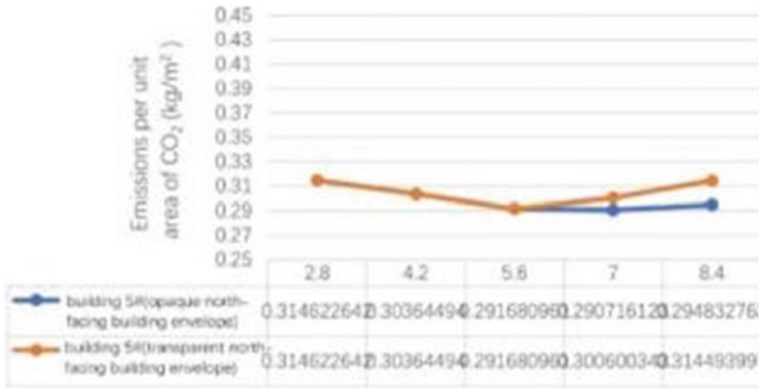


Fig. 6 Building 5# CO₂ emissions versus height of sunroom

floor area unchanged, the width of the sunroom was changed, and five experimental groups of 3.6, 4.2, 4.8, 5.4, and 6 m were set up in 0.6 m steps respectively (Table 9).

Results show that, with the same total floor area, the building heating load and CO₂ emission per unit area is the lowest when the width of south-facing sunroom is 4.8 m (Fig. 7).

The Depth of Sunroom. This experiment is conducted only for the south-facing sunroom of Building 5#. First, keep the total floor area and change depth of the sunroom. Detailed setting are shown in Table 10.

Results of analysis shows that, the south-facing sunroom with a depth of 3.9 m has the lowest heating load and CO₂ emissions per unit area (Fig. 8). The changes of carbon emission per unit area for the remaining four control groups were +7.32, +8.50, +0.23, and +2.54% respectively, compared with the original model.

Then, keep living space area and change depth of the sunroom to 2.7, 3.3, 3.9, 4.5, and 5.1 m respectively. Detailed setting are shown in Table 11.

Results shows that, with the same living area, the south-facing sunroom with a depth of 3.9 m has the lowest heating load and CO₂ emissions. Changes of carbon

Table 9 Experimental grouping of sunroom width

Plans					
Sunroom width/m	3.6	4.2	4.8	5.4	6
Sunroom area/m ²	12.30	14.49	16.69	18.89	21.08

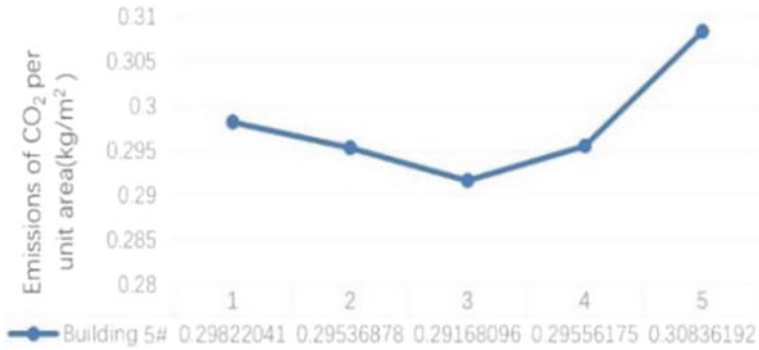


Fig. 7 CO₂ emissions versus width of sunroom

Table 10 Experimental grouping of sunroom depth (building area remains unchanged)

Plans					
Sunroom depth/m	2.7	3.3	3.9	4.5	5.1
Sunroom area/m ²	11.22	13.95	16.69	19.94	22.16

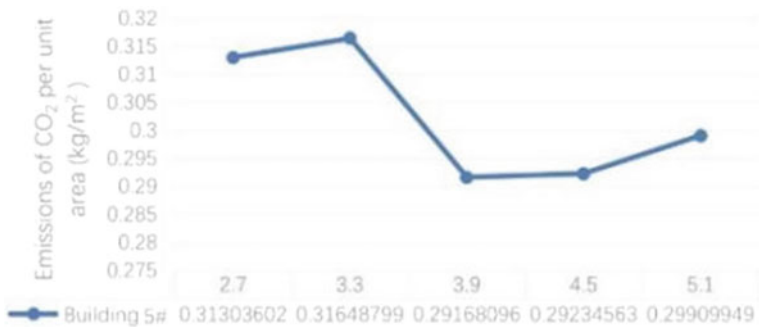







Fig. 8 CO₂ emissions versus depth of sunroom (building area remains unchanged)

Table 11 Experimental grouping of sunroom depth (living space area remains unchanged)

Plans					
Sunroom depth/m	2.7	3.3	3.9	4.5	5.1
Building area/m ²	460.9	463.7	466.4	469.7	471.9
Sunroom area/m ²	11.22	13.95	16.69	19.94	22.16

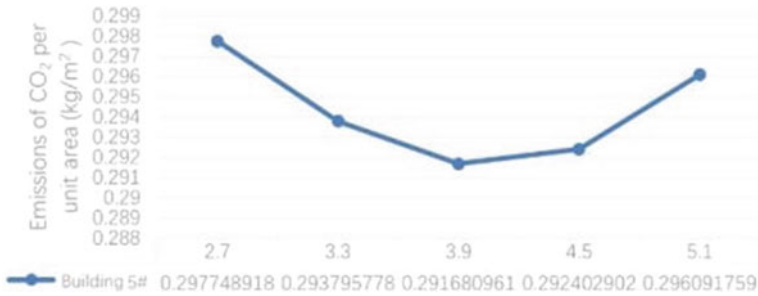


Fig. 9 CO₂ emissions versus depth of sunroom (living space area remains unchanged)

emission in the remaining four control groups are +2.08, +0.72, 0.24, and 1.51%, respectively (Fig. 9). Compared with the previous analysis, change of depth has smaller impact on carbon emission.

6 Conclusion

Compared with rural houses without sunroom, the rural houses with sunroom can reduce winter heating load Carbon emission by about 20%.

For the atrium sunroom, it is recommended to increasing the southward slope of sunroom roof to provide better daylight conditions, at the same time to reduce the heating load of the building. For the south-facing sunroom, the roof slope has little impact on the building’s carbon emissions, so can be set at the same angle of geographic latitude to facilitate installation of solar panels at a later stage.

The height of the sunroom is not recommended to be higher than the back wall. If the sunroom has to be higher than the back wall, it is recommended to extend the

solid wall upwards to improve the thermal performance of the building, instead of using transparent envelope.

Keep current building construction area, the width and depth of the south-facing sunroom are recommended to be 4.8 and 3.9 m respectively, its outer contour is recommended to be in a relatively straight line with the building's outer wall so that the body shape factor is not too large while volume of the sunroom can be expanded as much as possible.

Acknowledgements 1. The research of this paper was supported by The National Natural Science Foundation of China (No.52078422) 2. Thanks to Prof. Cho Seigen from the Institute of Urban Innovation at Yokohama National University and to A/Prof. David Hou Chi Chow from the School of Architecture at Liverpool University for their valuable advice and suggestions along with the research and writing of this paper.

References

1. China Building Energy Consumption Research Report (2021) [J]Building Energy Conservation 1–6,2021–02–25
2. Liu Y, Liu J, Yang L, Li J et al (2008) Test and research on passive solar traditional residential buildings in Lhasa [J]. *J Solar Energy* (04):391–394
3. Baiyang (2017) Research on optimization of residential morphology in severe cold regions based on solar energy utilization potential [D]. Harbin Instit Technol
4. Weixian J (2020) Research on the design of collective housing in western China using radiation energy conservation [D]. Xi'an Univ Architect Technol. <https://doi.org/10.27393/d.cnki.gxazu.2020.000134>
5. Yang X (2022) Post-use evaluation study on passive solar energy utilization of new residential buildings in Qinghai[D]. Northwestern Polytechnical University

Watertightness Design and Experimental Evaluation of a Solar Panel Structure for Building Integrated Photovoltaics (BIPV) Roofs



Dingqiu Chen and Shaohang Shi

Abstract Building integrated photovoltaic (BIPV) roof technology is gaining popularity and its durability is of concern to different interest groups—watertightness is an important aspect. This study proposes an optimized solar panel structure for BIPV roofs, which aims to achieve watertightness performance; further, watertightness experiments with static and dynamic rainfall (the max wind speed level was 12) were conducted based on GB/T 15227–2019 standard through third-party testing. The results show that the BIPV roof system proposed has good watertightness performance; the water leakage grade is “not severe”. In addition, this study compares the technology application differences of three BIPV roof prototypes and discusses the effectiveness of red dyed test strips in characterizing water leakages. The proposed structure can be a reference for architects and engineers in the early design stage of BIPV roofs, which effectively enhances the durability and the cost investment of waterproofing materials.

Keywords Building integrated photovoltaic (BIPV) · Watertightness performance · Design optimization · Third-party testing

D. Chen

Tianjin University, No. 92 Weijin Road, Nankai District, Tianjin, China

GuangDong Bright Dream Robotics Co., Ltd, Panpu Road, Bijiao Town, Shunde District, Foshan, Guangdong, China

S. Shi (✉)

Tsinghua University, No. 30 Shuangqing Road, Haidian District, Beijing, China

e-mail: 846525618@qq.com

Key Laboratory of Eco Planning & Green Building, Ministry of Education (Tsinghua University), No. 30 Shuangqing Road, Haidian District, Beijing, China

1 Introduction




As global warming caused by climate change becomes more and more severe, countries begin to pay attention to energy saving and emission reduction in various fields [1]. The building sector accounts for more than 30% of the world's total primary energy consumption [2], and the application of renewable energy integration technology in buildings provides an effective solution path. Building integrated photovoltaic (BIPV) roof technology has received a lot of attention from researchers in recent years [3], which is especially valid in nearly zero energy buildings [4]. Compared to BIPV facades [5], PV roofs have many advantages and potential for development because they receive higher radiation intensity and do not affect the view of building users, which also reflects significant economic advantages.

The construction design and shape parameters of BIPV roofs determine the performances of building envelopes [6], which include building energy balance, PV panel heat dissipation, thermal insulation factor, waterproofing, sound insulation, etc. Correspondingly, countries have codes and standards to qualify the structure design of BIPV roofs. Waterproofing of buildings has always been an issue of close attention for architects and engineers—in particular, it affects the energy, economic and safety performance of BIPV roofs.

Building waterproofing usually has two technical paths: building construction design [7] and building advanced material integration [8]. Typical BIPV roof construction design solutions include ventilated BIPV roofs, BIPVs tile products and BIPV skylights (Table 1). In addition, there are differences between BIPV roofs in terms of the heat dissipation effects of PV collectors and whether the angle of PV panels can be adjustable. Ventilated BIPV roofs can reduce excessive PV panel temperatures through thermal convection, which can effectively reduce the power generation losses due to photovoltaic efficiency decreasing when heated up.

The building advanced material applied in roof systems achieves waterproofing through the hydrophobic nature. Gonçalves et al. [11] compared the life-cycle performance of different flat roof waterproofing solutions, considering environmental and economic aspects; this study found that the bituminous membranes were the best option for all roof types. But if the weight of cost is reduced, then Thermoplastic polyolefin (TPO) film will be the best choice. Talib et al. [12] investigated waterproofing materials in real buildings in Malaysia and the UK; based on the results of case studies, this study found that the causes of the building water leakage are basically the same in both countries, although the climatic zones are different. The study also noted that most contractors have a 10–15 years warranty on waterproofing materials and that choosing the best solution during project construction stage will ensure the best performance. Building waterproofing materials are usually utilized in BIPV roof systems, however, they are also usually affected by aging (leading to loss of effectiveness), short service life, material cycling stability, material deformation due to temperature increase and high maintenance costs [13]. By choosing a reasonable construction design solution in early design stage, the costs of roof system maintenance can be reduced, thus providing advantages from economic and

Table 1 A comparison study of different BIPV roof prototypes

Case studies	(a) Ventilated BIPV roofs	(b) BIPV's tile products	(c) BIPV skylights
Waterproofing techniques	Roof waterproofing layer, architecture advanced materials integrations	Roof waterproofing layer (architecture advanced materials integrations)/rolled metal edges (building construction design)	Sealing glue, architecture advanced materials integrations; constructing connections building construction design
Relationship between PV panels total area (A_{PV}) and roof area (A_{ROOF})	A_{PV} can be larger than A_{ROOF}	A_{PV} should be less than A_{ROOF}	A_{PV} should be less than A_{ROOF}
PV heat dissipation	Good	Not good	Not good
PV angle	Flexible	Same as roof slopes	Same as roof slopes
Diagram (figure <i>source</i> references [9, 10])			

environmental perspectives. Among the various BIPV roofs, ventilated BIPV roofs have better heat dissipation (higher energy production under the same solar radiation) and flexible construction for the parameter shape design—it is worth exploring waterproofing construction design for this type of BIPV roof. In summary, there is a research gap on how to better the waterproofing of BIPV roof systems through PV panel structures without relying on advanced building materials such as TPO or sealing glue.

Therefore, this study proposes a new PV panel structure which can ensure roof waterproofing for ventilated BIPV roofs (Fig. 1). This solar panel structure has the following features (1) the angle of the PV panels can be flexible according to the local sunlight conditions in the early design stage and not same as roof slopes—this makes sure improving the energy efficiency of the PV system and also enhance the roof drainage; (2) Through natural convection flow, the ventilated BIPV roofs can avoid the loss of power generation efficiency due to the high temperature of the PV panels, which ensure a long service life of the PV system; (3) This PV structure is of lightweight, which can save labor and material costs in the construction process.

In this study, a PV panel structure was developed for watertightness purposes, and then a prototype (scale 1:1) was constructed. Subsequently, third-party testing experiments were introduced, and the testing party was China Academy of Building Research Testing Center Co., Ltd. Finally, the watertightness of the proposed BIPV roof system was discussed based on the experiment results.

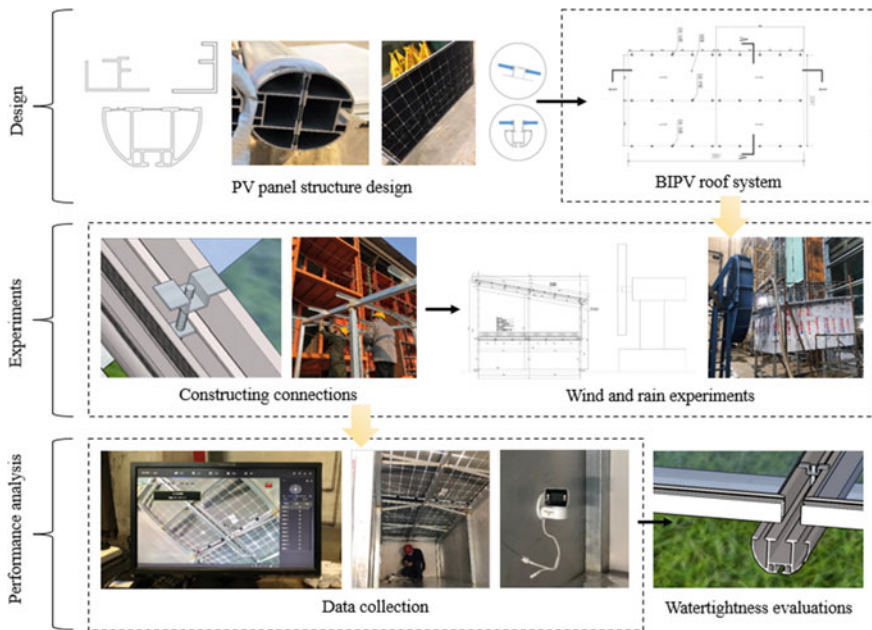


Fig. 1 Research framework

2 Materials and Methods

2.1 Related Codes and Standards

BIPV roofs of different constructions have restrictions in the early design stage by corresponding codes and standards. For example, when PV products act as skylights, they need to meet safety glass codes. The relevant standards include GB 15,763.3–2009 “Safety glazing materials in building—Part 3: Laminated glass” in terms of stiffness requirements, etc., which makes roof constructions costly. For ventilated BIPV roofs, this study uses GB/T 29907 “Test method for watertightness of curtain walls under dynamic wind pressure” to investigate the watertightness performance of the PV panel structure. The dynamic rain experiment results are determined according to GB/T 15227 “Test method of air permeability, watertightness, wind load resistance performance for curtain walls”. In addition, the observation and recording method is used to determine whether there is water leakage [14]; the leakage status of the structure for experiments includes five levels (Table 2).

2.2 Case Description and Watertightness Experiments

In this study, a third-party test was introduced to verify the watertightness performance of the BIPV roof with the proposed PV panel structure of water conductor (Fig. 2). This test is conducted to investigate the watertightness of the PV panel structures by simulating dynamic rainfall in the laboratory, so as to evaluate the durability of the proposed structure against rain of different levels. The wind speed in the experiment gradually increased from 0 to 12 wind levels, where the wind speed value corresponding to 12 wind levels reached 32.7 m/s or more. When water leakage occurred in the BIPV roof during experiments, the corresponding wind level would be recorded, and the water leakage would be judged as severe or non-severe grade according to leakage grade determination method in Table 2; meanwhile, the number of water leakage points would be recorded.

The workflow of the experiment was performed in the following procedure: (1) Preparation of BIPV roof specimen integrated with PV panel of water conductors. The BIPV roof specimen in experiments was built 1:1, and the structure from top

Table 2 Leakage level of the test structure

Number	Leakage situation	Leakage degree
1	Appearance of water droplets	–
2	Water droplets are linked in a line	–
3	Small amount of water splashing	–
4	Continuous splashing of water	Severe
5	Continuous water outflow	Severe

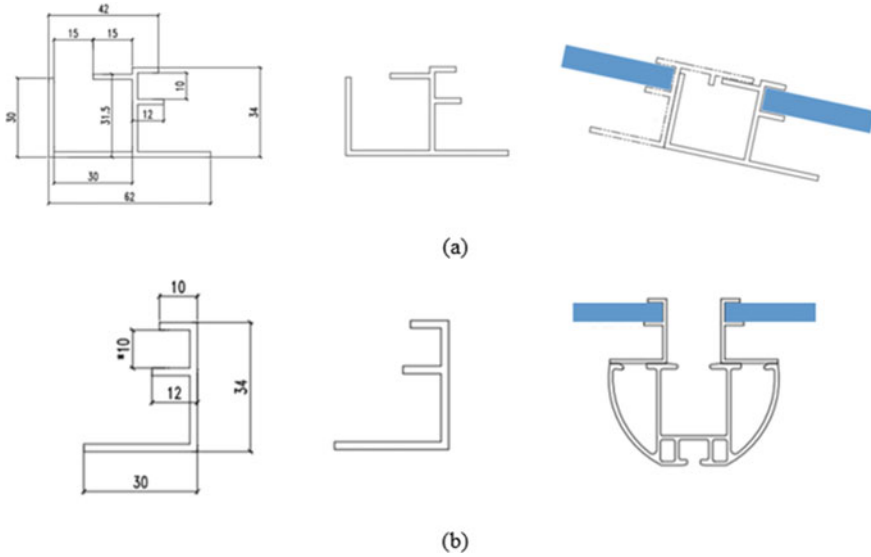


Fig. 2 Water conductors for PV panel in BIPV roof experiments, **a** structure design of the horizontal water conductor for PV panel, **b** structure design of the longitudinal water conductor for PV panel

to bottom included PV panels (including water conductors), BIPV roof cavity, steel frames, roof structure with insulation layers, the fixing bracket for specimen, etc. (2) The BIPV roof specimen is fixed at the test height, where the wind simulator fan (Fig. 3a) is directly in front of the BIPV roof (Fig. 3b). (3) Equipment arrangement and experimental staff work assignment. Third-party experimental staff set up the rain simulator equipment on top of the BIPV roof specimen parallelly. It was ensured that cameras, monitors and other auxiliary recording tools were set up in place. Meanwhile, third party staff (fan controllers, rain sprinkler controllers, water leakage observation recorders, video monitors, etc.) were ready in place. (4) Subsequently, static rainwater and dynamic rainwater experiments would be conducted; the wind speed is continuously increased during dynamic rainwater experiments. The water leakage conditions on the back of the BIPV panel (Fig. 4) was recorded by HD video recorder (Fig. 5) in real time to determine which type of leakage exists in the BIPV roof; experiment results were recorded qualitatively and quantitatively at the same time.

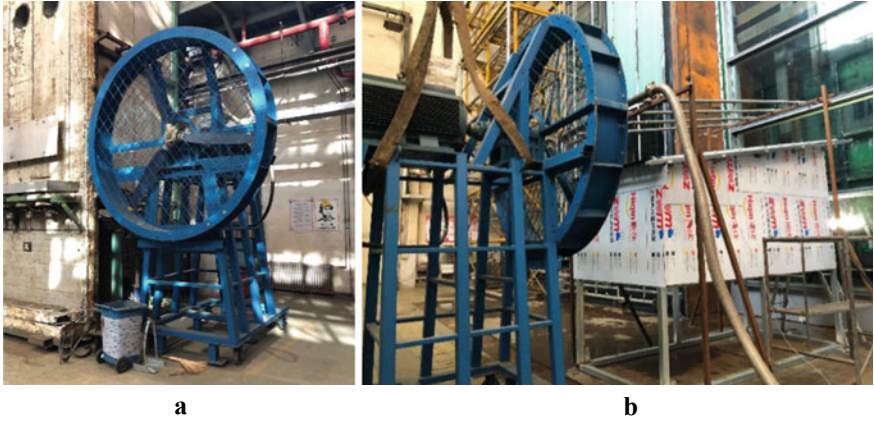
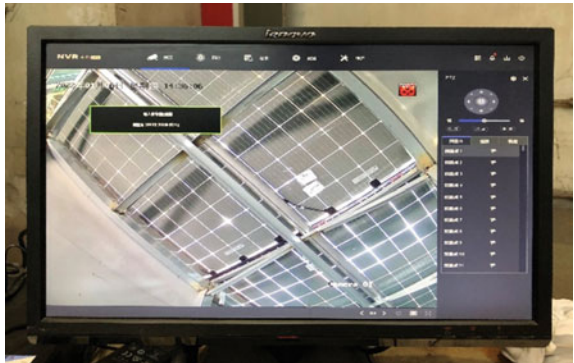


Fig. 3 a Wind simulator fan in experiments; b relative positions of fan and BIPV roof

Fig. 4 The view of the back of the BIPV roof system



Fig. 5 Video-recording interface



3 Results and Discussions

3.1 Watertightness Experiments with Dynamic Rain

Watertightness experiments' results can be seen in Table 3. Experiments with static and dynamic rainwater were conducted and no leakage occurred in the BIPV roof specimen when the wind speed degree was under 6 (the corresponding wind speed was less than 11.1 m/s) according to the experimental results. When the wind speed of dynamic rain is 6 degree, there was a water leak and the corresponding leakage degree is minor; when the wind speed of dynamic rain is 9 degree or more (the corresponding wind speed was greater than 20.8 m/s), the second water leakage appears, and the corresponding leakage degree is minor. It can be found that the BIPV roof with proposed PV panel structure design has a good water insulation capacity.

3.2 Watertightness Performance Comparison of Different BIPV Roofs

For BIPV skylights, light and radiant heat can be collected, but the cost is relatively high and the waterproof sealant is easy to deteriorate. For BIPVs tile products, watertightness is usually achieved by using TPO waterproofing membrane in the roof, and it is suitable for energy-saving renovation of existing buildings; this technology is relatively flexible because the total area of PV panels is not necessarily the same as the total area of roofs. However, the disadvantage of BIPVs tile products is that it is less effective to dissipate heat and may lose solar energy utilization under high PV panel temperature conditions. In this study, proposed ventilated BIPV roofs have great heat dissipation effects and the water conductors designed for PV panels can effectively achieve the watertightness purpose and effectively improve the service life of BIPV roof systems. Therefore, this kind of structure watertightness design for PV panels has the value of promotion.

Table 3 Results recorded of dynamic rainwater experiments

Rainfall	Wind speed	Number of leakage locations	Leakage degree
Static	0	–	–
Dynamic	4	–	–
Dynamic	6	1	Not severe
Dynamic	9	2	Not severe

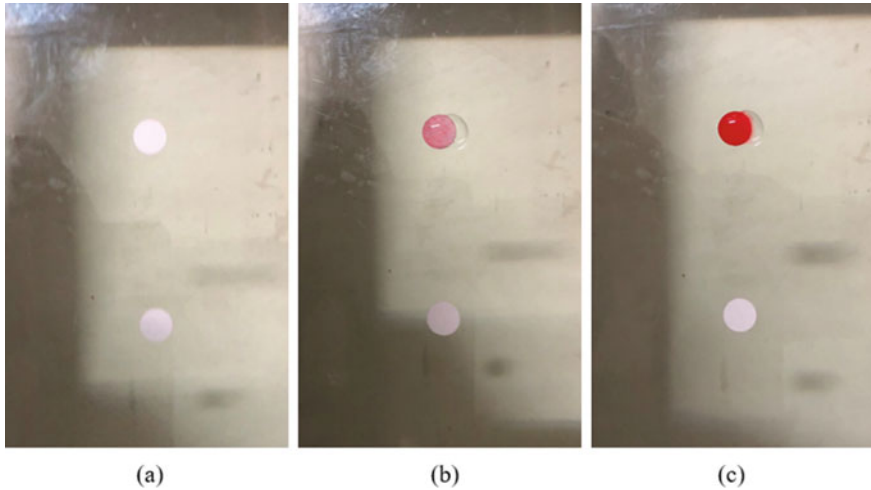


Fig. 6 The color change process of the test paper that turns red in water, **a** no water on the red dyed test strip, **b** a drop of water on the red dyed test strip—after several seconds, **c** a drop of water on the red dyed test strip—after several minutes

3.3 An Experimental Method to Mark Water Leakage

In GB/T 15227–2019 “Test method of air permeability, watertightness, wind load resistance performance for curtain walls”, the observation and recording method is required for the determination of the degree of water leakage. This study proposes an optimized experimental method to detect water leakage by means of red dyed test strips (Fig. 6). At the same time, the location of water leakage can be marked.

4 Conclusion

This study proposed a solar panel structure for building integrated photovoltaics (BIPV) roofs and conducted an experimental study for this structure; this experiment investigated the watertightness performance of this BIPV roof based on static and dynamic rainfall. The wind speed level increased continuously during experiments. The results show that the degree of water leakage is minor according to GB/T 15227–2019 “Test method of air permeability, watertightness, wind load resistance performance for curtain walls”—the proposed solar panel structure has great watertightness performance for BIPV system. In summary, the main research highlights are as follows:

- (1) A new PV panel structure was proposed with the aim of achieving watertightness reaching the degree of minor water leakages. The BIPV roof specimen was built and experiments were conducted under static and dynamic rainfall (the max wind

speed level is 12); after experiments, the expected watertightness performance was proven.

- (2) Through case studies, the characteristics of several types of BIPV roofs are compared, including application scenarios, installation methods and durability.
- (3) Based on GB/T 15227–2019, a discussion of marking water leakage by red dyed test strips is presented, which provides a new path to make the recording of water leakage more visual and permanent.

This research also provides insights for architects and engineers that building structure design can effectively improve building performance. In future studies, the application of artificial intelligence technology is also of research value to monitor of BIPV system risks [15] or track maximum power point [16].

Acknowledgements The project is supported by National Key R&D Program of China (2022YFC3803805) and R&D Program of THAD (K52022-033).

References

1. Lehtola TA, Zahedi A (2020) Technical challenges in the application of renewable energy: a review. *Int J Smart Grid Clean Energy* 689–699
2. Kou F, Shi S, Zhu N, Song Y, Zou Y, Mo J, Wang X (2022) Improving the indoor thermal environment in lightweight buildings in winter by passive solar heating: an experimental study. *Indoor Built Environ* 31:2257–2273
3. Abdelrazik AS, Shboul B, Elwardany M, Zohny RN, Osama A (2022) The recent advancements in the building integrated photovoltaic/thermal (BIPV/T) systems: an updated review. *Renew Sustain Energy Rev* 170:112988
4. Shi S, Yu L, Liu CH, Wang Y, Zhu N (2022) Application of synergic evidence-based design and sustainable technology strategies in off-grid residential NZEBs in the severe cold zone of China: a case study of The Steppe Ark. *IOP Conferen Series Earth Environ Sci* 1074:012023. IOP Publishing
5. Shi S, Sun J, Liu M, Chen X, Gao W, Song Y (2022) Energy-saving potential comparison of different photovoltaic integrated shading devices (PVSDs) for single-story and multi-story buildings. *Energies* 15:9196
6. Mao Q, Yang M (2020) Study on heat transfer performance of a solar double-slope PCM glazed roof with different physical parameters. *Energy Build* 223:110141
7. Wang X, Ramakrishnan S (2023) Environmental sustainability in building design and construction
8. Zhang C, Shen C, Zhang Y, Zheng K, Pu J, Zhao X, Ma X (2023) Experimental study of indoor light/thermal environment with spectrally selective windows using ATO nanofluids in winter. *Energy Build* 278:112597
9. Shukla AK, Sudhakar K, Baredar P (2017) Recent advancement in BIPV product technologies: a review. *Energy Build* 140:188–195
10. Kurz D, Nawrowski R (2019) Thermal time constant of PV roof tiles working under different conditions. *Appl Sci* 9:1626
11. Gonçalves M, Silvestre JD, de Brito J, Gomes R (2019) Environmental and economic comparison of the life cycle of waterproofing solutions for flat roofs. *J Build Eng* 24:100710
12. Talib R, Boyd D, Hayhow S, Ahmad AG, Sulieman M (2015) Investigating effective waterproofing materials in preventing roof leaking. *Init Comparat Study: Malaysia, U.K. Procedia Manuf* 2:419–427

13. Müller A, Martins I (2022) Recycling of building materials: generation-processing-utilization. Springer Nature
14. State administration for market regulation (China) (2019) Standardization Administration of the People's Republic of China: GB/T 15227-2019, Test method of air permeability, watertightness, wind load resistance performance for curtain walls
15. Olabi AG, Abdelkareem MA, Semeraro C, Radi MA, Rezk H, Muhaisen O, Al-Isawi OA, Sayed ET (2023) Artificial neural networks applications in partially shaded PV systems. *Therm Sci Eng Progr* 37:101612
16. Memaya M, Moorthy CB, Tahiliani S, Sreeni S (2019) Machine learning based maximum power point tracking in solar energy conversion systems. *Int J Smart Grid Clean Energy* 8:662-669

Evaluation of PV Utilization Potential of University Building Roofs Based on PVsyst Software Simulation



Yufei Zou, Yu Liu, Jie Song, Yiming Zhang, Minmin Yang, and Wenqiang Li

Abstract Solar energy utilization is an important way to reduce energy consumption of university buildings and build a green low-carbon campus environment. With usually large and plain form, the roofs of college bulidin (CB) in universities may possess good basic conditions for PV utilization. To explore the actual potential of PV utilization of the roofs of existing FBC, this paper takes a FBC in a university in Xi'an area as an case for analysis. First of all, a CB close to the campus center with a moderate total area was selected as a typical research object; second, a roof PV utilization scheme was proposed based on the situation of the case building; third, PVsyst software was used for modeling and simulation, based on which calculation was conducted to evaluate the energy saving and economic benefits that the roof of the case building may generate; finally, the overall PV utilization potential of the roofs of all FBC in the university was calculated, limitations of this research were addressed and further researches was recommended.

Keywords Potential · Building roofs · Simulation · University · Evaluation

1 Introduction

China has a large number of colleges and universities, huge university construction area and the characteristics of dense personnel and high energy consumption. Solar energy utilization is an important way to reduce energy consumption of university buildings and build a green low-carbon campus. The roof area of university buildings is usually large, so the use of roof photovoltaic (PV) production may become an effective way of solar energy utilization in universities.

However, there is still little PV utilization on the roofs of existing university buildings in China. In order to promote the PV utilization of university buildings, it is necessary to first clarify their PV utilization potential. To this end, this paper takes

Y. Zou (✉) · Y. Liu · J. Song · Y. Zhang · M. Yang · W. Li
Northwestern Polytechnical University, Shaanxi Province, Xi'an, China
e-mail: 2021261822@mail.nwpu.edu.cn

a college building (CB) in Xi'an area as an case to evaluates and analyzes the PV utilization potential of university building roofs based on PVsyst software simulation, hoping to provide a reference for the actual PV utilization of such buildings in colleges and universities.

2 Overview of Existing Studies

The concept of PV utilization in university buildings was first proposed by Germany, and was first applied in the "solar school" project. Subsequently, the United States, Australia, the United Kingdom, Japan and other countries have responded by promoting PV activities on campus and related research also started to increase gradually. For example, Taravella et al. conducted an energy and economic analysis of large-scale integration of PV system on a Spanish university campus. Choi et al. evaluated the potential for distributed PV at Penn State University, USA, considering the effect of roof shading. Yang Kim and Yang-Young Choi conducted a three-dimensional (3D) modeling approach using GIS for the design of regional PV systems, energy production, and resulting potential economic benefit calculations for the Pusan university campus in South Korea. Daniela Mewes used PVsyst software to evaluate a roof PV utilization potential for the Royal Institute of Technology, Sweden (KTH).

The research in the field of university building PV utilization in China started relatively late. Existing researches include: Peng Jinyin (2014) took Hainan Institute of Science and Technology as an case to review the advantages and benefits of the application of PV building integration technology in colleges and universities; Targeting Haikou and Shanghai regional colleges and universities respectively, Ke Hongfeng (2014) and Ma Qiang (2016) proposed that the application of PV building in colleges and universities not only can well meet the requirements of teaching and scientific research, but also had good economic and social benefits, and had a wide application prospect. Yan Lu (2016) took the teaching complex building of Xiamen Campus of Huaqiao University as an example, combined the roof PV system with roof space renovation to carry out virtual design of PV building integration, simulated the installed capacity and power generation of the virtual design scheme using PVsyst software, and demonstrated the feasibility of the proposed estimation method of PV utilization potential, which provides direct reference for the research of this paper.

3 Solar Resource Conditions in Xi'an Area

Located in the solar energy resource category 3 area, with abundant and stable solar energy resources, Xi'an possesses good basic conditions for solar energy utilization (Table 1), including PV utilization.

Table 1 Meteorological data of Xi'an area

	Horizontal plane global radiation (MJ/m ² .mth)	Scattered radiation in the horizontal plane (MJ/m ² .mth)	Average temperature (°C)	Average wind speed (m/s)
Jan	58.9	34.1	-1.1	1.90
Feb	71.3	51.2	3.1	2.40
Mar	91.3	62.8	10.0	2.70
Apr	120.6	78.0	15.6	2.70
May	145.6	93.0	20.9	2.59
Jun	143.4	94.7	25.6	2.60
Jul	158.1	92.2	28.0	2.90
Aug	144.2	92.5	25.5	2.70
Sept	101.6	61.3	19.8	2.40
Oct	76.7	54.6	14.0	1.99
Nov	57.0	36.7	6.6	1.90
Dec	51.3	37.1	0.5	1.89

Source database in Pvsyst

4 Tool and Methods of Research

Pvsyst is one of the most commonly used analysis software in the field of PV design. Developed by André Mermoud at the Faculty of Environmental Sciences of Geneva University in Switzerland, it has a powerful database that includes information on geometeorological data from around the world, all PV modules and inverter models on the international market, specific parameters of PV cables, batteries, pumps and other equipment used in PV system [1].

Based on this software, the roof PV utilization potential of a CB in Xi'an was evaluated and analyzed. First, a typical CB of the university was selected as a case building; second, Pvsyst software was used to propose a PV utilization design scheme for the typical building with the goal of obtaining the best power generation efficiency; third, the monthly and annual power generation of the mentioned scheme was simulated and calculated to evaluate its energy saving and economic benefits; finally, based on the evaluation results, the overall PV utilization potential of all CBs of the university was projected.

5 Selection of Case Building

According to the Technical Guidelines for the Construction of Energy-saving Supervision System for University Buildings of Higher Education Institutions of China, which was released in 2009, university buildings can be divided into 13 categories,

such as administrative office buildings, libraries, comprehensive buildings, research buildings, venue buildings, cafeterias and restaurants, student dormitories, large or research laboratories, university hospitals and exchange centers. The annual energy consumption monitoring data of typical buildings in typical universities are selected for analysis, and the energy consumption composition of university buildings is obtained (Fig. 1).

FBC is different from the above building types which is a building complex with teaching, office, scientific research and experimental functions. It can be characterized by high frequency and long time of use with high energy consumption per unit area. It is one of the several major building types in its belonged university. Its energy consumption accounts for a large proportion of the total energy consumption of the university. Self-sufficiency of the energy supply of such kind of buildings plays an important role in promoting the green and low-carbon construction of the university. At present, there are four clusters of CB on the researched university (A, B, C and D), the roofs of which are shown in the red area (Fig. 2).

Field research shows that the CBs of the university generally have flat roofs, moderate building heights, and are not affected by the shadows of surrounding vegetation and adjacent buildings, so have good conditions for PV design. In this paper, the easternmost building (CB C-1) in CB Group C, which is close to the center of the university and has a moderate total floor area, was selected as a case for the study.

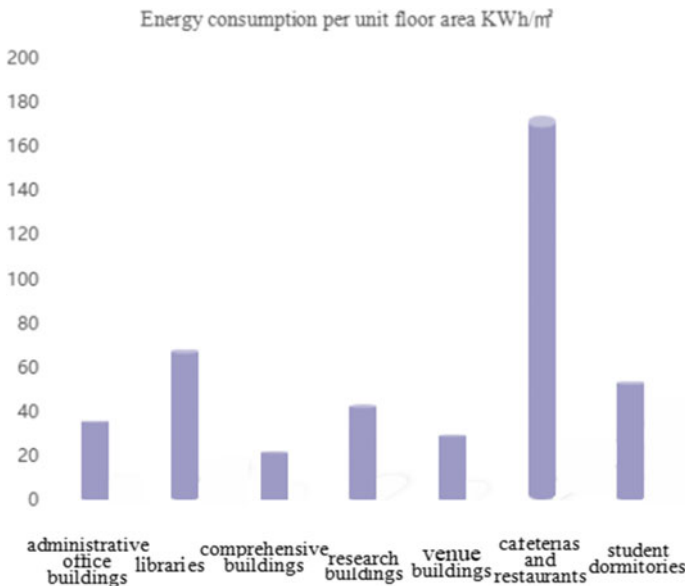


Fig. 1 Energy consumption per unit area of different types of buildings on campus (Source data from literature [2])



Fig. 2 Schematic view of the roof area of the CB building (shown in red)

6 Modeling and Simulation

6.1 Available Roofing Area

In order to assess the PV utilization potential of the selected case, it is necessary to first count its PV available area. At present, there are a number of methods for calculating the available area of PV roofs [3]. The calculation should generally take into account the utilization of translucent roofs and opaque roofs. Among them, in the transparent roof area (such as atrium space, transition space, traffic space, etc.), the roofing could usually facility potential PV utilization while satisfying the lighting demand of its under-space; in the opaque roof area, the PV utilization is realized by integrating PV panels and shading scaffolding, etc.

The roof of CB C-1 includes 3 parts (Fig. 3). Among them, ① and ③ are ordinary hard-paved roofs, which is completely impervious to light; ② are roof garden, which includes part of translucent roof. When calculating the PV available area of the roof, it is usually necessary to consider daylight shading and actual roof occupancy. Since the roof of this building is basically free from sunlight shading, only the actual occupancy should be considered. the discount factor for the PV available area of the opaque roof is set at 0.8; the discount factor for the PV available area of the transparent roof is set at 0.5 [4].

Based on the above setting, the effective area of the roof for PV application are shown (Table 2).

6.2 Layout Scheme of PV Array

According to the existing construction drawing information, the 3D model of the CB C-1 can be constructed and imported into the PVsyst software (Fig. 4).

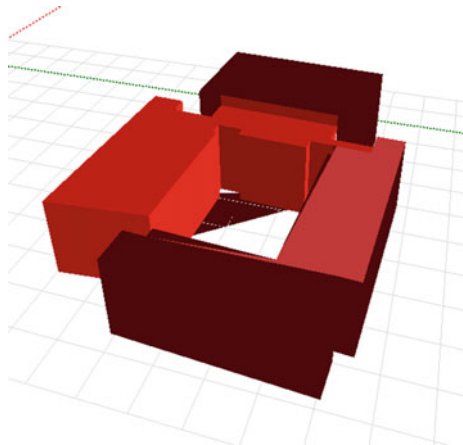
Fig. 3 Illustration of the roof area and type of the College Building C



Table 2 Calculation of the effective area of the roof that can be used for PV

Area code	Roof area (m ²)	Discount factor	Available area
①	1106	0.8	884.8
②	1194	0.5	597
③	933	0.8	746.4
Total effective area (m ²)	2228.2		

Fig. 4 PVsyst 3D model of CB C-1



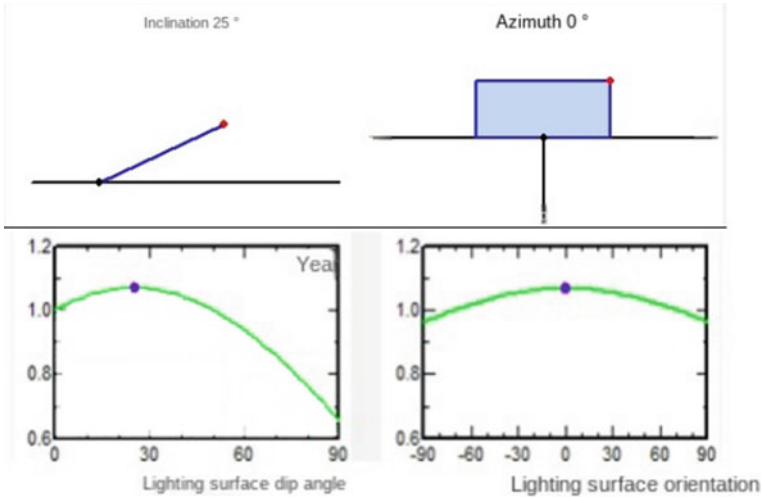


Fig. 5 Diagram of the best orientation and inclination of PV arrays in Xi'an

The Best Orientation and Inclination Angle. In order to obtain the highest PV power generation efficiency, it is necessary to determine the optimal orientation and inclination angle of the PV array first [5]. Results of PVsyst software simulation shows that the optimal orientation of the PV array for power generation in Xi'an area is south and the optimal inclination angle is 25° (Fig. 5).

Spacing of PV Array. According to “Design Code for PV Power Station” GB 50,797–2012, the distance between PV arrays should ensure that the solar cells will not be blocked during the daily 9:00–15:00 h of the year. Based on this, the PV array spacing was calculated with the following formula:

$$D = L \cos \beta + L \sin \beta \frac{0.707 \tan \varphi + 0.4338}{0.707 - 0.4338 \tan \varphi} \tag{1}$$

Eq.

D is the minimum PV array spacing.

L is the height difference between the highest end of the PV array module in the front row and the lowest end of the PV array module in the back row.

β is the tilt angle of the PV array.

φ is the latitude (positive in the northern hemisphere and negative in the southern hemisphere).

The latitude of the location site is 33.42° north latitude.

The calculation results show that the PV array spacing should be not less than 5.19 m (Fig. 6).

Based on the above PV array spacing can be derived in the front and rear row array without shading premise [6], the corresponding PV array area and the ratio of its occupied roof area is 0.6, the value is the theoretical maximum. Based on the

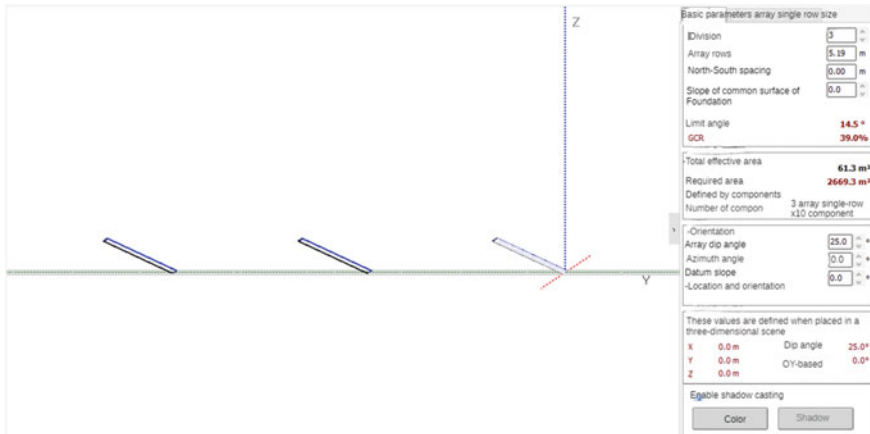


Fig. 6 Simulated PV array spacing schematic

above conclusion of the effective roof area, the PV array area can be calculated to be about $2228.2 \text{ m}^2 \times 0.6 = 1336 \text{ m}^2$.

Installed Capacity of PV Arrays. Considering that polycrystalline silicon cells are more cost-effective than monocrystalline silicon cells in areas with good solar radiation resources, a first-tier brand polycrystalline silicon module RT-340-355 M battery component was selected [7]. Based on which the roof PV utilization layout scheme can be simulated and the installed PV capacity is 206.5 kWp.

7 Simulation and Evaluation

7.1 Estimation of Generation Potential

PVsyst software and its own meteorological data (Fig. 7) were used to simulate the power generation of the selected typical case under the aforementioned PV array layout scheme [6]. The specific operation steps include: (1) geographic location information setting (Fig. 7); (2) system setting (including installed capacity, PV array orientation and inclination, array layout, array spacing, PV cell material and module type, installation site, installation method, etc.) (Fig. 8); (3) simulation calculation of solar radiation available on the surface of PV array, as well as month-by-month and yearly power generation.

The software comes with the parameters of power generation per unit area and system efficiency throughout the year, with high power generation per unit and low system efficiency in summer months and the opposite in winter months. The highest system output per unit area is 4 kWh/kWp/day in July and the highest system efficiency is 0.927 in January (Fig. 9).

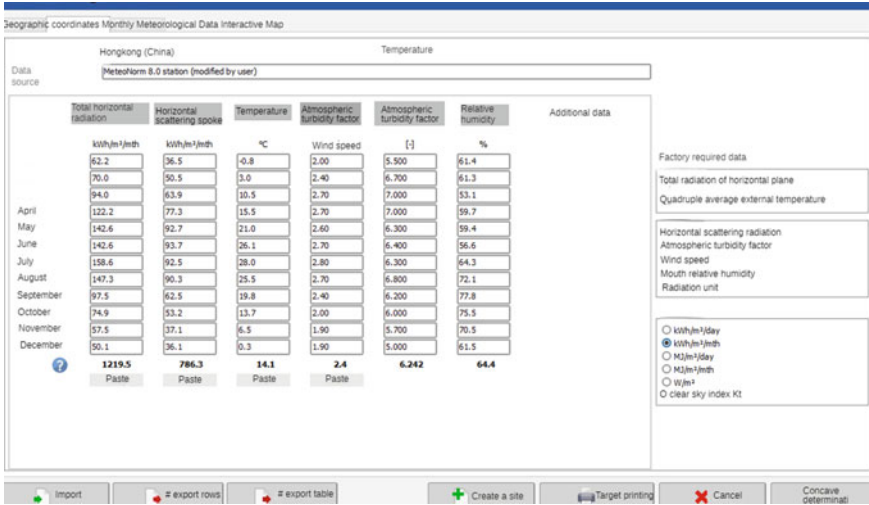


Fig. 7 Illustration of meteorological data settings in PVsyst software

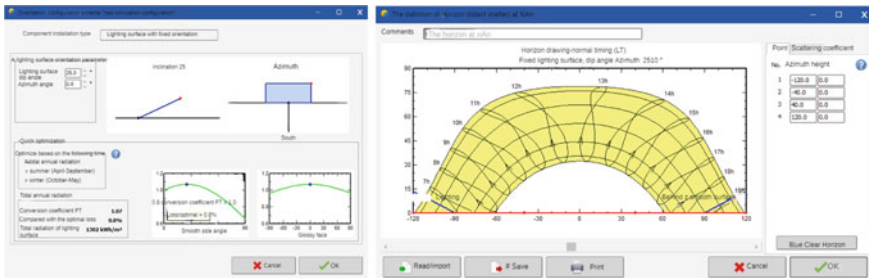


Fig. 8 Screenshot of simulation setup process

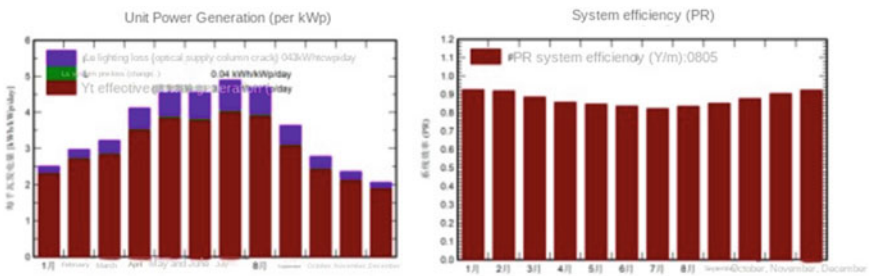


Fig. 9 System simulation data

Table 3 First-year power generation profile of the case building

Parameters	System production	System production power	System efficiency	Annual unit power generation
Numerical value	519.8 MWh/year	466 kWp	86.51%	1117 kWh/kWp/year

According to results of the simulation, the total power generation of the case building in the first year of the described PV system is 519.8 MWh, the system efficiency is 86.51%, and the annual power generation per unit area is 1117 kWh/kWp/year (Table 3).

7.2 Analysis of the Benefits

According to the data of the “National Implementation Plan for Transformation and Upgrading of National Coal Power Units” released by the National Development and Reform Commission of China in 2021 [8], the current 1 kWh PV power generation can be converted to standard coal 305.5 g. The average emission of 1 t coal is 2620 kg, 15 kg of dust, 22 kg sulfur dioxide and 7.0 nitrogen oxide 7.4 kg (Table 4).

According to the conversion of the data in Tables 3 and 4, it can be seen that the comprehensive environmental benefits of the case building roof PV utilization scheme are considerable, with a first-year power generation of about 519.8 MWh, equivalent to a saving of 158.8 t of coal, reducing 416.1 t of CO₂ emissions, and an annual energy-saving benefit of about 407,000 RMB.

7.3 Assessment of the Overall Power Generation Potential

Converting the power generation in the first year of the typical case into power generation per unit roof area, the result is about $519.8 \text{ MWh/year} \div 3233 \text{ m}^2 = 160.8 \text{ kWh/m}^2 \cdot \text{year}$. The total roof area of the CB A-D group is 35,732.9 m², without considering the decay of PV module power generation efficiency, it can be estimated that the overall potential PV power generation is about $160.8 \text{ kWh/m}^2 \cdot \text{Year} * 35,732.9 \text{ m}^2 = 5745.7 \text{ MWh/year}$, generating energy-saving economic benefits of about 4.502 million yuan/year (Table 5).

Table 4 Calculation table of PV power generation benefits

Calculation category		Quantity/unit
PV power generation per 1 kWh	Equivalent to standard coal	305.5/g
Emissions per 1 t of standard coal burned	Carbon dioxide	2620/kg
	Sulfur dioxide	22/kg
	Nitrogen oxides	7.4/kg
	Dust	15/kg
Unit consumption reduction and energy efficiency	Coal	750 RMB/ton
	Carbon dioxide	208.5 RMB/ton
	Sulfur dioxide	1260 RMB/ton
	Nitrogen oxides	2000 RMB/ton
	Dust	550 RMB/ton
System benefits	Annual power generation	519.8/M kWh
	Coal	158.8/t
Annual emission reduction	Carbon dioxide	416.1/t
	Sulfur dioxide	3.5/t
	Nitrogen oxides	1.2/t
	Dust	2.4/t
Annual earnings	Coal	31.2 million
	Carbon dioxide (million yuan)	87,000 yuan
	Sulfur dioxide (million yuan)	0.4 million
	Nitrogen oxides (million yuan)	0.2 million
	Dust (million yuan)	0.1 million
	Total (million yuan)	407,000

Source calculated based on literature [8]

Table 5 Calculation of the overall PV power generation potential of the FBC

	CB A	CB B	CB C	CB D	Total
Roof area (m ²)	4372.4	15,360.7	7459.6	8540.2	35,732.9
Potential power generation capacity (MWh)	703.1	2470.1	1199.6	1373.3	5745.7
Potential energy saving benefits (million yuan RMB)	55.1	193.5	93.2	106.8	450.2

8 Conclusion

In this paper, a CB of a university in Xi'an was used as an case and its PV utilization potential was evaluated and analyzed using PVsyst software. The results show that the roof of the CB has an overall PV potential of about 160.8 kWh/m². The potential of

PV power generation is about 160.8 kWh/m². per year, which can generate potential energy saving benefits of about 4.502 million RMB/year. Therefore, it is of practical significance and application value to apply PV on the roofs of existing buildings in colleges and universities in Xi'an.

It should be noted that the estimation of effective roof area and PV array area are two key points in the process of roof PV utilization potential assessment, and there are often errors in this estimation, and the PVsyst simulation software has its own limitations, so the actual project PV power generation efficiency may be lower than the estimated value, and the specific differences are yet to be discussed and clarified through further research. In this study, the evaluation of the PV utilization potential of university buildings is only focused on CBs and flat roofs, and the PV utilization potential of other building types, sloped roofs and facade curtain walls in universities can be further explored in subsequent studies.

Acknowledgements The research of this paper was supported by the National Natural Science Foundation of China (project number: 52078422)

References

1. Mewes D, Monsalve P, Gustafsson I et al (2017) Evaluation methods for PV installations on existing buildings at the KTH campus in Stockholm, Sweden [J]. *Energy Procedia* 115:409–422
2. Li P (2015) Analysis of university energy use data based on the energy conservation supervision system [J]. *Smart Build City Inform* 05:85–87
3. Zhang H (2014) Research on the application potential of photovoltaic building integration in campus environment [D], Tianjin University
4. Yan L (2016) Research on the application of photovoltaic building integration in Chinese universities [D], Huaqiao University
5. Bernasconi D, Guariso G (2021) Rooftop PV: potential and impacts in a complex territory [J]. *Energies* 14(12):3687
6. Wei C, Hui S, Yong L (2009) Theoretical study on the influence of photovoltaic array orientation and inclination on performance in BIPV [J]. *Solar Energy J* 30(02):206–210
7. Li F, Xi H (2013) Preliminary discussion on the application and design of photovoltaic building integration technology in teaching building [J]. *Henan Sci Technol* (09):238–9
8. (2022) National implementation plan for transformation and upgrading of national coal power units [J]. *Electric Power Technol Environ Protect* 38(1)

Reallocation of Supply Air in Large Indoor Spaces Considering Thermal Coupling



Bo Lan  and Gongsheng Huang 

Abstract In large public indoor spaces, such as railway station and airport waiting halls, indoor thermal environment is not always homogenous due to non-uniform indoor occupant distributions. A conventional air conditioning system, which adopts a uniform air supply, easily leads to local overcooling or overheating. Therefore, this paper proposes a supply air reallocation method for a large indoor space to enhance the uniformity of the thermal environment and improve the occupants' thermal comfort. In the proposed method, the large space is firstly divided into several subzones according to the layout of the supply air terminals. Then, a co-simulation platform, including a building energy model and a computational fluid dynamics (BEM-CFD) model, is established to simulate and identify the thermal coupling between different subzones. The supply air volume of each subzone is then optimized considering the thermal coupling characteristic. The proposed method was applied to a high-speed railway station in China to evaluate the feasibility of the proposed method. The results showed that, compared with the conventional uniform air supply method, the indoor thermal uniformity could be improved by 15.61–31.11% after reallocating supply air, being able to reduce the risk of local overcooling or overheating.

Keywords Large space buildings · Thermal environment · Supply air reallocation · BEM-CFD co-simulation · Thermal coupling

1 Introduction

Persons spend about 90% of their time indoors in average [1] and thus indoor environment is important for persons. Unlike residential buildings, large buildings, such as airport terminals and railway stations, are characterized by a large number of

B. Lan · G. Huang (✉)

Department of Architecture and Civil Engineering, City University of Hong Kong, Kowloon, Hong Kong SAR, China

e-mail: gongsheng.huang@cityu.edu.hk

passengers and significant variations in passenger flows [2], which represents challenging in creating and maintaining comfortable indoor thermal environment for occupants in such buildings [3]. Figure 1 illustrates the typical thermal environment in a large space. The thermal environment is affected by both external and internal loads. External loads are from the outdoor weather conditions, such as solar radiation, air temperature and humidity [4]. Internal heat sources include occupants, lighting, and other devices. The locations, geometry, and power of the internal loads can directly influence the indoor thermal environment [5].

Unlike lighting and other internal heating sources that normally will not move their locations, occupant can move freely in a large space and their movements may be unpredictable. The movement and randomness can lead to the different occupancy. For example, Ken et al. showed significant uneven distributions in the occupancy in Japanese railway stations [6]. People tended to gather in the ticket zone rather than in the aisles, resulting in a heavy load in ticket zone and a small load in the aisles. However, in the design of heating, ventilation, and air conditioning (HVAC) systems, it is impossible to address all unevenly distributed occupancy just by optimizing the locations of terminal units [5]. Besides, in large public transportation places, due to the high occupant density, the occupant load may contribute a high percentage to the total load. According to the HVAC design reports of seven hub airports in China

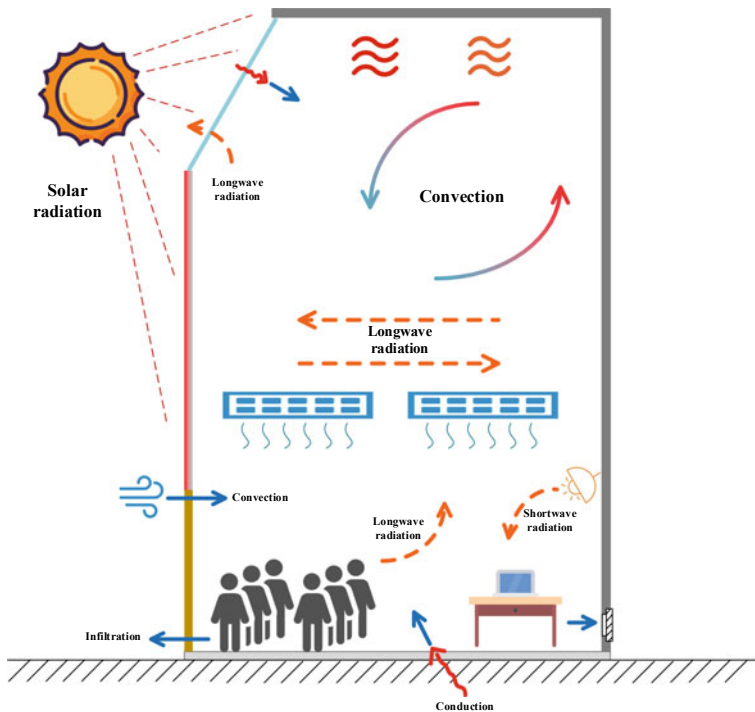


Fig. 1 Indoor thermal environment and heat transmission diagram in a large space

[7], three main types of the internal heat source load including occupant, mechanical ventilation, lighting and equipment account for about 50–90% of the total cooling load. The occupant load always accounts for 13–50% [8]. For high-speed railway stations, this percentage may be even higher. Therefore, occupant uneven distribution should be considered in the operation of HVAC systems in large indoor spaces.

Previous studies have demonstrated that the non-uniformity in the thermal environment may lead to local thermal discomfort and a high thermal dissatisfaction rate [5]. Furthermore, if the air supply volume is not adjusted according to the real-time occupancy condition, it will easily lead to local overcooling or overheating phenomena, resulting in energy wastage and occupants' uncomfortable thermal feelings [9]. Therefore, it is necessary to reallocate the supply air volume following the variations of occupancy condition.

When studying the uneven distribution of the thermal environment, it was suggested to divide the large space into different subzones based on the indoor thermal environment's simulation results [10]. For example, Zhou et al. proposed a method based on a K-means clustering algorithm and extreme learning machine to partition the large space according to the temperature and air velocity results obtained from computational fluid dynamics (CFD) simulations. However, they did not study how to improve the indoor thermal environment after zoning [11]. Later, different ways were proposed to improve the indoor subzones environment [9]. Shide et al. divided a large open-plan office into different zones based on the activities of occupants and the number of HVAC terminals in each zone. Based on actual data on the stochastic behaviors of occupants, temperature set points and lighting intensity in different zones were optimized to reduce building energy consumption and occupant discomfort time. They showed that their strategy improved the thermal environment by 50% while saving 2% energy consumption [12]. Wang et al. divided a large office into different patches and used an indoor positioning system (IPS) to monitor occupancy in each patch. To simplify the model, the authors regulated each patch independently and did not supply air in unoccupied areas [13]. Wang et al. also proposed a ventilation method based on the occupancy in the room through Wi-Fi networks. Combined with the k-Nearest Neighbors (kNN) algorithm and a random walk model to collect high-resolution occupancy information, and adjust the supply air volume of different areas [14].

However, while the above studies considered adjusting the thermal environment of different subzones according to the distribution of occupants, they ignored the thermal coupling between different subzones. Since there is no physical partition between different subzones in a large space, there are coupling changes in the spatial temperature of adjacent subzones through air convection, causing the actual temperature not to track the set temperature. Therefore, to improve the thermal uniformity of the large space, supply air reallocation is proposed in this study for a large space by considering the thermal coupling between subzones. Firstly, by establishing a building energy and computational fluid dynamics (BEM-CFD) co-simulation platform, the thermal coupling between the zones of the large space is modelled. According to this model, the method of reallocating the supply air for different occupant distributions is developed. A high-speed railway station in China is used as a case study to verify

the effectiveness and applicability of the proposed method by comparing with the conventional air supply method that uses a constant supply air volume.

2 Methodology

2.1 CFD and BEM Coupling Framework

To achieve the indoor supply air reallocation, an external coupling method is adopted through the mutual call between CFD and BEM for co-simulation [15]. The framework is illustrated in Fig. 2 Firstly, a BEM is established after specifying the boundary conditions for the large space, such as weather conditions, building construction information, and so on. Then, the initial boundary of the HVAC air supply system can be obtained, including the supply air volume, air temperature, and the heat flux of the envelope. With these boundaries, the CFD model is used to simulate the large-space temperature distribution with the conventional constant air supply.

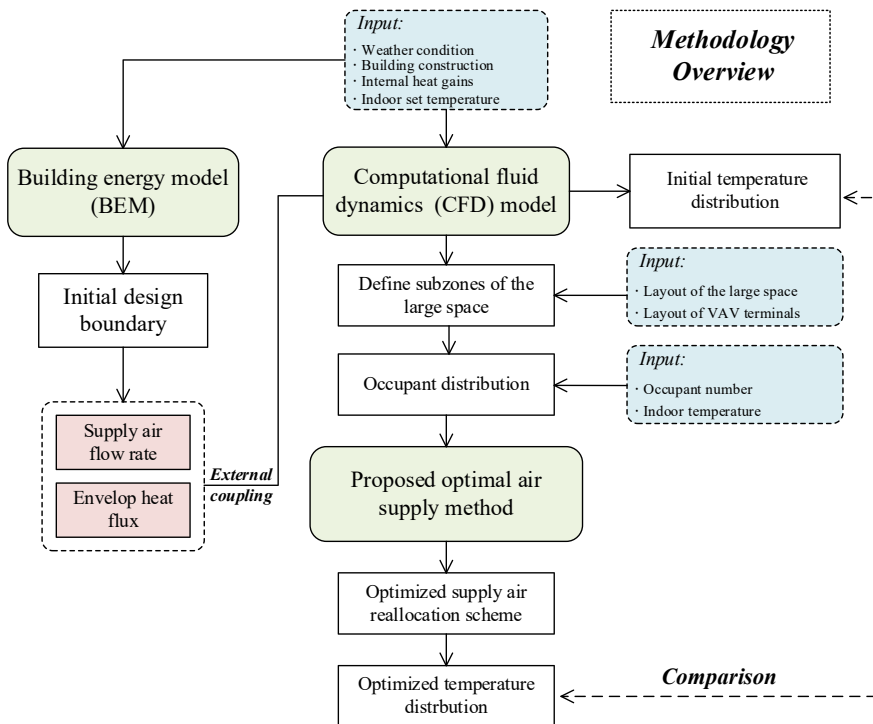


Fig. 2 Methodology of coupling framework of optimal supply air reallocation for large space

The large space is divided into multiple subzones according to the layout of terminals in the large space. Then the supply air is reallocated by the proposed method based on the occupant distribution scenario and indoor temperature distribution. The supply air volume of each subzone is adjusted coordinately and simultaneously to improve the uniformity of the temperature field. The specific optimization model is introduced in the following subsection. Finally, the non-uniformity indicator is proposed to quantitatively analyze and compare the optimized temperature field distribution with the temperature field distribution under the conventional air supply method.

2.2 Optimal Supply Air Reallocation Model

After zoning the space, the whole large space is divided into n subzones. The indoor average temperature (T_i) of the i -th subzone can be obtained. Define the difference between the indoor average temperature and the set temperature ($T_{i, set}$) as the temperature difference, as shown in Eq. (1). Since there is a thermal coupling between different subzones, that is, when the temperature in subzone i is adjusted, the temperature in other subzones of the large space will also be influenced. Therefore, the temperature change of each subzone ($\Delta V_1, \dots, \Delta V_n$) is affected by the change of the supply air volume of the other subzones, which can be expressed as a functional relationship as Eq. (2). Zhou et al. [16] pointed out that this phenomenon could be expressed as an approximately linear relationship, so a linear matrix is used for description, as shown in Eq. (3). The matrix coefficients in Eq. (3) can be identified by model identification.

$$\Delta T_i = T_i - T_{i, set} \tag{1}$$

$$\begin{cases} \Delta T_1 = f(\Delta V_1, \dots, \Delta V_n) \\ \vdots \\ \Delta T_n = f(\Delta V_1, \dots, \Delta V_n) \end{cases} \tag{2}$$

$$\begin{pmatrix} \Delta T_1 \\ \vdots \\ \Delta T_n \end{pmatrix} = \begin{pmatrix} \alpha_{11} & \dots & \alpha_{1n} \\ \vdots & \ddots & \vdots \\ \alpha_{n1} & \dots & \alpha_{nn} \end{pmatrix} \begin{pmatrix} \Delta V_1 \\ \vdots \\ \Delta V_n \end{pmatrix} \tag{3}$$

Based on the above relationship, the air volume in each subzone (V_1, \dots, V_n) can be reallocated to ensure the thermal uniformity of the whole space. This problem can be solved by optimizing the air volume change in different subzones ($\Delta V_1, \dots, \Delta V_n$). To solve this optimization problem, the objective functions are formed in Eqs. (4) and (5). The aim is to reduce the temperature difference between various subzones. The constraint condition is that the total air volume is constant, as shown

in Eq. (6). Equation (7) gives the feasible range of air volume adjustment. The air volume in each subzone cannot exceed the maximum air volume that can be adjusted, namely, the design air volume (V_{design}).

$$[\Delta V_{1,\text{opt}}, \dots, \Delta V_{n,\text{opt}}] = \arg \min_{\Delta V_1, \dots, \Delta V_n} \phi \quad (4)$$

$$\phi = \sum_{i=1}^n \sqrt{(\Delta T_i)^2} \quad (5)$$

$$s.t. \sum_{i=1}^n \Delta V_i = 0 \quad (6)$$

$$\Delta V_i \in [-V_{i,\text{set}}, V_{\text{design}} - V_{i,\text{set}}] \quad (7)$$

All in all, according to the actual occupant and temperature distributions, the large space's temperature distribution and the thermal environment can be improved by reallocating each subzone's supply air volume. Besides, more accurate indoor temperature adjustment can be achieved by obtaining the thermal coupling relationship between different subzones.

3 Case Study

3.1 BEM-CFD Co-Simulation

A building energy model of a large high-speed railway station in China was built in Design Builder, a BEM simulation software, as displayed in Fig. 3. According to the actual dimensions of the case building (231 m (L) \times 177 m (W) \times 21.8 m (H)), the building's thermal environment boundary and supply air parameters of the air conditioning system were simulated. The building is with a central skylight made of low-radiation glass and glass curtain walls. Other specific design parameters are shown in Table 1.

The CFD model was created by Airpak 3.0, and a 1:1 scale CFD model was developed. To simplify the simulation, 1/4 of the station was modeled because of the symmetry of this station. The internal heat sources (lights, equipment) are uniformly distributed on the floor. The occupant model is represented by rectangular blocks in Fig. 3. There are two types of occupants: standing and seated occupants distributed in standing and seated areas. Air is supplied by nozzles and vents, which are demonstrated in the CFD model in Fig. 3. The CFD boundaries, including the supply air volume, temperature, and heat flux of the envelope, can be obtained from BEM simulation results.

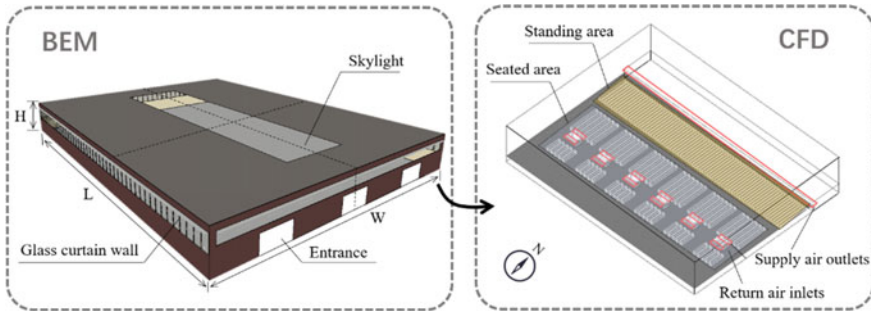


Fig. 3 Developed building model in BEM and CFD co-simulation platform

Table 1 Basic settings for BEM simulation

No	Types	Value	Unit
1	Window-to-wall ratio	0.4	–
2	Occupancy	0.67	p/m ²
3	Indoor setting temperature	26	°C
4	Indoor setting relative humidity	55	%
5	Fresh air flow rate	10	m ³ /(h·p)

To verify whether the method can effectively adjust the indoor thermal environment according to different occupant distributions. The scenario of uneven occupant distribution is set. Assume that occupants are gathered in the seated area, and no one is in the queuing area. Under this condition, the conventional uniform air supply method and the optimized air supply method are compared.

3.2 Model Validation

To validate the simulation model, we compared the BEM and CFD simulation results with the actual measurement results, respectively. Firstly, for the validation of the BEM, the actual outdoor temperature on October 4 was selected as the BEM input with a time step of 1 h. Figure 4 gives the actual outdoor temperature variation (black line). The simulated and measured temperatures of the north wall are displayed in blue and green lines, respectively. The relative error is given in the bar graph. It can be seen that the maximum temperature difference is 1.38°C at 17:00, and the maximum relative error is 3.37%. Therefore, the numerical model can reflect the temperature changes of the actual building envelope. Therefore, BEM model simulation results were further used as simulation boundaries in the CFD model to provide accurate indoor thermal environment simulations [17].

Based on the BEM simulations, the thermal environment on October 4 was given by CFD simulation. The simulation selected a 10:20 a.m. scenario for comparison. In

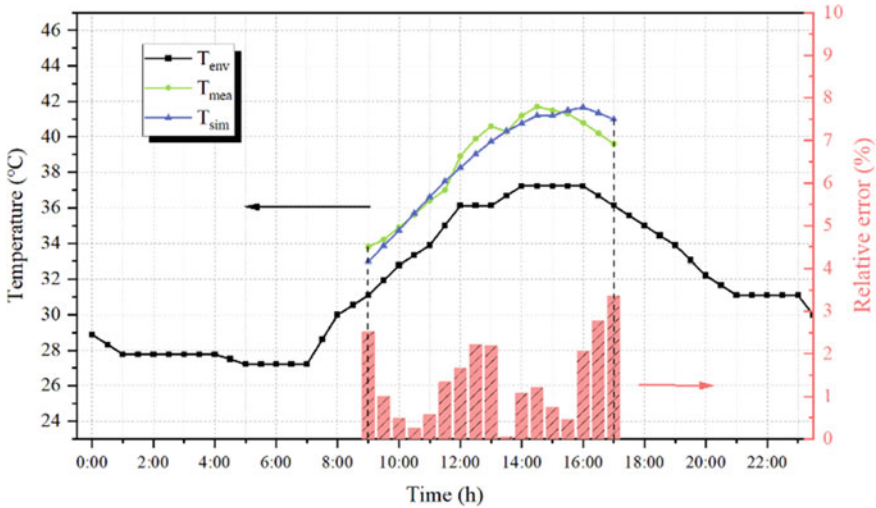


Fig. 4 Measured and simulated results for BEM model validation

this scenario, the outdoor meteorological parameters, the measured building envelope temperature, and the number of occupants in the standing and seated areas were used as inputs to simulate the thermal environment for comparison. We selected several measurement points at the height of 1.1 m. Compared with the actual measured temperature, it is found that the temperature difference is 0.3–0.4°C. And the temperature distribution character is the same as the actual measurement results: the lower temperature at the center supply air outlet and the higher temperature around the supply air outlet. Therefore, the BEM-CFD co-simulation model can be used to analyze the thermal environment of large space public buildings under different occupant distributions.

4 Results and Discussions

According to Sect. 3.1, the uneven occupant distribution in a large space (occupants all gathered in the seating area) is set as an example to verify this method. The optimized thermal environment at 1.1 m is analyzed and discussed from both qualitative and quantitative aspects.

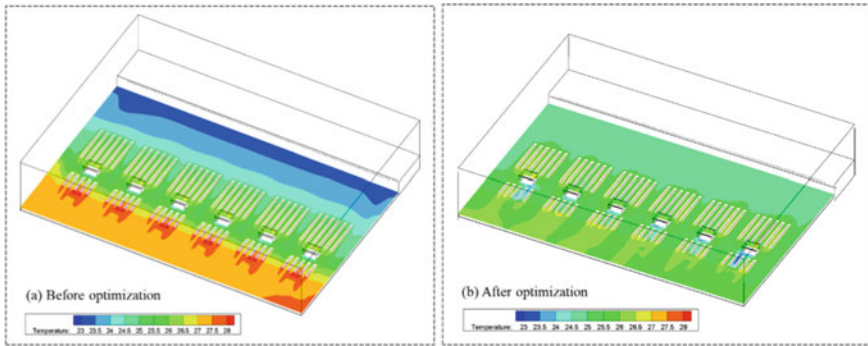


Fig. 5 Comparison of temperature field before and after optimization

4.1 Qualitative Analysis of Thermal Environment Non-Uniformity

Figure 5a shows the temperature field using the conventional uniform air supply under uneven occupant distributions. The temperature in the unoccupied area is lower than the set temperature of 26°C, while in the high-density seated area (occupancy = 1.01 p/m²), located under the skylight, resulting in a local maximum temperature of 28°C. The maximum temperature difference becomes more than 4°C. After being optimized using Eqs. (1–7), Fig. 5b illustrates the optimized CFD simulation results of temperature field. By increasing the 22.8 m³/s of air flow rate to the seated area while reducing the air supply to the standing area, it can effectively reduce the occurrence of local over-cooling, and the temperature was raised to 25°C. In contrast, the temperature of the over-heated area under the skylight is reduced to near 26°C. It makes the temperature distribution of the whole space more uniform and meets the thermal comfort demand of the human body.

4.2 Quantitative Analysis of Thermal Environment Non-Uniformity

To quantitatively analyze the effect of optimization, a non-uniformity index is proposed in this paper for quantification. As shown in Eq. (8), the Euclidean distance (ω^h) is used to calculate the difference between the temperature (T_i^h) in different subzone i and the average temperature ($\overline{T_i^h}$) of the whole plane at different heights (h). When ω^h is larger, the thermal non-uniformity is more pronounced and vice versa. In addition, β^h is added to express the relative value of the improvement of temperature uniformity on different planes after optimization, expressed as a percentage, as shown in Eq. (9).

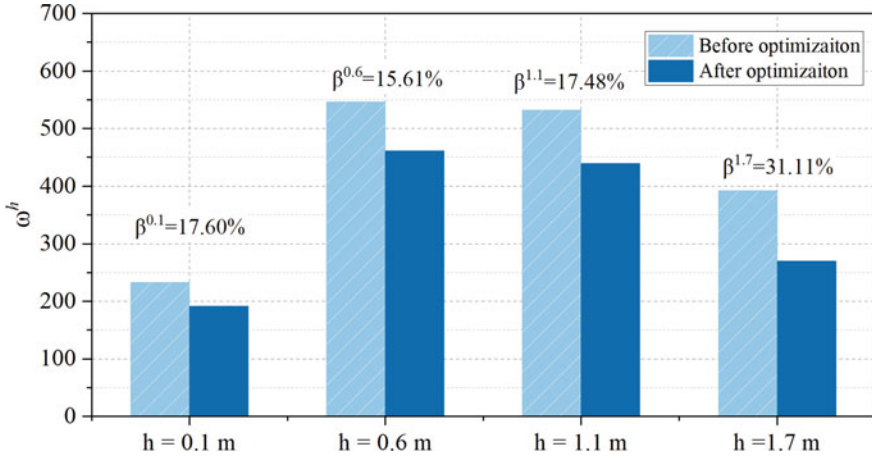


Fig. 6 Comparison and statistics of non-uniformity index under different planes

Figure 6 shows the comparison results. The thermal uniformity on different planes is improved by 15.61–31.11% after adopting the optimized air volume reallocation method proposed in this paper. Combined with the qualitative analysis in Sect. 4.1, this method can effectively avoid local overcooling or overheating by reducing the extreme temperature difference and improving the thermal uniformity. Besides, it can also enhance the occupants’ thermal comfort when staying in large space public buildings.

$$\omega^h = \sqrt{\sum_{i=1}^n (T_i^h - \overline{T_i^h})^2} \tag{8}$$

$$\beta^h = \frac{|\omega_{op}^h - \omega^h|}{\omega^h} \times 100\% \tag{9}$$

5 Conclusion

The conventional air supply method considers the occupants to be evenly distributed in large spaces and thus fixed the supply air speed. However, the distribution of occupants is always dynamic and not uniform, and it is necessary to consider this impact on the thermal environment under different occupant distributions. Therefore, this paper proposes a supply air reallocation method, which divides the whole large space into several subzones and adjusts the supply air volume according to the variation of the occupant distributions. A better uniform temperature distribution in

the large space could be achieved and as well as a better thermal environment for indoor occupants when compared with the conventional air supply method. The main conclusions are listed as bellow:

- (1). Thermal coupling exists between different subzones. When adjusting the supply air volume speed in a zone, the adjacent zones will be affected. This feature needs to be considered when performing the supply air allocation.
- (2). Occupant distribution may have a significant influence on the indoor thermal environment. In the case study, when the supply air was not adjusted, the zones with high occupancy density were 1–4 °C higher than those with low occupant density.
- (3). The occurrence of local overcooling and overheating can be effectively avoided through supply air volume reallocation. The case study showed that the thermal uniformity could be improved by 15.61–31.11% under different occupant distribution scenarios.

References

1. United States Environmental Protection Agency Homepage. Retrieved from <https://www.epa.gov/report-environment/indoor-air-quality>. Accessed on 17 Oct 2022
2. Du XH (2020) Investigation of indoor environment comfort in large high-speed railway stations in Northern China. *Indoor Built Environ* 29(1):54–66
3. Yang L, Xia J (2015) Case study of space cooling and heating energy demand of a high-speed railway station in China. *Procedia Eng* 121:1887–1893
4. Mao N, Song M, Pan D et al (2017) Numerical investigations on the effects of envelope thermal loads on energy utilization potential and thermal non-uniformity in sleeping environments. *Build Environ* 124:232–244
5. Lu YY, Dong JK, Liu J (2020) Zonal modelling for thermal and energy performance of large space buildings: a review. *Renew Sustain Energy Rev* 133:110241
6. Misawa K, Nakano J, Tanabe SI (2007) Field survey of thermal environment and occupancy condition of passengers in railway station. *Cytopathology* 27(4):297–299
7. Huang W, Lin Y, Lin B et al (2019) Modeling and predicting the occupancy in a China hub airport terminal using wi-fi data. *Energy Build* 203:109439
8. Tao Z, Liu X, Liu X et al (2018) Design, operating status and research prospects of air-conditioning systems in airport terminals. *Heat Ventilat Air Condition* 48:53–59
9. ANSI/ASHRAE 62.1 (2019) Ventilation for acceptable IAQ. ASHRAE, Atlanta
10. Lan B, Yu ZJ, Zhou P et al (2022) Optimal zoning for building zonal model of large-scale indoor space. *Build Environ* 225:109669
11. Hiyama K, Kato S, Ishida Y (2010) Thermal simulation: response factor analysis using three-dimensional CFD in the simulation of air conditioning control. *Build Simul* 3:195–203
12. Yu LK (2015) Optimization analysis of winter heating system in waiting hall of railway passenger station. *J Central South Univ* 46:1900–1908
13. Hussain S, Oosthuizen PH (2012) Validation of numerical modeling of conditions in an atrium space with a hybrid ventilation system. *Build Environ* 52:152–161
14. Wang W, Chen J, Hong TZ (2018) Occupancy prediction through machine learning and data fusion of environmental sensing and Wi-Fi sensing in buildings. *Autom Constr* 94:233–243
15. Djunaedy E, Hensen JLM, Loomans M (2005) External coupling between CFD and energy simulation: implementation and validation. *ASHRAE Trans* 111(1):612–624

16. Pei Z, Huang G, Zhang L et al (2015) Wireless sensor network-based monitoring system for a large-scale indoor space: data process and supply air allocation optimization. *Energy and Buildings* 103:365–374
17. Shan X, Luo N, Sun K et al (2020) Coupling CFD and building energy modelling to optimize the operation of a large open office space for occupant comfort. *Sustain Cities Soc* 60:102257

Investigation on the Influence of Insolation on Winter Thermal Comfort of Outdoor Activity Space on Campus in a Cold Region of China



Jie Song, Yu Liu, Wenqiang Li, Yufei Zou, Minmin Yang, Yiming Zhang, and Hui Liu

Abstract With the development of various outdoor activities on campus, students are spending increasingly more time in the outdoor space, so the outdoor environment has a more important impact on students' physical and mental health. Targeting a typical outdoor activity space of a university in Xi'an city, which is located in the cold region of China, this paper investigated its winter thermal comfort performance through on-site measurement, a questionnaire survey, and statistical analysis. The collected data were analyzed by SPSS software, and the functional relationship between TCV (thermal comfort voting value) and outdoor environmental parameters was established. Along with the questionnaire survey, solar radiation, wind speed, and air temperature of two specific positions (P1 and P2) was measured and recorded in real time. The results showed that, under similar clothing thermal resistance, in the area without sunlight (P1), the measured air temperatures range between 3.2 °C and 13.1 °C and wind speed range between 0 and 1.8 m/s. The survey respondents wanted to improve thermal comfort by increasing the temperature. In contrast, in the area with sunlight (P2), the temperature range between 3.6 °C and 16.2 °C and wind speed range between 0 and 1.9 m/s, the survey respondents wanted to improve the thermal comfort by decreasing the outdoor temperature. Such results imply that insolation significantly affects the winter thermal comfort sensation of outdoor activity space on campus.

Keywords Insolation · Thermal comfort · Outdoor space · Campus · Cold region

J. Song · Y. Liu (✉) · W. Li · Y. Zou · M. Yang · Y. Zhang · H. Liu
School of Mechanics, Civil Engineering and Architecture, Northwestern Polytechnical University, Xi'an, China
e-mail: liuyu@nwpu.edu.cn

J. Song · Y. Liu · W. Li · Y. Zou · M. Yang · Y. Zhang
Sustainable Building and Environmental Research Institute, Northwestern Polytechnical University, Xi'an, China

J. Song
School of Architecture, University of Liverpool, Liverpool, United Kingdom

© The Author(s), under exclusive license to Springer Nature Singapore Pte Ltd. 2024
M. Casini (ed.), *Proceedings of the 3rd International Civil Engineering and Architecture Conference*, Lecture Notes in Civil Engineering 389,
https://doi.org/10.1007/978-981-99-6368-3_40

1 Introduction

As an important place for students and faculty to relax, entertain and socialize, the quality and comfort of outdoor spaces on campus affect the likelihood and frequency of use, which in turn has an impact on the cultural atmosphere and vitality of campus as well as the psychological and physiological well-being of students. Susceptible to climatic factors (insolation and wind), outdoor campus activities may decrease in wintertime. This paper investigates the thermal comfort of campus outdoor activity spaces in a cold region and winter time, taking a university in Xi'an, a city in northwest China, as an example.

Existing relevant research in China has mainly focused on outdoor thermal comfort research in urban areas [1], such as in parks, and residential areas [2], public squares, and pedestrian streets, et [1, 3]. In 2020, Hu [4] conducted a literature review and synthesis of outdoor thermal comfort-related research at home and abroad in the past 20 years, summarizing the effects of different influencing factors and research methods. At the same time, according to the factors considered in the more commonly used thermal comfort evaluation indexes, the development trend that solar radiation among microclimatic factors is gradually included in the scope of consideration in the outdoor environment was summarized. Huang [5] conducted a study on the actual measurement of outdoor activity thermal environment of the university campus in the Mianyang area. In addition, he also conducted a study on the thermal comfort range of outdoor activity crowds in the Mianyang area, based on ENVI-met thermal environment simulation. In 2017, Chun Mingyang focused on the relationship between the behavioral activity of older people and outdoor thermal comfort in a cold settlement square. Through the field research and records of the cold settlement square, it was found that the activity time of the elderly in summer is longer than that in spring and using the correlation analysis in statistical analysis, it was concluded that the temperature environment has the most influence on the behavioral activity of the elderly, and the design strategy of the cold settlement square was proposed. Wang et al. [6] showed that the evaluation of overall thermal comfort in non-uniform thermal environments had not been fully clarified, and proposed steady-state and non-steady-state overall thermal comfort models.

Relevant researches from outside China include: 2020 Salman et al. [7] reviewed that differences in outdoor thermal comfort in cities depend on site characteristics and reviewed past and present thermal comfort in Australia research on how to help improve urban livability. Very early on, Thorsson et al. [8] selected parks and squares in Tokyo to study the relationship between thermal comfort and behavioral activities and concluded that people spend more time in comfort zones, but found a weak correlation between the number of people in their sites and thermal comfort. Matzarakis et al. [9] conducted an outdoor thermal comfort study of two different types of shaded spaces on campus in Malaysia and found that the shaded environment created by plants had better PET values than the other environment created by buildings and structures.

By sorting out the existing studies on the effect of insolation on the thermal comfort of the outdoor environment in cold regions, Sun [10] illustrated the effect of outdoor physical parameters on the outdoor thermal comfort of panelized residential buildings in Xi'an by analyzing outdoor physical parameters and then concluded that daylight makes a huge difference in the average radiation temperature between shaded and non-shaded areas during daytime in cold regions, and ensuring sufficient daylight spacing can significantly enhance the outdoor thermal environment in winter.

In summary, established studies have explored the relevance of outdoor thermal comfort at different scales. There are apparent regional and climatic aspects in the scope of the study, so there are certain differences and seasonal variations in the results of the study in different regions.

It is important to investigate the impact of regional and climatic differences in outdoor thermal comfort on the people who use it, it is also of great social application value. Based on the micro-scale and seasonal characteristics, this paper investigates and compares the wintertime thermal comfort of university outdoor activity space with and without sunlight.

2 Methods

The investigation includes two parts: field measurement and a questionnaire survey. The questionnaire survey was conducted to understand the subjective feelings of students on the outdoor thermal environment in winter. In the specific operation process, while obtaining the time-by-time data of the thermal environment parameters from the field measurement, a questionnaire survey was conducted on the people within the scope of the measurement area to obtain their subjective thermal comfort feelings under the thermal environment conditions.

The investigation was conducted on November 28, December 1, and December 2 in 2021, which were typical winter meteorological days with all-clear weather. The specific meteorological data and measurement periods at the time of actual measurement are detailed in Table 1.

The square in front of the Student Activity Square was selected for the investigation and two specific sites (P1, P2) were selected for the on-site measurement, as shown in Fig. 1. P1 was located on the southeast side of the square with trees on the south side of it, which provides shading during the whole test period. P2 was located in the central and western part of the square, with a landscape vegetation belt in the

Table 1 Research dates and weather conditions

Date of research	Research time	Weather	Temperature (°C)
November 28th, 2021	9:30–17:30	Sunny	3–13
December 1st, 2021	9:30–17:30	Sunny	0–10
December 2nd, 2021	9:30–17:30	Sunny	–1–15

northwest and south side of P2, and insolation during the test period. The relationship among the differences at the two measurement points in different sunlight conditions in the same outdoor site and the user population is studied.

The physical environment data collected in the investigation included outdoor temperature (T_a), relative humidity (RH), wind speed (V), solar radiation (G), and black-bulb temperature (T_g). The test apparatus was arranged with a test height of 1.5 m, (Fig. 4) closer to the subject's neck and head height, and a data recording interval of 30 min (Figs. 2 and 3). The measurement period was 9:30–17:30, during which P1 was always in the shade of trees without direct sunlight P2 always had sunlight.

Fig. 1 Research site layout map. *Source* taken by the author

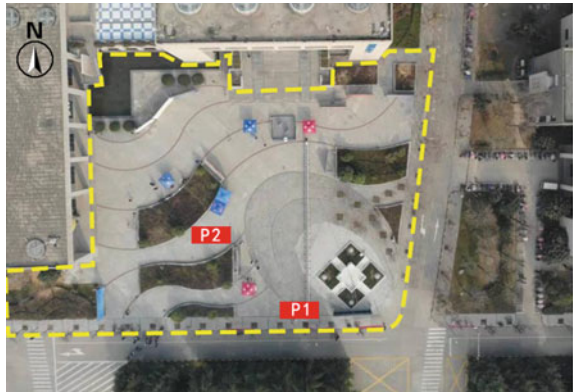


Fig. 2 Test instrument at P1

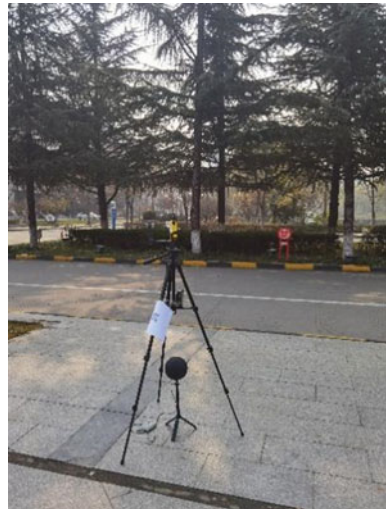


Fig. 3 Test instrument at P2

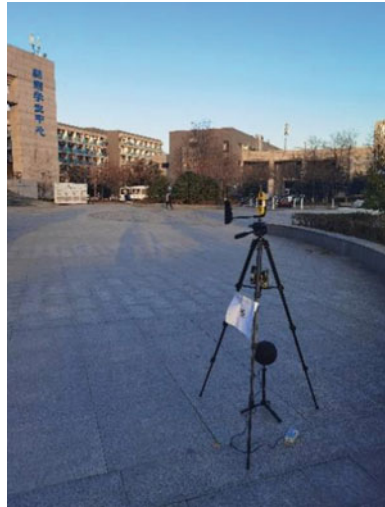


Fig. 4 On-site survey



Microclimate data including air temperature, relative humidity, wind speed, and solar radiation at different measurement points of the site were also recorded in real-time. The physical factors of the site were measured and recorded. The distribution and activities of the active population around the measurement points were observed to investigate the impact of the climatic factors on the population. The physical factors are the main climatic factors affecting human thermal comfort.

3 Results and Discussions

3.1 On-Site Measurement

Air Temperature. Firstly, the changes air temperature at the two measurement points were different, the temperature of P1 started to raise from 9:30 until 15:00 when it became stabilized; while the temperature of P2 showed a clear upward trend between 9:30 and 14:00 and a clear decreasing trend between 14:00 and 17:30. The highest temperatures all appeared between 13:00 and 16:00. It showed that different sunlight conditions affected the changing pattern of temperatures of the two measurement points. Secondly, the average temperature of P1 was always lower than that of P2 during the research period (3 days), and temperatures in the area under direct sunlight were significantly higher than that in the shaded area. Thirdly, the temperature variation of P1 was relatively small, and the highest temperature of P1 was usually lower than that of P2, which reached 16.2 °C during the investigation (Fig. 5).

Relative Humidity. Firstly, the changing of relative humidity of P1 and P2 were similar, both gradually decreases from 9:30 am onward, and gradually increased after 15:00. Secondly, the average relative humidity of P1 was always higher than that of P2 during the research period, with the average relative humidity of P1 and P2 being 55.32% and 51.84% respectively. The humidity of P2 was significantly lower than that of P1, which may be due to the evaporation of moisture from the surrounding environment caused by direct sunlight (Fig. 6).

Wind Speed. Firstly, both P1 and P2 belonged to open space, where the wind speed variation did not show obvious patterns. The range of wind speed variation was between 0–1.8 and 0–1.9 m/s for P1 and P2 respectively. Secondly, on November 28, the wind speed of P1 gradually increased during 9:30–14:00, while the wind speed of P2 showed no obvious change pattern; the wind speed of P1 was generally smaller than that of P2 on December 1 and 2. Thirdly, the average and maximum

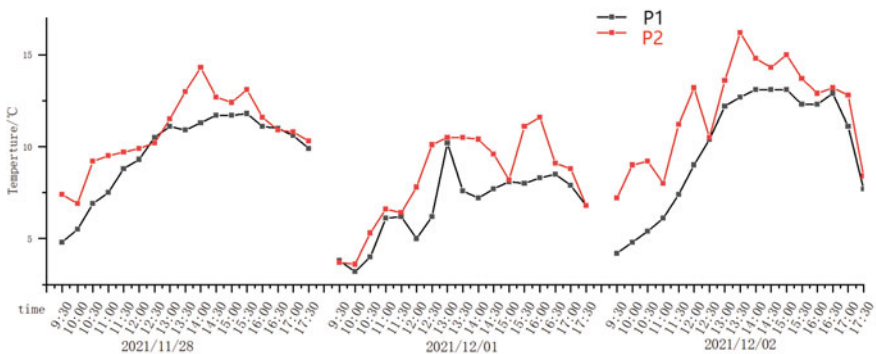


Fig. 5 Three days of measured air temperature change

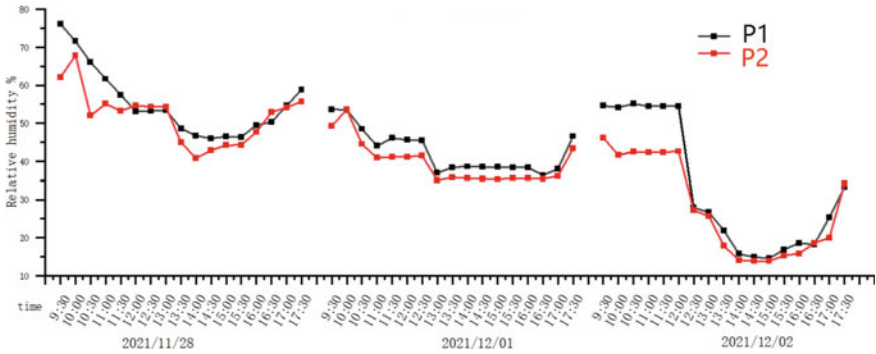


Fig. 6 Three days measured relative humidity change

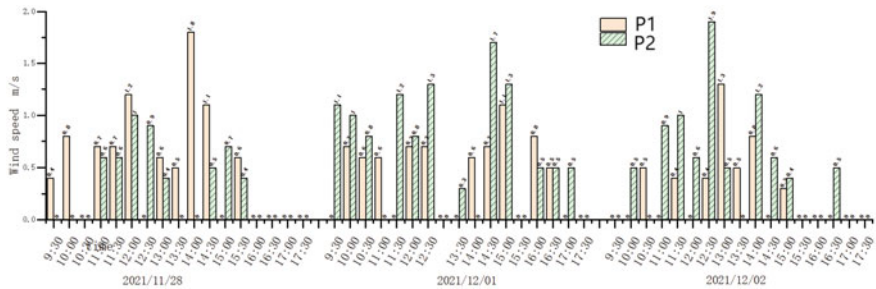


Fig. 7 Three days measured wind speed change

wind speed of P1 was 0.38 and 1.8 m/s, while that of P2 was 0.47 and 1.9 m/s. There were trees on the south side of P1, which may be the main reason why the wind speed of P1 was smaller than that of P2 (Fig. 7).

Solar Radiation. Firstly, the solar radiation of P1 was always lower than that of P2. The trend of solar radiation changes was in line with the regular sunshine variation. Secondly, the total and the highest solar radiation of P1 was 4967.9 W/m² and 464.5 W/m², while that of P2 was 12,883.5 W/m², and 605.2 W/m², which showed that the point in a sunlight area received significantly higher solar radiation than that in the shaded area of the same site (Fig. 8).

3.2 Overview of the Survey

The questionnaire survey was conducted within a distance of 2 m from the aforementioned measurement points. The questionnaire was divided into two parts, the first part involved basic information about the respondents, including age, gender, clothing, and activity status, and the second part involved subjective feelings of the

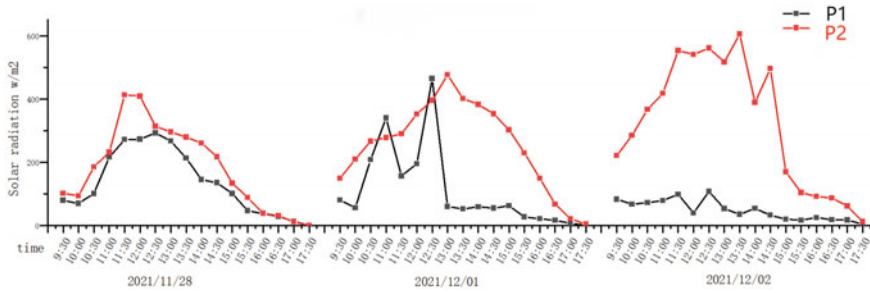


Fig. 8 Three days measured solar radiation change

respondents regarding the microclimate thermal environment, including Thermal Comfort Vote (TCV, using a 5-point scale) and Thermal Sensory Vote Value (TSV, using a 7-point scale).

The questionnaires were collected from students who frequently engage in outdoor activities in the SAS. 251 valid questionnaires were collected near the two measurement points. Among them, 123 (49%) were near P1 and 128 (51%) were near P2.

The gender distribution of respondents was relatively even (57.4% male, 42.6% female), and the age distribution of respondents was mainly focused on 18–28 years old, and respondents between 19 and 23 years old accounted for the main group (79.2%). 70 male respondents (56.9%) and 53 female respondents (43.1%) were received in P1. 74 male respondents (57.8%) and 54 female respondents (42.2%) were received in P2. 57.8%) and 5 (42.2%) female respondents.

3.3 Thermal Comfort

The outdoor winter environment was relatively cold. The clothing thermal resistance (clo) at P1 and P2 were generally between 0.39 and 2.4 clo, and 0.67 and 2.03 clo, while individual clothing thermal resistance varied greatly. The average clothing thermal resistance of respondents at P1 was 1.50 clo, and the maximum value was 2.40 clo. The average clothing thermal resistance of respondents at P2 was 1.47 clo. The average and maximum thermal resistance of clothing for P1 respondents was higher than that of P2 respondents, which implied that the sunshine site, (P2) may attract more active people with lighter clothes; while the shaded site (P1) may be suitable for people with thicker clothes (Fig. 9).

The top three thermal sensation votes for P1 was “Slightly cold” 46.3%, “Moderate” 24.4%, and “Cold” 20.3%, while for P2 was “Slightly cold” 53.1%, “Slightly hot” 14.1% and “Moderate” 13.3% respectively. Besides, 14.1% of the respondents in P2 indicated a feeling of radiant heat. The results of the heat sensation questionnaire are shown in Fig. 10. The deviations in the heat sensation poll indicate that

Fig. 9 Distribution of thermal resistance of garments at two points

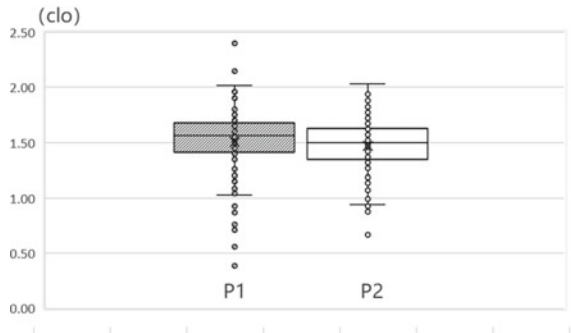
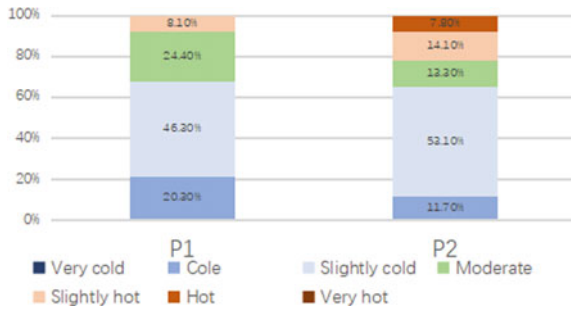


Fig. 10 Thermal sensory percentage. *Source* On-site research and the questionnaire survey



human comfort is not only affected by outdoor physical meteorological factors but also related to individual adaptation differences, different dressings, and different activity states. The outdoor activity space in winter needs sufficient sunlight as well as a suitable amount of solar radiation.

Results of the thermal comfort questionnaire survey showed that the number of “Moderate” and “Very comfortable” in P2 was higher than that in P1, and the number of “Very uncomfortable” and “Uncomfortable” was lower than that in P1, which indicated that the outdoor activity areas with sunlight are more preferred by people in winter. “Moderate”, “Comfortable” and “Very comfortable” all indicate that the human body felt good outdoor thermal comfort. Among them, the total proportion of “Moderate”, “Comfortable” and “Very comfortable” in P1 and P2 was 42.3% and 38.3%, respectively. The proportion of respondents who felt poor thermal comfort in P1 and P2 were 57.7%, and 61.7% respectively, which showed that the thermal comfort situation of outdoor activity sites was generally poor, while P1 possesses a relatively better overall performance of thermal comfort and thermal sensation than that in P2.

The above results indicated that the presence or absence of sunshine has a certain influence on the thermal comfort of outdoor activity space. It was also noted that suitable sunshine was needed, while too much solar radiation may also cause a decrease in comfort level in winter (Tables 2 and 3, Figs. 10 and 11).

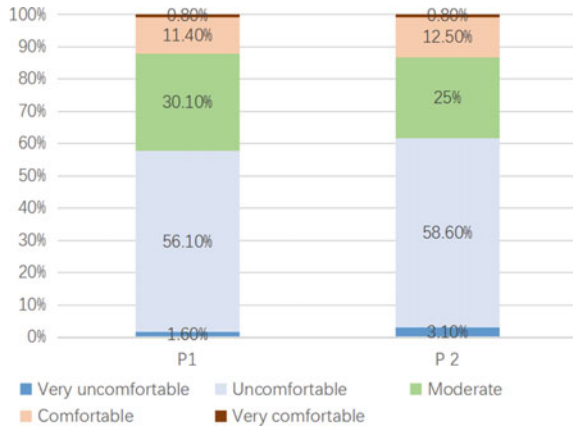
Table 2 Thermal comfort voting statistics for P1 and P2

Site	Very uncomfortable	Uncomfortable	Moderate	Comfortable	Very comfortable
P1	2	69	37	14	1
P2	4	75	32	16	1

Table 3 Thermal sensation voting statistics for P1 and P2

Site	Very cold	Cold	Slightly cold	Moderate	Slightly hot	Hot	Very hot
P1	1	25	57	30	10	0	0
P2	0	15	68	17	18	10	0

Fig. 11 Thermal comfort share. *Source* On-site research and the questionnaire survey



3.4 Influence of Outdoor Space with and Without Insolation

Voting on the Perception of Solar Radiation at P1. According to the vote on the perception of solar radiation at P1, 75.6% of the respondents had a weak perception of solar radiation, 14.6% had a moderate perception of solar radiation, and 9.8% had a significant perception of solar radiation (Fig. 12). According to the results of the solar radiation expectation poll for P1, 54.5% of the respondents expect the solar radiation to remain the same and accept the sunlight situation in P1 at the investigation time, while 38.2% of the respondents expected the solar radiation to be stronger (Fig. 13).

Voting on the Perception of Solar Radiation at P2. Firstly, 21.9% of the respondents felt moderately about solar radiation. About 32% of the respondents felt strongly, and 46.1% felt weak about solar radiation (Fig. 12). Secondly, 50% of the respondents expected solar radiation to remain the same, while 26.6% of the respondents expected solar radiation to be stronger. Thirdly, 23.4% of the respondents expect solar radiation to be weaker. Thus, it can be concluded that 50% of the respondents accept the

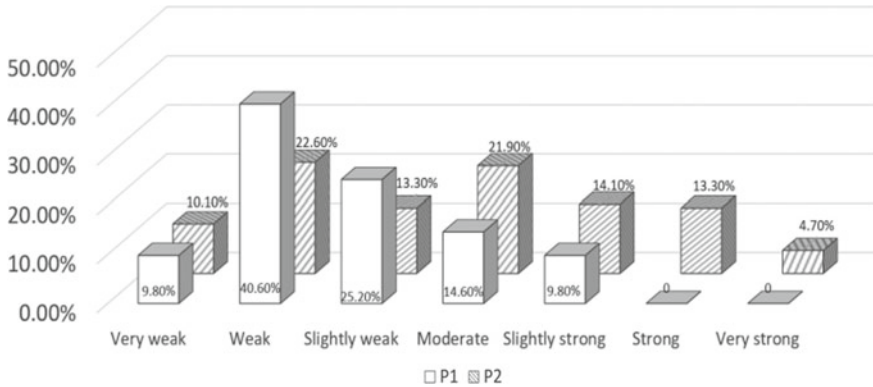
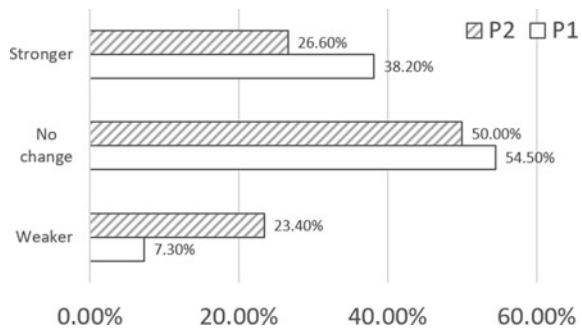


Fig. 12 Solar radiation perception vote at 2 points

Fig. 13 Respondents' expectations for changes in sunlight at 2 points



current sunlight conditions, while 26.6% of respondents expect more sunlight on-site (Fig. 13).

3.5 Multiple Linear Regression Analysis

In the investigation of outdoor thermal comfort, it is found that several factors influence the results of the investigation at the same time. Therefore, multiple linear regression was used to further analyze the results. Using outdoor physical parameters as independent variables and TCV as dependent variables, a regression model of outdoor thermal comfort of P1 was established and the following Eq. (1) was obtained.

$$TCV = 0.066 Ta + 0.006 RH + 0.29 V - 1.472 \tag{1}$$

A P2 winter outdoor thermal comfort regression model was developed and the following Eq. (2) was obtained.

$$TCV = 0.008 RH - 0.017 Ta + 0.269 V - 0.758 \quad (2)$$

(RH stands for relative humidity, Ta stands for air temperature and V stands for wind speed in the equation).

The above formula shows that the important factors affecting the winter outdoor thermal comfort of P1 and P2 are wind speed, air temperature, and humidity in order. Outdoor physical parameters of P1 have a positive relationship with winter outdoor thermal comfort; wind speed and humidity of P2 have a positive relationship with winter outdoor thermal comfort, and air temperature has a negative relationship with winter outdoor thermal comfort. The air temperature is negatively related to outdoor thermal comfort in winter.

The equation indicates that, for P2, when the temperature varies between 3.6 °C and 16.2 °C, the outdoor thermal comfort of respondents decreases as the outdoor temperature increases. This may be because direct sunlight causes more heat gain than needed which leads to a decrease in outdoor thermal comfort. In contrast, for P1, when the temperature varies between 3.2 °C and 13.1 °C, the outdoor thermal comfort of respondents increases as the outdoor temperature increases. Solar radiation, as the main factor influencing outdoor air temperature in winter, showed a significant difference in the thermal sensation of respondents. The regression model of outdoor thermal comfort in winter from the two measurement points showed that the physical factor of relative humidity had a weak effect on outdoor thermal comfort as well as on outdoor thermal comfort.

4 Conclusion

This paper investigated the use of an outdoor activity space on campus and analyzed the clothing thermal resistance, thermal feeling, and thermal comfort of the respondents from the perspective of time and space. Correlation analysis was also conducted based on the measured climate data and the thermal comfort of the research object.

It was found that different sunshine conditions changed the temperature, humidity, and solar radiation of the two measurement points significantly, and had no general effect on the wind speed. For sites with different sunshine conditions, different strategies should be considered to improve thermal comfort. The thermal resistance of respondents' clothing was also related to the sunshine conditions. The average clothing thermal resistance of P1 was lower than that of P2, and the clothing thermal resistance of respondents in the shadow area was generally lower than that of the insolation area. This study focused on the respondents' choice of feelings about solar radiation. In P1 75.6% felt less about solar radiation, and the respondents in P2 had a higher intensity of solar radiation than in P1. By analyzing the two test-point thermal senses, P1 thermal comfort performs better than P2 under both temperature

and solar radiation. From the above analysis, it can be seen that when the temperature ranges between 3.2 °C and 13.1 °C, it was more important to improve the outdoor temperature in the shadow area; when the outdoor temperature range in the insolation area was 3.6–16.2 °C, thermal comfort of the respondents was negatively related to the outdoor temperature. Under different sunshine conditions in the same site, the thermal comfort of the respondents was significantly affected by solar radiation. The seasonal characteristics of winter in cold regions are a key challenge for the design of outdoor spaces in buildings. Therefore, designers and planners need to better understand the built environment, meteorological conditions, and important factors that hinder users' outdoor activities in winter, and on this basis, explore the relationship between meteorological conditions and outdoor space design.

It should be noted that the research period of this paper was short in winter, and the number of valid questionnaires collected was limited, so the conclusion has limitations. Follow-up studies can be conducted to expand the investigation under the influence of multiple factors for more outdoor activity spaces of different scales on the university campus in this region. Besides, most of the current studies have shown that there is a certain separation between thermal comfort and thermal sensation subjective studies; therefore, subsequent studies could also consider the relationship between the subjective factors of outdoor thermal comfort voting and thermal sensation voting and the objective factors affecting the outdoor physical thermal environment and assign weights for analysis.

Acknowledgements The research of this paper was supported by The National Natural Science Foundation of China (52078422).

References

1. Zhen M, Dong Q, Chen P et al (2021) Urban outdoor thermal comfort in western China. *J Asian Archit Build Eng* 20(2):222–236
2. Li W (2015) Research on outdoor thermal environment in winter in urban residential areas in cold regions. Xi'an University of Architecture and Technology
3. Hong J, Liang Q, Peng C (2021) Research on winter thermal comfort of campus in severe cold regions based on outdoor activities. *Build Sci* 3(8):87–92, 103. <https://doi.org/10.13614/j.cnki.11-1962/tu.2021.08.11>
4. Hu X, Li B, Chen H (2020) Research review and evaluation framework of outdoor thermal comfort. *Build Sci* 36(04):53–61. <https://doi.org/10.13614/j.cnki.11-1962/tu.2020.04.09>
5. Huang Z (2020) Investigation on the design strategy of outdoor activity space of university campus in Mianyang area based on comfort. Southwest University of Science & Technology
6. Wang YM, Lian ZW, Chang HY, The correlation between the overall thermal comfort, the overall thermal sensation and the local thermal comfort in non-uniform environments with local cooling. *Indoor Built Environ*
7. Shoosharian S, Lam CKC, Kenawy I (2020) Outdoor thermal comfort assessment: a review on thermal comfort research in Australia. *Build Environ* 177
8. Sofia Thorsson T, Lindberg F, Eliasson I, Lim E-M (2007) Thermal comfort and outdoor activity in Japanese urban public places. *Environ Behav* 39(5):660–684

9. Matzarakis A, Rutz F, Mayer H (2007) Modelling radiation fluxes in simple and complex environments—application of the RayMan model. *Int J Biometeorol* 51(4):323–334
10. Sun C (2016) Research on the morphology and layout of Xi'an plate residential complex based on outdoor heat and comfort. *Xi'an Univ Archit Technol* 2(5):99–110

A Novel Low-Temperature Personalized Radiant Cooler: Thermal Environment and Local Thermal Comfort Evaluation



Yuying Liang and Gongsheng Huang

Abstract A new personalized radiant cooler (PRC) is presented in this study, which uses an air-layer integrated radiative cooling unit (AiRCU) to create a microthermal environment for individuals. The AiRCU separates the air-contact surface from the radiant surface, which is able to enhance cooling capacity and reduce condensation risk simultaneously. An interesting issue is if the thermal comfort of the thermal environment built by the PRC should be satisfied. In this study, the PRC was experimentally prepared and a model for the thermal environment was developed using computational fluid dynamic. The cases of the PRC with the supply air temperature of 26.8 °C, 27.1 °C, 27.5 °C and the radiant surface temperature of 15 °C, 10 °C, 5 °C, which achieved the same operative temperature for the workstation, were investigated. The temperature and velocity distributions, and the thermal comfort indices were analyzed. The results indicated that the local thermal comfort of the PRC satisfies the comfort criteria specified in the ASHRAE Standard.

Keywords Personalized radiant cooler · Energy saving · Thermal comfort · Local cooling

1 Introduction

Personalized comfort systems (PCSs) allow individuals to regulate the microthermal environment for specific body parts to meet their own comfort requirements rather than regulating the whole conditioned space (i.e., all-air conditioning system) [1]. PCSs is also an efficient technique for energy saving as it allows higher ambient temperatures under the same thermal requirement. It has been reported that using PCS can increase the ambient temperature up to 4.2 °C [2] and achieve the highest energy savings of 51% [3] compared with all-air systems. Generally, PCSs in indoor

Y. Liang · G. Huang (✉)

Department of Architecture and Civil Engineering, City University of Hong Kong, Hong Kong, China

e-mail: gongsheng.huang@cityu.edu.hk

cooling are mainly two types: (i) personalized ventilation systems (PVSs) and (ii) personalized radiant cooling systems (PRCSs). PVSs has been wildly applied to target the uncomfortable upper body parts in a microenvironment [4]. However, the cool air with a high velocity in PVSs will produce the unwanted feeling of local thermal discomfort due to fan noisy and cold-draft. For example, using ductless PVSs near the breathing zone results in significant thermal stratification with the vertical air temperature differences (e.g., up to 5 °C) between the head and ankle height levels [5]. In addition, exposing to cold-draft for a long time will increase the risk of chronic diseases like headache and pains in the back and joints [6].

To address the above problems, PRCSs were proposed in conditioned space with three types: the radiant cooling cubicle [7, 8], radiant cooling desk [9], and the radiant cooling board integrated drainage grooves [10]. The PRCS is considered as a more comfortable PCS because of its smaller vertical temperature differences and less cold-draft risk to avoiding local thermal discomfort. Comfortable condition with standard effective temperature of 23.2–26.1 °C and 60% energy saving can be achieved when the supply water temperature is 15–19 °C by using PRCSs in a radiant cooling cubicle type compared the ceiling radiant system [7]. In addition, using PRCs in a desk type with a supply water temperature with 22.8–25.5 °C in workstation can reduce warm sensation and increase both comfort and acceptability of subjects, which extends acceptable temperature range up to 32 °C [9]. However, these two PRCSs need to control a low relative humidity of the indoor air and keep the radiant surface temperature above dew-point temperature to avoid condensation problem, which adds the cost of dehumidification device and narrows the radiant cooling temperature range. Furthermore, in order to collect water drops from the PRCSs when condensation, the PRCS integrated drainage grooves combined with naturally ventilated office buildings was designed under two high ambient temperature (28 °C and 30 °C), five radiant surface temperatures (10–30 °C) and relative humidity of 45% [10]. But this design results in a cooling capacity reduction as the condensation in low-temperature radiant surface will decrease the emissivity of the radiant surface.

Therefore, to enhance the flexibility in regulating the microthermal environment with a wide range radiant surface temperature, we proposed a novel personalized radiant cooler (PRC) integrated with an air-layer integrated radiative cooling unit (AiRCU) to separates the air-contact surface from the radiant surface [11–13], which improves cooling capacity and reduce condensation risk simultaneously. By using this design, the purpose of this paper is to studies the thermal environment and thermal comfort characteristics under the regulation by a novel PRC based on the CFD simulation.

2 Theory of the Thermal Environment and Thermal Comfort

The local thermal comfort was evaluated through the percentage dissatisfied with the radiant temperature asymmetry caused by the radiant cooling panel (PD_r) and with the vertical air temperature difference ($PD_{a(0.1-1.1m)}$), which are calculated by

$$PD_r = 100/[1 + \exp(9.93 - 0.5\Delta T_{pr})] \tag{1}$$

$$PD_{a(0.1-1.1m)} = 100/[1 + \exp(5.57 - 0.856\Delta T_{a,v})] \tag{2}$$

where ΔT_{pr} represents the radiant temperature asymmetry, limited inside 15 °C; $\Delta T_{a,v}$ represents the vertical difference of air temperature between height levels of 1.1 m and 0.1 m, limited inside 3.0 °C. The limit of the local thermal comfort indices is summarized in Table 1.

The surface temperature $T_s \sim T_m$ under the PRC is modelled by combining the radiative and conductive heat transfer models on the CFD fluent platform. The energy equation of the PRC can be expressed as [16]

$$\frac{\partial}{\partial t}(\rho E) + \nabla \cdot (\vec{v}(\rho E + p)) = \nabla \left[\lambda_{eff} \nabla T - \sum_j h_j \vec{J}_j + (\vec{\tau}_{eff} \cdot \vec{v}) \right] + S_h \tag{3}$$

where E , ρ , \vec{v} , p and T represent the total energy, the density, the velocity vector, the pressure and the temperature; h_j represents the sensible enthalpy of the j th species; \vec{J}_j represents the diffusion flux of species j ; $\vec{\tau}_{eff}$ represents the deviatoric stress tensor; λ_{eff} represents the effective conductivity; and S_h represents volumetric heat sources, including the radiation energy source.

The discrete ordinates (DO) radiation model [16] was used to solve the radiation intensity equation inside the semi-transparent PE membrane that is optically thin. The realizable $k-\epsilon$ model was used to calculate the turbulent viscosity, the turbulence kinetic energy and the dissipation rate. The isometric view of the simulated chamber was shown in Fig. 1. ANSYS Fluent 2020 was used as the CFD software to construct the simulation platform. In the CFD simulation, the residual errors of eight governing equations for continuity, (x, y, z) velocity, k , ϵ , energy and do-intensity was 10^{-3} , 10^{-3} , 10^{-3} , 10^{-3} , 10^{-6} and 10^{-6} , respectively [11]. For ensuring the reliability

Table 1 Indices and their limits of local thermal discomfort factors. [14, 15]

Radiant temperature asymmetry	Floor temperature	Vertical air temperature difference	Draft
Cooling wall < 15 °C	19–29 °C (Feet in contact)	< 3 °C for seated posture between 0.1 to 1.1 m	0.2 m/s

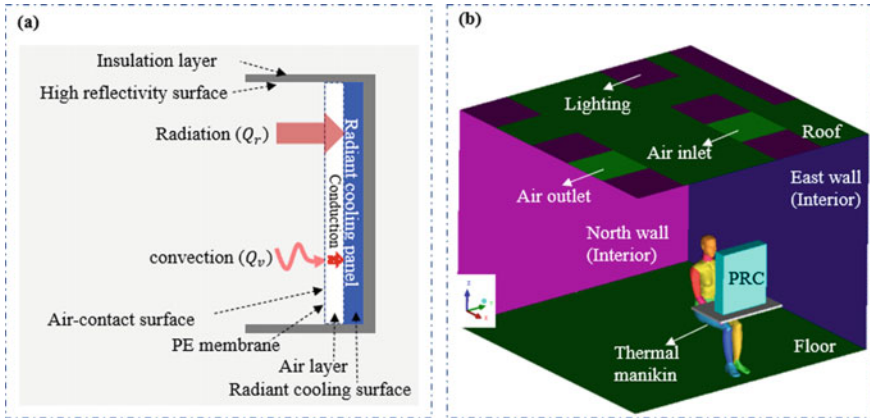


Fig. 1 a The structure of the PRC and b the isometric view of the simulated chamber

of the simulation data, the 0.1% CFD convergence was set in membrane temperature, radiant surface heat flux and membrane heat flux before stop criterion.

3 Case Studies

3.1 Setup of Cases

The structure of the PRC was demonstrated in the Fig. 1a, consisting of an insulation layer, high reflectivity surface, radiant cooling panel and an air layer combined with PE membrane. The PRC (0.3 × 0.6 m) was installed in a chamber (3 × 3 × 2.4 m) and a ventilation system to maintain ensure the thermal comfort in a specific thermal environment together with a ventilation system, where a thermal manikin was located near the PRC in the workstation, as shown in Fig. 1b.

With the application of the PRC at different indoor air temperatures, the supply air temperature was adjusted from 25.9 °C to 27.5 °C with constant air velocity of 0.15 m/s to maintain the constant local operative temperature of 24 °C under different radiant surface temperature of the PRC in the range of 15 °C to 5 °C. The wall surface temperature of east/south/north/west wall/ceiling specified 28 °C, which was close to the indoor air temperature to eliminate the effect of the wall surface on the radiative heat flux between the PRC and the human body. The floor was 27 °C that is approximately equal to the air temperature near floor. The roof was equipped with fluorescent lighting with constant heat flux of 69.5 w/m² as an internal heat source. The thermal manikin in the thermal chamber was with total heat flux 70 W·m⁻² (i.e., metabolic rate of 1.2 met) and the summer clothing conductivity of 0.0129 W·m⁻¹·K⁻¹ (i.e., clothing insulation of 0.5 clo). The detail boundary condition setup is shown in Table 2.

Table 2 Boundary conditions of the simulated chamber

Boundary	Simulation conditions
Supply air inlet/outlet (0.6 m × 0.6 m)	Inlet velocity, 0.15 m·s ⁻¹ , Inlet temperature, 25.9, 26.8, 27.1, 27.5 °C Outlet pressure out
East/south/north/west wall/ceiling	28 °C, internal emissivity, 0.9
Floor	27 °C, internal emissivity, 0.9
Radiant cooling panel (0.6 m × 0.3 m)	Temperature, 5, 10, 15 °C Internal emissivity, 0.95
Fluorescent lighting	25 W per unit lamp (69.5 W·m ⁻²)
Thermal manikin	Heat flux, 70 W·m ⁻² (1.2 met), emissivity, 0.98
Clothing	Summer clothing thickness, 0.001 m Emissivity, 0.90 Clothing thermal conductivity, 0.0129 W·m ⁻¹ ·K ⁻¹

Three radiant cooling temperatures the PRC, namely 15, 10, and 5 °C, were investigated to understand the influence of the radiant cooling temperature on the PRC thermal environment. The corresponding supply air temperatures were 26.8, 27.1, 27.5 °C respectively, which were set to maintain the local operative temperature at 24.0 °C in order to meet the requirement in the European design criteria in an office building [14], i.e. $T_{op} = 24.5 \pm 1$ °C. The three cases were denoted as PRC_S26.8_T15, PRC_S27.1_T10 and PRC_S27.5_T5, respectively. In the three cases, the membrane temperature could be maintained around 22 °C, higher than the dew point temperature of 19.5 °C ± 0.8 °C in the indoor environment with $T_{a,max} = 28$ °C and relative humidity of 60%. Thus, there was no condensation risk on the surface of the PE membrane. The case of air cooling with the supply air temperature of 25.9 °C was used as a benchmark, entitled as AC_S25.9_27.9, which achieved the same local operative temperature of 24 °C.

3.2 Personalized Thermal Environment Analysis

Figure 2a–d show the indoor air temperature contour inside the chamber at $y = 1.5$ m, of the cases AC_S25.9_T27.9, PRC_S26.8_T15, PRC_S27.1_T10 and PRC_S27.5_T5. In Fig. 2a the air temperature near the floor was below 27.1 °C, lower than the temperatures of other places of the thermal chamber. In comparison, the air temperature over the head and around the upper space of the human body was over 29.3 °C, higher than that of the other spaces around the human body between the pelvis level (0.6 m) and the ankle level (0.1 m). This was because the heat flux around the upper part of the thermal manikin was upward due to the buoyancy effect.

In Fig. 2b–d the indoor air temperature increased with the supply air temperature increasing from 25.9 °C to 26.8 °C and the radiant surface temperature decreasing

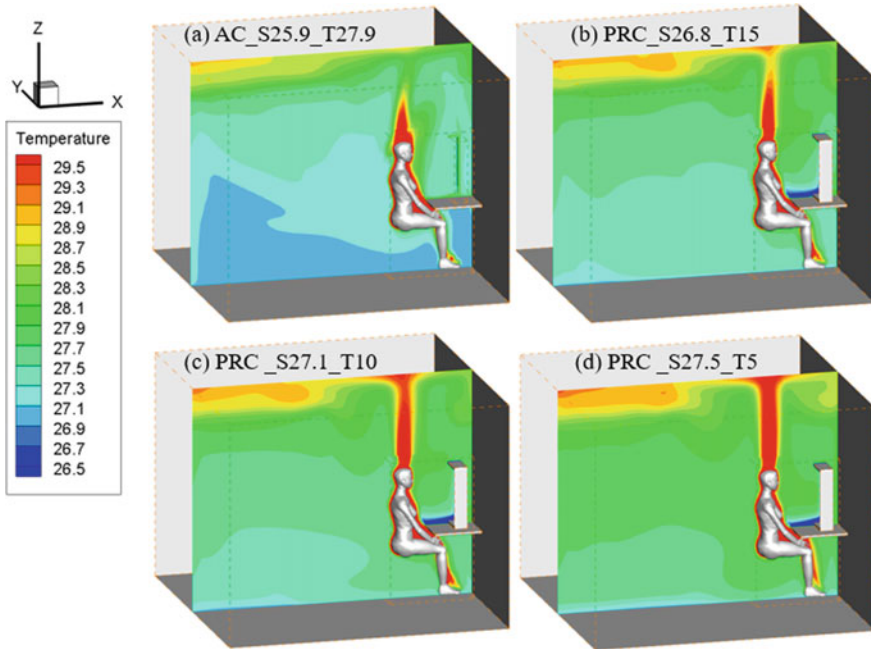


Fig. 2 The temperature distribution in the four cases: **a** AC_S25.9_T27.9; **b** PRC_S26.8_T15; **c** PRC_S27.1_T10; **d** PRC_S27.5_T5

from 15 °C to 5 °C. Compared to all air case AC_S25.9_T27.9, the PRC cases showed a larger space of hot air over the head and around the human body as the supply air temperature increased. When the supply air temperature became higher, the phenomenon of hot air ascending over the head became prominent. This was because the increase of air temperature around the human body led to an increase in its surface temperature, and thereby increased the temperature difference between the roof and the human body. The air temperature of the chamber was in the range of (27.1 °C, 28.7 °C). Due to the influence of the low radiant cooling surface temperature in PRC, the air temperature of lower part of the PRC cases facing the human body was the relatively low (below 26.5 °C), which reduce the air temperature of hot zone near the front torso.

Figure 3a–d showed the air velocity distribution of the four cases at the section of $y = 1.5$ m, respectively. Overall, the air velocity of the chamber was inside the range of 0–0.2 m/s. Figure 3a showed that the air velocity at the top of the head and between the head and torso level near the human body was the maximum (~0.2 m/s); while that of the back of the human body and the space above the desk presented the minimum velocity inside the range of 0–0.04 m/s. The other space of the chamber had a relatively non-uniform air velocity distribution inside the range of 0–0.14 m/s. In Fig. 3b–d the low-velocity zone (0–0.02 m/s) at the back of the manikin had an increasing area along with the decrease of T_c from 15 °C to 5 °C. The high-velocity

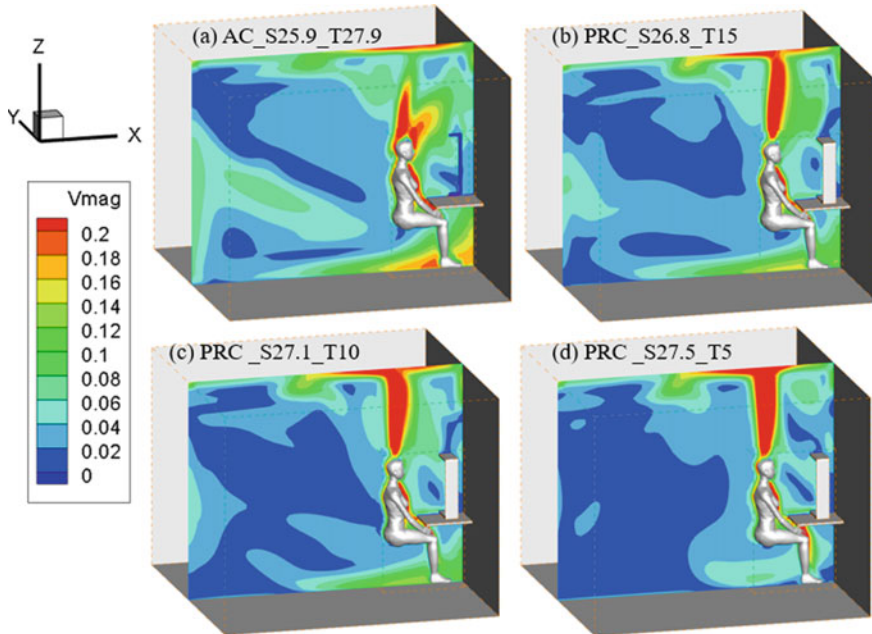


Fig. 3 Comparisons of velocity distribution: **a** AC_S25.9_T27.9; **b** PRC_S26.8_T15; **c** PRC_S27.1_T10; **d** PRC_S27.5_T5

zone right overhead became more prominent with the decrease of T_c , especially in PRC_S27.1_T10 and PRC_S27.5_T5. This was because the buoyancy effects on the thermal plume of the manikin was stronger at a higher air temperature. Therefore, the low-velocity zone around the manikin became larger when T_c become lower.

The average air temperature and air velocity at the typical height levels of a seating human body, i.e., 0.1 m for the ankle level, 0.6 m for the waist level, 1.1 m for the head level, as well as 1.7 m for the height of a standing position, were further analyzed with area weighted average simulation data for the four cases, as shown in Fig. 4a and b, respectively.

In Fig. 4a the overall air temperature was in the range of (27.0–27.9 °C) and the temperature difference between 0.1 and 1.7 m was less than 0.4 °C in all the four cases. The average air temperature in the three PRC cases was larger than that in the AC_S25.9_T27.9. With the increase of the height, the average air temperature increased, and its increasing rate decreased due to the PRC installed at the height level of 1.1 m. For instance, in the case PRC_S27.5_T5, the average air temperature at 1.1 m was slightly smaller than that at 0.6 m. This indicated that the average air temperature at the height of 1.1 m was much influenced by the PRC. Figure 4b showed that the overall air velocity was ranged in 0.02–0.08 m/s and decreased with the decrease of T_c . For instance, when T_c was decreased from 15 °C to 10 °C and 5 °C, the average air velocity at the height of 0.1 m decreased from 0.057 to 0.044 and 0.025 m/s, respectively. With the decrease of the height from 1.7 to 0.1 m, the average

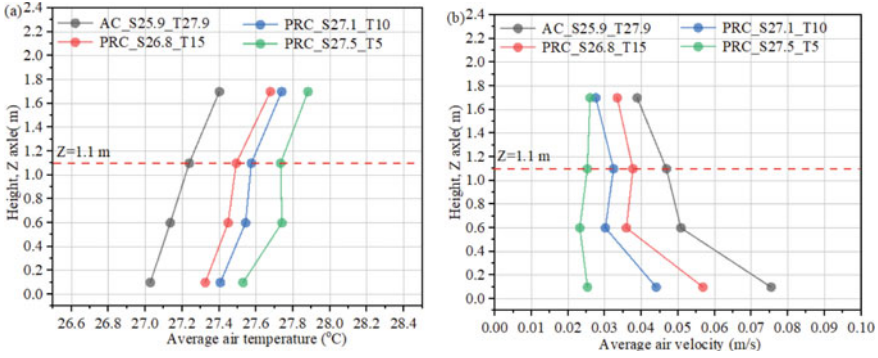


Fig. 4 Thermal environmental parameters as a function of the vertical heights of the chamber: **a** the average air temperature; **b** the air velocity

air velocity of the cases AC_S25.9_T27.9, PRC_S26.8_T15 and PRC_S27.1_T10 slightly decreased, with the difference being less than 0.04 m/s. In comparison, the difference of the average air velocity in PRC_S27.5_T5 was maintained at 0.025 m/s approximately.

3.3 Personalized Thermal Comfort Analysis

The radiative heat exchange between the radiant cooling surface and the human body was illustrated and compared between the four cases, as shown in Fig. 5. It was observed that the radiative heat flux of the thermal manikin surface was in a range of 0–70 W·m⁻². The radiative heat flux in AC_S25.9_T27.9 was significantly smaller than that in other three PRC cases. It should be noted that the radiative heat flux of the concave surfaces of the human body (i.e., eyes and the rib) was larger than that of the convex surfaces (i.e., chest). This is because the concave surface has a larger angle factor between the human surface and the radiant cooling surface; while the convex surface has a smaller one. Therefore, the application of the PRC can effectively enhance the radiative heat exchange between the radiant surface and the human body.

The vertical air temperature differences and the radiant temperature asymmetry are two main important indices for the local thermal comfort analysis. Figures 6a, b illustrated the comparisons of the percentage dissatisfied ($PD_{a(0.1-1.1\text{ m})}$, PD_r) relative to the vertical air temperature differences ($\Delta T_{a,v}$) between the ankle level (0.1 m) and the head level (1.1 m) and the radiant temperature asymmetry (ΔT_{pr}) for different cross sections. In Fig. 6a the vertical air temperature differences were inside the range of (0.17 °C, 0.21 °C), which was far smaller than the upper limit of 3 °C [15]. The maximum $\Delta T_{a,v}$ was 0.21 °C in AC_S25.9_T27.9, whereas the minimum $\Delta T_{a,v}$ was 0.17 °C in PRC_S27.1_T10, which resulted in the $PD_{a(0.1-1.1\text{ m})}$ between the ankle

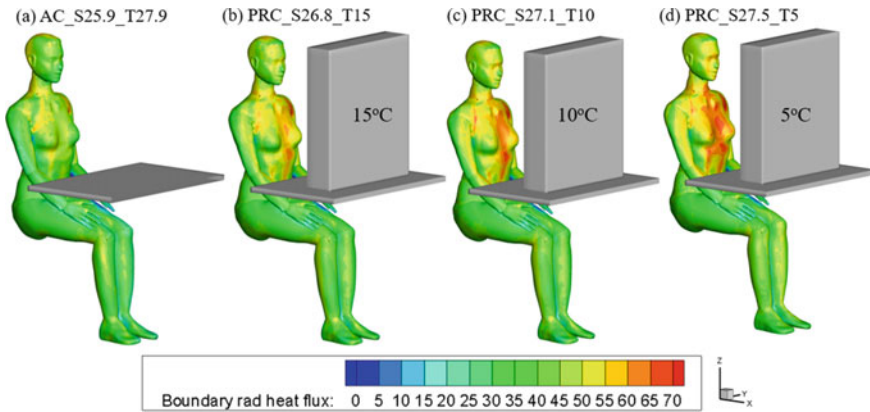


Fig. 5 Local radiative heat flux distribution of the thermal manikin

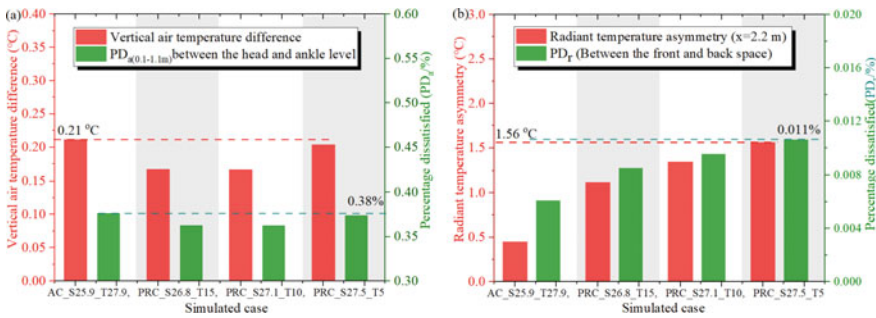


Fig. 6 Local thermal comfort indices of a the vertical air temperature differences and b the radiant temperature asymmetry for cross section $x = 2.2$ m for cases

level and the head level for the four simulated cases within 0.38%. Figure 6(b) shows that ΔT_{pr} in the cross section of $x = 2.2$ m increased with the decrease in the radiant surface temperature within a range of (0.45 °C, 1.56 °C). The maximum ΔT_{pr} could reach up to 1.56 °C in PRC_S27.5_T5, which was significantly larger than that in AC_S25.9_T27.9, only 0.45 °C. Accordingly, the PD_r if the three PRC cases caused by the ΔT_{pr} was inside the range of (0.009%, 0.011%), which was larger than that of the AC_S25.9_T27.9, 0.006%.

4 Conclusion

The thermal environment and thermal comfort created by the proposed PRC have been investigated. A benchmark case, AC_S25.9_T27.9, and three PRC cases, PRC_S26.8_T15, PRC_S27.1_T10 and PRC_S27.5_T5, were compared. The model of the

thermal environment for the PRC has been developed using CFD techniques. The PRC played a role in local regulation of the air temperature of the workstation, and its average air velocity decreased with a difference within 0.04 m/s with the decrease in the heights from 0.1 to 1.7 m. The vertical air temperature differences between the head and ankle levels were in a range of 0.17–0.21 °C and the radiant temperature asymmetry for all cross sections was within 1.56–3.75 °C, which met the requirement of thermal discomfort limits.

References

1. Xie J, Li H, Li C, Zhang J, Luo M (2020) Review on occupant-centric thermal comfort sensing, predicting, and controlling. *Energy Build* 226:110392
2. Zhang H, Arens E, Zhai Y (2015) A review of the corrective power of personal comfort systems in non-neutral ambient environments. *Build Environ* 91:15–41
3. Schiavon S, Melikov AK, Sekhar C (2010) Energy analysis of the personalized ventilation system in hot and humid climates. *Energy Build* 42:699–707
4. Yang B, Ding X, Wang F, Li A (2021) A review of intensified conditioning of personal micro-environments: moving closer to the human body. *Energy Built Environ* 2:260–270
5. Liu J, Li Z, Kim MK, Zhu S, Zhang L, Srebric J (2020) A comparison of the thermal comfort performances of a radiation floor cooling system when combined with a range of ventilation systems. *Indoor Built Environ* 29:527–542
6. Xia Y, Niu J, Zhao R, Burnett J (2000) Effects of turbulent air on human thermal sensations in a warm isothermal environment. *Indoor Air* 10:289–296
7. Khare VR, Garg R, Mathur J, Garg V (2021) Thermal comfort analysis of personalized conditioning system and performance assessment with different radiant cooling systems. *Energy Built Environ* (In press)
8. Ismail N, Ouahrani D (2022) Modelling of cooling radiant cubicle for an office room to test cooling performance, thermal comfort and energy savings in hot climates. *Energy* 244:123185
9. He Y, Li N, He M, He D (2017) Using radiant cooling desk for maintaining comfort in hot environment. *Energy Build* 145:144–154
10. Teufl H, Schuss M, Mahdavi A (2021) Potential and challenges of a user-centric radiant cooling approach. *Energy Build* 246:111104
11. Liang Y, Zhang N, Wu H, Xu X, Du K, Yang J et al (2021) Thermal environment and thermal comfort built by decoupled radiant cooling units with low radiant cooling temperature. *Build Environ* 206:108342
12. Zhang N, Liang Y, Wu H, Xu X, Du K, Shao Z et al (2021) Heat transfer modeling and analysis of air-layer integrated radiant cooling unit. *Appl Therm Eng* 194:117086
13. Liang Y, Zhang N, Wu H, Xu X, Yang J, Huang G (2022) Cooling load characteristics of indoor spaces conditioned by decoupled radiant cooling unit with low radiant temperature. *Build Simul* 15:2067–2079
14. ISO7730 (2005) Ergonomics of the thermal environment—analytical determination and interpretation of thermal comfort using calculation of the PMV and PPD indices and local thermal comfort criteria
15. American Society of Heating, Refrigerating, Air-Conditioning Engineers (2017) Thermal environmental conditions for human occupancy: ASHRAE Standard 55-2017. ASHRAE Inc., Atlanta, USA
16. Ansys (2013) ANSYS fluent theory guide 15.0. Ansys Inc., Canonsburg, PA, USA

An Empirical Study of the Effects of Green Roof on the Outdoor and Indoor Thermal Environment of a College Buildings in Winter



Minmin Yang, Yu Liu, Yiming Zhang, Yufei Zou, Jie Song, and Ni Zhang

Abstract With the continuous progress of urbanization, urban ecological problems have been widely concerned. The heat island effect produced in cities affects people's lives, and it is increasingly urgent to solve the problem of heat island. Roof greening is closely related to buildings. It is a new greening method, which has advantages in improving ecology, regulating climate and building energy conservation. The campus not only meets the greening needs of teachers and students for the environment, but also pays more and more attention to the energy-saving utilization of teaching buildings, college buildings and other buildings. In this context, campus roof greening came into being. In different seasons, roof greening will have a certain impact on the indoor and outdoor thermal environment of campus buildings. By means of on-site measurement, this paper scientifically and quantitatively explores its impact, and then analyzes the data to obtain experimental conclusions such as the insulation effect of the top floor indoor. It is hoped that this article can provide some reference for whether to use roof greening in buildings.

Keywords Green roof · Thermal environment · Empirical study

M. Yang · Y. Liu (✉) · Y. Zhang · Y. Zou · J. Song · N. Zhang
School of Mechanics, Civil Engineering and Architecture, Northwestern Polytechnical University,
Xi'an, China
e-mail: liuyu@nwpu.edu.cn

M. Yang · Y. Liu · Y. Zhang · Y. Zou · J. Song
Sustainable Building and Environmental Research Institute, Northwestern Polytechnical
University, Xi'an, China

J. Song
School of Architecture, University of Liverpool, Liverpool, United Kingdom

© The Author(s), under exclusive license to Springer Nature Singapore Pte Ltd. 2024
M. Casini (ed.), *Proceedings of the 3rd International Civil Engineering and Architecture
Conference*, Lecture Notes in Civil Engineering 389,
https://doi.org/10.1007/978-981-99-6368-3_42

501

1 Introduction

Rooftop greening has been recognized as helpful in improving ecology and thermal environment of buildings. Existing researches have mainly been focused on the effect of green roof in summer time; however, people may still like to go to the roof areas for outdoor leisure, snow watching and other activities in winter time, so how green roofs may affect its surrounding environment in wintertime is question that also worthy of exploration.

2 Existing Researches

Research involving this field has been advanced from 2004 to 2021 in China, with 2013 reaching its climax in the number of published papers. For example, Gao et al. [1] carried out an experimental study of green roofs on indoor thermal environment, showing that such roofs can effectively reduce indoor air temperatures in summer. Yao et al. [2] analyzed three adjacent green roofs in an industry park, in terms of their improvement and regulation of microclimate in summer. The study of Yuan et al. [3] showed that the green roof layer had a significant effect on the thermal environment of residential building in spring. Some other researches explored the potential of green roofs as a way to improve energy saving and reduction of CO₂ emission [4]. In 2018, Chen [5] analyzed the effect pattern of green roofs on the indoor and outdoor thermal environment of building roofs by four locations in Xi'an area. Jin [6] used PHOENICS software in his master's thesis to analyze a university in Jinan, showing that the external surface temperature of the roof surface of the building was reduced after setting up green roofs, which had a better effect on reducing the air-conditioning cooling load in summer. Dong et al. [7] studied Tongji University and simulated the effects of no greenery, ground greenery, rooftop greenery, and lawn-type rooftop greenery combining ground greenery and rooftop greenery on campus temperature using ENVI-met version 4.4.2, respectively. Lin et al. [8] explored green roofs with vine frames in a hot summer and warm winter area in the suburbs of Xiamen. Cai [9] has discussed effective ways to improve urban ecological environment in a journal paper, mentioning that green roofs have important significance in new urbanization construction, such as regulating urban microclimate, beautifying urban landscape and other roles. So far, many relevant studies have focused on office, commercial or residential buildings, few has been put on educational buildings on campus.



Fig. 1 Master plan of the university campus and location of the measured building

3 Object and Method

3.1 Object of the Study

The object of this study was the green roof of a college building in Xi'an, which locates in the cold climate zone of China. Plants on this green roof were mainly trees, low shrubs and herbs. The plant area of the roof was 335.65 m², accounting for 36.79% of the total roof area. The hard-paved area of the roof was basically cement rendered with a few color paintings and some wood-panel pavement (Figs. 1 and 2).

3.2 Method of the Study

Continuous measurements were conducted from January 22 to February 8, which are representative dates of winter climate in Xi'an.

For comparative purpose, the object was divided into two parts: one was the outdoor roof space with a plant-covered green area and an ordinary hard-paved area;

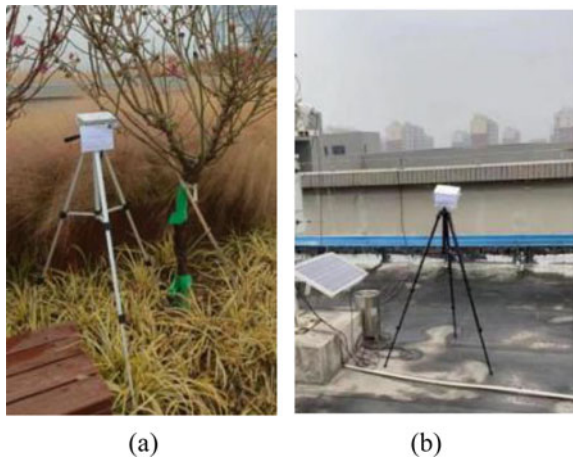


Fig. 2 The measured green roof with different types of ground

the other was the indoor public space on the top floor of the building, which locate just beneath the outdoor roof area.

Four points were selected for the measurements. Among them: point 1 was the planting green roof area (Fig. 3 left); point 2 was the hard-paved area of the roof (Fig. 3 right); point 3 was the indoor area corresponding to point 1 (Fig. 4 left); point 4 was the indoor area corresponding to point 2 (Fig. 4 right).

Fig. 3 a Point 1 (green roof area); b point 2 (hard roof area)



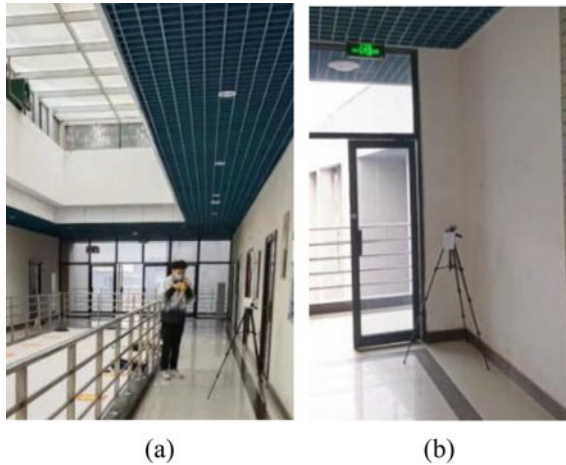


Fig. 4 a Point 3 (corresponding to the green roof area); b point 4 (corresponding to the hard roof area)

4 On-Site Measurement

4.1 Process of Measurement

Outdoor Thermal Environment. HOBO MX1101 temperature and humidity logger was placed at point 1 and 2 and started to operate at 14:00 pm on January 21. The logger was set to automatically record at every 30 min, and a total of 863 sets of data were recorded (Fig. 3).

Indoor Thermal Environment. After laying out the outdoor measurement equipment, HOBO MX1101 temperature and humidity recorder were then placed in point 3 and 4 to record the indoor temperatures and humidity (Fig. 4).

4.2 Results of Investigation

Indoor and Outdoor Temperatures. The measured data from 00:00 on January 22 to 00:00 on February 8 show that, in the time interval from 09:30 to 15:30, the temperature of point 1 (green roof area) varied slightly less dramatically comparing to that of point 2 (hard roof area), showing that green roof area may help in slightly mitigating fluctuation of the outdoor temperature (Fig. 5).

The measured data at every half hour between 00:00 ~ 23:30 on January 22 showed that the highest outdoor temperature of point 2 was 0.44°C, which appeared at 13:00, and the lowest temperature was -0.93°C, which appeared at 22:00, with a temperature fluctuation value of 1.37°C (Fig. 6).

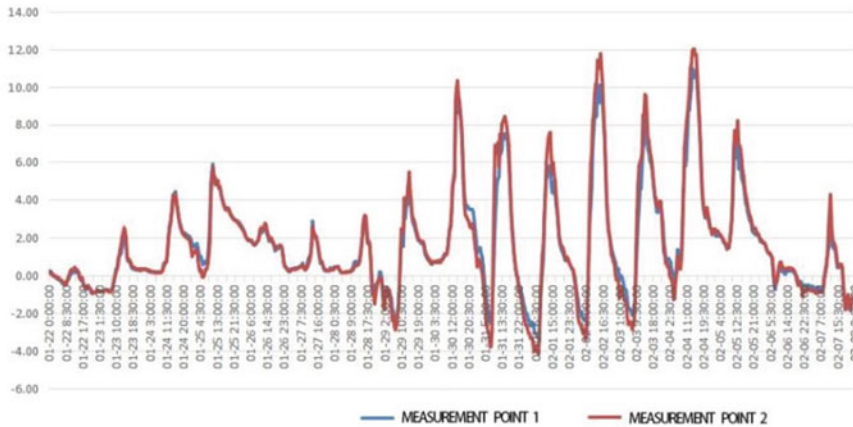


Fig. 5 Outdoor temperatures of point 1 and 2 (Jan. 22 to Feb. 8)



Fig. 6 Outdoor temperatures of point 1 and 2 (Jan. 22)

The measured indoor temperature between 00:00 of January 22 and 00:00 of February 8 show that, temperatures of point 3 were mostly higher than that of point 4. The highest temperature at point 3 was 10.4 °C, which appeared at 14:30, and the lowest was 5.9 °C, which appeared at 8:00; while, The highest temperature at point 4 was 9.5 °C, which appeared at 14:30, and the lowest was 5.3 °C, which appeared at 8:30. The overall fluctuation of temperatures at point 3 and point 4 were both quite small (Figs. 7 and 8).

Outdoor Relative Humidity. The overall outdoor relative humidity of point 2 (hard roof area) was slightly larger than that of point 1 (green roof area), while detailed data shows that, the outdoor relative humidity of point 1 was lower than that of point

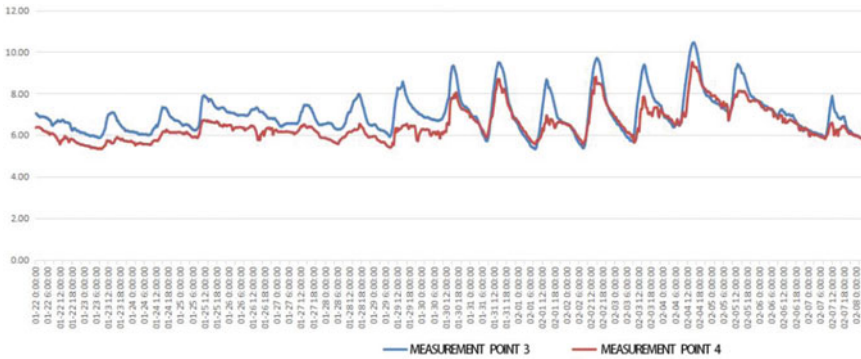


Fig. 7 Indoor temperatures of point 3 and 4 (Jan. 22 to Feb. 8)

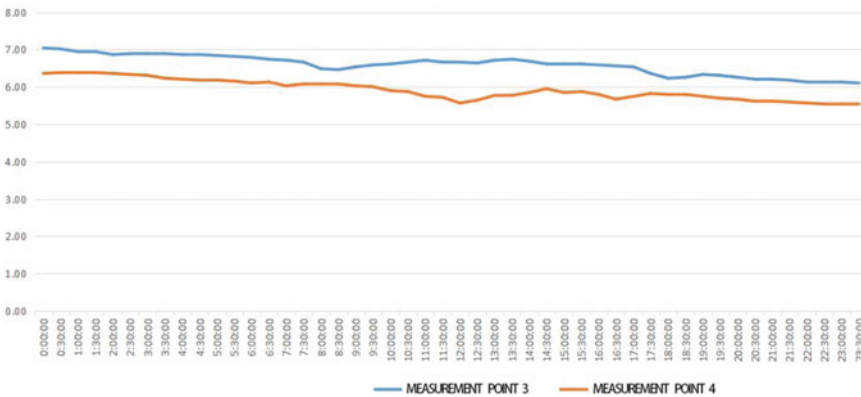


Fig. 8 Indoor temperatures of point 3 and 4 (Jan. 22)

2 at 0:00~3:00 on January 22, it tended to coincide with that of point 2 at 3:00~10:00, and it was higher than that of point 2 at 10:00~22:00 (Figs. 9, 10 and 11).

Indoor Relative Humidity. During the measurement period, the relative humidity at point 4 varied from 55.40% to 62.74% between 23:30 and 9:00 on January 22, with an average value of 57.78%; during the same period, the relative humidity at point 3 varied from 52.36% to 58.01%, with an average value of 54.28%. All the relative humidity data fall in a basically comfortable range, while the relative humidity of point 3 was significantly higher than that of point 4 (Figs. 12 and 13).

Overall, the relative humidity of the outdoor environment at point 4 (hard roof area) was higher than that at point 3 (green roof area), throughout the measurement period. (Fig. 14).

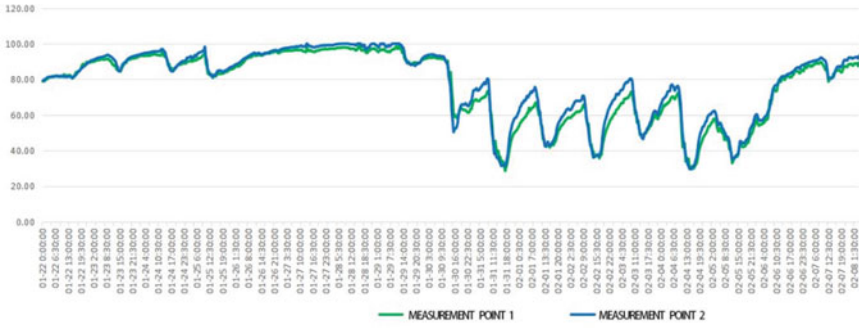


Fig. 9 Outdoor relative humidity of point 1 and 2 (Jan. 22 to Feb. 8)



Fig. 10 Outdoor relative humidity of point 1 and 2 (Jan. 22)

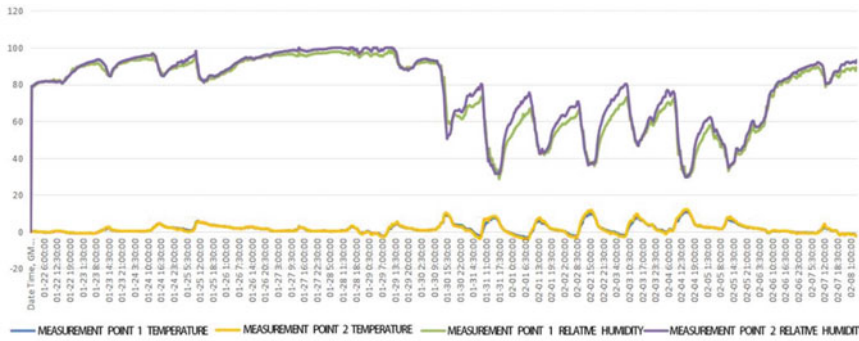


Fig. 11 Outdoor temperature and relative humidity of point 1 and 2 (Jan. 22 to Feb. 8)

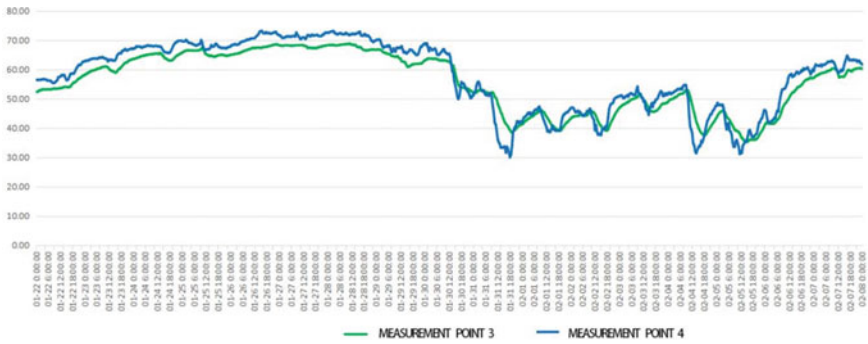


Fig. 12 Indoor relative humidity of point 3 and 4 (Jan. 22 to Feb. 8)



Fig. 13 Indoor relative humidity of point 3 and 4 (Jan. 22)

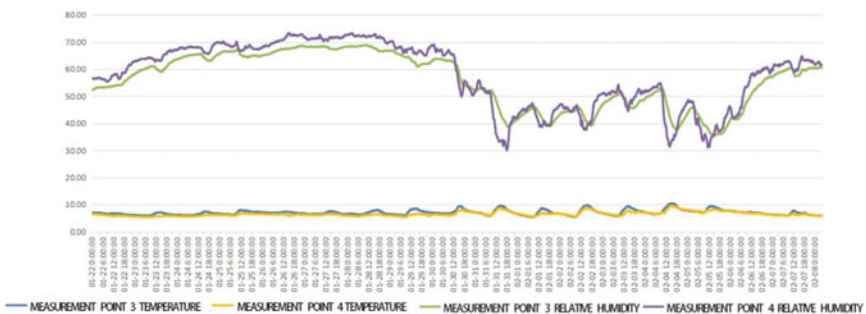


Fig. 14 Indoor temperatures and relative humidity of point 3 and 4 (Jan. 22 to Feb. 8)

5 Conclusion

The effect of green roof on the indoor and outdoor thermal environment of a college building in Xi'an was measured during January 22 to February 8, 2022.

The Overall Measured Data Showed that: Outdoor temperatures of the green roof area were slightly lower and fluctuated less obviously compared to that of the hard roof area.

Outdoor relative humidity in the green roof area varied in the same direction and slightly less obviously compared to that in the hard roof area.

The Measured Data Between 00:00 and 23:00 on January 22 showed that: Indoor temperatures corresponding to the green roof area were higher than that of the hard roof area, indicating that the former has positive thermal insulation effect, which may help reducing heating energy consumption in winter.

Indoor relative humidity corresponding to the green roof area were lower than that of the hard roofing area, indicating a potential need to humidify the indoor environment in case there is a green roof above.

Considering that this investigation was only conducted for about two weeks, which is a short time in general, and the object was only one building, so the conclusions have obvious limitations. Future studies could be further developed on this basis, e.g. to investigate more green roofs of different buildings and to identify their effects in different seasons.

References

1. Gao XD, Jin S, Dui YD (2007) Study on the effect of green roof on indoor human thermal comfort. *J Chongqing Univ Archit* 5:44–48
2. Xiong Y, Jin MJ, Lu HW (2017) Review of wind and thermal environment of green roof in summer from microclimate perspective. *Archit Culture* 9:26–29
3. Yuan PP, Chen XY, Yan HY, Wang LY (2017) Test study on the effect of green roof layer on the thermal environment of roofs. *Build Energy Conserv* 4507:119–122+136
4. Hang, Tan, Xi, et al (2019) Building envelope integrated green plants for energy saving. *Energy Explor Exploit* 381:222–234
5. Chen Q (2018) Research on the impact of green roofs on the thermal environment of buildings in Xi'an. Xi'an University of Architecture and Technology
6. Jin M (2017) Study on outdoor thermal environment simulation and optimization strategy of a university campus in Jinan. Shandong University of Construction
7. Dong NN, Wu J (2020) Thermal environmental impact of green roof based on ENVI-met simulation. *China Urban Forestry* 1804:61–66
8. Lin YH, Shi F (2021) Study on the effect of vine shelf green roof on building thermal environment. *Urban Archit* 1813:31–34
9. Cai WY (2022) Exploring the effective way to improve urban ecological environment—taking green roof as an example. *Low Carbon World* 1208:94–96

Sustainable and Creative Architectural Design

Passive Design Strategies with Thermal Capacity in Contemporary African Educational Architecture



Yen-Khang Nguyen-Tran , Minato Hashimoto , and Ryo Murata 

Abstract In the harsh environment of Africa, the vernacular architecture detaches the indoor from the outdoor environment through natural materials with high thermal capacities. This method, inherited from craftsmanship and knowledge of local materials and climate, is essential in sustainable design. With the rise in construction in Africa, a new trend inspired by vernacular architecture seeks to renew its passive strategies to adapt to the outdoor climate. The challenge of affordable building in educational architecture requires methods to optimize the indoor environment inspired this study. This research aims to clarify the characteristics of contemporary educational architecture in Africa by illustrating how the regional style was reinvented by comparing the vernacular models and their modern derivations. The results demonstrate the design solution to combine spatial composition and wind environment. Further, the technique and knowledge of using the thermal capacity of local materials is a solution for the built environment in the climate change era.

Keywords Vernacular architecture · Schools · Materiality · Wind environment · Spatial composition · Africa

1 Introduction

Africa is facing a challenge of infrastructure such as housing, schools, and hospitals in many parts of the continent admit to the growing population. Addressing this challenge, Benimana and architects like Kunlé Adeyemi and Diébédo Francis

Y.-K. Nguyen-Tran (✉)
Shimane University, Matsue, Japan
e-mail: khng.ntr@riko.shimane-u.ac.jp

M. Hashimoto
TAISEI Corporation, Tokyo, Japan

R. Murata
Tokyo Institute of Technology, Tokyo, Japan

Kéré are working to build a unique African model for sustainable development while attempting to use indigenous experience and vernacular wisdom. Rudofsky [1] described the wonders of this architecture as “*audacious “primitive” solutions that anticipate our cumbersome technology*”, and Schittich [2] believed that the vernacular method is an “*enormous wealth of experience that has been passed from generation to generation*” and has potential for application in contemporary architecture. Besides, based on the recommendations for the global environment from Japan [3], harsh environments tend to prioritize closed-type space that isolates the indoor space from the outside environment. This recommendation is based on the climate situation where often the building envelope is made of sun-dried bricks and mud to prevent heat from entering. As airflow is uncomfortable when the temperature rises above 35 °C, the openings decrease to minimize exchange with outdoor air. However, Fathy [4] found that relying on the material is not enough to solve the issues with climate. Unlike others, Fathy used night ventilation to exhaust remaining heat from indoors and provide moderate comfort for occupants. These principles of vernacular architecture value were considered in the recent scientific approach from the evaluation viewpoint of sustainable performance [5]. The above literature inspired an investigation into the interaction between the building and its surroundings to enhance the indoor environment. Firstly, the vernacular method opted to protect the dwelling spaces by limiting the exchange between indoors and outdoors. Then, how to adapt vernacular principles with modern technology is an attempt to enhance the indoor environment by natural airflow and the cold storage effect of materials. Furthermore, optimal use of the material in terms of embodied energy reduces the built environment’s impact on the natural habitat [6]. These intentions challenge the traditional composition of spatial openness and the use of local material by reinventing passive design and the relationship between openness-closeness and heaviness-lightness. Hence, this study aims to investigate the tendencies of spatial composition with indoor airflow while looking at the passive design potentials to find a balance between indoor and outdoor environments. We analyze contemporary educational facilities via their spatial openness, local materials, and natural airflow. Via comparison, the finding clarifies the possibilities of passive design using thermal mass materials in contemporary African architecture.

2 Methodology

2.1 Framework

This study investigated the interior spaces through spatial openness and wind environment. Firstly, for spatial openness, we extracted parameters such as: the ratio between floor area and ceiling height, the shape and size of openings (door, window, clerestory), the ratio of windows-to-wall (WWR), the presence or absence

of skylights and the ratio of thermal capacity materials used for the floors, walls, and ceilings.

Secondly, we simulated the wind flow indoors using CFD software. We built three typologies of rural houses as a base for comparison from the literature [7]. As shown in Fig. 1, all models have a small opening and a simple floor plan. In terms of thermal capacity material in walls and roofs, all three models differ in the presence of high thermal mass material (HTMM) and roof shape. In terms of the wind environment, we assume that the airflow direction is from the South and the openings are on the windward side to make the simulation. Then we applied the following method for contemporary buildings: First, we define the area of wind speed of 0.4 m/s and above as the wind path area (WPA). Secondly, we calculate the ratio of this area to the floor area of each room. Thirdly, we define the area of night airflow, called the cool storage area (CSA) and finally, we determine the range of wind speed within this area.

Thirdly, we selected contemporary African educational architecture for comparison and extracted the interior spaces. Then, by following the above analysis steps, we analyzed and classified them into different patterns. Figure 2 shows an analysis sample of how we define the pattern for each parameter. The classification related to spatial openness is called Composition Pattern, consisting of the spatial composition of the floor, roof, eaves, and windows, defined as Open or Closed, and the characteristic of HTTM making up these components, defined as Heavy or Light. The classification related to the Wind environment consists of the size of WPA, as Narrow or Wide, and the range of wind speed in CSA, as Strong or Weak. Finally, we combined all the interior spaces into the building to illustrate their characteristics in terms of spatial composition and wind environment. Then, we compared them to the traditional models. The discussion focuses on the similarities and differences in tendencies

Vernacular model	Model 1	Model 2	Model 3	
<p>Model illustration</p> <p>Floor area : 12 m² Window area : 0.5 m²</p>				
Spatial Composition				
Material	Wall	brick, soil	straw, wood	straw, wood
	Roof	brick, soil	brick, soil	straw, wood
Opening ratio		4.2%	4.2%	4.2%
Ratio of HTMM in walls & ceilings		98.8%	52.6%	0%
Wind Environment				
Wind Path Area		31%	0%	52%
Cool Storage Area		around 0.1m/s	around 0.1m/s	around 0.1m/s

Fig. 1 Opening ratio of all interior spaces in vernacular model

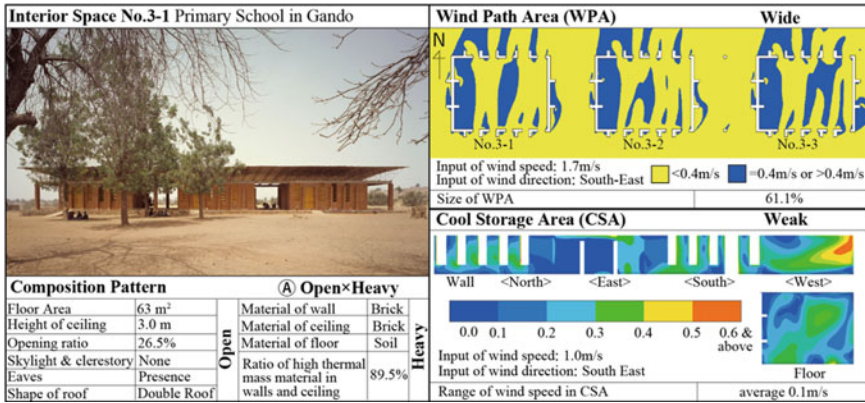


Fig. 2 Analysis of interior spaces No. 3-1, 3-2, 3-3 [8]

to clarify the relationship between indoor and outdoor, the strategy of spatial composition and airflow to illustrate the value of African vernacular indigenous architecture heritage.

2.2 Case Studies

The case studies are African educational architecture because its unique spatial composition is essential for social life with a gathering function among others. And there is a need for that in Africa due to its growing population. Also, in these buildings, natural materials are incorporated with other materials to maximize the structural capacity and adapt to the harsh African environment. We focused on how the material’s thermal capacity provides cooling effects at night and ventilation during the day.

For the database, we chose buildings from the period after 2000 from several architectural mediums worldwide, such as ArchDaily, ArchiDatum, Designboom, Shinkenchiku, and Divisare. As shown in Table 1, the case studies consist of 42 education facilities, presenting a variety in terms of the Köppen climate located in the region, such as Tropical (Am, Aw, Af), Arid (BW, BS), and Temperate (Cw) climates. And we extracted 105 interior spaces to analyze. The case studies need to be schools or facilities with education functions located in several climate conditions across the African continent and with enough information to create a 3D simulation model.

Table 1 Case studies of African schools

Case studies no.	Köppen climate	Number of interior spaces
1, 11, 12, 16, 19, 20, 21, 24, 25, 29, 30, 31, 33, 38, 39, 40, 41, 42	Tropical (Am, Aw, Af)	61
2, 3, 5, 6, 7, 13, 14, 15, 22, 26, 27, 34, 36	Arid (BW, BS)	23
4, 8, 9, 10, 17, 18, 28, 32, 37	Temperate (Cw)	21

3 Results

This chapter summarizes the results, consisting of two categories:

- The Spatial Composition examines the Spatial Openness and Thermal Mass Material of components made up the interior spaces. Spatial Openness summarizes the characteristics of each interior space in terms of floor area and ceiling height, size of windows, clerestory and skylight, roof shape, and eaves. Thermal Mass Material summarizes the primary material in each component in terms of specific heat capacity, material composition, and the ratio of HTMM in building components.
- The Wind Environment outlines the simulation settings and analyzes the ratio of wind path area (WPA) and the range of wind speed in the cool storage area (CSA).

3.1 Spatial Composition

Spatial Openness: Here is the summary of spatial composition in 105 interiors. As for floor area, the average is 92.6 m², and the maximum and minimum are 451 and 10 m², respectively, showing a large gap. As for the ceiling, the average height is 3.3 m, and the maximum is 4.7 m, nearly double the minimum of 2.4 m. For windows and roofs, as they represent the boundary between indoors and outdoors, we focused on the opening ratio as the ratio of openings (doors, windows) to the floor area. Based on the recommendation for a WWR for African schools [9], the percentage of opening ratio has a threshold value of 22.5%. A ratio higher than the threshold is considered Open, and a lower one is Close. As seen in Fig. 3, 87 spaces are in the category Open. Concerning the opening ratio of the vernacular model of 4.2% (cf. Figure 1), 103 have a higher opening ratio, representing 90% of samples. It indicates that the WWR of contemporary facilities tends to be higher than the vernacular model. Finally, clerestory, skylight, roof shape, and eaves are examined as the elements to promote airflow. The clerestory is present in half of the samples (52/105), while Skylights are about 10% (14/105). Meanwhile, pitched roofs account for 53 and double roofs for 35. These shapes prevent rainwater and promote the stacked effect to exhaust hot air from indoors. As for eaves, 90 have eaves, and 78 cases among them are recreation spaces, indicating a tendency to connect indoors and outdoors.

Thermal Mass Material: we analyzed the material of each building component (floor, wall, and ceiling). There are materials with high thermal mass, such as stone,

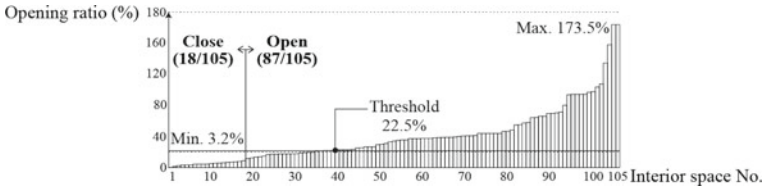


Fig. 3 Opening ratio of all interior spaces in contemporary architecture

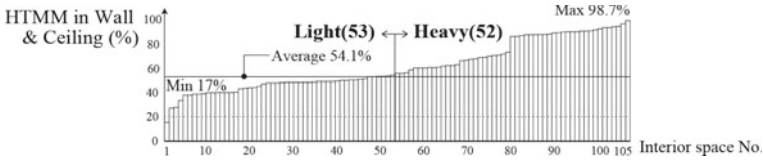


Fig. 4 High thermal mass in materials of all interior spaces

concrete, soil, plaster, tile, and brick, and those with low thermal mass, such as steel, wood, fabric, straw, and bamboo. More than 102 samples have floors and walls made of high thermal mass materials (HTMM), and about 87 have ceilings made of low thermal mass materials. Also, since the surface of the wall and ceiling resulted from the opening size, we calculated the ratio of HTMM in walls and ceilings (Fig. 4). With an average of 54.1%, the lower ratio of HTMM is classified as Light, while the other is Heavy. The distribution of HTMM in all 105 interior spaces ranges from 17 to 98.7%. By comparing with the vernacular model (cf. Fig. 1), we can see the average is close to Model 2, while the maximum tends toward Model 1.

3.2 Wind Environment

CFD simulation was done by STREAM (Fig. 5). Since the case studies are in the suburbs, we did not build the surrounding buildings, but we selected surface roughness classification II, which is the situation of low-height and low-density surroundings, as per recommendations from the Japan Ministry of Construction to calculate wind pressure in urban situations [10]. The climate data is from a meteorology program called WEADAC, which shows the estimated hourly frequent wind speed and direction. Then, we selected the months with the highest outdoor air temperature for the simulation period. During this month, the daytime is the operating period of classes. Also, the night ventilation simulation is the period with the lowest temperature. The wind parameters are selected according to the case study location.

Wind Path Area (WPA): To simulate the airflow during the daytime, we started by defining the analysis area at 1.1 m from the actual floor level of interior spaces. This height corresponds to the sitting position of pupils during daytime classes, which is

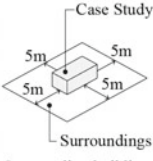
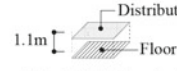
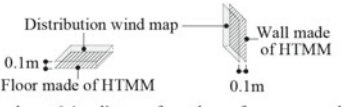
Simulation model  Case Study Surroundings Surrounding buildings are not modeled. The surrounding is a rectangular area offset by 5m from the case study perimeter.	Software (STREAM ver.2021.1) Turbulence model: Standard k-εmodel Boundary condition: All surfaces are smooth Route block: Standard length x,y,z = 0.1m Limit width x,y,z = 0.01m Surface roughness classification: II Power exponent α=0.15	Analysis method for wind during daytime  1.1m Distribution wind map Floor A plan at 1.1m height from the floor to simulate wind flow during the day, called the distribution wind map.
	Climate data source (WEADAC) Station: closest to the city located case study Season: month with highest temperature	Analysis method for wind during nighttime  0.1m Distribution wind map Floor made of HTMM Wall made of HTMM 0.1m A plan at 0.1m distance from the surface concerned to create distribution wind map for cold storage area.
Simulation period Daytime for WPA: 7:00-12:00 Night time for CSA: 00:00-5:00 Wind direction: WEADAC hourly average Wind speed : WEADAC hourly average		

Fig. 5 Settings for CFD simulation

also the activity time of schools. A distribution wind map is simulated at this height for all interior spaces. Referring to a previous experiment [11], the wind speed that brings comfort in hot temperatures is 0.4 m/s as the minimum threshold. Based on this threshold, the WPA is defined as the area with speed ranges from 0.4 m/s and higher. Then, we determined the ratio of WPA (Fig. 6). With an average of 56.4%, below is considered a Narrow WPA, and above means a Wide WPA. It indicates a diverse distribution with a high concentration of WPA ratios around 10, 60, and 90%.

Range of Wind Speed in Cool Storage Area (CSA): To simulate the cooling potentials of the night purging by using the thermal mass of materials, we started by defining the analysis area at 0.1 m away from each surface of the ground and walls. A distribution wind map is generated at this distance, defined as the cool storage area (CSA). Same as the above, 0.4 m/s is the minimum threshold. After simulating the average speed in CSA, we combined all case study CSA in Fig. 7. The results show the Weak range (speed less than 0.4 m/s) accounts for 76. One explanation for this phenomenon is a lower speed during nighttime. Also, 38 spaces in this category show extremely Weak velocity (less than 0.1 m/s). On the other hand, some spaces in the Strong range (speed more than 0.4 m/s) have a speed as fast as 1.5 m/s.

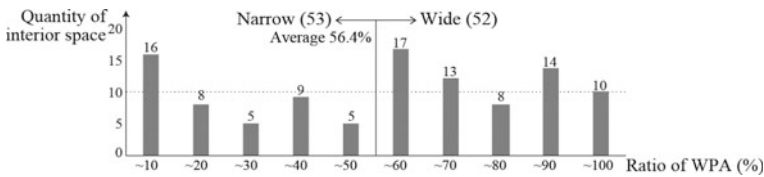


Fig. 6 WPA ratio of all interior spaces

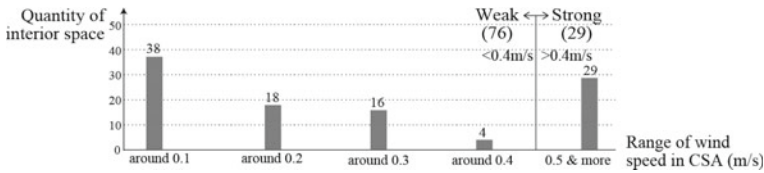


Fig. 7 Range of wind speed in CSA of all interior spaces

4 Discussion

We defined the composite characteristics of interior spaces by combining the patterns from the analysis of Spatial Composition and Wind Environment (Fig. 8). All interior spaces were classified into Composition Patterns focusing on the opening ratio (distinguished between Open and Close patterns) and the HTMM ratio (distinguished between Heavy and Light). There are four patterns, as detailed in the following: Pattern A: Open \times Heavy account for 36 interior spaces, Pattern B: Open \times Light account for 51 spaces, Pattern C: Close \times Heavy account for 16 spaces, Pattern D: Close \times Light account for 2 spaces. Then we included vernacular models in the patterns. The results indicate that Model 1 belongs to Pattern C, Model 2 and Model 3 to Pattern D. For the wind environment, Pattern B mostly has a Wide WPA ratio (speed higher or equal to 4 m/s) and appears in the Strong or Weak range of CSA. On the other hand, most Patterns A and C have a Narrow WPA ratio (speed lower than 4 m/s) and a Weak range of CSA. This result reveals a clear distinction between the vernacular models in terms of spatial composition and wind environment compared to the spaces in contemporary case studies. Furthermore, we interpreted these results by considering interior spaces in the building. As a side note, for interior spaces that have the same shape, we applied only the typical one. The result is an overview of the comparison between contemporary buildings and vernacular models. As shown in Fig. 9, the vernacular models are set as the base of comparison, characterized by four aspects: the opening ratio (Close and Open), the HTMM ratio (Light and Heavy), the WPA ratio (Narrow and Wide) and range of CSA (Weak and Strong). By grouping similar tendencies, three dominant groups emerged as the following:

- Group 1 consists of 12 contemporary buildings like Model 1. This group concentrates on a Heavy ratio of HTMM with an opening ratio of less than 50%, indicating a tendency toward the Close system. For the wind environment, the WPA ratio is more than 30% compared to Model 1, and all case studies have a Weak range of CSA. However, all the case studies contain double roofs and have a skylight, which illustrates an enclosed form, Heavy in HTMM with openings to the sky.
- Group 2 consist of 23 contemporary buildings like Model 2. Most cases in this group have diverse tendencies in terms of HTTM ratio and opening ratio.
- For the wind environment, most case studies exceed the WPA ratio of Model 2 and the Strong range of CSA. This finding indicates a different wind environment in daytime and nighttime compared to Model 2. For example, case 10 has a Close

Interior space No.	Cleaves/ Skylight	Roof Shape	Eaves	Opening ratio	HTMM ratio	WPA ratio	Range of CSA	Composition Pattern	
9-1	b	P	×	Open (36)	Light (36)	Wide	Strong	(A) Open×Heavy (36)	
9-2	b	P	×						
9-3	b	P	×						
14-1	d	T	×						
17	b	P	×						
27	b	P	×						
2-1	d	D	×						
2-3	d	D	×						
3-1	d	D	×						
3-2	d	D	×						
3-3	d	D	×						
15	c	D	×						
22-1	a	D	×						
22-2	a	D	×						
37-2	d	D	×						
8-2	b	T	×						
18-1	b	P	×						
19-5	d	D	×						
21-3	c	D	×						
1-4	d	D	×						
1-5	d	D	×						
1-6	d	D	×						
2-2	d	D	×						
5-1	a	D	×						
5-2	a	D	×						
11-1	b	P	×						
11-3	b	P	×						
11-4	b	P	×						
19-2	d	D	×						
19-4	d	D	×						
20	b	P	×						
21-1	c	D	×						
21-2	c	D	×						
24-4	d	P	×						
26	b	P	×						
34	d	F	×						
4-1	b	D	×	Open (36)	Light (36)	Wide	Strong	(B) Open×Light (51)	
4-2	b	D	×						
4-3	d	D	×						
4-4	d	D	×						
8-1	b	T	×						
8-3	b	T	×						
8-4	b	T	×						
29-1	a	T	×						
29-2	a	T	×						
32-1	b	T	×						
32-2	b	T	×						
38-1	b	T	×						
38-2	b	T	×						
41	b	P	×						
42-2	b	D	×						
1-2	d	D	×						
1-7	d	D	×						
16	d	P	×						
18-2	d	P	×						
24-1	d	P	×						
24-2	d	P	×						
24-3	d	P	×						
29-3	b	T	×						
30-1	b	P	×						
31-1	b	P	×						
31-2	b	P	×						
31-3	b	P	×						
31-4	b	P	×						
31-5	b	P	×						
35	d	F	×						
39-2	d	P	×						
39-7	d	P	×						
40	d	P	×						
19-1	d	D	×						
42-1	b	D	×						
1-1	d	D	×						
1-3	d	D	×	Open (15)	Light (30)	Narrow	Weak	(C) Close×Heavy (16)	
11-5	b	P	×						
12	a	P	×						
19-3	d	D	×						
25	d	P	×						
30-2	b	P	×						
31-6	b	P	×						
31-7	b	P	×						
31-8	b	P	×						
31-9	b	P	×						
39-1	d	P	×						
39-3	d	P	×						
39-4	d	P	×						
39-5	d	P	×						
39-6	d	P	×						
6	c	P	×	Close (18)	Heavy (16)	Narrow	Weak		(D) Close×Light (2)
28-1	d	D	×						
28-2	d	D	×						
37-1	d	D	×						
10	b	P	×						
23	d	T	×						
7-1	d	P	×						
7-2	a	P	×						
11-2	d	P	×						
13	c	D	×						
14-2	d	T	×						
33-1	d	P	×						
33-2	b	P	×						
33-3	b	P	×						
33-4	b	P	×						
36-1	d	P	×						
Model 1	d	F	×						
36-2	d	P	×						
33-5	b	P	×						
Model 2	d	P	×						
Model 3	d	P	×						

Fig. 8 Composition pattern and wind environment of interior spaces

- opening ratio, Narrow WPA and a Strong range of CSA, indicating a possibility of night purging despite less connection to the outdoors.
- Group 3 consists of 2 contemporary buildings like Model 3. This group is in Light HTMM ratio and Open opening ratio. The presence of a clerestory pitched roof or double roof to promote stack effects might be a reason for this tendency.
- 5 case studies do not belong to any groups.

Besides, in terms of climate classification, various tendencies emerge depending on the climate zone. Among 14 cases in Arid (BS, BW), 8 cases belong to Group 1, indicating a tendency toward a Close system with HTMM. Among 19 cases in Tropical (Am, Aw, Af), 14 cases belong to Group 2, which shows a tendency for a diverse approach in terms of opening ratio, HTMM ratio, and wind environment. The last 9 cases in Temperate (Cw, Cs) are distributed in every group, characterized by a Wide WPA ratio and a Strong range of CSA, affirming flexibility in terms of design strategy.

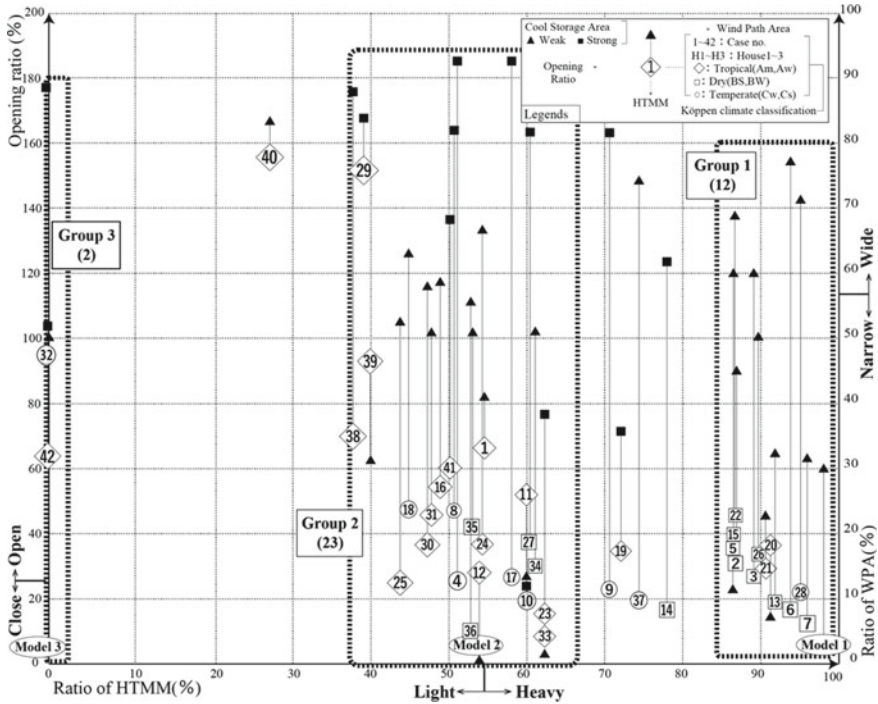


Fig. 9 Comparison of case studies with vernacular models

5 Conclusion

In conclusion, the analysis revealed some aspects of the transformation inherited from the vernacular models. The findings clarify various applications of the thermal capacity of material in design strategy according to different climates. The result shows the relationship between vernacular and contemporary as:

- Despite using a similar material to the vernacular model, the contemporary case studies have a higher opening ratio that allows more wind during the daytime. The spatial composition also being less enclosed, promoting the relationship with the outdoors, as suitable for the characteristics of the educational facilities.
- The use of night purging, as was mentioned by the literature [4], was somehow present in contemporary case studies but not yet a clear tendency.
- In terms of the Köppen climate, the findings show several tendencies which clarify the trends to develop the environment performance from the vernacular architecture and a passive design strategy for educational facilities in Africa.
- These findings are interpreted as various architectural solutions to experiment with using high thermal material in designing buildings while enhancing the relationship between indoor and outdoor environments.

Regarding the scope of the study, three vernacular typologies were selected from the rural housing of Africa from the reference literature [7]. However, African vernacular houses vary between regions and cannot be represented using only these models. Further study is required to grasp the richness of African vernacular typology and the diversity of African architecture, not only in educational facilities. Besides, regarding night purging, a wind distribution map was generated via CFD simulation to examine the potential of night ventilation regarding high thermal mass material. However, the effect of airflow can also depend on other factors, such as the difference in temperature allowing convective heat transfer and the frequency of airflow. As the model excluded the trees and vegetation despite their relevancy in the passive design principle, we need to optimize the model for an accurate simulation. Finally, the analysis finds various usages of materials in building components, showing the efforts of African architects to promote craftsmanship and local knowledge, reflecting the potential of self-efficiently for affordable construction, and demonstrating the creativity of architects to optimize embodied energy through design. Finding a new balance between the spatial composition and wind environment can enhance the passive design strategy and create sustainable alternatives for African countries and other developing countries seeking sustainable design for the future in this era of climate change.

References

1. Rudofsky B (1984) *Architecture without architects: a short introduction to non-pedigree architecture*. University of New Mexico
2. Schittich C (2019) *Vernacular architecture: atlas for living throughout the World*. Birkhäuser
3. Architecture Institute of Japan (2009) *Recommendations for global environmental architecture*. Shokokusha
4. Fathy H (2000) *Architecture for the poor: an experiment in rural Egypt*. University of Chicago Press
5. Murakami S (2008) *Environmental assessment of vernacular architecture. Exploring the origin of sustainable architecture via CASBEE evaluation*. Keio University Press
6. Benjamin D (2018) *Embodied energy and design: making architecture between metrics and narratives*. Columbia University GSAPP and Lars Müller Publishers
7. Brasseur G (1974) *A collection of housing in West Africa*. Enda tiers monde
8. AV Monographs 201 (2018) *Francis Kere practice aesthetics*. Avisa
9. Dierckx R (2002) *Cool schools for hot suburbs: models for affordable and environmentally responsive schools in Nairobi, Kenya*. Technische Universiteit Eindhoven
10. Oura R, Miyamoto S (2015) Study on the range of wind speed to be the thermal comfort in thermally neutral to hot environment the thermal comfort in thermally neutral to hot environment. In: 39th symposium on human-environment system, pp 125–128
11. Ministry of Construction Japan Homepage. [https://www.mlit.go.jp/jutakukentiku/build/conttent/H12-1454.pdf](https://www.mlit.go.jp/jutakukentiku/build/content/H12-1454.pdf). Last accessed 12 Oct 2022

Sustainable House Design Thru Passive and Active Strategies with Python Language. Case Study Ras Al Khaimah (RAK), UAE



Aysha Alsheraifi, Lindita Bande, Alyazia Alsheraifi, and Muhammad Iqbal

Abstract Based on the values of the electricity consumption in the residential stock in the Middle East it's time to apply more and more sustainable strategies from the design stage by using advanced tools. It is our generation responsibility to improve the building design in order to reduce electricity consumption, therefore, to reduce CO₂ emissions. Referring also to the SDG 11, UAE has done great effort in the green building sector. This study follows these efforts. This research evolves on the main points: active and passive strategies in a sustainable house in the United Arab Emirates. 1. Analyze the site selection (location, climate, microclimate), 2. Design Process, 3. Project progress: Active and Passive strategies, 4. Tools and resources, 5. Results. In conclusions, the aim of this study is to use the advanced tools available to explore the possibilities of active design strategy of sustainable house projects. In addition passive strategies are applied in order to have an economically sustainable building. The findings might help the industry to integrate advanced tools in early stages of design.

Keywords Sustainable house · Passive strategy · Active strategy · Rhino · Python language

A. Alsheraifi · L. Bande (✉) · A. Alsheraifi · M. Iqbal
United Arab Emirates University, Al Ain, UAE
e-mail: lindita.blande@uaeu.ac.ae

A. Alsheraifi
e-mail: 202016059@uaeu.ac.ae

M. Iqbal
e-mail: mmiqbal@uaeu.ac.ae

1 Introduction

Seven plan geometries are studied: square, rectangle, trapezoid, L, U, H and T shapes. A well-designed passive-solar building can provide 45–100% of daily heating requirements (ASHRAE 2007). Rectangular shape is considered as the optimal building shape for passive solar design and the most energy efficient. In cold climate, the ideal aspect ratio for a rectangular shape solar house design ranges from 1.3 to 1.5. The solar potential of various shapes of two-story houses is evaluated in this paper [1].

Sustainable slum redevelopment guidelines in India is a policy gap that needs immediate attention. A rational design and planning route is necessary to ensure sustainability of the upcoming low-income (LIG) housing stocks. Results show that the current form of LIG houses had a poor indoor environment and social interaction spaces [2].

A new student housing complex on the campus of the University of Patras, Greece, was used as a test-bed for experimentation with parametric design algorithms. Bio-climatic considerations that involve solar radiation analysis and computational fluid dynamic (CFD) simulations have been integrated into the parametric model [3].

The most significant interactions in a solar house involve non-design parameters such as infiltration, internal gains, temperature setpoints, and major geometry parameters. Grouping them into a single area was shown to under-predict energy use by as much as 15%. This suggests that for certain modeling issues, a relatively high level of modeling resolution should be applied—even for early stages of design [4].

Energy management and parametric optimization of an integrated PV solar house.

A solar house is designed to satisfy the main requirements of electrical power and space heating. It has a south facing PV module and an air solar collector integrated behind it. Simulation results show that an area of 2 m² of the PV module would satisfy an acceptable room temperature in the season of winter [5].

Possible solutions for zero energy building design in UK are discussed in this paper. Various design methods are compared and optimal design strategies for typical homes and energy systems are provided. The study investigates the feasibility of zero energy houses with renewable electricity, solar hot water system and energy efficient heating systems under Cardiff weather conditions [6].

The demand for low-energy building in the market is growing in Korea. Transition of the market has been slow mainly due to shortage of relevant information. Analysis show that education for thermal bridge free design is required and solar heat gain coefficient (SHGC) of glazing should be addressed more seriously [7].

Typological transformation of single-family houses in Riyadh from attached courtyards to detached setback houses has affected the inhabitants' outdoor experiences. In Riyadh, 49.02% of the year is classified uncomfortable heat period. Findings support the argument for revising setback regulations to increase thermal comfort and the quality of life for inhabitants [8].

A parametric analysis for an innovative prototype of passive building, located in south Italy and for residential use. The investigation was addressed by considering

the aspect of sustainability, by employing natural materials such as dry sand and wood fiber. These materials increase the building thermal capacity, which represents a crucial aspect for hot climates [9].

An approach in architectural design of energy-efficient timber buildings with a focus on the optimal glazing size in the south-oriented façade. The aim of the study is to offer architects a simple shortcut to energy-efficient design of prefabricated timber-frame buildings. A parametric analysis is performed on the variation of the glazing-to-wall area ratio (AGAW) for six different exterior wall elements with different thermal properties [10].

2 Methodology

2.1 RAK Weather and Site Conditions

The UAE has an arid desert climate with only two main seasons, winter and summer separated by two transitional periods. The winter season (December to March) has a mean temperature ranging from 16.4 °C to 24 °C. The summer season (June to September) is characterized by extremely high temperature which can be expected to climb up to 50 °C, especially over the southern parts. In Ras Al-Khaimah, the summers are long, muggy, and arid; the winters are comfortable and dry; and it is mostly clear year-round. Over the course of the year, the temperature typically varies from 12.8 °C to 43 °C and is rarely below 9 °C or above 45 °C. Best times of year for hot-weather activities are from late March to early May and from mid-October to late November. The site of the project is located in Jas mountain in RAK, the site is an uneven land, in which the project will have to adapt to the natural topography of the location (Figs. 1 and 2).

2.2 Design Selection

After analysing the site and the topography lines, the design phase started to take place. The first thing that comes to mind when designing on a natural terrain is organic architecture and merging the shape and Volume of the villa with the terrain and its geometry. I started designing 4 alternatives divided into two groups. Alternative 1 and 3 fall under curved lines organic architectural style, whereas Alternative 2 and 4 fall under linear lines organic architectural style. At first, it was difficult to identify the ideal Alternative, however after working on Alternative 1 and alternative 4 via Revit and Rhino programs, I have come to the conclusion that Linear lines would work best with the proposed site selection, considering that Jabal Jais is renowned for its jagged slopes and abrupt edges. Alternative 4 was the chosen design since it

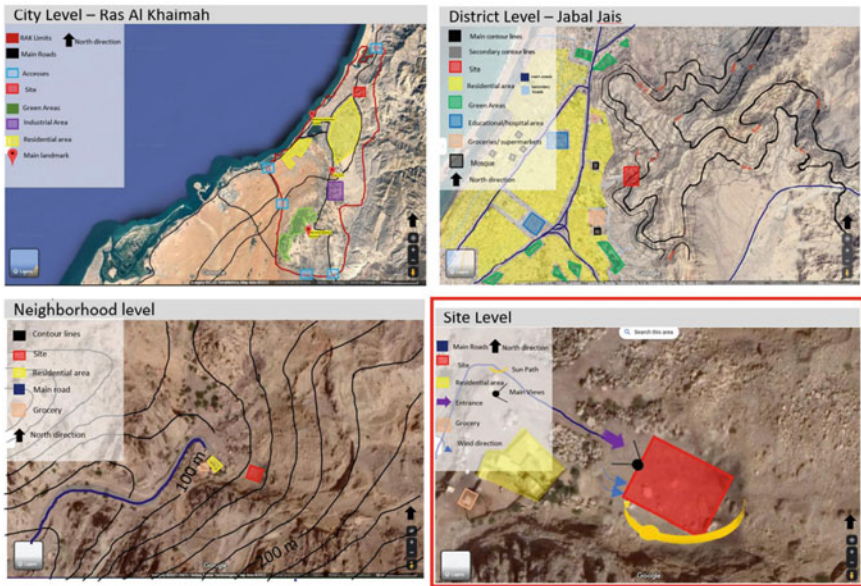


Fig. 1 Site analysis of the project location

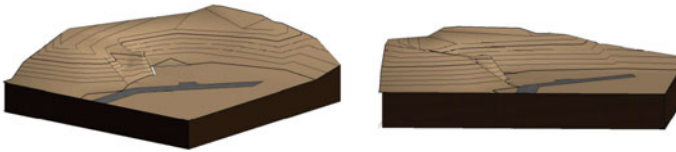


Fig. 2 Terrain 3D of the project location

best fits the site requirements moreover it will merge in with the environment without altering or harming the terrain (Fig. 3).

2.3 Project Progress

According to the proposed design, there are 2 storeys total—a first floor and a raised ground floor. To begin with, a Revit landscape model was created to help with building placement. The design was altered to better fit the landscape after taking a look at it. The ground floor elevated 2 m above the ground to create a place for the water coming from the mountain's slope to pass and enter into a collecting tunnel, which will eventually be utilized for irrigation and cooling techniques. The major alterations occurred to the first floor, which was divided into two blocks, an L-shaped and a rectangular block. Part of the L-shaped block of the first floor will be sitting on

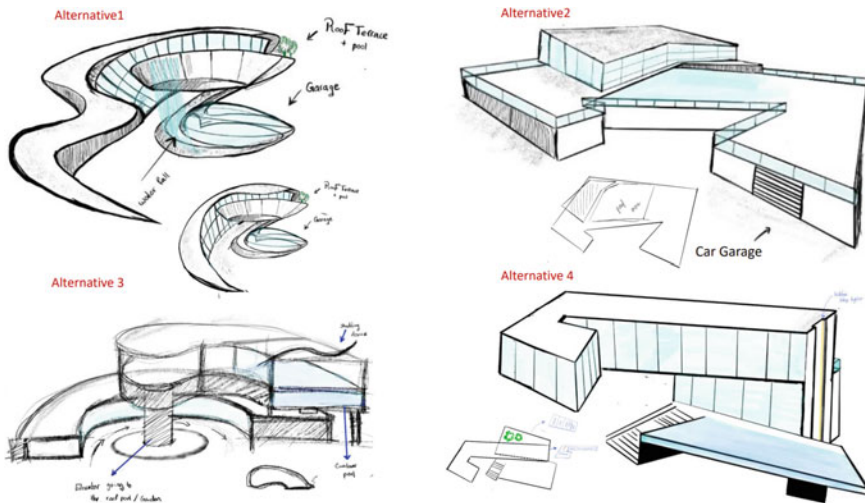


Fig. 3 Conceptual development of alternative 1, 2, 3 and 4

the elevated part of the mountain, fusing it with the Structure. The orientation of the structures was chosen to blend in with the surroundings and, most importantly, to fully appreciate the stunning view of the mountains and the sea (Figs. 4 and 5). Although the orientation will shade some parts of the building, the view lies on the west direction meaning if glass walls will be used, the building will experience significant daytime heat gain. This is where Rhino Grasshopper came into play, a shading device was generated using rhino grasshopper to help with preventing the heat from entering while still enjoying the mountain sea view (Figs. 6 and 7).

2.4 *Passive Strategies*

When designing the villa, Passive strategies were added to it that will enhance its value, appearance, and role in the field of sustainability and environmental preservation. The orientation of the villa is subjected to merge in with the site and work on self-shading. The first floor was designed to shade the ground floor and outdoor areas as well as areas where openings are needed. Openings towards the South directions were reduced, in order to reduce the heat gain during the day. Another passive strategy is the use of water as a cooling strategy to cool down the area. The pool and the water collecting tunnel will work on the evaporative cooling system for a better thermal comfort during humid climate. All points mentioned above will work on reducing the energy consumption of the villa which will then lower greenhouse gas emissions and other pollutants, while on the economical aspect lower the utility bills.

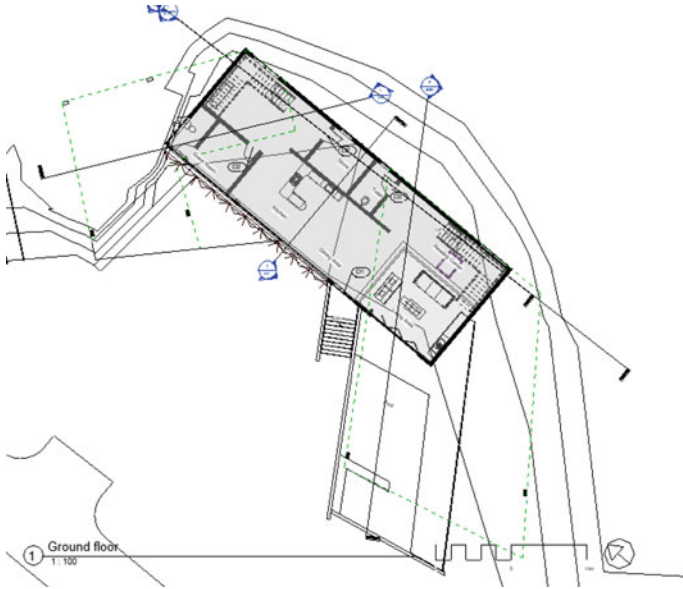


Fig. 4 Ground floor plan



Fig. 5 First floor plan



Fig. 6 Sections of the building

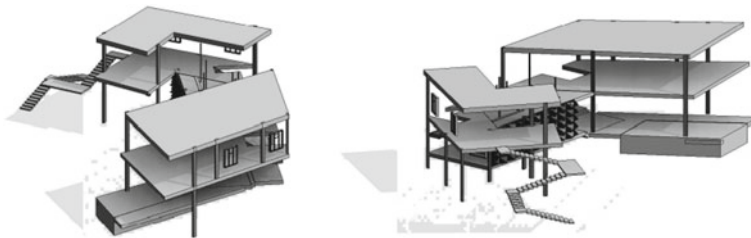


Fig. 7 3D of the building structure

2.5 Active Strategies

In order to ensure the reduction of the energy consumption of the villa, along with the passive strategies, active strategies were used. Glass wall was used in the west direction to capture the wonderful view of the mountain and the sea. However, the west direction is known to receive heat during the day. Here is where the active strategy will take place, the active shading strategy consists of squared panels generated using grasshopper plug in, that will read the heat temperature and sun path, if the sun is directed towards the glass wall the squares will shut closed preventing any heat gain, while still allowing some natural light penetration due to the material used. Moreover, once the sun is read to be farther away from the structure, the squares will open to allow the client to enjoy the splendid vie of the site (Fig. 8).

2.6 Tools and Resources

The Revit application was mostly used in the process of modeling the 3D construction. The topography plug-in in Revit was used to create the terrain landscape. To better comprehend the shape and volume of the construction, I first assigned the levels

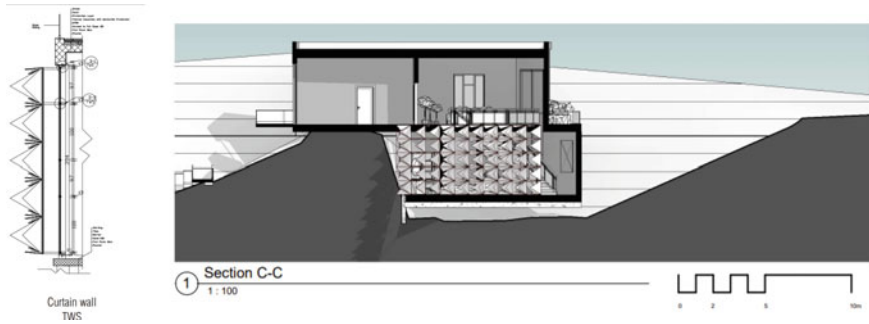


Fig. 8 Details of the active strategy

of each floor before creating the form. A gap was created between the two first floor blocks after the shape had been built. The inner atmosphere and external environment were connected by modeling the void to be a roof garden. The different volumes gave the structure an attractive quality and the impression of mountains' irregularity. The rest of the building's elements such as walls windows, floors, roof, etc., was also modeled using Revit and customized with different Finishes and behind the scene layers for thermal and acoustic comfort. Rhino grasshopper was used to model the Active Structure that was utilized to shade the west façade. The created script allows us to select the shading form that best matches our project; in our instance, a rectangular shape was most suitable. The Shading device consists of squared shapes spread over a given area, the squares are divided into triangles allowing a smooth opening and closing movement of the structure. To check that the design was comprehensive and to record any extraneous points, a Visual Reality experiment was conducted when the modeling phase was about to come to a close. Following the VR trial, certain adjustments were done, and mistakes were corrected such as adding space between the shading structure and the Glass wall, making the pool bigger, and connecting the slab to the stairs (Figs. 9, 10, and 11).

3 Results

This research aim was to design a sustainable house in the mountain of Jebel Jais thru various strategies. Based on the various steps described above the results show a sustainable house by the application of passive strategies and active strategies in order to achieve a sustainable project.

- (a) **Passive Strategies:** The passive strategies applied are several. The first one is the selection of the orientation of the building. The various areas avoid openings of windows in the south direction. In the case of the bedroom in the first floor, there is a roof extension providing natural shade as shown in Fig. 12. The second point of passive sustainable solution is the overlap of volumes to create shade in the

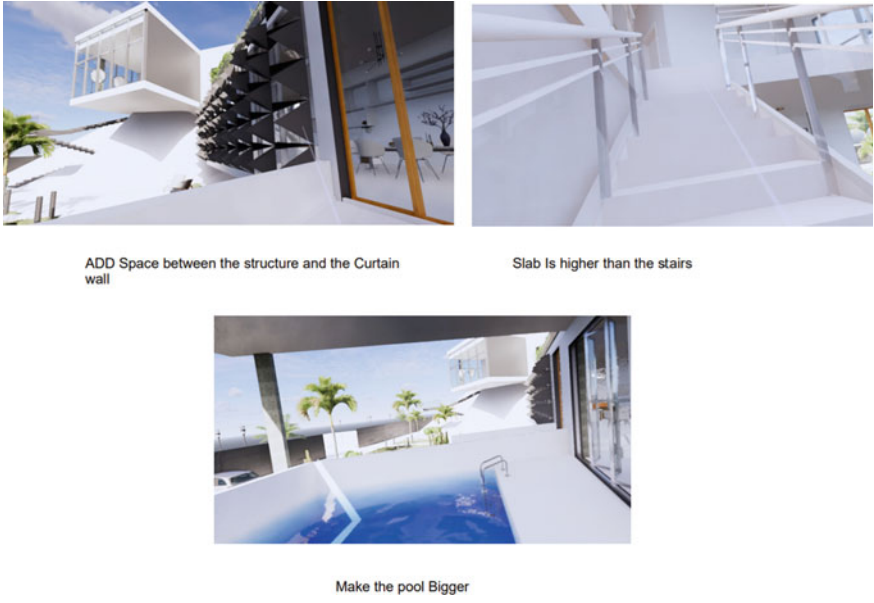


Fig. 9 Use of VR to detect errors in early stage of design

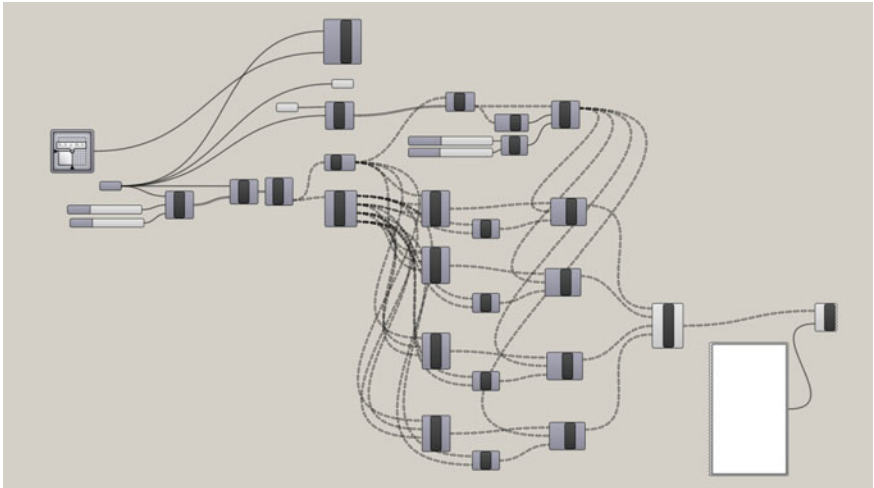


Fig. 10 Python script used for the active façade in rhino

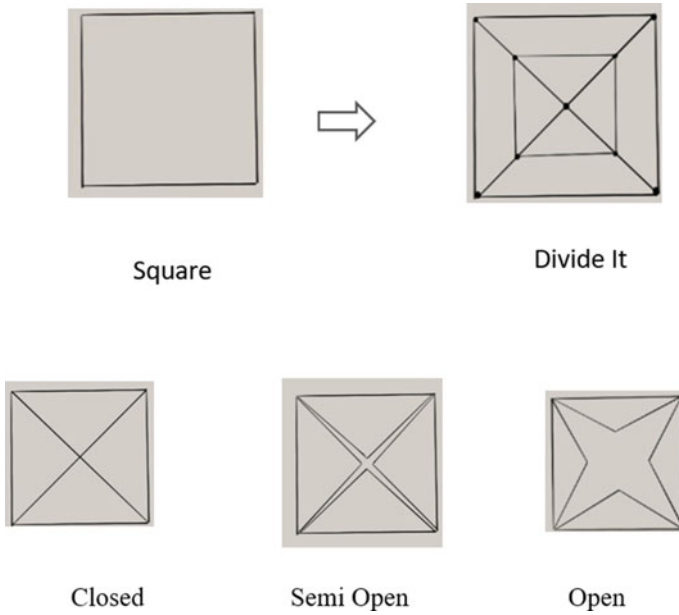


Fig. 11 Conceptual explanation of the active facade



Fig. 12 Application of shading from the roof

lower floor as shown in Fig. 13. The third passive strategy is the use of water bodies to cool down the surrounding air. These water bodies are the pool and the water collection under the house that collects the rainwater as shown in Fig. 14. The fourth strategy is adapting the structure to the terrain. This adaptation of the masses to the shape of the mountain is a sustainable architectural solution in providing an organic and efficient composition of the shape of the building as shown in Fig. 15.



Fig. 13 Application of cooling body



Fig. 14 Overlap of masses creating shading in the lower floor



Fig. 15 Adaptation of the form to the surrounding landscape

(b) Active Strategies: The active façade applied in this project is located in the west façade, reduction get direct solar radiation therefore the energy consumption for the internal energy use. Advanced tools were used such as VR to detect errors



Fig. 16 View of the active façade applied in the west facade



Fig. 17 Detailed view of the active facade

in early stages of design, rhino/grasshopper thru the python language in order to design the active façade (Figs. 16 and 17).

4 Conclusion

The main scope of this research was to achieve a sustainable house design based on several types of strategies. Based on the results, the sustainable house thru passive an active strategy in the country of UAE is a process that requires the application of advanced tools (Fig. 18). The discussion is divided in the below three main points:

- (a) The application of advanced tools: The rhino/grasshopper is an advanced tool used in this project for the active façade. This tool helps optimize the design and detect errors in early stages of design. However more work is needed in analyzing the solar radiation of the full building an energy simulation with and without the strategies.



Fig. 18 Conceptual development of alternative 1

- (b) The active strategies are elements of architecture that were successfully applied in this project. However, more investigation shall be done to understand how these strategies are connected to heritage houses in the country.

The active façade was successfully applied in this project, however more work is needed to understand the impact into the internal cooling load and energy consumption.

In conclusions, the applications of advanced tools in the design of the sustainable house in Jabal Jais is proven effective. This research might be helpful to professionals working in their field. Furthermore, authorities in the housing programs in UAE might find this research beneficial in applying effective strategies for sustainable housing.

References

1. Hachem C, Athienitis A, Fazio P (2011) Parametric investigation of geometric form effects on solar potential of housing units. *Sol Energy* 85(9):1864–1877
2. Bardhan R, Debnath R, Malik J, Sarkar A (2018) Low-income housing layouts under socio-architectural complexities: a parametric study for sustainable slum rehabilitation. *Sustain Cities Soc* 41:126–138
3. Chronis A, Liapi KA, Sibetheros I (2012) A parametric approach to the bioclimatic design of large scale projects: the case of a student housing complex. *Autom Constr* 22:24–35
4. O'Brien W, Athienitis A, Eng P, Kesik T Parametric analysis to support the integrated design and performance modeling of net-zero energy houses. Carleton, CA. <https://carleton.ca/hbilab/wp-content/uploads/parametric-analysis-to-support-the-integrated-design-final.pdf>
5. Matrawy KK, Mahrous AF, Youssef MS (2015) Energy management and parametric optimization of an integrated PV solar house. *Energy Convers Manag* 96:377–383
6. Wang L, Gwilliam J, Jones P (2009) Case study of zero energy house design in UK. *Energy Build* 41(11):1215–1222
7. Lee B, Jang Y, Choi J (2020) Multi-stage optimization and meta-model analysis with sequential parameter range adjustment for the low-energy house in Korea. *Energy Build* 214:109873
8. Alkhoudiri A, Navarro I, Fort JM, Alumran S (2022) Parametric comparative analysis of outdoor thermal comfort in a desert climate: a case study of single-family houses in Riyadh. *Urban Clim* 46:101300

9. Bruno R, Arcuri N, Carpino C (2015) The passive house in Mediterranean area: parametric analysis and dynamic simulation of the thermal behaviour of an innovative prototype. *Energy Procedia* 82:533–539
10. Leskovaar VŽ, Premrov M (2011) An approach in architectural design of energy-efficient timber buildings with a focus on the optimal glazing size in the south-oriented façade. *Energy Build* 43(12):3410–3418

The Art of Sustainable Architecture Creation and Evaluation



Dalia Augustinaite

Abstract The article is the study of the logics to create and evaluate the sustainable architecture. As it focuses on the solving of sustainability challenges, such as environmental crisis, their origin is revised with the purpose to investigate in ‘curing the roots rather than the fruits’. The study consists of two parts. The first is the search of the parallels in variety of concepts of sustainability interacting physical and mental attributes. Their constitution is revised, patterns of behavior or, alternatively, performance questing possibilities to make a change. It is theoretical considerations on analogy of particularities of sustainability in different fields, such as sociology, education, architecture, economy, and in the variety contexts of time as a result of study of national and international scientific literature, documents, and initiatives. The second part is the case study of clay possibilities for molding architectural solutions in such a form illustrating the prototype of evaluation of the levels of sustainability. The notion of the *art* embodies suggestion of the way of thinking as guidelines to create quality sustainable solutions rather than only the ultimate end by itself. Conclusions and proposals are given.

Keywords Sustainable architecture solutions · Levels of sustainability · Sustainability creation logics · Sustainability degree evaluation · Human behavioral patterns · Impact of architecture on sustainable human living

1 Introduction

The search of the concepts for thriving of civilization, such as applied principles of *democracy* [1], emerged far earlier than the Planet was first touched by the ecological disbalance, for example, by rapid depletion of forests at the beginning of eighteenth century [2]. As a concept of holistic approach, dependent on time and space, the *Baroque* laid foundation to contemporary perception of sustainability [3]. The later

D. Augustinaite (✉)

Vilnius Gediminas Technical University, 01132 Vilnius, Lithuania

e-mail: dalia@augustinaite.lt

© The Author(s), under exclusive license to Springer Nature Singapore Pte Ltd. 2024
M. Casini (ed.), *Proceedings of the 3rd International Civil Engineering and Architecture Conference*, Lecture Notes in Civil Engineering 389,
https://doi.org/10.1007/978-981-99-6368-3_45

539

attempts, such as movement of *Bauhaus*, continues to evolve the creation of the wealth principles for humanity via interaction between the art and technologies [4]. So appears the tendency for novel forms of sustainability duplicating the fundamentals in alternative contexts and in more sophisticated ways compared to prototypes. In terms of sustainable architecture, the concept represents the structural logics of quality human-made solutions—the *art of design*. H. L. Cox, formulates that the *art of design* “*may be defined as the attempt to achieve a precise object only vaguely known, by the application of strict rules only imperfectly understood*” [5]. Alternatively, inability to put the issue in an absolute meaning of sustainability [6], determines further study to be uncovered as the direction on freedom of creativity rather than *one size fits all* approach.

1.1 The Issue

The nature of environment itself is to ensure the balance and vitality while the nature of human beings is driven by cognition and therefore inaccurate following the laws of nature [7]. The sustainability occurs within alignment of social-mental and natural-physical patterns acting in synchrony with the circumstances, such as time. Therefore, it matters if the deviation from the absolute mimicking the nature in human-made solutions lead to depletion or abundance, for example, by McDonough and Braungart [8] named, *upcycling*. As a response to issue, American professor of science and technology Haraway [9] metaphorically calls humanity to “*make kin not babies! It matters how kin generate kin*”. The iconic manifest identifies human actions being as powerful as mechanical aggregates to make significant footprint on Earth. Therefore, it is reasonable to state that (un)conscious decisions are the ultimate cause of such phenomenon as the climate change.

1.2 The Solution

World Health Organisation in 2021 by *Behavioural sciences for better health initiative* approved insights of human thinking and behaviour relationship to “help to accelerate the achievement of the sustainable development goals” [10]. For example, Thaler and Sunstein [11] employ these findings to formulate strategy of *Nudge* in touch with architecture composing. In terms of the art, based on Alfred Gells’ arguments, thinking and behaviour is alternative to cause-and-effect phenomenon. Specifically focussing on transplanting this analogy on the interrelationship between creator and creature, Gell [12] both members in system names being the same ontological status *agents* which interact mutually. Therefore, exchange of the status of *agency* between involved is inevitable, i.e., stimulus creates response and vice versa. Long-term artefacts, such as architecture, for sustainable thinking and behaviour guidance

therefore is a perspective tool and ‘clay’ for ‘moulding’. Moreover, mutual interrelationship between impact maker and impacted urges the vital need for considerations to take into account the logics of sustainable masterpiece—architecture—structure and the logics of its user—human—constitution together with other collaboratives despite if they are natural or anthropogenic.

2 The Concepts of Sustainability and the Role of the Hierarchy

The modern form of concept of sustainability, first formulated by United Nations in 2005, determines to treat sustainable development as the synergy between *environment, society and economy* domains [13]. Later, in 2015, the principals of *partnership and peace* were added [14]. They are enablers of the concept demonstrating properties of the structure—methods—under which the model is constructed and managed. In practice such ways of structural engineering act as interacting and overlaying systems likewise subsystems in ecosystem. Therefore, while dividing them into separate parts to schematize, the author of the article suggests to name enablers *patterns*. The enablers empowering the approaches on sustainability discussed in this article are: *circularity, holism, vitality and hierarchy* (Fig. 1). Further study focuses on the *hierarchy* to consider possibilities for evaluation of the levels of sustainability and change of structure *operation*. The term *operation* used further in the study demonstrates generalized alternatives to meanings of terms of *behavior* of live creatures and *performance* of artificial creatures, such as building or architecture.

Following hypothesis of all elements in system being of equal capacity to affection—*agency*—on each other, the chosen leading *pattern* is also an *agent* therefore accordingly influences other *patterns-agents* involved. By individual selection of the *pattern* the changes appear in a *form* determining *operation* but not in the essence of the components. To illustrate, the *universal* model of sustainability demonstrating absence of specific *pattern*, composed by United Nations, and *hierarchical* model, suggested by American ecologist and economist Daly [15], are compared (Fig. 2). According to Caradonna [16], *hierarchical* construction of the structure embodies

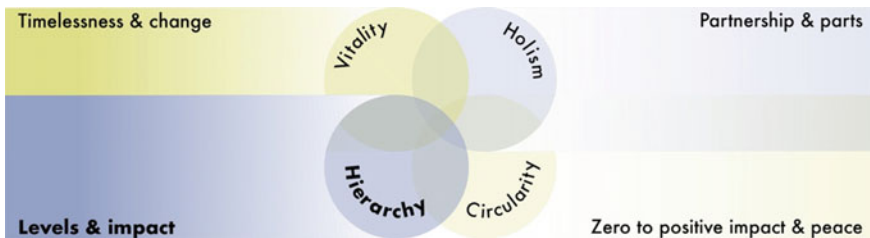


Fig. 1 The range of enablers of the concept of sustainability and their alternative meanings considered in the study

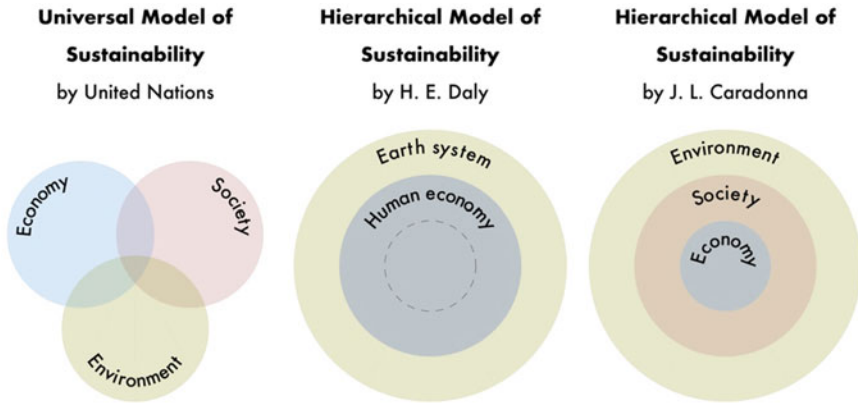


Fig. 2 The schemes of the models of sustainability in universal and hierarchical forms

priority to *environment* as being the fundamental and all involving discourse under which any other exist. Such attitude correlates with the logics of development and interaction of physical and mental capital emerged from behavioral sciences.

According to American psychologist Abraham Harold Maslow, *hierarchical* constitution is natural for intellectual *agent*. In 1943 Maslow suggested the model of *hierarchy of human needs* dividing the scale into five domains: *physiological, safety, love and belonging, esteem, self-actualization* [17]. The division varies in alternatives, for example, the later version of the range by professional in human psychology Robert Dilts, presented in 1990, composes six domains: *environment, behavior, capabilities, values and believes, identity, spirit* [18]. A German social theorist Jürgen Habermas, based on theories, such as formulated by Anthony Giddens, summarizes natural constitution of structure to model of education consisting of tree domains of knowledge: *technical, practical and emancipatory* [19]. Originally Habermas theory arises from his study of principles of *democracy* [20]. Comparing the discussed models with the historic concepts of architecture, such as by Marcus Vitruvius Pollio, formulated in fifteenth century BC, the clear image appears of the analogy of meanings of the *firmness, commodity and delight* despite the differing contexts of the time and space [19] (Fig. 3).

According to Robert Dilts and later *levels of logics* conceptualists, such as Alfred North Whitehead and Bertrand Russell or Gregory Bateson, “each level synthesizes, organizes and directs the class of activity at the level below it. So changing something at a higher level will necessarily change something at a lower level; however, change at a lower level would not necessarily change the element above” [18]. Such dualistic approach is an analogy to interactivity between the discourses of sustainability, argued by H. E. Daly, driven by *patterns of circularity* [15]. Therefore, the parallel also occurs between the repetitive human behavior *patterns* and the recurrent architecture performance *patterns*. For the development of strategy of design, tendencies on levels interactivity demonstrates the competing methodologies on creation

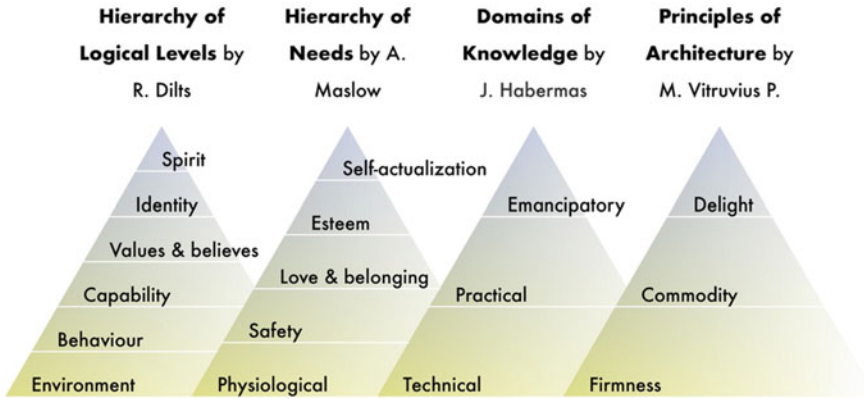


Fig. 3 The alternatives of the levels of sustainability

of *evolutionary design vs design of innovation*. For the further discussion the difference between identified *art of design* ways is formulated as *bottom-up* and *top-down* approaches.

2.1 Bottom-Up Approach

The ground levels of the model are of *environmental* origin and of double meaning. The meaning consists of *formations*, i.e., matters, for example, materials, energy, medium, and their *performance*. Variety ways of *formation-performance* is determined by the laws of nature, excluded from intellectual properties and therefore are of *non-human* [9] mode. In a scale of sustainability of artificial creatures such position embodies attributes of sustainable building. The upper layers are analogy of nature’s evolution, demonstrate the levels of intellectual development. Every upper four levels are reached through the deeper insights on life and living therefore are accomplished gradually, not overleaped. The two middle levels of the model demonstrate applied *strategy* for *status*, in other words, acquired habits for likely results [21]. *Strategy* by itself is of *universal* mode, determines *status* only if likely results are of *consensus* mode, i.e., accepted by others, commons [22]. The *vernacular* architecture is the example of applied *strategy* and the *traditional* solutions of the specific culture reflect its *status*. As *ethnical* architecture applies communal design principles [23], the level of *status* is the ultimate for any *traditional* or alternative structure in the scale of sustainability. The top of model shows *reflexivity* of orders. According to Anthony Giddens that is the capacity of *agent’s* conscious decisions to change a structure and self (agent’s) position in it [24]. *Authenticity* therefore demonstrates the reach of highest possible potential to *operate* in specific way under common *patterns* through application of principles of mechanics of systems transformation. In such a way the search of individuality is so-called stimulus to employ



Fig. 4 The *bottom-up* approach for the evolving states of sustainable design

imagination to *contribute* to obtaining new meaning and purpose of solutions that unnecessarily is natural, by Alfred Gell named as *abductive* [12]. *Authenticity* exists disconnected from *contribution* (universality or (non)materiality) only if the *form* of the structure causing change in *operation* (unprecedented way of acting) is in already existing means and purposes, unnecessarily natural. Accomplishment of all levels determines the state of *thriving*—the level beyond *sustainability*. If solution does not satisfy quality of *environmental patterns*, such as the *pattern* of *circularity*, it is under the category of *sustainability* at the state of *survival* [17] (Fig. 4). According to such concepts, as of Japanese *Ma*, the model of architecture without hesitation is a *holistic* approach [25], therefore accordingly unaccomplished levels translate incomplete structural *form* and therefore *operation*.

2.2 Top-Down Approach

The model of sustainability, as a specific philosophy, is analogy to the structurization theory in terms of structural mechanics [24]. In a *hierarchical* form it demonstrates impact rate on change in structures *operation*. In *innovation design* constitution—*top-down* approach—the more structure acquires the characteristics of the higher levels of sustainability, the more changes in *form* are feasible and crucial for making change in *operation*. Compared with the *natural*, *artificial* structure has particularity of double level of innovation: the innovation on technical levels and innovation on social levels. According to the theory of Dilts, therefore innovation on technical levels arise embodying artificial solutions and necessarily cause change in building's *performance* but not necessarily change human *behaviour*; innovation on social levels necessarily change both—the human *behaviour* and therefore thinking, the building *performance* and therefore matter, such as phenomenon of climate change. The notion of *change* is used universally in this study as for natural so for intellectual creatures, although, specifically for human, notion of *alter* is used in terms of *change* of thinking [26]. Aligned to the formulated issue of the study, the second level,



Fig. 5 The *Top-down* approach for the revolutionary states of sustainable design

i.e., on social levels, artificial innovation is alternative to metaphor of ‘core curing instead of fruit’, i.e., treating ‘health’ of the Planet, ecosystem, through elimination of the cause. Change in technical levels appears over *circular patterns*, in artificial—nearly *circular*, i.e., *spiral patterns*, so-called *repetition* (Fig. 5). To add, *patterns* that cause change in a *positive* way also demonstrate the *pattern* of *vitality* and in such a case dichotomy between *growth* and *novelty* is impossible. *Novelty* in *top-down* approach focuses on abundance, unlimited solution possibilities, while *bottom-up* approach prioritises improvement of limits, not necessarily acquiring beyond existing patterns characteristics.

3 The Prototype of Evaluation of Level of Sustainable Solutions: Case Study

The original detailed study of evaluation system of architectural sustainability includes the exploration of the properties of the environmental—sustainable building—design and is the material for the following article. This study is limited to the evaluation of level of sustainability of architectural solutions. Therefore, the case study essentially focuses on problem solving in a range of society and economy originating in the artificial levels of *strategy*, *status*, *authenticity* and *contribution*.

3.1 Strategy

The level of *strategy* is dedicated to applied scientific or, in folklore cases, revealed by practice after long-term trial and error [27] approaches that definitely makes an impact on human health, comfort, capabilities to evolve and safety. For example, the *biophilic* [28], already discussed *vernacular design* [27], *European Green Deal*



Fig. 6 The case of *Life Cersuds* by E. De Miguel & E. Fernández Vivancos. Photos by ©Milena Villalba (on the left) [32] and © Life Cersuds (on the right) [31]

[29], *Sustainable Development Goals* [30] are the sustainable origin strategies applicable in contemporary context. To illustrate the level of *strategy* the case of *Life Cersuds* by E. De Miguel & E. Fernández Vivancos, in Spain, completed in 2019, is explored (Fig. 6). This is European project of Ceramic Sustainable Urban Drainage System (SUDS) that “uses ceramic tiles of low commercial value as a flooring filter system” [31]. It is solution of commodity for migration of pedestrians and by vehicles, in appearance reflecting pure interaction with the nature. Strategically it is creative way of enabling the *pattern* of *circular* economy also changing the standard means and application methods of the clay tiles, therefore is an innovation on technical levels. The solution does not provide any properties of investigation neither in specific context, nor in unique needs therefore is of *universal* origin—applicable in *international* levels [33, 34].

3.2 Status

The *status* of sustainable architecture solution means regard to specific macro and micro attributes of bioregion, topographical [35], geographical, temporal, social and cultural context as the necessities of reasonable norms and standards [36]. For example, the particularities of Japanese or Lithuanian culture, the heritage [37], the forms of expression of common social values [38]. *Status* is important in case of quality adapting the solutions to *local*, *national* levels [33, 34]. To illustrate the level of *status* the case of *Rest House in Forest* by ArchiDesign, Akiko Tutltyts, in Lithuania, completed in 2014, is presented (Fig. 7). It is a “restoration of already existing previously project, guided by the Council for the Safeguarding of Ethnic Culture manual on vernacular architecture” [39]. Although the project includes abundance of novel solutions, such as mixing of Japan and Lithuanian attributes, *local* cultural *status* is the leading magnitude and demonstrates respect to Lithuanian traditions, for example, preserve rammed clay flooring. The rammed earth is a prototype of wide spectrum of later alternatives, innovations in technical level, such as baked clay tiles which are also applied in discussed building. The possibilities to make



Fig. 7 The case of restoration of *Rest House in Forest* by ArchiDesign, Akiko Tutllys. Photos by © Lina Fisheye [39]

a significant alteration of human *behavior* by this or analogue case is average due to shift in technical *performance*, i.e., from raw to processed clay features as the quality standards in Lithuanian case, but inhabitants’ habits, rituals and thinking will not necessarily change.

3.3 Authenticity

According to Jürgen Habermas, the level or *authenticity* demonstrates the *insight* element and in terms of design is the result of interaction between designer and user [19]. Such collaboration is the priority also in many other design guidelines and documents that include even much more creative *agents*. For example, according to The American Institute of Architecture (AIA), International Union of Architects (UIA) *authenticity* management depends on professionals, building industry, customers and society [40]. Green building council of Lithuania to the list adds the academical institutions [41]. By the very first concept of architecture by Vitruvius, the level of *authenticity* demonstrates the origin of *delight* in artificial solutions appearing as an accomplishment of *innovative form* and so the expression of common sense, not ‘communal’ sense. *New European Bauhaus* strategy is the contemporary way to explain and engage in the issue [42]. To illustrate the case of the level of authenticity, the *House in Takaya* by Suppose Design office, in Japan, completed in 2011, is considered (Fig. 8). The entrance zone is the object of the interest. First, it is of *vernacular* origin and so demonstrates the level of *strategy*. Second, “the design of the property is informed by the traditional Japanese concept of a *doma*, which is an area of compacted dirt typically found between a house’s entrance and living spaces” [43]. Therefore, the sustainability level of *status* is completed. Third, the project is formatted for individual client and possibilities to adopt building to the change of users’ needs later in the future. Thus, comparing to traditional appearance of *doma*, the space in between boundaries, the case is absent of mental as well as material limits, clay is only symbolic sign of traditional function, nontypical. The solution of *doma* also links the outside surroundings of the building with the inside.



Fig. 8 The case of *House in Takaya* by suppose design office photos by © Toshiyuki Yan [43]

Attention to such specific details cares for the residents needs from very individual position and is the illustration of the level of sustainability of *authenticity*. To add, in appearance—form—transformed *traditional* solution of the *doma* sticks to the essence of ethnicity and is the example of *vitality* of cultural heritage in attractive way to cultivate instead of to neglect.

3.4 Contribution

Contribution, or alternatively called *mission*, *vision*, *purpose* [44], *transcendence* [45], *trans-mission* [46], in some concepts, including by Dilts, appears as additional level—beyond *self* and *system*. The author of the study suggests to name it the *contribution*—the spark—to ignite the matter which in very first state of existence is in a form of *idea*. For example, the case of *Second Hand* by Zhanna Kadyrova, in the Kiev Film Copy Fabric, Ukraine, demonstrated in 2017, is studied (Fig. 9). The *idea* of the possibilities to use the building secondary, for example, to reconstruct, inspired the author to use the clay tiles as a ‘fabric’ in *abductive* meaning to manifest analogy of human clothes in *second hand* concept. It is an unexpected very *aesthetical* way to touch the consciousness of humanity to think about the consumerism differently—to engage in secondary use of goods. On one hand such artificial solution is the educational tool, on the other—the advertisement of *circular* economy. The building of Kiev Film Copy Fabric “was wrecked, and the newest residential, shopping and entertainment complex is slated in its place” [47]. Although the physical matter extinct, the *idea* in a form of artificial solution sticks in human memory for long if not forever and hopefully *alters* the *patterns* of human *behavior*, *change* cultural standards and industrial *performance*—giving the second chance is *beautiful*.



Fig. 9 The case of *Second Hand* by Zhanna Kadyrova. Photos by © Zhanna Kadyrova [47]

3.5 Insights on Levels of Sustainable Architecture

Every level of sustainable architecture serves for specific purpose in a range of the scale and cannot exist independently unless it is of the deeper perception of the initial. The experimentally evaluated levels of sustainable architecture show the possibility not necessary to be engaged in all the attributes of the scale. Under hypothesis of cause-and-effect such solutions alternatively ‘program’ lack of quality human decisions in life and living comparing with the possibilities to thrive. As there exists no need for neither absolute meanings nor absolute purposes in practice, the solution could be to choose which of the parts of the artificial artefact meets the properties of each of the level, or, in other words, are leaders to either *alteration*, improvement or support of behavior. Such criteria as of *material, site, pedestrian and vehicle management, waste management, health and well-being* [48–50] was involved in a study in selected forms of architecture and is the criteria correlating with such sustainable building assessment systems as *Leadership in Energy and Environmental Design (LEED), Building Research Establishment Environmental Assessment Method (BREAM), Lithuanian Buildings Sustainability Assessment System (LBSAS)*. Therefore, it exists the possibility to evaluate the quality of architectural sustainability in unison with the requirements of national and international sustainable building assessment systems what is the goal for research for upcoming publications.

4 Conclusion

As the article discuss the *art* of sustainable architecture creation and evaluation, the study of the *hierarchy* particularities of the concept uncovered its possibility to be the universal tool for guidelines as well as assessment system. The experimental part of the study proves possibilities to apply the strategical architecture development-assessment prototype in practice. Moreover, case study is promising in finding links with the already existing in practice sustainable building assessment systems. The

model of artificial sustainability as the solution for change of *patterns* of consumerism is also determinant of the high quality of human living in essence and so is the illustration of impossible dichotomy between development of body and mind. Under the theory of cause-and-effect the artificial solutions have the higher potential for managing human footprint on earth comparing with the technological innovation alone.

References

1. Guy S, Farmer G (2001) Reinterpreting sustainable architecture: the place of technology. *J Archit Educ* 3(54):140–148
2. Carlowitz HCV (2013) *Sylvicultura oeconomica* (1713). In: Robin L, Sörlin S, Warde P (eds) *The future of nature: documents of global change*. Yale University Press, New Haven, pp. 63–66. <https://doi.org/10.12987/9780300188479-008>
3. Frankl P (1914) *Entwicklungspbasen der neueren Baukunst*. Teubner, Leipzig, p 5
4. Beyme KV (1998) Art and politics: no “new unity.” In: Kentgens-Craig M (ed) *The Dessau Bauhaus building 1926–1999*. Birkhaeuser, Berlin, pp 66–85
5. Evans JH (1959) Basic design concepts. *Am Soc Naval Eng J* 671–678
6. Cook SJ, Golton BL (1994) Sustainable development concepts and practice in the built environment—a UK perspective. In: *Proceedings of the First International conference on sustainable construction*. Tampa University of Florida, Tampa, p 684
7. Valero A, Valero A (2019) Thermodynamic rarity and recyclability of raw materials in the energy transition: the need for an in-spiral economy. *Entropy* 21(9):873. <https://doi.org/10.3390/e21090873>
8. McDonough W, Braungart M (2013) *The upcycle. Beyond sustainability—designing for abundance*. North Point Press, New York
9. Haraway D (2015) Anthropocene, capitalocene, plantationocene, chthulucene: making kin. *Environ Hum* 6(1):159–165
10. World Health Organization (2022) Report adopted by the Director-General on 27 April 2022. Behavioural sciences for better health initiative. A75/25. https://apps.who.int/gb/ebwha/pdf_files/WHA75/A75_25-en.pdf
11. Thaler RH, Sunstein CR (2022) *Nudge. The Final Edition*. Penguin Random House UK, Great Britain
12. Gell A (1998) *Art and agency. An anthropological theory*. Clarendon Press, Oxford
13. United Nations (2005) Resolution adopted by the General Assembly on 16 September 2005. *World Summit Outcome*, 60/1
14. United Nations (2015) Resolution adopted by the General Assembly on 25 September 2015. *Transforming our world: the 2030 Agenda for Sustainable Development*, 70/1
15. Daly HE (1973) *Towards a steady-state economy*. W. H. Freeman and Company, San Francisco
16. Caradonna JL (2014) *Sustainability: a history*. Oxford University Press, New York, pp 9–10
17. Bergman D (2012) *Sustainable design. A critical guide*. Princeton Architectural Press, Hudson, New York, pp 19–21
18. Grimley B (2010) The NLP approach to coaching. In: Cox E, Bachkirova T, Clutterbuck D (eds) *The complete handbook of coaching*. SAGE Publications Ltd., London, pp 187–200
19. Brennan J (2011) Qualitative and quantitative traditions in sustainable design. In: Lee S (ed) *Aesthetics of sustainable architecture*. 010 Publishers, Rotterdam, pp 80–96
20. Huckle J (1993) Environmental education and sustainability: a view from critical theory. *Environ Educ Pathway Sustain* 43:68
21. Bourdieu P (1977) *Outline of a theory of practice*. Cambridge University Press, New York

22. Lizard O (2004) The cognitive origins of Bourdieu's habitus. *J Theory Soc Behav* 34(4):375–448. <https://doi.org/10.1111/j.1468-5914.2004.00255.x>
23. Puodžiukienė D (2014) Lietuvos architektūros istorija, VI. Lietuvos etninė architektūra nuo seniausių laikų iki 1918 m. Savastis, Vilnius, p 5
24. Giddens A (1984) *The constitution of society: outline of the theory of structuration*. Plity Press, Cambridge
25. Kodama M (2017) *Ma theory and the creative management of innovation*. Palgrave Macmillan, New York
26. Erickson MH (1998) *Life reframing in hypnosis. The seminars, workshops and lectures of Milton H. Erickson. Volume II*. Irvington Publishers, USA
27. Caves RW (2004) *Encyclopedia of the city*. Routledge, London, p 750
28. Kellert SR, Heerwagen JH, Mador ML (2008) *Biophilic design. The theory, science, and practice of bringing buildings to life*. Wiley, New Jersey
29. European Commission: European Green Deal. https://commission.europa.eu/strategy-and-policy/priorities-2019-2024/european-green-deal_en. Last accessed 13 Feb 2023
30. Mossin N, Stilling S, Bøjstrup TC, Hau IC (eds) (2020) *An architecture guide to the UN 17 sustainable development goals, vol 2*. Royal Danish Academy, Copenhagen
31. Life Cersuds. Life Cersuds homepage. <http://www.lifecersuds.eu/en>. Last accessed 14 Jan 2023
32. LIFE CerSuds. Archello homepage. <https://archello.com/project/life-cersuds>. Last accessed 14 Jan 2023
33. Association of University Leaders for a Sustainable Future (1990) *The Talloires declaration: 10 point action plan*. <http://ulsf.org/wp-content/uploads/2015/06/TD.pdf>. Last accessed 13 Feb 2023
34. United Nations (1992) *Earth summit: agenda 21. United Nations conference on environment and development, Rio de Janeiro, Brasil, 3 to 4 June 1992*, United Nations, United States
35. McLennan JF (2004) *The philosophy of sustainable design*. Ecotone, USA
36. General Assembly of Architects' Council of Europe (2009) *Architecture and sustainability: declaration and policy of the architects' Council of Europe*. https://www.ace-cae.eu/uploads/tx_jidocumentsview/Brochure_EN.pdf. Last accessed 13 Feb 2023
37. Larsen PB, Logan W (2018) *World heritage and sustainable development*. Routledge, London
38. Tsirogianni S, Sammut G, Park E (2014) Social values and good living. In: Michalos AC (eds) *Encyclopedia of quality of life and well-being research*. Springer, Dordrecht. https://doi.org/10.1007/978-94-007-0753-5_3666
39. Poilsio namas miške. ArchiDesign homepage. <https://archdesign.lt/projektai/virs-vilniaus-stogu-3-3-2-2-2-poilsio-namas-miske/>. Last accessed 14 Jan 2023
40. The American Institute of Architecture (AIA), International Union of Architects (UIA) (1993) *Declaration of interdependence for a sustainable future, at the UIA/AIA World congress of architects in Chicago, 18–21 June 1993*
41. Lithuanian Green Building Council Homepage, <https://www.lzpt.lt/apie-mus/>, last accessed 2023/01/17.
42. European Commission: New European Bauhaus. https://new-european-bauhaus.europa.eu/index_en. Last accessed 13 Feb 2023
43. Griffiths A. Suppose design office creates 21st-century take on traditional Japanese doma. Dezeen homepage. <https://www.dezeen.com/2018/06/03/house-in-takaya-doma-suppose-design-office-higashihiroshima/>. Last accessed 11 Jan 2023
44. Giebe C (2021) It's a pirate tale—a supplementary approach to coaching in business and management. *Int J Appl Res Bus Manage* 2(1):38–50
45. Mathes EW (1981) Maslow's hierarchy of needs as a guide for living. *J Hum Psychol* 21(4):69–72
46. Dilts R (1990) *Changing belief systems with NLP*. Meta Publications, USA
47. Second Hand. Kadyrova homepage. <https://www.kadyrova.com/second-hand-en>. Last accessed 15 Jan 2023
48. U.S. Green Building Council (2019) *LEED v4 for building design and construction*. https://www.usgbc.org/sites/default/files/LEED%20v4%20BDC_07.25.19_current.pdf. Last accessed 11 Jan 2023

49. Rezaallah A, Bolognesi C, Khoraskani RA (2012) LEED and BREEAM. Comparison between policies, assessment criteria and calculation methods. In: Proceedings of the 1st International conference on building sustainability assessment (BSA) 23–25 May 2012. Porto, Portugal
50. Lietuvos žaliųjų pastatų taryba. Lietuvos pastatų tvarumo vertinimo sistema: LPTVS 2018:1.1. Vilnius (2019).

The Effect of Geometry Parameters on Daylighting of School Buildings in the Gaza Strip



Tawfiq Jebril, Yang Chen, Saji Hamed, and Aly Hajjaj

Abstract School buildings have a significant potential for daylighting to improve school students' academic performance in terms of rational, behavioral, and physical aspects; of their education and activities. This paper discusses the role of geometry parameters, including building shape, annual sun exposure (ASE), and spatial daylight autonomy (sDA) of single-sided school buildings in the Gaza Strip, Palestine. The daylighting of five shapes was compared through computer simulations using ClimateStudio software. It has been noted that geometric shapes, such as L, C, H, F, and E-shapes, are the most popular shapes, especially in governmental schools in the Gaza Strip. Results showed that each shape has a different impact on daylighting. The E-shape performed the optimal shape, with 84.5% for sDA and 19.1% for ASE, with various design options to determine the stability of increasing or decreasing the amount of artificial light needed per day. A 40–60% window-to-wall ratio had the optimal daylighting quality performance. However, deeper rooms required a higher window-to-wall percentage to reduce the lighting demand.

Keywords Schools · Building geometry · Daylight · Gaza Strip

T. Jebril · Y. Chen

School of Human Settlements and Civil Engineering, Xi'an Jiaotong University, Xi'an, China

e-mail: chenyang@mail.xjtu.edu.cn

S. Hamed (✉)

College of Engineering and Urban Planning Department of Architecture Engineering, The University of Palestine, Al-Zahra City, Palestine

e-mail: saji@sajiarchitects.com

A. Hajjaj

Faculty of Architectural Engineering, Higher Technological Institute, Ramadan, Egypt

1 Introduction

1.1 Overview

Daylighting can give spaces and schools a quality that no other design element can match [1]. Since the nineteenth century, researchers have studied daylight conditions in educational facilities. Educational buildings are considered important architectural structures that consider daylighting [2]. Spatial Daylight Autonomy (sDA) and Annual Sunlight Exposure (ASE) assess whether a space receives sufficient daylight on a work plane during standard operating hours on an annual basis [3].

The Gaza Strip is located on the Mediterranean Sea's eastern coast, bordering Egypt to the west and the West Bank to the east and north [4], as shown in Fig. 1. Since 2005, the area has been effectively isolated. The combined effects of the rising population, the contaminated environment, and unsustainable construction raise doubts about Gaza's viability shortly [5]. Furthermore, the Gaza Strip has one of the world's youngest populations, and there is currently a shortage of schools that barely meet the population's needs [6]. This situation necessitates immediate action, and educational efforts must be accelerated to maintain the quality of education [7].

Additionally, building design in the Gaza Strip does not consider climatic considerations that could increase school daylighting rates [8]. Hence, climate-responsive building design is essential in the first design stage to achieve more comfortable classroom lighting [9]. Moreover, it would be logical for architects to pay attention to local climatic conditions during the design process [10]. Building form, orientation, and urban patterns are the most crucial design parameters affecting the building

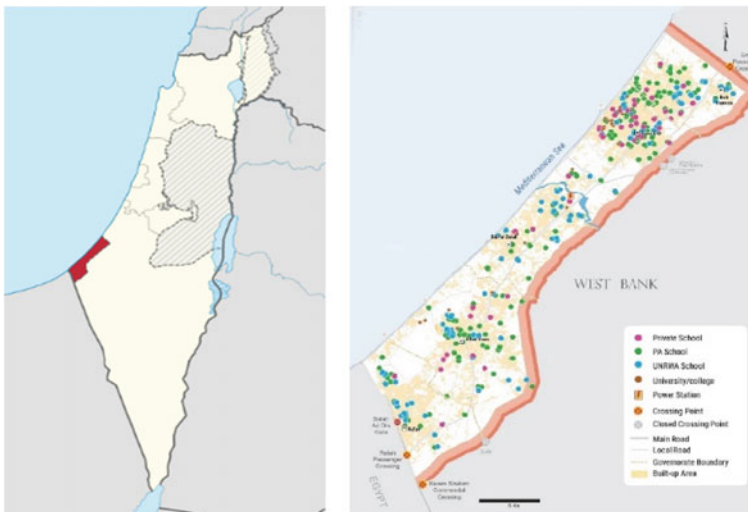
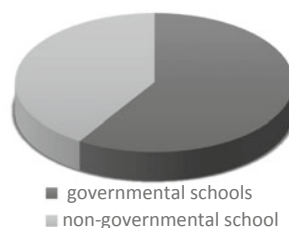


Fig. 1 Map of Palestine (left) and educational utilities in the Gaza Strip (right)

Fig. 2 Schools' structure in the Gaza Strip



scale of daylighting [11]. Suitable configuration and molding of the built form and its surroundings can considerably minimize glare in the building [12, 13].

In the Gaza Strip, over 460,000 children attend 688 elementary and secondary schools, of which 59% are government-run and 41% are privately run [14], as shown in Fig. 2.

1.2 Typical Features of School Buildings

The Gaza Strip has schools of many different shapes, which affects daylighting performance. It has been noted that geometric shapes, such as L, C, H, F, and E-shapes, are the most popular shapes, especially in governmental schools [15], as shown in Table 1.

According to the MoHE's¹ Annual Statistical Book for General Education in Gaza Governorates, 2020/2021, 299 government buildings in the Gaza Strip are distributed among seven directorates. Many of these school buildings have been built since 1994, and around 30 schools have been made in the last ten years [15]. The shapes or forms of the classrooms in these schools are distributed across the five main shapes (L, C, H, E, and F); only five schools have mixed shapes (L and C) shapes, which were funded by Oman [16].

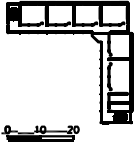
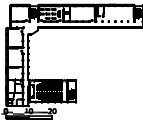
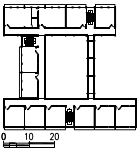
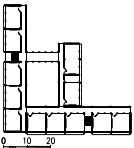
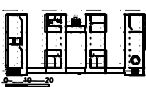
The L-shape is the most used in schools in the Gaza Strip and accounts for 50% of school building shapes, while the E-shape is used in only one school building. The newest 30 schools were designed using H- and F-shapes, apart from the five Omani schools discussed above [17].

2 Methodology

Our approach involved using the five most common shapes in the study field for a school building. ClimateStudio simulation engine is an environmental analysis software program based on Rhinoceros 3D (Rhino), which was chosen to evaluate school buildings' daylighting performance in the Gaza Strip. ClimateStudio was

¹ Palestinian Ministry of Education & Higher Education.

Table 1 Summary of school classroom' shapes and their features [15]

Plan	Shape	Area (m ²)	Number of schools	Proportion (%)
	L	630	165	55.2
	C	1050	104	34.8
	H	1115	19	6.4
	F	1070	5	1.7
	E	1095	1	0.3

selected due to its accuracy in analysing environmental performance for architecture. It can be approved by comparing the results with the light stanza, a widely used software for calculating daylight analysis. The results were the same, so we proceeded with Climate Studio.

Based on the above analysis, five school building models were created in Rhino (L, C, E, F, and H). Each of the five archetypes had a single-sided design² [18], a common design in the Gaza Strip. The corridor width was set at a constant of 2 m, with stair and toilet units for all models.

Figure 3 shows the five school models and their internal spatial organization patterns. General classrooms had a single-sided design. Additional spaces were arranged in the corners or connections of the buildings. The five models were three

² Single-sided design means the common arrangement classrooms with one side of classrooms and a corridor on the left side. However, the double-sided design has two classrooms with a middle corridor.

stories high, each floor having eight to 12 classrooms, one to six specialized classrooms, one to three toilet units, and two to three staircases. The general classrooms were modeled with a net size of 8 m × 6 m and the same area and dimensions as the specialized classrooms.

According to the Palestinian MoHE, most classrooms are 52 m², with 32 students organized in two shifts (from 8 am to 2 pm and 3 pm to 6 pm) [19]. Therefore, most schools are designed to have the maximum number of classrooms. Single-sided schools are primarily designed to provide natural lighting and ventilation due to Gaza's lack of electricity for over 14 years [20].

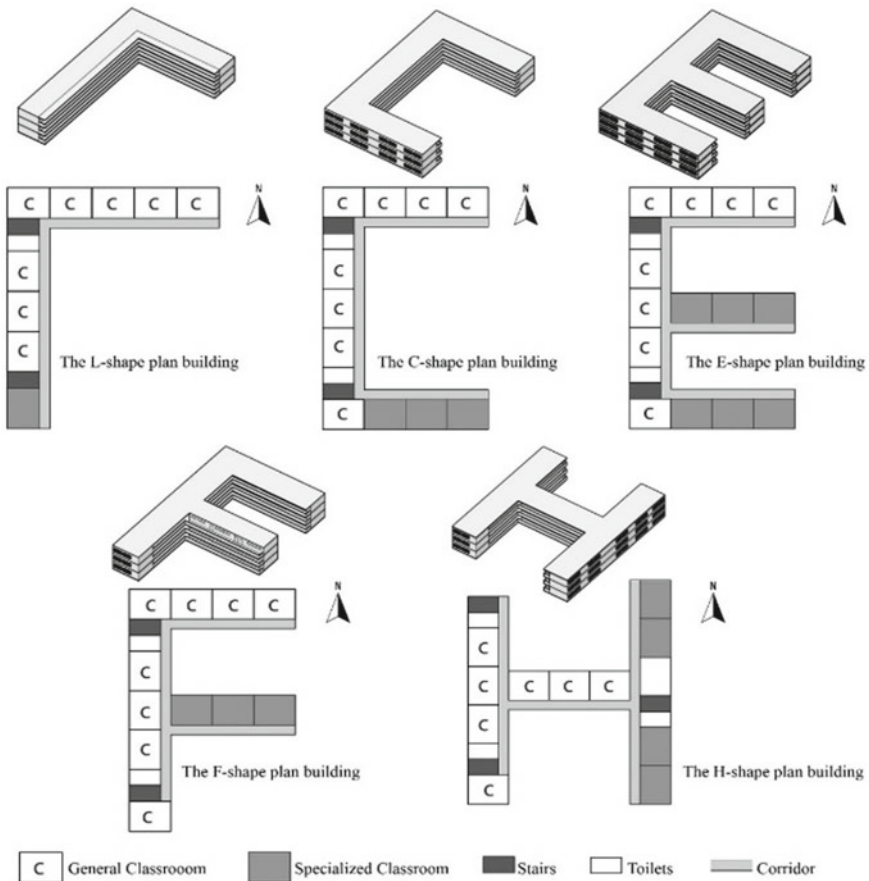


Fig. 3 The five school building shapes were analyzed in the study

3 Results

Daylighting calculations compared five different types of school buildings used in Gaza to assess their annual performance according to daylight analysis by including all types of geometric shapes used in Gaza's schools. Calculations were made for each shape with the same conditions and orientation (Optimal North with no rotation).

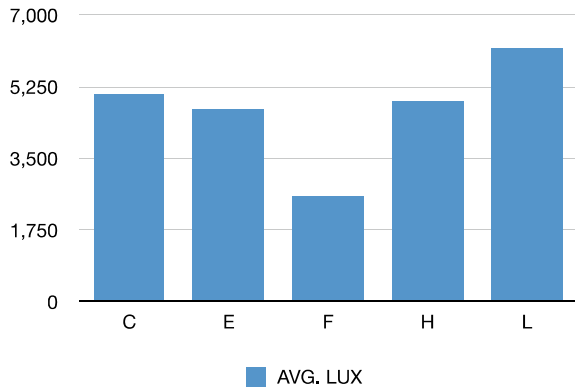
3.1 Daylight Analysis

Daylight is the controlled admission of natural light, direct sunlight, and diffused skylight into a building to reduce the amount of artificial lighting required and thus save energy [8, 21]. However, ASE with higher levels of daylight sufficiency leads to the potential for glare and solar heat gain [22].

ASE uses a simulated 1000 lx as an indicator for sunlight. Still, the simulated value can differ significantly from what is measured in the physical world, which considers secondary bounce-off surfaces. Like spatial daylight autonomy (sDA), ASE values range from 0 to 100%, with the latter suggesting that the entire floor area of the space in question exceeds the simulated value of 1000 lx for at least 250 h per year [23]. Thus, to reduce the potential for glare and thermal stress, designers should balance the amount of light entering the space with the least amount of glare and dark areas if not able to eliminate them [24].

As seen in Fig. 4, the results of most building shapes were different. When F- and H-shapes were used, the glare was significantly decreased; however, the dark areas increased in F, which reduced the need for artificial lighting. The glare was high for the C- and L-shapes due to the high ASE, with few dark areas, leading to greater demand for artificial lighting. Finally, the E-shape was the shape with the optimal average results when balancing the amount of ASE and dark areas in the building.

Fig. 4 AVG. LUX results



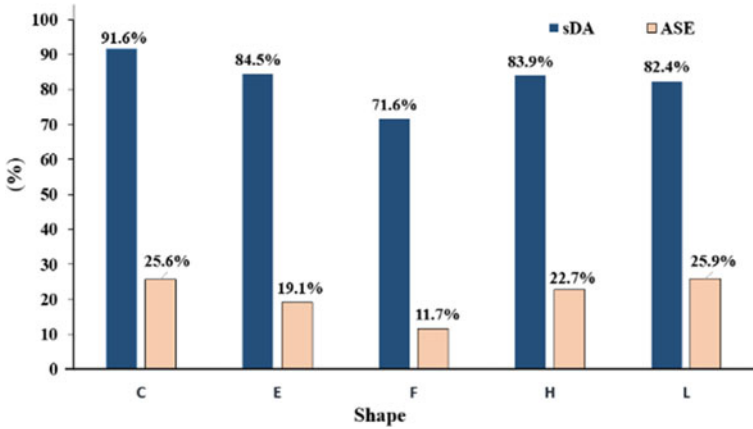


Fig. 5 Daylight analysis results: sDA and ASE

3.2 Illumination and SDA

Illumination is a term that describes the measurement of the amount of light falling into spreading over a given surface area [25]. Illumination also correlates with how humans perceive the brightness of an illuminated area [26]. Moreover, sDA examines whether a space receives enough daylight during standard operating hours (5 am to 6 pm). Furthermore, floor areas or grid points that achieve 300 lx for at least half of the analysis hours count as meeting the daylighting threshold in the building model. Accordingly, sDA values can range from 0 to 100% for the floor area. An sDA value of 75% indicates a space in which daylighting is “preferred” by occupants; that is, occupants would be able to work comfortably without any electric lights and find the daylight levels to be sufficient. An sDA value between 55 and 74% indicates a space where daylighting is “nominally accepted” by occupants. Lighting designers, therefore, should aim to achieve sDA values of 75% or higher in regularly occupied spaces, such as open-plan offices or classrooms, and at least 55% in areas where some daylight is essential [27]. However, the E-shape showed the optimal results regarding the highest or lowest numbers and balancing ASE and sDA throughout the year, as shown in Fig. 5.

4 Conclusion

Our research has highlighted the importance of geometric shapes in school buildings in the Gaza Strip. These geometry parameters included building shape, window-to-wall ratio, and orientation to highlight the proper design of geometric shapes in school buildings.

Several computer simulations were run to evaluate the daylighting improvement potential. The main findings of this study are outlined below:

- The E-shape was the optimal design when considering both SDA and ASE. With various design options, it achieved a maximum of 84.5% for SDA and 19.1% for ASE.
- Generally, a 40–60% window-to-wall ratio had the optimal daylighting quality performance. However, deeper rooms required a higher window-to-wall percentage to reduce the lighting demand.
- It was implemented in only one school as an E-shape in Gaza called Al Tafawuk School. The students set the feedback on the indoor atmosphere aside; however, shape E was chosen because of the elongation of the land lot and to provide the maximum number of classrooms.

These findings reveal that proper design regarding geometry parameters in school buildings in a temperate climate zone thus enhances students' subjective feelings. The findings of this study can provide a reference understanding of the influence of geometry in designs for daylighting for school buildings and students' preferences in the temperate climate of the Gaza Strip. However, it must be noted that one of the limitations of this study was that it did not include any shading systems in the school building models. Future research should aim to address this.

Further, these results may differ slightly according to the orientation, by rotating some shapes in different directions (by rotation by 90, 45, or 30 degrees). Finally, it must be noted that the analysis was based on the current conditions of school building shapes without any optimization. Therefore, future studies should be aimed at addressing this consideration.

References

1. Barrett P, Davies F, Zhang Y, Barrett L (2015) The impact of classroom design on pupils' learning: final results of holistic, multi-level analysis. *Build Environ* 89:118–133
2. Baker L, Bernstein H (2012) The impact of school buildings on student health and performance: a call for research. The Center for Green Schools and McGraw-Hill Research Foundation. Retrieved from <http://mcgraw-hillresearchfoundation.org/wp-content/uploads/2012/02/GreenSchoolsWP-2012.pdf>
3. Dogan T, Park YC (2019) A critical review of daylighting metrics for residential architecture and a new metric for cold and temperate climates. *Light Res Technol* 51(2):206–230
4. Bariche M, Sayar N, Balistreri P (2019) Records of two non-indigenous fish species *Synanceia verrucosa* Bloch and Schneider, 1801 and *Acanthurus sohal* (Forsskål, 1775) from the Gaza strip (eastern Mediterranean Sea). *BioInvasions Rec* 8:699–705
5. El Kichaoui AY, Bara'a A, El Hindi M (2017) Isolation, molecular identification and under lab evaluation of the entomopathogenic fungi *M. anisopliae* and *B. bassiana* against the red palm weevil *R. ferrugineus* in Gaza Strip. *Adv Microbiol* 7(01)
6. Abuzerr S, Nasseri S, Yunesian M, Hadi M, Mahvi AH, Nabizadeh R, Mustafa AA (2019) Prevalence of diarrheal illness and healthcare-seeking behavior by age-group and sex among the population of Gaza strip: a community-based cross-sectional study. *BMC Public Health* 19(1):1–10

7. Eldalo AS (2016) Prevalence and perception of smoking habits among the Palestinian population in the Gaza Strip. *J Multidiscip Healthc* 9:297
8. Abed HMM (2012) Effect of building form on the thermal performance of residential complexes in the Mediterranean climate of the Gaza Strip
9. Emmanuel R (2012) *An urban approach to climate sensitive design: strategies for the tropics*. Taylor & Francis
10. Esther MM, Sagada ML (2014) An evaluation of thermal comfort conditions in an urban entertainment centre in hot-dry climate of Nigeria. *Int J Energy Environ Res* 2(1):55–74
11. Van Esch M, Looman R, de Bruin-Hordijk G (2012) The effects of urban and building design parameters on solar access to the urban canyon and the potential for direct passive solar heating strategies. *Energy Build* 47:189–200
12. Barbeito I, Zaragoza S, Tarrío-Saavedra J, Naya S (2017) Assessing thermal comfort and energy efficiency in buildings by statistical quality control for autocorrelated data. *Appl Energy* 190:1–17
13. Elaydi H, Ibrki I, Khoudary EA (2012) Scheme for energy saving measures in Gaza Strip at no cost. *J Appl Sci Environ Sanitation* 7(4):257–262
14. Jalambo MO, Hamad A, Abed Y (2013) Anemia and risk factors among female secondary students in the Gaza Strip. *J Public Health* 21(3):271–278
15. M.o.E.a.H. Education (2021) Annual statistical book for general education in Gaza governorates 2020/2021. G.D.o.P.a.D.S.a.I.D.G.E.S. Division (Ed.), p 63
16. Al Shobaki MJ, Abu-Naser SS (2017) The reality of computerized MIS in the Palestinian ministry of education and higher education in Gaza Strip
17. Alzaneen R, Mahmoud A (2019) The role of management information systems in strengthening the administrative governance in ministry of education and higher education in Gaza. *Int J Bus Ethics Gov* 2(3):1–43
18. Bayoumi M (2021) Improving indoor air quality in classrooms via wind-induced natural ventilation. *Model Simul Eng* 2021
19. Shraim K, Khlaif Z (2010) An e-learning approach to secondary education in Palestine: opportunities and challenges. *Inf Technol Dev* 16(3):159–173
20. Bahloul AA (2013) The effect of differentiated instruction strategy on developing ninth graders' English reading comprehension skills at Gaza UNRWA schools
21. Ahmad A, Kumar A, Prakash O, Aman A (2020) Daylight availability assessment and the application of energy simulation software—a literature review. *Mater Sci Energy Technol* 3:679–689
22. Mohsenin M, Hu J (2015) Assessing daylight performance in atrium buildings by using climate based daylight modeling. *Sol Energy* 119:553–560
23. Fontoynt M (2014) *Daylight performance of buildings*. Routledge
24. Futrell BJ, Ozelkan EC, Brentup D (2015) Optimizing complex building design for annual daylighting performance and evaluation of optimization algorithms. *Energy Build* 92:234–245
25. Dutre P, Bala K, Bekaert P (2018) *Advanced global illumination*. AK Peters/CRC Press
26. Haans A, De Kort YA (2012) Light distribution in dynamic street lighting: two experimental studies on its effects on perceived safety, prospect, concealment, and escape. *J Environ Psychol* 32(4):342–352
27. Turan I, Chegut A, Fink D, Reinhart C (2020) The value of daylight in office spaces. *Build Environ* 168:106503

Analysis Model for Industrialized Housing Design and Assembly Process



Yidnekachew Tesmamma Daget and Hong Zhang

Abstract Industrialized housing construction comprises different connected activities that include many stakeholders and for which the plan of action is carried out itinerantly. This paper proposes and tests a conceptual analysis model for industrialized housing design and assembly process. Four projects from Ethiopia and China were selected as a comparative case study. Semi-structured interviews, document and literature reviews, and field studies were conducted. Abductive reasoning was applied for conceptual model development. The study's findings revealed that the complexity of the design-construction process of industrialized housing could be simplified through the building component-based design and assembly process. Further, it provides three basic dimensions (i.e., material, technical, and assembly order) to understand and analyze industrialized house buildings. The study contributes a conceptual model to the industrialized house-building body of knowledge for a systematic view of the industrialized housing design and construction process.

Keywords Analysis model · Industrialized house design · Design-construction efficiency · Design-construction analysis · Ethiopia · China

1 Introduction

The way of industrialized housing construction is known for its many benefits in housing development, including but not limited to: rapid construction [1], environmental and health-friendly [2–4], less labor [5], better life-cycle performance, and increased profit [6, 7]. While industrialized housing as a field of research still has the house as an object of study, it also consists of the spatial design and assembly processes, their industrialization, and the perspectives and significances of the housing result [8]. Spatial design and the assembly process are equally crucial regarding each housing project's design-construction efficiency (DCE) issues. Rather

Y. T. Daget · H. Zhang (✉)
Southeast University, Sipailou, Nanjing, China
e-mail: zhangh555@aliyun.com

© The Author(s), under exclusive license to Springer Nature Singapore Pte Ltd. 2024
M. Casini (ed.), *Proceedings of the 3rd International Civil Engineering and Architecture Conference*, Lecture Notes in Civil Engineering 389,
https://doi.org/10.1007/978-981-99-6368-3_47

563

than concerned with a particular result, industrialized housing construction is a systematic view of housing design and construction that has significance for the efficiency of house building.

However, there is a growing challenge in industrialized housing projects due to technological advancement, which widens the gap between the housing design approach and its consecutive realization process. To address the described difficulty and research gaps, the study aims to propose an analytical model to elucidate and simplify the potential of industrialized housing design that could improve the understanding of how buildings can be put together as a combination of prefabricated components and onsite construction.

2 Literature Review

Industry theory and industrialized manufacturing methods infer strict procedures and structures to ease or handle complexity. Since constructions have become more industrialized, most onsite processes have moved into a factory setting [9]. The links to the manufacturing industry and the motivation to draw on it become apparent. The production of industrialized building materials and components is as old as the industrial revolution, but the development is not increased to the same extent as the industry [10]. However, the linkage to the industry has recently been improved by the fact that the production of industrialized building materials and components has become based on the notion of mass production of standardized objects, new procedures, business models, and techniques, as well as individualized and customized products [11]. The approach of industrialized manufacturing helps achieve a better connection between architectural ideation and its construction, as it helps to increase construction efficiency [12].

3 Methodology

3.1 Research Methods and Techniques

This study sought to develop a conceptual model for analyzing the industrialized design and assembly approach. Based on the study's objective, an abductive reasoning and case study method was applied. The case study methodology is suitable for this purpose because it offers a variety of data collection methods [13] that contribute to understanding complex phenomena studied in their real-life context [14]. Four industrialized house buildings were selected as case studies from Ethiopia and China. The case studies were conducted over two years, enabling a variety of information and data collection to be carried out on several occasions, thereby increasing the validity of the work [15] and providing the case study with richer material.

A list of essential factors in the design-assembly process was summarized from the literature review and given to the selected experts to identify the most significant within the basic three categories (See Table 1). Twenty-eight experts were selected with an average of more than ten years of experience and participation in industrialized housing design and construction. Four primary sources of data collection were applied to investigate the case studies: site visits (observations and conversations), document studies, and semi-structured interviews. These multiple sources enabled triangulation and enhanced the reliability of the study [16]. Furthermore, four industrialized construction projects were chosen as case studies from Ethiopia and China. Finally, the case studies were reviewed, analyzed, and evaluated to understand their design and assembly approaches.

The notion of abductive reasoning inspires the approach to model development. To put the notion briefly, it can be described as proposing a credible or satisfying hypothesis about what needs to be explained. Abduction is not an exclusive way of inference. Rather it supplements or precedes the two other more common ways of deduction and induction. Thus, according to Kirkeby, an ‘ideal’ sequence for

Table 1 Issues in the material, technical, and assembly order dimensions

Main categories	Important issues	References
Material	Component/modular	[18–22]
	Raw materials	[23]
	Manufacture	[19, 24, 25]
	Production	[22, 26]
Technical	Design information (object)	[5, 22, 24, 26–32]
	Customer demand/satisfaction	[33, 34]
	Information mapping (BIM)	[20, 22, 23, 25, 26, 35–38]
	Life-cycle (Flexible and demountable)	[22, 35, 39]
	Environment/sustainability	[36, 40]
	Planning	[36, 40]
	Standard/guidelines	[21, 29, 32, 41]
	Lean/agile concept	[42]
Assembly order	Concurrent engineering	[43]
	Assembly	[19, 24, 26, 44, 45]
	Transport	[5, 19]
	Installation	[18–20]
	Supply chain/market condition	[23, 24, 32, 46]
	Equipment	[23]
	Flow efficiency	[22, 47, 48]
Lean/Agile concept	[22, 42]	

producing qualitatively new and validated knowledge would be abduction—deduction—induction [17]. This sequence and approach are followed and tested in this model development.

3.2 *Model Development*

The significance of the industrial production theory and industrialized production has triggered a system structure view to perceive architectural design and its realization. Kieran and Timberlake have developed a conceptual supply chain model to convey and analyze the components utilized in industrialized building projects [9]. The model's significant chains were offsite and onsite processes ended on the construction site. Each chain is divided into several tiers—three offsite and two onsite tiers representing the category of the building components applied. However, the model was limited to a specific project. In addition, it does not show the complete flow of materials ranging from raw materials to finished building components as a product [49].

Strongly encouraged by Kieran and Timberlake's supply chain model, Vibaek [8] proposed a revised form that combines offsite and onsite deliveries into one single hierarchy that integrates the advancement of integration levels with a slightly improved number of tiers (T1-5). The revised model can reduce the need for the resource-intensive and laborious transfiguration of architectural concepts into physical material and form. It also helps to control the limitless design options and gives a system structural view of the architectural design and how the buildings are put together.

The above-mentioned models on systematic design thinking help to analyze the impact of the design integration level and the construction process. However, it also needs comprehensibility to analyze the dimensions mentioned in each model prevalent in today's complex scenario of industrialized construction. Therefore, there is a need to outline and organize the material comprehensively, technical and assembly dimensions to get a complete picture of the industrialized housing construction. The proposed model is developed based on the model and system structure design thinking of Kieran and Timberlake [9] and Vibaek [8]. It intends to organize the dimensions systematically and for better analysis of design and assembly approaches (See Fig. 1). The material aspect focuses on component classification, material selection, and production. It is embodied in the integral molding and independent parts and standard characteristics of the physical system. The technical system includes the design principle, manufacturing rule, and structure of the building and its components that conform to the prefabrication and assembly of the construction process.

The assembly order focused on the connection law and its production process based on modular, standardized, generalized, and serialized design principles. The model can be used as an operational self-discipline construction process and embodies the assembly and connection process technology accumulation. The physical deliveries are combinations of materials, components, and assemblies to deliver

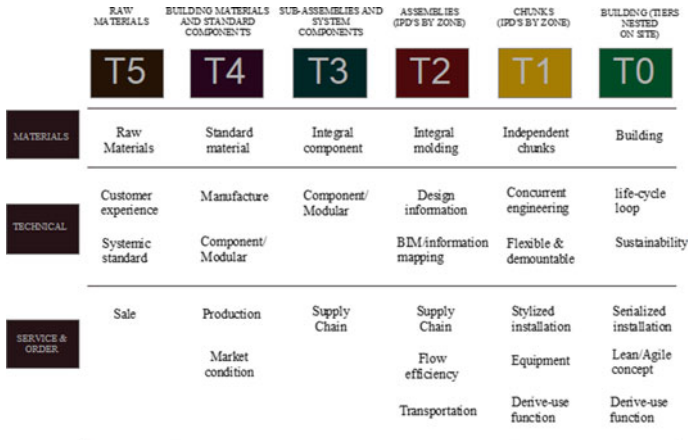


Fig. 1 Design-construction analysis model

and install them into a subsequent tier level (i.e., tier 0). The system structure is a result of different processes, just like the product architecture of an industrial product. As used in this research, it divides into different tier-levels, and the deliveries become nested into each other from the less complex upstream deliveries on tier 4 and tier 3 over the more difficult and integrated deliveries on tier 2 to the final tier 0—deliveries onsite.

3.3 Case Studies

Case Studies Data Collection and Analysis. The data on the four selected case studies were collected from Ethiopia and China (See Table 2). The cases were selected based on their attempt to promote the performance of DCE. Attention was given to contextual differences to minimize the possible effects. Qualitative data were collected through semi-structured field interviews and direct literature and document reviews. To reduce the potential impact of limited cases, a detailed case study was executed. Interviews with project participants were undertaken to draw lessons from their insights regarding the design approach in which they were involved. In the meantime, project documents were studied to enable thorough understanding and direct observations. In this section, based on the proposed model, the design-construction approaches of the case studies are analyzed.

Table 2 Summary of the design-assembly analysis of the project cases

Key application of industrialized design-construction dimensions		Typical Southeast university project	Typical part	Degree of application	Typical Ethiopian project	Typical parts	Degree of application
Material system	Integral molding (one piece)	Yi Hui Tang project	Components of the wall board panel	High	Apt 16 and Special housing project	Precast concrete Wall and components	High
	Independent system	Dreamhouse project	Whole (systematic)	Very high			Nothing
Technical system	Systematic and standard	Dreamhouse and Yi Hui Tang projects	Whole (systematic)	Very high	Apt 16	Residential whole	High
	Modularization						
	Generalization						
	Serialization lean-thought						
	Concurrent engineering						
	Sustainability						
BIM information			Solar panels (Self-sufficient energy) and waste treatment system	Very high	Nothing		
		Dreamhouse project	Information exchange	Very high		Residential whole	High

(continued)

Table 2 (continued)

Key application of industrialized design-construction dimensions		Typical Southeast university project	Typical part	Degree of application	Typical Ethiopian project	Typical parts	Degree of application
Order system	Flexible and demountable		Independent modular system				
	Assembly process	Dreamhouse and Yi Hui Tang projects	Whole (systematic)	Very high	Apt 16 and special housing project	Residential whole	High
	Stylized/serialized installation						
Derivative function							

3.4 Design-Construction Analysis of the Case Studies

Apt 16. The 16th apartment building (Apt 16) is one of the first of a series of prefabricated residential building projects in Addis Ababa (See Fig. 2). Based on the delivery mode of the construction work, the building has two discrete phases of assembly. The first part is the foundation and structural parts assembly phase which took only six months to complete. In contrast, the second part took more than seven years over an extended time. The Apt 16's system structure code and project features indicate that the Prefabricated Building Parts Production Enterprise (PBPPE) produced all structural framework deliveries (tier 4 to tier 2) before they were delivered for final assembly (tier 0) on the building site. The established system structures of the project (See Fig. 3a and b) comprise a relatively large number of tier 3 and 4 deliveries.

This can partly be described and examined by the production focus and the assembly mode of the deliveries. Equally, the system structure of Apt 16 (Fig. 3a) shows a collection of the more integrated (downstream) tier 4 and 3 deliveries that subsequently are nested as deliveries onsite (on tier 0). This structure can be understood as an approach directed at increasing the level of component-based building parts before delivery at the construction site (on tier 0). The system structure in Fig. 3b shows the typical conventional construction method.

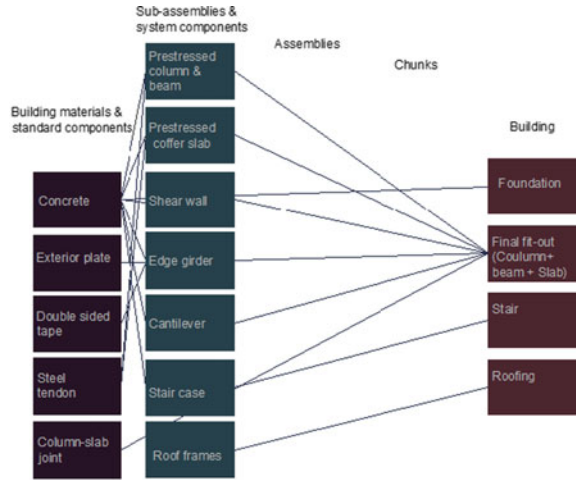
Special Housing Project (CMC). The project is situated in an area of approximately 22 hectares and is distributed among 56 buildings of varying architectural styles. Five hundred apartment units for diplomats, higher government officials, and various shops and service buildings were constructed (See Fig. 4). The buildings were constructed using modern technology of architectural precast concrete decorated walls, slabs, stairs, and columns, as well as the assembly of other precast parts. Having defined internally and being in the power of the overall framework, CMC enabled it to model the system structure towards a more industrialized approach

Fig. 2 Apt 16 building.

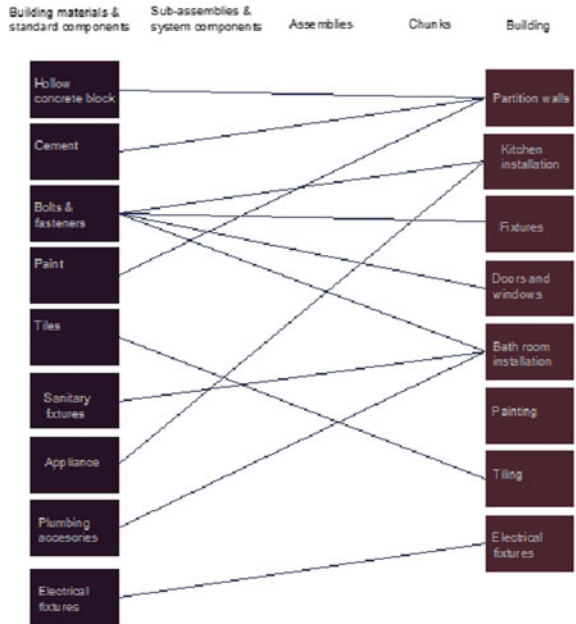
Source Author



Fig. 3 a System structure of structural framework assembly of Apt 16; **b** System structure of finishing onsite work assembly of Apt 16



(a)



(b)

without depending on decisions made by external consultants as in conventional project setup (See Fig. 5).

Fig. 4 CMC apartment buildings. *Source* CMC and Author



Yi Hui Tang's Project. The project type is a residential building funded and built by the Changzhou Institute of Building Science. The Southeast University industrialization of housing and construction industry research institute did the planning and design of the project. The project is located in the Changzhou Wujin green building industry cluster demonstration zone. This project is a new industrialization demonstration project with two floors with a total construction area of 350 m² (See Fig. 6). The building was completed and put into use within three months. The work packages behind the trade contracts of this project are parallel, as opposed to the traditional serial system. The deliveries in all work packages span from and include any sub-delivery from tier 4 (T4) to tier 0 (T0). The collaborative construction management approach creates the particular system structure of parallel deliveries spanning various tier levels (See Fig. 7).

Dreamhouse Project. The Dream House is located in Jiangsu green building expo Park, Wujin District, in Changzhou City. The building was a product of a new generation of solar and portable, lightweight modular integrated housing systems (See Fig. 8). The building was designed and developed by the Southeast University School of Architecture. The installation process was simple and fast and took only two weeks to complete. Being a modular and relatively highly standardized level of offsite manufacturing, the dream house system structure contains only a limited number of deliveries (See Fig. 9). The choice of modular steel lightweight structure units combined with movable solar panels made connectors easily accommodate the onsite assembly with little need for additional fixing solutions. The dream house thus has a few tiers 4 (t4) and tier 3 (T3) deliveries. It also has a few tier 0 (T0) deliveries on site due to the high degree of offsite fabrication (See Fig. 6). This means, on the

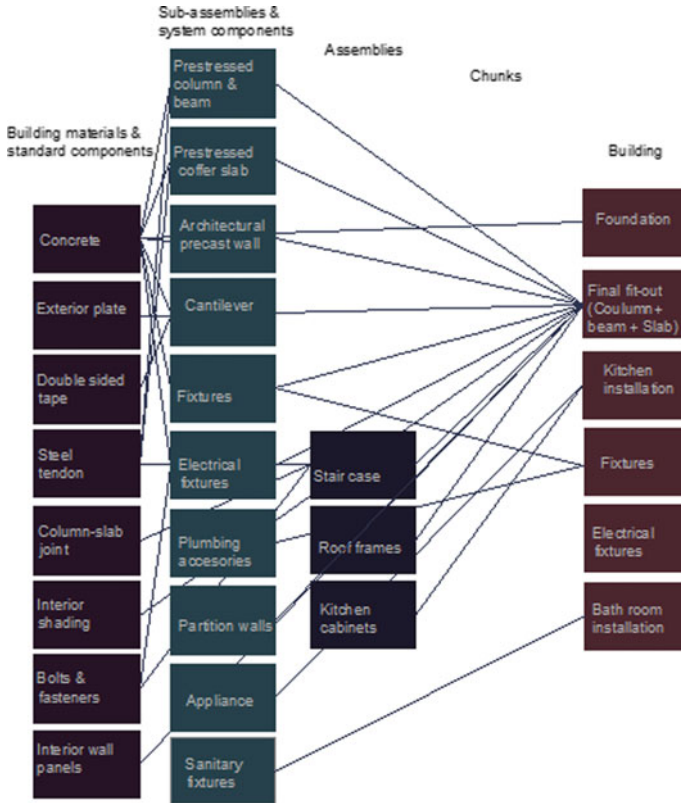


Fig. 5 System structure of the CMC project

other hand, that the two integrated system levels –tier 2 (T2) and tier 1 (T1) have a relatively high weight.

The T1 and T2 deliveries can be considered the primary elements of the dream house project. The T1 chunks had a 90% degree of completion upon onsite delivery, thus integrating most upstream deliveries from the factory, including several T2 deliveries and most partition wall panels. Others were integrated onsite, i.e., kitchen cabinets and bathroom pods (t1). Some partition walls and solar panels could not be factory integrated due to the specific onsite assembly sequence or the risk of transportation damage and were instead delivered to the site for final fit-out. Although the primary structural system, the steel frame becomes a (T3) subsystem to the chunks. The project was designed and controlled with the support of the BIM application.



Fig. 6 Yi Hui Tang building. Source SEU Zheng Studio

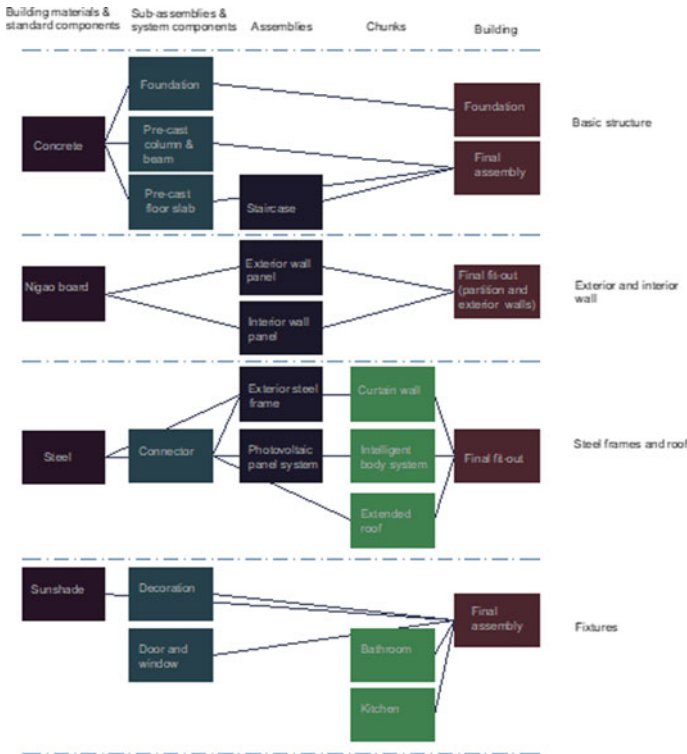


Fig. 7 System structure of the Yi Hui Tang building



Fig. 8 Dream-house building. *Source* SEU Zheng Studio

4 Analysis and Findings

4.1 Industrialization of a Material System

Integral Molding of Component. Integral molding is one of the main points of the production strategy of the building in the form of sub-assemblies and components. The building assembly results from the composite concept of integrating building components. Before the onsite assembly, integral molding is fabricated as a product based on the in-depth design. It is necessary to carry out the essential connection and secondary decoration treatment to avoid many component assemblies on site. This typical assembly strategy is applied to all case-study projects. For example, the precast concrete components in Apt 16 are manufactured and supplied based on the component level of building parts in the features of integral molding and do not require onsite modification (See Fig. 10). The dream house and Yi Hui Tang buildings were designed based on two types of prefabricated exterior wall panel components: aluminum panel insulation and a decoration-integrated component (See Fig. 11). The erection process is fast and straightforward. The integral molding of the component system can produce the enclosure to suit an extensive range of building facades.

Independent System of the Building. The independent system is the main point of the industrialization strategy and refers to similar functional components. It is a collection of components that becomes a relatively closed system. Each assembly (system) has a clear function, no cross-interference, and strong independence and systems. The implementation of the independent system was seen mainly in the Yi Hui Tang residential project (See Fig. 12). The roof structure also has a self-protection

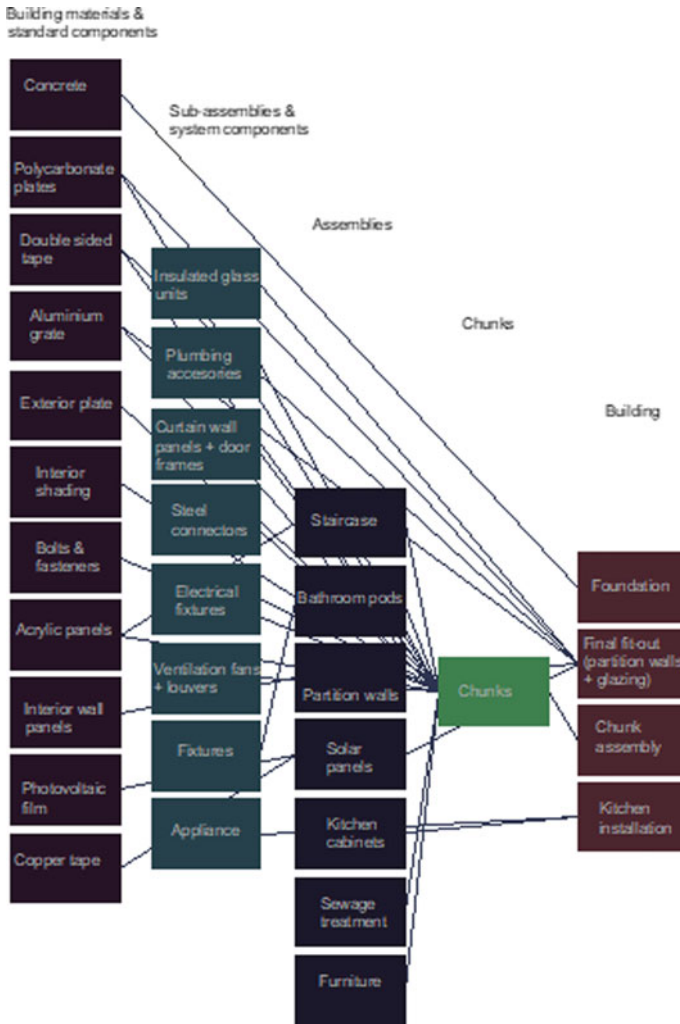


Fig. 9 System structure of Dreamhouse project

multifunctional activity room. To simplify the complexity of the building system, the design team organized it into independent structure systems such as peripheral (body) system, interior (body) system, and equipment (body) system.

The system's design (development) and construction ideas are the material composition order for implementing lean thinking and concurrent engineering technologies. Based on the analysis of the integral molding of the outer protective members and the independent system, it can be concluded that the building components displayed standard production strategy features.

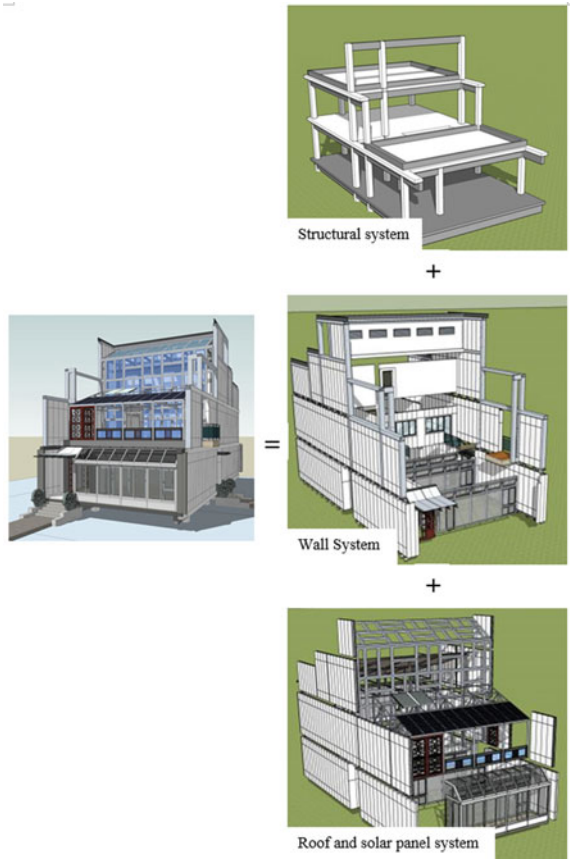


Fig. 10 Apt 16's integral modular component



Fig. 11 Yi Hui Tang's integrated modular components

Fig. 12 Independent system of Yi Hui Tang buildings.
Source SEU Zheng Studio



4.2 Industrialization of the Technical System

Design Principles and Strategies. Modularity, standardization, generalization, and serialization are the technical industrialization strategy’s design guidelines and end goals. The continuous development in research and practice of prefabrication strengthens and promotes the application of generalized and standardized design principles in prefabricated buildings. Prefabricated technology solves the problem of implementing the concept of blocking and the combination of good buildings. This typical building industrialization policy was applied to the Yi Hui Tang and dream house projects (see Figs. 13 and 14). The effective application of the principle in the design stage ensures the smoothness of the prefabricated technology in the subsequent production and construction phases. The principles of generalization and standardization also run through the entire construction process of designing, producing, and constructing lightweight structural buildings.

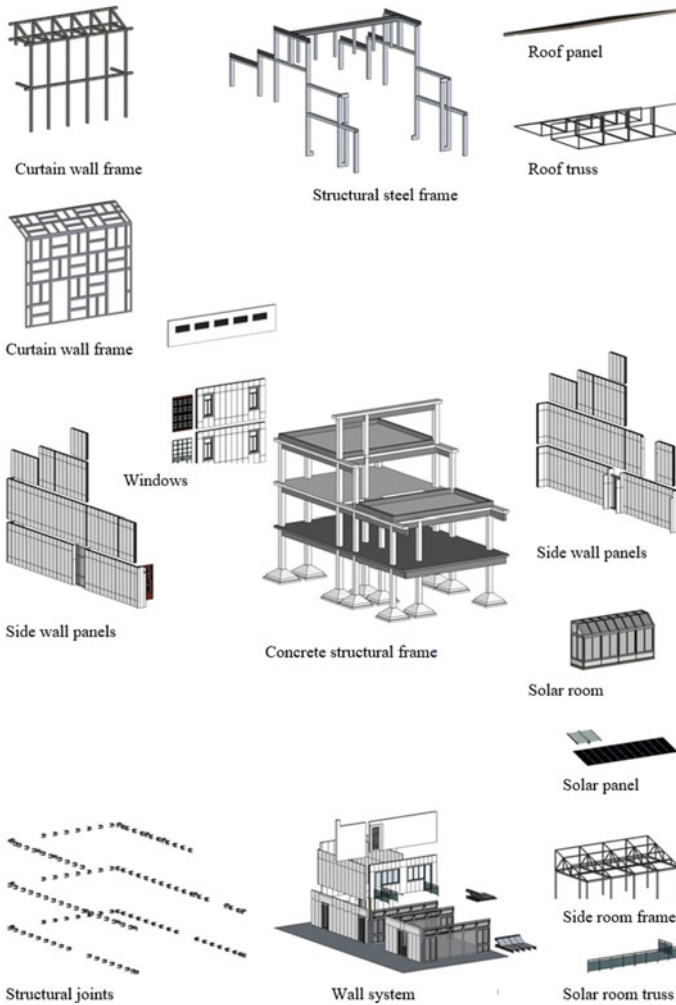
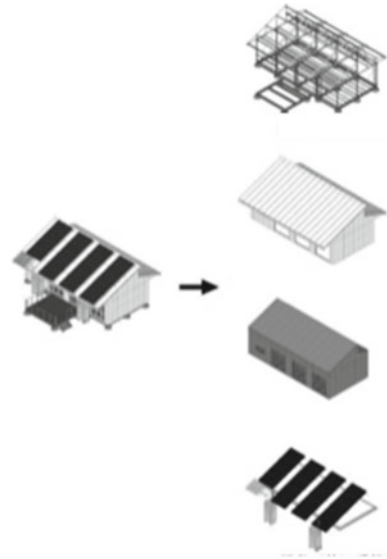


Fig. 13 Yi Hui Tang building’s standardized and modular component-based design. *Source* SEU Zheng Studio

Serial Design Goals. Serialization helps to achieve the industrialization strategy of buildings and design end objectives of hierarchy. The serialized design results from using simplified principles in product design through the systematization of objects. The serialized design is a basic form of standardization to achieve the structure’s unification and meet the technical activities of the multi-functionality of use.

The implementation of serialized products represents a mature application of modularization, standardization, and generalization of technology (See Fig. 15). The residential product series is based on the type of houses. CMC’s residential series are groups of different apartment buildings that can be divided into five-story apartment

Fig. 14 Modular unit of dream house building.
Source SEU Zheng Studio



buildings, two-story residential homes, and service buildings (See Fig. 16). This industrialization enables it to develop customized residential products that meet the market and customers' needs. In the prefabricated residential case of the above two projects, it can be seen that various types of prefabricated residential buildings are finally transformed into a series of residential products. The goal of listing products and the birth of serialized products, in turn, promote modularization, standardization, and generalization.

4.3 Industrialization of the Assembly Order

Assembly Process. The systemized approach of component assembly provides the possibility of the assembly process. Process efficiency plays an essential role in the final building quality. With progressive experience, the technical optimization for the assembly and joining process of the Yi Hui Tang project was inclined to standardization and stylization (See Fig. 17). At PBPPE in Ethiopia, stylized assembly and joining procedures play an important role in prefabricated building projects. Such as a standardized connection method and assembly process of the post-tensioning connection system. The worker only needs to tighten the bolt sleeve on the top of the prefabricated component to assemble the component conveniently and quickly.

Derived Use Function. Mobile transportation and maintenance are the main points of the industrialization strategy of the building at the derivative use function (system purpose) level. Using a car to move the building module due to a change of location needs fast disassembling and assembling methods. The movement of modules and

Fig. 15 SEU's Lighthouse series building. *Source* SEU Zheng Studio



their maintenance convenience has always been one of the essential goals of the Dreamhouse project. The team used to divide the building into a container sizes. The main module (box unit) is transported and hoisted using existing vehicles and equipment to achieve mobile transport (See Fig. 18). This is achieved by applying the principles of modularization, standardization, and generalization of building components.

Fig. 16 CMC's series buildings



4.4 The Analytical Model

The model enabled a systematic view for analysis of the design-construction approaches of industrialized housing constructions. The model has two functions that are, however, closely related: One is to show how the outcome, the building, production-wise, is constructed or assembled by different elements. Another is how these elements sometimes are embedded in each other forming supply chains that lead to more or less integrated product deliveries to be installed or nested into the building. The model analysis showed that each project applied different design-assembly and delivery approaches which can be demonstrated through their various system structure analysis diagrams. The appropriate degree of prefabrication and different levels of industrialization is and will always be project and context dependent. It is never an either/or choice between onsite and offsite processes.

The discussion of offsite vs. onsite construction is an explicitly integrated part of concepts and processes. This proposes that the explanative power of the model is

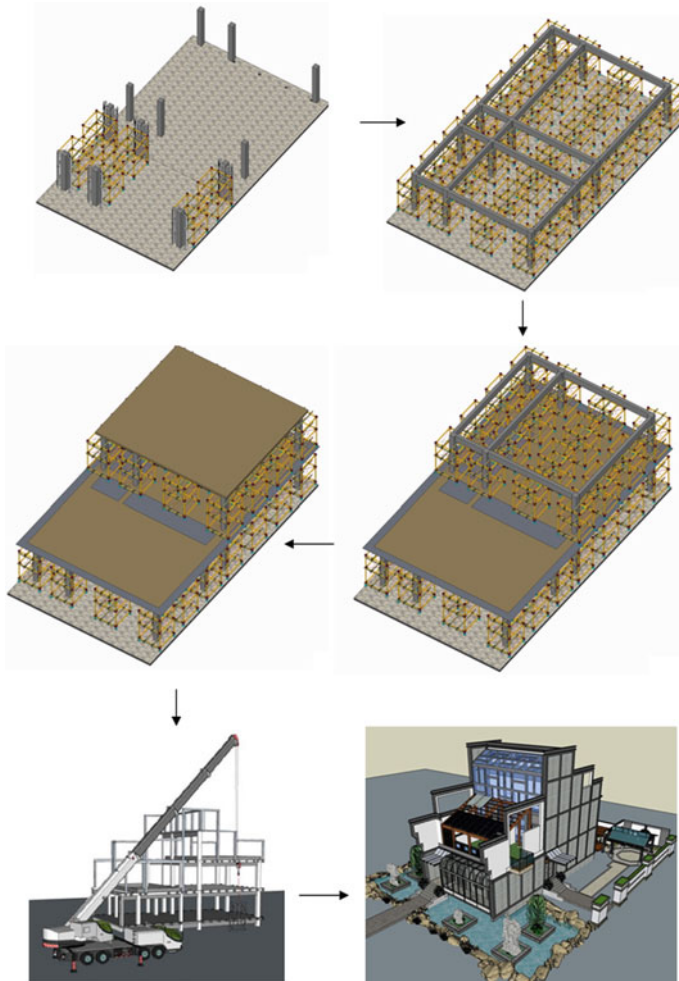


Fig. 17 Stylized assembly of Yi Hui Tai building construction

reasonable to the project's features and a particular focus on production. For example, the Yi Hui Tang project has certain chunk deliveries (T1), and the Dreamhouse goes much further into that realm. In the Yi Hui Tang, the chunks (modules) are limited to the most system-intensive spaces, such as bathrooms and sunrooms. On the other hand, the dream house has a comparatively high level of prefab system integration due to the network of intelligent and mechanical systems into lightweight modular structures that are delivered as assemblies with plug-and-play system connections. One of the main reasons for the (T1) chunking strategy applied for the Dreamhouse was the two-week time limitation allocated for the onsite assembly. Where the Dreamhouse is mainly assembled onsite as chunks by zone, the Yi Hui Tang project is mainly assembled onsite as assemblies by component groups supplemented with



Fig. 18 Module part transportation of dream house project. *Source* SEU Zheng Studio

the proposed building components such as (a) concrete structural framework, (b) external steel enclosure, (c) Nigao panels and partitions walls, (d) intelligent body systems with the solar room, and (e) the final fit-out.

The Apt 16 and special housing project, on the other hand, the nesting of upstream deliveries (T4-T2) into the site (T0) is deliberately maximized due to limitations in transportation and the site constraints such as difficult access and little space for laying out construction elements as in the case of Apt 16 project. Although time, economy, and site constraints were critical for the projects, the vision was similar regarding fast onsite assembly based on a high degree of prefabrication.

Summing up, the notion of the design approach model can help express the industrialized construction's capacity as enabling the architectural design imagination rather than limiting its potential. Though the projects displayed varying degrees of complexity, the model visualizes how the architectural design approach is appropriately organized and assembled in the construction site (See Table 2).

5 Conclusion

The current approach for housing that is built to meet the increasing demands has called for construction methods to be provided in a timely and quality manner. However, due to technological development, architectural design and construction have become highly multifaceted issues and disintegration of the knowledge required to act in accordance. There are also restrictions/gaps in examining and understanding

the design-construction approach. The study addresses this gap. Based on the findings of the study, the following conclusions are made.

The idea of a system structure view on the design-construction analysis model is a way to conceptualize a systemic level in architecture and construction that lies between general construction techniques and specific architectural results. Pivotal in the present research endeavor is that the conceptual model seeks to establish a system view on industrialized housing design and its realization as assemblies of what the present and upcoming building industries are capable of delivering. Such a system view can decrease design-assembly complexity and help make a more competent decision regarding a housing development project. Additionally, it supports strategically identifying and outsourcing the portions that need external assistance.

The analytical model is also reflected as a second essential contribution to knowledge in architectural industrialization in a present industrialized context. It is not an effort to create a new paradigm or a changed style. It does, however, signify an adapted way to look at what is already there. The observation and methodological approach can help ease a more vigorous applied use of the current and upcoming building industry to make industrialized housing specifically attached to time, place, and cultural context, as well as not just the manifestation of smooth procedures or cost-efficient and affordable housing development solutions.

References

1. Chen Y, Okudan GE, Riley DR (2010) Sustainable performance criteria for construction method selection in concrete buildings. *Autom Constr* 19(2):235–244
2. Fan Y et al (2016) An approach of measuring environmental protection in Chinese industries: a study using input–output model analysis. *J Clean Prod* 137:1479–1490
3. Law EP, Diemont SAW, Toland TR (2017) A sustainability comparison of green infrastructure interventions using energy evaluation. *J Clean Prod* 145:374–385
4. Matic D et al (2015) Economically feasible energy refurbishment of prefabricated building in Belgrade, Serbia. *Energy Build* 98:74–81
5. Mao C et al (2016) Cost analysis for sustainable off-site construction based on a multiple-case study in China. *Habitat Int* 57:215–222
6. Polat G (2008) Factors affecting the use of precast concrete systems in the United States. *J Constr Eng Manage* 134:169–178
7. Samani P et al (2017) Pre-fabricated, environmentally friendly and energy self-sufficient single-family house in Kenya. *J Clean Prod* 142:2100–2113
8. Vibaek KS (2014) Architectural system structures: integrating design complexity in industrialised construction. Routledge, London
9. Kieran S, Timberlake J (2003) Refabricating architecture: how manufacturing methodologies are poised to transform building construction. McGraw Hill
10. Bachman LR (2003) Integrated buildings - the systems basis of architecture. Wiley, Hoboken (NJ)
11. Pine II BJ, Gilmore JH (2000) The experience economy: work is theater & every business a stage. Harvard Business School Press, Boston
12. Mikkelsen H et al (2005) Integrated product deliveries in construction - a preliminary account. Institut for Produktion og ledelse, DTU, Kgs Lyngby

13. Stake RE (1995) *The art of case study research*. Sage Publications, London
14. Yin RK (2003) *Case study research: design and methods*, 3rd ed. Sage Publications, Thousand Oaks, CA
15. Merriam SB (1998) *Qualitative research and case study applications in education revised and expanded from "Case study research in education"*. ERIC, San Francisco, USA
16. Lincoln YS, Guba EG (1990) Judging the quality of case study reports. *Int J Qual Stud Educ* 3(1):53–59
17. Kirkeby OF (1994) Abduktion IN. In: Andersen H (ed) *Philosophy of science and scientific methodology*, vol. I. Samfundslitteratur, Frederiksberg, DK
18. Yildirim SG (2012) Design education of industrialised building systems. *Procedia Soc Behav Sci* 51:84–89
19. Yuan Z, Sun C, Wang Y (2018) Design for manufacture and assembly-oriented parametric design of prefabricated buildings. *Autom Constr* 88:13–22
20. Zhang J et al (2016) BIM-enabled modular and industrialized construction in China. *Procedia Eng* 145:1456–1461
21. Gan Y et al (2017) Critical factors affecting the quality of industrialized building system projects in China. *Sustainability* 9:216
22. Li X et al (2019) Integrating building information modeling and prefabrication housing production. *Autom Constr* 100:46–60
23. Čuš-Babič N et al (2014) Supply-chain transparency within industrialized construction projects. *Comput Ind* 65(2):345–353
24. Razkenari M et al (2018) A systematic review of applied information systems in industrialized construction
25. Yin X et al (2019) Building information modelling for off-site construction: review and future directions. *Autom Constr* 101:72–91
26. Li Z, Shen GQ, Xue X (2014) Critical review of the research on the management of prefabricated construction. *Habitat Int* 43:240–249
27. Ekholm A, Wikberg F (2009) Design with architectural objects in industrialised house-building. *EWork and eBusiness in architecture, engineering and construction*. Taylor & Francis, pp 213–222
28. Knotten V et al (2015) Design management in the building process - a review of current literature. *Procedia Econ Financ* 21:120–127
29. Jansson G, Viklund E, Lidelöv H (2016) Design management using knowledge innovation and visual planning. *Autom Constr* 72:330–337
30. Delfani M et al (2016) Towards designing modular of industrialized building systems, vol 78, pp 387–391
31. Sadafi N, Zain MFM, Jamil M (2012) Adaptable industrial building system: construction industry perspective. *J Archit Eng* 18:140–147
32. Bari NAA et al (2012) Factors influencing the construction cost of industrialised building system (IBS) projects. *Procedia Soc Behav Sci* 35:689–696
33. Jansson G (2016) Flow-oriented contracting in industrialized house-building. In: *International conference on construction and real estate management 2016*. ASCE, Edmonton, Canada
34. Haron N et al (2015) Quality function deployment (QFD) modelling to enhance industrialized building system adoption in housing projects, vol 26
35. Beucke K et al (2005) Applications of virtual design and construction in the building industry. *Struct Eng Int* 15(3):129–134
36. Hosseini MR et al (2018) Critical evaluation of off-site construction research: a scientometric analysis. *Autom Constr* 87:235–247
37. Tan T et al (2019) Barriers to building information modeling (BIM) implementation in China's prefabricated construction: an interpretive structural modeling (ISM) approach. *J Clean Prod* 219:949–959
38. Abanda FH, Tah JHM, Cheung FKT (2017) BIM in off-site manufacturing for buildings. *J Build Eng* 14:89–102

39. Jaillon L, Poon CS (2014) Life cycle design and prefabrication in buildings: a review and case studies in Hong Kong. *Autom Constr* 39:195–202
40. Mohammad M (2013) Construction environment: adopting IBS construction approach towards achieving sustainable development. *Procedia Soc Behav Sci* 85
41. Wu G et al (2019) Factors influencing the application of prefabricated construction in China: from perspectives of technology promotion and cleaner production. *J Clean Prod* 219:753–762
42. Mostafa S, Chileshe N, Abdelhamid T (2016) Lean and agile integration within offsite construction using discrete event simulation: a systematic literature review. *Constr Innov* 16:483–525
43. Armacost R et al (1994) An AHP framework for prioritizing customer requirements in QFD: an industrialized housing application. *IIE Trans* 26:72–79
44. Schmidt R, Vibæk KS, Austin S (2014) Evaluating the adaptability of an industrialized building using dependency structure matrices. *Constr Manag Econ* 32(1–2):160–182
45. Tam VWY et al (2015) Best practice of prefabrication implementation in the Hong Kong public and private sectors. *J Clean Prod* 109:216–231
46. Shukor ASA et al (2016) Towards improving integration of supply chain in IBS construction project environment. *Procedia Soc Behav Sci* 222:36–45
47. Wernicke B, Lidelöw H (2016) Foundation for balancing resources and flow efficiency in industrialized construction. In: ICCREM. American Society of Civil Engineers
48. Teng Y et al (2017) Analysis of stakeholder relationships in the industry chain of industrialized building in China. *J Clean Prod* 152:387–398
49. Nagurney A (2006) *Supply chain network economics: dynamic of prices, flows, and profits*. Edward Eglar Publishing, Cheltenham Glos

Visioning New Methodology for Creative Architecture in the Third Millennium of Knowledge Society



Abeer Samy Yousef Mohamed 

Abstract The most effective utilization of information and cutting-edge scientific understanding is essential to the fourth technological revolution of the twenty-first century. As new ideas frequently encounter a negative response from society, it is crucial to constructively use new technology, particularly in building systems and creative architectural design. A person needs substantial knowledge, a holistic approach, the ability to synthesize information about an item, and the development of new human values to interact positively with these technologies. Philosophy, science, art, architecture, and technology are all seen in today's knowledge as components of a single, interacting cognitive system. According to the new techniques provided to help design and enhance thought translating to physical forms, the paper will study and analyze the effects of the thinking transformation shift in the third century on architectural space and design methodologies. In addition, the paper will introduce a methodology for future vision based on existing and emerging technologies and methods, which will shift lifestyle and improve quality of life. The psychological impossibility of inaction is the inability of thought, and technology and mass media can affect how a new thing is seen in advance.

Keywords Visioning · New methodology · Innovation · Creative architecture · Knowledge society

1 Introduction

The century that began with radio and cinema and finished with satellites, genetic engineering, computers, and the Internet saw life globalization with the emergence of the global market and communications revolution with its rapid information methods

A. S. Y. Mohamed (✉)

Effat University, PO Box 34689, Jeddah 21478, Saudi Arabia

e-mail: asmohameddawod@effatuniversity.edu.sa; drabeersamy@hotmail.com

Tanta University, Tanta 31111, Egypt

[1]. Communication electronics have developed rapidly, so the Internet has become like the air we breathe between day and night. By increasing the capacity of information network waves, network bandwidth provides communication and immediate, practical, two-way visual way capabilities [2]. The capabilities of hyperlinking on the Internet suddenly made it palatable and accessible to many users. This is reflected in a huge amount of information that changed all lifestyle features and intellectual patterns.

The term “innovation” has gained prominence as the information society has evolved. The information society is based on innovation, which contributes to global prosperity. The desire for innovation has arisen as the guiding concept of the period, working as a catalyst for personal progress, business success, state prosperity, and a comeback of the country [3]. The goal of building design is to create a variety of amenities, settings, and other end products for the building group, individual buildings, and the region as a whole [2]. Innovative architectural thinking is critical in architecture because it allows for rapidly resolving exceedingly complex problems. If an architect is creative, he will be at risk in a competitive environment, especially in the age of globalization and information technology.

The paper attempts to theorize the implications of an invented Visioning of a New Methodology for Creative Architecture in the Third Millennium of knowledge Society in a new mental analysis to achieve Innovative architectural thoughts.

1.1 Research Aim

Architectural design innovation does not necessarily entail creating something novel; every architect strives to give their creations a unique personality and set of qualities that make them appealing to the eye. However, this does not imply that a novel idea is out of the ordinary. This is to be aligned with society’s needs and cultural criteria to be respected and involved in design creativity. When developing architecture, innovation should be expressed in the fusion of community and modern architectural elements, architectural design, urban development, and the enhancement of the design work’s culture, function, and layout. All these Features target the achievement of The Quality of Life for the community they design for by improving city patterns within saving local identity.

1.2 Research Objectives

- Innovative thought emerges and analyzes the principles for transforming and reconfiguring the architecture of the new architectural technology.
- The coming decades will witness amazing new inventions no one ever thought about to facilitate lifestyle and enhance the Quality of Life.

- This research is aimed to theorize invented New Methodology Visioning for Creative Architecture in the Third Millennium of knowledge Society. This will be through a new mental analysis to achieve Innovative architectural thoughts in the era of unlimited technologies that align with their society and target The Quality of Life and local identity.

1.3 Research Methodology

According to the research objectives, the research methodology is formulated as follows:

- A theoretical study about architectural design, theories of architectural design within the Pragmatist Philosophy Vision.
- An analytical study to identify Innovative Architectural Thought and New Visioning to achieve the targeted methodology.

2 Architectural Design

Design is a sophisticated way to enhance architectural work, while creativity allows one's feelings and imagination to run wild while attempting to solve a design issue. Visualizing the architectural form is a way to interact with and simulate the surroundings during the design process [3]. It is an elicitation process influenced by various variables, including the environment, geography, space, construction, technology, the kind of structure, and the standard of the needed solution.

We have realized that scientific reasoning is no longer sufficient to address issues of expanding complexity globally. The only way to find the solution is through a transdisciplinary, global, integrated approach that involves all parties and is built on lateral, creative, and critical thinking. This requires an integrative design with definite, all-encompassing, consistent guiding principles.

2.1 Theory of Architectural Design Creativity via Pragmatist Philosophy Vision

Architectural Design must be seen as a knowledge and scientific enterprise, different from what we normally see as knowledge. The pragmatist has been chosen as an appropriate philosophical foundation for design theoretical reasoning. It can integrate scientific, reflective, and interpretative methods in the social sciences and humanities. John Dewey's philosophy of art is written primarily as theories for promoting better human action and life. Applying his ideas to the design approach produces a new perspective on design research.

Architectural design is both commercial and artistic. Aesthetic experience remains an important factor in design production. In John Dewey's design theory, aesthetic experience can touch on real problems and real situations rather than being reduced to conceptualization and reasoning at an abstract level [4]. Design theory is responsible for critiquing the ethical statements and assumptions or hidden or implicit ethical agendas often used as the basis of design thinking.

Using a full life cycle approach, Architectural Design can provide services to meet any facility's or client's needs. The architectural design aims to organize information as science, art, and business and transform it into knowledge. Design thinking involves making trade-offs between ideals and reality, taking full account of often conflicting goals.

2.2 The Epitome of New Era Architectural Design Innovative Thought

Innovation in architectural design does not necessarily imply the creation of something brand-new. Each architect strives to give their creations a unique personality and set of qualities that make them appeal to the eye. However, this does not imply that a novel concept is necessarily innovative. Combining traditional and modern architectural art, architectural design, and urban development, including regional local culture when creating architecture [5], and improving the culture, function, and layout of design work are all examples of how innovation could be expressed.

However, innovation lacks architecture, a profession, and a management system while having millions of corporate devotees. The term "innovation" today refers to a fragmented pastiche of approaches, references, procedures, contexts, instruments, and techniques. It floats in the airy space of inventive heroes and creative geniuses, occasionally touching down with useful advice and a range of consultants, academics, and alchemists who claim to have the secret recipe to turn corporate lead into shareholder gold. It lacks a coherent "architecture" and a profession, and it belongs simultaneously to everyone yet to no one.

Architecture Innovation Dilemma. Architecture profited from two aspects of innovation as the corporate invention age got underway: innovative tools and methods (such as brainstorming, psycho-cybernetics, and Synectic, Systematic Inventive Thinking Methodology, etc., with the turn of the millennium, a new way of thinking emerged: invention was now considered as only one type of innovation. A systematic innovation architecture is required to enable decision-makers to approach innovation challenges like financial, technical, or construction issues. Therefore: Architecture Innovation is the systematic discipline that integrates, configures, transforms, and aligns diverse elements resulting in the creation, design, or building of the era features.

Changing Motivations. Collaboration and critical thinking are the cornerstones of architectural design as a force for change. The diversity of people's views, beliefs, and values is encouraged by designers. Design-related activities can improve our capacity for free thought and heighten our understanding of cultural diversity. Integrative thinking develops from holistic, natural, and synergistic practice paradigms. The design has numerous facets and layers and expresses various messages.

Innovation is being driven by creativity to provide value. The design focuses on creating objects to achieve objectives and how things should be. Our activities require interaction between the arts and sciences since architectural design expertise is the most valuable "commodity" of our day. Empathy-driven and problem-solving-focused, design is a per se inventive, heuristic, and exploratory process. It deals with issues with ambiguous borders and stakeholders and seeks solutions across disciplines. The design focuses on scientific and artistic techniques but combines them into a singular strategy fueled by lateral thinking to enhance The Quality of Life.

Innovation Irrational Conflict. Opposition Resistance is a response to people's attachment to the traditional and well-known, which is overcome by new interventions in the current architectural environment, whether good or bad. A negative response from society is common to almost every new concept, direction, or plan, even one good on paper. People instinctively (or intentionally) start by looking for flaws, underestimate the importance of a concept, and search for (and are certain to discover) anything negative [6]. The research will examine how people react to new architecture and design in urban settings and why people respond positively or more optimistically to new works in certain nations. In contrast, in others, they are completely rejected or even incite hostile behavior. A modern creation that deliberately blends ancient architectural styles into what appears to be a historical edifice, although a phony one, is viewed more subtly and calmly. Professionals frequently criticize this design as "poor taste," while spectators generally approve it.

Pathway

- It is founded on a set of ideas, procedures, and methods that are universally applicable to all circumstances; some of these ideas are timeless, while others are timeless [7].
- Requires ongoing practice, learning, and application; has strict criteria attest to the practitioner's worth as an expert in their field.
- Great architecture has a strong bond with a fundamental "Natural" Truth. Natural truth is connected to what happens in naturally occurring biological forms or imitates the conditions that endure under the continual rigors of nature. Since the brain's neural networks are not linear, neither are fully linear processes; the brain can use linear logic and non-linear creativity.
- The innovative architect acts with freedom of idea in the foreground and route within the background because of the non-linear nature of innovation. Thus, for the accomplished inventor, pathways become a liberating force rather than a constraint.

Methodical

- Architecture must be systematic and embrace the harmony and coherence of all its components to be effective [8]. Innovation that does not adopt this all-encompassing perspective will inevitably forget some of its most important objectives and tactics. If there is not enough discord, the design could not be adequately resilient for the system. However, too much will cause the system to collapse.

Individual and Societal Perception Psychology Analysis. It is easier for people to perceive the novel, adopt new forms, and use new technology the more evolved society and the person are. This is caused by a greater amplitude scale when input is filtered, which discovers a subliminal inventory of recognized images. Psychological habituation and form cognition result from new forms, constructs, and styles becoming the norm. In challenging crisis conditions, societies in various nations exhibit a sluggish response to the novel, contemporary, and unusual. Society, technology, and the media can psychologically prepare an individual to have a favorable or unfavorable opinion of a novel object. To combat these technologies, one must possess a high level of knowledge, a global perspective, and information synthesis.

3 Architectural Design Creativity

3.1 Architectural Design

A set of principles, procedures, and practices that enable the architect's innovation teams to produce and repeat sustainably are necessary to turn dreams into realities, visions into value, and possibility into action.

Architectural design is the fusion of art and mechanical science, of the tangible and the fleeting. Here, the world of the twenty-first century is brimming with an abundance of instruments and trade secrets. To continually deliver excellent outcomes, the inventive architect must be able to assist innovation teams in determining which procedures, methods, equipment, and strategies to employ.

3.2 Architectural Creativity

The twenty-first century differs from previous ages in speed and hybridization. Innovation has been happening much faster lately. Organizational, functional, and disciplinary borders are all where many innovations break through [9]. This hybridization fosters a new kind of creativity that puts the innovation team rather than the person at the center. A crucial concern for the innovation architect is the dynamic ability of differentials in thinking to produce new paradigms. Harnessing this co-creative energy and ensuring differentials converge to avoid paradigm and pathway reliance.

As a result, synthesis, and the mental process of genesis (creation) must be closely related (union). This will be a significant change for most colleges that have traditionally emphasized analytical excellence (compartmentalization) and for businesses that have historically benefited from recruiting managers with strong left-brain functions.

There is no shortage of creative thoughts and energy. Still, it is equally important to establish innovation coalitions that allow analytical and linear thinkers to collaborate in non-linear, relational breakthrough teams. Building innovation teams requires fusing the appropriate skill sets with the proper mindsets.

4 Innovative Architectural Thought New Visioning

4.1 Architectural Innovative Pillars

Synthesis, Functionality, Metamorphosis, and Synchronization. Four architectural pillars should be implemented innovatively to achieve responsive architecture generated from society and aligned with the features of millennium technology and techniques. These pillars are (Synthesis, Functionality, Metamorphosis, and Synchronization). It takes a distinct combination of viewpoints, specialties, linkages, and interdependencies to master architecture. The architect, who integrates art and engineering, is the overarching master of all trades and subspecialties, as the ancient Greeks recognized.

Synthesis. Architecture is the fusion of art and science, human behavior, technology, the ephemeral and the concrete, the sublime; the facts, the creative and the analytic; and the heart and the mind. Two basic cognitive abilities, analysis, synthesis, and genesis, must be present for something to be integrated, configured, or transformed [10]. The technical, organizational/social, and business systems, as well as the languages, outlooks, and skill sets required to foster a synergy between these systems, must all be reasonably well understood by the innovation architect. Organizational integration is only one more integration that is crucial.

Functionality. The innovation architect must possess the configuration skill to connect the parts of a challenging jigsaw in the proper sequence, order, and priority for the invention to materialize. It combines the functions of the left and right brains, the analytical and relational, the scientific and the creative, the discipline and the freedom, and it frequently combines linear and non-linear systems. Architecture must highlight how a design is configured for use, production, utility, and service; if the configuration lacks beauty, its inherent ugliness may send it to the dungeon.

Metamorphosis. It is the metaphysical component of the innovation architect's role and is its physical outcome. The process of altering physical objects into something new, more useful, or better suited for their surroundings is called Metamorphosis [11]. Knowledge is not as vital as creativity, and transcendence involves both the head and the heart. One must first embrace the enthusiasm of a Champion of Innovation before

trying to be an Architect of Innovation. People must accept others in the invention process because imagination is the first creative step.

The typical lonesome hero suffers from the radical ego degeneration that Innovation Champion has personally experienced. The transformational rise of the innovation champion as a spiritual warrior who bravely challenges the status quo coincides with the degeneration of the ego. Undoubtedly, eccentrics frequently present as innovators. The energy force of the innovation champion enables everyone in their sphere to realize the untapped potential and co-creative possibilities. In this way, creative culture offers people a richer sense of purpose in their lives and a secure setting to engage both individually and as a group in exploration, imagination, and innovation. Thinking and cultural realignment. It takes great strength of heart and mind.

Synchronization. Effective systems, strategy, and structure synchronization are necessary for innovation. The first alignment is the alignment of purpose, which entails that each system, and its subsystems are directed toward a single aim. At the strategic level, it is critical to focus on certain competitive advantages that result from a particular invention. The function of the innovation architect includes forming internal and external alliances to align the strategic, cultural, and operational components of innovation for it to materialize and have a real-world impact. The innovation process will stall if one organizational division, department, or coalition is out of alignment since this will send conflicting messages to the populace about the importance of innovation.

4.2 Architectural Design Innovation Thought Stages—Proposed Roadmap

Preparedness Stage. This stage targets research of the innovation object. Primary innovative thinking has been highlighted as a crucial problem that has to be solved, information gathered, and an attempt to systematize and generalize it. Begin looking for new approaches and solutions simultaneously, but these approaches are frequently unworkable, which causes the problem-solving process to stall. The construction plan is the primary component of this process. The architect eventually assumes the designer's function, concentrating on taking in and comprehending the project's purpose statement. Research into design goals is important to understand the different connected objective situations, and preparation is necessary to load and process external data. The data should include urban planning requirements, environmental factors, user needs, community conditions, engineering economy estimates, specific requirements, cultural context, historical and cultural aspects of the proposed building, etc., to create useful design outcomes. Innovative thinking will be sparked as we discover the tiny valuable information during the initial design, and thoughts will flow.

Innovative Ideas Generative Stage/Conceptual Invention. A significant amount of excellent architectural design is done during the Innovative Ideas Generative Stage/Conceptual invention, further divided into blueprints and clear stages. Choosing information and posing design concerns are the main goals of the first part of the architectural design idea, which corresponds to the blueprint stage. The architects should now be using more logical reasoning. Procedures, logical conclusions, summative statements, and recording are frequently crucial components. Due to the rationale of the time, the information was chosen with partial knowledge, which supports the designer's rational decision. Generating architectural design concepts is produced via a sudden feeling of innovation when a unique revelation startles the architect. This period typically yields stronger architectural accomplishments, is clearly marked by strong emotions, and can fluctuate more dramatically; this rapid, dramatic mood change may inspire the architect.

Pinnacle Reaching Stage/Creativity Completion. The goal of this stage is to determine whether the program is sound. After establishing the fundamental concept, the building program considers the numerous issues related to environmental elements, cultural factors, and other variables like those previously mentioned. Since the following project is directly related to this stage and involves making final design tweaks that make architectural design tend to be more aesthetically pleasing, we should pay special attention to the thorough study of specific technical concerns. Since each profession should be closely combined at this point, even unresolved problems will be detrimental to the overall design idea.

5 Innovative Architectural Thought Optimal Practicing Initiative

All creative architecture adheres to fundamental principles, procedures, and practices that form the basis of the fieldwork, with alignment and inspiration from society's real needs, culture, and natural environment integration and real implementation. This will never be isolated from the millennium's new technologies, techniques, and innovation, which should be the architect's third hand to achieve innovative creativity that will help formalize a high standard of The Quality of Life. Configuring place figure print and saving city identity with innovative architecture that applies up-to-date technology for human benefit is a powerful architect's most important focal point. Innovative Architectural Thought Optimal Practicing Initiative is an efficient criterion as a self-evaluation manual of Innovation Architecture to guarantee the effectiveness and longevity of the results: (see Fig. 1).

The most crucial decision in this text is that the concept should be feasible, understandable, verifiable, quantifiable, controllable, diagnosable, perceivable, reusable, trainable, beneficial, repeatable, and consistent. It is also actionable, understandable, measurable, controllable, diagnosable, and transcribable. These specifics aid in

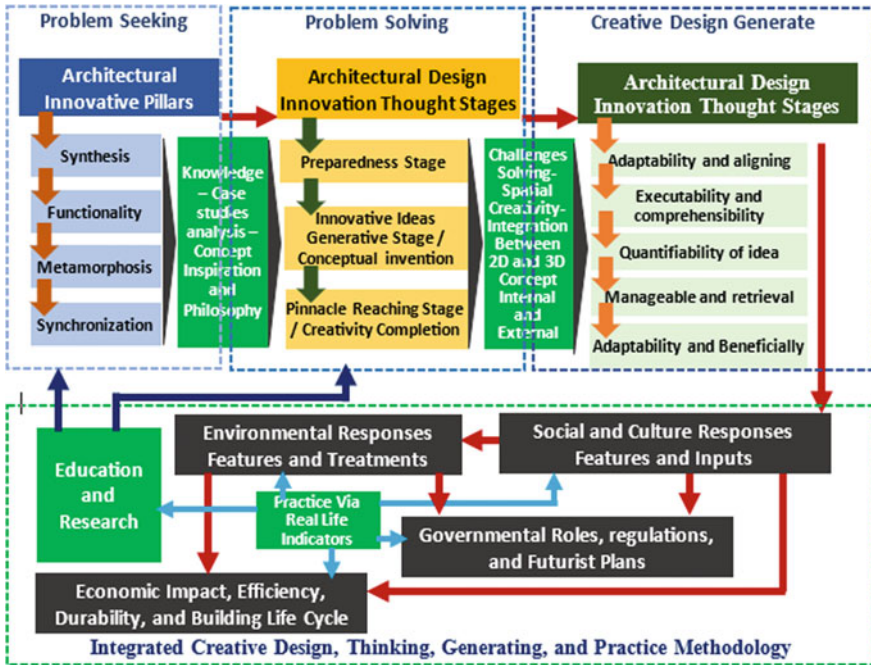


Fig. 1 New methodology for creative architecture in the third millennium of knowledge society— an integrated framework aligned with the quality of life for livable city

establishing whether the idea will remain true in practice and whether it is necessary or just an extraneous nicety:

- Adaptability and alignment of all circumstances and social cultures.
- Executability and comprehensibility of ideas via design criteria.
- Quantifiability of idea to be applied according to design regulation.
- Manageable and retrieval: of applications principle effectively.
- Adaptability and beneficially of the design idea and the necessity of the project.

6 Conclusion

The main objective of architecture is to design and then construct something that will remain, not because of its size or grandeur but because it combines beauty and function, vision and truth, and underlying meaning and worth in an elegantly simple way.

- In each era, there will be new emerging technologies that will help in adding something new to the architecture field. Here the innovation of the architect should be seen in dealing with these technologies and re-orient them in a positive combination. Architects will never be able to ignore the development which became an updated lifestyle but should pick the proper and reuse them in the thought's inventions.
- Creativity can be achieved in all design stages within a solid foundation of knowledge and research. This could be reflected in the spaces and math in a complete scenario of the design process with one target, making the human always needs a focal point of design thinking and technology features.
- Culture, environment, economy, and, most importantly, governmental roles will always remain vital in architecture's creative thought formation and never prevent innovation. Still, the opposite enhances and improves innovative architectural outcomes.

References

1. A Saggio 2003 Chapter 6: Other challenges, in architecture in the digital age, design and manufacturing Spon Press, Taylor & Francis New York, London 231 337
2. Danfulani BI, Khairul AMK (2015) Concept of creativity and innovation in architectural design process. *Int J Innov Manage Technol* 6(1)
3. M Carpo 2017 The second digital turn: design beyond intelligence The MIT Press Cambridge, MA
4. S Zuboff 2019 Surveillance capitalism and the challenge of collective action *New Labor Forum* 28 1 10 29 <https://doi.org/10.1177/1095796018819461>
5. K Xing 2009 Impact of progressive 111 sustainable value assessment on building design *J Harbin Inst Technol* 10 1563 1566
6. Kolarevic B, Jose PD (2019) From massive to mass customization and design democratization. In: *Mass customization and design democratization*. New York: Routledge, pp 2–12
7. GT Zou 2006 The relationship between integrated design and safety on construction projects *J Harbin Inst Technol* 07 1120 1123
8. O Ataman 2005 Integrating digital and building technologies: towards a new architectural composite *Int J Archit Comput* 3 2 181 189 <https://doi.org/10.1260/1478077054214442>
9. F Liu 2010 Analysis of architectural design innovation thinking *Chin Overseas Archit* 04 66 67
10. Asadullah M, Raza A (2016) An overview of home automation systems. In: *2nd International conference on robotics and artificial intelligence*, pp 27–31
11. K Xing 2008 Bilayer structure of architectural design innovation thinking methods *Huazhong Archit* 12 42 46

Lumiducts Implementation and Their Relation to Luminous Comfort in High Andean Homes in the District of Huamancaca-Peru in 2021



L. Katherine Brañez , P. Paola Segura , and T. Vladimir Montoya 

Abstract The insufficient research on lighting comfort in high Andean housing is irrelevant compared to thermal comfort. Therefore, the following study presents an eco-technique called lumiduct that allows increasing lighting in the required spaces; the design and construction process considers factors that must contribute to developing a low-cost and environmentally friendly model. The study research is on observing the influence of a lighting duct implemented in a House kitchen built with adobe in the southeastern district of Huamancaca, province of Chupaca, Junín region, Peru. The encountered problem shows that 75% of the district's population uses the kitchen constantly, even when 48% say it is the darkest and most inefficient space. This study is an Applied Research. It has been based on testing theories and performed on correlative levels, which aims to measure the relationship between two variables (lighting pipelines and high Andean housing). On the other hand, the results obtained allowed us to understand the lack of lighting comfort through the implementation of a lighting duct; evaluated through measurements with properly calibrated lux meters, showing a significant increase in internal illuminance, comparing the results obtained through the Dialux software.

Keywords Traditional housing · Adobe · Light pipe · Luminous comfort · Illuminance · High Andean housing · Ecotechnics

L. Katherine Brañez (✉) · P. Paola Segura · T. Vladimir Montoya
Continental University, Huancayo 12002, Perú
e-mail: 73045544@continental.edu.pe

P. Paola Segura
e-mail: 73175379@continental.edu.pe

T. Vladimir Montoya
e-mail: vmontoya@continental.edu.pe

1 Introduction

Adobe is one of the ancestral constructions legacies of Peruvian culture, and its principal material is based on mud (adobe). For example, the Chan Chan citadel in Trujillo city had houses, water reservoirs, irrigation canals, and public use areas built with adobe or Tapia [1], both mud-made materials. This construction system has been a widespread tradition in the coastal, highland, and jungle regions. Focusing on the department of Junín, 34% of houses are made of adobe, quincha, and tapia. Within the Mantaro Valley, A group of districts provides “collective, historical, and natural memory” [2]. However, since its origins, natural illumination has had difficulties. The principal fact is that the adobe construction system is limited to the non-window opening technique to provide a seismic-resistant structure and to maintain thermal comfort.

Zenithal lighting is an alternative solution for dark spaces lacking lateral lighting, such as conventional windows. The various dark environments are not favorable for everyday use, and artificial lighting is required during the day, being negative in the following aspects: economic, health (physiological and psychological), lighting, and environmental comfort.

The first refers to savings in 2 factors. In construction (due to modifications in the house such as roofs and enlargement of windows), and electricity bills (due to the increase of halogen bulbs). Regarding health, artificial light generates the “sick building syndrome” (SBS) due to the lack of natural light, which has repercussions on human health and gives rise to physiological and psychological problems. The first problem is related to the circadian rhythm that is synchronized by environmental factors such as light, showing that the functioning of the organism has schedules to present pulsations, and these secretes hormones and enzymes. This process has its origins in the photoreceptors in the eye, and if these are affected or there is a change, pathologies can occur in the life of the human being [3]. The psychological problems it can cause are also: sleep, eating and emotional disorders, as for the first one, light can affect the hours of sleep that a person should have; although eating disorders are not a direct consequence of the limited lighting, the proper use of light can contribute to the improvement of people with cases of bulimia or anorexia. Nevertheless, a poor perception of light and reception can be a primary cause of emotional difficulties such as anxiety or depression, which as in eating disorders, are treatable through phototherapy by adequate exposure [4].

Lighting comfort and health have a direct relationship because they are perceived by the human senses to indicate if there is discomfort through internal sensory responses. However, the poor analysis of the previous light study as the quantity and quality of light can generate, in the first case, an environment that creates fatigue when performing a task; and the second case the “effort made by the eye to prolonged and constant exposure to artificial light causes deformations and optical disorders” [5].

Finally, regarding the environmental impact, 86% of the primary energy used causes pollution effects, and it derives from the use of fossil fuels causing inconveniences in the process of extraction, transportation, and consumption; likewise, the increase of the greenhouse effect is the principal cause of climate change leading to changes in time, space, temperature, winds, humidity, and rainfall. Besides, not only the production of energy causes polluting effects, but the development of lighting systems generates harmful components such as mercury, a heavy and toxic metal [6].

For this reason, one of the eco-technologies used is the lumiducts. These have a simple structure that, through its elements, captures, transports, and propagates diffuse sunlight, which is emitted in different directions maintaining the intensity [7] towards the interior of the environment. This lighting alternative can be used in various infrastructures that cannot be illuminated by lateral or zenithal windows. However, commercial lumiducts are too expensive and not accessible to the entire population.

The present research is based on a lighting duct built with easily accessible materials for adobe houses, to make it more energy-efficient and avoid artificial lighting during the day. This will be evaluated with the help of a lux meter that will measure the amount of lux emitted in a traditional kitchen before and after the implementation of the lighting duct. Finally, the research is to make known this type of low-cost lighting, which guarantees an improvement in the visual quality of environments lacking natural lighting.

2 Materials and Methods

According to Hernández Sampieri the research applies the quantitative approach, correlational type, and with the quasi-experimental design that is tested in the study with a convenience sample. This sample has been selected because the results of an experimental study and a controlled study were contrasted in order to compare the results obtained in each study object [8].

2.1 *Population and Sample*

The population “is the set of all cases that match a series of specifications” [8]. According to the analysis, 1669 adobe and brick houses were found. Being these 668 (40.02%) from the district of Huamancaca.

The sample “is, in essence, a subset of elements that belong to that set defined in its characteristics that we call population” [8]. For this reason, the non-probability sample was taken into account, which was chosen by convenience, considering 60 houses selected by the characteristics of the state of conservation and housing typology.

“The unit of analysis is also known as cases or elements, what or who are the participants, objects or events or collectivities of study, this depends on the scope approach of the research” [8]. From the sample mentioned before, a dwelling was selected meeting the characteristics of an-adobe high Andean dwelling that had lighting difficulties in environments of common use.

2.2 Instruments

See Table 1.

3 Context

Within the department of Junín, according to the National Institute of Statistics and Informatics [10], the provinces with the highest percentage of adobe houses are Huancayo, Chupaca, Jauja, and Tarma (Fig. 1). The last three have 2% of houses with the construction material, were chosen in the province of Chupaca as the place

Table 1 Types of instruments

Observation sheets	“During the initial immersion observation, we may or may not use a format. Sometimes, it can be as simple as a sheet of paper divided in two: on one side, the descriptive annotations of the observation are recorded and on the other interpretative one” [8]. Sixty observation sheets were made to collect descriptive data on the condition of the houses in the district of Huamancaca, in order to analyze the typology of existing houses in the district and the number of windows on their facades. Additionally, another observation sheet format was used to obtain the results of the measurements at different points in the kitchen where the lumiduct was implemented
Survey	“It consists of a set of questions related to one or more variables to be measured. It must be congruent with the statement of the problem and hypothesis” the questions to be formulated can be of type: closed or open as appropriate [8]. For the development of the investigation, 52 inhabitants of the district of Huamancaca were questioned in order to analyze the current situation of their house rooms to find the lighting deficiencies
Dialux	“It is a free software designed for lighting projects. It allows documenting the results obtained through photorealistic visualizations [9]”. Through this software, it is possible to perform the lighting analysis of the selected room in a state before the implementation and after implementation. It will be represented through waves that describe the expansion of light without and with the lumiduct
Model	Two prototype models of the house with the lumiduct were made as a verification method with the help of a lux meter calibrated on the illumination received by the environment. One prototype is in the natural state of the kitchen, and another is in an improved state with the lumiduct

of analysis, and within this the district of Huamancaca Chico where there is 40.02% of adobe houses.

This district is located in western Huancayo, on the right bank of the Mantaro River, where vulnerable adobe homes and people living modestly were identified (Fig. 2). 80% are engaged in economic activities such as agriculture, livestock, and construction workers; acquiring a monthly income of 100 to 1000 soles (\$25–250), which prevents them from paying electricity bills. The houses registered in this environment did not have adequate natural lighting in their interior spaces due to the absence of windows, which causes the use of artificial lighting, generating electricity bills of between 20 to 30 soles (5\$–6.5\$). For this reason, implementing lighting ducts inside these houses to generate lighting efficiency and energy savings is proposed.

According to the survey mentioned before, 69% of the population is not satisfied with the natural lighting that enters their homes, which is a common problem in adobe dwellings. The data obtained are presented (See Figs. 3, 4, 5, 6, 7, 8, and 9 in Table 2).



Fig. 1 Location map

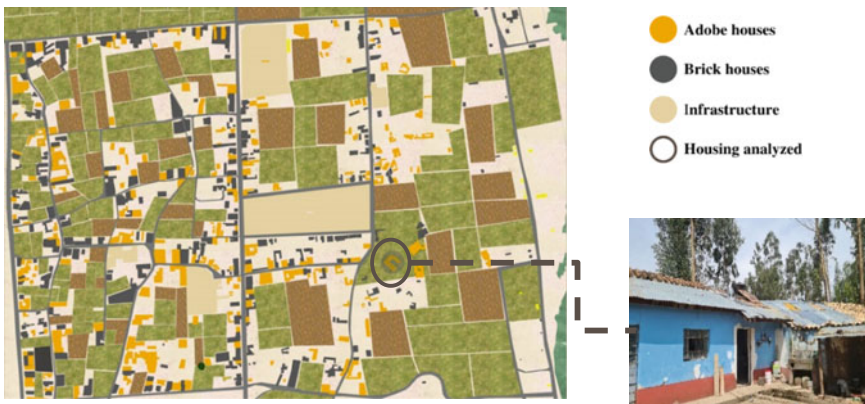


Fig. 2 Material plan of Huamancaca

Fig. 3 Satisfaction with lighting

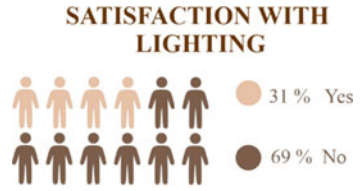


Fig. 4 Economic activity

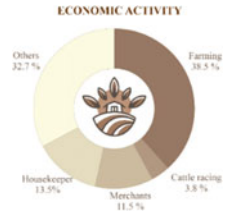


Fig. 5 Salary



Fig. 6 Remodeling

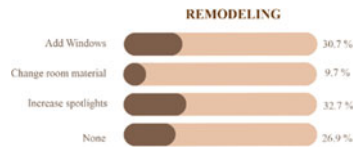


Fig. 7 Roof type

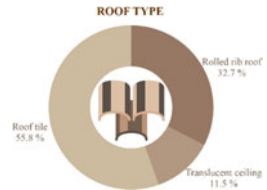
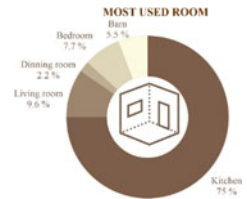


Fig. 8 Most used room



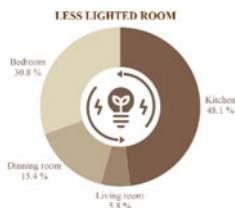


Fig. 9 Less lighted room

Table 2 Statistical data

See Fig. 3	See Fig. 4	
69% of the population indicates that the amount and size of light coming through their windows is insufficient	13.5% of the population are housewives who frequently use the kitchen	
See Fig. 5	See Fig. 6	
According to the economic activities of the population, 66% receive a monthly salary between S./100-S/0.1000 (\$25-\$25), which is less than the minimum wage in Peru	73.08% of the population remodeled their homes to increase lighting, which generates an increase in budget expenditures	
See Fig. 7	See Fig. 8	See Fig. 9
The shingle roof is a predominant material by 55.8%	The kitchen has a 75% of use in homes, because it is the space of family union	48.1% of the population said that the kitchen is the darkest environment, despite being the most used

4 Proposal

4.1 Housing

According to the previous analysis of the measurements on the mock-ups and the DIALUX software, it was considered appropriate to remodel the environment with respect to the color of the walls and ceiling (Table 3). This choice was crucial because, depending on the color, the lighting can be absorbed or reflected. Prior to the selection of the materials, the reflection value was considered to prevent them from absorbing (such as the black color) or increasing the ambient light causing glare (such as the glossy finish paint). Two steps were taken before the implementation. The first one was to change the color of the walls to white due to its absorbent property. “Since if the body is white, it reflects all the white light, but if the surface is black, it absorbs all the white light without reflection” [11]. The second point considered was the

Table 3 State of the intervened dwelling

See Fig. 10

See Fig. 11

Fig. 10 Housing in initial condition



Fig. 11 Improved and implemented housing



ceiling. We decided to implement a false ceiling because the high Andean houses have sloping ceilings causing the lighting to be uneven (Figs. 10 and 11).

4.2 Lumiduct

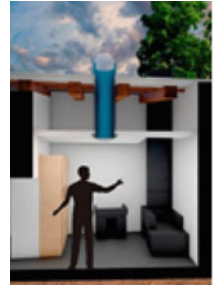
For the construction of the lumiduct, 3 parts were taken into consideration: the collector, conductor, and diffuser. Internally, each of these has parts for its installation. For the collector, a dome with UV protection was used, with a diameter of 35 cm. This part was assembled to a stainless-steel connection ring of 35.2 cm in diameter and 15 cm in height using rivets and screws.

As for the conductor, a stainless-steel tube of 35 cm in diameter was considered, which was spliced to the connection ring mentioned above; this tube maintains a height of 120 cm. This measure is since the lighting duct must protrude to the Rolled rib roof of the house, as well as the internal height of the ceiling to the false ceiling installed must also be considered. Finally, for the diffuser, three tests of possible elements that could be used were carried out. The first one was a metallic ring where different types of glass could be interchanged. The first one was sandblasted glass observed that it does not have great diffusion capacity, then cathedral glass was used, but the material only allowed projecting the light in a vertical direction, and finally, a matte plastic diffuser was tested, perceiving an improvement compared to the first 2 tests, lighting every corner of the environment, being implemented with screws to a ring using metallic hooks (Figs. 12 and 13). After having the environment restored

Fig. 12 Section B



Fig. 13 Section A



and the lumiduct system installed, we proceeded with the implementation in the room, following the procedure (Fig. 14).

5 Results

5.1 Analysis in the Dialux Software

The previous analysis using Dialux (Table 4) allows two important aspects: to corroborate or disprove the data of the scale models and to know if one or two lumiducts should be used to achieve the objective of 150 lx to 300 lx.

5.2 Model with Lumiduct

According to Andrea Pattini, if the scale models are well constructed, the lighting levels obtained will be equal to those of the actual scale built [12]. For this reason, a comparison of the measurements in the scale model with the measurements of the actual kitchen in the house was made, with the result that the measured values are quasi-similar. Likewise, the measurement points were considered at a height of

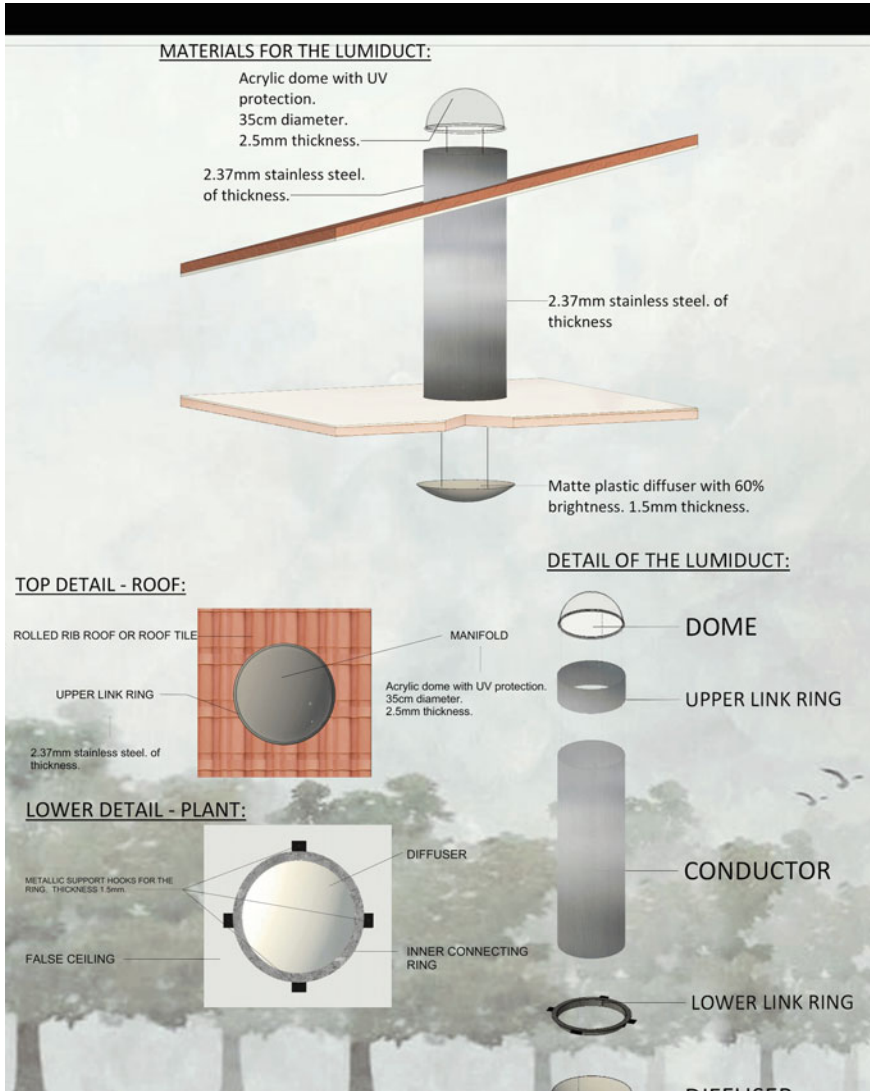


Fig. 14 Materials lumiduc

0.80 cm in the work plane, being this value a standard and an average as mentioned by Julian Restrepo [12]. However, the various authors only choose their measurement points for convenience (Table 5). For example, Julian Restrepo projects measurements that are taken in the four corners of the space and at the crossing of the diagonals to finally get a final average but do not consider the work area. For this reason, the five measurement points that were chosen are supported with the formula of the ratio of the area index and the number of measurement zones. This allowed

Table 4 Compare of results of the lighting behavior of the kitchen by means of the software Dialux

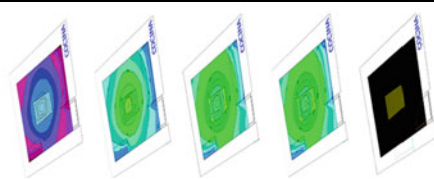
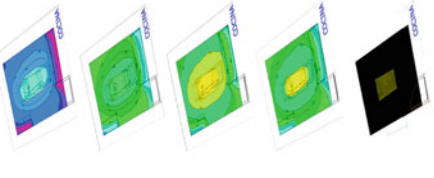
LUMINIC BEHAVIOR	
 <p><i>HOUR: 6:00 am. E (nominal): 2.02 lx. E minimal: 0.31 lx. E maximum: 10.3 lx</i></p> <p><i>HOUR: 9:00 am. E (nominal): 16.8 lx. E minimal: 2.55 lx. E maximum: 85.3 lx</i></p> <p><i>Highest hour of natural lighting</i> <i>Hour: 12:00 pm. E (nominal): 18.6 lx. E minimal: 2.83 lx. E maximum: 94.5 lx</i></p> <p><i>Hour: 15:00 pm. E (nominal): 12.71 lx. E minimal: 1.92 lx. E maximum: 64.2 lx</i></p> <p><i>Hour: 18:00 pm. E (nominal): 0.0 lx. E minimal: 0.0 lx. E maximum: 0.0 lx</i></p>	 <p><i>Hour: 6:00 am. E (nominal): 19.0 lx. E minimal: 2.31 lx. E maximum: 34.8 lx</i></p> <p><i>Hour: 9:00 am. E (nominal): 234 lx. E minimal: 28.9 lx. E maximum: 430 lx</i></p> <p><i>Highest how of natural lighting</i> <i>Hour: 12:00 pm. E (nominal): 439 lx. E minimal: 62.5lx. E maximum: 808 lx</i></p> <p><i>Hour: 15:00 pm. E (nominal): 298 lx. E minimal: 42.5 lx. E maximum: 549 lx</i></p> <p><i>Hour: 18:00 pm. E (nominal): 0.0 lx. E minimal: 0.0 lx. E maximum: 0.0 lx</i></p>
<p>Preliminary conclusions</p> <ul style="list-style-type: none"> • The highest average illuminance (nominal E) with One humidict at a fixed time is 162 lx at 12:00 pm; the maximum illuminance (E max) is 386 lx at the same time; and the minimum illuminance (E min) was 0.00 lx at 18:00 pm. The data from 9:00 am to 15:00 pm exceeded the target of 150 lx • The illumination acquired at 15:00 pm is higher than at 9:00 am. In view of the previous analysis of the current state, it was possible to identify the problem of the accelerated loss of luxes during the afternoon (table N°96); therefore, it was decided to make a minimum 5% inclination of the collector toward the Southwest, in order to control the accelerated loss of illuminance during the afternoon 	<p>Preliminary conclusions</p> <ul style="list-style-type: none"> • The highest average illuminance (nominal E) with One humidict at a fixed time is 162 lx at 12:00 pm; the maximum illuminance (E max) is 386 lx at the same time; and the minimum illuminance (E min) was 0.00 x at 18:00 pm. The data from 9:00 am to 15:00 pm as exceeded the target of 150 lx • The illumination acquired at 15:00 pm is higher than at 9:00 am. In view of the previous analysis of the current state, it was possible to identify the problem of the accelerated loss of luxes during the afternoon (table N°96); therefore, it was decided to make a minimum 5% inclination of the collector toward the Southwest, in order to control the accelerated loss of illuminance during the afternoon



Table 5 Relationship between the area index and the number of measurement zones

Area index	Number of zones to evaluate	Number of zones to be considered by the limitation
$IC < 1$	4	6
$1 \leq IC < 2$	9	12
$2 \leq IC < 3$	16	20
$3 \leq IC$	25	30

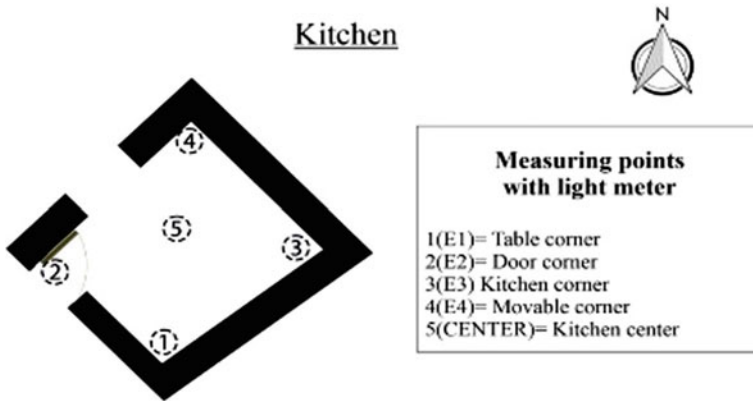


Fig. 15 Measuring points in the kitchen

us to know which points or corners are the lowest in illuminance and thus determine which will be the location of our lumiduct (Fig. 15).

5.3 Housing with Lumiduct

For the measurements with the luminous pipeline, the same 5 points mentioned above were considered (graph N°28). In addition, measurements were taken every hour from sunrise to sunset for 2 days (December 18 and 21, 2021) with different types of ceilings: clear ceiling and partially overcast. It might be considered that the sunset and sunset were obtained from the SunEarth Tools software. As a result, the final project is shown in Table 6.

Table 6 Illuminance measurement data in the kitchen with lumiduct, day 21–12-21

Illuminance measurement sheet with the lumiduct implemented—door open													
General Specifications													
Date: December 21, 2021		Sunset: 18:24:26		Half day: 11:59:15									
Atmospheric conditions													
SKY: clear													
Measurement zone		Dimensions						Area index (IC)				No of measurement points	
Area	Length A	Length B	Width A	Width B	Height								
Kitchen	11.6	3.5	3.59	3.5	3.02	2.4	0.73						5
Measurement equipment data													
								Maker		Innovative industrial			
								Model		Lux29			
								Team series		August 14, 2021			
								Date of calibration		0.5 s			
Measurement data with the light duct implemented													
Illuminance: Value measured in luxes		Measuring points											
Hour	Exterior (lx)	E1 (lx)	E2 (lx)	E3 (lx)	E4 (lx)	Center (lx)	Inside						
05:34	262	11	259	15	19	38	68						
07:00	676	40	734	51	58	227	222						
08:00	866	69	1182	63	76	259	330						
09:00	1185	154	1231	83	112	284	373						
10:00	1039	146	907	70	98	267	298						
11:00	1397	187	1333	135	227	304	437						
11:59	1647	259	1816	268	379	641	673						
13:00	1570	207	1549	167	304	462	537.8						
14:00	1097	151	1470	114	168	274	435.4						

(continued)

Table 6 (continued)

Measurement data with the light duct implemented										
Hour	Exterior(lx)	E1 (lx)	E2 (lx)	E3 (lx)	E4 (lx)	Center (lx)	Inside			
15:00	645	98	1006	59	93	217	294.6			
16:00	1468	196	1224	126	212	287	409			
17:00	1056	141	947	83	143	201	303			
18:24	129	14	201	10	16	24	53			
Average	341									
Illuminance measurement sheet with the lumiduct implemented—door close										
Illuminance: Value measured in luxes										
Hour	Exterior(lx)	E1 (lx)	E2 (lx)	E3 (lx)	E4 (lx)	Center (lx)	Inside			
05:34	262	5	9	4	7	15	8			
07:00	676	25	31	23	29	53	32			
08:00	866	49	65	44	63	82	61			
09:00	1185	105	129	88	114	156	118			
10:00	1039	99	118	85	109	140	154			
11:00	1397	136	170	116	134	214	110			
11:59	1647	197	206	178	167	324	214			
13:00	1570	153	178	169	160	301	192.2			
14:00	1097	103	113	89	110	226	128.2			
15:00	645	23	35	30	28	59	35			
16:00	1468	149	182	123	172	292	183.6			
17:00	1056	99	110	88	103	53	90.6			
18:24	129	3	6	3	6	10	5.6			
Average	103									

Table 7 Summary table of the implementation of the lighting duct in the kitchen

Summary table of the implementation of the lighting duct in the kitchen	
Did you meet the target luxes? Yes/no	<p>Yes</p> <p>The main objective of the implementation was to reach an average of 300 lx with the door open and 150 lx with the door closed during the hours of use (in this case the hours of use of the kitchen are from 11:00 h to 13:00 h). The values obtained with the door open were the following: 437 lx, 281 lx, and 549.27 lx; and the values obtained with the door closed were 166 lx, 115.13 lx, and 172.1 lx, increasing considerably the illuminance with the door closed</p>
Did you meet the target luxes? Yes/no	<p>No</p> <p>Since the standard establishes an optimum of 300 lx</p>
Did you comply with the luxes proposed by the standard? Yes/no	<p>Yes</p> <p>Since it is not an artificial light (1157.4 lm to 154,302 lm) and there is no standard for natural light, it was considered that the lumiduct should reach a minimum of 1000 lm. The objective was fulfilled because the light pipeline obtained an average value of 1081.4 lm</p>
Did you meet your target lumens?? Si/no	<p>Yes</p> <p>The perceived difference is minimal. For example, the room with open door has values between 353 lx (tile) and 341 lx (metal), and with closed door values of 71 lx (tile) and 103 lx (metal)</p>

6 Conclusion

It was determined that natural lighting has a positive influence on the lighting comfort of the users of the high Andean adobe houses in the district of Huamancaca - Chupaca—2021. Taking into account the results of the scale models and the DIALUX analysis, the implementation of the lighting duct in the kitchen was carried out, showing average illuminance values of 296 lx and 341 lx with the door open. According to standard EM.010 Indoor Electrical Installations—Table 7 of illuminances for indoor environments, mentions that kitchens in homes generally require 300 lx. According to the measurements taken in the kitchen of the house where the project was implemented, the space is most used from 11:00 am to 2:00 pm, with values of 66.66% of the total of the measurements taken exceeding 300 lx, showing an improvement over the initial condition of 134.97 lx, 140.93 lx and 176.03 lx. Finally, the analysis of the measurements in the environment with the 2 types of ceilings does not show great contrasts because the existing difference is 12 lx in open door condition and 32 lx with closed door concluding that the ceilings will not be difficult to adequately implement the lighting duct.

References

1. Gisela A et al (2021) CHAN CHAN Patrimonio Cultural de la Humanidad Ministerio de Cultura
2. Jorge Burga Bartra CMGMPMJSCJTS (2014) Tradición y modernidad en la arquitectura del Mantaro_2014
3. van Bommel IWJM, van den Beld IGJ (2004) La iluminación en el trabajo: Efectos visuales y biológicos
4. Hidalgo LA (2020) Arbona - Estudio de la influencia de la iluminación en la percepción de los estudiantes universit...'. Available: <https://riunet.upv.es/bitstream/handle/10251/161277/Arbona%20-%20Estudio%20de%20la%20influencia%20de%20la%20iluminación%20en%20la%20percepción%20de%20los%20estudiantes%20universit....pdf?sequence=1>. Accessed 13 Aug 2022. [Online].
5. Aguilera AO (2014) Eficiencia en iluminancia del ducto vertical de luz solar con colector plano y semiesférico. Instituto Politécnico Nacional
6. Jesús Zapata Giraldo N (2008) Impacto Ambiental de los Sistemas de Iluminación Contaminación Lumínica
7. Pattini A (2012) Sistemas de iluminación natural
8. Roberto Hernández Sampieri CFCPBL (2014) Metodología de la investigación
9. Madrid UC (2014) DIALux [Online]. Available: <https://www.ucm.es/pimcd2014-free-software/dialux#:~:text=DIALuxesunsoftwaregratuitofabricanteslíderesanivelmundial>
10. INEI (2018) RESULTADOS DEFINITIVOS TOMO XIV. RESULTADOS DEFINITIVOS CUADRO ESTADISTICO DE POBLACION, VIVIENDA Y HOGAR. https://www.inei.gob.pe/media/MenuRecursivo/publicaciones_digitales/Est/Lib1576/12TOMO_14.pdf. Accessed 06 Aug 2022
11. Pattini A Capítulo 11 Luz Natural e Iluminación de Interiores
12. Restrepo JAQ (2015) ESTUDIO SOBRE ILUMINACION NATURAL EN LUGARES CON POCO ACCESO DE LUZ

Mars Habitat Design Thru Parametric Structures Based on United Arab Emirates Heritage



Jose Berengueres, Lindita Bande, Aysha Alsheraifi, Afra Alnuaimi, Entesar Alawthali, and Alanoud Ablooshi

Abstract Mars exploration has started for decades; however, the recent missions show possibility of building a colony. Therefore, the design of a habitat for human colony is relevant. Life on Mars is challenging due to the excessive radiation. Therefore, the habitat design shall consider all elements of radiation protection, in addition to the atmosphere. The methodology followed in this study is as per the below steps: 1. Analysis of Mars conditions; understand the Mars soil, climate, and radiation. 2. Schematic Design, standards of living in space; analyze standards of habitat and evaluate schematic design options. 3. Connection to UAE Architectural Heritage. 4. Modelling and Simulations; Create and analyze the models in Rhino Grasshopper. 5. Findings and results. The aim of this study was to design a human habitat on Mars using parametric structures based on the heritage architecture of the United Arab Emirates (UAE). The study followed a set of steps including an analysis of Mars conditions, schematic design, connection to UAE architectural heritage, modeling and simulations, and findings and results. The main tools used in the study were *Rhino* and *Grasshopper*. The final design was selected based on the modeling and simulation results, with the goal of creating a habitat that is adapted to the conditions on Mars and the humans who will live in it. The findings of this study contribute to the ongoing efforts to define new spaces in other planets.

Keywords Mars habitat · Minimalism · Radiation · Rhino · Python language

1 Introduction

In the continuous improvement for a space architecture, Foster and Partners worked on a project that would inhabitate four people in a minimal space. The possibility of building such residential units could be done by using 3D printing [1].

J. Berengueres · L. Bande (✉) · A. Alsheraifi · A. Alnuaimi · E. Alawthali · A. Ablooshi
United Arab Emirates University, Al Ain, UAE
e-mail: lindita.bande@uaeu.ac.ae

© The Author(s), under exclusive license to Springer Nature Singapore Pte Ltd. 2024
M. Casini (ed.), *Proceedings of the 3rd International Civil Engineering and Architecture Conference*, Lecture Notes in Civil Engineering 389,
https://doi.org/10.1007/978-981-99-6368-3_50

617

The International Competition named “Moontopia” is another effort into understanding and improving the space architecture, namely the lunar architecture. Building the designed structure would require 3D printing. The jury of this competition included scientist from NASA in order to evaluate the durability of such design [2].

Furthermore, there are efforts in creating experimental space in the earth conditions, but with the aim of investigation mars conditions. Such project is March Science City, shown in 2017 by Mohamed Bin Rashid Space Center in collaboration with BIG. This center would use local materials from the Emirates including 3D printing technology in order to understand the behavior of this structure [3].

Robots were involved in building the design of the project “Marsha”. This design project aims to use Martian materials and recycled materials to build advanced prototypes that can withstand the mars conditions. The focus here is in having a livable space indoors, considering the harsh conditions of the planet [4].

In a recent study from NASA based on usage of the constellation system there were diverse solutions on Mars inhabitation and exploration. The strategy and example implementation concepts that are described here are not a formal plan for the human exploration of Mars, but rather provide a common framework for future planning of systems concepts, technology development, and operational testing as well as potential Mars robotic missions, research that is conducted on the International Space Station, and future potential lunar exploration missions. This summary of the Mars DRA 5.0 provides an overview of the mission approach, how to go about exploring the surface and exploration goals, as well as the key systems and challenges for the first three concepts for human missions to Mars [5].

Proposed architectures for human journeys to Mars need to take note of the two competing constraints of an executable program. These two constraints include inflation and participation of stakeholders, such as the public. In this article we describe a stepwise approach for human journeys to Mars using a minimal architecture. We refer to this architecture as minimal because it would minimize large new development efforts and rely largely on elements currently being developed or planned by NASA [6].

New research describes the analysis of heat and mass transfer phenomena in a greenhouse dome. This is developed with the aim of activating the agricultural environment in Mars. In this structure there is the possibility of converting the solar energy in plant biomass. Agricultural products will be used as food sources and the waste will enter into the recycling process of the structure [7].

Additionally another interesting study was done in the project: Moon Village. In this habitat several units connect making the space larger and more flexible. The aim of the project was to create a self-sufficient village of lunar habitat [8].

An ideal house was shown in the project Mars Case. Here the minimalistic aspect of the design is quite notable. The aim is the use the technology of re-heating and recycling the materials in order to have a fully sustainable build habitat [9].

Another advanced design is proposed by Foster and Partners where robots contribute to the building of the units in the Martian environment. Using the mars

rocks and the 3D printed modules, the robots shall assembly the full habitat in one functioning Martian habitat [10].

German firm ZA Architects, through the Mars Colonization project proposes to build a massive underground network of tunnels to begin populating the red planet. Through technology and robotics, they would first carve out large caverns in the planet's basaltic rocks to later insure the oxygen and water supply through the production of an underground glacier in a basalt processing plant [11].

Mars Utopia is a project that proposes introducing bio life to the planet in order to create living conditions. Fungus for example could be used for structural purposes and luminescent bacteria can be used for natural lighting [12].

1.1 Analysis of Mars Conditions

Mars is bombarded with radiation. Without a protective magnetic shield and a thick atmosphere like Earth's the red planet surface is almost fully deadly to human life to this radiation. Radiation-hardened machines like the Curiosity Rover can roam around on the surface and face all that radiation with impunity [13].

Based on a recent study there are two possible solutions to shield from the radiation: use a lot more mass as a barrier or use less mass and efficient shielding materials. In the first case, the sheer volume of material surrounding a structure would absorb the primary and secondary energy particles of the radiation before they could reach the astronauts. However, the use of heavy equipment means more energy for the launch of the capsules. Finding more efficient materials that can reduce the radiation helps save budget and equipment. NASA is conducting various research programs in finding efficient materials for the astronaut suits the Mars habitat [14].

Lightweight magnetic shields could be a way to protect from deadly radiation as they travel to Mars and on Mars. Harmful radiation in space can be classified in two groups; protons emitted by the Sun, and cosmic rays. Naturally, as with any radiation, extended exposure to radiation would lead to increase in the risk of developing cancer. Increasing the thickness of walls would be enough to protect astronauts from any low-energy particles from the sun including protons. High-energy cosmic rays would initially be stopped too. Unfortunately, after extended exposure the shield would become radioactive itself, emitting so-called secondary radiation in all directions [15].

Regarding radiation in the visible spectrum, rocks and soil surface layers absorb and reflect incoming solar radiation immediately at the surface. Ice on the other hand, whilst opaque in the infrared, is partially transparent in the visible spectral range. These properties are responsible for the "solid-state greenhouse effect" (SSGE), which may play an important role in the energy balance of icy surfaces. To model the SSGE, one needs to know not only thermal properties but also optical properties such as the albedo and the absorption scale length of the ice. The absorption scale length, also known as e-folding scale, of snow/dust mixtures within the scope of a project directed at investigating the behavior of the Martian polar caps has been

studied. After measuring the e-folding scale of recrystallized snow we can now also relate the dust content of contaminated snow to the penetration depth of sunlight into the mixture. Equally important, however, is our observation that light penetration through the mixture is dramatically affected by small-scale inhomogeneities [16].

Foster + Partners have Foster and Partners, been working on a NASA-backed competition for a 3d-printed modular habitat on Mars. The design for the Mars Habitat plans for a settlement constructed by a swarm of pre-programmed, semi-autonomous robots prior to the eventual arrival of the astronauts. The habitat—created in collaboration with industrial and academic partners—envisions a robust 3D-printed dwelling for up to four astronauts constructed using regolith—the loose soil and rocks found on the surface of Mars [17].

Atmosphere and Weather: The Martian atmosphere is composed primarily of carbon dioxide. However unlike Venus, the Mars atmosphere is very thin, subjecting the planet to a bombardment of cosmic rays and producing very little greenhouse effect [18].

Astronauts living on Mars will need to grow some of their own food in order to survive and stay healthy. To successfully grow plants on Mars, greenhouse structures will be necessary to provide similar growing conditions to those on Earth. Greenhouses on Earth are structures with transparent glass or plastic walls and roofs that allow as much of the available sunlight as possible to reach the plants inside. This begs the question, is there enough light to grow plants on Mars? Several factors influence the amount of light that would be available on Mars [19].

Radiation Shielding on Mars Future space missions to Mars will require radiation shielding to be optimized for two main purposes. The first optimization shall be on space transit. The second optimization shall be on the extended stay on the surface. In deep space, increased shielding levels and material optimization will reduce the exposure from most solar particle events but are less effective at shielding against galactic cosmic rays. This result is significant for optimization of vehicle and shield designs effective on the Martian surface [20].

Protecting astronauts during the voyage from Earth to Mars is also an issue to consider. In this case, the amount of payload is a constraint of the mission. An alternative relatively heavy passive shields are active shields based on an electrically induced magnetic field. However, in the majority of the cases they are not practical. Several studies are developing technologies based on superconducting magnetic fields in space [21].

Ukrainian architecture practice Makhno Studio has designed a 3D-printed settlement for Mars named Plan C that would encircle the edge of a crater. In response to this, Makhno Studio developed a proposal for an underground bunker that made headlines internationally. This later led to Plan C, a concept for a Martian settlement. The proposal sees a bagel-shaped settlement located on the inside of a crater, which would protect the development from Mars' environmental conditions—including frequent sandstorms, meteor showers and solar radiation [22].

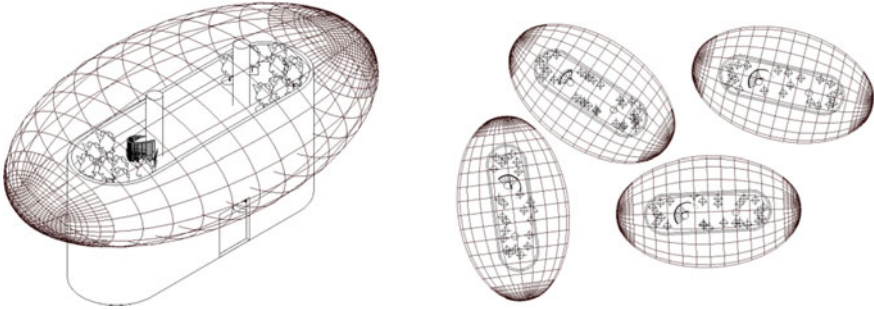


Fig. 1 Conceptual development of alternative 1

1.2 Schematic Design, Standards of Living in Space

The design is based on different units related and connected to each other by serving their functions, the units consist of 3 different levels. The ground level is main entrance and access, then the main function layer and last layer is the greenhouse layer. The green house layer is protected by inflatable material to give access to sunlight and produce oxygen for the units. The construction of the design is 3D printed using martial materials of which will lower the expenses for transporting construction materials, it will provide as well natural isolation (Fig. 1).

The fundamental design comprises of many capsules with unique interiors that are used by astronauts and researchers. A huge dome that will cover them all will link each of the capsules. The Dome is the project's focal point or major component. The design of the dome could incorporate many designs. The recommended designs were created after studying the cultural history of the UAE. The proposed designs were mostly inspired by the emblem for Expo and the conventional palm tree (Figs. 2 and 3). The dome might be created for future study so that it can both connect the capsules and give oxygen. In which the dome will serve as a location where astronauts and researchers may conduct study without donning space suits and explore the outside of the capsule (Figs. 4 and 5).

1.3 Connection to UAE Architectural Heritage

Alternative 2 and 3 were generated after analyzing the UAE's past, present and future. The first alternative was inspired by the biggest event that happened to the UAE, which is Dubai's hosting of EXPO 2020. Our first design was inspired by the expo's logo, which was initially based on a civilization that lived in a region that stretched from Abu Dhabi to Dubai. It continued from Sharjah to Ras Al Khaimah. It reached finally to Al Fujairah 4000 years ago. The region was claimed to display a global culture that is interconnected. We developed this idea further by designing

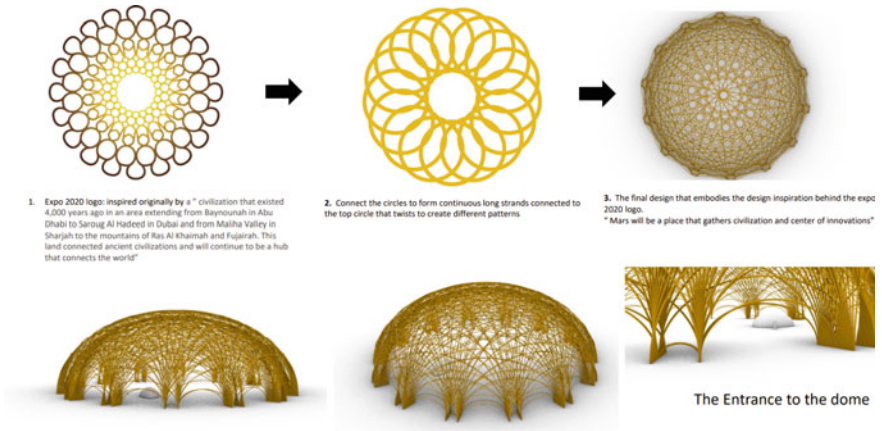


Fig. 2 Conceptual development of alternative 2

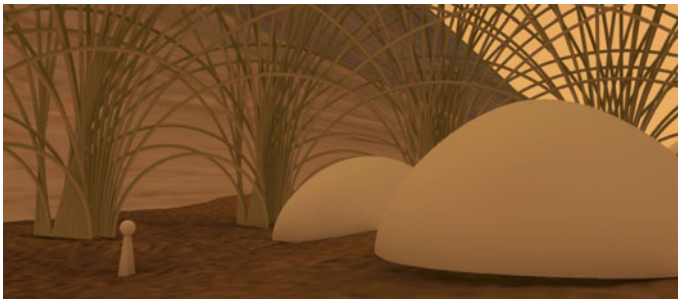


Fig. 3 Conceptual 3D of alternative 2

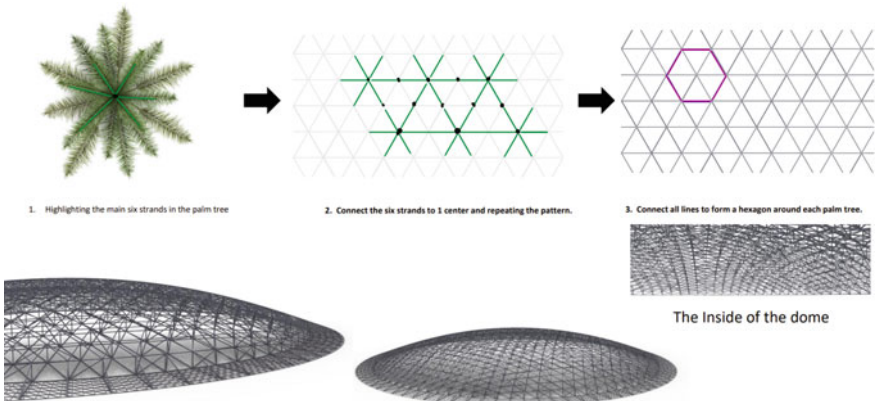


Fig. 4 Conceptual development of alternative 3

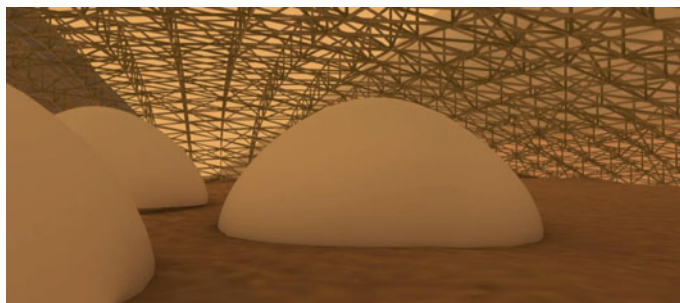


Fig. 5 Indoor conceptual view of alternative 3

the first dome to display the Expo's emblem, with the idea that Mars will serve as a hub for innovation and a location where civilizations may interact. The second alternative's designed was inspired from the leaves of the traditional palm tree. The dome will be a steel structure with a hexagonal shape pattern. The branches of the palm tree will connect to make 1 hexagon shape, creating repetitive hexagon pattern.

1.4 Modelling and Simulation

The modelling of booth domes was designed using Rhino Grasshopper plug in the python language allowed the making and altering of the design easily. The first alternative's script mainly consists of assigning a surface and surface point, in which each point will present a support element (Figs. 6, 7 and 8). The supports consist of number of pipes like structures that connects with the other supports, creating a network of pipes that generate more complex when the support's number increase. On the other hand, the making of the second hexagon steel dome structure, was generated using python programming language as well. However, the script of the second dome was more complex because of the use of different plug-in's such as lunchbox, and pufferfish to create the repetitive hexagon pattern (Figs. 9 and 10).

2 Results

The findings of this study suggest that it is possible to design a human habitat on Mars using parametric structures based on the heritage architecture of the UAE. This should come as no surprise, as the omnidirectional radiation profile of the summer months in UAE is similar to the omnidirectional cosmic radiation profile on Mars surface. The use of Rhino and Grasshopper allowed for the creation and analysis of models that could withstand the harsh conditions on Mars, such as excessive radiation and lack of an atmosphere. The final design proposal was selected based on these

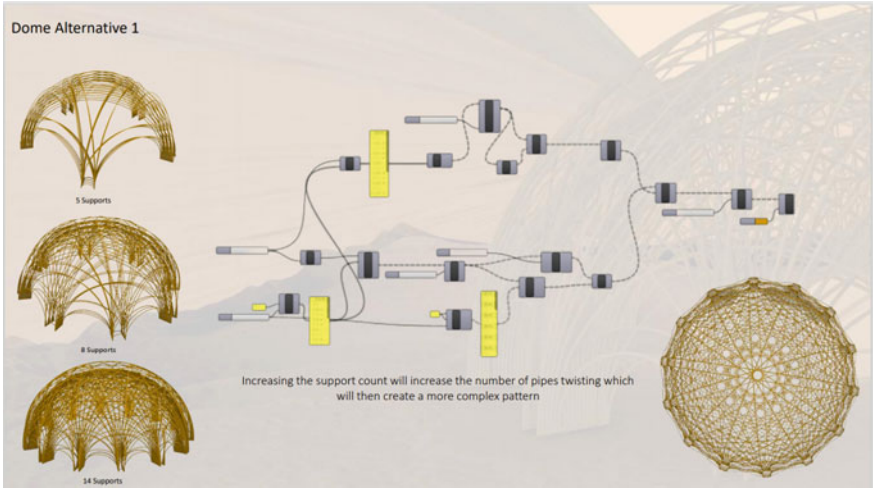


Fig. 6 Script in python, alternative 2

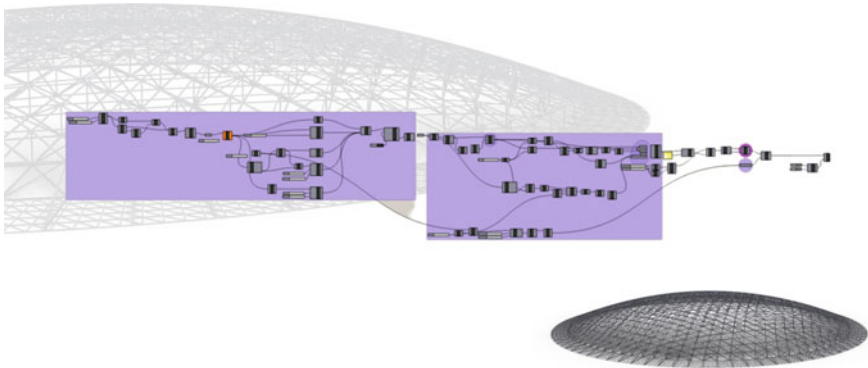


Fig. 7 Script in python, alternative 3



Fig. 8 Script in python, trials 1

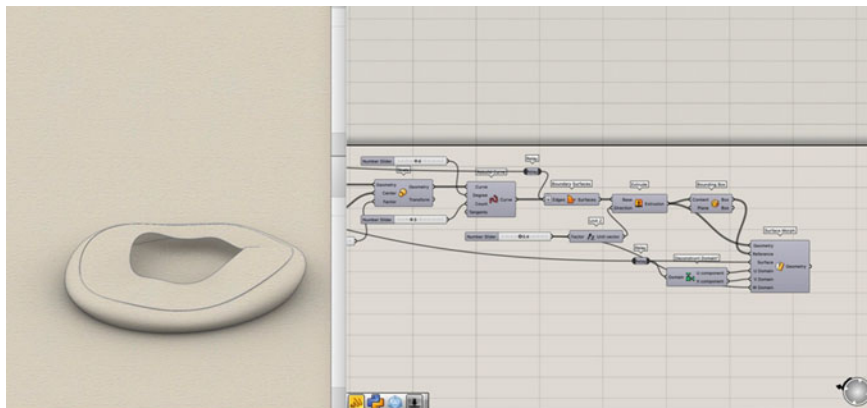


Fig. 9 Script in python, trials 2

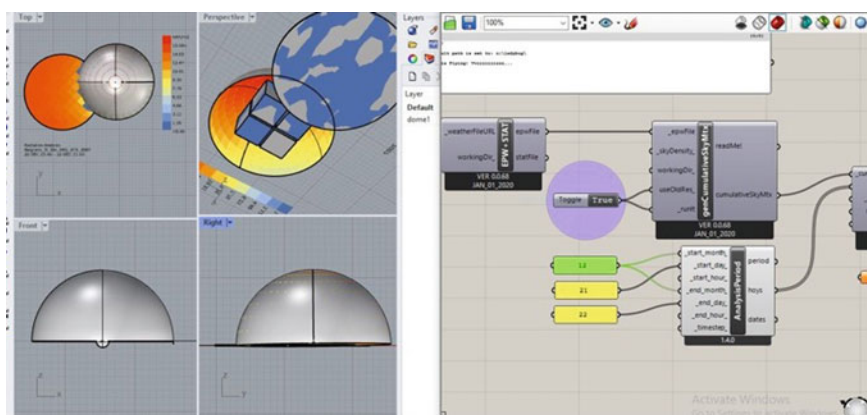


Fig. 10 A figure caption is always placed below the illustration

simulations, ensuring that it would be suitable for human habitation on the red planet (Figs. 11 and 12).

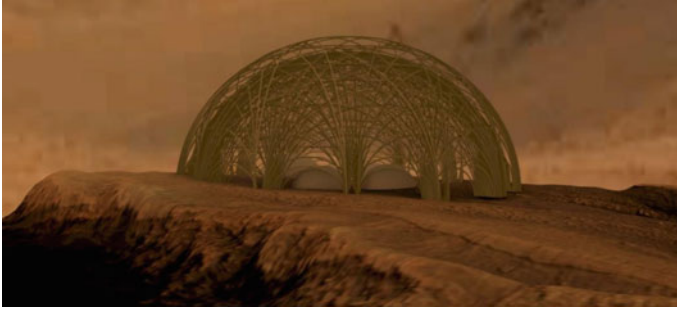


Fig. 11 Conceptual 3D of alternative 2

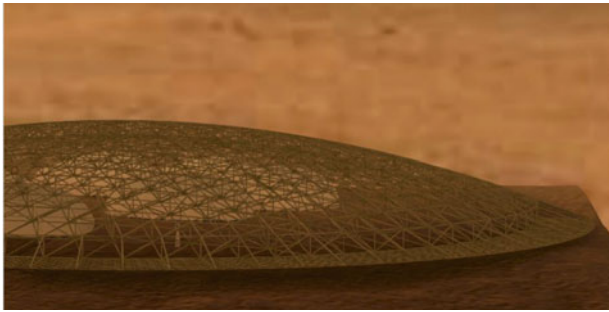


Fig. 12 Conceptual 3D of alternative 3

3 Conclusion

While the design of a human habitat on Mars is a challenging task, this study shows that it can be realized by considering the specific conditions of the planet and incorporating elements of radiation protection and atmosphere control. The use of parametric structures and 3D printing technology, as demonstrated by other successful space architecture projects, also holds promise for the construction of a functional and sustainable habitat on Mars.

However, further research is needed to fully understand the challenges and limitations of building a human habitat on Mars. This could include conducting more detailed simulations and experiments, as well as exploring new materials and technologies that can be used in the design and construction of such a habitat. Additionally, further collaboration with space agencies and experts in the field will be crucial to the success of this project. Overall, the findings of this study provide a promising starting point for the development of a human habitat on Mars.

References

1. Foster + Partners to 3D Print Structures on the Moon ArchDaily [Online]. Available: <https://www.archdaily.com/326429/foster-partners-to-3d-print-structures-on-the-moon>. Accessed 20 Dec 2022
2. 9 Visions for lunar colonies selected as winners in Moontopia competition. ArchDaily [Online]. Available: <https://www.archdaily.com/803985/9-visions-for-lunar-colonies-selected-as-winners-in-moontopia-competition>. Accessed 20 Dec 2022
3. UAE announces \$140 Million BIG-designed Mars Science City. ArchDaily [Online]. Available: <https://www.archdaily.com/880528/uae-announces-140-dollars-million-big-designed-mars-science-city>. Accessed 20 Dec 2022
4. "AI SpaceFactory [Online]. Available: <https://www.aispacefactory.com/post/ai-spacefactory-builds-3d-printed-mars-habitat-prototype-green-lighted-by-nasa-for-final-phase>. Accessed 03 Oct 2021
5. Drake BG, Hoffman SJ, Beaty DW (2010) Human exploration of mars, design reference architecture 5.0. In: IEEE Aerospace Conference Proceedings
6. Price H, Baker J, Naderi F (2015) A minimal architecture for human journeys to Mars. *New Space* 3(2):73–81. <https://home.liebertpub.com/space>
7. Yamashita M et al (2006) An overview of challenges in modeling heat and mass transfer for living on Mars. *Ann N Y Acad Sci* 1077(1):232–243
8. SOM unveils vision for first human settlement on the Moon. ArchDaily [Online]. Available: <https://www.archdaily.com/914813/som-unveils-vision-for-first-human-settlement-on-the-moon>. Accessed 20 Dec 2022
9. OPEN architecture and Xiaomi unveil MARS case housing prototype at China House Vision 2018. ArchDaily [Online]. Available: <https://www.archdaily.com/903198/open-architecture-and-xiaomi-unveil-mars-case-housing-prototype-at-china-house-vision-2018>. Accessed 20 Dec 2022
10. Foster + Partners awarded top prize in NASA's 3D-printed Mars habitat challenge. ArchDaily [Online]. Available: <https://www.archdaily.com/870686/foster-plus-partners-awarded-top-prize-in-nasas-3d-printed-mars-habitat-challenge>. Accessed: 22 Apr 2022
11. ZA Architects propone una colonia subterránea en el planeta Marte. ArchDaily en Español [Online]. Available: <https://www.archdaily.cl/cl/02-290476/za-architects-propone-una-colonia-subterranea-en-el-planeta-marte>. Accessed 20 Dec 2022
12. Mars Utopia towers could terraform red planet's atmosphere [Online]. Available: <https://www.dezeen.com/2016/01/06/mars-utopia-concept-alberto-villanueva-galindo-bacteria-towers-breathable-environment/>. Accessed 20 Dec 2022
13. Mars is bombarded with radiation, but we may have just found natural shelter. ScienceAlert [Online]. Available: <https://www.sciencealert.com/these-martian-features-could-serve-as-natural-radiation-shelters>. Accessed 20 Dec 2022
14. Garner R (2015) How to protect astronauts from space radiation on Mars
15. Radiation shielding to protect a mission to Mars. *Research and Innovation* [Online]. Available: <https://ec.europa.eu/research-and-innovation/en/horizon-magazine/radiation-shielding-protect-mission-mars>. Accessed 20 Dec 2022
16. (5) (PDF) Use of in situ ice to build a sustainable radiation shielding habitat on Mars [Online]. Available: https://www.researchgate.net/publication/342145558_Use_of_in_situ_ice_to_build_a_sustainable_radiation_shielding_habitat_on_Mars. Accessed 20 Dec 2022
17. Foster + Partners awarded top prize in NASA's 3D-printed Mars habitat challenge. ArchDaily [Online]. Available: <https://www.archdaily.com/870686/foster-plus-partners-awarded-top-prize-in-nasas-3d-printed-mars-habitat-challenge>. Accessed: 20 Dec 2022
18. N. N. W. S. US Department of Commerce, The Planet Mars
19. Tomatosphere, Is there enough light on Mars to Gr [Online]. Available: <http://tomatosphere.letstalkscience.ca/Resources/library/ArticleId/5421/is-there-enough-light-on-mars-to-grow-plants.aspx>. Accessed 20 Dec 2022

20. Slaba TC, Mertens CJ, Blattnig SR, Mertens CJ, Blattnig SR (2013) Radiation shielding optimization on Mars
21. Durante M (2014) Space radiation protection: destination Mars. *Life Sci Sp Res* 1(1):2–9
22. Makhno Studio designs conceptual settlement within Martian crater [Online]. Available: <https://www.dezeen.com/2022/01/24/makhno-plan-c-mars-settlement-concept-architecture/>. Accessed 20 Dec 2022

An Experimental Study and Sensitivity Analysis of Design Parameters of Building Integrated Photovoltaic (BIPV) Roofs for Rain Noise Reduction



Dingqiu Chen and Shaohang Shi

Abstract Building integrated photovoltaic (BIPV) roof performance in different types of buildings has attracted the attention of architects and engineers in recent years—sound reduction of lightweight buildings is a typical scenario. Laboratory experiments with artificial rain (rainfall intensity: 2 mm/min) were conducted to investigate the sound insulation performance of a lightweight BIPV roof; in addition, sensitivity analysis was conducted for five design parameters, including floor area, room height, length to width ratio of room (LWR), air temperature and atmospheric pressure intensity (310 cases in total). The results show that the A-weighting sound pressure level (L_{IA}) ranges from 18.25 dB to 29.01 dB, with LWR having the greatest effect (decrease of 10.76 dB) on rain noise reduction and air temperature having the least effect (decrease of 0.70 dB). The data and analysis presented in this study can provide a reference for the performance evaluation of BIPV technology, so as to create a healthy and comfortable indoor acoustic environment through parameter optimization design.

Keywords Building integrated photovoltaic (BIPV) · Rain noise · Lightweight building · Sound environment optimization

D. Chen

Tianjin University, No. 92 Weijin Road, Nankai District, Tianjin, China

GuangDong Bright Dream Robotics Co., Ltd, Panpu Road, Bijiao Town, Shunde District, Foshan, Guangdong, China

S. Shi (✉)

Tsinghua University, No. 30 Shuangqing Road, Haidian District, Beijing, China

e-mail: archieandie@163.com

Key Laboratory of Eco Planning and Green Building, Ministry of Education (Tsinghua University), No. 30 Shuangqing Road, Haidian District, Beijing, China

1 Introduction

Globally, fossil fuel consumption leads to an increase in greenhouse gases and a corresponding growth in climate warming; countries actively adopt various levels of strategies to develop and promote the utilization of renewable energy in order to achieve energy saving and emission reduction [1]. In the world's total energy consumption, the building sector consumes more than 30%, and it is important to realize source-developing and energy-saving through renewable energy building integration technology [2]. In recent years, building integrated photovoltaic (BIPV) technology has received plenty of attention from architects and engineers, and this technology can effectively reduce the energy consumption level of buildings. Depending on where the PV panels are integrated in buildings, this technology can be usually divided into BIPV facades [3] and BIPV roofs [4]. In smaller areas of buildings, the application of BIPV roof technology has higher payback benefits [5]—the closer the area of the PV roof is to the floor area, the easier it is for the net energy consumption of the building to approach zero during building operation. Lightweight fabrication technology is widely used in small-scale buildings, which have short construction periods and favorable economics; structural insulated panels (SIPs) in lightweight buildings, for example, combine good insulation and structural properties. However, due to lighter mass, the roofs of such lightweight buildings result in poor sound insulation, especially under rainfall conditions. The application of BIPV roofs in lightweight buildings requires assessments of the impact of rain noise.

The parameter design of the building envelope greatly affects the building energy consumption and the establishment of a healthy indoor environment [6], and the optimization of the indoor acoustic environment is an important aspect. Previous studies have been carried out to investigate the effects of different optimization strategies on the indoor acoustic environment. Traditional technical strategies include vibration dampers, sound barriers and anechoic chambers. Yan [7] investigated the effect of rain noise on the roof of lightweight buildings by comparing the effect of increasing the roof mass, adding acoustic wool or layers of roof construction materials; at the same time, the differences between natural and artificial rainfall were compared. In another study, Yan et al. [8] investigated the features of rain noise by means of artificial rainfall and the technical strategies to simulate rain noise scenarios. Donohue et al. [9] also explored the rain noise isolation effect of SIPs buildings and found that the difference in impact velocity and droplet distribution of simulated rainfall were the main differences between artificial and natural rainfall. In another study, Donohue et al. [10] explored the sound insulation effect of lightweight roofs by constructing an experimental platform to simulate natural rainfall; it was found that the presence of a water film during rainfall could moderate rain noise, and therefore the relationship between rainfall amount and rain noise was not necessarily linear. Hopkins [11] experimentally simulated artificial rainfall to test the rain noise reduction effectiveness of ETFE roof element, Polycarbonate roof element, ETFE with rain suppressor Type 1, ETFE with rain suppressor Type 2 and 6-12-6.4 (laminated) glazing; it is found that ETFE roof element has the worst sound insulation effect

and 6-12-6.4 (laminated) glazing has the best sound insulation effect. Toyoda et al. [12] investigated the sound insulation performance of Ethylene/Tetrafluoroethylene membrane structures through an experimental study, demonstrating the rain noise isolation potential through acoustic layers and damping materials.

Based on the discussion of the above studies, it can be seen that there is still a research gap on the rain noise reduction effects of BIPV roof systems in lightweight buildings. In addition, the sensitivity of various design parameters of BIPV roof systems and climate zone applications have not been explored and analyzed.

Therefore, this study focuses on the rain noise insulation performance of a lightweight BIPV roof system—experimental studies and sensitivity analyses were conducted; in addition, this study investigates the numerical regularity of the optimization effect of a lightweight BIPV roof system design parameter optimization on the indoor physical sound environment. As for the research process (Fig. 1), the prototype design of a lightweight BIPV roof system was first carried out. Then, a full-scale model for experiments was built. Further, artificial rainfall simulation and acoustic measurements of the room environment were conducted in the acoustic laboratory (Acoustics Laboratory, Building Environment Testing Centre, Tsinghua University) to investigate the rain noise insulation effect of the proposed lightweight BIPV roof system. Based on the experiments' results, sensitivity analysis of BIPV roof design parameters was conducted to investigate the influence of spatial shape and other indicators on the rain noise insulation effect. This study provides experimental and analytical data on the rain noise reduction capability of lightweight BIPV roof system. At the same time, the applied sensitivity parameter analysis method provides BIPV system design ideas for the exploration of application scenarios of lightweight roof.

2 Methods

2.1 Experimental Studies

In this study, a lightweight BIPV roof system with a cavity was proposed (Fig. 2), based on which an experimental platform was built to test the rain noise isolation performance of this system. The rainfall conditions were simulated in the laboratory to obtain the sound power levels of the BIPV roof at different frequencies (frequency = 125, 250, 500, 1000, 2000, 4000 Hz) to characterize the sound insulation capability. The measurement index used for the roof insulation performance is the A-weighting sound pressure level (L_{IA} , dB). After obtaining the experimental data, the sensitivity analysis was carried out based on 8.4.1 of GB/T 6881.1-2002 "Acoustics—Determination of sound power levels of noise sources using sound pressure - Precision methods for reverberation rooms", methods for reverberation rooms" to evaluate the LIA of the target room under different BIPV roof design parameters, which reflects the sound insulation effect of the lightweight system.

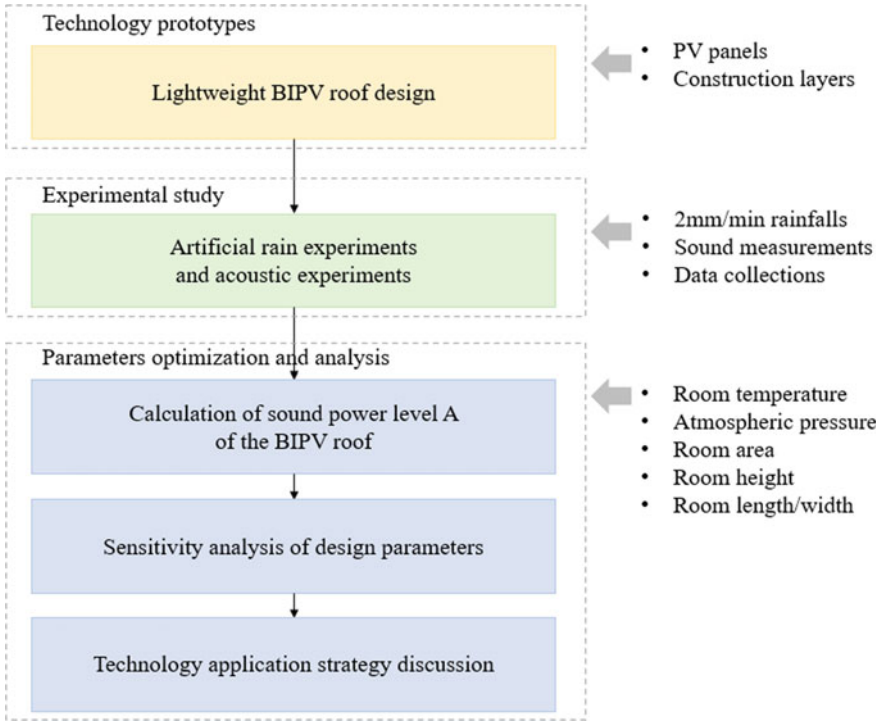


Fig. 1 Workflow

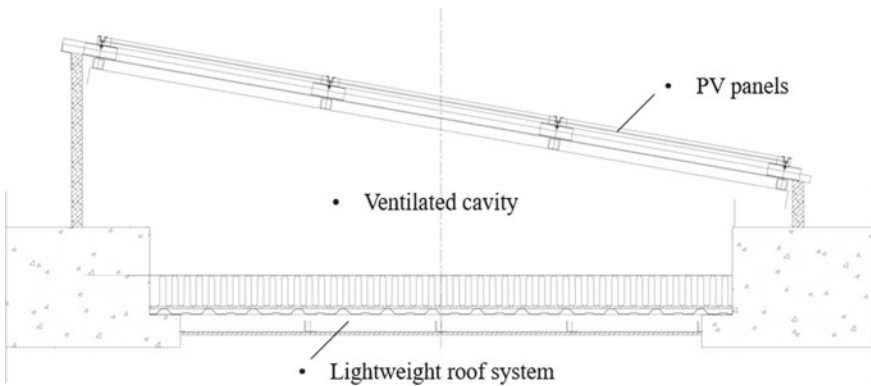


Fig. 2 Lightweight BIPV roof system in experiments

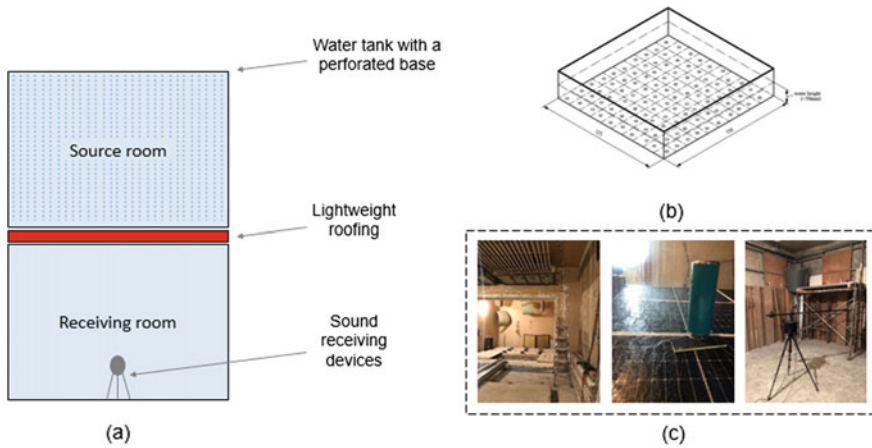


Fig. 3 **a** The section diagram of the rain noise experiment; **b** Water tank for rain simulation (picture source: reference [8]); **c** Experiments setup and photos during measurements

The experimental equipment and experimental site in this study were provided by Tsinghua University [7, 8] (Acoustics Laboratory, Building Environment Testing Centre), and a third-party testing approach was introduced. The laboratory space is divided into two parts, the rain noise simulation room (source room) and the sound measurement room (receiving room), which are shown in Fig. 3a. The rainwater simulation device structure used in experiments is shown in Fig. 3b. The rain collector and Norsonic acoustic recorder used in experiments are shown in Fig. 3c.

Before the start of formal experiments, the rainfall simulation equipment needs to be pre-tested. During the pre-testing process, the rainfall amounts of different experimental conditions will be recorded by rain gauges to guarantee the rainfall intensity to achieve heavy rainfall conditions (2 mm/min). Further, the sound power level of the lightweight BIPV roof system was converted by Eqs. (1) [13], (2) and (3) under heavy rainfall conditions, and the sound insulation capability of the roof structure was characterized. Finally, the sound pressure level will be converted into the A-weighting sound pressure level by using Eq. (4) [14] for the conversion of the sound pressure level. When calculating the sound absorption effect of the receiving room, the sound absorption factor is shown in the Table 1.

$$L_w = \bar{L}_p + \left\{ 10 \lg \frac{A}{A_0} + 4.34 \frac{A}{S} + 10 \lg \left(1 + \frac{Sc}{8Vf} \right) - 25 \lg \left[\frac{427}{400} \sqrt{\frac{273}{273 + \theta}} \cdot \frac{B}{B_0} \right] - 6 \right\} \quad (1)$$

$$c = 20.05 \sqrt{273 + \theta} \quad (2)$$

Table 1 Sound absorption factor in receiving room

f [Hz]	125	250	500	1000	2000	4000
Sound absorption factor	13.95	19.16	23.95	22.81	23.95	23.56

Data source Acoustics Laboratory, Building Environment Testing Centre, Tsinghua University

$$A = S \cdot \bar{\alpha} \quad (3)$$

$$L_{IA} = 10 \lg \sum_{j=1}^{j_{\max}} 10^{0.1(L_j + C_j)} \quad (4)$$

In Eqs. (1), (2), (3) and (4), L_w means the sound power level; A means absorption area; S means the surface area of the room; c means sound velocity; V means the room volume; θ means air temperature; B means the atmospheric pressure intensity. A_0 and B_0 are taken as 1 m^2 and $1.013 \cdot 10^5 \text{ Pa}$ [13].

2.2 Sensitivity Analysis of Design Parameters of the BIPV Roof System

The sensitivity analysis study was conducted to investigate the sound insulation effect of lightweight BIPV roof of different design parameters. There is set a base case to evaluate its indoor rain noise levels. The relevant design parameter values are shown in Table 2. When investigating the effect of specific design parameters' relationship with the sound insulation, the other parameters were kept the same as the base case.

Table 2 Parameters design of BIPV roof's base case

Parameters	Value
Room height (m)	4
Room width (m)	6
Room length (m)	6
Length to width ratio of room	1
Air temperature (θ , °C)	25
Atmospheric pressure intensity (B, Pa)	1.013×10^5

Table 3 Sound power levels at different frequencies of the lightweight BIPV roof under 2 mm/min rainfall conditions

f (Hz)	125	250	500	1000	2000	4000
Sound power level (dB)	50.40	42.39	37.67	27.68	21.43	20.15

3 Results

3.1 Sound Power Levels of the Room

The sound power level of the lightweight BIPV roof was tested at different frequencies under 2 mm/min rainfall conditions (Table 3), which characterizes the ability of the roof to block the rain noise.

3.2 Sensitivity Analysis of Room and BIPV System Design Parameters for Rain Noise Reduction

Sensitivity analyses were conducted for different design parameters, including floor area, room height, length to width ratio of room (LWR), air temperature and atmospheric pressure intensity.

Figure 4 shows the rain noise level of a room with different floor area, which contains 60 cases. When the parameters such as room LWR are kept constant, it can be seen that the increase in floor area makes the rain noise level gradually decrease. Specifically, the A-weighting sound pressure level of rain noise changes from 29.01 to 24.69 dB as the room area changes from 36 to 144 m² (step size of width and length = 0.1 m).

Figure 5 shows the rain noise level of the room with different LWR, containing 50 cases. It can be seen that as the room LWR increases (step size of LWR = 0.02), the rain noise level decreases; at the same time, it can be seen that the degree of noise reduction gradually decreases (in all cases, design parameters such as room area and height remain the same). In cases presented, the rain noise decreases from 29.01 to 18.25 dB as the room aspect ratio increases from 1 to 2.

Figure 6 shows the rain noise level of a room with different height and contains 60 cases. It can be seen that the level of indoor rain noise decreases as the room height increases, while the room size and shape are kept constant. In cases presented, the rain noise level is reduced from 29.01 to 26.53 dB for room heights from 4 to 10 m (step size of room height = 0.1 m).

Figure 7 shows the rain noise level of the room with different air temperature, containing 70 cases. It can be seen that as the air temperature increases (step size of air temperature = 0.5 °C), the rain noise level decreases. In the above cases, the rain noise decreases from 29.52 to 28.82 dB as air temperature increases from 0 to 35 °C.

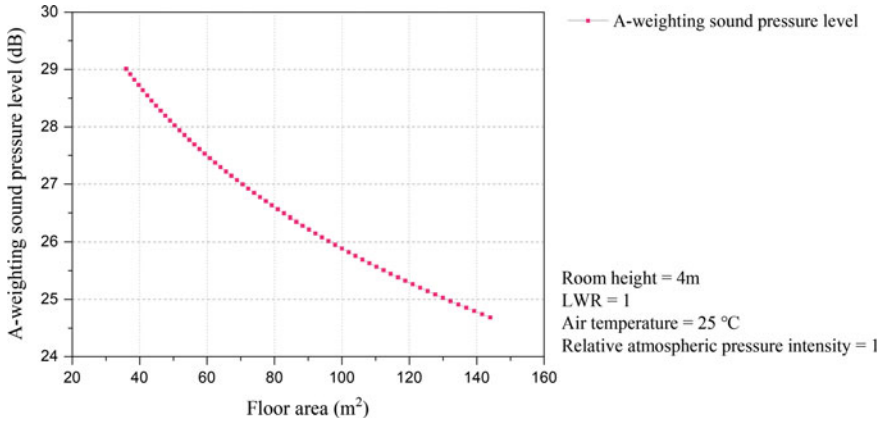


Fig. 4 Rain noise level with different floor area of the room

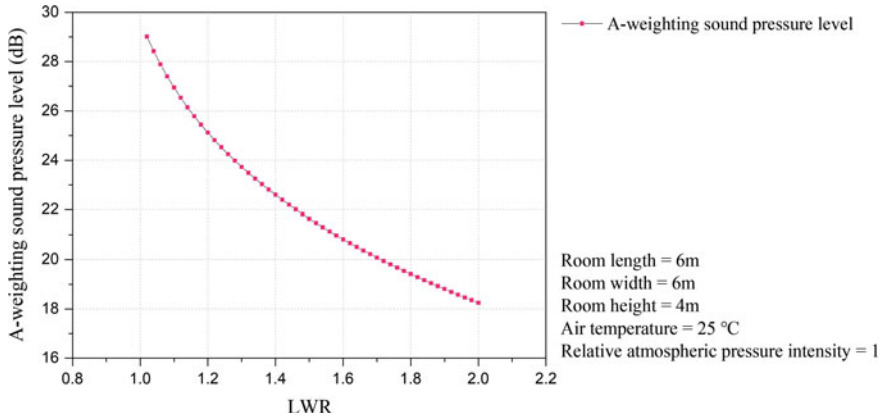


Fig. 5 Rain noise level with different room LWR

Figure 8 shows the rain noise level of a room with different atmospheric pressure intensity and contains 40 cases. As the relative atmospheric pressure increases (which is usually caused by the low altitude of the area where the BIPV building is located), the rain noise level increases gradually. In the case discussed, the relative atmospheric pressure rises from 0.6 to 1.0 and the rain noise rises from 23.47 to 29.01 dB.

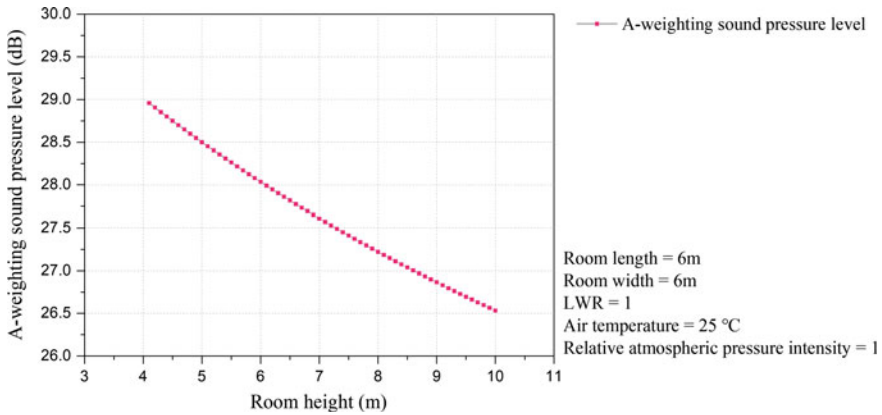


Fig. 6 Rain noise level with different room height

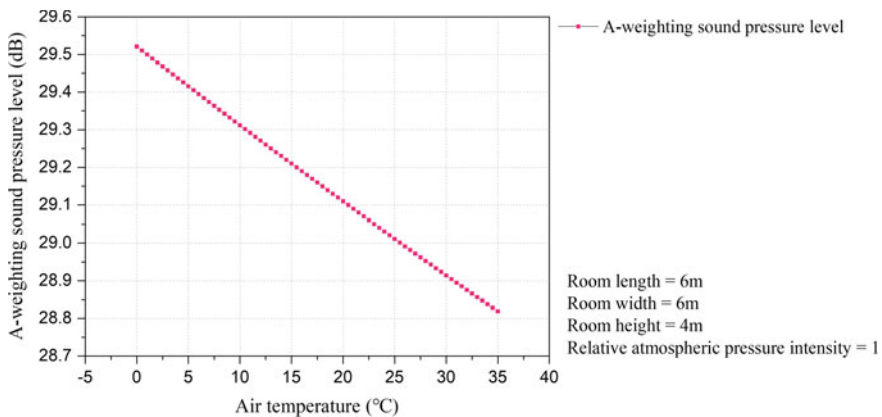


Fig. 7 Rain noise level with different air temperature

4 Discussion

According to the results of the above experiments and sensitivity analysis, the A-weighting sound pressure level values are all below 30 dB—according to GB55016-2021 “General Code for Building Environment”, the standard requirement for bedroom indoor acoustic environment is less than 30 dB at night [15], so this lightweight BIPV roof prototype can meet the acoustic application standard requirements.

The increase of floor area, room height, LWR and air temperature values leads to the decrease of rain noise A-weighting sound pressure level; the change in LWR resulted in the largest reduction in rain noise of 10.76 dB. The increase of relative atmospheric pressure intensity leads to the increase of rain noise A-weighting

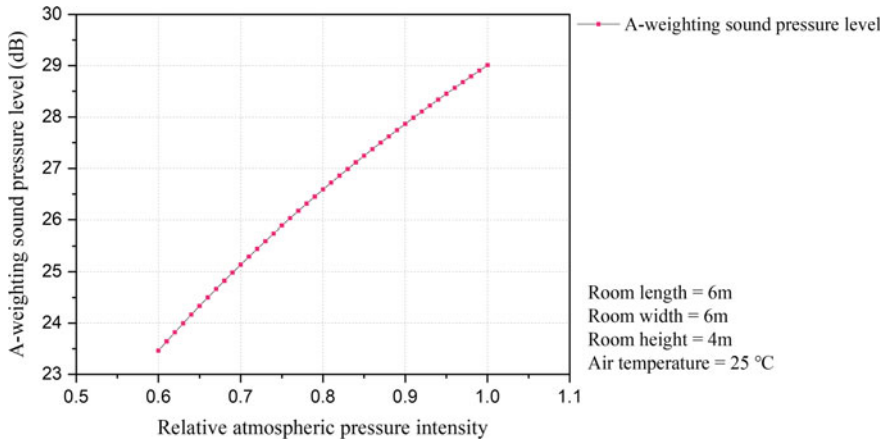


Fig. 8 Rain noise level with different atmospheric pressure intensity of the room

sound pressure level increases. It can be found that spatial design parameters, climate zone application (different temperatures throughout the year) and regional altitude (different atmospheric pressures) all have an effect on the rain noise reduction performance of lightweight BIPV roofs. The optimization strategy of room space and form can be attributed to the increase of the sound absorption area of the building interior. Meanwhile, temperature has some effect on rain noise, but the reduction is less than 1 dB between 0 °C and 35 °C, so there is a small difference in rain noise between different climate zones applying lightweight BIPV roofs. But the relative atmospheric pressure has more than 5 dB effect on the rain noise (relative atmospheric pressure 0.6 raised to 1). Therefore, at different altitudes, the change in atmospheric pressure makes a large difference. This is related to the change of sound propagation in different temperature and pressure environments. In addition, the cavity of the BIPV roof in experiments ensures the sound insulation performance to a certain extent.

At the objective level of building physical environment optimization, excessive rain noise may have negative impact on people's health; noise reduction is considered to be an effective way to improve people's concentration or work performance. However, from the perspective of subjective evaluation of sound, rain noise can be transformed into a beneficial physical element. For example, the soundscape formed by rainwater sounds from nature may cause comfort and appointments, which may appropriately increase people's tolerance to rain noise [16]. Moreover, people's acoustic preferences [17] for rainfall all have an impact on sound environment evaluations.

5 Conclusion

In this study, the rain noise reduction performance of a lightweight BIPV roof was tested based on laboratory artificial rainfall conditions; also, a sensitivity analysis was conducted. The main findings are as follows:

1. Based on GB55016-2021 “General Specification for the Built Environment”, the BIPV roof with the cavity has a good ability to isolate rain noise (< 30 dB), so it can be applied in lightweight buildings. This provides insight for architects and engineers in a specialized design of acoustics. It is possible to take the steps of “prototype design—experimental study—performance analysis”.
2. The early design stage of building envelope systems and building site evaluation are critical for rain noise reduction performance. This is not only related to the development of a healthy indoor acoustic environment, but also indirectly affects the economics of BIPV roofs, etc. There is also a revelation that optimization of multiple performance objectives should be taken when applying new technologies.
3. Achieving less rain noise may not necessarily be the best design conception for a room. In future research and practice, in addition to optimizing the objective physical environment, the subjective preferences of building occupants can also be considered.

In summary, the data and analysis methods presented in the study can contribute to promoting and supporting the application of BIPV roof in lightweight buildings.

Acknowledgements The project is supported by National Key R&D Program of China (2022YFC3803805) and R&D Program of THAD (K52022-033).

References

1. Lee S, Paavola J, Dessai S (2022) Towards a deeper understanding of barriers to national climate change adaptation policy: a systematic review. *Clim. Risk Manage.* 100414 (2022)
2. Ahmed A, Ge T, Peng J, Yan W-C, Tee BT, You S (2022) Assessment of the renewable energy generation towards net-zero energy buildings: a review. *Energy Build.* 256:111755
3. Shi S, Sun J, Liu M, Chen X, Gao W, Song Y (2022) Energy-saving potential comparison of different photovoltaic integrated shading devices (PVSDs) for single-story and multi-story buildings. *Energies* 15:9196
4. Wijeratne W, Samarasinghalage TI, Yang RJ, Wakefield R (2022) Multi-objective optimisation for building integrated photovoltaics (BIPV) roof projects in early design phase. *Appl. Energy* 309:118476
5. Shi S, Yu L, Liu C-H, Wang Y, Zhu N (2022) Application of synergic evidence-based design and sustainable technology strategies in off-grid residential NZEBs in the severe cold zone of China: a case study of The Steppe Ark. In: *IOP conference series: earth and environmental science*, vol 1074. IOP Publishing, pp 012023
6. Kou F, Shi S, Zhu N, Song Y, Zou Y, Mo J, Wang X (2022) Improving the indoor thermal environment in lightweight buildings in winter by passive solar heating: an experimental study. *Indoor Built Environ.* 31:2257–2273

7. Yan X (2008) Research on rain noise of lightweight roofing. Tsinghua University
8. Yan X, Lu S, Li J (2016) Experimental studies on the rain noise of lightweight roofs: natural rains vs artificial rains. *Appl Acoust* 106:63–76
9. Pearse J, Donohue B (2020) Structural insulated panels (SIP) and Rain Noise
10. Donohue B, Pearse J (2019) Rain noise. Universitätsbibliothek der RWTH Aachen
11. Hopkins C (2006) Rain noise from glazed and lightweight roofing. BRE Information PAPER IP 2
12. Toyoda M, Takahashi D (2013) Reduction of rain noise from Ethylene/TetraFluoroEthylene membrane structures. *Appl Acoust* 74:1309–1314
13. Nanjing University (2002) The Institute of Acoustics of the Chinese Academy of Sciences: GB/T 6881.1-2002, Acoustics - Determination of sound power levels of noise sources using sound pressure - Precision methods for reverberation rooms. General Administration of Quality Supervision, Inspection and Quarantine of the People's Republic of China, Beijing, China
14. Tsinghua University (2017) China Academy of Building Research, The Institute of Acoustics of the Chinese Academy of Sciences: GB/T 19889.18-2017, Acoustics-Measurement of sound insulation in buildings and of building elements - Part 18: Laboratory measurement of sound generated by rainfall on building elements. General Administration of Quality Supervision, Inspection and Quarantine of the People's Republic of China; Standardization Administration of the People's Republic of China, Beijing, China
15. Ministry of Housing and Urban-Rural Development of the People's Republic of China (2021) GB 55016-2021, General code for building environment. Ministry of Housing and Urban-Rural Development of the People's Republic of China, State Administration for Market Regulation, Beijing, China
16. Kang J, Aletta F, Oberman T, Mitchell A, Erfanian M, Tong H, Torresin S, Xu C, Yang T, Chen X (2023) Supportive soundscapes are crucial for sustainable environments. *Sci Total Environ* 855:158868
17. Liu X, Kang J, Ma H, Wang C (2021) Comparison between architects and non-architects on perceptions of architectural acoustic environments. *Appl Acoust* 184:108313

Low Carbon Design Strategy of Regional Airport Terminal Based on *Building Carbon Emission Calculation Standard*



Xia Ye, Tao Li-ke, and Guo Qin-en

Abstract The construction of regional airports in China is growing vigorously, which is in sharp contrast to the continuous operating losses. The low-carbon design of the terminal is of great significance to reduce the construction and operating cost of the project. Through the analysis of Building Carbon Emission Calculation Standard, combined with the case studies of domestic and foreign regional airports, based on the perspective of the whole life cycle of buildings, the low-carbon design strategy of regional airport terminals is analyzed and summarized from the three stages of building materials production and transportation, construction and demolition, and building operation respectively; The results were shown that the carbon emissions in the production and transportation stages of building materials can be reduced by modular and expandable systems, digital models for full process control, selecting building materials with low carbon emission factors and recyclable building materials, local building materials and lightweight structures; The carbon emissions in the construction and demolition stages can be reduced by adopting the prefabricated assembly technology and the reconstruction and reuse of existing buildings; The carbon emissions in the operation stages can be reduced by introducing natural lighting and ventilation, using renewable energy and increasing building carbon sinks. These design strategies can provide suggestions and ideas for the sustainable development of relevant venues in the future.

Keywords Calculation standard of building carbon emission · Regional airport terminal · Low-carbon design strategy

X. Ye · T. Li-ke · G. Qin-en (✉)

School of Architecture, South China University of Technology, Guangzhou 510641, China

e-mail: qegu@scut.edu.cn

© The Author(s), under exclusive license to Springer Nature Singapore Pte Ltd. 2024
M. Casini (ed.), *Proceedings of the 3rd International Civil Engineering and Architecture Conference*, Lecture Notes in Civil Engineering 389,
https://doi.org/10.1007/978-981-99-6368-3_52

641

1 Introduction

Climate change is a common challenge facing all mankind. At the 75th United Nations General Assembly in September 2020, China solemnly committed itself to “strive to achieve a peak in carbon dioxide emissions by 2030, and strive to achieve carbon neutrality by 2060”.

The regional airports are widely distributed and have a large number, but their operating conditions have suffered losses year after year. At the same time, the terminal building has a large space and numerous equipment, and the envelope structure often uses large area glass curtain walls, resulting in high building energy consumption. The energy consumption per unit area of the terminal building is 129–281 kWh/(m² a), which is far higher than the power consumption per unit area of the national public buildings in the same period of 61.96 kWh/(m²·a) [1]. As a high energy consumption public building, the low-carbon design strategy for widely distributed regional terminal buildings is of great significance for achieving the carbon reduction targets of the construction industry.

The Calculation Standard for Building Carbon Emissions issued by the Ministry of Housing and Urban Rural Development of the People’s Republic of China in 2019 is the accounting basis for the carbon emissions of airport terminal and other types of buildings.

The definition of “building carbon emissions” in the Calculation Standard for Building Carbon Emissions (GB/T 51366-2019) is: the sum of greenhouse gas emissions generated during the production, transportation, construction, demolition and operation of building materials, expressed in carbon dioxide equivalent [2]. The calculation formulas for carbon emissions at different stages are shown in Table 1.

Table 1 Calculation formula of carbon emission in each stage

No.	Calculation formula	Stage	Variable factor
1	$C_{sc} = \sum_{i=1}^n M_i F_i$	Production and transportation stage of building materials	M_i —Consumption of the <i>i</i> th main building materia; F_i —Carbon emission factor of the <i>i</i> th main building material
2	$C_{ys} = \sum_{i=1}^n M_i D_i T_i$		M_i —Consumption of the <i>i</i> th main building material (t) D_i —Average transportation distance of the <i>i</i> th building material (km) T_i —Carbon emission factor of unit weight transportation distance under the transportation mode of the <i>i</i> th building material [kgCO ₂ e/(t · km)]

(continued)

Table 1 (continued)

No.	Calculation formula	Stage	Variable factor
3	$C_{JZ} = \frac{\sum_{i=1}^n E_{jz,i} E F_i}{A}$	Building construction and demolition stage	$E_{jz,i}$ —Total consumption of type i energy in building construction stage (kWh or kg) $E F_i$ —Carbon emission factor of type i energy (kgCO ₂ /kWh or kgCO ₂ /kg) A—Floor area(m ²)
4	$C_{cc} = \frac{\sum_{i=1}^n E_{cc,i} E F_i}{A}$		$E_{cc,i}$ —Total consumption of the ith energy in the building demolition phase (kWh or kg) $E F_i$ —Carbon emission factor of type i energy (kgCO ₂ /kWh or kgCO ₂ /kg) A—Floor area (m ²)
5	$C_M = \frac{[\sum_{i=1}^n (E_i E F_i) - C_p] y}{A}$	Building operation stage	E_i —Annual consumption of the ith energy of buildings (/a) $E F_i$ —Carbon emission factor of type i energy (kgCO ₂ /kWh or kgCO ₂ /kg) C_p —Annual carbon reduction of building green space carbon sink system (kgCO ₂ /a) y—Design life of building (a) A—Floor area(m ²)

2 Production and Transportation Stage of Building Materials

According to Formula 1, to reduce the consumption of main building materials M_i , can be realized by adopting modular and expandable system and using digital models for full process control; To reduce the carbon emission factor of main building materials F_i , building materials with low carbon emission factor and recyclable building materials can be selected.

According to Formula 2, reduce the average transportation distance of building materials D_i , local materials can be used for this purpose; Reduce the carbon emission factor of unit weight transportation distance T_i . That is to say, the weight of building materials can be reduced by lightening the structure.

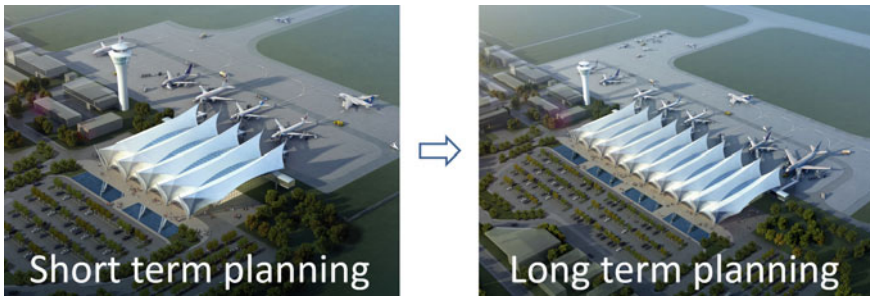


Fig. 1 Yueyang airport terminal modular and expandable system

2.1 Adopt Modular and Expandable System

The expansion of terminal buildings often leads to many inconveniences in the connection between new and old terminals. Adopting a modular and expandable system can not only form a unified design logic for the new and old terminals, but also effectively achieve the sharing of equipment resources between the new and old terminals. The construction method of modular standard components has a high degree of industrialization and high reuse rate. Due to its standardization, it can be quickly installed on site, which is not only conducive to reducing construction difficulty, but also can improve efficiency and reduce pollution.

For example, the terminal of Yueyang Airport adopts a unified planning and phased construction approach, so during the early planning, a modular expansion model for long-term development was determined. It can not only form a rhythmic architectural shape, but also achieve efficient and rapid terminal construction in the long term with sufficient preparation for early component production, while also achieving non-stop renovation of the terminal. (Fig. 1).

The results of the study show that modular building results in a reduction of 46.9% equivalent greenhouse gas emissions as compared to a conventional site-built building [3].

2.2 Using Digital Models for Full Process Control

Using digital models to optimize design can conduct qualitative and quantitative analysis on various technical indicators, so as to optimize the design scheme, ensure the effective configuration and accurate use of materials, and achieve the goal of material saving.

For example, the terminal building of Hulunbeier Hailar Airport uses BIM technology for full process control. Through design collaborative shape finding, simulation, and optimization, the curvature and surface of aluminum panels are analyzed and classified. The complex surface is simplified into three curvature aluminum

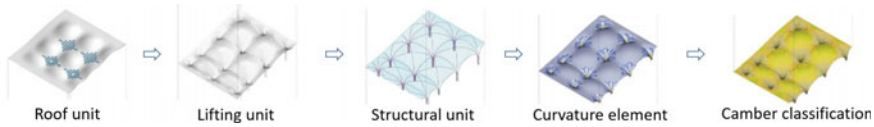


Fig. 2 BIM whole process design of Hailar airport terminal building

panel modules, thereby minimizing process difficulty and cost, avoiding errors and conflicts caused by repeatedly modifying drawings, and achieving accurate design (Fig. 2).

2.3 Select Building Materials with Low Carbon Emission Factor

The carbon emission factors of some main building materials are listed in Fig. 3. It can be seen that the difference between the Gravel with the lowest value and the electrolytic aluminium with the highest value is nearly ten thousand times, and the resulting carbon emissions will also vary widely.

Wood can play a role in carbon fixation and oxygen release by plants during the growth process. It also generates small carbon emissions during the acquisition, processing and manufacturing processes, and has a strong recyclability. It is almost considered a natural green building material with zero carbon emissions. For example, the terminal building of Mactan-Cebu Airport has an area of 53,000 square meters, and the wooden structure uses local spruce. The roof is supported by a continuous span of 30 m of plywood arches (Fig. 4).

The engineering wood materials used for wood structures have a carbon emission factor of 50.5 kgCO₂/m³ [4], 0.4 m per square meter of timber. It is estimated that the carbon emissions from the production of wood structural materials per square

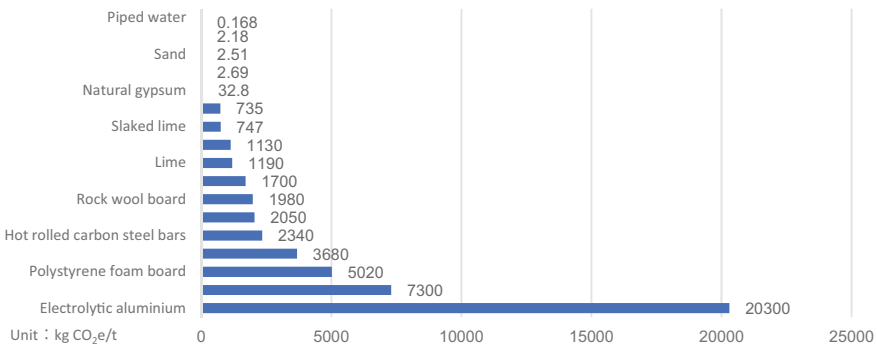


Fig. 3 Carbon emission factors of some building materials



Fig. 4 Wood structure in Cewu airport

meter are about $20.2 \text{ kgCO}_2/\text{m}^3$, while the carbon emissions from the use of cast-in-situ reinforced concrete materials are about $317.5 \text{ kg}/\text{m}^2$. With the same material consumption, the carbon emissions from wood structures per square meter are reduced by about 297.3 kg compared to reinforced concrete structures.

2.4 Use Recyclable Building Materials

According to Calculation Standard for Building Carbon Emission, when other recycled raw materials are used, it shall be calculated as 50% of the carbon emission of the raw materials replaced [2].

For example, Schiphol Airport in the Netherlands recycles 110 tons of materials from the demolition of old buildings, and also uses materials such as columns, trusses, stairs, and doors of old buildings. The Building Circularity Index is as high as 64%. Taking steel structure buildings as an example, the carbon emission factor of ordinary carbon steel is about $2050 \text{ kgCO}_2/\text{t}$ [2]. Based on the steel consumption per square meter of about 50 kg , the carbon emission can be reduced by 102.5 kg per square meter of steel recycling.

2.5 Select Local Materials

Local materials can not only minimize the energy consumption caused by long-distance transportation, but also avoid the material loss caused by long-distance. At the same time, some local materials can also show the sense of place and regionality of buildings.

The ceiling of the terminal building at Madrid Barajas Airport was decorated with $230,000 \text{ m}^3$ of fireproof bamboo sheets (Fig. 5), which was the largest bamboo application project in the world at that time. Bamboo itself was also an environmentally friendly building material with a low carbon emission factor. However, all

Fig. 5 Madrid Barajas airport airport



the bamboo materials used in the project were imported from Zhejiang in China, and reached Spain through container shipping [5], with a shipping carbon emission intensity of about 14 tons/million ton kilometers, The process of long-distance sea transportation will generate about 13,800 tons of carbon emissions, and its carbon reduction effect can be described as outweighing the gain.

2.6 Lightweight Steel Structure

Airports are mostly large span structures, and the lightweight of large span structures can be considered mainly from two aspects: first, starting from structural materials, using lightweight and high-strength materials to reduce the dead weight of the structure; The second is to maximize the effectiveness of the structure by optimizing the structural form, component layout, and force transmission routes from the perspective of the structure itself.

The terminal building of Chibougamau Chapais Airport in Canada has created a lightweight large-span roof through the combination of materials and structures. Firstly, the use of high-performance materials such as locally glued wood and cross laminated wood (CLT) structural panels has brought into play the lightweight and high-strength characteristics of wood, enabling a span of up to 12 m. Secondly, optimize the structural form of the roof, using engineering wood and steel components. The CLT panel is supported by wooden columns at both ends, and the columns are reinforced with high-strength steel rods, which are connected from the center to the four walls. The structural support of the skylight can be used as a load-bearing shaft without the need for additional structural beams (Fig. 6).

Fig. 6 Chibougamau Chapais airport



3 Building Construction and Demolition Stage

The carbon emission of structural engineering mainly comes from ready mixed concrete, accounting for more than 55% of the carbon emission in the whole construction stage, which can be achieved by using prefabricated buildings.

In the stage of building demolition, the reconstruction and reuse of existing buildings can directly avoid demolition from the source and reduce carbon emissions.

3.1 Structural Engineering—Adopt Prefabricated Technology

The components of prefabricated assembly technology are produced in a factory, which can control errors and reduce material consumption; During the construction process, the auxiliary materials such as formwork and mortar required for cast-in-situ construction are greatly reduced, and temporary supports such as scaffolding are not required. At the same time, the construction waste generated on site is also greatly reduced, making the construction process more green and environmentally friendly. Compared to cast-in-place buildings, prefabricated buildings can reduce carbon emissions by 2.65 kg/m^2 during the construction phase.

The fourth terminal building of Madrid Barajas Airport adopts prefabricated steel structures, and the entire building is assembled with prefabricated steel structures. It has greatly improved construction efficiency and accelerated the entire construction process. At the same time, many key components are specifically designed and manufactured for this project, such as biofilm exhaust systems, floor flushing systems, Vietnamese hat style lighting, and so on. Now these specialized design components have been put into large-scale production and applied to other projects (Fig. 7).

Fig. 7 Prefabricated technology



3.2 Reconstruction and Reuse of Existing Buildings

Due to the rapid development of airports, it is inevitable to update and iterate the terminal. Although the old terminal cannot keep up with the development of the times due to various reasons such as building scale, process layout, equipment and facilities, its complete structure and open space are valuable land and spatial resources. If its service life can be extended through renovation and reuse, it can not only reduce the carbon emissions generated by demolishing existing buildings, but also significantly reduce the carbon emissions of rebuilding existing buildings compared to new venues.

The terminal building of New York's Kennedy Airport, designed by Little Sarin, is a masterpiece of organic architecture. After completing the historical mission of the terminal, it was transformed into a hotel, not only extending the life of classic buildings, maximizing the use of the original building skeleton, but also greatly reducing the carbon emissions of new buildings.

4 Operation Stage

According to the calculation formula 5, to reduce the annual energy consumption E_i , can be achieved through passive energy conservation strategies, such as natural lighting and natural ventilation; To reduce the carbon emission factor EF_i of energy. can be achieved by using renewable energy; To increase the annual carbon reduction of building green space system C_p . That is, increase the building carbon sink.

4.1 Natural Lighting

The energy consumption of building lighting is about 20–40% of the total energy consumption. Due to the long streamline and large depth, the internal space of the terminal lacks natural lighting. The following methods can be used to introduce natural light (Fig. 8):

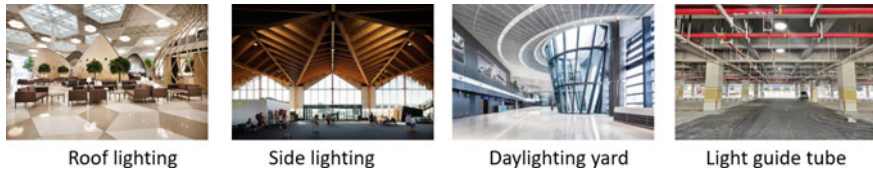


Fig. 8 Natural light methods

1. **Roof lighting:** Opening a skylight on the top to provide natural lighting, which is the most commonly used lighting method in the terminal lobby. For example, in the design of the Azerbaijan's Heydar Aliyev Airport terminal, the roof lighting not only reduces the energy consumption of artificial lighting, but also forms a rich variety of light and shadow.
2. **Side lighting:** The main disadvantages of side lighting are easy to generate glare, uneven illumination and low lighting efficiency. Therefore, the side lighting mainly plays an auxiliary role. Side lighting is the most commonly used lighting method due to its simple structure, convenient layout, and clear directionality of light. For example, The roof of Nelson Airport imitates the undulating mountain contours around it, so it mainly introduces indoor lighting through side glass curtain walls.
3. **Daylighting yard:** For example, Shangrao Mount Sanqing Airport introduces natural light through three daylighting yard in the internal space of the terminal.
4. **Light guide tube:** In some areas where natural lighting cannot be directly used, the use of light guide system can make up for the dependence of indoor light environment on artificial Lighting. This type is commonly used in large airports, such as the underground area of Nanning Airport.

The energy consumption per unit area of the terminal is 129–281 kWh/(m² a). Natural lighting can reduce energy consumption during building operation by about 15% [6]. Therefore, natural lighting can reduce the energy consumption per unit area of the terminal building by 19.4–42.2 kWh/(m² a) equivalent to reducing 15.2–33.1 kg of carbon emissions per square meter per year.

4.2 Natural Ventilation

The air conditioning system in the terminal consumes approximately 35% of the terminal's power consumption [7].

The regional airport is small in size and has the conditions and advantages of adopting natural ventilation during the transition season. Natural ventilation can be achieved by optimizing the building envelope. For example, the skylight on the top of the terminal building of Leshan Airport can achieve natural ventilation; The curtain wall of the terminal building of Yancheng Airport is equipped with pneumatic windows, which are opened for natural ventilation during the transition season.

4.3 Renewable Energy

As renewable energy does not produce carbon emissions and pollutants during its use, it can be regarded as a natural green energy with carbon emission factors approaching zero.

Wind Power Generation System. Aircraft takeoff and landing can generate huge winds, so the wind resources around the terminal are abundant. Wind power plants have been installed on the top of the Edinburgh Airport terminal and around the runway. However, due to high safety limits, the use of wind power in airport terminals is not common.

PV System. The solar photovoltaic system is combined with the building, which is divided into two types: BAPV (Building Attached Photovoltaic) and BIPV (Building Integrated Photovoltaic). BAPV is to fix the PV modules on the existing buildings without affecting the original functions of the buildings; As a building component, BIPV is a solar photovoltaic power generation system designed and constructed simultaneously with the building and integrated with the building.

The BIPV method used in Terminal 2 of Daraman Airport in Turkey, solar photovoltaic panels are combined with the sunshade to filter and block the sun while helping to generate some of the energy required by the terminal (Fig. 9).

According to the solar photovoltaic panel installed capacity of 100 w per square meter, in a region with a moderate level of solar energy resources with annual sunshine hours of 2200–3000 h, solar photovoltaic panels can generate 143–195 degrees of electricity per square meter per year, equivalent to reducing carbon dioxide by 112–153 kg.

Heat Pump System. Haikou Meilan Airport uses air source heat pumps to provide hot water, with a proportion of up to 70%.

Yancheng Airport adopts a ground source heat pump system to provide more than 60% of the cooling and heating capacity of air conditioning.

Fig. 9 The BIPV system in terminal 2 of Daraman Airport



According to existing data, the application of heat pump systems per square meter can reduce carbon emissions by about 30 kg per year [8].

4.4 Building Carbon Sink System

Building carbon sequestration refers to the amount of carbon dioxide absorbed and stored by greening and vegetation from the air within the designated scope of the building project. Increasing green space in buildings can not only fix carbon and release oxygen, but also regulate environmental temperature and humidity, effectively reducing the temperature of the building surface, with a significant thermal insulation effect, helping to reduce building energy consumption. At the same time, passengers desire to be close to nature and relax from the ecological environment after a long journey with the cabin closed. Therefore, the arrangement of landscape greening space will undoubtedly become the highlight and focus of the terminal building.

For example, a pair of atriums called “green lungs” have been set up on both sides of the dome in the terminal building of Ordos Airport, creating two four-level evergreen “botanical gardens”, forming a new way of dialogue with the desert. Liuzhou Bailian Airport introduces an ecological atrium into the interior of the airport to create a green and ecological waiting environment (Fig. 10).

According to existing research, the annual carbon sequestration per square meter of green space is about 5.4 kg [9].

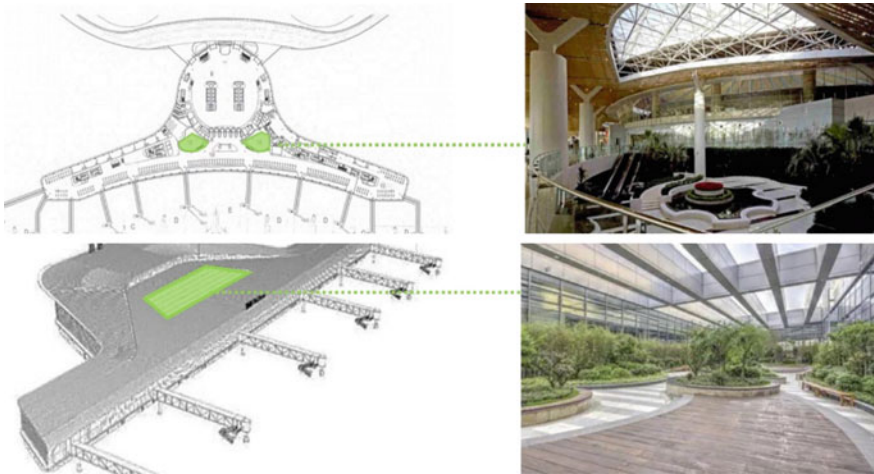


Fig. 10 Building carbon sink system

5 Conclusion

The low-carbon design of the regional airport terminal needs to be grasped from three stages: production and transportation of building materials, construction and demolition, and building operation.

During the production and transportation stages of building materials, the consumption of main building materials can be reduced by adopting modular and expandable systems, digital models for full process control; The use of low carbon emission factor and recyclable building materials can reduce the carbon emission factor of building materials; The average transportation distance of building materials can be reduced by using local building materials; The carbon emission factor per unit weight transportation distance can be reduced through lightweight structure.

During the construction and demolition stages, the use of prefabricated buildings can reduce carbon emissions during the construction stage, and the reuse of existing buildings can reduce carbon emissions during the demolition stage.

During the construction operation stage, adopting passive energy-saving technologies such as natural lighting and ventilation can reduce the carbon emissions generated by the use of energy; The use of renewable energy reduces the carbon emission factor of energy; Carbon sequestration can be increased by increasing green space in buildings.

References

1. Juan Y, Borong L, Yanxiang H et al (2016) Investigation and actual measurement analysis on energy consumption and indoor environmental quality of china's terminal buildings. *Journal of Tsinghua University: Natural Science Edition*
2. GB/T51366–2019 (2019) Calculation standard for building carbon emission. China Construction Industry Press, Beijing; De Lillo F, Cecconi F, Lacorata G, Vulpiani A, *EPL* 84 (2008)
3. Pervez H, Ali Y, Petrillo A (2021) A quantitative assessment of greenhouse gas (GHG) emissions from conventional and modular construction: a case of developing country. *J Clean Prod* 294:126210
4. Hongpeng X, Kaiwen L, Zherui L (2021) Carbon emission analysis of passive wooden structures in severe cold regions based on type comparison. *Build Tech* 52(03):324–328
5. Ying Z (2018) Do “bamboo” articles and create a good “bamboo” meaning. *Fujian Daily*, August 2nd (9)
6. Yiqun P, Jinjie W, Yumin L et al (2022) Evaluation of carbon emission reduction potential of green building energy conservation technology in typical public building operations. *HVAC* 52(04):83–89
7. Pengfei S, Xiangyang R, Lijun S, Zhengwu Y, Xichen L (2019) Airport airlines case study on energy consumption composition characteristics of station buildings. *HVAC* 49(06):63–67
8. Beijing Municipal Development and Reform Commission (2019) Beijing municipality issued the implementation opinions on further accelerating the application of heat pump systems to promote clean heating. *Constr Tech* 6(2)
9. Min W, Wen Z (2021) The path and spatial characteristics of urban green space affecting carbon neutrality: a case study of Huangpu District Shanghai. *Landsc Arch* 38(10):11–18

Hydraulic Engineering and Flood Control

Coupled Hydrologic-Hydraulic Modeling-Based Flood Inundation Mapping for a Segment of the Tullahan River in Valenzuela City, Philippines



Hiyasmine S. Pili, Franz D. Santos, Charena P. Baluyot,
Kyla M. Manzanade, and Yunika Aloha P. Cruz

Abstract Anthropogenic activities brought about by accelerated urban expansion trigger changes in the hydrologic response of watersheds. The Philippines, being prone to the occurrence of extreme weather events and urban development, has experienced more frequent and more devastating floods that have caused damage to life and property throughout the years. Thus, the need for modern approaches to disaster risk and preparedness is essential to lessen the extent of damage that flood events bring to communities. This study was conducted to exhibit the capability of using a coupled hydrologic and hydraulic model to produce a flood inundation map for a segment of the Tullahan River in Valenzuela City, Philippines. A hydrology model was set up and calibrated using the Hydraulic Engineering Center Hydrologic Modeling System (HEC-HMS), and simulations show that the peak discharge for the 10-year and 100-year return periods ranges from 11.88 cubic meters per second (cms) up to 23.48 cms. Based on the produced flood inundation map using Hydrologic Engineering Center-River Analysis System (HEC-RAS), the maximum flood depths reach up to 2.91 m, and the inundated area covered 0.9419 km² for a storm with a 100-year return period which occurred close to the banks of the river at mid-stream. The findings of this study could help local planners in promoting the use of modern tools, such as computer models, in disaster-risk preparedness toward resilient communities.

Keywords Flood inundation mapping · Hydrologic modeling · Hydraulic modeling · Tullahan river

H. S. Pili · F. D. Santos (✉) · C. P. Baluyot · K. M. Manzanade · Y. A. P. Cruz
Department of Civil Engineering, National University, 1008 Manila, Philippines
e-mail: fdsantos@national-u.edu.ph

© The Author(s), under exclusive license to Springer Nature Singapore Pte Ltd. 2024
M. Casini (ed.), *Proceedings of the 3rd International Civil Engineering and Architecture Conference*, Lecture Notes in Civil Engineering 389,
https://doi.org/10.1007/978-981-99-6368-3_53

1 Introduction

Global warming is the world's most dangerous environmental challenge [1]. Scientists and professionals are interested in extreme events, including heat waves, widespread flooding, and extremely violent storms, because of their potential to create significant harm and repercussions on people, infrastructure, and the environment [2]. As a result of global warming, extreme meteorological events occur more frequently [3]. Rainfall patterns have changed because of global warming, resulting in floods or drought that varies from place to place [4].

Floods are the most common and widespread catastrophic natural disaster, affecting many people worldwide [5]. Flooding is usually brought on by frequent typhoons and heavy rains [6] and it is also the world's most costly type of natural hazard in terms of economic losses and fatalities [7]. Moreover, flood-related damages can be severe and could impact human health, both infectious and noninfectious [8].

The Philippines is at risk of typhoons commonly occurring in the Northwest Pacific because of its geographic location and socio-economic conditions [9]. Each year, approximately 20 typhoons occur in the coastal area, equal to 25% of all identical events throughout the world. Additionally, 856 tropical cyclones entered Philippine waters from 1970 to 2013, and 322 were destructive [10]. Typhoon damage is defined through three interconnected factors including wind speed, floods, extreme rainfall, or storm surge [11]. With the country being more vulnerable to typhoons but also has limited capability for response due to lack of resources, proper planning toward disaster preparedness is essential.

One of the most common and hazardous natural disasters, inflicting significant damage to property and causing many fatalities, is floods. From a continental perspective, Asia experiences the most floods and has the largest flood-affected population [12]. Since the Philippines is in a part of the Pacific Ring of Fire, natural disasters and risks are common events where catastrophic typhoons originated, making them vulnerable to typhoons, floods, earthquakes, storm surges, and tsunamis [13]. Furthermore, it experiences an average of 20 typhoons yearly, with severity ranging from moderate to extreme events [14].

According to [15], the various disasters and extreme events pose different health hazards, such as waterborne and vector-borne disease. Waterborne diseases are typically spread by water ingestion and are closely related to drinking water quality. Diarrheal illnesses, cholera, shigella, typhoid, hepatitis A and E, and poliomyelitis are significant waterborne illnesses [16]. Leptospirosis, another waterborne disease, can be developed by contacting an open wound and contaminated water, such as rat urine [15]. The water caused by heavy rains and flooding is the breeding site of mosquitos carrying vector-borne diseases such as dengue, malaria, chikungunya, and Zika [17]. Moreover, severe flooding causes loss of livelihood, property damage, and fatalities [18]. Since floods pose a threat to public health, the use of tools for its prediction and mitigation is deemed necessary for flood-prone communities around the world.

Hydrological models are essential for studying water resource changes and simulating the water cycle. Real-world observations are used to choose model parameters as part of a calibration process to produce realistic model simulation results [19]. Different software was utilized to produce the best model near to reality, including the Geographic Information System (ArcGIS) and The Hydrologic Modeling System (HEC-HMS). ArcGIS is a software tool used for analyzing maps, geographic data, and spatial analysis [20]. After mapping the study area using the ArcGIS software, it is now possible to proceed with the hydrologic modeling using the HEC-HMS software to produce the discharge and precipitation-runoff processes [21].

According to [22], it has become crucial to estimate the amounts of runoff by knowing the amounts of rainfall to determine the necessary water storage in reservoirs and to predict the possibility of floods. The topography and surface features of the modeled region were considered while using the HEC-HMS program to convert the rainfall data into the direct flow (e.g., length of the reach). The runoff computation in the software also considers routing, loss, and flow transformation. The data were verified, and the HEC-HMS model was constructed, producing files for the basin, the meteorological model, and several HEC-HMS parameters.

When predicting and issuing a flood warning, the river stage and discharge are considered variables. Among the many hydraulic factors, the roughness coefficient (also known as Manning's) is crucial, particularly in hydraulic modeling [23]. The Hydrologic Engineering Center-River Analysis System (HEC-RAS) model was created by the US Army Corps of Engineers and can be utilized to simulate flood development in either one or two dimensions. It offers four primary river study options: the steady flow rate in a river profile, simulation of an unsteady flow of water, calculations of the sediment transport and modifications of the riverbed and water quality analysis [24].

A study [25] used HEC-RAS and ArcGIS for floodplain mappings. This study has a flood model containing hydrologic, hydraulic, flood-plain mapping tools, and geospatial extraction. The digital elevation model (DEM) used data from Interferometric Synthetic Aperture Radar (ISFAR) helped create 2D models for processing the outcome of flood progression since it contains terrain elevation parameters, while the HEC-RAS modeling setup was generated to produce the floodwater level and simulate flood-inundated areas across different return times.

Having mentioned the risk of exposure of the Philippines to typhoon events, flooding as a result of urbanization, and the need for modern tools in the prediction and mitigation of flood events, this paper aimed to exhibit the use of a coupled hydrology and hydraulic model to capture the extent of flooding through inundation maps along a segment of the Tullahan River in Valenzuela Philippines, one of the flood prone areas in the country.

2 Materials and Methods

2.1 The Study Area

The City of Valenzuela, a part of the third district of Metro Manila (i.e. CAMANAVA), often known as the “Gateway to the North,” is one of the progressive places that transformed from being a bucolic town into a bustling city [26]. A highly urbanized, wealthy industrial and residential suburb in a low-lying location surrounded by the Tullahan, Polo, and Meycauyan rivers. Currently, it is known as the 13th most populous city among 144 cities in the Philippines, with an area of 47.02 square kilometers or 18.15 square miles [27]. As recorded by the Philippine Statistics Authority (PSA), the city has a population of 714,978, representing 5.30% total population of the National Capital Region as determined during the 2020 census. Shown in Fig. 1 is the administrative boundary of the Philippines highlighting Valenzuela City, the site of interest of this paper. According to [28], the City of Valenzuela seems to be at risk of natural calamities like flooding, earthquakes, liquefaction, and tsunamis. One of the most common problems the city experiences is flooding due to the average elevation of the city being just 2 m above sea level. Approximately 13.22% of the city is made up of tidal flats with unstable soil and low-lying topography. Moreover, the number of low-income families and informal settlers is still rapidly growing; thus, urban catastrophes like fires and flooding are typical.

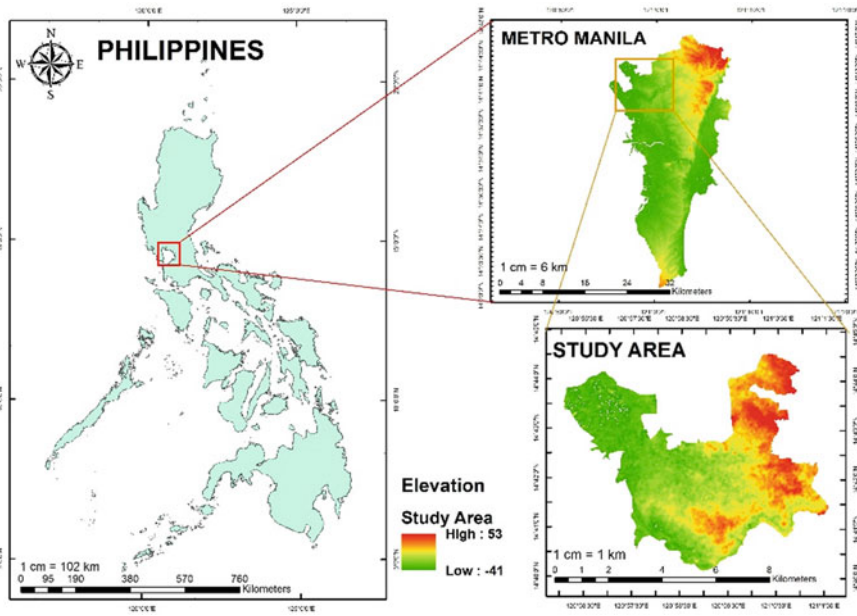


Fig. 1 Valenzuela City, Metro Manila

Table 1 Data sets used for the study

Type	Data	Purpose	Source
Spatial information	Digital topography (DEM)	Delineation of watershed	USGS
	Land use/land cover map	Curve number and manning's roughness determination	ESRI
Meteorologic data	Rainfall	Model input for rainfall-runoff simulation	PAGASA
River data	Discharge	Calibration and validation of hydrology model	DPWH

2.2 Data for Modeling

For this study, a coupled hydrology and hydraulic model were utilized to produce flood inundation maps and capture the flooding extent for a segment of the Tullahan River in Valenzuela City, Philippines. Enumerated in Table 1 are the data that were necessary to meet this objective.

Data gathering was done by requesting secondary data from government agencies and open-source websites while other model inputs were derived from these initial data sets. The digital topography of Valenzuela City was downloaded from EarthExplorer of the United States Geologic Survey (USGS) while the Land Use/Land Cover Map was downloaded from the website of ESRI. In setting up the hydrology model, the daily precipitation as well as the Rainfall Intensity Duration Frequency (RIDF) data was acquired from the Philippine Atmospheric Geophysical and Astronomical Services Administration (PAGASA). To ensure realistic model behavior [19], actual observed discharges that was used for calibration was acquired from the streamflow website of the Department of Public Works and Highways (DPWH).

2.3 Methodology

To achieve the objectives of this study, modeling and simulation was the general method utilized. Depicted in Fig. 2 is the general flow of the study.

The DEM was first delineated using ArcGIS to capture the watershed boundary and generate the watershed properties such as drainage area, curve number, and identify the watershed outlet. The delineated watershed was then used for hydrologic modeling in HEC-HMS to set-up the rainfall-runoff parameters to produce calibrated discharges which will then be used as an input for the hydraulic model. HEC-RAS was used to model the hydraulic behavior of the Tullahan River and produce flood inundation maps of the study area.

Watershed Delineation Using ArcGIS. The watershed containing the segment of the Tullahan river that runs from upstream Marulas up to the downstream in Malinta in Valenzuela City was delineated in ArcGIS. The digital terrain was processed to

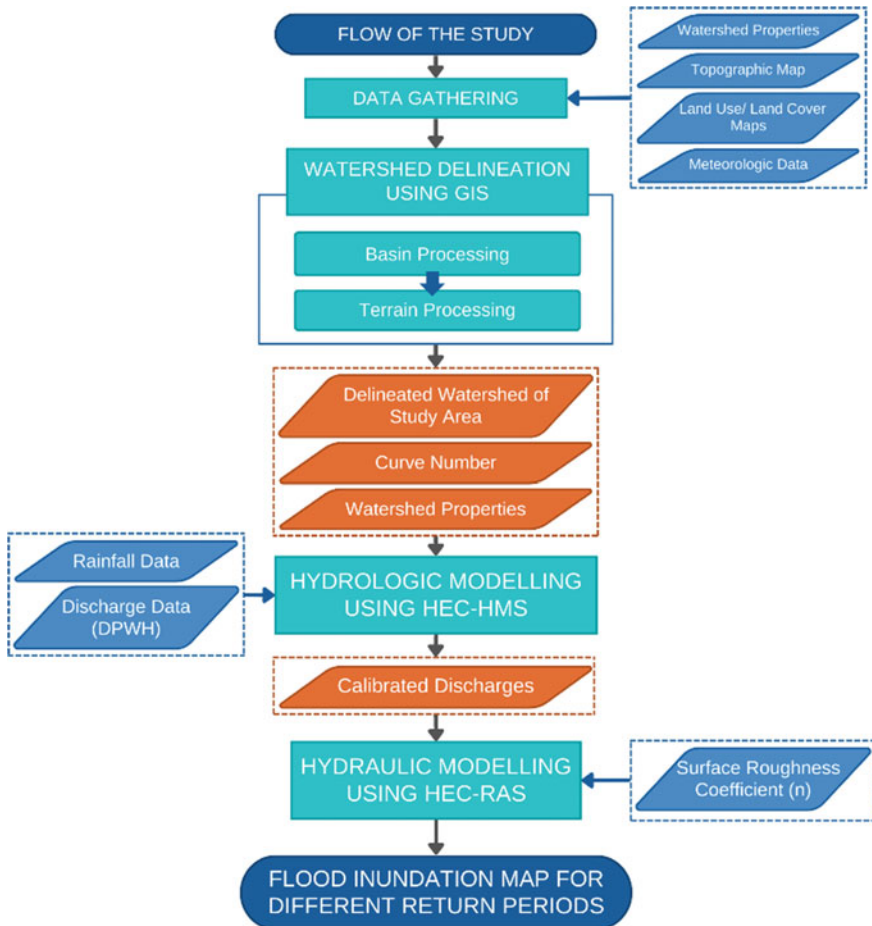


Fig. 2 Flow of study showing the data, models, and processes used

yield the hydrologic elements that will be necessary in representing the behavior of the study area [29].

Hydrology Modeling Using HEC-HMS. Hydraulic Engineering Center—Hydrologic Modeling System (HEC-HMS) is a software developed by the US Army Corps of Engineers for representing the rainfall-runoff process in a watershed [30]. The delineated watershed from ArcGIS was imported to HEC-HMS to assign parameters based on the different hydrologic processes.

Calibration of Hydrology Model. Calibration of the chosen was done to ensure a realistic model behavior [19]. The simulated discharges from the model were compared to observed data from DPWH for the period of October 26 to November 21, 2017. Model acceptability was based on statistical parameter of the Nash–Sutcliffe

Table 2 Model performance based on statistical rating [31]

Performance rating	NSE	PBIAS (%)
Very good	$0.75 < \text{NSE} \leq 1.0$	$\text{PBIAS} \leq \pm 15$
Good	$0.65 < \text{NSE} \leq 0.75$	$\pm 15 \leq \text{PBIAS} \leq \pm 30$
Satisfactory	$0.50 < \text{NSE} \leq 0.65$	$\pm 30 \leq \text{PBIAS} \leq \pm 55$
Unsatisfactory	$\text{NSE} \geq 1.0$	$\text{PBIAS} \geq \pm 30$

Efficiency (NSE) and Percent Bias (PBIAS). Shown in Table 2 is the general performance rating that was used in assessing model acceptability based on the study of [31].

After reaching a satisfactory model behavior, RIDF from PAGASA was used to simulate a frequency storm to produce discharges for a 10, 25, 50, and 100-year return period. These discharges were used as input in the hydraulic model to generate the flood inundation maps for the study area.

Hydraulic Modeling using HEC-RAS. Hydraulic Engineering Center—River Analysis System (HEC-RAS) is another software developed by the US Army Corps of Engineers. It is capable of performing one-dimensional steady flow hydraulics as well as one and two-dimensional unsteady river hydraulics [32]. Flow hydrograph boundary condition was utilized for the upstream, while a normal depth boundary condition was used for downstream. Surface roughness (n) was adjusted based on land cover to get a good representation of the river behavior through calibration of the unsteady flow model [32]. A twenty-four-hour frequency storm (10, 25, 50, and 100-year return periods) was simulated and the resulting inundation areas were plotted on map to see the extent of flooding for the study area as the general objective of this study.

3 Result and Discussion

3.1 Watershed Delineation and Hydrology Model Calibration

A total of 52 subbasins were generated with a total drainage area of 4.182 km². The largest subbasin was found with an area of 203,210 m² while the smallest subbasin was recorded at 2809.3 m². The hydrology model of the study area underwent calibration process to ensure realistic model behavior by fine-tuning watershed parameters that were selected to represent the different hydrologic processes. Simulated discharges from the period of October 26 to November 21, 2017, were compared with observed DPWH discharges and acceptability was based on statistical parameters of NSE and PBIAS. Calibration hydrograph was also produced by HEC-HMS to show the behavior of the simulated discharges as compared to the observed data on field.

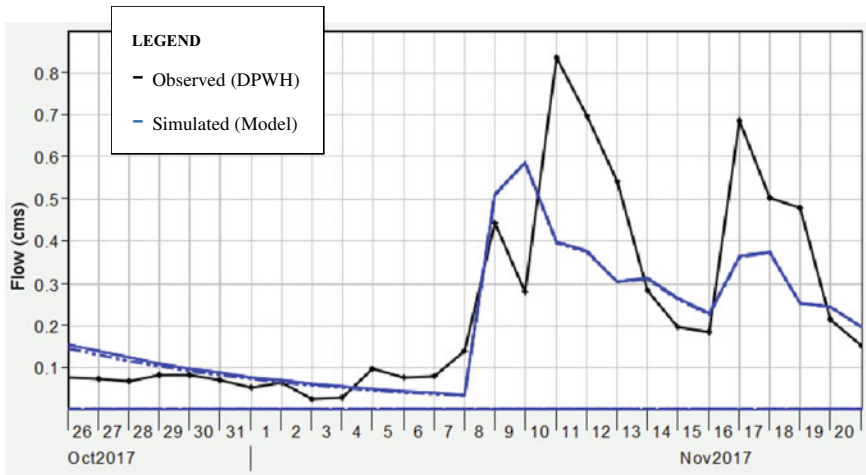


Fig. 3 Outlet hydrograph showing calibrated discharges imported from HEC-HMS

Shown in Fig. 3 is the outlet hydrograph from HEC-HMS for the watershed model after calibration process.

The Nash–Sutcliffe Efficiency is a statistical parameter that measures residual variance to the measured standard variance of data [33] while the goodness of the model that includes uncertainty measurement is described by the Percent Bias (PBIAS). The hydrology model showed an NSE of 0.536 and a PBIAS of -14.44% after the calibration of parameters. From the study of [31], the model exhibits a satisfactory performance based on the NSE and in terms of the PBIAS, it is rated as a good model.

The calibrated hydrology model was now used to simulate frequency storms corresponding to the 10, 25, 50, and 100-year return periods. Depicted in Fig. 4 are the outlet hydrographs for the different return periods that were simulated using a 24-h frequency storm in HEC-HMS. As shown by results of the simulation, peak discharge for the 10-year and 100-year return periods ranges from 11.88 cubic meters per second (cms) up to 23.48 cms. From these results, it is evident that the outlet discharge increases significantly as the rainfall intensity increases. The peak precipitation occurs at 12:10 p.m. and the peak discharge arrives about 4 h later (3:50 p.m. to 4:10 p.m.). The discharges from the frequency storm simulation were then used as boundary condition (input) for the hydraulic model in HEC-RAS.

3.2 Hydraulic Modeling Using HEC-RAS

The objective of this paper is to capture the extent of flooding through inundation maps along a segment of the Tullahan River in Valenzuela Philippines. A hydraulic

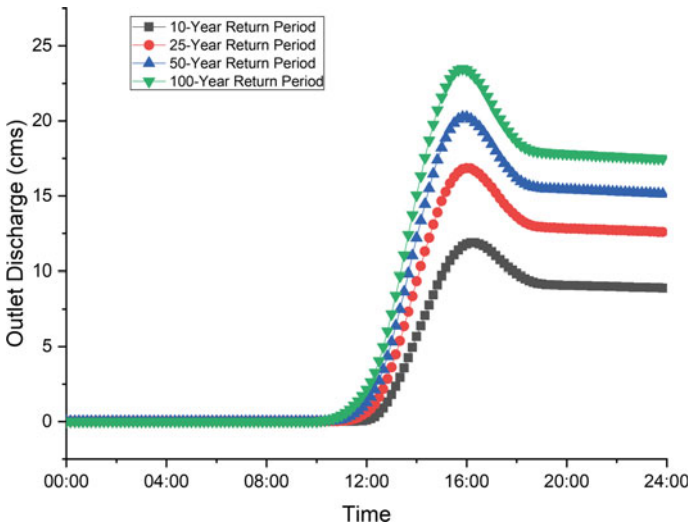


Fig. 4 Outlet hydrograph for watershed model after calibration

model was set-up using HEC-RAS and the calibrated discharge from the hydrology model were used as input for upstream boundary condition while the normal depth was used for downstream boundary condition. A twenty-four-hour frequency storm (10, 25, 50, and 100-year return period) was simulated to produce flood inundation maps. Shown in Fig. 5 are the generated flood inundation maps for the different return periods.

The inundation map depicts the extent of flooding of the study area as well as the flood depths for the corresponding return periods. Maximum flood depth for the 100-year return period was calculated to reach as high as 2.91 m that occurs at the middle of the reach that can be attributed to its topography and the noticeable river bend on that segment of the river. Table 3 summarizes the outputs from HEC-RAS in terms of maximum flood depths and estimated inundated areas corresponding to the return periods used.

Based on the outputs of the hydraulic model, the depth of flood and inundated area increases as the intensity of rainfall increases. An increase of 27.25% in maximum flood depth and 34.56% increase in the total inundated area can be seen when comparing the results for a 50-year and a 100-year return period. Taking note from simulation results of the hydrology model that the time to peak is approximately four hours, these simulation results would be of aid to disaster management offices in their planning for instances of extreme weather events.

Results of this study could further be improved by using a better resolution of digital topography in modeling the hydrology of the area and as suggested by [34], to achieve high-accuracy models for flood hazard maps, it is recommended to use actual values of river discharge as input to the hydraulic model as compared to simulated discharges.

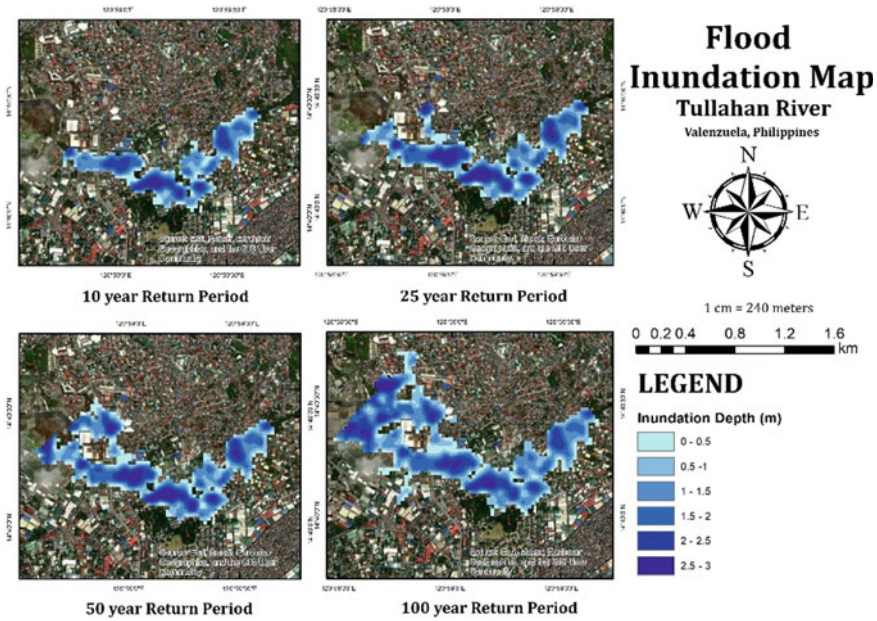


Fig. 5 Flood inundation map output from HEC-RAS

Table 3 Summary of calculated flood depths and flood inundated area

Return period	Max. Flood depth (m)	Estimated inundated area (km ²)
10-year	2.08	0.4492
25-year	2.19	0.5774
50-year	2.29	0.7002
100-year	2.91	0.9419

4 Conclusion

In this study, a coupled hydrologic and hydraulic model was used to produce flood inundation maps to assess the extent of flooding for a segment of the Tullahan River in Valenzuela City, Philippines.

Results from the calibrated hydrology model simulation indicate that the peak discharges range from 11.88 cms reaching up to 23.48 cms during a 100-year return period storm. The time of peak was also estimated to arrive 4 h after the maximum precipitation based from frequency storm generated discharges.

From the produced flood inundation map, it was found that areas close to the riverbanks were more prone to flooding having maximum flood depths of 2.08, 2.19, 2.29, and 2.91 m for the 10, 25, 50, and 100-year return periods, respectively. Flood levels are also found to be greater at the bend of the river midstream as compared to

upstream which can be attributed to the topography but in terms of flood inundated area, the flood water spreads after the bend thus causing a greater area affected downstream.

With flood events worsening over the years due to the changing climate, rapid urban development, and disruption of the natural hydrologic response of watersheds, modern tools such as computer models are now found to be useful in generating decision support information towards community resilience. Findings of this study could help planners and policy makers in disaster-risk response and management of areas that are prone to flooding. Moreover, results generated from this paper could still be improved by using a higher resolution digital topography and validating the hydraulic model by comparing it to observed data of water level from local agencies.

Acknowledgements The proponents would like to acknowledge government agencies who were generous in giving access to the data, The Philippine Atmospheric, Geophysical and Astronomical Services Administration (PAGASA) for the rainfall data and The Department of Public Works and Highways (DPWH) for their open-access streamflow data. Lastly, the proponents also would like to thank National University—Manila particularly the Research and Development (NURD) Office for their support in this research undertaking.

References

1. Bayeh B, Alemayehu M (2019) Scientific community debates on causes and consequences of global warming: review. *J Agric Environ Sci* 4(1)
2. McPhillips LE et al (2018) Defining extreme events: a cross-disciplinary review. *Earths Future* 6(3):441–455. <https://doi.org/10.1002/2017EF000686>
3. Liu G, Li X, Wang J, Kou Y, Wang X (2020) Research on the statistical characteristics of typhoon frequency. *Ocean Eng* 209. <https://doi.org/10.1016/j.oceaneng.2020.107489>
4. Yadollahie M (2019) The flood in Iran: a consequence of the global warming? *Int J Occupat Environ Med* 10(2):54–56. NIOC Health Organization. <https://doi.org/10.15171/ijoom.2019.1681>
5. Mignot E, Li X, Dewals B (2019) Experimental modelling of urban flooding: a review. *J Hydrol* 568:334–342. <https://doi.org/10.1016/j.jhydrol.2018.11.001>
6. Cabrera JS, Lee HS (2019) Flood-prone area assessment using GIS-based multi-criteria analysis: a case study in Davao Oriental, Philippines. *Water (Switzerland)* 11(11). <https://doi.org/10.3390/w11112203>
7. Nogueira K et al (2018) Exploiting ConvNet diversity for flooding identification. *IEEE Geosci Remote Sens Lett* 15(9):1446–1450. <https://doi.org/10.1109/LGRS.2018.2845549>
8. Dayrit JF, Bantanjoyo L, Andersen LK, Davis MDP (2018) Impact of climate change on dermatological conditions related to flooding: update from the international society of dermatology climate change committee. *Int J Dermatol* 57(8), 901–910. <https://doi.org/10.1111/ijd.13901>
9. Gray J, Lloyd S, Healey S, Opdyke A (2022) Urban and rural patterns of typhoon mortality in the Philippines. *Prog Disaster Sci* 14. <https://doi.org/10.1016/j.pdisas.2022.100234>
10. Holden WN, Marshall SJ (2018) Climate change and typhoons in the philippines: extreme weather events in the Anthropocene. In: *Integrating disaster science and management: global case studies in mitigation and recovery*, Elsevier, pp 407–421. <https://doi.org/10.1016/B978-0-12-812056-9.00024-5>
11. Strobl E (2019) The impact of typhoons on economic activity in the Philippines: evidence from nightlight intensity (EWP No. 589). <https://doi.org/10.22617/WPS190278-2>

12. Hu P, Zhang Q, Shi P, Chen B, Fang J (2018) Flood-induced mortality across the globe: spatiotemporal pattern and influencing factors. *Sci Total Environ* 643:171–182. <https://doi.org/10.1016/j.scitotenv.2018.06.197>
13. Cabrera JS, Lee HS (2020) Flood risk assessment for Davao oriental in the Philippines using geographic information system-based multi-criteria analysis and the maximum entropy model. *J Flood Risk Manag* 13(2). <https://doi.org/10.1111/jfr3.12607>
14. Stephenson V, Finlayson A, Morel LM (2018) A risk-based approach to shelter resilience following flood and typhoon damage in rural Philippines. *Geosciences (Switzerland)* 8(2). <https://doi.org/10.3390/geosciences8020076>
15. Clamor WL, Lamberte E, Demeterio FP, Tanhueco RM, Regadio C (2020) The state of health in flood-prone areas in the Philippines: the case on the cities of Iligan and Cagayan de Oro. *J Hum Behav Soc Environ* 30(6):797–808. <https://doi.org/10.1080/10911359.2020.1757008>
16. Cissé G (2016) Food-borne and water-borne diseases under climate change in low- and middle-income countries: further efforts needed for reducing environmental health exposure risks. *Acta Tropica* 194:181–188. <https://doi.org/10.1016/j.actatropica.2019.03.012>
17. Chowell G, Mizumoto K, Banda JM, Poccia S, Perrings C (2019) Assessing the potential impact of vector-borne disease transmission following heavy rainfall events: a mathematical framework. *Philosoph Trans Royal Soc B: Biol Sci* 374:1775. <https://doi.org/10.1098/rstb.2018.0272>
18. Alcantara JC, Christopher J (2019) Briefing note regional fellowship program overview of the societal impacts of floods in the Philippines
19. Mostafaie EF, Safari A, Schumacher M (2018) Comparing multi-objective optimization techniques to calibrate a conceptual hydrological model using in situ runoff and daily GRACE data. *Comput Geosci* 22(3):789–814. <https://doi.org/10.1007/s10596-018-9726-8>
20. Arifjanov SA, Akhmedov I, Atakulov D (2019) Evaluation of deformation procedure in waterbed of rivers. In: *IOP Conference Series: Earth and Environmental Science*, vol 403, no 1. <https://doi.org/10.1088/1755-1315/403/1/012155>
21. Al-Mukhtar M, Al-Yaseen F (2019) Modeling water quality parameters using data-driven models, a case study Abu-Ziriq marsh in south of Iraq. *Hydrology* 6(1). <https://doi.org/10.3390/hydrology6010021>
22. Hamdan NA, Almukhtar S, Scholz M (2021) Rainfall-runoff modeling using the hec-hms model for the al-adhaim river catchment, northern Iraq. *Hydrology* 8(2). <https://doi.org/10.3390/hydrology8020058>.
23. Abbas SA, Al-Aboodi AH, Ibrahim HT (2020) Identification of manning’s coefficient using HEC-RAS model: upstream Al-amarah barrage. *J Eng (UK)*. <https://doi.org/10.1155/2020/6450825>
24. Marimin NA, Razi MAM, Ahmad MA, Adnan MS, Rahmat SN (2018) HEC-RAS hydraulic model for floodplain area in Semborong River. *Int J Integrated Eng* 10(2):151–157. <https://doi.org/10.30880/ijie.2018.10.02.029>
25. Romali NS, Yusop Z, Ismail AZ (2018) Application of HEC-RAS and Arc GIS for floodplain mapping in Segamat town, Malaysia. *Int J Geomate* 15(47):7–13. <https://doi.org/10.21660/2018.47.3656>
26. ECOLOGICAL_PROFILE_2021
27. Patrocina M, Mateo LC (2015) Inside Stories on climate compatible development Inside Stories on climate compatible development Building resilience to climate change locally: the case of Valenzuela City, Metro Manila Authors
28. Rei J et al Assessment of Valenzuela City’s resilience in times of disaster using the ten essentials for making cities resilient toolkit recycled concrete aggregates view project carbon fiber reinforced polymer view project assessment of valenzuela city’s resilience in times of disaster using the ten essentials for making cities resilient toolkit. <https://doi.org/10.13140/RG.2.2.21662.15689>
29. Santos FD, Sablan KAD, Gonzales KAD, Gonzales WE (2021) Assessment of the impact of changing land use and land cover on the peak discharges of a tropical watershed: a study of the Davao River Basin. In: *IOP conference series: earth and environmental science*, vol 822, no 1. <https://doi.org/10.1088/1755-1315/822/1/012018>

30. Feldman (2000) Hydrologic modeling system technical reference manual. Hydrologic modeling system HEC-HMS technical reference manual, no. March, p 148
31. Moriasi DN, Gitau MW, Pai N, Daggupati P (2015) Hydrologic and water quality models: Performance measures and evaluation criteria. *Trans ASABE* 58(6):1763–1785. <https://doi.org/10.13031/trans.58.10715>
32. HEC-RAS River Analysis System User's Manual (2016). [Online]. Available: www.hec.usace.army.mil
33. Nash EI, J'tcliff SI River flow forecasting Throigh conceptual models part i-a disclission of principles*
34. Lagmay MF, Paringit EC (2015) Flood forecasting and flood hazard mapping for Mandulog River Basin, disaster risk exposure and assessment for mitigation (DREAM), DOST grants-in-aid program, vol 56

Modeling of the Submersible Plate System to Counteract Erosion in the Huallaga River, Case: Yurimaguas—Loreto



Amanda Giron, Stefano Rottiers, and Mitchel Jara

Abstract At present, the lack of optimal riparian defense systems in the Peruvian Amazonian rivers has allowed the occurrence of natural disasters. The main objective of this report is to model different alternatives of plate batteries and simulate in IBER with flow rates and bathymetry of the area to find the most optimal alternative. The HEC-HMS software was also used to obtain the maximum flood flows for return periods of 25, 50, 100, 100, 200 and 500 years for use in IBER, which allows hydrodynamic simulations of rivers and watercourses, calculating floods and delimiting zones. The simulations were performed with the 200-year return flow, 21,749.6 m³/s. For this research 3 simulations were performed, which were divided into 3 different distributions of plate batteries, these in turn were divided into 2 different angles of attack. As the most relevant results, according to the distributions of water velocity, bottom stress, specific flow and erosion along the channel, and considering that the maximum values are far from the margin to be protected, the alternative distributions of the battery of plates that gave the best results in the channel were alternatives 1 and 3. Finally, it is concluded that the most optimal alternative and angle of attack is alternative 1 and the angle of 20°, thus counteracting erosion. Therefore, with the support of ANSYS software, the same conclusion was reached as for alternative 1, but with an angle of 25°, so that the optimal angles are 20–25 degrees.

Keywords Erosion · Submerged vanes · IBER software · Angles of attack · Amazon rivers

A. Giron · S. Rottiers · M. Jara (✉)
Civil Engineering, Universidad Peruana de Ciencias Aplicadas, Lima 15023, Perú
e-mail: pccinjar@upc.edu.pe

A. Giron
e-mail: u201715663@upc.edu.pe

S. Rottiers
e-mail: u201714850@upc.edu.pe

1 Introduction

At present, the high number of river flooding events coupled with the lack of optimal river defense systems, clogged riverbeds, insufficient and/or non-existent vegetation cover on riverbanks, among other factors, have allowed natural disasters to cause damage and/or collapse of houses, loss of agricultural land and damage to infrastructure, even threatening the lives of people in the Amazonian areas of the country.

Erosion is understood as the removal, transport and deposition of soil particles, organic matter, and soluble nutrients as a natural phenomenon. It occurs with varying degrees of intensity and gradually. This phenomenon is caused by active factors such as magnitude, duration of discharge, flow velocity and shear stress; similarly. However, biological factors such as root strength and vegetation function as stabilizers [1]. Erosion is produced by turbulent flow, which is one of the most important characteristics of the flow pattern in bends. Affecting several other fluvial processes, including sediment transport, bed morphology and natural channel shape [2].

To modify the secondary flow in the river bends, the implementation of submersible plates was proposed. These have the function of redistributing sediment within the channel cross section and, consequently, reducing scour at the bends [3]. Submersible plates are small structures designed to modify the flow pattern. These structures are installed on a riverbed at an angle to the flow direction and change the flow pattern by producing a secondary rotation [4]. In recent years, submersible plates for riverbank protection have been increasingly used due to their quick and easy way of installation compared to other traditional methods such as dikes and groins [5]. As an environmentally friendly structure, submersible slabs are also designed to improve habitat. Several studies have been conducted on the plates. The effectiveness of the plates in reducing near-bank velocity considering different angles of attack was investigated [6]. In Colombia, 5 projects were carried out using submersible plates, which were Barrancabermeja, Sinu River in Trementino, Metica River, in Puerto Lopez, Sector 2, Cauca River, Guarumo Site and Cruce Puerto Rico—Ye de Granada Road. Where the authors demonstrated that there is sediment control and bank protection, they also show favorable effects on the environment, as well as cost reduction [7].

Marelius and Sinha, performed a detailed analysis of the flow field passing through submersible plates with a high angle of attack of approximately 40° . Were identified the crossflow of sediment transport. They determined that the maximum value is between 36 and 45° . The use of a small plate length (or height) can also result in a small scour hole. They consider that the next step of their research would be to fully analyze the circulation force caused by the transverse velocity component [8]. The use of different angles of attack helps to redistribute sediment and decrease flow velocity. The research will seek to obtain optimal parameters for modeling different submersible plate battery systems in the Iber software, simulating with maximum flow rates, which will also find the levels of erosion, bottom stress, velocity, and flow rate.

2 Materials and Methods

2.1 Materials

The software used for the simulations were IBER [9] and HEC HMS [10]. IBER is a two-dimensional mathematical model which simulates free sheet flow in natural channels with preprocessing and post-processing, from which we are going to use the responses of velocity, bottom stress, erosion, and flow. The HEC HMS is a software designed to simulate the rainfall-runoff processes of a dendritic watershed system.

2.2 Basin in HEC HMS Software

In principle, to obtain the design flows, we proceeded to extract the rainfall from the San Ramon station of SENAMHI [11], ranging from 1969 to 2014, was extracted, we proceeded to perform the DOUBTFUL DATA TEST (using the Water Resources Council Method), from which it was determined that there were no doubtful data. After this, the goodness-of-fit test was performed in which, based on our critical delta calculated according to our amount of data and with a significance level of 5%, a comparison was made with the deltas calculated for each distribution. Concluding that the Log-Normal fit is the most appropriate. The Log-Normal adjustment was used to obtain the corrected maximum annual rainfall. Subsequently, the intensities and maximum precipitations were determined. From the intensities determined for the different return periods, the intensity- duration-frequency (IDF) graph can be obtained. Finally, to obtain the design hietograms for return periods of 25, 50, 100, 200 and 500 years.

Subsequently, to obtain the maximum flood flows, a hydrological simulation was carried out for the return periods with the help of the HEC- HMS software. For this purpose, input data such as the basin area, length of the main river, slope, curve number and rainfall hietograms were used. For the calculation of the curve number, the shapefile of vegetation cover and soil type of Peru provided by MINAN was used and together with the delimited watershed (Fig. 1) with the help of ArcMap, the map algebra calculations were performed to determine the curve number (CN) of our watershed. The result was a CN of 71.

2.3 Simulations in IBER Software

For the simulation in IBER software, the topobatimetry points of the area were first processed to fill the gaps in the topobatrimetry (Fig. 2) with the help of QGIS and SAGA GIS software.

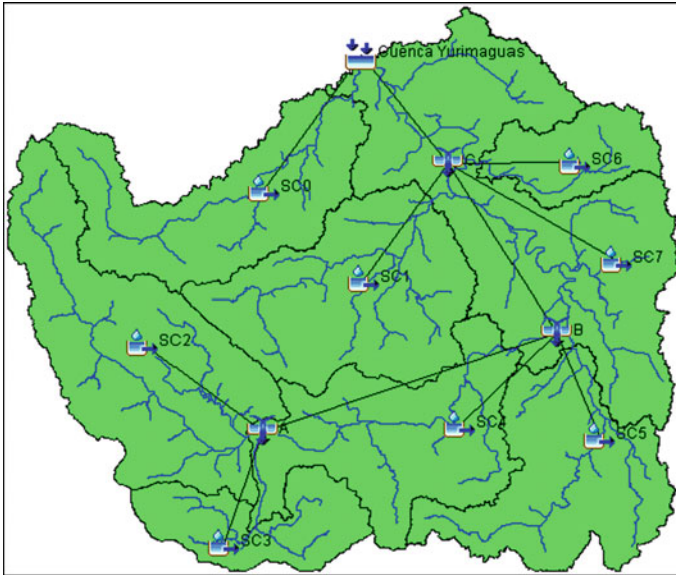


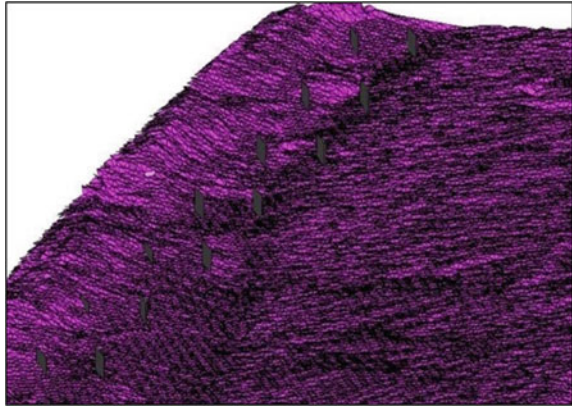
Fig. 1 The study basin is divided into 8 sub-basins



Fig. 2 Filling of topobathymetry gaps

With the topo-bathymetry of the area, which was delivered by the Water Research and Technology Center—UTECH [12], and already processed. It was entered into the IBER software (Fig. 3). For these simulations we used the input data for a return period of 200 years of inflow ($21,749.6\text{m}^3/\text{s}$), manning number (0.028), diameter of sediment in suspension (0.000015 mm).

Fig. 3 Topobatismetry of the area entered in IBER



For the design of the plates, the design guidelines of the book “River Training and Sediment Management with Submerged Vanes” by Jacob Odgaard were followed. Having to use a plate height of 0.2 to 0.4 times the average depth(d_0), a plate thickness of 0.05 to 0.20 m, a plate length and lateral spacing between plates of up to 3 times the plate height, a spacing between plate groups of 10 to 30 times the plate height, a distance from bank to plate of up to 3 times the plate height and an angle of attack of 10 to 20 degrees.

The geometry of the plates was made in plan with the hollows tool of the IBER software. Based on the design indications given by Jacob Odgaard in his book “River Training and Sediment Management with Submerged Vessels” (Fig. 5). Three alternatives (Table 1) of plate sizing were carried out.

Continuing with the simulations, 4 simulations were carried out, the three design alternatives with the flow values for the 200-year return period; the simulation without plates was also carried out for comparison (Fig. 4). The responses for comparison given by IBER will be the velocity, erosion, bottom stress and specific flow are found in the post process (Figs. 6, 7, 8 and 9).

Table 1 Sizing of plate batteries

Variable	Alter.1	Alter.2	Alter.3
Number of lates per group	2	1	3
Design flow depth	6.35	6.35	6.35
Plate height	6.5	6.5	6.5
Plate thickness	0.2	1.2	1
Plate length, L	20	20	20
Lateral separation δn	20	20	20
Longitudinal spacing δs	88	88	88
Distance to benchor tap δb	19.6	19.6	19.6
Angle of attack α	20	25	25

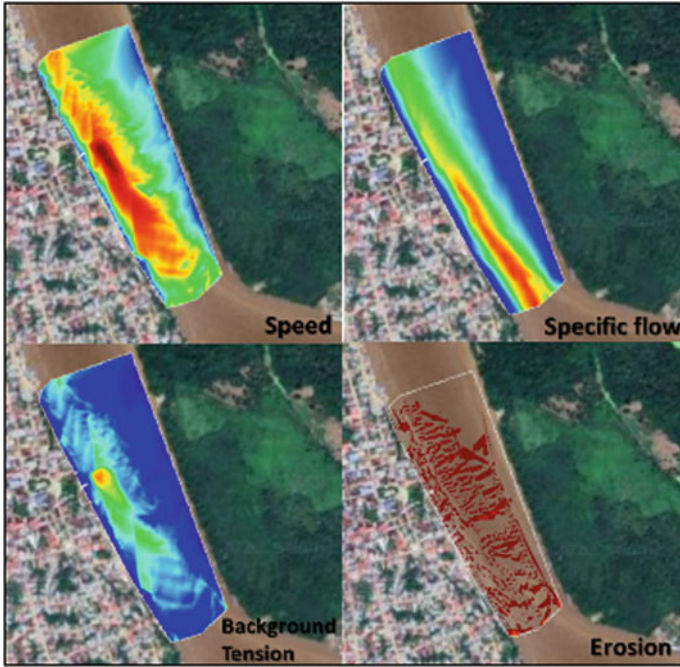


Fig. 4 IBER software answers from the river without plates

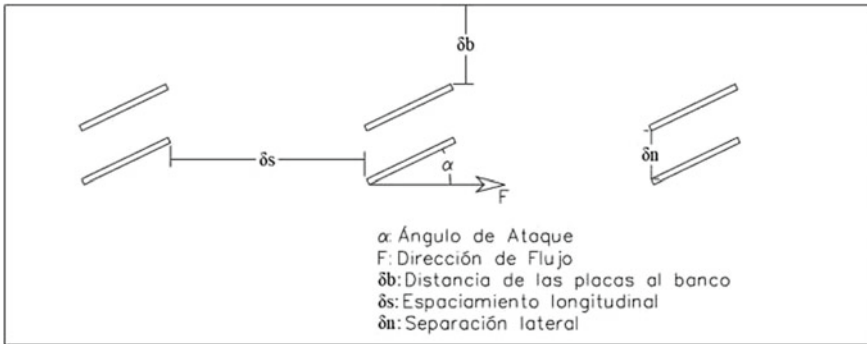


Fig. 5 Sizing of plate batteries

2.4 Simulation in ANSYS Software

On the other hand, simulations of submersible plates in a typical channel were carried out with the consideration of using different distribution alternatives (Fig. 10) and angle of attack of the plate array to complement the previous simulations carried out in IBER.

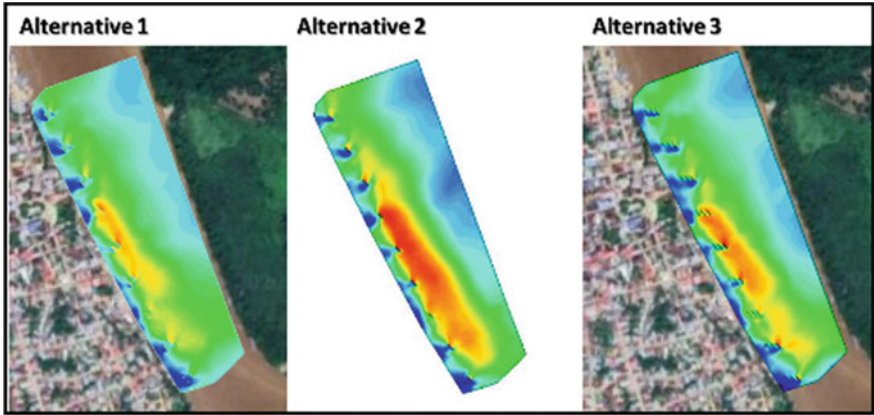


Fig. 6 Channel velocity of the 3 alternatives

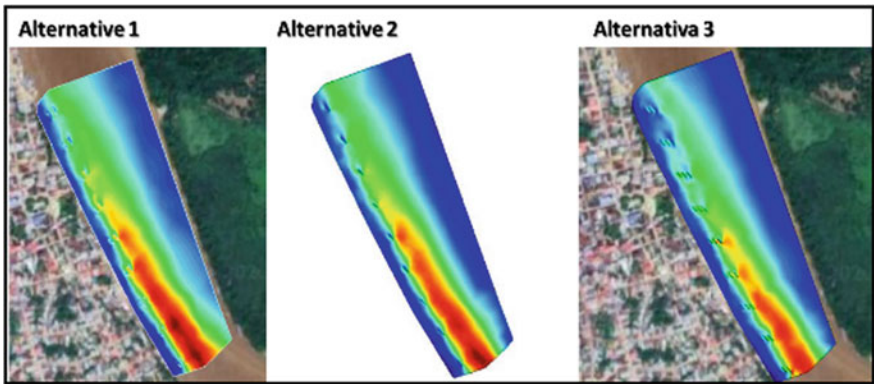


Fig. 7 Specific flow rate of the channel of the 3 alternatives

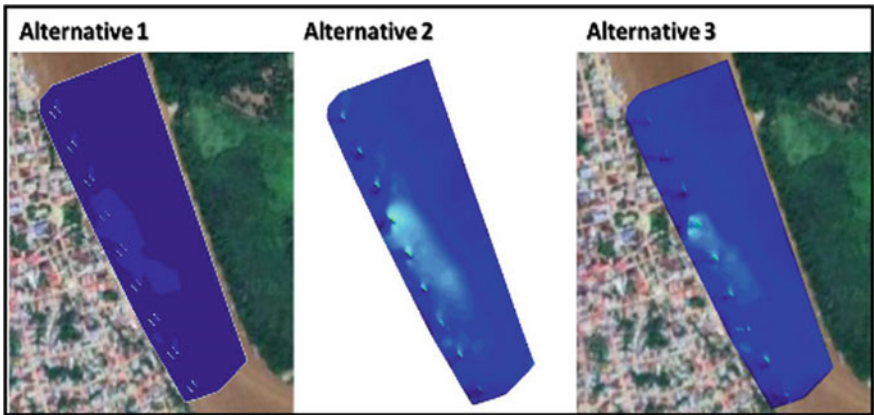


Fig. 8 Tension at the bottom of the channel for the 3 alternatives

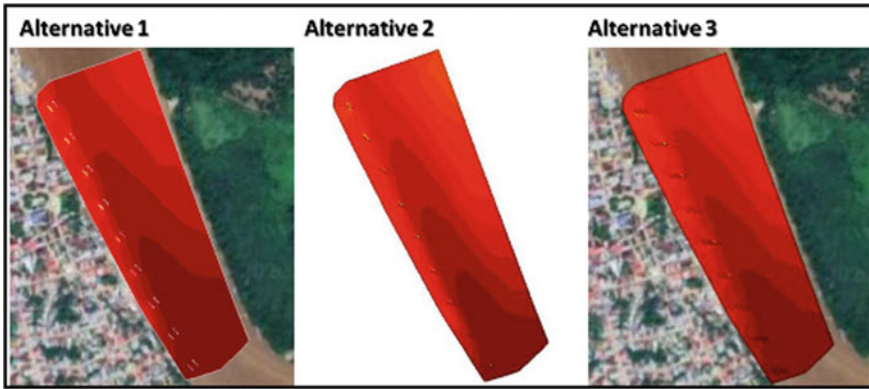


Fig. 9 Channel erosion of the 3 alternatives

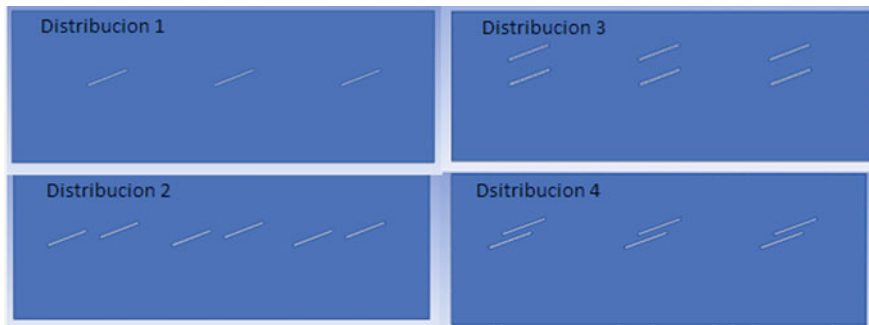


Fig. 10 The 4 distributions made in ANSYS

Once the 3 simulations were carried out, a comparative table of all the answers according to the alternatives was made. Since Iber gave us graphic results of erosion, bottom stress, specific flow, and velocity.

3 Results and Analysis

3.1 Iber Software Results

From the simulations performed at Iber we obtained the results shown in Table 2.

From the images obtained from the modeling in the Iber software (Fig. 11), it can be observed that the plates redirect the concentration of suspended sediments to the left bank of the river, thus counteracting the erosion produced by the river. Figure 8 shows that the velocity in the scenario without plates is more pronounced and closer

Table 2 Summary of maximum results obtained in IBER software

Alternatives	Speed m/s	Specific flow m ² /s	Tension of bottom N/m ²
Without plates	19.332	224.92	2659
Alternative 1	22.38	177.91	40,518
Alternative 2	19.057	187.91	4118.8
Alternative 3	20.479	197.87	4781.4

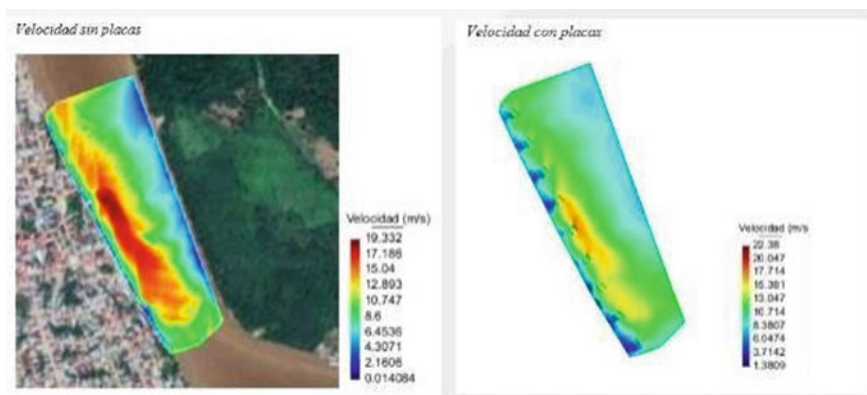


Fig. 11 Comparison of velocity scenarios for a return period 200

to the left bank, but with plates the velocity is less pronounced and farther from the left bank. Thus, the areas between the riverbank and the plates have a lower velocity.

3.2 Ansys Software Results

From the results obtained from the software (Table 3), considering only the results of the left side of the channel, since this is the margin to be protected, a graph was made comparing the different distributions and their corresponding angles of attack (Fig. 9). The best distributions are 1 and 3, in which the most favorable results for the protection of the left side of the channel are found with angles of attack ranging from 20° to 30°.

3.3 Discussion of IBER Software Results

According to the responses of the river without plates (Fig. 4), of velocity, flow, tension bottom, and erosion, we can observe the intensity of the velocity near the

Table 3 Summary of maximum results obtained with ANSYS software

Degree	Distribution1			Distribution2			Distribution3			Distribution4		
	Left	Center	Right	Left	Center	Right	Left	Center	Right	Left	Center	Right
20°	1.344	0.308	1.517	1.618	0.09	1.469	1.377	0.363	1.489	1.648	0.638	1.14
25°	1.237	0.581	1.33	1.657	0.693	1.548	1.391	0.541	1.484	1.697	0.745	1.473
30°	1.511	1.052	1.531	1.988	0.751	1.864	1.435	0.53	1.55	1.129	1.282	1.657
35°	1.713	1.352	1.12	1.643	0.912	1.46	1.482	0.658	1.521	1.609	0.564	1.86
40°	1.691	1.36	2.018	2.243	0.437	2.66	1.586	1.74	1.467	1.797	0.35	2.071
45°	1.599	1.862	2.147	1.548	0.592	2.349	1.521	0.954	2.224	2.047	1.723	3.283

left margin, the margin that we want to protect, so that alternative 1 (Fig. 11) can be observed as the velocity is better distributed and the intensity is lower and the left margin has lower velocities (Fig. 6). According to the specific flow rate, it can be observed that in the river without a plate the flow is more intense; however, there is a better distribution of the flow in alternative 3 (Fig. 7).

The bottom stress can be observed to be better distributed with plates of 1, 2 or 3 batteries (Fig. 8), since without plates the shear stress at the bottom of the channel is greater. Unlike the simulation without plates, the simulation with plates shows that there is no erosion, only sedimentation (Fig. 9).

3.4 Discussion of the Ansys Software Results

Each plate distribution has 6 simulations in ANSYS. For distribution 1, the 20, 25 and 30° plates have the lowest maximum velocities; in contrast, the 40 and 45° distributions have the highest values. On the other hand, the 40° (Fig. 13) and 35° have a better distribution of lower velocities according to their legend which would be an optimal choice. But the 45° angle (Fig. 12) in this case is detrimental to the margin to be protected since the highest velocity is on the left margin.

For the simulations of distribution 2, angles 20, 25 and 30° have lower maximum velocities compared to the other angles, but in this case the angle of 35° (Figs. 12 and 14) would be the most appropriate since it has a better distribution of velocities, and the maximum velocity is far from the margin to be protected. In the case of angles 25, 40 and 45° (Fig. 13), the highest concentration of velocities is found in the margin to be protected, which would not be convenient to have.

For the simulations of distribution 3 the angles 20, 25 and 30° have lower maximum velocity values. In this case the optimal angles would be 25 and 45° (Fig. 15) since they have a better distribution of the maximum velocities and the greatest concentration of velocity is away from the margin being protected.

For the simulations of distribution 4, angles 20°, 25° and 30° have lower maximum velocities, but with a less effective distribution since the highest velocity is found in the margin to be protected. A better distribution of lower velocities is in the angles

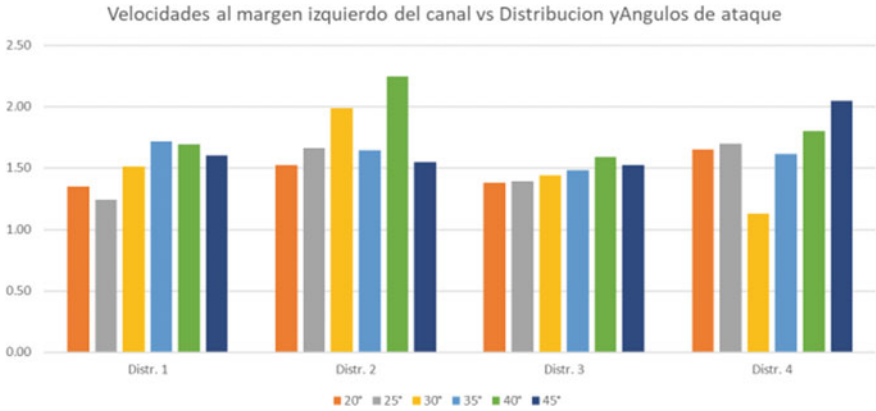


Fig. 12 Velocity at left channel margin versus distribution and angle of attack. Velocities in the left margin of the channel according to their respective distributions and angles of attack

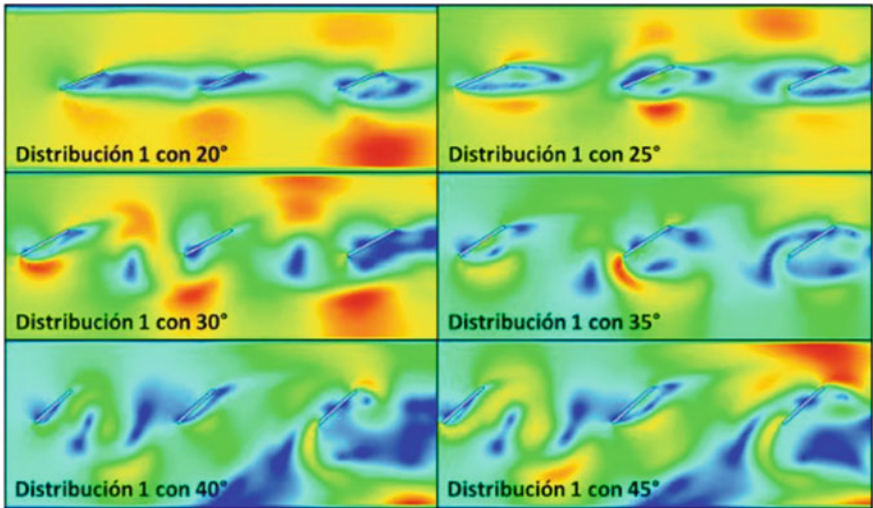


Fig. 13 Speeds of distribution 1 with its different angles of attack

40 and 35 degrees, however in the angle of 40° (Fig. 16) the highest velocity is in the margin to be protected as compared to angle 45. In any case, the best option of an angle would be 35° (Fig. 16).

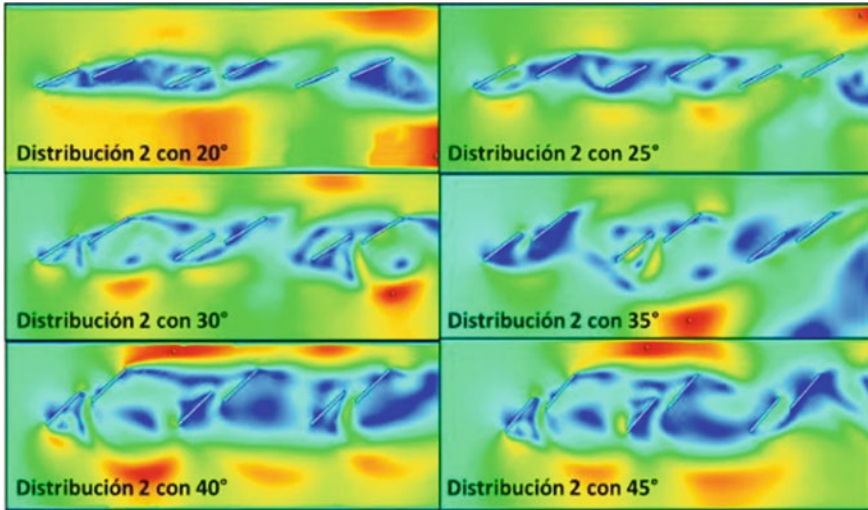


Fig.14 Speeds of distribution 2 with its different angles of attack

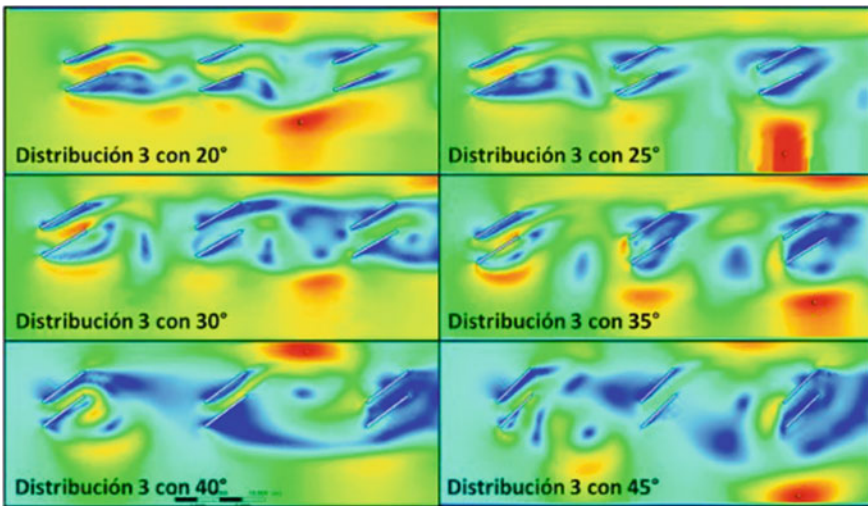


Fig. 15 Speeds of distribution 3 with its different angles of attack

3.5 Validation of Results

To validate the results obtained in this work, we use previous studies by Odgaard & Kennedy, in which they performed simulations with different angles of attack, concluding that for an angle of attack greater than 20°, a scour hole is formed at the upstream edge of the plates [6]. On the other hand, Sharma, Jain & Ahmad,

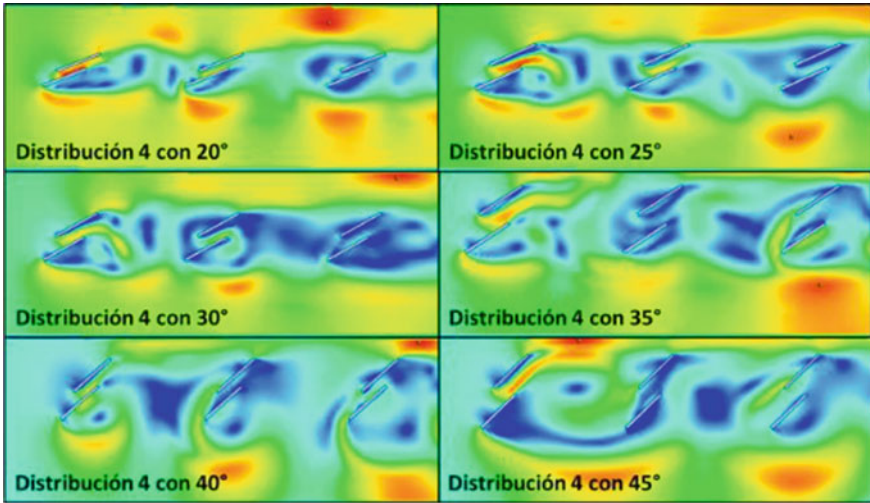


Fig.16 Speeds of distribution 4 with its different angles of attack

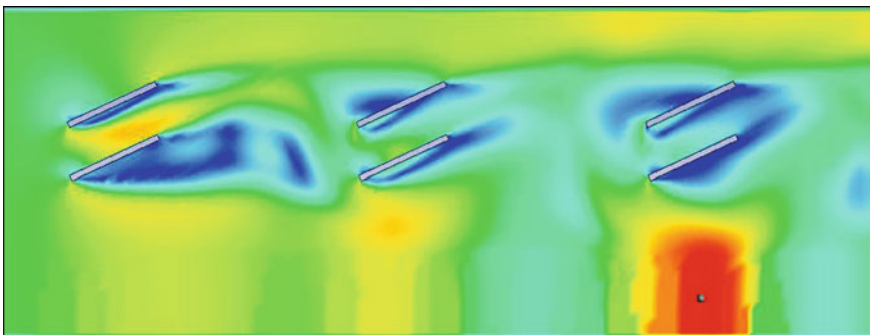


Fig. 17 Optimal choice of distribution and angle

according to the numerical and physical analyses they performed, concluded that for an angle of attack of 30° , an optimum vorticity force is generated [10]. Likewise, the study conducted by Marelius and Sinha, concluded that, according to a sediment transverse transport analysis to counteract erosion, the optimum angle of attack is between 35° and 45° [8].

4 Conclusion

4.1 IBER

Based on the IBER modeling images for a return time of 200 years, it can be observed that the maximum velocity reaches values of approximately 19 m/s. For a return period of 200 years, it can be observed that erosion occurs in certain sections along the study area ranging from 0.05 m to approximately 1 m. From the images it can be observed that the concentration of suspended sediments is higher in the river margins. Since the plates have the function of redistributing the sediments towards the margins. According to the simulations, erosion decreases since, with plates on the left margin, only sedimentation is found. According to the simulation with plates, the specific flow for the 200-year return year decreases, generating a better distribution.

4.2 ANSYS

According to the 24 simulations in ANSYS, it has been possible to evaluate the different angles of attack for different distributions of plate batteries (Fig. 17), in order to determine the most optimal angle for the sizing of the submersible plate batteries; since, as we know, water velocity is an important factor for erosion, since the higher the water velocity, the greater the erosive force and the greater the wear on the margin of the channel. Finally, based on the data obtained and together with the studies carried out previously, we conclude that the optimum angle of attack for the sizing of the submersible plate batteries is 25° , since the velocity distribution with this angle presents lower values in the margin to be protected, thus counteracting erosion. According to the IBER design, the best alternative is 1, since it is within the design limitations of J. Odgaard, and has better distributions and lower results in velocity, bottom stress, specific flow and erosion, the answers in the ANSYS software support the optimal alternative given by IBER.

References

1. Ramos R, Alva M (2020) Geomorphological analysis and fluvial dynamics of the Hualaga River in the locality of Yurimaguas. *Investigaciones sociales. Investigaciones Sociales* 23(43):71–85
2. Abdi C, Vaghefi M (2019) Experimental study of the effect of displacement of vanes submerged at channel width on distribution of velocity and shear stress in a 180 degree bend. *J Appl Fluid Mech*
3. Odgaard J, Mosconi C (1987). Streambank protection by submerged vanes. *J Hydraul Eng* 113(4)
4. Odgaard J, Wang Y (1991) Sediment management with submerged vanes. I: theory. *J Hydraul Eng* 117(3)

5. Barbhuiya AK, Biswas P (2017) Experimental study on bank erosion and protection using submerged vane placed at an optimum angle in a 180 laboratory channel bend. *Geomorphology* 283:32–40
6. Jacob Odgaard A, Kennedy (1983) River-bend bank protection by submerged vanes. *J Hydraulic Eng* 109(8)
7. Rodríguez C, Durán A, Duarte S (2020) Submerged vane technology in colombia: five representative projects. *Water* 12(4):984
8. Marelius F, Sinha SK (1998) Experimental investigation of flow around a submerged vane at high angles of attack. *J Hydraul Eng* 124(5):542–545
9. IBER. <https://www.iberaula.es/space/54/downloads>
10. HEC-HMS. <https://www.hec.usace.army.mil/software/hec-geohms/downloads.aspx>
11. SENAMHI. <https://www.senamhi.gob.pe/?p=descarga-datos-hydrometeorological>
12. CITA UTEC. <https://cita.utec.edu.pe/>

Soft Computing Method for Settling Velocity Prediction of Fine Sediment in Retention Structure



Ren Jie Chin, Sai Hin Lai, Wing Son Loh, Lloyd Ling,
Eugene Zhen Xiang Soo, Yuk Feng Huang, and Ya Qi Yeo

Abstract Most of the retention structures were polluted by various pollutants, particularly fine sediment carried by rainwater due to erosion. Fine sediment is the main cause of siltation which may cause numerous health and environmental problems. To date, the study on fine sediment is limited due to the technology constraint. Therefore, there is a need to formulate a mathematical model which is able to provide an acceptable level of accuracy for the settling velocity prediction of fine sediment. In this study, Radial Basis Function Network (RBFN) and Gradient Boosted Trees (GBT) models were developed and trained by using the experimental data from Particle Image Velocimetry (PIV) tests. Flow rate, particle sizes, vertical displacement and maximum depth were considered as the input while the settling velocity of fine sediment was kept as the output. The developed models were evaluated using a series of statistical analyses. For RBFN and GBT, model VI and model V respectively, has achieved the best performance in terms of coefficient of determination, mean absolute error, and root mean squared error. The findings show that GBT is more suitable than RBFN for the settling velocity prediction of fine sediment with a R^2 value of 0.9591, MAE value of 0.000177 and RMSE value of 1.03E-05.

Keywords Decision trees · Fine sediment · Machine learning · Radial basis function · Settling velocity · Siltation

R. J. Chin (✉) · L. Ling · E. Z. X. Soo · Y. F. Huang · Y. Q. Yeo
Department of Civil Engineering, Lee Kong Chian Faculty of Engineering and Science, Universiti Tunku Abdul Rahman, 43000 Kajang, Malaysia
e-mail: chinrj@utar.edu.my

S. H. Lai
Department of Civil Engineering, Faculty of Engineering, Universiti Malaya, 50603 Kuala Lumpur, Malaysia

W. S. Loh
Department of Mathematical and Actuarial Sciences, Lee Kong Chian Faculty of Engineering and Science, Universiti Tunku Abdul Rahman, 43000 Kajang, Malaysia

1 Introduction

Due to rapid urbanization process and climate changes, controlling the quantity and quality of stormwater runoff has become a challenging task. It is a common practice to construct the retention structures to serve the purpose of runoff prevention and rainwater acquisition, especially during the high precipitation events where large volumes of rainwater flow over a wide range of urban surfaces. It can be seen as an important component for flood control in urban drainage systems [1–3].

However, it is common that the retention structures in Malaysia face erosion, a typical soil degradation which will then lead to issues such as sedimentation, siltation and etc. The problems may cause a series of destructive effects in retention structures, i.e. low level of dissolved oxygen, death of aquatic life, bad odour smell, poor aesthetical view and in some cases, the retention structures even evolved into dead pond status [4–7].

Series of researches have been conducted on sedimentation in past decades and the knowledge development of the field has appeared as an important focus point due to the environmental protection awareness worldwide. Wynants et al. [8], through their study, have provided a solid foundation for targeted land and water management strategies to safeguard water security and environmental health in the lake. Chinellato et al. [9] developed a taphofacies model for coquina sedimentation in lakes, which considered the domination of wave and storm-current activity that related to the water energy of the environment.

In contrast, the studies on siltation are limited, thereby it becomes the main concern of this study. Fine sediment (i.e. clay and silt) is the major cause of siltation. Due to technical constraints, it is impossible to study the fine sediment directly at sites. In addition, the current method for studying the hydrodynamic behaviours of fine sediment is costly as it involved the uses of advanced technology and laboratory tests such as rheological test, particle image velocimetry (PIV) technique and etc. [10–14]. Therefore, there is a need to formulate a mathematical computational model using machine learning techniques for such a problem which is complex and the knowledge behind is yet not well-established [15–19].

This study aims to apply machine learning approaches which are Radial Basis Function Network (RBFN) and Gradient Boosted Trees (GBT) to predict the settling velocity of the fine sediment in retention structure. It is expected that the developed model may beneficial to relevant parties while designing the stormwater management plan as well as dealing with the siltation problem in coming future.

2 Materials and Methods

A foundation study focusing on the hydrodynamic behaviours of fine sediment was carried out by Kashani et al. [13] with the aid of particle image velocimetry (PIV). A prototype of the retention structure was set up in the laboratory while seeding

particles which has the similar density to the actual fine sediment and can trace the movement of fine sediment in water were used during the experiments to mimic the real-life situation. The laboratory works were conducted under several experimental conditions, i.e. particle sizes, flow rate, and depth.

A total number of 297 datasets were extracted from Kashani et al. [13] and divided according to a ratio of 80% to 20%. 80% of the datasets were used to train and validate the machine learning model while the rest 20% were used for the testing purpose.

The RBFN models were developed using particle sizes, flow rate, vertical displacement, maximum depth and depth fraction while settling velocity was kept as the output. The software used for the model development is Waikato Environment for Knowledge Analysis (WEKA). The architecture of the RBFN model was shown in Fig. 1.

It is essential to determine some parameters while designing the architecture of Weka RBFN. For this cases, trial and error method was applied while selecting the values of the parameters, where the number of clusters was placed within the range of 50–60, the random seed to be used by K-means was ranged from –95 to –100, while the range of minimum standard deviation for the clusters was set in between 0.1 and 0.5.

On the other hand, the GBT models were developed using the same series of experimental data [13] where particle size, flow rate, vertical displacement, maximum and depth fraction were set as input while settling velocity was put as output. In this study, the GBT models were constructed using different combinations of the number of trees, maximal tree depth, minimum number of rows, specific number of bins and learning rate. The number of trees was set within the range of 500–2500, 1–20

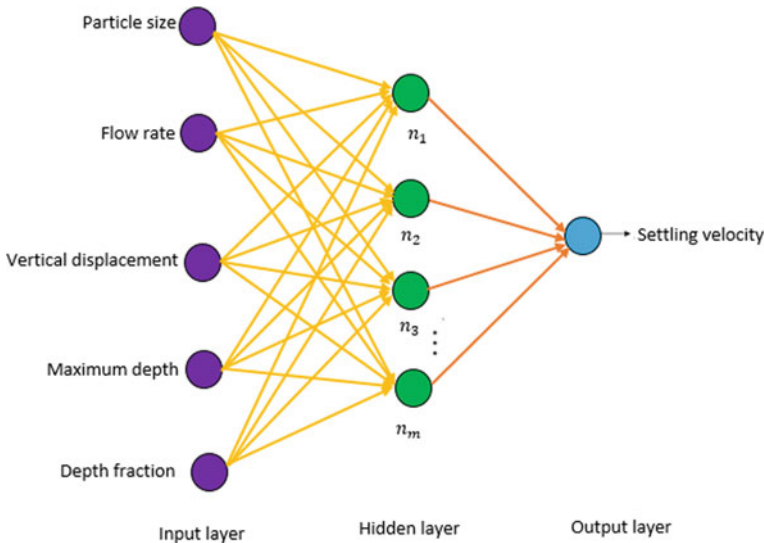


Fig. 1 Architecture of the RBFN model

in maximal tree depth, 1–5 for the minimum number of rows to assign to terminal nodes, 10–50 in the specific number of bins to build a histogram and 0.1–0.5 for the learning rate.

All the developed machine learning models were evaluated using a series of statistical analyses to determine their appropriateness for the settling velocity prediction of fine sediment in retention structure. The statistical performance indicators consist of coefficient of determination (R^2), mean absolute error (MAE), and root mean squared error (RMSE).

3 Results and Discussion

Through the RBFN approach, numerous models were developed, however, only the selected models (as shown in Table 1) were presented and discussed under this section.

The statistical performance for each RBFN model is tabulated in Table 2. Coefficient of determination (R^2) shows the correlation between the actual value and the predicted value. A higher R^2 -value indicates a stronger correlation. As shown in Table 2, the highest R^2 -value is seen in model VI which means that it is the best-performed model from the aspect of coefficient of determination.

From the perspective of MAE and RMSE, since both of the performance indicators are closely related to the difference between the actual value and the prediction value, a smaller value is always favorable. From Table 2, model VI has the lowest MAE and RMSE values among the examined models.

In sum, model VI appears as the most suitable RBFN prediction model for the settling velocity prediction as it has achieved the highest R^2 -value, as well as the lowest MAE and RMSE.

Table 1 Parameters combination with respect to the selected RBFN model

Model	Number of clusters, B	Random seed to be used by K-means, S	Minimum standard deviation for the clusters, W
I	56	−95	0.1
II	56	−96	0.1
III	56	−98	0.1
IV	56	−99	0.1
V	56	−100	0.1
VI	56	−99	0.4
VII	56	−99	0.5
VIII	56	−99	0.6

Table 2 Statistical performance for each RBFN model

Models	R ²	MAE	RMSE
I	0.2285	0.000813	4.72E-05
II	0.1696	0.000875	5.08E-05
III	0.2689	0.000880	5.11E-05
IV	0.4669	0.000950	5.51E-05
V	0.2964	0.000880	5.11E-05
VI	0.5545	0.000678	3.93E-05
VII	0.4170	0.000774	4.49E-05
VIII	0.4207	0.000761	4.42E-05

On the other hand, a series of GBT models were developed using different parameters combination. Due to a large number of the developed model, the result presentation and discussion were mainly focused only on the selected models as shown in Table 3.

The statistical performance for each GBT model is contained in Table 4. From the aspect of R²-value, model V records the highest value at 0.9591, showing the correlation between the actual value and the predicted value is the strongest on the model.

On the hand, among the examined models, model V has the lowest MAE and RMSE values, recorded at 0.000177 and 1.03E-05 respectively. These point out that the model is the most suitable model for the settling velocity prediction of fine sediment.

For each RBFN and GBT approach, the best-performed model is identified based on the evaluation result of their statistical performance. Table 5 compares the best-performed RBFN and GBT model through the statistical analyses. It is noticed that the overall performance shows an improvement from RBFN to GBT. In other words, GBT can provide a prediction model for the settling velocity with better accuracy in terms of R², MAE, and RMSE.

Table 3 Parameters combination with respect to each GBT model

Model	No. of trees	Max. depth	Min. rows	No. of bins	Learning rate
I	1000	10	1	30	0.1
II	1000	10	1	50	0.1
III	1000	10	1	70	0.1
IV	1000	10	1	90	0.1
V	1000	10	1	50	0.2
VI	1000	10	1	50	0.3
VII	1000	10	1	50	0.4
VIII	1000	10	1	50	0.5

Table 4 Statistical performance for each GBT model

Models	R ²	MAE	RMSE
I	0.9331	0.000212	1.23E-05
II	0.9459	0.000192	1.11E-05
III	0.9451	0.000195	1.33E-05
IV	0.9458	0.000194	1.12E-05
V	0.9591	0.000177	1.03E-05
VI	0.9532	0.000191	1.11E-05
VII	0.9414	0.000207	1.20E-05
VIII	0.9449	0.000191	1.11E-05

Table 5 Model comparison according to the statistical analyses

Model	RBFN (model VI)	GBT (model V)
R ²	0.5545	0.9591
MAE	0.000678	0.000177
RMSE	3.93E-05	1.03E-05

4 Conclusion

Siltation has become a major issue in water bodies. The main factor that causes the siltation issue is fine sediment. However, the study on fine sediment is limited due to the technology constraint. It is essential to have a mathematical model which is able to perform the task of predicting the settling velocity of fine sediment in water bodies.

The prediction model was developed using two machine learning approaches which are Radial Basis Function Network (RBFN) and Gradient Boosted Trees (GBT). The developed models were evaluated using coefficient of determination (R²), mean absolute error (MAE), and root mean squared error (RMSE).

According to the evaluation outcomes, RBFN model V has appeared as the best-performed model as it has the highest R²-value (0.5545), as well as the lowest MAE (0.000678) and RMSE (3.93E-05). Meanwhile, from the perspective of GBT, model V has achieved the best performance in terms of R² (0.9591), MAE (0.000177), and RMSE (1.03E-05). By comparing the RBFN and GBT approaches, the latter appears as the more favourable machine learning technique while developing the prediction model for the settling velocity of fine sediment in retention structure.

The model can be further improved by training it with a wider range of data. The other more advanced machine learning techniques may also be utilised to achieve the purpose of model improvement.

Acknowledgements This research was supported by the Ministry of Higher Education (MoHE) Malaysia through the Fundamental Research Grant Scheme project (FRGS/1/2021/WAB07/UTAR/02/1), KURITA Overseas Research Grant 2022 (8128/0002), and Universiti Tunku Abdul Rahman Research Fund (IPSR/RMC/UTARRF/2022-C2/C04).

References

1. Ayub KR, Sidek LM, Ainan A, Zakaria NA, Ghani AA, Abdullah R (2005) Stormwater treatment using bio-ecological drainage system. *Int J River Basin Managem* 3:215–221
2. Jones GD, Wadzukm BM (2013) Predicting performance for constructed storm-water wetlands. *J Hydraul Eng* 139:1158–1164
3. Persson J, Somes N, Wong T (1999) Hydraulics efficiency of constructed wetlands and ponds. *Water Sci Technol* 40:291–300
4. Hamm NT, Dade WB, Renshaw CE (2009) Fine particle deposition to initially starved, stationary, planar beds. *Sedimentology* 56:1976–1991
5. Harrison ET, Norris RH, Wilkinson SN (2008) Can an Indicator of river health be related to assessments from a catchment-scale sediment model? *Hydrobiologia* 600:49–64
6. Kirby R (2013) Managing industrialised coastal fine sediment systems. *Ocean Coast Manag* 79:2–9
7. Lowe DR, Guy M (2000) Slurry-flow deposits in the Britannia formation (Lower Cretaceous), North Sea: a new perspective on the turbidity current and debris flow problem. *Sedimentology* 47:31–70
8. Wynants M, Millward G, Patrick A, Taylor A, Munishi L, Mtei K, Brendonck L, Gilvear D, Boeckx P, Ndakidemi P, Blake WH (2020) Determining tributary sources of increased sedimentation in East-African Rift Lakes. *Sci Total Environ* 717:137266
9. Chinelatto GF, Vidal AC, Kuroda MC, Basilici G (2018) A taphofacies model for coquina sedimentation in lakes (Lower Cretaceous, Morro do Chaves Formation, NE Brazil). *Cretac Res* 85:1–19
10. Adrian RJ, Westerweel J (2011) Particle image velocimetry. Cambridge University Press, New York
11. Blanc F, Peters F, Lemaire E (2011) Particle image velocimetry in concentrated suspensions: application to local rheometry. *Appl Rheol* 21:23735
12. Kashani MM, Lai SH, Ibrahim S, Bargani PO (2016) Design factors affecting the dynamic performance of soil suspension in an agitated, baffled tank. *Chin J Chem Eng* 24:1664–1673
13. Kashani MM, Lai SH, Ibrahim S, Meriam NSN (2016) A study on hydrodynamic behavior of fine sediment in retention structure using particle image velocimetry. *Water Environ Res* 88:2309–2320
14. Kashani MM, Lai SH, Ibrahim S, Sulaiman NM, Teo FY (2016) An investigation into the effects of particle texture, water content and parallel plate's diameters on rheological behavior of fine sediment. *Int J Sedim Res* 31:120–130
15. Azari B, Tabesh M (2018) Optimal design of stormwater collection networks considering hydraulic performance and BMPs. *Int J Environ Res* 12:585–596
16. Chin RJ, Lai SH, Shaliza I, Wan Zurina WJ, Ahmed Elshafie AH (2019) New approach to mimic rheological actual shear rate under wall slip condition. *Eng with Comput* 35:1409–1418
17. Chin RJ, Lai SH, Shaliza I, Wan Zurina WJ, Elshafie A (2019) Rheological wall slip velocity prediction model based on artificial neural network. *J Exp Theor Artif Intell* 31:659–676
18. Vasto-Terrientes LD, Kumar V, Chao TC, Valls A (2016) A decision support system to find the best water allocation strategies in a Mediterranean river basin in future scenarios of global change. *J Exp Theor Artif Intell* 28:331–350
19. Zhang Y, Chen H, Yang B, Fu S, Yu J, Wang Z (2018) Prediction of phosphate concentrate grade based on artificial neural network modeling. *Results in Phys* 11:625–628

Research on Scour Monitoring Techniques for Bridge Pile Foundations



Wenting Qiao, Qianen Xu, and Yang Liu

Abstract The scour of pile foundation is a key problem of the wading bridge structure, and the underwater pile foundation lies in a complicated environment, which is difficult to inspect directly. Therefore, the effective monitoring of scour for the bridge pile foundation is very important to ensure the safety of the bridge structure operation. The research status of scour monitoring techniques for the bridge pile foundation is summarized from two aspects of direct monitoring methods and indirect monitoring methods. At the same time, the research progress of determining whether the bridge pile foundations scour occurs, identifying the depth of bridge scour, identifying the degree of bridge scour and the protection of bridge scour are described and discussed. The development trend of scour monitoring techniques of the bridge pile foundation is proposed, and it is suggested that more attention should be paid to the research of direct monitoring equipment of the pile foundation for the underwater complex environment, embedded sensors with higher survival rate and accuracy, and the collaborative working method for monitoring the bridge pile foundation and other components of bridge.

Keywords Bridge pile foundation · Scour monitoring · Optical fiber sensing technology · Vibration monitoring

W. Qiao

Inner Mongolia Research Institute of Transportation Science Development, Hohhot 010050, China

W. Qiao · Q. Xu · Y. Liu (✉)

School of Transportation Science and Engineering, Harbin Institute of Technology, Harbin 150090, China

e-mail: ly7628@hit.edu.cn

1 Introduction

Scour monitoring of the bridge pile foundation is an important part of the bridge structural health monitoring. There are a large number of bridges and the proportion of wading bridges is high. Therefore, it is a key research issue for researchers in various countries to ensure the safe operation of bridges in the complex water environment. According to the difference of monitoring equipment, bridge scour methods can be divided into two categories: direct monitoring techniques and indirect monitoring techniques based. In the direct monitoring techniques, radar, sonar, ultrasonic and various kinds of scour monitoring sensors are used to monitor the scour depth of the bridge pile foundation. The principle of this monitoring technology is mainly to identify the changes of soil and water interface so as to conduct scour monitoring. Therefore, this monitoring technology is greatly affected by equipment, and due to the complex water environment, underwater sensors are easy to be damaged. At the same time, the sensor monitoring range is limited.

In the indirect monitoring techniques, point sensor or distributed optical fiber is used to monitor the scour depth through the change of vibration signal of the bridge structure. Compared with the direct monitoring techniques, indirect monitoring techniques use modal parameter changes identified by strain sensors or acceleration sensors to identify scour, which are not affected by water environment. The precision of indirect monitoring techniques is greatly affected by the number of sensors. At the same time, these monitoring techniques often realize scour monitoring through the vibration signal of the superstructure, but neglect the most sensitive foundation part to scour. Therefore, these monitoring techniques are subject to the damage of other bridge components and the environmental impact is not easy to separate, which poses an obstacle to the further development of indirect monitoring techniques. The above scouring monitoring techniques can be expressed in terms of a diagram, Fig. 1.

This paper summarizes the research status of scour monitoring techniques for the bridge pile foundation. Meanwhile, the research progress of determining whether or not bridge scour occurs, identifying the depth of bridge scour, identifying the degree

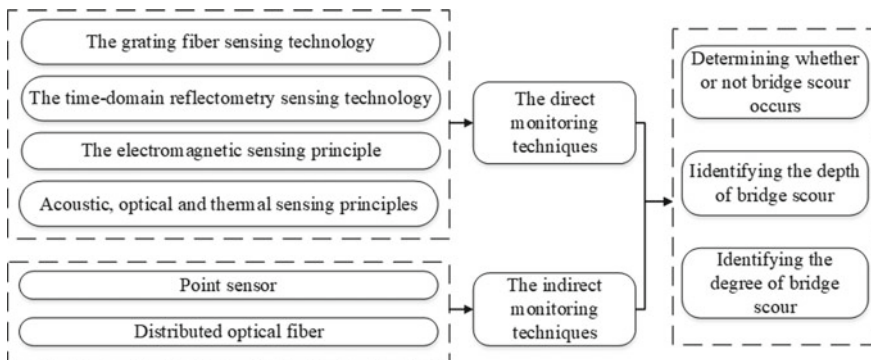


Fig. 1 The scour monitoring techniques for bridge pile foundations

of bridge scour and the protection of bridge scour are analyzed and summarized, and the development trend of scour monitoring techniques of the bridge pile foundation is prospected.

2 Scour Monitoring for the Bridge Pile Foundation Based on the Direct Monitoring Technique

2.1 Scour Monitoring Based on the Grating Fiber Sensing Technology

Fiber Bragg grating (FBG) is a kind of sensing element, which can obtain the change of wavelength by measuring the change of refractive index of light in its interior, and then obtain the change of environmental parameters, including temperature and stress, by measuring the change of wavelength. Zhou et al. [1] proposed an FBG scour monitoring sensor system. FBG sensors were installed on both sides of the neutral axis to measure the tensile and compressive strain of the beam under dynamic water pressure, and then the scour monitoring was carried out by identifying different strain states under soil and water environment. Laboratory tests have proved the effective performance of the sensor system. Similarly, Kong et al. [2] embedded FBG sensors into the riverbed by an equivalent cantilever beam and protected it from damage in the water by an external protective shell, thus realizing scour monitoring.

In contrast to the above, Manzoni et al. [3] coupled a temperature sensor array based on fiber Bragg grating to the heating device. Heat generated by the equipment is dissipated through conduction phenomena in the riverbed and convection phenomena in the flowing water. Due to the different heat exchange efficiency of the two processes, the temperature increase of the temperature sensor in flowing water should be less than that of the temperature sensor buried in the riverbed. The different behavior of the two sensors can be a reliable tool for monitoring scour. Kong et al. [4] connect FBG with water-expanding polymer. In the presence of water, the volume of the polymer material expands and bends the optical fiber sensor. This method can monitor the whole scouring process. Liang et al. [5] designed a bridge scour monitoring system with fiber Bragg grating pressed with a roller mechanism. The fiber Bragg grating was embedded in silicone rubber, and the two ends of the rubber were fixed on the metal plate. When the rubber is pressed, the depth of scour can be obtained by measuring the wavelength offset of the reflective center of the FBG sensor. In addition, Yong et al. [6] proposed a method to determine bridge scour depth based on lateral earth pressure by using FBG sensors. Due to the advantages of simple measurement principle and low production cost, the fiber Bragg grating has been paid more and more attention in scour monitoring in recent years. However, the fiber Bragg grating needs to be embedded in the structure, which is easily affected by the complex environment in the water.

2.2 *Scour Monitoring Based on the Time-Domain Reflectometry Sensing Technology*

Time domain reflectometer (TDR) is a new bridge scour monitoring technology, which has been used in recent years. During scour monitoring, electromagnetic pulse is emitted at the top of TDR, and the pulse signal is reflected back to the signal tower when it passes through the interface of water and soil, and then the scour location is judged according to the reflected signal information.

In recent years, researchers have made a lot of explorations in the algorithm and hardware of the time domain reflectometer. In 2009, Yu et al. [7] proposed a search signal analysis algorithm for bridge scour monitoring based on time domain reflectometry. This algorithm has strong robustness and can be used for automatic signal interpretation. The performance of scour monitoring system is verified by simulation test. In order to further improve the algorithm, Yu et al. [8] developed a reliable and accurate TDR signal analysis method, and studied the influences of sediment type, river water salinity, suspended sediment and inclusion bubble on the depth of scour measurement in the experiment. The experimental results show that the algorithm is accurate for different types of sediment and river conditions. The program can be developed into an automatic scour assessment algorithm, which expands the application scope of TDR in the field of bridge scour monitoring. On this basis, Lin et al. [9] proposed a new TDR induction waveguide in the form of induction rod or induction line. The sensing rod consists of a hollow channel steel rod paired with a metal strip on the insulating groove. The sensing line consists of two strands of steel strand, one of which is coated with an insulating sheath. A simplified method of scour depth estimation and a two-step calibration method of propagation velocity are presented. The test results show that the new TDR sensing waveguide can accurately measure the scour depth.

In terms of hardware equipment research, Wang et al. [10] proposed a new bottom-up binding sensor cable to improve the durability of the sensor. In addition, a new time-delay differential waveform data reduction method is used to further enhance the robustness of system calibration and scour estimation. On this basis, in 2020, Wang et al. [11] proposed a new TDR scour sensor, which greatly improved the scour monitoring effect of TDR sensor under harsh flow conditions. This method can improve the measurement sensitivity and overcome the adverse effects of coating wear and the limitation of measurement range. In addition, Gao et al. [12] proposed a new spiral TDR sensor, which consists of a parallel copper wire waveguide wound on the mounting rod. By using the spiral waveguide, the TDR sensor achieves higher sensitivity than the traditional straight TDR probe, and the electromagnetic wave propagation distance per unit length of the spiral probe is longer. The scour monitoring accuracy can reach 2 cm, and the sensitivity of the spiral TDR sensor is four times that of the traditional straight TDR probe. Yu et al. [13] developed anti-corrosion protection on the coating of the TDR sensor. At the same time, the finite element method was used to conduct numerical simulation research on the design of the new sensor, and the effective sampling area of the sensor was determined.

The experimental results show that the sensor is sensitive to scour process and can provide accurate scour depth measurement.

Compared with FBG sensors, TDR has a much lower cost and better adaptability in complex water environments. However, TDR is not immune to the pitfalls of needing to be re-debugged and re-installed each time it is used. In addition, the salinity interferes greatly with the signal of TDR, and the reflection at the end of the probe can no longer be recognized when the salinity is too high.

2.3 Scour Monitoring Based on the Electromagnetic Sensing Principle

Similar to TDR, the principle of using electromagnetic sensing to monitor scour depth is the difference between the electrical conductivity of water and soil interfaces. Researchers have designed different scour depth monitoring sensors according to the principle of electromagnetism. Fitzgerald et al. [14] proposed a bridge scour monitoring method based on the free vibration monitoring of cantilever piezoelectric energy harvesting device (EHD). It has been shown that the installation of EHD on piers enables scour monitoring by monitoring the frequency shift due to stiffness loss due to scour under the support. Funderburk et al. [15] developed a piezoelectric drive rod scour monitoring system. The sensor used in the system is a thin polymer rod with a thin strip of polyvinylidene fluoride along the center line. The system can directly calculate the exposure length of the long rod after fluid excitation by extracting the fundamental frequency, and then identify the change of scour depth. Azhari et al. [16] proposed a low-cost and simple scour depth sensor—piezoelectric polyvinylidene fluoride (PVDF) polymer strip. PVDF-based sensors can be embedded in the riverbed and placed where the depth of the scour needs to be measured. When scour occurs and part of the PVDF sensor is exposed, the water flow stimulates the sensor to generate a time-varying voltage signal. Due to the dynamics of the voltage time-history response are related to the exposure length of the sensor, the scour depth can be determined.

Tang et al. [17] have also made a smart rock, which is a super-strong magnet embedded in a concrete ball. It is dropped around the pier and the location of the smart rock can be located by comparing the magnetic field changes before and after the smart rock is placed. The monitor smart rock has a permanent service life and is of high strength, but may be washed away and cannot monitor the refilling process of live bed scour. In the same year, Tang et al. [18] also proposed two kinds of intelligent rocks for scouring monitoring, namely intelligent rocks of arbitrary orientation system and intelligent rocks of automatic guidance system. Chen et al. [19] made two kinds of intelligent rock monitoring bridge scour with unknown direction and known direction. Based on the theory of magnetic field, the distribution law of induced magnetic field of two kinds of intelligent rock is deduced, and two kinds of positioning algorithms of intelligent rock are proposed. Field experiments

show that the algorithm has high positioning accuracy, but it is greatly affected by external environmental factors, especially passing vehicles. Zhang et al. [20] combined intelligent rock with unmanned aerial vehicle (UAV) technology. Smart rock in the traditional sense requires a magnetometer mounted on a truck crane, which is time-consuming to measure and requires blocking traffic. The UAV can be used as a mobile base station to measure the Earth's magnetic field, which improves the above problems, and the accuracy of the positioning algorithm also meets the needs of practical engineering.

2.4 Scour Monitoring Based on Acoustic, Optical and Thermal Sensing Principles

Similar to electromagnetic sensors, acoustic, optical and thermal sensors also realize bridge scour monitoring according to the different properties of water and soil materials. Zhao et al. [21] proposed a submarine pipeline scour monitoring system based on the distributed Brillouin fiber optic sensor that can actively measure temperature. The system consists of a thermal cable running parallel to the pipe, which captures the frequency shift of the optical sensor during the heating and cooling process and can directly indicate the temperature change. The water and soil interfaces are identified by differences in heat transfer behavior between different media. Zhao et al. [22] proposed a three-indexes estimator based on active temperature measurement, thus designing a new type of nearshore and landfill scour monitoring system. Heat dissipates in different ways in water and sand. By analyzing the time history of temperature changes during heating and cooling, the three indexes, including temperature intensity, consistency of temperature curve and temperature fluctuation during heating, can well characterize the difference of heat transfer behavior between liquid and solid. By calculating these three indexes, it is possible to determine whether a location along the pipe is surrounded by water or soil. In 2013, Zhao et al. [23] developed a submarine pipeline scour monitoring system based on active temperature measurement. The thermal cable is the main component of the system, which consists of heating belt, armored optical fiber and heat shrink tube running parallel with the pipe. During heating and cooling, the exposed portion caused by scouring can be monitored by the different heat transfer behavior of water and sediment. In 2019, Lin et al. [24] proposed a scour monitoring system for offshore wind turbines. The monitoring system consists of a series of small VLC (visible light communication) modules. The system is directly connected to the pile foundation structure and uses the underwater optical wireless sensor network to realize remote data acquisition. The test results show that the system is highly sensitive to scour process.

Other types of sensors used for scour monitoring include sonar, radar, ultrasonic, image sensors, etc. Sonar, radar and ultrasonic sensors can not carry out dynamic real-time monitoring of scour, which requires a lot of labor, time and effort. Image sensor has developed well in recent years. In 2016, An et al. [25] proposed a new

contact image sensor (CIS) to monitor the local scouring process around piles in water flow. CIS is an optical sensor that tracks changes at the interface between water and soil by the fact that two media have different reflectance. The sensor has successfully detected local scour development around vertical piles under steady flow and tidal current. In addition, Fisher et al. [26] proposed a new instrument system that can determine scour formation and replenishment in real time. Turbulent pressure sensors are distributed evenly on a support plate and then buried in the riverbed. The turbulence pressure sensor contains an accelerometer that measures the acceleration time-history response of the plate to determine whether the material around the sensor is water or sediment.

In conclusion, in the direct monitoring technique, the sensor performance directly affects the monitoring accuracy and quality. At the same time, regardless of the type of sensor, the monitoring range is limited and the cost is very high due to the need for frequent replacement.

3 Scour Monitoring for the Bridge Pile Foundation Based on the Indirect Monitoring Technique

Conventional scour monitors are often expensive to install and maintain, and are vulnerable to damage during floods. In order to solve this problem, the indirect scour monitoring technique uses the dynamic response of structures to detect and measure the scour depth around the structure. Dynamic measurements have the advantage of being easily installed above the waterline and require low maintenance costs compared to the direct scour monitoring technique.

Lin et al. [27] built fractal dimension and topological degree, two important indexes for scour monitoring, using vibration data of bridge superstructure. The experimental results show that these indexes have high sensitivity to bridge scour, which provides a new choice for the bridge scour monitoring method. Through numerical simulation and experiments, Elsaid et al. [28] proved that the horizontal displacement mode was more sensitive to scour than the vertical displacement mode. Meanwhile, the finite element numerical simulation results show that the natural frequency of the vertical displacement mode has no significant change under different scour levels. However, the natural frequency of the horizontal displacement mode decreases with the increase of scour levels, which can be used to identify scour and determine the degree of damage. Lin [29] proposed a real-time bridge scour monitoring system. In this system, vibration signals are divided into structural vibration set and rigid body motion set. The structural vibration set is mainly sensitive to the change of structural frequency, while the rigid body motion set is dominated by the rigid body motion. The applicability of the system is verified by three different experiments.

Xiong et al. [30] proposed a method to identify and analyze the scour depth of Bridges by tracking the dynamic behavior of the superstructure. This method

mainly depends on the influence of bridge scour on the natural frequency and mode change of the superstructure. This method does not require the use of underwater instruments for continuous and long-term monitoring, and can be easily integrated into the bridge structure monitoring system. Xiong et al. [31] also proposed four dynamic characteristics reflecting scour, and discussed the feasibility and effect of each index on scour identification of cable-stayed bridges by analyzing the data of a real bridge. In addition, Xiong et al. [32] conducted two vibration measurements in 2013 and 2016 by installing acceleration sensors on the beams and towers of a bridge. Through modal analysis, the natural frequencies of the superstructure under different modes are calculated. Furthermore, by comparing the dynamic characteristics of the two measurements in 2013 and 2016, the difference of the support boundary of the bridge foundation was detected, and the existence of bridge foundation scour was qualitatively identified. Khan et al. [33] proposed a monitoring method based on the relative change of pier mode amplitude under scour. The frequency domain decomposition method is used to track the relative change of pier mode amplitude under scour. The modal shape value of each pier is compared with the average of the remaining piers to generate the average normalized modal shape and further identify the bridge scour.

4 Conclusion

As many bridge pile foundation structures are damaged due to continuous scour, scour monitoring has attracted more and more attention. In this paper, the research progress of bridge pile foundation scour monitoring techniques is summarized, and the key problems solved in bridge pile foundation scour monitoring are analyzed and summarized.

- (i) By using the direct scour monitoring technique, the location of soil and water interface can be directly obtained, but regardless of the type of sensor, the monitoring range is limited and the cost is very high due to the need for frequent replacement. In addition, many sensors do not work well underwater, and their accuracy and resolution are greatly affected by the uncertainties in the water.
- (ii) The indirect scour monitoring technique have the advantage of being easily installed above the waterline and require low maintenance costs compared to the direct scour monitoring technique. However, the most sensitive structure to erosion is the pile foundation. As a result, the indirect scour monitoring technique is generally less accurate than the direct scour monitoring technique, and the overall effect of scour cannot be observed unless high-density instruments are used near the scour critical area.

With the progress of sensing technology and the improvement of structural monitoring methods, some future development trends of scour monitoring of bridge pile foundation are summarized as follows.

- (i) The underwater working effect of the existing sensors is poor, and the accuracy and resolution are often low. To solve this problem, it is of great significance to study the direct monitoring equipment of pile foundation for the complex underwater environment.
- (ii) The impact of scour on pile foundation is significant. The embedded sensor is easy to install and the monitoring location is closer to the scour affected area. Therefore, the research on the embedded sensor with higher survival rate and higher precision is helpful to improve the scour monitoring effect of bridge pile foundation.
- (iii) The existing indirect monitoring equipment for pile foundation scour is poorly coordinated with the overall monitoring system of the bridge structure, so it is necessary to further study the collaborative working method for monitoring the bridge pile foundation and other components of bridge.

Acknowledgements This study is supported by the Key Research & Development Program of Heilongjiang Province of China (Grant No: GA21A303) and 2022 Excellent Postdoctoral Program of Inner Mongolia Autonomous Region.

References

1. Zhou Z, Huang M, Huang L et al (2011) An Optical Fiber Bragg Grating Sensing System for Scour Monitoring. *Adv Struct Eng* 14(1):67–78
2. Kong, X., Cai, C. S., Hu, J. X., et al.: Field Application of an Innovative Bridge Scour Monitoring System with Fiber Bragg Grating Sensors. *Journal of aerospace engineering* 30(2), B4016008.1–B4016008.10 (2017).
3. Manzoni S, Crotti G, Ballio F, Cigada A, Inzoli F, Colombo E (2011) A fiber optic sediment. *Flow Meas Instrum* 22(5):11–18
4. Kong, X., Ho, S., Song, G., et al.: Scour Monitoring System Using Fiber Bragg Grating Sensors and Water-Swellable Polymers. *Journal of Bridge Engineering* 22(7), 04017029.1–04017029.11 (2017).
5. Liang, T., Wu, P., Huang H., Yang, C.: Design a bridge scour monitoring system by pressing the fiber Bragg grating with a rolling pulley mechanism. *Microsystem Technologies*, B4016008 (2018).
6. Yong, D., Yao, Q., Zhang, Z., et al.: A new method for scour monitoring based on fiber Bragg grating. *Measurement*, S0263224118302380 (2018).
7. Yu X, Xiong Y (2009) Time Domain Reflectometry Automatic Bridge Scour Measurement System: Principles and Potentials. *Struct Health Monit* 8(6):463–476
8. Yu X, Xiong Y (2011) Assessment of an Automation Algorithm for TDR Bridge Scour Monitoring System. *Adv Struct Eng* 14(1):13–24
9. Lin, C. P., Wang, K., Chung, C. C., et al.: New types of time domain reflectometry sensing waveguides for bridge scour monitoring. *Smart Materials and Structures* 26(7), (2017).
10. Wang, K., Lin, C. P., Chung, C. C.: A bundled time domain reflectometry-based sensing cable for monitoring of bridge scour. *Struct Control Health Monitor* 26(5), e2345.1–e2345.14 (2019).
11. Wang, K., Lin, C. P., Jheng, W. H.: A New TDR-Based Sensing Cable for Improving Performance of Bridge Scour Monitoring. *Sensors* 12(2), (2020).
12. Gao, Q., Yu, X. B.: Design and evaluation of a high sensitivity spiral TDR scour sensor. *Smart Materials and Structures* 24(8), (2015).

13. Yu X, Zhang B, Tao J et al (2013) A new time-domain reflectometry bridge scour sensor. *Struct Health Monit* 26:1–14
14. Fitzgerald, P. C., Malekjafarian, A., Bhowmik, B., et al.: Scour Damage Detection and Structural Health Monitoring of a Laboratory-Scaled Bridge Using a Vibration Energy Harvesting Device. *Sensors* 19(11), (2019).
15. Funderburk, M. L., Huang, S. K., Loh, C. H., et al.: Chin-Hsiung Loh, Kenneth J Loh. Densely distributed and real-time scour hole monitoring using piezoelectric rod sensors. *Advances in Structural Engineering* 22(16), (2019).
16. Azhari F, Tom C, Benassini J et al (2014) Design and characterization of a piezoelectric sensor for monitoring scour hole evolution. *Smart Structures* 11(12):22–33
17. Tang, F., Chen, Y., Guo, C., et al.: Field Application of Magnet-Based Smart Rock for Bridge Scour Monitoring. *Journal of Bridge Engineering* 24(4), 04019015.1–04019015.14 (2019).
18. Tang, F., Chen, Y., Li, Z., et al.: Genda Chen, Yan Tang. Characterization and field validation of smart rocks for bridge scour monitoring. *Structural Health Monitoring* 18(5–6), (2019).
19. Chen, Y., Tang, F., Li, Z., et al.: Bridge scour monitoring using smart rocks based on magnetic field interference. *Smart Materials and Structures* 27(8), (2018).
20. Zhang, H., Li, Z., Chen, G., et al.: UAV-based smart rock localization for bridge scour monitoring. *Journal of Civil Structural Health Monitoring* 24(4), 04019015.1–04019015.14 (2021).
21. Zhao, X. F., Le, L., Qin, B., et al.: Jinping Ou. Scour monitoring system of subsea pipeline using distributed Brillouin optical sensors based on active thermometry. *Optics and Laser Technology* 44(7), 2125–2129 (2012).
22. Zhao XF, Le L, Qin B et al (2012) A three-index estimator based on active thermometry and a novel monitoring system of scour under submarine pipelines. *Sens Actuators, A* 18(6):115–122
23. Zhao X, Li W, Song G et al (2013) Scour Monitoring System for Subsea Pipeline Based on Active Thermometry Numerical and Experimental Studies. *Sensors* 44(7):2125–2129
24. Lin YB, Lin TK, Chang CC et al (2019) Visible Light Communication System for Offshore Wind Turbine Foundation Scour Early Warning Monitoring. *Water* 11(7):1486
25. An H, Yao W, Cheng L et al (2016) Detecting Local Scour Using Contact Image Sensors. *J Hydraul Eng* 131(4):330–334
26. Fisher M, Atamturktur S, Khan AA (2013) A novel vibration-based monitoring technique for bridge pier and abutment scour. *Struct Health Monit* 12(2):114–125
27. Lin TK, Wu RT, Chang KC et al (2013) Evaluation of bridge instability caused by dynamic scour based on fractal theory. *Smart Mater Struct* 22(7):075003
28. Elsaid A, Seracino R (2014) Rapid assessment of foundation scour using the dynamic features of bridge superstructure. *Constr Build Mater* 79(8):42–49
29. Lin T, Chang YS (2017) Development of a real-time scour monitoring system for bridge safety evaluation. *Mech Syst Signal Process* 16(2):221–230
30. Xiong W, Cai CS, Kong B et al (2018) Identification of Bridge Scour Depth by Tracing Dynamic Behaviors of Superstructures. *KSCE J Civ Eng* 22(4):1316–1327
31. Xiong, W., Kong, B., Tang, P. B., Ye, J. S.: Vibration-Based Identification for the Presence of Scouring of Cable-Stayed Bridges. *Journal of Aerospace Engineering* 22(4), (2018).
32. Xiong, W., Cai, C. S., Kong, B., et al.: Bridge Scour Identification and Field Application Based on Ambient Vibration Measurements of Superstructures. *Journal of Marine Science and Engineering* 31(2), (2019).
33. Khan MA, Mccrum DP, Prendergast LJ et al (2020) Experimental demonstration of a mode shape-based scour-monitoring method for multispan bridges with shallow foundations. *J Bridge Eng* 25(8)

Infrastructure Projects and Municipal Engineering

A Review of Approaches to Drainage System Management: Current Status and Future Research Directions



Gabriel Lloyd C. Malinay, Clariz D. Santos, Gayle Ann Marie B. Sarmiento, Franz D. Santos, and David B. Sanson

Abstract Throughout humans' existence, drainage systems have been a very vital part of civilization and sanitation development. Drainage systems are coined to have purposively given way to the improvement of modern-day sanitation, through which disposal and transport of wastewater and stormwater were given priority in aid of public health and flood concerns. However, through time, the practices in drainage system management have also gradually changed. In this paper, approaches to drainage system management are reviewed through scholarly articles worldwide. Historical accounts of drainage system development are consulted to formulate the current approaches. Governmental action, especially governing legislations and ordinances to public utilization and prevention of urbanization-related problems (e.g., flooding) are also analyzed. Lastly, a greener approach to a drainage system is also viewed as essential in this review. Hence, Sustainable Drainage Systems and the technological approaches in this regard are reviewed to shed light on the current standing of drainage systems around the globe.

Keywords Drainage system management · Urban drainage system · Government approach · Sustainable drainage system

1 Introduction

In the course of the continuous progression of the world, from its oldest stance of evolution up to the earliest technological advances, drainage systems are playing a crucial role in helping humankind shape the world. Drainage simply means the

G. L. C. Malinay · C. D. Santos · G. A. M. B. Sarmiento · D. B. Sanson
Department of Environmental and Sanitary Engineering, National University, 1008 Manila, Philippines

F. D. Santos (✉)
Department of Civil Engineering, National University, 1008 Manila, Philippines
e-mail: fdsantos@national-u.edu.ph

© The Author(s), under exclusive license to Springer Nature Singapore Pte Ltd. 2024
M. Casini (ed.), *Proceedings of the 3rd International Civil Engineering and Architecture Conference*, Lecture Notes in Civil Engineering 389,
https://doi.org/10.1007/978-981-99-6368-3_57

707

'draining' of liquid [1] from one point source to another. By incorporating a systematized approach to this concept, it becomes a system of waterworks that enables the transport or storage [2], depending on the complexity of the structure.

Earliest accounts of the utilization of drainage systems date back to the archaic cultivation of land [3], which influenced drainage's application to irrigation practice. Because of this, as an ancient idea coinciding with the start of agriculture, drainage boasted a historic unconsciousness as a sign of early civilization. However, the simplicity of the concept does not equate to the present situation, especially considering the millennial gap. The need for comprehensive drainage system management is required to attest to the underlying problems of today.

Fundamental concepts aligned to its evolution must also be reviewed in grasping drainage system management. For example, Butler et al. [4] have noted in their book that wastewater and stormwater are the two types of water being serviced by urban drainage systems (mutually varying in water quality, physicochemical characteristics, and disposal). In a nutshell, a drainage system aims to either remove or transport a type of liquid from one place to another. The facility where it is being done can be delineated into the natural versus the humanmade. In this regard, each type of system explores different complexity. Piped drainage system can be classified into combined and separate, for which the battle which is better to be used remains a debate in the realm of drainage system management [5]. Meanwhile, natural drainage system obviously refers to the innate path of waterbodies [6]. Varying conditions, especially considering the differences between the two marginal epoch, have amplified the need for drainage system while preserving the purpose throughout the years.

The world no longer tries to survive the problem of irrigation alone, but also the arising urban and modern problem that may or may not be related to the lack of drainage systems or the poor utilization of its facility. Urbanization is seen as a significant driving factor for the need for drainage system within the regions of densely populated areas, often called as urban drainage system [7]. The trend, however, is not caged to citification alone, but also with the migration of people [8] due to the socioeconomic stability that these areas promise. The inherent problem with this trend is the lingering domino effect it brings to environment, economy, and public health. As argued by Pratiwi Adi and Imam Wahyudi [7], urbanization calls for growth of population that demands higher consumption, that eventually leads to the unmanageable solid waste generation and increased risk of land disruption brought by incorrect land use.

Climate change is another factor that proposes the need for the analysis of drainage system management. This phenomenon challenges the utilization in terms of management, since it becomes unprecedented as time progresses. Climate change disrupts the normal hydrologic patterns that induces extreme rainfall within the areas [9]. This, therefore, draws the relationship of higher volume of flood and increased flood risks, especially in the highly urbanized areas with poor urban drainage system [10]. The aftermath of flooding then affects public health, as more hazards and risks regarding the safety of the masses are under question. Concerns like drowning, flood-related diseases, and disrupting smell threaten the health of the people exposed to flood [11].

Flooding is one of the natural disasters that has been occurring throughout the world and has damaged the lives and properties of communities [12]. Urbanization and improper implementation of government policies towards drainage system management resulted to problems like flooding. Accordingly, this paper discussed the different approaches worldwide for properly managing drainage systems.

2 Method of Collection

The backbone of this paper relies on the collated papers and studies sourced from reputable databases such as Elsevier, ResearchGate, MDPI, Springer, and ScienceDirect. General topics, retrieved from 2000 to 2022, were sourced using under the umbrella terms “Urban drainage systems,” “Sustainable Urban Drainage Systems,” “History of drainage systems,” “General policies of government and environmental institutions,” and the “Effectivity of Sustainable Urban Drainage Systems in mitigating floods.”

Google Scholar and ScienceDirect were utilized as the primary search engines for scholarly works and Mendeley for a systematic citation of sources.

3 Result and Discussion

3.1 *Brief Ancient Historical Development of Drainage System Management*

To fully understand the ways and means of drainage system management as a tool to alleviate urbanization-related problems (e.g., flooding) in today’s world, it is best to have a quick stroll down the history of how it evolved.

The very concept of drainage system presented itself naturally in the environment. Before the drainage system concept was even thought of, nature had its way of transporting and draining the excess liquids on its surface. Natural processes have ruled and managed the earliest signs of flood and waste disposal [5]. Only through the natural course, the waterways being paved by massive floodings in ancient times did the idea of a drainage system finally come into the public realm. Khan et al. [13], through their paper, have believed that Indus and Minoan Civilizations paved the way for the earliest designs of drainage systems. For instance, the paper has demonstrated that Indus Civilization (Harappa) was believed to have mastered water engineering even in the earliest times through a comprehensive linkage of residential lines connected to the main sewer (see Fig. 1). Meanwhile, from 2800 to 1100 BC, the Minoan civilization incorporated stone to build the facility away from the residential areas [14]. However, these ancient innovations seem to be still true and in practice



Fig. 1 Shows traces of Ancient Indus Drainage System in India. *Source* Adapted from [21]

today, except for the materials being incorporated and with a more elaborate plan in consideration of urbanization.

However, Valipour et al. [1], citing the work of Gilmore et al. [15], have argued that the Mesopotamian Civilization showed the most primitive utilization of artificial water management found in the channel of Iran in aid of the drainage system. In the strengths of these ancient civilizations, the drainage management systems of today continue to flourish. In fact, an interesting account of history has been revealed by Yazdanfar and Sharma [16], stating that the combined sanitary sewers being used today is an idea that stemmed from the ancient Romans as they worked with runoff drainage. On the other hand, ancient Chinese civilization boasts their innovation about stormwater management. According to Cun et al. [17], there is an excellent interconnection between the modern and ancient philosophy of stormwater management, which upholds the “practical” style amidst the intricate urbanization trends and culture.

These archaic civilizations have given the way for modern urban drainage systems to flourish. However, the civilizations that have sprouted simultaneously around the world cannot fit into writing for this paper. Table 1 shows other featured ancient civilizations and their historical accounts related to drainage systems.

Table 1 Summary of drainage system historical accounts of other ancient civilizations

Epoch	Highlight	Source
Mycenaean Civilization	Use of dykes	[1]
Ancient Egypt	Productivity in Agricultural Irrigation	[18]
Persian Civilization	The sacredness of drainage system; pollution equates to moral disobedience	[14]
Babylonian Civilization	Use of baked clay pipelines	[19]
Etruscan Civilization	Incorporated cistern to private versus public use in aid of urbanization	[20]

3.2 *Government Action on the Management and Public Utilization of Drainage System*

Planning and implementation of the government on the proper management of drainage systems are beneficial to prevent flooding, landslide, and potential health hazards. Climate change and urbanization are some of the factors that cause problems in drainage systems [22]. These factors can often lead to problems, especially if there are water quality problems, which may affect the health of the people when they are exposed to stormwater.

Government actions are often done through the conventional management of drainage systems to minimize the risk of flooding through directing the surface runoff, leading them to discharge and drains [23]. However, the conventional management of drainage systems is still not enough for the future problems that may happen. Drainage systems should be managed properly as it helps the people in their needs and provide solutions to the problems they encounter because of stormwater [17]. Government actions such as policies, ordinances, or environmental laws are some of the most common methods in the management of drainage system which can be sustainable for flood management [24]. Furthermore, the different methods on the management of drainage system that are used worldwide was shown in Table 2.

Local Regulations on the Proper Waste Disposal. Implementation of the laws or ordinances by the government contributes to the management of drainage system worldwide. This includes the programs which motivates the public to participate in cleaning, storing, and properly dispose their waste in appropriate places to prevent drainage overflow. Laws regarding flood risk management can help in preventing flood risks [25], while ordinances on proper waste disposal contributes to the management of drainage systems. Since floods affects both life and properties, measures and policies are implemented worldwide to act for this problem. The Ghanaian government uses early warnings for flood and implements strategies that would help mitigate the risks of flooding [26]. This indicates that problems on drainage systems can be minimized through planning and developing strategies.

Implementation of Environmental Related Laws. Environmental laws that are proposed and implemented to protect the environment was also beneficial in the management of drainage systems. The Ecological Solid Waste Management Act of 2000 or the Republic Act 9003 is an environmental related law in the Philippines where the reduction of solid waste as well as the proper disposal of solid waste were implemented in the country [27]. The United States also have environmental related laws which is the Pollution Prevention Act of 1990. This act focuses on the prevention of pollution through source reduction, whereas prevent improper disposal of waste indicating that waste should be disposed in an environmentally safe way [28]. This indicates that environmental laws are also implemented to properly dispose waste, which not only protects the environment, but also helps in the management of drainage systems through preventing problems like drainage overflow caused by improperly disposed garbage.

Table 2 Laws/ordinances implemented in different countries for the management of drainage system

Country	Law/ordinance	Objective of the law/ordinance	Approaches to drainage system management
Philippines	Metropolitan Manila Development Authority (MMDA) Regulation No. 96-009 or the (<i>Anti-Littering Law</i> , 1996)	To prevent littering and throwing of garbage in public places and to maintain cleanliness in public or private establishments	Implementation of the Anti-Littering Law allowed the citizens to be more responsible in the disposal of their waste to proper places. This approach helps to handle the management of canals in the Philippines to prevent drainage overflow due to improper waste disposal
Japan	Law No. 137 of 1970 or the (<i>Waste Management and Public Cleansing Law</i> , 1970)	To restrict the improper disposal of waste to public places and help in maintaining a clean environment	Government restrictions in Japan towards the disposal of waste in public places can help lessen the problems in canals which affects the drainage systems
Australia	(<i>Litter Act</i> , 1979)	To punish people who are littering and do not follow the act, in which offenders will be required to pay for the fines especially to offenders who are caught on the spot littering	Through the strict implementation of the Litter Act 1979, the public can prevent the disposal of waste in public places because it can even lead to court if they would refuse to pay for fines. They will motivate the people to follow the act, leading to proper management of drainage systems since it would be free from garbage which causes drainage overflow
Washington	2020 Revised Code of Washington Chapter 70A.200 or the (<i>Waste Reduction, Recycling, and Model Litter Control Act</i> , 2020)	To control littering in public places as well as produce programs which can help in effectively reducing the amount of waste being generated	Proper implementation of this act can help in establishing this act to be a permanent program which can improve the control of littering and reduce the amount of waste in drainage systems

Different countries worldwide who have poor drainage systems often experience problems such as flooding due to heavy rains. These countries implement flood prevention measures; however, these measures only help in the redistribution of floodwater, but do not resolve the root cause of flooding [29]. Furthermore, laws should encourage people to follow the measures that can help mitigate flooding [30].

Responsibility of the Public Towards the Participation on Drainage System Management. The public benefits from drainage systems since it transports waste material and helps in preventing flood occurrence caused by accumulation of water



Fig. 2 Storm Water Management in Boise City, Oklahoma. *Source* Adapted from [34]

in households. However, responsibility of the public towards the management of drainage systems should also be considered. Legal and environmental laws are implemented to manage the drainage systems, but public participation is also needed. Community involvement should be considered in the management of drainage systems [31]. Thus, stating the importance of the management of stormwater can help in encouraging the citizens to actively participate in the laws and ordinances by the government [32].

Interactions with communities particularly to citizens can also help in spreading awareness and allow them to analyze the importance of proper drainage system management [33]. The citizens and the government should equally help each other in the implementation of laws and ordinances [31] (Fig. 2). Moreover, the management of drainage systems should be through the cooperation of the government and the public to properly manage and minimize the problems encountered on drainage systems.

3.3 Sustainable Urban Drainage System (SuDS)

Drainage system management across the globe progresses as the environment changes caused by rapid urbanization and increased surface runoffs. From a broader perspective, this has been the main goal of introducing the Sustainable Urban Drainage System (SuDS) to most countries worldwide. This system provides the best management practices, low-impact developments (LI), and water-sensitivity design due to its imitation of natural hydrological processes such as infiltration, evapotranspiration, filtration, retention, and reuses [24]. It further intends to improve water quality and prevent the possibility of flooding to strengthen the city's resilience [11]. It can be classified as green roofs, rainwater harvesting systems, permeable paving, swales, rain garden, etc. all under one purpose of reducing runoff volume

and improving water quality control through infiltration, absorption, and channeling rainwater to avoid it from flowing directly to the sewage system [35]. The climate, on the other hand, is one of the influencing factors for the design of SuDS. This intends to state that while the climate varies, parameters and factors to be considered also change due to their hydrologic condition differences [23].

In the European Union, this intervention was seen as a “transitional pathway from conventional to sustainable flood management” [24]. Moreover, this sustainable way of transition works together with Green Infrastructure (GI) which focuses on the lenses of the environmental landscapes and was quoted to be a smart approach to preserving and making use of natural spaces within the city [11]. Despite the numerous findings on the efficacy of SuDS, Brazil is still challenged by its management toward mitigating urban floods due to insufficient legislation mainly in semi-arid regions [35]. Table 3 shows the different considerations for SuDS that are based on climate.

As seen in Table 3, climate is a driving factor to consider for designing SuDS with varying parameters and factors. The parameters for the sub-tropical and semi-arid countries are almost the same, specifically the design consideration for the size of the pipes. As already mentioned, SuDS are designed for the management of stormwater runoff, and this depends on the volume of runoff a certain area receives. Consequently, for the sub-tropical countries, rainfall rate and total precipitation are valuable factors while the semi-arid considers soil moisture and dry periods for the location and details of the design [35]. Moreover, it has been found that subtropics are the best climate for SuDS application due to its high pollutant removal brought by high-intensity rainfalls [23].

SuDS Approach Technologies. The need for urban drainage management arises due to the continuous growth of the population over the years. As a response to this ongoing dilemma, global attention is geared toward the SuDS that creates a simultaneous result of both water quantity and quality for the drainage management systems. However, transitional frameworks shall be considered in accordance with the diverse adaptability of the cities involved [31]. Flood Mitigation, Pollutant Removal, and Aesthetics are one of the multicriteria Analysis for the design of SuDS depending on the place and its specifications such as the size and filter to be utilized [36].

Despite the positive agenda of this implementation to mitigate flooding, there are still barriers that are beyond the grasp of the engineering design which are the financial provisions and higher management approval. Russia, Belarus, and Ukraine justified

Table 3 Considerations for SuDS depending on climate

Climate	Parameters	Factors	Source
Sub-tropical (Hongkong, Manila)	Size, filter media, and vegetation	Rainfall rate and total precipitation	[23]
Semi-Arid (Campina Grande, Brazil)	Size of pipes and channels Land-use legislation based	Soil moisture and previous dry periods	[35]

Table 4 Surface runoff reduction of different SuDS in Brazil, Vietnam and Berlin

Country	SuDS surface runoff reduction (%)			Source
	Green Roof (GR)	Pervious Pavements (PP)	Rain Gardens (RG)	
Brazil	13.8	55.2	48.3	[35]
Vietnam	19.75	13.27	6.27	[36]
Berlin	28	38	39	[39]

this concern by highlighting the aggravated regulatory frameworks, as well as the major funding, powered by international sponsors promoted by the non-Government office (NGO) [37]. England and Wales on the other hand are not fully confident in this sustainable solution due to their separate call for addressing the concern in water quality and quantity which impedes the possibility of maximizing outputs with lower economic cost [38]. While some of the countries halted due to barriers present, most of the countries are welcoming this proposal with different approaches to SuDS and its effectiveness towards the reduction of surface runoff compared to conventional drainage management systems. Shown in Table 4 are some studies that highlighted the different SuDS and their corresponding the surface runoff reduction in different countries.

The table above shows the percentage of the reduced surface runoff for Brazil, Vietnam, and Berlin. As seen, different approaches were maximized for each country wherein Brazil showed favorability to pervious pavements on sidewalks (Fig. 3a) as recorded with decreased flow volumes upon adaptation. But as compensation for areas where pervious pavements are not advisable such as free spaces, rain gardens are utilized instead [35]. In the case of Vietnam, the green roof (Fig. 3b) showed the most effective response to flood mitigation while considering the load capacity of roofs, existing piping systems, and other relevant parameters that were specifically analyzed [36]. Berlin on the other hand also showed a different SuDS approach through Rain Gardens or the intervention of green spaces. Rain garden boasts a visual statement for passerby, which offers more function than stated as seen in Fig. 3c. This intervention was studied for a year suggesting situating SuDS downstream of streets to maximize its purpose [39]. Overall, it can be inferred that SuDS varies depending on the adaptation of the countries. Technical factors such as climate, topography, and population can come up with the best solution suited for the location.

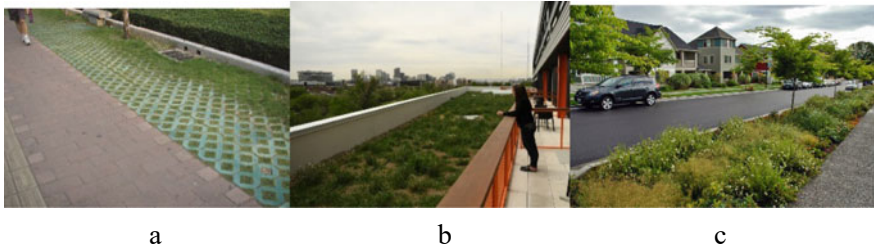


Fig. 3 **a** Pervious pavements. *Source* Adapted from [40], **b** Green roof at the Flight office building, Denver. *Source* Adapted from [41], **c** Rain Gardens between a road and sidewalk. *Source* Adapted from [42]

4 Conclusion

Countries worldwide experience rampant problems involving drainage systems. Heavy rains lead to problems in drainage systems such as flooding where the discharge of water goes beyond the drainage capacity [43] affecting the lives and properties of communities as well as risks that these problems impose on public health. This paper discussed the different approaches for the proper management of drainage systems worldwide. The management of drainage systems is important to prevent problems such as flooding, drainage overflow, and health-related concerns. In order to manage drainage systems, different approaches were taken by countries worldwide.

Approaches such as (1) Historical development of drainage system management (2) Government actions on the management and public utilization of drainage system, (3) Management of drainage system resources through Sustainable Urban Drainage System (SuDS) including the application of technological innovation in the management of drainage systems.

Historical Development of Drainage System Management. Archaic civilizations have allowed the innovation of stormwater management which gave way to a practical and modern way for the modern urban drainage system to flourish.

Government Actions on the Management and Public Utilization of Drainage System. The relationship between the citizens and the government should be analyzed to determine the impacts of cooperation toward the proper management of drainage systems.

Management of Drainage System Resources through Sustainable Urban Drainage System (Suds). The SuDS varies on the factors such as climate, topography, and population which can help provide the best practical solution to the problems of drainage system management. Modeling and simulation through technological innovation of drainage systems should also be emphasized to generate future ideas that may help resolve problems in drainage systems.

Moreover, identifying the different approaches to drainage system management can help other countries to determine the best practice and approaches suitable for

them. Furthermore, among the different approaches towards the proper management of drainage systems, it is important to know the most appropriate approach considering the available resources and practices that are most suitable for the needs and capabilities of the country.

Acknowledgements The proponents would like to express our most incredible gratitude and acknowledge National University—Manila particularly the Research and Development (NURD) Office for their support towards the presentation and publication of this research in the international stage.

References

1. M. Valipour et al., “The evolution of agricultural drainage from the earliest times to the present,” *Sustainability (Switzerland)*, vol. 12, no. 1. MDPI, 2020. doi: <https://doi.org/10.3390/SU12010416>.
2. L. García, J. Barreiro-Gomez, E. Escobar, D. Téllez, N. Quijano, and C. Ocampo- Martinez, “Modeling and real-time control of urban drainage systems: A review,” *Adv Water Resour*, vol. 85, pp. 120–132, Nov. 2015, doi: <https://doi.org/10.1016/j.advwatres.2015.08.007>.
3. G. O Schwab, P. W. Manson, J. N. Luthin, R. C. Reeve, and T. W. Edminster, “Engineering Aspects of Land Drainage,” 1957.
4. D. Butler, C. Digman, C. Makropoulos, and J. Davies, “Urban Drainage Fourth Edition,” 2018.
5. D. Butler and J. Davies, “Urban Drainage, 2nd Edition,” 2004.
6. J. Parkinson, “Drainage and stormwater management strategies for low-income urban communities,” 2003.
7. H. Pratiwi Adi and S. Imam Wahyudi, “Integrated Solution to Overcome the Climate Change Impact on Coastal and Delta Areas Semarang,” 2015.
8. Bach PM, Rauch W, Mikkelsen PS, McCarthy DT, Deletic A (2014) A critical review of integrated urban water modelling - Urban drainage and beyond. *Environ Model Softw* 54:88–107. <https://doi.org/10.1016/j.envsoft.2013.12.018>
9. K. Arnbjerg-Nielsen et al., “Impacts of climate change on rainfall extremes and urban drainage systems: A review,” *Water Science and Technology*, vol. 68, no. 1. 2013. doi: <https://doi.org/10.2166/wst.2013.251>.
10. Q. Zhou, G. Leng, J. Su, and Y. Ren, “Comparison of urbanization and climate change impacts on urban flood volumes: Importance of urban planning and drainage adaptation,” *Science of the Total Environment*, vol. 658, 2019, doi: <https://doi.org/10.1016/j.scitotenv.2018.12.184>.
11. Hoang L, Fenner RA (2016) System interactions of stormwater management using sustainable urban drainage systems and green infrastructure. *Urban Water J* 13(7):739–758. <https://doi.org/10.1080/1573062X.2015.1036083>
12. J. Costa, “The World’s Largest Floods, Past and Present.” [Online]. Available: <http://www.usgs.gov/>
13. S. Khan, E. Dialynas, V. K. Kasaraneni, and A. N. Angelakis, “Similarities of minoan and indus valley hydro-technologies,” *Sustainability (Switzerland)*, vol. 12, no. 12, 2020, doi: <https://doi.org/10.3390/SU12124897>.
14. Burian SJ, Edwards FG (2002) Historical perspectives of urban drainage. *Global Solutions for Urban Drainage*. [https://doi.org/10.1061/40644\(2002\)284](https://doi.org/10.1061/40644(2002)284)
15. Gillmore GK et al (2009) Irrigation on the Tehran Plain, Iran: Tepe Pardis - The site of a possible Neolithic irrigation feature? *Catena (Amst)* 78(3):285–300. <https://doi.org/10.1016/j.catena.2009.02.009>

16. Z. Yazdanfar and A. Sharma, "Urban drainage system planning and design - Challenges with climate change and urbanization: A review," *Water Science and Technology*, vol. 72, no. 2. 2015. doi: <https://doi.org/10.2166/wst.2015.207>.
17. C. Cun, W. Zhang, W. Che, and H. Sun, "Review of urban drainage and stormwater management in ancient China," *Landscape and Urban Planning*, vol. 190. Elsevier B.V., Oct. 01, 2019. doi: <https://doi.org/10.1016/j.landurbplan.2019.103600>.
18. S. Abdel-Dayem, S. Abdel-Gawad, and H. Fahmy, "Drainage in Egypt: A story of determination, continuity, and success," *Irrigation and Drainage*, vol. 56, no. SUPPL. 1, 2007, doi: <https://doi.org/10.1002/ird.335>.
19. G. de Feo *et al.*, "The historical development of sewers worldwide," *Sustainability (Switzerland)*, vol. 6, no. 6. 2014. doi: <https://doi.org/10.3390/su6063936>.
20. N. Angelakis, G. de Feo, P. Laureano, and A. Zourou, "Minoan and etruscan Hydro-Technologies," *Water (Switzerland)*, vol. 5, no. 3. 2013. doi: <https://doi.org/10.3390/w5030972>.
21. B. Gagnon, "A water well in Lothal," Wikipedia, Feb. 13 2020, [Online] Available: https://en.wikipedia.org/wiki/Sanitation_of_the_Indus_Valley_Civilisation#/media/File:Lothal_-_ancient_well.jpg
22. D. Jato-Espino, E. I. Toro-Huertas, and L. P. Güereca, "Lifecycle sustainability assessment for the comparison of traditional and sustainable drainage systems," *Science of The Total Environment*, vol. 817, Apr. 2022.
23. S. S. Chen *et al.*, "Designing sustainable drainage systems in subtropical cities: Challenges and opportunities," *Journal of Cleaner Production*, vol. 280. Elsevier Ltd, Jan. 20, 2021. doi: <https://doi.org/10.1016/j.jclepro.2020.124418>.
24. M. Gimenez-Maranges, J. Breuste, and A. Hof, "Sustainable Drainage Systems for transitioning to sustainable urban flood management in the European Union: A review," *Journal of Cleaner Production*, vol. 255. Elsevier Ltd, May 10, 2020. doi: <https://doi.org/10.1016/j.jclepro.2020.120191>.
25. Mehryar S, Surminski S (2021) National laws for enhancing flood resilience in the context of climate change: potential and shortcomings. *Climate Policy* 21(2):133–151. <https://doi.org/10.1080/14693062.2020.1808439>
26. A. Almoradie *et al.*, "Current flood risk management practices in Ghana: Gaps and opportunities for improving resilience," *J Flood Risk Manag*, vol. 13, no. 4, Dec. 2020, doi: <https://doi.org/10.1111/jfr3.12664>.
27. Ecological Solid Waste Management Act. 2000. Accessed: Dec. 17, 2022. [Online]. Available: <https://www.officialgazette.gov.ph/>
28. Pollution Prevention Act. 1900. Accessed: Dec. 17, 2022. [Online]. Available: <https://www.epa.gov>
29. I. B. Lourenço, L. F. Guimarães, M. B. Alves, and M. G. Míguez, "Land as a sustainable resource in city planning: The use of open spaces and drainage systems to structure environmental and urban needs," *J Clean Prod*, vol. 276, Dec. 2020, doi: <https://doi.org/10.1016/j.jclepro.2020.123096>.
30. W. A. Adebayo, "Environmental Law And Flood Disaster In Nigeria: The Imperative Of Legal Control," *International Journal of Education and Research*, vol. 2, no. 7, 2014, [Online]. Available: www.ijern.com
31. Andrés-Doménech I, Anta J, Perales-Momparler S, Rodríguez-Hernandez J (2021) Sustainable urban drainage systems in Spain: A diagnosis. *Sustainability (Switzerland)* 13(5):1–22. <https://doi.org/10.3390/su13052791>
32. V. Pappalardo and D. la Rosa, "Policies for sustainable drainage systems in urban contexts within performance-based planning approaches," *Sustain Cities Soc*, vol. 52, Jan. 2020, doi: <https://doi.org/10.1016/j.scs.2019.101830>.
33. Ramsey MM, Muñoz-Erickson TA, Mélendez-Ackerman E, Nytech CJ, Branoff BL, Carrasquillo-Medrano D (2019) Overcoming barriers to knowledge integration for urban resilience: A knowledge systems analysis of two-flood prone communities in San Juan, Puerto Rico. *Environ Sci Policy* 99:48–57. <https://doi.org/10.1016/j.envsci.2019.04.013>

34. City of Bose, "Stormwater and Drainage Control," (n.d.), Accessed: Feb. 13, 2023. [Online]. Available: <https://cob.azureedge.net/cache/7/0/2/7/2/9/702729ac62bf38dde3bf6aa6c22199e994500f2a.jpg>
35. P. B. R. Alves, I. A. A. Rufino, P. H. C. Feitosa, S. Djordjević, and A. Javadi, "Land-use and legislation-based methodology for the implementation of sustainable drainage systems in the semi-arid region of Brazil," *Sustainability (Switzerland)*, vol. 12, no. 2, Jan. 2020, doi: <https://doi.org/10.3390/su12020661>.
36. Loc HH, Duyen PM, Ballatore TJ, Lan NHM, das Gupta A (2017) Applicability of sustainable urban drainage systems: an evaluation by multi-criteria analysis. *Environ Syst Decis* 37(3):332–343. <https://doi.org/10.1007/s10669-017-9639-4>
37. Shkaruba A et al (2021) Development of sustainable urban drainage systems in Eastern Europe: an analytical overview of the constraints and enabling conditions. *J Environ Planning Manage* 64(13):2435–2458. <https://doi.org/10.1080/09640568.2021.1874893>
38. Ellis JB, Lundy L (2016) Implementing sustainable drainage systems for urban surface water management within the regulatory framework in England and Wales. *J Environ Manage* 183:630–636. <https://doi.org/10.1016/j.jenvman.2016.09.022>
39. M. Riechel et al., "Sustainable urban drainage systems in established city developments: Modelling the potential for CSO reduction and river impact mitigation," *J Environ Manage*, vol. 274, Nov. 2020, doi: <https://doi.org/10.1016/j.jenvman.2020.111207>.
40. S. Ink, "Pervious pavement," National Association of City Transportation Officials, July 24, 2015. [Online]. Available: <https://nacto.org/publication/urban-street-design-guide/street-design-elements/stormwater-management/pervious-pavement/>.
41. J. Murray, "Denver's Green Roof Initiative may face big changes that provide less-costly options - but its lead backer is OK with that," *The Denver Post*, May 15, 2018. [Online]. Available: <https://www.denverpost.com/2018/05/14/denver-green-roof-initiative-big-changes/>.
42. N. Wakefield, "Incorporating sustainable urban drainage systems into landscape design," *Node*, November 22, 2016. [Online]. Available: <http://www.thisisnode.com/2016/11/22/incorporating-sustainable-urban-drainage-systems-into-landscape-design/>.
43. Q. Sholihah, W. Kuncoro, S. Wahyuni, S. Puni Suwandi, and E. Dwi Feditasari (2020) The analysis of the causes of flood disasters and their impacts in the perspective of environmental law. *IOP Conf Ser: Earth Environ Sci* 437(1). <https://doi.org/10.1088/1755-1315/437/1/012056>

Influence of Parameter Variation of Saturated–Unsaturated Soil on Deformation and Stability of Foundation Pit



Yongbiao Xu, Yinzhen Dong, Yingyuan Jiang, Jianfen Zhou, and Qian Mao

Abstract The soil–water interaction of unsaturated soil has a significant impact on the characteristics of the soil. Capillary action makes the distribution range of unsaturated cohesive soil deep, and the effect of matric suction changes the characteristic parameters of the soil, affecting the deformation and stability of the foundation pit. In this paper, the theory of zonal shear strength of saturated–unsaturated soil is established. The physical and mechanical initial parameters of soil are obtained through tests. The deformation and slope stability of foundation pit are studied by finite element method. The theory is applied to the deformation and stability analysis of the foundation pit of the drainage pump station in Lanxi. When the excavation reaches a depth of 5 m, the error between the monitoring value of the horizontal displacement of the top of the foundation pit and the simulation result of the model is within 10% when considering the change of the unsaturated soil characteristic parameters; When the excavation reaches the depth of 9 m, considering the change of unsaturated soil characteristic parameters, the extreme value of stability coefficient of the foundation pit slope before and after adding steel support increased by 16.0% and 6.7% respectively. The theoretical model and numerical simulation results of saturated unsaturated soil in this paper are more consistent with the actual situation. The research results can be applied to the slope stability analysis of foundation pit excavation engineering.

Y. Xu

Lanxi Urban Investment Group Co., Ltd, Jinhua, Zhejiang, China

Y. Dong

Lanxi Town Planning Office, Jinhua, Zhejiang, China

Y. Jiang

Chengtou Reservoir Management Office of Lanxi Water Bureau, Jinhua, Zhejiang, China

J. Zhou (✉) · Q. Mao

Key Laboratory for Technology in Rural Water Management of Zhejiang Province, Zhejiang University of Water Resources and Electric Power, Hangzhou, China

e-mail: zhoujf@zjweu.edu.cn

Keywords Saturated and unsaturated soil · Water and soil characteristic parameters · On-site monitoring · Finite element simulation · Horizontal displacement · Slope stability

1 Introduction

The majority of geoenvironmental applications occur in the unsaturated, or vadose zone, which can be up to hundreds of metres in depth depending on the ground profile and climate. Unsaturated soil applications include foundation pit excavations, foundations and buried infrastructure. The pump station is the key engineering project of flood control. The foundation pit project of the pump station has the characteristics of complexity, concealment and temporary. Once an accident occurs, it will cause casualties and property losses. In recent years, deep foundation pit accidents occur frequently in China. The report of the Ministry of Housing and Urban–Rural Development shows that the safety accidents of deep foundation pit projects have accounted for more than 30% of the construction safety accidents in China [1]. The excavation of the foundation pit brings about the deformation and stability of the foundation pit slope. Excessive deformation or accelerated development is the prelude to the slope instability, and also causes the deformation or settlement of the surrounding buildings. During the excavation of the foundation pit, it is necessary to ensure the safety of the foundation pit itself, as well as the safety and stability of the adjacent buildings and underground structures.

The theory and engineering application of deformation and stability analysis of foundation pit slope need to be further deepened. Previous research mainly focused on field monitoring, model simulation, experimental research, theoretical exploration, etc. [2, 3]. Scholars have done a lot of research in this area, and have made relatively rich research results. Aiming at the problem of anti-uplift stability of foundation pit support in water conservancy projects, it is deduced the safety calculation model of anti-uplift stability applicable to soft soil areas [4]. The formula of foundation bearing capacity is revised, and the formula of shear force on the failure surface is deduced [5]. Ter-Martirosyan Z. G. and Pei Q. developed a method for determining the stressed state component in the reduced engineering problem, accounting for the nonlinear deformation properties of soils to determine the settlement over time of the foundation near the pit [6, 7]. After an excavation in the sand-gravel layer was supported by soldier pile, the displacement and stress of the surrounding rocks are reduced [8]. After studying the geoenvironmental applications in the vadose zone, the bearing capacity model of pile foundation of unsaturated soil is established [9]. It was found that the bearing capacity of unsaturated soil can reach 7 times of that of saturated soil with the increase of matric suction of unsaturated soil [10–13]. Recent studies have shown that as principles of unsaturated soils become more understood and demand increases for incorporating climate change effects in design, use of unsaturated soils, principles in practice will continue to increase [14]. Previous studies have mostly considered the physical and mechanical properties of saturated soil, and

less involved the influence of the strength change caused by unsaturated soil on the stress–strain field. This paper studies the stability of foundation pit slope from the mechanical properties of saturated–unsaturated soil.

2 Theoretical Model

In the past, the deformation and strength of unsaturated soil were only studied according to the total stress state, which was quite different from the actual situation, resulting in a large deviation between the analysis results and the actual situation. For the analysis of foundation pit stability, it is necessary to find a more reasonable expression, taking the matric suction of unsaturated soil into consideration, so that the volume strain, water content and shear strength are consistent. The soil mass of foundation pit slope is divided into saturated and unsaturated regions, which follow the strength theory of saturated and unsaturated soil respectively. From the ground to the bottom, the saturation of slope soil gradually increases as the depth increases, as shown in Fig. 1. The saturation of capillary zone changes greatly, which has a significant impact on the deformation and stability of cohesive soil.

The strength of saturated–unsaturated soil is closely related to the change of water content. The strength of saturated soil is determined according to the Mohr–Coulomb law to determine the failure envelope, and then determine the strength index. The shear strength of unsaturated soil is a combination of effective shear strength in saturated state and additional strength caused by matric suction [15]. It can be expressed as

$$\tau_{fw} = \tau_{fs} + \tau_s = c' + (\sigma - u_a)\tan\phi' + (u_a - u_w)\tan\phi^b \tag{1}$$

where τ_{fw} is the shear strength of unsaturated soil; τ_{fs} is the shear strength of unsaturated soil; τ_s is the additional strength caused by matric suction; c' is the cohesion; $(\sigma - u_a)$ is the effective stress; ϕ' is the effective friction angle; $(u_a - u_w)$ is the matric

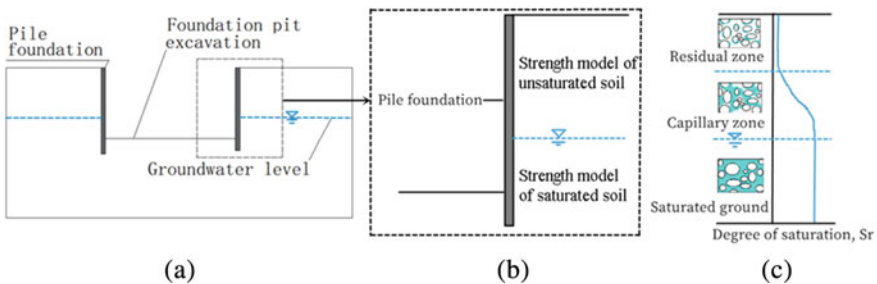


Fig. 1 Saturated and unsaturated soil in foundation excavation: **a** Cross section of foundation pit; **b** foundation pit soil strength model; **c** Schematic diagram of saturated–unsaturated soil

suction; φ^b is the adsorption internal friction angle. The additional strength caused by matric suction can be expressed by saturation and other parameters [16]. It was calculated according to Eq. (Eq. 2).

$$\tau_s = \left[(u_a - u_w) \frac{S - S_r}{1 - S_r} \right] \tan \varphi' = [(u_a - u_w) S_e] \tan \varphi' \tag{2}$$

where S is the saturation; S_r is the residual saturation; S_e is the effective saturation. The relationship curve between water content and permeability coefficient is obtained through test. The relationship between matric suction and permeability coefficient of saturated–unsaturated soil is expressed by subsection function, as shown in Fig. 2 [17]. After simplifying the water and soil characteristic curve of van Genuchten, Eqs. (3) and (4) are used to express the relationship between matric suction and permeability coefficient.

$$u_a - u_w \in [0, 10] [(u_a - u_w) \leq (u_a - u_w)_b] \tag{3}$$

$$u_a - u_w = \frac{k_i - k_w}{c} + (u_a - u_w)_b [(u_a - u_w) > (u_a - u_w)_b] \tag{4}$$

where $(u_a - u_w)_b$ is the generalized limit value of suction between saturated and unsaturated regions; k_w is the permeability coefficient of unsaturated soil; k_s is the permeability coefficient of saturated soil; c is the fitting coefficient of Eq. (4).

In this way, the effective friction angle, cohesion, permeability coefficient and other relevant parameters of saturated–unsaturated soil can be obtained through the test, and the shear strength can be obtained by substituting Eqs. (1) and (Eq. 2), and then the deformation and stability of the slope can be judged after comparing with the numerical analysis results.

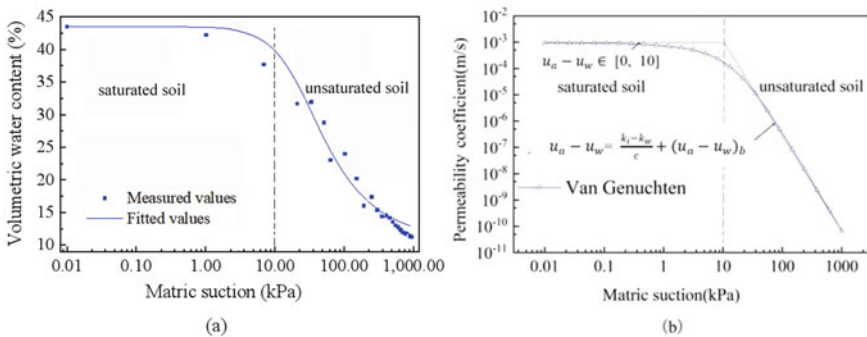


Fig. 2 Relation of saturated–unsaturated soil volumetric water content and matric suction: **a** Soil–water characteristic curve; **b** permeability coefficient and matric suction curve

3 Case Application

3.1 Project Overview

At present, the main specifications for the design of foundation pit engineering are the *Technical Code for Building Foundation Pit Support* (JGJ120-2012) and the *Code for Design of Building Foundation* (GB50007-2011) of the Ministry of Housing and Urban–Rural Development, and the *Technical Code for Building Foundation Pit* (DB33/T1096-2014) of Zhejiang Province. The current foundation pit stability design theory does not consider the soil and water characteristics of unsaturated soil, and the calculation results have a large deviation from the actual situation. In this paper, the strength formula of saturated–unsaturated soil is simplified, and the relevant parameters are measured in combination with the field and laboratory tests, which are applied to the deformation and stability analysis of the foundation pit of the drainage station. The project is located in Lanxi, a city in southern China, at the intersection of Qu River, Jinhua River and Lan River. It is the intersection of Lanxi urban flood embankment and urban drainage. The geographical location of the project and the layout of the foundation pit are shown in Fig. 3. When the rainstorm comes, the waterlogged water in the urban is discharged to the Lan river by pump station. The flood control standard of the project is once in 50 years.

3.2 Engineering Geological Conditions

The site of this engineering is a structurally stable section, and the geological and foundation pit section are shown in Fig. 4. The artificial fill of layer I is mainly silty clay with gravel, which is unevenly distributed. The gravels and pebbles in layer II are mainly slightly dense, and the gravels and pebbles are mainly volcanic rocks, which are sub-rounded. The gravels are filled with sand and a small amount of silt and clay. Layer III pelitic siltstone is purplish red, silty structure, medium-thick layer, argillaceous cementation, soft rock, gentle occurrence, widely distributed, and undeveloped structural plane. See Table 1 for the physical parameters of each soil layer measured by the clay plate compression test, triaxial consolidation undrained test and variable head permeability test.

3.3 Finite Element Model and Horizontal Displacement

The typical section of the foundation pit is selected. The ground elevation of the foundation pit is 32.3 m, the bottom elevation is 23.3 m, the depth is 9 m, and the width is 28.3 m. The reinforced concrete cast-in-place pile is 0.5 m below the bedrock, and the pile length is 17.6 m. The elastic modulus of artificial fill, sandy

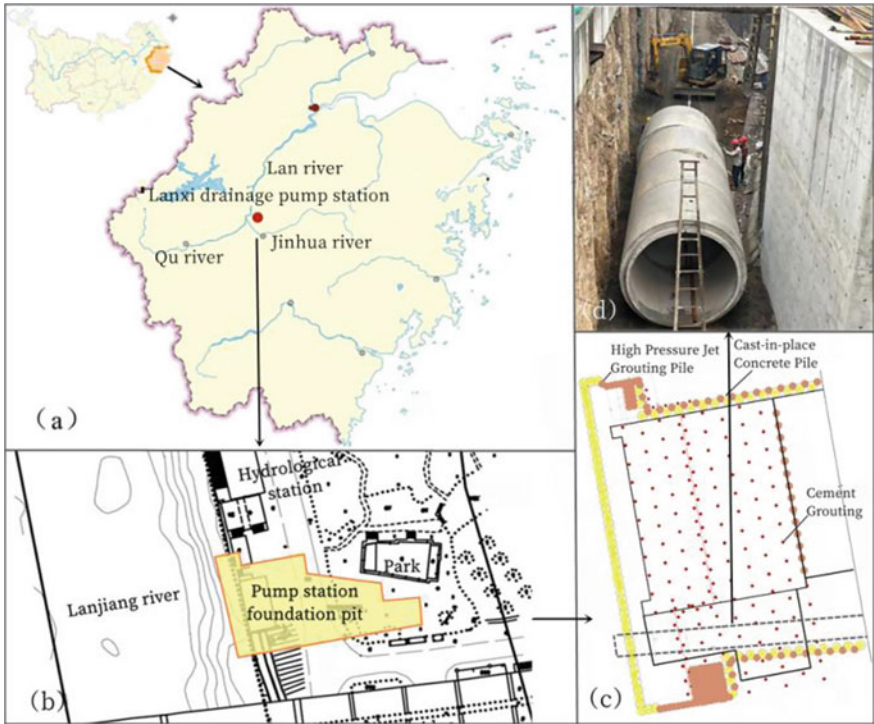


Fig. 3 Geographic location and engineering layout: **a** Geographic location of the engineering; **b** plane position of pump station; **c** Pile foundation; **d** diversion construction of pump station

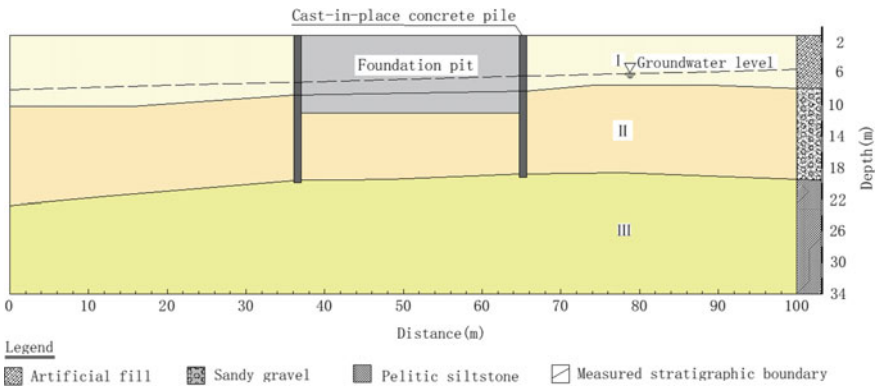


Fig. 4 Typical geological and foundation pit section

Table 1 Physical and mechanical indexes of soil layer in the typical section

Number	Name	Thickness	Natural density	Volume water content	Void ratio	Friction angle	Cohesion	Initial permeability coefficient
		m	$\text{kN}\cdot\text{m}^{-3}$	%	/	°	kPa	$\text{cm}\cdot\text{s}^{-1}$
I	Artificial fill	6.5	15.6	42.8	1.08	26.5	2.3	9.7×10^{-3}
II	Sandy gravel	10.6	17.9	37.6	1.20	35.0	0	4.1×10^{-3}
III	Pelitic siltstone	> 7	20.3	/	/	40.0	6.5	/

pebble foundation and argillaceous siltstone are 19.0, 21.0 and 30.0 MPa respectively, and Poisson's ratio is 0.32, 0.30 and 0.33 respectively. The elastic modulus of cast-in-place pile is 25.0 MPa, and Poisson's ratio is 0.33. In order to compare the influence of unsaturated soil parameters on the calculation results, the deformation and stability of the foundation pit are calculated and analyzed with and without considering the soil and water characteristic curve.

The foundation pit construction is divided into three working conditions, namely, 0.5, 5 and 9 m below the excavation surface, as shown in Table 2. The numerical model is a quadrilateral elastic–plastic element, and the groundwater level elevation is 27.8 m. The cell grid division is shown in Fig. 5., with 3331 cells and 3854 nodes in total.

Displacement monitoring 1 # and 2 # clinometers are set in the cast-in-place concrete piles to monitor the change of horizontal displacement value during excavation, as shown in Fig. 6.

When the foundation pit is excavated to a depth of 5 m, it is the depth of groundwater level. Numerical simulation calculation is carried out with and without considering the water and soil characteristic model. The results are compared with the monitoring values, as shown in Table 3. It can be seen that when the variation of unsaturated soil parameters is considered, the simulation results are close to the monitoring values, and the horizontal displacement deviation at the top of the cast-in-place concrete piles are within 10%. It can be seen that this model and the selection of relevant parameters can better simulate the deformation of foundation pit. When the

Table 2 Foundation pit construction condition

Stages of process	Construction condition
1	Excavate to 0.5 m below the ground surface, construct crown beam and set steel support
2	Excavate to 5 m below the ground surface
3	Excavate to 9 m below the ground surface

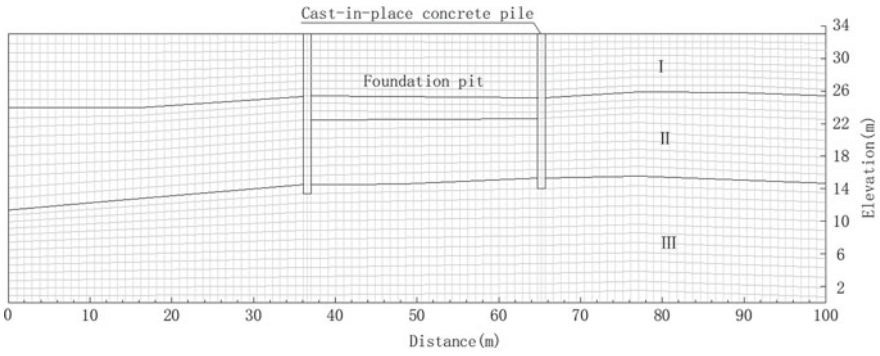


Fig. 5 Cell grid division of the model

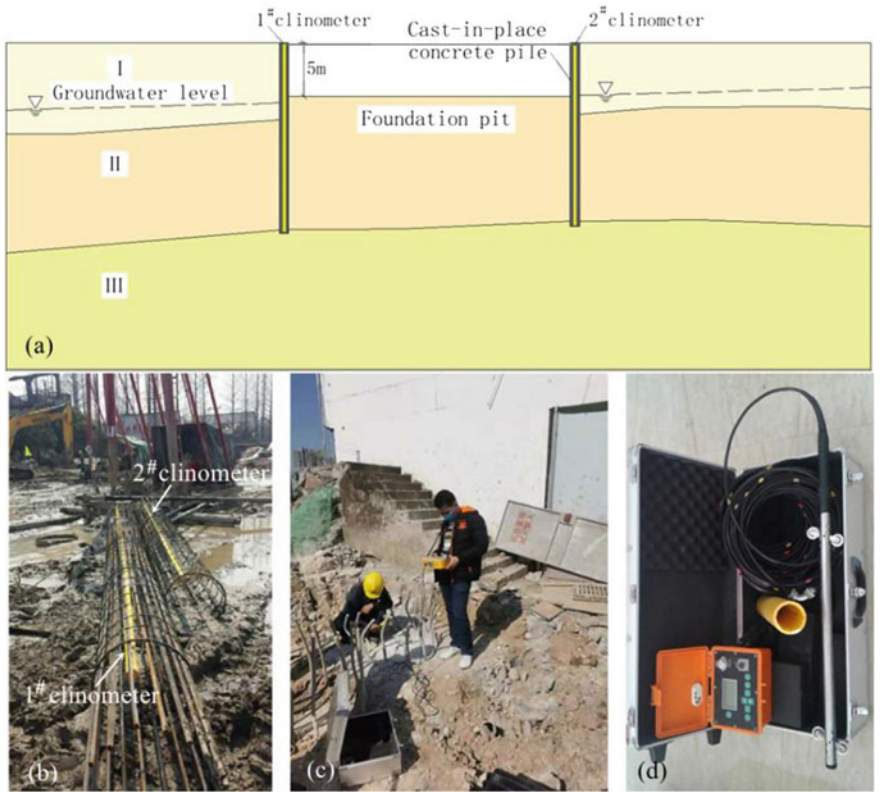


Fig. 6 Horizontal displacement monitoring of foundation pit: a Layout diagram of clinometer; b installation of clinometer; c horizontal displacement monitoring; d clinometer

Table 3 Monitoring value and simulation value of displacement at the top of foundation pit

Number	Excavation depth	Horizontal displacement monitoring	Numerical simulation results (unsaturated soil is considered)	Deviation ratio	Numerical simulation results (unsaturated soil is not considered)	Deviation ratio
	m	cm	cm	%	cm	%
1#	5	2.5	2.7	8.0	3.1	24.0
2#	5	2.1	2.2	4.8	2.6	23.8

variation of unsaturated soil parameters is not considered, the horizontal displacement deviation at the top is within 25%. It shows that considering the influence of soil–water characteristics of unsaturated soil on the deformation is more practical. And then apply this numerical model to study the stability of the foundation pit.

3.4 Results and Analysis

The overall stability of the foundation pit is simulated numerically when it is excavated to 9 m, and the slope stability without steel support and steel support is analyzed respectively, as shown in Fig. 7. Lines 1 and 2 show the slope sliding surface without steel support, and lines 3 and 4 show the slope sliding surface after steel support. Lines 1 and 3 are the most dangerous sliding surface without considering the influence of unsaturated soil parameters on strength, and lines 2 and 4 are the most dangerous sliding surface after considering unsaturated soil parameters. According to the analysis results, the corresponding safety factors of slope stability in the four cases are 1.065, 1.268, 2.171 and 2.325 respectively. After considering the change of unsaturated soil parameters, the extreme value of slope anti-sliding stability coefficient increased by 16.0% before and 6.6% after adding steel support. It can be seen that in the slope stability analysis, the slope stability coefficient is improved after considering the parameter variation of unsaturated soil, which has a guiding role for the design of foundation pit excavation and steel support.

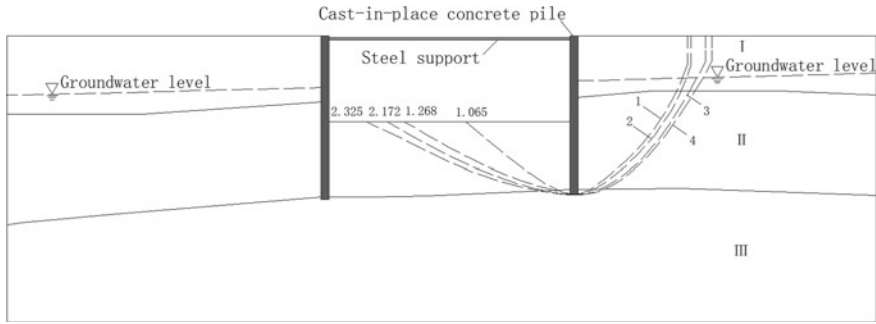


Fig. 7 Stability coefficient of foundation pit slope

4 Conclusion

In this paper, the current stability analysis theory of foundation pit slope is improved theoretically, and the stability analysis method of foundation pit with complex soil structure considering the variation of soil and water characteristics parameters of unsaturated soil is established. Taking the foundation pit engineering of the pump station in Lanxi as an example, the changes of displacement and slope stability in the foundation pit excavation engineering are analyzed, and the following conclusions are got:

- (1) In the foundation pit support engineering, the slope soil mass is divided into saturated and unsaturated regions. Due to the capillary effect, the soil and water characteristic parameters in the unsaturated region have a certain impact on the stress and strain of the soil mass. In this paper, the relationship between matric suction and effective friction angle, cohesion and permeability coefficient in saturated and unsaturated regions is established.
- (2) In the past, the stability analysis method of foundation pit only had been considered a single parameter of soil mass. In this paper, the variation model of soil and water characteristics parameters of saturated and unsaturated soil is established. The comparison between the field displacement monitoring values and the simulation results shows that the stability analysis method in this paper is more in line with the actual situation. When this method is applied to analyze the stability of the foundation pit of the drainage pump station in Lanxi, the stability coefficient of the foundation pit slope increases when the variation of the soil and water characteristics parameters of the unsaturated soil is considered, compared with the single parameter of the soil.
- (3) The cohesive soil is widely distributed in foundation pit support engineering, and the variation of soil and water characteristics parameters of unsaturated soil are significant. The analysis results of the mathematical model of saturated–unsaturated soil in this paper are close to the actual situation. The research results can be applied to the slope stability analysis of foundation pit excavation engineering.

Acknowledgements The authors thank Lanxi Water Construction Engineering Investment Limited Liability Company for their support and funding acquisition. This research was Supported by Major Science and Technology Plan Project of Zhejiang Provincial Department of Water Resources (RA1904).

References

1. Ministry of Housing and Urban-Rural Development of the People's Republic of China: Circular of the General Office of the Ministry of Housing and Urban-Rural Development on the production safety accidents of housing and municipal engineering in 2019, 13–16 (2020).
2. Zhao YH, Tong LY et al (2020) Prediction and analysis of the influence of foundation pit dewatering on the surrounding environment under different water stop curtain insertion depth. *Water Resources and Hydropower Engineering* 51(5):126–131
3. Cheng L (2022) Monitoring and analysis of stability of supporting structure for narrow deep foundation pit on weak soil base. *Port Engineering Technology* 59(5):77–81
4. Ye M (2022) Analysis of Anti-heave Stability of Excavation for Water Conservancy Projects in Guangdong. *Guangdong Water resources and hydropower* 12:122–127
5. Liu YF, Ye JJ (2022) Improvement of the checking calculation formula of heave resistant stability of excavations in soft soil areas. *Natural Science Journal of Hainan University* 40(4):400–406
6. Ter-Martirosyan ZG (2022) Mathematical computations of long-term settlement and bearing capacity of soil bases and foundations near vertical excavation pits. *Axioms* 11:679–686
7. Pei Q, Ding X (2019) Optimized back analysis method for stress determination based on identification of local stress measurements and its application. *Bull Eng Geol Environ* 78:375–396
8. Jiang Xie, Xiaojia Lu, et al: Force Chain Effect of Deep Foundation Pit Supported by Soldier Piles in the Sand-Gravel Layer. *Shock and Vibration*, Article ID 9617807 (2021).
9. Vanapalli, S.K., & Mohamed, F.M.: Bearing capacity of model footings in unsaturated soils. *Springer Proceedings in Physics*, Berlin (2007).
10. Khalili N, Zargarbashi S (2010) Influence of hydraulic hysteresis on effective stress in unsaturated soils. *Géotechnique* 60(9):729–734
11. Zhang C, Fan W (2015) A new twin-shear true triaxial strength criterion of unsaturated soils and its validations. *Journal of tongji university (Natural Science)* 43(9):1326–1331
12. Zhang L, Chen Z (2017) Test verification of stress state variables for unsaturated soils. *Chinese Journal of Geotechnical Engineering* 39(2):380–384
13. Kang L, Jian Y (2022) Analytical analysis of infinite heterogeneous slope stability considering suction influence. *Geofluids* 29(5):156–169
14. Greg A (2018) Unsaturated soil mechanics - bridging the gap between research and practice. *Can Geotech J* 55:909–927
15. Fredlund DG, Xing A (1994) Equations for the soil-water characteristic curve. *Can Geotech J* 31(4):521–532
16. Vanapalli SK, Fredlund DG (1996) Model for prediction of shear strength with respect to soil suction. *Can Geotech J* 33(3):379–392
17. Zhou JF, Dong ZY et al (2023) Influence of induced variability of unsaturated soil parameters on seepage stability of ancient riverbank. *Appl Sci* 13(3):1481

An Urban Public Transport Resilience Assessment Methodology Based on a Two-Carbon Context



Keyuan Ding , Xueliang Liu, Ran Peng , and Hanbang Ning

Abstract In 2020, China has proposed “peak carbon” and “carbon neutral” targets, of which active guidance for low-carbon travel will be crucial. Urban public transportation has the advantages of high capacity and high intensification, and its per capita energy consumption is extremely low compared with that of small cars. Therefore, the proportion of people traveling by public transportation in a city will directly affect the overall traffic resilience level of the city. In this regard, this paper takes Wuhan City, Hubei Province as an example, and through an extensive survey of residents’ travel characteristics, we count the threshold of residents’ willingness to still choose public transportation when faced with the phenomenon of connections, detours and transfers in public transportation. The total motorized trips were classified into four modes, including active public transportation mode, easy to replace the car mode, passive public transportation mode and not easy to replace the car mode. By fitting the relationship curves between their thresholds and the proportion of each type of travel mode, the corresponding assessment system of urban public transportation resilience is established, and finally the key nodes in the curves are identified according to the fitting results. And accordingly, the overall public transportation resilience characteristics of the city and the distribution of public transportation resilience in each region within the city are analyzed.

Keywords Connections · Detours · Transfers · Public transport resilience · Wuhan

1 Introduction

Since the beginning of the twentieth century, environmental problems have become increasingly serious, and the trajectory of human carbon emissions has had a significant impact on the ecological environment. In order to address climate change and environmental problems caused by human carbon emissions, countries around

K. Ding · X. Liu · R. Peng (✉) · H. Ning

School of Civil Engineering and Architecture, Wuhan Institute of Technology, Wuhan, China

e-mail: pengran@wit.edu.cn

© The Author(s), under exclusive license to Springer Nature Singapore Pte Ltd. 2024
M. Casini (ed.), *Proceedings of the 3rd International Civil Engineering and Architecture Conference*, Lecture Notes in Civil Engineering 389,
https://doi.org/10.1007/978-981-99-6368-3_59

733

the world have successively proposed carbon reduction targets. Cities are the main contributors to carbon emissions, and transport is one of the main sources of urban carbon emissions. According to the International Energy Agency (IEA), the transport sector accounts for 37% of the 36.3 billion tons of global carbon emissions in 2021, and urban transport is the fastest growing contributor to carbon emissions. Residents are the basic unit of carbon emissions from urban transport, and their daily travel patterns have a significant impact on reducing urban carbon emissions and achieving the “dual-carbon” target. Public transport is a green mode of transport, with low energy consumption and low emissions compared to private car travel and has a significant contribution to carbon reduction.

“Resilience” is originally a physical concept that refers to the ability of a material to absorb deformation forces as it deforms. The “resilience” in scientific term was first introduced by C. S. Holling in 1973 as a concept of “ecological resilience”, which refers to the ability of an ecosystem to sustain itself and to maintain the same relationships between populations or state variables after absorbing change and disturbance. It is a measure of the ability of an ecosystem to sustain itself and maintain the same relationships between populations or state variables after absorbing changes and disturbances [1]. Murray-Tuite et al. proposed 10 dimensions for resilient transportation systems, which have been refined by many scholars, and the application of resilience theory has been extended to passenger and freight transportation, transportation energy efficiency, and natural disaster response, etc. [2–4]. Raymond et al. defined resilience in transport as the ability of a transport system to return to a normal operating state within an acceptable period after a disruption [5]. Krumdieck et al. propose a classification of residential travel characteristics according to the degree of necessity and impact in their assessment of urban transport resilience [6].

This paper defines the level of resilience of urban transport as the degree of stability in the daily travel and efficiency of urban residents in an unstable external environment, especially when subjected to shocks caused by unexpected situations. The urban transport system is a complex and large system that is inevitably affected and impacted by various unexpected situations (e.g. traffic accidents). The higher the traffic flow on urban roads and the more complex the road environment, the higher the probability of traffic accidents. A study by Yaqin He et al. showed that as the traffic flow on urban roads increases, the delay of vehicles in the event of a traffic accident gradually increases, the greater the impact on road access. Compared to private car travel, public transport has greater transport capacity, greater intensification and greater operational stability [7]. Therefore, increasing the proportion of urban residents travelling by public transport can effectively reduce the volume of traffic on urban roads, reduce the probability of traffic accidents and the extent to which road traffic is affected by unexpected conditions such as traffic accidents, and improve the overall resilience of urban traffic.

2 Data and Methods

2.1 Source of Data

Wuhan is an important node city in the middle in China and lower reaches of the Yangtze River. The city's two rivers meet and divide the city into three main parts, and there are many rivers and lakes in the city. The study is based on a combination of these factors, and the riverside city of Wuhan has been chosen as the subject of the study.

In order to obtain a sample of Wuhan residents' travel characteristics, the data was sampled by means of a questionnaire with the option of geographic coordinates embedded in the file information to facilitate the extraction of OD (Origin–Destination) data of the residents' daily travel origins and destinations. A team of more than ten people conducted a combination of online promotion and offline field visits to collect a total of 9282 valid questionnaires, covering the respondents' daily travel OD data, main modes of transport and public transport interchange. there is still considerable room for Wuhan to increase the proportion of public transport.

2.2 Methods

Definition of Connections, Detours and Transfers In this paper, it is hypothesized that in the context of the “dual-carbon”, more people will need to shift from car (including private cars, car-hailing service and taxis) to public transport in their daily travels, so as to analyze the feasibility of using public transport instead of car travels under the “dual-carbon” goal and its suitable scope. This paper proposes the “Maximum willingness to connect distance as a percentage” (MWCDP), and “Maximum willingness to connect distance as a percentage” (MWDDP) for the public transport mode to indicate the maximum distance that people are willing to pay for connecting and detouring when choosing public transport modes under ideal conditions, considered with “the number of interchanges” (n) in the trip.

Using the Baidu Maps API, it is possible to achieve detailed calculations of the OD data of residents' daily trips, thus extracting detailed information on the different transport options taken by residents in their daily trips. To clarify the connection problem of public transport in actual travel, all segments except the main travel mode are defined as the connection process, and the walking connection distance between different modes of transport is calculated in the same cumulative manner. The ratio of the total feeder distance to the distance of the entire transport process is defined as the feeder distance share (see Fig. 1).The commuting distances between different modes of transport are significantly different. This paper focuses on the energy saving and emission reduction benefits of public transport in the process of achieving the double carbon target. Therefore, the ratio of the total distance of public transport modes to the total distance of small car travel is defined as the

bypass distance share (see Fig. 2). With complex traffic routes, whether a transfer is required during travel is an important basis for route selection in the public transport process. The number of interchanges for the whole process is accumulated to give the number of interchanges for the process, which is considered as a separate variable in the analysis.

Mode of Travel. The classification of residential travel patterns is based on the concept of “travel mode shift”, and accordingly a model is proposed to assess the level of transport resilience with MWCDP thresholds and MWDDP thresholds. The model can better reflect the optimization priorities and problem-solving directions of urban transport systems when they are fully transformed into public transport modes.

As a result, daily trips made by Wuhan residents are classified into four modes: active public transport mode, replaceable car mode, passive public transport mode, and non-replaceable car mode. The “active public transport mode” refers to those who travel within the MWCDP and MWDDP range, and already choose public transport for their daily trips. The “replaceable car mode” includes residents whose connecting distance and detour distance fall within the MWCDP and MWDDP range, but have not chosen public transport as their mode of travel. This group of residents is more adaptable to switching to public transport and can make the transition more quickly without requiring additional development of the public transport system and infrastructure. The “passive public transport mode” refers to those who choose to travel by public transport for specific reasons, even when their connecting distance and detour distance are outside the range of MWCDP and MWDDP. Although these individuals



Fig. 1 Schematic diagram of public transport connections and interchanges for travel



Fig. 2 Diagrammatic representation of diversions issues

may face inconvenience while using public transport, they contribute to reducing carbon emissions in the urban transport system. Finally, the “non-replaceable car mode” is for residents whose connecting distance and detour distance exceed the MWCDP and MWDDP range, and must rely on private cars for their daily travel. This group of residents face significant challenges in transitioning to public transport due to deficiencies in the urban public transport system and infrastructure. Therefore, this group’s real-life problems are the primary focus of this study (see Fig. 3).

2.3 Calculation of Resilience

The connecting distance ratio reflects how easy it is for residents to reach a public transport station. The calculation process is as follows Eq. (1):

$$i = \frac{X_c}{X_p} = \begin{cases} \frac{W_1+W_2}{W_1+B+W_2} \\ \frac{W_1+B_1+B_2+W_2}{W_1+B_1+S+B_2+W_2} \end{cases} \quad (1)$$

i represents the proportion of connecting distance, X_c represents the total connecting distance, X_p represents the total distance of the travel, W_1 and W_2 represent the walking distance, B_1 and B_2 represent the distance travelled by other transport modes

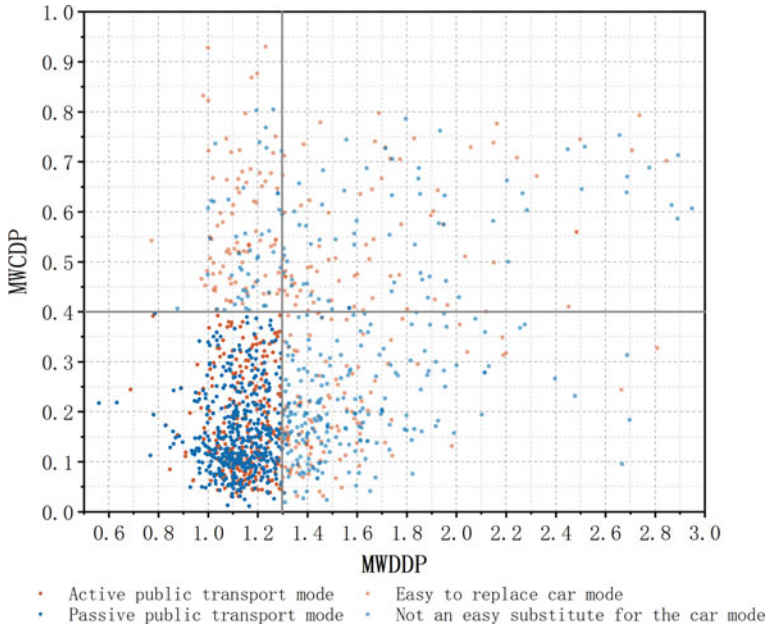


Fig. 3 Diagram of the four modes of travel when MWCDP = 0.4, MWDDP = 1.3

before and after the main transport mode, B and S represent the distance travelled by the main transport mode (see Figs. 4 and 5).

The detour distance share reflects the increase in the total number of miles travelled when residents travel by public transport. The calculation process is as follows

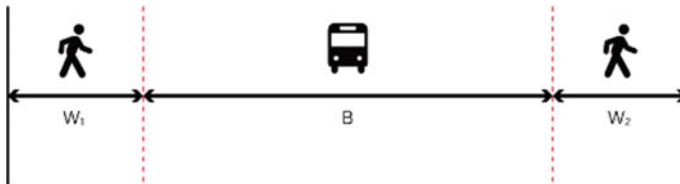


Fig. 4 Schematic representation of connections under a single public transport mode



Fig. 5 Schematic representation of the connection when the metro is dominant

Eq. (2):

$$j = \frac{X_p}{X} \tag{2}$$

j represents the percentage of detour distance, X_p represents the total distance travelled by public transport modes and X represents distance travelled by small cars.

Figures 6 and 7 show the distribution of the proportion of connection distance and the proportion of detour distance from which it can be seen that the proportion of connection distance is distributed between 0 and 1, and the proportion of detour distance is distributed between 0.5 and 3.0.

A preliminary classification of the traffic situation can be made by comparing the proportion of connection distance and the proportion of detour distance with the MWCDP and MWDDP. As there is no direct correlation between the connection

Fig. 6 Connection distance distribution as a percentage

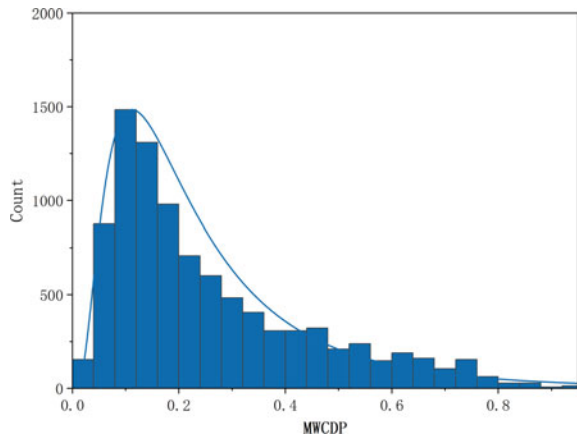
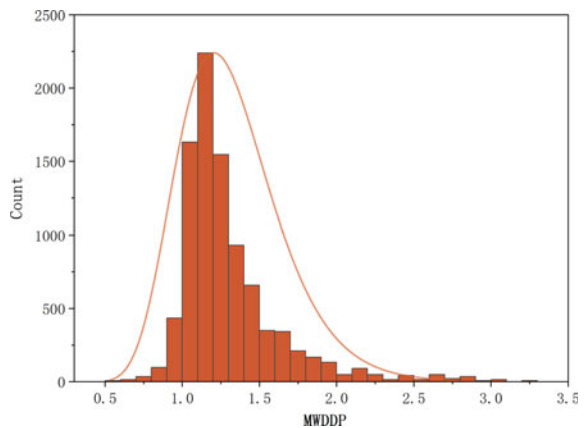


Fig. 7 Detour distance distribution as a percentage



distance share and the detour distance share, this paper will separately analyze the influence of the connection distance share and the detour distance share on residents' daily travel choices.

With the connection problem, the calculation is as follows Eq. (3):

$$P_c = \frac{1}{S} \times \sum_{i=0, i \leq MWCDP}^n W_i \times 100\% \quad (3)$$

With the detours problem, the calculation is as follows Eq. (4):

$$P_d = \frac{1}{S} \times \sum_{j=0, j \leq MWCDP}^n W_j \times 100\% \quad (4)$$

P_c represents the proportion of public transport trips in the corresponding MWCDP scenario, P_d represents the proportion of public transport trips in the corresponding MWDDP scenario, i and j represent the proportion of connection distance and the proportion of detour distance, W_i represents the number of people who choose public transport trips when the proportion of connection distance is i , and W_j represents the number of people who choose public transport trips when the proportion of detour distance is j . S represents the total number of people in the sample.

By calculating the cumulative urban transport resilience based on the proportion of connection distance, and the urban transport resilience based on the proportion of detour distance, an integrated urban transport resilience can be obtained by combining the two indicators. The calculation process is illustrated by Eq. (5):

$$R = P_c + P_d \quad (5)$$

R represents the level of traffic resilience for the city as a whole or for the urban area.

The variable number of interchanges was further introduced to analyze the impact of the number of interchanges on the number of residents who choosing public transport for their trips. Its relationship to the level of transport resilience R is as the following calculation Eq. (6):

$$R = R_1 + R_2 + \dots + R_t \quad (6)$$

R represents the traffic resilience level of the city, t represents the number of interchanges, and R_t represents the traffic resilience level of the city when the number of interchanges is t .

3 Analysis of Results

3.1 Overall Urban Transport Resilience Assessment

Each resident’s travel is influenced by a variety of personal factors, and individual differences between samples result in differences in both the respondent’s own MWCDP and MWDDP. To analyze the level of urban transport resilience for green and low-carbon travel under different feeder distances and bypass distances, this paper constructs one scenario for each set of MWCDP and MWDDP values. The city-wide survey data were then imported into the scenario, and the respective percentages of the four travel modes under different scenarios were calculated to further fit the relationship between MWCDP and MWDDP and the overall traffic resilience of the city. Table 1 shows the 12,726 scenarios for the overall traffic resilience assessment in Wuhan.

Using the assumptions of the above scenarios, the overall traffic resilience of the city under different scenarios is calculated according to the calculation method of urban traffic resilience in the above section. If Wuhan’s overall traffic resilience level reaches 100%, it means that all city residents can use public transport modes to travel in a dual-carbon context to save energy and reduce carbon emissions, while the urban transport system can be less affected by daily operational contingencies such as congestion.

To visually analyze the variation of the overall traffic resilience level in Wuhan with the MWCDP and MWDDP values, the change curves of the resilience level were plotted respectively with the MWCDP and MWDDP values as independent variables. After discarding some of the discrete data, the range of values of the curves was determined. On the change curve with MWCDP as the independent variable, the starting point of the curve was (0, 0%) and the maximum value of MWCDP was 1. The change curve shown in Fig. 8 was fitted to the actual change curve shown in Fig. 8a by the logistic four-parameter fitting algorithm, then “S-shaped” fitting curve shown in Fig. 8b could be obtained as follows, and the fitting results are shown in Table 2.

Table 1 Assumed scenarios for integral transportation resilience assessment in Wuhan

MWCDP	MWDDP							
	0.5	0.52	0.54	0.56	0.58	...	2.98	3
0	1	2	3	4	5		125	126
0.01	127	128	129	130	131		251	252
0.02	253	254	255	256	257		377	378
...						...		
0.99	12,475	12,476	12,477	12,478	12,479		12,599	12,600
1	12,601	12,602	12,603	12,604	12,605		12,725	12,726

Note In the table 1-12,726 are the numbers of the 12,726 hypothetical scenarios

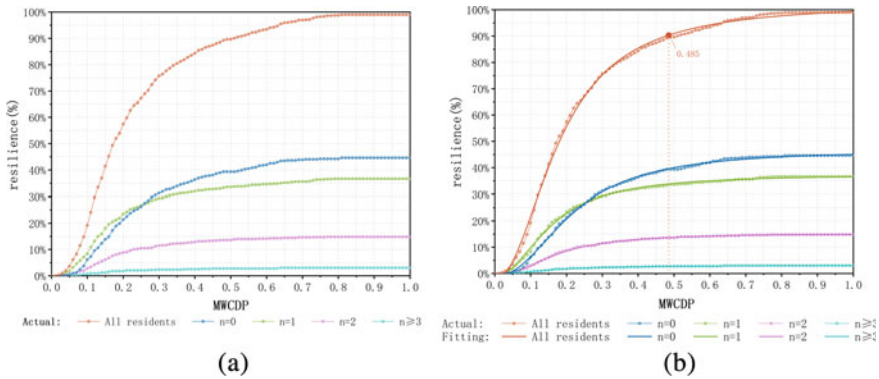


Fig. 8 **a** Curves of change in urban transport resilience levels with MWCDP as the independent variable (actual); **b** curve of change in urban transport resilience levels with MWCDP as the independent variable (fitting)

On the change curve of MEDDP as the independent variable, the starting point of the curve is (0.5, 0%) and the maximum value of MWDDP is 3. The change curve shown in Fig. 8 is fitted to the actual change curve shown in Fig. 9a by the logistic four-parameter fitting algorithm, and the “S-shaped” curve shown in Fig. 9b can be obtained, and its fitting results are shown in Table 3.

It can be deduced that the fitting process for both curves conforms to the equation represented by Eq. (7):

$$R = A_2 + \frac{A_1 - A_2}{1 + \left(\frac{x}{x_0}\right)^p} \tag{7}$$

Based on the fitted curves for the overall traffic resilience level in Wuhan shown in Figs. 8b and 9b, it can be further analyzed that as the MWCDP and MWDDP values gradually increase, so does the level of traffic resilience in Wuhan. The increase in the number of residents travelling by public transport is then conducive to the development of a low-carbon and energy-efficient urban transport system. When the resilience level of urban transport is greater than 90%, the resilience level has reached an extremely high level, 90% of the city’s residents can complete their daily trips by public transport. But continuing to increase the MWCDP over the MWDDP value, the resilience level of urban transport increases extremely slowly and has no significant value. At this point MWCDP = 0.485 and MWDDP = 1.65, meaning that residents would need to accept nearly half of the total distance travelled by feeder and over 50% of the total distance travelled by detour to travel by public transport. The MWCDP and MWDDP analysis of the current state of the urban transport system can provide city managers with a new perspective to quantify the public transport coverage and the rationality of public transport route design in their cities. It helps to identify weaknesses and determine problems in the public transport system.

Table 2 Fitting results of the “S-shaped” curve in Fig. 8b

	All residents	n = 0	n = 1	n = 2	n ≥ 3
A_1	-0.02293 ± 0.00526	-0.01041 ± 0.00225	-0.00944 ± 0.00243	$-0.00216 \pm 8.29E-4$	$-0.0014 \pm 4.53E-4$
A_2	1.02311 ± 0.00343	0.46739 ± 0.00182	0.37374 ± 0.00135	$0.15185 \pm 4.94E-4$	$0.03145 \pm 3.04E-4$
x_0	0.18018 ± 0.00139	0.21757 ± 0.00156	0.15815 ± 0.00154	0.17778 ± 0.00141	0.17127 ± 0.00378
p	2.06465 ± 0.0319	2.17622 ± 0.03443	2.04597 ± 0.03775	2.22614 ± 0.03694	1.88393 ± 0.07786
$R^2(COD)$	0.99865	0.99869	0.99796	0.99839	0.9906
Adjusted R^2	0.99861	0.99865	0.9979	0.99834	0.99031

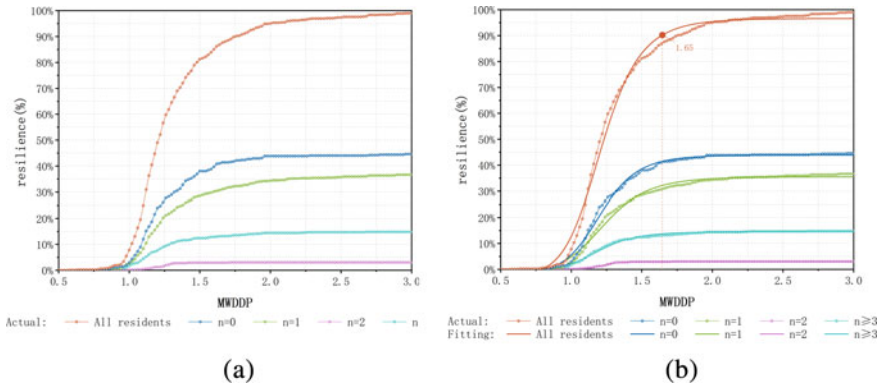


Fig. 9 **a** Curves of change in urban transport resilience levels with MWDDP as the independent variable (actual); **b** curve of change in urban transport resilience levels with MWDDP as the independent variable (fitting)

3.2 Urban Transport Resilience Assessment with Different Number of Interchanges

On the fitted curves for the changing levels of urban traffic resilience about the interchange problem, a similar trend is maintained between the curves for the different number of interchanges. But the trend is not clear as there is a crossover before the different interchanges. The number of public transport interchanges does not have a linear effect on the change in the level of transport resilience due to connection distance in this Figure. It can be argued that, compared to the impact of the proportion of feeder distances, the number of interchanges does not significantly change the level of urban transport resilience. For the issue of feeder distance, the number of interchanges shows a linear relationship with connection distance, characterizing that the number of interchanges is positively related to the share of detour distance of public transport modes, which together affects urban transport resilience.

Table 3 Fitting results of the “S-shaped” curve in Fig. 9b

	All residents	n = 0	n = 1	n = 2	n ≥ 3
A_1	-0.2142 ± 0.00585	-0.00912 ± 0.00237	-0.00902 ± 0.00261	$-0.00358 \pm 9.68E-4$	$9.09E-5 \pm 1.08E-4$
A_2	0.96647 ± 0.00324	0.43903 ± 0.0013	0.35554 ± 0.00149	$0.14519 \pm 5.15E-4$	$0.03009 \pm 6.32E-5$
x_0	1.21688 ± 0.00405	1.21021 ± 0.00351	1.23481 ± 0.00519	1.19252 ± 0.00428	1.2178 ± 0.0018
p	8.82201 ± 0.22174	9.29401 ± 0.21402	7.95596 ± 0.23013	9.00517 ± 0.24792	18.94583 ± 0.45568
$R^2(COD)$	0.99634	0.99702	0.99491	0.99566	0.99819
Adjusted R^2	0.99625	0.99695	0.99479	0.99555	0.99815

4 Conclusion

This paper classifies the travel patterns of urban residents into four modes: active public transport mode, the replaceable car mode, passive public transport mode and the non-replaceable car mode. This classification is different from other studies on urban transport, which have categorized travel patterns statically according to the mode of transport, the characteristics of the population, the purpose of travel and the distance travelled. The paper also proposes the concept of “Maximum willingness to connect distance as a percentage (MWCDP)” and “Maximum willingness to connect distance as a percentage (MWDDP)” for urban residents’ travel, and then uses MWCDP and MWDDP thresholds as the core variables of the urban public transport resilience assessment model. This resulted in a fitted curve describing the change in overall traffic resilience levels in the city. The fitting formulae are further derived, and the results can be used as a reference for the formulation of transport countermeasures when survey data are insufficient due to limited conditions.

In addition to the above innovations, the following important conclusions can be drawn from this paper:

1. When assessing the level of urban transport resilience in Wuhan, the curves of MWCDP and MWDDP as independent variables are almost identical, with the important inflection points of $MWCDP = 0.485$ and $MWDDP = 1.65$ respectively. It is needed to be reached to optimize the resilience of urban transport in a dual-carbon context and to reach the critical point of the marginal decreasing effect.
2. In terms of urban public transport systems, the number of interchanges is in a weak position compared to the share of feeder distances, but there is a linear relationship with bypass distances. In the face of the urgency of urban construction, consideration can be given to completing coverage of the imperfect part of urban public transport through interchange routes first. Further consideration is given to building direct routes and fewer detour routes to improve the comfort of residents in their daily travels.

The urban transport resilience assessment method proposed in this paper can, in a certain extent, help city managers to construct an assessment model through a survey of residents’ travel characteristics, so as to identify the key thresholds for sudden changes in urban transport resilience, and to improve public transport facilities and formulate relevant policies with a view to meeting residents’ demands for public transport and increasing the proportion of public transport in their daily travels. In this way, the resilience of the urban transport system can be enhanced, and its operational efficiency and anti-risk ability improved.

References

1. Holling CS (1973) Resilience and stability of ecological systems. *J Annu Rev Ecol Syst* 4:1–23
2. Koetse MJ, Rietveld P (2009) The impact of climate change and weather on transport: an overview of empirical findings. *J Transp Res Part D Transp Environ*
3. Cutter SL, Ash KD, Emrich CT (2014) The geographies of community disaster resilience. *J Glob Environ Change* 29:65–77
4. Meerow S, Newell JP, Stults (2016) Defining urban resilience: a review. *Landsc Urban Plan* 147:38–49
5. Chan R, Joseph et al (2016) Measuring transportation system resilience: response of rail transit to weather disruptions. *J Nat Hazards Rev* 17(1):5015004
6. Krumdieck S, Page S, Dantas A (2010) Urban form and long-term fuel supply decline: a method to investigate the peak oil risks to essential activities. *J Transp Res Part A: Policy Pract* 44(5):306–322
7. He YQ, Zou JC (2021) A traffic impact analysis of urban-road traffic accidents based on coupling influences of accident characteristics. *J Transp Inf Saf* 01:45–51+63

Advanced Intervention Phase of High-Speed Rail Construction Catenary and Track Synchronization Precise Measurement Fine Adjustment Exploration



Yonggui Li and Yajun Wang

Abstract In order to achieve high smoothness and high stability of high-speed railway catenary, the exploration of high-speed railway catenary equipment and track synchronous precise measurement and adjustment is carried out in early intervention stage. On the basis of elaborating the relationship between catenary and precise measurement network, this paper explores the implementation of synchronous precise measurement and adjustment of catenary and track in high-speed railway from four aspects of key contents, important guarantee, basic method and necessary measures, and lays a solid foundation for implementing ‘zero defect’ of dynamic acceptance of catenary through early intervention and whole process control.

Keywords High-speed railway catenary · Track; precise measurement · Fine adjustment

1 Introduction

In order to make the high speed, smooth and safety operation of the trains running on passenger-dedicated lines, design standards of high-speed railways pose higher requirements on track regularity. The chief means of effectively controlling the high track regularity is to inspect the track geometry state by precise track inspection technology and adjust the rail fastening system by precise adjustment of tracks [1, 2]. With the continuing development of ballastless tracks, the improving of operating speed and the increase of carrying capacity, some light, small and intelligent

Y. Li
Wuhan Railway Vocational College of Technology, Wuhan 430205, China

Y. Wang (✉)
School of Civil Engineering and Architecture, Wuhan Institute of Technology, Wuhan 430074,
China
e-mail: yajun11616@163.com

track-surveying trolleys equipped with multi-sensor have replaced traditional manual inspection methods and have become indispensable track static inspection tools for track construction and maintenance in high-speed railways[3, 4]. Especially, the track inspection technology and track-surveying trolleys for track geometric parameters, which use the static high-precision three-dimensional discrete measurement mode, are widely used to inspect the track regularity state and adjust the track [5].

Because Catenary is in direct contact with high-speed trains in the traction power supply system, its operational condition is directly connected to the safety of high-speed train operation [6, 7]. Unlike the Catenary of a general-purpose railroad, the Catenary of a high-speed railroad focuses on high smoothness and stability during the construction, joint commissioning, and subsequent operating stages. It is based on the data of the precision measurement plane control network (hereinafter referred to as “precision measurement network”) and carries out “precise measurement and fine adjustment” simultaneously by accompanying the track during the early intervention stage of high-speed railroad construction [8]. It may remove all types of faults impacting Catenary smoothness and stability in advance, laying a firm platform for attaining “zero defect” dynamic acceptance.

2 Catenary’s Relationship with Precision Measurement Network

The fine measurement network is separated into four tiers based on the distribution principle: frame plane control network (CPO), foundation control network (CP I), line plane control network (CP II), and railroad track control network (CP III). The precision measurement network establishes coordinate standards for station construction, project acceptance, and subsequent operation and maintenance, as well as providing the conditions for Catenary’s high precision construction [9, 10]. The new high-speed railroad Catenary project’s pillar foundation placement measurement, wrist arm and crane chord measurement calculation installation, contact line detection, and fine adjustment shall be carried out in accordance with CP II and CP III. In the later phases of common compliance, catenary and line track professional measures should also be based on the fine measurement network, and as the basis for the construction, operation, and maintenance of the public works and power supply professionals. The following five elements depict the link between Catenary and Precise Measurement networks.

- (1) During the construction phase of the “Four Electricity Projects” (collectively referred to as the four professional projects of power supply, electricity, communication and signal, sometimes also referred to as “post-station projects”), the starting points of the Catenary stations and sections of the high-speed railroad are measured and approved according to the CP II Precise Measurement network data to achieve accurate positioning of the pile foundations.

- (2) During the Catenary column foundation construction phase, the positions of the pre-determined tunnel slots, post-planted anchor bolts, and lower anchor sections in the tunnel section were measured using the CP II Precise Measurement network data. The position of the pillar and tie line foundation in the roadbed section was measured using CP II Precise Measurement network data. The placement of Catenary pillars and tie wire foundations reserved on the bridge body were measured in the bridge section using CP II Precise Measurement network data to fulfill design criteria.
- (3) The pillars and pillars (including various installation bases) were uniformly numbered during the Catenary upper support installation phase based on the CP III Precise Measurement network data, measurement of the deviation of the vertical line centerline of the Catenary pillars, accuracy of the upper hole position, and deviation of the installation of the pillars and anchor bolts in the tunnel.
- (4) The CP III Precise Measurement network data is utilized throughout the Catenary suspension installation phase to assess if the height of the load-bearing cables and contact wires meets the design criteria, as well as to measure and compute the length of the suspension chord.
- (5) The Catenary was adjusted in three passes during the joint adjustment and testing stage, based on data from the CP III Precise Measurement network, to further analyze and judge the coupling condition of the Catenary and the track, and to make it meet the requirements of relevant standards through subsequent adjustments.

3 Precise Measurement Implementation of Fine Adjustment

Key Content. Catenary Precise Measurement is divided into three stages: survey and design, construction, and Catenary Precise Adjustment. The cornerstone and foundation of Precise Measurement fine adjustment is data interchange, sharing, and recognition between the public works and power supply departments.

- (1) Create a communication and contact system. During the construction stage, the power supply department should establish a communication and contact mechanism with the public works department, understand the public works department's construction plan on a regular basis, determine the precise pounding and fine adjustment time nodes of each section, and prepare for joint fine adjustment later on.
- (2) Measure and calculate everything. The foundation pile in the CPIII Accurate Measurement network data is utilized as the construction data baseline throughout the Catenary erection stage, and precise measurements and calculations are performed using a total station and a contactless Catenary laser static

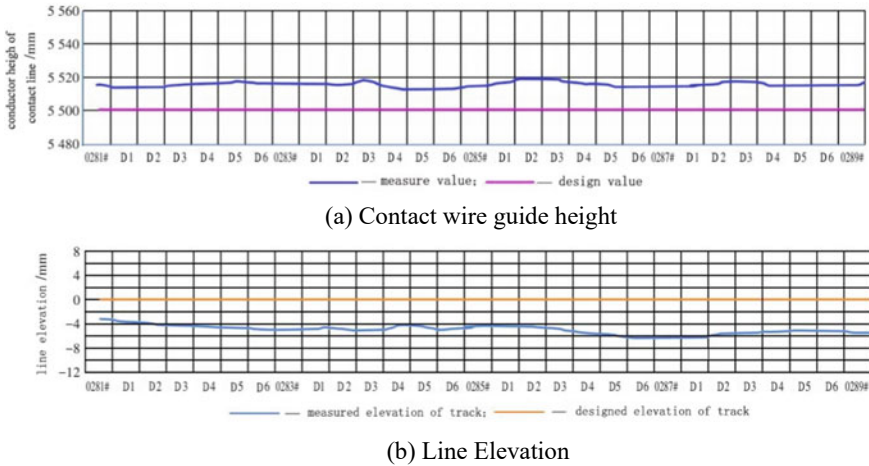


Fig. 1 Contact line guide height and line elevation comparison curve

measuring equipment. Ensure the uniformity of power supply equipment installation form, geometric measurements, and other criteria from the beginning of the installation process.

- (3) Create a curve that compares contact line guide height and line elevation. After receiving the measured data with the base pile as the baseline in CP III Precise Measurement network data, the design layout points are matched to the measured points in the field during the Catenary fine adjustment stage. It calculates and draws the matching curve after calibrating the contact line guide height and pull-out value based on the interval and pole number. Figure 1 depicts a comparison curve for contact line guide height and line elevation.

According to Fig. 1, it takes the pole number as the coordinate to find out the actual track surface elevation of the corresponding line, and the public works and power supply departments each find out the deviation from the design value as the basis for adjustment by both sides and common compliance.

Critical Assurance. According to the principle of “professional responsibility, problem-oriented, joint management, and synchronous optimization,” it strengthens equipment management in the combination of public works and power supply, implements joint design and comprehensive utilization of construction “skylights,” and closely collaborates with professionals from public works and power supply. As a result, the cooperative design of public works “windows” and power supply is an important assurance for Precise Measurement.

- (1) We collected the real measurement data by using the base pile as the baseline in CP III Precise Measurement network data. The data interchange, sharing, and recognition between public works and power supply departments is then combined to correctly define the Catenary equipment adjustment plan and give support for the cooperative design of construction skylight.

- (2) To the greatest extent possible, the Catenary fine-adjustment construction is integrated into or followed by the construction of public works track fine-adjustment, and the construction “skylight” outline plan is dovetailed with the public works department in advance, and the “skylight” joint design network diagram is drawn, so that the fine-adjustment construction of public works and power supply can be effectively integrated and the risk of professional construction “skylight” collision is reduced.
- (3) In response to the reality of changing conditions, fine-adjustment construction period, it is to adhere to daily communication, dynamic adjustment, timely resolution and elimination of uncoordinated, unreasonable, unsafe problems, to ensure the smooth implementation of public works, power supply construction “daylight”.

Basic Method. The basic method of Precise Measurement fine-adjustment is mainly to carry out equipment leveling inspection in phases. According to the former Ministry of Railways issued by the Railway Office in 2008 No. 176 “Guidance on the early intervention of the Railway Bureau in the management of passenger dedicated lines” and the former Transport Bureau of the Ministry of Railways issued by the Transport Installations and Power Supply in 2010 No. 212 “Guidance on the early intervention of the traction power supply and electric power professional in the construction and operation of passenger dedicated lines to take over” documents, before the opening of the operation of high-speed railroad Catenary, it needs to finish 3 times of leveling inspection. In the process of each leveling inspection, the content and focus of Catenary Precise Measurement fine-adjustment are different. The specific requirements are as follows.

- (1) The initial pushing level examination. Before the leveling inspection, the public works department must arrange a joint coordination conference to identify the extent of their separate actions, avoiding the public works fine-adjustment section in order to minimize mutual effect. The scope of the examination covers the type and installation criteria for the equipment. It must finish the initial tightening of parts and remove issues like as loosening, stripping, jamming, grinding, and breaking. After the public works department has completed track fine-adjustment, it must arrange the public works fine-adjustment data and comprehend the standard line data of line rail surface. Then, the subsequent beginning volume, dialing volume, line slope, and other data must be analyzed, together with the timely adjustment and perfection of each power supply equipment’s pre-assignment parameters, in order to conduct the Catenary 2nd level pushing inspection and establish a solid foundation.
- (2) The second degree of pushing inspection. It is based on the line pounding advancement crosswalk chart of the engineering department, and the Catenary Precise Measurement team is created after the basic completion of pounding. It is measured and recorded contact line, bearing cable geometric characteristics and anchor section joints, line fork varied sizes and side limitations, and other data, and data waveform diagrams are drawn by anchor section to determine the relationship between the line and Catenary. It calculates the contact

line guide height and pull-out value fine-adjustment parameters based on the wave line diagram after work hammering, together with the plane, longitudinal section, and curve over-height data and Catenary design requirements. Then, the overrun data must be corrected in a timely manner such that the Catenary geometric parameters are essentially altered in situ and the indicators are in a standard state.

- (3) Pushing level inspection for the third time. It will follow up the Catenary's 3rd pushing level inspection in time after the pounding of the work line has totally attained the standard. It implements continuous measurement of Catenary static geometric characteristics using a laser inspection device measuring trolley. It docks the data with the engineering department in all aspects and jointly decides the adjustment plan based on the measurement findings. Then, it delicately adjusts individual Catenary parameters that do not match the norms to provide as much smoothness of the contact line and line as feasible. It coats the examined equipment with anti-loosening adhesive and reflective marks to keep pieces from coming loose. It applies mark management for all installed critical equipment, video archives, and then intervenes with workers to monitor control, acceptance, and signing on site in order to achieve equipment traceability management. At the same time, it uses the Catenary static geometric characteristics and other inspection data measured by three times of pushing level inspection as the foundation for comparing the engineering department's track surface elevation data. The Catenary static parameters waveform diagram is then created, followed by the Catenary "one pole, one file" equipment file. It serves as the foundation for future operation and maintenance. The information shown above can be implanted into the line's "RF chip" and subsequently used in the intelligent maintenance control system's portable or vehicle-mounted interface. It scans the "RF chip" on the Catenary pillar and updates the Catenary's maintenance, inspection, monitoring, and fault data. It will give a more comprehensive maintenance record for Catenary intelligent operation and maintenance, as well as future correct maintenance.

Necessary measures. Track and catenary synchronization Precise Measurement fine-adjustment is performed with the primary goal of promoting professional management space integration through the sharing of professional data resources, in order to maximize resource allocation optimization and ultimately achieve the synchronization of engineering and power supply equipment to overcome defects. As a result, equipment synchronization is a crucial measure of Precise Measurement fine-adjustment, which goes through the entire process of three times of pushing level.

- (1) Catenary's own local flaw. The study proved that there was a local Catenary issue, and the power supply department was in charge of coordinating prompt correction in connection with the equipment's three times-pushing level. Figure 2 depicts the Catenary local fault.
- (2) The line structure causes local problems. Analysis confirms local faults induced by the line structure. The station unit is responsible for referring to the site

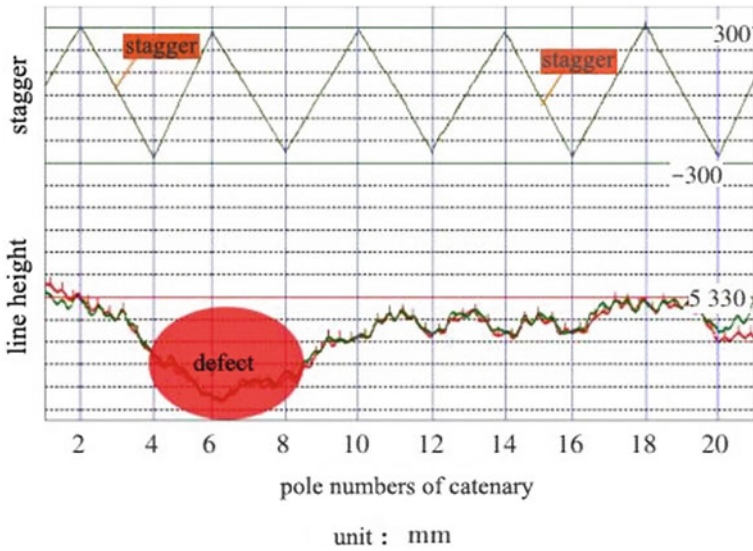


Fig. 2 Catenary local defects

Precise Measurement data and organizing the implementation of structural fault rectification such as triangle pits and variable slope points.

- (3) Defects in smoothness. The research reveals that the change in line settling or ballast line characteristics caused by smoothness is not acceptable. It is accountable to the public works department, and when integrated with public works, it exchanges power supply data, shares and recognizes the situation, and adjusts to discover the line parameters.

4 Conclusion

The track parameters are used to determine the contact line geometry parameters. Consequently, if the track parameters change, so will the geometric characteristics of the contact line. In the past, because the technical specifications were not shared by the sub-discipline management, the Catenary equipment parameters were frequently exceeded after the public works department altered the track parameters. It is not conducive to the operation, maintenance, or management of equipment. Catenary and track synchronization Fine-tuning of Precise Measurement. It has been evaluated for construction management, early intervention, joint adjustment, and joint testing on the Shiji Passenger Dedicated Line. In the course of dynamic acceptance testing for Catenary equipment, a “zero defect” acceptance effect has been realized. In the railroad site, synchronous overcoming of joint flaws has increasingly become an effective method for enhancing the degree of Precise Measurement fine-adjustment,

which is crucial for ensuring the long-term safety and efficiency of the new line after its opening.

References

1. Catenary Operation and Maintenance Rules for High-Speed Railways: Railway General Transportation [2015] No. 362 [S]. Beijing: China Railway Publishing House, 2016.
2. General Railway Catenary Operation and Maintenance Rules: General Railway Transport [2017] No. 9 [S]. Beijing: China Railway Publishing House, 2017.
3. Wang Zhehao. High-speed Railway Catenary Project High Accuracy Construction Technology Discussion [J]. Railway Standard Design, 2011, 39(3): 106–108. Author, F.: Contribution title. In: 9th International Proceedings on Proceedings, pp. 1–2. Publisher, Location (2010).
4. Ministry of Railways, Department of Labor and Health, Ministry of Railways, Bureau of Transportation. High-speed railroad Catenary maintenance post [M]. Beijing: China Railway Publishing House, 2012.
5. Beijing Railway Bureau (2012) High-speed railroad Catenary knowledge book [M]. China Railway Publishing House, Beijing
6. Akpınar B (2013) Railway track geometry determination using adaptive Kalman filtering model [J]. Measurement 46(1):639–645
7. Akpınar B (2012) Multisensor railway track geometry surveying system [J]. IEEE T Instrum Meas 61(1):190–197
8. Bai L, Liu R, Sun Q, Wang F (2016) Classification-learning-based framework for predicting railway track irregularities [J]. Proceedings of the institution of Mechanical Engineers, Part F: Journal of Rail and Rapid Transit 230(2):598–610
9. Chen Q, Niu X, Zhang Q, Cheng Y (2015) Railway track irregularity measuring by GNSS/INS integration [J]. Journal of The institute of Navigation 62(1):83–93
10. Chia cchiari L., Loprencipe G. Measurement methods and analysis tools for rail irregularities: a case study for urban tram track [J]. Journal of Modern transportation, 2015,23(2):137–147.

Research on the Integrated Design Method of Construction and Maintenance in the Whole Life Cycle of Expressway



Xue-Feng Zhang

Abstract Aiming at the drawbacks of “emphasizing construction and ignoring operation” in the current engineering construction mode, the author studies the influencing factors and design methods of the integrated design of construction, management and maintenance of expressway bridges in the whole life cycle. According to the cost function curve of the whole life cycle, the method of optimizing the life cycle cost analysis is given. The integrated design of construction, management and maintenance throughout the life cycle can ensure the stability and continuity of the construction, management and maintenance of transportation facilities, realize the seamless connection of its construction, management and maintenance, and realize the continuity and traceability of engineering responsibilities. Reference is provided throughout the life cycle.

Keywords Whole life cycle · Integrated design of construction and maintenance · Expressway · Cost optimization analysis

1 Introduction

To realize the transformation and upgrading of transportation development, it is necessary to comprehensively improve the level of scientific and technological progress in the industry [1]. At present and in the future, the overall demand for transportation is still strong, the development space continues to expand, the rigid constraints continue to increase, the technical difficulty of infrastructure construction and maintenance is increasing, and the industry management efficiency and public service level need to be improved urgently [2]. Technological innovation in the industry should focus on the development of the “four transportations”. In various fields such as improving the durability and reliability of infrastructure, promoting

X.-F. Zhang (✉)

Research Institute of Highway Ministry of Transport, M.O.T, Beijing 100088, People’s Republic of China

e-mail: 28144484@qq.com

the green, circular, and low-carbon development of transportation, and enhancing safety assurance and emergency response capabilities, breakthroughs in a number of common key technologies will be fully implemented [3, 4]. Improve the level of scientific and technological progress, and promote the transformation and upgrading of industry development.

Therefore, to carry out the integrated construction of expressway construction, management and maintenance throughout the life cycle is to respond to the spirit of the document of the state and the Ministry of Transport, thoroughly implement the five development concepts of “innovation, coordination, green, openness and sharing”, and implement the development requirements of “four transportation”, to implement the needs of national strategies such as the strategy of building a strong transportation country [5–7].

2 Comparative Analysis of Traditional Design and Full Life Cycle Design Process

Traditional design methods include pre-feasibility study, engineering feasibility study, preliminary design, construction drawing design, construction, and completion acceptance [8], while full-life design includes maintenance management, maintenance and reinforcement, life and economic analysis, demolition and reuse, etc. content, as shown in Fig. 1.

3 Research on Influencing Factors

3.1 Technical Factors

(1) Design level

The design stage is the soul of a project, and the level of design directly determines the performance of the construction project in the use stage [9]. The design level is limited by the existing design concepts, calculation methods and engineering materials, and often cannot meet the new requirements arising from the long-term operation of the project during the operation period. This requires more and more designers, and the connotation of engineering design is also added Contents, anti-collision design, anti-seismic design, anti-flood design and some risk control designs that may occur during various construction and operation periods.

(2) Construction quality

There are many reasons for quality problems in engineering projects. From design to construction, from system regulations to construction supervision, every link may

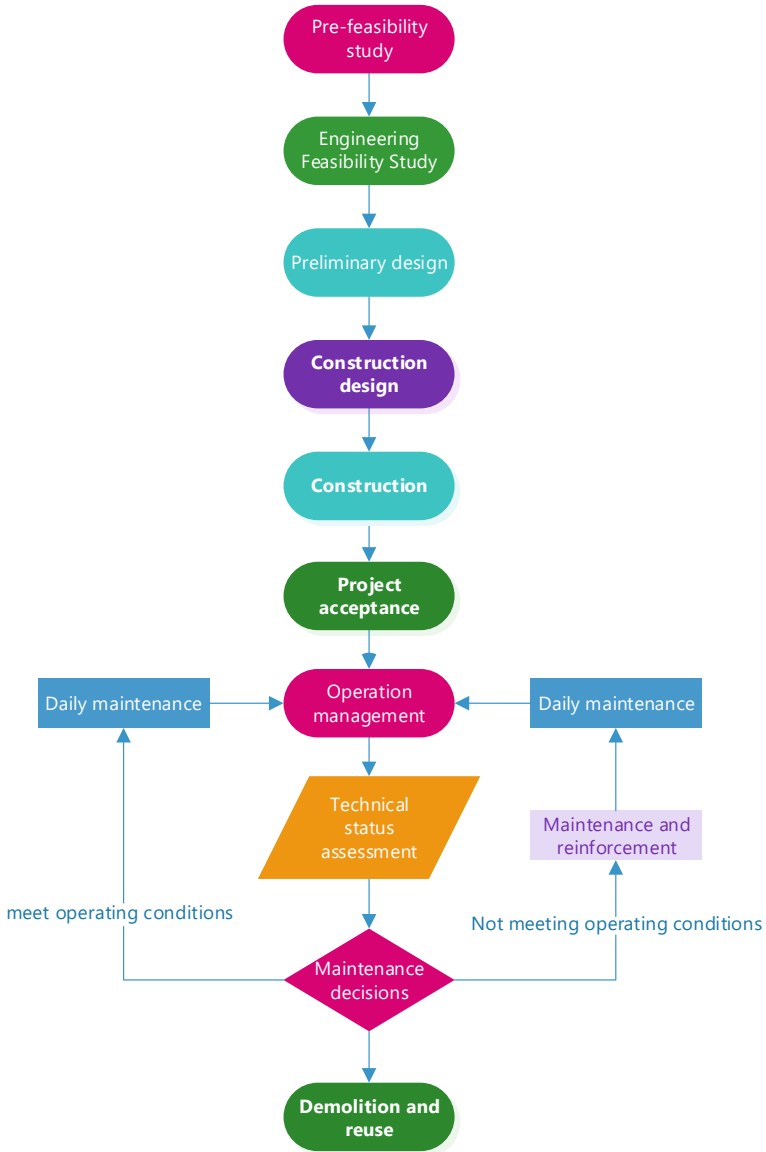


Fig. 1 Design process of the whole life cycle

become an incentive for engineering quality problems. The appearance of quality problems is directly related to the construction process. Some construction teams have low quality and poor business level; they have weak safety awareness and lack technical strength; in terms of construction technology, construction technology,

etc., the level is poor, and they are completely unable to follow relevant technical regulations, Construction specification construction.

(3) Maintenance level

In the process of expressway development, there has always been the problem of “emphasizing construction and ignoring maintenance”, which only pays attention to the process of starting a project from scratch and neglects its performance in the use stage [10]. In terms of maintenance costs, the American Society of Civil Engineers (ASCE) proposed the fivefold rule, that is, if the civil structure is not maintained in time, the maintenance and repair costs in the operation phase will increase by 5 times the cost in the construction period. The development of American highways was relatively early. From the 1950s to the 1980s, a large-scale construction stage was carried out. The construction management mode gradually changed from focusing on construction to focusing on both construction and maintenance, and now it has turned to the stage of focusing on maintenance.

3.2 Institutional Factors

From the perspective of the main units responsible for the management of expressways, there are mainly three management modes: business type, enterprise type and mixed type [11]. These three modes mainly have the following problems: the main body of construction management is a wholly state-owned enterprise, and the issue of capital implementation affects the development of expressways; expressway projects involve a wide range, and the overall coordination and coordination of various types of approvals are not efficient; construction management enterprises have construction management maintenance. Separation phenomenon, in terms of system (business, management, personnel) and information sharing, the unified planning, unified management and unified standards of the construction management system and the maintenance system have not been achieved.

3.3 Economic Factors

Highways are part of the economy and are also influenced by the country’s large economic background [12]. From the perspective of economic and social development needs in the new era, planning and building a national expressway network is a basic prerequisite for affecting the overall situation. Judging from the actual needs of expressway construction and development, a unified and comprehensive overall plan is urgently needed to guide expressway layout and investment decisions.

3.4 Environmental Factors

The impact on the environment of the expressway project's life cycle is mainly in the construction period and the operation period. During the construction period, the impact time is relatively short, but the impact scope is wide and the intensity is high [13]. During the operation period, the impact time is long, the impact scope is small, and the intensity is low. Considering the impact of the two main stages of the expressway project on the environment comprehensively, the impact factors are divided into six aspects: ecological environment, air quality, water pollution, noise pollution, solid waste and living environment according to the affected objects.

4 Research on the Design Method of Expressway Life Cycle

The traditional bridge design procedure considers the various stages of bridge construction separately, focusing only on the construction stage. The focus of the design work is mainly on the optimization of the construction cost and the short-term performance of the completed bridge during the construction stage. Its primary goal is to optimize during construction. efficiency and minimize costs. The traditional bridge design concept and construction and management system are the key to the current bridge durability problems and the failure to reach the design service life. As a new design concept, the life-based bridge design approach considers all aspects of bridge construction, from planning, design, construction and life-time management, all the way to demolition and material recovery. For sustainable development, the traditional short-term method needs to be extended to the entire life cycle of the bridge, and all feasible solutions should be optimized considering various performance indicators during the entire design life of the bridge. The integrated design of bridge life cycle construction and maintenance needs to seek appropriate methods and measures from all aspects of bridge structure planning, design, construction, operation, management and maintenance and demolition to meet the overall performance of the bridge structure life cycle. sex, humanities, ecology, etc.

4.1 Design Requirements

The basic principles of the integrated design of the whole life cycle of construction and maintenance are: practicality, economy, safety, beauty, environmental protection and sustainable development. The integrated design of the construction and maintenance of the bridge throughout its life cycle must meet the following performance requirements:

- (1) Safety performance

The most basic principle in the use of bridges is to maintain the safety performance during use. Its whole and various internal components should have sufficient strength, rigidity and stability during construction and use. The strength requirement means that the bearing capacity of all the components and the connecting structure of the bridge has sufficient safety reserves. Capacity, etc., including seismic performance and stiffness requirements means that the deformation of the bridge under load should be controlled within the allowable range. Therefore, not only the ultimate bearing capacity of the bridge, but also the deformation capacity should be considered, and the vehicle should also be considered as needed. impact. The stability requirement is to require the bridge structure to have the ability to maintain the original shape and position under the action of various external forces.

(2) Use performance

The usability of a bridge includes the functionality and usability of the structure. The so-called functionality means that the structure should function as expected or required, and it is related to the service level of the structure. For example, the number of lanes of the bridge can meet the actual vehicle traffic demand and other functions have the characteristics of improving its service level year by year according to the needs of use. The so-called usability basically includes characteristics that change year by year with use, such as deformation, vibration, or water resistance. In a broad sense, in addition to other performances such as safety performance, they can be collectively referred to as use performance.

(3) Aesthetic properties

A bridge should have a beautiful shape, and this shape should be beautiful from any angle, the structural arrangement must be simple, and there must be harmonious proportions in space. The bridge type should be in harmony with the surrounding environment. For urban bridges and bridges in tourist areas, more consideration can be given to the requirements of architectural art. Reasonable layout and outline are the main factors of aesthetics, in addition, construction quality also has a significant impact on the aesthetics of bridges. For different forms of structures, rust or cracks caused by degradation during use will also affect the aesthetics of the structure.

(4) Durability

The requirement of durability is to ensure that the bridge structure can meet the design requirements for a long time during the service life, and various technical indicators, such as corrosion of steel, fatigue and aging of component materials, etc.

(5) Sustainability

The bridge design should consider the requirements of environmental protection and sustainable development. The environmental requirements are comprehensively considered in terms of bridge location selection, bridge span layout, foundation scheme, pier shape, superstructure construction method, construction organization design, etc. Necessary engineering control measures shall be established, and an

environmental monitoring and protection system shall be established to minimize adverse effects.

In addition, it analyzes and predicts the environmental impact during the use of bridges, and takes measures to minimize the consumption of resources and energy and the adverse impact on the environment during design.

(6) Economical

Bridge design should follow the principles of adapting measures to local conditions, using local materials and facilitating construction. An economical bridge type should be the one with the most comprehensive cost and maintenance cost. In the design, the convenience of maintenance and low maintenance cost should be fully considered, and maintenance should not be interrupted as much as possible. The bridge location considered for the shortest time of traffic or interruption of traffic should be geological, with good hydrological conditions and short bridge length. The bridge location should be considered to shorten the transportation distance between the two sides of the river, promote the economic development of the area, and produce the greatest benefits., for the bridge toll collection should be able to attract more vehicles to pass through, to achieve the purpose of recovering the investment as soon as possible.

4.2 *Design Contents*

Life-cycle design is the most important link in engineering construction. It transforms the needs of owners, users and society into performance requirements of bridge structural systems, and establishes and optimizes structural solutions to achieve these needs. To ensure good performance over the design life cycle of the bridge, the full life design should include the following.

- (1) Determine the design life of the entire project and each replaceable part.
- (2) Performance design. Functional design of structural systems and components and their possible future flexibility design; In order to meet the requirements of bridge safety performance, structural design such as strength and stability is required; In order to meet the requirements of bridge durability performance, durability design is required; Safety analysis and design to meet the user's requirements for travel safety; risk analysis and countermeasure design, so that the bridge will not cause large economic losses and casualties after encountering a certain probability of risk events, and clarify the engineering insurance cost.
- (3) Aesthetic design. Including modeling design and landscape design to meet people's needs for bridge aesthetics and landscape appreciation.
- (4) Eco-design. Including environmental protection design, recycling and reuse design.
- (5) Control design during construction to ensure good construction quality and faithfully express design results.

- (6) Management and maintenance design of bridges. Including monitoring, maintenance, repair, management, etc. during the operation period of the bridge, so that the bridge can always maintain good performance during the service life and meet the requirements of the use function.
- (7) Life cycle cost analysis is one of the indispensable contents in the whole life design of bridges. To choose the optimal design scheme, it is necessary to carry out a life cycle cost analysis, compare all costs (including financial costs and environmental costs) incurred in the entire life cycle, and select the life cycle cost under the premise of balancing various needs lower scheme.

5 Design Cost Analysis of Whole Life Cycle

The whole life design of expressway is a design theory of expressway based on the overall structural performance such as safety, practicability, economy, durability, etc. and method. Engineering design based on the concept of life cycle should not only consider the initial function and cost of project construction, but also fully consider all designs in the entire life cycle. On the basis of overall consideration of structure, material, load, economy, environment and humanities The lowest total cost is the economic optimization index to achieve the best combination of both mechanical index and functional index, and pay more attention to the quality, safety, economy, comfort, beauty, coordination and sustainable development of the project. Life-cycle design is different from traditional design, considering more and more complex factors.

The whole life cycle cost includes the design cost C_1 , the construction cost C_2 , the operation cost C_3 and the disposal cost C_4 . Realize the life cycle cost optimization $LCC = \min(C_1 + C_2 + C_3 + C_4)$. The cost function curve of the whole life cycle is established, as shown in Fig. 2. The higher the cost in the construction period, the higher the degree of functional completion, the lower the cost in the operation period, the lower the cost in the construction period, and the higher the cost in the operation period. The cost-function curve M point is obtained through the whole-life optimization design, so that the whole-life cost is minimized. The key to the optimization is the establishment of the structural deterioration model.

6 Conclusions

The whole life design of expressway is a design theory of expressway based on the overall structural performance. The integrated model of construction, management and maintenance throughout the life cycle can ensure the stability and continuity of the construction, management and maintenance of transportation facilities, realize the seamless connection of its construction, management and maintenance, and realize the continuity and traceability of engineering responsibilities. Adhere to equal emphasis on

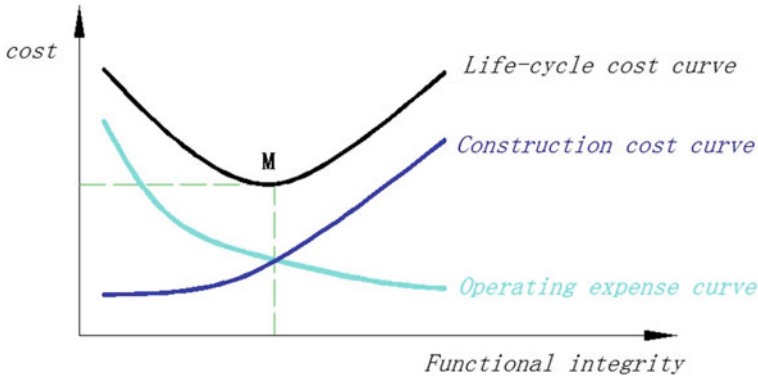


Fig. 2 Cost-Function curve

construction, maintenance, transportation and management, scientific development, people-oriented, and taking into account the development needs of stakeholders. Pay attention to the safety, information management, environment and landscape of expressways A sustainable” transportation system has achieved steady and rapid development.

Acknowledgements This study was funded by financially supported by the National Key Research and Development Program of China (2020YFC1511905) and Chinese Central Government for Basic Scientific Research Operations in Commonweal Research Institutes (2021-9072a). We thank the anonymous reviewers and the Editor for their constructive comments and advice, which greatly improved the quality of this paper.

References

1. S Labò, Passoni, C. , Marini, A. , & Belleri, A. . Design of diagrid exoskeletons for the retrofit of existing rc buildings. *Engineering Structures*, 220, 110899 (2020).
2. Jia, X. , Liu, C. , Neale, Z. G. , Yang, J. , & Cao, G. . Active materials for aqueous zinc ion batteries: synthesis, crystal structure, morphology, and electrochemistry. *Chemical Reviews*, 120(15) (2020).
3. Jr, A. , Sl, A. , Cd, B. , Jx, B. , Sz, C. , & Fei, W. A. , et al. Effect of heteroatom doping and morphology tuning of cnt-derived material for potassium-ion hybrid capacitors. *Chemical Engineering Journal*, 410 (2021).
4. Parise, G. , Parise, L. , Allegri, M. , Marco, A. D. , & Anthony, M. A. . Operational resilience of hospital power systems in the digital age. *IEEE Transactions on Industry Applications*, PP(99), 1–1 (2020).
5. Kim, B. G. , Dong, W. K. , Park, G. , Park, S. H. , & Choi, J. W. . Electrospun li-confinable hollow carbon fibers for highly stable li-metal batteries. *Chemical Engineering Journal*, 130017 (2021).
6. Qi, S. , Wang, H. , He, J. , Liu, J. , & Ma, J. . Electrolytes enriched by potassium perfluorinated sulfonates for lithium metal batteries. *Science Bulletin* (2020).

7. Gonzalez, A. G., Cabal, J., & Sciubba, E. . Csp quasi-dynamic performance model development for all project life cycle stages and considering operation modes. validation using one year data. *Energies* (2020).
8. Bian X, Chen D, Han L (2022) Taking full advantage of the structure and multi-activities of mineralized microbial surface-displayed enzymes: portable three-in-one organophosphate pesticides assay device. *Chem Eng J* 429:132317
9. Dionne E, Hanson ML, Anderson JC, Brain RA (2021) Chronic toxicity of technical atrazine to the fathead minnow (*pimephales promelas*) during a full life-cycle exposure and an evaluation of the consistency of responses. *Sci Total Environ* 755(Pt 2):142589
10. Sangare, N. , Lo-Yat, A. , Moullac, G. L. , Pecquerie, L. , & S Andréfout. Impact of environmental variability on *pinctada margaritifera* life-history traits: a full life cycle deb modeling approach. *Ecological Modelling*, 423, 109006 (2020).
11. Ye X, Chen H, Sun Q, Chen C, Yuan R (2020) Life-cycle reliability design optimization of high-power dc electromagnetic devices based on time-dependent non-probabilistic convex model process. *Microelectron Reliab* 114:113795
12. Luo H, Cheng F, Yu B, Hu L, Zhang J, Qu X et al (2021) Full-scale municipal sludge pyrolysis in china: design fundamentals, environmental and economic assessments, and future perspectives. *Sci Total Environ* 795:148832
13. Best RE, Kalehbasti PR, Lepech MD (2020) A novel approach to district heating and cooling network design based on life cycle cost optimization. *Energy* 194

Urban Architectural Image and Urban Planning

Architectural Identity of the City of Tirana, Albania. Overview of the Past, Present, and Future Expectations with Focus on the Residential Buildings (Inner Circle)



Lindita Bande and Brunilda Babameto

Abstract The city of Tirana, the capital of Albania is undergoing thru large developments in the city center and suburbs. Will aspirations to enter int eh European Union the value of properties in the capital is increasing. Due to the fast development of the city, there is a need of the architectural assessment of this development with focus on the residential buildings. The city has an interesting history of architecture. The methodology of this study follows the below steps:

- Analysis of the city urban development
- Evaluation of the architectural history influences
- Current architectural language
- Future expectations of the city architectural identity
- Findings and results.

The aim of this study is to understand and draw guidelines on how the future of the architectural identity of the city, referring to the residential buildings, might be. This result shall be based on the past and current developments of residential buildings. Since Albania is a developing country, this research might have an impact to the local authorities in understanding the critical need of preserving the architectural identity of the city for the future generations.

Keywords Architecture · Identity · Communist impact · Colors · Green design

L. Bande (✉)
United Arab Emirates University, Al Ain, UAE
e-mail: lindita.bande@uaeu.ac.ae

B. Babameto
Tirana, Albania

1 Introduction

This study is focused on the architectural identity of residential buildings in the city of Tirana. This goal aims to find results that would bring a sustainable development of residential buildings by maintaining the identity of the city. In order to achieve results and guidelines, it is relevant to have an overview on the country vernacular architecture; the Italian influence in architecture; the communist period impact into such buildings; the modern transition; the current situation.

The Country of Albania has a compelling history of development with the ancient roots into the Illyrians more than 2000 BCE, Fig. 1. The language is Indo-European. The influence of Ancient Greek and Ancient Roman architecture is still visible today in several cities such as Butrint, Epidamus (Durrës), Apollonia (near Vlora). However, several cities have their own history of development based on local construction materials such as Gjirokastra and Berat (Fig. 2) [1–3].

The country went to a history of continuous wars with the Byzantine and Ottoman Empire, until having the independence in 1912, with the center in the city of Vlora.



Fig. 1 Map of a Illyrians, b current Albania [4, 5]



Fig. 2 Historical picture of the traditional city of a Berat, b Gjirokastra [6, 7]

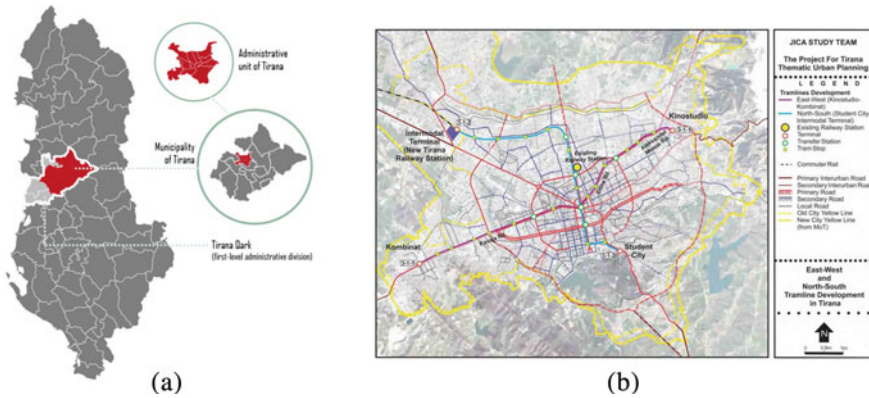


Fig. 3 Map of a Tirana location in the country, b inner, outer Ring of Tirana [11, 12]

However in 1920 Tirana was declared the capital, following the Balkanik continues wars with the neighbouring countries [8].

The city of Tirana, declared as capital in 1920, has two main division, inner and outer circle. The inner circle consists of the historical city center, governmentail, religious and residential buildings. The outer circle developed mainly after the fall of communism into residentials (low-rise, mid-rise and industrial buildings, Fig. 3). The central square of the city underwent significant transformations during all stages of its development. In the communist period, it was destroyed and the form that had begun to be given at the time of fascist Italy, leaving it with a gigantic surface, outside of any urban dimensions, to show the greatness of the dictatorship of the proletariat in the eyes of the citizens. After the fall of the communist regime in 1992, the uncontrolled movement of the population brought about a chaotic expansion of the city.

Buildings without criteria occupied the green spaces between the existing buildings and entire informal neighborhoods were developed. For more than 10 years, the city developed without any plan, buildings sprouting everywhere with a hybrid architecture, without a name. Only in 2004, Architecture Studio, winner of the international competition, brought a completed urban study, which, among other things, proposed the central square as a pedestrian zone, as well as the construction of towers around its center [9, 10].

2 Methodology

The methodology of this study follows the below steps (Fig. 4):

- Analysis of the city urban development,
- Evaluation of the architectural history influences, residential buildings,

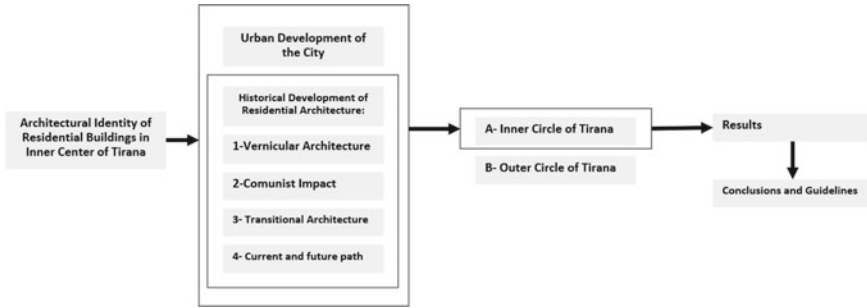


Fig. 4 Methodology path followed in in this study

- Current architectural language,
- Future expectations of the city architectural identity, residential buildings,
- Findings and results.

2.1 Analysis of the City Urban Development

In order to understand the architectural development of Tirana, residential buildings, it is relevant to make an analysis of the urban development of the city. The development of the city of Tirana has many historical layers that are linked to the political changes of several decades. The city center falls into the inner circle, defined by large roads surrounding the core. The outer circle developed mainly after the fall of communism. The city center is the best example of such influence. Starting from the impact of the Ottoman empire, the Italian influence, the communism, the post-communism transition era until the today development, the city center has been modified as per the political aspirations of the governing parties [13].

In a recent study relating the urban identity of Tirana it was shown that the older urban layers are more of an identity to the citizens rather than the new layers of the postmodern. The methodology was based on the physical approach based on evidences over the years and phenomenological, based on the people's perception [14].

Tirana possesses a rich cultural, social, microeconomic, historical heritage. The current construction process of the "ordinary" contemporary city with buildings that create the idea of the superblocks is a fast development that perhaps risks all the diversity and interesting language of architecture that the city currently has [15].

The residential stock in the capital represents the largest number of buildings. In a recent study it was found that the main residential typologies are detached houses, apartments, mass housing, social housing, gated communities, informal detached houses and housing with in/formal additions. This study shows a heterogeneous typology of buildings in the city [16].

As part of the post-communist transition phase in the suburbs of the city there were new areas developed as informal settlements. In a recent research the analysis showed that even though these buildings were built in a transitory time with fragile regulations there is still a common language of architecture and land use of these buildings [17].

2.2 *Evaluation of the Architectural History Influences*

Historical buildings of Tirana, Vernacular Architecture: The city was founded in 1614 with a strong influence of the Ottoman Empire. The initial residential buildings in the city center were one-story, two-story villas with inclined roofs. This is the base of the vernacular architecture. The walls were made of mud bricks and wood was used to design the beams and roof. Several of these houses are still standing today and many are opened to the public as historical buildings. Tirana began to develop as a city since 1920 (when declared capital of Albania), when it was declared the capital of Albania. The urban development of Tirana, in all its stages, is inextricably linked with its political developments. Tirana's evolution makes it come across as an urban laboratory of layered ideas of interest to local and foreign architects and urban planners, who have been contributing to its completion (Fig. 5). **Italian influence into architecture:** The city has a great Italian influence in the urban planning and architecture. During the years 1923–1943 (Fig. 6). This influence is divided into two main periods: the first one under the monarchy of the self-declared king Zog. And the second period is after the occupation of Albania from Italy in the period of 1939–1943. The main fields of this impact are in urbanism: constructions of new roads; governmental buildings: the municipality and ministries located around Skanderbeg Square and the residential building: low-rise residential mainly houses of one or two stories [18].

Communism impact into architecture: With the coming to power of the communist party in 1944, the urban and architectural development took a different direction. Influence was already coming from Eastern Block countries. The architects and engineers were Albanians but educated in the Soviet Union. The city had already grown to an area of 1200 ha and a population of 12,000 inhabitants. Subsequently, the city developed into a radial and circular road system. The development of these residential buildings was relevant due to the expansion of the population of the city. Therefore these buildings were mainly 5 floors with minimal internal spaces and concrete-looking exterior. The units were prefabricated. However, the composition of the units allowed internal green areas and the distance among them allowed direct sunlight and natural ventilation (Fig. 7) [19]. In a study evaluating the rapid development of Tirana's built environment, it was found that the interviewed citizens expressed nostalgia for the communist approach towards urban planning and built environment. The main points of the nostalgia show that the socialist city positively evaluated the built environment [20].



Fig. 5 The city center in with the first historical buildings, vernacular architecture [21]



Fig. 6 House design in the city center influenced by the Italian architecture [22]

Transition Architecture: The post-communist transition period started in 1990 when the communist system fell of power. The new fragile democratic system would go on until the recent years. These political changes had a drastic impact in to the urban planning and architecture of the city. In this transition period there were many approvals of new building without fulfilling the urban regulations, construction safety, the existing infrastructure and so on. Even though in the recent years the regulatory system has improved, there is still much work to be done in order to have a contemporary architectural language in the city. The residential building was built in previous internal parks between the communism influenced blocks. The height reached ten floors [23, 24]. From concrete to color: This is an attempt to bring some colors to the city after the grey concrete blocks of the communist era. It was an attempt to re-vitalize the city by use of street art into concrete looking residential blocks (Figs. 8, and 9).



Fig. 7 Residential buildings from the communism period, area Zogu I Zi, Tirana. *Photo by Arch. B. Babameto, 16 December 2022*



Fig. 8 Colored buildings from the communist period [25]



Fig. 9 Street art in a residential building from the communist period [26]

2.3 *Current Architectural Language*

This research refers to the residential buildings architecture in the Inner Circle of Tirana. The current buildings, referring to a timeline of 5 years are shown in the below pictures. There is a large number of skyscrapers built near to the main boulevard. The function of this buildings is mainly residential but also offices or malls. The majority of this towers have a mix use. These buildings enter in the already defined architectural language of the Italian influence, communism buildings and transitional structures (Fig. 10).

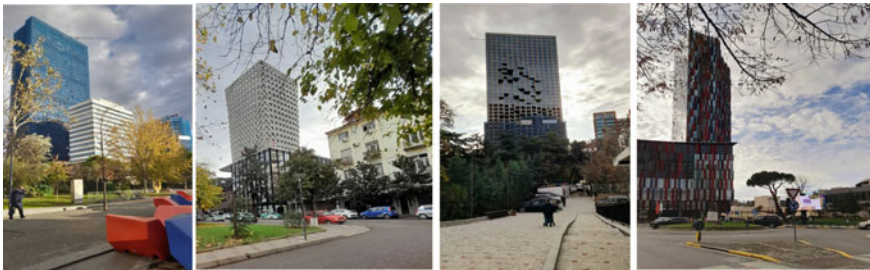


Fig. 10 New towers in Tirana, from left to right: “Tirana International” Hotel in “Skanderbeg” Square; “Maritim Plaza” Hotel near “Sulejman Pasha” Square; “Downtown” Tower in Elbasani Street; Tower of “Air Albania” Stadium, near “Mother Teresa” Square. *Photos by Arch. B. Babameto, 16 December 2022*

2.4 Future Expectations of the City Architectural Identity

Based on the current architectural competitions mainly directed to international studios, the current trend will continue and there will be more skyscrapers in the city Inner Circle (Fig. 11). However, there is an attempt to shift to more green buildings based on the new building codes that are being adapted to the European Union Standards. There is an attempt to add local elements to the architecture of the buildings [27].

It is also notable an influence from Italian recent architects and architecture such as Boeri with Bosco Verticale done in Milan, or Mario Cucinella Architects. Well known for the green buildings they are building in Italy and Europe where the upper floors of the buildings have vertical gardens as a mean to replace the green land where they are built (Fig. 12).



Fig. 11 Future of architecture in Tirana [28]



Fig. 12 Images of future projects a Boeri, b Mario Cucinella Architects [29, 30]



Fig. 13 Buildings under construction around Skanderbeg Square. *Photo by Arch. B. Babameto, 16 December 2022*

3 Results

Based on the above analysis of the architectural identity of the residential buildings in the Inner Circle of Tirana, referring to the urban analysis as well, the result is the city currently has an architectural identity of residential building with predominant feature based on the communist architecture that shaped this identity.

The Italian architecture is part of the identity but with a minor impact compared to the first. The new towers in the city center for residential and mixed use are an attempt to create a new modern architectural language based on sustainability principles of including greenery in the higher floors (Fig. 13).

4 Conclusion

Based on the results, we can define that the new constructions shall be in coordination with the current architectural identity of the city. The authors believe that adapting to the historical layers referring to the communist and Italian identity of the residential buildings when designing new buildings will help the inner circle of the city maintain an established identity. The new residential building design shall be referring to the existing identity, proportions of residential building but with the latest regulation on green buildings and sustainable development.

The new building residential architecture can possibly follow the recent development of other European cities such as Milan. This since as per the results the city



Fig. 14 Green Tower, Resurrection of Christ Orthodox Cathedral, Ministries buildings. *Photo by Arch. B. Babameto, 16 December 2022*

of Tirana clearly continues to have an impact from the modern Italian architects and architecture. Surely, this shall be connected to the identity of the city.

However, further studies shall be conducted to analyze elements of the architecture of the residential buildings in the outer circle of the city, in order to create a relationship among both administrative zones.

In conclusion, respecting the past architectural identity by considering the architectural features, proportions, forms the new residential and mixed-use towers being built in the Inner Circle of the city will make a better transition into a futuristic architecture by preserving the identity of Tirana (Fig. 14).

References

1. “The Tribes of Albania: History, Society and Culture—Robert Elsie—Google Books.” [Online] Available: https://books.google.ae/books?hl=en&lr=&id=bbeKDwAAQBAJ&oi=fnd&pg=PP1&dq=albania+history&ots=zLZxJNGIVl&sig=aWnKGENIq-LY1mHu869Yc6kcD3A&redir_esc=y#v=onepage&q=albaniahistory&f=false. Accessed: 05-Feb-2023
2. “Berat—Albania.” [Online]. Available: <https://albania.al/destinations/berat/>. Accessed: 05-Feb-2023
3. Gjirokastra—Albania. [Online]. Available: <https://albania.al/destinations/gjirokastra/>. Accessed: 05-Feb-2023
4. Wilkes JJ (1992) The Illyrians, p 351
5. “Albania | History, Geography, Customs, & Traditions | Britannica.” [Online]. Available: <https://www.britannica.com/place/Albania>. Accessed: 05-Feb-2023
6. “Fotografi të mahnitshme bardhezi të qytetit të Beratit - ObserverKult.” [Online]. Available: <https://observerkult.com/fotografi-te-mahnitshme-bardhezi-te-qytetit-te-beratit/>. Accessed: 05-Feb-2023

7. “Gjirokaštër | Julien Maury | Flickr.” [Online]. Available: https://www.flickr.com/photos/julien_maury/44727881752. Accessed: 05-Feb-2023
8. “Albania—Neil Olsen—Google Books.” [Online]. Accessed: 05-Feb-2023
9. Aliaj B, Lulo K, Myftiu G (2003) Tirana, the challenge of urban development, p 221
10. Gjoka E, The Masterplan of Tirana. Sustain Arch Urban Des
11. “City of Tirana, Sustainable Urban Mobility Plan—TRT Trasporti e Territorio.” [Online]. Available: <http://www.trt.it/en/PROGETTI/sustainable-urban-mobility-plan-of-tirana/>. Accessed: 05-Feb-2023
12. “(No Title).” [Online]. Available: https://www.scad.gov.ao/ReleaseDocuments/CCI_Q3_2015-EN-V2.pdf. Accessed: 31-May-2021
13. Pojani D (2014) Urban design, ideology, and power: use of the central square in Tirana during one century of political transformations 30(1):67–94. <https://doi.org/10.1080/02665433.2014.896747>
14. Manahasa E, Manahasa O (2020) Defining urban identity in a post-socialist turbulent context: the role of housing typologies and urban layers in Tirana. *Habitat Int* 102:102202
15. Naselli F (2021) Tirana-next: a complementary development strategy (and consequent urban tactics) for the informal and historical urban fabrics within Tirana Super Blocks. *Urban B Ser*, pp 61–77
16. Manahasa E, Özsoy A, Manahasa O (2022) A hierarchical definitional framework for a heterogeneous context: housing typologies in Tirana, Albania. *Open House Int* 47(2):254–281
17. Manahasa E, Rasha A (2021) Searching for aesthetical values in an upgraded informal neighborhood in Tirana. *Technol Appl*
18. Capolino P (2011) Tirana: a capital city transformed by the Italians 26(4):591–615. <https://doi.org/10.1080/02665433.2011.601610>
19. Vokshi A, Pino S, Balilaj E, Tirana 1920–2020 : përmes arkitekturës, p 173
20. Manahasa E, Manahasa O (2022) Nostalgia for the lost built environment of a socialist city: an empirical study in post-socialist Tirana. *Habitat Int* 119:102493
21. “Pamje ajrore nga Tirana. Aerial view. Vue aréienne du cent... | Flickr.” [Online]. Available: <https://www.flickr.com/photos/44425842@N00/9687083948/in/pool-1149247@N21/>. Accessed: 05-Feb-2023
22. Resuli P, Dervishi S (2014) Architectural decorative elements of Tirana Traditional Villas: The Italian Impact
23. Nepravishta F (2016) Contemporary architecture in Tirana during the transition period. *South East Eur J Archit Des* 2016:1–10
24. Manahasa E (2021) An observation on residential complexes as a new housing typology in post-socialist Tirana. *Technol Appl*
25. “8 views of Tirana, Albania—with its bright, multicolored building | TED Blog.” [Online]. Available: <https://blog.ted.com/9-views-of-tirana-albania-with-its-bright-multicolored-building/>. Accessed: 17-Dec-2022
26. “Arti mural, atraksioni më i ri turistik në Tiranë.” [Online]. Available: <https://www.kultplus.com/arti-pamor/arti-mural-atraksioni-ri-turistik-ne-tirane/>. Accessed: 17-Dec-2022
27. “(99+) Contemporary Architecture in Tirana During the Transition Period | Florian Nepravishta—Academia.edu.” [Online]. Available: https://www.academia.edu/en/22615226/CONTEMPORARY_ARCHITECTURE_IN_TIRANA_DURING_THE_TRANSITION_PERIOD. Accessed: 17-Dec-2022
28. “Projektet në ndërtim në Tiranë—Revista Monitor.” [Online]. Available: <https://www.monitor.al/projektet-ne-ndertim-ne-tirane-2/>. Accessed: 17-Dec-2022
29. “Stefano Boeri designs Tirana Vertical Forest in Albania.” [Online]. Available: <https://www.dezeen.com/2019/03/01/tirana-vertical-forest-albania-stefano-boeri-architetti/>. Accessed: 05-Feb-2023
30. “Idea 2962764: MET Tirana residential building by Mario Cucinella Architects in Tirana, Albania.” [Online]. Available: <https://architizer.com/idea/2962764/>. Accessed: 05-Feb-2023

Factors Affecting the Formation of Architectural Space and Construction Systems in the Jordanian Vernacular Architecture



Mohannad Tarrad and Umamah Ahmad

Abstract The research includes studying architectural space in heritage houses to identify the value of architectural spaces in Jordanian social life. The different structural systems, their characteristics, building materials, and the constituent elements of buildings were defined in the context of vernacular Jordanian architecture. This investigation has provided insights into the impact of the structural system on the architectural and interior spaces from several aspects. By highlighting on the abandonment of these inherited in the contemporary ages of Jordan. The study emphasizes the great advantages missed by this practice, as they represent a sustainable housing solution by adopting local building materials and promoting social sustainability. In addition, this form of buildings has a long lifespan, especially compared to different types of concrete buildings. However, despite the modern movements of abandoning inherited methods, there have been some attempts by local architects to revive these traditions. The research aims at explaining and clarifying interconnected construction design solutions in Jordanian vernacular architecture in a manner that promotes environmental sustainability, taking into account the material cost of the building, as a key role in choosing the building construction method, from an economic sustainability point of view. In its methodology, the research relied on description, analysis, and comparison through case studies of heritage buildings from different regions, in addition to modern buildings following inherited construction methods to illustrate the idea of the research.

Keywords Construction systems · Vernacular architecture · Traditional architecture · Architectural space · Environmental context · Jordanian architecture · Sustainability

M. Tarrad (✉) · U. Ahmad
Al AlBait University, Mafraq 130040, Jordan
e-mail: ms-tarrad@aabu.edu.jo

© The Author(s), under exclusive license to Springer Nature Singapore Pte Ltd. 2024
M. Casini (ed.), *Proceedings of the 3rd International Civil Engineering and Architecture Conference*, Lecture Notes in Civil Engineering 389,
https://doi.org/10.1007/978-981-99-6368-3_63

781

1 Introduction

Life in the past was characterized by a simple lifestyle and an economy based on traditional agriculture and self-sufficiency through home production and construction with simple tools, in contrast to modern lifestyle, which depends on an industrial and profit-making economy [1]. This has had a major impact on the human-physical environment interactions, including construction methods, as historic architecture was characterized by its dependence on natural local building materials [2]. Local socioeconomic, climatic, and topographic constraints have been considered in the building processes [3]. Architecture acted a material manifestation of this interaction between man and nature from one side, and between human civilizations from the other. These organic interactions have been disturbed by modern technological innovations as they significantly altered building methods, resulting in the modern building systems and technologies [4]. In this process, inherited building techniques have been alienated and abandoned, transforming architecture from a symbol for local identities, cultures, and belief systems to a globalized product with unified characters and construction methods [5, 6].

Traditionally, local builders have been able to adapt and develop building techniques by using local resources to produce ‘contextual’ architecture, that is linked to distinctive construction methods that meets their needs [7], and the balance between man and nature was one of the most important inherited concept [8]. However, with the emergence of globalized architecture, local architectural identities became under irreversible risk [9]. This matter does not only represent a loss of cultural diversity, but also a loss of the diversity found in the inherited construction methods [10].

This research aims to explore construction systems and materials of Jordanian vernacular architecture, explaining the relationships between systems, materials, and local contexts. And as the study demonstrates the abandonment of inherited systems, it highlights the efforts of modern Jordanian architects to revive this heritage with different approaches. This was accomplished by site observations to explore traditional structural and architectural features of Jordanian traditional architecture. Additionally, interviews were conducted with the architects who designed two case studies examined in this study; Arch Ikrima Gharaibeh and Arch Maher Azmi Abu-samra, both based in Jordan.

2 The Relationship Between Building Materials and Architecture

Ever since the Industrial Revolution, the relationship between building materials and architecture has become more complex [11, 12]. Before that, local materials were used for their availability and durability. Therefore, builders chose building materials based on the form, function, and affordability. Post industrial revolution, architects

began to rely on laboratory-tested materials instead of relying on experience and practice.

Jordanian vernacular houses had a distinguished layout that reflected the social class of its residents. In some cases, the space is divided into two areas of different levels [13]. The ground level which is near the entrance and service, and the higher level that is used for sleeping and living. These houses were gathered around courtyards where extended families lived in adjacent houses [14], connected courtyards depending on the degree of kinship between the inhabitants; thus, it can be said that the courtyard constitutes a semi-private family gathering where daily business and activities take place [15].

These houses were constructed by the load-bearing wall system that carries the weight from the roof and upper floors. Including roofing systems that used tree trunks where wooden joists rest on the load-bearing walls, supported from the inside by arches and vaults consisting of two opposite layers of reeds. Then, thick layers of clay are mixed with hay [16]. In other cases, domes and vaults were adopted for roofing, mainly in cities, where natural stones were used as building material, and the walls were thick to support the roof [17]. This construction method was influenced by previous civilizations that inhabited Jordan [10], in terms of formation and architectural construction.

Modern migrations have affected Jordanian architecture by the mixture of different cultures, such as, Chechens, Syrians, and Palestinians [8]. In addition to the characteristics of Ottoman architecture [18]. This resulted in an architecture characterized by rationality, simplicity, and local materials [10]. In conclusion, heritage buildings in Jordan have mainly relied on the material available in the construction area [19].

3 Traditional Construction Systems

This section investigates the inherited construction systems, from different areas in Jordan. Starting with clay and limestone as the materials of load-bearing walls, followed by illustrating the use of basalt as the material of construction and roofing in the Badia region. Aiming to set a base and background for the main topic of this research.

3.1 Architectural Formation Using Clay and Limestone as Building Materials, and the System of Load-Bearing Walls

Most Jordanian cities are mountainous where natural stones are the available building material, considered a sustainable building material by providing a long lifespan [20, 21]. Houses built of stone and clay are an ancient expression of the development of

human civilizations and the emerging needs of humans throughout history. Using local resources did not overburden owners, nor did they burden the face of the earth by digging it, hammering iron skewers, and pouring blocks of cement in it, with alien materials that look like implanted foreign bodies. Instead, architecture had a harmonious form with its environment; depending on raw materials such as mud and straw [22]. The resulting space depended on the loading capacity of the building system. To achieve that, builders have used vaults and arches, and in some cases, domes [23].

As for natural stone, it was used more in cities [24], most notably in mountainous areas such as Amman [25]. Load-bearing stone walls with multiple roofs, such as the cross-arch, single-dome, or multi-domed roof, provided durability and an architectural space that serves the required function (Fig. 1) [26]. The walls transmit loads from roofs, distributing them on a layer of soil suitable for the foundation. In this case, the thickness of the walls increases the closer we get to the foundation, as the loads that the wall is exposed to are increasing. In this sense, future changes on the walls are complicated, precautions must be taken to avoid structural failures and the risk of collapsing. Openings were decreased to the least possible, as their presence weakens the walls [27]. When existing; the ratio of openings was of low width to larger height to ensure the construction safety, moreover, this practice plays a key role in thermal insulating.

In the case of horizontal roofs, parallelly arranged tree trunks, wooden bridges, or iron bridges resting on the load-bearing walls were used to distribute loads evenly and homogeneously (Table 1). Reeds were placed over secondary wooden bridges, straws were spread over the ceiling, and clay and straw were covered with a wet, cohesive coarse soil [28]. In other cases, arcades were used as each span is carried by two arcades facing one another, and the load-bearing walls from the other two sides (Table 1). However, by the end of the nineteenth century, more specifications of the functions of residential units were noticed by the influence of Western architectural patterns [29].

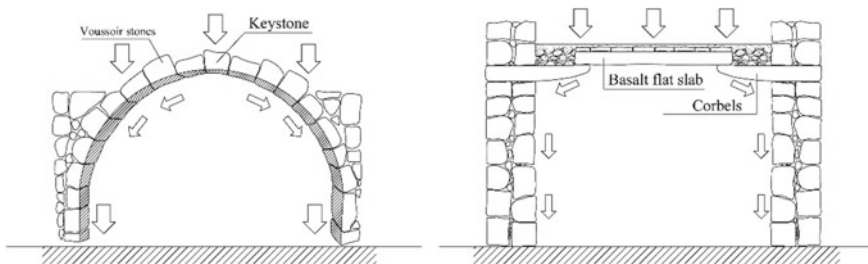






Fig. 1 (Left): Stone transverse arches (limestone or basalt) to support the roof and transfer the loads to load-bearing walls and then to the foundations. (Right): Corbelling system where two parallel basalt corbels support the flat slab to transform the loads to the load-bearing walls





Table 1 Examples of using clay and limestone as building materials from around Jordan

	
<p>A clay house using domes for roofing [30]</p>	<p>System of parallel transverse stone arcades</p>
	
<p>A flat roof based on iron bridges and reeds</p>	<p>A two-story house, with intersecting domes</p>

3.2 Roofing and Construction in the Northern Badia Region with Black Volcanic Stones (Basalt)

Construction methods in the Badia relied on basalt stones as construction material [31]. Alhara region is highly dependent on stones for construction, as everything in it was built of stone, including some doors and windows [32]. Historically, Byzantine and Umayyad builders made their buildings safer and more durable by using basalt load-bearing walls. In this case, the adopted roofing techniques used to create flat slabs have mainly depended on corbelling system. Corbels act as load-transferring elements, from the slab to the load-bearing wall to the foundations. Systems of single or double rows of corbels were used based on the slab’s span (Fig. 1 and Table 2). Historical evidence of this technique is not only limited to dwellings, as they are also observed in churches and other public buildings. As another evidence of its durability, this technique has prospered in roofing stone water tanks. It is worth mentioning that these buildings were still inhabited by local residents until the end of the twentieth century. As a previous study of the Badia region conducted by the author has emphasized on the relationship and interactions between Bedouins and their environment using building techniques that meet their basic needs in physical and cultural aspects [33].

Table 2 Examples of using basalt stones as building material in the Northern Badia region



	
<p>Corbels supporting a flat slab in Um Al-Jimal</p>	<p>Parallel transverse arches to carry the flat slab</p>
	
<p>Stone rows intertwined to form a barrel vault</p>	<p>Basalt corbels to form cantilevered staircase</p>

4 Modern Construction Techniques in Jordan, Adopting Load-Bearing Walls

Modern constructions depend on skeleton system of reinforced concrete. Technological developments have affected the construction sector in Jordan. This has contributed to creating faster and cheaper projects than old inherited methods [34], in addition to developing building techniques to prevent environmental risks that threaten human life.

Although inherited methods have been abandoned by modern practices, and the vast demand for reinforced concrete, these developments did not take over the architectural scene. There are many cases of modern buildings that are designed and constructed according to inherited systems, whether in the formation of architectural spaces or structural system. Few Jordanian architects have made notable efforts to revive traditional construction methods. Of these, this research concentrates on the works of two aspiring Jordanian architects; Arch. Ikrima Gharaibeh, and Maher Azmi Abu-samra.

Table 3 Details of The A.E.A.J. building in the Ghor area

	
<p>Exterior view of the building in Al Karama</p>	<p>Interior of a ceiling loaded on parallel arches</p>

By Arch Ikrima Gharaibeh

4.1 *First Case Study: Jordanian Agricultural Engineers Association*

Among these buildings is the building of the Agricultural Engineers Association in the southern Ghor area. In an interview with the architect, he demonstrated how he agreed with the association on following traditional construction methods in the buildings’ construction, as the formation of spaces and the structural system was based on live-loaded walls. Building materials were extracted from the building site, using local materials. And laborers from the local population were hired in phases of construction.

To ensure building safety, the architect relied on structural calculations of the loading system based on construction heritage. Although the architect has adopted traditional materials and structural systems, he made his own modifications to the forms of structural elements such as arches and domes. This modification has also affected the formation and aesthetic of multiple interior spaces as shown in Table 3.

4.2 *Second Case Study: Dar Al-Uquod*

Another project adopting traditional techniques, is Dar Al-Uquod in Amman. A personal residential building designed by architect Maher Azmi Abu-samra, founder of MAS design studio. It is important to note that his works are influenced by traditional techniques that rely on practical experience, and by the theoretical ideas of architects such as Hassan Fathy and Abdel Wahid Al-Wakil, as he has been a student of the latter.

In an interview, the architect has elaborated on his motive behind choosing traditional construction methods for building his own house, it is in an attempt to create a house that represents the saying: “*My father’s house... in which each step has meaning*” a concept that was first brought by Hassan Fathy. The project is primarily built with limestones in a load-bearing walls system. In his recently published paper,

Table 4 Construction and aesthetic details of “Dar Al-Uquod”, a residential project by Arch Maher Azmi Abu-Samra (photos are obtained from the architects’ archive)

	
<p>The detail of stairs loaded on an arch</p>	<p>The interior of the pointed cross vaults</p>

the architect mentioned the thickness of the walls as approximately one meter thick [35]. For roofing, different types of vaults and domes have been used (Table 4). In addition to being effective structural elements, they also perform as natural lighting and ventilation provident and present eye-appealing interior and exterior aesthetic forms. The building is considered an environmentally designed building as well, as it gradually adopts the site terrain at different levels. Besides using stone extracted from the building site, the architect has trained labor from different origins of the levant to revive the methods of traditional construction which are common around the levant region as inherited these methods are a result of the cultural exchange in the region.

5 Discussion

It is our responsibility, as architects, to keep searching for and developing sustainable construction methods to solve modern issues in the most functionally and aesthetically appropriate solutions. This study shows the important role traditional construction techniques play in this regard. There is no doubt that heritage buildings reflect and enhance the architectural identity, and that inherited construction methods reflect the beauty and distinctive architectural creativity and historic continuity.

In a practical sense, the study has revealed some present challenges and obstacles that must be put forward to achieve better results in conserving and reviving traditional building methods. In an attempt to propose practical solutions, a set of recommendations have been developed, in addition to the expected advantages of employing inherited building methods. This research summarizes these challenges, recommendations, and advantages in the following (Table 5).

Table 5 The set of challenges, recommendations, and expected advantages of employing inherited traditional construction methods in Jordan

Challenges	Lack of experienced craftsmen in this type of construction
	Educational gap in teaching architects and engineers about the system of load-bearing walls, domes, and vaults
	The absence of craft institutes to teach construction using the principle of load-bearing walls
Recommendations	Enactment of laws that encourage traditional construction and distinguish them from reinforced concrete buildings
	Spreading awareness of the importance of traditional construction for owners, especially in tourism
	Emphasizing on the sustainability of such buildings, as the life span is significantly higher than other building methods
Expected Advantages	The long life span role in saving resources, energy, and labor
	Saving the authentic architectural identity of Jordanian cities
	Good thermal insulation that provides thermal comfort in summer and winter (thick walls and high ceilings)
	Obtaining greater aesthetic values, as the flow of weights from the ceilings to the floor and columns are constructed in an aesthetic arrangement without being overly pretentious
	Reviving traditional crafts and encouraging craftsmanship training provides new job opportunities and, in its turn, ensuring a more equitable distribution of wealth in society
	Reducing environmental pollution knowing that every ton of cement produces a large amount of carbon dioxide. Which can be reduced by using local stone and building materials

6 Conclusion

Jordanian vernacular architecture has witnessed many changes over different eras. From the early stages of its formation and flourishing as a material manifestation of cultural exchanges in the region. To the modern stage of replacement with reinforced concrete. Abandoning traditional methods that used arches and vaults to create aesthetic interior space in addition to its structural function, has affected the image of Jordanian cities from being vibrant towns with identified aesthetic architectural styles to anonymous and monotonous units of concrete.

Despite the major abandonment of traditional building techniques in Jordan, a prospering movement to conserve and renovate these methods is rising and gaining momentum among local architects. This research provided evidence and emphasis on the cultural and architectural advantages of such a movement. In this respect, future studies might extend the research on adopting and renovating traditional construction systems of Jordanian vernacular architecture within modern contexts and using modern technologies. In addition to considering the impacts of socioeconomic forces and factors on the construction sector and vernacular architecture in Jordan.

References

1. Barber WJ (2021) A history of economic thought. Wesleyan University Press
2. Alves S (2017) The sustainable heritage of vernacular architecture: the historic center of oporto. *Procedia Environ Sci* 38:187–195
3. Downton PF (2009) *Ecopolis: Architecture and cities for a changing climate*, vol 1, Springer Science & Business Media, Australia
4. Lu Y, Li Y, Skibniewski M, Wu Z, Wang R, Le Y (2015) Information and communication technology applications in architecture, engineering, and construction organizations: a 15-year review. *J Manage Eng* 31(1)
5. Ali A (2002) *Mud Villages (Qura al-teen)*. Historical Engineering Study, Arabic language book, Ministry of Culture Publications, Syrian Arab Republic, p 11
6. Onishchenko AN, Petrova TI, Kartseva EV (2020) Features Of Space Organization In: The Modern Regional Architecture. In: IX All-Russian Festival Of Science Collection of reports, Nizhny Novgorod State University of Architecture and Civil Engineering, pp 624–626
7. Toole TM (1998) Uncertainty and home builders' adoption of technological innovations. *J Constr Eng Manag* 124(4):323–332
8. Aldabbas AHM, Atiyat ADI (2016) The impact of population migrations in contemporary Amman city architecture. *Arts and Design Stud* 49:66–75
9. Salman M (2018) Sustainability and vernacular architecture: rethinking what identity is. In: *Urban and architectural heritage conservation within sustainability*. IntechOpen
10. Tarrad M, Ibrahim M (2021) Detection of limestone quarries in Jordan through remote sensing data to achieve sustainable utilization in vernacular architecture. *Planning* 16(4):661–674
11. Kurtuluş M, Güner S (2020) Changes in the use of materials in the field of architecture after the industrial revolution. In: XIV international theory and history of architecture conference November 6, 2020, (Industrial Revolution), pp 249–256
12. Menga L (2022) Industrial revolution and the birth of modern architecture. *Int Scientific J Vis* 7(1):105–123
13. Shaikhli NA, Shafie IA (2020) The effect of natural energy sources on the sustainable form of vernacular architecture. *International J Adv Res Eng Technol* 11(6):378–391
14. Alhusban A, Al-Shorman A (2011) The social, political and economic functions of courtyard houses in Umm Qais, Northern Jordan. *Int J Hist Archaeol* 15(1):1–9
15. Tarrad M, Al-Omari O, Mohammed AR (2012) Natural stone in Jordan: characteristics and specifications and its importance in interior architecture. *J Environ Sci Eng B* 1(6B):720
16. Qtaishat Y (2021) *Integrated eco-cultural architecture framework for sustainable housing design in Jordan* (Doctoral dissertation, University of Bath)
17. Almatarneh RT (2013) Sustainability lessons learnt from traditional architecture: a case study of the old city of As-Salt Jordan. *IOSR-JESTFT* 5(3):100–109
18. Shawash J, Marji N, Marji N (2022) A century of Jordanian architecture: narrating the development of the nation. *Archnet-IJAR: Int J Architect Res Vol.* ahead-of-print, No. ahead-of-print
19. Alzoubi HH, Almalkawi AT (2019) A comparative study for the traditional and modern houses in terms of thermal comfort and energy consumption in Umm Qais city, Jordan. *J Ecologic Eng* 20(5)
20. Al-Shatnawi Z (2022) The environmental performance of earth construction systems in Jordan's mediterranean climatic zone. In: *Proceedings of 2021 4th international conference on civil engineering and architecture*, Springer, Singapore, pp 17–25
21. Zhong W, Schröder T, Bekkering J (2022) Biophilic design in architecture and its contributions to health, well-being, and sustainability: a critical review. *Front Architect Res* 11(1):114–141
22. Tarrad M (2020) A vision to revive mud architecture, a community heritage architecture in Jordan, for low income. *Int J Design Nat Ecodynam* 15(2):269–275
23. Aldeek Z (2020) Green architecture and sustainability in the complex transformation of the built urban environment in Jordan. *Int J Design Nat Ecodynam* 15(1):113–120

24. Malkawi FK, Al-Qudah I (2003) The house as an expression of social worlds: Irbid's elite and their architecture. *J Housing Built Environ* 18(1):25–48
25. Atiyat D (2015) The stone as a main building material. *J Multidisciplin Eng Sci Technol (JMEST)* 2(4):509–514
26. Mofleh NJJ (2009) Rehabilitation and Conservation of the old Center of Awarta Village (Doctoral dissertation)
27. Baglioni I (2015) Jordanian vernacular architecture. In: *Vernacular architecture: towards a sustainable future*, 105–110. CRC Press/Balkema
28. Al-Jokhadar A, Jabi W (2017) Applying the vernacular model to high-rise residential development in the Middle East and North Africa. *Archnet-IJAR: Int J Architect Res* 11(2):175–189
29. Abu-Azizeh W, Tarawneh MB (2015) Out of the harra: Desert kites in south-eastern Jordan. New results from the South Eastern Badia Archaeological Project. *Arabian Archaeol Epigraphy* 26(2):95–119
30. Ammar K (2022) A photograph of mud house in south-east of Tel Deir Alla, Central Jordan Valley, Jordan, taken in 1983 by Ammar Khammash. Retrieved from <https://www.facebook.com/photo/?fbid=914441315292871&set=a.907196532684016>. Accessed on 2022/12/10.
31. Meister J, Knitter D, Krause J, Müller-Neuhof B, Schütt B (2019) A pastoral landscape for millennia: Investigating pastoral mobility in northeastern Jordan using quantitative spatial analyses. *Quatern Int* 501:364–378
32. Dodge H (1984) Building materials and techniques in the Eastern Mediterranean from the Hellenistic period to the fourth century AD (Doctoral dissertation, Newcastle University)
33. Tarrad M (2014) Study on a Heritage Town in the Northern Badia of Jordan—Al Aqeb. *J Civil Eng Architect* 8(2):221–230
34. Semenyuk O, Abdrashitova T, Belousova E, Nechay N, Listkov V, Kurbatova V, Niyazbekova S (2018) The influence of ecology and economic factors on eco-architecture and the design of energy efficient buildings. *World Transact Eng Technol Educ* 16(2):186–192
35. Abu-samra MA (2022) Dar Al Uquod: a traditional house in amman. *J Tradit Build Architect Urban* 3:158–181

The Construction Typology and Its Relationship in the Architectural Image of the Buildings in the City of Oxapampa, a South German Colony Located Within the High Forest of the Department of Pasco in Central Peru



Diana Villegas and Vladimir Montoya

Abstract Our investigation had as objective, the study of the constructive typology that was developed in Oxapampa, this given that people from Germany and Austria arrived in Peru, who upon arriving in Oxapampa began with the development of an architecture which has both Austrian and German architecture that differs from the entire jungle region and even from the entire country, the architecture that the settlers impose is very well suited to the area due to the configuration of its climate, and they begin to exploit natural resources such as wood, for this reason it was possible to identify the constructive typology and the relationship it has with the architectural image. A data collection was carried out through observation sheets of the typological characteristics of the buildings located within the “Monumental Urban Environment”, this to analyze to what extent the constructive typology influences the architectural image of the buildings of the city. With the use of the descriptive statistical system we obtained results that define the architectural typology, the predominant materiality based on wood and how it relates to the architectural image. It was determined that the construction style contributes to safeguard the cultural heritage of Oxapampa; whose architectural use can be seen in the frontal elevation of each building within the zoning called “Monumental Urban Environment”, as well as the state of conservation influences the cultural valuation of the buildings under study, which represent a vernacular manifestation.

Keywords Constructive typology · Architectural image · Monumental urban environment · Cultural heritage · Wooden construction · Austro-German architecture

D. Villegas (✉) · V. Montoya
Universidad Continental, Huancayo 12002, Perú
e-mail: 71329997@continental.edu.pe

V. Montoya
e-mail: vmontoya@continental.edu.pe

1 Introduction

In the present investigation, the constructive typology of the city of Oxapampa was analyzed, in which we found very marked design criteria different from the criteria of other regions of Peru, this is due to the history of Oxapampa, in the year 1853 a group of German and Austrian immigrants arrived in Peru due to the German revolution, this group went through various journeys upon arrival in Peru, since at that time it was not known where they were going to settle, for which they had to travel through several provinces of our country after passing through many regions of Peru, for this reason it is not until 1859 that they manage to reach Pozuzo. Upon reaching this part of the Peruvian jungle, they are amazed by the beauty of its landscapes, where they settle and begin to develop a colony, they begin to replicate their houses with German and Austrian characteristics, thus introducing the Austro-German typology, in 1891 a group of settlers decided to extend their colony and thus arrived in Oxapampa, the year in which the city was founded on August 30, 1891 [1], they also began to share their culture with the inhabitants of the area, from this they began to build houses with Austro-German characteristics with materials from the area such as wood, which was abundant in the valley at that time, these replicas of Austrian and German buildings adapted to the area due to the configuration of its climate, its location.

Over the years, houses and buildings continued to be built as the first settlers did, until 1957 when new construction technology (reinforced concrete) was brought in and the famous Cine Lido [2] was built, which broke with the immediate environment in those years, because of its shape that was not related to the urban parameters of that time and because of its materiality that no wood was used in the structure and façade. Since then, construction began in a mixed way, integrating new construction technologies over the years, for this reason, in 2003, after a council session, municipal ordinance No. 007–2003-MPO [3] was created, which regulates the shape of the facades, and which preserves the continuity of the roof of the buildings in the Austro-German style.

The study problem in this research was chosen to be able to establish the necessary guidelines for future urban interventions, which safeguard the existing cultural heritage, and it does not happen as in 1957 when, as a result of a lack of correct guidelines, a building was built that was not consistent With all the urban parameters, after this event the urban landscape of Oxapampa was transformed [2].

The method used in the development of the investigation is the scientific method at a descriptive level, this as a consequence that it was sought to define what is the architectural typology that predominates in the facades of the buildings within the zoning called “Monumental Urban Environment”, this at a rate that the method makes it possible to describe each of the existing typological characteristics. Observation sheets were used to characterize the buildings within the “Monumental Urban Environment”, questionnaires were also addressed to the inhabitants of Oxapampa, who know the Oxapampa culture and are the most interested in preserving the essence of the buildings with their characteristics marked as is the material, a high-sloped, gabled roof, preserving the patterns of vernacular architecture [4].

2 Background

2.1 In the Thesis “Architectural Patterns of the Traditional Architecture of the Historic Center of Concepción—JUNIN 2017” [5]

The author begins by referring to the traditional buildings found in Concepción and poses the following problem: “What are the Architectural Patterns of the Traditional Architecture of the Historic Center of Concepción in Junín?” [5]. Due to a previous study of the city and its current urban landscape, and to the fact that architecture changed over time, traditional buildings were gradually replaced by buildings with a modern or period typology, which was not the case in Concepción since the buildings still maintain the architecture typical of the area, therefore its general objective is to Identify and Characterize said Architectural Patterns [6], for which they delimited the study area, which is the Historic Center of Concepción, for their investigation, because in In this area, the architectural typology of the place was easily recognized, during the study time I identified the traditional architecture that was developed in Concepción, highlighting the cultural heritage of great historical value that was found, it details the materials of these such as stone, adobe, wood among others, and the way in which the houses evolved over the years, also in the investigation Referring to architectural patterns, the methodology was descriptive and sought to recognize the patterns of existing architecture, for this the author collected data through a control sheet that was applied to 108 traditional buildings randomly chosen from the historic center of Concepción, After a long observation and filling in the sheets with data that refer to the main façade, the use of the building, the type of coverage, construction systems, among other characteristics, at the end the data was processed, obtaining as results the dominant patterns found in the study buildings and it was concluded that because the study buildings have the architecture of the colonial era: “The Traditional Architecture of the Historic Center of Concepción, presents a series of architectural patterns of functional and formal order” [5].

3 Results and Discussions

In the present investigation, in the first instance, do not use quantitative or qualitative instruments, which contribute to the investigation, for this reason we had to design an instrument that helps us to demonstrate the results, which we can see in Fig. 1, this instrument is based on references of the theoretical bases, in order to appreciate the current characteristics of the architectural typology of the city of Oxapampa, given that “Oxapampa is located within the so-called Central Jungle stands out as a protected natural area” [7], then it will be presented a data record sheet of a total of 92 of which are attached in their entirety in the annexes chapter.



LOT TYPE		CODE: 015-MZ-B		
MEDIATOR				
CORNERBACK				
DOUBLE FRONT				
				
DATA ABOUT MATERIALITY				
STRUCTURAL SYSTEM	ENVELOPE (WALLS)	FACADE	COVERAGE	
SUPPORTED	CONFINED MASONRY	CONFINED MASONRY	METALLIC	
WOOD		WOOD	CALAMINE	
BEARING WALL	WOOD	GLASS	ROOF TILE	
MIXED	DRYWALL	MIXED	LIGHTENED SLAB	
FACTS ABOUT ZONING				
APPLICATIONS	BUILDING HEIGHT	STATE OF CONSERVATION	YEAR OF BUILDING	
COMMERCIAL	15 m	VERY GOOD	FROM 0 TO 5 YEARS	
		GOOD	FROM 5 TO 10 YEARS	
FINANCIAL	NUMBER OF FLOORS	REGULAR	FROM 10 TO 20 YEARS	
HOUSING		BAD	FROM 20 TO 50 YEARS	
INSTITUTIONAL		4	UNINHABITABLE	MORE THAN 50 YEARS
SUPPLEMENTARY DATA				
FACADE ELEMENTS				
NUMBER OF BALCONIES	BALUSTER MATERIAL	NUMBER OF WINDOWS		NUMBER OF INCOME
5	WOOD	1ST FLOOR	7	6
	METAL	2nd FLOOR	7	
NUMBER OF PILASTS	ALUMINUM	3rd FLOOR	7	
	GLASS	4th FLOOR	6	
	DOESN'T COUNT	ROOF	2	
ROOFING ELEMENTS				
PERCENTAGE OF SLOPE	TYPE OF SLOPE	BLESSED WINDOW	COVER TYPE	GABLE IN FACADE
0% to 10%	PRONOUNCED	0	ROOF TO A WATER	YES
10% to 15%	MODERATE		GABLE ROOF	NOT
20% to 30%	SHORT	ATTIC WINDOW	ROOF WITH THREE WATERS	STEPPED ROOFING
30% to 40%	DOESN'T COUNT	2	FOUR WATER ROOF	YES
MORE THAN 40%				NOT

Fig. 1 Registration form model. Source Self made

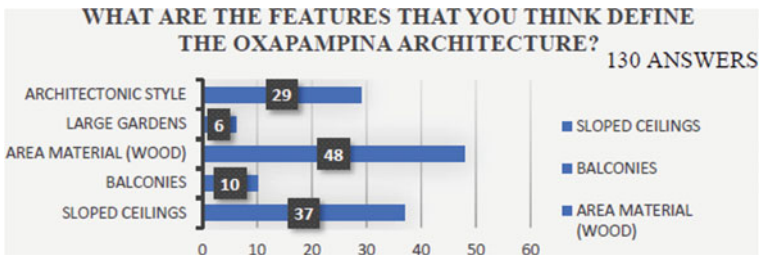
3.1 Analysis of the Typology of Dwellings in the Monumental Urban Environment Through the Use of the Opinion Survey

After having carried out a survey on the constructive typology in the buildings of Oxapampa, we were able to capture different appreciations about what exists.

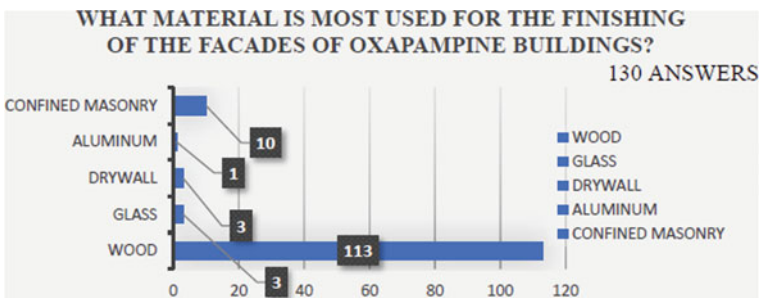
As we can see in Graph 2, According to 37% of the population that carried out the survey, the feature that defines Oxapampina architecture is the use of local material (wood), 28% consider that the feature that defines the oxapampina architecture are the sloping roofs, 22% consider that the feature that defines the oxapampina architecture is the architectural style.

This data was important for the investigation since it shows that 37% of the population is wrong, given that currently wood is only being used for the details of the façade, and not for its volumetry, and only 22% is in the correct thing, because it is the architectural style that defines the architecture of the Oxapampa.

As we can see in Graph 2, 87% of the population that carried out the survey identifies wood as the most used material for finishing facades, 8% determines that it is confined masonry.



Graph 1 Features that define the Oxapampina architecture. Source Self made



Graph 2 Most used material for finishing the facades of Oxapampa buildings. Source Self made

This data is very important since it shows that the population that carried out the survey was able to identify that the details of the finishes of the facades of the buildings in Oxapampa are mostly made of wood.

3.2 Comparative Chart Between Austro-German Architecture in the City of Oxapampa—Peru, in Germany and in Austria

A comparison was made of the architectural typology of 3 different countries that have the same architectural concept which we can see in Table 1, this comparison was made with the sole purpose of finding the similarities and differences between the architecture of their homes, given that it was the native settlers of Germany and Austria who brought the architectural trend to the Oxapampa Biosphere Reserve in Peru [8] (Illustrations 4, 5).

4 Discussion of Results

In our investigation, the background of our theoretical framework was taken into account as references to be able to carry out the discussion of the following conclusions.

The discussion is carried out with the following criterion “In the geometric aspect of the building, it is mostly represented by an irregular parallelepiped, the color that tints these buildings corresponds to a pure white, the character corresponds to residential dwellings where they show representative elements such as balconies, gates and double pane windows. For the roofs, they are covered with 2 waters” [5] (Arnesquito and Pio 2019), on the other hand, in my research a high level of affinity was found with the buildings analyzed since the owners mostly have the facades of monochromatic colors that make contrast with the color of the wood that in most are white and green, additionally another similar characteristic with the background is the use of balconies for their facades, being in our buildings in study wooden balconies with finishes typical of the area such as rustic balusters or in some cases carved wooden balusters and finally gabled roofs are also used on roofs with the difference that in our buildings the slope is steep due to the Austro-German architectural style that these and that adapt very well to the climate due to the constant rainfall, all these characteristics found in the houses of the Monumental Urban Environment of Oxapampa are defined in the Urban Development Plan of the year 2016 for Oxapampa [9].

Table 1 Summary table of characteristics of Austro-German architecture in Oxapampa-Peru, Germany and Austria

Criteria	Oxapampina housing Austro German style in Peru	German housing (Germany)	Austrian housing (Austria)
Facade	 <p>Illustration 1: Oxapampina house museum</p>	 <p>Illustration 2: German house</p>	 <p>Illustration 3: Typical house in the alps</p>
Materials	<p>In most of the buildings, wood predominates as a construction material, it is also used</p>	<p>Most of the houses have a basement, so the material to be used in this space is concrete, in the same way the upper floors are made of concrete with wood applications</p>	<p>Concrete for the first levels and wood for upper levels</p>
Construction system	<p>Structural system provided</p>	<p>Structural system provided</p>	<p>Structural system provided</p>
Coverage	<p>Catamine, tile, metallic structure</p>	<p>Roof tiles, light bituminous roof tiles</p>	<p>Tile imitation bituminous plates</p>
Roof slope	<p>In most buildings the slope is steep</p>	<p>In most buildings the slope is steep</p>	<p>In most buildings the slope is steep</p>
Balconies	<p>Many of the buildings have balconies on their upper levels</p>	<p>Most buildings do not have balconies, since they have larger windows</p>	<p>Many buildings have balconies on the top floors, they are small balconies</p>
Ventana En Techumbre	<p>In most of the buildings we find pious windows and dormer windows, the latter being the most used</p>	<p>Devout style windows could be seen on the roofs of the buildings</p>	<p>Gabled attic-style windows could be seen on the roofs of the buildings</p>

(continued)

Table 1 (continued)

Criteria	Oxapampina housing Austro German style in Peru	German housing (Germany)	Austrian housing (Austria)
Coverage type	In most of the buildings we find that the coverage is gabled	In most of the buildings we find that the coverage is gabled	Many of the buildings have four water coverage, finding buildings that also have two or three water coverage, but it is a minority
Gable on facade	There are few buildings that have a gable, but most do not	No buildings were found that present this architectural element	Some buildings were found that present this architectural element
Stepped roof	The minority of buildings have this type of roof, since they use it because the terrain is not symmetrical and in order to have a coverage	No buildings were found that present this architectural element	No buildings were found that present this architectural element

Source Self-made



Illustration 4 Virtual idealization Austro-German style housing. *Source* Self made



Illustration 5 Virtual idealization of the museum, Austro-German style. *Source* Self made

5 Conclusions

After having carried out the analysis of the city of Oxapampa, we realize something very important in the process of architectural mixing, which leads us to reflect on mixing, connecting the dualisms that constitute it with the socio-cultural context [10]. This is thanks to the fact that in Oxapampa there was a miscegenation not only of an architectural nature, but also of a social nature, since OXAPAMPA comes from the Quechua “OCSHA”, which means “straw”, and “PAMPA”, which means plain (pampa de straw), the native Yánesha (Amueshas), for their part, call it Mon Konma. In these two meanings it also means plain of reeds or pajonal [11], after carrying out the analysis of the city of Oxapampa we also analyze the buildings within the Monumental Urban Environment from which we can conclude with the following:

It was determined that there is a high and significant level of influence between the constructive typology and the architectural image of the buildings in the city of Oxapampa, this is because in the field work we were able to identify the current constructive typology of each building within the environment. monumental urban area in which it focuses largely on the finish of its facades, thus giving a pleasant image that is related to the immediate environment. This is supported by the results of the façade analysis indicator in which 42, 39% are related to each other by having a confined masonry façade.

After having analyzed the buildings within the Monumental Urban Environment, it was possible to determine that there is a great influence between the construction style and the cultural heritage, because in the field work we were able to identify very marked characteristics in different buildings currently considered part of the heritage. such as the main church, the representative house of Oxapampa, the house of Alpentel, among others, with few buildings having a very marked architectural pattern that is the gable on the façade, a feature that is still preserved in Austrian architecture. German brought by the first settlers, this is supported by the results of the Hastial analysis indicator in which 19.57% have the presence of the architectural element in their buildings.

It was determined that the Architectural Use has contributed to a great extent in the frontal elevation of the buildings of the Monumental Urban Environment, this is because in the field work we were able to identify that the buildings with commercial use mostly have a different frontal elevation than buildings for institutional use or residential use, mostly having confined masonry envelopes, which is clearly supported by the results of the analysis indicator of the Envelope (walls) of buildings in which 67.39% are related to each other for having a confined masonry envelope.

References

1. Provincial Municipality of Oxapampa (2019) History and culture. History of the Province of Oxapampa. [Online] 2019. Retrieved from https://www.peru.gob.pe/Nuevo_Portal_Municipal/portales/Municipalidades/1911/entidad/PM_MUNICIPALIDAD_DETALLE.asp?pk_id_entidad=1911&pk_id_tema=93600&pk_id_sub_tema=10964. Accessed on 20 Oct 2022
2. Zabanick J (2018) Wooden container: constructive Memory in Oxapampa
3. Provincial Municipality of Oxapampa (2003) Ordinance 007/2003/MPO
4. Luis M (2018) Residential vernacular architecture patterns in the Mantaro valley-Ahuac District Case-2018
5. Amesquito J, Trixy P (2019) Architectural patterns of the traditional architecture of the historic center of concepción—JUNIN 2017
6. Christopher A (1980) A pattern language
7. Jessica A (2014) Application of the principles of landscape architecture in the design of a tourist recreational center-Oxapampa for a perception of integration to the environment
8. UNESCO (2022) UNESCO recognizes Oxapampa as a biosphere reserve. [Online] June 3, 2010. Retrieved from <https://www2.congreso.gob.pe/Sicr/Prensa/heraldo.nsf/1234/749ecda11f072d4305257738005d9cb3/?OpenDocument>. Accessed on 20 Oct 2022
9. Provincial Municipality of Oxapampa Urban Development Plan. Oxapampa: MPO, 2017–2026.
10. Castillo L, Vélez J (2020) Miscegenation, a binary construction in the Latin American context
11. Maria Jesus Fung L (2017) Marketing application and tourism development of the district of Oxapampa, Pasco-Peru, period 2013–2015. 2017.

Transformation of Architectural Elements of *Rumah Gaba-Gaba* in Merauke Old Town, South of Papua: An Embodiment of Adaptation



Yashinta Irma Pratami Hematang  and Harry Kurniawan 

Abstract Based on its history, the city of Merauke was a city that developed from the Old Town of Merauke which was formed because it was a post for the Dutch government in the early twentieth century. At that time, the Catholic Missionaries came along with old teachers from the Moluccas who taught education for indigenous Merauke people in the rural area. When the old teachers were on duty in the rural area of Merauke, they need housing in the city area that serves as a place for their families to live which later developed as the *Rumah Gaba-Gaba*. Then the purpose of this study is to find the form of adaptation that occurs in the architectural elements of the *Rumah Gaba-Gaba* which later became the forerunner of the uniqueness of the Old Town of Merauke and the development of other sectors in Merauke. The method used in this study is a qualitative method with direct observation and interview techniques (primary data) for 5 observed cases at the location of the Merauke Old Town residential area as well as content analysis and visual analysis (secondary data) in the architectural analysis of the original residence and the Merauke Old Town. The results of this study include an analysis of the adaptation and transformation of the architectural elements of the *Rumah Gaba-Gaba* (foundations, floors, walls, and roofs) brought by the Moluccans in Merauke.

Keywords Moluccan migration · Migrant architecture · Influencing context · City development

Y. I. P. Hematang (✉)

Department of Architecture, Faculty of Engineering, Universitas Musamus, South of Papua, Merauke, Indonesia
e-mail: yashinta@unmus.ac.id

Y. I. P. Hematang · H. Kurniawan

Department of Architecture and Planning, Faculty of Engineering, Universitas Gadjah Mada, Yogyakarta, Indonesia

1 Introduction

The phenomenon of architectural migration in the world was studied by [1] who studied housing as residential architectural construction in the migration process. For her, migration is an urgent field in this age that is also emerging in architecture. The global impact of migration is evident in the increasing cultural diversity of cities and in urbanization. Examples of the massive exodus of postwar migrants from Southern Europe—Italy, Greece and Yugoslavia—were sent along labor migration trajectories to Sweden, Germany, Switzerland and other European countries, and to the United States, Canada and Australia, this prompted industry and economic growth of these host countries. Research conducted by [2] explains that a broader and more inclusive understanding of early modern cities in refugee camps stems from the Venetian colonialist expansion.

The phenomenon of migration occurs in all provinces in Indonesia. Badan Pusat Statistik of the Republic of Indonesia explained that the problem of migration in Indonesia is related to the density and uneven distribution of the population. More than half of recent migrants come from the working age group (20–39 years). Meanwhile, the percentage of recent migrants decreases with age. Of these migrants, nationally most of the recent migrant households have lived in their own homes (52.8%) [3]. From this data, there is an opportunity for the emergence of an influence on the design of housing owned by migrants located in the migration destination. In Yogyakarta, there is a phenomenon of the construction of several houses owned by Balinese people. Research conducted by [4] explains that there is a significant consistency of the *Pamerajan-Paon* concept of an ancient Balinese house in a Balinese house in Yogyakarta as a binary diametric space.

This migration phenomenon more specifically occurs in Papua Province which has been explained by the Badan Pusat Statistik of the Republic of Indonesia that the migration process occurs between districts in Papua [5]. PhD Thesis [6] explains that since Papua became part of Indonesia in 1963, hundreds of thousands of people have migrated to Papua and by 2000, more than a third of Papua's population were non-indigenous people, with most of these immigrants living in areas more developed cities along the coast. According to [6], if Papuans are to be fully incorporated into the Indonesian nation, an understanding of the impact of migration on the Papuan population is essential.

Papua as a country has long been occupied by many powers from many countries since ancient times, leaving an influence on the remaining building artifacts today. Book [7] explains that the name Papua for Irian Jaya or West Irian has been known for a long time where it was first given by the first Portuguese governor in Maluku named Jorge de Meneses in 1528. In 1770, James Cook rediscovered Papua. Following the French sailors, even Italy and Russia joined the expedition to the island of Papua. In 1902, the Dutch post in Merauke was built in the south. This post is famous as a center for hunting for the birds of paradise and before the war with Japan there had been immigration of Javanese people to the north of Merauke to open fields and make rice fields.

Book [8] explains that since 1570, most of the territory of West Irian was under the Tidore Sultanate. Book [9] explains that the people who inhabit the northwestern tip of the island of Papua and the entire north coast, have long been influenced by the inhabitants of the Maluku islands (Ambon, Ternate, Tidore, Seram and Key). Even the influence of Maluku has been since the megalithic era as explained by [10] who explains that since prehistoric times, to be precise, the megalithic period according to Reinsfeld, the Papua region has received megalithic influences from Southeast Asia through 2 (two) directions which are one of them came from the west through the southern Indonesian archipelago, through the Maluku islands to the western part of Papua.

The mobility of the migration of the Moluccans to Merauke in ancient times in the Old City of Merauke was due to several things. Book [11] explains that trade contacts were people from Seram which began in 1600 (maybe even earlier) namely several small islands in Seram spread towards the Banda Sea until 1645 trade expeditions reached Papua New Guinea east of Merauke. Then the entry of catholic missionaries in Merauke also brought teachers on educational missions from Tanimbar Kei and Langgur (Kei Island) [12].

Missionaries are required to come to Merauke bringing old teachers from Moluccas. Old teachers and Dutch government posts then formed an old settlement, namely the old city of Merauke. The origin of the name of the city of Merauke itself comes from the name of the Dutch for the plains at the Maro river divider which was obtained from a misunderstanding of communication between the indigenous people and the Dutch who came to Merauke in the 1900s [13].

There is a residential area within the Old Town of Merauke. The house that was formed and still survives to this day in Merauke with wall construction from sago midrib (*gaba-gaba*) in Merauke is known by the public as *Rumah Gaba-Gaba*. [14] explained that the *Rumah Gaba-Gaba* known to the people of Merauke with the material that makes up the wall, which is part of the sago plant, namely the midrib.

On the other hand, this *gaba-gaba* wall system is also owned by Merauke indigenous, especially those who live in coastal areas who also have houses with house walls made of sago fronds in Merauke. The indigenous people of Merauke, namely the Marind-Anim, are also known to have *gaba-gaba* wall houses. The Marind-Anim tribe who inhabited *gaba-gaba*, who lived on the coast, became known as the Marind Pantai. Report [15] explained that the Marind-Anim people live in residential locations along the Merauke coast and some live in the inland. Meanwhile [16] explains that in the inland, the houses are not built on stilts and are not made of sago leaves but are covered with eucalyptus bark. For all the Marind-Anim houses on the coast are rectangular in shape, five to six meters wide and six to seven meters long, standing on stilts erect above the ground. The walls are made of sago leaf stalks that are plugged into the ground between flat poles of wood or bamboo. Report [15] explained that generally Marind-Anim houses are long houses and only have one room, no windows, two doors on the west and east side, with the direction facing the house to the north. This building has a roof made of sago leaves, the pillars of the house are made of wood and bamboo, while the walls are made of sago fronds (*gaba-gaba*).

This study wants to see how the form of adaptation that occurs in the architectural elements of the *Rumah Gaba-Gaba* in the old city of Merauke, which is inhabited by immigrants but has been entrenched and rooted for a long time for the people of Merauke, is marked by several houses still surviving to this day. This form of adaptation then becomes a variety of visible creativity. How about the adaptation to the transformation of the architectural elements of these migrants to a new location in Merauke. Then it undergoes acculturation between its original influences, indigenous architecture (*Marind Anim*), colonial influences, and the influence of natural locations and the environment where the case is located.

2 Research Methods

This study uses a qualitative paradigm with the analytical techniques used are content analysis and visual analysis by comparing the original residential architecture and the new residential architecture that has been adapted to the new location. In addition, the primary data collection model with direct observation surveys and interviews was conducted for five observed cases. The form of analysis is descriptive textual from the results of data collection. The data collection technique comes from primary data in the form of interviews and observations on the object of research and secondary data comes from the results of research that has been carried out and published previously both by the researchers themselves and other researchers in the field of science, from books and from research reports and reports of relevant activities. This research was conducted from August to October 2022. The location of this research is Merauke, Papua, Indonesia. The research case consisted of 5 houses, which were non-probability samples by purposive sampling with consideration of the selection being the *Rumah Gaba-Gaba* which was not yet extinct in Merauke.

The area where the *Rumah Gaba-Gaba* is located in the research case as seen in Fig. 1 is in the Old Town of Merauke. Report [13] explains that although the local people had customary rights, the Dutch post at that time bought a piece of land which later turned the area into a Merauke Post. It was this area which later became the Old Town of Merauke and grew to become the City of Merauke. The boundaries of the postal area of the Dutch government referred to by [13] have the following boundaries:

1. The eastern and western parts are bounded by the outer parts of the two sand ridges.
2. The northern part is bordered by the banks of the Maro River.
3. The southern part is limited by a tread road that connects the two sand ridges to the tread road to Noari [13].

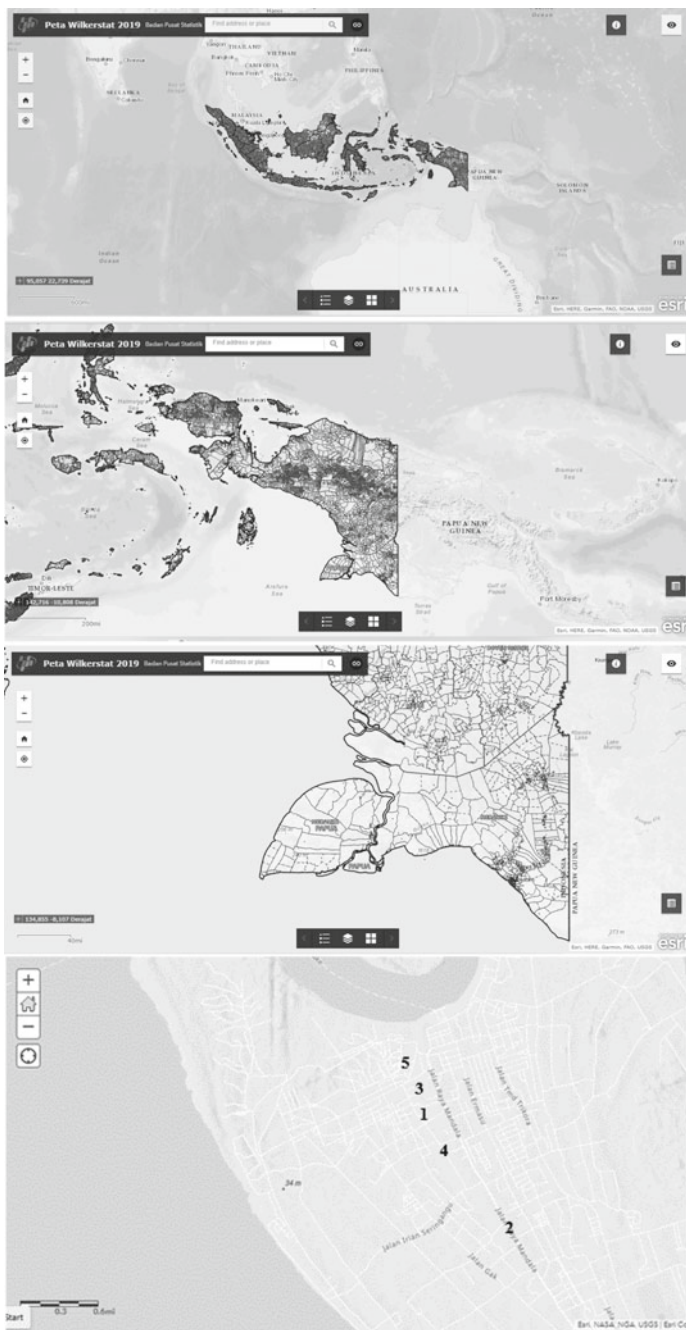







Fig. 1 Sample research in Merauke old town. Source [17]

Table 1 Research observation case table

Case number	Rumah <i>Gaba-Gaba</i> in Merauke old town	The origin house
Case 1		<i>Rumah Rahan Teli</i> in Tanimbar Kei, <i>The House</i> in Kei Besar Island, and <i>Rumah Sombalatu</i> in Seram
Case 2		
Case 3		
Case 4		
Case 5		

3 Result and Discussions

The basic elements of architecture should not be thought of as objects in their own right but in the way they can be used (individually or in combination) to identify places. When built, the basic elements are given a physical form, various additional factors come along. In its realization and in the subject’s experience of it. The basic elements identify the place and are modified by light, color, sound, temperature, air movement, smell (and possibly taste), the quality and texture of the materials used,

using scales and effects and the experience of time. There are endless possibilities in modifying the basic elements in their possible configurations [18]. In terms of making modifications in a creative process, book [19] explains that without an understanding of the relationship between the concepts of real and unreal, imagination and fantasy, it is impossible to have a clear understanding of the prerequisites. for the creative process, or to begin the task of cultivating and developing it. Fantasy is the catalyst of imagination, while imagination is the filter of fantasy to become a material of reality. Creativity is the process by which imagination exists in reality.

The process of building changes can occur because of new thoughts from the community to change their traditional residences because of the emergence of curiosity about modernity but sometimes it takes place very differently from their traditional residences. Book [20] explains that in the case in Kenya the Bomas of Kenya where this open space has representation with those outside Nairobi such as the Kikuyu, Kuria or Pokot people.

3.1 Elements Under the Floor

The foundation as one of the elements on Seram Island, book [21] displays the documentation of the river stone continuous foundation on the *Rumah Sombalatu*. In the case of migrant houses found in Merauke, namely the *Rumah Gaba-Gaba*, there is a continuous foundation but the filling material is different. This foundation is made of glass bottle filling material which is glued together with a mixture of sand, broken sea shells and cement into concrete.

According to the original residential architecture, the architecture of *Rumah Rahan Teli* and the house in Kei Besar has a stilt under the construction of wooden poles. This area under *Rahan Teli's* house is called *lavovan* [22]. This process of change is inseparable from the adjustment of Merauke's natural conditions. Explained that concrete materials consisting of quality sand and gravel were not available in Merauke City, so the materials had to be imported from other cities, such as Palu or Surabaya City [23].

This explains that from the past stone material could not be found naturally in Merauke. The thought of importing materials from outside the city in ancient times was substituted by replacing stone materials with used glass bottles of liquor and bottles of tomato sauce as seen in Fig. 2.

In the observed case, it was found that the first access to the house was through a footing made of concrete mix. In the original architecture in the form of a house on stilts (Tanimbar Kei Architecture and The House in Kei Besar), there is a ladder as the first step into the house. At *Rahan Teli's* house there are wooden stairs, while in Kei Besar there are steps made from piles of stones in front of the center of the house before entering the front porch.

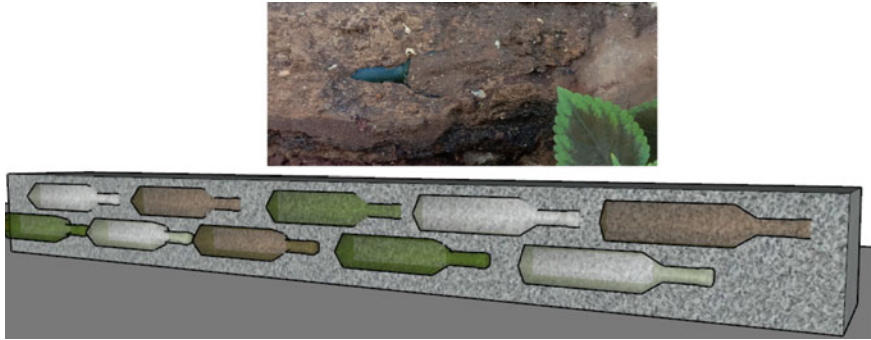


Fig. 2 The arrangement of glass bottles in the foundation structure of *Rumah Gaba-Gaba* in Merauke

3.2 Floor Elements

The owner of the *Rumah Gaba-Gaba* in the case observed in this study explained that initially it had a floor structure in the form of compacted soil without a floor layer but since the 1980s, the floor was then plastered with cement mortar. In terms of original residential architecture, it is known [21] that the floor structure of the *Rumah Sombalatu* is in the form of hardened soil without being covered with cast cement. Then the treatment of how to process the floor at the *Rumah Gaba-Gaba* at the beginning of its construction also has similarities to its origin. However, it is known that is also inhabited by people on Kei Besar Island and also on Tanimbar Kei Island. The original residential architecture there, namely *Rumah Rahan Teli*, has a different floor structure, namely from wood planks, this is different from what happened in the *Rumah Gaba-Gaba* in Merauke Old Town. As for the floor of the house, the tendency is to follow what happened in the architecture of *Rumah Sombalatu*.

At the bottom of each door of the *Rumah Gaba-Gaba* in the Old Town of Merauke, it is also found that there is a wooden bar that is installed sleeping on every room boundary, especially under the door of the house. This concept of thought can also be found in the original architecture, namely the *Rumah Sombalatu*. These horizontal pillars add to the rigidity of the wall structure of the house, which we can observe in a rigid system like this in the *Rumah Kancingan* in Merauke. Explained that *Rumah Kancingan* is a semi-permanent house which is generally located in the city of Merauke with the main structure used is wood although the walls use bricks [24].

3.3 Wall and Column Elements

The walls of the *Rumah Gaba-Gaba* have changed into a masonry wall. The reason for this change is the unavailability of natural *gaba-gaba* material in urban areas which is related to the scarcity of sago plants in urban areas. In addition to the

reasons above, it was found that this *gaba-gaba* construction system when it began to be fragile was very easy to break or damage, thus creating a feeling of worry over criminal activities if the walls of the house were left with rotting *gaba-gaba*. Homeowners change the *gaba-gaba* wall is at the *Rumah Kancingan* which is more easily weathered than the top side of the house. There is a view that the aesthetics of the *gaba-gaba* house are more attractive so that even though they change to masonry walls, the homeowners still maintain certain parts of the walls of the house with the material still *gaba-gaba*.

This *gaba-gaba* wall is also found in the original Merauke house, which is a residence owned by the Marind Anim community. The process of maintaining the *gaba-gaba* wall is a form of harmonization for local houses that have existed previously in Merauke, namely houses belonging to the Marind Anim community.

When the people of Merauke changed the wall structure system from *gaba-gaba* to masonry walls, the main structural system of the house, namely the wooden frame structure, was not changed. Likewise, the roof structure and also the layout of the house plan. So, this change is a practical wall that has the function of a house envelope. When changing pairs of walls, the house remains intact. The people of Merauke then called the *Rumah Gaba-Gaba*, whose walls had been renovated, to be the *Rumah Kancingan*.

In terms of variations and creativity carried out on the walls of the house, there is a change in the walls of the house into ventilation (as seen in Fig. 3). This process is carried out after the house is built, namely in the area behind the house, namely in the kitchen to drain the smoke produced from women's domestic activities, namely cooking. This shows that the *gaba-gaba* wall opens up various creative opportunities after the wall is applied. Various architectural tectonic variations then occur after the walls are applied and after the house is used.



Fig. 3 Variation of ventilation in the walls of *Rumah Gaba-Gaba* in Merauke

The shape of the ventilation has an affinity with that found in the *Rumah Sombalatu* and also with the Dutch colonial heritage church style in Papua in other areas, namely in Wasior. The shape of the motif is like a rhombus [21, 25] there are also oblique variations in the placement of the list on the window of the house. The ventilation of the house has also been influenced by the Dutch colonial, namely the use of ramp has wire with a rectangular box-shaped frame. The shape of the window of the house with the main geometry of the box / rectangle is maintained from the original. On the windows of the house, there is a series of vertical lists to protect the windows of the house, which are patterned as found in the *Rahan Teli*. The shape of the main door of the house is entirely in the form of a board with the basic shape of a rectangular box that is opened with two doors. The location of the door is symmetrical in the middle of the house. This is more influenced by colonial architecture, because in the original architecture the location of the main door of the house is not exactly in the middle of the house. In colonial-era residential architecture in Merauke, for example, the Merauke Lepro House, known to have a symmetrical position of doors and windows [26].

3.4 Roof Elements

The proportion of roof height on the house of Tanimbar Kei is quite tall but in the case of *Rumah Gaba-Gaba* the proportion of roof height changes. In Dutch colonial heritage houses in Papua, the roof of the house is also a gable roof with a short proportion of roof height [26, 27]. This context factor affects the adaptation of the proportion of the roof height of the *Rumah Gaba-Gaba* in Merauke as well as the removal of additional roofs on the left and right sides of the house.

The *Rumah Gaba-Gaba* in Merauke was originally also made of sago leaf material (such as the *Rahan Teli* and the Marind Anim Tribal House) but underwent renovations to make zinc material. This is because it has been difficult to obtain material from sago plants. The frame structure of the *Rumah Gaba-Gaba* in Merauke Old Town is still the same since the beginning of the house being built, what has changed is the structure of the roof covering.

4 Conclusions

The process of foundation, floor, wall, and roof transformation in *Rumah Gaba-Gaba* is influenced by the adaptation process from the original house in Moluccas which adapts to the influence factors. The process of transforming architectural elements in the *Rumah Gaba-Gaba* in Merauke Old Town underwent adaptation due to influencing factors, including: the colonial style of residential houses in Papua, the architectural form of the Marind Anim Tribe, and the availability of natural materials in Merauke.

The process of wall transformation in *Rumah Gaba-Gaba* is then grouped into several typologies. These typologies include: (1) *gaba-gaba* walls are maintained, (2) *gaba-gaba* walls become Rumah Kancingan, (3) *gaba-gaba* walls become ventilation openings, (4) *gaba-gaba* walls become boards, and (5) board walls are maintained.

Acknowledgements The Indonesian Education Fund Management Institute (LPDP-Indonesia) which has funded, field assistants in data collection Moh. Iqbal Fauzi, Sukayo, and Fransiskus Eko P. Kumuni, to the research sources: Mr. Pius Weliken, Mrs. Fanny Hematang, Leftungun Family, Tatipikalawan Family, Mr. Lexi Letsoin, Mr. Maryono, Father Yerem from Merauke Cathedral Church, secretariat employees of the Merauke Cathedral Diocese, employees at Radio Republik Indonesia (RRI) Merauke Regency. The author also thanks Mrs. Rini Maryone, a researcher at the Papua Archeology Center.

References

1. Lozanovska M (2019) *Migrant housing: architecture, dwelling, migration*. Routledge Taylor & Francis Group, London and New York
2. Abdon D (2021) *Sheltering refugees: ephemeral architecture and mass migration in early modern Venice*. *Urban Hist* 1–21. <https://doi.org/10.1017/S0963926821000444>
3. Rosiana N, Soblia HT, Prabawa PD, Firdaus PI (2020) *Migrant profile result of socio-economics national survey 2019*, Jakarta
4. Subroto TYW, Malangyudo AS (2014) The continuity of binary diametric space of Balinese house in Yogyakarta, Indonesia, City. *Cult Soc* 5(1):33–42. <https://doi.org/10.1016/j.ccs.2014.02.001>
5. dan T Kerja SSMP (2016) *Statistics of Migration Papua*, Jakarta
6. Upton S (2009) *The impact of migration on the people of Papua, Indonesia: a historical demographic analysis*, University of New South Wales
7. Usman S, Din I (2010) *Pasang Surut Sejarah Papua dalam Pangkuan Ibu Pertiwi*. Planet Buku, Yogyakarta
8. Kesselbrenner G (2003) *Irian Barat Wilayah Tak Terpisahkan Dari Indonesia*. TePLOK PRESS dan IJCC, Jakarta
9. Frank SAK, Nurmaningtyas AR, Lewakabessy B, Balingga N, Homba-Homba A (2012) *Kajian Arsitektur Tradisional Suku Arfak Manokwari*. Balai Pelestarian Nilai Budaya Papua Universitas Cenderawasih, Jayapura
10. Handoko W (2007) *Asal-Usul Masyarakat Maluku, Budaya dan Persebarannya: Kajian Arkeologi dan Mitologi*. *Kapata Arkeol.* 3(November):1–27. <https://doi.org/10.24832/kapata.v3i5.66>
11. Muller K (2008) *Introducing Papua*. Daisy World Books, Indonesia
12. Keuskupan Agung M (1999) *Sejarah Gereja Katolik di Irian Selatan: Menghantarkan Suku-Suku Irian kepada Kristus*. Keuskupan Agung Merauke, Merauke
13. Samkakai TE et al (2000) *Penyajian Data Dari Seksi Sejarah Panitia HUT Kota Merauke Ke-100 Tentang Tanggal HUT Kota Merauke*
14. Hematang YIP, Alahudin M, Susanti DS (2021) *Kajian rumah gaba-gaba (rumah material dinding dari pelepah sagu) di perkotaan merauke: sambungan dinding, potensi, dan tantangan pelestarian*. *J Arsit NALARs* 21(1):35–44
15. Djubiantono T et al (2005) *Laporan Hasil Penelitian Arkeologi : Survei Kehidupan Sosial Budaya di Wilayah Kediaman Suku Marind-Anim di Kabupaten Merauke, Jayapura*
16. Muller K (2011) *Pesisir Selatan Papua*. DW Books, Indonesia
17. Esri, “Peta Geoportat Badan Pusat Statistik,” (2022). Retrieved from <https://geoportal.bps.go.id/maps/home/webmap/viewer.html?useExisting=1>. Accessed on Oct 13, 2022

18. Unwin S (2014) *Analysing architecture* fourth edition. Routledge Taylor & Francis Group, London and New York
19. Antoniadis AC (1992) *Poetics of architecture: theory of design*. John Wiley & Sons Inc., Canada
20. Oliver P (2006) *Built to meet needs cultural issues in vernacular architecture*. Elsevier Ltd., Oxford. <https://doi.org/10.4324/9780080476308-22>
21. Juwita R et al. (2020) *Tipologi Arsitektur Indonesia Timur: Sulawesi-Maluku-Papua*. Kementerian Pekerjaan Umum dan Perumahan Rakyat, Makassar
22. dkk Kaloeti PP (2020) *Perjalanan Arsitektural Tanimbar Kei*. CV. Al-Hikmah Jaya Pratama, Makassar
23. Octavia S, Raubaba HS, Hematang YIP, Topan A (2018) The Feasibility of the Kancingan House Structure in Merauke City. In: *Atlantis highlights in engineering (AHE)*, vol 1, no ICST, pp 421–425. <https://doi.org/10.2991/icst-18.2018.88>
24. Topan A, Octavia S, Soleman H (2018) Analysis of the semi-permanent house in Merauke city in terms of aesthetic value in architecture. *J Phys Conf Ser* 1025(1). <https://doi.org/10.1088/1742-6596/1025/1/012021>
25. Tolla M (2018) Ornament on Zending Architecture in Roon and Wasior Islands, Wondama Bay, West Papua. *Kalpataru* 27(2):117–129. <https://doi.org/10.24832/kpt.v27i2.456>
26. Hematang YIP, Sarina P (2017) *Tipologi Bangunan Bersejarah Rumah Lepro Merauke*. *Mustek Anim Ha* 6(3):262–274
27. Sukandar SC (2012) *Tinggalan Kolonial di Pulau Doom*. *Papua* 4(1):29–41. Retrived from <https://jurnalrkeologipapua.kemdikbud.go.id/index.php/jpap/article/view/74>

Research on the Reconstruction Strategy of Historic Districts Under the Background of Carbon Neutrality—Taking Qinzhou Historic Districts in Guangxi as an Example



Chuwei Ban and Fuqiang Li

Abstract With the change of urban development mode and the continuous improvement of people's living standards, the renovation and transformation of historical blocks is imperative for a city. The transformation process under the background of carbon neutrality should pay more attention to the concept of green, ecology and low carbon, while avoid blind and excessive transformation. Taking Qinzhou historic district as an example, this paper puts forward six transformation strategies, including overall planning, energy consumption reduction, micro-transformation, lighting transformation, traffic system transformation and tourism value development, based on the background of "Carbon Neutrality" and the three principles of 'integrity, applicability and economy', which provides a reference for the transformation of old blocks under the new situation.

Keywords Carbon neutrality · Historic district · Climate adaptability · Renovation strategy

1 Introduction

In recent years, under the background of increasing urban scale and environmental pressure, in order to successfully achieve the goal of carbon neutralization, urban development is undergoing a huge reform of green, low carbon, energy saving and consumption reduction. The development mode of cities is gradually changing from incremental development to destocking development. The renewal and transformation of old urban areas or historical blocks has received more and more attention.

C. Ban

Beibu Gulf University, Guangxi Zhuang Autonomous Region, Qinzhou, China

F. Li (✉)

Jiangsu University, Zhenjiang, Jiangsu Province, China

e-mail: lifq1987@163.com

In the transformation of historical blocks in the past, some places have experienced chaos such as excessive commercialization, disrespect for history and culture, and lack of environmental awareness, and even turned the historical blocks into a 'newly old street' full of copper odor.

Under the 'double carbon' target background, it is imperative how to integrate new development concept of green, low-carbon, intelligent, livable in urban reconstruction. There are many research results and specific practice from domestic and foreign scholars. Newman studied the green transformation strategy of urban blocks from a single or multiple spatial fields [1]. KP Klo explained the process and measures of German historical building protection, taking the protection of historical building areas in Stadtnulon and Steblischer as an example [2]. Engel et al. took the pre-war urban areas of the Netherlands as an example to study the urban transformation and renewal strategies in terms of economic activities, infrastructure and public space design. Domestically, the research on the green transformation of old blocks and buildings has gradually increased [3]. Cui Jianfeng et al. put forward an effective green transformation strategy for block buildings by strengthening space utilization, building material reuse, function optimization, etc., taking the historical and cultural block of Daci Temple in Chengdu as an example [4]. Li Qin studied the evaluation of green transformation of old blocks, and established the evaluation system of green reconstruction value of old blocks, which provided a strong reference for solving the problems of resource waste, low environmental protection and non-compliance with green development requirements in the process of reconstruction of old blocks [5]. Hu Xianjun of South China University of Technology systematically studied the spatial micro-transformation strategy of the old city blocks in Lingnan area from the perspective of improving the microclimate of the blocks, and constructed the spatial micro-transformation strategy of the old city blocks in Lingnan based on climate adaptability [6]. Taking a community in Chizhou as an example, Shu Ping and Xu Lei et al. studied the specific application of sponge city scheme in the process of old residential area transformation, and put forward specific implementation suggestions for the economical utilization of urban water resources [7].

To sum up, many factors such as livability, tourism, business, ecology, culture, history, etc. should be comprehensively considered for the reconstruction of blocks, especially historical and cultural blocks. Under the premise of green and low-carbon, this reconstruction can not only retain urban heritage, but also help economic development. This paper takes Qinzhou historic district in Guangxi as an example, analyzes its reconstruction status, and puts forward strategies and suggestions for further optimization and transformation. The results with a view to providing useful guidance and support for the transformation of Qinzhou traditional arcade blocks, as well as the similar type of historical blocks in Guangdong, Guangxi, and so on.

2 Qinzhou Historical District and Transformation Status

Qinzhou historical district, commonly known as Qinzhou Old Street, was built in the Song Dynasty, total area about 0.28 square kilometers. The existing historical buildings are mainly composed of vertical Zhan'ao Alley, Zhongshan Road, Bangui Street and horizontal Yima road, Erma road, Sanma Road and interlaced street network, as shown in Fig. 1.

At present, the traffic connection between the old street and the main urban area is weak, and there is no coach and tourist guide, so it is difficult for tourists to arrival directly. The road inside the block is narrow and not systematic. The width of the main road surface is 4–10 m, and the remaining streets and lanes are about 2 m wide. Parking lots are not enough for vehicles, which can easily cause traffic congestion.

The local government has carried out a series of renovation and upgrading of the old streets in recent years, including road network laying, house reinforcement, and repair of the former residence of celebrities. The appearance of Yima Road, Zhongshan Road, Zhan'ao Alley and Su Tingyou 's former residence have been greatly improved, which has played a certain role in improving the living quality of the masses and developing the historical and cultural value of the blocks, as shown in Fig. 2. However, the current transformation projects of the old street focused on the surface update, lacking of long-term, holistic considerations. Furthermore, the present transformation has not given full consideration to the ecological environment and block climate adaptability, and the reformation didn't stimulate the local tourism obviously.

3 Suggestions on Reconstruction Strategy of Qinzhou Historic District

In the process of historic district reconstruction, we should follow three principles: integrity, applicability and economy [8]. In terms of integrity, block transformation includes levels of block (road traffic planning, municipal facilities, block greening, etc.) and building (scale, shape, material, etc.). It is necessary to consider local climate characteristics, block use, etc. Only by systematically planning, the transformation goals can be achieved. In terms of applicability, the transformation should be combined with the climate and environmental characteristics of the block, including the building shape, layout, natural ventilation, orientation, lighting and structural maintenance and so on. As to economic principles, considering that the block renovation is a long-term project with high investment and slow effect, the input–output ratios should be emphasized to avoiding excessive waste of resources.

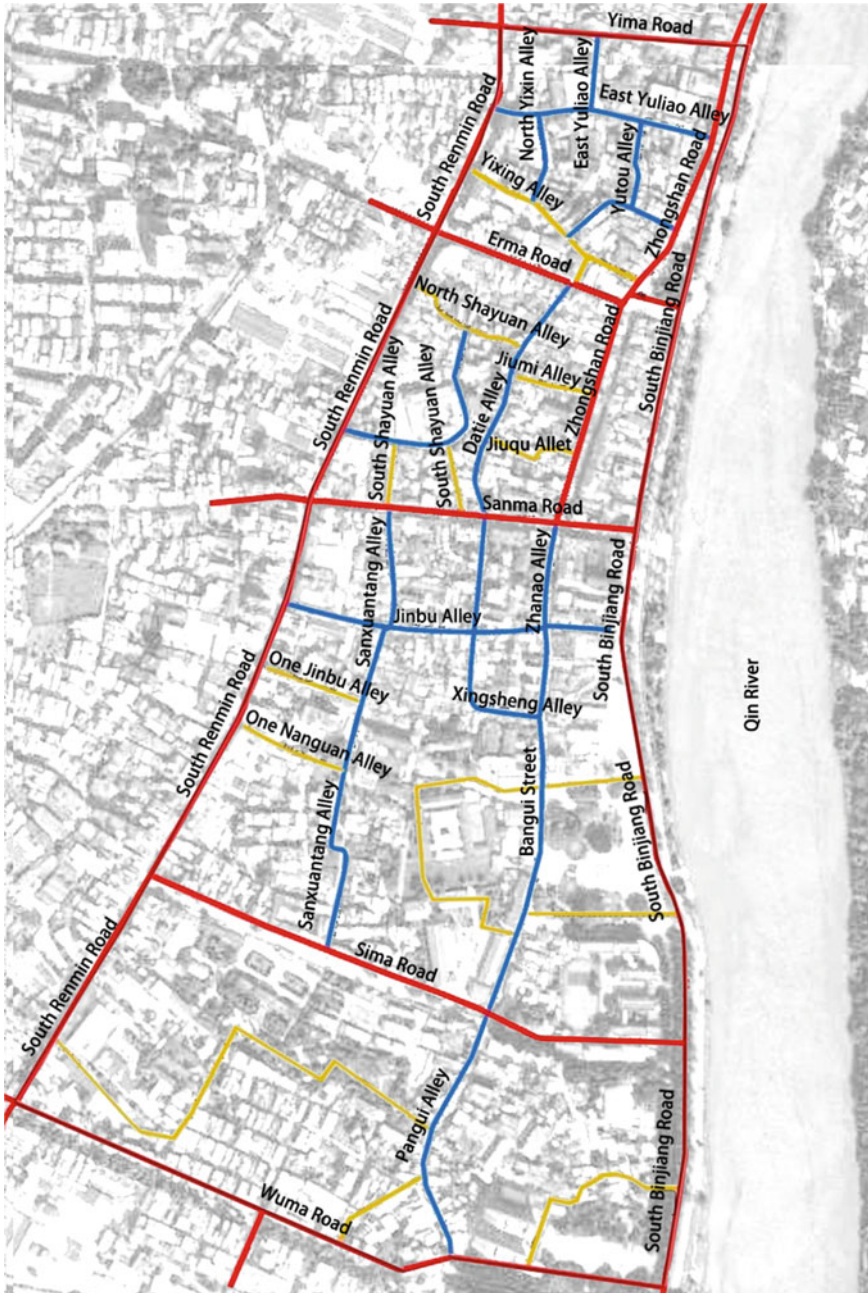


Fig. 1 The regional schematic diagram of Qinzhou historic district



Fig. 2 Comparison of block appearance before and after reconstruction of Qinzhou old street

3.1 Overall Planning Strategy

As a response to the principle of integrity mentioned above, this paper proposed an overall criterion of ‘one path and four belt’ relying on the area riverside advantages, which can revitalize the old street.

Riverside green walking path along South Binjiang Road, which can provide fitness sites, leisure fishing, square entertainment, boating and children’s entertainment district.

Traditional arcade style and feature belt along Zhongshan Road which is planned as a commercial and cultural pedestrian street. Stores of local industrial arts and traditional local featured delicious food can be proposed for displaying and selling.

Cultural industry belt along Sanma Road, which provides necessary venues for projects such as incubation of cultural and creative emerging industries, research and development of cultural media technology and so on. At the same time, modern catering such as creative coffee and fashionable restaurants can be planned.

Folk culture experience belt along Bangui Street, which offers chance of visit and participation to experience Nixing pottery product fabrication and Cantonese opera. Public welfare lectures and training can be hold as well.

Boutique homestay belt along Zhan’ao Alley, which can create a street of Boutique Homestay with Lingnan style, offering family-style hotels, farmhouses and other projects, so that travelers can truly experience the characteristics of local traditional living style.

3.2 *Energy Consumption Reduction Strategy*

On the spatial pattern Qinzhou old street has preserved complete arcade block buildings, forming a longitudinal bamboo tube combination. According to research result [9], the overall layout and architectural mode of traditional arcade blocks have significant advantages over modern cities in terms of climate adaptability such as ventilation and heat dissipation, showing adaptability to southern coastal climate such as Guangdong, Guangxi and Hainan. In the process of transformation, the climate adaptability characteristics of the arcade block should be fully utilized. The urban heat island effect can be effectively alleviated and the urban energy consumption reduced.

On the conceptual guidance. The lifestyle of green and low-carbon should be advocated, such as walking or using of bicycles when going out, reducing energy consumption and environmental pollution.

3.3 *Micro—Transformation Strategy of Block Building*

In the process of renovation, the internal space of the house should be functionally updated and repaired for most of the residential buildings in the block have problems such as poor safety, poor environmental conditions, and inadaptability to modern life requirements. But the reparation should avoid large-scale demolition and construction, reducing the impact to the original lifestyle of the surrounding residents. Small-scale and gradual ‘micro-renewal’ should be adopted.

Aiming at different building functions, different repair methods can be applied such as ‘demolition-repair-mending-decoration’. ‘demolition’ refers to demolishing some buildings that are inconsistent with the style of the block, ‘repair’ means repairing damaged old buildings with old style materials and traditional techniques, ‘mending’ means restoring part of the old building and filling in the blanks, connecting the whole, ‘decoration’ refers to burying all kinds of wires and pipelines, and decorating modern facilities such as air conditioning.

3.4 *Lighting Transformation Strategy*

Lighting projects should be conducted to the old street and both sides of Qin River, combined with cultural characteristics, spatial patterns and human behavior, which can create a hierarchical lighting night block. Analyzing comprehensively from entrance point of view, the long-term point of view and the pedestrian tour point of view, intelligent lighting system can be installed to control the brightness, color and time of the lighting system, creating a historical atmosphere and theme artistic conception while taking care of the actual living needs of local residents.

Nightscape atmosphere lighting color construction. The main landscape lighting belt is arranged along Zhongshan Road- Guangzhou Hall- Yongfu Cultural Square, with warm yellow as the main color. Some commercial streets are appropriately decorated with ' Chinese red ' to highlight the business atmosphere. The forest lighting on both sides of Qin River is mainly green to create a lively atmosphere.

Important historical building nodes Former residences of historical celebrities such as Liu Yongfu, Su Tingyou, Huang Wenlan, etc. have unique and important value of both culture and tourism. The lighting effect should create different sceneries by excavating the details of the buildings one by one, to show the beautiful details of the building.

Hiddenness and demonstration of the lamp shape. The lamps related to the building node such as lamp bands and contour lights can be concealed in the daytime to achieve the effect of 'seeing light but not lamps'. The lamps along the roads or around the squares can be revealed as embellishment, combined with the traditional elements of the old street for artistic expression.

3.5 Traffic System Transformation Strategy

Three priorities of historic district protecting, slow traffic and traffic order should be reflected in traffic network reconstruction. The internal traffic of the block can be organized by one-way traffic style under the premise of block's texture protecting, traffic congestion easing and full use of the surrounding bus stations. Main road such as Zhongshan Road, Renmin Road can be set as a single-lane motor way, while other narrow alleys can be planned as pedestrian way. The tour bus line connected to the outside is opened to facilitate the direct access for tourists to the block.

In modern society, the parking demand of local residents and tourists is increasing. To overcome the current situation of land shortage in the old street, the empty space left by the demolition of dilapidated houses can be made full use of to establish point-like parking lots, and mechanical three-dimensional parking lots.

3.6 Tourism Value Development Strategy

Certain commercial development can not only create cash flow for block protection, but also provide catering, rest, souvenir purchase and other services for citizens and tourists, which is essential in block reconstruction.

Creating hierarchical tourist routes According to the existing characteristic historical buildings, hierarchical tour routes can be formulated for different tour duration. Three tourist routes are formulated, including one-hour sightseeing, three-hour sightseeing, and all-day residential tourism. The tour route is connected in series with cultural landmarks such as public welfare lectures, local theaters, and museums.

The advanced concept of interaction, allowing viewers to participate in the history and present of the old street, and realizing the real revitalization of the block.

Focusing on cultural heritage and development It is suggested to set up a cultural and artistic center, transform part of the arcade space and street corner green space into a small theatre, and perform classic local plays of 'tea picking' and 'Cantonese opera' to meet the daily cultural demand for the surrounding people. Brand activity of 'Qinzhou Culture and Art Week in Arcade' can be launched regularly, inviting domestic and foreign troupes to perform, so as to display local plays and Nixing pottery techniques, and enhance the radiation and influence of Qinzhou culture.

Developing smart tourism projects. The reconstruction of old streets should be combined with smart city construction. Modern network communication technology should be fully utilized to develop multimedia map tour, AI characteristic clothing virtual fitting room and other apps to create a smart tourism brand.

4 Conclusion

In the background of global warming and carbon neutrality, the development and renovation of old blocks has become an important issue for every city to restrict the expansion of city size. Taking the transformation of Qinzhou historic district as the breakthrough point, this paper puts forward the transformation strategy in six aspects of overall planning, energy consumption reduction, micro-transformation, lighting transformation, traffic system transformation and tourism value development, under the guidance of the three principles of 'integrity, applicability and economy'. The proposed reconstruction strategy takes Qinzhou historical block as an example, but the transformation thought can provide reference for the transformation of historic blocks in Beibu Gulf area and other areas.

Acknowledgements This Project is funded by the Project of Improving Scientific Research Basic Ability of Young and Middle-aged Teachers in Universities of Guangxi (Study on Climate Adaptability of Traditional Arcade Blocks in Beibu Gulf Area under the Background of Carbon Neutralization, 2022KY0427).

References

1. Newman P, Kenworthy J (1999) Sustainability and cities: overcoming automobile dependence[J]. *Landsc Urban Plan* 44(4):219–226
2. Klo KP (2004) City-renewal and conservation of monumental buildings in historic city-centers—the transformation process of the cities in eastern Germany after the reunification in 1990 at the example of Brandenburg[J]. *Architectural J*
3. Engel H, Velzen EV, Van D (2013) Renewing city renewal: a call for strong design[J]. *Trancity Valiz*

4. Jianfeng C, Le F, Yanyu W et al (2019) Measures and key points of green renovation of historical and cultural block—a case study of Daci temple historical and cultural block in Chengdu [J]. *Sichuan Architect* (2):30–32,34
5. Qin L, Xiaonan G. Study on green reconstruction value estimation of old neighborhoods under the background of urban renewal—a case of Chuangye coffee block in Xi'an[J]. *Urban Architect* 393(18):24–28
6. Xianjun H (2019) The design strategies research on spatial micro-renovation of Lingnan old city district based on climate response[D]. South China University of Technology
7. Ping S, Lei X, Ping Z (2018) Sponge rebuilding of existing residential area based on simulation optimization[J]. *Energy Conserv* 46(7):83–86,107
8. Yan Y (2021) Research on planning and design strategy of green reconstruction of urban block[J]. *Resident Technol* 41(5):33–41
9. Shi Y (2019) Research on climate adaptation of traditional neighborhoods morphology in hot-humid climate [D]. South China University of Technology

Identifying the Influencing Factors for the Walkability of Business Streets Based on Urban Multi-source Data



Chendi Yang , Siu Ming Lo , and Rui Ma 

Abstract Walkability tends to be crucial to the brick-and-mortar store in the current context. This study aims to identify the potential influencing factors of the business street, and reveal the multivariate causal relationship between street attributes and walking behavior. To explore such associations, we employed a structural equation model (SEM) to explain the links of multiple latent constructs and their observable indicators based on urban multi-source data and image segmentation techniques. The result revealed that Spatial Form, Street Facility, Retail Mix and Accessibility, these variables of the built environment, have a significant influence on pedestrians' walking behavior in the business street. People prefer the wider street with shade from buildings on both sides rather than trees when shopping, which is unlike some previous studies at the community level. Moreover, convenient facilities for the subway and cars are more important to local customers compared with the bus.

Keywords Built environment · Street quality · Walking behavior · Business street · Structural equation modeling

1 Introduction

1.1 Importance of Walkability to Business Environment

The traditional commercial area tends to be the core area of a city, which plays a central role in the political, economic, cultural and living functions of urban development. The growth of online shopping has put massive pressure on traditional brick-and-mortar retail for the past few years, and it has been especially true since the wake of COVID-19 [1]. A walkable business street deserves a higher rent because of its greater probability of capturing potential customers walking in shopping areas

C. Yang (✉) · S. M. Lo · R. Ma
City University of Hong Kong, Hong Kong, China
e-mail: chendyang2-c@my.cityu.edu.hk

© The Author(s), under exclusive license to Springer Nature Singapore Pte Ltd. 2024
M. Casini (ed.), *Proceedings of the 3rd International Civil Engineering and Architecture Conference*, Lecture Notes in Civil Engineering 389,
https://doi.org/10.1007/978-981-99-6368-3_67

for more revenue [2]. For this reason, a pleasant walking and shopping experience in the street is particularly important in terms of attracting pedestrians.

The business streets with the hustle and bustle of shoppers usually accompany many aspects of features, specifically, good locations, high-quality design and convenient transportation [3]. First, the location is often related to spatial configuration based on topology theory, as well as those characterized by easy-to-find (e.g., located in the intersection) [4]. Second, the streets with humanization design and visual aesthetic can be more attractive to shoppers by influencing human perception [5]. This kind of favorable experience partially derives from enough shade of trees and open spaces that provide resting places [6]. Third, customers prefer to go window-shopping in an accessible area with a wide selection of transportation facilities [7]. Shorter distance, fewer crossings and lower car speeds invite pedestrians [8].

1.2 Street Quality Related to Walkability

Some scholars have conducted research in the field of the relationship between street quality and walking behavior. In 1997, researchers proposed that density, diversity and design these three elements can affect people's travel, and it is commonly known as the 'three Ds' [9]. Whereafter, the other two 'D' - destination accessibility and distance to transit were put forward [10]. In the meanwhile, Handy et al. brought up more specific environmental characteristics for streets and suggested that street quality is in connection with connectivity, scale and design of streets, as well as the development intensity and land use on both sides of the street [11]. Ewing et al. depicted such influencing factors using indicators called 'imageability', 'enclosure', 'human scale', 'transparency', and 'complexity' [12].

1.3 Factors Affecting Customer's Experience

The quality of surroundings impacts consumers' experiences while they wander in business streets. Previous studies on customer satisfaction and service quality have illustrated that the physical design, layout, functionality and some environmental features of the space can affect customers' mood and desire [13, 14]. This leads to people being willing to spend more time there, and therefore more money [15]. Specifically, the atmosphere significantly impacts retail attractiveness [16]. Some factors associated with transport, like parking conditions and accessibility, occasionally affect customers' satisfaction [17]. In addition, physical design can bring a visual impact that influences the perception of ambience, thus serving as a reference for customers to evaluate the overall service [18].

1.4 Research Gaps and Objectives

To uncover the associations between the built environment and pedestrian walking behavior, researchers have mainly studied the following two areas: consumer satisfaction with store's physical attributes based on preference surveys and environmental components effects based on measuring. The explorations of the first field only concentrate on customers' subjective feelings about some of the store settings, the potential connection between them is usually revealed through the stated preference survey. However, it can only be used to narrowly explain the relation of the shopping experience to some environmental components because of the limitation on satisfaction expression. The studies in the second field pay more attention to the community environment than the commercial one. They attempt to use experimental data to make objective inferences about the environmental factors that attract pedestrians, and yet the walking behavior may differ in these two conditions due to people's diverse travel purposes.

Considering the inadequacy of empirical studies on business streets' influence factors, this study aims to identify the built environmental factors that directly and indirectly impact pedestrians in traditional retail streets taking Hong Kong as an example. We attempt to investigate the multivariate causal relationships for such streets by using multi-source urban data and image segmentation techniques.

2 Methodology

2.1 Study Area

The site is Mong Kok, a typical commercial area in Yau Tsim Mong District, Hong Kong. It is one of the bustling traditional retail districts with a mix of office and residential buildings. It used to be a popular shopping and leisure destination for tourists and residents before the COVID-19 pandemic in 2019. Some of the old buildings along the streets have a variety of retail stores on the ground floor, and several malls are located among them. The core area comprises catering, clothing, beauty, living and office functions. We took the boundary of 500 m around the MTR station — the most representative part of this area (Fig. 1).

2.2 Data and Samples

Further investigation is conducted using data gathered from multiple sources, derived from Hong Kong Geodata, Open Street Map (OSM), Google Maps and Baidu Map. For basic street and building information, we used the digital maps provided by the land and highways department of Hong Kong and OSM. For the location information

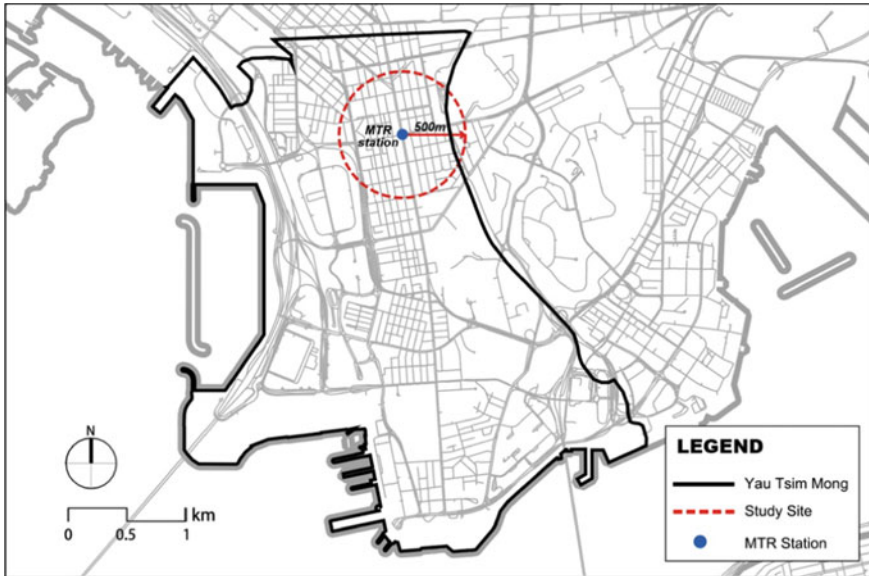


Fig. 1 Study site in Hong Kong

of bus and metro stations, we used the data from the transport department of Hong Kong. The street view image (SVI) and function distribution data were acquired from Google Maps and Baidu Map, and the pedestrian volume data came from SVI.

2.3 Statistical Analysis

We employed a structural equation model (SEM) to infer the direct and indirect environmental factors influencing pedestrian walking behavior in the commercial area. SEM can help identify those variables that are regarded as existing but hard to be observed. They are called latent variables, which need to be measured by some observable indicators. For this reason, it is widely used to reveal the potential relationships between people’s perception and satisfaction in the field of business marketing and real estate [19, 20]. SEM contains two parts: the structural model, which verifies the relations of endogenous and exogenous variables, and the measurement model, which shows the relationships among these variables and their observable indicators.

2.4 Endogenous and Exogenous Variables

In this study, our endogenous variable is pedestrians' Walking Behavior represented by instantaneous and cumulative pedestrian volume in each business street segment. The pedestrian volume indicates the possibility that passersby are appealed by the street or willing to choose the route, therefore it is suitable for measuring walking behavior. Our exogenous variables can be divided into four categories. We hypothesized that the following variables are able to influence people walking behavior in business streets: Spatial Form, Street Facility, Retail Mix, and Accessibility. They depict the built environment from multiple angles.

2.5 Latent Variables and Observable Indicators

The latent variables were measured by their observable indicators. First, for Spatial Form, we considered the indicators: street width, street length, building height, D/H ratio (the ratio of street depth to building height), street density and street enclosure. Second, Street Facility related to business streets includes border trees, buildings and street signboards extracted by semantic segmentation method via pre-trained PSPNet model [21] shown in Fig. 2a, as well as the street lamps, bus station, MTR station, charging station, gas station and parking lot that come from Hong Kong Geodata. Third, Retail Mix means the heterogeneity of stores, represented by the number of malls, restaurants, café, clothes stores, and cosmetics stores and the retail diversity index shown in Eq. (1). We gathered the point of interest (POI) data within fifty meters of each street to show the number of different types of retail.

$$\text{Retail diversity index} = - \sum_{i=1}^S (p_i \times \ln p_i) \quad (1)$$

where S represents the total number of retail categories, p_i is the proportion of the i th retail type to the total.

Fourth, Accessibility concerns road networks, including betweenness and closeness calculated according to space syntax theory. Betweenness is the possibility that a street is selected as the potential shortest path. Closeness refers to the difficulty from one street to all the other streets within a certain radius.

In addition, the Walking Behavior is proxied by instantaneous and cumulative pedestrian volume in each segment of business streets. The cumulative volume is the total number of people passing the street segment in a given period of time obtained from a field survey, indicating the possibility of passersby entering stores in the street. The instantaneous volume is the number of people that stay in the street at a given moment, implying the attraction of streets that capture potential customers to stay. The number of pedestrians is extracted from SVI by using the instance segmentation method. The method, applying google SVI for pedestrian counts via image detection,

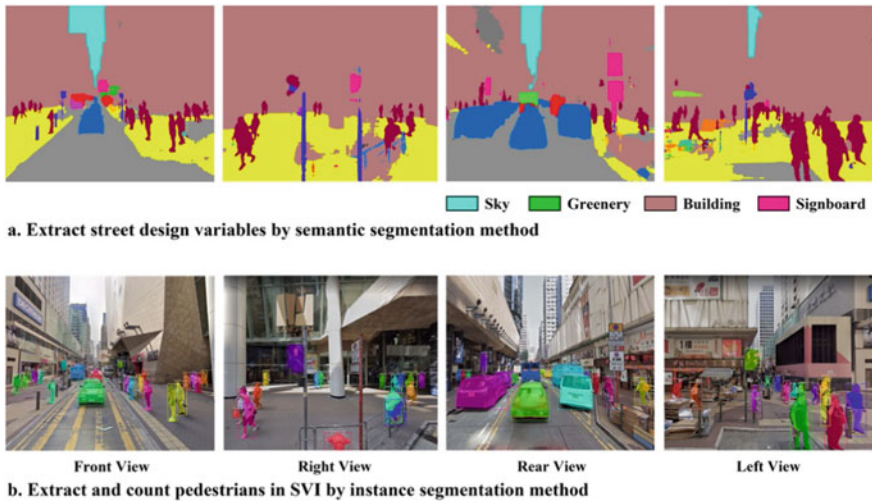


Fig. 2 Observable indicator extraction using image segmentation method

was verified to be feasible and reliable with the value of Cronbach's alpha higher than 0.70 [22]. In this study, we chose the pre-trained model based on Mask R-CNN framework [23], and Fig. 2b shows the result of image segmentation.

3 Results

3.1 Measurement Model Test

We eliminated the indicator that lacked reliability after conducting the estimation test for all indicators of the measurement model (Table 1). As a result, the indicator "street length" and "closeness" were excluded according to the process of the check. Then we tested the validity of the remaining indicators, and it showed a practicable result: KMO (Kaiser–Meyer–Olkin Measure of Sampling Adequacy) = 0.559, χ^2 (df, p) = 743.775 (253, <0.001).

3.2 Analytical Result

The analytical results of the relationships among constructs in SEM are shown in Table 2, and the importance of each construct is shown in Fig. 3. For the relationship between endogenous and exogenous variables, the latent constructs of the built environment (Spatial Form, Street Facility, Retail Mix and Accessibility) are statistically

Table 1 Reliability test of the measurement model

Variable	Indicator	CITC	Cronbach's α
Spatial form	Building height	0.083	0.631
	Street width	0.752	
	D/H	0.162	
	Enclosure	0.416	
	Density	0.618	
Street facility	Border tree	0.057	0.630
	Signboard	0.195	
	Street lamp	0.174	
	Bus station	0.380	
	MTR station	0.380	
	Charging station	0.663	
	Gas station	0.772	
	Parking lot	0.616	
Retail mix	Mall	0.493	0.834
	Cosmetics	0.365	
	Clothes	0.790	
	Café	0.856	
	Restaurant	0.715	
	Diversity	0.138	
Accessibility	Betweenness	–	–
Walking behavior	Instantaneous volume	0.559	0.717
	Cumulative volume	0.559	

significant at a 5% level to pedestrian Walking Behavior. These four variables are confirmed to have an influence on people’s choices when walking in business streets. Among them, Spatial Form, Retail Mix and Accessibility all have positive impacts on Walking Behavior, while Street Facility shows a contrary impact. It indicates pedestrians prefer to choose streets with good spatial form, mixed retail type, high accessibility and fewer street facility.

When it comes to the association between latent variables and observable indicators, the results present some differences compared to our hypothesis. In Spatial Form, all of the indicators have statistically significant positive effects at a 5% level. Street density has the most impact on walking activities, which means people prefer to hang out where the streets are more concentrated. Moreover, street width and D/H ratio suggest that they prefer wide spaces rather than those that bring a sense of narrowness. However, the coefficient of the enclosure is positive, implying that the more covered streets are more attractive for pedestrians due to providing shade in strong sunshine.

Table 2 Analysis of the relationships among constructs

Exogenous and endogenous variables			Unstandardized Coef.	<i>p</i>
Spatial form	→	Walking behavior	0.397	***
Street facility	→	Walking behavior	-1.002	***
Retail mix	→	Walking behavior	120.265	***
Accessibility	→	Walking behavior	0.105	**
<i>Variables and indicators</i>				
Spatial form	→	Density	3.983	**
Spatial form	→	Enclosure	1.720	***
Spatial form	→	D/H	1.189	**
Spatial form	→	Street width	2.284	***
Spatial form	→	Building height	1	-
Street facility	→	Parking lot	-0.203	0.760
Street facility	→	Gas station	1.703	**
Street facility	→	Charging station	0.563	**
Street facility	→	MTR station	3.236	***
Street facility	→	Bus station	-5.208	***
Street facility	→	Street lamp	-2.498	***
Street facility	→	Signboard	-0.073	0.910
Street facility	→	Border tree	1	-
Retail mix	→	Restaurant	240.894	***
Retail mix	→	Café	289.238	*
Retail mix	→	Clothes	266.637	***
Retail mix	→	Cosmetics	90.030	0.780
Retail mix	→	Mall	142.094	***
Retail mix	→	Diversity	1	-
Accessibility	→	Betweenness	1	-
Walking behavior	→	Cumulative volume	0.871	***
Walking behavior	→	Instantaneous volume	1	-

Note * $p < 0.1$, ** $p < 0.05$, *** $p < 0.01$

In Street Facility, indicators except for street signboard and parking lot are statistically significant at a 5% level. The coefficient of border tree and street lamp are contrary, suggesting that pedestrians prefer to walk in the streets with more lamps and fewer trees. For basic facilities, greater distance to MTR station, charging station and gas station has a negative effect, while bus station has a contrary result, meaning locals are used to going shopping by subway or private cars. According to the standardized coefficient, facilities for the subway play a more vital role than those for cars.

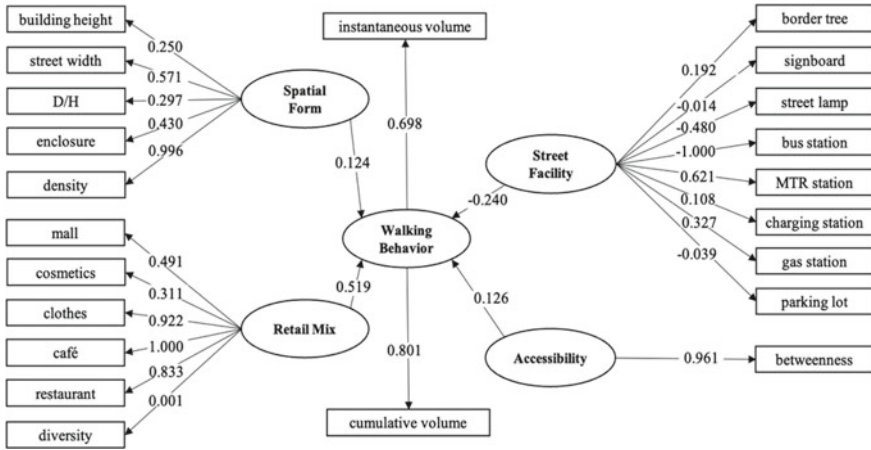


Fig. 3 The importance of each construct in SEM

In Retail Mix, only mall, clothes store and restaurant have a statistically significant positive relationship at a 5% level. Among them, the standardized coefficient of clothes and restaurant are higher than mall, which indicates that pedestrians are more likely to be appealed by these two types of retail.

Finally, in Accessibility, betweenness is a positive indicator with a high coefficient as predicted, reconfirming the importance of centrality in the walkability of the street. This phenomenon also exists in the business district.

4 Conclusion

This research aims to identify the potential factors affecting pedestrian walking behavior in the business street in Hong Kong. For this purpose, we acquired latent variables and observable indicators related to the retail environment via multi-source geodata and image segmentation techniques, and established multivariate causal relationships among them by SEM. Some of our analytical results are consistent with commonly accepted theory. For instance, people like commodious and intensive streets rather than narrow ones; the centrality of the road network has a positive impact on pedestrians’ choices. But beyond that, some findings are contrary to previous studies. People prefer to walk within spaces with towering buildings instead of streets full of trees; they are more concerned about the type of retail, especially the clothes stores and restaurants, other than the richness of stores.

In addition to the above, our research still has some limitations. The street data were only collected from one district, so there is a lack of diversity in the samples. In further studies, we can take into account more business streets from diverse areas to enhance the universality of results. Besides, the visit purpose of people in the street

can also affect their walking behavior and drive them to have various route choices, further consideration is necessary for judging pedestrian purposes.

This study employed new methods and techniques to conduct a quantitative analysis of the associations between people's behavior and the retail environment in business streets, which is based on objective urban data instead of a stated preference survey. Our approach and findings provide a fresh perspective for the revitalization of business streets, and encourage more consideration of the effect of design quality on walkability in urban regeneration.

References

1. Moon J, Choe Y, Song H (2021) Determinants of consumers' online/offline shopping behaviours during the COVID-19 pandemic. *Int J Environ Res Public Health* 18:1593
2. Fuerst F, van de Wetering J (2015) How does environmental efficiency impact on the rents of commercial offices in the UK? *J Prop Res* 32:193–216
3. Saelens BE, Handy SL (2008) Built environment correlates of walking: a review. *Med Sci Sports Exerc* 40:S550
4. Boumezoued S, Bada Y, Bougdah HJIRfSP, Development S (2020) Pedestrian itinerary choice: between multi-sensory, affective and syntactic aspects of the street pattern in the historic quarter of Bejaia, Algeria 8:91–108
5. Tang J, Long Y (2019) Measuring visual quality of street space and its temporal variation: Methodology and its application in the Hutong area in Beijing. *Landsc Urban Plan* 191:103436
6. Speck J (2013) Walkable city: how downtown can save America, one step at a time. Macmillan
7. Southworth M (2005) Designing the walkable city. *J Urban Plan Dev* 131:246–257
8. Schneider RJ (2015) Walk or drive between stores? Designing neighbourhood shopping districts for pedestrian activity. *J Urban Des* 20:212–229
9. Cervero R, Kockelman K (1997) Travel demand and the 3Ds: density, diversity, and design. *Transport Res Part D-Transport Environ* 2:199–219
10. Ewing R, Cervero R (2010) Travel and the built environment. *J Am Plann Assoc* 76:265–294
11. Handy SL, Boarnet MG, Ewing R, Killingsworth RE (2002) How the built environment affects physical activity: views from urban planning. *Am J Prev Med* 23:64–73
12. Ewing R, Handy S, Brownson RC, Clemente O, Winston E (2006) Identifying and measuring urban design qualities related to walkability. *J Phys Act Health* 3:S223–S240
13. Wakefield KL, Baker J (1998) Excitement at the mall: Determinants and effects on shopping response. *J Retail* 74:515–539
14. Baker J, Grewal D, Parasuraman A (1994) The Influence of store environment on quality inferences and store image. *J Acad Mark Sci* 22:328–339
15. Teller C, Reutterer T (2008) The evolving concept of retail attractiveness: what makes retail agglomerations attractive when customers shop at them? *J Retail Consum Serv* 15:127–143
16. Teller C, Elms J (2010) Managing the attractiveness of evolved and created retail agglomeration formats. *Mark Intell Plan* 28:25–45
17. Teller C, Elms JR (2012) Urban place marketing and retail agglomeration customers. *J Mark Manage* 28:546–567
18. De Nisco A, Warnaby G (2013) Shopping in downtown: the effect of urban environment on service quality perception and behavioural intentions. *Int J Retail Distrib Manage*
19. Hui ECM, Zheng X (2010) Measuring customer satisfaction of FM service in housing sector. *Facilities* 28:306–320
20. De Nisco A, Warnaby G (2014) Urban design and tenant variety influences on consumers' emotions and approach behavior. *J Bus Res* 67:211–217

21. Zhao H, Shi J, Qi X, Wang X, Jia J (2017) Pyramid scene parsing network. In: 2017 IEEE conference on computer vision and pattern recognition (CVPR), pp 6230–6239
22. Yin L, Cheng Q, Wang Z, Shao Z (2015) ‘Big data’ for pedestrian volume: exploring the use of Google Street View images for pedestrian counts. *Appl Geogr* 63:337–345
23. He K, Gkioxari G, Dollár P, Girshick R (2017) Mask R-CNN. In: 2017 IEEE international conference on computer vision (ICCV), pp 2980–2988

Drawing the Invisible: Visualizing Patterns of Occupation in Two Streets in Shanghai



Glen Wash Ivanovic  and Shinya Miyazaki

Abstract From the many dynamics and urban planning features encountered in Shanghai, perhaps the two most iconic and recognizable are, on the one hand, the western urbanistic principles of the international settlements, and on the other, the Dan Wei-derived modern gated communities. Their foundations and historical contexts could not be further apart, yet the interaction between them has generated one of the world's most iconic and unique cities. These two approaches have been researched and compared from numerous perspectives, but the patterns of occupations taking place in their public spaces remain overlooked. This research proposes a methodology for mapping information in order to record and compare these patterns of occupations, aiming to understand their differences and similarities better, while also identifying findings that could be incorporated into modern architectural and urban design.

Keywords Information visualization · Digital visualization · Place theory · Patterns of occupation · Social spaces

1 Introduction

The unprecedented urbanisation process in China has reshaped the country at a scale and speed that is impressive, representing a unique opportunity for researching and designing the built environment. In aiming to achieve its goal of 70% of urban population by 2035, China has created some of the newest and most extensive urban areas in history. Nevertheless, despite this significant progress, the urbanisation process has also presented numerous challenges, which can be tackled as opportunities. For instance, it has generated a substantial gap between urban life and rural development.

G. Wash Ivanovic (✉)
Xi'an Jiaotong-Liverpool University, Suzhou, China
e-mail: glen.wash@xjtlu.edu.cn

S. Miyazaki
Fukuoka University, Fukuoka, Japan

© The Author(s), under exclusive license to Springer Nature Singapore Pte Ltd. 2024
M. Casini (ed.), *Proceedings of the 3rd International Civil Engineering and Architecture Conference*, Lecture Notes in Civil Engineering 389,
https://doi.org/10.1007/978-981-99-6368-3_68

The government has also addressed this by implementing different rural revitalisation policies in order to create a more balanced development of the country, enabling unique approaches to rural design [1]. These two dualities (urban and rural) are very easy to identify and compare, resulting in specialized and focalized efforts to address their specific problems. However, it is becoming more and more evident that some of these dramatic gaps can be found not only between villages and cities but also within cities themselves, where co-existing urban fabrics might require radically different, yet integrated approaches to guide their interaction and development. The city of Suzhou is a great example of this, where we can find very modern developments (like Suzhou Industrial Park) located just a few kilometres away from Suzhou's old town, one of the oldest in the world. What makes these two completely different urban fabric parts of the same city? It is easy to assume that, due to the centralised planning of cities, the edges and differentiation between these different urban fabrics are consistently very clear and controlled, but this is not always the case. There are many instances in which different urban fabrics intertwine and interact with each other in ways that are not always evident or entirely planned. One of the unique characteristics of Chinese architecture and planning is using confinement and inward focus to organise and enhance spaces. Traditional courtyard houses, Dan wei units, new workers' villages and modern gated communities: all seem to share, in their own way, an inward vocation to dwelling [2, 3]. This configuration presents both advantages and disadvantages. From the perspective of traffic and connectivity, it is inefficient to have large portions of the city inaccessible for public circulation and traffic. Because of this, the government started to discourage the construction of gated communities, yet this was met with opposition from residents [4]. While this is an ongoing debate involving multiple facets, we wanted to further understand this duality by comparing an open street with a closed one, trying to record and represent the public habitability which they generate. In order to do so, we undertook a case study in two streets Shanghai's former French Concession, testing a methodology for visualising their planning, character and patterns of occupation by residents.

2 Background: Representing Intangible Information

Modern architectural visualization can be used not only for generating images which represent the material features of the built environment, but it can also provide new theoretical and spatial distinctions so we can represent intangible information. Architecture makes use of a wide range of visualization tools for improving or modifying the design process. These visualizations are generally focused on representing perceivable, yet invisible, natural phenomena. The sequence is quite clear; the phenomena is first perceived, then measured and finally translated into a visual representation that can lead to a better understanding of the phenomena. However, architecture also defines and establishes spatial relationships with cultural, social and historical factors which may not have clear material implications, yet they

permeate and determine our environments in ways which can be even more categorical than pure physical boundaries. When studying patterns of occupation in streets in Shanghai we are not confronted with a natural phenomenon, but an anthropological one. This demands a rather different sequence: through observation and analysis, certain aspects of the dwelling are theoretically understood and then, based on that understanding, a visual representation is created, which ultimately allows perception of what was initially theoretically intuited. Hence, architectural visualizations can be used not only for supporting new approaches and possibilities to the design process, but also for revisiting old problems from a new perspective [5]. Digital representation and visualization can generate new ways of perceiving and understanding old yet relevant, essential concepts, allowing us to represent invisible information interacting with the built environment [6, 9].

3 Case Study: Introduction

For our research, we decided to undertake a case study by comparing two iconic streets in Shanghai's former French Concession; Jinxian Road and Simming Village. These streets offer an excellent opportunity for comparison due to their similarities and differences. Jinxian Road is a fully open public street, while Simming village is a gated street of public access. They are very close to each other -less than 300 m apart- and their length is very similar- between 200 and 250 m. They both belong to the same area of Shanghai with comparable flow and activity levels, which is essential for undertaking a meaningful comparison of their patterns of occupation. Their two main differences are their orientation and their role in the city, since one is open and the other one is gated (Fig. 1).

3.1 Case Study: Methodology

The proposed methodology is for visualising quantitative information in a qualitative way, and is divided in three main parts: Data collection, map generation and analysis.

Data Collection Focused primarily on collecting external references like the historical profile, architectural styles and available data regarding past and current building regulations and occupation profile of the studied streets. The second step is the place survey, which is executed in the streets themselves. Initially, we surveyed the architectonic elements (space-defining elements) responsible for boundary demarcation and identification, so we could divide the street into workable segments. The second step was to record the visual scenery of each segment, which later could be subdivided into "character categories". The third step will be the Facade's survey for each side of the street. The final step was the recording of occupation in both streets.



Fig. 1 Top view and street view of the two studied streets: Jinxian Road (top) and Simming village (bottom)

Maps Generation Once the information has been collected, we will generate the “place-maps”, which are maps that can convey not only physical and geographical information, but also intangible information related to place coordinates. We will do so by applying two methodologies of visualisation overlapping historical, physical and photographic information with the patterns of occupations.

Analysis Once the maps are generated, we will analyse them by searching for different patterns of occupation, character correlation and presence/use of architectural elements, resulting in a complete overview of both streets. We argue that the “place-maps” have the potential to reveal relationships and conclusions that otherwise would not be possible or evident to visualise, allowing for a deep comparative analysis.

3.2 Case Study: Execution

The first steps of the research were focused on producing all the necessary material for supporting the site survey, starting with an initial site visit, rendering of the first plans of the two streets, modelling of 3d digital models, followed by a basic morphological study and comparison. The second step was to produce a historical overview of the studied streets, adding this information to the initial maps, which served as the base and support for the fieldwork. For the fieldwork and data collection, we visited the streets multiple times, surveying and mapping the following information: elements, character and activity.

Elements The first step of the survey was to map and draw all the space-defining elements (architectonics elements) that play a role in creating spatial boundaries, with a special focus on identifying intermediate and weak boundaries. These are boundaries that exist in a site and play a role in organising the space and occupation of a place, but due to their size and nature, they are rarely indicated in plans at an urban scale. Occasionally, these types of boundaries are established informally by the residents themselves. Hence, they do not appear in the official documentation. Examples of these boundaries are sidewalks, curbs, small fences, changes of pavement, etc. The second step was to map the activity-defining elements. These elements are not very important or categorical when defining or demarcating spaces, but they are crucial for allowing certain activities to take place. Examples of these elements are benches, tables, or luminaries. Some of these elements can even be moved from one place to another by the residents (like foldable chairs). Again, this kind of information is rarely present in ArcGIS databases or official documentation, yet they play a significant role in determining the activities, occupation and overall experience of a place.

Character The character of a street is not easy to define: We can all understand and experience it, yet it is very challenging to break down the concept into measurable and mappable elements. It involves the historical periods in which its buildings were constructed, materials, details and design features. Building functions play a crucial role in defining the character of a street, determining either its variety or uniformity. Generally speaking, a purely residential street will appear more uniform and homogeneous than a mixed-use street, affecting its overall vibrancy and atmosphere. In order to incorporate this variable in our comparison, we first mapped the functions of the buildings in the studied streets. We also included typological research, collecting some of the housing types found in Jinxian Road and Simming Village. Additionally, we did a facade study, recording every facade of each building facing the street and combining them into one continuous image of the streets' elevations. Progressively, we started to explore ways this information could be combined into single maps or images (Fig. 2).

Activity In order to fully understand and compare these two streets, we must incorporate the patterns of occupation which take place in them. Both streets have substantial pedestrian traffic. Jinxian Road is fully embedded in the urban fabric, yet it spans only one block, resulting in low traffic of vehicles and a visible high occupation of its public space by both residents and visitors. Simming village also spans only one block, connecting a main artery (Yan'an Road) with Julu Road, one of the most iconic streets of the French Concession. Because of this we wanted to investigate the implication of these different conditions in defining the occupation of the streets. In order to do so, we registered the places where people gathered and stayed in both streets by using video recordings, mapping down their location and length of stay. We recorded ten minutes videos for every hour, from 9:00AM until 6:00PM, on the same day in both streets, making sure that the weather conditions (partially cloudy) were the same consistently throughout the day. This sample time for data recording has been proven dependable in numerous urban surveys, and allows for



Fig. 2 Sample image showing part of the survey conducted in Siming Village, showcasing a roof plan of the street, existing typologies and gates and facades details

reliable information for data extrapolation [7]. This data would enable us to study both the location and concentration of activity in the studied streets. In order to do so, we introduced a tool for visualising the recorded information so it would allow us to analyse it quantitatively. For this, we introduce the Activity Counter Maps.

3.3 Case Study: Using the Activity Counter Maps

The Activity Counter Maps (ACM) is a digital tool that allows representation and visualization of different kinds of data in a geographical context. What the ACM does is to assign an area of influence to an object or location in the space. The radius and height of the area of influence can be assigned accordingly to the specific needs of varied researches (Fig. 3). When x areas of influence meet, the highest point where they are intersected is multiplied by x , generating a new common area of influence [8]. The process continues until every area of influence is combined with the others into a resultant common area, allowing visualization of both the shape of the combined personal spaces and the intensity of activity, since the combined spaces grown vertically. Hence, the intensity of activity can be expressed three-dimensionally, just like topographic contour lines. Especially for this research, here is where it lays the potential of this tool; it can be used not only for generating graphics, but also to generate form, and therefore, space [9].

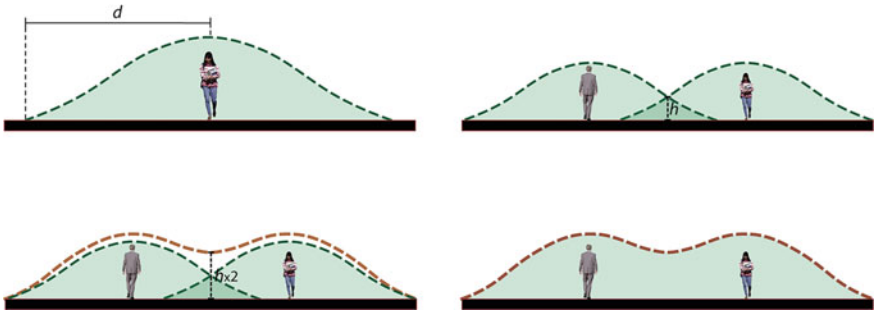


Fig. 3 Diagram showing the logic behind the Activity Counter Maps

3.4 Case Study: Generating the Maps

In order to generate the ACM for both streets, we first created digital files containing the location and number of people staying in the streets. We generated one digital file for each studied hour, plus one file combining all the occupation of the day, resulting in 10 files for each street and 20 files in total. Additionally, it is possible to change the area of influence in the activity counter maps, allowing us to generate many results depending on the area which we want to visualise. After testing different areas of influence, we finally assigned a social area of 9 m for each user, which is also an established proxemic for public distance in public places (Fig. 4). Once the maps were generated, we could quickly identify the areas with occupation concentration and recognise changes throughout the day. This would allow us to see if there is a correlation between the patterns of occupation and the other collected data for both streets.

Additionally, we generated several other maps with the rest of the collected information. For instance, we did not only recorded the location and quantity of activity, but we also categorised it, indicating if it was a social or individual activity, passive

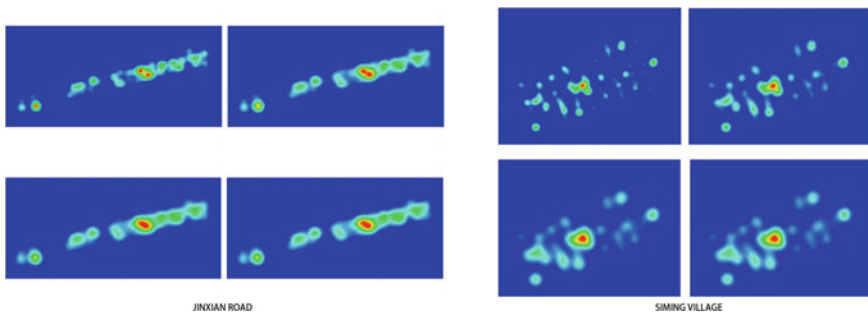


Fig. 4 Image showing selected sample of the concentration of occupation for different times of the day in the studied streets, testing different areas of influence. Jinxian Road (left) and Siming Village (right)

or active activity, and so on. We also mapped the location and quantity of restaurants, cafes and stores on both streets, aiming to see the impact of these commercial functions on the occupation. We identified and categorised the level of openness in both streets, mapping the public, semi-public and private open areas, seeing how extruded walls and balconies could be transformed into temporary kitchens and gathering areas. Another important map was the one showing service and infrastructure, in which we mapped the location and quantity of the many elements that may populate and allow streets to function, like generators, bicycle parking areas, garbage collection areas and self-made mailboxes, which added a unique identity to the streets.

One of the most exciting and unexpected maps was the one about planting and vegetation. Besides the public trees, which are part of the streets, many residents engage in claims of public space for placing their own plants and vegetables, once again blurring boundaries between public and private and concentrating a big deal of activity and occupation.

3.5 Case Study: Combining the Maps

Once we finished all of our maps, we ended up with a total of 42 maps (21 maps per street) showcasing all the surveyed information. At that point, we understood that, while we could compare and study all the maps individually, there was much potential for visualising deeper correlations if we could combine all the data into one single map for each street. There were a couple of problems in executing this. First, the amount of data was too large, which resulted in very concentrated maps that were almost impossible to read and understand. The other problem was the type of data. The occupation patterns, building facades and typologies, location and size of informal planting and vegetation, stores and restaurants; They all needed different representational languages to be effectively integrated into the line maps of the streets, creating a problem of visual consistency. Finally, we managed to generate the map by switching from a 2D map to a 3D one, creating a tridimensional, layered poster containing different types of information in different translucent surfaces, allowing each type of data to be independent yet integrated at the same time (Fig. 5). This also allowed us to include vertical information (like the height and facade of the buildings), which emphasised even more the vertical quality of the ACM. The resultant maps were compelling in showing the correlation between the different variables, like vegetation and activity, or history and facades, allowing for more accessible and unforeseen opportunities for analysis.

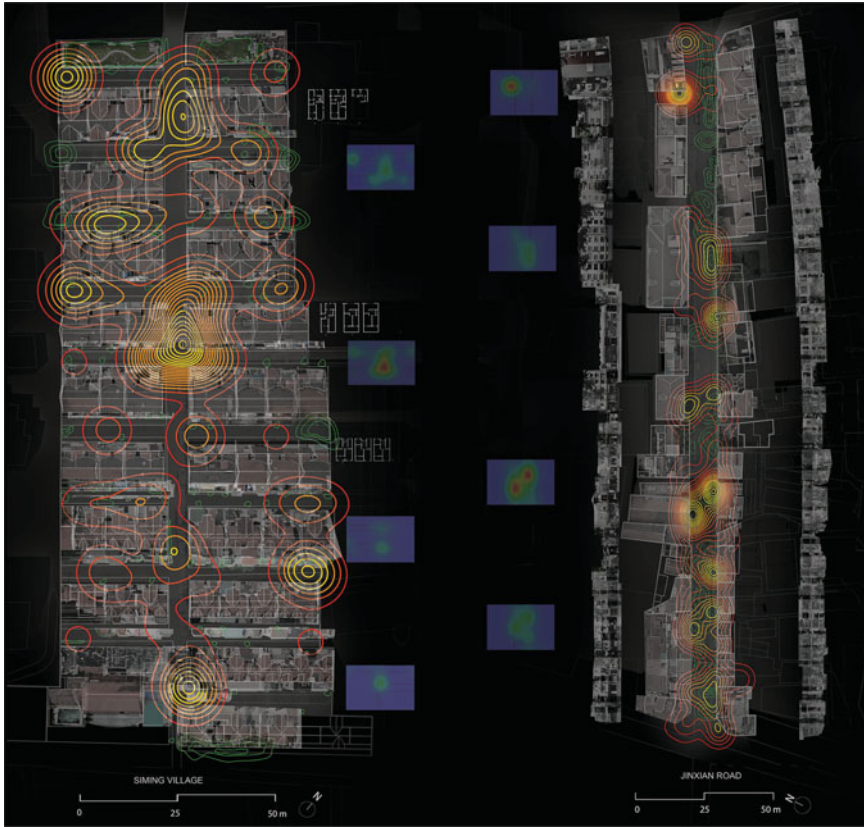


Fig. 5 2D representation of one of the 3D illustrations which combines different layers of information of the two studied streets into one final map

4 Conclusion

After combining the data, we were able to see correlations and distinctions within each street and between them. Regarding the elements, both streets showed several informal interventions by the inhabitants, creating users-made boundaries that altered the patterns of occupation of the original planning. Surprisingly, Jinxian Road presented more of these interventions, which was unexpected considering that it is a fully public street. They range from self-made post boxes to installing benches and chairs. The most common one on both streets was the growing of plants and greenery. Spaces around planting revealed themselves as powerful places for congregation. Neighbours would take care of plants, which would attract other neighbours, creating moments of socializing. This was shared by both streets, and while this was initially intuited before the analysis, it was surprising to see how substantial and important these informal greeneries are for determining patterns of occupation.

Regarding the character of both streets, they were quite distinctive. Simming village is mostly residential, dominated by three types of buildings with similar details and consistent heights. However, users have played a great role in modifying the buildings over the years, creating a unique community. Jinxian Road has evolved into a very concentrated and mixed street, which combines residential buildings with stores, restaurants and services. The type of stores is also very varied, ranging from traditional and old local restaurants to modern cafes and boutiques. All of the above, combined with low traffic of vehicles and the presence of trees and shades, has resulted in a street that is not only constantly occupied by locals, but also highly visited by other people, creating a mixed and unique street in which the occupation is ever-changing and flexible. The patterns of occupation in Simming village were also quite unexpected and surprising. The branch-like organization of the alleys produces public spaces which are more secluded and intimate, where residents are more likely to meet with each other. In opposition, the main central street acquires a semi-public identity in which residents and passing citizens can indirectly (or directly) interact. However, this type of indirect interaction also becomes important in defining patterns of occupation because people passing by would draw attention from people in the alleys, creating a constant exchange of gaze.

While both streets are different in their urban role, their level of activity and occupation had more similarities than initially presumed. We believe that there are many lessons to be learned from Simming village: its semi-public condition seems to create a good balance between openness and concealment. Perhaps this is a way forward for planning parts of Chinese cities, in which gated communities could become more fragmented and numerous, incorporating semi-public streets within them. Regarding the methodology, its innovation is that it successfully represented and combined different categories of information, allowing for meaningful comparisons and unexpected conclusions, showing new opportunities for analysing a variety of places and phenomena. We expect to expand and advance this methodology so it can be applied in other cities and urban scenarios, since we believe that it has the potential to provide meaningful information and new perspectives for better understanding and designing our built environment.

References

1. Bolchover J, Lin J (2013) Rural urban framework: transforming the Chinese countryside. Birkhäuser, Basel
2. Chai Y (2014) From socialist danwei to new danwei: a daily-life-based framework for sustainable development in urban China. *Asian Geogr* 31(2):183–190
3. Zhang D (2016) Chinese courtyard housing under socialist market economy. *China Curr: J China Res Center* 15:8 p
4. Wang H, Pojani D (2019) The challenge of opening up gated communities in Shanghai. *J Urban Des* 25(4):1–18
5. Ware C (2004) Information visualization: perception for design. Morgan Kaufmann Publishers, San Francisco

6. Wash G (2020) Lifestyle as heritage: a methodology for visualizing the space-activity relationship in rural China. In: 1st IconA international conference on architecture “creativity and reality. The art of building future cities”. Edizioni Nuova Cultura, Rome, pp 628–633
7. Gehl J, Gemzøe L (2004) Public spaces, public life. The Danish Architectural Press, Copenhagen
8. Fujii A (1978) Study of activity contour—Part 1: Report on the structural concept “Ridge” of a closed curve. *Trans Architect Inst Jpn* 267:121–128
9. Wash G (2014) People as place-making coordinate: a methodology for visualizing personal spaces. *Front Architect Res Elsevier* 1(1):36–43

The ‘Integration Mode’ of Regeneration of Industrial Heritage, Magna Science Adventure Centre



Chen Zhang and Zishen Bai

Abstract The concept that valuable industrial heritage should be wisely conserved and reutilised in post-industrial societies has gradually been a consensus. Practices of heritage regeneration have become widespread in industrially developed countries. This study summarises current industrial heritage regeneration practices into three modes: ‘Continuation’, ‘Replacement’, and ‘Integration’. The third mode is rare in practice but regarded as significant research and practice value. This unique mode is detailly analysed through the literature review, archival research, and field research on a case, Magna Science Adventure Centre. The success of this case is thus attributed to its innovative regeneration design, which organically integrates the original and new identities of the steelworks in the fields of theme, function, structure, architectural form, etc. Further, the strengths, inadequacies and applicability of the third mode represented by this case are discussed. The ‘Integration’ mode of industrial heritage regeneration is considered worthy of further study and promotion if the relatively stringent prerequisites for implementing this mode can be achieved.

Keywords Industrial heritage · Regeneration · Magna Science Adventure Centre · Integration mode · Identity

1 Regeneration of Industrial Heritage

Industrial heritage is the remains of industrial culture, including buildings, machinery, workshops, factories, mines, refineries, warehouses, energy conversion sites, transport and all other infrastructures, as well as places of social activity associated with the industry [1, 2]. Some scholars have recently proposed expanding the

C. Zhang (✉) · Z. Bai
School of Architecture, The University of Sheffield, Sheffield, UK
e-mail: czhang120@sheffield.ac.uk

Z. Bai
e-mail: zbai5@sheffield.ac.uk

definition of industrial heritage by including non-material factors, such as production environments, technologies and processes, into the category of industrial heritage [3, 4]. Industrial heritage can be summarised to represent the collective memory of industrial culture, history and landscape in the modern history of a territory [5].

‘Industrial heritage may not evoke the same overpowering moral emotions and impulses as Romantic ruins, but instead has an unpredictable internal impression and emotions [6]’. Besides providing multiple sensory experiences, industrial heritage possesses unique values [7, 8] (see Fig. 1).

Since the second half of the twentieth century, the significance of industrial heritage has been gradually aware in many developed industrial countries, and regeneration has gradually become one of the essential means of perpetuating the value of industrial heritage [9]. Scholars have various views on the classification of industrial heritage regeneration. For example, Fuying classifies the regeneration into four broad categories: public, residential, landscape, and integrated mode, while Li classifies that into historical reproduction mode, economic revival mode, adaptive use mode, environmental optimisation mode, and integrated mode [8, 10]. The existing modes of industrial heritage regeneration can arguably be divided into three main categories (Table 1). Even though the third mode has many merits, it has fewer examples than the first and second modes. The Magna Science Adventure Centre in the traditional industrial belt of central England is a typical example of the third mode.

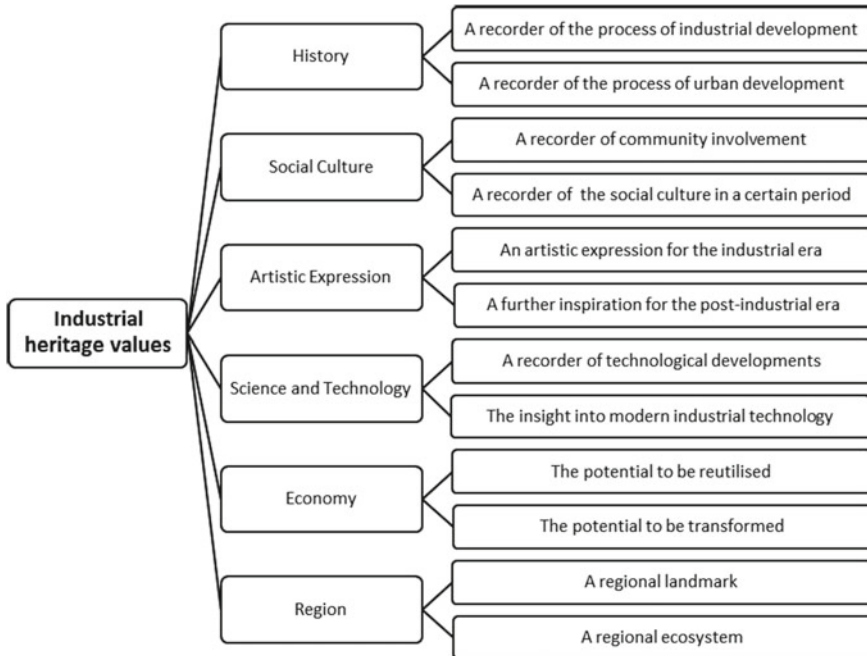


Fig. 1 Industrial heritage values

Table 1 Three modes of industrial heritage regeneration

Modes	Characteristics	Cases	Descriptions
Mode I Continuation	The original identity of the industrial heritage is continued to be maintained or displayed	Chongqing Industrial Museum, China	Much original steelwork structure is well preserved and has been transformed into a museum relevant to the steel industry
		Museum of Steel, Mexico	The original steelworks have been transformed into a new steel museum, and the most distinctive structural features have been retained
Mode II Replacement	A newly implanted identity has largely replaced the original identity of the industrial heritage, and the new identity is mainly displayed	The Main Pavilion of the 11th Jiangsu Horticultural Expo, China	The equipment of the cement factory was utterly dismantled, and the industrial heritage was transformed into an exhibition building unrelated to the original cement factory, housing the new horticultural exhibition
		Bonbon Town, Sugar Hall renovation, China	The formerly dark industrial warehouse has been transformed into a sunlit event space that does not continue the warehouse's own historical story and narrative
		Site Verrier de Meisenthal, France	The old industrial building has been entirely transformed into a new cultural centre
Mode III Integration	The old and new identities of the industrial heritage are integrated and presented	Magna Science Adventure Centre	(Details are described below)

The methodology of this study consisted of a literature review, archival research and field research. Through months of in-depth research, the background, conservation methods, renewal techniques, exhibition design and social evaluation of the Magna Science Adventure Centre are clarified. The strengths, inadequacies, and applicability of the 'Integration' mode, represented by this case, are further explored. This study could be seen as a preliminary exploration of the possibilities of regenerating industrial heritage.

2 Regeneration of Magna Science Adventure Centre

2.1 *Historical Context*

Britain is an essential representative of industrial civilisation. From the first industrial revolution onwards, factories have gradually been a unique part of Britain's human geographical landscape. Many British factories are usually structurally sound and had a broad impact on the local community, but have been abandoned in recent years due to de-industrialisation. These factories deserve to be preserved, renewed and reused. The Magna Science Adventure Centre can be described as one of the successful examples of the third mode of industrial heritage regeneration.

Templeborough, where the Magna Science Adventure Centre is located, is steeped in history. In the mid-fourteenth century, small rolling mills and some facilities were built on this land that can be seen as the basis of the future factory. In 1871, steelworks were established on the site. Later, the steelworks were expanded during the First World War due to military production, and by the 1920s, it became the largest steelworks in Europe. During that period, the factory became known for its worker welfare, creating a vibrant and close-knit local community. After World War II, the factory was developed again. In 1967 the British steel industry was nationalised, and the factory became the Sheffield division of British Steel. After the 1980s, the factory fell into decline because of transformations in British manufacturing and the economy. At the end of 1993, the entire factory ceased production [11]. This industrial heritage was once a symbol of Templeborough and even the industrial glory of the British Empire. It has great potential for conservation and renovation.

2.2 *Heritage Conservation*

Work began in 1998 when The Magna Trust commissioned the Wilkinson Eyre team to transform this 37,000 m² factory into the UK's first science museum [12]. The US\$60 million project was officially completed in 2001 [13, 14]. As Chris Wilkinson, responsible for the project, says, 'Steelmaking building and its artefacts have been retained [13].' The main structure of the steelworks was required to be preserved as far as possible in the transformation. Apart from the dismantling of the two small auxiliary buildings, the original 250-ton gantry, crane rails, hoppers and other steel structures, and even the plant's electricity supply system, were preserved and reused for the new centre [12, 13, 15]. The renovated building is painted black, contrasting with the contemporary red Glass Reinforced Plastic (GRP) cladding on the building's surface. During the daytime, the flame-coloured curtain wall of the façade permeates inwards with red light from the sun; at night, the interior light, in turn, permeates outwards through the surface. The 'glowing' interior and exterior facades imply enormous energy emitted during steel production in the past factory. That design both alludes to the old identity of a bygone factory time and creates a new

appearance befitting the science adventure centre, which can be seen as a valuable attempt to integrate the old and new identities of the heritage. Some landscapes transformed from the industrial remains are retained, and two new playgrounds for the junior and community are constructed.

2.3 Heritage Regeneration

The highlight of the Magna regeneration is the organic blend of new and old in terms of theme, space, function, and narrative. As a designer says: 'We were struck by its immense scale and the drama of its dark, empty spaces. This huge piece of industrial archaeology has many qualities of a Gothic cathedral, and we were determined to maintain its integrity' [14]. Apart from preserving the steelmaking equipment and structure, four exhibition spaces are implanted, separated from the original heritage at different heights, suspended or deep underground, and a new transport complex with aerial walkways, bridges, and vertical lifts. These new elements constitute the new identity of the heritage, the main exhibition space of the science adventure centre (see Fig. 2). The design of the entire exhibition theme is inspired by the most prominent character of the original steelworks, steelmaking. The themes of the four new spaces are taken from the philosopher Aristotle's view of the four elements that make up the world: earth, air, fire and water, which are also necessary for steel production [16]. 'Raw material (of the steel) comes from the earth, and it is extracted with fire and air before being quenched with water [13]'. These four elements perhaps also correspond to the four states of matter: solid (earth), liquid (water), gas (air) and plasma (fire). 'The form, location, and appearance of these spaces relate to the respective elements and, together with the artefacts retained from the previous steelmaking processes, combine to make a new narrative [17]'. This blend narrative of old and new themes forms a practical approach to the integration of the old and new identities of the heritage.

The visiting route of the Magna Science Adventure Centre is appealing, with a strong narrative and spatial links between the new exhibitions and the original remains. A long-axis section was drawn to expatiate the Magna museum's spatial design (see Fig. 3). Visitors first enter a light-filled foyer connected to a large multi-purpose hall with dining, lounge and toilet functions. The 'adventure' begins when people then walk through a multimedia gallery made of fake concrete called 'The Human Element', which tells the story of the steelworks and steelworkers' life. Then visitors are greeted by the front of a nine-storey furnace workshop, a towering space with several experiential exhibition installations to explore. Visitors then move from the new transport core in front of the workshop to the mysterious suspending walkway, 10 m high and deep into the vast core space of the factory. Here, they are free to plan their visit. Most visitors are appealed by the vast dark space around the bridge, which is more than 30 m high and four football pitches long [13]. The space is poorly lit and retains much historically active but now rusted steelmaking equipment, illuminated by new spotlights of various colours and aided by sound,

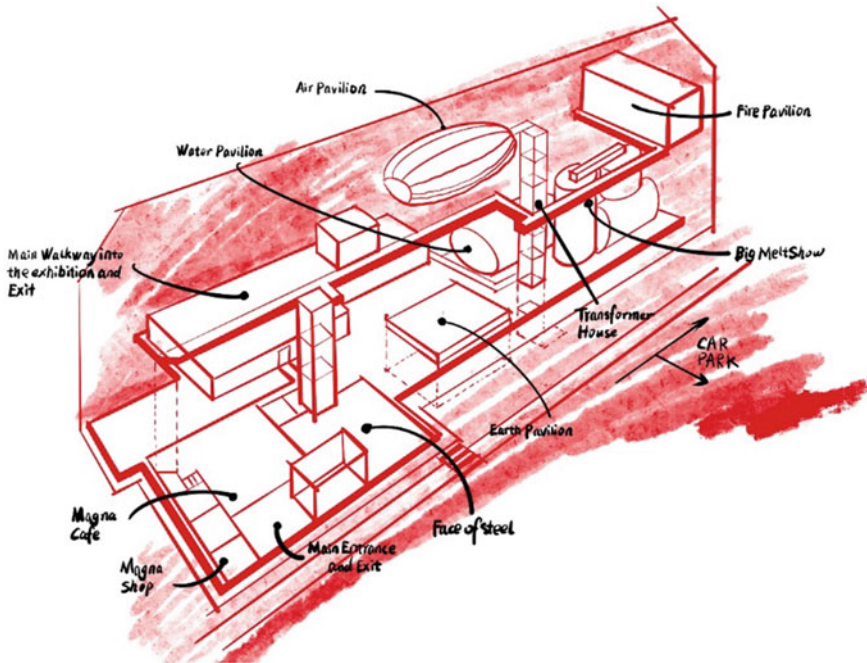


Fig. 2 Exhibition space layout

presents a vibrant scene of old steelmaking days. Visitors walk on a suspended walkway viewing audio-visual presentations of the old production processes and freely operating several large searchlights to appreciate the dim details of the factory and furnaces. This interactive approach, much appreciated by young generations, allows visitors to explore the space actively.

After crossing the long walkway, visitors arrive at the first gallery, the Fire Pavilion, an ample matte black space wrapped in black steel cladding suspended from the main structure with main support trusses [12, 14]. The pavilion focuses on the knowledge of fire, with presentations of electricity, heat and steelmaking processes. Several interactive installations, such as a spectacular fire tornado and immersive images of lightning-induced fires, with textual interpretation, keep family visitors lingering.

Most visitors then return to the transport core and go up to the top floor to the second gallery, the Air Pavilion. The pavilion is lightweight and like an airship 'hovering' 12.5 m above the steelmaking furnace. 'This blimp is wrapped by three layers of Ethylene Tetrafluoroethylene (ETFE) foil cushions, clipped to aluminium extrusions, and a steel ring provides a framework for the pavilion structure [13, 14]'. The exhibition is about air and steel making, with facilities such as a simulated typhoon, air-sound devices and airflow simulations.



Fig. 3 Section and scenic shots of the Magna Science Adventure Centre

Visitors then go through the traffic core again to the Water Pavilion, slightly above the horizon and like a spiral ellipsoidal, wrapped in an intricate steel structure [14]. This gallery looks full of dynamics under blue light. Visitors pass through a narrow corridor flanked by two foggy pools, which simulate a rainy climate, to enter the interior. This pavilion's theme relates to water characteristics, like steel production and water transport. This pavilion was observed to be a 'haven' for children since many interactive exhibits encourage children to get in touch with water.

Finally, visitors go down by lift to the final exhibition, The Earth Pavilion, located five metres below the original factory horizon [13, 14]. This pavilion consists of several irregularly shaped rusted steel walls and roofs, symbolising the unevenness of the earth's crust. The Earth Pavilion focuses on the knowledge of the soil and mining industry and the historical reasons steel production flourished in this area. Visitors can interact with a series of installations in the pavilion, learning the process of mining from extraction to transportation. This pavilion contains fascinating installations, the three small-scale JCB-sponsored excavators. Visitors can sit in the cockpit and operate two gear levers to dig up 'coal', which is a unique experience for visitors. Visitors finish their visit by returning from this pavilion to the multi-purpose hall at the entrance.

2.4 Reputation

The Magna regeneration project has been highly acclaimed. It has won some awards, such as the RIBA Stirling Prize 2001, Design Week Awards, etc. In terms of visitors, the Magna served 225,000 visitors in the first four-month operation and has been one of the most visited museums in South Yorkshire [18]. For the locals, ‘since opening its doors 17 years ago, Magna has been at the heart of the South Yorkshire community [19]’. Magna’s success is considered inextricably linked to its unique regeneration approach.

3 Result and Discussion

3.1 Strengths

The third mode of regeneration, represented by the Magna, is distinguished from the first and second modes in that it neither ‘faithfully’ continues the old identity of the heritage nor retains the old ‘surface’ only and implants an entirely new identity to replace the old one. The ‘Integration’ mode preserves a large portion of the original identity of the industrial heritage, including architecture, appearance, machinery, demonstration of industrial processes, impact, etc., while introducing a new identity tied to the original closely. The Magna’s old and new identities are organically integrated and easily perceived by visitors. This harmonious connection is considered the most significant value of this case and this mode.

There are many other commendable points of this case, such as the relatively flexible visitor route. Although an official route guide exists, visiting pavilions in a different order does not affect the presentation of the core theme of the exhibition, as the sub-themes of the various pavilions are relatively independent and reversible. Further, as the RIBA Stirling Prize described, ‘(The designers) allow the existing building to speak for itself and to tell its own story [13].’ Apart from unique thematic integration, this accolade is also due to the fascinating and interactive nature of the exhibition. While providing essential information, the exhibition encourages visitors to interact with the objects on display and allows them to explore some zones with their actions. The exhibition’s empathetic interpretation of the past lives of the local steelworkers is also praiseworthy. In addition, Magna’s success in gaining visibility and financial benefits through various academic, media, and family events, as well as its contribution to the community’s cultural identity, are admirable. These illustrate that inclusive, interactive and caring consideration of exhibitions should be an essential principle of industrial heritage regeneration.

3.2 *Inadequacies*

The Magna inevitably has some flaws. Some exhibition installations were under deterioration. For visitors, most of the Big Melt area is inaccessible and only can be viewed from a distance from the suspended walkway, probably due to visitor safety or heritage conservation, which is a visiting pity. The conservation of much of the original space and equipment has led the newly implanted building with limited and fixed space and form, which is not conducive to potential exhibition renovation and temporary exhibition events. However, these shortcomings are not overshadowed its status. the continued patronage of this old case is a testament to its unique value and the superiority of the third regeneration mode [16].

3.3 *Applicability*

As mentioned above, cases of the 'Integration' mode are still rare. The reasons can be attributed to the following assumptions.

Firstly, the variety of support during the renovation of this case was robust. In addition to the close collaboration and the high level of professionalism of the entire design team, the practice's success was also due to the complete client trust from Magana Trust. This kind of teamwork between professionals and highly qualified clients is not common in heritage renovations widely. Adequate financial support is also necessary. The Millennium Commission, established in 1997, planned to set 46 million pounds for the Magna project budget [19]. As mentioned, the Magna was finally built at a cost far over that budget. The financial support enabled the design team to show their creativity, implanting new features and facilities with a significant amount of industrial heritage retained.

The second is the perfect conditions of the heritage. The unique meaning, decent structure and facility condition, and original heritage theme give the designers a solid platform. Such excellent heritage conditions are rare. The progress of industrial regeneration is sometimes in line with the game theory where, for example, the value of the industrial physical assets largely influences decisions. When the economic benefits of recycling and selling assets outweigh the reuse, such regeneration may not meet some stakeholder groups' needs, and regeneration implementation will be challenging.

The third relates to the positive relationship between the centre and the local community. Magna's industrial heritage was the community pride and has provided benefits to the community. During the design phase, the Magana design team built a great relationship with the community, and then Magana provided event venues, jobs and tax revenue to the community during its operation. This mutually beneficial interaction between the heritage and communities was essential.

The combination of these conditions has shaped the success of the third regeneration mode represented by the Magna Science Adventure Centre. This is also why the number of such heritage regenerations is low.

4 Conclusion

Industrial heritage, the remains of industrial culture, has significant values and should be conserved and regenerated for the current society's requirements. The existing modes of industrial heritage regeneration could be divided into three main modes: 'Continuation', 'Replacement', and 'Integration'.

The Magna Science Adventure Centre can be described as one of the successful examples of the 'Integration' mode. Its regeneration integrating the old and new identities is the biggest highlight: (1) the structure and form of this heritage are mostly conserved while some new appearance elements are implanted. These additions do not harm, but some even enhance the visual presentation of the heritage. (2) the new theme, educational exhibitions of four states of matter, is introduced and coincide with the original theme of the heritage, steelmaking. (3) the new architectural spaces, such as four exhibition pavilions, suspended walkways and transportation core, are organised in various locations in the original dark giant space. Each new space presents an exhibition theme while visually relating to the original industrial space. Apart from these organic integrations, the application of interactive exhibition equipment and flexible visitor route is worth mentioning. Owing to these innovative designs, Magna has gained visitors and a high reputation.

The successful implementation of the third regeneration mode represented by the Magna depends on the complete client trust and various supports, perfect heritage conditions, and a positive relationship with the local community, which perhaps are not common in every case. Considering the excellent outcome of the Magna, the third regeneration mode has potential worth further research and application.

References

1. Loures L (2008) Industrial heritage: the past in the future of the city. *WSEAS Trans Environ Dev* 4(8):687–696
2. TICCIH. The Nizhny Tagil Charter for the industrial heritage. The International Committee for the Conservation of the Industrial Heritage. http://orcp.hustoj.com/wp-content/uploads/2016/04/Nizhny_Tagil_PUN_15.pdf. Last accessed 13 Jan 2023
3. Jixiang S (2006) Focus on a new type of cultural heritage - the conservation of industrial heritage. *China's Cultural Heritage* 4(11):38
4. Xiangqi Z, Yufan Z (2021) From heritage to legacy: an overview of research on the development of industrial site landscaping. *Landscape Architect* 1:80–86
5. Huanzhou X, Xuyi S, Maoying W (2015) A study on the preservation of industrial heritage in waterfront areas and the continuation of urban memory—A case study of industrial heritage in West Gongchenqiao of Hangzhou Canal. *Geogr Sci* 35(2):183–189

6. Edensor T (2005) Waste matter—the debris of industrial ruins and the disordering of the material world. *J Mater Cult* 10(3):311–332
7. Yu L (2015) Research on the conservation and reuse strategies of China's industrial building heritage in the post-industrial era. Doctoral dissertation. Tianjin University
8. Li Z (2017) Research on the conservation and cultural regeneration of industrial building heritage. Doctoral dissertation. Xi'an Academy of Fine Arts
9. Bell D (1976) The coming of the post-industrial society. In: *The educational forum*, vol 40, no 4. Taylor & Francis Group, pp 574–579
10. Fuying L (2016) A study on the spectrum of industrial heritage conservation and reuse modes—Based on the perspective of scale hierarchy. *Urban Plan* 9:84–96
11. Magna. Magna overview—visitmagna.co.uk. https://www.visitmagna.co.uk/wp-content/uploads/2019/05/Magna_Overview.pdf. Last accessed 15 Dec 2022
12. Anonymous (2022) Magna—The New Science Adventure Centre in Rotherham. *Facilities* 20(1):16–18
13. Hart S (2001) Projects-Magna Science Adventure Centre, UK—An English steel-processing plant is remade as a science centre. *Archit Rec* 189(11):122–127
14. Davey P, Forster KW (2007) Exploring boundaries: the architecture of Wilkinson Eyre. Walter de Gruyter
15. Troth N (2003) Magna Science and Adventure Centre-Fire Safety Strategy, Magna is housed in a vast former steelwork. *Fire Safety Eng* 10(1):12–15
16. Jin J (2014) Different user experience and interactions design sensitivities for children; adult and family inside Modern Science Centre. In: *Museum studies at Leicester 50th anniversary conference*, University of Leicester, UK
17. Wilkinson C, Eyre JA (2001) Universal space. Bridging art and science. Wilkinson Eyre architecture. Booth-Clibborn Editions
18. Magna Trust. Templeborough history. Magna Science Adventure Centre. <https://www.visitmagna.co.uk/science-adventure/history-of-steel/templeborough-times-a-brief-history-of-the-site/>. Last accessed 03 Dec 2022
19. Magna Trust. Magna on a mission. Available at <https://www.mymagnaevent.co.uk/news/magna-on-a-mission/>. Last accessed 05 Dec 2022

Interpreting the Urban Historical Area-Huishan Ancient Town as a Case Study



Ting Zhang, Fangqian He, Di Wang, and Li Tao

Abstract This paper examines the historical change process of urban historic districts through morphological research. This paper uses morphological theory to construct an analytical framework. Taking the ancient town of Huishan in Wuxi as an example, the relationship between the evolution process of spatial structure and spatial function is analyzed. Meanwhile, the transitional morphological characteristics are closely related to the social cultural background of each period. The conclusion of the study proposes that from the perspective of urban culture, the design of heritage sites should not only consider the conservation of physical forms, but also the social forms behind the physical forms are worth further consideration. In addition, this study also aims to provide the feasibility of western morphological theories in urban studies in China.

Keywords Morphology study · Urban heritage area · Social culture context

1 Introduction

China has experienced a very huge urban renewal movement in the last decades. Many studies have reviewed this process in detail from different perspectives. In the new round of urban renewal, the <14th Five-Year Cultural Plan>¹ explicitly proposes to improve the protection of urban culture, for example, by paying more attention to local characteristics in urban planning.

As the epitome of the historical evolution of the city, the urban historic area is an important part of the urban physical structure. At the same time, it is also

¹ Notes 1.

T. Zhang (✉) · F. He · D. Wang · L. Tao
Wuxi Taihu University, Wuxi 214064, China
e-mail: zhangt_wxu_edu@163.com

T. Zhang
Department of Architecture and Design, Politecnico di Torino, Torino, Italy

the most basic unit of cultural bearing from an urban perspective, and its research direction is more focused on the interaction of human activities, physical elements, and local culture. As the most central part of urban heritage, historic buildings play an important role in local cultural expression. The current study on historical building is less associated with local culture and identity, mainly because of the massive demolition process that has destroyed the original social fabric. The same approach of regeneration has resulted in the convergence of urban heritage areas and the loss of the urban cultural identity.

Over the past decades, a large number of researchers have conducted studies on Chinese cities. Some scholars have examined the urban regeneration through governance perspective [1, 2]. Some researchers have studied the transformation process of an urban heritage space through social process and governance logic [3–6], and the property perspective [7]. Many studies have also examined urban transformation and heritage areas in Beijing, such as Fang and Zhang and Fang, who examined hutong neighborhoods that were demolished and replaced by commercial buildings [8, 9]. The relationship between public–private partnerships and local residents of transformation project was proposed by Zhang in 2002 [10]. Scholars such as Chen Fei studied urban heritage areas from the perspective of morphological change combined with urban design, and proposed some suggestions for the further design of historical areas [11, 12]. However, few studies have investigated the relationship between historical areas and local culture from the perspective of physical form.

This study attempts to use the morphological theory of Western into Chinese studies. By constructing an analysis framework, one suitable methodology for studying historical areas is explored. In addition, further design ideas that consider local culture are presented for designers and decision makers. The Huishan ancient town in Wuxi was selected as a case area because of its unique historical changes and architectural characteristics.

2 Methodology

This study adopts a morphological approach to construct an analysis framework. First, the morphological process is defined by studying history; Second, the relationship between physical form and social culture of each period is analyzed; Third, by discussing the morphological process of case area, the suggestion is proposed. In the end, the limitations of this study and future research directions are provided. Due to the lack of some historical information, the spatial structure is mapped in this paper based on historical information.

3 Case Study-Huishan Ancient Town, Wuxi, China

3.1 Introduction

Huishan Ancient Town is located in Wuxi, Jiangsu Province. Wuxi covers an area of more than 4000 km², and the south of the city is connected to Taihu Lake. It is a well-known city with rich resource since ancient times. Due to Wuxi's commercial prosperity, it became a center of commerce in the late Ming Dynasty (1368–1644). During the Qing Dynasty (1611–1911), this area became a gathering place for merchants and politicians. Huishan Ancient Town is the most representative historical area in Wuxi (Fig. 1), and its history is closely related to the urban development.

According to the investigation, the development of Huishan ancient town can be divided into four main periods: the first, the formation period-Ming-Qing period (1368–1644), refers to the formation stage according to the main characteristics of historical buildings; the second is the continuation period-the period of the Republic of China (1840–1912), based on the original architecture, western elements have been incorporated under the social background at that time; the third period is the rupture period-from the Republic of China to 2000s, the physical form of the previous period was destroyed due to social instability, and some poor-quality buildings were formed. The fourth period is the new transformation period-from 2008 to the present, the formation of new historical space by selecting historical elements into new space.

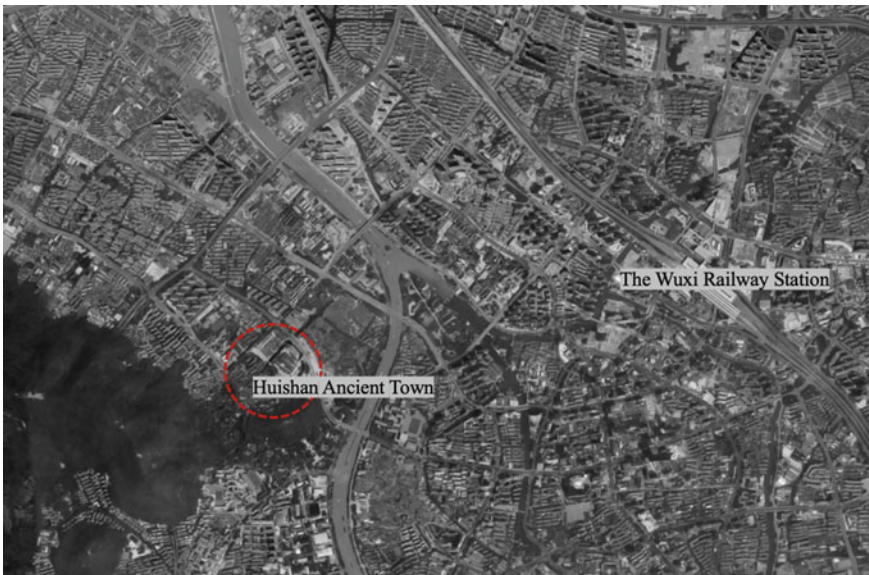


Fig. 1 The location of case area

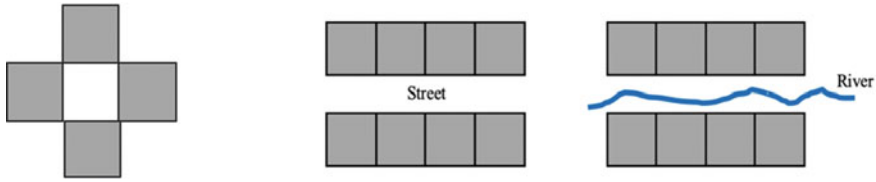


Fig. 2 The basic building form (the left) and the physical forms of this area

3.2 Morphological Analysis of Each Period

The Formation Period-Ming-Qing Period Before the Ming Dynasty, ancestral halls basically belonged to official temples, and during the Jiajing period (1522–1566), private ancestral halls were allowed. A unique type of historical building—ancestral temple building was born in this period. Wuxi is adjacent to the Beijing-Hangzhou Grand Canal and has become one of the main places for industrial and commercial development.

In order to offer sacrifices to ancestors and demonstrate their social status, local noble families began to build their own buildings for worshipping ancestors. These buildings mainly located on the both sides of the water system of this area. The basic spatial form of Huishan Ancient Town was gradually formed during this period (Fig. 2).

The Continuation Period-The Period of the Republic of China During this period, a large number of western cultural elements poured into China. The architectural and spatial structure of this period has the characteristics of combining Chinese and Western elements, such as architectural space (in the form of Huizi), materials and decorations. The Yang Oufang ancestral hall is the most distinctive historical building of this period (Fig. 3).

The Rupture Period-from the End of Republic of China to 2000s After the founding of New China (after 1949), many local property rights were taken back by the government and these property rights were changed from private to public. During this period, the buildings were used by the government to relocate housing displaced people. One building was usually used to house several families that caused the courtyard gradually became the shared space. With the urban development, the population began to increase, which led to many illegal building parts being added to the existing buildings. The living environment in this area began to deteriorate and gradually failed to meet the needs of the residents (Fig. 4).

From 2008 to Present With the development of the city, the dilapidated area could not represent the contemporary urban image of Wuxi. Since 2006, the government has started the transformation project, selecting historically representative elements to insert into the new space. Some illegal buildings and other structures were demolished during the transformation process. At the same time, local residents were relocated to other parts of the city. The new heritage space consists of the heritage as the core



Fig. 3 The Yang Oufang ancestral hall



Fig. 4 The Huishan ancient town before 2003

element, with commercial and tourist elements implanted (Fig. 5). The historical buildings are given new functions and become new representatives of the urban culture.

The designers selected the most representative morphological characteristics of the historical evolution process. The ancestral hall and the street pattern follow the main morphological characteristics of the first two periods.



Fig. 5 The new historical space

4 Discussion

According to the morphological analysis, the case area has gone through four main historical morphological periods (Table 1), and the changes in its morphological characteristics are strongly related to the social and cultural context of each morphological period. During the historical periods, the morphological system kept changing and adapting to the changing social culture and local daily life. The morphological characteristics of different morphological periods have specific memory, such as the selected representative historical elements. These physical elements have the identity of local culture and are a symbol of local culture.

However, in the latest transformation process, the residents were relocated in order to develop tourism and commerce. This has led to the destruction of the original social structure, as the daily lives of the inhabitants are very closely related to the physical form. The new heritage space was implanted with commercial and tourism elements, which reflects the designers wants to enhance the attractiveness of the space with these elements. The new space constructs the relationship between people and space through heritage, which provides culture meaning to the experience of tourists. This new type of visitor-oriented spaces needs to rely on the dissemination and experience of culture to maintain the vitality of the space.

In the new round of urban planning, the cultural revival has been emphasized. As the most representative urban heritage area of Wuxi, the further renewal of Huishan Ancient Town has an important role in urban development.

Table 1 The morphological process of case area

Morphological period	The characteristics	Function
The formation period-Ming-Qing period	The ancestral halls; the courtyard house; the terraced houses	Residence, worship ancestors, commerce
The continuation period-the period of the Republic of China	The western building elements, materials	Residence, commerce
The rupture period- from the end of Republic of China to 2000s	Illegal building	Residence
From 2008 to present	The representative morphological characteristics of historical process	Tourism, commerce

5 Conclusion

Currently, urban conservation in China has entered into a new process—from physical structure conservation to the integration of overall resources with more attention to local residents. This paper illustrates that the morphological characteristics of physical spaces are related to the social culture of different periods. Therefore, while focusing on the restoration of physical space, the relationship between social attributes and local culture also needs to receive attention. In addition, there is a relationship between morphological characteristics and changes in the function of the space, that is, the needs of the users of the space.

Morphological studies can help decision makers understand the dynamic factors of transition of physical form. Due to the driven force of physical spatial change are easier to explain at a small scale than at the urban scale, this helps to clarify the dynamic relationship between the physical structure and socio-cultural characteristics of heritage areas. This relationship should receive more attention in the further design of heritage areas.

The urban design perspective is a complex system because it is associated with various aspects of the city. This study only provides a superficially interpretation of the relationship between morphological characteristics and social culture in different periods. In further research, other aspects should be considered, such as the connection of morphological characteristics with environmental quality and the psychological and spiritual needs of users. These factors are major factors in constructing urban spatial quality and local culture, which should be paid more extensive attention.

Notes

The 14th Five-Year Cultural Plan was issued by the State Council in 2022.

Acknowledgements Part of the data of this study comes from first author's Ph.D. research at Polytechnic University of Turin, Italy.

Funding This study is supported by Philosophy and Social Science of Jiangsu Higher Education (2021SJA0913), Natural Science foundation of Jiangsu Higher Education, the project number is 20KJB560011.

References

1. Ye L (2011) Urban regeneration in China: policy, development, and issues. *Local Econ* 26(5):337–347
2. Wu F (2022) *Creating Chinese urbanism: Urban revolution and governance changes*. UCL Press
3. Ren X (2008) Forward to the past: historical preservation in globalizing Shanghai. *City Commun* 7(1):23–43
4. Ren X (2011) *Building globalization: transnational architecture production in Urban China*. University of Chicago Press, Chicago
5. Ren X (2018) A genealogy of redevelopment in Chinese cities. In: Ye L (ed) *Urbanization and Urban Governance in China*. Governing China in the 21st century. Palgrave Macmillan, New York
6. Ren X (2020) Historical preservation in Rust-Belt China: the life and death of Jihong Bridge in Harbin. *J Chin Architect Urban* 2(2):916
7. He S, Wu F (2005) Property-led redevelopment in post-reform China: a case study of Xintiandi redevelopment project in Shanghai. *J Urban Aff* 27(1):1–23
8. Fang K (2001) Contemporary redevelopment in the inner city of Beijing (当代北京旧城更新). China Architecture & Building Press, Beijing
9. Zhang Y, Fang K (2004) Is history repeating itself? From urban renewal in the united states to inner-city redevelopment in China. *J Plan Educ Res* 23(3):286–298
10. Zhang Y (2008) Steering toward growth: symbolic urban preservation in Beijing, 1990–2005. *Town Plan Rev* 79(2–3):187–208
11. Chen F (2008) Typomorphology and the crisis of Chinese cities. *Urban Morphol* 12(2):45–47
12. Romice O, Chen F (2014) Preserving the cultural identity of Chinese cities in urban design through a typomorphological approach. In: Tian Y, Gu K, Tao W (eds) *Urban morphology, architectural typology and cities in transition*. Science Press Beijing, Beijing, pp 172–197. ISBN 9787030402189

Before Becoming an Independent Building: A Study of the Mixed Nature of Chemistry Laboratory Space from the 16th-18th Centuries



Mingzhu Lei  and Tong Cui

Abstract With the rapid development of science, the value of study in laboratory building for scientific research is becoming increasingly prominent. Focusing on the chemical science, this paper presents a historical study of the chemistry laboratory space before the formation of independent building from an architectural perspective. It is found that with the development and independence of chemistry, chemistry laboratory space passed through a state of mixture with private residence space, court space and pharmacy space, and eventually became independent building in institutions such as science societies and universities. Such a process also indicates a shift from practical-oriented chemistry practices to purely scientific research-oriented experimental activities. The study of the mixture of chemistry laboratory space helps to establish a systematic lineage of the evolution of laboratory building and provides a historical basis and broader perspective for the subsequent research.

Keywords Chemistry · Chemistry laboratory · Chemistry laboratory building · Space · Mixture · Laboratory building

1 Introduction

The three major crisis that occurred in the late Middle Ages destroyed the prosperity of the mid-medieval scientific revival. The population decline caused by the Great Famine and the Black Death, the political conflicts caused by people's revolts and noble wars, and religious turmoil greatly inhibited the development of science during this period. With the arrival of the Renaissance, the interweaving of the humanities, arts and sciences took on a new intertwined scene. The collision and fusion of ideas is fully reflected in literature, art, architecture, politics, philosophy and science. Among them was the intertwining of art and science in the Renaissance resulting in the communication between artists and scientists that lasted throughout

M. Lei (✉) · T. Cui
University of Chinese Academy of Sciences, Beijing 100190, China
e-mail: leimingzhu16@mailsucas.ac.cn

© The Author(s), under exclusive license to Springer Nature Singapore Pte Ltd. 2024
M. Casini (ed.), *Proceedings of the 3rd International Civil Engineering and Architecture Conference*, Lecture Notes in Civil Engineering 389,
https://doi.org/10.1007/978-981-99-6368-3_71

871

the fifteenth century. Along with the background of the rapid rise of the capitalist economy in the seventeenth century, modern science began to formally come to the forefront of history. A great change in the conception of science occurred in the process, witnessing the rise of experimental science (experimental natural philosophy). These transformations eventually led to the completion of the scientific revolution in the seventeenth century, when the natural philosophy led by Aristotle's theory was replaced by a radically new system. During the eighteenth century of the Enlightenment, scientific knowledge not only broke through the narrow circle of academic elites and spread to the public on a wider scope, but also was widely applied to serve human society and improve the quality of human life.

Laboratory space existed long before the formation of modern science, but they were significantly different from the space in which scientific research is done in the modern world. It usually refers to a place where manual work and practices are carried out, and is often highly relevant to chemical practice. With the scientific revolution in the seventeenth century and the chemical revolution in the eighteenth century, the science represented by chemistry began to be independent. Against this background, the chemistry laboratory gradually transitioned from a mixed space to an independent building.

A review of the early literature on chemistry laboratory shows that research was mainly conducted in the field of the historiography of science. For example, Owen Hannaway's comparative investigation of early seventeenth century "Uraniborg" and "The Chemical House" emphasizes the differences in the social responsibilities of scientists as citizens [1]. Graeme Gooday proposed exploring the history of the laboratory in a broader context of concepts [2]. Ursula Klein's study of early experimental spaces and their histories [3], etc. There are also studies of the laboratory by Gieryn [4], Kohler [5], Smith [6], and others that combine the historiography of science with the sociology of science. However, there is still a notable lack of research on the physical spaces of chemistry laboratory. As Robert G.W. Anderson said: "Chemistry laboratories, as buildings, have been surprisingly little studied by historians of science; interest has been focused on them more as sites of specific scientific activity, with particular emphasis on the personalities who worked within them." [7]

Based on an architectural perspective, this paper aims to study the state of existence of chemistry laboratory space before the emergence of independent chemistry laboratory building, as well as to sort out the changing stages of chemistry laboratory space combined with the history background of early chemical research, and to comprehensively present the process of early chemistry laboratory space from mixture to independence.

2 The Mixed Nature of Early Chemistry

Being a space for chemical experimental activities, the evolution of chemistry laboratory space is inevitably closely related to the development of chemistry, and is a concrete representation of the history of chemistry in space. Just like the mixed

nature of the chemistry laboratory space, early chemistry was similarly mixed until it became an independent science in the late eighteenth century. Therefore, a review of the development of early chemistry can help clarify the essential causes and historical background of the evolution of chemistry laboratory space, and present a complete overview of the changes in early chemistry laboratory space.

Chemistry had already sprouted as early as the primitive period of science. The ancient Mesopotamians acquired partial knowledge of the properties of natural chemicals and applied them in the manufacture of pottery, glass and metal [8]. In the classical period of science, the exploration of the basic composition of the material world in natural philosophy directly influenced the early development of chemical theory. Aristotle's theory of the four elements assumes that matter is all composed of the four elements of earth, water, air and fire, and that change in matter is accomplished by transformation of the underlying states of matter instead of by rearrangement of atoms [9]. The theory of the four elements developed in the Middle Ages as an important theoretical basis for alchemy, one of the prototypes of early chemistry. During the Renaissance, Aristotle's philosophical view of nature was challenged from Paracelsusism. Paracelsus added a third component, salt, to Jabir's *حيان بن جابر* "mercury-sulphur theory" and argued that all matter, including metals and minerals, is composed of these three components. Medical chemistry, represented by Paracelsusism, was another prototype of early chemistry. The practical goal is the preparation of drugs by metal extraction, while the theoretical goal is to explain human metabolic process and diseases by chemistry [10]. One of the most important achievements of medical chemistry was to facilitate the entry of early chemistry into universities as an adjunct to medicine, laying the foundation for the acceptance of chemistry as an independent subject in the eighteenth century. With the rise of mechanistic philosophy and experimentalism in the seventeenth century, Aristotelianism and Paracelsusism were replaced by Robert Boyle's mechanistic chemistry. Robert Boyle used mechanistic philosophy as a theoretical guide, while conducting observations and chemical experiments to liberate chemistry from old modes [11]. Robert Boyle introduced chemistry to science in the seventeenth century, Antoine-Laurent de Lavoisier achieved the chemical revolution (Gas mechanics revolution) by studying gases, and transformed chemistry into a rational and quantitative science in the eighteenth century. Meanwhile, chemistry was gradually separated from medicine in the university and became independent.

Before chemistry became an independent science, the practice of chemistry did not usually take place in a specialized space. Early chemical practices, represented by alchemical experiments, generally occurred in the residences of alchemists and in the courts. The practice represented by pharmaceutical experiments is widely found in pharmacies and some universities. It was not until the emergence of institutionalized scientific organizations, represented by the Royal Society, that a model of scientific research for the purpose of purely chemical studies developed. The chemistry laboratory space, which was once mixed with other spaces, was gradually separated and the need for an independent building began to sprout. In this process, the interest in chemical practice shifted from personal to institutional, from the mysticism of alchemy and the utilitarianism of metallurgy and pharmaceuticals to the pursuit of

pure scientific research, and the laboratory space that contained the practical activities was a visual reflection of this transformation.

3 Chemistry as a Personal Hobby: Mixture of Chemistry Laboratory Space and Private Residence Space

Historians of science have found that early practical activities related to scientific experiments did not take place in a specially designed space at first, but often in the humble space of a researcher's private residence. At this time, the role of scientist had not yet been formed, and the social identities of those who did these practices were varied and included artisans, doctors, philosophers and scholars, merchants, nobles, etc. In such a case, using a part of the domestic space in a private residence as a space for experimental activities is an obviously easier way. In this mixed space with the experimental site, the private residence is not only used as a living place for the researcher, but also given additional functions such as thinking, writing, observing and experimenting. The private residence thus became one of the important places where different people pursued and explored natural knowledge in the early development of science, and largely witnessed the emergence of various natural knowledge [6]. Alberti's ideal study, proposed by Feon Battista Alberti, is considered to be the prototype of the image of academic space for families and scientific institutions [12] (see Fig. 1). Typical examples of this mixture of chemistry laboratory space and private residence space are "Uraniborg" by Tycho Brahe and "The Chemical House" by Andreas Libavius.

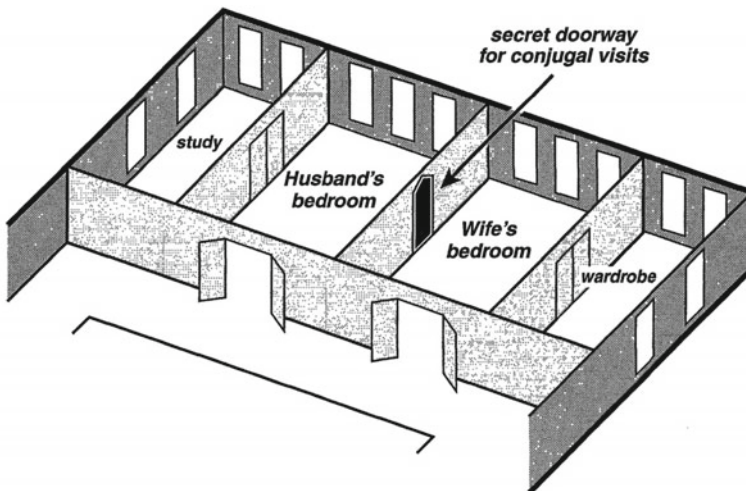


Fig. 1 Alberti's ideal study

3.1 “*Uraniborg*” by Tycho Brahe

In 1576, Frederick II, King of Denmark, gave the island of Hven to Tycho Brahe and sponsored the construction of “Uraniborg”, including the main house, the observatory and other ancillary facilities for his residence and research and practical work in astronomy and chemistry (see Figs. 2 and 3). The main building of the “Uraniborg” consists of a quadrangular central square and circular bays located on the north and south sides. The domestic space is mainly located within the central square and consists of two floors and a basement. On the first floor, D is described as the winter dining room, while the other three rooms E, F and G are used as spare bedrooms, but contain desks and beds for the Brahe’s students. It seems to suggest the possibility that the research activity has been spill over into the bedroom area. The second floor contains the summer dining room, rooms for the king and queen, etc. A partial third floor space is designated as an assistant’s room. The circular bays on the north and south sides are the main areas where scientific research activities are taking place. The observation deck on the second floor is mainly used for astronomy observation and study. Under the decks of the south bay stood Brahe’s own circular study on the first floor. The main chemistry laboratory is located on the basement level, under the study [1]. The chemistry laboratory is a circular space with a central pillar surrounded by circular worktables. Sixteen furnaces are placed around the peripheral wall in an orderly way. Additionally, there is another special laboratory space in the “Uraniborg”, described by Brahe as “a small hidden chemistry laboratory”. It is the space known as “winter dining room” (D) on the first floor. Its function is mixed that it is considered to be Brahe’s own bedroom, while also serving as a living room and dining room for the whole family.

3.2 “*The Chemical House*” by Andreas Libavius

Andreas Libavius tried to introduce chemistry as a natural philosophy into the university curriculum [13] and in 1597 he published his book “Alchemia”. In the second edition, he proposed the idea of a chemistry laboratory building named “The Chemical House”. Although one of the purposes was to criticize the so-called “aristocratic, indifferent and isolated castle science” expressed in “Uraniborg”, “The Chemical House” still reflects the spatial arrangement of the period and has influenced the chemistry laboratory buildings of later times. (see Figs. 4 and 5).

The study and practice of chemistry as a personal hobby usually comes in the form of alchemy. As the above two examples suggest, the practice of alchemical chemistry usually takes place in private residences. The form of mixture of chemistry laboratory space and residential space is exactly how the early scientific experimental space generally existed, and also expresses a metaphor for the secrecy of early chemistry represented by alchemy to some extent.

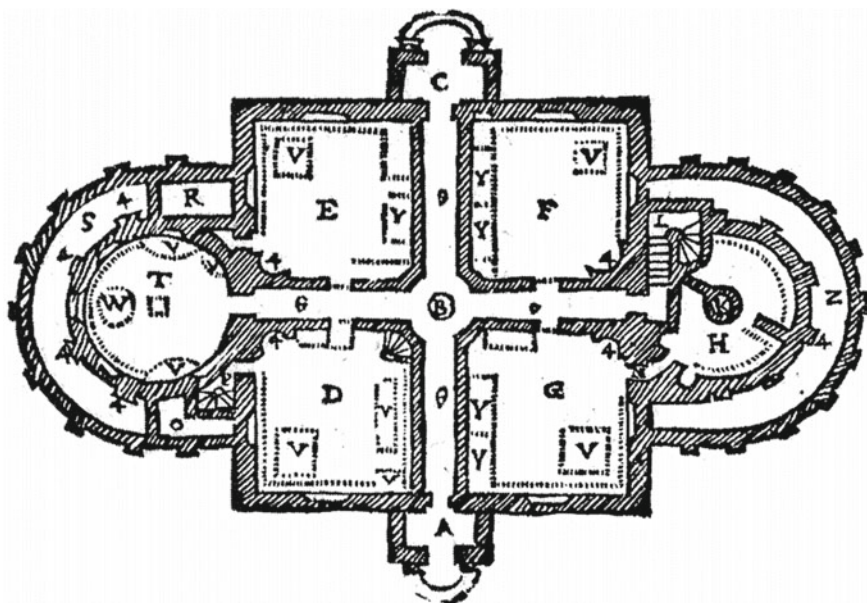


Fig. 2 “Uraniborg”: ground plan

4 Chemistry as a Court Economic Instrument: Mixture of Chemistry Laboratory Space and Art Space

Experimental activities related closely to chemistry were highly prevalent in the noble courts of the sixteenth century. The reason why the court nobles actively pursued alchemy-related chemical practices, besides the personal interests of some nobles, was that the exploitation of natural resources was the core of the political and economic policies of the sixteenth century court. The chemical practices involved alchemy are considered to be closely related to mining metallurgy, and although differences exist are equally applicable in improving the technology of mining and metallurgy [14]. The court’s pursuit of economic goals led directly to the flourishing of scientific activity focused on the practice of chemistry, exemplified by the Medici family in Florence during the Renaissance.

4.1 *The Casino Di San Marco*

Originally a palace, the Casino di San Marco was rebuilt in 1576 by Francesco I de’ Medici, Grand Duke of Tuscany, who planned and added a court art studio and a chemistry laboratory to accommodate his patronage in the arts and sciences. One of the chemistry laboratories, famous for its alchemy and other chemical practices, is



Fig. 3 “Uraniborg”: front (east) elevation

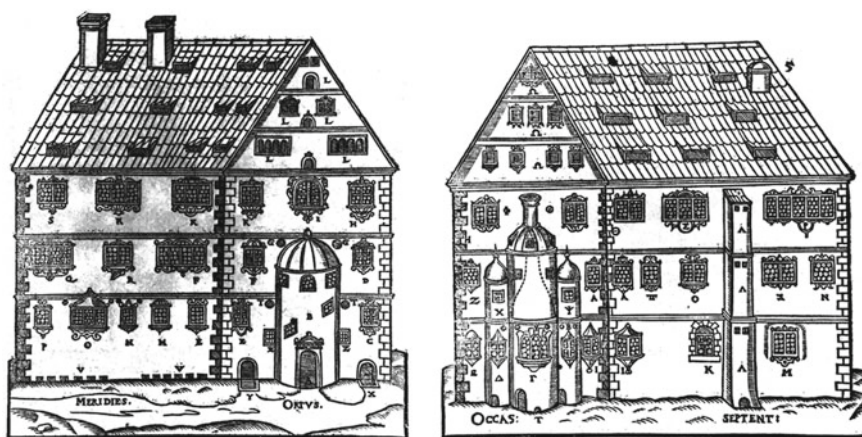


Fig. 4 “The Chemical House”: front (southeast) elevation and rear (northwest) elevation

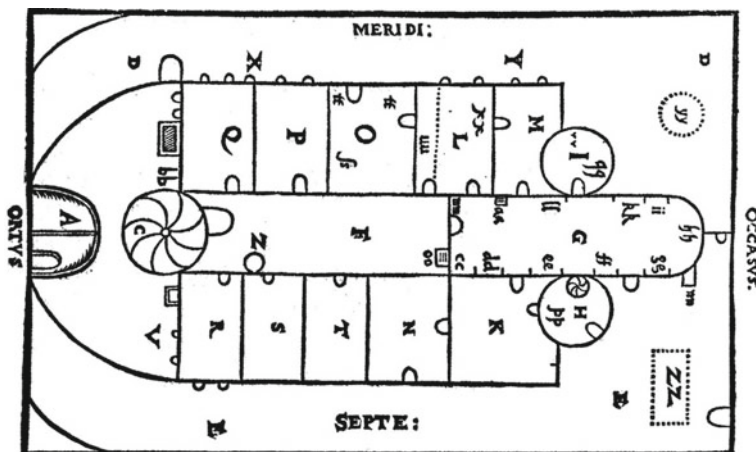


Fig. 5 “The Chemical House”: ground plan. A East gate. B: Porticoed terrace (not marked, but presumably between gate and entrance to house). C: Spiral staircase to lower- and middle-level atria. D: Garden. E: Northern walkway. F: Lower atrium or vestibule of the laboratory. G: Laboratory. H: Adytum with spiral stair to study. I: Assay room tower. K: Storage room for chemicals. L: Preparation room. M: Laboratory assistants’ bedroom. N: Apparatus storage room. O: Coagulatorium. P: Wood storage room. Q: South storeroom. R: Vegetable storage room. S: Wash room or wood storage room. T: Room for undressing. V: Cellar for provisions. X: Wine cellar. Y: Laboratory cellar. Z: Aqueduct (not marked). aa: Entrance to laboratory cellar. bb: Entrance to wine cellar. cc: Steam bath. dd: Ash bath. ee: Simple water bath. ff: Downward distillation apparatus. gg: Sublimation apparatus. hh: Central hearth (focus communis). ii: Reverberatory furnace. kk: Stepped-down distillation apparatus. ll: Serpentine distillation apparatus. mm: Dung bath. nn: Bellows. oo: Coal cellar. pp: Philosophical furnace. qq: Assay furnace. rr: Assay balance. ss: Vessels for coagulation. tt: Distillation using cloth fibers. uu: Press stand. xx: Desks, preparation tables, and mortars for grinding. yy: Fishpond. zz: Site for saltpeater, alum, and vitriol works

known as “Fonderia”. Chemistry practices such as melting crystal, imitating porcelain, making jewels and alchemy were conducted in the Casino di San Marco as well as art practices such as painting, sculpture. The practices are arranged in various rooms and include a distillation room, a smelting room, a forge, a pharmacy, an alchemy laboratory, and an important art glass workshop.

4.2 Uffizi Gallery

In 1560, the Uffizi Gallery was designed by Italian architect Giorgio Vasari for Cosimo I de’Medici, the first Grand Duke of Tuscany, as an office space. The third Grand Duke, Ferdinando I de’Medici, was renovated to include laboratory space for scientific practice. The “Fonderia” also exists in the Uffizi Gallery and is considered to be a laboratory for art that uses fire. “Fonderia” contains a pharmacy, equipped with cabinets, counters with scales and benches; a distillation laboratory, equipped with

stills, pots and benches, to undertake the practice of alchemy, medicine preparation; a blacksmith's workshop with a terrace [15] (see Fig. 6). Goldsmiths, jewellers, furniture makers, painters, sculptors and alchemists are able to share and exchange not only laboratories and their equipment and instruments, but also theoretical and technical knowledge.

Unlike the private alchemy laboratory spaces mixed with residential spaces, the mixture of chemistry laboratory spaces in the noble court is reflected in a more complicated mixture among spaces such as galleries, museums, artists' studios and various chemical practice spaces. The interweaving of art and science practices has been described as an "encyclopedic" gathering of knowledge [15]. The collaboration between artists, artisans and scientific researchers aggregates different types of knowledge in the same space. A new order is constructed in which artistic, artificial and natural research coexist, and the spatial organization becomes a reflection of this new order.

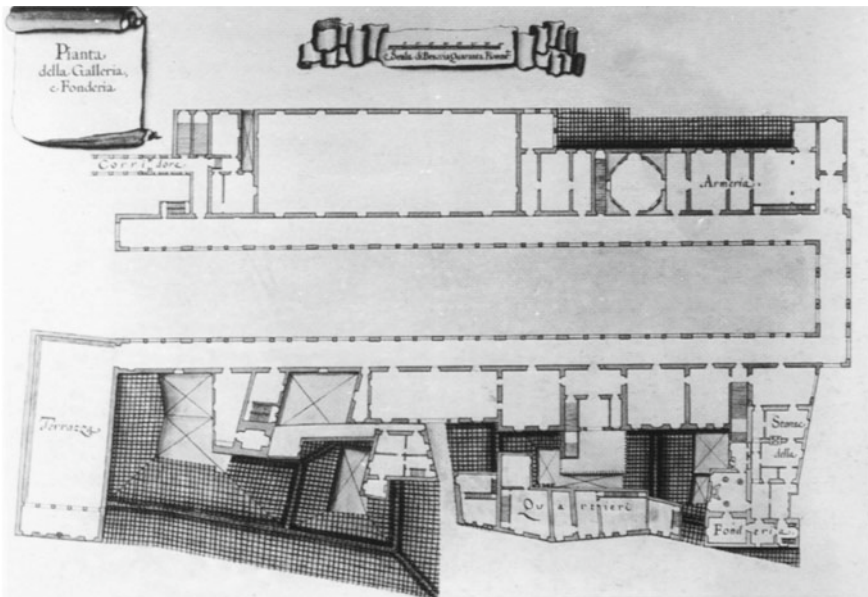


Fig. 6 The "Fonderia" in the Uffizi Gallery

5 Chemistry as an Adjunct to Medicine and Pharmacy: Mixture of Chemistry Laboratory Space and Pharmacy Space

Medical chemistry, one of the important branches of early chemistry, was widely practiced in the pharmacies in secular society, guided by the theory of Paracelsusism. Plenty of chemistry laboratory related to medicine preparation exist in pharmacies and have had a profound impact on the development of chemistry laboratory space. As Ursula Klein said: “There was a particularly strong similarity between pharmaceutical and academic laboratories.” [3]

The plan of the seventeenth century pharmacy shows that the chemistry laboratory was mixed with other practice spaces such as the pharmacy, apothecary’s parlor, kitchen and so on. (see Fig. 7) On the one hand, the close relationship between early chemistry and medicine and pharmacy is the essential reason why the mixture of chemistry laboratory space and pharmacy space occurred. On the other hand, the mixed nature of the space is also the spatial reflection of the development of early chemistry.

6 Chemistry as Institutional Research: The Emergence of an Independent Chemistry Laboratory Building

Whether it was an alchemy laboratory in a private residence, a chemistry laboratory at court, or a chemistry laboratory in a pharmacy, the chemical experiments were conducted for practical reasons rather than for scientific research purposes. Influenced by the ideas of experimentalism of Francis Bacon, the pursuit of independent building for the pure purpose of scientific research emerged for the first time in institutions included scientific societies and universities. Although this attempt is still in the initial stage and the space used for chemistry experiments has not achieved a real sense of independence, the significance of this transformation is revolutionary.

6.1 The Royal Society’s “College” Plan and the Ashmolean Museum at Oxford University

In the early days of the Royal Society, influenced by the “Salomon’s House” in “New Atlantis”, the founders had a vision for a scientific research institution. The so-called new “College” is an institution for research, an independent building dedicated to science research and discussion [16]. Although this plan did not materialize for financial reasons, three versions of architecture design proposals were born from this attempt. They were proposed by Robert Hooke, Christopher Wren, and John Evelyn. These proposals demonstrate for the first time the vision of an independent building

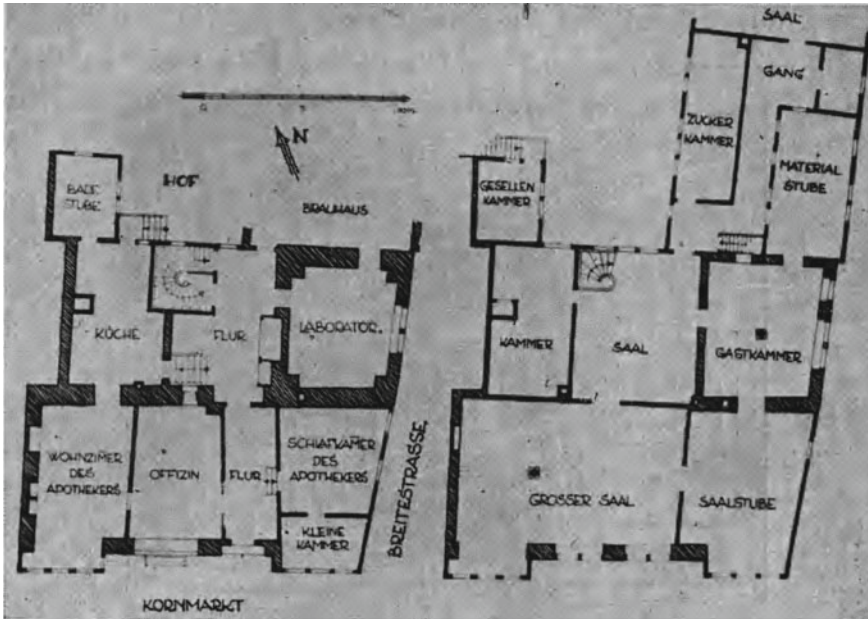


Fig. 7 The plan of the seventeenth century pharmacy. Laborator: Laboratory. Küche: Kitchen. Flur: Foyer. Wohnzimmer des apothekers: Pharmacist’s parlor. Offizin: Pharmacy. Schatzkammer des apothekers: Treasury of pharmacists. Kleine kammer: Small chamber. Kornmarkt: Grain market. Gesellen kammer: Journeyman chamber. Kammer: Chamber. Saal: Lobby. Grosser saal: Gathering hall. Gang: Corridor. Zucker kammer: Sugar chamber. Material stube: Material room. Gastkammer: Guest room. Saalstube: Lobby room. Breitestrasse: Broad street. Hof: courtyard. Brauhaus: Brewhouse. Badestube: Bathroom

for the purpose of scientific research, which has a high research value. The science research building designed by Wren consists of two floors and a basement. The first floor contains the conference room and the second floor is the curator’s room. The loft is a corridor that contains research rooms for members. The roof has an experimental platform that may also assume the function of an anatomical theater. The basement contains a cellar, workshop, kitchen and storage room [16]. However, financial problems made it difficult to accept his proposal, and Robert Hooke was therefore assigned to carry out another architecture design with the premise of meeting the economic requirements. The layout of Evelyn’s “College” consists of a “Pavilion”, a “chapel”, six cells with gardens, a laboratory, a “conservatory of rare plants” and stables. All of this is organized around a central courtyard and an adjoining forecourt [16]. His proposal was considered by the supporters of the new science as a suitable building for science research.

The Ashmolean Museum at Oxford University was built in 1682 by the same architect, Christopher Wren, who is considered to be one of the architects of the Royal Society’s “College” plan. The Ashmolean Museum is breakthrough in that it is not limited to being a storage room for exhibits, but rather as the first institutional

building established in a university for the purpose of science research [17]. It was built to provide a research space for the practice of experimental science, while open to all members of the university, and is fundamentally different from the earlier private chemistry laboratory. It integrated a museum, lecture hall and laboratory [18], and was the first institution designed specifically to study most of the sciences of that period, such as chemistry, anatomy, astronomy, experimental physics, mechanics, etc. According to the documents, the Ashmolean Museum consists of ten rooms, of which the most important and largest spaces in three parts are public spaces. The second (top) floor is the museum, used for the display of the collection; the first floor is the office and public lecture room (“School of Natural Historie”); and the basement is the chemistry laboratory, one of the best custom laboratories in Europe. The remaining rooms are the accommodation rooms and the study of the museum administrator [17, 19–21]. The most important experimental science in the Ashmolean Museum is chemistry. In 1683 Dr Robert Plot was appointed director of the museum and given the title of “Professor of Chemistry”, giving lectures on chemistry three times a week in the lecture theatre on the first floor.

6.2 Chemistry Laboratory Building at Uppsala University

While the seventeenth century Ashmolean Museum in Oxford was the first attempt at independent building, the eighteenth century chemistry laboratory building at Uppsala University is a truly independent institutional chemistry laboratory building. In Johan Gottschalk Wallerius’s chemistry laboratory building, the larger room is an auditorium, prepared for public demonstrations, while the smaller room is a chemistry laboratory [22] (see Fig. 8). His chemistry laboratory building intends to convey a transformation from the private to the public domain of scientific research. His successor, Torbern Bergman, combined the lecture demonstration space with the chemistry laboratory space again in the chemistry laboratory building after the fire reconstruction. In the new building plan, the former smaller chemistry laboratory has been slightly enlarged and marked as a composite space of “auditorium” and “laboratory” [22] (see Fig. 9).

7 Conclusion

The process of chemistry laboratory moving from different forms of mixed spaces to independent building is closely related to the process of chemistry becoming an independent science. Early chemical practices usually took place in spaces such as private residences, courts, and pharmacies, showing a mixture with personal living spaces, art spaces, and pharmacy spaces. In the context of this mixed state, the economic utilitarianism of chemistry was considered to be paramount, and the pursuits of both individual alchemists, aristocratic chemistry enthusiasts and apothecaries were often

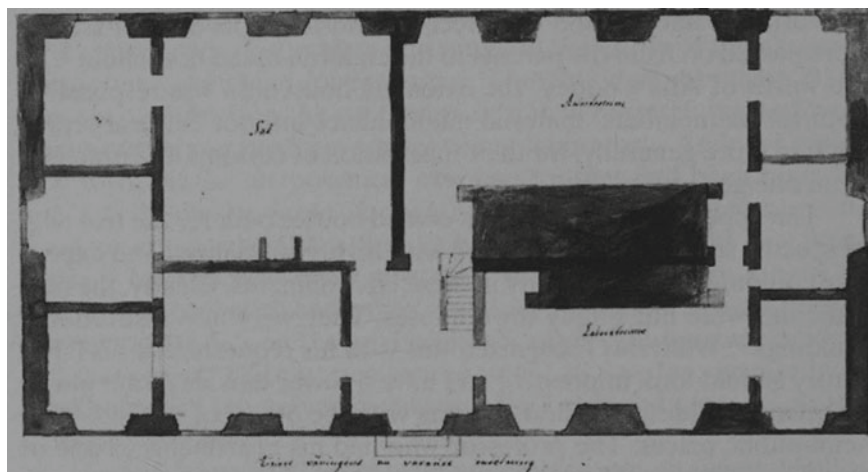


Fig. 8 Johan Gottschalk Wallerius's chemistry laboratory building: ground plan

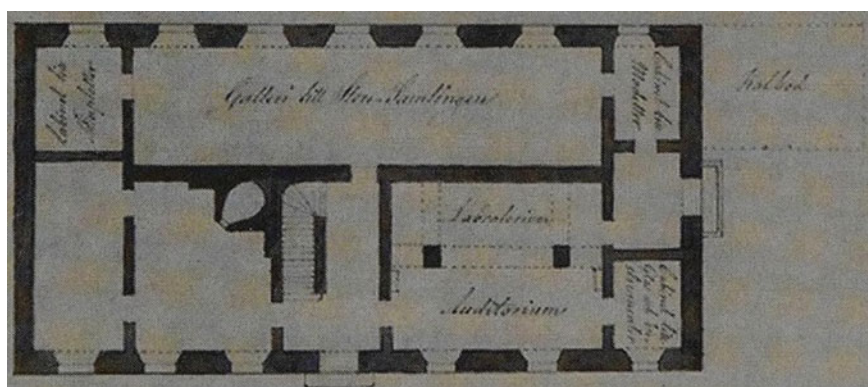


Fig. 9 Torbern Bergman's chemistry laboratory building: floor plan

associated with the practical and economic aspects of chemistry. With the rise of experimental science as well as organized science, pure chemical research developed in institutions represented by science societies and universities. Independent science building including chemistry laboratory began to sprout, and the space of chemistry laboratory changed from early mixed to independent, and finally formed independent chemistry laboratory building in the late eighteenth century. The trend toward independent chemical laboratory building marked the emergence of chemistry as a pure scientific study.

With the rapid development of science, laboratory building, represented by chemistry laboratory building as a space carrier, plays an important role in science (chemistry) research. As a physical space for scientific experiments, the laboratory building

is a direct site for the production of science, and its space layout and related structures have a straightforward impact on experiments. On the contrary, the progress of science will also lead to adaptive changes in the laboratory building space, and the two influence each other. To clarify the existence state of chemistry laboratory space before the formation of chemistry laboratory building is the historical foundation and basis for understanding the formation and evolution of modern chemistry laboratory building space. It also helps to establish a complete historical lineage of the development of laboratory building space and provides broader ideas for research related to laboratory building.

References


1. Hannaway O (1986) Laboratory design and the aim of science: Andreas Libavius versus Tycho Brahe. *Isis* 77(4):585–610
2. Gooday G (2008) Placing or replacing the laboratory in the history of science? *Isis* 99(4):783–795
3. Klein U (2008) The laboratory challenge: some revisions of the standard view of early modern experimentation. *Isis* 99(4):769–782
4. Gieryn TF (2008) Laboratory design for post-Fordist science. *Isis* 99(4):796–802
5. Kohler RE (2008) Lab history: reflections. *Isis* 99(4):761–768
6. Jones A, Bowler PJ, Shank MH et al (2003) *The Cambridge history of science: vol 3, early modern science*. Cambridge University Press
7. Anderson RGW (2013) Chemistry laboratories, and how they might be studied. *Stud History Philos Sci Part A* 44(4):669–675
8. McIntosh J (2005) *Ancient Mesopotamia: new perspectives*. ABC-CLIO
9. Lloyd GER (1968) *Aristotle: the growth and structure of his thought*. Cambridge University Press
10. Weyer J (1992) Alchemie an einem Fürstenhof der Renaissance. Graf Wolfgang II. von Hohenlohe (1546–1610) und Schloß Weikersheim. *Chemie in unserer Zeit*. 26(5): 41–249
11. Hudson J (1992) *The history of chemistry*. Macmillan, London
12. Galison P, Tompson EA, Edelman S (1999) *The architecture of science*. MIT Press, Cambridge, pp 497–540
13. Clericuzio A (2010) “Sooty empiricks” and natural philosophers: the status of chemistry in the seventeenth century. *Sci Context* 23(3):329–350
14. Nummedal T (2008) *Alchemy and authority in the Holy Roman Empire*. University of Chicago Press
15. *Laboratories of art: Alchemy and art technology from antiquity to the 18th century* (2014). Springer
16. Hunter MCW (1989) *Establishing the new science: the experience of the early Royal Society*. Boydell & Brewer Ltd.
17. MacGregor A, Mendonça M, White J et al (2000) *Ashmolean Museum Oxford: manuscript catalogues of the early museum collections 1683–1886: The Vice-Chancellor’s consolidated catalogue, 1695*. Archaeo Press
18. Martínón-Torres M (2012) Inside Solomon’s house: an archaeological study of the Old Ashmolean Chymical Laboratory in Oxford. *Ambix* 59(1):22–48
19. Morrell J, Richards G, Morris PJT (2009) *Chemistry at Oxford: a history from 1600 to 2005*. Royal Society of Chemistry
20. Gunther RWT (1933). *The Old Ashmolean: the oldest museum for the history of the natural sciences and medicine, prepared for the 250th Anniversary of the Opening of the Museum*. Ashmolean Museum (Oxford, GB), University of Oxford, University Press

21. Ovenell RF (1986) *The Ashmolean Museum, 1683–1894*. Oxford University Press, USA
22. Fors H, Wallerius JG, *Laboratory of Enlightenment* (2006). Taking place: the spatial contexts of science, technology, and business. Science History Publications Ltd., p 3

Information Technology and Modeling in Construction

Building Information Modeling-Based Virtual Reality System for Four-Dimensional Progress Simulation and Construction Safety Training



Kun-Chi Wang , Yuan-Hsiu Chou, Guan-Yu Chen, and Jun-Jie Jiang

Abstract In recent years, BIM models have been regarded as a necessary item to be delivered in engineering projects. The owner's demand for BIM is no longer limited to the model itself, and further requires the subsequent application of BIM, of which 4D simulation is the most common extension application. Construction safety in AEC industry is an important issue. In practice, the planning of construction safety must be carried out in advance. That is, the occupational safety planning of the project should be taken into consideration at the design stage. In this way, the chance of reducing construction hazards can be greatly reduced. This research integrates BIM and virtual reality to develop "4D Progress Simulation" and "Occupational Safety Training Simulation" System to present the 4D simulation of the construction process in an immersive way. Through the immersive visual effects, the construction sequence and details of each activity in the 4D simulation can be clearly presented, so as to facilitate the identification of key construction problems and object conflicts in the process. In addition, designers can use the simulation system to check the occupational safety precautions and possible hazards during the construction process due to the immersive nature of immersive VR. An actual project is used for case studying to test the applicability of the system developed by this research. The results show that the simulation system developed by this research can indeed assist the engineers to grasp the construction sequence and construction details at the design stage. It can also prevent possible construction hazards in advance.

Keywords Building information modeling · Virtual reality · Four-dimensional progress simulation · Construction safety training

K.-C. Wang (✉) · Y.-H. Chou · G.-Y. Chen · J.-J. Jiang
Department of Civil and Construction Engineering, Chaoyang University of Technology,
Taichung 413310, Taiwan
e-mail: wkc@gm.cyut.edu.tw

© The Author(s), under exclusive license to Springer Nature Singapore Pte Ltd. 2024
M. Casini (ed.), *Proceedings of the 3rd International Civil Engineering and Architecture
Conference*, Lecture Notes in Civil Engineering 389,
https://doi.org/10.1007/978-981-99-6368-3_72

889

1 Introduction

Prevention measures to ensure safety in both domestic and overseas construction industries have transformed from their conventional forms to promote construction safety and planning. Experienced on-site personnel can improve safety and planning through construction schematics and occupational safety regulations. To improve the effectiveness of occupational hazard prevention, construction safety must be taken into consideration at the design stage, such as through Prevention through Design (PtD). PtD is proposed mainly because the construction industry often regards construction site safety as the responsibility of construction companies. Making plans to ensure construction site safety before construction begins can reduce the probability of occupational disasters [1].

Following a growth in development, virtual reality (VR) technology has been introduced to the education and training of real estate agents, military and police personnel, and medical personnel. A high degree of immersion in VR makes it suitable for application in the construction industry; VR can warn construction workers about occupational hazards and deepen their understanding of potential dangers without undergoing actual harm.

Building information modeling (BIM) and VR technology have not been widely applied in the construction industry because the cost and time required for model building are often only accounted for in architectural design. Although VR can improve the interactive and immersive experience of building information models, third-party experts are often required, which increases the overall construction time and cost [2].

In this study, Unity 3D game engine was used as a platform for integrating BIM with four-dimensional (4D) simulation. The game engine's intuitive design and model compatibility allow designers or engineers to expand the system's functions and simulate integration, which saves additional time and costs from third-party experts. Progress information derived from 4D simulation enables personnel to simulate occupational safety in construction. VR can also be used as a medium for workers to acquire knowledge of work procedures and occupational safety.

2 Literature Review

2.1 4D Progress Simulation

The 3D model displays its geometric and model information through BIM. Combining a construction project schedule with a 3D model is defined as 4D progress simulation. Before 4D simulation was developed, scheduling work procedures for construction projects often required engineers to plan and evaluate projects based on their expertise and experience to determine the optimal construction period and the feasibility of the project [3, 4]. 4D simulation has become a major communication

tool. In addition to benefitting engineers and saving time, 4D simulation provides a more intuitive display through BIM. Thus, 4D simulation has become a powerful tool for designers to preassess construction site hazards [5, 6].

2.2 Integration of BIM into VR

VR requires a head-mounted display and a controller to navigate a virtual environment. VR users can view, interact, and move in the virtual environment through the VR device to experience immersion. VR has a wide range of applications. When applied to engineering education in the construction industry, VR can improve students' motivation and concentration. The clear visual effects of VR facilitate understanding of various construction designs [7, 8]. Additionally, VR can be used to visualize model data, such as labeling model information or describing work procedures; therefore, students can understand complex engineering more effectively [7, 9].

2.3 Integration of 4D Progress Simulation into VR

Boton [6] created a 4D simulation model by using Navisworks and Microsoft Project and converted the model material through 3ds Max to import the model into Unity3D. During the research, Boton [6] found that importing the 4D simulation into Unity3D by using Navisworks causes time loss. BIM and time information must be imported separately into the development platform for 4D simulation development. Although many studies have discussed 4D and VR, no comprehensive construction framework exists for applying 4D to VR. Discussions on 4D construction are mainly centered on synchronous operations and displays rather than on the construction and interaction of BIM in 4D.

2.4 Integration of BIM into Occupational Safety

In occupational disasters in Taiwan, an average of approximately 200 people are injured or killed in the construction industry each year. Effectively carrying out construction safety plans is challenging because conventional safety plans still depend on 2D floor plans and construction schedules to understand the safety facilities required for construction sites [10]. In the early stages of a project, planning the design and the construction safety was not performed simultaneously, which forces engineers to participate in several meetings. Consequently, integrating information and reaching consensus in meetings is difficult, and occupational safety personnel

may find it relatively challenging to plan safety measures corresponding to certain times and places [11].

In many construction projects, occupational safety personnel are often forced to examine the construction plan in the later stages of a construction project rather than proactively participating in creating and modifying the construction plan in the early stages. Thus, the safety assessment of the construction site is overly reliant on the personal experience of on-site operation supervisors or occupational safety personnel. In the event of a complex and highly variable construction project, such personal experience affects the accuracy of identifying potential hazards in the workplace [12].

3 System Development

By using BIM as the foundation, this study provided VR users with a 4D progress simulation and identified potential areas of occupational safety training that users should pay attention to in VR. The 4D progress simulation model was used to engage users in occupational safety training and to remind users to pay attention to hazards in the corresponding engineering stage. Immersive characteristics of VR and temporal characteristics of progress simulation are integrated into the occupational safety training to deepen users' understanding of hazards. In this study, the process of developing the system was divided into four parts: BIM construction, construction schedule development, simulation system development, and simulation system display, as shown in Fig. 1.

3.1 *BIM Construction*

This study used construction engineering as the subject, BIM as the VR simulation environment in Revit, and the construction schedule of the model to implement 4D progress simulation and occupational safety.

To achieve system development and model versatility, this study mainly constructed structural components, such as columns, beams, walls, slabs, stairs, and other preset components. During this process, other nonstructural components were considered and component types or names were self-defined. For example, decorative columns or grilles were built using general model components. This study did not use decorative material components. Any subsequent requirements for progress simulation of finished materials could be fulfilled by creating a standardized method for naming component types during model construction. The new naming rule was incorporated into the model filter for in-depth progress simulation.

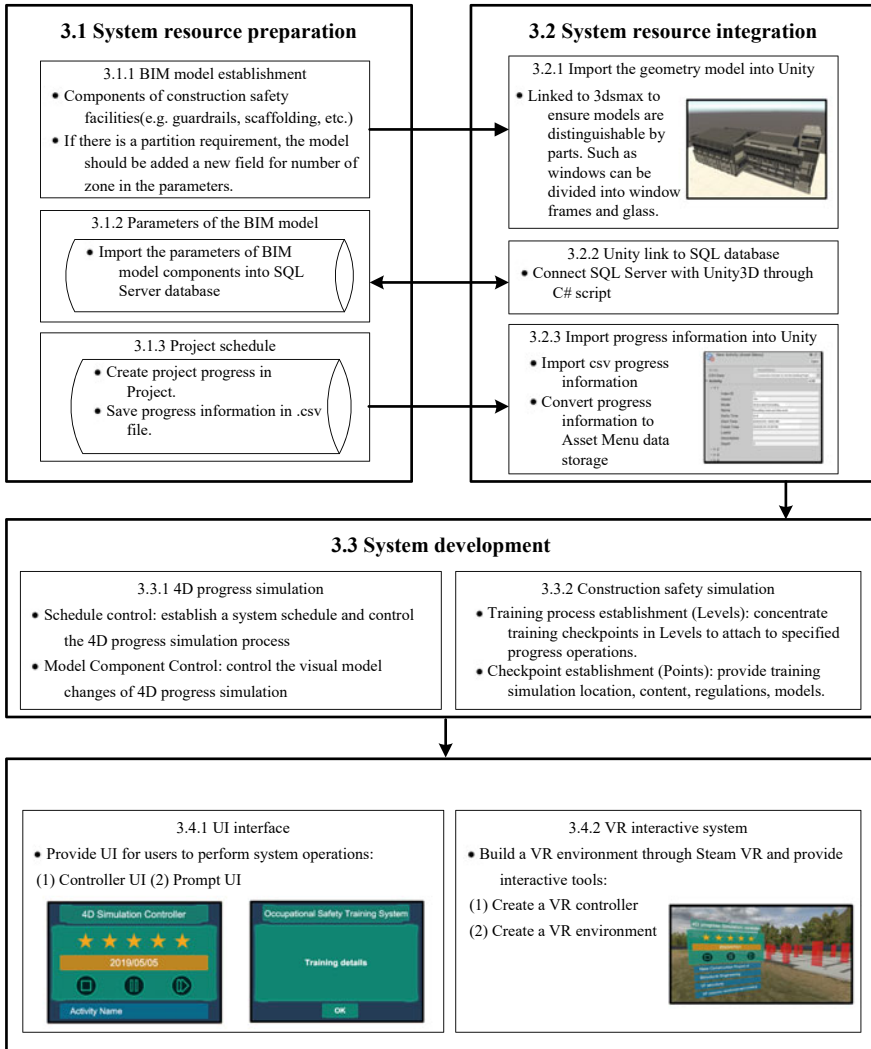


Fig. 1 System development model

3.2 Construction Schedule Development

In this study, the construction schedule was planned using Microsoft Project, and all the job names, durations, start times, finish times, and other information were created in Microsoft Project. After the schedule was created, the mpp file of the project was exported as a csv file to store and use progress information in Unity3D for subsequent reading and modification.

3.3 *Simulation System Development*

This study used Unity3D as the final collection platform to develop system functions. The development method of the simulation system was divided into two parts, namely 4D progress simulation and occupational safety simulation.

1. 4D progress simulation: 4D progress simulation involved combining the model with the schedule activity. After time and the schedule activity were input into the system, the corresponding model was initiated. During the display process, the degree of completion of the construction project was presented based on the cumulative schedule activity. This study divided the control functions of 4D progress simulation into schedule control, SQL server control, and model control to primarily follow the schedule and include additional items (e.g., database or model components) in the schedule. When the time simulation began, the corresponding schedule activity was initiated according to the time, which created the 4D progress simulation display.
2. Occupational safety simulation: In addition to the 4D progress simulation, the proposed system displayed the project completeness level to users. During progress simulation, multiple schedule activities were selected to incorporate simulation levels of occupational safety. After the selected schedule activities were performed, training began by triggering levels. The occupational hazards were examined individually. Users were informed of labor and safety-related precautions and information during the VR experience. VR deepened users' understanding of the causes of common hazards at a construction site and the appropriate safety measures. The 4D progress simulation also provides the time that hazards occur most frequently during construction projects.

4 **Case Study**

This study conducted 4D simulations through the schedule and BIM of a construction case and added occupational safety simulation levels to the selected schedule activity to establish a VR simulation system.

4.1 *BIM Construction*

To enable the simulation system to correctly read the BIM information, the engineers must pay attention to whether the components correspond to their component group types during the construction process, and the offset of the floors should not exceed one floor. If offset is necessary, engineers must record the model ID and pay attention to the correct schedule activity when setting the simulation system. If subsequent progress simulations of finished materials are necessary, finished components may

be added to the model. A standardized method for naming component types should be established, and the new naming rule should be incorporated into the model filter for an in-depth progress simulation.

4.2 Construction Schedule Development

1. Develop a construction schedule on Microsoft Project.
2. Convert the Microsoft Project file to an Excel file after confirming the required work procedure schedule.
3. Confirm whether the name, start time, end time, and outline level have been successfully exported to the Excel file.
4. Delete the columns that are not required (e.g., comment, active, task mode) and then export the Excel file to a.csv file.

4.3 Simulation System Development

Through the 4D progress simulation and occupational safety simulation, the complete geometric model, BIM information, and progress information of the case project were integrated into the scene as necessary to conduct each step of the simulation.

4.4 4D Progress Simulation

The 4D progress simulation method combined the schedule activity with the BIM model and activated the added model components after inputting the time and schedule activity. During the display process, the degree of completion of the case project was presented on the basis of the cumulative schedule activity. The application was introduced as follows:

1. Schedule establishment: When performing 4D progress simulation, the schedule was the foundation of the simulation, and all functions were assigned to the schedule activity to arrange the order of the display. However, information on the current progress was stored as Asset Menu data in the project. Schedule activity must be converted from data to objects to facilitate the execution of subsequent functions.
2. Activity Obj: The present study used the schedule activity as the foundation of the simulation, and Activity Obj was used as a column, shown as Fig. 2. Carried data in Activity Obj were the basic data of schedule activity, the model ID added to the activity, the model components added to the activity, and occupational safety simulation levels.

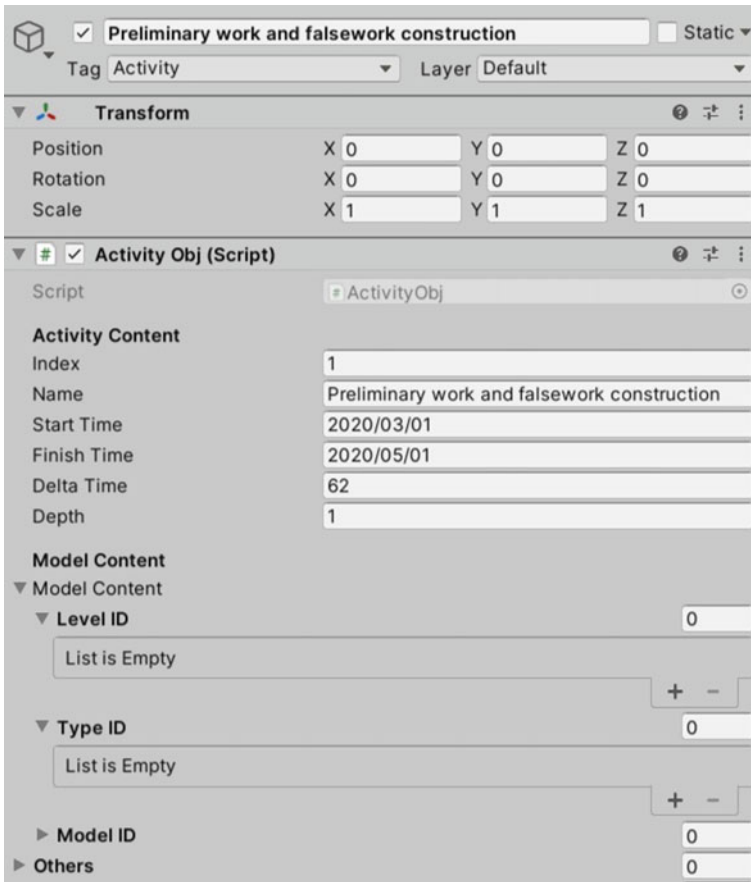


Fig. 2 Activity Obj columns

4.5 Simulation of Occupational Safety Training

With schedule activity as the primary focus, the system implemented the trigger point of the occupational safety stimulation. When the schedule activity was executed, if the occupational safety level was input in the hazards level column of the Activity Obj, the system ceased to run the 4D simulation and asked the user whether they wished to enter the occupational safety level. The users could press the confirm button to enter the level and complete the examination points in sequence. The procedure for setting up the Occupational Safety level and establishing points is detailed as follows and shown in Fig. 3:

1. Create a level as the basis for triggering the schedule activity.
2. Create subitems in the level; the subitems are stored in the level as examination points.

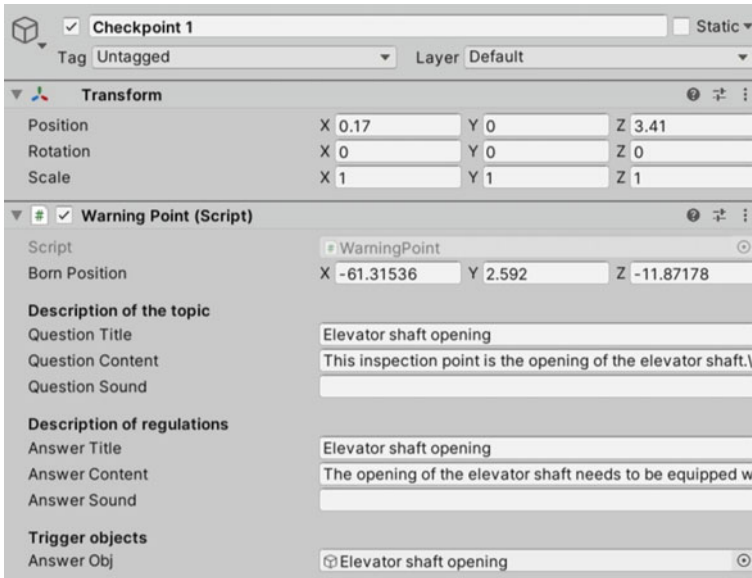


Fig. 3 Completed examination point setting

3. Add the script “Warning Points” to the examination points and complete the examination point setting. The examination point script provides users with the experience location, experience questions (guidance), experience answers (regulations), and the occupational safety facility components that are displayed.

4.6 System Display

After completing the addition to the model, the 4D progress simulation test could begin. During the simulation process, the study activated the execution model and created the color change function in the model while executing the schedule activity. The color change made the updated model easier to read during examination. After the system was activated, the time simulation (i.e., the countdown) began. The 4D simulation was affected by the countdown; if the time equaled the start time of the schedule activity, the schedule activity was activated and the model began running, shown as Fig. 4.

To use the time element from the 4D simulation, this study added the construction occupational safety simulation to the schedule activity to improve understanding of occupational safety events. Examination point 1 at the edge of the opening or at the elevator hoistway opening was used as an example to explain the steps of the experience and the implementation process.

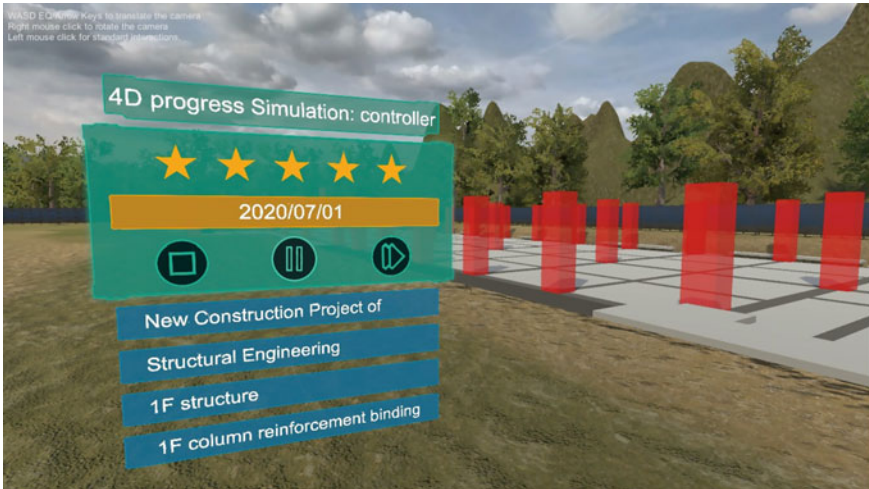


Fig. 4. 4D progress simulation from the perspective of VR users

1. Examination point 1 is explained to users, and users are guided to find the components of the construction occupational safety facilities and understand the purpose of training (Fig. 5).
2. After the user clicks on the hint in the scene (Fig. 6), they can recognize the locations that require occupational safety facility components and read the relevant regulations presented in a pop-up window, shown as Fig. 7.

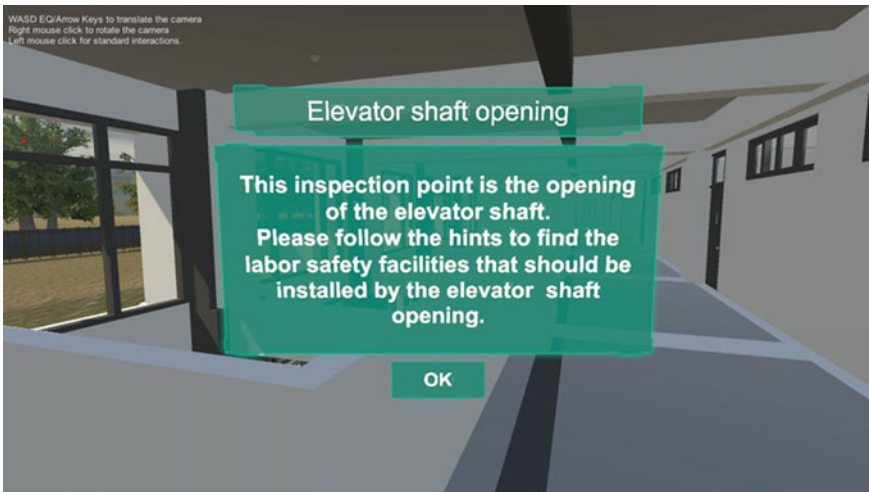


Fig. 5 Window explaining the Point questions



Fig. 6 The level hint button of the scene

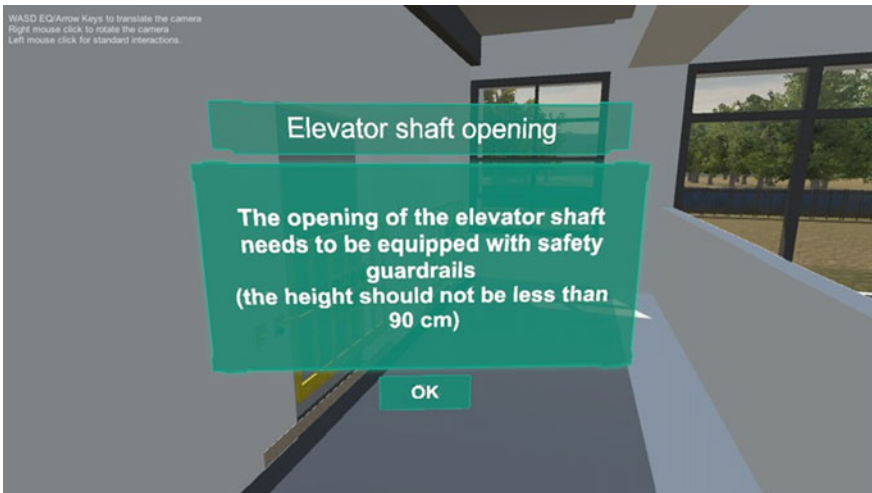


Fig. 7 Display of regulations on occupational safety facility

3. After pressing the confirm button, the user can continue running the 4D progress simulation.

5 Conclusion

This study used the Unity3D game engine as a development environment for BIM, 4D, and VR. During the process, the BIM information is saved in the database through the SQL server, and the BIM model, BIM information, and construction schedule are integrated into Unity3D. In this study, two simulations, namely 4D progress simulation and occupational safety simulation, are performed in Unity3D. Through C# script compilation, a time concept is established in the system for the time simulation. The schedule structure requires that the 4D progress simulation is developed on the basis of the construction schedule. After connecting to SQL server, models are filtered and added to the construction schedule. Finally, by using additive models, occupational safety levels are added to address operations at a particular stage of construction. During the 4D simulation, users can view the visualized BIM model and interact with the occupational safety levels.

Two simulations have been created using VR to achieve an immersive experience. During the VR experience, users interacted with the 4D progress simulation, occupational safety simulation, and various training levels. Users also understood how a construction project starts and ends and received practical engineering knowledge about occupational safety.

References

1. Schulte PA, Rinehart R, Okun A, Geraci CL, Heidel DS (2008) National prevention through design (PtD) initiative. *J Safety Res* 39(2):115–121
2. Horne M, Roupé M, Johansson M (2005) Visualisation using building information modelling. Jorge JA (ed in chief), Dias JMS et al (guest eds). CONVR
3. Coyne K (2008) Leveraging the power of 4D models for analyzing and presenting CPM schedule delay analyses. *AACE Int Trans* 31–39
4. Mezrag Y, Botton C (2021) Integrating 4D simulations and virtual reality environments: an innovative prototype. In: International conference on cooperative design, visualization and engineering. Springer, Cham, pp 103–114
5. Sulankivi K, Kähkönen K, Mäkelä T, Kiviniemi M (2010) 4D-BIM for construction safety planning. In: Proceedings of W099-special track 18th CIB world building congress, vol 2010, pp 117–128
6. Botton C (2018) Supporting constructability analysis meetings with immersive virtual reality-based collaborative BIM 4D simulation. *Autom Constr* 96:1–15
7. Li X, Yi W, Chi HL, Wang X, Chan AP (2018) A critical review of virtual and augmented reality (VR/AR) applications in construction safety. *Autom Constr* 86:150–162
8. Kamath RS, Dongale TD, Kamat RK (2012) Development of virtual reality tool for creative learning in architectural education. *Int J Qual Assur Eng Technol Educ (IJQAETE)* 2(4):16–24
9. Huang Y, Shakya S, Odeye T (2019) Comparing the functionality between virtual reality and mixed reality for architecture and construction uses. *J Civil Eng Architect* 13(1):409–414
10. Chantawit D, Hadikusumo BH, Charoenngam C, Rowlinson S (2005) 4dCad-safety: visualizing project scheduling and safety planning. *Constr Innov*
11. Bansal VK (2011) Application of geographic information systems in construction safety planning. *Int J Project Manage* 29(1):66–77

12. Zhang S, Teizer J, Lee JK, Eastman CM, Venugopal M (2013) Building information modeling (BIM) and safety: automatic safety checking of construction models and schedules. *Autom Constr* 29:183–195

A Method for Semantic City Modeling



Rui Ma , Jiayu Chen , Chendi Yang , and Xin Li 

Abstract Semantic city models have been widely used in computer graphics, geomatics, gaming, planning, construction, and urban simulation. Different from the traditional geometric models which serve for visualization purposes only, semantic city models contain more information, such as location, classification, thematic attributes, functional aspects, and their logical and spatial interrelationships, which facilitate computers to understand the built environment better. However, the availability of such models, case-specificity of city object type and features, and unclear spatial semantics bring challenges to their application. Therefore, this study proposes a method, called OSMsc, for constructing semantic city models, including generating analytical layers for building, vegetation, waterbody, transportation, and UrbanTile objects, exploring the spatial semantics between city objects, calculating geometric properties, and outputting semantic city models in CityJSON format. In the end, this study selected a study area of Paris to demonstrate the construction process of the semantic city models, showing the potential of OSMsc in improving the availability, consistency, and spatial semantics of such models.

Keywords Semantic city model · CityJSON · OpenStreetMap · Python

1 Introduction

With the acceleration of urbanization worldwide, many application domains and use cases at the urban scale benefit from semantic city models. Such semantic city models can be regarded as computer representations of the city objects and their features in the urban built environment [1]. These features not only include geometric and

R. Ma · C. Yang · X. Li (✉)

Department of Architecture and Civil Engineering, City University of Hong Kong, Hong Kong, China

e-mail: xinli87@cityu.edu.hk

J. Chen

School of Civil Engineering, Tsinghua University, Beijing, China

appearance information, but also describe spatial and thematic properties of urban entities. Compared to city visualization models such as Google Maps or Bing Maps, the main advantage of semantic city models is that they integrate heterogeneous data from multiple sources. Such data from different domains are usually related to specific urban objects, and this integration process can be easily achieved by linking domain-specific data with their respective city model objects, which further facilitates machines to utilize rich semantic information for identification, query, and simulation. Therefore, many cities developed and maintained their semantic city models, such as New York, Berlin, and Zurich, to describe their physical environment and solve complex problems in the urban system.

However, there are still three obstacles in the application of semantic city models. First, most cities in the world do not have their city semantic models, and the lack of semantic data limits the potential of these cities to address city-level challenges. Second, the available semantic city models are mainly established by mapping departments at municipal, state, or country levels [1] and universities or academic communities. It results in these models being generally inflexible and case-specific in terms of size, scale, and city object type. Third, the semantic information of a city object is not only related to its inherent information, but also should consider its spatial context. For example, the same two buildings, when located in the city center and the suburbs respectively, can have large differences in building density, vegetation density, and connectivity of the surrounding street network. Considering this, it needs to clarify the spatial relationship and features between objects in semantic city models. To fill these gaps, this paper proposes a method for constructing semantic city models, known as OSMsc, where OSM means that the current data is mainly derived from OpenStreetMap [2], “sc” refers to the semantic city. OSMsc can help city researchers, managers, and decision-makers to easily build such models for a specific city or region and further improve the availability, consistency, and generalizability of semantic city models.

2 Background

Semantic city models are typically being used to represent the physical objects in the urban built environment [1]. The reason why these models need semantics is that humans can easily recognize city objects just based on geometrical representations of the urban surface, but computers hardly divide them into meaningful individuals. Therefore, information such as location, classification, thematic attributes, functional aspects, and their logical and spatial interrelationships would help computers understand city objects more accurately. The international standard for semantic city models is City Geography Markup Language (CityGML), issued by the Open Geospatial Consortium (OGC) [3]. CityGML not only represents the graphical appearance of city models but specifically addresses the representation of the semantic and thematic properties, taxonomies, and aggregations. To make CityGML readable and easily editable for users, Ledoux et al. [4] proposed CityJSON, a

JSON-based encoding for a subset of the CityGML data model. CityJSON re-defines methods to describe common 3D city objects and the interrelationships between them and promotes the establishment, reading and modification of semantic city models. At present, the construction of the semantic model usually requires a great deal of manual fine-tuning or even manual construction [5, 6]. Therefore, this research aims to create an algorithm that can automatically build a semantic city model in CityJSON format for any city and overcome the shortcomings of data unavailability, low coverage, inconsistent features, etc.

Semantic city models are generally composed of geometric and semantic information. Geometric information originally came from observation methods, such as 2D terrestrial views from mobile mapping and 3D point clouds from laser scanning. And semantic information is used to further distinguish the above geometries. For example, semantic tags turn a solid into a building, and turn spatial polygons into roof surfaces, ground surfaces, or wall surfaces. Models with mere geometry are like a collection of polygons or solids, and they may be useful in visualization, but their potential in spatial analysis or related simulations are hindered by the lack of semantics [7, 8]. Thus, semantic enrichment would bring new possibilities for the application of semantic models. In this regard, some scholars have carried out related work. Verdie et al. [9] proposed a method that produces a semantically rich 3D city model from a triangular mesh. Their classification step relies on a Markov Random Field to distinguish between four classes—ground, trees, facades, and roofs. Slade et al. [10] used computer vision techniques to develop a semantic enrichment method, which can automatically locate subclasses of windows and doors in CityGML models. Similarly, Goetz [5] explained how to generate highly detailed CityGML LoD4 (levels of detail) models with interior structures from OpenStreetMap. The above methods mainly classify geometries into several urban semantic objects, especially for constructing a higher LoD semantic model of buildings. However, these semantic studies usually have only one or several city objects, which may be affected by the study scale or research preferences and lack the practice of establishing a more comprehensive semantic city model for other cities or regions. Meanwhile, in the current semantic enrichment methods, few focus on the spatial context of city objects, which can clarify the spatial relationship between these objects and help to quantify the surrounding environment of each city object. Therefore, the construction method of semantic city models proposed in this paper not only can easily create city objects for any city worldwide, but also can explore the spatial semantics and features between these city objects.

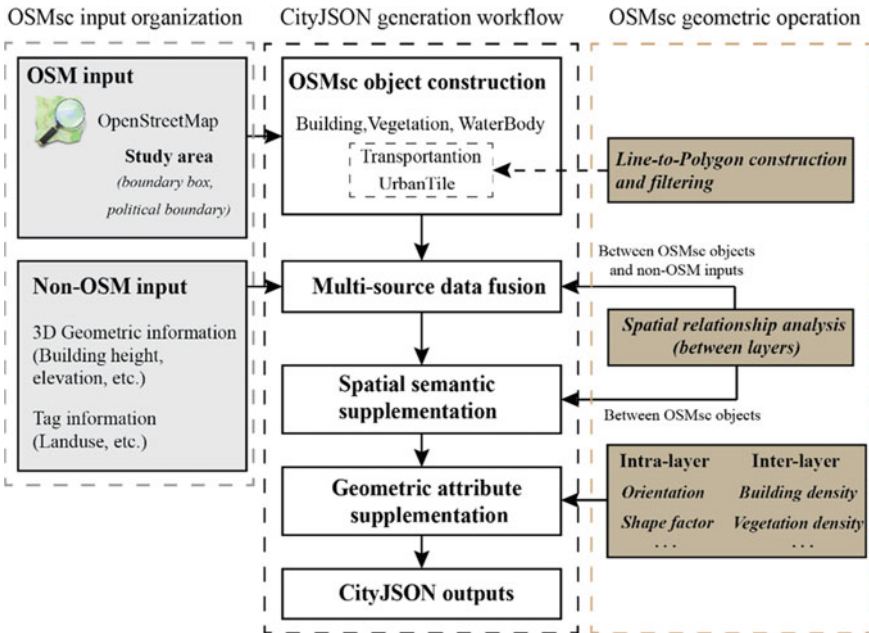


Fig. 1 OSMsc algorithm workflow. Source Created by the authors

3 Methodology

3.1 Overview

The construction method of the semantic city model proposed in this study aims to solve the problems of lack of urban semantic data, incomplete urban model, and unclear spatial semantics. Figure 1 presents the general flow chart of the OSMsc algorithm, which mainly includes three parts, OSMsc input organization, OSMsc geometric operation, and CityJSON generation workflow. Each OSMsc object (Building, Vegetation, WaterBody, Transportation and UrbanTile) has a unique osmscID, remaining stable over the lifetime and allowing to keep track of them in different OSMsc operations. And their geometry is georeferenced with respect to a regional or global coordinate reference system (CRS), which efficiently facilitates spatial queries and analyses at the city level.

3.2 OSMsc Layers

Before constructing a semantic city model, it is required to determine the study area. There are two ways to represent it: (1) boundary box (bbox). Such a bbox is

Table 1 Default tags for building, vegetation and WaterBody objects

Layer name	City object	OSM tags
BldgLayer	Building	key is “building”
VegLayer	Vegetation	natural = wood; natural = scrub; natural = wetland; leisure = park; leisure = garden; leisure = pitch; leisure = playground; landuse = grass; landuse = farmyard; landuse = meadow
WatLayer	WaterBody	natural = water; landuse = swimming_pool; leisure = ice_rink; leisure = swimming_pool; reservoir = water_storage

surrounded by two longitudes and two latitudes and equal to (min lon, min lat, max lon, max lat). (2) political boundary. Unclear official place names or addresses can be found or determined on Nominatim website [11]. In OSMsc, Building, Vegetation and WaterBody objects are obtained directly from OSM, and Transportation and UrbanTile objects are constructed by processing OSM road network.

3.3 BldgLayer, VegLayer and WatLayer

By internally calling the Overpass API [12], OSMsc directly downloads Building, Vegetation, and WaterBody geometries inside the study area from OSM. This study pre-saved some default tags (tag structure: key = value) for these objects, as listed in Table 1. For Vegetation and WaterBody tags, there is no rule to follow, and different cities usually contain different types of Vegetation and WaterBody tags. Thus, the current default tags, which cannot be fully applicable to each city, should be adjusted appropriately according to the actual situation. The construction process of each layer is as follows:

3.4 TransLayer and TileLayer

Since the OSM database lacks sufficient street width and urban Tile boundary information, the Transportation and UrbanTile objects need to be constructed in this section.

Step1: Determine the study area (boundary box or political boundary) and download the street networks from OSM within the study area.

Step2: Construct street polygons with the assumed street width. The default width of a single lane is 3 m,

Step3: Generate TransLayer.

Step4: Fully merge all the previous Transportation objects.

Step5: Since Transportation and UrbanTile are complementary in the 2D urban plane, the area enclosed by the merged streets is regarded as an UrbanTile object.

3.5 Spatial Semantic Supplementation

This part aims to explore the spatial relationship among OSMsc objects, and it mainly establishes the spatial relationship between UrbanTile and internal city objects, including Building, Vegetation and WaterBody. This exploration process is achieved by considering different OSMsc objects in different layers and inferring their spatial relationship through Geopandas.sjoin(op = "intersects"). The result is represented by the corresponding osmscIDs; namely, the osmscID of UrbanTile is stored in the "within_UrbanTile" attribute of Building, Vegetation and WaterBody, and the osmscIDs of these three objects are stored under the "contains_Building", "contains_Vegetation" and "contains_WaterBody" attribute of UrbanTile. Currently, the spatial semantic analysis takes a layer as a computing unit, and OSMsc only analyzes the spatial relationship between the two layers each time.

3.6 Geometric Attribute Supplementation

OSMsc mainly calculates the geometric properties of polygon objects, including intra-layer and inter-layer properties. Intra-layer properties include polygon area, polygon perimeter, area of minimum rotated rectangle (mrr), area of minimum circumscribed circle (mcc), shape factor (ratio of polygon area to the area of its mcc) and orientation, and demonstration examples of intra-layer geometric attributes are shown in Fig. 2. Inter-layer properties are calculated based on the spatial semantics between two OSMsc layers, including Building/Vegetation/Waterbody density, average height of Building objects, average area of Building/Vegetation/Waterbody objects, average perimeter of Building/Vegetation/Waterbody objects.

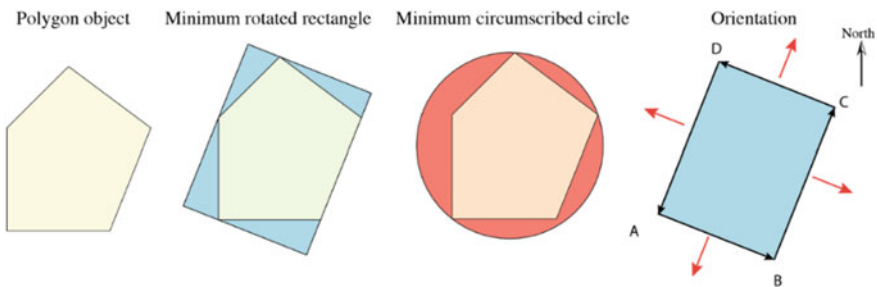


Fig. 2 Demonstration examples of intra-layer geometric attributes

3.7 OSMsc Layer Output

After constructing OSMsc layers, supplementing spatial semantics and geometric attributes, the next step is to produce city objects in each layer as corresponding CityJSON-schema objects. OSMsc city object inherits the geometry type specified by CityJSON [13]. For those that do not explicitly name the object type by CityJSON, OSMsc considers the output object type as GenericCityObject, such as UrbanTile. This study internally calls the cjio [14], a Python package to process and manipulate CityJSON files, to create semantic city objects. Such CityJSON objects mainly contain three main parts: “type”, “geometry”, and “attributes”, where “type” specifies the object type defined by CityJSON, “geometry” stores the geographic location and “attributes” stores the related spatial semantics and geometric information. This section takes each OSMsc layer as a unit to extract the geometric and semantic information of the internal city objects and construct semantic models.

4 Case Study

OSMsc allows researchers and other users to acquire, construct and analyze multi-layer semantic city models. It automates the construction and analysis process and makes semantic city models consistent in research and application. The following section illustrates its functionality with a simple case study in Paris. The boundary box of it is (48.8695, 2.3908, 48.8825, 2.4108), and the study area is about 2.5 km². Following the proposed algorithm in Sect. 3.2, OSMsc constructs BldgLayer, VegLayer, WatLayer TransLayer and TileLayer. The spatial distribution and total amount of each city object are shown in Fig. 3.

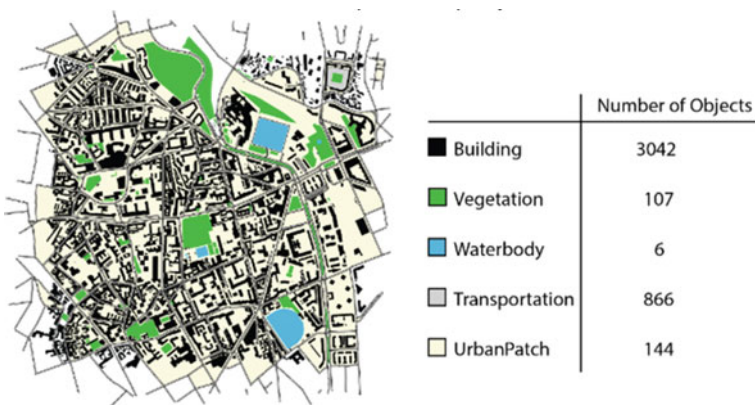


Fig. 3 Superimposed multi-layered city objects

Then, this study used `Geopandas.sjoin(op = "intersects")` to infer the spatial semantics between OSMsc layers. Semantic labels, like "within_UrbanTile", "contains_Building", "contains_Vegetation" and "contains_WaterBody", are filled in corresponding city objects. Based on the spatial connections, OSMsc enriches the spatial features for UrbanTiles. For geometric attributes, this case study calculated the typical intra-layer and inter-layer features of Paris. Figure 4a shows the calculation results of intra-layer features, including mrr, mcc, shape factor, and orientation. All area and perimeter are calculated by Shapely, a python package. The shape factors of Paris range from approximately 0 to 0.95, indicating that the shape of the UrbanTiles in Paris is diverse. In addition, UrbanTiles are mostly east–west facing. Figure 4b presents the inter-layer geometric features in three cities, including average building height, building density, vegetation density, and waterbody density. The average building height of Paris's UrbanTiles varies widely, from 3 to 30m, where high-rise buildings are mainly concentrated in the western region. The building density in the study area changes steadily, less than 0.4. The distribution of vegetation density and water density is discrete, even if those attributes of some UrbanTiles exceed 0.7.

Finally, OSMsc outputs the constructed city objects as the CityJSON-schema semantic model. Figure 5 is the visualization result when uploading the CityJSON models to ninja [15]. The surrounding sub-images are samples of each object in JSON format. Among them, "type" specifies the type of CityJSON object, "geometry" includes geometry type (such as Solid, MutliSurface), LoD and boundary information (footprint nodes of polygons), "attributes" include osmscID, geometric attributes, and spatial semantic information, etc. The red boxes highlight the representation method of the semantic information, which semantically links city objects in OSMsc different layers.

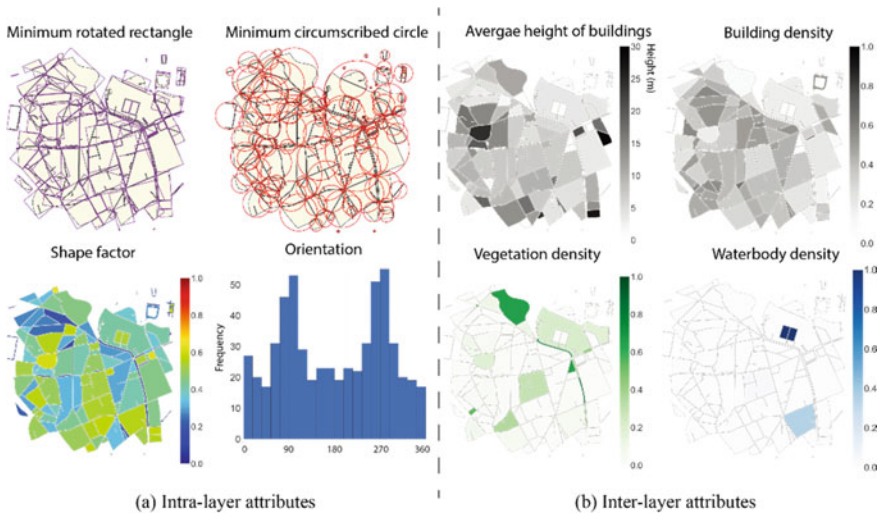


Fig. 4 Geometric attributes of UrbanTile objects

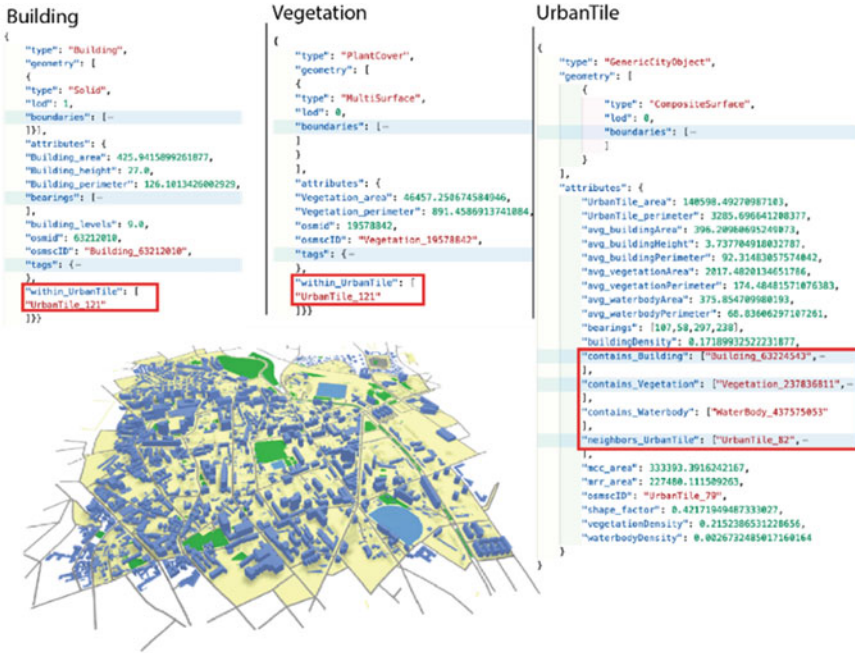


Fig. 5 Visualization of CityJSON semantic models

5 Conclusion

Semantic city models play an important role in computer graphics, geomatics, gaming, urban planning, and urban simulation [1]. And the Open Geospatial Consortium (OGC) has proposed the international standard for semantic city models, i.e., CityGML. However, at present, only New York, Berlin, and Zurich have their own semantic models, while most cities in the world still do not. Even though available, most of them are case-specific, and inconsistent with city object types and features. These semantic models ignore the spatial semantics of each city object, i.e., the spatial relationship between city objects in the urban context. To fill these gaps, this study proposed OSMsc algorithm for semantic city model construction. The city semantic model constructed by OSMsc includes city object types, well-defined LoDs, spatial and thematic attributes, and relations. A simple case in Sect. 4 demonstrates the above workflow of OSMsc, and the generated city objects can be parsed by the CityJSON software. From a macro point of view, the urban semantic model constructed by OSMsc is not just a simple superposition of multi-layer urban objects but has a vertical hierarchy with rich spatial semantics.

Although OSMsc demonstrated its practicality and scalability in this study, it is still subject to limitations and can be improved in future studies. First, CityGML defines five consecutive levels of detail (LoD). But limited by the current public data

sources, the city objects constructed by OSMsc are mainly at LoD0 and LoD1. Thus, the LoD level needs to be improved. Second, the CityGML data model is extended for specific applications through so-called Application Domain Extensions (ADEs). OSMsc lacks such extensions currently, and future work needs to connect to the ontology knowledge graph of some application fields, such as materials, energy, and transportation. Third, OSMsc only calculates Polygon-based geometric features at present. Regarding more complex network and spatial weights analysis, it needs to be combined with OSMnx [16], PySAL [17], momepy [18] and other Python packages for a more comprehensive quantitative analysis of urban scenes.

At present, OSMsc is freely available online at <https://github.com/ruirzma/osmsc>.

References

1. Kolbe TH, Donaubaue A (2021) Semantic 3D city modeling and BIM. In: Urban informatics, pp 609–636. https://doi.org/10.1007/978-981-15-8983-6_34
2. OpenStreetMap. <https://www.openstreetmap.org/>. Last accessed 15 Nov 2021
3. OGC (2012) OGC city geography markup language (CityGML) encoding standard. https://portal.ogc.org/files/?artifact_id=47842
4. Ledoux H, Arroyo Ohoi K, Kumar K, Dukai B, Labetski A, Vitalis S (2019) CityJSON: a compact and easy-to-use encoding of the CityGML data model. Open Geospatial Data Softw Stand 4:4. <https://doi.org/10.1186/s40965-019-0064-0>
5. Goetz M (2013) Towards generating highly detailed 3D CityGML models from OpenStreetMap. Int J Geogr Inf Sci 27:845–865. <https://doi.org/10.1080/13658816.2012.721552>
6. Kelly T, Wonka P (2011) Interactive architectural modeling with procedural extrusions. ACM Trans Graph 30:1–15. <https://doi.org/10.1145/1944846.1944854>
7. Brodeur J (2011) Geosemantic interoperability and the geospatial semantic web. In: Springer handbook of geographic information. Springer, Berlin, Heidelberg, pp 291–310. https://doi.org/10.1007/978-3-540-72680-7_15
8. Henn A, Römer C, Gröger G, Plümer L (2012) Automatic classification of building types in 3D city models. GeoInformatica 16:281–306. <https://doi.org/10.1007/s10707-011-0131-x>
9. Verdie Y, Lafarge F, Alliez P (2015) LOD generation for urban scenes. ACM Trans Graph 34:1–14. <https://doi.org/10.1145/2732527>
10. Slade J, Jones CB, Rosin PL (2017) Automatic semantic and geometric enrichment of CityGML building models using HOG-based template matching. https://doi.org/10.1007/978-3-319-25691-7_20
11. Nominatim. <https://nominatim.openstreetmap.org/>. Last accessed 15 Nov 2021
12. OpenStreetMap Wiki. Overpass API. https://wiki.openstreetmap.org/wiki/Overpass_API. Last accessed 15 Nov 2021
13. Ledoux H. CityJSON specifications 1.0.1. <https://www.cityjson.org/specs/1.0.1/>. Last accessed 15 Nov 2021
14. Dukai B. cjjio, or CityJSON/io. <https://github.com/cityjson/cjio>
15. Vitalis S. ninja. <https://ninja.cityjson.org/>. Last accessed 15 Nov 2021
16. Boeing G (2017) OSMnx: new methods for acquiring, constructing, analyzing, and visualizing complex street networks. Comput Environ Urban Syst 65:126–139. <https://doi.org/10.1016/j.compenvurbsys.2017.05.004>
17. PySAL Developers. PySAL. <https://pysal.org/>. Last accessed 15 Nov 2021
18. Fleischmann M (2019) momepy: urban morphology measuring toolkit. J Open Source Softw 4:1807. <https://doi.org/10.21105/joss.01807>

Analyzing the Awareness, Drivers, and Barriers of Building Information Modelling (BIM) Implementation for Sustainable Construction: Indonesia Construction Industry



Cakraningrat Kencana Murti and Fadhilah Muslim

Abstract The increasing sustainability issues that occur have encouraged the construction sector to adopt green and sustainable construction strategies. In Indonesia itself, regulations have been issued regarding the guidelines for the implementation of sustainable construction, which are contained in Indonesia's Ministry of Public Works and Housing Regulation Number 9 of 2021. On the one hand, technological advances encourage us to continue innovating, and there is one technology in the construction field, namely building information modelling (BIM). The application of BIM allows for improved performance in the application of sustainability concepts in a project. To be able to implement something new into the existing workflow, it is necessary to measure the level of awareness, as well as the driver and barrier factors. A questionnaire survey was conducted to 60 respondents, and it was found that construction service players in Indonesia already have a high level of awareness of sustainable construction, BIM technology, and its regulations. Based on the knowledge of the construction service actors, the factors in the implementation of sustainable construction and BIM technology are also known. The knowledge of construction service actors in Indonesia regarding the implementation of BIM-based sustainable construction shows that the most relevant drivers are construction waste reduction (SC) and better visualization for stakeholder (BIM) and the most relevant barriers are lack of experts in sustainable construction (SC) and BIM implementation requires higher initial investment than conventional methods (BIM).

Keywords Building information modelling (BIM) · Sustainable construction · Awareness · Driver factor · Barrier factors · Indonesia

C. K. Murti · F. Muslim (✉)

Faculty of Engineering, Universitas Indonesia, Pondok Cina, Beji, Depok, West Java 16424, Indonesia

e-mail: fadhilahmuslim@ui.ac.id

C. K. Murti

e-mail: cakraningrat.kencana@ui.ac.id

1 Introduction

The concept of sustainable development is rapidly evolving to achieve a sustainable relationship between social, economic and environmental systems. This is reinforced by the growing debate in recent decades about the influence of building construction on the sustainability of the environment and human life [1]. Due to increasing sustainability issues, such as the construction sector being responsible for the use of 42% of energy, 30% of raw materials, and 25% of clean water worldwide [2], a number of building projects have been encouraged to adopt green and sustainable construction strategies, which are gradually being recognized as a useful way to promote the development of the construction industry [3]. Innovation in science and technology plays an important role to support the transition to sustainable development, especially for cleaner production and operational processes. Speaking of innovation in science and technology, its ability to rely on advanced technology and effective construction processes makes Building Information Modelling (BIM), a breakthrough innovation in construction industry, considered as an opportunity that can bring great benefits to the architecture, engineering, and construction (AEC) industry [4].

Building Information Modelling (BIM) is one of the technologies that can be used in creating and monitoring digital information of a construction project throughout its life cycle. The application of BIM itself has received great attention from both academics and practitioners, given its ability to bring its novelty in replacing conventional project delivery [5]. Speaking of the concept of sustainability, the application of BIM itself allows for improved performance in the application of the concept of sustainability for each different stage in a project life cycle [6]. However, the overall potential of using and operating BIM has not been utilized to achieve sustainability throughout the life of a building due to the overlap of features and services provided by BIM with indicators and criteria for achieving sustainability [7]. On the one hand, practitioners have indirectly used BIM to measure, evaluate, and support several sustainability-related indicators, given the breadth of BIM functions that make it possible for every involved and responsible party in the project to exchange knowledge related to the ongoing project in each different dimensional model, such as three-dimensional models (3D), time-related models (4D), cost-related models (5D), energy and performance analysis models (6D), and facilities management-related models (7D) (Chong et al. [6]). To maximize this, there is a need for an integrated approach or a model that allows the application of BIM in the application of each sustainability indicator for each life phase of each project [7].

According to a report from the United Nations Environment Programme (UNEP), the construction sector consumes up to 40% of global energy consumption, 20% of annual water use, and contributes to 40% of total annual waste as a result of construction and demolition activities [8]. The significant influence of the construction sector makes the application of sustainable construction concepts more relevant. To date, there are many methods that have been applied in the success of sustainable construction, and one concept that is currently experiencing increased interest is the

use of building information modelling (BIM) technology, due to the advantages it can provide when compared to conventional methods. However, despite the various advantages offered, the application of BIM in the Asian region is arguably lagging behind when compared to countries in other major continents [9]. Some of the obstacles that arise in Asian countries are the confusion of construction service providers regarding how they should apply BIM due to the absence of clear standards and guidelines in its application [10]. In Indonesia itself, as one of the Asian countries, the application of BIM technology has received more attention from the government, with the issuance of Indonesia's Ministry of Public Works and Housing Regulation Number 9 of 2021 concerning guidelines for the implementation of sustainable construction in Indonesia, which also includes BIM technology as one of the methods in the implementation of sustainable construction [11]. However, with the lagging level of BIM application in Asia, and Indonesia's Ministry of Public Works and Housing Regulation Number 9 of 2021 which is still quite new, this encourages the author to examine the level of awareness, knowledge, and readiness, of construction service actors in Indonesia. This is because awareness and knowledge are the first obstacles that need to be overcome in order to apply the concept of sustainable construction that is capable and feasible [12]. Considering that the application of BIM technology is one of the methods in implementing sustainable construction, these two barriers need to be overcome so that the application of sustainable construction will enter the implementation stage. In this implementation stage, the author would like to further examine the readiness of construction service actors in Indonesia. The three factors (awareness, knowledge, and readiness) are then analyzed against the level of implementation of sustainable construction with the use of BIM technology based on Indonesia's Ministry of Public Works and Housing Regulation Number 9 of 2021.

This research has the following research questions (RQs):

1. What is the level of awareness of construction service actors in Indonesia towards the implementation of sustainable construction, the use of BIM technology, and related regulations governing its implementation?
2. How is the knowledge of construction service actors in Indonesia regarding the driver factors on the application of sustainable construction and BIM technology in its implementation according to related regulations?
3. How is the knowledge of construction service actors in Indonesia regarding the barrier factors on the application of sustainable construction and BIM technology in its implementation according to related regulations?

2 Literature Review

The concept of sustainability was first defined in "Our Common Future" or often referred to as the "Brundtland Report". The book was published by the Brundtland Commission, in 1987, and in it explains the concept of sustainability as a concept in which there is a fulfillment of the needs of the present without compromising

the ability of future generations to meet their own needs [13, 14]. The Brundtland Report at times provided fundamental action in the introduction of the concept of sustainability into legislative frameworks, which could raise public awareness while providing guidelines and other legislative needs related to the application of the concept of sustainability [15]. From there, the concept of sustainability slowly began to be considered and applied in every aspect of human life at that time [16]. The factors that will drive the sustainability movement are knowledge and awareness. With that, comes interest and demand, followed by implementation [12].

Awareness and knowledge are the first barriers to overcome in creating a capable and viable sustainability sector. As there have been many efforts made by the government and professional bodies to raise awareness and knowledge about the concept of sustainable construction among construction developers, it is expected that developers will realize this concept and start incorporating it into their projects. This knowledge needs to be imparted to encourage acceptance of this new concept. Through implementation, they will learn from experience and start making improvements. Building Information Modelling (BIM) is an advanced technology used to support decision-making about a building throughout its life cycle. BIM is both a technology and a process. The National Building Information Modelling Standards (NBIMS) defines BIM as a digital representation of the physical and functional characteristics of a facility. The technology component of BIM helps project stakeholders to visualize what will be built in a simulated environment to identify potential design, construction, or operational issues. The process component enables close collaboration and encourages the integration of the roles of all stakeholders in a project. The Associated General Contractors of America (AGC) defines as: "Building Information Modelling is the development and use of computer software models to simulate the construction and operation of facilities. Indonesia's Ministry of Public Works and Housing Regulation Number 9 of 2021, or what has been abbreviated as Indonesia's Ministry of Public Works and Housing Regulation Number 9 of 2021, is a regulation issued by the Ministry of PUPR of the Republic of Indonesia, in order to provide a guideline for the implementation of sustainable construction for construction service actors in Indonesia. In Indonesia's Ministry of Public Works and Housing Regulation Number 9 of 2021, there are technical provisions that fulfill the principles of sustainable construction. These principles include general planning, programming, implementation of construction consulting, and implementation of construction work.

From a research conducted by Abidin [17], a path is proposed to be able to implement sustainable construction, which involves many stakeholders (contractors, consultants, owners). The road in implementing sustainable construction is based on the awareness and knowledge of these stakeholders as an essential first step in achieving sustainable construction. Then, when discussing the application of BIM to sustainable construction, it is reinforced by research submitted by Rahman [18], it is stated that BIM technology is still relatively "new" and not thoroughly known by construction service actors. This makes the review and analysis of awareness and knowledge factors, in this case the knowledge of construction service players in Indonesia regarding the driver and barrier factors, as the important main step to

Table 1 Variable for awareness factor [19–22]

Code	Variable of awareness	Indicator
X1.1	Sustainable construction	What is the level of awareness of the institution where you work towards the implementation of sustainable construction
X1.2	BIM	What is the level of awareness of the institution where you work on the use of BIM in the project workflow
X1.3	Regulation	What is the level of awareness of the institution where you work on the regulated requirements for the implementation of sustainable construction according to Indonesia's Ministry of Public Works and Housing Regulation Number 9 of 2021
X1.4	Implementation of sustainable construction	What is the level of awareness of the company/agency/organization where you work on the regulated procedures for implementing sustainable construction according to Indonesia's Ministry of Public Works and Housing Regulation Number 9 of 2021
X1.5	Implementation of BIM for sustainable construction	What is the level of awareness of the company/agency/organization where you work on the recommended use of BIM in the implementation of sustainable construction according to Indonesia's Ministry of Public Works and Housing Regulation Number 9 of 2021

take before knowing whether the construction service players are ready and able to implement the application of BIM technology and sustainable construction itself [12, 18].

3 Research Methodology

In this research, several variables are also used, where each variable represents research for RQ1 (looking for the level of awareness), RQ2 (looking for driver factors), and RQ3 (looking for barrier factors), as shown in Tables 1, 2, and 3 consecutively.

4 Data Analysis

The first stage of data collection was conducted as the first stage of RQ1, RQ2, and RQ3. Expert validation stage the expert validation stage was carried out in parallel for the three problem formulations, which began with conducting a literature study. The literature study is intended to find out what variables are relevant to the research being carried out based on the following relevant to the research being conducted based on

Table 2 Variable for driver factor [22–27]

Variable	Code	Indicator
SC driver	X3.1.1	Improving energy efficiency
	X3.1.2	Resource conservation
	X3.1.3	Improved indoor environmental quality
	X3.1.4	Construction waste reduction
	X3.1.5	Reduction impacts of buildings on the environment
	X3.1.6	Increased productivity
	X3.1.7	Reduced operation and maintenance costs after construction
	X3.1.8	Increased job opportunities
	X3.1.9	Increased health and safety factor
	X3.1.10	Increased worker welfare
BIM driver	X3.2.1	Effective design process
	X3.2.2	Reduction of errors, risks, and design time
	X3.2.3	Availability of building life cycle data for operations and maintenance
	X3.2.4	As lessons learned from previous projects
	X3.2.5	Form the basis of a design (in line with regulatory standard codes)
	X3.2.6	Centralized reuse of information stored in the database
	X3.2.7	Overall project cost efficiency
	X3.2.8	Better visualization for stakeholders
	X3.2.9	More controlled project scheduling
	X3.2.10	Improved work safety on projects

Table 3 Variable for barrier factors [22–27]

Variable	Code	Indicator
SC barrier	X2.1.1	Lack of training and education on sustainable construction
	X2.1.2	The cost of implementing sustainable construction tends to be high
	X2.1.3	Lack of experts in sustainable construction
	X2.1.4	Lack of demand from clients
	X2.1.5	Tendency not to adapt into sustainable construction
BIM barrier	X2.2.1	BIM implementation temporarily reduces work efficiency due to the unwillingness of related parties to adapt
	X2.2.2	BIM implementation requires higher initial investment than conventional methods
	X2.2.3	BIM implementation is not required/required by the client
	X2.2.4	BIM implementation causes delays in the project due to lack of experience in the use of BIM by related parties
	X2.2.5	BIM implementation feels like additional work that must be done

previous studies. After obtaining the formulation of the temporary variables, then the then an expert validation questionnaire can be made to be distributed to experts who are experts in their fields according to the criteria. experts in their fields according to predetermined criteria. Output The expected output of the validation process using the questionnaire is valid variables for the three research questions (RQs) proposed. At this stage of expert validation, the author distributed questionnaires and discussed with three experts, in accordance with the predetermined criteria, to validate the variables to be used.

After knowing what variables are valid for use in each RQ, the author then conducted a pilot survey to find out whether the questions used in the third stage of data collection (respondent survey) were easy to understand or not. The pilot study survey was delivered in the form of a questionnaire with the answer options “easy to understand” or “difficult to understand”, so that the author could improve the preparation of the final questionnaire later which would be distributed to real respondents.

The third stage of data collection was carried out after the pilot study was completed, and the questions used were considered easy to understand by potential respondents later. In this third stage of data collection, the author targeted a minimum number of 30 respondents, and ended up with a total of 63 respondents. The number of respondents obtained has also met the minimum limit standards/criteria needed for this research to run and be considered valid. From the 63 respondents who have filled out the questionnaire has been categorized as their respective education, length of work experience, and the sector where they currently work. With the following profile grouping:

From the research respondents obtained, it is known from Fig. 1 that the distribution of data for the latest education with the latest education Bachelor (S1)/Equivalent is 54 people (86%), and Masters (S2)/Equivalent is 9 people (14%).

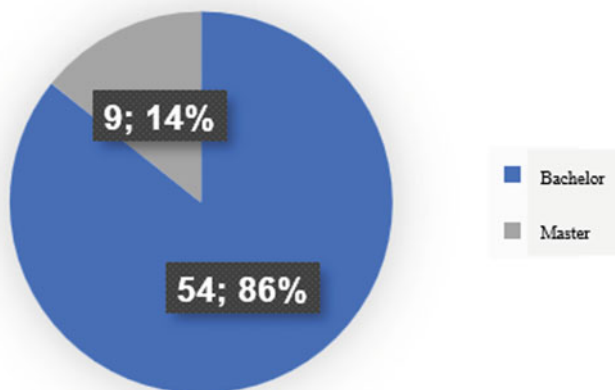


Fig. 1 Education level of respondents

From the research respondents obtained, it is known that the distribution of data for work experience with a length of 1–5 years is 35 people (56%), 6–10 years is 16 people (25%), 11–15 years is 5 people (8%), and 16–20 years is 7 people (11%) as we can see from Fig. 2.

From the research respondents obtained, it is known from Fig. 3 that the distribution of data for the respondent’s work sector with respondents working in contractors as many as 33 people (52%), owners as many as 13 people (21%), consultants as many as 12 people (19%), suppliers / vendors as many as 2 people (3%), and architects as many as 3 people (5%).

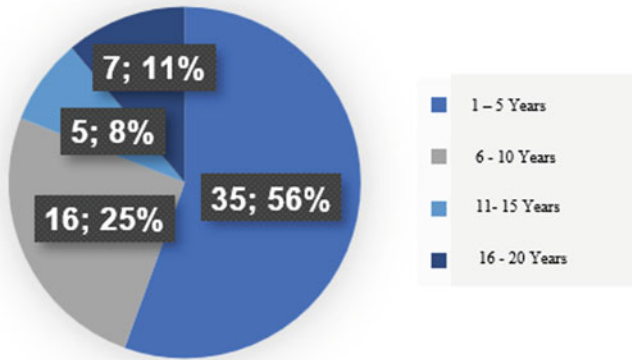


Fig. 2 Work experience of respondents

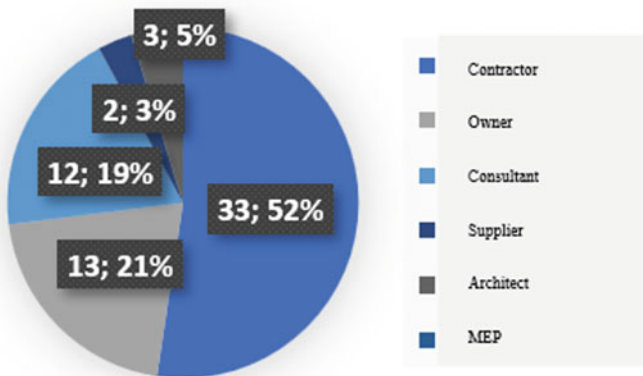


Fig. 3 Type of respondents institution

Data analysis starts from RQ1, where this analysis is carried out using frequency analysis to calculate the level of awareness viewed from a Likert scale of 1 to 5. The Likert scale used in this study itself is: 1 = very low; 2 = low; 3 = neutral; 4 = high; 5 = very high. The author reviewed several aspects of awareness in this research, including awareness of the application of sustainable construction, BIM technology, sustainable construction requirements, sustainable construction implementation methods, and recommendations for implementing BIM into the workflow of implementing sustainable construction itself based on Indonesia's Ministry of Public Works and Housing Regulation Number 9 of 2021. From the 63 sample respondents, data on the level of awareness of the construction service actors themselves were obtained. The analysis was conducted by calculating the frequency of each respondent's answer, from 1 to 5, and then weighted by percentage to obtain the awareness level. It is found that the level of awareness for the five areas under review is at the "very high" level. For RQ2 and RQ3, the author wants to review what factors are included in the barriers and benefits contained in the practice of applying BIM technology to sustainable construction. For this reason, the author has first conducted a literature study to find out what variables are included in the barriers and drivers. From there, a ranking of the drivers and barriers is then carried out, to find out which factors are most influential in its application. The ranking is done with the Relative Importance Index (RII) approach.

5 Finding and Discussion

The findings of RQ1 were derived from the frequency analysis of the Likert scale that was administered to the study participants. On the basis of this study, statistics on each component's level of awareness were acquired, giving the following results, with the line at the 80% mark indicating a high awareness value:

From the graph, it can be seen the level of awareness for each predetermined criterion, where each variable explains the level of awareness in the following aspects:

In the graph, it can be seen the level of awareness of the construction service actors of the aspects that have been determined in the table above. This shows positive results, where for all five criteria there is a very high level of awareness. It can be seen from the horizontal line that becomes the threshold at 80%, where the value of 80% is the lower limit of the range for very high awareness criteria, as shown in Fig. 4.

With the explanation for each variable, such as X1.1; X1.2; X1.3; X1.4; and X1.5 are mentioned in Table 4.

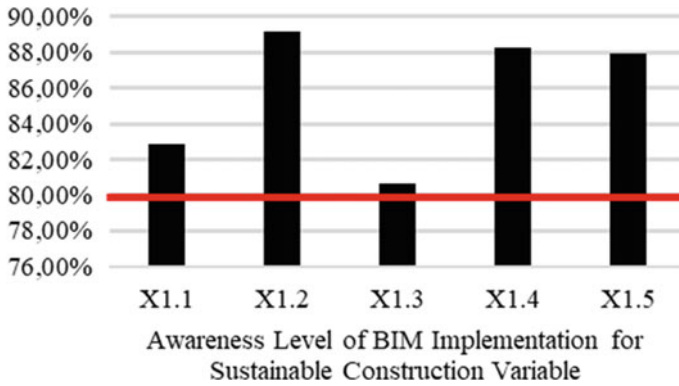


Fig. 4 Awareness level for each component

Table 4 Details of each awareness variable

Code	Variable of awareness	Indicator
X1.1	Sustainable construction	What is the level of awareness of the institution where you work towards the implementation of sustainable construction
X1.2	BIM	What is the level of awareness of the institution where you work on the use of BIM in the project workflow
X1.3	Regulation	What is the level of awareness of the institution where you work on the regulated requirements for the implementation of sustainable construction according to Indonesia’s Ministry of Public Works and Housing Regulation Number 9 of 2021
X1.4	Implementation of sustainable construction	What is the level of awareness of the company/agency/ organization where you work on the regulated procedures for implementing sustainable construction according to Indonesia’s Ministry of Public Works and Housing Regulation Number 9 of 2021
X1.5	Implementation of BIM for sustainable construction	What is the level of awareness of the company/agency/ organization where you work on the recommended use of BIM in the implementation of sustainable construction according to Indonesia’s Ministry of Public Works and Housing Regulation Number 9 of 2021

To be able to understand more about the range of awareness criteria shown in Fig. 4, there are divided into 5 different categories, which categorized value of awareness level for each different variable as we can see from Table 5.

Therefore, from the frequency analysis that has been carried out, it is found that the level of awareness of construction service actors in Indonesia regarding the issue of applying BIM technology to sustainable construction based on Indonesia’s Ministry of Public Works and Housing Regulation Number 9 of 2021 is high.

Table 5 Range of awareness criteria

Criteria	Range		
Very low	0%	–	20%
Low	20%	–	40%
Neutral	40%	–	60%
High	60%	–	80%
Very high	80%	–	100%

From the test results, it was found that the level of awareness of construction service actors in Indonesia was at a high to very high level, with no one answering low to very low by more than 5%. However, this is still an obstacle, because it was found that the implementation of BIM technology in Indonesia itself is still low, which is at a level of 38% [28]. In Indonesia itself, the obstacle to the implementation of BIM is “the function of BIM which is still not needed”, with a percentage of answers of 38% [29]. The main obstacle as mentioned by that research is that they do not really need BIM at the moment. This is because the current document approval method is still based on conventional 2D drawings. Therefore, some respondents do not see any demand or need to move to BIM as their current working methods are considered sufficient. This unwillingness to implement BIM itself is in line with the study proposed before, where the low implementation is due to a lack of awareness of what BIM is [30]. However, in this study, it was found that the level of awareness of the construction service actors themselves was relatively high.

In research question 2 and 3, testing with the relative importance index (RII) method approach was carried out to determine the knowledge of practitioners in the field regarding the level of importance and also the ranking of drivers and barriers in the application of BIM technology to sustainable construction. From the test, the following results were obtained (see Table 6 for relevant driver factors and Table 7 for relevant barrier factors):

Table 6 Relevant Driver factors

Driver factors	Indicator	RII	Rank
Sustainable construction	Construction waste reduction	0.847	1
	Reduction of adverse impacts of buildings on the environment	0.837	2
	Increased productivity	0.813	3
BIM	Better visualization for stakeholders	0.913	1
	Centralized reuse of information stored in the database	0.897	2
	Reduction of errors, risks, and design time	0.897	2

Table 7 Relevant barrier factors

Barrier factors	Indicator	RII	Rank
Sustainable Construction	Lack of experts in sustainable construction	0,830	1
	The cost of implementing sustainable construction tends to be high	0,787	2
	Lack of training and education on sustainable construction	0,783	3
BIM	BIM implementation requires higher initial investment than conventional methods	0,857	1
	BIM implementation is not required/required by the client	0,687	2
	BIM implementation temporarily reduces work efficiency due to the unwillingness of related parties to adapt	0,680	3

6 Conclusion

From this research, writer can take several conclusions, such as:

1. The level of awareness of construction service actors in Indonesia regarding the implementation of BIM-based sustainable construction based on Indonesia’s Ministry of Public Works and Housing Regulation Number 9 of 2021 is at a high to very high level.
2. The knowledge of construction service actors in Indonesia regarding the implementation of BIM-based sustainable construction shows that the most relevant drivers are construction waste reduction (SC) and better visualization for stakeholder (BIM).
3. The knowledge of construction service actors in Indonesia regarding the implementation of BIM-based sustainable construction shows that the most relevant barriers are lack of experts in sustainable construction (SC) and BIM implementation requires higher initial investment than conventional methods (BIM).

References

1. Balaban O, Puppim de Oliveira JA (2017) Sustainable buildings for healthier cities: assessing the co-benefits of green buildings in Japan. *J Clean Prod* 163:S68–S78. <https://doi.org/10.1016/j.jclepro.2016.01.086>
2. Hashemkhani Zolfani S, Pourhossein M, Yazdani M, Zavadskas EK, (2018) Evaluating construction projects of hotels based on environmental sustainability with MCDM framework. *Alexandria Eng J* 57(1):357–365. <https://doi.org/10.1016/j.aej.2016.11.002>

3. Alireza AFF, Rashidi TH, Akbarnezhad A, Waller ST (2017) BIM-enabled sustainability assessment of material supply decisions. *Eng Constr Archit Manage* 24(4):668–695. <https://doi.org/10.1108/ECAM-12-2015-0193>
4. Abanda FH, Vidalakis C, Oti AH, Tah JHM (2015) A critical analysis of building information modelling systems used in construction projects. *Adv Eng Softw* 90:183–201. <https://doi.org/10.1016/j.advengsoft.2015.08.009>
5. Wang HCX (2016) The outlook of building information modeling for sustainable development. *Clean Technol Environ Policy* 18(6):1877–1887. <https://doi.org/10.1007/s10098-016-1170-7>
6. Chong H, Wang J, Shou W, Wang X, Guo J (2014) Improving quality and performance of facility management using building information modelling*. pp 44–50
7. Mohammed AB (2022) Applying BIM to achieve sustainability throughout a building life cycle towards a sustainable BIM model. *Int J Constr Manag* 22(2):148–165. <https://doi.org/10.1080/15623599.2019.1615755>
8. Wimala M, Akmalah E, Sururi MR (2016) Breaking through the barriers to green building movement in indonesia: insights from building occupants. *Energy Procedia* 100(September):469–474. <https://doi.org/10.1016/j.egypro.2016.10.204>
9. Jung W, Lee G (2015) The status of BIM adoption on six continents, vol 9, no 5, pp 512–516
10. Zahrizan Z, Ali NM, Haron AT, Marshall-Ponting A, Hamid ZA (2013) Exploring the adoption of building information modelling (BIM) in the Malaysian construction industry: a qualitative approach. *Int J Res Eng Technol* eISSN pISSN:2319–1163
11. PUPR (2021) Permen PUPR No. 9 Tahun 2021: Pedoman Penyelenggaraan Konstruksi Berkelanjutan, vol 2021, Available <https://jdih.pu.go.id/detail-dokumen/2882/1>
12. Zainul Abidin Nazirah N (2010) Investigating the awareness and application of sustainable construction concept by Malaysian developers. *Habitat Int* 34(4):421–426. <https://doi.org/10.1016/j.habitatint.2009.11.011>
13. Borowy I (2013) Defining sustainable development for our common future: A history of the world commission on environment and development (Brundtland Commission), 1st edn. Routledge, London. <https://doi.org/10.4324/9780203383797>
14. World Commission on Environment and Development (1987) The Brundtland report: “our common future.” Oxford University Press, Oxford. <https://doi.org/10.1080/07488008808408783>.
15. Klein L, Arts K (2022) Public participation in decision-making on conservation translocations: the importance and limitations of a legislative framework. *Restor Ecol* 30(1):1–11. <https://doi.org/10.1111/rec.13505>
16. Mondini G (2019) Sustainability assessment: from brundtland report to sustainable development goals. *Valori e Valutazioni* 2019(23):129–137
17. Abidin NZ (2010) Investigating the awareness and application of sustainable construction concept by Malaysian developers. Elsevier. <https://doi.org/10.1016/j.habitatint.2009.11.011>
18. Rahman MM (2017) Awareness of BIM adoption in Brunei. *AIP Conf Proc* 1887(September):2017. <https://doi.org/10.1063/1.5003515>
19. Alsanad S (2015) Awareness, drivers, actions, and barriers of sustainable construction in Kuwait, vol 118, pp 969–983. <https://doi.org/10.1016/j.proeng.2015.08.538>
20. Son H, Kim C, Chong WK, Chou J (2009) Implementing sustainable development in the construction industry: constructors’ perspectives in the US and Korea. *Sustain Dev* 347(November 2009):337–347
21. Gamil Y, Rahman IAR (2019) Awareness and challenges of building information modelling (BIM) implementation in the Yemen construction industry. *J Eng Des Technol* 17(5):1077–1084. <https://doi.org/10.1108/JEDT-03-2019-0063>
22. Serpell A, Kort J, Vera S (2013) Awareness, actions, drivers and barriers of sustainable construction in Chile. *Technol Econ Dev Econ* 19(2):272–288. <https://doi.org/10.3846/20294913.2013.798597>
23. Chan APC, Darko A, Olanipekun AO, Ameyaw EE (2018) Critical barriers to green building technologies adoption in developing countries: the case of Ghana. *J Clean Prod* 172:1067–1079. <https://doi.org/10.1016/j.jclepro.2017.10.235>

24. Durdyev S, Zavadskas EK (2018) Sustainable construction industry in Cambodia : awareness , drivers and barriers. *Sustainability* 1–19. <https://doi.org/10.3390/su10020392>
25. Azhar S, Khalfan M, Maqsood T (2012) Building information modeling (BIM): now and beyond. *Aust J Constr Econ Build* 12(4):15–28. <https://doi.org/10.5130/ajceb.v12i4.3032>
26. Arayici Y, Egbu C, Coates P (2012) Building information modelling (BIM) implementation and remote construction projects: Issues, challenges, and critiques. *Electron J Inf Technol Constr* 17(May 2016):75–92
27. Barlish K, Sullivan K (2012) How to measure the benefits of BIM—A case study approach. *Autom Constr* 24:149–159. <https://doi.org/10.1016/j.autcon.2012.02.008>
28. Sopaheluwakan MP, Adi TJW (2020) Adoption and implementation of building information modeling (BIM) by the government in the Indonesian construction industry. IOP Publishing. <https://doi.org/10.1088/1757-899X/930/1/012020>
29. Hatmoko JUD et al. (2019) Investigating building information modelling (BIM) adoption in Indonesia Construction Industry. In: MATEC Web of Conferences. <https://doi.org/10.1051/mateconf/201925802006>
30. Elhendawi A et al. (2019) Practical approach for paving the way to motivate BIM non-users to adopt BIM. *Int J BIM Eng Sci*. <https://doi.org/10.54216/IJBES.020201>

Integrating Cumulative Prospect Theory into a Cellular Automata Model for Building Evacuation with Obstacles



Dongli Gao , Eric Wai Ming Lee , Wei Xie , Xuanwen Liang ,
Ruifeng Cao , Qian Chen , and Nan Jiang 

Abstract A reliable evacuation model plays an important role in building design, emergency systems, and safety management. The cellular automata (CA) model, widely applied in simulating evacuations, determines evacuees' movement by probabilities in discrete space and time, and provides evacuees with rational moving decisions. However, people are not always rational. To fill this gap, in this study, cumulative prospect theory (CPT), a realistic decision-making model to describe the subjective outcomes and probabilities, was integrated into the CA model (i.e., CPT-CA) to mimic actual human decision-making behavior during evacuation in a room with obstacles. Two types of evacuation scenarios were used to validate our proposed model: one exit and two exits in the classrooms. The results showed that when the classroom with only one exit, the CPT-CA model can provide a relatively close, realistic evacuation time for building evacuation, while the advantages of this model are diminished when there are two exits. Our proposed CPT-CA model can help architects and engineers to adopt this building evacuation model for their building designs.

Keywords Evacuation model · Cellular automata · Decision-making · Cumulative prospect theory

1 Introduction

Efficient building evacuation plays an important role in saving lives from both manmade and natural disasters, e.g., during an emergency situation when fire outbreaks. Evacuation routes in cases of emergency should be carefully designed to ensure that all evacuees can leave the building in the least possible time. Therefore,

D. Gao · E. W. M. Lee (✉) · W. Xie · X. Liang · R. Cao · Q. Chen · N. Jiang
City University of Hong Kong, Hong Kong, China
e-mail: ericlee@cityu.edu.hk

N. Jiang
University of Science and Technology of China, Hefei, China

© The Author(s), under exclusive license to Springer Nature Singapore Pte Ltd. 2024
M. Casini (ed.), *Proceedings of the 3rd International Civil Engineering and Architecture Conference*, Lecture Notes in Civil Engineering 389,
https://doi.org/10.1007/978-981-99-6368-3_75

927

building evacuation modeling is invaluable for designing, optimizing, and assessing emergency systems and building safety management.

Several models have been widely adopted for this purpose, including social force models [1–6], agent-based models [7–10], lattice gas models [11–13], and cellular automata (CA) models [14–19]. CA models have become one of the most widespread discrete models for simulating evacuations [17]. In a CA model, a floor map is discretized into grids, and evacuees move from grid to grid. Thus the CA models require fewer computational resources and perform simulations faster, and they are able to investigate individual behavior (e.g., the effect of memory [20], familiarity [21], limited vision [22], etc.) and social interactions (e.g., small groups [23], information exchange [24], etc.).

However, although there has been some improvement in CA models to increase the realism of models, it is still challenging to use these models to describe real evacuation behavior [17]. These models were proposed from the researchers' perspective [16], assuming that people have an outstanding ability to perceive information from the environment and others, and they are able to make rational decisions. Clearly, this assumption does not correspond to the real world, as the observation from Tversky [25], people do not always act rationally in reality. Moreover, Our previous study [26] has provided clear evidence that evacuees' exit choice was observed to be a pattern reference rather than fully rational.

A small number of researchers have noticed this gap. Wang and Jiang [27] improved the CA model to take into consideration of the evacuees' bounded rational behavior, which was defined by the individuals' perception of information. Wang et al. [28] proposed a route choice model to present boundedly rational decision-making behavior during an evacuation. In our previous study [16], cumulative prospect theory (CPT), a descriptive decision-making model, was integrated into the CA model to make the most prospective decision in movement, namely the CPT-CA model, and this model has been validated by two case studies. However, the evacuation movement in these studies did not consider the influence of obstacles. This should be of primary importance because many actual emergency evacuations take place in such spaces as theaters, airplanes, classrooms, etc. [29]. Therefore, The objective of this study is to describe evacuees' real decision-making behavior with consideration of the influence of obstacles. First, in Sect. 2, we introduce how to integrate CPT into the CA model. Then, in Sect. 3, two case studies in the classroom are used to validate our proposed CPT-CA model. Finally, in Sect. 4, we conclude the results.

2 Model

In a CA evacuation model, the room is discrete into a rectangular grid. Each cell can be empty or occupied by an evacuee or an obstacle. For the next movement, an evacuee can either stand still in the current cell or move to one of eight adjacent cells in the absence of obstacles. The group of these nine available moving cells is known

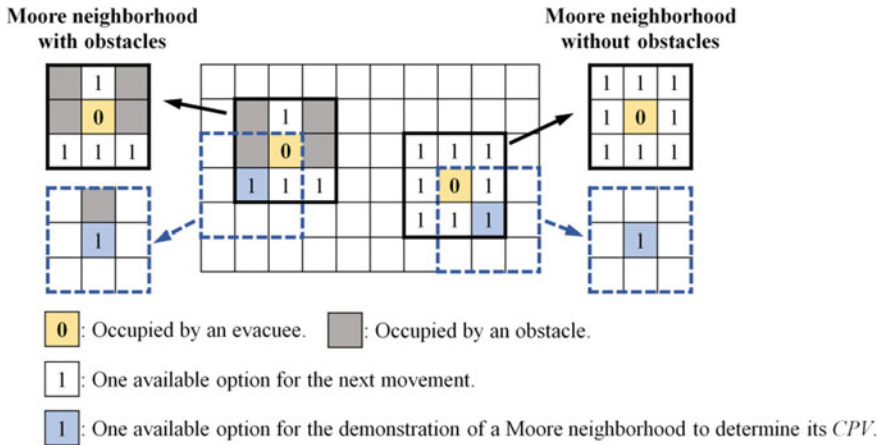


Fig. 1 Schematic illustration of a CA evacuation model in our study

as the Moore neighborhood [14], as shown in Fig. 1. There are fewer moving options if some of the nine cells are occupied by obstacles or other evacuees.

Our previous study [16] has successfully integrated CPT into a CA model to mimic exit/route choice behavior during building evacuation without obstacles. The CPT model was applied to introduce actual decision-making human behavior into the CA model (CPT-CA) by converting each of the floor fields into the outcomes and probabilities of the available options in the next movement direction, and CPT can be applied to determine the most prospective moving direction from the available options.

In this study, we propose to improve this CPT-CA model to make it available in a room with obstacles. The CPT-CA model includes two main parts: (1) obtaining outcomes and probabilities in a CA model; (2) integrating CPT into the CA model.

2.1 Obtaining Outcomes and Probabilities in a CA Model

Firstly, the outcome x of an evacuee making-decision in the next movement can be determined by Eq. (1), the difference in estimated evacuation time T between the current cell c and the available option cell j , where the estimated evacuation time is given by Togawa [30].

$$x = T_c - T_j \tag{1}$$

Secondly, the transition probability p_j is determined by the state of cell j and the integration of static floor field S_j , dynamic floor field D_j , and the inertia effect I_j with the sensitivity parameters k_S , k_D and k_I , respectively [16]:

$$p_j = N \exp(-k_S S_j + k_D D_j + k_I I_j)(1 - n_j)\xi_j \tag{2}$$

where occupation number $n_j = 0, 1$; obstacle number $\xi_j = \begin{cases} 0, & \text{for obstacles} \\ 1, & \text{otherwise} \end{cases}$, and N for ensuring $\sum_j p_j = 1$. In our previous study [16], the static field value S_j was given by the minimum Euclidean distance from cell j to the exit cells. However, in a room with obstacles, e.g., desks and chairs, the method to calculate the static field should be modified to improve the realism of the CA model [31]. Since the arbitrary geometries are divided by obstacles in space, the distance between the current position and exits can't be directly given by Euclidean distance. In this study, referring to the common path planning algorithms used in robotics, A "A*" search-based planning algorithm (<https://github.com/zhm-real/PathPlanning>) is applied to calculate the static floor field in space with obstacles. Moreover, our previous verification study of integrating CPT into CA model in spaces without obstacles found that the herding and inertia parameters can be omitted [16]. Thus, Eq. (2) can be simplified as follows with $k_S = 3$ [32]:

$$p_j = N \exp(-k_S S_j)(1 - n_j)\xi_j \tag{3}$$

2.2 Integrating CPT into the CA Model

Transforming Objective Outcomes and Probabilities into Subjective Terms CPT reveals an individual's subjective perception of the outcomes in which people are more concerned with loss than gain [25]. To reflect the effect of this human subjective perception on outcomes, a transformation from objective outcome obtained from Eq. (1) to subjective outcome $v(x)$ was proposed by Tversky [25] as shown in Eq. (4), where λ and α are the model parameters estimated to be 2.25 and 0.88 [25], respectively.

$$v(x) = \begin{cases} x^\alpha, & \text{if } x \geq 0 \\ -\lambda(-x)^\alpha, & \text{if } x < 0 \end{cases} \tag{4}$$

CPT was found from observations of the following behaviors [25]. When the probability of an event is low, people focus on how much they can gain rather than lose (i.e., risk seeking). Conversely, when the probability of an event is high, people are more focused on the loss than on the gain of the event (i.e., risk aversion). Thus, the probability of transformation is different between a loss and a gain. The following transformation, i.e., Eq. (5) was proposed by Tversky [25], where $\gamma^+ = 0.61$ and $\gamma^- = 0.69$ are the weighted probabilities in gain and loss situations, respectively. The probability p is obtained from Eq. (3).

$$w(p) = \frac{p^\gamma}{[p^\gamma + (1 - p)^\gamma]^{1/\gamma}}, \gamma = \begin{cases} \gamma^+, \text{ gain} \\ \gamma^-, \text{ loss} \end{cases} \tag{5}$$

Determining Cumulative Prospect Value For one available option j , the cumulative prospect value CPV_j is determined by its Moore neighborhood, which consists of m cells ($m \leq 9$) except the one occupied by other evacuees or obstacles (see Fig. 1). The m cells are sorted from loss to gain in ascending order and when the outcome of k th is loss or neutral, and $(k + 1)$ th is gain, CPV_j is given by:

$$CPV_j = \left[\sum_{i=0}^k \pi_i^- v(x_i) + \sum_{i=k+1}^m \pi_i^+ v(x_i) \right] (1 - n_j) \xi_j \tag{6}$$

where occupation number $n_j = 0, 1$; obstacle number $\xi_j = \begin{cases} 0, \text{ obstacles} \\ 1, \text{ otherwise} \end{cases}$; and

$$\pi_i^- = \begin{cases} w^-\left(\sum_0^i p_i\right) - w^-\left(\sum_0^{i-1} p_i\right), & i > 0 \\ w^-(p_0), & i = 0 \end{cases} \tag{7}$$

$$\pi_i^+ = \begin{cases} w^+\left(\sum_i^m p_i\right) - w^+\left(\sum_{i+1}^m p_i\right), & i < m \\ w^+(p_m), & i = m \end{cases} \tag{8}$$

Updating the Movement After obtaining the CPV of all available options, the evacuee moves to the target cell with the highest cumulative prospect value. All evacuees update synchronously at each time step. It is possible that two or more evacuees choose the same cell during a congested evacuation, and would arise conflicts due to the competition. To resolve the conflict, one of the evacuees is allowed to move to the target at random with a probability of 80%, while the unsuccessful evacuees remain in their current cell, and the conflict cannot be resolved with a probability of 20%, and all evacuees involved in the conflict remain in their current cell [32].

3 Case Studies

3.1 Case Study 1: One Exit

To study the application of CPT in route choice with obstacles, the experimental data in a classroom with one exit reported by Guo et al. [33] was analyzed. As shown in Fig. 2, The classroom in the simulation was divided into a series of $0.4 \times 0.4 \text{ m}^2$ cells. There were obstacles, i.e., desks and chairs, which were presented by light grey rectangles, and the initial positions of evacuees were denoted by red circles

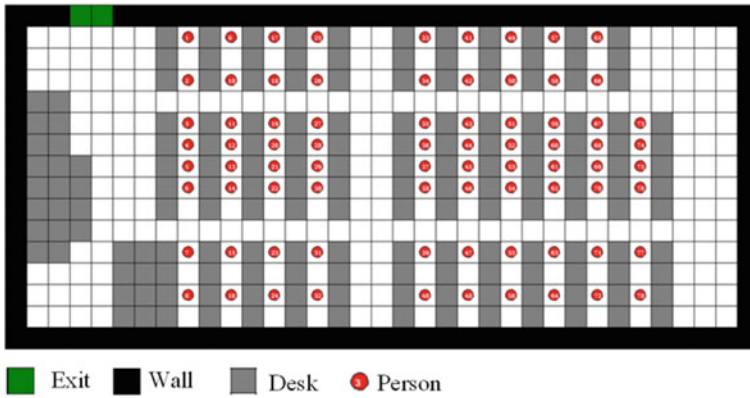


Fig. 2 Schematic of simulation in a one-exit classroom with obstacles

which were numbered from 1 to 78. The evacuees moving velocity was assumed to be 2.0 m/s, and thus each time step represents 0.2 s [34].

The correlation coefficient between the simulation and experiment for the times of repetition varying from 3 to 20 was calculated, and the results are shown in Fig. 3a. When the times exceeded 10, the correlation coefficient remained at around 0.91, so the further analysis was based on the results for 10 times. As shown in Fig. 3b, the correlation coefficient of the potential model which was proposed by Guo et al. [33] is less (0.831), and it is higher in the CA model, i.e., 0.885 while the correlation coefficient of the CPT-CA model is the largest one (0.903) and the closest to 1. That is to say; the CPT-CA model can be well to reflect the route choice behavior in a classroom with one exit.

3.2 Case Study 2: Two Exits

The case scenario in a two-exit classroom with furniture was referred to the experiment [34] with two exits (Exit A and Exit B), each of which has two doors (see Fig. 4). The classroom was divided into 27×23 grids with each size of 0.5×0.5 m². The walking velocity was the same as in the case above, i.e., 2 m/s, and the time step was assumed to be 0.25 s. Forty evacuees were arranged in rows and columns, and both two exits were opened.

The relation between the simulation and experimental evacuation time of each evacuee and correlation coefficient was built, as shown in Fig. 5a. The correlation coefficient of CPT-CA model and the experiment was around 0.85, and it is in accord with that for CA model. Figure 5b presents the output flux of Exit A, and the results in CPT-CA model are well consistent with that in CA model while they are obviously divergent in the experiment. Compared to the experiment, the number of evacuees choosing Exit A each time was relatively less than that in the simulations using both

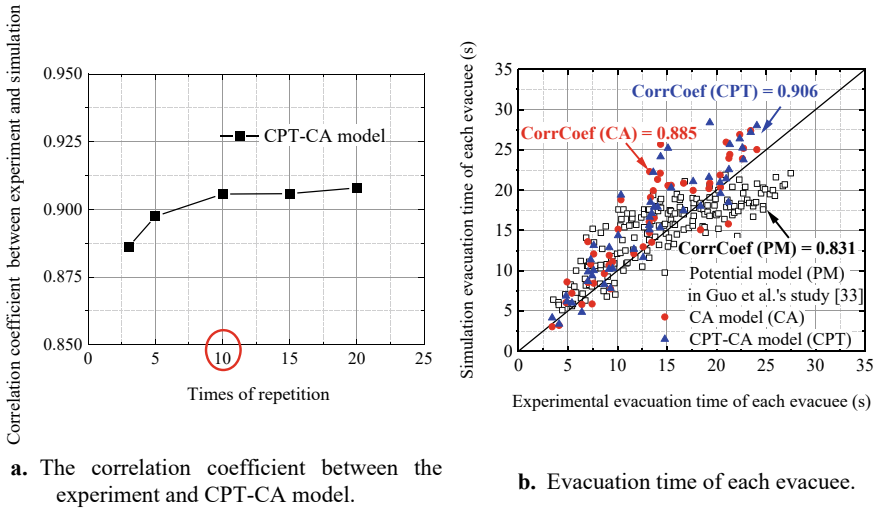


Fig. 3 Comparison between experimental data and simulation results

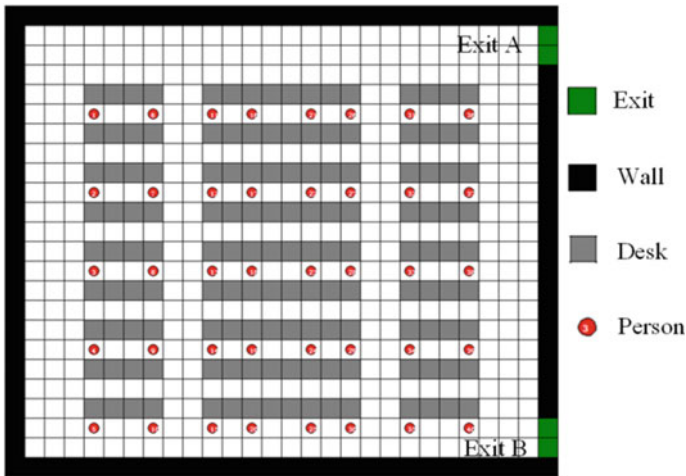


Fig. 4 Schematic of simulation in a two-exit classroom with obstacles

CA and CPT-CA model, and more evacuees chose the nearest exit, i.e., Exit B. There are several possible explanations. First, the walking velocity used in the simulation is a little high. Although Liu et al. [34] stated that the evacuees' walking velocity was not confined by the small people density, and 2 m/s can be reached in an emergency, actually, a lot of obstacles in the classroom may slow down people. Second, in their experiments [34], one participant chose an unreasonable way, and consequently, he/she took a long time to escape from Exit A.

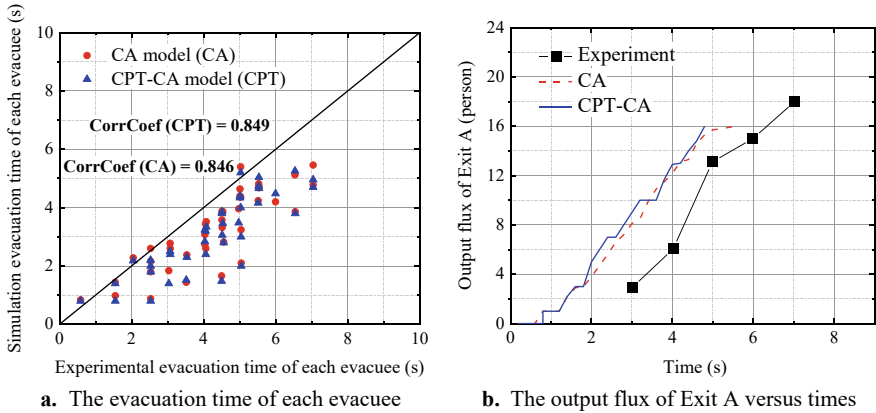


Fig. 5 Comparison between simulation and experiment [34] in a two-exit classroom

When there are two exits during evacuations, once evacuees start to move, they need to make global and local decisions, i.e., corresponding to the exit choice and the route choice [35]. The global choice (exit choice) would not be involved in the movement in the one-exit classroom, while both exit choice and route choice are involved in each movement in the two-exit choice. The exit choice would be dominant in the two-exit choice instead of the route choice. However, in both CA and CPT-CA models, we only considered the influence of other evacuees nearing the decision-makers and ignored the impact of evacuees' density around exits which seems as an important factors by Liu et al. [34] in the multiple exit choices. Therefore, in the near future, we must modify our model to consider the influence of evacuees' density around exits on modeling evacuations.

4 Conclusion

To mimic evacuees' real decision-making behavior in the evacuation with obstacles, we proposed an improved CA model, i.e., the CPT-CA model, which embedded the CPT into a CA model. In order to validate this model, two case studies with one exit or two exits were conducted by replicating a previously reported experiment in the classroom. The results demonstrated that, in general, our proposed CPT-CA model could simulate a much closer realistic evacuation time during escaping from a classroom with obstacles, while this advantage was reduced when there were two exits in the classroom. The possible explanation for this failure is that our proposed model didn't take into account the evacuees' density around the exits which might play an important role in making a decision between multiple exits. Considering this limitation, our future study will modify our proposed model with consideration of exit choice under different evacuees' densities around the exits.

Acknowledgements The work was supported by the Research Grants Council of the Hong Kong Special Administrative Region China (Project No. CityU 11208119) and by a grant from CityU (Project No. SRG-Fd 7005769).

References

1. Helbing D, Molnár P (1995) Social force model for pedestrian dynamics. *Phys Rev E* 5(51):4282–4286
2. Helbing D, Farkas I, Vicsek T (2000) Simulating dynamical features of escape panic. *Nature* 6803(407):487–490
3. Xie W, Gao D, Lee EW (2022) Detecting undeclared-leader-follower structure in pedestrian evacuation using transfer entropy. *IEEE Trans Intell Transport Syst* 1–10
4. Xie W, Lee EWM, Lee YY (2022) Simulation of spontaneous leader–follower behaviour in crowd evacuation. *Autom Constr* 134
5. Cao RF, Lee EWM, Yuen ACY, Chan QN, Xie W, Shi M, Yeoh GH (2021) Development of an evacuation model considering the impact of stress variation on evacuees under fire emergency. *Saf Sci* 138
6. Cao RF, Lee EWM, Yuen ACY, Chen TBY, De Cachinho Cordeiro IM, Shi M, Wei X, Yeoh GH (2021) Simulation of competitive and cooperative egress movements on the crowd emergency evacuation. *Simul Model Practice Theory* 109
7. Augustijn-Beckers E-W, Flacke J, Retsios B (2010) Investigating the effect of different pre-evacuation behavior and exit choice strategies using agent-based modeling. *Procedia Eng* 3:23–35
8. Chen X, Li H, Miao J, Jiang S, Jiang X (2017) A multiagent-based model for pedestrian simulation in subway stations. *Simul Model Practice Theory* 71:134–148
9. Edrisi A, Lahoorpoor B, Lovreglio R (2021) Simulating metro station evacuation using three agent-based exit choice models. *Case Stud Transport Policy* 3(9):1261–1272
10. Hu Y, Liu X, Wang F, Cheng C (2012) An overview of agent-based evacuation models for building fires. In: *Proceedings of 2012 9th IEEE international conference on networking, sensing and control*, pp 382–386
11. Tajima Y, Takimoto K, Nagatani T (2001) Scaling of pedestrian channel flow with a bottleneck. *Physica A* 1(294):257–268
12. Tajima Y, Nagatani T (2001) Scaling behavior of crowd flow outside a hall. *Physica A* 1(292):545–554
13. Helbing D, Isobe M, Nagatani T, Takimoto K (2003) Lattice gas simulation of experimentally studied evacuation dynamics. *Phys Rev E* 6(67):067101
14. Burstedde C, Klauck K, Schadschneider A, Zittartz J (2001) Simulation of pedestrian dynamics using a two-dimensional cellular automaton. *Physica A* 295:507–525
15. Kirchner A, Schadschneider A (2002) Simulation of evacuation processes using a bionics-inspired cellular automaton model for pedestrian dynamics. *Physica A* 312:260–276
16. Gao DL, Ming Lee EW, Lee YY (2022) Integration of cumulative prospect theory in cellular automata model for building evacuation. *Int J Disaster Risk Reduct* 74
17. Li Y, Chen M, Dou Z, Zheng X, Cheng Y, Mebarki A (2019) A review of cellular automata models for crowd evacuation. *Physica A: Stat Mech Appl* 526
18. Li X, Geng Z, Kuang H, Bai X, Fan Y (2019) Effect of dangerous source on evacuation dynamics in pedestrian counter flow. *Physica A: Stat Mech Appl* 533
19. Shi M, Lee EWM, Ma Y (2019) A dynamic impatience-determined cellular automata model for evacuation dynamics. *Simul Model Practice Theory* 94:367–378
20. Geng Z., Li X, Kuang H, Bai X, Fan Y (2019) Effect of uncertain information on pedestrian dynamics under adverse sight conditions. *Physica A: Stat Mech Appl* 521:681–691

21. Li D, Han B (2015) Behavioral effect on pedestrian evacuation simulation using cellular automata. *Saf Sci* 80:41–55
22. Li X, Guo F, Kuang H, Geng Z, Fan Y (2019) An extended cost potential field cellular automaton model for pedestrian evacuation considering the restriction of visual field. *Physica A: Stat Mech Appl* 515:47–56
23. Lu L, Chan C-Y, Wang J, Wang W (2017) A study of pedestrian group behaviors in crowd evacuation based on an extended floor field cellular automaton model. *Transport Res Part C: Emerg Technol* 81:317–329
24. Wang X, Guo W, Zheng X (2016) Information guiding effect of evacuation assistants in a two-channel segregation process using multi-information communication field model. *Saf Sci* 88:16–25
25. Tversky AKD (1992) Advances in prospect theory: cumulative representation of uncertainty. *J Risk Uncertain* 5:297–323
26. Gao DL, Xie W, Ming Lee EW (2022) Individual-level exit choice behaviour under uncertain risk. *Physica A: Stat Mech Appl* 604
27. Wang L, Jiang Y (2019) Escape dynamics based on bounded rationality. *Physica A: Stat Mech Appl* 531
28. Wang X., Mohcine C, Chen J, Li R, Ma J (2022) Modeling boundedly rational route choice in crowd evacuation processes. *Saf Sci* 147
29. Varas A, Cornejo MD, Mainemer D, Toledo B, Rogan J, Muñoz V, Valdivia JA (2007) Cellular automaton model for evacuation process with obstacles. *Physica A* 2(382):631–642
30. Togawa K (1955) Study on fire escapes basing on the observation of multitude currents. Building Research Institute, Ministry of Construction
31. Nishinari K, Kirchner A, Namazi A, Schadschneider A (2004) Extended floor field CA model for evacuation dynamics. *IEICE Trans Inf Syst* 3(87):726–732
32. Yanagisawa D, Haghani M, Sarvi M (2020) Exit-choice behavior in evacuation through an L-shaped corridor. *Traffic Granular Flow* 2019:283–289
33. Guo RY, Huang HJ, Wong SC (2012) Route choice in pedestrian evacuation under conditions of good and zero visibility: experimental and simulation results. *Transport Res Part B: Methodol* 6(46):669–686
34. Liu S, Yang L, Fang T, Li J (2009) Evacuation from a classroom considering the occupant density around exits. *Physica A* 9(388):1921–1928
35. Lovreglio R (2016) Modelling decision-making in fire evacuation based on random utility theory. Politecnico of Bari, Milan and Turin

Describing Construction Hazard Images Identified from Site Safety Surveillance Video



Wen-Der Yu, Wen-Ta Hsiao, Tao-Ming Cheng, Hung-Sheng Chiang, and Chia-Yu Chang

Abstract Construction accidents are a major cause of occupational fatalities globally. On-site hazard identification is crucial to prevent such accidents. CCTV is commonly used for safety surveillance on construction sites, and can be utilized for machine learning-based automatic hazard identification. A Construction Hazard Description System (CHDS) was developed in this study to systematically label site objects and describe hazard scenarios. CHDS builds on the ontology of Taiwan Occupational Safety and Health Administration (TOSHA) for hazard classification and construction accident risk scenarios. The system produces site images and associated hazard descriptions that can be used to train automated construction accident risk identification systems through machine learning. According to domain experts, CHDS is effective in assisting construction safety personnel in describing hazard images collected on site, achieving high accuracy rates in both attribute description and hazard classification. It is concluded the system has great potential in improving the task of captioning construction hazard images.

Keywords Construction safety · Hazard identification · Hazard ontology · Risk scenarios · Image processing

1 Introduction

The construction industry is a crucial driving force for economic growth in many countries. In Taiwan, the industry employs over 913,000 workers and accounts for 3.77% of the gross national product [1]. However, the per capita GDP of the construction industry is only about 60% of the national average, making construction workers a relatively economically disadvantaged labor force. Unfortunately, the construction industry also poses significant safety risks, with construction accidents being

W.-D. Yu · W.-T. Hsiao (✉) · T.-M. Cheng · H.-S. Chiang · C.-Y. Chang
Chaoyang University of Technology, Taichung 413310, Taiwan
e-mail: wdshiau@cyut.edu.tw

© The Author(s), under exclusive license to Springer Nature Singapore Pte Ltd. 2024
M. Casini (ed.), *Proceedings of the 3rd International Civil Engineering and Architecture Conference*, Lecture Notes in Civil Engineering 389,
https://doi.org/10.1007/978-981-99-6368-3_76

937

the highest percentage of industrial occupational accidents and major occupational accidents worldwide.

According to statistics from the Directorate-General of Budget, Accounting, and Statistics, Executive Yuen, the construction industry accounted for 46.32% of major occupational accidents in Taiwan from 2009 to 2020, with a death rate 4.78 times higher than the national average of all industries [2]. Although the government has invested in research and legal systems, there is a shortage of professional occupational safety managers on construction sites, making it challenging to achieve site risk control and immediate prevention measures [3].

Studies have linked site environmental hazards and unsafe labor behaviors to construction accidents [4]. However, identifying hazards relied on occupational safety personnel and real-time image monitoring couldn't identify and correct hazards quickly enough to prevent accidents [5]. To improve construction site safety and productivity, this study proposes a semantic analysis and automatic image captioning model for identifying and monitoring site hazards. The proposed model aims to address this limitation by providing an automated solution for hazard detection and management.

2 Review of Relevant Works

This section provides a review of relevant theoretical literature to enhance our understanding of the key areas and topics addressed in this study.

2.1 *Disaster Causation Theory and Site Hazard Identification*

The causes of occupational disasters can be classified into direct, indirect, and basic causes [6]: Direct causes are related to energy release and exposure to hazardous substances, while indirect causes include unsafe environmental conditions and unsafe behavioral actions. Basic causes refer to the employer's management deficiencies. Unqualified facilities and equipment may also cause hazards. Heinrich's "Domino Theory," proposed in 1931, was the earliest theory to study the causes of occupational accidents [6]. It classifies accidents into five factors that interact with each other in a cause-and-effect manner: social and family environment, individual deficiencies, unsafe behaviors or conditions, accidents, and injuries and losses. Widner developed the "New Domino Theory of Disaster" based on Heinrich's theory [7]. Both theories suggest that eliminating one factor will prevent the occurrence of subsequent factors.

Occupational accidents are caused by hazards, which are defined as potential factors that can cause harm or damage to human health. Hazard identification is the process of identifying hazards and defining their characteristics [8] The "Hazard Identification" is a procedure to identify the existence of hazards and define their characteristics [9]. Traditional hazard identification and risk assessment techniques

include checklists, What-If analysis, and risk matrix [9]. However, most of these techniques are used during the design and planning period and are not suitable for hazard identification in field operations. Additionally, existing methods rely on the experience of human safety personnel, emphasizing the importance of hazard identification training and coaching [10].

2.2 Ontology of Hazard Descriptions

The knowledge ontology describes domain-specific knowledge. Previous ontologies for site safety management were related to Building Information Modeling (BIM) applications [11]. They lacked actual engineering validation and only focused on a few disaster-causing factors. To build a more comprehensive ontology for construction safety, Liu et al. proposed a linguistic schema for describing hazards in construction images of common activities [12].

The model in Fig. 1 comprises white boxes for main objects, green boxes for actions, and blue ellipses for basic attributes. The framework also adds attributes, such as workers' gestures for greater precision. Liu et al.'s [12] ontology is more dynamic than Collinge et al.'s risk ontology [13]. This study aims to establish a set of linguistic schemas based on the above frameworks for describing construction safety hazards.

2.3 Image Captioning

Image captioning combines computer vision and natural language processing to describe the contents of an image in human language [14]. Traditional methods include sentence-based templates [15], image search [16] and deep learning-based approaches [14]. Deep learning-based methods have made remarkable progress and won the MS COCO image caption generation challenge, showing great potential for complex construction site descriptions [14].

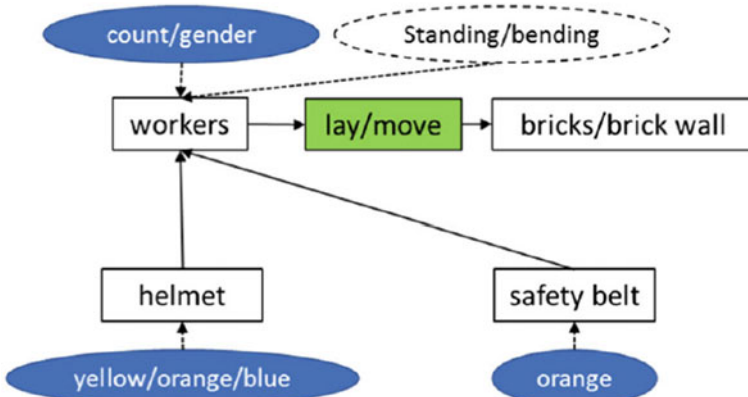
3 Research Problems and Objectives

3.1 Research Problems

Two key issues are preventing the realization of automated hazard identification for construction, which will be discussed in this paper. Firstly, there is currently no image semantic description linguistic schema available to describe complex construction hazards, such as falling and rolling hazards caused by temporary structures. To



(a). Scene images of masonry work



(b). Scene analysis of masonry work

Fig. 1 Linguistic schema model for describing bricklaying operation activity [12]

address this, a formal and shareable image semantic description linguistic schema must be established. Relevant regulations and regular safety inspections can provide knowledge on prevention and control measures for related risk situations. Secondly, there is no image description dataset for construction site safety hazard scenarios, which limits the accuracy of image descriptions. Current deep learning models need further training and fine-tuning to account for unique semi-finished and temporary structures, diverse laborers, machinery and equipment found on construction sites. Establishing an adequate dataset of OSH-related images and professional descriptors of safety hazards is the second research problem to be addressed.

3.2 Objectives

The current research has two primary objectives to address the research problems identified in Sect. 3.1: (1) Establish a linguistic schema that effectively describes safety hazards on construction sites, is processable by computer language, and can be understood and shared by site safety personnel; (2) Establish a benchmark dataset of images and the associated safety hazard descriptors related to construction sites to

aid in the identification of occupational safety hazards. For this end, the study hired an external professional OSH consultant, established standard operating procedures (SOP), and trained construction senior college students to build the database.

4 System Development for Construction Hazard Description

4.1 Research Procedure

To achieve the objectives defined in the last section, a research procedure is planned as shown in Fig. 2. A research procedure is planned to achieve the objectives. Steps include: (1) Review of state-of-the-art technologies, (2) Linguistic schema model for safety hazard scene image captioning, (3) Occupational safety hazard image caption labelling SOP, (4) Collecting video data of construction site safety inspections, (5) Site occupational safety hazards image framing and description, (6) Expert review, (7) Establishing hazard identification image captioning dataset stored in the “Construction safety hazard image captioning benchmark dataset (CSHICBD)”, and (8) Machine Learning testing using Matlab[®] Deep Learning Toolbox for validation.

4.2 Hazard Classification System of TOSHA

The Occupational Safety and Health Agency of Taiwan (TOSHA) has a classification system for worksite hazards, but it's not specific to construction. The Construction Agency of Taoyuan City has modified the system to better fit construction hazards. [17]. The TOSHA hazard classification system includes 19 major types of construction hazards such as falls, collisions, and cuts. This system forms the basis for the hazard ontology used in this research. (<https://www.osha.gov.tw/>), e.g., ‘H01-Fall from height’, ‘H02-Fall down’, ‘H03-Collision’, ‘H04-Object flying down’, ‘H05-Collapse’, ‘H06- Struck-by’, ‘H07-Trapped and clamped’, ‘H08-Cut’, ‘H09-Step through (roof)’, ‘H10-Drown’, ‘H11-Heated’, ‘H12-Contact with harmful substances’, ‘H13-Electric shock’, ‘H14-Explosion’, ‘H15-Object broken’, ‘H16-Fires’, ‘H17-Improper action’, ‘H18-Others’, and ‘H19-Management faults’. This system forms the basis for the hazard ontology used in this research.

4.3 Linguistic Schema of Safety Hazard Image Captioning

This study proposes a linguistic schema for image description of OSH hazards based on a hazard classification system. The schema includes ontology of safety knowledge,

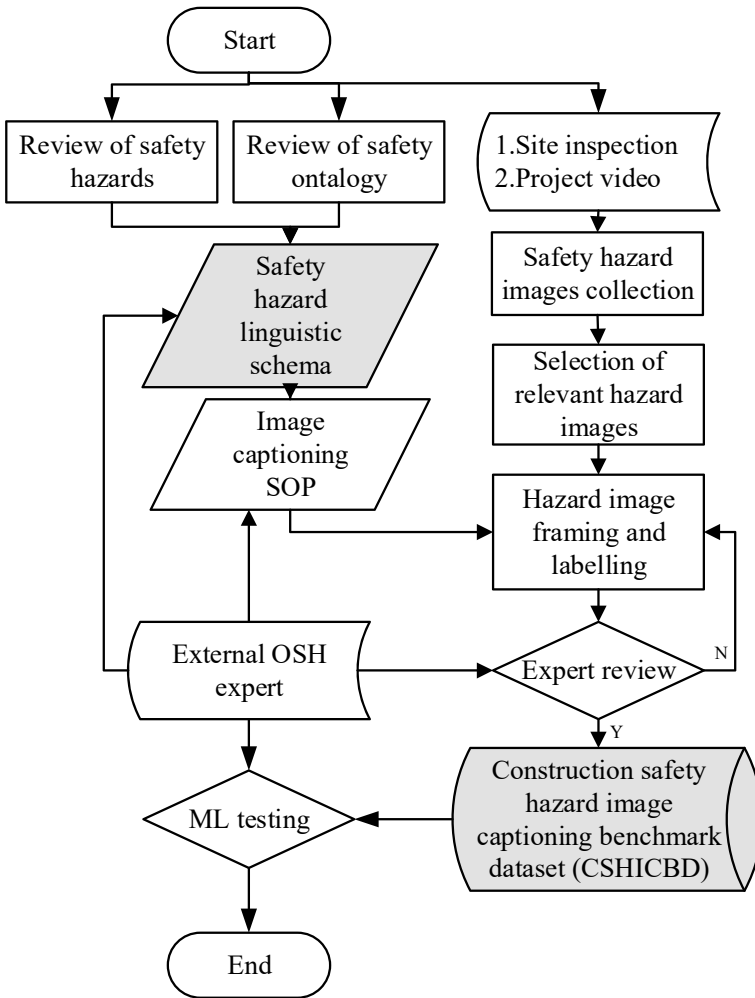


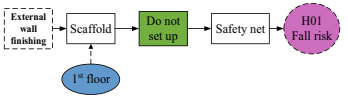
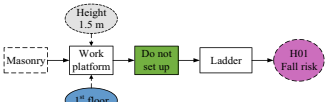
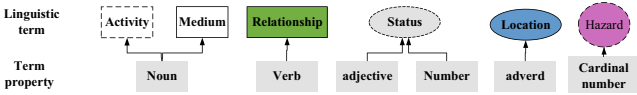


Fig. 2 Research procedure

image captioning phrases from the MS COCO database [18], and the 1,680 linguistic files accumulated by the research team [17]. The proposed schema meets the ontology requirements suggested by Borst [19] and Collinge et al. [13]. Using the linguistic schema from Table 1, domain experts (primarily professional safety personnel) can describe multiple image captioning sentences.

Table 1 Linguistic schema for image captioning of safety hazards

<p>Safety hazard images</p>		
<p>Hazard description</p>	<p>Safety net is not used on the gap between scaffold and wall during exterior wall finishing, creating a risk of H01 falling</p>	<p>No ladder with work platform over 1.5 m when finishing first floor masonry creates H01 falling risk</p>
<p>Linguistic schema</p>		
<p>Speech elements</p>		

4.4 Development of Construction Hazard Description System (CHDS)

The CHDS is introduced in this section for training an Automated Construction Hazard Image Captioning System (ACHICS). Previous studies [14] used public domain datasets like MS COCO [18], Flickr8k [20], Flickr30k [21] for image captioning, which are not appropriate for construction hazard description. Such generic datasets cannot effectively train an ACHICS to recognize construction hazards. The proposed CHDS interface graphics are shown in Figs. 3 and 4. Figure 3 labels and frames frequently seen objects (workers, equipment, machinery, materials, etc.) with their locations in the image, stored in XML format in an independent ‘.xml’ file.

In Fig. 4, the worker at the indoor basement area is at risk of falling from height (H01) due to unprotected edge openings (no guardrails).

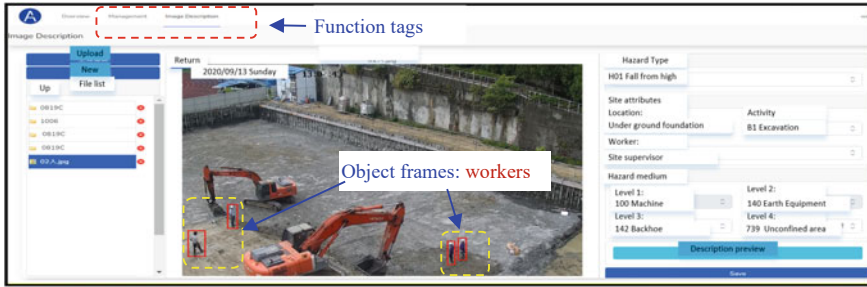


Fig. 3 System interface of the proposed CHDS—Object labeling

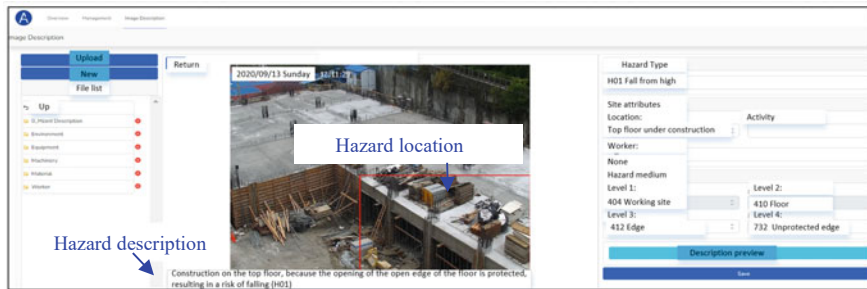


Fig. 4 System interface of the proposed CHDS—Hazard description

5 System Testing and Preliminary Results

The CHDS was tested for two functions: (1) labeling common objects found onsite, and (2) captioning hazard images with attribute information. Object labeling was tested using Matlab Deep Learning Toolbox[®] (MLDLT); while hazard image captioning was validated by TOSHA safety-certified domain experts.

5.1 Site Object Framing and Labeling Testing with ML

To test the proposed CHDS for image framing and categorization, 224 collected images were labeled using CHDS and tested with MLDLT’s image classification functions. Faster R-CNN with 4 CNN layers was used for object recognition, with 200 images used for training and 24 for testing. The resulted confusion matrix comprising Recall and Precision performance indexes are shown in Table 2, with Recall = 68.3% and Precision = 100%, indicating a fair Recall but perfect Precision performance.

The low Recall and Precision indexes of some objects were investigated, considering factors such as small images, insufficient samples for ML training, complicated

Table 2 The confusion matrix of object recognition by Faster R-CNN

	Actual with target	Actual without target	Precision
Predicted with target	97	0	100%
Predicted without target	45	0	
Recall	68.3%		

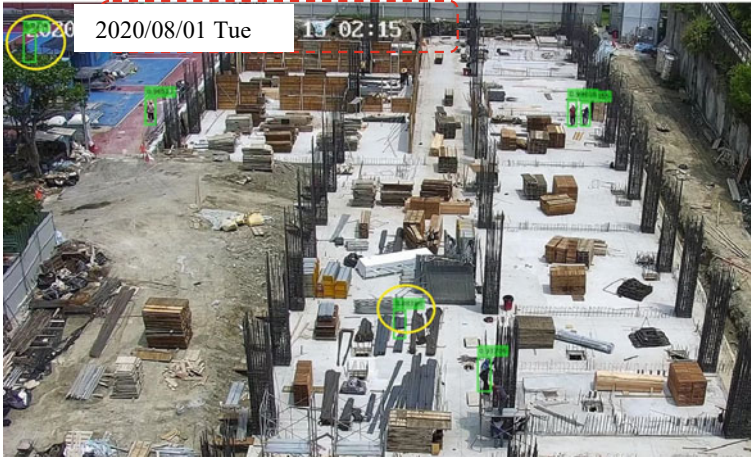


Fig. 5 Misrecognition of site objects (workers) by Faster R-CNN

site environment, and illumination issues. Figure 5 illustrates an example of image recognition for a worker, where false recognitions occurred for rebar laying images.

5.2 Hazard Image Captioning by Domain Experts

The feasibility of the proposed CHDS for image captioning of onsite hazard scenarios was tested using expert evaluation. The hazard attributes, such as hazard type, work location, activity type, worker types, and hazard medium (classified into four levels), were collected and stored in SQL database format as depicted in Fig. 6.

image_name	image_path	xml_path	attributes	created_at	updated_at
IMG_7976.jpg	/storage/hazard_image/image/IMG_7976.jpg	hazard_image/xml/00001001.XML	"{"hazard": "1", "location": "2022-05-22 08:06:39"	2022-07-23 13:11:53	2022-07-23 13:11:53
FN560pacAEHhA.jpg	/storage/hazard_image/image/01FN560pacAEHhA.jpg	hazard_image/xml/01FN560pacAEHhA.xml	"{"hazard": "0", "location": "2022-10-23 12:31:39"	2022-10-23 12:31:39	2022-10-23 12:31:39
FNuKqgVUAi2_LG.jpg	/storage/hazard_image/image/01FNuKqgVUAi2_LG.jpg	hazard_image/xml/01FNuKqgVUAi2_LG.xml	"{"hazard": "0", "location": "2022-10-23 12:31:39"	2022-10-23 12:31:39	2022-10-23 12:31:39
FNVEapHUYAOipQ.jpg	/storage/hazard_image/image/01FNVEapHUYAOipQ.jpg	hazard_image/xml/01FNVEapHUYAOipQ.xml	"{"hazard": "0", "location": "2022-10-23 12:31:39"	2022-10-23 12:31:39	2022-10-23 12:31:39
FO11hsaQAc0Yv05.jpg	/storage/hazard_image/image/01FO11hsaQAc0Yv05.jpg	hazard_image/xml/01FO11hsaQAc0Yv05.xml	"{"hazard": "0", "location": "2022-10-23 12:31:39"	2022-10-23 12:31:39	2022-10-23 12:31:39
FOhP1QeacVYndqj.jpg	/storage/hazard_image/image/01FOhP1QeacVYndqj.jpg	hazard_image/xml/01FOhP1QeacVYndqj.xml	"{"hazard": "0", "location": "2022-10-23 12:31:39"	2022-10-23 12:31:39	2022-10-23 12:31:39
FN560pacAEHhA.jpg	/storage/hazard_image/image/01FN560pacAEHhA.jpg	hazard_image/xml/01FN560pacAEHhA.xml	"{"hazard": "0", "location": "2022-10-23 12:50:22"	2022-10-23 13:04:56	2022-10-23 13:04:56
FNuKqgVUAi2_LG.jpg	/storage/hazard_image/image/01FNuKqgVUAi2_LG.jpg	hazard_image/xml/01FNuKqgVUAi2_LG.xml	"{"hazard": "0", "location": "2022-10-23 12:50:22"	2022-10-23 12:50:22	2022-10-23 12:50:22
FNVEapHUYAOipQ.jpg	/storage/hazard_image/image/01FNVEapHUYAOipQ.jpg	hazard_image/xml/01FNVEapHUYAOipQ.xml	"{"hazard": "0", "location": "2022-10-23 12:50:22"	2022-10-23 12:50:22	2022-10-23 12:50:22
FO11hsaQAc0Yv05.jpg	/storage/hazard_image/image/01FO11hsaQAc0Yv05.jpg	hazard_image/xml/01FO11hsaQAc0Yv05.xml	"{"hazard": "0", "location": "2022-10-23 12:50:22"	2022-10-23 12:50:22	2022-10-23 12:50:22
FOhP1QeacVYndqj.jpg	/storage/hazard_image/image/01FOhP1QeacVYndqj.jpg	hazard_image/xml/01FOhP1QeacVYndqj.xml	"{"hazard": "0", "location": "2022-10-23 12:50:22"	2022-10-23 12:50:22	2022-10-23 12:50:22

Fig. 6 Data of image captions for hazards identified from site hazardous scenarios

Table 3 Evaluation of image captioning for proposed CHDS

Hazard type	No	Attributes (%)	Hazard (%)	Overall (1–5)
H01-Fall from height	13	90	100	4
H02-Fall down	5	100	100	5
H04-Object flying down	1	100	100	5
H05-Collapse	6	100	100	5
H06-Struck-by	3	100	100	5
H08-Cut	3	100	100	5
H18-Others	2	70	0	4
H19-Management faults	17	100	100	5
Sum/Average	50	96.2	96.0	4.7

The proposed CHDS for hazard image captioning was evaluated by safety experts using a Likert-5 scale. Attribute descriptions and hazard classifications were assessed for correctness, as different scenarios may result in different hazards based on attribute conditions. Results of the preliminary evaluation of 50 hazard images collected by CHDS are presented in Table 3. The evaluation showed very high accuracy in both attribute description and hazard classification, achieving an overall score of 4.7 (94% accuracy) on the Likert 5-point scale.

6 Summary from Preliminary Testing Results

The preliminary testing results of CHDS highlights the importance of correct attribute description for hazard classification in complicated site conditions. An orientation for the user was held to ensure correct use of the system. The preliminary results also show promise for generating useful image captions for hazard scenarios onsite, which can be used to develop the Automated Construction Hazard Image Captioning System (ACHICS) in the future. However, identification of onsite objects was difficult due to remote filming, which can be improved by using a PTZ zoomable camera. This creates a chicken-and-egg problem that needs to be resolved in future work.

7 Conclusion

This article presents a recent work on developing a Construction Hazard Description System (CHDS) to systematically describe hazard scenarios using a hazard description ontology. A web-based CHDS was developed to assist safety personnel in describing hazard images collected from a CCTV surveillance system installed on a real-world construction site. Testing results show promising potentials for the

CHDS in captioning construction hazard images with high accuracy in both correct attribute description and hazard classification. The proposed CHDS can expedite the task of captioning construction hazard images.

The proposed CHDS shows promising results, but improvements are needed. The complicated construction site environment poses challenges to object recognition. A larger database of close-up images is needed, and other DL techniques can be used to improve recognition rates. Correct attribute description and hazard type classification are also challenging, and a standard operation procedure is needed. Additionally, generating enough training sets for ACHICS requires collecting at least 5000 images and 25,000 safety hazard descriptors related to construction sites, which is labor-intensive and time-consuming.

Acknowledgements This project (MOST 111-2221-E-324-011-MY3) was funded by the National Science and Technology Council of Taiwan. The authors gratefully acknowledge her support.

References

1. DGB (2018) Summary analysis of the preliminary statistical results of the 2016 industrial and commercial and service industry census. Directorate-General of Budget, Accounting and Statistics, Executive Yuan, R.O.C. (Taiwan), Published 27 Apr 2018, web document: <https://www1.stat.gov.tw/public/Attachment/8427181926BYT9Y7B1.pdf>. Accessed 24 Oct 2022
2. TOSHA (2020) 2020 Labor inspection annual report. Web document. <https://www.osha.gov.tw/1106/1164/1165/1168/34345/>. Occupational Safety and Health, Taiwan. Accessed 24 Oct 2022
3. MOL (2022) Enforcement rules of the Occupational Safety and Health Act. MOL regulation search system. <https://laws.mol.gov.tw/>. Accessed 24 Oct 2022
4. Jeong BY (1998) Occupational deaths and injuries in the construction industry. *Appl Ergon* 29(5):355–360. [https://doi.org/10.1016/S0003-6870\(97\)00077-X](https://doi.org/10.1016/S0003-6870(97)00077-X)
5. Ding L, Fang W, Luo H, Love PED, Ouyang X (2018) A deep hybrid learning model to detect unsafe behavior: Integrating convolution neural networks and long short-term memory. *Autom Constr* 86:118–124
6. Heinrich HW (1931) *Industrial accident prevention*. McGraw-Hill, New York
7. Widner JT (1973) *Selected readings in safety*. Academy Press, Macom
8. *Occupational Health and Safety Management Systems-Requirements, OHSAS 18001:2007* (2007) British Standards Institution, London
9. Yeh GY (2009) Application of event tree analysis in occupational safety risk assessment. Master thesis, MS Program of Environment Engineering, National Central University
10. Chang RN (2012) Training of potential hazard identification on construction site using virtual reality. Master thesis. MS Program of Environmental Engineering, National Chiao Tung University
11. Wang H-H, Boukamp F (2011) Ontology-based representation and reasoning framework for supporting job hazard analysis. *J Comput Civ Eng* 25:442–456. [https://doi.org/10.1061/\(ASCE\)CP.19435487.0000125](https://doi.org/10.1061/(ASCE)CP.19435487.0000125)
12. Liu H, Wang G, Huang T, He P, Skitmore M, Luo X (2020) Manifesting construction activity scenes via image captioning. *Autom Constr* 119:103334
13. Collinge WH, Farghaly K, Mosleh MD, Manu P, Cheung CM, Osorio-Sandoval CA (2022) BIM-based construction safety risk library. *Autom Constr* 141:104391. <https://doi.org/10.1016/j.autcon.2022.104391>

14. Li SC (2021) Image caption with object detection and self-attention mechanism. MS Program of Artificial Intelligence, National Yang Ming Chiao Tung University
15. Farhadi A, Hejrati M, Sadeghi MA, Young P, Rashtchian C, Hockenmaier J, Forsyth D (2010) Every picture tells a story: generating sentences from images. In: ECCV 2010. Lecture notes in computer science, vol 6314, pp 15–29
16. Mitchell M, Han X-F, Dodge J et al (2012) Midge: generating image descriptions from computer vision detections. In: EACL'12: proceedings of the 13th conference of the European chapter of the association for computational linguistics, pp 747–756
17. Hsiao WT, Yu WD (2020) Analysis and prevention of the critical factors causing safety hazards of building construction. To be present in the proceedings of the 2nd international conference on architecture, construction, environment, and hydraulics (ICACEH 2020), 25–27 Dec, Hsinchu, Taiwan
18. Chen X, Fang H, Lin T-Y, Vedantam R, Gupta S, Dollár P, Zitnick CL. Microsoft coco captions: data collection and evaluation server. ArXiv Preprint
19. Borst WN (1997) Construction of engineering ontologies for knowledge sharing and reuse. Universiteit Twente. <https://research.utwente.nl/en/publications/construction-of-engineering-ontologies-for-knowledge-sharing-and->
20. Hodosh M, Young P, Hockenmaier J (2013) Framing image description as a ranking task: data, models and evaluation metrics. J Artif Intell Res 47:853–899. <https://doi.org/10.1613/jair.3994>
21. Young P, Lai A, Hodosh M, Hockenmaier J (2014) From image descriptions to visual denotations: new similarity metrics for semantic inference over event descriptions. Trans Assoc Comput Linguist 2:67–78. https://doi.org/10.1162/tacl_a_00166

A Computationally Efficient Method for Simulation-Based Evacuation Guidance Optimization



Zhang Botao  and S. M. Lo 

Abstract Effective evacuation guidance can help evacuees reach the exit as soon as possible in an emergency evacuation process to ensure their safety. However, due to the unstable mobility condition and crowd distribution, the guidance plan made in advance by comparing the distances to exits may not be the most effective, so it is necessary to provide real-time optimal guidance information in the plan. This study presents a computationally efficient evacuation plan optimization method that combines CTM (Cell Transmission Model)-based simulation and DRF (Directed Rooted Forest)-based planning. In this method, the simulation module predicts evacuation dynamics at a computational cost that does not grow with crowd size, while the planning module takes advantage of the simulation feedback to optimize the evacuation plan efficiently. The high efficiency is achieved by a DRF structure suitable for representing the evacuation plan and a node assignment optimization algorithm highly coupled with the CTM simulation. In addition, the feedback from the simulation is employed to evaluate the performance of new solutions, making the search more directional and accelerating the algorithm convergence. The proposed method may serve as the foundation for developing real-time evacuation guidance plans for large-scale crowded buildings.

Keywords Emergency evacuation · Crowd dynamics · Real-time evacuation plan · Cell transmission model · Directed rooted forest

1 Introduction

As the population migration caused by urban agglomeration promotes economic growth, it also leads to myriad public safety problems [1]. In many densely populated urban cores, large-scale facilities have been built but can hardly meet the surge in demand. As a result, overcrowding during peak hours becomes a potential root cause

Z. Botao (✉) · S. M. Lo
City University of Hong Kong, Kowloon Tong, Hong Kong SAR, China
e-mail: botzhang2-c@my.cityu.edu.hk

© The Author(s), under exclusive license to Springer Nature Singapore Pte Ltd. 2024
M. Casini (ed.), *Proceedings of the 3rd International Civil Engineering and Architecture Conference*, Lecture Notes in Civil Engineering 389,
https://doi.org/10.1007/978-981-99-6368-3_77

949

of crowd disasters such as progressive crowd collapse and crowd crush [2]. In an emergency (e.g., fire, earthquake, or terrorist attacks), the crowdedness increases safety risks further. Targeting vulnerabilities of gathering people in emergencies, the issue of pedestrian evacuation management has raised interest among researchers in traffic engineering, computer science, operational research management, and many other fields [3].

Undoubtedly, pedestrian evacuation management consists of interdisciplinary scientific problems that must be solved by combining multiple methods and technologies. For one thing, the unabated empirical studies and mathematic modeling facilitate the analysis and reproduction of pedestrian dynamics and underlie the research on evacuation planning [4]. For another, intelligent techniques provide more methods for crowd monitoring and anticipation of crowd disasters, thereby enabling the integration of theoretical research into engineering practice [5]. However, to the best of our knowledge, most of the model-driven research shows two deficiencies. On the one hand, current research tends to take advantage of the existing models, which are more suitable for reproducing the self-organization phenomenon instead of predicting the performance of evacuation plans. On the other hand, a dearth of discussion on coupling simulation models with the optimization method may lead excessive computational overhead, especially for the evacuation from a large-scale pedestrian facility. Considering the above discussion, research that can formulate management strategies based on effective modeling is urgently needed.

2 Literature Review

Extensive research effort has been devoted to developing pedestrian movement models and optimizing the evacuation with the model. According to the difference in the granularity of the problem, they can be divided into two categories: mathematical programming-based network flow optimization and physical simulation-based route planning.

Most of the early studies classified as network-based planning treated the evacuation scenario as a transport network. This strand of research focused on building a comprehensive pedestrian network model and applying mathematical programming to find optimal flow assignment strategies that can shorten evacuation time. To find an efficient evacuation plan under the interference of fire and smoke, Lin et al. [6] firstly abstracted the evacuation system as a multi-source multi-sink network and established a multi-stage time-varying quickest flow approach for calculating the clearance time of the network. Similarly, Chen and Feng [7] converted the large-scale evacuation to multiple-narrow problems and developed two fast-flow control algorithms: multiple-narrow doors flow control algorithm and k-limited flow control algorithm. Considering Lin's network model, Park et al. [8] proposed a time-dependent optimal routing algorithm that can take temporal databases as input. Taking the capacity of the network into consideration, Lim et al. [9] constructed a capacitated and time-dependent network flow model with a greedy algorithm for

flow generation to determine the starting time for executing the evacuation process, recommended evacuation paths, and their flow for priority. For a similar pedestrian evacuation network, Aalami and Kattan [10] designed a more efficient planning algorithm and analyzed the fairness of evacuation plans with the Gini coefficient and Lorenz curve. Because of the simplification of crowd dynamics in the network, these planning methods normally possess high computational efficiency. Nonetheless, another side of the coin is the inaccuracy in flow calculation. Since the paths in the pedestrian space are not controlled-access highways, pedestrian flows to the same location interfere with each other in intertwined paths.

Another strand of research labeled as individual-based guidance emphasized individual pedestrian movement during evacuation. With the development of modeling research, some microscopic models with great expansibility perform well in reproducing evacuees' behavior at the operation layer. And they have been widely adopted for analysis and discussions at the decision-making layer. Gao et al. [11] developed a set of algorithms composed of a macroscopic route choice model at the top layer and a modified social force model (SFM) at the bottom layer. They planned the pedestrians' routes based on the dynamic user optimal criterion. Abdelghany et al. [12] proposed a similar two-layer framework, which simulated pedestrians' local maneuvers with the cellular automaton (CA) model at the bottom layer. Matching with empirical research, Crociani and Lämmel [13] presented a novel CA model that can induce the microscopic pedestrian dynamics in line with fundamental diagrams (FDs) to find Nash equilibrium and the system optimum. In their research, the route assignment was achieved with an iterative learning process where the individual pedestrian can adapt their strategies based on previous experiences. Jiang et al. [14] modified the dynamic navigation field in SFM which aiming at reducing the total instantaneous walking cost. Although the abovementioned research can provide detailed information on evacuation processes, the unacceptable computational requirement limits their applicability. To solve this problem, Zhang and Jia [15] suggested a two-layer method including a strategic guidance model for leaders and a modified cell transmission model (CTM) for followers. However, this method seems questionable since the egg-and-chicken problem that followers' behavior will also affect the leaders' decisions is not well-discussed.

This research will combine the advantages of the two types of research to develop an optimization method based on crowd simulation feedback for evacuees in large-scale facilities. To reduce the computational complexity associated with simulation, the optimization method will be required to find an acceptable approximation of the optimal guidance solution for a certain number of simulations.

3 Methodology

3.1 CTM-Matched Graph Construction and Guidance Initialization

The cell Transmission Model (CTM) is a typical mesoscopic simulation model for predicting crowd dynamics [16]. Since it focuses only on the mesoscopic parameters within the discretized cells, its computational complexity is not affected by the crowd size, but only by the discretization method. Among all types of regular polygons that can seamlessly fill the entire plane, we choose regular hexagon which can maximize the reproduction of anisotropy of the crowd movement at the same cell scale.

After the discretization, all cells share a boundary with obstacles or walls, each cell has limited connections with up to six neighbors. By treating the centroids of cells as nodes, and the connection between the nodes and their neighbors as links, the scenario where evacuees are initially distributed can be mapped onto a connected graph $G = (N, P)$ (Note that N here contains not only the internal nodes obtained from discretization, but also the exit nodes $e_1, e_2 \dots, e_n$ which represent the central positions of all exits). On this basis, all evacuees can be subsequently distributed to nodes based on their initial positions. For node c_i , a_i denotes the walkable area of unoccupied space in its corresponding cell and ρ_i tells the local density of evacuees in this cell.

To ensure that evacuees in each cell can reach the exit by continuously following the guidance at each node without circling around, we introduce the concept of DRF to decompose the graph G . After loading the key node attributes onto the graph, the initial DRF can be obtained with the following procedure shown in Table 1.

Through the above steps, the graph will be decomposed into a rooted forest containing multiple disjoint rooted trees. Taking all edges in an anti-branching structure (from the node to its parent node), an initial evacuation plan represented by the DRF can be obtained. These steps are illustrated in Fig. 1.

Table 1 DRF initialization procedure

Step 1: Create tree sets $T_1, T_2 \dots, T_n$, each of which initially contains only one exit node $e_1, e_2 \dots, e_n$
Step 2: Construct the adjacency matrix A with the distance of each node to its neighbors as the weight. And then calculate the distance $d_{i,m}$ from each internal node c_i to the exit node e_m by inputting the matrix into Dijkstra’s algorithm
Step 3: Find the tree set T_m with the smallest total number of evacuees $\operatorname{argmin}_m \left\{ \sum_{c_i \in T_m} \rho_i \cdot a_i \right\}$, then add a node connected to nodes in C_m that has the smallest $d_{i,m}$ from the unassigned nodes and put it into T_m
Step 4: Repeat Step 3 until all nodes in N are assigned to the tree sets
Step 5: For each internal node in tree T_m , set its parent node to be the neighbor node that belongs to the same tree set and has the smallest $d_{i,m}$

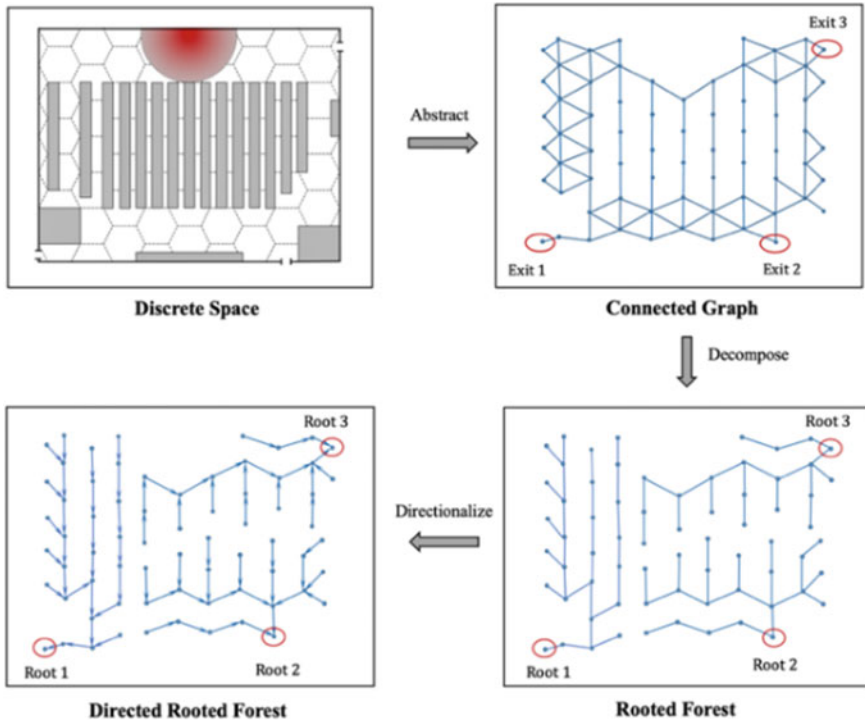


Fig. 1 The schematic diagram of evacuation planning with DRF

3.2 Flow Calculation in CTM

With the guidance directions in the DRF-based evacuation plan, the flow direction of the evacuees in the different cells in the simulation model for performance evaluation can be determined. The CTM simulates the evacuation process by updating the evacuee stocks of all the nodes at a fixed frequency. The time step is denoted by Δt . In the case of a regular hexagonal discretization, it can be calculated in the following manner,

$$\Delta t = \sqrt{3}l/v_{\text{free}} \tag{1}$$

where v_{free} denotes the velocity of evacuees in the free flow situation (no interruptions), and $\sqrt{3}l$ is the path length from one node to another neighboring node. Using n_i^{max} to represent the maximum capacity of cell i , it can be approximated as follow,

$$n_i^{\text{max}} = \lfloor a_i \cdot \rho_{\text{jam}} \rfloor \tag{2}$$

where $[x]$ is the function to obtain an integral part of x ; and ρ_{jam} represents the jam density (maximum density) of the evacuees in the local area.

As this model is designed only to evaluate the performance of evacuation plan when all evacuees in the node will receive a uniform set of instructions. As for the calculation of flow rate q_{ij} which direction is from cell i to its downstream cell j , following formula can be applied,

$$q_{ij} = \rho_{ij} \cdot v(\rho_{ij}) \cdot b_{ij} \tag{3}$$

where ρ_{ij} is calculated by averaging the local density of evacuees in cell i and cell j , and $v(\rho_{ij})$ indicates the function for the corresponding velocity of evacuees there. The function that shows the relationship between ρ_{ij} and $\rho_{ij} \cdot v(\rho_{ij})$ is normally obtained from the study on pedestrian fundamental diagrams (PFDs) [17]. With the PFD, the evacuees' velocity can be maintained at the level of free flow velocity v_{free} when the local density is below the critical density ρ_{cri} , but when beyond this threshold, the flow-density curve falls with a fixed slope $-v_{wave}$. So, the flow rate that is influenced by the real-time state of cell i and cell j can be calculated with the following equation,

$$q_{ij}(t) = \min\{\rho_i(t) \cdot v_{free} \cdot b_{ij}, (\rho_{jam} - \rho_i(t)) \cdot v_{wave} \cdot b_{ij}\} \tag{4}$$

where b_{ij} represents the length of the passible boundary between cell i and cell j .

In the same way as in a bathtub, both the upstream and downstream stock supply limit the actual flow volume. A cell may contain multiple upstream nodes despite having just one downstream node. When the flow from different cells merges, the upstream inflow is constrained by the downstream capacity. As such, the restricted inflow can be calculated by looking at the inflow rates of the downstream cell,

$$o_i(t) = \begin{cases} \Delta t \cdot q_{ij}(t), & \text{if } \sum_k \Delta t \cdot q_{kj}(t) \leq n_j^{max} - n_j(t) \\ \left[n_j^{max} - n_j(t) - \sum_k \Delta t \cdot q_{kj}(t) \right] * q_{ij}(t) / \sum_k q_{kj}(t), & \text{else} \end{cases} \tag{5}$$

where $o_i(t)$ represents the outflow from the cell i in the time step t .

Then the outflow of cell i can be determined, and the number of evacuees in the cell can be updated after each time step with the following equation,

$$n_i(t + 1) = n_i(t) - o_i(t) + \sum_{k \in U_i} o_k(t) \tag{6}$$

At each time step in the CTM, the stock of evacuees in the cell will be calculated and updated according to the above equations. When the evacuee moves toward the directed edge in the DRF, the flow update direction in the cells should be the out-forest direction due to the information transformation. Specifically, the cells corresponding

to the nodes at the lower hierarchy in each DRT will preferentially generate outflows and update the number of evacuees. In comparison, the cells corresponding to the nodes at the higher hierarchy will generate their outflows as the inflow of downstream cells based on the updated status of all downstream cells. In a timestep, the above process will be continuously executed in each DRT until the number of evacuees in all cells is updated. The simulation proceeds with time steps until the number of evacuees in all cells is all 0.

3.3 Guidance Optimization Based on Simulation Results

As the simulation proceeds, the cumulative outflow from each exit is counted for each time step and recorded in the corresponding time series. For e_k that takes a total of X_k time steps to evacuate, its time series is $R_k = \{r_{k,1}, r_{k,2}, \dots, r_{k,X_k}\}$. To reduce the total evacuation time $\max\{X_1, X_2 \dots, X_n\}$, the optimization method constantly balances the gap between evacuation times at each exit. The range θ can represent this gap, and the minimization of this metric becomes our optimization goal.

$$\theta = \max\{X_1, X_2 \dots, X_n\} - \min\{X_1, X_2 \dots, X_n\} \tag{7}$$

For this purpose, the evacuation time required for each node (i.e., time required for all evacuees whose initial location is within the cell corresponding to the node to leave the indoor space) can be approximated by linear interpolation. For $c_i \in T_k$, its evacuation time t_i^E can be calculated with the following equation,

$$t_i = t + \left(\sum_{j, d_{j,k} < d_{i,k}} n_j - r_{k,t} \right) / (r_{k,t+1} - r_{k,t}) \tag{8}$$

When all nodes' evacuation times are obtained, their imbalance can also be defined. For $c_i \in T_k$, if it has at least one neighbor node belonging to another tree, then its imbalance δ_i is calculated according to the following equation,

$$\delta_i = \max_{j, c_j \in U_i} \{t_i - t_j\} \tag{9}$$

where U_i denotes the set of nodes that meet the above requirements. According to such information, the node with the largest imbalance in the tree with the highest evacuation time is defined as the most "vulnerable" node. In the adjusted DRF, it will be reconnected to the "target" node c_h where $h = \operatorname{argmax}_{j, c_j \in U_i} \{t_i - t_j\}$. After completing this process, the time required to evacuate both trees T_k and T_h , to which c_i and c_h belong respectively, needs to be re-estimated.

$$(X'_k = X_k \cdot (1 - n_i / r_{k,X_k})) \tag{10}$$

Table 2 DRF optimization procedure

Step 1: Determine the DRT with the longest evacuation time based on the simulation results and calculate the imbalance of all nodes in it with Eqs. (8) and (9)
Step 2: Find the node with the that have highest imbalance value and reconnect it to its “target” node
Step 3: Re-evaluate the evacuation times of DRTs affected by node reconnection and time series of cumulative outflows at their corresponding exit with Eqs. (10–13)
Step 4: Recalculate the range value θ with Eq. (7). If it is still higher than the preset target value θ , repeat Steps 1–3

$$X'_h = X_h \cdot (1 + n_i / r_{h,X_h}) \tag{11}$$

Depending on these evacuation time lengths, the time series R_k and R_h are truncated or extended in the following manner,

$$r'_{k,t} = \begin{cases} r_{k,t}, & t \in (0, X'_k) \\ r_{k,X_k} - n_i, & t = X'_k \end{cases} \tag{12}$$

$$r'_{h,t} = \begin{cases} r_{h,t}, & t \in (0, X_h] \\ r_{h,X_h} + (t - X_h) / (X'_k - X_h) \cdot n_i, & t \in (X_h, X'_k) \\ r_{h,X_h} + n_i, & t = X'_k \end{cases} \tag{13}$$

According to the above calculation method, a round of optimization can be performed in the following steps shown in Table 2.

To obtain an evacuation guidance scheme that is expected to perform well enough, the optimization and simulation modules are normally needed to be run in iterative rounds. After each round of optimization, the CTM simulation will predict the evacuation time. The whole optimization method process is terminated only when the θ calculated from the direct output of the simulation is lower than the target value θ^* . Then the resulted DRF will be employed as the basis for developing the evacuation guidance scheme.

4 Validation and Test

The key parameter of CTM in this method can be validated with the experimental data extracted from video resources which is available at Pedestrian Dynamics Data Archive [18]. The position of evacuees after each time step in the video could be counted for comparison. Setting l as 2 m, we determined the most suitable value parameters: $v_{free} = 1.3$ m/s, $\rho_{cri} = 6.5$ ped/m² and $v_{wave} = 0.64$ m/s. Under such value, in addition to the clearance time of each node position, the self-organization

phenomenon in spatial dimensions, e.g., arching, can also be reproduced in the simulation (shown in Fig. 2).

When the simulation module is refined, the whole optimization method can be run by setting the target value of range $\theta^* = 1 \text{ timestep}$. To test the effectiveness and efficiency of the method in numerical tests, we chose a canteen at Beihang University as the initial evacuation scenario. It is a 26 m × 23 m single-story building containing several irregular obstacles inside, and about 750 customers are unevenly distributed during the peak hours of the midday meal. As shown in Fig. 1, this facility contains three asymmetrically distributed emergency exits, so three DRTs are partitioned according to the exit nodes during the optimization process, and the simulated evacuation time of the DRTs are recorded in Fig. 3.

In Fig. 3, it can be observed that the performance of the DRF-based plan in the simulation gets better evaluation results as each round of optimization is completed. This is reflected in the gradually balanced evacuation time for each exit and the gradual reduction of their maximum values, which means that the time required for the last evacuee to leave the facility is reduced. The number of reconnections in the iterative optimization is not continuously decreasing, mainly due to the unstable but gradually increasing accuracy of the reevaluation calculation in the optimization. Since the time complexity of the DRF initialization and node reconnection algorithm is extremely low, the computational cost is mainly determined by the number of times the simulation is executed. At the current task size, the optimization process requires a total of 12 simulations to be executed, which has vastly reduced the computational time cost compared to the planned optimization based on the metaheuristic algorithm.

As the current optimized evacuation plan results can be replicated by microsimulation, we also compared the results obtained by the genetic planning (GP) optimization method relevant to social learning [19]. With the Apple M1 chip, starting from an initial plan requiring 191.7 s in the micro simulation, GP-based method took 307 s to reduce evacuation time by 27.46%, while DRF-based optimization took 54 s to reduce it by 29.11%. It can be found that the currently proposed method not only

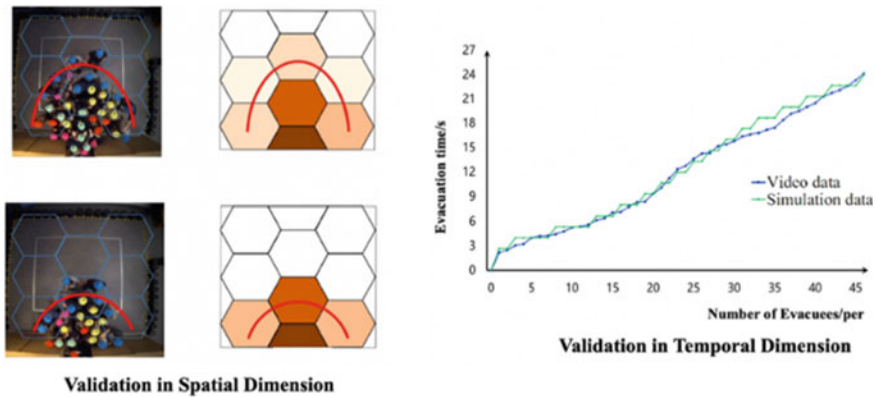


Fig. 2 Comparison between experimental data and simulation results

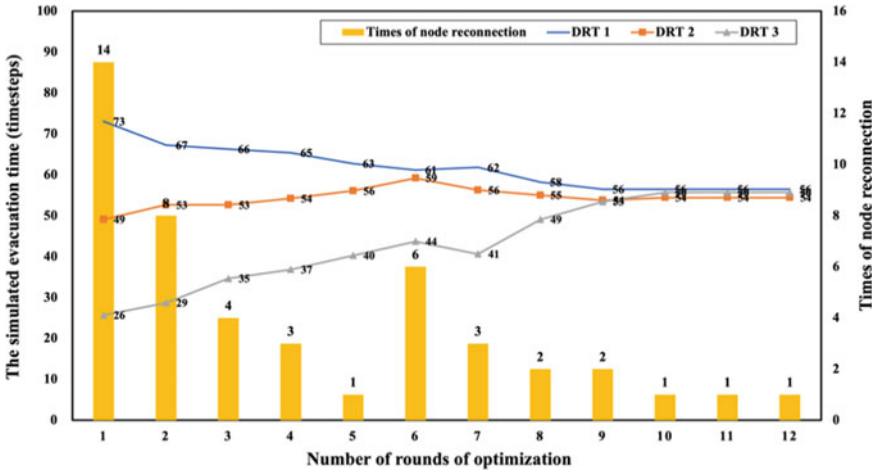


Fig. 3 Optimization process and simulation evaluation results

powerfully saves computational time but also gets better optimization results in a limited time.

In addition, we compare the optimization efficiency of the method at different network sizes and crowd sizes. For this purpose, we adjust the degree of discretization to obtain different numbers of nodes in the same scenario on the one hand and change the total number of evacuees in the facility on the other hand. We set the number of evacuees as 500, 750, 1000, 1500, and 2000, while that of nodes are set as 47, 123, 224, 378, and 826. The test results under their combination are shown in Fig. 4. It can be found that the crowd size does not have a significant impact, while the increase in the number of nodes leads to an increase in the computational cost. This is due to the fact that the crowd size only affects the attributes of the nodes, while an increase in the number of nodes leads to a higher frequency of node reconnection. However, the increase in the number of optimization rounds does not grow linearly with the network size, which demonstrates the potential of the method to be applied in large-scale scenarios.

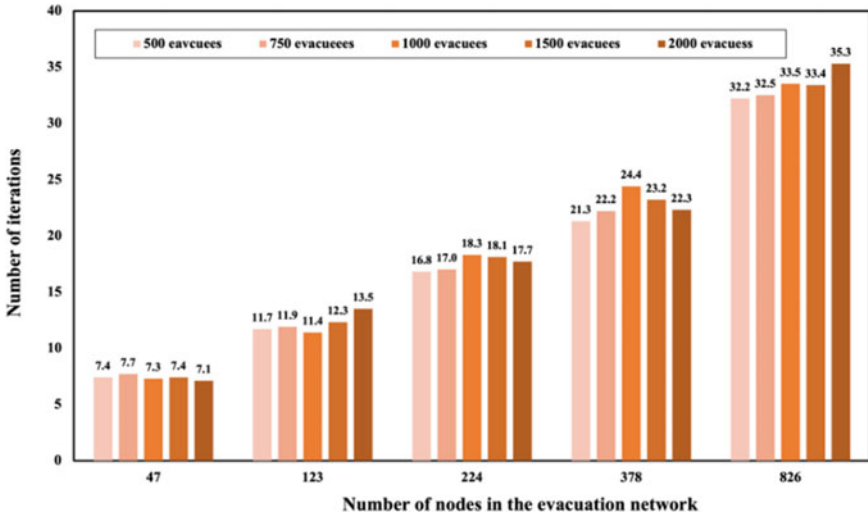


Fig. 4 Optimization efficiency at different population sizes and network sizes

5 Conclusion

In this study, we proposed a DRF-CTM joint method for evacuation guidance optimization. In this method, a DRF structure is introduced to store guidance information to ensure the feasibility of the evacuation plan. Two algorithms for DRF initialization and node reconnection are developed to cooperate with the simulation module. To make full use of the simulation result, the clearance time of each node is counted, and the outflow from the exits is recorded by segment with a time series. Then both are employed to evaluate new solutions, making the search more directional and maximizing the algorithm’s efficiency. During this process, CTM, the mesoscopic simulation model, can output the above data quickly, further amplifying the method’s advantages. In addition to the above advantages, in the tests, we also find that the optimization efficiency is especially high when the number of nodes is relatively small, and its computational complexity does not expand rapidly as the size of the network increases. So, this method has the potential to be the basis for developing a real-time evacuation guidance plan.

However, generating guidance information according to the current method is still based on the strong assumption of full compliance. Further studies will include more realistic factors from architectural, behavioral, and strategical aspects. For example, the number and location of guidance signs could be determined, and evacuee compliance should be quantified to further improve the evaluation accuracy of the impact of the evacuation plan.

References

1. Huang HJ, Xia T, Tian Q, Liu TL, Wang C, Li D (2020) Transportation issues in developing China's urban agglomerations. *Transp Policy* 85:A1–A22
2. Kok VJ, Lim MK, Chan CS (2016) Crowd behavior analysis: a review where physics meets biology. *Neurocomputing* 177:342–362
3. Liu H, Chen H, Hong R, Liu H, You W (2020) Mapping knowledge structure and research trends of emergency evacuation studies. *Saf Sci* 121:348–361
4. Vermuyten H, Beliën J, De Boeck L, Reniers G, Wauters T (2016) A review of optimisation models for pedestrian evacuation and design problems. *Saf Sci* 87:167–178
5. Ibrahim AM, Venkat I, Subramanian K, Khader AT, Wilde PD (2016) Intelligent evacuation management systems: a review. *ACM Trans Intell Syst Technol (TIST)* 7(3):1–27
6. Lin P, Lo SM, Huang HC, Yuen KK (2008) On the use of multi-stage time-varying quickest time approach for optimization of evacuation planning. *Fire Saf J* 43(4):282–290
7. Chen PH, Feng F (2009) A fast flow control algorithm for real-time emergency evacuation in large indoor areas. *Fire Saf J* 44(5):732–740
8. Park I, Jang GU, Park S, Lee J (2009) Time-dependent optimal routing in micro-scale emergency situation. In: 2009 Tenth inter-national conference on mobile data management: systems, services and middleware. IEEE, pp 714–719
9. Lim GJ, Zangeneh S, Baharnemati MR, Assavapokee T (2012) A capacitated network flow optimization approach for short notice evacuation planning. *Eur J Oper Res* 223(1):234–245
10. Aalami S, Kattan L (2020) Fairness and efficiency in pedestrian emergency evacuation: modeling and simulation. *Saf Sci* 121:373–384
11. Gao Z, Qu Y, Li X, Long J, Huang HJ (2014) Simulating the dynamic escape process in large public places. *Oper Res* 62(6):1344–1357
12. Abdelghany A, Abdelghany K, Mahmassani H, Alhalabi W (2014) Modeling framework for optimal evacuation of large-scale crowded pedestrian facilities. *Eur J Oper Res* 237(3):1105–1118
13. Crociani L, Lämmel G (2016) Multidestination pedestrian flows in equilibrium: a cellular automaton-based approach. *Comput-Aided Civil Infrastruct Eng* 31(6):432–448
14. Jiang Y, Chen B, Li X, Ding Z (2020) Dynamic navigation field in the social force model for pedestrian evacuation. *Appl Math Model* 80:815–826
15. Zhang Z, Jia L (2020) Optimal guidance strategy for crowd evacuation with multiple exits: a hybrid multiscale modeling approach. *Appl Math Model* 90:488–504
16. Moustaid E, Flötteröd G (2021) Macroscopic model of multidirectional pedestrian network flows. *Transport Res Part B: Methodol* 145:1–23
17. Zhang J, Klingsch W, Schadschneider A, Seyfried A (2011) Transitions in pedestrian fundamental diagrams of straight corridors and T-junctions. *J Stat Mech: Theory Exp* 2011(06):P06004
18. Data archive of experimental data from studies about pedestrian dynamics. <http://ped.fzjuelich.de/database/>. Last accessed 02 Nov 2020
19. Tang TQ, Zhang BT, Wang T (2022) An improved optimization framework for evacuation planning in facilities considering pedestrian dynamics. *J Transport Saf Secur* 14(4):693–722

Optimization of the Construction Subcontractor Selection Process for Residential Building Projects by Applying Blockchain Technology Through a Smart Contract



Josue Janampa , Jean Pierre Pinedo , Sandra Rodriguez ,
and Karem Ulloa 

Abstract Nowadays, the construction industry has become the main and great engine of the global economic recovery after the effects of covid-19, generating around 10.7 trillion dollars worldwide, and it is residential construction, specifically, the one in charge of driving growth in the short term, thanks to the constant demand for residential spaces. In this sense, various challenges such as new technologies, the complexity of projects, and a growing competitive environment, force the main contractor to subcontract between 80 and 90% of the activities, thus evidencing that subcontracting is an applied and necessary process in every construction project, and making subcontractors the backbone of the procurement strategy. However, one of the main risks of subcontracting is the inadequate selection of the construction subcontractor, which is often based solely on the criteria of selecting the known subcontractor and the lowest price, which often leads to risks regarding the time, cost and quality of the project. For this reason, the present research aims to improve the selection of the construction subcontractor carried out by the main contractor, through the development of a new subcontractor selection process, adapted to the current selection process, in which a Smart Contract is incorporated to greatly contribute to trust in the selection process, thanks to the contribution of Blockchain technology, in this process, through security against data manipulation, transparency of the selection process executed, traceability of information in real time pertaining to the process followed, and automation in the selection of the subcontractor under pre-established criteria.

Keywords Subcontractor · Selection · Smart contract · Blockchain · Ethereum · Optimization · Trust · Construction

J. Janampa · J. P. Pinedo · S. Rodriguez (✉) · K. Ulloa
School of Civil Engineering, Peruvian University of Applied Sciences, Lima, Peru
e-mail: sandra.rodriguez@upc.edu.pe

© The Author(s), under exclusive license to Springer Nature Singapore Pte Ltd. 2024
M. Casini (ed.), *Proceedings of the 3rd International Civil Engineering and Architecture Conference*, Lecture Notes in Civil Engineering 389,
https://doi.org/10.1007/978-981-99-6368-3_78

961

1 Introduction

According to a study carried out by the transnational Marsh, the construction industry currently accounts for around 13% of global GDP and, thanks to the post-pandemic recovery, is expected to reach more than 13.5% by 2030, making it the key industry in the recovery of the global economy, with residential building construction driving this rapid growth [1]. As construction is such an important but complex sector, a large number of contractors prefer to outsource construction project activities and only perform management activities such as project financing, contract administration and monitoring of project progress [2]. Thus, according to Rostiyanti, Hansen and Ponda, the subcontractor forms a fundamental part of any construction project when specialisation and work is required in certain activities that cannot be carried out by the main contractor [3]. However, one of the main risks of subcontracting is the inappropriate selection of the subcontractor, which can have a major negative impact on the success of the project [4]. The selection of the subcontractor is one of the main and essential processes in any construction project; however, due to the risk of subcontracting to unknown personnel and the profit margin of awarding the subcontract to the lowest bidder, the final selection is often based on the criteria of the known subcontractor and the lowest bid, which sometimes leads to risks in time, cost and quality of the project. This is why a proper selection of subcontractors is considered an important criterion for the successful management of many construction projects [5]. Therefore, as subcontractors directly manage an important part of the construction activities in any project, thus playing a vital role in the industry, it is necessary and of utmost importance to have a proper selection of subcontractors. In this sense, three studies are mentioned below that propose criteria and models for an adequate selection of subcontractors. In the study conducted by El-khalek, Aziz and Morgan, the appropriate criteria for evaluation and pre-qualification of the construction subcontractor were identified as “on-time delivery of materials”, “no financial problems impeding contract performance”, “reputation” and “bid price”, which were considered relevant and important to be taken into account in the subcontractor selection process [6]. Also, regarding the techniques or methodologies used by the authors for subcontractor selection, Chen, Ding, Cory, Hu, Wu and Feng propose a decision support model for subcontractor selection that considers the specific requirements of construction companies. This research designs a three-stage construction subcontractor selection model by introducing Quality Function Deployment (QFD) to achieve the transmission of “what is needed” in the subcontractor selection process, in order to take into consideration the project objectives and company needs, and also designs an allocation method using an Analytic Hierarchy Process (AHP) in conjunction with an Improved Grey Correlation Analysis (IGCA) to determine the weight of relevant selection indicators. Thus, by integrating the proposed weight calculation method and the QFD method, the results of subcontractor selection become more reasonable and objective [7]. In the same way, Abbasianjahromi, Sepehri and Abbasi propose a Kano model able to identify the main requirements of a customer for a product

or service in terms of quality attributes and TOPSIS (Technique for Order of Preference by Similarity to Ideal Solution) concepts to select the best subcontractor, allowing to classify the selection criteria into three categories including: “essential”, “one-dimensional” and “attractive”. Thus, despite the diversity of selection criteria that projects demand, by applying the concept of the Kano model, contractors manage to solve this complex challenge, thanks to this systematic approach provided to identify the necessary criteria in the subcontractor selection process [8]. However, despite the aforementioned previous research on criteria and models for construction subcontractor selection, the underlying problem of contractor mistrust, due to possible selection of unreliable and unsuitable subcontractors, remains one of the main factors of inadequate subcontractor selection. In that sense, for the present research, the application of Blockchain technology, through a Smart Contract created on the Ethereum Blockchain, is proposed in the subcontractor selection process as a solution to the problem of mistrust, thanks to the following research below which states that this technology brings and creates trust. In the study conducted by Qian and Papadonikolaki, the authors claim that the application of Blockchain technology in the supply chain causes a change in the paradigm of trust contributing positively in the same, with a greater basis in the system and cognition, thus reducing the need to establish trust based solely on relationships [9]. Also, in the third limited edition of the digital book “Blockchain for Dummies” published by IBM, the main business benefits of Blockchain technology in conjunction with Smart Contracts are explained, being mainly “enhanced security”, thanks to the protection against manipulation of encrypted data or records, fraud and cybercrime; “time savings”, as Smart Contracts reduce human intervention and dependence on third parties to verify, in an automated way, that pre-established terms or conditions have been met; “Increased transparency” and “instant traceability”, as participants in the Blockchain network have authorised access to the same information at the same time, being able to verify the full history of all transactions or movements recorded in the Smart Contract with immutability and time-stamped seal, which provides full transparency and traceability, virtually eliminating any opportunity for fraud or modification [10]. In the same way, in the study carried out by Dakhli, Lafhaj and Mossman, the authors affirm that Smart Contracts in the long term will replace the decision-making processes of a business organization, allowing to significantly reduce personnel at the management level [11]. For these reasons, the objective of this research focuses on the optimization of the construction subcontractor selection process carried out by the main contractor, through the development of a subcontractor selection process that implements a Smart Contract to contribute to the trust in the selection process, thanks to the contribution of security, transparency, traceability and automation that Blockchain technology provides.

2 Method

The Blockchain technology can be applied to the selection of subcontractors belonging to any type of project without any restrictions. However, this research focuses on residential projects, such as multi-family buildings, since it is in these projects where the number of subcontracts is greater. The sample evaluated for this study includes the projects listed in Table 1.

In order to carry out the present study, the research methodology is developed by following the processes shown in Fig. 1.

For the recording and analysis of the information, interviews are conducted with nine resident engineers of three different multi-family building projects to determine the root cause of an inadequate selection of construction subcontractors, as well as the specialty of the projects that present a higher incidence of subcontracting. For the determination of the traditional selection process surveys are conducted to forty engineers and architects with extensive experience working on these projects in order to collect information about the selection process followed by current construction companies and the most suitable subcontractor pre-qualification criteria respectively. For the development of the new selection process, a flowchart of the new selection process is drawn up in which Blockchain technology is applied for the selection of construction subcontractors. Likewise, it is necessary to use Remix IDE, an integrated development environment of the Ethereum Blockchain, which offers the possibility to compile and deploy Smart Contracts coded with the programming language Solidity.

Finally, the new selection process is implemented in the Project 3 (P3) through of a simulation of a selection process. Thus, it is possible to measure the degree of contribution to trust in the selection process of construction subcontractors, by providing security, transparency, traceability and automation in this process.

Table 1 Summary of the projects evaluated

	Project 1 (P1)	Project 2 (P2)	Project 3 (P3)
Number of floors	15	12	15
Company size	Medium	Medium	Medium
Project type	Multi-family building	Multi-family building	Multi-family building
Use	Residential		



Fig. 1 Investigation process

3 Results

3.1 Recording and Analysis of Information

The interviews and surveys are necessary to identify that the activities within the specialty of architecture require a higher index of subcontracting compared to the activities within the other specialties, such as structures and installations in general (electrical, sanitary and mechanical). It is also confirmed that the adequate selection of the construction subcontractor has a positive impact on the results of the project in terms of cost, time and quality of work. Finally, it is confirmed that the most recurrent cause of the inadequate selection of subcontractors is the tendency to choose the known subcontractor due to mistrust, which generally leads to risks in the project. In this way, the purpose of the research is aimed at improving the selection process through the contribution to trust. Tables 2, 3, 4, 5 and 6 list the 20 construction subcontractor prequalification criteria validated by the professionals at through individual surveys carried out.

Table 2 Subcontractor prequalification criteria in terms of time

ID	Description of the criterion
CRT01	Punctual delivery of materials
CRT02	Cope with critical activities during the construction phase
CRT03	Compliance with the deadline to complete the works under contracts already executed
CRT04	Flexibility and cooperation in resolving delays

Table 3 Subcontractor pre-qualification criteria in terms of cost

ID	Description of the criterion
CRC01	Fulfillment of the contract without any financial problems
CRC02	Financial backing of the subcontractor company to manage and cover the work of its staff prior to payment for appraisals
CRC03	Bidding price
CRC04	Financial stability

Table 4 Pre-qualification criteria of the subcontractor in terms of quality

ID	Description of the criterion
CRQ01	Satisfactory results despite the technological difficulty of the project
CRQ02	It has certificates of quality standards
CRQ03	Results history
CRQ04	Compliance with the requested quality specifications

Table 5 Subcontractor pre-qualification criteria in terms of reputation

ID	Description of the criterion
CRR01	Subcontractor reputation
CRR02	Percentage of previous works completed within the planned period
CRR03	Demonstrate experience in similar projects
CRR04	It does not have claims, arbitrations and contractual conflicts in previous projects

Table 6 Pre-qualification criteria for the subcontractor in terms of technical capability

ID	Description of the criterion
CRTC01	Competences of the workers of the subcontracting company
CRTC02	Has previous experience on a project of a similar type and size
CRTC03	Appropriate qualifications and experience of the company’s technical staff
CRTC04	Availability, condition and adequacy of equipment

3.2 *Determination of the Traditional Selection Process*

With the information provided by the resident engineers of the three residential building projects assessed, the traditional process of selection of construction subcontractors followed by these medium-sized construction companies is determined.

Among those involved in this process is the Head of Subcontracts (HSC), Resident Engineer (RES), Subcontracts Officer (SO), Head of Technical Office (HTO), Head of Site Quality (HSQ), Legal Area (LA) and Subcontractor (SC). This process is sequential and starts with the submission and update of the procurement schedule by the (RES), where the (HSC) reviews and maintains updated the backlog of subcontractors, after which the (SO) requests, proposes and submits shortlists for each specific subcontract and evaluates the operability of the subcontractors; then, the (HSC) is in charge of inviting the operational subcontractors so that the (SO) and the (HTO) can request, from the operational subcontractors, the documentations of their validated technical information, SSOMA, quality, among other requested documentations; then, the operational subcontractors must develop their final proposal. Subsequently, a meeting is scheduled with the finalist bidding subcontractors organized by the (SO) and the Head of the technical office and then a budget comparison of the bidders is carried out, thus selecting the winning subcontractor. Finally, the (HSC), (RES) and (LA) award the subcontract to the selected subcontractor.

3.3 Development of the New Selection Process

The proposal to optimize the construction subcontractor selection process is based on the development of a new selection process, adapted to the traditional process, which not only allows pre-qualification of the appropriate subcontractor under validated criteria in terms of time, cost, reputation, technical capacity and quality and not tending to select only the well-known subcontractor or with the cheapest proposal, but also allows contributing to trust in the selection process; thanks to the contribution, in this process, of the security, transparency, traceability and automation that Blockchain technology offers. To do this, a Smart Contract is created in Remix IDE, which is programmed to select the subcontractor with the highest score regarding the prequalification criteria (with a score greater than or equal to 4 on a 5-point Likert scale), and with the offer that best fits the contractual budget at the same time.

The application of Blockchain technology in the selection process is carried out by incorporating the Smart Contract created in the new subcontractor selection process. The new selection process which implements the Smart Contract is reflected in the flowchart shown in Fig. 2.

The flowcharts of Figs. 3 and 4 explain the functionality of the Smart Contract that is implemented in the new selection process (Fig. 2) with the activities to follow for the prequalification and final selection of the winning subcontractor.

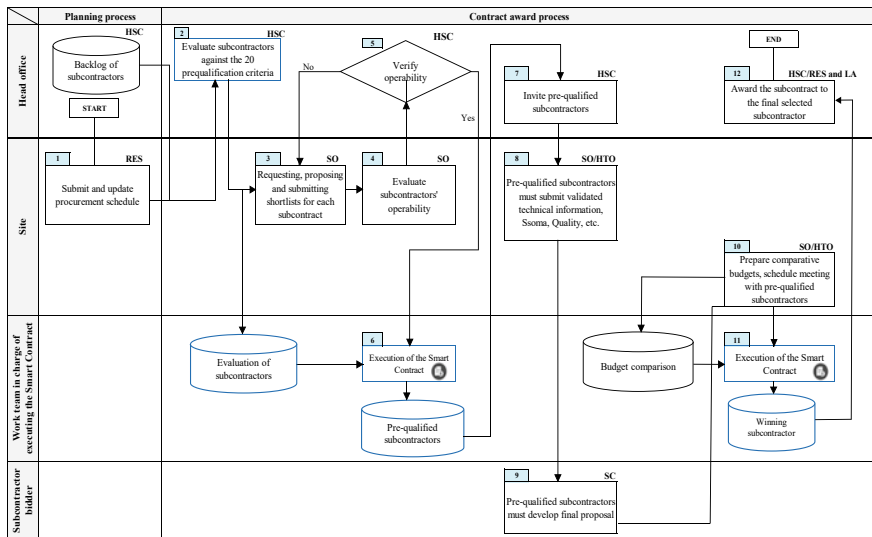


Fig. 2 Flowchart of the new construction subcontractor selection process

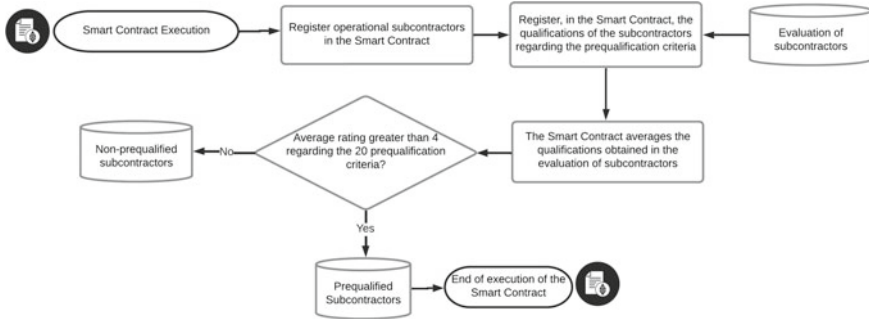


Fig. 3 Smart Contract execution process for obtaining pre-qualified subcontractors

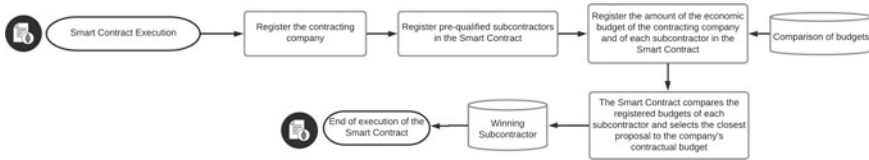


Fig. 4 Smart Contract execution process to obtain the winning subcontractor

3.4 Implementing the New Selection Process

The proposal is implemented in project 3, through a simulation of a selection process of a subcontractor for the Painting requirement, where the contractor in charge of “Project 3” and three subcontractors belonging to this project participate. The selection process begins with the prequalification stage of the participating operating subcontractors carried out by the HSC based on the subcontractor’s references from previous projects in or outside the company, but for the simulation the contractor is in charge of the evaluation. In Fig. 5 it is shown the evaluation of the subcontractors with respect to the prequalification criteria (corresponding to the “Quality” criteria for the example), as well as the result of the execution of the Smart Contract for prequalification with the prequalified subcontractors evaluated with respect to the 20 prequalification criteria, these being SC2 and SC3 since they are those with an average final score equal to 4 on the established five-point Likert scale (1 = Totally dissatisfied; 2 = Dissatisfied; 3 = Neither satisfied nor dissatisfied; 4 = Satisfied; 5 = Totally satisfied).

Finally, the Smart Contract is executed again, but this time for the final selection to obtain the winning subcontractor for the Painting requirement. To do this, the contractual budget determined by the contracting company and the budgets presented by each prequalified subcontractor must be registered in the Smart Contract. Thus, following the execution process of the Smart Contract shown in Fig. 6, human intervention is reduced by automatically selecting the winning subcontractor of the subcontract (SC3), who is the one that presents the offer closest to the established contractual

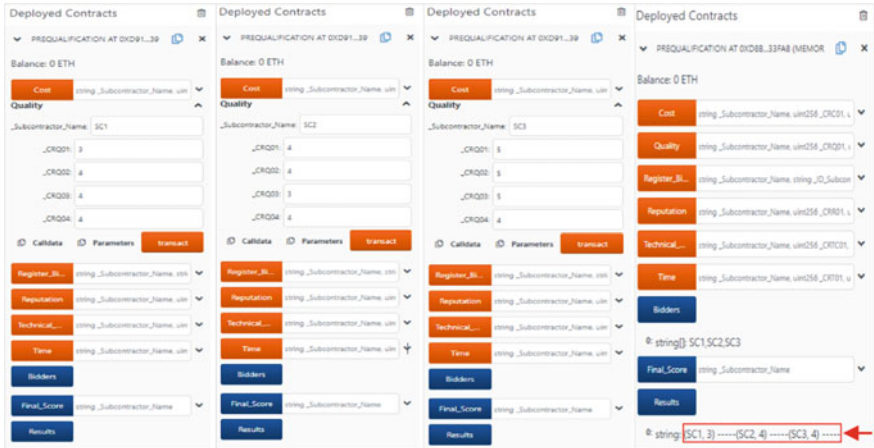


Fig. 5 Subcontractor prequalification process

budget, and it is to whom the subcontract is awarded for the requirement of the Painting item.

In this way, all the data (names and budgets) and qualifications (with respect to the prequalification criteria) of the participating subcontractors are registered and stored in the Ethereum Blockchain, protected against any possible manipulation of the information entered and allowing verification of the complete history of all the actions executed in the Smart Contract with date and time, thus providing greater transparency, traceability and security in the selection process. In Fig. 7 it is illustrated the result of storing the data of each subcontractor in the Ethereum Blockchain.

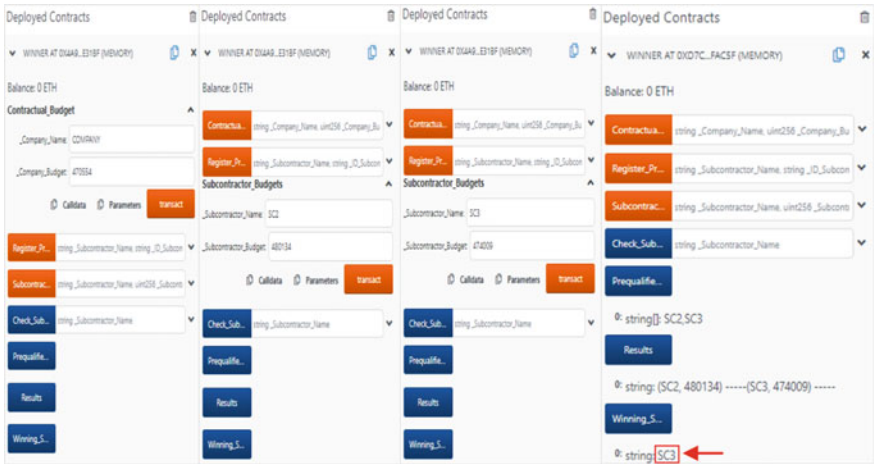
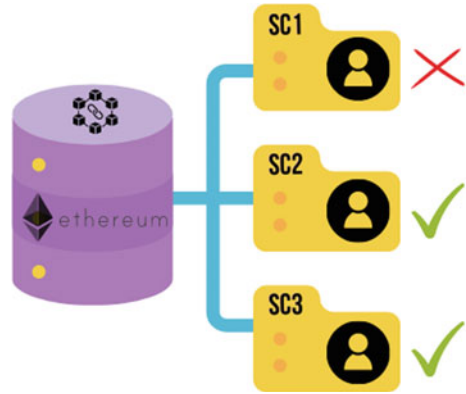


Fig. 6 Winning subcontractor selected by the Smart Contract

Fig. 7 Process of storing the data in the Ethereum Blockchain



To validate the proposal and measure the contribution to trust offered by Blockchain technology, the resident engineer who participated in the subcontractor selection simulation shown above is interviewed. The scale to validate the proposal is a 5-point Likert scale, where 5 = Totally agree, 4 = Agree, 3 = Neither agree nor disagree, 2 = Disagree, and 1 = Totally disagree. Figure 8 shows the comparative analysis between the contribution to trust in the traditional process and in the new selection process, obtaining as a final result that the engineer agrees that there is a degree of contribution to trust of 80% in the traditional process (average equal to 4, on a scale of 1 to 5), but he totally agrees that there is a degree of contribution to trust of 100% in the new selection process (average equal to 5, on a scale of 1–5) by applying the Blockchain technology through a Smart Contract, thus validating the optimization proposal.

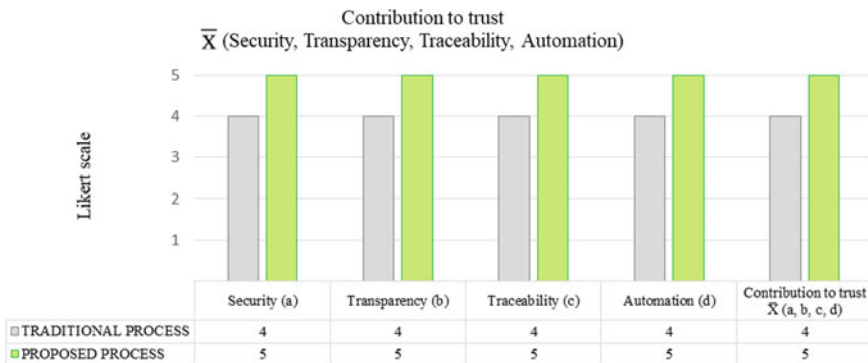


Fig. 8 Comparative analysis of the contribution to trust

4 Conclusion

This paper aims to propose a new construction subcontractor selection process through the programming of a Smart Contract by applying Blockchain technology. The present research proves that a Smart Contract is not only used to execute legal contracts but also serves for decision-making in a decentralized network free from manipulation by third parties, transparent and traceable by allowing authorized access to information in real time and automatable, by instantly executing the pre-established conditions in the smart contract.

Thus, by corroborating that mistrust when choosing the construction subcontractor is the main cause of an inadequate selection and identifying that the specialty of architecture is the one that presents a higher rate of subcontracting in multi-family building projects carried out by medium-sized construction companies, it is concluded that the application of Blockchain technology in subcontracting, through the development of an adequate selection process that implements a Smart Contract, contributes to 100% trust, thanks to the contribution of security against manipulation of the data, transparency by making visible the authorized information of the process, traceability by recording with date and time each process that is followed in the selection of the subcontractor, and automation, by instantly verifying that the prequalification and budget criteria programmed in the Smart Contract are met.

References

1. Marsh & Guy Carpenter (2021) Future of construction
2. Artan Ilter D, Bakioglu G (2018) Modeling the relationship between risk and dispute in subcontractor contracts. *J Leg Aff Dispute Resolut Eng Constr* 10(1):1–9
3. Rostiyanti SF, Hansen S, Ponda TN (2020) Cause and effect of conditional payments provision to subcontractors. *J Leg Aff Dispute Resolut Eng Constr* 12(1):1–6
4. Mohaghar A, Faqhei MS, Khanmohammadi E, Jafarzadeh AH (2013) Contractor selection using extended TOPSIS technique with interval-valued triangular fuzzy numbers. *Glob Bus Econ Res J* 2(5):55–65
5. El-Kholy AM (2019) A new technique for subcontractor selection by adopting choosing by advantages. *Int J Constr Manage* 22(7):1171–1193
6. El-khalek HA, Aziz RF, Morgan ES (2018) Identification of construction subcontractor prequalification evaluation criteria and their impact on project success. *Alex Eng J* 58(1):217–223
7. Chen X, Ding Y, Cory CA, Hu Y, Wu K-J, Feng X (2021) A decision support model for subcontractor selection using a hybrid approach of QFD and AHP-improved grey correlation analysis. *Eng Constr Archit Manage* 28(6):1780–1806
8. Abbasianjahromi H, Sepehri M, Abbasi O (2018) A decision-making framework for subcontractor selection in construction projects. *Eng Manage J* 30(2):141–152
9. Qian X, Papadonikolaki E (2020) Shifting trust in construction supply chains through blockchain technology. *Eng Constr Archit Manage* 28(2):584–602
10. IBM (2020) *Blockchain for dummies*, 3rd edn. Wiley
11. Dakhli Z, Lafhaj Z, Mossman A (2019) The potential of blockchain in building construction. *Buildings* 9(4):77

Identifying the Stages of Fire Development from Compartment Temperatures with GMM-HMMs: A Case Study of Room Fires



Hongqiang Fang  and S. M. Lo

Abstract It is essential for firefighters to identify the stages of fire development when conducting the fire emergency response operation. However, at present, the approaches for firefighters to identify the stages of fire development on the fireground mainly rely on subjective observation and judgment to the signs and symptoms changing on-site, which is highly unreliable and ambiguous. Therefore, to enhance firefighters' situational awareness, a machine learning approach by using Gaussian Mixture Models and Hidden Markov Models (GMM-HMM) to automatically identify the stages of fire development from compartment temperatures is proposed in this paper. To provide enough data samples for unsupervised model training, the CFD-based fire simulation—Fire Dynamics Simulator (FDS)—is applied to generate a large volume of simulated training data. Taking the ISO 9705 fire test room as our case study environment, we collect simulation data under 100 fire scenarios within this room to formulate the recognition model. By using the difference between the fire growth time in terms of the model estimated value and the actual value from HRR to evaluate the accuracy of the recognition, we find that the recognition model indicates an average of 98% accuracy within the 2 min error range in cross-validation, and acceptable performance of recognition are also found from the case examined by the real experimental data.

Keywords Stages of fire development · Machine learning · GMM-HMM · Compartment room fires · Fire simulation

H. Fang (✉) · S. M. Lo

Department of Architecture and Civil Engineering, City University of Hong Kong, Hong Kong, China

e-mail: hqfang3-c@my.cityu.edu.hk

1 Introduction

Among various types of fires, building fires are the most frequent and significant threat to life and property in urban and rural areas. According to the data [1] from Fire Service Bureau, the Ministry of Public Security of China, over 252,000 fires were reported in mainland China in 2020, and 43.4% of them occurred in residential buildings, which caused the highest proportion among all venues. Therefore, fire-fighting in buildings is especially important for fire emergency response. To conduct building fire emergency response operations, the first thing that firefighters need to do is to 'read' the fire, which is also known as situational awareness (SA).

SA is the perception of elements in the environment within a volume of time and space, and the comprehension of their meaning, and the projection of their status in the near future [2]. By conducting the SA in building fires, firefighters can observe changes that are likely to occur in their surroundings and comprehend their meanings, and most importantly, predict future fire development. These are essential for employing the appropriate firefighting strategies and protecting firefighters from dangers. Although firefighters have been trained to conduct SA from a long time ago, at present, the approach for firefighters to understand their surroundings and identify the stage of fire development still depends on their feelings (see, hear, or feel) and experience to the signs and symptoms changing on-site [3]. However, as the interior design of buildings become more and more complex, blocking the signs of flame and smoke, such an observation-based SA approach might become harder to operate. Furthermore, evaluation of the fire behavior indicators in mind highly relies on firefighters' experience and knowledge, so the judgments can vary from person to person. Therefore, it is welcomed to develop an approach analyzing the surrounding fire environment and automatically identifying the stages of fire development.

As the world is moving towards digitalization and intelligence, a wealth of data containing valuable information is now available to be captured before and during the fire. Artificial intelligence (AI) and big data technology become more and more important in fire safety. Using various machine-learning methods, extensive research has studied enhanced fire detection in buildings. By processing the data collection from multiple environmental sensors, such as temperature, CO₂ level, and CO level, many researchers have achieved early fire detection using artificial neural networks [4–6]. Moreover, by employing deep convolutional neural networks (CNNs) to process the video image from building surveillance systems, image-based intelligent fire detection algorithms were also developed [7–9]. Even though various machine learning approaches have been widely used in firefighting, most of them focused on the early detection of fires, and less attention was paid to helping firefighters during the fire emergency response. Thus, we consider embracing machine-learning methods to mine the essential information not only at the beginning of the fire but also during the fire.

In this study, a machine learning-based approach to automatically determine the stages of fire development from compartment fire temperature data was proposed. Considering that the stages of fire development change as the fire develops, the

proposed model should be able to deal with time-series data. Meanwhile, unlike the inversion of HRR or fire location, we tried to build the nonlinear relationship directly between the compartment temperatures and the corresponding fire stages, such as incipient, growth, and fully developed. Since the fire stage information is often vague and hard to distinguish, unsupervised pattern recognition needs to be used in the modeling process. To these ends, the Gaussian Mixture Model and Hidden Markov Model (GMM-HMM) was applied. The GMM-HMM is a combination of Gaussian Mixture Models (GMMs) and Hidden Markov Models (HMMs) [10]. It can be trained with unsupervised approaches. Owing to its strong ability in solving the recognition problem in time series, the GMM-HMM was widely used in speech recognition to identify the spoken word by finding out the best alignment between the current speaker's voice features and a given speech model. Therefore, by taking fires in an ISO 9705 fire test room as our case study, we developed a GMM-HMM-based fire stage recognition model for this case.

2 GMM-HMMs

GMM-HMMs are the Gaussian Mixture Model and Hidden Markov Model, also known as the Hidden Markov Model with Gaussian mixture emissions. Generally, an HMM can be defined as [11]:

$$\lambda = (N, V, \pi, A, B) \tag{1}$$

where N is the number of hidden states, and V is the observation symbol per states. π denotes the initial state distribution, A is the state transition probability distribution (the transition probabilities), and B represents the observation symbol probability distribution (the emission probabilities).

By considering fire development as a series of discrete events at a certain spaced time, we can divide the fire into several stages that undergo a movement from one state to another. This simplified state transition process is suitable to be modeled by HMMs. According to the fire dynamics in enclosure spaces [12], a compartment fire exists four stages of fire development. They are incipient, growth, fully developed, and decay. Since the recognition model discussed here is mainly applied to the emergency response operations where firefighters carry out reconnaissance, fire attack, and rescue of trapped occupants at the beginning of the fire, only the first three stages of fire development were considered in our HMM model. Moreover, we assumed that the fire starts from an incipient stage to a growth stage then to a fully developed stage, so state transitions of the HMM model strictly follow in this way. With a state transition probability matrix A to describe the transitions of stages of fire development in HMM model, the formula is given as follows:

$$A = [a_{ij}]_{N \times N} = \begin{bmatrix} a_{11} & a_{12} & a_{13} \\ a_{21} & a_{22} & a_{23} \\ a_{31} & a_{32} & a_{33} \end{bmatrix} = \begin{bmatrix} a_{11} & a_{12} & 0 \\ 0 & a_{22} & a_{23} \\ 0 & 0 & 1 \end{bmatrix} \tag{2}$$

where $a_{ij} \in [0, 1]$ is the probability of the event switches from state i to state j . N is the number of the states, which is 3 in this model. It is noted that fire development follows a designated pattern, so a_{13} is 0 in the transition matrix representing that the fire will never directly switch from an incipient stage to a growth stage. Similar explanations can be made for $a_{21} = 0$, $a_{13} = 0$, $a_{31} = 0$, and $a_{32} = 0$. Besides, $a_{33} = 1$ represents that fire remains in the fully developed stage after fire is burning sufficiently.

For the emission probabilities B , unlike typical HMM using discrete feature symbols to describe observation distributions per state, GMM-HMM describes the change of observations with GMMs. GMMs are parametric models of probability distributions that attempt to model the underlying probability distribution of multi-dimensional data comprised of several Gaussian distributions [10]. Thus, the continuous multi-dimensional values of observations can be included in the HMM model via GMMs. In this study, modeled by the GMM, emission probabilities of a mixture of M -dimensional multivariate Gaussians for each state can be defined as:

$$b_j(O) = P(O|q = S_j) = \sum_{l=1}^M \omega_{jl} g(O|\mu_{jl}, \Sigma_{jl}) \tag{3}$$

$$g(O|\mu_{jl}, \Sigma_{jl}) = \frac{1}{2\pi^{\frac{n}{2}} |\Sigma_{jl}|^{\frac{1}{2}}} e^{-\frac{1}{2}(O-\mu_{jl})^T \Sigma_{jl}^{-1} (O-\mu_{jl})} \tag{4}$$

where O is a particular observation sequence of the model. ω_{jl} represents the mixing weight for l -th component in state j and $\sum_{l=1}^M \omega_{jl} = 1$. Besides, $g(O|\mu_{jl}, \Sigma_{jl})$ denotes the multivariate Gaussian function summarizes the probability density of a Gaussian component, completely parameterized by its mean vector μ_{jl} , and covariance matrix Σ_{jl} .

After defining the configuration of the model, we then need to determine the parameters in both the GMM and HMM models. As a machine learning-based approach, parameters of the GMM-HMM can be directly learned from the data related to the event that the model described. Thus, after collecting a large volume of data describing fire development from fire simulations, we applied the expectation-maximization algorithm (EM algorithm) to learn the model parameters. As a special case of the EM algorithm, the Baum-Welch algorithm, also known as the forward-backward algorithm, can be employed. With the iterative process to conduct the calculation, parameters of the GMM-HMM model that best fit the observed data samples can be finalized.

3 A Room Fire Study

3.1 Sampling Data

Fire Simulation. Taking ordinary compartment room fires as our case study, we employed the fire simulation under the ISO 9705 test room environment to generate the data samples for model training. The geometry of the ISO 9705 test room is a compartment of 3.6 m by 2.4, 2.4 m high, and an opening of 0.8 m wide and 2.0 m high to supply the air [13], as shown in Fig. 1.

Furthermore, scenarios of the room fire were carefully designed. Fire in a room can start from anywhere and possess completely random fire loads and types of combustibles, so fire events were often treated as a non-deterministic random phenomenon [14]. By using sampling methods to discretize the probability distribution of some key factors in fire scenarios into multiple individual samples and then input them into the fire model for calculation, we can transfer the stochastic fire events into a problem regarding multiple deterministic fire scenarios. Therefore, we simulated 100 random fire scenarios in this study to generate the data samples representing all possible fire development in the case study room.

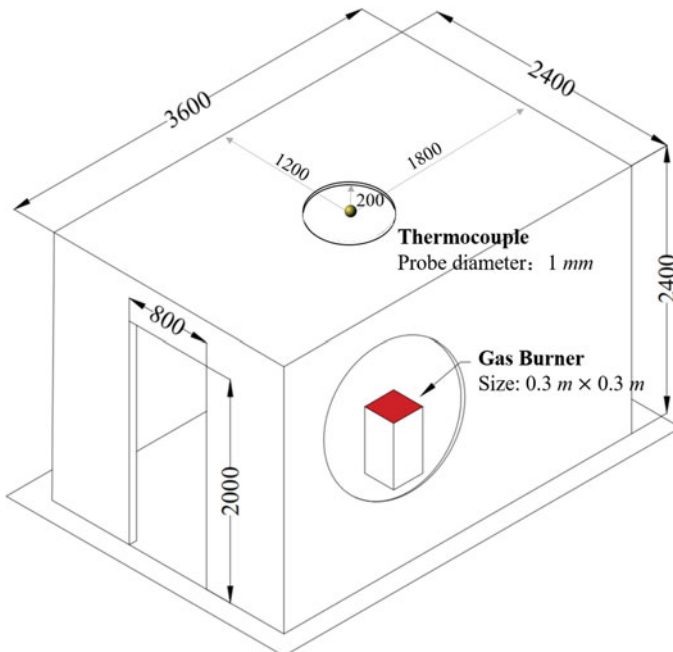


Fig. 1 The geometry of the ISO 9705 fire test room and the location of the fire source and the measurement probe in the simulation

For each of the fire scenarios, uncertainties in two aspects were considered. One is the location of fire sources, and another is the heat release rate (HRR) of the room fire. We assume that the location of fire sources follows a uniform probability distribution. As for the HRR curve, randomness in parameters of a t^2 fire was considered. The HRR curve of a t^2 fire is approximated by [15]:

$$Q(t) = \begin{cases} \alpha t^2 & 0 \leq t \leq t_{grow} \\ Q_{max} & t \geq t_{grow} \end{cases} \tag{5}$$

where $Q(t)$ is the HRR (kW) at time t (s); α is the fire growth rate (FGR) (kW/s²); t_{grow} denotes the time (s) when HRR reaches its peak value, and Q_{max} represents the maximum HRR (kW) of the fire.

The maximum HRR and FGR are two key parameters customizing the HRR curve. According to the study of Hopkin et al. [16], maximum HRR and FGR in residential building fires follow a lognormal probability distribution. Thus, using the lognormal distribution to describe the HRR curve and the uniform probability distribution to describe the location of fire sources, we list the details of the parameters in the fire scenarios in Table 1.

After this, with the sampling method—Latin Hypercube sampling (LHS) [17]—to sample the value of parameters from certain distributions, multiple fire scenarios with different parameter combinations were generated. In this study, a total of 100 individual fire scenarios were selected. By simulating fire development within 900 s throughout all fire scenarios and collecting the hot gas layer temperatures in every 0.9 s, we eventually obtained 100,000 temperature data points preparing for model training.

Feature Extraction. To facilitate the training of the recognition model, certain features regarding the training data need to be extracted. In this study, two features in terms of the temperatures were extracted. They were Final-First-Average (FFA) and Final-First-Difference (FFD). FFA refers to the average temperature over a period, and FFD is the difference between the final and first temperature data point over the

Table 1 Probability distributions of uncertainty parameters in the fire scenarios

Parameters	Symbol	Unit	Probability distributions	μ	σ	Max.	Min.
Maximum HRR	\dot{Q}_{max}	kW	Lognormal	6.29	1.27	3394 ^a	100
FGR	α	kW/s ²	Lognormal	-6.37	1.60	0.1876	0.00293
Fire source (X-axis)	L_{x-axis}	m	Uniform	-	-	3.6	0
Fire source (Y-axis)	L_{y-axis}	m	Uniform	-	-	2.4	0

^aThe maximum heat release rate for a completely ventilation-controlled fire is computed by $\dot{Q}_V \approx 1500A_0\sqrt{H_0}$, where A_0 and H_0 is the area and height of ventilation openings, respectively [15]

period. By dividing the entire simulation time into one hundred portions, we got 100 time intervals with every 10 data points included. For each time interval, the feature of FFA and FFD was calculated as follows:

$$FFA^{(k)} = \frac{\sum_{r=1}^R \lg(\Delta T_r^{(k)})}{R} \quad (6)$$

$$FFD^{(k)} = \frac{\lg(\Delta T_R^{(k)}) - \lg(\Delta T_1^{(k)})}{\lg(t_R^{(k)}) - \lg(t_1^{(k)})} \quad (7)$$

where k is the k -th time interval, and R is the amount of the data points contained inside the time interval. Moreover, $\Delta T = T_c - T_a$ denotes the difference between the upper layer compartment temperature ($^{\circ}\text{C}$ or K) T_c and the ambient gas temperatures ($^{\circ}\text{C}$ or K) T_a . In this study, R equals to 10, and T_c is the upper compartment temperatures obtained from thermocouples set in the simulation.

It is noted that a log function was applied to the temperature data. Since the hot gas layer temperature in a ventilated compartment is approximated to an exponential function of the HRR, and the HRR was designed in a t^2 fire following a squared function varied by time, employing a log function to training data can help the extraction of the temperature features at the early stage of fires. Finally, with the extraction of the temperature features from all the simulation cases, we established our training dataset.

3.2 Formulating Models

As introduced in the method, due to the nature of fire development in an enclosure space, the proposed model is designated to be a three-state HMM with multivariate Gaussian emissions. Thus, the model under this configuration was defined. With the parameter learning algorithm to train the model parameters from the established training dataset, we formulated the GMM-HMM model describing the temperature characteristics of different stages of fire development. Using the Viterbi algorithm to decode the temperature observations under the proposed model, we can have a glimpse of the model recognition performance in categorizing the stages of fire development. Taking all the training data as the model inputs, we obtain the results of the classification, as shown in Fig. 2.

The pattern of the classification results indicates that three clusters were explicitly recognized. The first cluster represents the incipient stage of fires. In this fire stage, most of the data samples are concentrated at the beginning of the fire, and meantime, along with an increase in the value of FFD and low value of FFA. After that, with a decline in the value of FFD and a rise in the value of FFA, the temperature data samples were successfully allocated to another cluster representing the fire growth

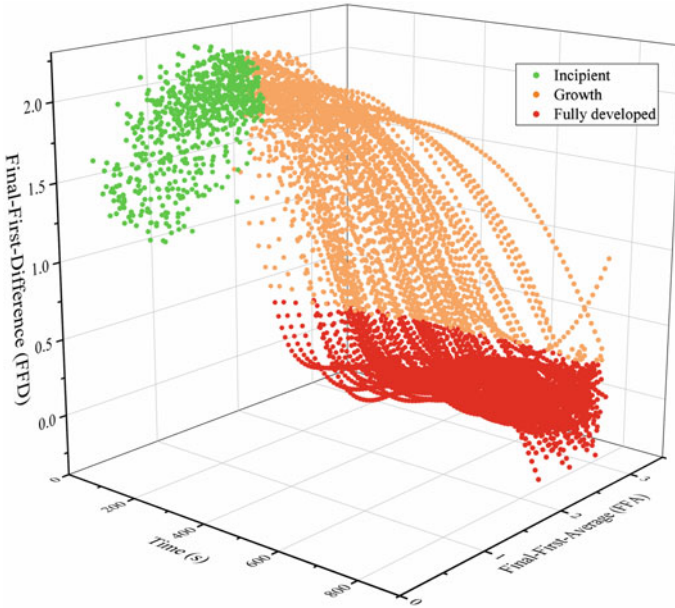


Fig. 2 Classification of the stages of fire development via the decoding of the features in temperature observations in formulated GMM-HMM model

stage. Finally, with the value of FFA and FFD fluctuating at a certain level, the last portion of the data samples was assigned to the cluster for the stage of fully developed.

3.3 Testing Results

Evaluation Methods. To ensure the proposed model can work well on the data that have not been seen before, we first proposed a method to evaluate the accuracy of the model recognition. The actual stages of fire development are usually determined by HRR values, so we considered using the difference between the fire growth time in terms of the model estimated value and the actual value from HRR to evaluate the accuracy of the recognition.

Take the temperature and HRR data from one simulation case as an example. Decoding by the formulated GMM-HMM model, we obtained the classification of the stages of fire development of this case in Fig. 3. The model estimated fire growth time ($t_{grow_estimated}$) could then be computed by counting the time from the fire start to the identified fully developed stage. As for the actual value of the fire growth time (t_{grow_actual}), we determined t_{grow_actual} by finding out the peak of the HRR. Marking out these two indicators on the figure, we find a difference existed between the identified stages of fire development and the actual stages of fire development exhibited

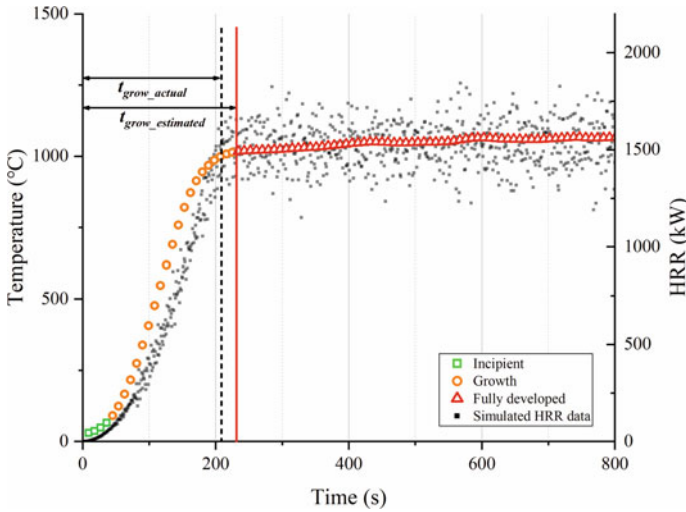


Fig. 3 Comparison of the difference between the model estimated stages of fire development and the actual fire development in HRR

from the HRR. Therefore, we calculated the difference between the $t_{grow_estimated}$ and t_{grow_actual} , and made it an indicator to evaluate whether the model estimated stage of fire development is appropriate to reflect the actual fire development.

Cross-validation. In this study, a fivefold cross-validation was conducted. All the simulation data samples were divided into five subsets, and each subset contained training data from 20 different simulation scenarios. Then, using any four subsets of data to train the model, we got 5 well-trained models. By calculating the difference between the $t_{grow_estimated}$ and t_{grow_actual} within these models, we obtained the results of the cross-validation shown in Table 2. It is indicated that model 1 exhibits the best performance in identifying the stages of fire development. The mean value of the difference between the $t_{grow_estimated}$ and t_{grow_actual} is 35 s for model 1. The average value of all five models is 46 s. Besides, cumulative probabilities of the differences between the $t_{grow_estimated}$ and t_{grow_actual} within 30, 60, 90, and 120 s were also computed. The result indicates that the errors of the most cases are less than 120 s.

Experiment data validation. Even though the proposed GMM-HMM-based approach behaved well in the cross-validation, the data we used to examine the model was still the simulation data. Fire development can be more complicated in a real fire environment. Therefore, temperature measurements from a real fire experiment were applied to test the model accuracy in this part. Taking the experiment data from NIST full-scale compartment fires in ISO 9705 room [18], we adopted data in two experimental cases—case 1 (ISOHept9) and case 2 (ISOPP18)—to validate our approach. The histories of the compartment temperatures and their HRR data are depicted in Fig. 4. By extracting the FFA and FFD from the temperature data and inputting them into the formulated recognition model, we identified the stage of

Table 2 Results of the difference between fire growth time in terms of the model estimated value and the actual value from HRR

Model number	Mean	SD	Cumulative probabilities			
			Within 30 s	Within 60 s	Within 90 s	Within 120 s
1	35.37	23.38	0.30	0.90	0.95	1.00
2	43.65	29.47	0.45	0.75	0.95	0.95
3	57.15	25.25	0.10	0.60	0.85	1.00
4	52.56	37.17	0.35	0.60	0.95	0.95
5	42.21	27.48	0.40	0.75	0.90	1.00
Average	46.19	28.55	0.32	0.72	0.92	0.98

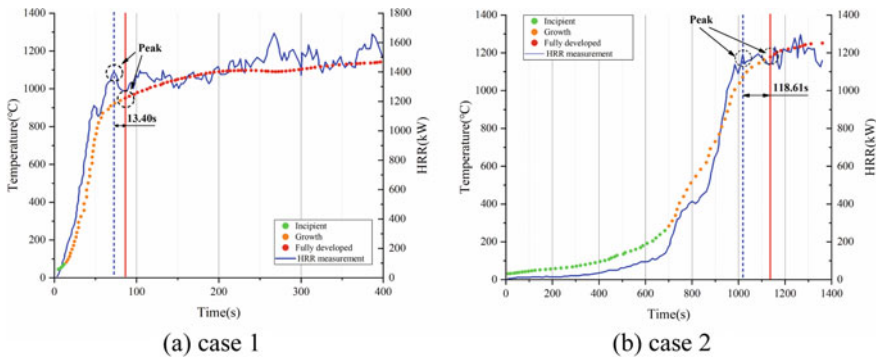


Fig. 4 Two cases that identifies the stages of fire development from real experimental temperature inputs with the proposed GMM-HMM model

fire development for every observation point. From the result, it is obvious that three different stages of fire are clearly identified. Moreover, by estimating the difference between the $t_{grow_estimated}$ and t_{grow_actual} , we found a 13.40 s lag for case 1 and 118.61 s for case 2. The lags of these cases are within an acceptable level, so we reckon that it is practical to identify the stages of fire development from compartment temperatures with GMM-HMMs.

4 Conclusion

SA known as ‘read’ the fire is an essential ability for firefighters to conduct emergency response operations. With the identification of the stage of fire development on the fireground, firefighters can keep safe and make appropriate tactic actions in advance. Therefore, a GMM-HMM-based approach identifying the stages of fire development from compartment temperatures was proposed. Taking ISO 9705 room fire as our case study, we examined our proposed GMM-HMM approach. From the test of the

formulated model, we found that the proposed GMM-HMM approach provides an effective way to learn the complex nonlinear relationship between the sequences of compartment temperatures and target fire stages. Given a series of compartment temperature observations, the formulated recognition model could properly identify the stages of fire development. Tested under the cross-validation, the proposed model indicated an average of 98% accuracy within 2 min error range. Besides, the model also showed a good adaptation to the real fire experiment cases. The difference between the fire growth time in terms of the model estimated value and the actual value from HRR in two real experiment cases were 13.40 s and 118.61 s, respectively. The availability of the proposed approach is indicated since the lags of these two cases are within an acceptable level.

References

1. China fire services (2020) China Personnel Press, Beijing (in Chinese)
2. Endsley MR (1995) Measurement of situation awareness in dynamic systems. *Hum Fact* 37(1):65–84
3. Fire Development and Fire Behavior Indicators. Retrieved from <http://www.firehouse.com/article/10494291/fire-behavior-indicators-and-fire-development-part-1>. Accessed on 2022/10/21
4. Park JH, Lee S, Yun S, Kim H, Kim WT (2019) Dependable fire detection system with multifunctional artificial intelligence framework. *Sensors (Basel)* 19
5. Sarwar B, Bajwa IS, Jamil N, Ramzan S, Sarwar N (2019) An intelligent fire warning application using IoT and an adaptive neuro-fuzzy inference system. *Sensors (Basel)* 19(14)
6. Sarwar B, Bajwa I, Ramzan S, Ramzan B, Kausar M (2018) Design and application of fuzzy logic based fire monitoring and warning systems for smart buildings. *Symmetry* 10(11):615
7. Muhammad K, Ahmad J, Mehmood I, Rho S, Baik SW (2018) Convolutional neural networks based fire detection in surveillance videos. *IEEE Access* 6:18174–18183
8. Saeed F, Paul A, Karthigaikumar P, Nayyar A (2019) Convolutional neural network based early fire detection. *Multimedia Tools Applicat* 79:9083–9099
9. Majid S, Alenezi F, Masood S, Ahmad M, Gündüz ES, Polat K (2022) Attention based CNN model for fire detection and localization in real-world images. *Expert Syst Appl* 189:116114
10. McLachlan GJ, Basford KE (1988) Mixture models: Inference and applications to clustering. M. Dekker New York
11. Jiang J, Chen R, Chen M, Wang W, Zhang C (2019) Dynamic fault prediction of power transformers based on hidden Markov model of dissolved gases analysis. *IEEE Trans Power Delivery* 34(4):1393–1400
12. Karlsson B, Quintiere J (1999) Enclosure fire dynamics. CRC press
13. ISO (1993) Fire tests—full-scale room test for surface products. International Standard Organization, Geneva
14. Ramachandran G, Charters D (2011) Quantitative risk assessment in fire safety. Routledge
15. Staffansson L (2010) Selecting design fires. *Brandteknik och Riskhantering*. Lunds tekniska högskola Lund
16. Hopkin C, Spearpoint M, Wang Y, Hopkin D (2020) Design fire characteristics for probabilistic assessments of dwellings in England. *Fire Technol* 56:1179–1196
17. Helton JC, Davis FJ (2003) Latin hypercube sampling and the propagation of uncertainty in analyses of complex systems. *Reliab Eng Syst Saf* 81:23–69
18. Lock A, Bundy M, Johnsson EL, Hamins A, Ko GH, Hwang C, Fuss P, Harris R (2008) Experimental study of the effects of fuel type, fuel distribution, and vent size on full-scale underventilated compartment fires in an ISO 9705 room. NIST Technical Note 1603:53–54

Determination of the Most Suitable Location of Evacuation Center for a Flood-Prone Community Using Multi-criteria Decision Analysis: The Case of Barangay Sapang Bayan, Bulacan, Philippines



Charena P. Baluyot, Franz D. Santos, Clariz D. Santos, Hiyasmine S. Pili, and Allan R. Alzona

Abstract Damage brought about by natural calamities is often hard to anticipate because of its sudden and unexpected timing. There have been modern approaches such as Geographic Information Systems (GIS) that are now being explored to store, communicate, and display spatial data. Since engineering decisions often involve multiple factors to consider, the Analytical Hierarchy Process (AHP) as a Multi-criteria Decision Analysis (MCDA) method implies value judgment to come up with the best recommendations as solutions. Because of the unpredictability of natural calamities such as flooding and the extent of damage that they may bring, disaster risk management and planning have become important for communities across the world. This paper aimed to determine the most suitable location for an evacuation center for Barangay Sapang Bayan in Calumpit, Bulacan using GIS and AHP. The criteria that were considered and given weights were flood hazard parameters, flood risk parameters, and accessibility parameters. The weights that were used in overlaying the maps were generated using normalized values after the pair-wise comparison of each parameter. The results produced a suitability map showing that 8.98% of the study area is the most suitable locations for an evacuation center which can be found in places with far distances from the adjacent river and in areas of high elevation. Moreover, 25.86% of the total study area are suitable areas or can be considered evacuation center locations, and the rest of the barangay, 65.14%, was found to be the least to non-suitable locations. The findings of this study could aid planners and

C. P. Baluyot · F. D. Santos (✉) · H. S. Pili · A. R. Alzona
Department of Civil Engineering, National University—Manila, 1008 Manila, Philippines
e-mail: fdsantos@national-u.edu.ph

C. D. Santos · A. R. Alzona
Department of Environmental and Sanitary Engineering, National University—Manila, 1008 Manila, Philippines

© The Author(s), under exclusive license to Springer Nature Singapore Pte Ltd. 2024
M. Casini (ed.), *Proceedings of the 3rd International Civil Engineering and Architecture Conference*, Lecture Notes in Civil Engineering 389,
https://doi.org/10.1007/978-981-99-6368-3_80

985

officials in imposing mitigation measures and guide them in improving their disaster response in times of calamities.

Keywords Analytical hierarchy process · Bulacan · Flooding · GIS · MCDA

1 Introduction

Natural calamities have long affected communities due to the implications they bring to the economy in the aspects of agricultural production and infrastructure [1]. Severe disturbances like earthquakes, floods, and cyclones are considered disasters when they adversely and seriously affect human life, livelihood, and property [2]. Furthermore, the effects of these disaster to operations of society result in widespread human, material, or environmental losses [3]. Communities in coastal regions are the areas that are drastically affected and are more vulnerable to natural calamities [4]. Because of these effects of natural calamities, knowledge and information about the environment should be achieved [5] through the collection and processing of available data towards planning mitigating measures to lessen the risk that these natural phenomena would bring to communities.

Flood Mitigation should be considered where options such as engineering solutions and nature-based solutions can be applied [6]. Other approaches such as controlling from the storm water source can also be considered in managing flood problems of the community [7]. Another risk management strategy that is often an option during flood events is evacuation. Individuals that are displaced from their homes are transferred to Evacuation centers that provide shelter and safety from direct exposure to floods. Since floods can affect both life and property, proper monitoring and mitigation should be considered along with proposing possible solutions through flood risk management [8].

The disaster management community has been evolving over the past years. The use of modern technology has provided more specific disaster risk assessments, enhanced forecasts, minimized human losses with effective early warning systems, and strengthened resilience-building approaches of communities. In addition, the development of new approaches to disaster management may reveal various forms of collaboration, tools, techniques for gathering and managing data risks, communication, and knowledge-sharing approaches [9]. With the aid of technological innovations, people can better comprehend the intricacies of natural disasters that have atmospheric, geological, hydrological, and biological causes, analyze the transformation of these hazards into disasters [10] and provide a higher chance of survivability and safety during catastrophic events.

Geographic Information System (GIS) is a new emerging and powerful tool that collects, stores, retrieves, and analyzes geographic data. It can also be used in integrating various real-world geographic data elements [11] and displaying geospatial data [12]. Through databases on computer-generated maps, information sharing between all departments in one place is made possible. The use of GIS in assessing

the flood-risk of communities across the world had been explored [13–17]. However, the hydrologic response of an area varies depending on the topography, land cover, soil type as well as the climatic condition therefore saying that the flood risk of every community is different and must be assessed so that proper planning and management can be applied to the area.

Flood-risk management requires consideration of natural and man-driven factors [18] to come up with a more reliable direction for urban planning in cases of extreme storm events. Geographical data is combined with value judgements to arrive at appropriate tools for better decision-making [19] and this is known as the multi-criteria decision analysis (MCDA). GIS gives the spatial visualization of data while MCDA complements it by evaluating and prioritizing alternatives thus getting a better benefit from output and solution for spatial problems [20]. There are various techniques of value judgements that has been used in coupled GIS-MCDA studies [13, 19, 21] but among them, the Analytical Hierarchy Process (AHP) has been one of the most explored [22–27] because it is easy to understand and cost-effective [28, 29].

2 Materials and Methods

Site selection for evacuation centers is a crucial decision in disaster management as the location of the center can significantly affect the efficiency and effectiveness of the evacuation process. The use of GIS and MCDA as tools allow for integrating and studying various spatial and non-spatial data to determine the most suitable locations for evacuation centers. This paper aims to use a coupled GIS-MCDA methodology utilizing AHP in identifying a suitable location of an Evacuation Center of a flood-prone barangay in Calumpit, Bulacan.

2.1 *The Study Area*

Sapang-Bayan is a barangay in Calumpit, Bulacan, with a population of 3140, as recorded in the 2020 Census, accounting for only 2.65% of Calumpit's total population [30]. Figure 1 shows the location map of the chosen study area where the terrain was a shot from Google Earth.

Flooding is a persistent issue in Calumpit, especially in Sapang Bayan, where high tides and heavy rains often cause the river to overflow. During the recent typhoon (Typhoon Ulysses), the barangay experienced severe flooding with four to eight feet of water, making it one of the most affected areas in Calumpit [31]. The community faces three problems during typhoons: flooding, inadequate evacuation centers, and mobility difficulties. The proponents of this paper decided to focus on the problem of the lack of an evacuation center, as it is observed to be a problem for every family during a calamity since they have to evacuate in neighboring Barangay.

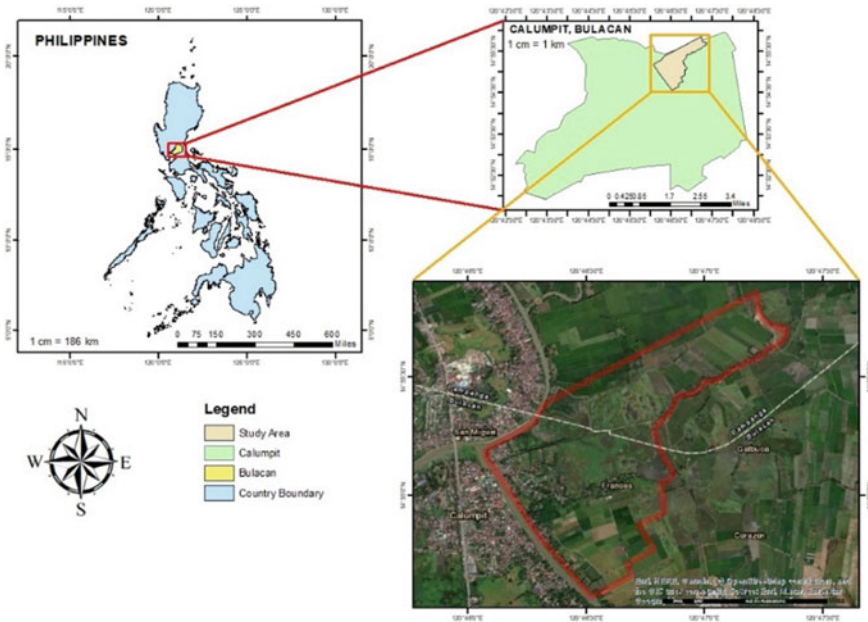


Fig. 1 Barangay Sapang Bayan in Calumpit, Bulacan

2.2 Data Collection

Data gathering is a very crucial phase in this study to arrive with the most suitable location of an evacuation center based on the different factors to meet the objective of this paper. In this site suitability study, the most desirable location for an evacuation center that will be safe from flooding was based on three criteria namely (i) flood hazard, (ii) flood exposure, and (iii) accessibility. In terms of flood hazard criteria, the following were considered as inputs: slope, elevation, soil type, and flood depth. For the flood exposure criteria: population density and land cover. And for the accessibility parameters, the following were considered: proximity to major roads and distribution of evacuation centers. Depicted in Fig. 2 is the framework used in the selection process.

2.3 Criteria Determination for Evacuation Center Site Selection

Three parameters were considered for Evacuation Center Site Selection: Flood Hazard Parameters, Flood Exposure Parameters, and Accessibility Parameters. They

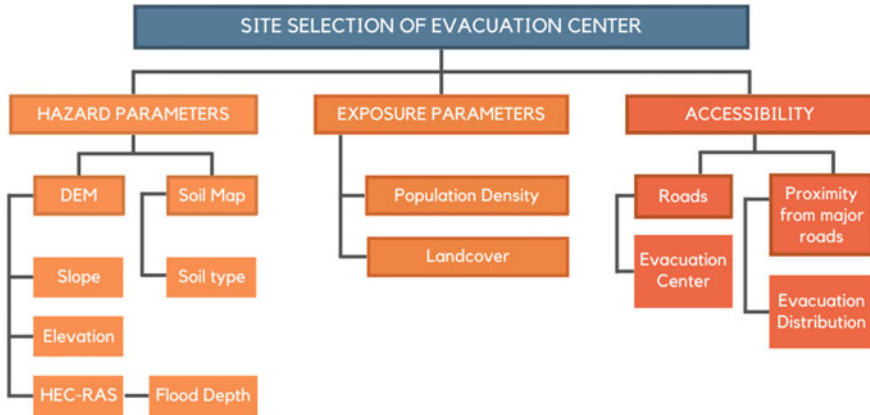


Fig. 2 Criteria-based site selection framework

are essential for ensuring that the evacuation center can meet the needs of evacuees and function effectively during an emergency.

Flood Hazard Parameters. The location to be selected should be away from potential flood hazards and structurally sound to withstand the hazard’s potential impacts. Shown in Table 1, the identified flood hazard elements were slope, elevation, soil type, and flood depth. The Digital Terrain Model (DTM) came from the National Mapping and Resource Information Authority (NAMRIA) and the Soil Map was downloaded from the website of the Food and Agriculture Organization (FAO). Flood depth was generated from the flood inundation map that was simulated using the coupled Hydraulic Engineering Center—Hydrologic Modeling System (HEC-HMS) and Hydraulic Engineering Center—River Analysis System (HEC-RAS) for a 100-year storm (Table 1).

Flood Exposure Parameters. The exposure analysis was intended to identify the life and property elements exposed during flooding events. Population density and land use/cover in raster format were identified as exposure elements as shown in Table 2.

Accessibility Parameters. The site should be easily accessible to the population that will be evacuating and with adequate transportation available to reach the site. This may include proximity to major roads and highways and the availability of

Table 1 Flood hazard parameters and data used

Flood hazard parameters	Data type	Source	References
Slope	DTM	NAMRIA	[32–38]
Elevation	DTM	NAMRIA	[32, 37–39]
Soil type	Soil map of the world	FAO	[32, 33, 37]
Flood depth	Raster	HEC-HMS and HEC-RAS simulations	[37, 40]

Table 2 Flood exposure parameters and data used

Flood exposure parameters	Data type	Source	References
Population density	Raster	WorldPop Website	[32, 34, 36, 40]
Landcover	Raster	NAMRIA	[32–35, 37]

Table 3 Accessibility parameters and data used

Accessibility parameters	Data type	Source	References
Proximity to major roads	Shapefile	Geofabrik	[32, 33, 35–38]
Evacuation center distribution	Excel	DSWD/Google Map	[33–36]

public transportation. The identified accessibility elements were Proximity to Major Roads in shapefile format and Evacuation Center Distribution in coordinates as listed in Table 3.

2.4 Parameter Weighing Using Analytical Hierarchy Process (AHP)

GIS as a tool was used analyze and visualize data related to site selection for evacuation centers in Sapang Bayan, Calumpit. It was used to map the affected area, the population that must be evacuated, and the resources and infrastructure required at the evacuation centers. Location of possible site evacuation centers based on parameters such as flood hazard, flood exposure, accessibility, and suitability for the intended use was also assessed in this paper.

Pair-wise Comparison of Parameters. AHP was used to assess and compare the probable sites based on predetermined criteria such as slope, elevation, soil type, flood depth, population density, land cover, proximity to major roads, and evacuation center distribution. The AHP method involves breaking down the evaluation criteria into a hierarchy and assigning weights to each level to reflect the criteria’s relative importance using Pairwise Comparison.

The normalized value for each criterion after pair-wise comparison was obtained and was used to calculate the weights that will be used in combining the layers. The potential sites are then evaluated based on these standards and weights shown in Table 4, and a final ranking of all the parameters is produced. This combination of ArcGIS and AHP allows for a systematic and comprehensive analysis of potential sites for an evacuation center in the area, helping to provide that the most suitable location is selected.

Table 4 AHP of all parameters

Flood risk parameters						
	Item description	Slope	Elevation	Soil type	Flood depth	Weight
1	Slope	0.27	0.27	0.27	0.27	26.9%
2	Elevation	0.23	0.23	0.23	0.23	22.9%
3	Soil Type	0.28	0.28	0.28	0.28	28.1%
4	Flood Depth	0.22	0.22	0.22	0.22	22.1%
Flood exposure parameters						
	Item description	Population	Land cover	Weight		
1	Population	0.50	0.50	50.1%		
2	Land cover	0.50	0.50	49.9%		
Accessibility parameters						
	Item description	Roads	Evacuation Center	Weight		
1	Roads	0.40	0.40	40.1%		
2	Evacuation center	0.60	0.60	59.9%		

3 Results and Discussion

Secondary data from the local government agency and other open-source websites were processed and analyzed according to the different criteria using ArcGIS. The map layers for each output are presented in this chapter.

3.1 Flood Hazard Parameters

Shown in Fig. 3 are the maps of parameters under flood hazard criteria. It can be noticed that based on the slope and elevation map, the areas that are more prone to flooding are the ones at the inner portions north-west. Due to a lower elevation ranging up to 0.90 m above mean sea level, it is expected that overflowing water from the river as well as runoff generated by storm events might come flushing down this area also because of the nature of the sloping terrain.

The soil map shows that the study area is made from Loam that may have an effect on the infiltration which is an important factor to consider in estimating and predicting overland flow [41]. The flood map generated from rainfall-runoff simulation of HEC-HMS and flood inundation mapping of HEC-RAS showed that the part of the study area adjacent to the river is the most prone to flooding with depths up to 2.1 m which makes the area not suitable for the construction of the evacuation center.

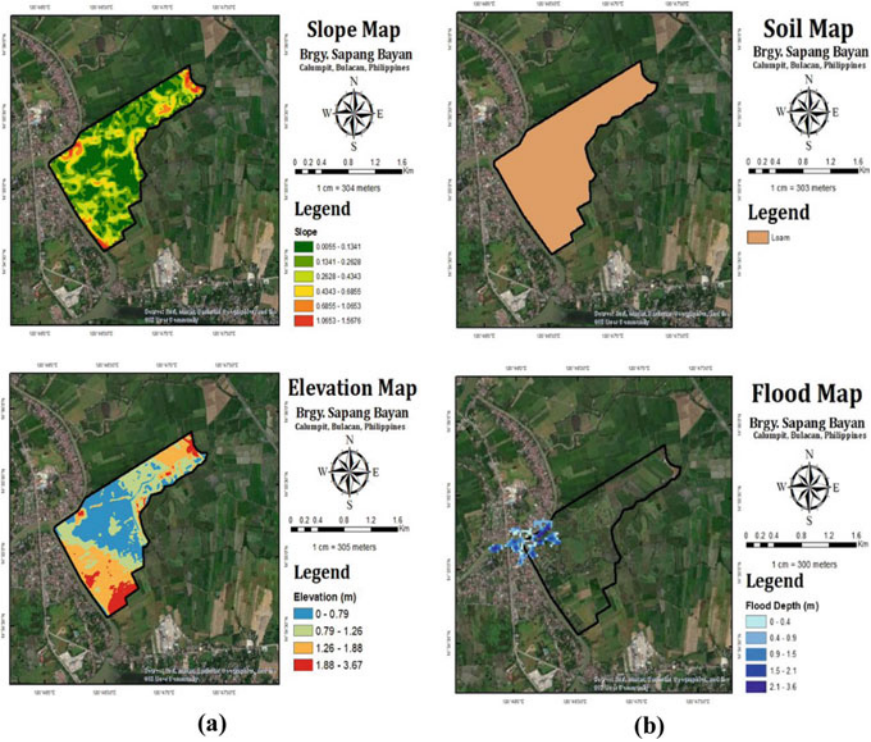


Fig. 3 Maps of study area considering flood hazard parameters **a** slope and elevation, **b** soil and flood map

3.2 Flood Exposure and Accessibility Parameters

Illustrated in Fig. 4 are the maps of the flood exposure parameters and accessibility parameters that were processed in ArcGIS. It can be seen on the population density map that majority of inhabitants are concentrated on the riverbank areas where they are of risk to flooding when an extreme weather event happens. Moreover, based on the location of evacuation centers in the area, no evacuation center is located within the boundary thereby strengthening the need for the objective of this paper that is to identify the most suitable location for an evacuation center considering the flood-prone nature of the area.

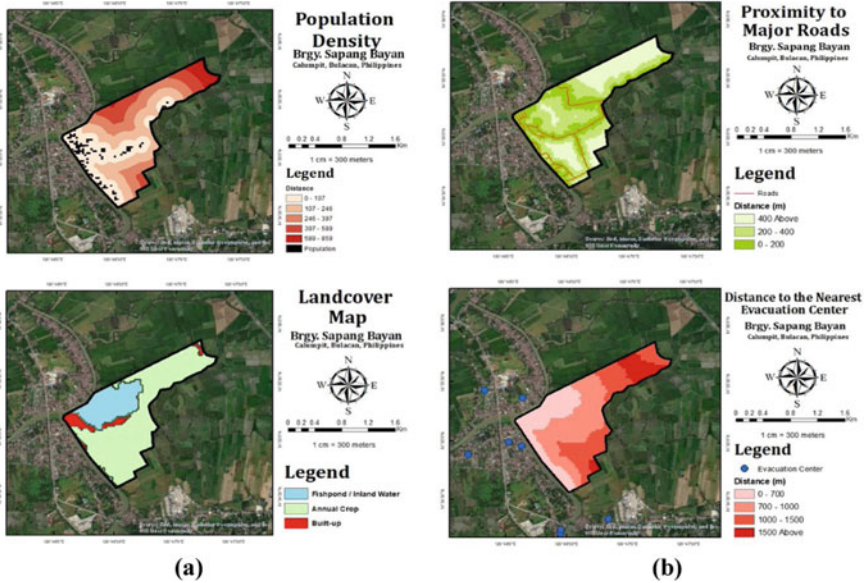


Fig. 4 Maps of study area considering flood hazard parameters a population density and land cover map, b proximity from major roads and distance to nearest evacuation center

3.3 Determination of Most Suitable Location for an Evacuation Center

Overall weights for the criteria were derived from normalized values of AHP. Based on Table 5, heavier weight was given to flood hazard parameters to ensure that the location that will be selected will not be susceptible to flood events having a weight of 55.7%. Following hazard parameters, the number of inhabitants and type of land cover was given second highest importance with a weight of 32% to consider not only the susceptibility of the study area, but also to minimize the risk of people that are residing in flood-prone areas of Sapang Bayan.

Output maps considering hazard parameters, exposure parameters and accessibility parameters were then combined and overlain in ArcGIS considering the weights that were derived from the AHP. Four classes (regions) were identified for the final

Table 5 Weight of criterion for suitability selection

	Item description	Accessibility	Hazard	Exposure	Weight (%)
1	Accessibility	0.12	0.14	0.10	12.3
2	Hazard	0.50	0.57	0.60	55.7
3	Exposure	0.38	0.29	0.30	32.0

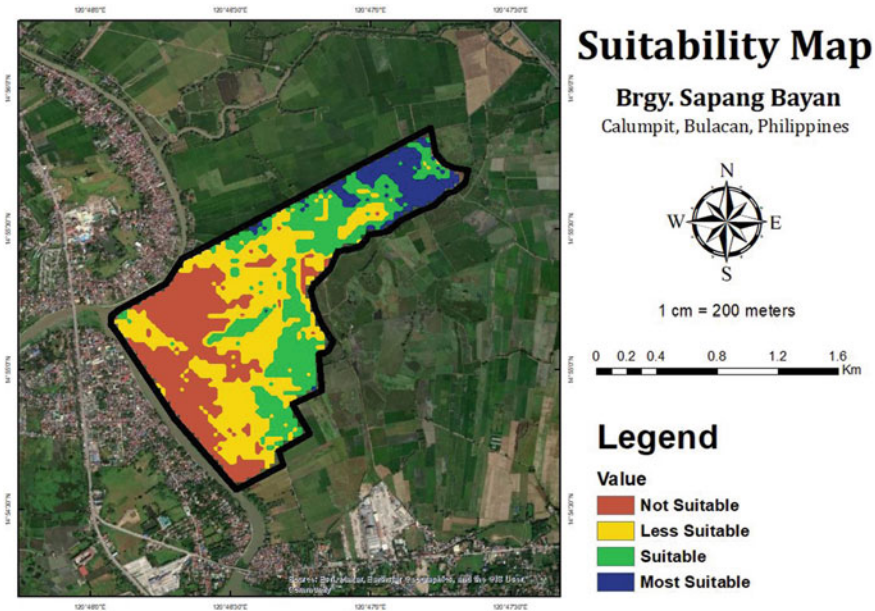


Fig. 5 Maps of study area considering flood hazard parameters a slope and elevation, b soil and flood map

map: most suitable, suitable, less suitable, and not suitable. Shown in Fig. 5 is the derived suitability map for the evacuation center.

Based on the suitability map output from GIS, it was found out that 8.98% of the total study area is highly suitable and can be recommended to be the location for the evacuation center. Majority of these areas can be found at the North-East side of the barangay where it is far from inundation that will come from the river as well as overland flow brought about by the topography. For areas that can be considered, 25.86% of the total study area can be said to be suitable enough to be the location of the evacuation center. Although majority of these suitable locations can be seen at the central part of the area, probably the consideration for accessibility of roads to be used in transporting evacuees are also seen to be interconnected in this region. In total, 65.14% of the total study area is at high risk of flooding being located near the riverbanks therefore getting a less to not suitable rating from the layered maps.

4 Conclusion

This paper explored the capability of GIS and multi-criteria decision analysis to determine the most suitable locations for an evacuation center of a flood-prone barangay, Sapang Bayan, in Calumpit Bulacan, Philippines.

Multiple Criteria Decision Analysis (MCDA) using Analytic Hierarchy Process (AHP) was used to combine spatial information with value judgements in choosing the most suitable location of an evacuation center in the area. A combination of Flood Hazard Parameters, Flood Exposure Parameters, and Accessibility Parameters were evaluated by assigning importance based on the assessment of proponents. Highest overall importance was given to Flood Exposure Parameters where it received a weight of 55.7% ensuring that priority in choosing the location was its safety from flooding. Second priority was given to exposure considering the population this is at risk to flooding in the area. With these importance ratings, the different layers were overlain to produce the final suitability map.

Results of the study identified that there is an 8.98% area of Sapang Bayan that was most suitable for an evacuation center that is safe from flooding. These are the areas that are far north-east of the study site due to its distance from the riverbank and its topographic characteristics. In addition, the central part of Sapang Bayan can be considered as location for an evacuation center since it was determined to be part of the 25.86% suitable area while the rest of the barangay (65.14%) was found to be least suitable to non-suitable for an evacuation center.

With the use of modern tools such as GIS and criteria-based methodology such as AHP, findings could help in the disaster preparedness of the barangay and the methodology of this study could also be applied to other flood-prone municipalities in their future urban planning.

Acknowledgements The proponents would like to acknowledge the open-access data sources that were utilized in this mapping study specially the National Mapping and Resource Information Authority (NAMRIA). The proponents also would like to thank National University—Manila particularly the Research and Development (NURD) Office for their support in this research undertaking.

References

1. Hussain M et al (2020) A comprehensive review of climate change impacts, adaptation, and mitigation on environmental and natural calamities in Pakistan. *Environ Monitor Assess* 192(1). <https://doi.org/10.1007/s10661-019-7956-4>
2. Pelling M et al (2004) Reducing disaster risk: a challenge for development
3. Khan H, Vasilescu LG, Khan A (2008) Disaster management cycle-a theoretical approach. *J Manage Market* 6(1):43–50
4. Jaisankar I, Velmurugan A, Swarnam TP (2018) Bioshield: an answer to climate change impact and natural calamities? In: *Biodiversity and climate change adaptation in tropical Islands*, Elsevier, pp 667–698. <https://doi.org/10.1016/B978-0-12-813064-3.00024-7>
5. Asio JMR (2020) Natural calamity, its impact and level of preparations: significance and implications to the community. [Online]. Available: <https://ssrn.com/abstract=3718496>
6. Edmonds DA, Caldwell RL, Brondizio ES, Siani SMO (2020) Coastal flooding will disproportionately impact people on river deltas. *Nat Commun* 11(1). <https://doi.org/10.1038/s41467-020-18531-4>

7. Hu M, Zhang X, Li Y, Yang H, Tanaka K (2019) Flood mitigation performance of low impact development technologies under different storms for retrofitting an urbanized area. *J Clean Prod* 222:373–380. <https://doi.org/10.1016/j.jclepro.2019.03.044>
8. Cvetkovic VM, Martinović J (2020) Innovative solutions for flood risk management. *Int J Disaster Risk Manage* 2(2):71–99. <https://doi.org/10.18485/ijdrm.2020.2.2.5>
9. Fontes de Meira L, Bello O (2020) The use of technology and innovative approaches in disaster and risk management: a characterization of Caribbean countries' experiences
10. Rathore V (2016) Technology in disaster management and disaster risk reduction: a review of applications. *Technology (Singap World Sci)* 6(4)
11. Madhloom HM, Al-Ansari N (2018) Geographical information system and remote sensing for water resources management case study: the Diyala River. *Int J Civil Eng Technol (IJCIET)* 9:971–984
12. Chang K (2016) Geographic information system. *International Encyclopedia of Geography: People, the Earth, Environment and Technology: People, the Earth, Environment and Technology*, pp 1–9
13. Wang Y, Li Z, Tang Z, Zeng G (2011) A GIS-based spatial multi-criteria approach for flood risk assessment in the Dongting Lake Region, Hunan, Central China. *Water Resour Manage* 25(13):3465–3484. <https://doi.org/10.1007/s11269-011-9866-2>
14. Hu S, Cheng X, Zhou D, Zhang H (2017) GIS-based flood risk assessment in suburban areas: a case study of the Fangshan District, Beijing. *Nat Hazards* 87(3):1525–1543. <https://doi.org/10.1007/s11069-017-2828-0>
15. Kabenge M, Elaru J, Wang H, Li F (2017) Characterizing flood hazard risk in data-scarce areas, using a remote sensing and GIS-based flood hazard index. *Nat Hazards* 89(3):1369–1387. <https://doi.org/10.1007/s11069-017-3024-y>
16. Ullah K, Zhang J (2020) GIS-based flood hazard mapping using relative frequency ratio method: a case study of Panjkora river basin, eastern Hindu Kush, Pakistan. *PLoS One* 15(3). <https://doi.org/10.1371/journal.pone.0229153>
17. Lyu HM, Sun WJ, Shen SL, Arulrajah A (2018) Flood risk assessment in metro systems of mega-cities using a GIS-based modeling approach. *Sci Total Environ* 626:1012–1025. <https://doi.org/10.1016/j.scitotenv.2018.01.138>
18. Danumah JH et al (2016) Flood risk assessment and mapping in Abidjan district using multi-criteria analysis (AHP) model and geoinformation techniques, (cote d'ivoire). *Geoenviroin Disast* 3(1). <https://doi.org/10.1186/s40677-016-0044-y>
19. Boroushaki S, Malczewski J (2010) Using the fuzzy majority approach for GIS-based multicriteria group decision-making. *Comput Geosci* 36(3):302–312. <https://doi.org/10.1016/j.cageo.2009.05.011>
20. Greene R, Devillers R, Luther JE, Eddy BG (2011) GIS-based multiple-criteria decision analysis. *Geogr Compass* 5(6):412–432. <https://doi.org/10.1111/j.1749-8198.2011.00431.x>
21. Yao Y, Zhang Y, Yao T, Wong K, Tsou JY, Zhang Y (2021) A GIS-based system for spatial-temporal availability evaluation of the open spaces used as emergency shelters: the case of Victoria, British Columbia, Canada. *ISPRS Int J Geoinf* 10(2). <https://doi.org/10.3390/ijgi10020063>
22. Ouma YO, Tateishi R (2014) Urban flood vulnerability and risk mapping using integrated multi-parametric AHP and GIS: methodological overview and case study assessment. *Water (Switzerland)* 6(6):1515–1545. <https://doi.org/10.3390/w6061515>
23. Antronisamy TK, Din NM, Omar RC, Mustafa IS (2020) Analytical hierarchy process and power method for flood evacuation route selection
24. Gacu JG, Monjardin CEF, Senoro DB, Tan FJ (2022) Flood risk assessment using GIS-based analytical hierarchy process in the municipality of Odiongan, Romblon, Philippines. *Appl Sci (Switzerland)* 12(19). <https://doi.org/10.3390/app12199456>
25. Ali SA, Khatun R, Ahmad A, Ahmad SN (2019) Application of GIS-based analytic hierarchy process and frequency ratio model to flood vulnerable mapping and risk area estimation at Sundarban region, India. *Model Earth Syst Environ* 5(3):1083–1102. <https://doi.org/10.1007/s40808-019-00593-z>

26. Junian J, Azizifar V (2018) The evaluation of temporary shelter areas locations using geographic information system and analytic hierarchy process. *Civ Eng J* 4(7):1678. <https://doi.org/10.28991/cej-03091104>
27. Şentürk E, Erener A (2017) Determination of temporary shelter areas in natural disasters by GIS a case study for GÖLCÜK/TURKEY. *Int J Eng Geosci* 2(3):84–90. <https://doi.org/10.26833/ijeg.317314>
28. Ajim Ali S, Ahmad A (2018) Using analytic hierarchy process with GIS for Dengue risk mapping in Kolkata Municipal Corporation, West Bengal, India. *Spatial Inf Res* 26(4):449–469. <https://doi.org/10.1007/s41324-018-0187-x>
29. Güler D, Yomralıoğlu T (2017) Alternative suitable landfill site selection using analytic hierarchy process and geographic information systems: a case study in Istanbul. *Environ Earth Sci* 76(20). <https://doi.org/10.1007/s12665-017-7039-1>
30. Sapang Bayan, Calumpit, Bulacan Profile—PhilAtlas. <https://www.philAtlas.com/luzon/r03/bulacan/calumpit/sapang-bayan.html> (accessed 11 Jun 2022)
31. Velez F (2020) 45,000 families in Bulacan affected by flood reaching 8 ft—Manila Bulletin. https://mb.com.ph/2020/11/16/45000-families-in-bulacan-affected-by-flood-reaching-8-ft/?fbclid=IwAR3Cj5VdUsD7M8ZOkII4C6S6Z6pn2tkZMx7o9XEy5TTX9ji45c6YMI9Hs_I (accessed 08 Jun 2022)
32. Erkan TE, Elsharida WM (2020) Combining AHP and ROC with GIS for airport site selection: a case study in Libya. *ISPRS Int J Geoinf* 9(5). <https://doi.org/10.3390/ijgi9050312>
33. Rahmat ZG et al (2017) Landfill site selection using GIS and AHP: a case study: Behbahan, Iran. *KSCE J Civ Eng* 21(1). <https://doi.org/10.1007/s12205-016-0296-9>
34. Boyacı AÇ, Şişman A (2022) Pandemic hospital site selection: a GIS-based MCDM approach employing Pythagorean fuzzy sets. *Environ Sci Poll Res* 29(2). <https://doi.org/10.1007/s11356-021-15703-7>
35. Pasalari H, Nodehi RN, Mahvi AH, Yaghmaeian K, Charrahi Z (2019) Landfill site selection using a hybrid system of AHP-Fuzzy in GIS environment: a case study in Shiraz city, Iran. *MethodsX* 6. <https://doi.org/10.1016/j.mex.2019.06.009>
36. Tripathi AK, Agrawal S, Gupta RD (2022) Comparison of GIS-based AHP and fuzzy AHP methods for hospital site selection: a case study for Prayagraj City, India. *GeoJournal* 87(5). <https://doi.org/10.1007/s10708-021-10445-y>
37. Alkaradaghi K, Ali SS, Al-Ansari N, Laue J, Chabuk A (2019) Landfill site selection using MCDM methods and GIS in the Sulaimaniyah Governorate, Iraq. *Sustainability (Switzerland)* 11(17). <https://doi.org/10.3390/su11174530>
38. Yousefi H, Hafeznia H, Yousefi-Sahzabi A (2018) Spatial site selection for solar power plants using a gis-based boolean-fuzzy logic model: a case study of Markazi Province, Iran. *Energies (Basel)* 11(7). <https://doi.org/10.3390/en11071648>
39. Bandira PNA, Mahamud MA, Samat N, Tan ML, Chan NW (2021) GIS-based multi-criteria evaluation for potential inland aquaculture site selection in the george town conurbation, Malaysia. *Land (Basel)* 10(11). <https://doi.org/10.3390/land10111174>
40. Barzehkar M, Dinan NM, Mazaheri S, Tayebi RM, Brodie GI (2019) Landfill site selection using GIS-based multi-criteria evaluation (case study: SaharKhiz Region located in Gilan Province in Iran). *SN Appl Sci* 1(9). <https://doi.org/10.1007/s42452-019-1109-9>
41. Diamond J, Shanley T (1998) Infiltration rate assessment of some major soils end of project report ARMIS 4102 Author

Bridge Safety State Classification Based on Unsupervised Machine Learning



Wei Xiang, Xiao Li, and Feng-Liang Zhang

Abstract With the development of artificial intelligence and big data technology, it is becoming a research trend to combine structural health monitoring (SHM) with these new techniques in order to make the analysis more intelligent. Due to the complexity and uncertainty of the structure environments, there are still problems such as low feature extraction efficiency and low accuracy in the research on the multivariable correlation features for structural perception data. Recently, the advantages of generative adversarial networks for nonlinear feature extraction have been noticed and this method has the potential to be applied to structural health monitoring. In this paper, an abnormal state detection model of monitoring data will be designed through the generative adversarial network of unsupervised learning. The abnormal state caused by bridge damage will be detected from a data-driven perspective, which provides support for the classification of bridge safety state abnormalities.

Keywords Structural state · Classification · Unsupervised learning · Structural health monitoring

1 Introduction

In the past two decades, some scholars have done a lot of research on the emerging field of Structural health monitoring (SHM) [1], such as the damage detection technology based on the change of modal characteristics in the frequency domain [2] (vibration frequency, mode shape, modal compliance and modal strain energy). These methods are aimed at objective structural damage detection and structural integrity

W. Xiang
Technical Center, Shenzhen Road and Bridge Group, Shenzhen 518055, China

X. Li (✉) · F.-L. Zhang
School of Civil and Environmental Engineering, Harbin Institute of Technology,
Shenzhen 518055, China
e-mail: 21b354009@stu.hit.edu.cn

assessment through the measurement data of sensors [3]. Due to various technological developments in this field, SHM has emerged as a promising solution to allow inspectors, and managers to gain a more rapid and accurate understanding of the state of structures [4].

Problems addressed by SHM include structural damage detection [5], damage quantification [6] and remaining useful life prediction [7]. This information can be used for feedback on structural design, maintenance decisions after evaluation, and post-disaster management. The modern SHM system is mainly composed of various sensors, which are connected through data acquisition and transmission systems. A large amount of measurement data is collected to extract useful information through physical parameter methods [8], so as to facilitate the decision-making process. Although some studies have proposed many different SHM methods [9], their wide application in practical engineering structures is limited due to the cumbersome installation of sensor networks and data acquisition systems.

In order to ensure the safety and durability of structural operations, the SHM combined with artificial intelligence and big data technology has become an effective technique for structural intelligent management [10]. The structural health monitoring system has accumulated a large amount of monitoring perception data with the growth of the structure's operating life, which could be used to reflect the health status of the objective structure. Although the structural health monitoring technology has achieved fruitful research results [11], there are still some deficiencies in the recognition of multi working conditions [12]. Due to the complexity and uncertainty of structure environments, a joint model on multivariate time series is yet to be constructed [13].

In this work, taking the classification of structural damage states under multiple working conditions as the research object, a generation countermeasure network is proposed on the basis of unsupervised learning. A structural state anomaly detection model is designed from a data-driven perspective, providing new methods for the structural state anomaly classification.

2 Methodologies

After the generative adversarial network (GAN) was developed [14], it has been applied in the field of image classification and achieved good classification results, but in the damage detection of Bridge, few studies were carried out. In this work, a bridge safety state classification method will be proposed based on the GAN, in which, the power spectral density spectra will be used as the input and training set to identify the bridge health states. Based on convolutional neural network, an unsupervised generative adversarial network classification model is designed for the classification of structural damage states. It mainly includes three parts: generative adversarial networks (GAN), network structure (CNN), and evaluation method. Unsupervised classification algorithms can effectively solve the problems of labeling difficulties

and insufficient samples in model training, so as to realize the classification of bridge safety states.

2.1 Generative Adversarial Networks (GAN)

Generative adversarial network (GAN) of unsupervised learning is a new algorithm proposed by Ian Goodfellow [14]. Figure 1 shows the structure of generative adversarial network. Generative adversarial network consists of two neural network, i.e., generator (G) and discriminator (D) [15], where the generator (G) disguises the Gaussian white noise z as the “real” data distribution $G(z)$ by learning the real sample distribution $x(z)$. The discriminator outputs classification information ranging from 0 to 1, which is used to distinguish whether the input data comes from real samples or generated samples. When the output of the discriminant network is “1”, the input sample is a real sample. While the output of the discriminant network is close to “0”, the input is a fake sample [16]. The authenticity of the input sample is determined by the objective function V :

$$\min_G \max_D V(D, G) = E_{x \sim P_{data}} [\log D(x)] + E_{z \sim P_z} [\log(1 - D(G(z)))] \quad (1)$$

$$E_{x \sim P_{data}} [\log D(x)] = \int_x P_{data}(x) \log(D(x)) dx \quad (2)$$

$$E_{z \sim P_z} [\log(1 - D(G(z)))] = \int_z P_z(z) \log(1 - D(g(z))) dz \quad (3)$$

where the subscript $x \sim P_{data}(x)$ and $z \sim P_z(z)$ represent the real data and the false data input to the generator, respectively. P_{data} and P_z denote the probability distribution of input data random variables, respectively. The discriminator model is trained to maximize $E[\log D(x)]$, while the generator model is trained to minimize $E[\log(1 - D(G(z)))]$ until the Nash equilibrium is reached. E represents the expectation of

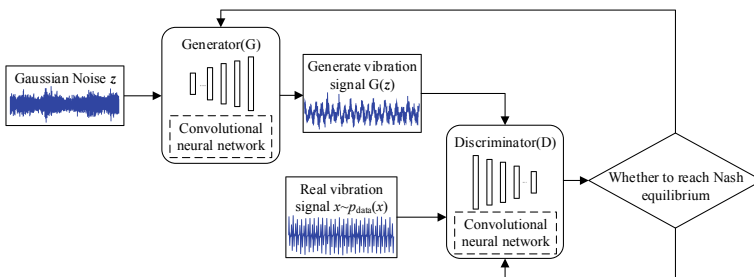


Fig. 1 Generative adversarial network training model

the variable. During the training process of the generative adversarial network, it is found that the better the discriminator is trained, the more obvious its gradient disappears. As the discriminator D can distinguish the real data from the generated data with a high probability, it will cause the problem that the gradient of the generator disappears.

2.2 Network Structure

In this part, The network structure is combined by CNN and GAN in unsupervised learning to form a new network structure with stable training. The batch normalization (BN) is successfully used on each layer network structure of the generator and the discriminator, which alleviates the problem of model collapse and effectively avoids model oscillation and instability.

Generally, the generator is fixed once, and then the discriminator is trained twice in the training process [17]. During the forward propagation of the network, the input data of the network includes unlabeled samples and random noise. The unlabeled data in the training set are input into the discriminator as real samples for training, while random noise is input into the generator.

The random noise is synthesized to fake samples by the generator, which will be sent to the discriminator to train with real samples. Both the discriminator and the generator use convolutional neural networks for high-level feature extraction. In the classification of structural damage state, the power spectrum of each working condition can be regarded as an independent sample. The high-level feature can be extracted by the convolutional layer, and the dimensionality of the extracted feature information can be reduced by the pooling layer. The pooling layer can simplify the computational complexity of the network and avoid overfitting in training. At the same time, the pooling layer can be used for feature compression and extraction of main features.

Table 1 shows the structure of the discriminator and the generator in GAN. The discriminator of the unsupervised generative adversarial network consists of 5 sets of convolutional layer. Among the five sets of convolutional layers, the first fully connected layer is mainly used to convert the dimension of the input data, and the second fully connected layer has the same dimension of input data, which is simply used for feature extraction. By adding a full connection layer with the same number of neurons as the previous layer, the network depth can be increased and the nonlinear expression ability of the model can be improved.

In the first group of fully connected layers, the input data is 513-dimensional power spectrum data, which is converted into 256-dimensional through full connection for output. In the second and third layers, the dimensionality of the output data of each group is twice than the input data, and the dimensions of the output data are 256 and 512 dimensions respectively. There is only one fully connected layer in the fifth group, which is used to convert the 512-dimensional high-dimensional features into 256-dimensional category features as the output of the discriminator.

Table 1 Structure of the discriminator and the generator in GAN

Layer	Generator	Discriminator
1	Input: 1×200	Input: 1×513
	4×1 conv1:513, stride = 2	4×1 conv1:256, stride = 2
2	4×1 conv1:256, stride = 2	4×1 conv1:128, stride = 1
3	4×1 conv1:128, stride = 2	4×1 conv1:256, stride = 2
4	Linear:513	4×1 conv1:512, stride = 2
5	–	Linear:256

Similar to the discriminator, the generator also contains 4 sets of convolutional layers. But there is the difference that the input data of the first layer is 200-dimensional random noise in the generator and the output data is 513-dimensional. In the second group and the third group of fully connected layers, the dimensionality of the output data is half of the input data, and the dimensions of the output data are 256 and 128 dimensions respectively. There is only one fully connected layer in the fourth group, which is used to convert the 128-dimensional input feature into 513-dimensional, which output the pseudo power spectrum features.

2.3 Evaluation Methods

Clustering analysis belongs to the category of unsupervised machine learning, and the selection of objective clustering evaluation indicators is very important for the application of classification algorithms. The methods for evaluating the effectiveness of clustering algorithms can be roughly divided into two categories: external evaluation criteria and internal evaluation criteria. External evaluation indicators rely on the real labels that clustering data sets provide, and then verify whether the clustering results are consistent with the real labels.

External evaluation indicators mainly include: accuracy rate (*ACC*) [18], mutual information (*MI*) [19], adjusted rand index (*ARI*) [20]. In this paper, the external evaluation indicators are used to test the quality of the clustering results, and the validity of the clustering is verified by comparing the clustering labels with the real labels. This section will select two external indicators that are commonly used to test the clustering results: normalized mutual information (*NMI*) and adjusted rand index (*ARI*). The critical values of both indicators are all equal to 1.

When the normalized mutual information matches random variables, the entropy will be small. On the other hand, the mutual information of overlapping areas is considered, and the relationship between the two is successfully balanced. Therefore, the normalized mutual information has good robustness and can well reflect the degree of correlation between random variables. *NMI*'s function is expressed as:

$$NMI(X, Y) = \frac{I(X; Y)}{\sqrt{H(X)H(Y)}} \quad (4)$$

where $H(X)$ and $H(Y)$ represent the entropy of the predicted category label and the entropy of the real category label, respectively; $I(X, Y)$ represents the mutual information of X and Y . When NMI is closer to 1, the two sets of label distributions X and Y are completely correlated. When NMI is closer to 0, the two sets of label distributions X and Y are independent of each other.

The similarity between two clusters is calculated through the adjusted rand index (ARI), and the value range of ARI is $[-1, 1]$. When ARI value is larger, the clustering result is more consistent with the real category. While ARI value is negative, the clustering result is not similar to the real label. On the other hand, a positive value indicates that the clustering result is similar to the real label.

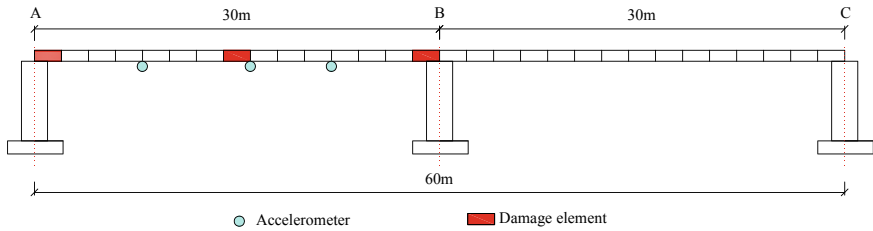
$$ARI = \frac{RI - E(RI)}{\max(RI) - E(RI)} \quad (5)$$

3 Damage State Classification of a Bridge

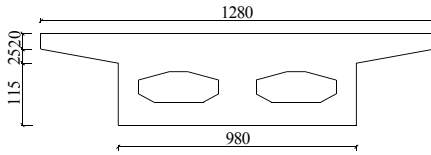
In order to verify the effectiveness of generative adversarial networks for the classification of structural damage states, a finite element model of a continuous beam bridge was established. Figure 2 shows the details of the bridge simulation and the excitation input. The span of the continuous beam is 60 m, and the cross-section adopts double boxes and single chambers which is shown in Fig. 2b. The cross-sectional area of the beam element is 7.756 m^2 , the moment of inertia of the section is 2.77 m^4 , and the elastic modulus is $3.45 \times 10^{10} \text{ N/m}^2$. In addition, the finite element model consists of 100 beam elements with 101 nodes, which is shown in Fig. 2a.

For simulating the bridge environment excitation, random white noise with mean value of 0 and variance of 1 m/s^2 is applied vertically on the structure as ground acceleration. The white noise excitation is shown in Fig. 2c. Generally, the environmental excitation was simulated by adding white noise excitation to the nodes, and the maximum acceleration of white noise is 0.01 g. The sampling time of structural dynamic response is 400 s, and the sampling frequency is 100 Hz. A total of 3 acceleration measuring points are arranged on the continuous beam, which are respectively arranged on node 13, node 25 and node 37, as shown in Fig. 2a.

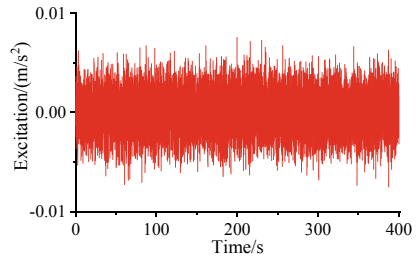
The damage of the structure will cause the change of its quality and stiffness, so the damage of beam element is simulated by reducing the elastic modulus. As shown in Table 2, three structural damage states at different positions are established, respectively denoted as State 2(S2), State 3(S3), and State 4(S4). The damage of the three structures is 30% of the elastic modulus of the beam element so that the elastic modulus is $2.415 \times 10^{10} \text{ N/m}^2$.



(a) Bridge damage location and acceleration sensor layout



(b) Cross section dimension of beam element



(c) The white noise excitation

Fig. 2 Bridge numerical experiment

Table 2 Description of the labels, damage element and degree in the numerical bridge dataset

Labels	State number	Damage element	Damage degree (%)	Young's modulus (N/m ²)
1	State 1 (S1)	–	–	3.45×10^{10}
2	State 2 (S2)	2	30	2.415×10^{10}
3	State 3 (S3)	25	30	2.415×10^{10}
4	State 4 (S4)	50	30	2.415×10^{10}

Based on this model, the vertical acceleration of nodes 13, 25, and 37 under environmental excitation are extracted for training. In the data preprocessing, the vertical acceleration signals are converted to the power spectrums through the Welch's PSD method [21]. Figure 3 shows the power spectrum curve of node 13 in the middle of the span.

From Fig. 3a, the structural power spectrum response of state 2 is basically the same as that of State 1, and the peak position does not change, basically located around 6, 12 and 25 Hz. Due to the influence of the unit at the mid-span position on the overall stiffness, the power spectra of State 3 and State 4 are quite different from the normal state (S1). Compared with State 1, the peak points of the power spectrum of State 4 are shifted to the left. However, the shift of the peak point of the power spectrum in State 3 is smaller but one additional peak appears. Three structural damage states exhibit different power spectrum features, which is beneficial for the neural network training.

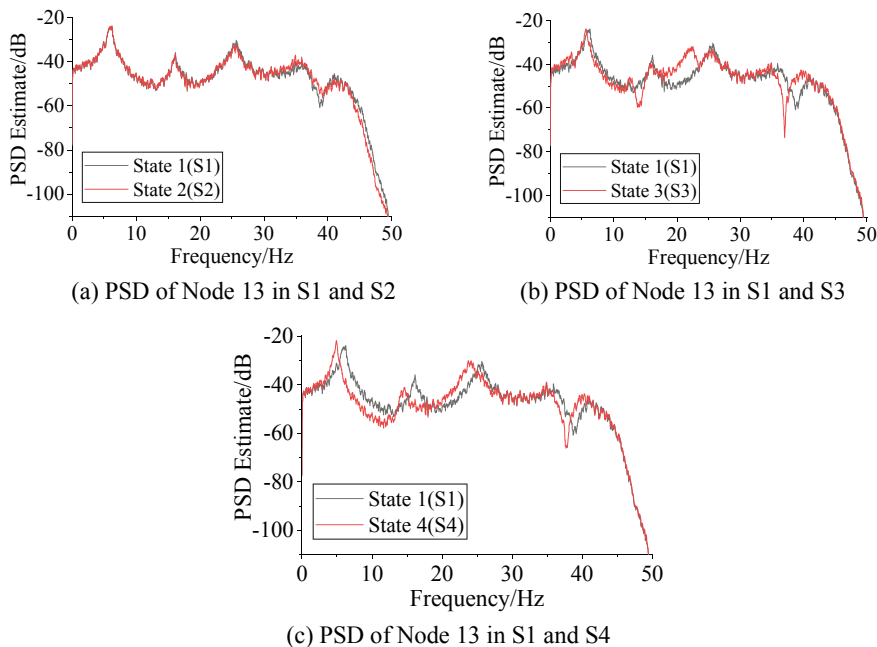


Fig. 3 The power spectral density of four structural states in the Node 13

In the model training, the acceleration signals obtained by the three measurement points are divided into 400 samples of each category with a total of 1200 samples. According to the ratio of 7:3 set, the samples are divided into a training set of 840 samples and a test set of 360 samples. When *ARI* value and *NMI* value are close to 1, the clustering result is more similar to the actual state.

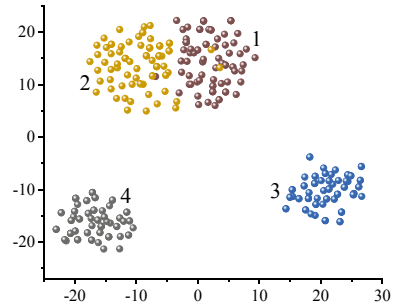
As shown in Table 3, the optimal number of clusters obtained by the spectral clustering algorithm [22] in Case-all is 3 categories, and the *ARI* and *NMI* values reach 0.782 and 0.885, respectively. It indicates that the GAN method has good robustness for the classification of structural damage states.

In order to further study the effect of generative adversarial networks on the classification of structural damage states, the learned features will be visualized by T-SNE [23]. The classification results under the C-all working condition are shown in Fig. 4. T-SNE is used to visualize the last layer of the discriminator output, while the high-order feature quantities of different states are projected into a two-dimensional

Table 3 Description of the fully-unsupervised tasks for test samples for each class in four structural states

Task	Data sets		Number of clusters	Adjusted rand index	Normalized mutual information
	Training set	Test set			
Case-all	All	All	3	0.782	0.885

Fig. 4 The clustering of test data from four structural states in case-all



map. Different colors in Fig. 4 represent high-level data of different structural states. The numbers 1, 2, 3, and 4 in the figure represent state 1, state 2, state 3, and state 4, respectively. The high-order feature quantities extracted by the unsupervised generative adversarial network can be effectively separated by T-SNE, and the four structural states can be clustered together. Since the power spectra of state 1 and state 2 have a high similarity, the cluster points of state 1 and state 2 tend to be identified as the same state type. This also indicates that the damage in the boundary has little effect on the dynamic responses.

4 Conclusion

In order to further obtain structural state information through data processing tools, this paper proposes an unsupervised state classification method based on generative adversarial networks for the different structural damage state of bridge. The structural response information of PSD spectra under multiple working conditions are used as the input of the generative confrontation network algorithm.

The model evaluation is performed on the training results through the normalization coefficient. The numerical acceleration data of two-span continuous girder bridge were used to illustrate the proposed method. The superiority of the anomaly detection method is verified based on the unsupervised generative adversarial network. At last, the two-dimensional visualization of the training results is performed by T-SNE, and a better clustering effect is obtained.

Acknowledgements This study is supported by the following projects: Shenzhen Technology and Innovation Commission (Grant No.: JSGG20201103093603016) and National Natural Science Foundation of China (52278298). The financial supports are greatly acknowledged.

References

1. Zhang FL, Gu DK, Li X et al (2022) Structural damage detection based on fundamental Bayesian two-stage model considering the modal parameters uncertainty. *Struct Health Monit* 2022:14759217221114262
2. Zhou YL, Maia NMM, Sampaio RPC et al (2017) Structural damage detection using transmissibility together with hierarchical clustering analysis and similarity measure. *Struct Health Monit* 16(6):711–731
3. Jun M, Xiao L, Jiangjiang X (2020) Numerical simulation of prefabricated prestressed bridge piers based on fiber beam element. In: 2020 International conference on intelligent transportation, big data and smart city (ICITBS). IEEE, 2020, pp 137–143
4. Al-Khateeb HT, Shenton HW III, Chajes MJ et al (2019) Structural health monitoring of a cable-stayed bridge using regularly conducted diagnostic load tests. *Front Built Environ* 5:41
5. Papatheou E, Manson G, Barthorpe RJ et al (2014) The use of pseudo-faults for damage location in SHM: an experimental investigation on a Piper Tomahawk aircraft wing. *J Sound Vib* 333(3):971–990
6. Nick W, Asamene K, Bullock G et al (2015) A study of machine learning techniques for detecting and classifying structural damage. *Int J Mach Learn Comput* 5(4):313
7. Li D, Wang Y, Wang J et al (2020) Recent advances in sensor fault diagnosis: a review. *Sens Actuators A* 309:111990
8. Ozer E, Feng MQ (2019) Structural reliability estimation with participatory sensing and mobile cyber-physical structural health monitoring systems. *Appl Sci* 9(14):2840
9. Sakiyama F I H, Lehmann F, Garrecht H.: A novel runtime algorithm for the real-time analysis and detection of unexpected changes in a real-size SHM network with quasi-distributed FBG sensors. *Sensors*, 21(8): 2871(2021).
10. Feng D, Feng MQ (2018) Computer vision for SHM of civil infrastructure: from dynamic response measurement to damage detection—a review. *Eng Struct* 156:105–117
11. Zhao R, Yan R, Chen Z et al (2019) Deep learning and its applications to machine health monitoring. *Mech Syst Signal Process* 115:213–237
12. Avendano-Valencia LD, Fassois SD (2017) Gaussian mixture random coefficient model based framework for SHM in structures with time—dependent dynamics under uncertainty. *Mech Syst Signal Process* 97:59–83
13. Zhang C, Mousavi AA, Masri SF et al (2022) Vibration feature extraction using signal processing techniques for structural health monitoring: a review. *Mech Syst Signal Process* 177:109175
14. Goodfellow I, Pouget-Abadie J, Mirza M et al (2020) Generative adversarial networks. *Commun ACM* 63(11):139–144
15. Yoon J, Jarrett D, Van der Schaar M (2019) Time-series generative adversarial networks. *Adv Neur Inf Process Syst* 32(2019)
16. Hong Y, Hwang U, Yoo J et al (2019) How generative adversarial networks and their variants work: an overview. *ACM Comput Surv (CSUR)* 52(1):1–43
17. Roth K, Lucchi A, Nowozin S et al (2017) Stabilizing training of generative adversarial networks through regularization. *Adv Neur Inf Process Syst* 30
18. Deng Z, Zhang H, Liang X et al (2017) Structured generative adversarial networks. *Adv Neur Inf Process Syst* 30
19. Belghazi MI, Baratin A, Rajeshwar S et al (2022) Mutual information neural estimation. *Int Conf Mach Learn PMLR* 2018:531–540
20. Wang X, Zhang C, Zhang Y et al (2022) IMGG: integrating multiple single-cell datasets through connected graphs and generative adversarial networks. *Int J Molecul Sci* 23(4):2082
21. Rahi PK, Mehra R (2014) Analysis of power spectrum estimation using welch method for various window techniques. *Int J Emerg Technol Eng* 2(6):106–109
22. Jia H, Ding S, Xu X et al (2014) The latest research progress on spectral clustering. *Neur Comput Appl* 24(7):1477–1486

23. Meyer BH, Pozo ATR, Zola WMN (2022) Global and local structure preserving GPU t-SNE methods for large-scale applications. *Expert Syst Appl* 201:116918